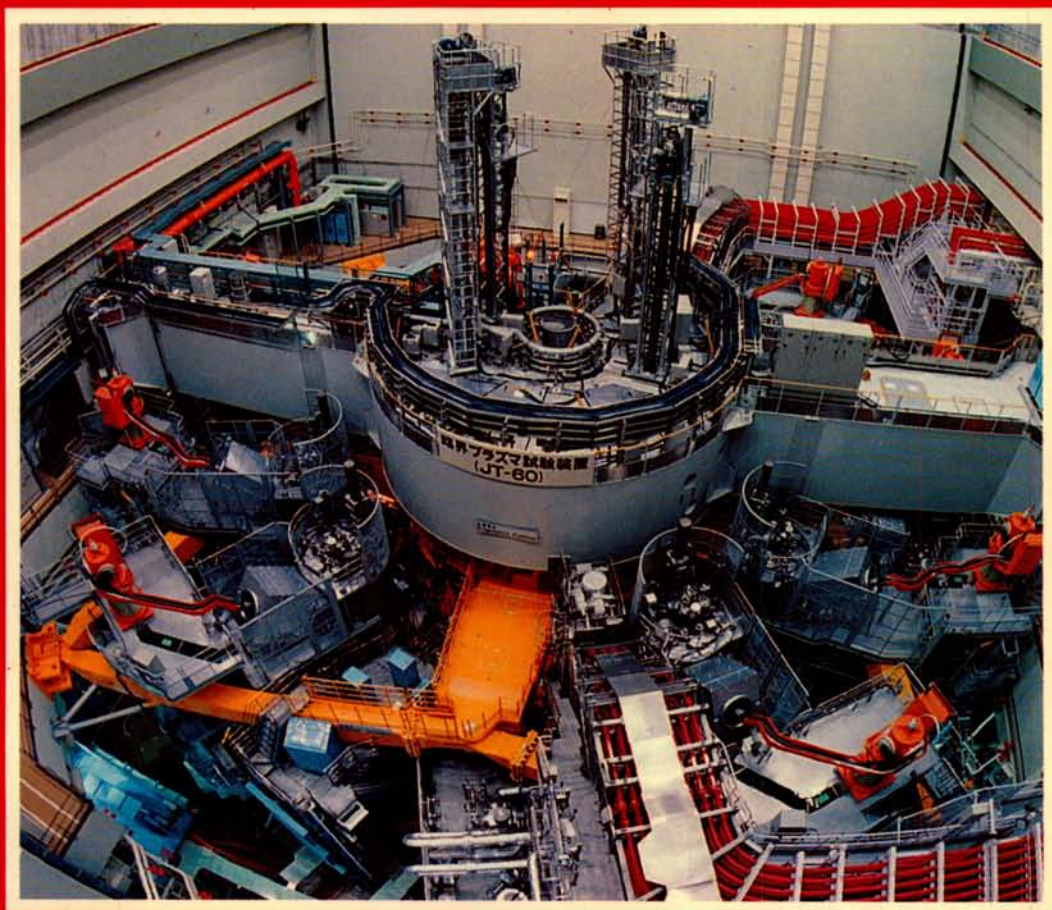


# Plasma Physics and Controlled Nuclear Fusion Research 1986

Vol. 2

ELEVENTH CONFERENCE PROCEEDINGS, KYOTO, 13-20 NOVEMBER 1986

Nuclear Fusion, Supplement 1987



INTERNATIONAL ATOMIC ENERGY AGENCY, VIENNA, 1987

The cover picture shows JT-60, one of the largest operational tokamaks.  
By courtesy of the Japan Atomic Energy Research Institute, Tokyo.

PLASMA PHYSICS  
AND CONTROLLED  
NUCLEAR FUSION RESEARCH  
1986

VOLUME 2

The following States are Members of the International Atomic Energy Agency:

AFGHANISTAN	GUATEMALA	PARAGUAY
ALBANIA	HAITI	PERU
ALGERIA	HOLY SEE	PHILIPPINES
ARGENTINA	HUNGARY	POLAND
AUSTRALIA	ICELAND	PORTUGAL
AUSTRIA	INDIA	QATAR
BANGLADESH	INDONESIA	ROMANIA
BELGIUM	IRAN, ISLAMIC REPUBLIC OF	SAUDI ARABIA
BOLIVIA	IRAQ	SENEGAL
BRAZIL	IRELAND	SIERRA LEONE
BULGARIA	ISRAEL	SINGAPORE
BURMA	ITALY	SOUTH AFRICA
BYELORUSSIAN SOVIET SOCIALIST REPUBLIC	JAMAICA	SPAIN
CAMEROON	JAPAN	SRI LANKA
CANADA	JORDAN	SUDAN
CHILE	KENYA	SWEDEN
CHINA	KOREA, REPUBLIC OF	SWITZERLAND
COLOMBIA	KUWAIT	SYRIAN ARAB REPUBLIC
COSTA RICA	LEBANON	THAILAND
COTE D'IVOIRE	LIBERIA	TUNESIA
CUBA	LIBYAN ARAB JAMAHIRIYA	TURKEY
CYPRUS	LIECHTENSTEIN	UGANDA
CZECHOSLOVAKIA	LUXEMBOURG	UKRAINIAN SOVIET SOCIALIST REPUBLIC
DEMOCRATIC KAMPUCHEA	MADAGASCAR	UNION OF SOVIET SOCIALIST REPUBLICS
DEMOCRATIC PEOPLE'S REPUBLIC OF KOREA	MALAYSIA	UNITED ARAB EMIRATES
DENMARK	MALI	UNITED KINGDOM OF GREAT BRITAIN AND NORTHERN IRELAND
DOMINICAN REPUBLIC	MAURITIUS	UNITED REPUBLIC OF TANZANIA
ECUADOR	MEXICO	UNITED STATES OF AMERICA
EGYPT	MONACO	URUGUAY
EL SALVADOR	MONGOLIA	VENEZUELA
ETHIOPIA	MOROCCO	VIET NAM
FINLAND	NAMIBIA	YUGOSLAVIA
FRANCE	NETHERLANDS	ZAIRE
GABON	NEW ZEALAND	ZAMBIA
GERMAN DEMOCRATIC REPUBLIC	NICARAGUA	ZIMBABWE
GERMANY, FEDERAL REPUBLIC OF	NIGER	
GHANA	NIGERIA	
GREECE	NORWAY	
	PAKISTAN	
	PANAMA	

The Agency's Statute was approved on 23 October 1956 by the Conference on the Statute of the IAEA held at United Nations Headquarters, New York; it entered into force on 29 July 1957. The Headquarters of the Agency are situated in Vienna. Its principal objective is "to accelerate and enlarge the contribution of atomic energy to peace, health and prosperity throughout the world".

© IAEA, 1987

Permission to reproduce or translate the information contained in this publication may be obtained by writing to the International Atomic Energy Agency, Wagramerstrasse 5, P.O.Box 100, A-1400 Vienna, Austria.

Printed by the IAEA in Austria  
July 1987

NUCLEAR FUSION, SUPPLEMENT 1987

PLASMA PHYSICS  
AND CONTROLLED  
NUCLEAR FUSION RESEARCH  
1986

PROCEEDINGS OF THE  
ELEVENTH INTERNATIONAL CONFERENCE ON PLASMA PHYSICS  
AND CONTROLLED NUCLEAR FUSION RESEARCH  
HELD BY THE  
INTERNATIONAL ATOMIC ENERGY AGENCY  
IN KYOTO, 13-20 NOVEMBER 1986

*In three volumes*

VOLUME 2

INTERNATIONAL ATOMIC ENERGY AGENCY  
VIENNA, 1987

**PLASMA PHYSICS AND CONTROLLED NUCLEAR FUSION RESEARCH 1986**  
**IAEA, VIENNA, 1987**  
**STI/PUB/723**  
**ISBN 92-0-130187-1**

## FOREWORD

The IAEA Conferences on Plasma Physics and Controlled Nuclear Fusion Research, organized biennially, are the largest and most important meetings in the field. They are a scientific forum not only for the presentation of the best results achieved in all laboratories performing fusion research but also for the co-ordination of international fusion efforts.

The Eleventh Conference, which was organized in co-operation with the Japanese Atomic Energy Research Institute, was attended by about 650 participants and observers representing 32 countries and two international organizations. About 200 papers were accepted for oral and poster presentations. The Conference opened with the traditional Artsimovich Memorial Lecture.

The Eleventh Conference became an important event for fusion scientists and engineers all over the world, for two special reasons. First, on the basis of the results achieved on several experimental devices, the plans for reaching plasma ignition within the next two years were presented. Second, the Conference not only marked 25 years of international co-operation under the auspices of the IAEA but also represented the starting point for a new international venture — an international thermonuclear experimental reactor.

These Proceedings, which include all the technical papers and five Conference summaries, are published in English as a supplement to the IAEA journal *Nuclear Fusion*.

The Agency promotes close international co-operation among plasma and fusion physicists and engineers of all countries by organizing these regular conferences on controlled nuclear fusion and by holding seminars, workshops and specialists meetings on appropriate topics. It is hoped that the present publication, as part of these activities, will contribute to the rapid demonstration of fusion power as one of the world's future energy resources.

## **EDITORIAL NOTE**

*The Proceedings have been edited by the editorial staff of the IAEA to the extent considered necessary for the reader's assistance. The views expressed remain, however, the responsibility of the named authors or participants. In addition, the views are not necessarily those of the governments of the nominating Member States or of the nominating organizations.*

*Although great care has been taken to maintain the accuracy of information contained in this publication, neither the IAEA nor its Member States assume any responsibility for consequences which may arise from its use.*

*The use of particular designations of countries or territories does not imply any judgement by the publisher, the IAEA, as to the legal status of such countries or territories, of their authorities and institutions or of the delimitation of their boundaries.*

*The mention of names of specific companies or products (whether or not indicated as registered) does not imply any intention to infringe proprietary rights, nor should it be construed as an endorsement or recommendation on the part of the IAEA.*

*The authors are responsible for having obtained the necessary permission for the IAEA to reproduce, translate or use material from sources already protected by copyrights.*

*Material prepared by authors who are in contractual relation with governments is copyrighted by the IAEA, as publisher, only to the extent permitted by the appropriate national regulations.*

## CONTENTS OF VOLUME 2

### MAGNETIC CONFINEMENT THEORY (Session E)

Sawtooth oscillations (IAEA-CN-47/E-I-1-1) .....	3
<i>J.A. Wesson, P. Kirby, M.F. Nave</i>	
Theory of sawtooth disruption (IAEA-CN-47/E-I-1-2) .....	11
<i>D. Biskamp, H. Welter</i>	
Sawteeth and ideal MHD (IAEA-CN-47/E-I-1-3) .....	17
<i>M.N. Bussac, K. Lerbinger, R. Pellat, M. Tagger</i>	
Discussion on Papers IAEA-CN-47/E-I-1-1 to E-I-1-3 .....	25
Second stability access in tokamak plasmas (IAEA-CN-47/E-I-2-1) .....	27
<i>K. Yamazaki, H. Naitou, T. Amano, Y. Hamada, K. Matsuoka, Y. Midzuno, Y. Nakayama, T. Sato, T. Tsunematsu, T. Tuda, S. Seki, M. Azumi, S. Tokuda, T. Ozeki, T. Nemoto, Y. Kishimoto, T. Takeda</i>	
Stable tokamak access to, and operation in, the second stability region (IAEA-CN-47/E-I-2-2) .....	37
<i>A.M.M. Todd, M. Phillips, M. Chance, J. Manickam, N. Pomphrey</i>	
Ellipsoidal shell tokamak (IAEA-CN-47/E-I-2-3) .....	45
<i>F.J. Helton, Mingsheng Chu, J.M. Greene, R.W. Harvey, J.K. Lee, T. Ohkawa, P.A. Politzer</i>	
MHD stability in low-aspect-ratio tokamaks (IAEA-CN-47/E-I-2-4) .....	53
<i>B.A. Carreras, L.A. Charlton, J.T. Hogan, J.A. Holmes, E.A. Lazarus, W.A. Cooper, T.C. Hender</i>	
Discussion on Papers IAEA-CN-47/E-I-2-1 to E-I-2-4 .....	63
Simulation studies of tokamak dynamics (IAEA-CN-47/E-I-3) .....	65
<i>M. Tanaka, T. Hayashi, K. Harafuji, Y. Nakayama, T. Sato</i>	
Stability conditions for helical MHD perturbations and disruptive instability in tokamaks (IAEA-CN-47/E-I-4-1) .....	75
<i>L.E. Zakharov</i>	
Bifurcation of plasma equilibrium in tokamaks (IAEA-CN-47/E-I-4-2) .....	89
<i>Yu.N. Dnestrovskij, D.P. Kostomarov, A.V. Pedorenko, A.M. Popov</i>	
Discussion on Papers IAEA-CN-47/E-I-4-1 and E-I-4-2 .....	99
Radiofrequency stabilization of ideal ballooning modes in a tokamak plasma (IAEA-CN-47/E-II-1-1) .....	101
<i>A. Sen, P.K. Kaw, A.K. Sundaram</i>	

Electromagnetic particle simulations of RF stabilization and ECRH of over-density plasmas (IAEA-CN-47/E-II-1-2) .....	109
<i>H. Abe, S. Nakajima, Y. Kadoya, H. Okada, R. Itatani, K. Sakai, S. Takeuchi, M. Matsumoto, R. Sugihara</i>	
Discussion on Papers IAEA-CN-47/E-II-1-1 and E-II-1-2 .....	117
Theory of resistive magnetohydrodynamic instabilities excited by energetic trapped particles in large-size tokamaks (IAEA-CN-47/E-II-2-1) .....	119
<i>H. Biglary, L. Chen, R.B. White</i>	
Alfvén wave phase mixing in a sheared magnetic field as a mechanism of ‘fishbone’ instability damping and oscillation energy pumping into the region of large $k_{\perp} \sim \omega_p/c$ (IAEA-CN-47/E-II-2-2) .....	127
<i>A.D. Beklemishev, O.P. Pogutse</i>	
Effects of energetic particles on tokamak stability (IAEA-CN-47/E-II-2-3) .	135
<i>J. Van Dam, M.N. Rosenbluth, H.L. Berk, N. Domínguez, G.Y. Fu, X. Llobet, D.W. Ross, D.P. Stotler, D.A. Spong, W.A. Cooper, D. Sigmar, D.E. Hastings, J.J. Ramos, H. Naito, T. Todoroki, S.T. Tsai, S.G. Guo, J.W. Shen</i>	
Discussion on Papers IAEA-CN-47/E-II-2-1 to E-II-2-3 .....	147
Nonlinear toroidal plasma dynamics by reduced fluid models (IAEA-CN-47/E-II-3-1) .....	149
<i>M. Kotschenreuther, A. Aydemir, R. Carrera, R.D. Hazeltine, J.D. Meiss, P.J. Morrison</i>	
Neoclassical MHD equations, instabilities and transport in tokamaks (IAEA-CN-47/E-II-3-2) .....	157
<i>J.D. Callen, W.X. Qu, K.D. Siebert, B.A. Carreras, K.C. Shaing, D.A. Spong</i>	
I. Plasma edge microinstability with up-down asymmetry.	
II. Theory of collisional tearing modes for arbitrary Larmor radii (IAEA-CN-47/E-III-1) .....	167
<i>A. Rogister, G. Hasselberg</i>	
Edge plasma oscillations in the H-mode: Effect or cause? (IAEA-CN-47/E-III-3) .....	177
<i>S.I. Krasheninnikov, A.S. Kukushkin, V.A. Pozharov</i>	
Magnetic islands and chaos induced by heat flow (IAEA-CN-47/E-III-4) ...	187
<i>P.H. Rebut, M. Brusati, M. Hugon, P. Lallia</i>	
Incomplete thermalization and enhanced transport in tokamak plasmas (IAEA-CN-47/E-III-5) .....	197
<i>S.-I. Itoh, K. Itoh</i>	
Effect of quasi-linear evolution of the minority ion distribution function on the wave dispersion and absorption and on the thermonuclear reaction rate (IAEA-CN-47/E-III-6) .....	205
<i>A.V. Longinov, S.S. Pavlov, K.N. Stepanov</i>	

Effect of x-point location on edge confinement in diverted tokamaks (IAEA-CN-47/E-III-24) .....	221
<i>T. Ohkawa, F.L. Hinton</i>	

## OPEN CONFINEMENT SYSTEMS (Session C)

TMX-U tandem mirror thermal barrier experiments (IAEA-CN-47/C-I-1) .....	231
<i>T.C. Simonen, S.L. Allen, D.E. Baldwin, J.D. Barter, L.V. Berzins, M.R. Carter, T.A. Casper, J.F. Clauser, F.H. Coensgen, D.L. Correll, W.F. Cummins, C.C. Damm, G. Dimonte, B.H. Failor, S. Falabella, J.H. Foote, T.K. Fowler, A.H. Futch, R.K. Goodman, D.P. Grubb, D. Hill, E.B. Hooper, R.S. Hornady, R.D. Horton, W.L. Hsu, B. Huff, A.L. Hunt, R.A. James, C.J. Lasnier, C.A. Leavitt, W.H. Meyer, J.M. Moller, A.W. Molvik, W.E. Nexsen, D.E. Perkins, W.L. Pickles, P.A. Pincosy, G.D. Porter, P. Poulsen, D.B. Ress, M. Shiho, E.H. Silver, B.W. Stallard, W.C. Turner, R.D. Wood, T.L. Yu</i>	
Discussion .....	241
Studies of potential formation and transport in the tandem mirror GAMMA 10 (IAEA-CN-47/C-I-2) .....	243
<i>T. Cho, M. Ichimura, M. Inutake, K. Ishii, A. Itakura, I. Katanuma, Y. Kiwamoto, A. Mase, S. Miyoshi, Y. Nakashima, T. Saito, K. Sawada, D. Tsubouchi, N. Yamaguchi, K. Yatsu</i>	
Discussion .....	250
Recent results from the Tara tandem mirror and the Constance-B mirror (IAEA-CN-47/C-I-3) .....	251
<i>R.S. Post, K. Brau, J. Casey, X. Chen, J. Coleman, H.R. Garner, M. Gerver, S. Golovato, D. Goodman, W. Guss, S. Hiroe, S. Hokin, S. Horne, J. Irby, J. Kesner, B. Lane, T. Moran, L. Pócs, E. Sevillano, D. Smatlak, D.K. Smith, J. Sullivan, R.P. Torti, X.Z. Yao</i>	
Discussion .....	262
Stabilization of MHD modes in an axisymmetric magnetic mirror by applied RF waves and initial results of Phaedrus-B (IAEA-CN-47/C-I-4-1) .....	263
<i>R.A. Breun, P. Brooker, D. Brouchous, J. Browning, G. Butz, J. Conrad, E. Dales, J. Ferron, R. Goulding, N. Hershkowitz, T. Intrator, C. Litwin, R. Majeski, S. Meassick, B. Nelson, L. Peranich, H. Persing, J. Radtke, D. Roberts, G. Severn, D. Sing, Enyao Wang, D.A. D'Ippolito, J.R. Myra, G.L. Francis</i>	

Axisymmetric mirror plasma produced, heated and stabilized by ICRF only (IAEA-CN-47/C-I-4-2) .....	273
<i>R. Itatani, H. Takeno, Y. Yasaka</i>	
Discussion on Papers IAEA-CN-47/C-I-4-1 and C-I-4-2 .....	281
A tandem mirror modelling code (IAEA-CN-47/C-II-1) .....	283
<i>W.M. Nevins, B.M. Boghosian, R.H. Cohen, W.F. Cummins, P.F. Dubois, A. Friedman, L.L. LoDestro, Y. Matsuda, L.D. Pearlstein, G.D. Porter, M.E. Rensink, T.D. Rognlén, G.R. Smith, J.J. Stewart, M. Phillips</i>	
Drift pumping of tandem mirror thermal barriers (IAEA-CN-47/C-II-2) ....	293
<i>D.E. Baldwin, J.A. Byers, Y.J. Chen, T.B. Kaiser</i>	
Stabilization of flute instability in axially symmetric mirror machines (IAEA-CN-47/C-II-3) .....	305
<i>I.A. Kotel'nikov, G.V. Roslyakov, D.D. Ryutov, G.V. Stupakov</i>	
Progress in plasma heating with powerful electron beams in open systems (IAEA-CN-47/C-II-4) .....	323
<i>A.V. Arzhannikov, V.T. Astrelin, A.P. Avrorov, B.N. Brejzman, A.V. Burdakov, V.S. Burmasov, V.V. Chikunov, I.V. Kandaurov, V.A. Kapitonov, A.D. Khil'chenko, B.A. Knyazev, V.S. Kojdan, V.V. Konyukhov, Eh.P. Kruglyakov, S.V. Lebedev, K.I. Mekler, O.I. Meshkov, V.V. Postupaev, D.D. Ryutov, A.L. Sanin, M.A. Shcheglov, S.L. Sinitskij, S.G. Voropaev, L.N. Vyacheslavov</i>	
Enhancement of radial transport by collective processes (IAEA-CN-47/C-II-5) .....	337
<i>D.L. Eggleston, J.D. Crawford, T.M. O'Neil, J.H. Malmberg</i>	
Radiofrequency plugging and tandem mirror experiments in a cusp-anchored mirror device (IAEA-CN-47/C-II-6) .....	343
<i>T. Sato, R. Kumazawa, S. Okamura, K. Adati, T. Aoki, H. Fujita, S. Hidekuma, T. Kawamoto, H. Masumoto, K. Nishimura, T. Hatori, K. Takayama, H.R. Garner, H.D. Price, A.M. Howald, B.J. Leikind, H. Ikezi, P.B. Parks, P. Andrews</i>	

#### ALTERNATIVE AND SUPPORTING SYSTEMS (Session D)

Studies on currentless Heliotron E plasma (IAEA-CN-47/D-I-1) .....	355
<i>K. Uo, A. Iiyoshi, T. Obiki, S. Morimoto, O. Motojima, M. Sato, S. Sudo, F. Sano, T. Mutoh, K. Akaishi, M. Nakasuga, K. Kondo, K. Hanatani, H. Zushi, S. Besshou, H. Kaneko, T. Mizuuchi, H. Okada, Y. Takeiri, N. Noda, I. Ohtake, Y. Ijiri, M. Iima, T. Kawabata, T. Senju, K. Yaguchi, T. Baba, S. Kobayashi, R. Takahashi, M. Murakami, H.C. Howe, D.L. Hillis, P.K. Mioduszewski, G.H. Neilson, J. Rice, J. Terry, E. Marmor,</i>	

<i>T. Yamashina, T. Hino, H. Minagawa, T. Oda, M. Hamamoto, T. Ohgo, Y. Sakamoto, H. Amemiya, K. Okazaki, H. Oyama, S. Kato, A. Amemiya, H. Sugai, S. Urano, K. Uchino, T. Koga, K. Muraoka, M. Akazaki, M. Maeda, S. Morita</i>	
Discussion .....	368
Plasma confinement in the Wendelstein VII-A stellarator (IAEA-CN-47/D-I-2) .....	369
<i>H. Wobig, H. Maassberg, H. Renner, W VII-A Team, ECRH Group, NI Group</i>	
Discussion .....	381
Physics studies for advanced stellarators (IAEA-CN-47/D-I-3) .....	383
<i>W. Dommaschk, F. Herrnegger, W. Lotz, P. Merkel, J. Nührenberg, A. Schlüter, U. Schwenn, R. Zille</i>	
Discussion .....	390
Transport theory in stellarators (IAEA-CN-47/D-I-4) .....	391
<i>K.C. Shaing, S.P. Hirshman, C.O. Beasley, Jr., E.C. Crume, Jr., W.I. Van Rij</i>	
Results from HBTX with improved confinement (IAEA-CN-47/D-II-1) .....	399
<i>B. Alper, V. Antoni, M.K. Bevir, H.A.B. Bodin, C.A. Bunting, P.G. Carolan, J. Cunnane, D.E. Evans, A.R. Field, S.J. Gee, C.G. Gimblett, R. Hayden, T.R. Jarboe, P. Kirby, A. Manley, A.A. Newton, P.G. Noonan, A. Patel, R.S. Pease, M.G. Rusbridge, K.P. Schneider, D.P. Storey, H.Y.W. Tsui, S. Whitfield, P.D. Wilcock</i>	
Discussion .....	410
Experimental and theoretical studies of the STP-3(M) reversed field pinch in the high current density regime (IAEA-CN-47/D-II-2) .....	413
<i>K. Sato, T. Amano, Z.X. Chen, H. Arimoto, S. Yamada, A. Nagata, K. Yokoyama, Y. Kamada, A. Matsuoka, S. Masamune, H. Shindo, K. Saito, H. Murata, H. Oshiyama, S. Shiina, T. Tamaru</i>	
Discussion .....	422
Reversed field pinch experiments in ZT-40M and ZT-P (IAEA-CN-47/D-II-3) .....	423
<i>K.F. Schoenberg, G.A. Wurden, P.G. Weber, J.C. Ingraham, C.P. Munson, D.A. Baker, C.J. Buchenauer, L.C. Burkhardt, T.E. Cayton, J.N. DiMarco, J.N. Downing, R.M. Erickson, P.R. Forman, A. Haberstich, R.B. Howell, F.C. Jahoda, R.S. Massey, G. Miller, R.W. Moses, Jr., R.A. Nebel, J.A. Phillips, M.M. Pickrell, A.E. Schofield, R.G. Watt, D.M. Weldon, K.A. Werley</i>	
Experimental studies of reversed field pinch in REPUTE-1 and ultra-low-q discharge (IAEA-CN-47/D-II-4) .....	433
<i>N. Asakura, A. Fujisawa, T. Fujita, Y. Fukuda, H. Hattori, N. Inoue, S. Ishida, K. Itami, Y. Iwata, H. Ji, Y. Kamada, K. Kusano, S. Matsuzuka, K. Miyamoto, J. Morikawa, C.P. Munson, Y. Murakami,</i>	

<i>Y. Nagayama, H. Nihei, S. Onodera, M.T. Saito, T. Sato, S. Shinohara, H. Toyama, Y. Ueda, M. Utumi, H. Yamada, K. Yamagishi, Z. Yoshida</i>	
Discussion .....	440
Heating and confinement studies in reversed field pinches (IAEA-CN-47/D-II-5) .....	441
<i>V. Antoni, A. Buffa, L. Carraro, S. Costa, P. De Simone, G. Flor, F. Flora, L. Gabellieri, M. Giubbilei, L. Giudicotti, P. Innocente, K. Jain, P. Martin, S. Martini, D. Merlin, S. Ortolani, R. Paccagnella, M.E. Puiatti, B. Sass, P. Scarin, H. Sorensen, M. Valisa, K. Weisberg, S. Zago, E. Zilli</i>	
Discussion .....	450
Results from the reversed field pinch experiment on TPE-1RM15 with a programmed vertical field (IAEA-CN-47/D-II-6) .....	453
<i>T. Shimada, Y. Hirano, Y. Yagi, A.A. Newton, K. Ogawa</i>	
Discussion .....	461
Plasma heating in stellarator/torsatrons and tokamaks by ion cyclotron waves (IAEA-CN-47/D-III-1) .....	463
<i>E.F. Jaeger, D.B. Batchelor, K. Imre, H. Weitzner</i>	
Discussion .....	472
ICRF heating of currentless plasma in Heliotron E (IAEA-CN-47/D-III-2) .....	473
<i>T. Mutoh, O. Motojima, M. Sato, H. Okada, H. Zushi, K. Kondo, N. Noda, H. Kaneko, T. Mizuuchi, S. Besshou, F. Sano, S. Sudo, Y. Takeiri, K. Akaishi, T. Kawabata, Y. Ijiri, K. Itoh, S. Morimoto, A. Iiyoshi, K. Uo</i>	
Discussion .....	479
I. Electron cyclotron resonance plasma heating by ordinary waves in the L-2 stellarator.	
II. Fast wave eigenmodes in the L-2 stellarator during ICR plasma heating (IAEA-CN-47/D-III-3) .....	481
<i>I. E.D. Andryukhina, D.K. Akulina, G.M. Batanov, V.A. Batyuk, M.S. Berezhetskij, M.A. Blokh, G.S. Voronov, S.E. Grebenshchikov, S.I. Dolgaev, N.P. Donskaya, K.S. Dyabilin, L.M. Kovrizhnykh, L.V. Kolik, N.F. Larionova, K.M. Likin, A.I. Meshcheryakov, P.E. Moroz, S.N. Popov, A.E. Petrov, V.I. Roshchin, A.V. Sapozhnikov, K.A. Sarksyian, N.N. Skvortsova, I.S. Sbitnikova, A.D. Smirnova, V.N. Sukhodol'skij, M.F. Ternovskaya, O.I. Fedyanin, S.I. Fedorenko, Yu.V. Kholnov, M.G. Shats, I.S. Shpigel'</i>	
<i>II. V.A. Batyuk, S.E. Grebenshchikov, A.I. Meshcheryakov, P.E. Moroz, I.S. Sbitnikova, I.S. Shpigel'</i>	
Discussion .....	487

Plasma potential and confinement in the Nagoya Bumpy Torus (NBT-1M) (IAEA-CN-47/D-III-4) .....	489
<i>H. Ikegami, M. Hosokawa, H. Iguchi, T. Shoji, T. Kamimura,</i>	
<i>H. Sanuki, K. Takasugi, F. Tsuboi, T. Takeuchi, A. Komori,</i>	
<i>K. Kadota, J. Fujita, C. Honda, M. Yokoo, M. Maeda, K. Muraoka,</i>	
<i>T. Yuyama, T. Michishita, H. Kubo, M. Fujiwara</i>	
Discussion .....	495
Effects on equilibrium and stability of high beta RF heated plasmas in the URAGAN-3 torsatron (IAEA-CN-47/D-III-5) .....	497
<i>V.L. Berezhnyj, N.T. Besedin, M.P. Vasil'ev, V.S. Vojtsenya,</i>	
<i>E.D. Volkov, Ya.F. Volkov, S.P. Gubarev, Yu.V. Gutarev, A.G. Dikij,</i>	
<i>V.M. Zaikind, G.V. Zelenin, V.K. Konovalov, V.I. Kononenko,</i>	
<i>V.D. Kotsubanov, B.V. Kravchin, A.E. Kulaga, Yu.K. Kuznetsov,</i>	
<i>G.G. Lesniyakov, A.P. Litvinov, Yu.K. Mironov, N.I. Nazarov,</i>	
<i>O.S. Pavlichenko, V.K. Pashnev, N.F. Perepelkin, V.V. Plyusnin,</i>	
<i>G.N. Polakova, N.P. Ponomarenko, T.Yu. Ranyuk, L.N. Remez,</i>	
<i>K.S. Rubtsov, S.I. Solodovchenko, A.I. Skibenko, A.S. Slavniy,</i>	
<i>I.S. Sushko, V.S. Taran, V.T. Tolok, T.O. Toryak, I.P. Fomin,</i>	
<i>A.N. Shapoval, O.M. Shvets, A.F. Shtan'</i>	
Experimental and theoretical studies of toroidal heliacs (IAEA-CN-47/D-III-6) .....	511
<i>B.D. Blackwell, R.L. Dewar, H.J. Gardner, S.M. Hamberger,</i>	
<i>L.E. Sharp, X.H. Shi, C.F. Vance, D.F. Zhou</i>	
Discussion .....	518
Helicity conservation and energy confinement in CTX spheromaks (IAEA-CN-47/D-IV-1-1) .....	519
<i>B.L. Wright, C.W. Barnes, J.C. Fernandez, I. Henins, H.W. Hoida,</i>	
<i>T.R. Jarboe, S.O. Knox, G.J. Marklin, R.M. Mayo, D.A. Platts</i>	
Confinement experiments and simulation on the CTCC-I spheromak (IAEA-CN-47/D-IV-1-2) .....	529
<i>N. Satomi, S. Goto, Y. Honda, Y. Kato, M. Nagata, M. Nishikawa,</i>	
<i>A. Ozaki, T. Takaishi, T. Uyama, K. Watanabe, T. Sato, T. Hayashi</i>	
Field reversed configuration transport: Theory and measurements of flux, energy, and particle lifetimes (IAEA-CN-47/D-IV-2-1) .....	541
<i>A.L. Hoffman, J.T. Slough, L.C. Steinhauer, N.A. Krall, S. Hamasaki</i>	
Slow formation and stabilization of FRC plasmas (IAEA-CN-47/D-IV-2-2) .....	551
<i>S. Okada, Y. Ito, M. Kako, R.E. Chrien, S. Ohi, S. Goto,</i>	
<i>T. Ishimura, H. Itô, T. Takahashi, M. Ohara, S. Shimamura,</i>	
<i>M. Machida, Y. Nogi</i>	
Discussion on Papers IAEA-CN-47/D-IV-2-1 and D-IV-2-2 .....	561

High beta plasma confinement with near-neoclassical transport in TPE-2 (IAEA-CN-47/D-IV-3) .....	563
<i>K. Hayase, I. Hirota, H. Kiyama, S. Kiyama, Y. Maejima, Y. Sato, S. Takeda, E. Yahagi, M. Kito, K. Koyama</i>	
Z-pinch experiments and theory (IAEA-CN-47/D-IV-4) .....	573
<i>M.G. Haines, A.E. Dangor, A. Folkierski, P. Baldock, C.D. Challis, P. Choi, M. Coppins, C. Deeney, M.B. Favre-Dominguez, E. Figura, J.D. Sethian</i>	
Discussion .....	582
Investigation of plasma dynamics and emission in dense plasma focus (IAEA-CN-47/D-IV-5-1) .....	583
<i>K. Hirano, T. Yamamoto, K. Shimoda, Y. Okabe, K. Wakabayashi, M. Yokoyama, Y. Yamamoto, Y. Yamada, Y. Kitagawa, M. Yamanaka</i>	
Investigation of collapse, pinch dynamics and fast particle emission in a plasma focus discharge (IAEA-CN-47/D-IV-5-2) .....	593
<i>S. Czekaj, S. Denus, A. Kasperczuk, R. Miklaszewski, M. Paduch, T. Pisarczyk, S. Sledziński, A. Szydkowski, Z. Wereszczyński</i>	
Discussion on Papers IAEA-CN-47/D-IV-5-1 and D-IV-5-2 .....	601
Impurity behaviour in the Wendelstein VII-A stellarator (IAEA-CN-47/D-V-1) .....	603
<i>H. Ringler, F. Sardei, A. Weller, W VII-A Team, ECRH Group, NI Group</i>	
Stable access to second stability regime in large-aspect-ratio torsatron/heliotron configurations (IAEA-CN-47/D-V-2) .....	615
<i>B.A. Carreras, L. Garcia, L.A. Charlton, J.A. Holmes, V.E. Lynch, P.H. Diamond</i>	
Three-dimensional MHD studies of ideal and resistive interchange modes in heliotron configurations (IAEA-CN-47/D-V-3) .....	625
<i>M. Wakatani, K. Ichiguchi, H. Sugama, K. Itoh, A. Hasegawa, J. Todoroki, H. Naitou</i>	
Self-consistent radial electric field evaluations for the TJ-II Helic (IAEA-CN-47/D-V-4) .....	633
<i>J. Guasp</i>	
Evolution, relaxation and transport in spheromaks and reversed field pinches (IAEA-CN-47/D-V-5) .....	639
<i>R.Y. Dagazian, J.P. Dahlburg, G. Doolen, G.J. Marklin, A.A. Mirin, J.P. Mondt, D. Montgomery, A.G. Sgro, L. Turner, J. Weiland</i>	
Experiments with a fully toroidal Extrap Z-pinch (IAEA-CN-47/D-V-6) ....	647
<i>J.R. Drake, J.E. Eninger, B.P. Lehnert</i>	
Characteristics of reversed field pinch plasmas with a resistive shell (IAEA-CN-47/D-V-7) .....	655
<i>T. Tamano, W.D. Bard, T. Carlstrom, C. Chu, R.R. Goforth, Y. Kondoh, R.J. La Haye, P. Lee, E.J. Nilles, M.T. Saito, M.J. Schaffer, P.L. Taylor</i>	

Energy confinement and nonlinear tearing mode dynamics in a high current reversed field pinch (IAEA-CN-47/D-V-8) .....	663
<i>Z.G. An, P.H. Diamond, T.S. Hahm, G.S. Lee, B.D. Scott, B.A. Carreras, L. Garcia, J.A. Holmes, V.E. Lynch</i>	
Theoretical and experimental studies of field reversed configurations (IAEA-CN-47/D-V-9) .....	673
<i>D.C. Barnes, W.T. Armstrong, E.J. Caramana, R.E. Chrien, W.N. Hugrass, H.R. Lewis, R.K. Linford, K.M. Ling, K.F. McKenna, D.J. Rej, J.L. Schwarzmeier, R.E. Siemon, M.M. Tuszewski, K.A. Werley, D.S. Harned, S. Okada, C.E. Seyler, D.E. Shumaker, H. Tuzcek, G. Vlases, R.D. Brooks, Z.A. Pietrzyk, K.D. Hahn, D. Lotz, R. Ramen, J. Wight</i>	
Experiment on relativistic electron beam ring core spherator (IAEA-CN-47/D-V-10) .....	687
<i>K. Narihara, T. Tomita, S. Kubo, M. Hasegawa, M. Matsui, T. Tsuzuki, A. Mohri</i>	
Three-dimensional MHD studies of the magnetic energy relaxation processes (IAEA-CN-47/D-V-11) .....	693
<i>T. Sato, K. Kusano, R. Horiuchi</i>	
Modelling and transport simulations of oscillating field current drive (F- $\theta$ pumping) in a reversed field pinch (IAEA-CN-47/D-V-12) .....	701
<i>R.A. Nebel, K.A. Werley, R.A. Scardovelli, G.H. Miley, D.S. Harned, H.R. Strauss, D.D. Schnack, Z. Mikić</i>	
Relaxation phenomena in reversed field pinches and tokamaks (IAEA-CN-47/D-V-13) .....	711
<i>A. Bhattacharjee, C.K. Chu, Y.-C. Kwok, E. Hameiri, H.R. Strauss, A.H. Boozer</i>	
Physics considerations on a fusion plasma in a field reversed configuration (IAEA-CN-47/D-V-14) .....	719
<i>H. Momota, M. Okamoto, Y. Nomura, K. Yoshikawa, M. Ohnishi, A. Ishida, K. Sato, S. Ohi, H.L. Berk, T. Tajima</i>	
Preliminary experiments in a compact toroid formed by four C-guns (IAEA-CN-47/D-V-15) .....	731
<i>S. Sinman, A. Sinman</i>	
Linear, high beta, $\ell = 1$ and heliac stellarator experiments (IAEA-CN-47/D-V-22) .....	739
<i>F.L. Ribe, M.E. Koepke, E.R. Hedin, C.M. Greenfield</i>	
Chairmen of Sessions and Secretariat of the Conference .....	747



**Session E**

**MAGNETIC CONFINEMENT THEORY**

## Chairmen of Sessions

**Session E-I**                      **D.B. NELSON**                      **USA**

*Papers E-I-1-1, E-I-1-2 and E-I-1-3  
were presented by J.A. Wesson as Rapporteur*

*Papers E-I-2-1 to E-I-2-4  
were presented by T. Amano as Rapporteur*

*Papers E-I-4-1 and E-I-4-2  
were presented by B.B. Kadomtsev as Rapporteur*

**Session E-II**                      **R.R. PARKER**                      **USA**

*Papers E-II-1-1 and E-II-1-2  
were presented by A. Sen as Rapporteur*

*Papers E-II-2-1, E-II-2-2 and E-II-2-3  
were presented by L. Chen as Rapporteur*

*Papers E-II-3-1 and E-II-3-2  
were presented by M. Kotschenreuther as Rapporteur*

**Session E-III (Posters)**

# SAWTOOTH OSCILLATIONS

J.A. WESSON, P. KIRBY<sup>1</sup>, M.F. NAVE  
 JET Joint Undertaking,  
 Abingdon, Oxfordshire,  
 United Kingdom

## Abstract

### SAWTOOTH OSCILLATIONS.

The recent observations of sawtooth oscillations having a very fast collapse phase call for a re-examination of the theoretical description of sawtooth behaviour. One possibility is that the instability involved is an ideal  $m = 1$  "quasi-interchange" mode. A calculation of the stability of this mode shows that flattening of the  $q$  profile reduces the critical  $\beta_p$  required for instability. Thus, contrary to previous expectations, the ideal mode can be unstable even at the low values of  $\beta_p$  observed experimentally. Non-linear simulations show the predicted cellular convection. The distinction between the behaviour of the quasi-interchange mode and a tearing mode is described and a comparison is made with experimental results from JET. Finally, attention is drawn to a fundamental difficulty in explaining the rapid collapse in precursorless sawtooth oscillations.

## 1. INTRODUCTION

With the advent of larger tokamaks it was found that the sawtooth collapse time did not increase as expected from the Kadomtsev scaling [1] and attention was drawn to this discrepancy by Campbell et al. [2]. An explanation of the observed behaviour was proposed by Wesson [3]. This predicted an mhd timescale for the collapse, in reasonable agreement with the experimental results. The model follows from a simple calculation showing that if the  $q$  profile is flat after the sawtooth collapse, then it will remain quite flat during the resistive diffusion of the ramp phase. Configurations of this type were shown to be unstable to an ideal  $m=1$  mode.

A further prediction of this model was that the form of the instability would not be a "rigid shift" of the plasma core, as predicted by previous models, but would be a cellular convective motion. This would then lead to the formation of a cold plasma bubble at the centre of the plasma. The magnetic field would not reconnect on this fast timescale, but reconnection would occur on a longer, resistive timescale after the collapse.

These predictions were confirmed by subsequent experimental studies on JET. Tomographic analysis of the soft X-ray emission from JET [4] indicated a broad convective motion and the formation of a plasma bubble. The existence of decaying "post-cursor"

---

<sup>1</sup> Euratom-UKAEA Fusion Association, Culham Laboratory, Abingdon, Oxfordshire, UK.

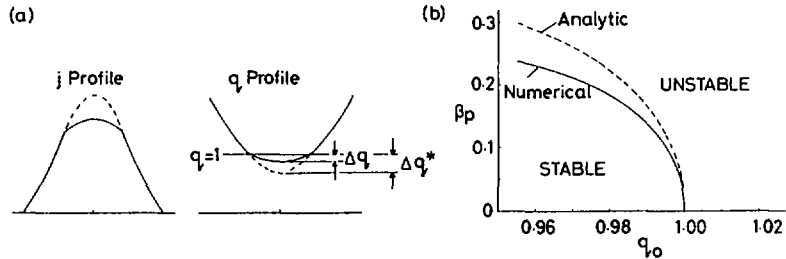


FIG. 1. (a) Form of assumed  $j$  and  $q$  profiles. (b) Stability diagram for critical  $\beta_p$  against  $q_0$ .

oscillations after the collapse seems to conform to the prediction of delayed reconnection.

In this paper we report further work on this model in the following areas:

- i) Mhd stability and its implications for the plasma motion.
- ii) Non-linear simulations of the sawtooth collapse
- iii) Distinction between ideal mode and tearing instability.

Finally, attention is drawn to a fundamental problem in understanding the trigger for the sawtooth collapse.

## 2. STABILITY OF THE IDEAL $m=1$ MODE

In reference [3], numerical calculations were presented, showing the crucial dependence of the stability of the ideal  $m=1$  mode on the flatness of the  $q$  profile within the  $q=1$  surface. These results can also be obtained analytically. In the large aspect ratio expansion the potential energy  $\delta W$  given by Bussac et al. [5] may be written in the form

$$\delta W = a + b\beta_p + c\beta_p^2 \quad \text{where} \quad \beta_p = \frac{2\mu_0 R^2}{r_1^4 B_\phi^2} r_1 \int_0^{r_1} (-dp/dr) r^2 dr \quad (1)$$

$r_1$  is the radius of the  $q=1$  surface and the coefficients are determined from the solution of a differential equation which gives the toroidal coupling to the  $m=2$  component. Taking the model illustrated in Fig.1a, for which

$$j = j_c \left(1 - \frac{r^2}{a^2}\right)^{\nu}, \quad r > r_1; \quad j = \frac{2B_\phi}{Rq_0} \left(1 - 2(1-q_0)\frac{r^2}{r_1^2}\right), \quad r < r_1$$

where  $j_c = (2B_\phi/R)(2-1/q_0)(1-(r_1^2/a^2))^{\nu}$ , the coefficients of eq.(1) were calculated and the criterion for instability was found to be

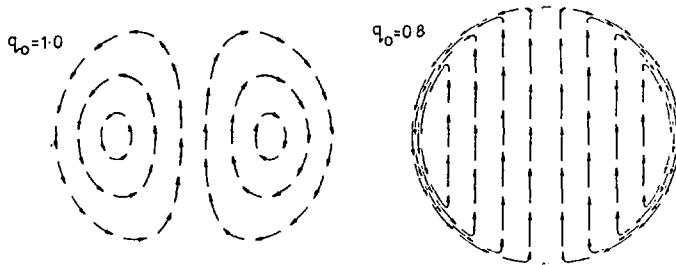


FIG. 2. Flow pattern of quasi-interchange ( $q_0 = 1.0$ ) and "rigid shift" ( $q_0 = 0.8$ ).

$$\beta_p > \frac{13}{144} \frac{3\Delta q}{\Delta q + 2\Delta q^*} \frac{1}{2}, \quad q_0 < 1; \quad \beta_p > 0, \quad q_0 > 1 \quad (2)$$

where  $\Delta q = 1 - q_0$  and  $\Delta q^* (= \nu r_1^2 / 2a^2)$  is the  $\Delta q$  which would have occurred without flattening.

It should be noted that in both cases there is a  $q=1$  surface at  $r=r_1$ . The stability boundary for criterion (2) is shown in Fig.1b for  $\nu=1$  and  $r_1/a=0.3$ , together with the result of a numerical calculation. It is seen that the toroidal stabilising effect is much reduced for a flattened  $q$  profile and furthermore that if  $q_0 > 1$ , while retaining the  $q=1$  surface, the  $m=1$  mode is unstable for arbitrarily small  $\beta_p$ .

It was pointed out in reference [3] that for flattened  $q$  profiles with  $1 - q_0$  sufficiently small, the calculation becomes invalid. The principal and important consequence of the changed ordering of  $1 - q$  is that the plasma flow associated with the instability is completely changed. The "rigid" displacement of the conventional case [6] is replaced by a convective flow in the reduced shear case. The two types of motion are illustrated in Fig.2. The physical basis of this distinction is that, for the more strongly sheared, unflattened  $q$ -profile the energy of the instability is inadequate to bend the magnetic field, whereas for small shear the magnetic field is carried with the fluid, preserving the flux surfaces but playing a negligible role in the mechanics. This type of behaviour could be called quasi-interchange.

### 3. SIMULATIONS OF SAWTOOTH COLLAPSE

A full simulation of the sawtooth collapse would require a toroidal calculation. However, the essential dynamical features of the present theory should be seen in the simpler case of cylindrical geometry. To this end, calculations have been carried out using a cylindrical, non-linear, incompressible,

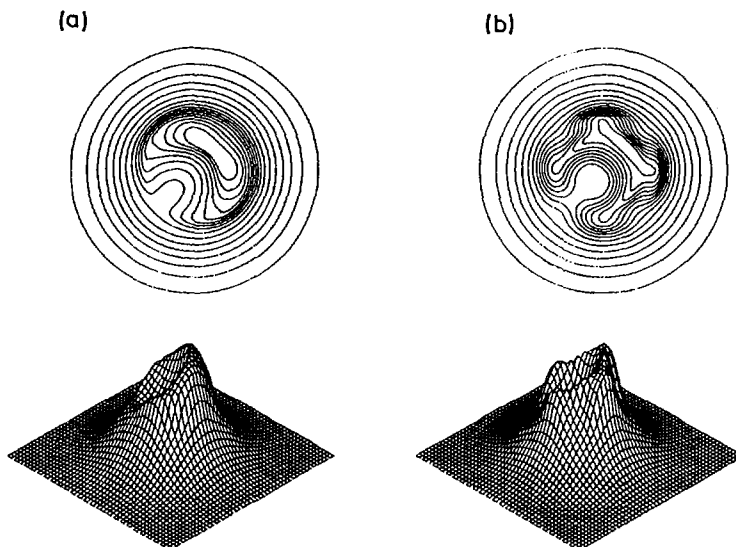


FIG. 3. Development of flux surfaces for (a)  $q_0 = 1.04$  and (b)  $q_0 = 1.005$ , together with associated soft X-ray emission.

mhd code with various  $q$  profiles. The code has finite resistivity, but for the simulations reported here the unstable modes are ideal and the resistivity has no significant effect.

To demonstrate the effect of a flattened  $q$  profile, simulations have been made using constant  $B_z$  and a model current profile given by

$$j_z = j_{z_0} = \text{const}, \quad r \leq r'; \quad j_z = j_{z_0} \frac{(c-r^2/a^2)^2}{(c-r'^2/a^2)^2}, \quad r > r'$$

This means that  $q$  is constant for  $r < r'$ , and then rises monotonically for  $r > r'$ . The runs described here had  $S=10^5$ ,  $r'/a=0.3$  and  $c=1.26$ . In these calculations the higher modes  $m/n=2/2, 3/3\dots$  are unstable, with growth rates comparable to that of  $m=1$ .

For a relatively large  $q_0$  the plasma is displaced a small amount by the  $m=1$  instability, as shown in Fig.3a for  $q_0=1.04$ . A small bubble forms but does not penetrate fully because of the magnetic shear. This may represent the behaviour of a partial sawtooth collapse.

As  $q_0$  is reduced, the instability is more able to sweep the fluid into a full cellular pattern. Figure 3b gives the result for  $q_0=1.005$ , showing deeper penetration of the bubble.

The corresponding time development of the X-ray emission can be calculated for a given initial profile on the assumption that (given the rapid collapse) the emission is convected with the plasma. The calculated profiles are shown in Fig.3 for the case

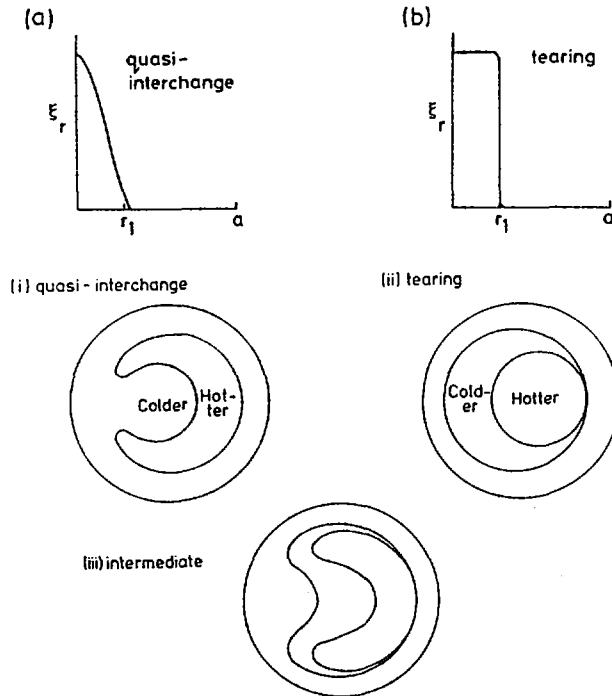


FIG. 4. Eigenfunctions  $\xi_r(r)$  for (a) quasi-interchange mode and (b) tearing mode, together with diagrams showing the contrasting non-linear topological development for these cases.

of an initially Gaussian emission profile. The general form of the development is very similar to that observed in the JET experiment [4]. A further comparison of theory and experiment is made in the following section.

#### 4. DISTINCTION BETWEEN QUASI-INTERCHANGE AND RESISTIVE INSTABILITY

The characteristic form of the radial displacement eigenfunctions for an ideal quasi-interchange mode and a tearing mode are shown in Figs. 4a and 4b. The general characteristics of these flows persist into the non-linear regime. The ideal mode leads to a convective flow on the scale of the radius of the  $q=1$  surface. The tearing mode leads to a Kadomtsev type reconnection, the core of the  $q < 1$  region moving almost rigidly to one side and the return flow taking place in a very narrow resistive layer.

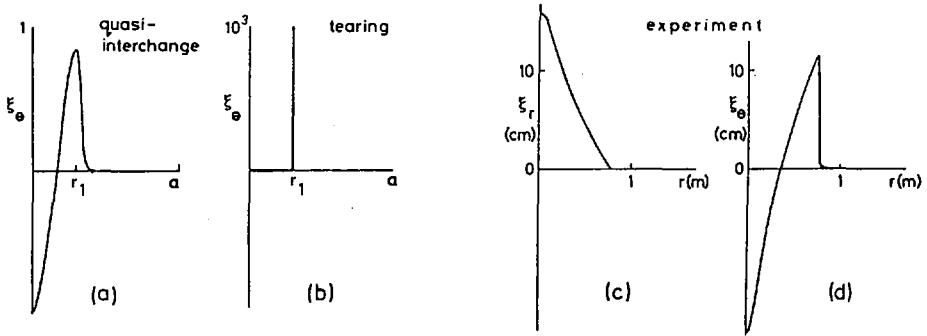


Fig. 5. Eigenfunction  $\xi_\theta(r)$  for (a) quasi-interchange mode and (b) tearing mode, together with experimental forms for (c)  $\xi_r(r)$  and (d)  $\xi_\theta(r)$  from the JET experiment.

The flux surfaces which would develop in the two cases are illustrated in Figs 4(i) and 4(ii). The contours of equal temperature and equal X-ray emission would have a similar topology. The distinction between the two cases is quite clear. It is possible that the type of behaviour will depend upon the plasma parameters and size. If there is a continuous transition from quasi-interchange (4(i)) to tearing (4(ii)), then an intermediate case would take the form shown in 4(iii).

The distinction between the quasi-interchange and the tearing mode is brought out most clearly by considering the azimuthal displacement eigenfunction  $\xi_\theta(r)$ . For  $R/r_1 \gg 1$ , this is related to  $\xi_r$  by  $\xi_\theta = -\frac{d}{dr}(r\xi_r)$ . The functions  $\xi_\theta(r)$  corresponding to the cases illustrated in Fig. 4 are shown in Figs 5a and 5b. Experimental forms for  $\xi_r$  and  $\xi_\theta$  have been derived from the X-ray emission at an early stage of a JET sawtooth collapse. The radial displacement is calculated from the initial emission profile and the profile after 50  $\mu$ s. The function  $\xi_r(r)$  and the derived  $\xi_\theta(r)$  are shown in Figs 5c and 5d. Comparison of Fig. 5d with Figs 5a and 5b gives clear evidence that the displacement has the form of a quasi-interchange.

## 5. A FUNDAMENTAL DIFFICULTY

In addition to the features described above, the model proposed by Wesson [3] also offered an explanation of the trigger for the rapid sawtooth collapse. Further examination of this problem shows that not only is the proposed explanation inadequate but also there is a fundamental difficulty for all models of "precursorless" sawteeth. This difficulty, which is associated with the rapidity of the onset of the collapse, is described below.

If the collapse time is  $\tau_c$ , it is necessary for a growth rate  $\gamma \sim \tau_c^{-1}$  to develop on a timescale  $\tau_c$ . Let the change in central  $q$  necessary to produce this  $\gamma$  be  $\delta q$ . If this change in  $q$  results from resistive diffusion, then

$$\delta q \sim \frac{\tau_c}{\tau_s} \Delta q \quad (3)$$

where  $\Delta q$  is the change in  $q$  during the ramp phase, the duration of which is approximately the sawtooth period  $\tau_s$ . The magnitude of this  $\Delta q$  can be estimated from the resistive diffusion of the current [3] and is given by

$$\Delta q \sim \frac{\Delta T}{T} \frac{\tau_s}{\tau_R} \quad (4)$$

where  $\Delta T/T$  is the fractional change in the temperature during the sawtooth, and the resistive diffusion time  $\tau_R = \mu_0 r_1^2 / 4\eta$ . Relations (3) and (4) determine the expected change  $\delta q$  during the collapse time. It is then necessary that the required instability growth rate can be switched on by this  $\delta q$ .

Typical JET values are  $\Delta T/T \sim 10^{-4}$  and  $\tau_s/\tau_R \sim 10^{-1}$ , giving  $\Delta q \sim 10^{-2}$ . Then, since  $\tau_s \sim 100\text{ms}$  and  $\tau_c \sim 100\mu\text{s}$ , relation (3) gives the required sharpness of the switch-on of the instability,  $\delta q \sim 10^{-3} \times 10^{-2} \sim 10^{-5}$ .

Even allowing for the uncertainty in the estimation, this  $\delta q$  seems to be improbably small. We can make an estimate of  $\delta q$  required to switch on the quasi-interchange mode as follows. Let the growth rate for zero shear be  $\gamma_0$ , then the destabilising energy density available for the instability is  $\sim \frac{1}{2} \rho \gamma_0^2 \xi^2$ . Putting  $d\xi/dr \sim \xi/r$  the stabilising energy density [3] is  $\sim (1-q)^2 (B_\theta^2 / 2\mu_0) (\xi/r)^2$ . Thus the dispersion relation can be characterised by

$$\gamma^2 = \gamma_0^2 - (1-q)^2 \tau_A^{-2} \quad \text{where} \quad \tau_A = r_1 / (B_\theta / (\mu_0 \rho)^{1/2}). \quad (5)$$

Although the initial switch-on,  $d\gamma/dq$ , at  $\gamma=0$  is very rapid, it is necessary for  $\gamma$  to grow to give a value (in JET) of  $\gamma^{-1} \sim 100 \mu\text{s}$ . Now, for the ideal  $m=1$  mode,  $\gamma_0 \sim \epsilon \beta_p / \tau_A$ , where  $\epsilon = r_1/R \sim 10^{-1}$ ,  $\beta_p \sim 10^{-1}$  and  $\tau_A \sim 1 \mu\text{s}$ . Thus,  $\gamma_0^{-1} \sim 100 \mu\text{s}$ , and this is of the order of the required growth time. Consequently, the change in  $q$  necessary to produce the required growth rate is given by equation (5) to be

$$\delta q \sim \gamma_0 \tau_A$$

Hence the theoretical switch-on width in  $q$  is  $\delta q \sim 10^{-2}$ , and this is orders of magnitude greater than the required experimental value of  $10^{-5}$ .

The problem is even more severe for tearing modes where the theoretical value for the  $\delta q$  necessary to provide a growth rate  $\gamma$  is [7]

$$\delta q \sim \gamma^{3/2} \tau_A \tau_R^{1/2}$$

The typical JET values given above, with  $\tau_R \sim 1$  s, give  $\delta q \sim 1$ , to be compared with a required switch-on  $\delta q \sim 10^{-5}$ .

It is clear therefore that a fundamental element is missing in our theoretical understanding of fast precursorless sawteeth. Thus, although the experimental evidence on the flow behaviour seems to support the quasi-interchange model, the validity of this model cannot be accepted while we still lack an explanation of the rapidity of the onset of the collapse.

## 6. CONCLUSIONS

- (i) A flattened  $q$ -profile inside the  $q=1$  surface allows instability of the ideal  $m=1$  mode which would otherwise be stable at low  $\beta_p$ .
- (ii) Non-linear simulations of the instability illustrate the quasi-interchange behaviour. The broad convective flow takes the outer plasma into the centre to form a colder "bubble".
- (iii) The behaviour of the quasi-interchange is quite distinct from that of a tearing mode and is in better agreement with experimental observations of sawteeth in JET.
- (iv) The sudden onset of the collapse in precursorless sawteeth presents a fundamental problem for all existing models.

## ACKNOWLEDGEMENTS

The authors would like to thank J.Hastie for discussions and R.Granetz for help in analysing the soft X-ray results.

## REFERENCES

- [1] KADOMTSEV, B.B., Sov. J. Plasma Phys. 1 (1975) 389.
- [2] CAMPBELL, D.J., et al., Nucl. Fusion 26 (1986) 1085.
- [3] WESSON, J.A., Plasma Phys. Contr. Fusion 28 (1986) 243.
- [4] EDWARDS, A.W., et al., Phys. Rev. Lett. 57 (1986) 210.
- [5] BUSSAC, M.N., et al., Phys. Rev. Lett. 35 (1975) 1638.
- [6] ROSENBLUTH, M.N., et al., Phys. Fluids 16 (1973) 1894.
- [7] COPPI, B., et al., Sov. J. Plasma Phys. 2 (1976) 583.

# THEORY OF SAWTOOTH DISRUPTION

D. BISKAMP, H. WELTER  
Max-Planck-Institut für Plasmaphysik,  
Garching, Federal Republic of Germany

## Abstract

### THEORY OF SAWTOOTH DISRUPTION.

Numerical investigations of the MHD processes related to the sawtooth oscillation have been performed, by using the full non-ideal MHD equations. Sawteeth are found to exist in cylindrical geometry, but the amplitudes become too small for small  $\eta$ . Toroidal effects are important, allowing larger energy storage.

### I. Introduction

The sawtooth oscillation is a well known relaxation phenomenon, observed in virtually all tokamaks. It periodically flattens the temperature, density and probably also current density profiles in the central part of the discharge column up to a certain radius  $r_1$ , the sawtooth inversion radius. While in Ohmic discharges or those with moderate amounts of auxiliary heating sawtooth amplitudes are small,  $\Delta T_e/T_e \sim 0.05$  typically, and seem to have an overall beneficial effect in preventing central impurity accumulation, discharges with strong additional power injection such as the ICRH experiments on JET exhibit sawteeth of much larger amplitudes, which strongly deteriorate the global confinement. Hence the sawtooth disruption has become a problem of major concern in tokamak research.

The traditional theoretical interpretation of the sawtooth phenomenon that until recently had been generally accepted is based on a model by Kadomtsev<sup>1)</sup>. If the  $q$ -profile in the plasma center drops below 1, the resistive  $m = 1$  kink mode becomes unstable giving rise to a rapid convective transport of the central plasma toward the  $q = 1$  surface and a flat current profile with  $q(0) > 1$ , from where the process restarts. In recent years, however, observational results in particular from the large tokamak devices such as TFTR and JET, indicate that the typical sawtooth oscillation shows features which cannot be reconciled with this simple model. Since skin times for major changes in the current profile far exceed the sawtooth period, the  $q$ -profile inside the inversion radius should remain flat close to unity. No  $m = 1$  oscillations preceding the sawtooth crash are observed, which should be present if the  $m = 1$  mode starts growing slowly accelerating gradually. The crash-time is very short, so that magnetic reconnection or other resistivity related processes do not seem to play a major role. In addition smaller disruptions occur at half period between main crashes, so called subordinate sawteeth, which are localized close to the inversion radius and indicate some local  $q$ -profile modification at this radius. Recent numerical simulations<sup>2)</sup> using the reduced resistive MHD equations including the selfconsistent evolution of the resistivity have successfully reproduced many features of these observations. They show that in fact the  $q$ -profile remains almost flat and that a weak skin current develops near the inversion radius, which under certain conditions gives rise to the subordinate sawtooth disruption. (A "magnetic trigger" of this kind has also been proposed in Ref. 3.)

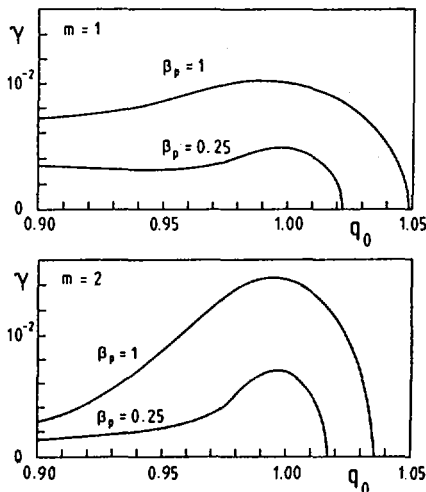


FIG. 1. Growth rates for cylindrical equilibria versus  $q_0$ , for  $\Delta q = 0$ .

The main shortcoming of these simulations is the use of the reduced MHD equations which neglect pressure driven effects. This is particularly restrictive for flat  $q$ -profiles, where shear effects become virtually negligible. In this case the  $m = 1$  mode is marginally stable in the reduced equations (or possibly weakly unstable including resistivity gradient effects), while it is known to be strongly unstable using the full equations, at least in the cylindrical approximation. In view of this deficiency the qualitative agreement of the results of Ref. 2 with experimental observations appears to be somewhat fortuitous. In the present investigation we therefore consider the full MHD equations with resistivity, heat conductivity and viscosity included, which are solved numerically in cylindrical as well as toroidal geometry. Section II outlines the numerical procedure and presents the results for cylindrical geometry: discussion of linear stability, nonlinear properties, and simulations of the full sawtooth period. In Section III the modifications of these results due to toroidal geometry are discussed. In Section IV the possibility of an alternative sawtooth model is investigated based on recent experimental observations<sup>4)</sup> that the current profile is peaked inside the inversion radius.

## II. Cylindrical Geometry

A numerical code has been developed for the solution of the full nonlinear MHD equations

$$\frac{\partial \vec{B}}{\partial t} = \nabla \times (\vec{v} \times \vec{B}) - \nabla \times \eta (\nabla \times \vec{B}) \quad (1)$$

$$\frac{\partial \vec{v}}{\partial t} = -\vec{v} \cdot \nabla \vec{v} - \nabla p - \vec{B} \times (\nabla \times \vec{B}) + \mu \nabla^2 \vec{v} \quad (2)$$

$$\frac{\partial p}{\partial t} = -\nabla \cdot \vec{v} p - \frac{2}{3} p \nabla \cdot \vec{v} + \nabla \cdot \vec{\kappa} \cdot \nabla p + \frac{2}{3} \eta (\nabla \times \vec{B})^2 \quad (3)$$

The density is assumed to be homogeneous,  $\rho = 1$ .

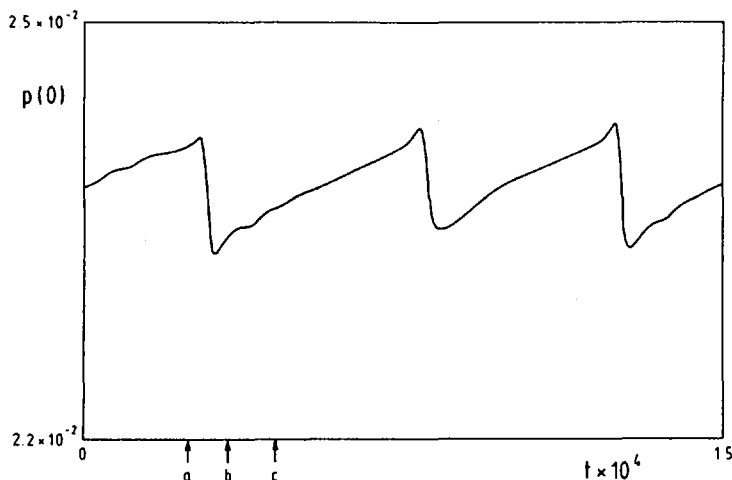


FIG. 2. Evolution of central pressure cylindrical geometry, for  $\eta_0 = 10^{-5}$ .

To eliminate the fast compressional Alfvén time step restriction a semi-implicit scheme suggested recently<sup>5)</sup> is used, which is efficient and accurate. Finite difference approximation is applied in radial direction, while Fourier expansion is used in azimuthal and axial directions. Linear mode properties for  $m = 1$  as well as  $m > 1$  have been investigated for various types of cylindrical equilibria by prescribing  $p'$ - and  $q$ -profiles. Guided by previous results<sup>2)</sup> and the sawtooth simulations given below, the  $q$ -profile is chosen to consist of a flat part  $q = q_0$  inside  $r_0$ , a shallow well with depth  $\Delta q$  between  $r_0$  and  $r_1$ , and a parabolic rise beyond  $r_0$ ,  $p'$  is characterized by a parameter  $\beta_p$ . The main results are:

- i) For small values of the transport coefficients  $\eta, \kappa_{\perp}, \mu \leq 10^{-7}$  (in units of  $av_{A1}$ ) unstable modes are essentially ideal modes. Choosing  $\kappa_{\parallel} \sim 10^2$  instead of  $\kappa_{\parallel} = 0$  has a negligibly small effect. Fig. 1 gives growth rates of the  $(m, n) = (1, 1)$  and  $(2, 2)$  modes for  $\beta_p = 1$  and 0.25, with  $\Delta q = 0$ .
- ii) Instability ranges have a sharp upper boundary in  $q_0$  and lower boundary in  $\beta_p$ ,  $\gamma \propto \sqrt{q_c - q}$  and  $\gamma \propto \sqrt{\beta_p - \beta_{pc}}$  respectively. Growth rates and mode structures are quite insensitive to the detailed pressure profile depending only on some average  $p'(\tau)$ , essentially  $p(0) - p(r_1)$ .
- iii) For  $q_0$  close to unity the instability is of the interchange type, i.e. many  $m$ -modes are unstable, not only  $m = 1$  as in the case of a peaked current profile with  $q_0 < 1$ . Maximum growth rates, which occur at  $q_0$  slightly below 1, increase with  $m$  and  $\beta_p$ ,  $\gamma \propto \sqrt{m\beta_p}$ , while the unstable band shrinks with growing wave number and decreasing pressure gradient  $\beta_p$ .
- iv) For  $q_0$  above the stability threshold as shown in Fig. 1 addition of a shallow well  $\Delta q$  also leads to instability. While eigenmodes remain global, growth rates depend on the value of the pressure gradient at  $r \approx r_1$ . A local flattening can suppress the instability, even if  $p(0) - p(r_1) > 0$ .

Concerning the nonlinear behavior of these instabilities, two questions are addressed. The first is the relationship between the linear growth rate  $\gamma_L$  and the "disruption time" defined by  $\tau = r_1/v_0$ , where  $v_0$  is the maximum value the velocity reaches in the center.

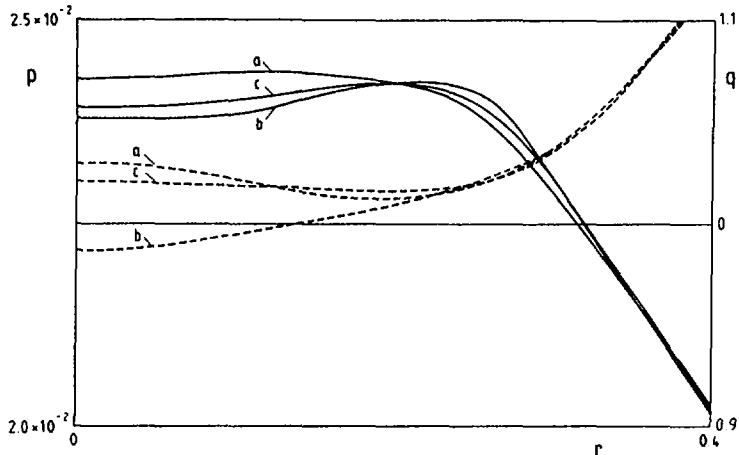


FIG. 3. Evolution of  $q$ - and  $p$ -profiles during sawtooth period. (a), (b) and (c) refer to the times indicated in Fig. 2.

For interchange type mode, i.e.  $q_0 = 1$ , varying  $\gamma_L$  by increasing  $\beta_p$  from 0.1 to 1 we find a strictly linear relationship  $\tau \approx 1.5\gamma_L^{-1}$ . Since  $\tau$  can directly be observed experimentally and the pure interchange mode probably gives the fastest nonlinear process, this relationship indicates a minimum value of the linear growth rate required to explain the disruption time. The second question concerns the transition from small amplitude saturation to disruption. We consider a sequence of equilibria with  $\beta_p = 0.25$ ,  $q_0 = 1.03$ , and  $\Delta q$  varying from 0.01 to 0.04. The saturation amplitude is defined by  $\Delta/r_1$ , where  $\Delta$  is the off center shift of the pressure maximum. The transition is in fact very sharp,  $\Delta/r_1 \approx 0.25$  for  $\Delta q = 0.02$  and  $\Delta/r_1 \approx 0.8$  for  $\Delta q = 0.03$ . It should be noted that the linear eigenmodes always have a global structure, also in cases saturating at small amplitudes.

We have performed simulations of the complete sawtooth cycle evolving selfconsistently under the effects of Spitzer-type resistivity, Ohmic heating and heat conduction. Starting from a resistive equilibrium with  $q_0 < 1$  the dynamical evolution has been followed over a sufficiently long time to reach dynamical behavior independent of the initial state. Steady sawtooth oscillations do in fact exist, as shown in Fig. 2, where the evolution of the central pressure is given. This phenomenon is by no means self-evident. Since for a flat  $q$ -profile with  $q_0 = 1$  any  $\beta_p = p(0) - p(r_1) > 0$  gives rise to instability with  $\gamma \propto \sqrt{\beta_p}$  leading to a rapid interchange motion, a stationary convective cell seems to be the most likely final state, as has recently been found under certain conditions in numerical simulations<sup>2)</sup> using the reduced MHD equations. The evolution of the  $p$  and  $q$  profiles during a sawtooth period is illustrated in Fig. 3, with  $\eta = 10^{-5}$ ,  $\mu = 10^{-6}$ ,  $\kappa_{\perp} = 3 \times 10^{-7}$ , and a), b), c) referring to the times indicated in Fig. 2. The disruption is due to an  $m = 1$  interchange-like instability excited by a slightly inverted  $q$ -profile, a). Note that the instability sets in while  $q_{min} > 1$  still. The rapid motion leads to an inverted  $p$ -profile (the actual dynamical process resembles strongly the tomographic results from JET<sup>5)</sup>) and a monotonic  $q$ -profile with  $q(0)$  slightly below 1 temporarily, b). Due to the relatively low pressure and corresponding large  $\eta$ ,  $q$  increases soon to  $q > 1$ , c).

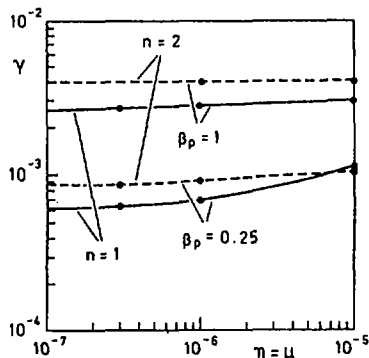


FIG. 4. Growth rates for toroidal equilibria versus  $\eta_0$ ,  $q_0 = 1$ ,  $\Delta q = 0$ .

Nevertheless, the cylindrical model cannot describe the sawtooth phenomenon in tokamaks, because of the inherent inefficiency of energy storage. This leads to a wrong  $\eta$ -scaling of the sawtooth amplitude. While the sawtooth period increases with decreasing  $\eta$  roughly as  $\tau \propto \eta^{-1/2}$ , the amplitude decreases  $\Delta p/p \propto \eta^{1/2}$ . In the case shown in Fig. 2 for  $\eta = 10^{-5}$ ,  $\Delta p/p \sim 0.03$  which is already rather small. These computations have been performed for  $\beta_p \sim 1$ . We expect that in the limit  $\beta_p \rightarrow 0$  and finite  $\eta$  the resistivity driven effects dominate as described in Ref. 2. For a qualitatively correct modelling of tokamak sawtooth oscillation, in particular at small but finite  $\beta_p$ , toroidal effects have to be taken into account.

### III. Toroidal Geometry

A toroidal version of the code described in section II has been set up in quasi-flux coordinates  $u, \theta, \varphi$ , where  $u(r, \theta) = \text{const}$  are circles with the axis shifted in such a way that the coordinate axis coincides with the magnetic axis of the equilibrium. The advantage as compared to numerically computed genuine flux coordinates is that all metric coefficients can be obtained analytically. For circular boundary to which the investigations have thus far been restricted, the deviation from exact flux surfaces is small. For nonlinear computations the equilibrium flux coordinates would lose their advantage anyway.

Equilibria are obtained by choosing a cylindrical configuration, which is allowed to relax into a toroidal equilibrium with the coordinate shift determined iteratively. Since  $\eta = 0$  in the relaxation process, the  $q$ -profile does not change and can thus be prescribed with high precision. This allows a direct comparison of cylindrical and toroidal equilibria.

Fig. 3 shows growth rates of the  $n = 1$  and  $n = 2$  modes as functions of  $\eta$  for a flat  $q$ -profile,  $q = 1$  inside  $r_1$ , for  $\beta_p = 1$  and 0.25. Growth rates seem to be independent of  $\eta$  for  $\eta \leq 3 \times 10^{-7}$ , hence there is ideal instability also in the toroidal case, but  $\gamma$  is proportional to  $\beta_p$ , instead of  $\beta_p^{1/2}$  in the cylindrical case. In addition the unstable  $q$ -range is narrower. These properties have a crucial effect on the sawtooth behavior, since they allow that free thermal energy may be accumulated much more easily than in the cylindrical model. On the other hand a certain problem arises in explaining the experimentally observed fast crash time scales. The toroidal configurations studies thus far yield growth rates that are somewhat too small. Since growth rates depend rather sensitively on details of the configuration, while the plasma will automatically find the fastest way of energy release, a

selfconsistent simulation of the full sawtooth cycle in toroidal geometry is required. Though such simulations have not yet performed, we expect that while much larger amplitudes  $\Delta p$  may be build up with  $\Delta p$  independent of the resistivity, the basic mechanism of energy release is essentially as in the cylindrical case, illustrated in Fig. 3.

#### IV. Alternate Model of the Sawtooth Oscillation

It has recently been observed experimentally<sup>4)</sup> that the current profile of a sawtooth tokamak discharge is peaked with  $q_0 \sim 0.7 - 0.8$ . This result would be in contradiction to the sawtooth model outlined in the previous sections where the current profile is flat inside  $r_1$  with  $q_0 \simeq 1$ . Such a behavior is in principle conceivable. The sawtooth disruption would be analogous to the major disruption, where the sudden outflow of thermal energy seems to be caused by the destruction of the magnetic surfaces rather than a convective process and where the current profile does not change appreciably. The basic problem in this concept is to explain the absence of the  $(m, n) = (1, 1)$  mode. A previous theory of the internal kink mode<sup>7)</sup> in toroidal geometry predicts stability (of the ideal mode) for sufficiently small  $\beta_p$ . Though the mode would still be resistively unstable, saturation at finite amplitude could occur as in the case of  $m > 1$  tearing modes, mainly due to a quasi-linear flattening of the current profile close to the  $q = 1$  surface. We have started to investigate this question numerically using the cylindrical as well as the toroidal code for  $\beta_p = 0.25$  and an aspect ratio  $R/a = 5$ . In both cases no stabilization, not even a substantial reduction of the growth rates, due to a local current- (and pressure-) profile flattening could be found. Though the results are still preliminary and nonlinear computations concerning this problem have not yet been performed, the indication is that a stabilization of the internal kink mode is not possible within the resistive MHD approximation and, if further corroborated experimentally, would require a more refined theoretical model.

#### Acknowledgements

The authors gratefully acknowledge valuable discussions with Dr. D. Harned and would like to thank Mrs. M. Walter for her assistance in the numerical computations.

#### REFERENCES

- [1] KADOMTSEV, B.B., *Sov. J. Plasma Phys.* **1** (1975) 389.
- [2] DENTON, R.E., DRAKE, F., KLEVA, R.G., BOYD, D.A., *Phys. Rev. Lett.* **56** (1986) 2477.
- [3] WESSON, J.A., *Plasma Phys.* **28** (1986) 243.
- [4] SOLTWICH, H., STODIEK, W., private communication, 1986.
- [5] HARNED, D.S., KERNER, W., *J. Comput. Phys.* **60** (1985) 62.
- [6] EDWARDS, A.E. et al., *Phys. Rev. Lett.* **57** (1986) 210.
- [7] BUSSAC, M.N., PELLAT, R., EDERY, D., SOULE, J.L., *Phys. Rev. Lett.* **35** (1975) 1638.

## SAWTEETH AND IDEAL MHD

M.N. BUSSAC, K. LERBINGER, R. PELLAT

Centre de physique théorique,  
Ecole polytechnique,  
Palaiseau

M. TAGGER

CEA, Centre d'études nucléaires,  
Fontenay-aux-Roses

France

### Abstract

#### SAWTEETH AND IDEAL MHD.

Recent experimental results support the idea that in tokamaks the sawtooth crash should be linked to an ideal MHD instability. Two possible interpretations, according to the current profile, are discussed.

Recent results on JET, TEXT, TFR, ALCATOR, etc. [1-5] have shown that the sawtooth crash has an  $m = 1$  structure with a growth rate much larger than the usual  $m = 1$  precursor, which may or may not be present. This supports the idea that the crash should be linked to an ideal MHD instability [6, 7]. In the following, we discuss two possible interpretations:

- (i) The first interpretation corresponds to a monotonically increasing  $q(r)$  profile with  $q(0) < 1$  ( $q(0)$  is the safety factor at the magnetic axis) and a partially reconnected topology with a finite magnetic island inside ( $q(r_0) = 1$ ).
- (ii) The second interpretation corresponds to a non-monotonic  $q$ -profile with  $q(0) > 1$ , but with a minimum  $q(r_0)$  away from the magnetic axis, which decreases in time and becomes equal to one, following the current penetration.

### 1. OBSERVATIONS

Recent tomography of sawteeth in JET has revealed a lot of interesting features; we shall discuss here the results of one of these experiments (shot 6320 with ICRH). Although a great variety of sawteeth exist (with or without precursor, postcursor; single partial, giant sawteeth...) it is believed [5, 10] that the observed behaviour of this shot is quite general.

According to soft-X ray reconstruction [1], the sawtooth collapse occurs essentially in two phases:

- (a) Initially, the region of maximum emissivity (the hot core) is rapidly displaced off axis. The volume of the hot core and the level of emissivity remain approximately constant. This phase, which lasts  $\sim 100 \mu\text{s}$ , has clearly an  $m = 1$  character and appears as a solid translation of the hot core (Fig. 3 of Ref. [1]). At the end of this first phase, an up-down asymmetric deformation is visible (Fig. 4 of Ref. [1]).
- (b) During the second phase (Fig. 4, C and D of Ref. [1]), this deformation increases, giving rise to a bubble-like structure of cold plasma. As a result, the hot core is pressed against the ' $q = 1$ ' surface and surrounds the bubble in a crescent (or island) shape. Its temperature, then, decreases rapidly (on a time-scale of  $\sim 100 \mu\text{s}$ ), while the bubble appears as a hollow temperature region.
- (c) In a third, much slower phase ( $\sim 1.5 \text{ ms}$ ), the central plasma develops a hollow, poloidally symmetric profile (Fig. 3 of Ref. [1]).

## 2. DISCUSSION

Comparison with ECE signals [2] shows that the observed emissivity is here mainly due to impurities (He-like nickel at  $5090 \text{ \AA}$ ). The temperature profiles seem, however, to follow the observed emissivity profiles.

The spatial resolution is  $\sim 7 \text{ cm}$  and an island less than  $10 \text{ cm}$  wide is not visible by tomography. Nevertheless, for a classical sawtooth with precursor, it has up to now been believed that the topology of the central plasma core is partially reconnected as a consequence of the resistive  $m = 1$  mode [17].

The detector configuration allows reconstructions with poloidal harmonics  $m = 0, \cos \theta, \sin \theta, \cos 2\theta$ . The outer ' $q = 1$ ' surface has an ellipticity  $(b - a)/(b + a) \sim 10\%$ .

## 3. FIRST INTERPRETATION

Let us first recall that all along the sawtooth cycle an inversion radius is observed, and that its position does not noticeably change on a time-scale of many sawteeth. Therefore, we favour the interpretation that a  $q = 1$  surface always exists in the plasma if one assumes a monotonically decreasing current profile. If  $q(0) < 1$  and the shear is infinite on  $q(r_0) = 1$ , the ideal MHD internal kink may be stable in toroidal geometry [11]. On the other hand, if unstable, this mode is expected to saturate to a low amplitude for finite shear [12]. In any case, an unstable resistive mode [18] allows magnetic field reconnection: a magnetic island grows on a very long time-scale ( $\sim \eta^{-1/2}$  or  $\eta^{-1/4}$ ), so that the size of that island cannot change substantially during the sawtooth crash phase.

The presence of that island can, however, affect the potential energy of the ideal MHD kink mode [6]:

$$\delta W = \delta W_{\text{T.IK}} + \delta W_{\text{shape}} + \delta W_{\text{island}} \quad (1)$$

where the first term describes the internal kink in toroidal geometry [11], the second term takes the shape of the plasma cross-section [8] into account, and the third term is due to the presence of the island causing the 'half-coalescence' instability [6] (we have neglected cross-terms in the modulation of the poloidal magnetic field). On the assumption of low shear and low  $\beta_p$  inside  $q = 1$  and finite shear outside, the toroidal contribution is of the order of

$$\delta W_{\text{T.IK}} \sim 2\pi^2 R \left( \frac{r_0 B}{R} \right)^2 \left[ \left( 1 - q_0 \right) \left( \frac{r_0}{R} \right)^2 - \beta_p^2 \left( \frac{r_0}{R} \right)^2 + O \left( \frac{r}{R} \right)^4 \right]$$

where  $q(r_0) = 1$ , and  $R$  is the major radius.  $B$  is the magnetic field;  $\beta_p$  is defined by Eq. (3).

For an elliptical cross-section,  $\delta W_{\text{shape}}$  takes the form:

$$\delta W_{\text{shape}} \sim 2\pi^2 R \left( \frac{r_0 B}{R} \right)^2 (1 - q_0)^2 \left( \frac{b - a}{b + a} \right)^2$$

Finally, the deformation of the hot core due to the presence of the island gives the contribution

$$\delta W_{\text{island}} = 2\pi^2 R \left( \frac{r_0 B}{R} \right)^2 (1 - q_0)^2 \left( \frac{\delta}{r_0} \right) f$$

where  $\delta$  is the island width and  $f$  is a measure of the poloidal magnetic field modulation along the separatrix. This factor can be positive or negative, depending on the detailed island shape.

It is very likely that, in different experiments, various terms in Eq. (1) can be dominant to drive (or stabilize) the mode, and that this should explain the different types of behaviour observed during sawteeth. There is an important feature to this MHD instability, whatever the origin of the potential energy. If  $\delta W$  becomes negative, then the well-known non-linear stabilizing effect [12], which limits the plasma displacement to the linear boundary layer, disappears: now the mode consists primarily of a solid displacement of the hot plasma core and a return motion in the island. The maximum solid displacement is expected to be of the order of the island size.

## 4. SECOND INTERPRETATION

According to [1, 2], it has been shown that JET sawtooth collapse may occur without any precursor. These results and the observation of a hollow temperature profile after the collapse [1, 19] led us to consider the possibility of skin currents forming at a finite radius. As is shown in numerical simulations [20], discharges with good central thermal confinement develop skin currents which grow stronger during the rise of the sawtooth. They become more pronounced and cause the safety factor  $q$  to fall below one, away from the magnetic axis, while  $q(0)$  remains larger than one. Another source of local enhancement of the current is the bootstrap current due to trapped electrons, which is proportional to the local pressure gradient. In a tokamak, when  $q(0) > 1$ , the ideal kink is linearly unstable if the safety factor  $q(r)$  has a minimum  $q(r_0) = 1$  away from the magnetic axis (as is shown in Fig. 1). In the limit of small  $(1 - q(0)) \sim s$  (but  $|s| \gg (r_0/R)^2$ ) and finite  $\beta_p$ , and keeping only terms up to first order in  $s$ , the available energy may be written as

$$\delta W_T = \frac{\pi R}{2} \left( \frac{r_0}{R} \right)^2 B_p^2(r_0) \times \left[ -\frac{\beta_p^2 (3 + Ae)}{1 - Ae + 8s} - \frac{5\beta_p s (3 + Ae)}{1 - Ae} + \frac{13}{8} s \right] \quad (2)$$

where  $B_p(r)$  is the poloidal magnetic field:

$$B_p = -\frac{8\pi}{B_p^2(r_0)} \int_0^{r_0} \frac{r^2}{r_0^2} \frac{dp}{dr} dr \quad (3)$$

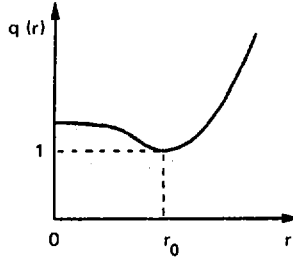


FIG. 1.  $q(r)$  profile of safety factor.

$$s = \int_0^{r_0} \frac{r^3}{r_0^4} dr \left( \frac{1}{q^2} - 1 \right)$$

$$Ae = \frac{r}{\xi_e} \frac{d\xi_e}{dr} \Big|_{r_0}$$

where  $\xi_e$  is the solution of the Euler equation for the harmonic  $m = 2$ ,  $n = 1$  which vanishes at the edge of the plasma and is equal to 1 on  $r = r_0$ . For a monotonically decreasing current density outside  $r = r_0$ , we obtain  $t - 3 < Ae < 0$ .

In the limit of vanishing  $\beta_p \ll s$ , the internal kink is stable for a monotonically decreasing current profile and unstable for a hollow current profile. Here, we notice that this instability is a purely toroidal effect, since, in cylindrical geometry, we obtain the opposite result if  $\beta_p \rightarrow 0$ .

Moreover, the linear growth rate is larger than in the regime where  $q(r)$  increases everywhere and  $q(0) < 1$ . Indeed, if the safety factor has minimum  $q(r_0) = 1$  away from the magnetic axis,

$$\frac{1}{q(r)} \approx 1 - \frac{q''(r_0)}{2} (r - r_0)^2$$

in the singular layer, and the lowest order in  $r_0/R$  the growth rate  $\gamma$  can be written as:

$$\gamma = \gamma_A \left( \frac{4}{\pi} \right)^{3/4} \frac{1}{(q''(r_0) r_0^2)^{1/4}} \left( \frac{-\delta W_T}{\frac{\pi}{2} R B_p^2(r_0)} \right)^{3/4}$$

where  $\gamma_A$  is the inverse poloidal Alfvén time:  $\gamma_A^2 = B_p^2(r_0)/(4\pi\rho r_0^2)$ . The singular layer  $\Delta$  scales as  $r_0 (\gamma/\gamma_A)^{1/2}$ , i.e. it is wider than for the usual kink with  $q(0) < 1$ , where it scales as  $\Delta \propto r_0 (\gamma/\gamma_A)$ .

More precisely, we obtain for a hollow current profile:

$$\frac{\Delta}{r_0} \approx \frac{1}{(q''(r_0) r_0^2)^{1/4}} \left( \frac{-\delta W_T}{\frac{\pi}{2} R B_p^2(r_0)} \right)^{1/4}$$

Therefore, in the non-linear regime, we may expect a saturation of the instability which limits the plasma displacement to the singular layer width.

The feature common to these two interpretations is to allow a large plasma displacement. The essential difference is the following: in the first case, the available potential energy becomes positive ( $\delta W < 0$ ) in time, the necessary  $q$ -profile being already settled. In the second case, the potential energy is available when the necessary current profile becomes accessible, i.e. when  $q(r)$  has a minimum equal to one, away from the magnetic axis where  $q(0) > 1$ .

We now discuss the non-linear evolution of this instability and its relevance to the explanation of the sawtooth crash.

In toroidal geometry (with or without non-circular cross-section) neither analytical nor numerical calculations exist, and one can only discuss the non-linear evolution qualitatively. In the first interpretation, where  $q(0) < 1$ , the surface  $q = 1$  is now distorted, and since the destabilizing terms  $\delta W_{\text{island}}$  are now of the order of the external kink, one can expect a non-linear evolution similar to that of the external kink which leads to bubble formation. In this process [14, 15], a configuration with hot plasma and strong current, surrounded by a vacuum, evolves to a state of lower energy where the hot plasma (and the current channel) surrounds the vacuum bubble. This evolution for the external kink in an axisymmetric configuration requires very low shear in the plasma. However, as was discussed in [6], this would be a natural evolution in the presence of an  $m = 1$  magnetic island, which would become the cold bubble. We note that the island topology is very favourable to this mechanism since

- (a) the island and the hot core have the same topology (forming two interlaced rings) and thus can exchange their cross-section shapes by a continuous, ideal MHD process;
- (b) the separatrix remains intrinsically a  $q = 1$  surface throughout this evolution, which might hence be less insensitive to shear.

In situations without an island, where the mode is due to skin currents and toroidal geometry (at least with very low shear), bubbles may also exist, but only by numerical simulations will we be able to discuss their extent, their importance and their sensitivity to shear.

In any of these situations, bubble formation leads to an inverted temperature profile. This inverted profile creates large temperature, pressure and current gradients at the  $q = 1$  surface, leading to very fast transport by diffusion, but, certainly, also causing enhanced stochasticity and microturbulence [16].

The same mechanism, with the bubble now remaining at the periphery of the  $q = 1$  region, could also explain the partial sawteeth observed in (large) tokamaks.

## REFERENCES

- [1] EDWARDS, A.W., et al., Phys. Rev. Lett. **57** (1986) 210.
- [2] CAMPBELL, D.J., et al., in Controlled Fusion and Plasma Physics (Proc. 12th Europ. Conf. Budapest, 1985), European Physical Society (1985).

- [3] KIM, J.B., et al., paper presented at Am. Phys. Soc. Meeting Boston, 1984.
- [4] DUBOIS, M.A., et al., Nucl. Fusion **19** (1979) 703.
- [5] CAMACHO, R., GRANETZ, R., paper presented at Am. Phys. Soc. Meeting Boston, 1984.
- [6] BUSSAC, M.N., PELLAT, R., SOULE, J.L., TAGGER, M., Phys. Lett., A **105** (1984) 51; **109** (1985) 331.
- [7] WESSON, J.A., Plasma Phys. Contr. Fusion **28** (1986) 243.
- [8] EDERY, D., LAVAL, G., PELLAT, R., SOULE, J.L., Phys. Fluids **19** (1976) 260.
- [9] ROBINSON, D., in Magnetic Reconnection and Turbulence, Editions de physique, Orsay (1985) 259.
- [10] SMEULDERS, P., *ibid.*, p. 239.
- [11] BUSSAC, M.N., et al., Phys. Rev. Lett. **35** (1975) 1638.
- [12] ROSENBLUTH, M.N., et al., Phys. Fluids **16** (1973) 1984.
- [13] KADOMTSEV, B.B., Sov. J. Plasma Phys. **1** (1975) 389.
- [14] KADOMTSEV, B.B., POGUTSE, D.P., Sov. Phys. — JETP **38** (1974) 283.
- [15] ROSENBLUTH, M.N., Phys. Fluids **19** (1976) 1987.
- [16] DUBOIS, M.A., SAMAIN, A., Nucl. Fusion **20** (1980) 1101.
- [17] BUSSAC, M.N., in Plasma Physics and Controlled Nuclear Fusion Research 1976 (Proc. 6th Int. Conf. Berchtesgaden, 1976), Vol. 1, IAEA, Vienna (1977) 607.
- [18] WADDELL, B., et al., Nucl. Fusion **18** (1978) 735.
- [19] BOYD, D.A., private communication, 1986.
- [20] DENTON, R.E., et al., Phys. Rev. Lett. **56** (1986) 2477.



## DISCUSSION

### ON PAPERS IAEA-CN-47/E-I-1-1 TO E-I-1-3

A. GIBSON: At the beginning of your oral presentation, you mentioned experimental results by the TEXTOR group at Jülich, showing that  $q$  is less than 1 throughout the sawtooth phase of some discharges. Cases have also been reported where the sawtooth is stabilized by lower hybrid current drive but where an  $m = 1$  oscillation remains; presumably,  $q = 1$  is still within the plasma. Can you say how these results affect the theoretical treatments which you discussed?

J.A. WESSON: I cannot answer this question in detail, but I would like to say the following. Firstly, it should be made clear that I accept Soltwisch's result that  $q_0 < 1$ . If these  $q_0 < 1$  profiles are smooth, they present a very serious problem for MHD because they should be highly unstable with respect to tearing modes. If, on the other hand, they are stable because of flattening around the  $q = 1$  surface, then, because of the large shear, the sawteeth must be different from those in JET.

K. McGUIRE: The new features in connection with sawteeth discovered over the past 4-5 years are the observed compound sawteeth, subordinate or partial relaxations and a fast collapse time. In your paper you deal with the problem of a fast sawtooth collapse time. Does your model also explain compound sawteeth, or subordinate relaxations?

There is another point. On TFTR, the collapse time for sawteeth may vary from 40  $\mu$ s to 10 ms and, even on one discharge, the crash time can vary by a factor of five. In your presentation you imply that all sawteeth crash in 100  $\mu$ s on JET. Is this true?

J.A. WESSON: It seems possible that the partial bubble formation which we see in the simulations for larger values of  $q_0$  can explain the partial relaxations. Then, the full collapse would occur when there had been a further reduction in  $q_0$ .

Regarding the collapse times on JET, I use 100  $\mu$ s as a typical value. Collapse times which appear to be longer are sometimes observed, but full reconstruction shows this to be a geometric effect. With neutral beam counter-injection, much longer collapse times sometimes occur. Of course, I emphasize the fast collapses because it is these which present the theoretical problem.

B. COPPI: What happens to the quasi-interchange mode when the theory for it is applied to toroidal geometry, with finite Larmor radius effects?

J.A. WESSON: Toroidal calculations have been carried out and they show that the quasi-interchange mode persists in toroidal geometry. Given the fast growth rate and the absence of any layer, I would not expect the quasi-interchange mode to be significantly affected by finite Larmor radius effects.

M.A. DUBOIS: A major problem with sawtooth models is that they have to explain not only the time-scale of the fast collapse but also the temperature profiles observed after the collapse, which are sometimes flat and sometimes hollow; also,

sometimes a very sharp temperature spike remains within the  $q = 1$  surface, as observed in TFR with ECRH. I feel that a sawtooth model should explain all observations. Do you think that with the models you presented a very sharp temperature spike can be kept motionless in the plasma centre?

J.A. WESSON: It is difficult to comment on the result you mention without knowing the details. As a general point, I think it quite possible that different types of sawteeth occur, but I also hope that one model would suffice to explain all results.

## SECOND STABILITY ACCESS IN TOKAMAK PLASMAS

K. YAMAZAKI, H. NAITOU, T. AMANO, Y. HAMADA,  
K. MATSUOKA, Y. MIDZUNO, Y. NAKAYAMA<sup>1</sup>, T. SATO<sup>1</sup>  
Institute of Plasma Physics,  
Nagoya University, Nagoya

T. TSUNEMATSU, T. TUDA, S. SEKI, M. AZUMI, S. TOKUDA,  
T. OZEKI, T. NEMOTO<sup>2</sup>, Y. KISHIMOTO, T. TAKEDA  
Naka Fusion Energy Research Establishment,  
Japan Atomic Energy Research Institute,  
Naka-machi, Naka-gun, Ibaraki-ken

Japan

### Abstract

SECOND STABILITY ACCESS IN TOKAMAK PLASMAS.

Methods of beta enhancement in a tokamak plasma are investigated. One is shaping optimization for a slightly indented cross-section, and the other one is optimization of plasma current profile for a circular or a dee-shaped cross-section. Access to the second stability region of the ballooning modes is demonstrated for both cases. The stability of external kink modes is also studied. The kink instability is of crucial importance for the exotic shape or current profile used in the analysis. The conducting shell placed at  $a_w/a \geq 1.2$  enhances the beta limit more than twice the conventional value ( $a_w$ ,  $a$  are, respectively, the horizontal minor radii of the conducting shell and the plasma). The non-linear evolution of the ballooning modes is studied by using a two-fluid model, and the fluctuation level of the magnetic field is evaluated.

### INTRODUCTION

One of the critical issues in tokamak fusion research is the improvement of the beta limit of a plasma ( $\beta$  is the ratio of plasma to magnetic pressure). We describe two different methods of beta limit enhancement in this paper. Part A demonstrates enhancement by using an indented cross-section. Shaping optimization is expected to reduce the indentation, and the pusher coil can be simplified. The effect of triangularity in the indented configuration on kink and ballooning beta limits in the first region of stability and on the accessibility to the second region of stability is studied. In Part B, enhancement by using

---

<sup>1</sup> Institute of Fusion Theory, Hiroshima University, Hiroshima, Japan.

<sup>2</sup> On leave from Fujitsu Ltd., Tokyo, Japan.

current profile optimization is described for circular and dee-shaped cross-sections. The accessibility to the second stability region of the ballooning modes is investigated. The stability of external kink modes is also studied for the equilibria that are stable against the ballooning modes. Beta enhancement by using this method reduces the plasma current and the current in poloidal coil systems, as well. In Part C, the non-linear evolution of the ballooning modes is studied by using a two fluid model, and the dependence of the magnetic field fluctuation level on the beta value is evaluated.

## Part A

### SECOND STABILITY ACCESS IN CRESCENT SHAPING<sup>3</sup>

A 'crescent' configuration [1] is characterized by optimal shaping with small indentation ( $i \approx 0.1$ ) but large triangularity ( $\delta > 0.5$ ) and moderately high ellipticity ( $\kappa \sim 2$ ). This high beta configuration ( $\beta > 10\%$ ) lies in the first region of stability and enables a smooth transition to the second region. This is an easily achievable extension from the conventional dee shaping of large tokamak design.

Figure A-1 shows a typical configuration related to the shaping effect on accessibility to the second region of stability. In the dee-shaped case, the first stability beta limit is  $\sim 3\%$ , and the second stability region near the centre appears at the toroidal beta value of  $\sim 25\%$  (Fig. A-1 (a)). By increasing the triangularity in addition to indentation (crescent shaping), the centre region passes to second stability (Fig. A-1 (b) and (c)), and, finally, the unstable region is diminished by enhancing the crescent shaping. Indentation without sufficient triangularity (kidney bean shaping) is not favourable for accessibility to the second region (Fig. A-1 (d)).

The change of local shear by adding triangularity is shown in Fig. A-2 for  $\beta \sim 13\%$  configurations. In the bad curvature region, the local shear is increased by raising triangularity, keeping the indentation constant.

As to first stability beta limits against  $n = \infty$  ideal ballooning modes, pressure optimized configurations are studied by using the FCT-BALLOON code, and a new beta scaling for a wide range of shapings (ellipse, dee and crescent) is obtained [1]. Higher elongation or a lower aspect ratio does not give rise to  $\beta$  enhancement unless sufficient triangularity is added. The effect of indentation-triangularity  $\delta^*$  is shown in Fig. A-3. Smoother but quicker transition to second stability is obtained by an indented configuration with a sharp tip (crescent shape,  $\lambda = 1$ ) than by shaping with a round tip (kidney bean shape,  $\lambda = 2$ ). In this

---

<sup>3</sup> K. Yamazaki, H. Naitou, T. Amano, Y. Hamada, K. Matsuoka, Y. Midzuno, Y. Nakayama, T. Sato.

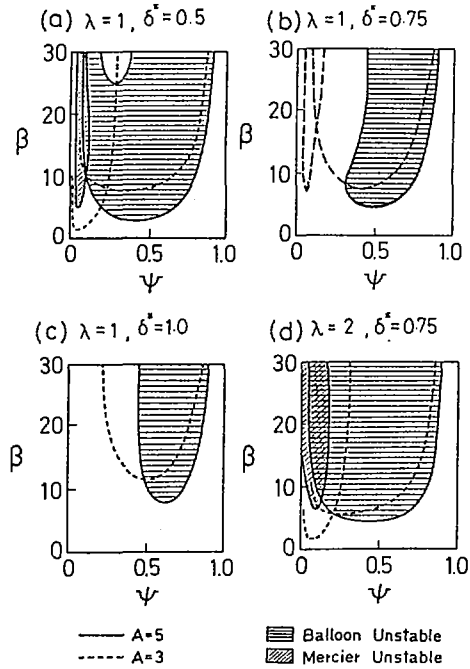


FIG. A-1. Effects of triangularity and indentation on accessibility to second regime of ballooning mode stability for  $A = 3.0$ ,  $\kappa = 2.0$ ,  $q_0 = 1.0$  and  $q_s = 3.0$ . The plasma shape is defined by  $(X/a^* + \delta^*(Z/\kappa^*\alpha^*)^2)^2 + (Z/\kappa^*\alpha^*)^{2\lambda} = 1$ .

- (a) Dee:  $\lambda = 1$ ,  $\delta^* = 0.5$ ,  $i = 0.5$ ,  $i = 0.0$ ,  $\delta = 0.5$   
 (b) Weak crescent:  $\lambda = 1$ ,  $\delta^* = 0.75$ ,  $i = 0.04$ ,  $\delta = 0.68$   
 (c) Crescent:  $\lambda = 1$ ,  $\delta^* = 1.0$ ,  $i = 0.11$ ,  $\delta = 0.76$   
 (d) Kidney bean:  $\lambda = 2$ ,  $\delta^* = 0.75$ ,  $i = 0.11$ ,  $\delta = 0.56$ .

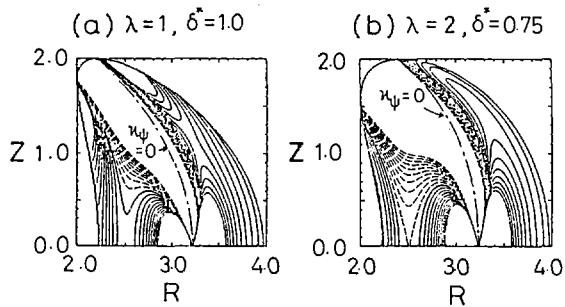


FIG. A-2. Contours of constant local shear for (a) crescent ( $\lambda = 1$ ) and kidney bean ( $\lambda = 2$ ) shaping at the same indentation of 0.11. Bad curvature region is on right hand side of  $\kappa_\psi = 0$  (zero principal normal) line.

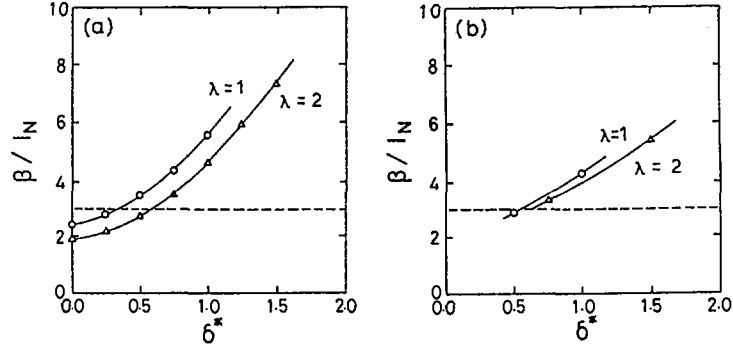


FIG. A-3. Permissible beta values normalized by  $I_n = I_p(MA)/(a(m)B(T))$  for  $n = \infty$  ballooning and (b) kink modes. In kink stability analysis, current profile is assumed as  $P' = cp_2(1 - \psi^2)\psi$  and  $TT' = cR_0^2(1 - \psi^\alpha)(t + (1 - t)\psi^2) - R_0^2P'$  ( $p_2$ ,  $\alpha$  and  $T$  are optimization parameters) for wall location of  $a_w/a = 2.0$ .

study, the  $q$ -profile is fixed at two positions only: at the centre,  $q_0 = 1.0$ , and on the surface,  $q_s = 0$ . When the same  $q$ -profile is assumed, a clearer transition to the second region of stability may be obtained.

The effectiveness of crescent shaping for low  $n$  kink modes is also clarified by using the ERATO code. Several current profile models have been taken into account to obtain optimal configurations for kink as well as Mercier and ballooning modes (Fig. A-3(b)). The coefficient  $g$  of the Troyon type beta scaling increases up to a 10 to 20% higher value for the  $\lambda = 1$  shape than for the  $\lambda = 2$  shape, by raising the triangularity of the indented shape. Higher beta values may be expected from a more accurate optimization of the profiles.

In connection with the achievement of these crescent configurations, axisymmetric mode stabilities are studied by using the linear ideal MHD code ERATO; in addition, bifurcation problems are investigated by using a full resistive MHD code [2], and transport processes accessible to the optimized profile are studied with a 1.5-D equilibrium transport code [3]; thus, the favourable stability features of crescent shapings in high beta regimes are confirmed. Several engineering merits related to this crescent shaping in reaction and ignition plasma experiments are also claimed [3, 4].

It is concluded that this crescent shaping makes the device more compact than normal dee shaping; it is supposed to be a more reliable extension, for beta enhancement, from conventional dee shaped design than is second stability bean shaping.

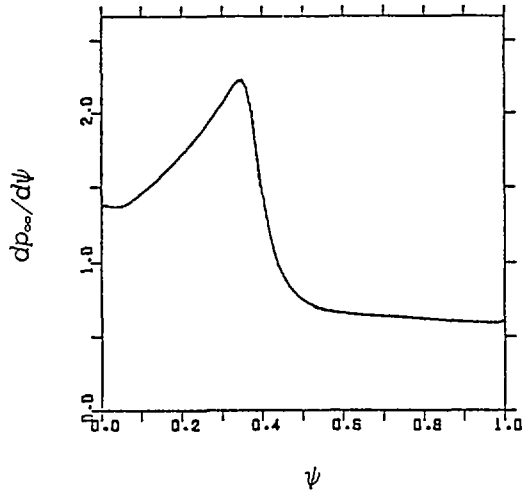


FIG. B-1. Pressure gradient versus  $\psi$  for  $A = 3$ ,  $q_0 = 1.4$ ,  $q_s = 3.1$ ,  $\kappa = 1.6$ ,  $\delta = 0.3$  and  $\beta = 8.1\%$ . Large pressure gradient is in low shear region.

## Part B

### SECOND STABILITY ACCESS IN CONVENTIONAL CROSS-SECTION<sup>4</sup>

When the region with negative local shear extends from the bad to the good curvature region, the plasma enters the second stability region for ballooning modes on magnetic surfaces with negative local shear. The local shear becomes negative more easily in a low shear and a large pressure gradient region [5]. By using this property, direct access to second stability, without passing the unstable region, can be realized for a plasma with conventional cross-section shape and  $q_0 > 1$  ( $q_0$  is the safety factor at the magnetic axis). For fixed  $q$ -profile, equilibrium is obtained by solving the Grad-Shafranov and the ballooning mode equations [6] iteratively. The ballooning mode equation determines the marginal pressure gradient,  $dp_\infty/d\psi$ , for a given equilibrium ( $\psi$  is the normalized poloidal flux). The equilibrium at the next iteration step is obtained by using the pressure gradient,  $C dp_\infty/d\psi$ . The constant  $C$  is adjusted so as to yield  $\Delta\beta = 0.2\%$ , where  $\Delta\beta$  is the increment of the volume averaged beta value. Figure B-1 shows the resulting pressure gradient of equilibria with a  $q$ -profile chosen as  $S_w = (q(\psi = 0.5) - q_0)/(q_s - q_0) \approx 0.05$ , where  $q_s$  is the safety factor at the plasma surface. In the low shear region, the pressure gradient is unlimited for ballooning modes, and the beta value increases

<sup>4</sup> T. Tsunematsu, S. Seki, M. Azumi, S. Tokuda, T. Ozeki, T. Nemoto, T. Takeda.

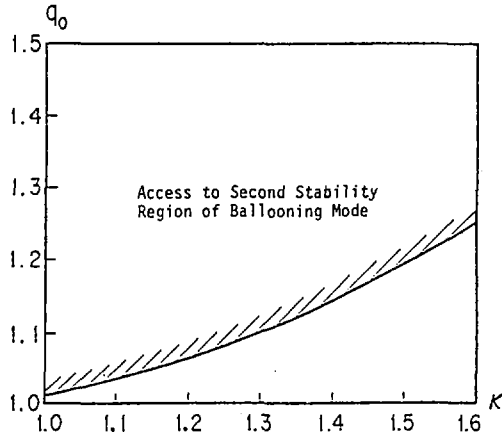


FIG. B-2. Critical  $q_0$  versus  $\kappa$  for the access to second stability region of ballooning modes.

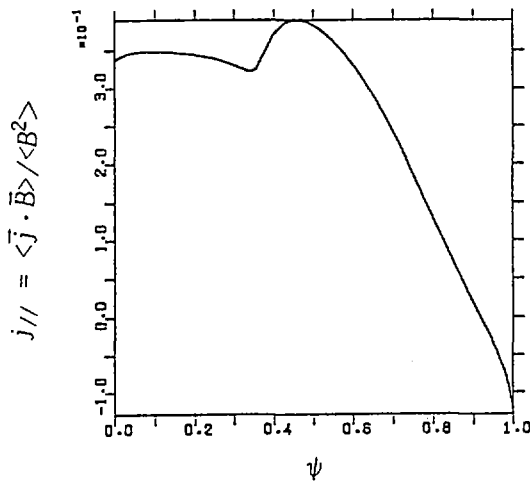


FIG. B-3. Parallel current  $j_{||} = \langle \vec{j} \cdot \vec{B} \rangle / \langle B^2 \rangle$ . Equilibrium is same as in Fig. B-1.

up to the limit of numerical accuracy of the toroidal current in the equilibrium calculation. Figure B-2 shows the critical value of  $q_0$  as a function of elongation,  $\kappa$ , for an aspect ratio of  $A = 3$  and  $q_s \approx 3.1$ . Above the critical  $q_0$ , direct access to the second stability region is possible.

For such an equilibrium, the profile of the current parallel to the magnetic field becomes hollow (Fig. B-3), which makes the stability of the external kink modes deteriorate. The stability of the  $n = 1$  external kink modes is studied

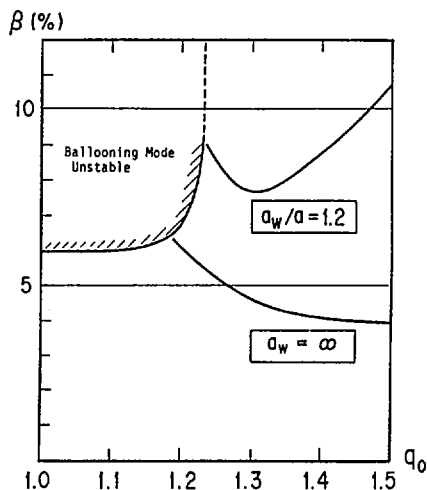


FIG. B-4. Beta limit of  $n = 1$  external kink modes versus  $q_0$  for  $\kappa = 1.6$ ,  $\delta = 0.3$ ,  $A = 3$ , and  $q_s \approx 3.1$ . In hatched region ballooning modes are unstable.

for the equilibria obtained in the analysis of the ballooning modes for the case of  $\kappa = 1.6$  and  $\delta = 0.3$ , where  $\delta$  is the triangularity. Figure B-4 shows the beta limit of the external kink modes. The upper and lower lines denote the cases of  $a_w/a = 1.2$  and  $a_w = \infty$ , where  $a_w$  and  $a$  are the horizontal radii of the conducting wall and the plasma, respectively. Because of the reduction of global shear, the beta limit decreases with  $q_0$  for the case where no conducting walls are present. When a conducting wall is placed close to the plasma surface,  $a_w/a = 1.2$ ,  $\beta \approx 11\%$  is possible for  $q_0 = 1.5$ . The beta limit due to the  $n = 1$  external kink modes is close to Troyon's beta limit,  $\beta = gI_p/aB$ ,  $\beta \approx 4\%$  for  $g = 3$  without conducting wall. A conducting wall placed at  $a_w/a = 1.2$  increases the beta limit up to  $\beta \geq 8\%$  and Troyon's  $g$  factor becomes  $g = 6-8$ . For the case of  $\kappa < 1.6$ , the factor  $g$  takes almost the same value. Above the beta limit, the dominant mode is  $m = 4$ ,  $n = 1$  for the case of no conducting walls, and the mode is localized near the plasma surface. When the conducting shell is placed at  $a_w/a = 1.2$ , the dominant component becomes  $m = 1$ ,  $n = 1$ .

By using current profile control, direct access to the second stability region of the ballooning modes is realized for plasmas with circular and dee shaped cross-sections and  $q_0 > 1$ . A plasma with  $q_0 > 1$  was shown to be possible in JT-60 experiments with clean plasmas [7] and in current drive experiments in ASDEX [8]. The ballooning modes do not limit the beta value but low  $n$  external kink modes determine the beta limit, and a conducting wall is required to increase the limit.

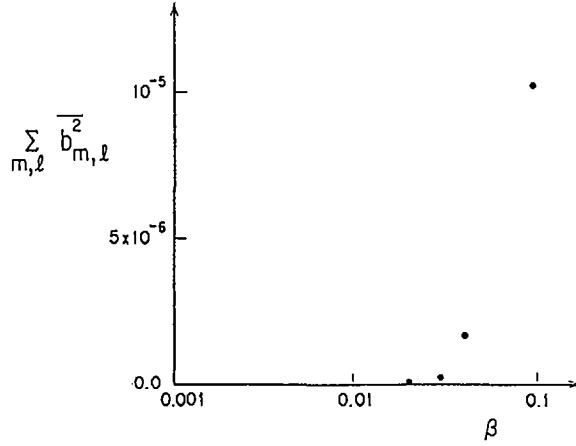


FIG. C-1. Time average of fluctuating magnetic energy versus beta value. Size of system normalized by ion gyroradius is  $16 \times 64$ , density scale-length is 100.

### Part C

#### SATURATION MECHANISM OF BALLOONING MODES<sup>5</sup>

Previous studies of the non-linear behaviour of electrostatic ballooning modes [9] are extended to the case of finite beta; the saturation mechanism and fluctuation level of the electromagnetic field are studied. We use a system of two-fluid equations with Maxwell's equation:

$$\frac{\partial}{\partial t} N = -v_* \frac{\partial}{\partial y} \Phi - v_M \frac{\partial}{\partial y} N + \frac{T_e}{eB} \{N, \Phi\} - \nu \Delta_{\perp}^2 N$$

$$\frac{\partial}{\partial t} \Delta_{\perp} \Phi = -v_M \frac{\partial}{\partial y} N - C_A^2 \nabla_{\parallel} \Delta_{\perp} A + \nu \Delta_{\perp}^2 \Phi$$

$$\frac{\partial}{\partial t} A = -v_* \frac{\partial}{\partial y} A + \nabla_{\parallel} (N - \Phi) + \frac{T_e}{eB} \{A, N\} + \eta \Delta_{\perp} A$$

$$N = \frac{\tilde{n}}{n_0}, \quad \Phi = \frac{e\tilde{\phi}}{T_e}, \quad A = \frac{e\tilde{A}}{T_e}, \quad v_* \equiv \frac{T_e}{eBL_n}, \quad v_M \equiv \frac{T_e}{eBR}$$

$$\{a, b\} \equiv \frac{\partial a}{\partial x} \frac{\partial b}{\partial y} - \frac{\partial a}{\partial y} \frac{\partial b}{\partial x}, \quad \Delta_{\perp} \equiv \frac{\partial^2}{\partial x^2} + \frac{\partial^2}{\partial y^2}$$

where  $L_n$  denotes the density scale-length.

<sup>5</sup> T. Tuda, Y. Kishimoto, T. Takeda.

For beta values below the critical value as derived by MHD analysis, the electrostatic ballooning modes are unstable, and moderate- $m$  ( $m$  is the poloidal mode number) eddies are formed. With increasing beta value, longer wavelength modes grow, and, finally, the  $m = 1$  mode dominates the other modes. Above the critical beta, magnetic fluctuations suddenly become large (Fig. C-1). Saturation occurs when the order of magnitude of the  $m = 0$  component that is excited non-linearly by the unstable modes becomes sufficiently large to cancel out the background density gradient. In the vicinity of the critical beta value, the ballooning modes degrade plasma confinement and induce a soft beta limit, but have no other effect. At higher beta values, however, they may cause a disruption of the current channel by large vortex formation.

### ACKNOWLEDGEMENTS

The authors wish to thank Dr. Y. Shimomura for helpful suggestions. They also express their gratitude to Drs M. Tanaka and M. Yoshikawa for continued encouragement.

### REFERENCES

- [1] YAMAZAKI, K., AMANO, T., NAITOU, H., HAMADA, Y., AZUMI, M., Nucl. Fusion **25** (1985) 2543.
- [2] NAKAYAMA, Y., et al., Res. Rep. HIFT-125, Hiroshima University (1986).
- [3] KITAGAWA, S., et al., in Fusion Engineering (Proc. 11th Symp. Austin, TX, 1985), Vol. 1, IEEE, New York (1986) 56.
- [4] YAMAZAKI, K., et al., Comments Plasma Phys. Controll. Fus. **10** (1986) 69.
- [5] SEKI, S., et al., submitted to Nucl. Fusion.
- [6] CONNOR, J.W., et al., Phys. Rev. Lett. **40** (1979) 396.
- [7] JT-60 TEAM, in Controlled Fusion and Plasma Physics (Proc. 12th Europ. Conf. Budapest, 1985), Vol. 1, European Physical Society (1985) 375.
- [8] McCORMICK, K., et al., in Controlled Fusion and Plasma Heating (Proc. 13th Europ. Conf. Schliersee, 1986), Vol. 1, European Physical Society (1986) 253.
- [9] TUDA, T., et al., in Plasma Physics and Controlled Nuclear Fusion Research 1984 (Proc. 10th Int. Conf. London, 1984), Vol. 2, IAEA, Vienna (1985) 179.



# STABLE TOKAMAK ACCESS TO, AND OPERATION IN, THE SECOND STABILITY REGION

A.M.M. TODD, M. PHILLIPS  
Grumman Corporation

M. CHANCE, J. MANICKAM, N. POMPHREY  
Princeton Plasma Physics Laboratory,  
Princeton University

Princeton, New Jersey,  
United States of America

## Abstract

STABLE TOKAMAK ACCESS TO, AND OPERATION IN, THE SECOND STABILITY REGION.

Tokamak operation in the second region of stability to ballooning modes holds promise for economic fusion reactor operation. A second region of stability is confirmed to exist in circular tokamaks with a nearby conducting shell for  $\epsilon\beta_\theta > 1$ . In addition to ballooning instabilities with high toroidal mode number  $n$ , the presence of low  $n$  internal pressure driven modes in low shear regions can pose serious problems for access to the second region. These modes can be present even when ballooning modes with infinite  $n$  are stable. Stable access to the second region for all ideal modes is demonstrated with current profile programming that raises the safety factor on axis above unity. Present calculations for stable access using this technique indicate that a conducting wall must be located close to the plasma edge ( $\sim 0.1$  plasma minor radius) to stabilize external modes. Pressure and shear profile optimization could be used to increase this value. As  $\epsilon\beta_\theta$  is raised above unity, the stabilizing wall can be moved to progressively larger major radii. This behavior is attributed to restabilization of the pressure driven component in low  $n$  kink modes. Finally, it is shown that poloidally discontinuous conducting structures are effective in stabilizing low  $n$  external kink modes.

## 1. INTRODUCTION

The economic advantage of high  $\langle\beta\rangle$  fusion reactor operation has long been recognized. Here,  $\langle\beta\rangle = 2\mu_0\langle p\rangle/B_0^2$ , where  $\langle\rangle$  denotes a volume average and  $B_0$  the nominal vacuum toroidal field at  $R$ , the major radius of the plasma center. It has traditionally been sought in Tokamak configurations by maximizing the  $\langle\beta\rangle$  limit through cross-sectional shaping and minimizing the aspect ratio,  $A$ . The widely used criterion for this 'first region' limit, the Troyon limit, is  $\langle\beta_T\rangle = 3 \times 10^{-8} I/aB_0$  [1]. It has been shown [2,3] that high toroidal mode number,  $n$ , ideal MHD pressure driven instabilities can restabilize at high values of  $\epsilon\beta_\theta > 1$ , giving rise to a 'second stable region' ( $\epsilon = a/R$ ,  $\beta_\theta = 8\pi \bar{p}/\mu_0 I^2$ ,  $a$  is the minor

radius,  $I$  the toroidal current,  $\bar{p}$  the cross-sectional pressure average - all units are SI). In general, a close conducting shell is required to simultaneously stabilize parallel-current-driven low- $n$  kink instabilities in this second stability region.

This paper explores the potential for high  $\langle\beta\rangle$  second stability region operation and access in moderate to large aspect ratio circular Tokamaks. Some of the benefits are that, within standard constraints such as wall loading, the higher power density second region reactor operates with significantly reduced toroidal field and current, when compared to first region Tokamak reactor concepts, or alternatively has the potential for advanced fuel operation. Additionally, a large aspect ratio circular configuration may have significant advantages from the important standpoint of accessibility and hence maintainability. The results described here span a parameter space ranging from that of the Compact Ignition Tokamak (CIT) [4] to a conceptual large aspect ratio second region experiment (SRX) [5].

## 2. SECOND REGION PARAMETER SPACE

Our parameterization of the second region boundary is not yet sufficiently comprehensive to permit the definition of an equivalent to the Troyon criterion. However, a few general remarks can be made. When the safety factor on axis,  $q_0 \sim 1$ , we find a wall stabilized second stable region when  $\epsilon\beta_\theta \sim 1.2$ . As  $q_0$  is allowed to rise above unity at fixed  $q_e$ , the edge safety factor, the first and second region  $\epsilon\beta_\theta$  boundaries shift downward in approximate proportion to  $q_0$ .

Figure 1 shows the lower bound on unstable toroidal mode numbers,  $n_c$ , using the ballooning mode formalism. It also shows the critical conducting wall location,  $(b/a)_c$  (expressed in units of the minor radius) for  $n=1$  stability. For clarity, the stability of  $n=2,3,4$  which has been calculated, is not shown. The  $n=2$  and 3 modes onset and begin to restabilize at successively higher  $\epsilon\beta_\theta$ . The first and second region  $\epsilon\beta_\theta$  boundaries for the  $n=3$  internal mode are  $\sim 0.7$  and  $\sim 1.1$  respectively. The  $n=4$  mode is stable with a wall at infinity for all  $\epsilon\beta_\theta$ . A circular  $A=9$  equilibrium sequence with  $q_0 = 1.01$ ,  $q_e = 4.1$  and  $q\alpha\psi^4$  was used for these calculations. The pressure profile was initially optimized to marginal  $n = \infty$  first region ballooning stability on all flux surfaces and then scaled to generate the  $\epsilon\beta_\theta$  variation. The purpose of Figure 1 is to illustrate that conventional ballooning theory is not a sufficient criterion for internal

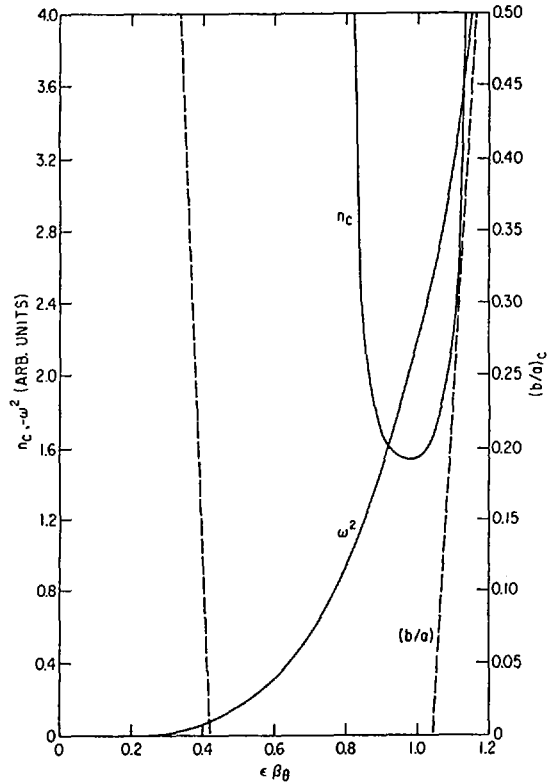


FIG. 1. Critical toroidal mode number,  $n_c$ , for ballooning stability ( $n \leq n_c$ );  $n=1$  mode growth rate,  $\omega^2$ , with a wall at infinity; and  $n=1$  mode critical conformal wall location for stability,  $(b/a)_c$ , expressed as the displacement from the plasma edge in units of the minor radius, as functions of  $\epsilon\beta_\theta$ .

mode stability, since low  $n$  modes onset long before the lower ballooning threshold and restabilize after the upper ballooning threshold. This also violates the ballooning mode picture of decreasing stability with  $n$ .

Conventional ballooning mode theory relies on an ordering where the wavelength transverse to the magnetic field is short in relation to other equilibrium variations. However, when the shear is weak, the ballooning mode ordering breaks down and a new higher order theory is required [6]. At the largest values of  $n \gg (\psi dq/d\psi)^{-2} \gg 1$ , the standard theory is recovered, but when  $(\psi dq/d\psi)^{-2} \gg n \gg 1$ , the new theory, which shows an oscillatory dependence of the growth rate  $\omega^2$  on  $1/n$ , is required (here  $\psi$  is the poloidal magnetic flux). However, when the shear is further weakened, we observe that even this theory breaks down and there is no longer a simple

behavior of the envelope of the oscillation. In particular, it is possible to have bands of instability, as  $1/n$  is varied, which do not extend to high  $n$ . Consequently, high  $n$  modes can be stabilized without stabilizing the low and intermediate  $n$  internal ballooning modes, the "infernal" modes. This situation can be remedied by increasing the shear or shifting the peak gradient in the pressure to regions of larger shear. Thus, the explicit form of the shear and pressure profiles is crucial to access and operation in the second stability region.

### 3. STABLE SECOND REGION ACCESS

Several mechanisms (see for example [5]) have been proposed for reaching the second region of stability. Here we will only consider current profile programming [7]. As  $q_0$  is raised,  $n_c$  rises, the first and second region boundaries move to lower values of  $\epsilon\beta_\theta$ , and the width of the unstable region,  $\Delta(\epsilon\beta_\theta)$ , decreases significantly. Peaking the pressure profile, flattening the safety factor profile or decreasing  $A$  will raise  $n_c$ . This dependence on  $A$  is similar to that observed when stable second region transition is obtained by indenting bean shaped plasmas. As  $A$  is increased in beans, the first and second region  $\langle\beta\rangle$  boundaries decrease and the width in  $\langle\beta\rangle$  of the unstable gap is reduced. However, the indentation required to access the second region in a stable manner increases.

Figure 2 demonstrates that stable second region transition with respect to all ideal MHD modes is possible, in principle, with current programming. A circular,  $A = 9$  equilibrium sequence with  $q_0 = 3.1$ ,  $q_0 \sim 4.1$  and  $q \sim \psi^4$  was used. The  $\epsilon\beta_\theta$  variation was generated by scaling a pressure profile  $\sim \psi^{2.5}$ . Optimization of the plasma profiles in the manner suggested above could be used to reduce the high  $q_0$  value and relax the constraint on the low  $n$  mode stabilizing wall.

We have also performed accessibility studies where the form of the pressure profile is iteratively modified to remain stable to  $n = \infty$  modes as  $\langle\beta\rangle$  is increased. When the shear near the axis is small and  $q_0 > 1.0$ , central surfaces in the low shear region are observed to have a stable transition to the second region. This leads to a centrally peaked two-region pressure profile, where a second region core is surrounded by a first region mantle, whose transition is inhibited by the peaked pressure. Such cases can be stable at twice the Troyon limit, for high and low  $n$  modes with  $(b/a)_c \sim 0.1$ . Resistive

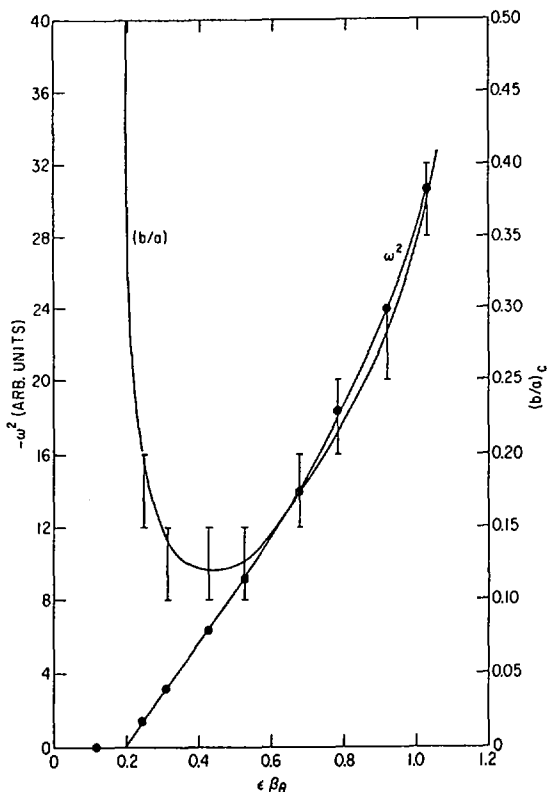


FIG. 2.  $n=1$  mode growth rate,  $\omega^2$ , and critical wall location,  $(b/a)_c$ , resolved to within 0.05, as functions of  $\epsilon\beta_\theta$ .  $n=\infty$  ballooning stability exists for all  $\epsilon\beta_\theta$ .

interchange instability near the first/second region boundary is a potential problem, since, if a resistive interchange stability requirement is included in the optimization procedure, then the central surface transition is inhibited. Alternatively, the shear profile can be adjusted to inhibit central transition and promote edge transition. We find that edge transition is difficult to achieve at high  $A$ , and at lower  $A$  it tends to be localized to the outermost flux surfaces. The transitioning region of the plasma does not propagate inwards towards the magnetic axis as  $\langle\beta\rangle$  is increased. Consequently, the edge pressure gradient grows with  $\langle\beta\rangle$  and leads to the development of unphysical profiles, as, for instance, in the case of a large parallel skin current. Similar localized edge transition is observed for  $q_0 \sim 1$ , and either high  $q_e$  ( $\sim 9$ ) circular equilibria that correspond to Tokamak Fusion Test Reactor (TFTR) supershot like parameters [8] or conventional  $q_e$  ( $\sim 3$ ) highly triangular

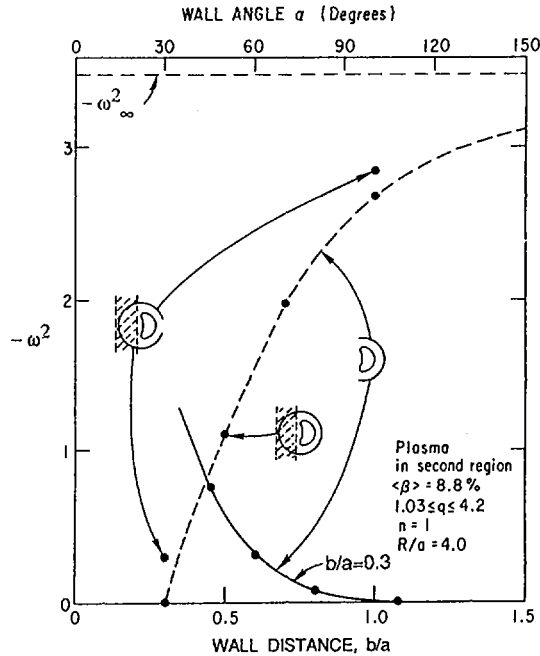


FIG. 3.  $n=1$  mode growth rate,  $\omega^2$  (solid curve), as a function of the angle,  $\alpha$ , subtended from the outboard midplane by a circular wall. The dotted curve shows the dependence on wall distance ( $b/a$ ).

and highly elongated CIT equilibria [4]. Since the local form of the shear profile is critical for transition, other transition scenarios will exist in addition to these examples.

#### 4. POLOIDALLY DISCONTINUOUS WALL STABILIZATION OF KINK MODES

Whereas the consequences of internal pressure driven modes can be minimized by tailoring the plasma profiles, low  $n$  global kink modes with significant surface perturbations require a conducting shell for stabilization. Since physical access to the plasma precludes a completely closed shell, we have calculated the effect of the presence of an axisymmetric gap in the shell. Typical results for the  $n=1$  mode are shown in Figure 3 for a bean-shaped plasma of elongation 1.38 and indentation 0.3 in the second region of stability. We see that, firstly, a partial wall at  $(b/a) = 0.3$  can stabilize the  $n=1$  mode if the angle  $\alpha$  subtended by the wall is  $\sim 100^\circ$ . Secondly, the inner major radius side of the shell plays an insignificant role in stabilization, so the hashed portions of the wall may be removed. Finally, a moderate gap on the outer major radius midplane can be tolerated.

## 5. CONCLUSIONS

Equilibria which are stable to all ideal MHD modes in the second region of stability are observed with  $\epsilon\beta_\theta > 1$ , provided a nearby conducting shell stabilizes the low  $n$  modes. Stable access to this region is not easy, but programming the current so that  $q_0 > 1$ , coupled with other access techniques [5], shows promise. Restabilization of low  $n$  as well as high  $n$  modes is observed as  $\epsilon\beta_\theta$  is increased above unity. The potential benefits of second region fusion reactor operation encourage further study of these issues.

## ACKNOWLEDGEMENTS

This work was supported by the United States Department of Energy, under Contracts Nos. DE-FG02-86ER53226, DE-FG02-86ER53222 and DE-AC02-CHO-3073, and by the Grumman Corporation.

## REFERENCES

- [1] TROYON, F., GRUBER, R., SAURENMANN, H., SEMENZATO, S., SUCCI, S., Plasma Phys. Controll. Fusion **26** (1984) 209.
- [2] STRAUSS, H.R., PARK, W., MONTICELLO, D.A., WHITE, R.B., JARDIN, S.C., CHANCE, M.S., TODD, A.M.M., GLASSER, A.H., Nucl. Fusion **20** (1980) 638.
- [3] COPPI, B., FERREIRA, A., MARK, M.W.-K., RAMOS, J.J., Nucl. Fusion **19** (1979) 715.
- [4] SCHMIDT, J., et al., Paper IAEA-CN-47/H-I-2, these Proceedings, Vol. 3.
- [5] NAVRATIL, G.A., et al., these Proceedings, Vol. 1, p. 299.
- [6] HASTIE, R.J., TAYLOR, J.B., Nucl. Fusion **21** (1981) 187.
- [7] SYKES, A., TURNER, M.F., in Controlled Fusion and Plasma Physics (Proc. 9th Europ. Conf. Oxford, 1979), UKAEA, Culham Laboratory, Abingdon (1979) 161.
- [8] HAWRYLUK, R.J., et al., these Proceedings, Vol. 1, p. 51.



## ELLIPSOIDAL SHELL TOKAMAK

F.J. HELTON, Mingsheng CHU,  
 J.M. GREENE, R.W. HARVEY, J.K. LEE,  
 T. OHKAWA, P.A. POLITZER  
 GA Technologies Inc.,  
 San Diego, California,  
 United States of America

*Presented by T. Amano*

### Abstract

#### ELLIPSOIDAL SHELL TOKAMAK.

The paper describes a novel toroidal plasma configuration, taking the shape of an elongated ellipsoidal shell, and some features of a realizable tokamak design which has been developed from it. The ellipsoidal shell tokamak (EST) has favourable high pressure MHD stability properties for a wide variety of shell geometries. Highly elongated tokamaks also have the possibility of achieving ohmic ignition at moderate toroidal field and moderate size. When the safety factor is held fixed, the current density is proportional to elongation and so the required high heating power density can be obtained. Empirical transport scaling laws indicate that ignition may be achieved at a range of aspect ratios, with a moderate plasma minor radius, using a feasible magnetic field. The considerations leading to the choice of an ellipsoidal shell configuration — the equilibrium and ballooning stability properties, global MHD stability, thermal instability and possible mitigating factors — are discussed and the parameters of a sample design for a modest proof-of-practicality EST are presented. The critical issues for the EST involve its behavior under transient conditions. It is important to determine whether the plasma configuration can be established quiescently and whether it can be sustained stably by active shape and position control.

### INTRODUCTION

This paper describes a novel toroidal plasma configuration and some features of a realizable tokamak design which has been developed from it. In this configuration the plasma takes the shape of an elongated ellipsoidal shell. The ellipsoidal shell tokamak (EST) has favorable high pressure MHD stability properties for a wide variety of shell geometries.

Highly elongated tokamaks also have the possibility of achieving ohmic ignition at moderate toroidal field and moderate size [1]. When the safety factor is held fixed, the current density is proportional to elongation, so the required high heating power density can be obtained. Empirical transport scaling laws indicate that ignition may be achieved

at a range of aspect ratios,  $3 \leq 1/\epsilon \leq 7$ , with a moderate plasma minor radius,  $a \cong 0.25$  m, using a feasible magnetic field,  $B_T \leq 6$  T.

We discuss the considerations leading to the choice of an ellipsoidal shell configuration, the equilibrium and ballooning stability properties, global MHD stability, thermal instability and possible mitigating factors, and present the parameters of a sample design for a modest proof-of-practicality EST.

## PLASMA SHAPING

The limitation on current density at the magnetic axis for which a favorable average magnetic well can be obtained (the Mercier criterion) is one of the constraints that suggests the geometry of this device. This limitation is relaxed by increasing the triangularity of the plasma shape. For the highly shaped EST devices, it is desirable to recast the triangularity in terms of the shape of the surface defined by the vanishing of  $B_z$ . If the radius of curvature of this surface is denoted by  $R_T$ , then in the usual notation [2]

$$\frac{R}{R_T} = \tau + \frac{1}{1 + 3\kappa^2} \left[ 1 + 2 \frac{1 + \kappa^2}{\kappa^2} \beta_p \right]$$

where  $R$  is the major radius of the magnetic axis, and  $\tau$  is the triangularity. In terms of  $R_T$ , the Mercier stability criterion is

$$\frac{\kappa^2}{(1 + \kappa^2)^2} \frac{R^2 \mu_0^2 j_\phi^2(0)}{B_0^2} = \frac{1}{q_0^2} < \frac{2}{1 + \kappa^2} - \frac{2(\kappa - 1)}{\kappa^2(\kappa + 1)} \beta_p + \frac{\kappa^2 - 1}{\kappa^2 + 1} \frac{R}{R_T}$$

where  $j_\phi(0)$  is the toroidal current density at the magnetic axis. With highly elongated shapes,  $q_0$  can be as small as unity when  $R_T = R$ . With this condition,  $B_z$  vanishes on a section of the surface of a sphere, leading naturally to a plasma which takes the shape of a section of a spherical shell and a device in which the vacuum chamber and poloidal field-shaping coil systems also conform to the spherical shell configuration. In practice, the shape can be relaxed to a prolate ellipsoid (e.g. 3:2 axis ratio —  $R_T = 9/4 R$ ), without undue degradation of the overall stability estimates.

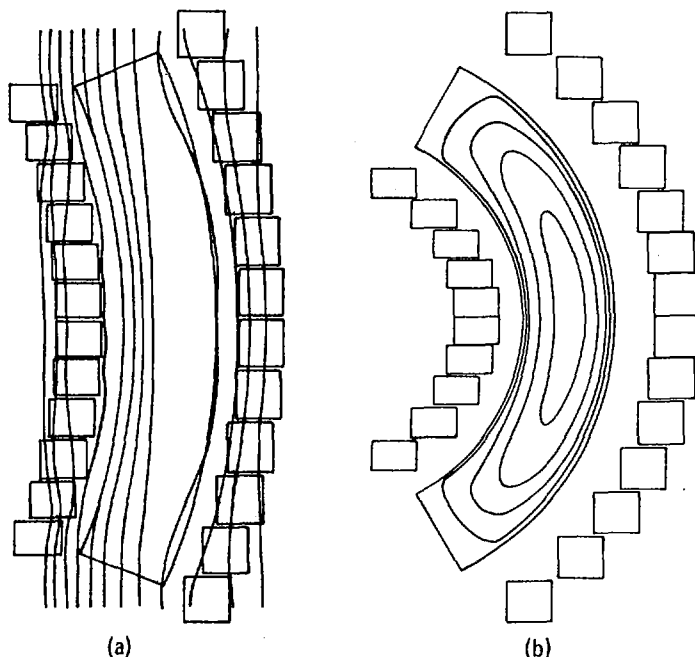


FIG. 1. (a)  $|B|$  contours for an EST plasma shape.  
 (b) EST equilibrium stable to ballooning and Mercier modes at 45%.

Ballooning mode instabilities are stabilized by strong magnetic shear and by reduction of the geodesic curvature. For a thin spherical shell, extending in latitude from  $-\theta_{\max}$  to  $+\theta_{\max}$ , geodesic curves are great circles. However, the safety factor is restricted to  $q(a) \leq 1$ , the equality holding for the geodesic field line that just reaches the top (maximum latitude) of the plasma and passes from the outer surface of the shell to the inner surface. The generalization to a thin ellipsoidal shell permits higher, tokamak-like values of  $q(a)$  — the maximum value of  $q$  depends on the elongation of the ellipsoid and on the maximum latitude of the shell plasma.

Minimizing geodesic curvature maintains nearly constant  $|B|$  on the outer magnetic surface. This partial omnigenicity arises because of the interplay between the variation of the toroidal field with major radius and the variation of the poloidal field with both major radius and vertical position. The major variation in  $|B|$  is at the top and bottom of the plasma, due to the finite thickness [see Fig. 1 (a)] of the shell. Using this property, the EST plasma shape should provide the possibility of improved confinement.

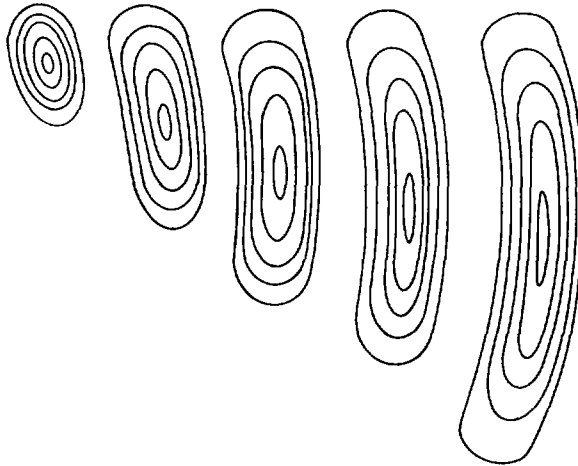


FIG. 2. Sequence of asymmetric equilibria demonstrating the startup of a  $\kappa = 6$  EST tokamak.

## EQUILIBRIUM AND BALLOONING STABILITY

Analysis of EST equilibria indicates that they are stable to ballooning and Mercier modes at very high  $\beta$ , without fine-tuning of the plasma shape. These equilibria can be obtained for a broad range of current profiles. Varying the width of the current profile from flat to ohmic changes the limiting  $\beta$  ( $\equiv \beta_c$ ) by less than a factor of 2. There are EST equilibria with  $\beta_c$  as high as 45% [see Fig. 1 (b)]. When EST equilibria are optimized, the shape becomes slightly pointed and there is a small increase in  $\beta_c$ , in agreement with the work of Todd and Phillips [3]. The equilibria are established with the limiters, flux loops, and field-shaping coils lying on nested ellipsoids, with corresponding flux loops and coils on orthogonal hyperboloids. The solutions are robust, that is they are not sensitive to small changes in plasma current or in the control flux values at the field-shaping coils.

We have obtained a sequence of asymmetric equilibria (see Fig. 2) which demonstrates the startup of a highly elongated tokamak [4]. These equilibria are limited by a physical limiter at the top of the resistive vacuum tank and a poloidal field null (divertor) at the lower side. By proper positioning of the the field null, the plasma evolves from low ( $\kappa \cong 2$ ) to high ( $\kappa \cong 6$ ) elongation on the time-scale given by the resistive tank.

We have compared the EST with equivalent racetrack and elliptical configurations. Racetrack equilibria have been obtained for  $\kappa \leq 11$ , but it is difficult to obtain any racetrack above  $\kappa = 7$ , and very flat current profiles are required as the elongation increases. The solutions are not robust and can have multiple magnetic axes. The non-existence of robust solutions is probably a consequence of the increased elongation of the central flux surfaces of the straight tokamak as compared to the EST. The racetrack solutions cannot be made stable to ballooning and Mercier modes at high  $\beta$  without fine-tuning the field-shaping coils. When the elliptical and racetrack equilibria are optimized the shapes become more EST-like. When elliptical and racetrack equilibria with the same plasma current (1.0 MA), aspect ratio (6.0), area and current half-width were optimized to ballooning and Mercier modes, the ballooning  $\beta$  of the elliptical equilibrium exceeded that of the racetrack equilibrium by a factor of 5.0.

## GLOBAL MHD STABILITY

Pressure and current driven global MHD instabilities for highly elongated tokamaks were analyzed using the initial value code CART [5] and the ideal stability code GATO [6].

The CART code employs the reduced tokamak equations in a Cartesian coordinate system. The CART results show that for a  $\kappa=6$  EST example the  $n=0$  mode can be stabilized with a conducting wall at  $0.3a$  while the  $n=1$  mode can be stabilized only with a very close conducting wall. For a  $\kappa=6$  racetrack the  $n=0$  mode can be stabilized with a conducting wall at  $0.3a$ , but the  $n=1$  and  $n=2$  modes cannot be stabilized even with a wall at the plasma boundary. For this fixed boundary case a double tearing mode was observed with a small growth rate. We have also analyzed the quasilinear evolution of the modes with  $n = 0, 1, \text{ and } 2$ .

Various stabilizing schemes were considered using CART. A toroidal limiter covering 20% of the poloidal plasma circumference reduces the growth rate by a factor of five for both  $n=0$  and  $n=1$  modes. The axisymmetric mode with  $n = 0$  is a shifting mode (see Fig. 3), generating perturbed flow pointing vertically upward in the plasma central region. It is more strongly stabilized by placing a conducting wall at the outboard side than at the top-bottom side. The ideal mantle with infinite conductivity does not significantly affect the  $n=0$  mode. It reduces

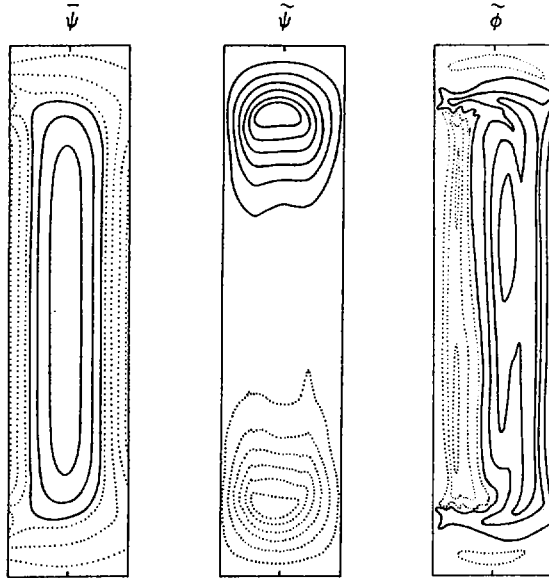


FIG. 3.  $n = 0$  shifting mode for a  $\kappa = 6$  racetrack equilibrium.

the growth rate of the  $n=1$  mode only slightly; the extent of the reduction depends on the open magnetic field configuration in the mantle region.

Ideal MHD kink instabilities for highly elongated tokamaks were analyzed using GATO. The  $n=0$  results for the  $\kappa=6$  EST were consistent with the CART results. The axisymmetric mode with  $n = 0$  is also a shifting mode for the EST. The position of the wall necessary to stabilize the  $n=0$  kink mode for an EST with  $\kappa = 6$  is greater than  $0.3a$ , except at low  $\beta_p$  and peaked current profile. We were not able to stabilize the  $n=0$  kink mode for a  $\kappa=6$  tokamak with an approximate racetrack plasma shape. The racetrack results are in agreement with other results [7] obtained for  $\kappa=3$  racetracks. Our equilibrium calculation is free boundary; it is possible to triangulate an approximate racetrack and stabilize the  $n=0$  kink mode with a very close wall.

## THERMAL INSTABILITY AND TRANSPORT

A major concern for EST plasmas is the ohmically driven thermal instability which can lead to central peaking of the current profile. This,

in turn, may prevent the stationary maintenance of elongated equilibria. We have carried out transport code simulations of the evolution of the current, and the central peaking is inhibited by several mechanisms. As usual in tokamaks, we assume a sawtooth instability when  $q(0) < 1$ , which flattens the profiles. This process is sufficient to prevent thermal instability if the equilibrium flux surfaces are assumed to be fixed ellipses.

However, in the EST equilibria, the  $q$ -values are observed to actually rise near the magnetic axis, being dominated by the flux surface shape rather than by the current profile. In the absence of the  $q < 1$  sawtooth instability, two further mechanisms are invoked to prevent the thermal instability. At low plasma density, MHD studies indicate that the  $n=1$  and higher  $n$  modes can be located well inside the plasma surface. These modes are taken to have current profile flattening effects equivalent to the sawtooth instability. In addition, at sufficiently high density but still below the Murakami limit, there is a regime of dominance of the ion neoclassical transport over the conventional empirical transport. The close coupling of the electrons and ions and the  $(1/r)^{3/2}$  variation of the ion diffusion coefficient give thermal stability.

## SAMPLE DESIGN

Figure 4 illustrates an engineering design for an ellipsoidal shell tokamak. The plasma shell is a portion of a prolate ellipsoid with a 3:2 ratio of axes. Thus, for the major radius of 0.69 m, the radius of curvature is 1.50 m.

A typical  $q$ -profile for an EST is inverted: it is maximum on axis, decreases to the minimum close to the limiter and then increases toward the limiter. When the current half-width of this equilibrium was varied from flat to ohmic,  $\beta_c$  decreased by less than 50%.

## SUMMARY

These analyses indicate that there are significant benefits inherent in the EST configuration. It provides the possibility of stable, high pressure plasmas, as well as the prospect of ignition with ohmic heating alone at feasible magnetic field strengths. The critical issues for the

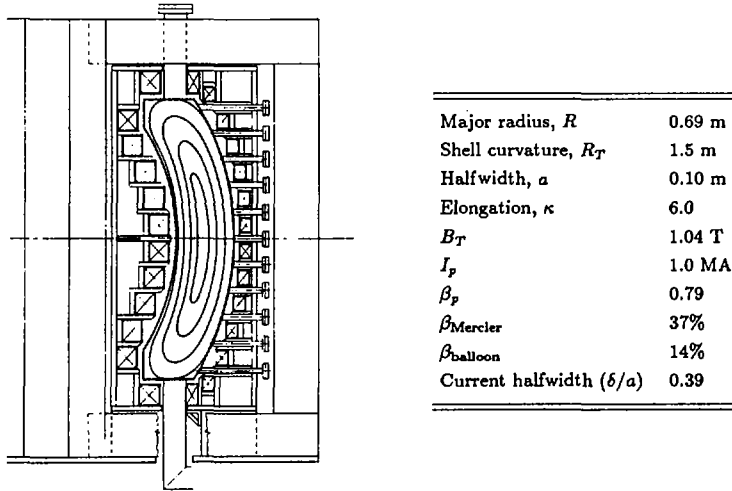


FIG. 4. Engineering design for an EST and typical  $q$ -profile for an EST equilibrium.

EST involve its behavior under transient conditions. It is important to determine whether the plasma configuration can be established quiescently and if it can be sustained stably by active shape and position control.

### ACKNOWLEDGMENT

This is a report of work sponsored by the U.S. Department of Energy under Contract No. DE-AC03-84ER53158 and by GA Technologies Inc.

### REFERENCES

- [1] CHU, M.S., HARVEY, R.W., POLITZER, P.A., YAMAGISHI, T., Nucl. Fusion 25 (1985) 835.
- [2] WEIMER, K., FRIEMAN, E., JOHNSON, J.L., Plasma Phys. 17 (1975) 645.
- [3] TODD, A.M.M., M.W. PHILLIPS, Bull. Am. Phys. Soc. 30 (1985) 1424.
- [4] MARCUS, F.B., JARDIN, S.C., HOFMAN, F., Phys. Rev. Lett. 21 (1985) 2289.
- [5] LEE, J.K., Phys. Fluids 29 (1986) 1629; Nucl. Fusion 26 (1986) 955.
- [6] BERNARD, L.C., HELTON, F.J., MOORE, R.W., Comp. Phys. Comm. 24 (1980) 377.
- [7] HOFMAN, F., MARCUS, F.B., TURNBULL, A.D., Plasma Phys. and Cont. Fusion 28 (1986) 705.

## MHD STABILITY IN LOW-ASPECT-RATIO TOKAMAKS\*

B.A. CARRERAS, L.A. CHARLTON<sup>1</sup>, J.T. HOGAN,  
J.A. HOLMES<sup>1</sup>, E.A. LAZARUS  
Fusion Energy Division,  
Oak Ridge National Laboratory,  
Oak Ridge, Tennessee,  
United States of America

W.A. COOPER  
Centre de recherches en physique des plasmas,  
Ecole polytechnique fédérale de Lausanne,  
Lausanne, Switzerland

T.C. HENDER  
UKAEA, Culham Laboratory,  
Abingdon, Oxfordshire,  
United Kingdom

### Abstract

#### MHD STABILITY IN LOW-ASPECT-RATIO TOKAMAKS.

Interest in tokamak configurations with high beta has led to renewed study of low-aspect-ratio tokamaks. The paper presents a quantitative estimate of the MHD  $\langle \beta_{\text{crit}} \rangle$  predicted for such configurations, with emphasis on experimentally feasible cases. Ideal MHD stability calculations, extending previous results to the regime with aspect ratio less than 2.5, show that stability follows the Troyon semi-empirical scaling law. We find this scaling law to be a reliable theoretical guide in the search for high beta configurations at low aspect ratio. Ideally, stable equilibria with  $\langle \beta \rangle \sim 40\%$  are found at an aspect ratio of 1.67. These calculations employ high-resolution equilibria to examine axisymmetric, low- $n$  ( $n \leq 3$ ), and infinite- $n$  ideal modes. Nonlinear resistive tearing mode calculations show that decreasing aspect ratio also leads to a reduction in the predicted saturation levels of  $m = 2/n = 1$ ,  $m = 3/n = 2$  islands and in their overlap region. The  $m = 1/n = 1$  reconnection time has been found to increase as the aspect ratio is reduced, leading to the possibility of sawtooth stabilization at low aspect ratio and high temperature.

---

\* Research sponsored by the Office of Fusion Energy, United States Department of Energy, under Contract No. DE-AC05-84OR21400 with Martin Marietta Energy Systems, Inc.

<sup>1</sup> Computing and Telecommunications Division, Martin Marietta Energy Systems, Inc.,

## 1. EQUILIBRIUM PROPERTIES OF LOW-ASPECT-RATIO CONFIGURATIONS

Many of the significant features of low-aspect-ratio equilibria have been pointed out by Peng and Strickler [1], who found a number of distinguishing properties:

- There is a natural shaping effect, so that little additional explicit external shaping current is needed to produce highly elongated shapes.
- The *magnetic* aspect ratio (defined as the ratio of poloidal to toroidal magnetic field at the periphery) is characteristically much larger in a low (geometric) aspect ratio tokamak than it is in a conventional tokamak with the same safety factor.
- The strongest differences in magnetic aspect ratio between low and high geometric aspect ratio tori are predicted to occur for  $A \leq 2.5$  (where the geometric aspect ratio  $A \equiv R/a$ ;  $R$  is the major and  $a$  the horizontal minor radius of the tokamak).

These attributes have some immediate implications for MHD stability:

- The absence of an externally applied quadrupole field for an elongated low- $A$  plasma means that the field index is 0; hence, axisymmetry will be improved relative to conventional tokamaks, in which this index is negative for elongated configurations.
- Since the magnetic aspect ratio is proportional to the well-known Troyon  $\beta$  scaling parameter  $I_p/aB_T$ , both empirical scaling and existing calculations lead us to expect improved stability at low  $A$ .
- Existing stability calculations (covering only  $A \geq 2.5$  in a systematic way) are not adequate to establish meaningful quantitative  $\langle\beta\rangle$  limits, since the major differences in magnetic aspect ratio occur for lower geometric aspect ratio.

The goal of our calculations is to make a quantitative estimate of the limiting  $\langle\beta\rangle$  values in low- $A$  tokamaks, with some important constraints.

We wish to consider cases for which the marginal  $\beta$  value does not lie at the extreme of tokamak operation; in such cases the confinement deterioration and increased disruptivity associated with  $q$  or density limits can either hinder the experimental study of the  $\beta$ -limiting physics or even prevent entirely the attainment of the theoretically expected  $\beta_{crit}$ . Our emphasis is thus placed on experimentally realizable cases: we require that the boundary safety factor lie in the range 3–4, we seek to minimize the central safety factor to coincide with the experimental observation that discharges with  $q(0) \sim 1$  are often observed, and we require that the shapes be compatible with those which can be constructed from realistic external shaping and OH coil sets. To support the last requirement and to provide a detailed basis for the stability analysis described here, we have extended the equilibrium work reported in Ref. [1].

A survey was carried out with the free-boundary EFIT code [2], including the effects of the Ohmic solenoid and of the finite size of the poloidal coil set. The equilibrium survey shows that the “natural” elongation is

dependent on the value of  $A$  and on the higher order fields applied. For example,  $\kappa_{\text{natural}} = 1.7$  at  $A = 1.67$ , with zero applied quadrupole field. Of relevance to non-axisymmetric stability, a large range of plasma shapes has been produced, with elongation  $\kappa$  up to 2.7, and triangularity  $\delta$  up to 0.5, for the specific case  $A = 1.67$ .

## 2. IDEAL MHD STABILITY

The results of a number of limiting  $\beta$  experiments are represented by the Troyon semi-empirical formula [3], which is based on ideal MHD stability calculations and predicts a strong improvement in  $\beta_{\text{crit}}$  as aspect ratio decreases. The improvement of ideal MHD  $\beta$  limits with decreasing aspect ratio has been regarded as "simple and predictable" for some time [4].

Our approach to investigating  $\beta$  limits for low  $A$  is to follow the trends suggested by the Troyon scaling law and to choose the direction for further improvement from its predictions. Thus, we begin by performing an aspect ratio scan, making the first systematic MHD stability study in the regime with  $A \leq 2.5$ , while keeping both the shape and the profiles fixed. Then, adopting an aspect ratio which is as low as possible, but still feasible for experimental implementation, we fix both the aspect ratio and the profiles to explore the detailed dependence of high- $n$  stability on plasma shaping. With this information, we proceed to our goal of estimating the maximum  $\langle \beta \rangle$  attainable with realistic values for both  $q_{\text{edge}}$  and  $q(0)$ .

Detailed calculations showing the general improvement of  $\beta_{\text{crit}}$  with decreasing  $A$  have, for example, been presented by Todd et al. [4] for  $A \geq 2.5$ . A summary of other recent work in low  $A$  stability is presented in the Proceedings of the IAEA Specialists' Meeting on Tokamak Concept Improvements [5]. In particular, we note that Degtyarev et al. report a degradation of  $\beta_{\text{crit}}$  compared with the Troyon parametrization for  $q_{\text{edge}} \leq 3$ .

Adopting the representation used by Troyon et al. for the JET configuration ( $\kappa = 1.68$ ,  $\delta = 0.3$ ) as a starting point, we have carried out the aspect ratio survey to explore the regime  $A \leq 2.5$ , with fixed shape, and pressure and  $q$  profiles. The aspect ratio scan includes an examination of axisymmetric ( $n = 0$ ) and low- $n$  free-boundary modes (for  $n \leq 3$ ), as well as fixed-boundary infinite- $n$  ballooning and Mercier modes.

The pressure and rotational transform profiles used for this study are those optimized by Troyon et al. for the JET analysis:

$$p = p(0) (1 - 0.2\psi - 2.6\psi^2 + 1.8\psi^3) \quad q = 1.62 \frac{1 + 1.95\rho^6}{1 + 0.6\rho^2}$$

where  $\psi$  is the (normalized) poloidal flux and  $\rho$  is the effective plasma radius ( $\sim (\text{volume})^{1/2}$ ). Since such a parametrization would lead to large edge current densities at low aspect ratio if applied literally, a local modification to  $q$  is made, which does not affect the central or edge  $q$  values, to null the current density at the edge.

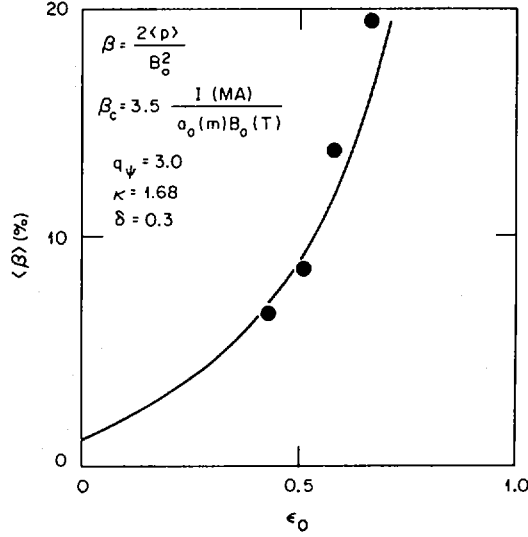


FIG. 1. Dependence of  $\beta_{\text{crit}}$  on inverse aspect ratio, following Troyon et al. [3].

We find that (Fig. 1.):

- a. The Troyon scaling law is a good extrapolation at low aspect ratio for  $q_{\text{edge}} = 3$ . The predicted  $\beta$  scaling agrees well with the numerical results. (The numerical coefficient is found to be somewhat larger than the value in [4], 0.035 rather than 0.027.) As no optimization was done at each  $A$ , the scaling law may be an underestimate.
- b. The  $\beta_{\text{crit}}$  values increase sharply with decreasing aspect ratio, especially for  $A \leq 2.5$  (in Fig. 1,  $\epsilon$  is the inverse horizontal aspect ratio  $a/R$ ).

As described earlier, we now fix the aspect ratio corresponding to the highest  $\beta$  from this scan, at  $A = 1.67$ , and carry out a study of the effects of plasma shape, with fixed profiles. This is intended to quantify the effect of increased  $\kappa$  and  $\delta$  on high- $n$  ballooning stability at this aspect ratio. Figure 2 shows the calculated dependence of  $\beta(0)_{\text{crit}}$  (for infinite- $n$  modes) on elongation for  $A = 1.67$ . For these profiles,  $\langle \beta \rangle \sim 1/2 \times \beta(0)$ . Two values of triangularity are shown:  $\delta = 0.3$  (the previous JET case) and  $\delta = 0.13$ , near the "natural" shape at low aspect ratio. Two features of special significance for our goal are that:

- $\beta_{\text{crit}}$  shows a weak optimum as a function of  $\kappa$ . (It should be borne in mind that, since we have not optimised the profiles, the  $\beta_{\text{crit}}^{\text{max}}$  versus  $\kappa$  curve could have a slightly different dependence than the one shown here for fixed profiles.)
- There is a decided improvement in  $\beta_{\text{crit}}$  with increasing  $\delta$  at a fixed elongation.

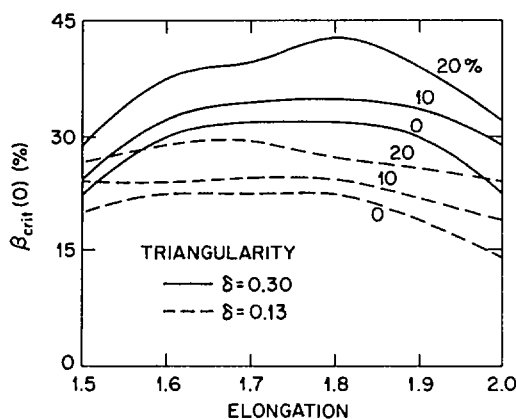


FIG. 2. Dependence of infinite- $n$   $\beta_{crit}$  on elongation for  $\delta = 0.13$  and  $0.30$ . The scan is taken with fixed aspect ratio and profiles. Curves are shown for the marginal case (0% unstable volume) and for the 10% and 20% unstable volume cases.

Thus, following the scaling law predictions, the route to higher  $\beta$  lies in the direction of increasing the triangularity.

Figure 2 exhibits the marginal case (no unstable volume,  $\beta = \beta_{crit}$ ) as well as cases with 10% and 20% ballooning unstable volume. According to the Connor-Taylor-Turner soft- $\beta$  limit picture [6], the high- $n$  unstable volume can be modelled as an effective reduction in energy confinement time, so that these curves could represent the  $\beta_{crit}$  attainable with, respectively, 10% and 20% more heating power than that required for the marginal case.

Although fixed-boundary equilibria have been used as input to these infinite- $n$  stability calculations, detailed free-boundary equilibria (including the effects of the OH solenoid and finite-size coils) have been found for configurations approximating those described here with  $A = 1.67$ .

The high- $n$  ballooning results suggest increasing the triangularity. Following this approach, the stable ( $\beta$ ) values at  $A = 1.67$  have been extended to the 40% range. We have used a  $q$ -profile similar to that in the original JET case,  $q = 1.61 + 1.89 \cdot \chi^{1.2}$  ( $q(0) = 1.61, q_{edge} = 3.5$ ). For a specific case the geometric parameters are  $\kappa = 2.35$ ,  $\delta = 0.55$ , and  $A = 1.67$ , and  $\langle \beta_{crit} \rangle = 41\%$ . A different parametrization of the pressure profile was required to reach this  $\beta$  value:

$$p = p_0 \left( e^{-(\chi/a)^2} - e^{-(1/a)^2} \right)$$

where  $a = 1.2$  and  $\chi$  is the toroidal flux normalized to the value at the edge. This configuration is stable to ideal low- $n$  modes with  $n \leq 3$ , to axisymmetric modes, and to high- $n$  ballooning modes. The equilibrium was computed with the ISLAND free boundary code, and low- $n$  stability was studied with the ERATO code.

The  $q$ -profile used for the cases thus far described, although widely used in MHD optimization studies, falls somewhat short of our goal, in

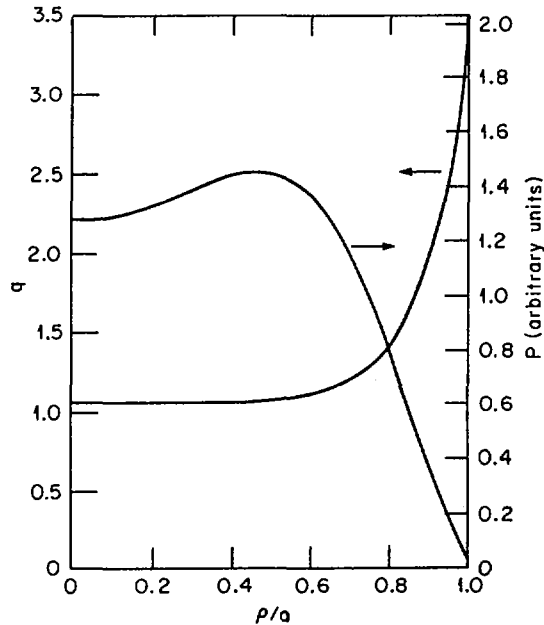


FIG. 3. Pressure and  $q$ -profiles for the  $\langle\beta\rangle = 20\%$  stable case, with  $A = 1.67$ .

that  $q(0) \geq 1.5$ . We have found, though, that this constraint can be relaxed by profile optimization. Stable  $\langle\beta\rangle = 20\%$  cases have been found with  $1.05 \leq q(0) \leq 1.5$ . Again, for a specific  $\langle\beta_{\text{crit}}\rangle = 20\%$  case, the geometric parameters are  $\kappa = 2$ ,  $\delta = 0.4$ , and  $A = 1.67$ . The pressure profile is broader, and the  $q$ -profile satisfies the criteria for our study,  $q_{\text{edge}} = 3.5$  and  $q(0) = 1.05$ :

$$p = p(0) [(1 - \psi^{2.5}) + 10\psi^3(1 - \psi)^{1.75}]$$

$$q = q(0) - (q(0) - q_{\text{edge}})\psi^8$$

The pressure and  $q$ -profiles for this case are shown in Fig. 3, and the corresponding flux surfaces are presented in Fig. 4. The equilibrium used was obtained from the Jardin-Monticello code [7], and ideal stability was determined from PEST 2 [8].

Thus, following the Troyon scaling formula, we have been led to discover a very promising direction for enlarging the  $\beta$ -stable tokamak operating regime with experimentally feasible configurations. The fact that ultra-high  $\beta$ -values can be found by following Troyon scaling, using the Troyon JET  $q$ -profile, means that there is substantial flexibility in the range of acceptable  $q$ -profiles which will produce  $\langle\beta_{\text{crit}}\rangle$  in the range of 20 to 40% for low aspect ratio.

We further note that these configurations fill the region inside the toroidal field coils relatively efficiently and thus do not provoke questions

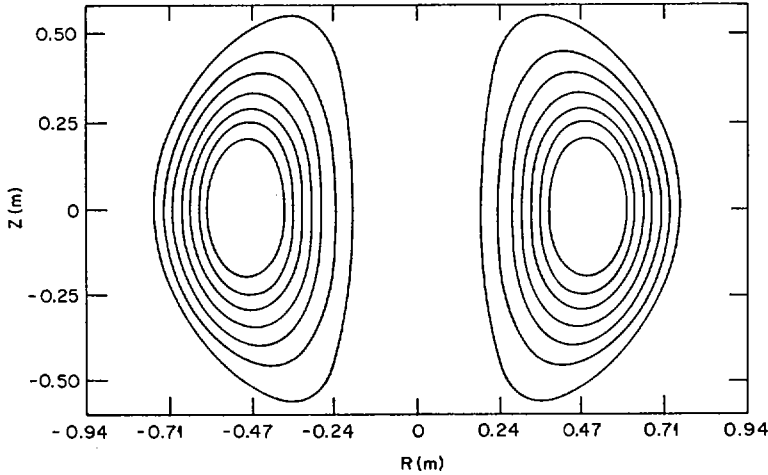


FIG. 4. Poloidal flux contours for the case in Fig. 3, showing the compactness of the configuration.

concerning the relevant definition of the (ultimately economic) value of  $\beta$ , as do more highly distorted shapes which do not effectively fill the magnetic volume.

### 3. AXISTABILITY

Attention is drawn to the fact that the stability studies described in Section 2 all include  $n = 0$  stability. The qualitative expectations noted in our discussion of equilibrium results in Section 1 have been borne out by detailed calculation. That is, axistability is improved at low aspect ratio.

### 4. TEARING STABILITY

The current density profiles used in the foregoing ideal stability calculations are relatively broad and, from the perspective of cylindrical calculations [9], might be considered liable to strong tearing instability and hence to disruption. Fully toroidal calculations show, however, that tearing stability actually improves in many respects with decreasing aspect ratio.

Linear calculations of the tearing growth rate of an  $m = 2/n = 1$  dominated eigenfunction show a weak equilibrium-induced stabilizing effect of increasing toroidicity on the current density profile. This favorable low-aspect-ratio effect competes with the potentially unfavorable development of coupling to toroidicity-induced satellite modes. Nonlinear studies have been carried out for a circular cross section using the full set of MHD equations, in toroidal geometry, with a nonlinear version of the FAR

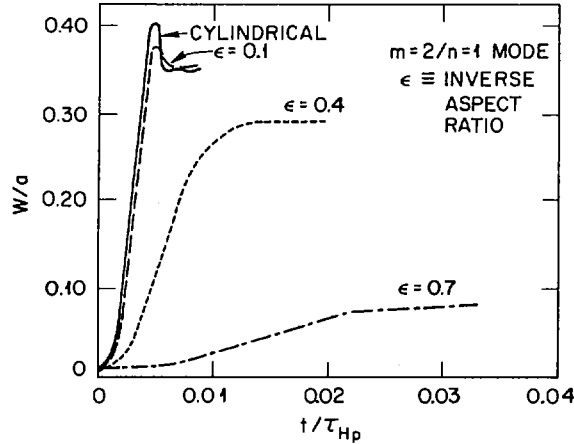


FIG. 5. Time evolution of the  $m = 2/n = 1$  island width for various aspect ratios.  $S = 10^5$  for his case.

code [10]. The calculations employed an incompressible model. Figure 5 shows the variation with  $\epsilon$  ( $\equiv A^{-1}$ ) of the  $m = 2/n = 1$  island width. We find a significant reduction in saturated island width with decreasing aspect ratio. This reduction is actually accompanied by an increase in the toroidally generated satellite activity. The low- $A$  improvement in the single-island-dominated result for the  $m = 2/n = 1$  mode is also found for the  $m = 3/n = 2$  behavior. Our nonlinear calculations show that the overlap volume is significantly reduced for lower aspect ratio. The simultaneous reduction of the island extent for these modes suggests an improved “disruption immunity” at low aspect ratio.

The deleterious effects of the  $m = 1/n = 1$  “sawtooth” instability are familiar, and the behavior of this mode assumes greater importance at low- $A$  with the discovery of high ideal MHD  $\beta_{\text{crit}}$  values, with  $q(0) \sim 1$ . At high temperature, as the resistive kink growth rate is slowed, recent linear calculations [11] show that a transition to a tearing-dominated situation is expected to occur, as the Lundquist number ( $S \equiv \tau_{\text{resistive}}/\tau_{\text{Alfvén}}$ ) increases, and as  $A$  decreases. In this case, the  $m = 1$  tearing mode is the relevant instability. We have examined the nonlinear behavior of the resistive  $m = 1/n = 1$  instability at different aspect ratios. The calculations were done with the full resistive nonlinear MHD equations, for a zero- $\beta$ , incompressible toroidal model. The configuration is circular, with a conducting wall on the surface. The profile has  $q(0) = 0.9$  and  $q_{\text{edge}} = 2.3$ . The computed prediction for the time required for the  $m = 1/n = 1$  mode to reconnect increases by a factor  $\sim 7$  as the aspect ratio in the calculation is decreased from 10 to 1.4, for  $S = 10^5$ . The trend is to longer reconnection time for the tearing mode as aspect ratio is reduced. The nonlinear calculations thus suggest that the  $m = 1/n = 1$  tearing mode could actually be stabilized at low aspect ratio, hence producing complete sawtooth

stabilization. It is important to note, however, that compressibility effects could modify these results.

The overall trend for resistive stability is a broadening of the operational regime, decreasing the likelihood of disruptions, as the aspect ratio is lowered.

## 5. SUMMARY

Quantitative estimates of the theoretically expected  $\langle \beta_{\text{crit}} \rangle$  in the low-aspect-ratio regime are quite favorable. Prospects for the experimental exploration of this area are encouraging. Both ideal and resistive stability are found to be improved for  $A \leq 2.5$ , and values of  $\langle \beta_{\text{crit}} \rangle$  in excess of 20% are indicated for tokamak operation with  $q_{\text{edge}} (\geq 3)$ .

The existence of ultra-high stable  $\beta_{\text{crit}}$  implies that the study of confinement at low aspect ratio can be decoupled from the enhanced losses thought to be associated both with marginal  $\beta$  behavior and with conventional current and density limits. The reduction in saturated island widths suggests a concomitant reduction in disruptivity. Stabilization of the resistive  $m = 1/n = 1$  instability at high  $S$  and low  $A$  may provide an intrinsic improvement in confinement. Improved axisymmetric stability should enable more efficient experimental exploration of the effects of cross-section shaping on confinement and stability, with reduced disruptivity due to vertical instability. Recent experimental results with diverted, shaped plasmas have suggested that operation at  $q_{\text{edge}} \sim 2$  may be an unrealistic goal [12]. If these experimental results are borne out, then the existence of high  $\beta_{\text{crit}}$  at  $q_{\text{edge}} \geq 3$  may mean that low  $A$  is *required* to access high  $\beta$  with the optimal (H-mode) confinement associated with divertor operation.

A new tokamak, the Spherical Torus Experiment (STX), has been proposed by ORNL [13] to exploit this predicted expansion in the  $\beta$ -stable tokamak operating regime.

## REFERENCES

- [1] PENG, Y.-K.M., STRICKLER, D.J., Nucl. Fusion **26** (1986) 769.
- [2] LAO, L.L., ST. JOHN, H., STAMBAUGH, R., et al., Rep. GA-A17910, GA Technologies, Inc., San Diego, CA (1985).
- [3] TROYON, F., et al., Comments Plasma Phys. Controll. Fusion **26** (1984) 209.
- [4] TODD, A.M.M., et al., Nucl. Fusion **19** (1979) 743.
- [5] INTERNATIONAL ATOMIC ENERGY AGENCY, Tokamak Concept Innovations (Proc. Specialists Meeting Vienna, 1986), IAEA-TECDOC-373, IAEA, Vienna (1986). See specifically PENG, Y.-K.M., et al., p. 567-570; BESPOLUDENNOV, S.G., et al., p. 571-574; TSUNEMATSU, T., et al., p. 575-579.
- [6] CONNOR, J.W., TAYLOR, J.B., TURNER, M.F., Nucl. Fusion **24** (1984) 642.
- [7] MONTICELLO, D., JARDIN, S., personal communication.
- [8] GRIMM, R.C., DEWAR, R.L., MANICKAM, J., J. Comput. Phys. **49** (1983) 94.

- [9] WADDELL, B.V., CARRERAS, B.A., HICKS, H.R., HOLMES, J.A., *Phys. Fluids* **22** (1981) 1131.
- [10] CHARLTON, L.A., HOLMES, J.A., HICKS, H.R., LYNCH, V.E., CARRERAS, B.A., *J. Comput. Phys.* **63** (1986) 107.
- [11] HASTIE, R.J., HENDER, T.C., CARRERAS, B.A., CHARLTON, L.A., HOLMES, J.A., Stability of Ideal and Resistive Internal Kink Modes in Toroidal Geometry, Rep. ORNL-TM-10331, Oak Ridge National Lab., TN (1987).
- [12] BURRELL, K.H., PRATER, R., EJIMA, S., et al., in *Plasma Physics and Controlled Nuclear Fusion Research 1984 (Proc. 10th Int. Conf. London, 1984)*, Vol. 1, IAEA, Vienna (1985) 131.
- [13] LAZARUS, E.A., ATTENBERGER, S.E., BAYLOR, L.R., BOROWSKI, S.K., BROWN, R.L., et al., A Feasibility Study for the Spherical Torus Experiment, Rep. ORNL-TM-9786, Oak Ridge National Lab., TN (1985).

## DISCUSSION

### ON PAPERS IAEA-CN-47/E-I-2-1 TO E-I-2-4

B.P. LEHNERT: Has the accuracy of MHD theory been examined in the present cases of high beta confinement, in which the ion Larmor radius does not become entirely negligible as compared to the characteristic dimensions of the system and of the relevant instability modes? In particular, kinetic effects may become significant for the fine structure — the high wave numbers — of such modes.

T. AMANO: None of the papers I have presented consider kinetic effects. It is generally believed that kinetic effects have a stabilizing influence on such MHD modes.

K. UO: The second stability region is frequently discussed at present and some of the designs for new fusion devices are based on concepts including this region. Is there really experimental evidence for a second stability region?

T. AMANO: Yes, there seems to be some evidence for a second stability regime in high beta torus experiments. Also, most of the systems I described have sufficiently high first stable critical beta ( $\geq 10\%$ ).

S. ITOH: With regard to the MHD stability in low-aspect-ratio tokamaks, described in paper E-I-2-4, the authors considered high n-modes as well as  $n = 1, 2, 3$  modes. Do you have any information on intermediate n-modes?

T. AMANO: Since this system has rather high shear, I assume that intermediate n-modes are stable.

K. ITOH: Could you comment on the compatibility of systems with high beta configurations, such as a highly elongated system or a low-aspect-ratio system with the separatrix at the surface?

T. AMANO: I think it is possible to install open divertors in these configurations.



## SIMULATION STUDIES OF TOKAMAK DYNAMICS

M. TANAKA, T. HAYASHI, K. HARAFUJI,  
Y. NAKAYAMA, T. SATO  
Institute for Fusion Theory,  
Hiroshima University,  
Higashisenda-machi, Naka-ku,  
Hiroshima, Japan

### Abstract

#### SIMULATION STUDIES OF TOKAMAK DYNAMICS.

Three new simulation approaches for tokamak studies are proposed. First, a new particle simulation code applicable to kinetic phenomena of time- and spatial scales comparable to the magneto-hydrodynamic (MHD) scales is developed and applied to tokamak current drive and sustainment. Second, a full MHD simulation model that can treat a plasma-vacuum-wall system for arbitrary plasma beta is developed and applied to a study of the bifurcation problem in a non-circular cross-section tokamak. Third, a full 3-D MHD simulation code is applied to the problem of suppression of major disruptions by a resonant helical field.

### 1. INTRODUCTION

There are many problems to be overcome in demonstrating the usefulness and practicability of computer simulations in fusion plasma research. Because of the subtleties of particle simulations, it has been believed that their application to real fusion plasmas is rather limited. As one method of getting rid of this drawback of particle simulations, we have developed a macroscale particle simulation code that can adequately deal with the MHD time- and spatial scales along with the kinetic aspects pertinent to the MHD scale phenomena. The code developed is successfully applied to tokamak current drive and sustainment by electron beam injection.

One main concern in MHD simulation is its numerical accuracy. To increase the accuracy it is necessary to develop a new code. On the other hand, it is also important to know the limit of applicability of a conventional code. In this paper, attempts are made to attack two tokamak problems that seem to require some effort to be solved by using the conventional Lax-Wendroff code. One is the bifurcation problem of non-circular cross-section tokamaks in which some uncertainties must always remain within the framework of the mathematical analysis. In this regard, two numerical issues must be clarified. One is the treatment of the plasma-vacuum interface, and the other is that of an arbitrary beta plasma. The code developed has discovered an interesting new fact that would otherwise remain unpredicted. The second problem is the suppression of the major disruption by application of a resonant helical field. Since this requires a three-dimensional, high resolution code, it was quite

unclear whether the full 3-D MHD code based on the Lax-Wendroff method could indeed solve the problem. The result has shown that a reasonably good solution can even be obtained with the Lax-Wendroff code.

These three problems will be described in order.

## 2. CURRENT DRIVE BY RELATIVISTIC ELECTRON BEAM INJECTION

Intense relativistic electron beam (REB) injection into tokamak plasmas has recently been studied as an efficient means of quasi-stationary current generation and sustainment [1-4]. The current drive method by REB injection is considered to have advantages over the Ohmic current drive method in that the electron injection system can be mechanically simple and efficient and the plasma particle and energy losses arising from the pulse mode operation, hence the device wall damages, might be reduced substantially.

A simulation study of the REB injection current drive has been performed by using the macroscale particle simulation code [5]. This new class of particle code can deal with spatially large and slow time-scale (MHD scale) phenomena in which particle effects and the scalar potential electric field are non-negligible.

Two types of REB current drive simulation are studied here. In the first type of simulation, the electron beam is continuously injected into a longitudinally magnetized plasma channel [6] to illustrate the physics process involved in the mono-energetic single REB injection. It is found that in an early stage of REB injection a plasma return current is excited by the electromagnetical beam induced electric field. The primary electron beam is decelerated by the induced electric field as long as the beam injection continues. The aforementioned plasma return current nearly cancels the primary beam current before anomalous collisions participate. The beam produced scalar potential electric field causes radially inward diffusion of the ions, which substantially reduces the radial expansion of the beam. When anomalous collisions take part in the process, further development of the plasma return current is prevented, and a net current, hence the azimuthal magnetic field, is created around the beam path. The radial extension of the azimuthal field is confined to the vicinity of the beam path, because of the global cancellation of the net current. The net saturation current increases remarkably with beam relativisticity as  $I_{\text{net}} \approx (mc^3/e)\beta\gamma$  [Fig. 1], where  $\beta = v_b/c$ ,  $\gamma = (1-\beta^2)^{-1/2}$  and  $v_b$  is the speed of the electron beam. On the other hand, the net saturation current is independent of the injection current intensity of the REB. When the beam relativistic factor is considerably large, a kink instability develops, and the net saturation current does not reach the previous scaling level (solid circle at  $\gamma \approx 5$  in Fig. 1). The instability is, however, easily suppressed by increasing the strength of the longitudinal magnetic field in such a manner that the q-value on the beam path does not fall below unity (open circle in Fig. 1). (Note that the results shown above are applicable to the flat profile electron beam, where the q-value on the beam path is comparable to unity.)

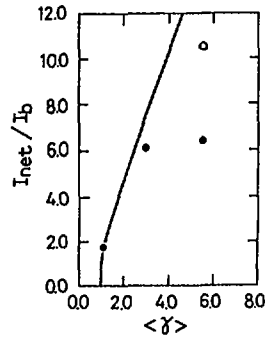


FIG. 1. Dependence of net saturation current,  $I_{net}$ , on relativistic factor  $\langle \gamma \rangle$  of electron beam injected into longitudinally magnetized plasma channel.  $I_b$ : injection beam current;  $\langle \gamma \rangle$ : average relativistic factor defined by  $\langle \gamma v_z \rangle / \langle v_z \rangle$ .

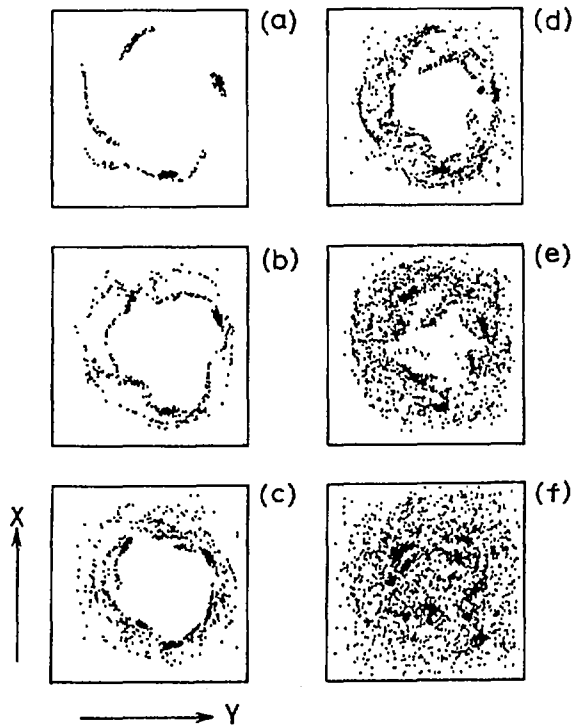


FIG. 2. Beam electrons passing the same poloidal cross-section  $(x, y)$  at several different times;  $t/\tau_A = 0.5, 1.0, 2.0, 2.5,$  and  $4.0$  (from a to f) (poloidal magnetic surfaces present).  $\tau_A$ : Alfvén transit time defined by using poloidal magnetic field at  $t = 4 \tau_A$ .

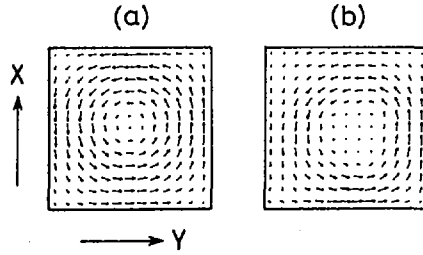


FIG. 3. Poloidal magnetic field in the same cross-section as in Fig. 2 at times (a)  $t = 0$  and (b)  $t = 4\tau_A$ . Maximum field strengths: (a) for  $\omega_{ce}/\omega_{pe} = 0.17$  and (b) for 0.28.

In the simulation of the second type, the REB is injected into a plasma where poloidal magnetic surfaces are present (such as tokamak plasmas). A toroidal (longitudinal) magnetic field is applied in the  $z$ -direction. The initial  $q$ -value is  $q \sim 4$ . In this simulation, the beam current is injected in a direction parallel to the initial toroidal current. In the early stage of the injection, the beam electrons make many round trips along the constant magnetic surface in the longitudinal (periodic) direction. This produces a current carrying thin annulus whose radius is comparable with the minor radius (Fig. 2(a)). A modulation of the annulus with the poloidal mode number  $m = 3$  is observed (Fig. 2(b)). The modulation is due to the beam produced poloidal magnetic field. The radius of the outer edge of the annulus in Fig. 2(b) is more or less bounded by the magnetic surface where the beam injector is located, but the inner edge lies distinctly inside.

With the passage of time, the beam electrons tend to gather at the inner edge of Fig. 2(a) [see Fig. 2(c)]; eventually, the central region is to be filled with beam electrons [Figs 2(e) and (f)]. The whole process occurs in a few Alfvén transit times when the magnetic pinch is taking place, since the electron population tends to be more dense at the inner edge of the annulus. (We note that our MHD simulation has shown that two current filaments with 200 kA placed 1 m apart merge in a few Alfvén transit times). The resultant poloidal magnetic field is shown in Figs 3(a) and (b). The initial poloidal field strength is maximum near the wall (Fig. 3(a)). When the electron beam is injected, the poloidal magnetic field is intensified and the distribution corresponding to the time shown in Fig. 2(f) becomes hollow (Fig. 3(b)). The maximum of the poloidal field strength appears near the inner edge of the beam electron annulus. There is a great possibility of a macroinstability such as the tearing mode instability participating in this process. However, we have not confirmed this possibility, so far.

From this study, it can be concluded that the electron beam injected from near the wall can penetrate into the central region of the tokamak plasma and form the toroidal current through the aforementioned process.

### 3. HIGH BETA TOKAMAK WITH NON-CIRCULAR CROSS-SECTION

It is maintained that shaping the poloidal cross-section to assume a non-circular form can increase the beta limit of tokamak plasmas. Shaping coils, however, exert additional external forces on confined plasmas, which may cause destruction of the plasma shape.

To study the stability of a non-circular cross-section tokamak, a compressible non-linear MHD simulation model is developed which can treat a finite beta plasma surrounded by a vacuum and a conducting wall [7].

The parameter range accessible to study depends strongly on the ability of the equilibrium code to obtain an initial equilibrium configuration of the non-circular cross-section. In our present study, the EQUICR code was used to obtain initial equilibria [8]. Since we found it rather difficult to obtain various bean shaped equilibria in a systematic way, we started with the study of elliptically shaped equilibria. Elliptically shaped equilibria were obtained in the range of  $\kappa = 2.4$  to 4.2 ( $\kappa$  is the ellipticity) and  $\beta = 1$  to 20% ( $\beta$  is the toroidal beta) for a fixed toroidal current.

It is found that the elliptical cross-section tokamak is always positionally unstable for the range surveyed and that the instability is of an ideal, current driven type. We thus assume that the positional instability is feedback stabilized. We then proceed to the bifurcation mode, i.e. the  $m = 2/n = 0$  mode. It is found that there is a beta limit for this bifurcation mode and that the beta limit is larger for smaller ellipticity. The stability diagram in the  $\beta$ - $\kappa$  plane is shown in Fig. 4. Along with the fact that there is a beta limit for the instability, comparison of the induced flow pattern and the pressure profile suggests that the instability is a pressure driven instability rather than a current driven instability (see Fig. 5). Simulation runs for a wide range of the resistivity (magnetic Reynolds number in the range of 2000 to infinity) indicate that the instability is of an ideal type. Thus, the initial linear instability is concluded to be an ideal, pressure driven instability.

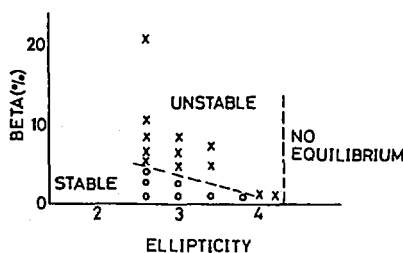


FIG. 4. Stability diagram of  $m = 2/n = 0$  (bifurcation) mode in  $\beta$ - $\kappa$  plane.

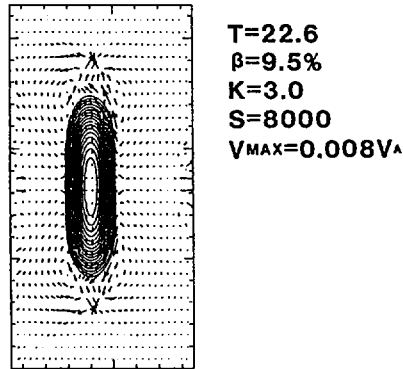


FIG. 5. Induced flow vectors overlaying pressure contours at early phase of linear instability development.

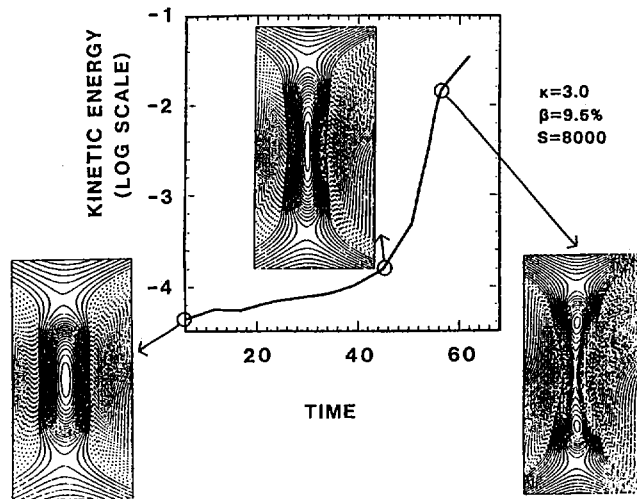


FIG. 6. Temporal development of induced flow energy and poloidal flux contours at three typical bifurcation times: initial, last stage of ideal pressure driven instability, and development stage of non-linear reconnection.

Another interesting finding is that when the ideal (pressure driven) instability develops, the original elliptical current distribution deforms vertically, and a current-sheet-like distribution is formed. As a consequence of the current sheet development, reconnection is non-linearly driven near the magnetic axis in the presence of resistivity; this behaviour is shown in Fig. 6. In this figure, the solid line indicates the development of the induced flow energy; also the poloidal flux contours at three times of the evolution are shown. The first, gradual growth ( $0 < t < 45\tau_A$ ,  $\tau_A$

being the Alfvén transit time) corresponds to the ideal pressure driven instability during which only elongation of the elliptical shape occurs. As is seen in this figure, a burst-like increase occurs at about  $t = 45 \tau_A$ . This burst-like phenomenon is closely associated with the onset of non-linear reconnection. It is, therefore, concluded that bifurcation of the elliptical cross-section takes place in two steps: ideal instability and subsequent non-linear reconnection.

Since a few bean shaped equilibria were obtained additionally by the EQUICR code, the positional instability and the bifurcation were also studied. It is likely that the growth rate of the positional instability is greatly reduced compared with the elliptical case although quantitative comparison is, in a strict sense, difficult. For the equilibria we have studied, no bifurcation instability was found, indicating that the bean shaped tokamak would be far more stable than the elliptical tokamak.

#### 4. SUPPRESSION OF TOKAMAK DISRUPTION BY RESONANT HELICAL FIELD

It is widely believed that a tokamak major disruption can be prevented if we can suppress the growth of the  $m = 2/n = 1$  magnetic island [9, 10]. One way to suppress the island growth is to apply an external helical field which resonates with the 2/1 magnetic surface [11]. However, complete control of the major disruption has not yet been attained experimentally by this method. Making use of a 3-D full MHD simulation code, we thus wish to investigate the stabilization effect of the resonant helical field in the island growth, thus verifying the viability of this method.

The initial condition of the tokamak is such that  $q_0 = 1.3$ ,  $q_a = 4.0$ ,  $\beta_0 = 0.5\%$ , and  $A = 20$  (aspect ratio). When the resonant helical field is absent,

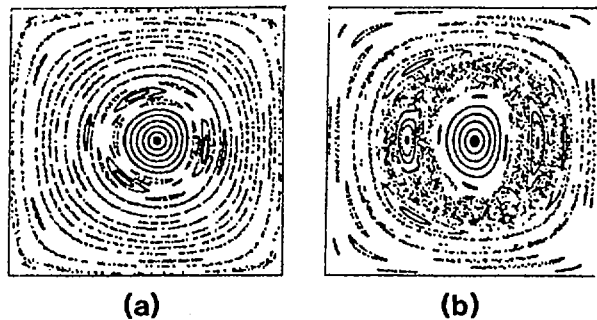


FIG. 7. Poincaré plots of magnetic field lines in poloidal plane observed at  $t = 3000 \tau_A$ : (a) resonant helical field (RHF) with  $\Delta B_p/B_p = 0.3\%$  and  $180^\circ$  out of phase from spontaneous 2/1 mode applied at  $t = 2000 \tau_A$ ; (b) no resonant helical field applied (spontaneous development of 2/1 mode).

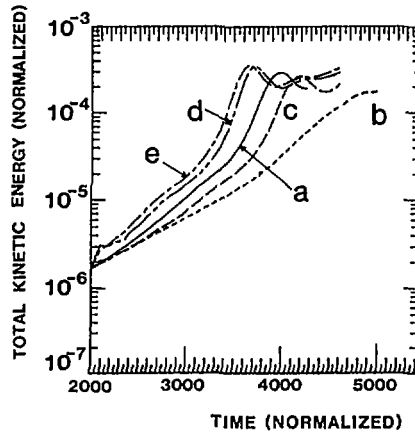


FIG. 8. Temporal development of total kinetic energy for (a) no RHF, (b)  $\Delta B_p/B_p = 0.3\%$  and out of phase, (c)  $\Delta B_p/B_p = 0.57\%$  and out of phase, (d)  $\Delta B_p/B_p = 1.1\%$  and out of phase, and (e)  $\Delta B_p/B_p = 0.57\%$  and in phase.

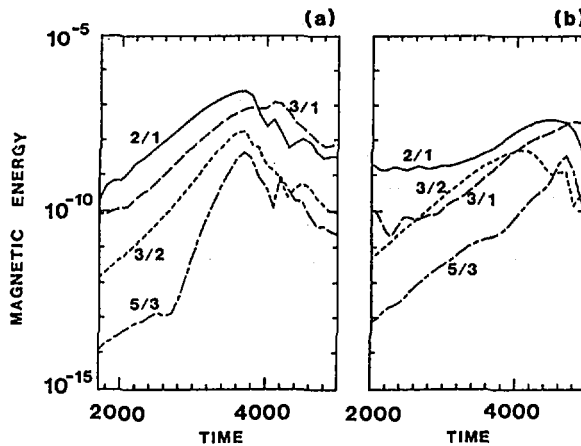


FIG. 9. Temporal development of several dominant Fourier modes: (a) case (b) of Fig. 7, and (b) case (a) of Fig. 7.

an ergodic region of the magnetic surface develops, due, primarily, to the overlapping of the islands of the 2/1 and 3/2 (and 3/1) modes (see Fig. 7(b)). When, however, a 2/1 resonant field is applied at the instant when the island width of the 2/1 mode grows up to about one-tenth of the minor radius  $a$ , the 2/1 mode is almost completely suppressed (see Fig. 7(a)). In this example, the width of the island created by the applied resonant field was about  $a/10$  ( $\Delta B_p/B_p \approx 0.3\%$ ), and the phase was  $180^\circ$  out of phase with the 2/1 mode ('out'). [Here, we assumed that the applied helical field was immersed instantaneously in the plasma.]

The temporal development of the total kinetic energy for different magnitudes and phases of the applied resonant field is shown in Fig. 8(a). It is observed that when the applied phase is in coincidence with that of the spontaneous one ('in'), the resonant field always accelerates the development of the instabilities. Even if the phase is 'out', it results in development of the 2/1 mode with the same phase as the resonant field when the resonant field is very strong.

The development of several dominant Fourier modes of the perturbed magnetic field is shown for the case without applied resonant field in Fig. 9(a), and for the case with applied resonant field in Fig. 9(b). The growth of the 2/1 mode is strongly suppressed by the resonant field. The growth rate of the 3/2 mode is also somewhat reduced because no steep current gradient, necessary for the excitation of the 3/2 mode, is generated, owing to the suppression of the 2/1 mode. Furthermore, the onset of the rapid growth of the 5/3 mode, which would occur as soon as the 2/1 and 3/2 islands overlap, disappears.

It is concluded that the resonant helical field can really act to stabilize the 2/1 mode. However, in the actual experiment, it might require special care to control the magnitude, phase and timing of the external helical field by which the 2/1 mode can be suppressed.

## 5. SUMMARY

Several investigations of the future prospects of numerical simulations, both particle and MHD, in fusion plasma research were attempted successfully. The first example, a macroscale particle simulation, has proven the usefulness of particle simulations in the extended area of fusion plasma research. The other two examples also indicate that the full MHD code can, to a greater extent, contribute to success than had been thought probable before. In particular, the last example suggests that by developing a new, slightly higher resolution MHD code, one can indeed solve even geometrically complicated stellarator problems.

## REFERENCES

- [1] BAILEY, V.L., Steady State Current Drive in Tokamaks, Rep. DOE/ET-0077 US Department of Energy, Washington, D.C. (1979).
- [2] WONG, K.L., ONO, M., WURDEN, G.A., Rev. Sci. Instrum. **53** (1982) 409.
- [3] MOHRI, A., et al., in Plasma Physics and Controlled Nuclear Fusion Research 1978 (Proc. 7th Int. Conf. Innsbruck, 1978), Vol. 3, IAEA, Vienna (1979) 311.
- [4] TANAKA, H., et al., Jpn. J. Appl. Phys. **24** (1985) 1644.
- [5] TANAKA, M., to appear in J. Comput. Phys. (1986).
- [6] TANAKA, M., SATO, T., Phys. Fluids **29** (1986) 3823.
- [7] SATO, T., NAKAYAMA, Y., MATSUOKA, K., in Plasma Physics (Proc. Int. School Varenna, Aug. 1985).

- [8] SHINYA, K., et al., An MHD Equilibrium Code 'EQUCIR Version 2' Applicable to Up-down Asymmetric Toroidal Plasma, Rep. JAERI-M-9278, Japan Atomic Energy Research Institute (1981).
- [9] CARRERAS, B., et al., Phys. Fluids **23** (1980) 1811.
- [10] KLEVA, R.G., DRAKE, J.F., BONDESON, A., Phys. Fluids **28** (1985) 2478.
- [11] KARGER, F., et al., in Plasma Physics and Controlled Nuclear Fusion Research 1974 (Proc. 5th Int. Conf. Tokyo, 1974), Vol. 1, IAEA, Vienna (1975) 207.

# STABILITY CONDITIONS FOR HELICAL MHD PERTURBATIONS AND DISRUPTIVE INSTABILITY IN TOKAMAKS

L.E. ZAKHAROV

I.V. Kurchatov Institute of Atomic Energy,  
Moscow,  
Union of Soviet Socialist Republics

## Abstract

### STABILITY CONDITIONS FOR HELICAL MHD PERTURBATIONS AND DISRUPTIVE INSTABILITY IN TOKAMAKS.

The effects of the current profile on the stability of kink and tearing modes are studied on the basis of the successive current layer principle. The dependence of the stability against disruptions on the global current profile parameters is analysed. Effects of local current redistribution near the resonant surface on the tearing modes are demonstrated. A complete model for quasi-linear saturation of the tearing modes is proposed. The stability of the edge localized kink modes is analysed, and the optimum current profiles are given. It is proved that  $q(a) = 2$  is the asymptotic theoretical limit, ensuring the stability against all kink and tearing modes. A characteristic exact solution for the  $m = 1$  mode equilibrium in a cylinder is given. The main reasons for the appearance of disruptions in a tokamak are mentioned.

## 1. PRINCIPLE OF SUCCESSIVE CURRENT LAYERS (SCL PRINCIPLE) AND STABILITY AGAINST DISRUPTIONS

The linear stability analysis of current driven MHD modes in the cylindrical tokamak model reduces to the study of a well-known equation and of the functional  $W$ :

$$\frac{d}{d\rho} \rho \frac{dY}{d\rho} - \frac{m^2}{\rho} Y = \frac{j'}{\mu - n/m} Y, \quad W = \int_0^{\infty} \left( \rho Y'^2 + \frac{m^2}{\rho} Y^2 + \frac{j' Y^2}{\mu - n/m} \right) d\rho \quad (1)$$

where  $\rho$  is the minor radius,  $\mu(\rho) = 1/q(\rho)$  is the rotational transform, and  $m$  and  $n$  are the wavenumbers. The current density is given in dimensionless units, i.e.  $j \rightarrow (4\pi/c)jR/B_0$ , so that  $q(0) = 1$  corresponds to  $j(0) = 2$ .

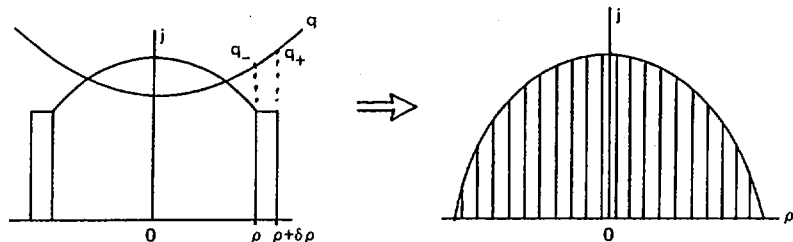


FIG. 1. Successive current layers.

Equation (1) is actually a perturbation of the equilibrium equation

$$\Delta\Psi = j(\Psi) - \bar{j}_{m/n} \quad (2)$$

where  $\bar{j}_{m/n} = 2nB_s/(mR) = \text{const}$ , and  $\Psi$  is the helical flux. The existence of a smooth solution of Eq. (1),  $\Delta' = 0$ , means that a linear near-equilibrium with continuous current density exists [1, 2]. When  $\Delta' > 0$ , the plasma column must pass into this near-equilibrium state, with the formation of magnetic islands. The fact that Eqs (1) and (2) are independent of the dissipative plasma properties explains the good agreement between theoretical conclusions and experiment.

Equation (1) alone does not, however, say anything about the consequences of the development of instabilities. Calculation of the instability growth rate does not help either, in this case. The SCL principle, which will be set forth below, clarifies the relationship between stability properties and the consequences of the instabilities.

According to this principle, any current profile is considered to be the sum of nested cylindrical current layers disposed around the initial axis (Fig. 1). The effect of each layering event on stability is analysed. Without conducting wall, this effect is simply determined by the sign of the expression

$$\delta V = j \frac{nq - (m-1)}{(nq_+ - m)(nq_- - m)} 2mq \frac{\delta\rho}{\rho} \quad (3)$$

where  $j$  is the current density in the layer added,  $\rho$  and  $\delta\rho$  are the radius and the thickness of a layer, and  $q_+$  and  $q_-$  are the values of  $q(\rho)$  on the outside and inside of the layer. When  $\delta V > 0$ , stability deteriorates with an additional layer, whereas when  $\delta V < 0$ , it improves [2].

Equation (3) is valid for the most general case, including discontinuities in the current density, presence of a resonant surface inside the layer, etc. In the presence of a casing, only the term  $(m-1)$  of Eq. (3) should be replaced by an explicit, simple function  $nq_m(\rho)$  [2].

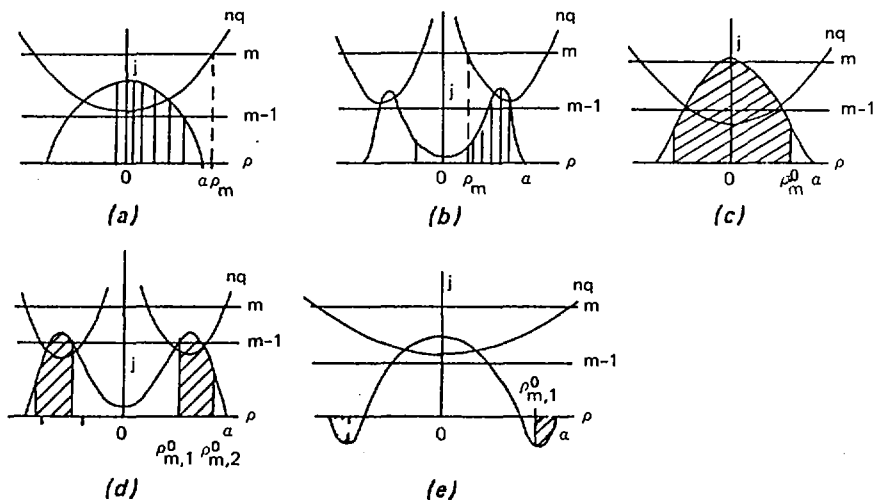


FIG. 2. Characteristic unstable current profiles: (a), (b): without supporting channel, subject to major disruption; (c), (d), (e): with supporting channel,  $\rho_m^0 < a$ , subject to minor disruption.

In spite of its simplicity, the SCL approach gives a practically exhaustive picture of the effect of current profile on the stability of kink and tearing modes and yields criteria on the disruptive instability.

### 1.1. Kink instabilities, $nq(a) < m$

Only when the layer added includes the resonant surface,  $nq(\rho_m) = m$ , does the sign of the dominator in Eq. (3) become negative. In all other cases, the sign of  $\delta V$  is determined only by the signs of the numerator and  $j$ .

We easily see that current distributions with  $j(\rho) > 0$  and  $nq(\rho) > m - 1$  (Fig. 2(a), (b)) are unstable against the  $m/n$  kink mode. This is obvious for a monotonic current distribution. The initial current channel,  $\rho \ll a$ , is certainly unstable (uniform current,  $m - 1 < nq(0) < m$ ). Further layer adding only makes the stability worse because  $nq(\rho) > m - 1$  yields  $\delta V > 0$  [1]. For a skin current distribution including an additional internal resonant surface  $nq(\rho_m) = m$  (Fig. 2(b)), the current channel with radius  $\rho_m + \epsilon$  is unstable (see Eq. (1)). An outer current layer,  $\rho > \rho_m + \epsilon$ , is destabilizing, which results in instability of the whole profile.

For  $j(\rho) > 0$ , only a distribution having a region with  $nq(\rho) < m - 1$  can be stable. For a monotonic current density, (Fig. 2(c)), the initial current channel  $\rho \ll a$  is stable because  $nq(0) < m - 1$ . Additional current layers up to the point  $\rho_{m-1}$ ,  $nq(\rho_{m-1}) = m - 1$  improve the stability. The next layers at  $\rho > \rho_{m-1}$  make the stability worse, and it is possible that a neutral stability will be reached

for a current cylinder with  $\rho = \rho_m^0$ . We shall call such a cylinder a supporting current channel for the  $m/n$  kink mode. The exact value of  $\rho_m^0$  is determined by the relationship

$$\left. \frac{\rho Y_i'}{m Y_i} \right|_{\rho_m^0} + 1 - \frac{j}{m\mu - n} \left|_{\rho_m^0} = 0 \quad (4)$$

where  $Y_i(\rho)$  is the internal solution to Eq. (1),  $Y_i(0) = 0$ .

The physical meaning of the supporting current channel consists in the fact that all bulk forces  $\vec{j} \times \vec{B}$  inside it are exactly balanced for a small helical deformation. There are no reasons for this balance to be violated seriously, even at a non-linear stage. Therefore, in the development of the  $m/n$  kink instability, the supporting current channel will not be modified significantly. In the absence of such a channel, the kink instability should completely remix the whole distribution because it is unable to reach a new stable equilibrium [4]. The absence of a supporting current channel means that the current profile is unstable against a major disruption.

For the most important mode, the 2/1 mode, the supporting channel exists only if  $q(0) < 1$ . This has made it possible to draw the conclusion [1], based on the stable regimes with  $q(a) \lesssim 2$  in T-10 and T-11, that  $q(0) < 1$  is not forbidden in tokamaks and that internal relaxation oscillations are not related to  $m = 1$  reconnection. For regimes with  $q(a) \lesssim 2$ , any  $m = 1$  reconnection should lead to a major disruption.

For a skin profile, the supporting current channel may be hollow. In the process of SCL adding, the internal unstable cylinder (Fig. 2(d)), where  $nq(\rho) > m-1$ , is surrounded by a stabilizing layer with  $nq(\rho) < m-1$ , and, thus, neutral stability is first reached for  $\rho_0 = \rho_{m,1}^0$ . The supporting current channel is situated at  $\rho_{m,1}^0 < \rho < \rho_{m,2}^0$ , where  $\rho_{m,2}^0$  is the radius where neutral stability is reached for the second time. The outer shell,  $\rho > \rho_{m,2}^0$ , destabilizes the whole current profile. Owing to the presence of a supporting current channel, such a linearly unstable current profile is, nevertheless, stable against a major disruption. A similar picture with a hollow supporting channel is also possible in the presence of a casing [2].

The addition of negative current density,  $j < 0$ , causes the stability to deteriorate if  $nq(\rho) < m-1$  and improves it if  $nq(\rho) > m-1$ . In this case, stabilization is possible even of a current profile with  $nq(\rho) > m-1$  everywhere [5] (Fig. 2(e)). In particular, this situation occurs in the Kadomtsev reconnection model, where  $q(\rho) \geq 1$  is established after remixing. The 2/1 mode, nevertheless, remains stable [6], because a negative  $\delta$ -function-type current sheet is generated at  $\rho = \sqrt{2}\rho_{1/1}$ . In this case, the supporting current channel for the 2/1 kink mode becomes hollow but is not destroyed. Later, however, because of the decay of this negative current, the supporting channel will disappear. If  $q(a) \lesssim 2$ , this

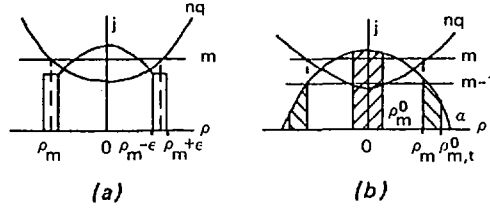


FIG. 3. (a) Stabilizing current layer embracing resonance surface; (b) unstable current profile with internal supporting channel,  $\rho_m^0$ , and with hollow supporting channel,  $\rho_m < \rho < \rho_m^0 < a$ , stabilizing the tearing mode.

should lead to the major disruption due to the kink mode  $2/1$ . Note that, in accordance with the SCL principle, the abovementioned negative current reduces the stability of the  $3/1$  mode because, for  $m = 3$  and  $n = 1$ ,  $nq(\sqrt{2}\rho_{1/1}) < m - 1$ .

The generation of a negative current at the plasma edge (Fig. 2(e)), where  $nq > m - 1$ , may create a hollow supporting channel which stabilizes the unstable interior part [5]. In particular, such a current is always generated during the non-linear stage of the kink instability [4], leading to its stabilization, a fact which was observed in numerical simulations [7]. However, such a stabilization cannot be stationary in a real plasma. Therefore, an unstable kink mode should either lead to a major or a minor disruption.

The examples given here show how we can analyse the stability of any conceivable current profile by using the SCL principle. This principle connects the linear stability properties with the stability criteria referring to the disruptions. A kink mode (as well as a tearing mode) is linearly stable only when a supporting current channel exists and has an external radius exceeding the plasma radius,  $\rho_m^0 \geq a$ . In the presence of a supporting channel with  $\rho_m^0 < a$ , the plasma is linearly unstable but the instability only leads to a minor disruption. The interior of the supporting channel cannot be modified significantly by such a kink instability. In the absence of a supporting channel, the kink instability leads to a major disruption.

## 1.2. Tearing modes, $nq(a) > m$ , $\rho_{m/n} < a$

Adding a positive current layer of width  $2\epsilon$ , which includes the resonant surface  $\rho_m$  (Fig. 3(a)), transforms a current distribution which is unstable against the kink mode ( $a = \rho_m - \epsilon$ ) into a distribution stable against the tearing mode ( $a = \rho_m + \epsilon$ ). In this case,  $\delta V \sim j/\epsilon$  is negative, because the denominator in Eq. (3) is negative ( $nq_+ > m$ ,  $nq_- < m$ ), although  $nq > m - 1$ . Adding further current layers only worsens the stability and may, finally, produce an unstable current distribution (Fig. 3(b)).

Thus, when the resonance surface is inside the current channel,  $\rho_m < a$ , there is always an additional hollow supporting channel,  $\rho_m < \rho < \rho_{m,t}^0$ , where the radius  $\rho_{m,t}^0$  limits a neutrally stable cylinder (the subscript t denotes the tearing mode supporting channel). The radius  $\rho_{m,t}^0$  is determined by the same rule – see Eq. (4) – as  $\rho_m^0$ , except that  $Y_i(\rho)$  intersects the resonance surface with a continuous derivative.

The stability of tearing modes is thus ensured by a current layer adjacent to the resonance surface. Like the kink mode, the tearing mode is stable only for  $\rho_{m,t}^0 \geq a$ . For  $\rho_{m,t}^0 < a$ , the tearing mode may be transformed into a kink mode or can pass into a new, quasi-linear equilibrium with magnetic islands [8], in which case it is not dangerous.

## 2. LOCAL INFLUENCES AFFECTING THE STABILITY OF TEARING MODES

The stability of tearing modes is sensitive to a number of local effects which were mentioned explicitly for the first time in Ref. [9].

One important example [2], given in Fig. 3(a), shows that a jump in the current density beyond the resonance surface stabilizes the tearing mode. Surprisingly, a similar case has been realized in H-regimes in tokamaks, stabilizing the 2/1 mode. In the general case, a negative jump in the current density just before the resonance surface destabilizes the tearing mode but, just beyond the resonance surface, stabilizes it (Figs 4(a), (b)). In accordance with the SCL principle, the addition of a positive current layer just at the resonant surface (Fig. 4(c)) stabilizes the tearing mode.

These examples are useful for understanding the interaction of different tearing modes by current redistribution during island formation. For example, the development of the 2/1 tearing mode, at the beginning, produces a jump-like current distribution beyond the resonant surface  $\rho_{3/2}$  and stabilizes the 3/2 mode. During the growth of the 2/1 island, this jump penetrates inside the radius  $\rho_{3/2}$ , immediately destabilizing the 3/2 tearing mode. Some authors consider this situation to be the start of a disruption. A non-linear effect of the internal 3/2 tearing mode on the 2/1 mode is always destabilizing because the 3/2 mode produces a jump before the surface  $\rho_{2/1}$ .

The example presented in Fig. 4(c) fully clarifies the nature of tearing mode stabilization by local current drive. An additional positive current layer will stabilize the tearing mode if it contains the resonant surface and will have a destabilizing effect if the resonant surface is outside this layer (Fig. 4(c)). The addition of a negative current layer (Fig. 4(d)) has exactly the opposite effect.

In all the examples described, the effect of the current jump is proportional to  $\Delta j/\epsilon$ , where  $\epsilon$  is the distance from the jump to the resonant surface. A weaker effect with  $\delta W \sim \Delta j' \ln \epsilon \sim \Delta j'$  is the formation of a break in the current profile

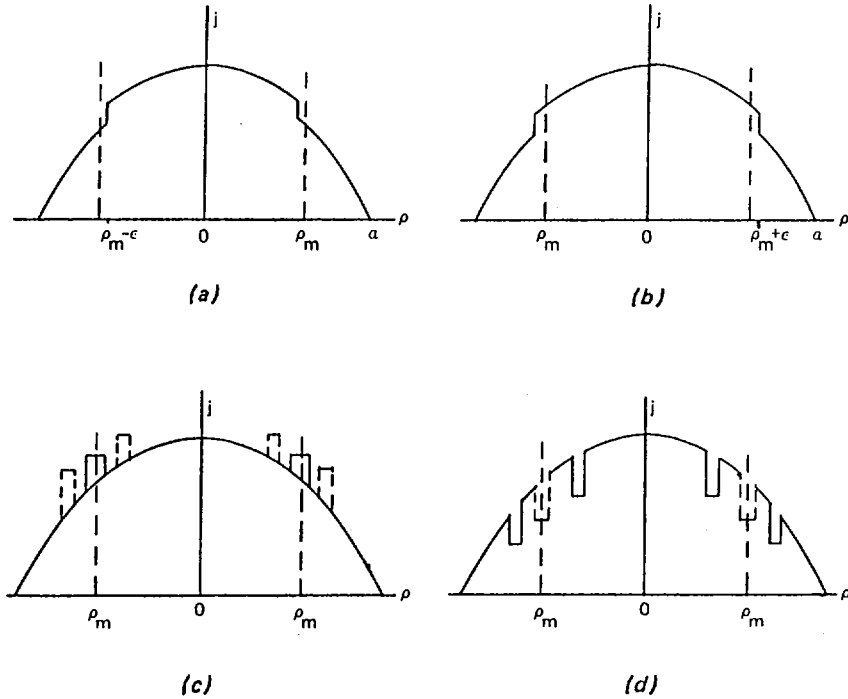


FIG. 4. (a) Unstable and (b) stable current density drops near resonance surface; positively directed (c) and negatively directed (d) stabilizing (solid line) and destabilizing (dashed line) locally driven current.

[9, 2]. It is clear that a break of the type presented in Fig. 5(a) localized close to the resonant surface stabilizes the tearing mode. This effect, which was pointed out, first, only theoretically in Ref. [2], was later realized on T-10 [10] by local ECR heating which produced a break in the  $T_e(\rho)$  and, consequently, the  $j(\rho)$  profiles in the heating zone. Although the experiment was initiated for other reasons, the suppression of the 2/1 mode has completely confirmed the analysis in Ref. [2]. Note that a break of the opposite sign,  $\Delta j' > 0$ , has a destabilizing effect (Fig. 5(b)).

In the next section, we shall show that finite amplitude effects, which are determined by the relationship between  $\epsilon$  and the island width  $w$  and by the poloidal position of the current drive or heating zone with respect to the island, do not significantly affect the active stabilization of the tearing modes. Therefore, linear stability considerations, indeed, yield complete information on the control of tearing modes by local current redistribution.

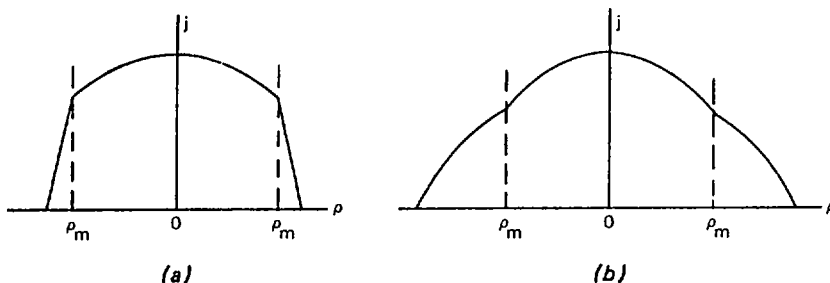


FIG. 5. (a) Stabilizing and (b) destabilizing breaks on the current profile.

### 3. QUASI-LINEAR MODEL FOR SATURATION OF TEARING MODES

To describe the equilibrium (see Eq. (2)) of a configuration with magnetic islands we have analysed the following model of current distribution near the islands:

$$j(\Psi) = j(\chi) = \begin{cases} J_0 - J'_1 (\sqrt{\chi + d_1^2} - d_1) + \frac{1}{2} J''_1 \chi \\ J_0 + \frac{1}{2} J''_1 \chi \\ J_0 + J'_r (\sqrt{\chi + d_r^2} - d_r) + \frac{1}{2} J''_r \chi \end{cases} \quad (5)$$

where  $\chi = 2(\Psi - \Psi_s)/(J_0 - \bar{j}_m/n)$ ,  $\Psi_s$  is the value of  $\Psi$  at the separatrix;  $d_1, d_r$  are the widths of the left and right hand parts of the magnetic islands  $d_1 + d_r = 2w$ ;  $J_0, J'_{\ell, r}, J''_{\ell, r, i}$  are constants determining the current distribution on the left ( $\ell$ ) and on the right ( $r$ ) of the separatrix and inside the island ( $i$ ). Unlike other models (e.g. [8]), the current distribution given by Eq. (5) does not contradict the stationary transport equations and is the simplest model for quasi-linear analysis. We have proved that the linear Eq. (1) can be used, with an accuracy to within  $\sim 1\%$ , up to the separatrix, permitting a maximum reduced number of terms in Eq. (5) for the remaining 2-D zone. Hence, the model given by Eq. (5) is practically exhaustive.

The parameters  $J_0, J'_{\ell, r}, J''_{\ell, r}$  are determined from the matching conditions for total current, current density and its derivatives. The quantity  $J''_i$  is a free parameter also affecting the equilibrium conditions.

The equilibrium conditions can be written in the following simplified form:

$$\rho_m \Delta'_w(0) = \frac{2.72J''_i w + 0.64(J''_\ell + J''_r)w + 0.28(J'_r - J'_\ell)}{J_0 - \bar{j}_{m/n}} \rho_m + 0.28 \frac{J'_\ell + J'_r}{J_0 - \bar{j}_{m/n}} \rho_m \frac{Y'_i + Y'_e}{2Y(\rho_m)} w \quad (6)$$

Here,  $\Delta'_w(0)$  is the standard value of  $\Delta'(0)$  calculated for a modified current profile (the subscript  $w$  indicates the current modification). In this case, the linear Eq. (1) is solved outside the separatrix, introducing the unperturbed value  $\chi = \chi_0$  in Eq. (5). Within the two-dimensional zone, Eq. (1) is solved with a zero right hand side. In Eq. (6),  $Y'_i$  and  $Y'_e$  on the right hand side are calculated at the radii  $\rho_m - d_\ell$  and  $\rho_m + d_r$ , respectively. Note that  $\Delta'_w(0)$  in Eq. (6) must be distinguished from the quantity  $\Delta'(w)$ , which is often incorrectly used in quasi-linear analysis. The first term in Eq. (6) describes the stabilizing effect due to negative second derivatives,  $J''_{\ell,i,r}$ , while the second term is usually destabilizing.

From Eq. (6), it follows:

- (i) Local heating of the internal and external parts of the islands has a favourable stabilizing effect. The position of the heating zone in the poloidal direction determines only the efficiency.
- (ii) A positive current drive inside the islands has a stabilizing effect, whereas the same current drive outside the islands is destabilizing. It must be noted that a positive current drive over both regions has a stabilizing effect, which is, however, not so effective as in the case of a positive current inside the islands alone.
- (iii) If  $w < \epsilon$ , the stabilization effects remain, because of the direct influence of the current redistribution on  $\Delta'_w(0)$ , as was analysed in the previous section.

These results, unlike the analysis in Ref. [6], show that synchronization of an external action with island rotation is not very important and that the island width,  $w$ , has virtually no influence on the stabilization effect.

#### 4. EQUILIBRIUM CONDITIONS FOR THE $m = 1$ PERTURBATION

For the main approximation,  $B_s \gg B_\theta$ , the equilibrium conditions of a helical,  $m = 1$  perturbation in a cylinder are elucidated on the basis of an exact solution of Eq. (2). In regions I and III (Fig. 6), the cross-sections of the magnetic surfaces are circular. The total current in region I corresponds to

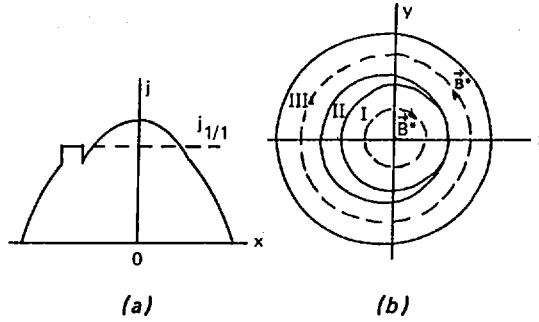


FIG. 6. Exact solution of equilibrium equation (2) for  $m = 1$  mode: (a) current distribution; (b) magnetic field geometry.

$q = 1$  at its boundary. Inside the island, the current density  $j_i(U) = \bar{j}_{1/1} = \text{const}$ , and  $\Psi = \text{const}$ .

Note that, as a result of any inductive process splitting the magnetic surfaces, the current density within the island cannot become greater than  $\bar{j}_{1/1}$  (in general,  $\bar{j}_{m/n}$ ). Artificial current drive, with  $j_i > \bar{j}_{1/1}$ , is also probably impossible, because reconnection conditions would come about within the island. For  $j_i(\Psi) < \bar{j}_{1/1}$ , equilibrium is impossible because the lesser total current in the island cannot compensate for the destabilizing force,  $\vec{j} \times \vec{B}_s$ , acting on the internal helical current channel, I. Thus, it will be clear that the Kadomtsev reconnection process cannot be stopped at a non-linear stage. Therefore, we should invoke some additional considerations to explain the existence, in a tokamak, of a zone with  $q(\rho) < 1$ .

Note that for the  $m = 1$  mode, in contrast to the  $m \geq 2$  modes, stabilization is possible only by current drive inside the island, provided  $j_i(\Psi) = \bar{j}_{1/1}$ . Of course, this becomes more and more difficult with decreasing  $w$ .

## 5. EDGE KINK MODES AND OPTIMUM CURRENT PROFILES

Optimum current profiles, which are stable against all the current driven modes and have a minimum  $q(a)$  value [11], should satisfy the following requirements: a)  $q(0) > 1$ , b)  $q(a) > 2$ , c) the 2/1 mode should be stabilized by local effects, such as a break in the current profile at  $\rho_{2/1}$  (Fig. 5(a)), or by local current drive at  $\rho_{2/1}$  (Fig. 4(c)). If necessary, the 3/2 mode should be stabilized in a similar manner.

In this case, only the problem of higher mode stabilization remains, because an unfavourable break in the  $j(\rho)$  profile at the plasma boundary  $\rho = a$  can

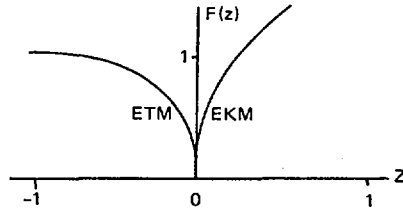


FIG. 7. Function  $F(z)$  for the criterion (7).

destabilize the edge localized modes with  $\rho_{m/n} \approx a$ . For such edge modes, the stability criterion can be written in the form:

$$aj'_a < \frac{S}{q(a)} mF\left(\frac{m - nq(a)}{S}\right) \quad (7)$$

where  $j'_a$  and  $S$  are the current density gradient and the shear at the current channel boundary, and the function  $F(z)$  is shown in Fig. 7;  $z > 0$  corresponds to the edge kink modes and  $z < 0$  to the edge tearing modes. When  $z \rightarrow 0$ , the function  $F(z) \propto 1/|\ln z| \rightarrow 0$ .

From Eq. (7), it follows that there can be a stable current channel boundary with a finite current density gradient:  $j'_a(a-0) = j'_a \neq 0$ ,  $j'_a(a+0) = 0$ . In fact, for an irrational  $q(a)$  value, the limitation on  $j'_a$  remains finite because the factor  $m$  compensates a comparatively slow decrease in  $F(z)$  for  $z \rightarrow 0$  when the resonance surface approaches the plasma boundary. In this case, the limitations on  $j'_a$  are imposed by the low  $m$  modes. The limiting  $j'_a$ , according to criterion (7), is shown in Fig. 8 as a function of  $q(a)$  for a tokamak of circular cross-section ( $S = 2$ ). If the 2/1 tearing mode is stabilized by the break of the current profile at  $\rho_{2/1}$ , the diagram given in Fig. 8 permits the construction of completely stable current profiles with  $j'_a \neq 0$  and  $q(a) = 2 + \epsilon$ , where  $\epsilon$  is an arbitrary, small quantity. Therefore, the theoretical limit for  $q(a)$  is actually 2, instead of the previous limit  $q(a) = 2.6$  [11]. The point which corresponds to the current profile of Ref. [11] is presented in Fig. 8.

The diagram of Fig. 8 gives a natural limitation on the current density gradient  $j'_a$ , due to the edge kink modes. When the  $q(a)$  value changes, the limiting current density corresponds to the right hand edge of the teeth, jumping from one to another with the variation in  $q(a)$ . From the diagram presented in Fig. 8 we see that there are some natural characteristic values of  $q(a)$  corresponding to the gaps between the teeth, the most representative being located near  $q(a) = 2.5$  and  $q(a) = 3$ .

Let us note that the limitation on  $j'_a$  due to the edge MHD modes is proportional to the shear,  $S$ . In tokamaks with a separatrix, because of the increase

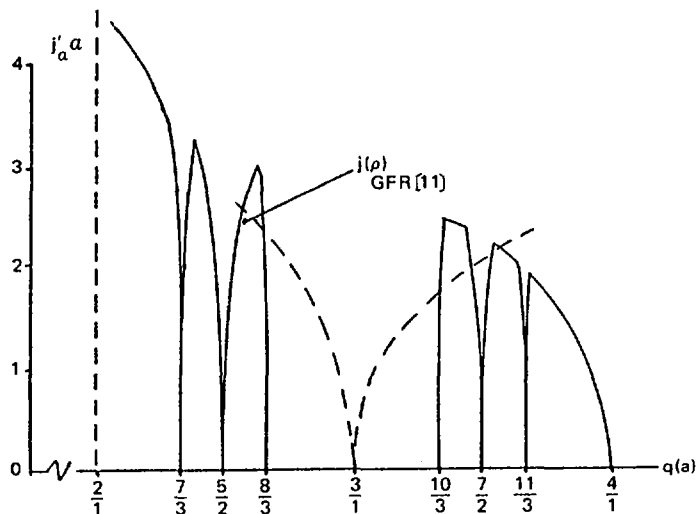


FIG. 8. Limiting  $j'_a$  at plasma boundary. Dashed line illustrates limitation due to 3/1 mode, as obtained from criterion (7), which is not well applicable to 3/1 mode. 2/1 tearing mode is assumed to be stabilized by a local effect in the same way as all  $m/n = 2/1$  modes.

in shear at the edge of the current channel,  $S > 2$ , the limiting values of  $j'_a$  are greater, making it more likely to stabilize the 2/1 mode by a fast drop in  $j(\rho)$  outside the resonance surface  $\rho_{2/1}$ . It is natural to assume that the difference in  $S$  permits an H regime only in tokamaks with divertors and not in tokamaks with limiters.

## 6. APPEARANCE OF DISRUPTIONS IN TOKAMAKS

From our point of view [4], the disruptive instability is a manifestation of a kink instability in a real plasma. This statement is based on the fact that kink modes ( $nq(a) < m$ ), being unstable, do not display saturation in a real plasma and cannot lead to a new equilibrium (with  $j(\rho) > 0$ ). In the presence of a supporting channel,  $\rho_{m/n}^0 < a$  (see Eq. (4)) corresponding to the existence of a region with  $nq(\rho) < m - 1$ , only the plasma outside  $\rho_{m/n}^0$  will be rearranged, which takes the form of a minor disruption. If there is no supporting channel,  $m - 1 < nq(\rho) < m$ , the whole current profile will be rearranged. This will appear as a major disruption.

Let us consider some examples of different disruption possibilities. During the current rise, four characteristic cases can be identified when  $q(a)$  crosses the resonance value [12]:

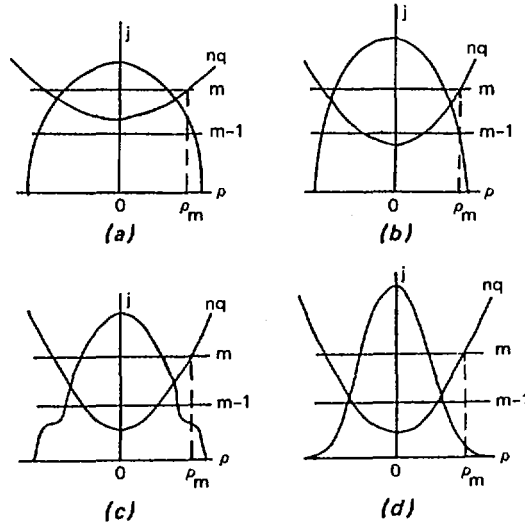


FIG. 9. Typical regimes of passage through resonance  $q(a)$  values at current rise phase: (a) with major disruption (b) with minor disruption, both without precursor; (c) with minor disruption preceded by Mirnov oscillations; (d) without MHD perturbations.

- (a)  $nq(0) > m - 1$ , and an abrupt current density decrease beyond the resonance surface  $\rho_{m/n}$  (Fig. 9(a)). In this case, the  $m/n$  tearing mode is stable. The kink mode leading to a major disruption is excited when the surface  $\rho_{m/n}$  crosses the plasma boundary.
- (b)  $nq(0) < m - 1$ , and the same abrupt decrease in current density (Fig. 9(b)). The kink mode only leads to a minor disruption, without precursor.
- (c)  $nq(0) < m - 1$ , and smooth current density outside the surface  $\rho_{m/n}$  (Fig. 9(c)). The tearing mode is in a saturated state (Mirnov oscillations). A slightly pronounced minor disruption arises from the Mirnov oscillations when the surface  $\rho_{m/n}$  crosses the plasma boundary.
- (d)  $nq(0) < m - 1$ , and the difference between  $nq(0)$  and  $nq(a)$  is sufficient to stabilize the  $m/n$  tearing mode. The resonance value of  $q(a)$  is crossed without MHD perturbations.

In the stationary state, the  $2/1$  tearing mode plays the main role. When  $q(a) \lesssim 2$ , any reconnection due to the  $1/1$  mode will always lead to a major disruption. For  $q(a) > 2$  and  $q(0) \gtrsim 1$ , the  $2/1$  tearing mode will always be unstable if no local mechanisms of stabilization are at work. There is a  $2/1$  magnetic island, which plays a basic role in current profile self-consistency [13]. In this case, disruption becomes possible when the separatrix of the island goes beyond the boundary of the current channel [2]. In this situation, the width of the islands can be estimated from quasi-linear theory (Eq. (6)). The last case corresponds to the transformation of the tearing mode into a kink mode.

## 7. CONCLUSIONS

The SCL principle is shown to be the most suitable method of analysing the stability of current driven modes. While the formal linear stability theory of the 1970s operated with badly defined concepts (such as 'peaked' or 'rounded' current profiles, etc.), the present approach elucidates the physics of the stability properties for any current profile. In addition to a new representation of linear stability it provides full information on current profile stability against disruption, even for the most exotic current distributions.

Let us also note that synchronization of the external impact with the island rotation frequency is not essential for tearing mode suppression by local current redistribution.

## REFERENCES

- [1] ZAKHAROV, L.E., *Fiz. Plazmy* 7 (1981) 1295.
- [2] BOGOMOLOV, L.M., ZAKHAROV, L.E., BLEKHER, P.M., *Nucl. Fusion* 27 (1987) 241.
- [3] BLEKHER, P.M., *Fiz. Plazmy* 10 (1984) 493.
- [4] ZAKHAROV, L.E., *Fiz. Plazmy* 7 (1981) 18.
- [5] DNESTROVSKIY, Yu.N., KOSTOMAROV, D.P., POPOV, A.M., *Zh. Tekh. Fiz.* 42 (1972) 1825.
- [6] IGNAT, D.W., RUTHERFORD, P.H., HSUAN, H., in *Course and Workshop on Applications of RF Waves to Tokamak Plasmas* (BEABEI, S., GASPARINO, U., SANDONI, E., Eds), Vol. 2, Monotypia Franchi (1985) 525.
- [7] ROSENBLUTH, M.N., MONTICELLO, D.A., STRAUSS, H.R., WHITE, R.B., *Phys. Fluids* 19 (1976) 1987.
- [8] WHITE, R.B., MONTICELLO, D.A., ROSENBLUTH, M.N., WADDELL, B.V., *Phys. Fluids* 20 (1977) 800.
- [9] BLEKHER, P.M., ZUEVA, N.M., YURCHENKO, E.I., Preprint, Keldysh Institute of Applied Mathematics, Moscow (1982) 121.
- [10] ALIKAEV, V.V., STEPANENKO, M.M., *Pis'ma Zh. Ehksp. Teor. Fiz.* 40 (1984) 327.
- [11] GLASSER, A.H., FURTH, H.P., RUTHERFORD, P.H., *Phys. Rev. Lett.* 38 (1977) 234.
- [12] ZAKHAROV, L.E., PUTVINSKIY, S.V., in *Itogi Nauki i Tekhniki, Ser. Fizika Plazmy* (SHAFRANOV, V.D., Ed.), Vol. 7, VINITI, Moscow (1985) 4.
- [13] OHYABU, N., LEE, J.K., DE GRASSIE, J.S., *Nucl. Fusion* 26 (1986) 593.
- [14] KURITA, G., AZUMI, M., TAKIZUKA, T., TUDA, T., TSUNEMATSU, T., TANAKA, Y., TAKEDA, T., *Nucl. Fusion* 26 (1986) 449.

# BIFURCATION OF PLASMA EQUILIBRIUM IN TOKAMAKS

Yu.N. DNESTROVSKIJ

I.V. Kurchatov Institute of Atomic Energy

D.P. KOSTOMAROV, A.V. PEDORENKO, A.M. POPOV

M.V. Lomonosov Moscow State University

Moscow, Union of Soviet Socialist Republics

## Abstract

### BIFURCATION OF PLASMA EQUILIBRIUM IN TOKAMAKS.

Helical equilibria for the  $m/n=2$  mode in a plasma cylinder are studied by numerical and analytical methods. These helical equilibria are shown to be present within the subrange  $q_{cr} < q_0 < 1$  of the kink instability range  $q_{cr} < q_0$ . Transition across the stability boundary,  $q_{cr}$ , corresponds to a bifurcation from axially symmetric equilibria towards helical equilibria with elliptical cross-section.

## 1. INTRODUCTION

Careful analysis of plasma behaviour in the presence of a linearly unstable helical mode is necessary for understanding the mechanism of discharge transition into a regime with low  $q_a = q(a_0)$ . The  $m/n = 2$  mode is the most dangerous one. The development of unstable motions for this mode, as has been shown in Refs [1, 2] by a numerical solution to the set of MHD equations, can result in stabilized states of the plasma column in a non-linear stage. This behaviour of the solutions demands a study of the helical equilibria.

Existence and properties of some helical equilibria have been considered in [3–6]. In particular, in [4], the bifurcation of a cylindrical equilibrium to a helical one is shown to be subcritical, and there are no adjacent helical equilibria for a homogeneous current. The bifurcation can be supercritical for an inhomogeneous current [3]. This implies that the evolution of unstable helical modes will result in a transition of the plasma column from a cylindrical equilibrium into an adjacent helical equilibrium without discharge destruction.

Helical equilibria in a plasma cylinder for the  $m/n=2$  mode are studied by numerical and analytical methods in this paper. Conditions for the bifurcation of axially symmetric equilibria to helical ones, the nature of bifurcation and its dependence on plasma parameters and current profile are found. The case of homogeneous current, is, from the viewpoint of bifurcation, found to be

degenerate. The bifurcation is always supercritical for a monotonically decaying inhomogeneous current. The bifurcations are studied by two methods, the first of which is based on the direct numerical solution of a 2-D helical equilibrium problem [6]. The second technique reduces the problem of helical equilibrium within an unlimited region to a one-dimensional integrodifferential equation [4], which is also solved numerically. It is possible to expand the bifurcation equation in terms of ellipticity in the neighbourhood of the bifurcation points and to obtain some analytical expressions for the bifurcation curve. The results for the two- and one-dimensional problems are in good agreement with each other.

## 2. 2-D PROBLEM OF HELICAL EQUILIBRIUM

Let us consider a plasma cylinder, with a length of  $L = 2\pi R$ , a radius of  $a_0$  and identified ends. All physical parameters characterizing the configuration depend only on two variables,  $r$  and  $\theta = \varphi - \alpha Z$ , in the presence of helical symmetry. Here,  $r, \varphi, Z$  are cylindrical co-ordinates with the  $Z$ -axis along the cylinder axis. The parameter  $\alpha = 2\pi n/mL = n/mR$  determines the pitch,  $n$  and  $m$  are the numbers of starts along  $Z$  and  $\varphi$ , respectively. The equation for a helical equilibrium has a form [5]:

$$\Delta\psi^* = -\frac{4\pi}{c} \left[ j(\psi^*) - j_B \right] \quad (1)$$

where  $\psi^*$  is the helical potential,  $j_B = c(4\pi 2\alpha B_z)$ , and

$$B_r^* = B_r = \frac{1}{r} \frac{\partial\psi^*}{\partial\theta}, \quad B_\theta^* = B_\varphi - \alpha r B_z = -\frac{\partial\psi^*}{\partial r}$$

The boundary condition for Eq. (1) is set on an ideally conducting casing of circular cross-section with radius  $r_w$ :

$$\psi^* \Big|_{r=r_w} = 0 \quad (2)$$

The longitudinal current density,  $j(\psi^*)$ , is given in 2-D calculations by the following relationship:

$$j(\psi^*) = j_0 \left[ 1 - \left( \frac{\psi^* - \psi_0^*}{\psi_p^* - \psi_0^*} \right)^k \right] (\psi^* < \psi_p^*), \quad j = 0 (\psi^* > \psi_p^*) \quad (3)$$

Here,  $\psi_0^*$  and  $\psi_p^*$  are the potentials at the magnetic axis and the plasma boundary, respectively. The parameter  $\psi_0^*$  is an arbitrary quantity.  $\psi_p^*$  is determined by the condition:

$$\psi_p^* = \psi_0^* \left( b_0, \pm \frac{\pi}{2} \right) \quad (4)$$

The parameter  $\kappa$  allows the localization of the current distribution and, thus, the ratio  $\gamma = q_a/q_0$  to be varied. The quantity  $j_0$  is found, in the process of solution, from the condition of total current conservation,

$$I_p = \int_{S_p} j(\psi^*) dS$$

where  $S_p$  is the plasma column cross-section. It is convenient to use the relation  $\nu = I_p / (S_p j_B)$  as the bifurcational parameter. For a circular plasma column cross-section, we have  $\nu = 2/q_a$ . If the parameter  $\nu$  is within the zone of linear stability for a kink mode ( $\nu > \nu_{cr}$ ), the plasma cross-section and the cross-sections of the internal magnetic surfaces will be a family of concentric circumferences for the equilibrium found. If the value of  $\nu$  passes into the zone of linear instability, two possibilities will appear: either there is no solution to the problem (1), (2), or the equilibrium plasma cross-section and the cross-sections of the internal magnetic surfaces are extended towards the fixed points (4), in spite of the circular cross-section of the casing (2). The configuration of these cross-sections is close to elliptical and can be characterized by the ratio  $\lambda = b/a$ , where  $b$  and  $a$  are the major and minor semiaxes of the magnetic surface cross-section. On the plasma surface,  $a = a_0$ ,  $b = b_0$ ,  $\lambda = \lambda_0 = b_0/a_0$ . For the case of homogeneous current within the plasma,  $\lambda = \text{const} = \lambda_0$ . For an inhomogeneous current,  $\lambda$  is a function of the magnetic surface. The results of calculations to be given below refer to a case with  $r_w/b_0 = 1.5$ ;  $m/n = 2$ .

Later on, the dependence of  $\lambda_0$  on  $\nu$  will be identified with a bifurcational curve. Some bifurcational curves for different  $\gamma$  are given in Fig. 1. The choice of  $\kappa$ , in (3), for a current profile is done to retain  $\gamma$  in the process of solution. The bifurcation points in Fig. 1 correspond to entering the zone of linear instability with respect to  $\nu$  (transition across  $\nu = \nu_{cr}$ ). There are no helical equilibria to the left of point  $\nu_{cr} = 2$  for  $\gamma = 1$  (homogeneous current, curve 1). This corresponds to the results of Ref. [4], and to the analytical dependence found there:

$$\lambda_0 = \nu - 1 + \sqrt{\nu(\nu - 2)} \quad (5)$$

For a parabolic current, when  $\gamma = 2$  (curve 2), a branch of the bifurcational curve corresponding to an elliptic plasma cross-section emerges at the point of

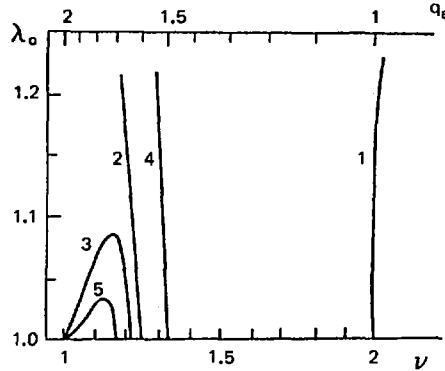


FIG. 1. Ratio of semi-axes,  $\lambda_0 = b_0/a_0$ , for elliptical plasma cross-section in helical equilibrium versus  $\nu$  (bifurcation curves). Curves 1, 2 and 3 correspond to  $\gamma = 1, 2.0$  and  $2.1$ ; they are calculated by 2-D model. Curves 4 and 5 correspond to  $\gamma = 2.0$  and  $2.5$  and are calculated by 1-D model.

entry into the linear instability zone. The bifurcation is, in this case, supercritical. Therefore, the evolutionary transition to a helical equilibrium should be of a 'soft' nature. This behaviour is confirmed by a numerical integration of the time dependent, non-linear MHD equations [1, 2].

When the current profiles are more peaked,  $\gamma > 2$  (curve 3), the bifurcation curve does not tend to infinity, but has a maximum within the instability range  $1 < \nu < \nu_{cr}$ . The values of  $\lambda_0$  on this curve are not large. Therefore, the temporal evolution of the unstable kink modes should only result in weak perturbations within the plasma column.

### 3. 1-D MODEL OF HELICAL EQUILIBRIUM

The helical equilibrium problem of Eq. (1) can be solved by the method of preset magnetic surfaces [4]. Let the cross-sections of the magnetic surfaces be a family of nested ellipses:

$$x = a \cos \theta, \quad y = \lambda(a) a \sin \theta$$

where  $a$  is the radial co-ordinate (marker) of magnetic surfaces and  $\lambda(a)$  is the ratio of the semi-axes of the nested ellipses. An equation for ellipticity  $\lambda(a)$  can be written in the following form:

$$t = \frac{a\lambda'}{\lambda} = \frac{A}{B} - 1 + \frac{1}{2} \left( \frac{B}{C} \right)^2 \pm \frac{1}{2} \left| \frac{B}{C} \right| \sqrt{4 \frac{A}{C} + \left( \frac{B}{C} \right)^2} \quad (6)$$

The following designations are introduced here:

$$\begin{aligned} A &= 2(3\lambda^2 + 1) f_0 + 2 f_1 - 8\lambda^2 f_2 \\ B &= 2(1 - \lambda^4) f_0 - 2\lambda^2 + 1) f_1 + 4(\lambda^4 - 1) f_2 \\ C &= 2(3 + \lambda^2) f_0 \lambda^2 - 2\lambda^2 f_1 - 8\lambda^2 f_2 \end{aligned} \quad (7)$$

$$f_0 = \lambda [j(a) - j_B]$$

$$f_1 = \frac{1}{a^4} \int_0^a j'(a) a^4 \lambda (\lambda^2 - 1) da, \quad f_2 = \frac{1}{a^2} \int_0^a j'(a) a^2 \lambda da$$

Equation (6) is a non-linear integrodifferential equation. To complete the posing of the problem, we have to prescribe the current distribution,  $j(a)$ , and the boundary condition on the plasma column edge,  $a = a_0$ :

$$\lambda(a_0) = \lambda_0 \quad (8)$$

Substituting condition (8) into (6), we find  $\lambda'$  and the field  $\vec{B}^*$  at the plasma column boundary. As a result, we obtain Cauchy's problem for Poisson's equation (1) for an external field. Using the method of separation of variables, for an external quadrupole field, we have [4]:

$$\begin{aligned} \psi_{\text{ext}}^* &= \frac{\pi}{c} (x^2 - y^2) F(\lambda_0) \\ F(\lambda_0) &= \frac{\lambda_0^2 - 1}{(\lambda_0 + 1)^2} j_B \\ &\quad - 4 \frac{(j - j_B) \lambda_0 - 1/a_0^2 \int_0^{a_0} j' a^2 \lambda da}{(\lambda_0 + 1)^2} \\ &\quad \times \frac{\lambda_0^2 - 1 + \lambda_0^2 a_0 \lambda'_0 / \lambda_0}{(\lambda_0^2 + 1) (1 + \sqrt{1 + a_0 \lambda'_0 / \lambda_0}) + \lambda_0^2 a_0 \lambda'_0 / \lambda_0} \end{aligned} \quad (9)$$

The helical equilibria in which we are interested satisfy the condition  $\psi_{\text{ext}}^* = 0$ , i.e.

$$F = 0 \quad (10)$$

which defines the permissible values of  $\lambda_0$  for boundary condition (8).

For a homogeneous current,  $j'(a) = 0$  and  $\lambda'(a) = 0$ , and Eq. (10) leads to (5). Solving Eq. (6), we use two different parametrizations for the current profile:

$$j = j_0(1 - a^2/a_0^2)^\gamma \quad (11)$$

$$j = j_0 \begin{cases} 1 & (0 < a < r_0) \\ \left[1 - \left(\frac{a - r_0}{a_0 - r_0}\right)^2\right]^\kappa & \end{cases} \quad (12)$$

Equation (6), with current profiles (11) and (12) and boundary conditions (8) and (10), has been solved numerically. The same parameters,  $\nu$  and  $\gamma$  as in the previous case have been used as variables. Curves 4 and 5 in Fig. 1 correspond to  $\gamma = 2.0$  and  $\gamma = 2.5$ . Curves 2 and 4 are slightly shifted with respect to each other. This shift is related to a different position of the casing for the 2-D problem ( $r_w/a_0 = 1.5$ ) and for the 1-D problem ( $r_w/a_0 = \infty$ ). From Fig. 1, we also see that, with the casing approaching the plasma, the modulus of the derivative  $d\lambda_0/d\nu|_{\nu=\nu_{cr}}$  is reduced, which implies a 'softer' bifurcation of the axially symmetric equilibria towards the helical ones.

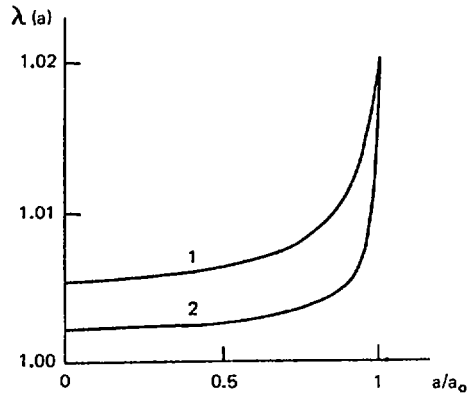


FIG. 2. Solution  $\lambda(a)$  to problem (6) to (10) at  $\gamma = 2.5$ ,  $\lambda_0 = 1.02$ . Curve 1 corresponds to  $\nu = 1.165$ , Curve 2 to  $\nu = 1.07$ .

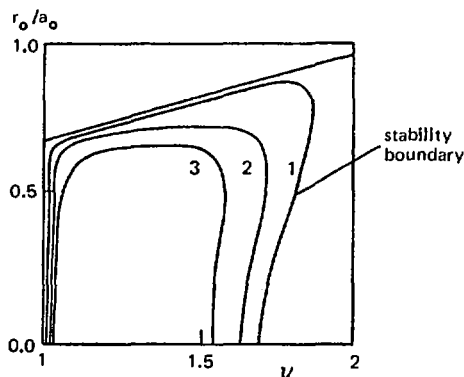


FIG. 3. Curves  $\lambda_0(r_0, \nu) = \text{const}$  for current distribution (12) at  $q_0 = 0.9$ . Curve 1 corresponds to  $\lambda_0 = 1.0$ ; Curve 2 to  $\lambda_0 = 1.1$ ; Curve 3 to  $\lambda_0 = 1.2$ .

When  $\gamma > 2$ , i.e. the current profile is more pronouncedly peaked than parabolic, each bifurcation curve has a maximum. In this case, there are two helical equilibria with the same boundary extension,  $\lambda_0$ , and with different values of  $\nu$ . Two curves,  $\lambda(a)$ , for  $\gamma = 2.5$  with the same  $\lambda_0 = 1.02$  and with different values of  $\nu$  —  $\nu = 1.165$  (Curve 1) and  $\nu = 1.07$  (Curve 2) — are shown in Fig. 2. The shape of these curves shows that  $\lambda(a)$  is close to unity at the plasma column centre, i.e. the magnetic surface cross-sections are almost circular and the extension of the magnetic surfaces only occurs close to the boundary  $a = a_0$ . The solutions to Eq. (8) are well approximated by the relationship

$$y = y^0 - (1 - y^0)x^n \quad (13)$$

where  $y = E/E_0$ ,  $E = \lambda(a) - 1$ ,  $E_0 = \lambda_0 - 1$ ,  $x = a/a_0$ ,  $n \cong [\gamma^2] - 1$ .

The results of calculations for current profile (12) are shown in Fig. 3. The cross-sections of the bifurcational surface,  $\lambda_0 = S(q_0, r_0, \nu)$  with the planes  $\lambda_0 = 1.0$ ; 1.1; 1.2 at  $q_0 = 0.9$  are given in the figure.  $\lambda_0 = 1$  is the stability region boundary. It consists of bifurcation points.

#### 4. ANALYTICAL RELATIONSHIPS FOR SOLUTIONS IN THE NEIGHBOURHOOD OF BIFURCATION POINTS

Analytical representations for the equilibrium solutions in the neighbourhood of the bifurcation points can be derived. Let us use a 1-D model and expand

Eqs (6) and (10) in terms of  $\epsilon_0$ . Terms of  $\epsilon_0$  with powers higher than one should be retained in order to derive the bifurcational relationships. As a result, we obtain:

$$\dagger (a_0) = \mathcal{L}\epsilon_0 + \mathcal{B}\epsilon_0^2 4F/j_B = \epsilon_0 D(\nu_{cr} - \nu) + \delta\epsilon_0^2 = 0 \quad (14)$$

where

$$\begin{aligned} \mathcal{L} &= 2A_2, \mathcal{B} = 2(A_2 - 1)(A_1 + A_2) + 3A_3 - 2A_2 \\ D &= 2 + \mathcal{L}, \nu_{cr} = \frac{4 + \mathcal{L}}{2 + \mathcal{L}}, \delta = \left( \mathcal{B} - \frac{\mathcal{L}^2}{2} - 1 \right) (1 - \nu) - 1 \end{aligned} \quad (15)$$

$$\text{Here, } A_k = \frac{1 - \gamma I_k}{1 - \gamma q_0/2} \quad (K = 1, 2, 3)$$

$$I_1 = \int_0^1 I(x^2 y)' dx, \quad I_2 = \int_0^1 I(x^4 y)' dx, \quad I_3 = \int_0^1 I(x^4 y^2)' dx$$

and  $y(x)$  is found as a solution to the non-linear integro-differential equation

$$xy' = y \left\{ 1 - \left[ \frac{1}{x^4 y} \int_0^x I(x^4 y)' dx - q_0/2 \right] \middle/ \left[ \frac{2}{x^2} \int_0^x I x dx - \frac{q_0}{2} \right] \right\} \quad (16)$$

with the boundary condition  $y(1) = 1$ .

It can be shown that Eq. (16) coincides with an equation for the eigenfunctions of a linear stability problem of external modes.

It follows from (14) that bifurcation is supercritical for  $\delta \neq 0$ . When  $\gamma = 1$ , which corresponds to a homogeneous current,  $\delta = 0$ , and terms of the order of  $\epsilon_0^2$  should be taken into account in expansion (14). For a parabolic current, relationships (15), with account of (13), yield  $d\epsilon_0/d\nu|_{\nu=\nu_{cr}} = D/\delta = -3.8$ . The numerical calculations, using the complete 1-D model, result in  $d\epsilon_0/d\nu|_{\nu=\nu_{cr}} = -4$ .

## 5. DISCUSSION

It is shown, by solving 2-D and 1-D problems, that bifurcation of axially symmetric equilibria towards helical ones occurs at the stability boundary for

helical modes. The bifurcation is supercritical for an inhomogeneous current, which results in a possible non-linear stabilization of external kink modes. The region where adjacent equilibria are present, for infinitely removed casing,

$$q_{cr} < q_0 < 1 \quad (17)$$

is located within the instability range  $q_{cr} < q_0$ . The case of homogeneous current is degenerate; in this case, bifurcation is subcritical, and no mode stabilization occurs. A casing approaching the plasma increases the stability range and changes the region where helical equilibria are present. For the most stable, piecewise current, we have  $q_{cr} = 1$ , and range (17) disappears.

Thus, the really dangerous zone,  $q_0 > 1$ , is determined by the most stable current profile. A search for the instability range boundaries at different current profiles is unnecessary since the results of such a search do not provide a complete picture of real plasma column evolution anyway. The consequences of the development of kink modes can be completely determined by non-linear effects.

#### ACKNOWLEDGEMENT

The authors express their gratitude to V.D. Shafranov for useful discussions and valuable remarks.

#### REFERENCES

- [1] ROSENBLUTH, M.N., MONTICELLO, D.A., STRAUSS, H.R., WHITE, R.B., *Phys. Fluid* **19** (1976) 1987.
- [2] DNESTROVSKIY, Yu.N., KOSTOMAROV, D.P., POPOV, A.M., SHAGIROV, E.A., *Fiz. Plazmy* **11** (1985) 1080.
- [3] SYKES, A., WESSON, J.A., in *Plasma Physics and Controlled Nuclear Fusion Research 1980* (Proc. 8th Int. Conf. Brussels, 1980), Vol. 1, IAEA, Vienna (1980) 237.
- [4] ZAKHAROV, L.E., *Fiz. Plazmy*, **7** (1981) 18.
- [5] ZAKHAROV, L.E., SHAFRANOV, V.D., *Voprosy teorii plazmy*, Vol. 11, Energoizdat, Moscow (1982) 118.
- [6] DNESTROVSKIY, Yu.N., KOSTOMAROV, D.P., PEDORENKO, A.V., POPOV, A.M., in *Controlled Fusion and Plasma Physics* (Proc. 11th Europ. Conf. Budapest, 1985), Vol. 1, European Physical Society (1985) 102.



## DISCUSSION

### ON PAPERS IAEA-CN-47/E-I-4-1 AND E-I-4-2

D.B. NELSON: Several years ago I considered a model similar to the current layer model described by you. I found the stability results to be very sensitive to whether the layer boundary occurred at a mode rational surface, and to the magnitude of the jump in current density at a mode rational surface. I therefore abandoned the model as being an unrealistic description of an actual current profile.

I wonder if you have encountered the same problem and, if so, what you have done about it?

B.B. KADOMTSEV: Yes, I believe that this problem has been found, but I would suggest that you discuss it with the authors of papers IAEA-CN-47/E-III-15 and E-III-16.

H.P. FURTH: I would like to comment on the finding of  $\Delta'$ -stable tokamak  $\tau(r)$  profiles. Ten years ago, the only known solutions had very close fitting shells or very high values of  $q(a)$ . Glasser et al. then found a  $\tau(r)$  model that was stable for  $q(a) = 2.6$  without a shell. We did not carry the  $\tau(r)$  profile optimization further at that time, because it seemed unlikely that such refinements could be realized experimentally. In recent experiments, however, the tokamak has turned out to be an excellent solver of the  $\Delta' < 0$  problem: this is an important part of the 'profile consistency' phenomenon. Inspired by this observation, Dr. F. Cheng at Princeton has carried through a full optimization study. Like Dr. Zakharov, he finds that  $q(a) \rightarrow 2$  is consistent with  $\Delta'$  stability, but he identifies not just a single  $\tau(r)$  solution for this case, but a whole family of them. They are all rather peculiar looking but perhaps the tokamak plasma will find them all.

B.B. KADOMTSEV: Thank you for the comment.

L. CHEN: It seems to me in the case of the quasi-linear saturation of ballooning modes that the choice of the trial function disregards the inertial layer physics. Specifically, one would expect the formation of singular current sheets which could affect the quasi-linear saturation process. Could you comment on this point?

B.B. KADOMTSEV: I don't know exactly, but quasi-linear saturation may resemble near-equilibrium, so that inertia can be disregarded.



# RADIOFREQUENCY STABILIZATION OF IDEAL BALLOONING MODES IN A TOKAMAK PLASMA

A. SEN, P.K. KAW, A.K. SUNDARAM  
Institute for Plasma Research,  
Bhat, Gandhinagar District,  
India

## Abstract

### RADIOFREQUENCY STABILIZATION OF IDEAL BALLOONING MODES IN A TOKAMAK PLASMA.

A new method of stabilizing ideal ballooning modes in a tokamak plasma through the use of radiofrequency waves is suggested. Model calculations show that ponderomotive forces produced by radial gradients in the RF energy can provide an effective stabilizing mechanism and create a stable window to the second stability regime.

## 1. INTRODUCTION

The maximum achievable beta (the ratio of plasma pressure to magnetic field pressure) in a tokamak plasma is limited to rather low values by the onset of the ideal ballooning instability. To improve the critical beta, several methods have been proposed, such as the use of bean shapes or crescent shapes for the plasma cross-section and the introduction of energetic particles [1-3]. One important aim of these investigations was to find a stabilization method permitting access to the second stability regime without having to burn through an unstable domain. In this paper, we propose the use of radiofrequency (RF) waves (close to characteristic frequencies such as the lower hybrid frequency and the ion cyclotron frequency) for stabilization of the ideal ballooning instability. We show that for rather modest amplitudes of the RF-fields a stable window to the second stability regime can be made available.

We take our cue from some recent experiments on magnetic mirrors [4, 5] demonstrating that Rayleigh-Taylor instabilities driven by bad magnetic curvature can be stabilized by application of RF waves near the ion cyclotron frequency. Theoretical calculations [6] indicate that the dominant physical effect responsible for RF stabilization is the non-resonant ponderomotive force which counteracts the effective gravitational force due to bad magnetic curvature; other competing effects contributing to RF stabilization are related to resonant mode coupling phenomena [7]. Our calculations reveal similar stabilizing effects on the ideal ballooning modes in a tokamak plasma.

## 2. BALLOONING EQUATION WITH RF FIELDS

We derive a model equation for the ideal ballooning modes from the following closed set of linear one-fluid equations:

$$\rho_0 \frac{\partial \vec{V}_1}{\partial t} + \rho_1 \langle (\vec{V}_{0E} \cdot \nabla) \vec{V}_{0E}^* \rangle = \frac{\vec{J}_1 \times \vec{B}_0}{C} + \frac{\vec{J}_0 \times \vec{B}_1}{C} - \nabla P_1 \quad (1)$$

$$E_1 + \frac{\vec{V}_1 \times \vec{B}_0}{C} = 0 \quad (2)$$

$$\frac{\partial P_1}{\partial t} + (\vec{V}_1 \cdot \nabla) P_0 = 0 \quad (3)$$

$$\frac{\partial \rho_1}{\partial t} + (\vec{V}_1 \cdot \nabla) \rho_0 = 0 \quad (4)$$

$$\nabla \cdot \vec{J}_1 = 0 \quad (5)$$

and Maxwell's equations. Here,  $\vec{V}_{0E}$  is the induced oscillating velocity of the fluid (ions) in the presence of an external RF field and the other symbols have their standard meanings. The term  $\rho_1 \langle (\vec{V}_{0E} \cdot \nabla) \vec{V}_{0E}^* \rangle$  is the ponderomotive contribution due to the RF field and can be rewritten as

$$F_P = \rho_1 \langle (\vec{V}_{0E} \cdot \nabla) \vec{V}_{0E}^* \rangle = \frac{\rho_1}{2} \langle \nabla |V_{0E}^2| \rangle$$

for electrostatic RF waves.

For simplicity, we assume that the ponderomotive force is radially symmetric (with respect to the minor radius) and look for effects arising from radial gradients in the RF energy. We also neglect for the moment other non-linear RF effects (for instance side-band coupling or modification of the equilibrium profile) and assume a model equilibrium with shifted circular magnetic surfaces. The procedure for determining the marginal stability of such an equilibrium to ballooning instabilities has been well developed and considerably simplified through the use of ballooning co-ordinates [8-10]. This procedure involves only the solution of an ordinary differential equation, which in our case is given by

$$\frac{\partial}{\partial \eta} [1 + (s\eta - \alpha \sin \eta)^2] \frac{\partial F}{\partial \eta} + \alpha [\cos \eta + \sin \eta (s\eta - \alpha \sin \eta)] F + P_{\text{rad}} \cdot F = 0 \quad (6)$$

where  $s = (r/q)(dq/dr)$  is the shear parameter,  $\alpha = -(2Rq^2/B^2)$ ,  $(dp/dr)$  is a measure of the maximum stable pressure gradient,  $q$  is the safety factor,  $\eta = s\theta$  is the ballooning co-ordinate and  $F$  is the normalized potential.

$$P_{\text{rad}} = \frac{1}{2k_{\perp}^2 V_A^2} \left( \frac{1}{\rho_0} \frac{d\rho_0}{dr} \right) \frac{d}{dr} |V_{0E}^2|$$

is an additional term due to the RF presence. Its physical origin is the leading contribution from

$$c\nabla \cdot \left[ \frac{B_0}{B_0^2} \times \left( \frac{\rho_1}{2} \nabla |V_{0E}^2| \right) \right] \cong -\frac{c\bar{B}_0}{2B_0^2} \cdot \nabla \rho_1 \times \nabla |V_{0E}^2|$$

For  $P_{\text{rad}} = 0$ , Eq. (6) reduces to the standard model equation for the ideal ballooning mode [8-10]. Our aim is to study the effect of the additional term due to RF waves on the stability properties of the ballooning mode.

### 3. NUMERICAL RESULTS AND ANALYTIC LIMITS

We solve Eq. (6) numerically, with the boundary conditions  $F \rightarrow 0$  as  $|\eta| \rightarrow \infty$ . Numerically, this involves setting  $F(\eta_0) = 0$  at some arbitrarily large  $\eta_0$  and iteratively obtaining the eigenvalue  $\alpha$  for a given  $s$ . For large  $s$ , the wave function  $F$  has a narrow mode width and falls off quite rapidly at moderate values of  $\eta$ . However, in the region of small  $s$ , it is necessary to integrate out to a large  $\eta$ , since the wave functions falls off rather slowly ( $\sim 1/s$ ). For  $P_{\text{rad}} = 0$ , we recover the standard results obtained by others, namely that in the  $s$ - $\alpha$  plane there is a zone of instability which extends all the way to the origin and separates the first and second stability regimes (solid lines in Fig. 1). For  $P_{\text{rad}} > 0$ , the instability zone is found to broaden. This is consistent with the physical effect that for  $P_{\text{rad}} > 0$  the RF forces enhance the gravitational forces due to bad curvature on the outside of the torus. For  $P_{\text{rad}} < 0$ , the instability zone shrinks and also moves away from the origin (dotted curves in Fig. 1), thus providing a stable window which connects the first and second stability regimes. This fundamental change in the  $s$ - $\alpha$  diagram is brought about by finite values of

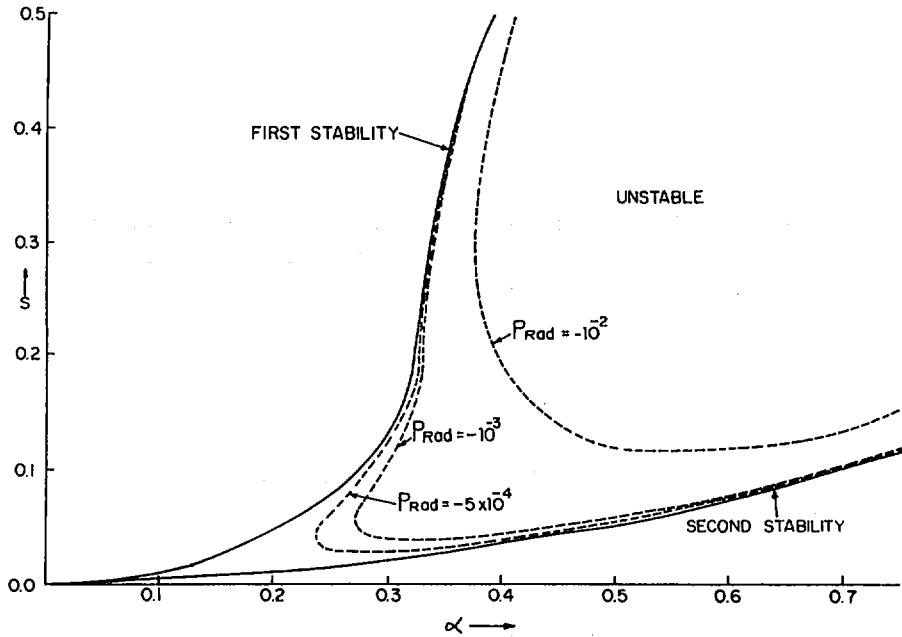


FIG. 1. Marginal stability curves for ideal ballooning modes in the  $s$ - $\alpha$  plane. The solid curves are for  $P_{\text{rad}} = 0$  and the dashed curves are for various values of  $P_{\text{rad}}$ .

$P_{\text{rad}}$  and is noticeable in our numerical solutions for even very small values of  $P_{\text{rad}}$  (about  $10^{-4}$ ). At large values of  $P_{\text{rad}}$  the window broadens considerably and the stability region is enhanced. The stabilization effect persists even at large  $s$ -values and is quite appreciable for  $P_{\text{rad}} \approx 10^{-1}$ .

To understand these numerical results, we have considered analytic approximations to Eq. (6) in two limits. In the limit of small  $s$  and  $\alpha$  – the ‘weak ballooning limit’ – the extent of the mode is large compared with  $2\pi$ , and a multiple scale analysis can be applied in order to solve the ballooning equation [9–11]. Basically, we allow variation in  $F$  on two length scales,  $\eta \approx 1$  and  $\eta \approx 1/s$ , to account for the rapid variation due to the periodicity of the equilibrium and to account for a lower secular decay due to shear. The slow variation is given by

$$Z = s\eta$$

and we expand the  $\eta$ -derivatives as

$$\frac{\partial}{\partial \eta} \rightarrow \frac{\partial}{\partial \eta} + \frac{\partial}{\partial Z}$$

and  $F$  as

$$F = F_0(Z, \eta) + F_1(Z, \eta) + \dots$$

To understand the behaviour near the origin, we also assume  $P_{\text{rad}}$  to be of order  $\alpha^4$ . Then, in zero order, we find that  $F_0 = F_0(Z)$  and, in first order,

$$F_1 = \frac{F_0}{1 + Z^2} (\cos \eta + Z \sin \eta)$$

Likewise, second- and third-order equations for  $F_2$  and  $F_3$  satisfy periodicity conditions and do not yield any constraint equation. In fourth order, however, periodicity of  $F_4$  results in an equation determining  $F_0$ :

$$s^2 \frac{\partial}{\partial Z} (1 + Z^2) \frac{\partial F_0}{\partial Z} + \frac{\alpha^2 (2s - 3\alpha^2/8)}{1 + Z^2} F_0 + P_{\text{rad}} F_0 = 0 \quad (7)$$

Equation (7) can be rewritten as a Schrödinger equation by setting

$$F_0 = \frac{\phi(Z)}{(1 + Z^2)^{1/2}}$$

to obtain

$$-s^2 \frac{\partial^2 \phi}{\partial Z^2} + V(Z) \phi = 0 \quad (8)$$

where the potential  $V(Z)$  is

$$V(Z) = \frac{1}{1 + Z^2} \left[ -P_{\text{rad}} + \frac{s^2}{1 + Z^2} + \alpha^2 \frac{2(3\alpha^2/8 - 2s)}{(1 + Z^2)^2} \right] \quad (9)$$

Equation (9) shows that if  $P_{\text{rad}} > 0$ , the potential is negative at sufficiently large  $Z$  and can lead to instability. This agrees with our numerical findings. A simple sufficient condition for stability is  $V(Z) > 0$  for all  $Z$ . This gives the stability criteria as

$$s^2 + |P_{\text{rad}}| + \alpha^2 \left( \frac{3\alpha^2}{8} - 2s \right) > 0 \quad (10)$$

From Eq. (10) we can obtain the two stability boundaries as

$$s = \alpha^2 \pm \left[ \frac{5\alpha^4}{8} - |P_{\text{rad}}| \right]^{1/2} \quad (11)$$

The two curves given by Eq. (11) approximately agree with the numerical  $s$ - $\alpha$  curves in the vicinity of the origin. Note that in the absence of  $P_{\text{rad}}$ ,  $s = \alpha = 0$  is a solution of Eq. (11), confirming the fact that the two curves emanate from the origin. However, such a solution is not possible for  $P_{\text{rad}} \neq 0$ . In addition, Eq. (11) also indicates that there is a minimum  $\alpha$ ,  $(8P_{\text{rad}}/5)^{1/4}$ , below which no instability is possible for any value of  $s$ . These features explain the moving away of the instability zone from the origin and the consequent creation of a stable window bridging the two regions.

Another interesting analytic limit is the high shear case or the strong ballooning limit ( $s \approx \alpha \gg 1$ ) where the mode is localized to a narrow range of  $\eta$ . To analyse this situation, we convert Eq. (6) to a Schrödinger form by putting

$$F = \frac{\phi}{\sqrt{1 + (s\eta - \alpha \sin \eta)^2}}$$

to obtain

$$\frac{-d^2 \phi}{d\eta^2} + V(\eta) \phi = 0 \quad (12)$$

with

$$V(\eta) = \frac{(s - \alpha \cos \eta)^2}{[1 + (s\eta - \alpha \sin \eta)^2]^2} - \frac{(P_{\text{rad}} + \alpha \cos \eta)}{1 + (s\eta - \alpha \sin \eta)^2} \quad (13)$$

Our numerical solutions show the wave function to be peaked at  $\eta = 0$  with a narrow mode width. It is thus appropriate to expand  $V(\eta)$  near  $\eta = 0$  and to retain terms up to second order in  $\eta$ . This reduces Eq. (12) to a Weber equation which can be studied analytically [12]. For our purpose, we can get a qualitative picture of the stabilizing influence of  $P_{\text{rad}}$  by considering the expanded potential

$$V(\eta) = a + b^2 \eta^2 \quad (14)$$

$$a = P_{\text{rad}} - \alpha + (s - \alpha)^2 \quad (15)$$

$$b^2 = \alpha \cdot [s - \alpha + \frac{1}{2} + (s - \alpha)^2] - 2(s - \alpha)^4 + (s - \alpha)^2 P_{\text{rad}} \quad (16)$$

For stability, we require  $b^2 < 0$ . The stability boundary can again be determined (within the present approximation) by solving  $b^2 = 0$ . An approximate solution is given by

$$s \sim \alpha \pm \left[ \frac{\alpha + P_{\text{rad}}}{2} \right]^{1/2} \quad (17)$$

which agrees roughly with the numerical curves, although the agreement is poor for the lower branch. For  $P_{\text{rad}} < 0$ , Eq. (17) indicates lowering of the upper branch and raising of the lower branch, whereby the instability regime shrinks. This is in qualitative agreement with our numerical results.

#### 4. DISCUSSION

We have carried out a model calculation to study the influence of externally imposed RF waves on the stability of ideal ballooning modes. Retaining the ponderomotive forces produced by radial gradients in the RF energy, we have obtained a modified marginal stability equation, which we have solved numerically and studied analytically in a few limits. Our results indicate significant stabilization effects and the creation of a stable window linking the first and second stability regimes. Thus the method offers the possibility of accessing the high beta regime of tokamak operation without having to burn through an unstable domain. The stabilization mechanism is significant at modest RF powers, for instance  $P_{\text{rad}} \approx \alpha^4$ , which corresponds to  $V_{\text{OE}}/V_{\text{thi}} \approx \alpha^2 \ll 1$ .

Some of the simplifying assumptions made for our calculation and the possible limitations they may impose on our results are the following: A major simplification is the neglect of other non-linear RF effects, notably side-band coupling phenomena. These can become quite significant near wave resonances and can affect the stability through parametric interactions. For interchange modes in mirror plasmas, side-band coupling has been shown to have a stabilizing influence [7], but for ballooning modes no such calculations have been performed. Our preliminary investigations show that the side-band coupling contribution can become comparable to the non-resonant contribution in some realistic parameter regimes (particularly in the edge plasma) and that side-band coupling should be incorporated into the stability calculations. Then, the model equation would no longer be so simple as Eq. (6) but would involve higher derivative modifications. Work on such a modified equation is in progress. The  $P_{\text{rad}}$  term in Eq. (6) is independent of  $\eta$  because of the assumed symmetry of the RF ponderomotive forces. Such an assumption is quite reasonable, judging from ray tracing and resonance cone results of lower hybrid waves, for example, which show that the RF energy is uniform over magnetic surfaces and changes as a function of  $r$ .

We have also ignored possible RF modifications of equilibrium profiles (e.g. distortion of magnetic flux surfaces) and this restricts the validity of our results at low RF power levels ( $V_0/V_{\text{thi}} \ll 1$ ). In the ponderomotive force term we have also neglected the electron contribution arising from the  $E \times B$  motion. This is justified in the limit  $\omega_{pe}^2/\Omega_e^2 \ll 1$  for lower hybrid waves. It is also clear that the present calculations are made with electrostatic RF waves in mind, but an extension to electromagnetic waves is not difficult. The basic stabilization mechanism arising from the radial ponderomotive force is, however, quite unambiguously shown by our simple model. This is the principal result of our calculations and it is not expected to be seriously modified by any of the above simplifications.

## REFERENCES

- [1] CHANCE, M.S., et al., *Phys. Rev. Lett.* **51** (1983) 1963.
- [2] YAMAZAKI, K., et al., *Nucl. Fusion* **25** (1985) 1543.
- [3] ROSENBLUTH, M.N., et al., *Phys. Rev. Lett.* **51** (1983) 1967.
- [4] FERRON, J.R., et al., *Phys. Rev. Lett.* **51** (1983) 1955.
- [5] INUTAKE, M., et al., in *Plasma Physics and Controlled Nuclear Fusion Research 1982* (Proc. 9th Int. Conf. Baltimore, 1982), Vol. 1, IAEA, Vienna (1983) 545.
- [6] MYRA, J.R., IPPOLITO, D.A., *Phys. Rev. Lett.* **53** (1984) 914.
- [7] McBRIDE, J.B., et al., *Phys. Rev. Lett.* **54** (1985) 42.  
McBRIDE, J.B., *Phys. Fluids* **27** (1984) 324.
- [8] CONNOR, J.W., HASTIE, R.J., TAYLOR, J.B., *Phys. Rev. Lett.* **40** (1978) 396.
- [9] STRAUSS, H.R., *Phys. Fluids* **24** (1981) 2004.
- [10] HENDER, T.C., et al., *Phys. Fluids* **24** (1984) 1439.
- [11] LORTZ, D., NÜHRENBERG, J., *Nucl. Fusion* **19** (1979) 1207.
- [12] HAZELTINE, R.D., MEISS, J.D., *Phys. Rep.* **121** (1985) 1.

# ELECTROMAGNETIC PARTICLE SIMULATIONS OF RF STABILIZATION AND ECRH OF OVER-DENSITY PLASMAS

H. ABE, S. NAKAJIMA, Y. KADOYA, H. OKADA, R. ITATANI  
Department of Electronics,  
Kyoto University,  
Kyoto

K. SAKAI, S. TAKEUCHI, M. MATSUMOTO, R. SUGIHARA<sup>1</sup>  
Department of Engineering,  
Yamanashi University,  
Kofu  
Japan

## Abstract

ELECTROMAGNETIC PARTICLE SIMULATIONS OF RF STABILIZATION AND ECRH OF OVER-DENSITY PLASMAS.

Employing a slab model and using 2½-D, electromagnetic particle simulation codes developed in two institutes of the Kyoto and Yamanashi universities, the authors study two subjects: (1) RF stabilization of flute and drift modes and (2) heating of an over-density plasma (ODP) by injection of an electron cyclotron resonance wave (ECRW).

## 1. RF STABILIZATION OF FLUTE AND DRIFT MODES

### 1.1. Model of the simulation

A slab plasma is immersed in a uniform magnetic field  $B_0(\parallel \hat{z})$  (Fig. 1(a)). The density is initially parabolic along the x-axis and uniform along the y-axis, except for a small perturbation. The RF is excited by sheet currents flowing parallel either to the y-axis (perpendicular antenna) or to  $B_0$  (parallel antenna). The system is uniform along  $B_0$ . So, the wave vector  $\vec{k}$  is always perpendicular to  $B_0$  (i.e.  $k_{\parallel} = 0$ ).

If no RF is applied, the flute mode grows as a result of the gravitational acceleration  $g(\parallel \hat{x})$ . The growth rate agrees with the theoretical value of  $\gamma_0 = (-g/\ell_n)^{1/2}$ . Here  $\ell_n \equiv n(dn/dr)^{-1}$  is the scalelength of the density gradient. The scalelength for the RF intensity  $\ell_E \equiv E^2/(dE^2/dr)^{-1}$  will also be used.

<sup>1</sup> Institute of Plasma Physics, Nagoya University, Nagoya 464, Japan.

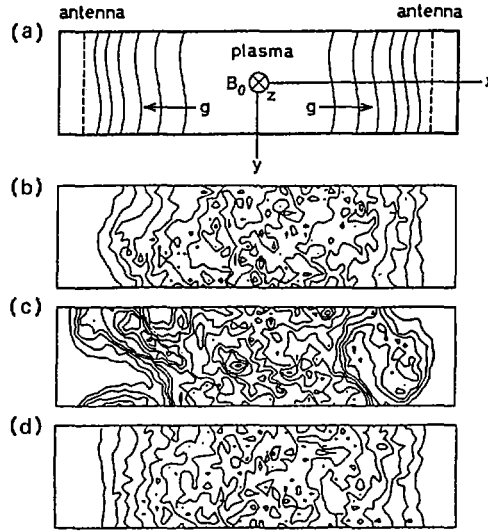


FIG. 1. (a) Configuration of the system. Contours show initial density. (b), (c), (d) Density contours at  $\Omega t = 348$ ; specifically, (b) with no RF, (c)  $\omega/\Omega = 1.25$ , (d)  $\omega/\Omega = 0.67$ .

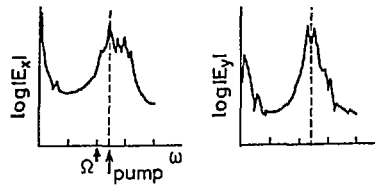


FIG. 2. Frequency spectrum. Pump at  $\omega = 1.25 \Omega$  mainly has  $x$ -component, while sidebands mainly have  $y$ -component.

## 1.2. Results of the simulation

### 1.2.1. Case 1: stabilization of drift mode by perpendicular antenna

Even if gravitation is absent, a slowly growing mode (a kind of drift mode) has been observed (Fig. 1(b)). This mode is stabilized when  $\omega < \Omega$  (ion cyclotron frequency), and destabilized when  $\omega > \Omega$  by RF with  $|e_x| \sim |e_y|$  excited by perpendicular antennas (Fig. 1(c), (d)). The growth rate of the drift mode is so slow that destabilization of the plasma by RF is shown clearly (Fig. 1(c)). In the case of destabilization, sidebands are observed in the frequency spectrum of the electric field (Fig. 2).

TABLE I. SUMMARY OF THE THEORETICAL AND SIMULATION RESULTS

		$\omega < \Omega$	$\omega > \Omega$	Dominant mechanism
$ \ell_E  \gg  \ell_n $		S( $\textcircled{S}$ )	U( $\textcircled{U}$ )	Sideband coupling
$ \ell_E  \ll  \ell_n $	$\ell_E > 0$	S	S	Ponderomotive force
	$\ell_E < 0$	U	U	

### 1.2.2. Case 2: stabilization of flute mode by perpendicular antenna

In the presence of gravitation, theory predicts that the flute mode is stabilized when  $\omega < \Omega$  and destabilized when  $\omega > \Omega$  by the RF with  $|\ell_E| \gg |\ell_n|$ , where the effect of the ponderomotive force is supposed to be negligible. Even though  $|\ell_E| \sim |\ell_n|$ , the abovementioned phenomenon may occur. Examples were already reported [1]. When the mode was stabilized, the growth rate  $\gamma$  decreased as the antenna current  $A$  increased, following the relation  $\gamma^2 = \alpha - \beta A^2$  ( $\alpha, \beta$  are positive constants). This indicates that the suppression is due to a non-linear process.

### 1.2.3. Case 3: stabilization of drift and flute modes by parallel antenna

Parallel antennas excite parallel electric fields. These fields do not propagate but are damped out at a relatively short distance. They were observed to stabilize both MHD modes, independently of the sign of  $\omega - \Omega$  in the simulations.

## 1.3. Interpretation of the results

A theory [2] has been presented on RF stabilization; it seems to be closely related to the present simulation. We briefly summarize the results of the theory. First, suppose that the high frequency waves are magnetosonic and the condition  $\omega_{pi}^2/k^2c^2 \ll 1$  holds. This corresponds to Case 2 (perpendicular antenna). The results are shown in Table I, where S and U stand for 'stabilization' and 'destabilization' or 'enhancement of instability'. The simulation results are also denoted by encircled S and U.

Let us compare simulation with theory. The simulation results for  $|\ell_E| \gg |\ell_n|$  in Case 2 are consistent with the theoretical prediction. Furthermore, the simulation results for  $|\ell_E| \sim |\ell_n|$  imply that sideband coupling is also dominant in this case. It should be noted that a case with  $|\ell_E| \ll |\ell_n|$  has not been realized in the present simulation. For Case 3 (i.e. parallel antenna), theory predicts that the effects

of sideband coupling are negligible and the ponderomotive force acting on the electron fluid is dominant in the stabilization. The simulation results are consistent with this notion.

#### 1.4. Discussions and conclusions

For the case of  $|\ell_E| \sim |\ell_n|$  and a magnetosonic pump wave, the theory does not give an explicit indication because the results, in a subtle manner, depend on the parameters and the polarization of the waves used.

The simulation results in the present parameter region and under the condition  $\omega_{pi}^2/k^2c^2 \ll 1$  (or  $\lambda$  (wavelength)  $\ll c/210\sqrt{n}$ ) imply that sideband coupling effects are dominant in flute mode suppression and consistent with the theory. Therefore, it is concluded that the simulation results are successfully explained by the theory although the parameter region covered by the simulation is limited.

Referring to Table I, we should understand the experimental results of Akimune et al. [3] and part of the results of Yasaka et al. [4]: If some experimental condition prevents sidebands, in addition to the condition  $\ell_E > 0$ , which seems to be the case for most of the experiments, the plasmas are stabilized, regardless of the sign of  $\omega - \Omega$ . In other words, polarization may offset the effect of the sign of  $\omega - \Omega$  included in the ponderomotive force term, in contrast to the simple picture that is still widely believed.

## 2. HEATING OF OVER-DENSITY PLASMA BY INJECTION OF ELECTRON CYCLOTRON RESONANCE WAVE (ECRW)

### 2.1. Introduction

According to the linear theory, an O-mode of ECRW with  $\omega_0 > \Omega_e$  injected from the low field side at the optimum incident angle is converted to an electron Bernstein wave (EBW) through the O-X-B mode conversion process [5].

On the other hand, a fast X-mode incident from outside the plasma tunnels through the evanescent region between the cut-off ( $\omega_0 = \omega_R$ ) and the upper hybrid resonance (UHR) and is converted into both the slow X-mode and the EBW [6].

In either case, the EBW propagates from the UHR to high density regions beyond the O-mode cut-off and X-mode cut-off ( $\omega_0 = \omega_L$ ) and is expected to heat the electrons in ODP (over-density plasma).  $\omega_R$  and  $\omega_L$  are the cut-off frequencies of the right and left hand elliptically polarized wave.

We have first observed ODP heating by injection of a fast X-mode and an O-mode, in the EM simulation results.

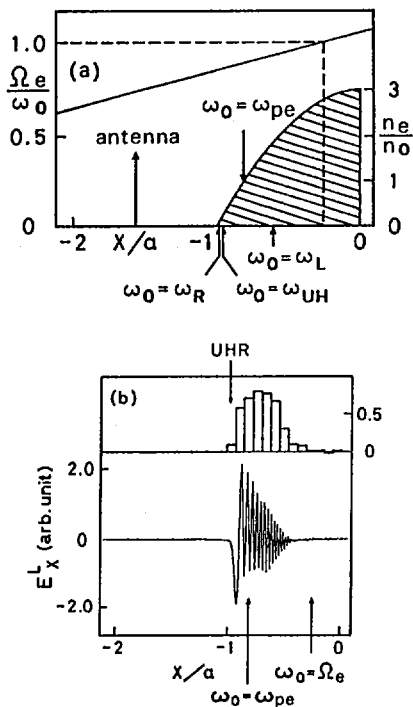


FIG. 3. (a) Profiles of external magnetic field  $B_0(\parallel y)$  and initial density distribution.

Initial electron temperature is 1.3 keV. (b) Interferogram of  $E_x^L$  and energy deposition to electrons  $\Delta(n_e T_e)/\bar{n}_e T_{e0}$  ( $a/\lambda_0 = 2.06$ ).

## 2.2. O-mode injection

A microwave with appropriate polarization is injected at the optimum incident angle ( $\theta_i = 46.7^\circ$ ). The initial plasma parameters are shown in Fig. 3(a). The EBW excited through the O-X-B process propagates to higher density regions, is gradually damped and heats the electrons between UHR and ECR (Fig. 3(b)).

Considering the results of ray tracing analyses [7], we know that the trajectories of the O-mode are distorted in the toroidal section near the cut-off ( $\omega_0 = \Omega_{pe}$ ), and that this three-dimensional effect prevents the O-mode from being converted to the X-mode.

## 2.3. Dependence of conversion efficiency of the fast X-mode on density gradients

The fast X-mode is observed to propagate up to the cut-off ( $\omega_0 = \omega_R$ ) (Fig. 4(a)) and to be converted to an EBW at UHR (Fig. 4(b), (c), (d)). A slow

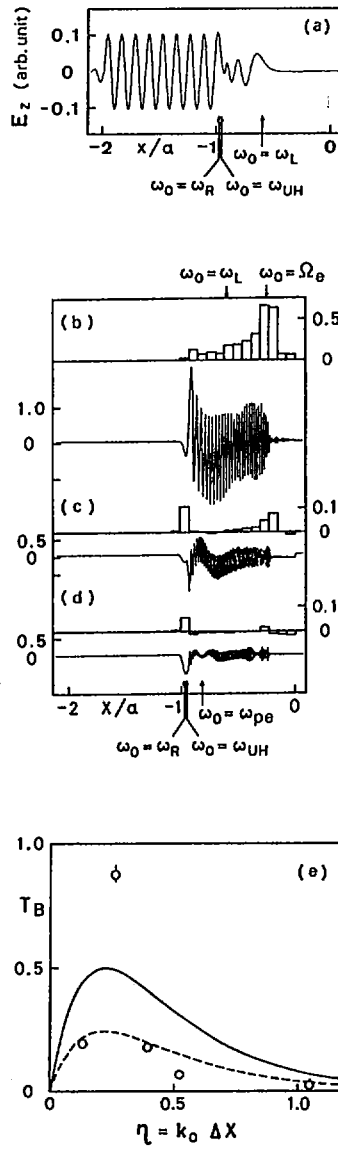


FIG. 4. (a) Interferogram of  $E_z$ ,  $a/\lambda_0 = 8.24$ . (b), (c), (d) Interferogram of  $E_x^L$  and energy deposition to electrons  $\Delta(n_e T_e)/\bar{n}_e T_{e0}$ ; specifically (b)  $a/\lambda_0 = 2.06$ , (c)  $a/\lambda_0 = 4.12$ , (d)  $a/\lambda_0 = 8.24$ . (e) Conversion efficiency to EBW of fast X-mode. Ordinate is  $T_B = I - R$ , where  $R$  is power reflection coefficient measured in vacuum region.

X-mode is also observed to be converted from the fast X-mode (Fig. 4(a)). The EBW propagates, first, with small damping until finally it is damped quickly at ECR. In accordance with wave damping, the electron energy increases near ECR, where the density is  $\omega_{pe}^2/\omega_0^2 = 2.72-2.93$ .

Figure 4(e) shows the total conversion efficiency  $T_B$  versus  $\eta = k_0\Delta x$ , where  $k_0$  is the wavenumber of the incident wave in vacuum and  $\Delta x$  is distance between the cut-off ( $\omega_0 = \omega_R$ ) and UHR. The parameter  $\eta$  is proportional to  $n/(dn/dx)$  and, therefore, to the minor radius in the case of a parabolic density profile.

The theoretical conversion efficiency from a fast X-mode to an EBW and a slow X-mode is  $T_{FB} = \exp(-\pi\eta) - \exp(-2\pi\eta)$  and  $T_{FS} = \exp(-\pi\eta)$ , respectively [8].

Here, we present a new idea on the ODP heating process referred to as the X-X-B process. The slow X-mode converted from the fast X-mode is reflected at the cut-off ( $\omega_0 = \omega_L$ ), partly converted to an EBW at UHR with a conversion efficiency of  $T_{SB} = 1 - \exp(-\pi\eta)$  (X-X-B process) and partly converted to a fast X-mode via tunnel effect. Neglecting phase effects of the two EBW, the total conversion efficiency is calculated to be  $T_B = 2\exp(-\pi\eta) (1 - \exp(-\pi\eta))$ , which is plotted as the solid line in Fig. 4(e), which includes a broken curve, showing for comparison the usual theoretical value  $T_{FB}$ .

As is seen in Fig. 4(e), the optimum density gradient is localized in a narrow parameter space  $\eta$ , and the maximum of  $T_B$  is close to unity. These two results are at variance with the theoretical prediction.

## 2.4. Discussions and conclusions

The accessibility condition of the EBW to the centre of the plasma, including three-dimensional effects [7], excludes the possibility of ODP heating by using the O-mode. In the case of X-mode injection, normal injection is possible and may avoid three-dimensional effects. Therefore, X-mode injection remains a candidate for ODP heating.

If a plasma manages to adjust an optimum density gradient at the plasma surface and to keep the electron temperature high enough to avoid collisional damping, the injected X-mode is well converted to an EBW, and high efficiency electron heating is expected in over-density regions, even for large scale plasmas, as is shown in the present simulations.

## REFERENCES

- [1] SAKAI, K., et al., in Mirror Fusion Research (Proc. IAEA Tech. Comm. Meeting Tsukuba, 1985).
- [2] D'IPPOLITO, D.A., MYRA, J.R., Rep. SAIC-85-1922/PRI-94, Science Applications, Inc., Pleasanton, CA (1986).
- [3] AKIMUNE, H., et al., J. Phys. Soc. Jpn. **50** (1981) 2729.

- [4] YASAKA, Y., ITATANI, R., Nucl. Fusion **24** (1984) 445.
- [5] PREINHAELTER, J., KOPECKY, V., J. Plasma Phys. **10** (1973) 1.
- [6] SUGAI, H., Phys. Rev. Lett. **47** (1981) 1899.
- [7] TAKEUCHI, K., et al., J. Phys. Soc. Jpn. **54** (1985) 2915.
- [8] BUDDEN, K.G., Radio Waves in the Ionosphere, Cambridge Univ. Press, London (1961) 476.

## DISCUSSION

ON PAPERS IAEA-CN-47/E-II-1-1 AND E-II-1-2

S. ITOH: In your calculation, for the stabilization of the ballooning mode the RF power must balance the excess energy of the unstable mode. How much power is needed for stabilization in the case of typical large tokamak parameters? When one considers an actual experiment, the dissipative effect on the RF power must surely be seriously taken into account.

A. SEN: In answer to the first part of your question, I would like to emphasize that the RF power ensures stabilization in a reactive manner and not by producing an additional damping mechanism to balance the growth of the ballooning mode. The magnitude of the RF power needed for access to the second stability regime can be estimated from the scaling  $(V_E/V_{thi}) \sim \alpha^2$ . In the low shear region near the centre of large tokamaks, our estimates show that a few megawatts of RF power with the correct profile should be able to provide a stable window. I agree with you that in an actual experiment the dissipation of this RF power must be seriously taken into account.

R. ITATANI: I would like to point out the importance of the profile of RF field intensities in plasmas. When using standing waves or mixing two waves, there is ponderomotive force in the azimuthal direction which produces convective motion across a confining magnetic field, because of the inhomogeneity of the field strength. Two-dimensional consideration is then always unavoidable for the RF field profile.



# THEORY OF RESISTIVE MAGNETOHYDRODYNAMIC INSTABILITIES EXCITED BY ENERGETIC TRAPPED PARTICLES IN LARGE-SIZE TOKAMAKS

H. BIGLARY<sup>1</sup>, L. CHEN, R.B. WHITE  
Princeton Plasma Physics Laboratory,  
Princeton University,  
Princeton, New Jersey,  
United States of America

## Abstract

THEORY OF RESISTIVE MAGNETOHYDRODYNAMIC INSTABILITIES EXCITED BY ENERGETIC TRAPPED PARTICLES IN LARGE-SIZE TOKAMAKS.

It is shown that, in present-day large-size tokamaks, finite resistivity modifies qualitatively the stability properties of magnetohydrodynamic instabilities resonantly excited by the unfavorable precessional drift of energetic trapped particles, the so-called "fishbone"-type instabilities. Specifically, it is found that (i) the  $n = 1$  energetic trapped particle induced internal kink ("fishbone") instability is strongly stabilized by resistive dissipation, and (ii) finite resistivity lowers considerably the threshold conditions for resonant excitations of high- $n$  ballooning/interchange modes. The possibility of exciting "fishbones" by alpha particles in ignition experiments is also considered.

## I. INTRODUCTION

In recent years, observations of magnetohydrodynamic (MHD) instabilities and associated particle loss in tokamak experiments with high-power near-perpendicular neutral beam injection<sup>1,2</sup> have stimulated considerable theoretical interest in MHD modes resonantly excited by the precessional drift of energetic particles trapped in the region with unfavorable curvature, i.e., the outside of a tokamak. These so-called "fishbone"-type MHD instabilities thus have, generically, mode frequencies,  $\omega$ , comparable to the trapped-particle precessional frequencies,  $\bar{\omega}_{dh}$ .<sup>3</sup> Theoretical models based on this resonance excitation mechanism have been rather successful in explaining many experimental features observed in both the  $n = 1$  "fishbone"<sup>4</sup> and high- $n$  "precursor"<sup>5,6</sup> events in tokamaks the size of PDX. Here,  $n$  is the toroidal mode number. To extend these theoretical

<sup>1</sup> Institute for Fusion Studies, University of Texas, Austin, TX, USA.

results to current high-field large-size tokamaks such as TFTR, JT-60 and JET, we must examine the validity of the core-plasma ideal MHD approximation employed in the theoretical models. Note that  $\bar{\omega}_{dh} \approx E/BR$ , with  $E = v^2/2$  and  $R$  the major radius. Hence, in large devices,  $\bar{\omega}_{dh}$  may become comparable to or even smaller than the characteristic resistive frequency  $\omega_R \equiv S_M^{-1/3} \omega_A$ , and finite-resistivity effects may be significant. Here,  $S_M$  is the magnetic Reynold number,  $\omega_A = (1 + 2 q_s^2)^{1/2} v_A/q_s R$  is the toroidal Alfvén frequency,  $q_s$  is the safety factor  $q$  at the singular surface  $r = r_s$ , and  $v_A$  is the toroidal Alfvén velocity.

In the next section, we first consider the effects of finite resistivity on the  $n = 1$  "fishbone" internal kink instability. The high- $n$  "fishbone"-type resistive ballooning/interchange instabilities are then considered in Sec. III. Finally, in Sec. IV, noting that fusion alpha particles will carry significant  $\beta$  ( $\equiv$  plasma pressure/magnetic pressure) values in future ignition experiments, we also consider the possible excitations of  $\alpha$ -particle induced "fishbone" instabilities.

## II. $n=1$ RESISTIVE "FISHBONE" INSTABILITIES<sup>7</sup>

As in the ideal "fishbone" theory<sup>4</sup>, we consider a large-aspect-ratio ( $\epsilon \equiv a/R \ll 1$ ) circular tokamak plasma consisting of core (c) and hot (h) components, and perturbations of predominantly the  $m=1$ ,  $n=1$  internal kink mode. Here,  $m$  is the poloidal mode number. We adopt the following formal orderings:  $\beta_{pc} \sim 1$ ,  $\beta_{ph} \sim \epsilon$ ,  $T_c/T_h \sim \epsilon^2$ , and  $|\omega/\omega_A| \sim |\bar{\omega}_{dh}/\omega_A| \sim \epsilon^2$ . In addition, we order  $\omega \sim \omega_R$ , i.e.  $S_M^{-1/3} \sim \epsilon^2$ , which represents an optimal ordering for the resistive effects. Consistent with these orderings, the hot component is described by the gyrokinetic equation, but the core plasma must be treated as a resistive MHD fluid obeying the Ohm's law

$$\delta \underline{B} = \underline{\nabla} \times (\underline{\xi} \times \underline{B}) - (\eta c^2 / 4\pi i \omega) \nabla^2 \delta \underline{B} \quad (1)$$

where  $\underline{\xi}$  is the (core-plasma) fluid displacement and  $\eta$  is the resistivity.

By separating the regions outside and inside the singular layer located at  $q(r_s) = 1$ , we can derive the dispersion relation variationally. Since resistivity is ignorable in the outside region, the only modification to the ideal "fishbone" theory is

the replacement of the inertial-layer Lagrangian by the following resistive-layer Lagrangian

$$D_R[\xi] = -2\pi R r_s^3 \int_{-\infty}^{\infty} dx [3\omega^2 \rho_m |d\xi_r/dx|^2 + iBk_{\parallel}' \times \xi_r^* d^2 \delta B_r/dx^2] \quad (2)$$

where  $x = r - r_s$ ,  $k_{\parallel}' = q'(r_s)/R$  and  $\delta B_r$  from Eq. (1) acts as the constraint.

Following the analyses of Coppi et al.<sup>8</sup>, it is straightforward to solve the resistive-layer Euler-Lagrange equation and match the solutions in the two regions. The final dispersion relation is then given by

$$\hat{\delta W}_{fc} + \hat{\delta W}_k + 8 S_M^{-1/3} \Omega^{-5/4} \frac{\Gamma[(\Omega^{3/2} + 5)/4]}{\Gamma[(\Omega^{3/2} - 1)/4]} = 0 \quad (3)$$

where  $\Omega = -i\omega/\omega_R$ ,  $\hat{\delta W}_{fc}$ , defined in Ref.[4], is the normalized core-plasma contribution to the ideal MHD  $\delta W$ ,

$$\hat{\delta W}_k = \frac{2^{3/2} M_h \pi^2}{B_0^2} \left\langle \int_{1-r/R}^{1+r/R} d(\alpha B) \int_0^{\infty} dE E^{5/2} \frac{K_2^2}{K_b} \frac{\omega}{\bar{\omega}_{dh} - \omega} \left( \frac{\partial}{\partial E} + \frac{\hat{\omega}_{*h}}{\bar{\omega}_{dh}} \right) F_{oh} \right\rangle \quad (4)$$

$\langle y \rangle \equiv (2/r_s^2) \int_0^r y r dr$ ,  $\alpha = v^2/v^2$ ,  $\omega_{*h} = -(i/\omega_c)(\underline{e}_{\parallel} \times \underline{v} \ln F_{oh}) \cdot \underline{v}$ ,  $K_b = \oint (d\theta/2\pi)(1 - \alpha B)^{-1/2}$ ,  $K_2 = \oint (d\theta/2\pi) \cos\theta (1 - \alpha B)^{-1/2}$ , and only  $m = 1$ ,  $n = 1$  perturbations are kept in Eq. (4).

In the  $|\Omega| \gg 1$  ideal limit, we recover from Eq. (3) the ideal "fishbone" dispersion relation<sup>4</sup>

$$\hat{\delta W}_{fc} + \hat{\delta W}_k - i\omega/\omega_A = 0 \quad (5)$$

and the corresponding threshold condition, using a model slowing-down distribution function as an example, is given by

$$\langle \epsilon \beta_{ph,t} \rangle_{cr}^I \sim \bar{\omega}_{dm}/\omega_A \quad (6)$$

where the subscript t denotes trapped particles and  $\bar{\omega}_{dm} = \bar{\omega}_{dh}(E=E_{inj})$ . Note that below the threshold, i.e. for  $\beta_{h,t} < \langle \beta_{h,t} \rangle_{cr}^I$ , the singularity associated with damped ideal "fishbone" modes is regularized by finite resistivity with a characteristic width of  $S_M^{-1/3}$ .

In the  $|\Omega| \ll 1$  regime of interest here, i.e. the resistive limit, Eq. (3) reduces to

$$\hat{\delta W}_{fc} + \hat{\delta W}_k = A_S e^{i5\pi/8} S_M^{-1/3} (\bar{\Omega})^{-5/4} \quad (7)$$

where  $\bar{\Omega} \equiv \omega/\bar{\omega}_{dm}$  and  $A_S = -8 (\bar{\omega}_{dm}/\omega_R)^{-5/4} \Gamma(5/4)/\Gamma(-1/4) > 0$ . The instability threshold condition then becomes, again, for a model slowing-down distribution function,

$$2^{9/4} > \langle \epsilon \beta_{ph,t} \rangle_{cr}^R S_M^{1/3} / A_S > 1 \quad (8)$$

and  $1/2 < \bar{\Omega}_{cr} < 1$ , that is,

$$\langle \epsilon \beta_{ph,t} \rangle_{cr}^R \sim A_S S_M^{-1/3} \sim \left( \frac{\omega_R}{\omega_{dm}} \right)^{9/4} \frac{\bar{\omega}_{dm}}{\omega_A} \sim \left( \frac{\omega_R}{\omega_{dm}} \right)^{9/4} \langle \epsilon \beta_{ph,t} \rangle_{cr}^I \quad (9)$$

Thus, in the resistive limit, the threshold  $\beta$  value of the energetic trapped particles is raised dramatically over the ideal-limit value. Since physically the threshold condition can be understood in terms of balancing negative dissipation due to the trapped-particle precession mode with positive dissipation of Alfvén wave resonance absorption at the singular layer, this stabilization then corresponds to enhancement of positive dissipation due to finite resistivity.

#### IV. HIGH-N RESISTIVE "FISHBONE"-TYPE BALLOONING/INTERCHANGE MODES<sup>9</sup>

This study is in part motivated by observations of high-n ( $n \sim 5$ ) "precursors" to "fishbones" in PDX experiments, which have been theoretically interpreted as high-n ideal MHD ballooning modes resonantly excited by trapped beam-ion precessional drift, i.e. similar to the  $n = 1$  "fishbone" instability. In addition to the above-mentioned issue concerning validity in large-size devices, the applicability of the ideal-MHD theoretical models

appears to be also severely restricted to either singular-type energetic trapped-particle distribution functions or regimes near ideal-MHD ballooning-mode marginal stability. Specifically, note that the dispersion relation of high-n ideal "fishbone"-type ballooning modes is of the same form as that of  $n = 1$  ideal "fishbone", Eq. (5), with appropriate replacements of  $\delta\hat{W}_{fc}$  and  $\delta\hat{W}_k$  in terms of surface quantities. For  $\epsilon\beta_{pc} \sim \epsilon \ll (\epsilon\beta_{p,MHD})_{cr}^I \sim 1$ , i.e. away from ideal-MHD marginal stability,  $\delta\hat{W}_{fc} \sim 1$ , due to field-line bending and, hence, balancing the real part of Eq. (5) dictates  $\text{Re}(\delta\hat{W}_k) \sim O(\epsilon\beta_{ph,t}) \sim 1$ , except for non-analytic  $F_{oh}$  such as the model slowing-down distribution function which yields logarithmically singular  $\delta\hat{W}_k$ . Since field-line bending and, hence,  $\delta\hat{W}_{fc}$  can be minimized by finite resistivity, in this case high-n resistive "fishbone"-type instabilities could be excited with regular  $F_{oh}$  and  $\epsilon\beta_{ph,t} \sim \epsilon^2$ , more consistent with experimental conditions.

Employing two small parameters,  $\epsilon$  and  $\lambda \equiv (n^2/S_M)^{1/3}$ , the orderings adopted here are  $\beta_{pc} \sim 1$ ,  $\beta_{ph} \sim \epsilon$ ,  $\omega_R = \lambda\omega_A$ ,  $\bar{\omega}_{dh} \sim \epsilon^{4/3}\omega_R$ , and, in a maximal scheme,  $\lambda \sim \epsilon^3$ . The frequency ordering,  $|\bar{\omega}_{dh}/\omega_R| \sim \epsilon^{4/3} < 1$ , corresponds to the resistive limit of interest in large-size tokamaks and also implies eigenmode properties similar to those of the electrostatic resistive interchange mode. The dispersion relation can then be straightforwardly derived and is given, in the incompressible limit and for the lowest (most unstable) eigenstate, by

$$\delta\hat{W}_k - D_{RC} + (-i\omega/\omega_R)^{3/2} = 0 \quad (10)$$

where  $D_{RC} \approx E + F \sim 0$  ( $\epsilon^2\beta_{pc}^2 < 0$ ) represents favorable average curvature.<sup>10</sup> We remark that inclusion of compressibility does not alter our final conclusions in any substantial way. Stability properties predicted by Eq. (10) have been analyzed via Nyquist technique for both model slowing-down and Maxwellian  $F_{oh}$  and are qualitatively similar. In particular, the instability threshold condition is given by

$$\langle\langle \epsilon\beta_{ph,t} \rangle\rangle_{cr}^R \sim \max [ |D_{RC}|, (\bar{\omega}_{dh}/\omega_R)^{3/2} ] \sim 0 (\epsilon^2) \quad (11)$$

Here,  $\langle\langle \rangle\rangle$  denotes surface average. Equation (11) indicates that, with the field-line bending stabilizing term minimized by finite resistivity, high-n resistive "fishbone"-type ballooning/interchange instabilities can be excited for  $\beta_{pc} \sim 1$

and  $\beta_{ph,t} \geq \epsilon$ , which is much lower than the ideal prediction [ $\epsilon(\beta_{pc} + \beta_{ph,t}) \sim 0$  (1) for a Maxwellian  $F_{oh}$ ] and, hence, appears to agree better with the PDX experiments. Also, we remark that, since the eigenmodes are highly localized around the mode-rational surfaces, finite banana width may assert a stabilizing influence. In this case, it can be shown that the threshold condition is increased by a factor  $(\rho_{bh}/\rho_R) \ln(\rho_{bh}/\rho_R)$ , where  $\rho_{bh}$  is the typical energetic trapped particle banana width and  $\rho_R \sim r_s(nS_M)^{-1/3}(\bar{\omega}_{dh}/\omega_R)^{1/4}$  is the typical mode radial width. Finally, we note that, by performing a three-region asymptotic matching, the usual high- $n$  resistive ballooning/tearing dispersion relation<sup>11,12</sup> can be generalized to include effects due to energetic trapped particles such that both ideal and resistive "fishbone"-type modes are derivable in the appropriate limits.

#### IV. ALPHA PARTICLE-INDUCED "FISHBONE" INSTABILITY<sup>13</sup>

In proposed tokamak ignition experiments, fusion  $\alpha$ -particles generally contribute a significant fraction of the total  $\beta$ -values, and, hence, the possibility of exciting "fishbone"-type instabilities and an associated anomalous loss of  $\alpha$ -particles needs to be seriously considered. Assuming typical reference parameters,  $R = 135$  cm,  $a = 42$  cm,  $B = 10^2$  KG, and  $n_0 = 10^{15}/\text{cm}^3$ , the precessional frequency of the 3.5 MeV  $\alpha$ -particles is then  $\bar{\omega}_{d\alpha} \sim 10^5 n$  and  $\omega_A \sim 2 \times 10^7$ . That is,  $\bar{\omega}_{d\alpha}/\omega_A \sim n 5 \times 10^{-3} \geq (n^2/S_M)^{1/3}$  for, typically,  $S_M \geq 10^7$ . We, therefore, need only to consider ideal "fishbone"-type modes. Furthermore, since  $\beta$ -values are usually sufficiently below  $(\beta_{MHD})_{cr}^I$ , high- $n$  modes are stable and only the  $n = 1$  "fishbone" instability may be excited. From Eq. (6), we find  $\langle \beta_{\alpha,t} \rangle_{cr}^I \sim 1.7 \times 10^{-3}$  or, noting  $n_{\alpha,t}/n_{\alpha} \sim 1/3$  for isotropic  $\alpha$ -particle distributions,  $\langle \beta_{\alpha} \rangle_{cr}^I \sim 0.5\%$ . Taking  $\beta_{\alpha}/\beta_{total} \sim 0.1$ ,<sup>14</sup> we then derive  $(\beta_{total})_{cr}^I \sim 5\%$  as the corresponding instability threshold condition, which may be exceeded in some designs. Finally, it is instructive to note the scaling  $\beta_{\alpha,t}/\langle \beta_{\alpha,t} \rangle_{cr}^I \sim n_{\alpha}/n_0^{1/2}$ , and, hence, high-density ignition experiments are more favorable with regard to the stability of the "fishbone".

#### ACKNOWLEDGMENT

This work was supported by United States Department of Energy Contract No. DE-AC02-76-CHO-3073.

## REFERENCES

- [1] McGUIRE, K., et al., Phys. Rev. Lett. **50** (1983) 891.
- [2] ARMENTROUT, C.J., STRAIT, E.J., Rep. GA-A-17891, GA Technologies, Inc., San Diego, CA (1986).
- [3] CHEN, L., et al., in Plasma Physics and Controlled Nuclear Fusion Research 1984 (Proc. 10th Int. Conf. London, 1984), Vol. 2, IAEA, Vienna (1985) 59.
- [4] CHEN, L., WHITE, R.B., ROSENBLUTH, M.N., Phys. Rev. Lett. **52** (1984) 1122.
- [5] WEILAND, J., CHEN, L., Phys. Fluids **28** (1985) 1359.
- [6] VAN DAM, J.W., ROSENBLUTH, M.N., Paper 1C-6, presented at Annual Controlled Fusion Theory Conference (Apr. 1985, Madison, WI).
- [7] BIGLARI, H., CHEN, L., Phys. Fluids **29** (1986) 1760.
- [8] COPPI, B., et al., Fiz. Plazmy **2** (1976) 961; Sov. J. Plasma Phys. **2** (1976) 533.
- [9] BIGLARI, H., CHEN, L., Phys. Fluids **29** (1986) 2960.
- [10] GLASSER, A.H., GREENE, J.M., JOHNSON, J.L., Phys. Fluids **18** (1975) 875.
- [11] CONNOR, J.W., HASTIE, R.J., MARTIN, T.J., in Plasma Physics and Controlled Nuclear Fusion Research 1982 (Proc. 9th Int. Conf. Baltimore, 1982), Vol. 3, IAEA, Vienna (1983) 403.
- [12] DRAKE, J.F., ANTONSEN, T.M., Phys. Fluids **28** (1985) 544.
- [13] WHITE, R.B., et al., Paper 2D-9, presented at Sherwood Controlled Fusion Theory Conference (Apr. 1986, New York).
- [14] HOULBERG, W.A., paper presented at Alpha Particle Effects Workshop, Courant Institute, New York University, Dec. 1985.



**ALFVÉN WAVE PHASE MIXING  
IN A SHEARED MAGNETIC FIELD  
AS A MECHANISM OF  
'FISHBONE' INSTABILITY DAMPING  
AND OSCILLATION ENERGY PUMPING  
INTO THE REGION OF LARGE  $k_{\perp} \sim \omega_p/c$**

A.D. BEKLEMISHEV, O.P. POGUTSE  
I.V. Kurchatov Institute of Atomic Energy,  
Moscow, Union of Soviet Socialist Republics

*Presented by B.B. Kadomtsev*

**Abstract**

ALFVÉN WAVE PHASE MIXING IN A SHEARED MAGNETIC FIELD AS A MECHANISM OF 'FISHBONE' INSTABILITY DAMPING AND OSCILLATION ENERGY PUMPING INTO THE REGION OF LARGE  $k_{\perp} \sim \omega_p/c$ .

New dynamic equations for the  $m = 1$  mode in a tokamak are obtained; they may be used to describe the 'fishbone' instability. Other types of Alfvén waves in a sheared magnetic field have an analogous property allowing them to transfer oscillation energy into the short wave region. This is used to explain the pumping of energy into the region  $k_{\perp} \sim \omega_p/c$  and to construct a non-linear model.

Theoretical simulation of the 'fishbone' instability is based on allowance for two processes: excitation of oscillations at the toroidal drift frequency of fast particles and wave induced fast particle radial transport [1, 2]. Experimental observations [3] have shown that low  $k_{\parallel}$  Alfvén modes, in particular the internal  $m = 1, n = 1$  kink mode, are excited by fast particles.

The first phenomenological 'fishbone' oscillation model was proposed by Gribkov et al. [4]. A more detailed study of  $m = 1, n = 1$  mode excitation and damping is presented in [2]. However, the ideal dispersion relation  $-i\omega/\omega_A + W = 0$  obtained there has a limited range of validity.

In this paper, dynamic equations for the  $m = 1, n = 1$  mode are obtained, enabling us to take finite viscosity, conductivity and ion Larmor radius effects into account.

The physical mechanism of phase mixing, studied in connection with 'fishbone' oscillations, has another, very interesting application: it enables us to explain the process of oscillation accumulation in the collisionless skin layer region,  $k_{\perp} \sim \omega_p/c$ , which is very important in collective transport processes in a tokamak [5].

1. DYNAMIC EQUATIONS FOR THE  $m = 1, n = 1$  MODE

Let us proceed from the dynamic equations for the  $m = 1, n = 1$  ideal kink mode in a tokamak, derived in [6]:

$$\left[ (\mu - 1)^2 + \frac{\partial^2}{\partial t^2} \right] x_1' - U_{11} x_1 = \hat{M}_{12} x_2 \quad (1)$$

$$[a^3 (\mu - \frac{1}{2})^2 x_2']' - 3a (\mu - \frac{1}{2})^2 x_2 = \hat{M}_{21} x_1 \quad (2)$$

Here,  $x_1$  and  $x_2$  are the poloidal harmonics of the radial component of plasma displacement ( $\vec{x} \cdot \nabla a = x_1 \cos(\theta - \zeta) + x_2(a) \cos(2\theta - \zeta)$ ) in an equilibrium co-ordinate system  $(a, \theta, \zeta)$ , in which the magnetic field lines are straight,  $\mu(a)$  is the rotational transformation,  $t$  is the time normalized to the poloidal Alfvén transit time,  $\tau_\theta = R/\mu c_A$ , and  $R$  is the major radius. Concrete forms of the coefficient  $U_{11}(a) \ll 1$  and of the differential operators  $\hat{M}_{12}$  and  $\hat{M}_{21}$  are given in Ref. [6].

It is well known that the function  $x_1(a)$  is well approximated by a stair-like function with a jump near the  $\mu = 1$  ( $a = a_1$ ) resonant surface for moderate frequencies ( $\omega^2 \tau_\theta^2 \ll (\mu(0) - 1)^2$ ). Thus, the derivative of  $x_1(a)$  has a small, bounded support.

Using Eq. (1), we easily derive the integral representation

$$\left[ (\mu - 1)^2 + \frac{\partial^2}{\partial t^2} \right] x_1' = \frac{1}{a^3} \int_0^a (U_{11} x_1 + \hat{M}_{12} x_2) da \quad (3)$$

where the right hand side is a weak function of the quantity near the resonance  $a = a_1$ . Hence, it can be calculated at this point by using a stair-like trial function:

$$\left[ (\mu - 1)^2 + \frac{\partial^2}{\partial t^2} \right] x_1' = \frac{1}{a_1} W x_1(0) \quad (4)$$

Here,

$$W = \frac{1}{a_1^2 x_1^2(0)} \int_0^{a_*} (U_{11} x_1^2 + x_1 \hat{M}_{12} x_2 + x_2 \hat{M}_{21} x_1 + a^3 (\mu - \frac{1}{2})^2 x_2'^2 + 3a (\mu - \frac{1}{2})^2 x_2^2) da \quad (5)$$

This expression was evaluated in [7, 8] and represents the potential energy of perturbation.

Let us introduce a new independent variable,  $z = (a/a_1) - 1$ , and consider only the first non-vanishing term of an expansion  $\mu - 1 = -\hat{s}z$  near  $a = a_1$ . Here,  $\hat{s} \equiv -\mu'(a_1)$ . The quantity  $a_1$  is the shear parameter.

Using the Fourier transformation

$$f(k) = \int_{-\infty}^{+\infty} x'_1 e^{ikz} dz$$

we obtain

$$\left[ \hat{s}^2 \frac{\partial^2}{\partial k^2} - \frac{\partial^2}{\partial t^2} \right] f = 2\pi W \delta(k) f \quad (6)$$

This equation governs the Alfvén wave phase mixing process in a sheared magnetic field.

Considering a wave of constant frequency, we can easily include the effects of viscosity, resistivity and finite ion gyroradius (for the core ions), to obtain:

$$\left\{ \hat{s}^2 \frac{\partial}{\partial k} (1 + ik^2/\omega S)^{-1} \frac{\partial}{\partial k} + 2i\hat{s}^2/\omega S (1 + ik^2/\omega S)^{-2} \right. \\ \left. + \omega(\omega - \omega_*)F(z) + i\omega\lambda k^2 \right\} f = 2\pi W \delta(k) f \quad (7)$$

Here,  $S = \tau_S/t_\theta \gg 1$  is the magnetic Reynolds number,  $\tau_S$  the resistive transit time,  $\lambda = \nu\tau_\theta a_1^{-2}$  the normalized viscosity coefficient,  $\omega_*$  the drift frequency,  $F(z) = (1 - I_0(z)\exp(-z))/z$ ,  $z = \rho_i^2 a_1^{-2}(1 + k^2)$  and  $\rho_i$  the core ion gyroradius. The first term in Eq. (7) characterizes the field line bending and the second term is the source of the tearing instability. The third and the fourth terms describe inertial and viscous effects, respectively.

## 2. PHASE MIXING AND SPECTRAL METHOD

Equation (6) describes the evolution of waves travelling along the  $k$ -axis and being scattered on the  $\delta$ -function-like barrier at  $k = 0$ . Thus, any initial perturbation will evolve to large values of  $k$ , and the maximum of the displacement will decrease roughly as  $x_1 \sim f/k$ . We shall call this process 'phase mixing'.

It is natural to assume the evolution of short, perpendicular wavelengths to result in a further decay, due to the dissipation. This is why Eq. (6) must be supplemented by the 'outgoing wave' boundary conditions, i.e. for  $|k| \rightarrow \infty$ ,

there will be only waves travelling away from the region of generation at small values of  $k$  towards still larger values of this parameter.

By matching the constant frequency solution around  $k = 0$ , we obtain the dispersion relation obtained previously in Ref. [2]:

$$-i\omega + \pi W/\hat{s} = 0 \quad (8)$$

In a more realistic situation, however, small effects may become important at large values of  $k$  and partially reflect the outgoing wave back into the region of generation or absorb it. If the return time of the reflected wave,  $t_r = k_r/\hat{s}$ , is shorter than, or comparable to, the time of instability evolution, Eq. (8) and the assumption of an outgoing wave are no longer applicable. In other words, the small effects may discretize the continuous Alfvén spectrum and, if the growth rate or the decay rate is smaller than, or comparable to, the difference between successive eigenfrequencies, it is only the spectral theory that is accurate.

Equation (7), with the usual boundary conditions  $\lim_{k \rightarrow \infty} f(k) = 0$ , predicts a tearing instability with a growth rate of  $\gamma_T \cong \hat{s}^2 W^{-4/5} S^{-3/5}$  for  $W > 0$ . With the inclusion of fast particles trapped in the region of unfavourable field curvature, a corresponding contribution to  $W$  is obtained and the excitation of an instability at their toroidal drift frequency becomes possible [2]. For this instability to be visible against a tearing background, it is necessary that  $\omega_{dh} \gtrsim \gamma \gg \gamma_T$ . For Eq. (8) to be applicable, still higher frequencies are necessary:  $\gamma^2 \omega_{dh} > \hat{s}^2/4S$  and  $\omega_{dh} > \omega_*$ . Therefore, the spectral method (7) is apparently more adequate for describing the 'fishbone' instability in large tokamaks.

### 3. ALFVÉN OSCILLATIONS WITH $m = 1$ AND ENERGY TRANSFER INTO THE REGION OF LARGE $k$

Modern theory of collective transport processes in a current carrying plasma (tokamaks) predicts a special role for oscillations in the region of wavelengths of the order of the collisionless skin layer width  $c/\omega_{pe}$  [5, 9]. However, there are no accepted mechanisms of energy pumping into the small scale fluctuations. In this paper, Alfvén wave phase mixing is shown to be a possible candidate for this role.

Oscillations with an  $m = 1$  poloidal wavenumber in a tokamak are of a specific nature since the eigenfunction is similar to a stair-like function. However, for  $m = 1$  it is also possible to obtain a dynamic equation in the Fourier space, and it will be a wave equation, although one of a more general form than that given by expression (6).

In the limit of long wavelengths, the Alfvén waves obey the well known equation

$$\frac{\partial^2}{\partial t^2} \Delta_{\perp} \varphi + c_A^2 k_{\parallel} \Delta_{\perp} k_{\parallel} \varphi = 0 \quad (9)$$

In a sheared magnetic field, the parallel wavenumber is a function of the radius. Expanding  $k_{\parallel}$  near the resonance point  $k_{\parallel}(a_s) = 0$ :  $k_{\parallel} = k'_{\parallel}\Delta x$ ,  $\Delta x = a - a_s$  and carrying out a Fourier transformation, we obtain:

$$\frac{\partial^2}{\partial t^2} k_{\perp}^2 \varphi_k - c_A^2 (k'_{\parallel})^2 \frac{\partial}{\partial k_x} k_{\perp}^2 \frac{\partial}{\partial k_x} \varphi_k = 0 \quad (10)$$

where  $k^2 = k_x^2 + k_y^2$ ,  $k_y^2 = m^2 a_s^{-2} \cong \text{const.}$

The wave equation (10) describes the shift of any perturbation into the region  $|k_x| \rightarrow \infty$ , the velocity of this shift being constant and equal to  $c_A k'_{\parallel}$ . As the wave approaches  $k_x \sim \rho_i^{-1}$ , its dispersion properties change. We shall immediately consider the limit  $k_x \rho_i \gg 1$ , where, instead of Eq. (10), we obtain:

$$\frac{\partial^2}{\partial t^2} \varphi_k - 2c_A^2 (k'_{\parallel})^2 \frac{c^2}{\omega_{pe}^2} \frac{\partial}{\partial k_x} k_{\perp}^2 \frac{\partial}{\partial k_x} \varphi_k = 0 \quad (11)$$

This equation describes the so-called kinetic Alfvén waves with a dispersion relation  $\omega^2 = 2c_A^2 k_{\parallel}^2 k_{\perp}^2 c^2 \omega_{pe}^{-2}$ ; all perturbations propagate into the large  $k$  region, with increasing velocity:  $k_x \sim k_x$ .

No energy change occurs during the spectral shift although there are certain changes in amplitude. These may be expressed as  $A \sim (k_x^2 + k_y^2)^{-1/2}$  for  $k_x \rho_i < 1$  and  $A \sim (k_x^2 + k_y^2)^{-1/4}$  for  $k_x \rho_i > 1$ .

Let us assume that at the very short wave end of the spectrum (where  $k_x \sim \omega_{pe}/c$ ), the level of oscillations reaches the maximum, strongly turbulent regime  $e\varphi/T \sim 1/k_{\perp} a \sim c/(\omega_{pe} a)$ . What amplitude of oscillations in the region  $k_x \sim 1/a$  is necessary to justify this assumption? Matching the asymptotic spectra at  $k_x \rho_i = 1$ , we easily obtain:

$$\bar{n}/n_0 \cong e\varphi/T \cong (m/M\beta)^{1/2} < 1 \quad (12)$$

This result yields  $\bar{n}/n_0 \cong 0.2$  for typical tokamak parameters ( $\beta \sim 1\%$ ), which is virtually always observed in experiments. It should be noted that (12) holds only for  $\beta > m/M$ , i.e.  $\rho_i > c/\omega_{pe}$ . In the opposite limit,  $\rho_i < c/\omega_{pe}$ , the  $\varphi_k \sim k_x^{-1}$  spectrum should be between  $1/a < k_x < \omega_{pe}/c$ , and the fluctuations at  $k_x a \sim 1$  should be of the order of unity for the strongly turbulent regime.

#### 4. NON-LINEAR MODEL

Full dynamics include transverse (drift) vortices and the Alfvén (or tearing) oscillations. For their general description we shall use the well known set of equations governing plasma behaviour in a strong magnetic field [10]:

$$c \frac{d}{dt} \Delta_{\perp} \varphi = -c_A^2 (\vec{b} \cdot \nabla) \Delta_{\perp} A \quad (13)$$

$$c(\vec{b}, \nabla) \left( \frac{T}{e} \ln n - \varphi \right) = \frac{\partial A}{\partial t} \quad (14)$$

$$\frac{dn}{dt} = -\frac{cB}{4\pi e} (\vec{b}, \nabla) \Delta_{\perp} A \quad (15)$$

where

$$\frac{d}{dt} \frac{\partial}{\partial t} + \vec{v}_{\perp} \cdot \nabla, \vec{v}_{\perp} = \frac{c}{B} [\vec{b} \times \nabla \varphi], \vec{B} = B_0 \vec{e}_z - [\vec{e}_z \times \nabla A], \vec{b} = \vec{B}/B,$$

$$T = \text{const}$$

These equations differ from the original ones [10] by the inclusion of an equation for the density [11], as was done in Refs [11, 12]. In particular, in Ref. [11] they were used to describe anomalous transport processes due to flutter. Here, we shall rewrite the system (13) to (15) in order to show the physics more clearly. To do this, we write for the density:

$$n = n_0(x) + \frac{e\varphi}{T} + \delta n \quad (16)$$

where  $\delta n$  describes the non-Boltzmann part of the distribution  $n$ . Subtracting Eq. (13) from Eq. (15), we obtain:

$$\frac{d}{dt} (\varphi - \rho^2 \Delta_{\perp} \varphi) = g \quad (17)$$

where

$$g = -\frac{T}{en} \frac{d}{dt} \delta n, \rho^2 = \frac{Mc^2 T}{e^2 B^2}$$

For the variable  $g$  we can obtain an equation by combining (13) and (15):

$$\left[ c_A^2 (\vec{b}, \nabla) \Delta_{\perp} (\vec{b}, \nabla) - \frac{\partial^2}{\partial t^2} \Delta_{\perp} \right] g = -\rho^2 \frac{\partial^2}{\partial t^2} \frac{d}{dt^2} \Delta_{\perp} \varphi \quad (18)$$

This equation is only an approximate one since small insignificant corrections were omitted in its derivation. Equations (17) and (18) may be rewritten as a single equation, but in the present form they are clearer; the vortices governed by Eq. (17) generate Alfvén perturbations (18), which in turn (through  $g$ ) feed the vortices.

The linear dispersion relation, following from (17) and (18), is well known [5]:

$$(\omega - \omega_* + \omega k_{\perp}^2 \rho^2)(\omega - k_{\parallel}^2 c_A^2) = \omega^3 k_{\perp}^2 \rho^2 \quad (19)$$

Strong interaction between Alfvén and drift waves occurs in the region  $\omega_* \cong k_{\parallel} c_A$ . To the right of the interaction point  $k_{\parallel} c_A > \omega_*$  and for the drift branch, we obtain, as an estimate from (18):  $g \sim \omega_*^3 \rho^2 (k_{\parallel} c_A)^{-2} \Delta_{\perp} \varphi$ . In this case, the correction with  $g$  on the right hand side of Eq. (17) is small, and we get a normal Hasegawa-Mima equation [13]. In the opposite limit,  $k_{\parallel} c_A < \omega_*$ , for the drift branch, we have  $g = -2(d/dt)\Delta_{\perp} \varphi$  and the chief non-linear terms in (17) vanish. This can lead to an additional concentration of oscillations in the region  $\Delta x < \rho \sqrt{\beta/\bar{s}} \epsilon \mu$ . In general, Eqs (17) and (18) describe the pumping of oscillations into the region of large  $k$ .

To demonstrate this statement, let us consider the case where  $\varphi$  is governed by the Hasegawa-Mima equation  $(d/dt)(\varphi - \rho^2 \Delta_{\perp} \varphi) = 0$ . Let us take the turbulent limit to describe the evolution in detail. It is well known that the Hasegawa-Mima equation gives a spectrum with a flux of the form  $\varphi^2 \sim k^{-\alpha}$ , where  $2 < \alpha < 4$  [14]. In the case  $\varphi^2 \sim k^{-4}$ , (18) has a solution in the  $k$ -space, independent of  $k$ :  $g \sim \omega_* \rho^2 k_x^2 \varphi \sim \omega_* \rho^2$  (let us recall that  $(b, \nabla)^2 \sim \partial^2 / \partial k^2$ ). The variable  $g$ , which is independent of  $k$ , leads to a  $\delta$ -function-type source (in real space), on the right hand side of Eq. (17). Taking multiple resonances into account, we write

$$g = \sum_{\Gamma} \delta(x - x_{\Gamma}) \varphi_{\Gamma}$$

$\sum_{\Gamma}$  is a sum over all resonances,  $\bar{\varphi}_{\Gamma}$  is the potential averaged over a cell with given helicity. It is a source of this form that describes the generation of small scale oscillations.

It is conceivable that this result, obtained for the  $\varphi^2 \sim k_x^{-4}$  model, has a much broader applicability since, in the general case, the operator on the left hand side of (18) provides an efficient averaging of the right hand side over  $k_x$ . The appearance of a source on the right hand side of (17) of the form  $\sum_{\Gamma} \delta(x - x_{\Gamma}) \bar{\varphi}_{\Gamma}$  will lead to a slower drop in the spectrum for large values of  $k_x$ , i.e. to the very effect that we discussed above.

These considerations suggest the possibility of two-dimensional simulation of a three-dimensional spectral problem in the large  $k$  region. In general, Alfvén oscillations may be replaced by a source of given magnitude localized near the resonant flux surface.

## REFERENCES

- [1] WHITE, R.B., GOLDSTON, R.J., et al., Phys. Fluids **26** (1983) 2958.
- [2] CHEN, L., WHITE, R.B., ROSENBLUTH, M.N., Phys. Rev. Lett. **52** (1984) 1122.
- [3] MCGUIRE, K., GOLDSTON, R.J., et al., Phys. Rev. Lett. **50** (1983) 891.
- [4] GRIBKOV, W.M., KADOMTSEV, B.B., POGUTSE, O.P., Pis'ma Zh. Ehksp. Teor. Fiz. **38** (1983) 14.
- [5] KADOMTSEV, B.B., in Voprosy teorii plazmy (LEONTOVICH, M.A., Ed.), Vol. 4, Atomizdat, Moscow (1964) 183.
- [6] MIKHAILOVSKIJ, A.B., *ibid.*, Vol. 9 (1979) 3.
- [7] BUSSAC, M.N., PELLAT, R., et al., Phys. Rev. Lett. **35** (1975) 1638.
- [8] ZAKHAROV, L.E., Fiz. plazmy **4** (1978) 898.
- [9] OHKAWA, T., Phys. Rev., A **67** (1978) 35.
- [10] KADOMTSEV, B.B., POGUTSE, O.P., Zh. Ehksp. Teor. Fiz. **65** (1973) 575.
- [11] KADOMTSEV, B.B., POGUTSE, O.P., Pis'ma Zh. Ehksp. Teor. Fiz. **39** (1984) 225.
- [12] COZZANI, F., HORTON, W., Preprint IFSR-214, Univ. of Texas at Austin (1985).
- [13] HASEGAWA, A., MIMA, K., Phys. Fluids **21** (1978) 87.
- [14] HASEGAWA, A., MacLENNAN, C.G., KODAMA, Y., Phys. Fluids **22** (1979) 2122.

## EFFECTS OF ENERGETIC PARTICLES ON TOKAMAK STABILITY

J. VAN DAM<sup>1</sup>, M.N. ROSENBLUTH<sup>1</sup>, H.L. BERK<sup>1</sup>,  
N. DOMINGUEZ<sup>1</sup>, G.Y. FU<sup>1</sup>, X. LLOBET<sup>1</sup>,  
D.W. ROSS<sup>2</sup>, D.P. STOTLER<sup>1</sup>

<sup>1</sup> Institute for Fusion Studies,

<sup>2</sup> Fusion Research Center,  
University of Texas at Austin,  
Austin, Texas,  
United States of America

D.A. SPONG, W.A. COOPER  
Oak Ridge National Laboratory,  
Oak Ridge, Tennessee,  
United States of America

D. SIGMAR, D.E. HASTINGS, J.J. RAMOS  
Plasma Fusion Center,  
Massachusetts Institute of Technology,  
Cambridge, Massachusetts,  
United States of America

H. NAITO, T. TODOROKI  
Institute of Plasma Physics,  
Nagoya University,  
Nagoya, Japan

S.T. TSAI, S.G. GUO, J.W. SHEN  
Institute of Physics,  
Academia Sinica,  
Beijing, China

### Abstract

#### EFFECTS OF ENERGETIC PARTICLES ON TOKAMAK STABILITY.

Energetic particles (for instance fusion product alphas or beam-injected/rf-heated ions) can excite MHD ballooning modes through wave-particle interaction at their large magnetic drift frequency. The use of a "sloshing" distribution avoids resonant destabilization, but tends to excite a new type of continuum instability. At higher energies, the usual MHD unstable modes are suppressed, although subtler instabilities related to shear Alfvén gap modes and global Alfvén waves occur. When these low growth rate modes are negligible, access to the high-beta regime of second stability can be attained with sufficiently hot energetic particles.

## 1. INTRODUCTION

Energetic particle species may be produced in tokamaks by neutral beam heating, by rf heating, or, in ignition devices, by alpha particle production. Due to their large magnetic curvature drift velocity and possibly super-Alfvénic parallel velocity, these hot particles can significantly affect the low frequency MHD and also the higher frequency Alfvénic stability properties of tokamaks, depending on their average energy. In this paper, we discuss and present detailed results on a number of such issues.

## 2. MHD BALLOONING MODES

### 2.1. Moderately Energetic Regime

A moderately energetic hot particle species whose typical magnetic curvature and gradient- $B$  drift frequency  $\bar{\omega}_{dh}$  is comparable to MHD frequencies can excite new resonant instabilities such as “fishbones” and their high-frequency precursor oscillations. These modes were observed in the PDX tokamak and have been associated, respectively, with trapped particle-induced internal kink and ballooning instabilities [1]. Here we consider the latter.

The behavior of high-toroidal-mode-number ballooning modes interacting with an anisotropic population of energetic trapped particles can be described with the vorticity equation

$$\begin{aligned} & \vec{B} \cdot \nabla \left[ \left( \frac{\sigma |\nabla S|^2}{B^2} \right) \vec{B} \cdot \nabla \Phi \right] + \omega(\omega - \omega_{*i}) \frac{|\nabla S|^2}{v_A^2} \Phi \\ & + \vec{e} \cdot \vec{\kappa} \left( \vec{e} \cdot \hat{\nabla} P_{\parallel} + \frac{\sigma}{\tau} \vec{e} \cdot \hat{\nabla} P_{\perp} \right) \Phi + \sigma B \vec{e} \cdot \vec{\kappa} \left( Q_{\parallel} - \frac{\sigma}{\tau} B \vec{e} \cdot \vec{\kappa} \Phi \right) = 0 \quad (1) \end{aligned}$$

and the perturbed pressure balance equation

$$\tau \left( Q_{\parallel} - \frac{\sigma}{\tau} B \vec{e} \cdot \vec{\kappa} \Phi \right) = \int d^3v \frac{\omega - \omega_{*h}}{\omega - \langle \omega_{dh} \rangle} \left( \frac{\partial F_h}{\partial E} \right) \mu^2 \langle Q_{\parallel} \rangle \quad (2)$$

Here,  $\Phi$  is related to the magnitude of the field line displacement;  $Q_{\parallel}$  is related to the parallel component of the perturbed (Lagrangian) magnetic field; angle brackets denote bounce averages: perturbed quantities are assumed to vary as  $\exp(iS - i\omega t)$ , where  $\vec{B} \cdot \nabla S = 0$ , with  $\vec{B}$  the equilibrium magnetic field; and  $P_{\perp, \parallel} = P_c(\psi) + P_{\perp, \parallel h}(\psi, B)$  are the total pressure components of the isotropic core plasma and anisotropic ( $P_{\parallel h}/P_{\perp h} \sim a/R \ll 1$ ) hot species. Also, we have  $\sigma = 1 + 4\pi(P_{\perp} - P_{\parallel})/B^2$ ,  $\tau = 1 + 4\pi(\partial P_{\perp}/B\partial B)$ ,  $v_A = (B^2/4\pi N_i M_i)^{1/2}$ ,  $\vec{\kappa} = [(\vec{B}/B) \cdot \nabla](\vec{B}/B)$ ,  $\vec{e} = \nabla S \times \vec{B}/B^2$ .  $\hat{\nabla} = \nabla - (\nabla B)(\partial/\partial B)$ ,  $\mu = Mv_{\perp}^2/2B$ , and  $Mv_{\parallel}^2 = 2(E - \mu B)$ . The hot particle

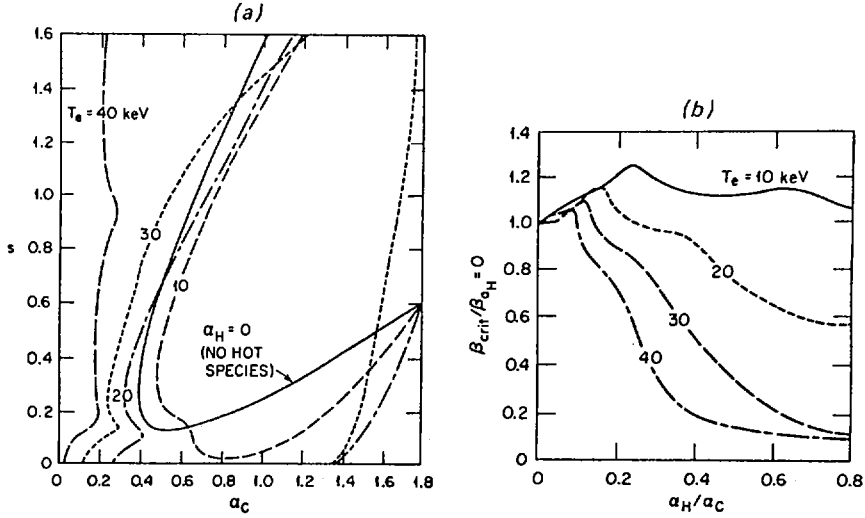


FIG. 1. (a) Dependence of  $(\hat{s}, \alpha_c)$  stability boundaries on  $T_e$  for  $\alpha_h/\alpha_c = 0.3$ ,  $q = 2$ ,  $k_{\perp}\rho_i = 0.28$ , and  $\epsilon_p = R|d \ln P_c/dr| = 6$ .

(b) Ratio of  $\beta_{crit} = (\epsilon_p/q^2)\alpha_{c,crit}$  with alphas to that without alphas, at  $\hat{s} = 0.6$ , versus  $\alpha_h/\alpha_c$  for various  $T_e$ .

diamagnetic frequency is  $\omega_{*h} = -(c/e_h Z_h)(\vec{e} \cdot \nabla F_h)(\partial F_h/\partial E)^{-1}$  and their magnetic drift frequency is  $\omega_{dh} = (c/e_h Z_h)\vec{e} \cdot (M v_{\parallel}^2 \vec{\kappa} + \mu \nabla B)$ . Also, the total ion diamagnetic frequency, including both core plasma and energetic ion species, is  $\omega_{*i} = (B/N_i M_i) \sum_j (\vec{e} \cdot \nabla P_{\perp j})/\Omega_j$ , with  $\Omega_j = e_j Z_j B/M_j c$ . Equations (1) and (2) were solved numerically to obtain the stability boundaries for these resonant modes, with various models for the energetic particle distribution function  $F_h$ .

The low-beta, large-aspect-ratio model tokamak equilibrium with shifted circular flux surfaces and steepened pressure gradients was adopted.

Figure 1(a) shows the results [2] for a collisionally slowing-down distribution of alpha particles with a deeply trapped pitch angle dependence:  $F_h(E, \mu) \propto (E^{3/2} + E_c^{3/2})^{-1} \delta(\mu B_0/E - 1)$ , where  $E_c$  is proportional to the core plasma electron temperature  $T_e$ . Increasing  $T_e$  is strongly destabilizing, which can be understood as increasing  $\text{Re}(\omega)$  through  $\omega_{*i}$  (if  $T_i \cong T_e$ ) and thus maintaining the destabilizing resonance condition  $\text{Re}(\omega) \simeq \bar{\omega}_{dh}$  at higher energies. In particular, the unstable region at low shear,  $\hat{s} = d(\ln q)/d(\ln r)$ , and high values of the normalized core pressure gradient,  $\alpha_c = -(8\pi q^2 R/B_0^2)(dP_c/dr)$ , is enlarged;  $q$  is the safety factor. This type of flat  $q$ , peaked pressure profile will be characteristic of low  $q(a)$  ignited plasmas, especially those with large alpha-driven sawtoothing. Figure 1(b) indicates the  $T_e$  effect in lowering the critical beta value. Results similar

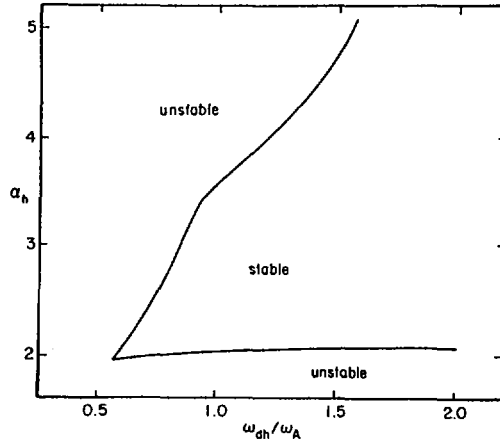


FIG. 2. Stability boundaries in  $\alpha_h$  versus  $\bar{\omega}_{dh}/\omega_A$  for the low-frequency MHD branch (lower curve) and the high-frequency precessional branch (upper curve).

to those of Fig. 1(a) have also been obtained for an isotropic pitch angle dependence: the ballooning mode is somewhat more stable at large shear. However, at low shear ( $\hat{s} \simeq 0.2$ ), both types of pitch angle distributions prevent entry into the second stability regime if  $T_e \gtrsim 40$  keV. This feature may provide an automatic burn control mechanism for ignited tokamaks.

As the hot particle transverse energy  $T_{\perp h}$  is raised such that  $\bar{\omega}_{dh}$  becomes comparable to the Alfvén frequency  $\omega_A = v_A/qR$ , the threshold for these resonant instabilities increases. Figure 2 shows that a stable operating window exists for intermediate values of the energetic particle pressure gradient  $\alpha_h = -(8\pi q^2 R/B_0^2)(dP_{\perp h}/dr)$  when  $\bar{\omega}_{dh}/\omega_A \gtrsim 0.6$ . For PDX parameters ( $B = 2$  T,  $N_i = 3 \times 10^{13}$  cm $^{-3}$ ,  $a = 25$  cm,  $q = 2$ ) and toroidal mode number  $n = 2$ , this would require  $T_{\perp h} > 500$  keV. Below the lower marginal stability boundary, which is independent of  $T_{\perp h}$ , the instability is a nearly purely growing MHD mode, whereas above the upper boundary, given approximately by  $\alpha_h > 3(\bar{\omega}_{dh}/\omega_A)$ , the unstable mode is characterized by a finite oscillation frequency  $\text{Re}(\omega) \approx \bar{\omega}_{dh}$ . The results of Fig. 2 were obtained [3] with the neglect of  $\omega_{*i}/\omega$  effects and for a Maxwellian distribution function of the form

$$F_h(E, \mu) \propto \frac{(\mu B_c - E) \exp(-E/T_{\perp h})}{1 + (\mu B_c - E)^2/(\Delta\lambda)^2}, \quad \mu > E/B_c \quad (3)$$

where  $B_c = B_0 \left(1 - \frac{r}{R} \cos \vartheta_0\right)$  is the field strength at the angle  $\vartheta_0$  that measures the poloidal extent of the trapped particles and where  $\Delta\lambda$  controls the peaking of the pressure profile.

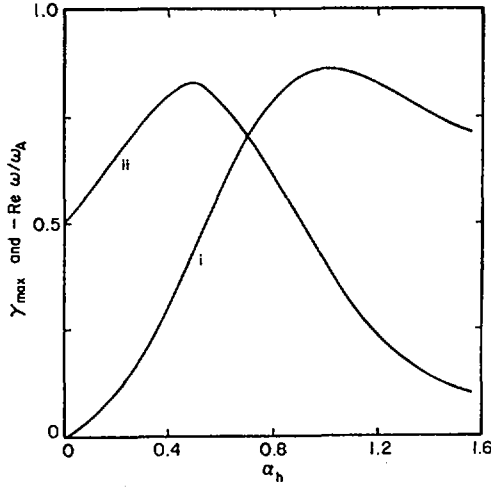


FIG. 3. Maximum growth rate  $\gamma_{max}$  (curve i) and frequency  $Re \omega$  (curve ii), normalized to the Alfvén frequency  $\omega_A$ , versus  $\alpha_h$  for a sloshing distribution.

A “sloshing” population of energetic particles strongly pressure-weighted in the favorable curvature region, which may be created by off-normal neutral beam injection or by cyclotron heating on the small-major-radius side, does not cause resonant destabilization, at least for those particles whose bounce-averaged magnetic precessional drift is reversed:  $\omega_{*h} \langle \omega_{dh} \rangle < 0$ . However, a study [4] of such a sloshing distribution, given by Eq. (3) with  $\Delta\lambda \ll 1$  and  $\vartheta_0$  close to  $\pi$ , reveals a new type of continuum instability. A circulating anisotropic component was added to the distribution of Eq. (3) to satisfy the mirror mode constraint,  $\tau > 0$ . For large  $\vartheta$ , where the extended poloidal angle  $\vartheta$  of the ballooning representation describes the variation along a field line, the wavenumber is secular,  $|\nabla S|^2 \rightarrow (\hat{s}\vartheta)^2$ ; also, the geodesic curvature dominates,  $\vec{e} \cdot \vec{\kappa} \rightarrow \hat{s}\vartheta \sin \vartheta$ . Thus, the asymptotic form of Eqs. (1) and (2) is

$$\frac{d^2\Psi}{d\vartheta^2} + \left(\frac{\omega}{\omega_A}\right)^2 \Psi + q^2 \sin \vartheta \left\{ \frac{\frac{B}{M_h \Omega_h} \int d^3v \frac{\mu^2 (\vec{e} \cdot \nabla F_h) \langle \Psi \sin \vartheta \rangle}{\omega - \langle \omega_{dh} \rangle}}{1 - \frac{B}{M_h \Omega_h} \int d^3v \frac{\mu^2 (\vec{e} \cdot \nabla F_h)}{\omega - \langle \omega_{dh} \rangle}} \right\} = 0 \quad (4)$$

The wavefunction  $\Psi(\vartheta) = \vartheta \cdot \Phi(\vartheta)$  in Eq. (4) can be expressed in Floquet form:  $\Psi(\vartheta) = \tilde{\Psi}(\vartheta) \exp(ik\vartheta)$ , where  $\tilde{\Psi}$  is periodic. Equation (4) is found to have a nearly purely growing solution, whose growth rate  $\gamma = \text{Im}(\omega)/\omega_A$ , shown in Fig. 3, is maximum when  $k = 1/2$ . An analytical estimate with a delta-function pressure model,  $P_{\perp h}(\vartheta) \propto \delta(\vartheta + \vartheta_0) + \delta(\vartheta - \vartheta_0)$ , confirms this

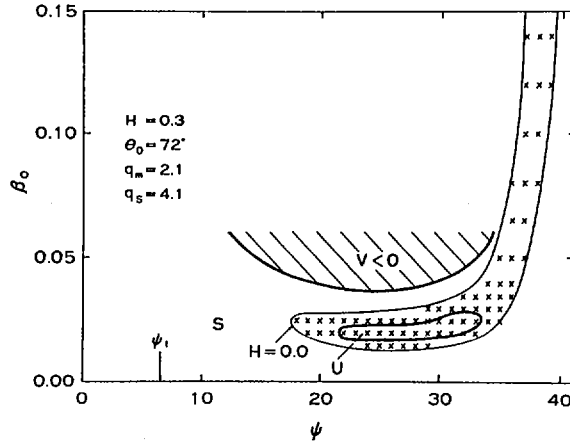


FIG. 4. Stability diagram in core plasma beta on axis,  $\beta_0$ , versus flux surface  $\psi$  for a fixed  $q$  profile. Unstable surfaces in the absence of hot particles ( $H = 0$ ) are shown by  $\times$ ; the small unstable region ( $U$ ) shown for  $H = 0.3$ , where  $H \approx (\beta_{\perp h}/\beta_c)$ , disappears for  $H \geq 0.5$ . Drift reversal ( $V < 0$ ) occurs above the upper curve.

zero-frequency instability above an  $\alpha_h$  threshold. At small  $\alpha_h$  values, however, as shown in Fig. 3, the mode converts to a finite-frequency resonantly unstable Alfvén gap mode, to be discussed in Sec. 3.1.

## 2.2. Highly Energetic Regime

On the other hand, energetic particles that are trapped in the large-major-radius, unfavorable curvature region of a tokamak and whose transverse energy is high enough to preclude resonant interactions can provide enhanced ballooning stabilization and access to the high-beta second regime of stability. This has been confirmed by 2D numerical computations [5] of ballooning stability for finite aspect ratio ( $R/a = 3$ ) anisotropic equilibria. Figure 4 shows that the number of unstable flux surfaces  $\psi$  decreases as  $H$ , which is approximately the ratio of the peak perpendicular pressure of the hot particles to the core plasma pressure on axis, increases; for  $H \geq 0.5$ , all surfaces are stable. Current programming has been assumed to raise  $q_m$  (on axis) above unity in order to reduce the second stability threshold below the drift reversal curve, where  $V = \omega_{*h}(\omega_{dh}) > 0$  and where the analysis yields a sufficient condition for stability.

Access to second stability has also been explored [6] by means of a time-evolved solution for the radial profile of the plasma pressure in a ballooning mode transport formalism. The hot-particle-enhanced marginal stability relationship between  $\alpha_c \propto (r/B_p)^2(dP_c/dr)$  and the shear  $\hat{s} = B_p d(r/B_p)/dr$  can be specified, where the poloidal field  $B_p$  is evolved self-

consistently with the pressure  $P_c(r)$ , and the thermal conductivity (normalized to INTOR scaling) is taken to be unity in the stable region and anomalously large but finite in the unstable region. Fairly high auxiliary heating power is found to be required for the plasma to penetrate the unstable zone and attain a second-stable steady state.

The detailed structure of the second stability regime for ideal ballooning modes was also investigated [7] for large pressure gradients, without hot particles. The threshold for first stability is most stringent for modes that peak on the tokamak midplane, whereas second stability is degraded for off-angle modes. The numerical results yield the empirical scaling  $\alpha_c \simeq 4.2\hat{s}^{1.25}$  for  $2 < \hat{s} < 100$  as the most stringent second stability boundary. At low shear, the computed boundary joints onto the known relationship  $\alpha = 2.13\hat{s}^{0.5}$ . Noting that the behavior of the eigenfunction is primarily determined by changes in slope at points where the local shear or the integrated local shear vanishes, one can analytically derive  $\alpha = 4.6\hat{s}^{1.25} (1 - 0.3\hat{s}^{-0.13})^{0.5}$  for  $\hat{s} \gg 1$  by taking into account only one such pair of neighboring points.

Finally, even if the ideal MHD modes and the alpha particle resonantly excited modes can be stabilized, resistive ballooning instabilities may persist. The  $\Delta'$  parameter that controls their stability was obtained [8] numerically and, in a low beta limit ( $\alpha_c \sim \alpha_h \sim \hat{s} < 1$ ), analytically from the solution in the ideal region with the presence of highly energetic, nonresonant particles. The dispersion relation  $\Delta'(\omega)$  was then derived by asymptotically matching to the solutions in the resistive and deeply resistive regions, with the inclusion of parallel compressibility and cross-field transport effects. The critical value for  $\Delta'$  indicates that the hot species in the nonresonant limit tends to stabilize the resistive modes, at least for  $\alpha_c$  values below the ideal threshold.

### 3. ALFVÉN MODES

#### 3.1. Continuum Gap Modes

At the high energies, such that  $\bar{\omega}_{dh}$  is comparable to or larger than  $\omega_A$ , interaction between the hot particles and shear Alfvén modes occurs. In particular, a new mechanism for continuum gap eigenmodes is found [9]. Note that the third term in Eq. (4), which is proportional to  $\alpha_h$ , introduces a Mathieu equation type of modulation. For a square-top hot pressure profile ( $\alpha_h = \text{const.}$  for  $|\vartheta| \leq \vartheta_0$ , zero elsewhere), the spectrum for the characteristic exponent  $k = k(\omega)$  can be derived. Frequencies within gaps of width proportional to  $\alpha_h$ , which are located in the MHD stable continuum near the points where  $\omega/\omega_A = 0.5, 1.0, 1.5, 2.0, \dots$ , lead to spatially amplifying solutions at  $|\vartheta| \rightarrow \infty$ . Within each such gap, however, there exists a discrete eigenmode that is spatially evanescent. This high-mode-number

localized gap mode can be resonantly excited, without threshold, by the hot particle-wave magnetic drift resonance. Its growth rate is proportional to  $\alpha_h$  but decreases inversely with  $\bar{\omega}_{dh}/\omega_A$ ; usually its magnitude is largest when  $\omega/\omega_A \sim 1$ . For the parameters used in Fig. 3, one observes the  $\omega/\omega_A = 0.5$  shear Alfvén gap mode instability at low  $\alpha_h$  values.

### 3.2. Global Alfvén Waves

Energetic particles whose parallel motion is super-Alfvénic can resonantly destabilize the global Alfvén eigenmodes. These MHD-like modes have discrete frequencies lying just below the Alfvén continuum, i.e.,  $\omega^2 < \min(\omega_A^2)$ , where  $\omega_A = v_A(nq + m)/qR$  and  $(n, m)$  are the toroidal and poloidal mode numbers. They are very weakly damped by electron Landau damping and are therefore more strongly destabilized than the kinetic Alfvén eigenmodes [10]. The instability is driven by the alpha particle density gradient. Coupling to sidebands occurs through the curvature and gradient- $B$  drift of the alphas. A necessary condition for instability is

$$\omega_{*\alpha}/\omega > (2T_\alpha/m_\alpha) \langle \partial F_\alpha / \partial v^2 \rangle_\pm / \langle F_\alpha \rangle_\pm \quad (5)$$

with  $\langle \dots \rangle_\pm \equiv \int d^3v (v_\perp^2/2 + v_\parallel^2) \delta(\omega - k_{\parallel, m \pm 1} v_\parallel) \dots$ ,  $T_\alpha \equiv \int d^3v F_\alpha m_\alpha v^2/3$ ,  $\omega_{*\alpha} \equiv T_\alpha c/eB_0 L_\alpha$ , and  $L_\alpha = -n_\alpha^{-1} dn_\alpha/dr$ . For low  $m$  axisymmetric modes ( $n = 0$ ) and typical CIT parameters, we find instability when  $L_\alpha/a < 0.5$  for a slowing-down distribution. Since the birth distribution of the alphas is expected to be narrower (roughly  $L_\alpha/a = 0.4$ ) than this critical value, the modes are likely to be unstable, leading to possible radial transport. (Studies employing Maxwellian alphas yield somewhat more optimistic stability estimates.)

Figure 5 shows the damping effect of increasing  $L_\alpha$  for the (0,-2) mode, as obtained from a full numerical calculation. A simpler analytic calculation gives nearly identical results. For the CIT parameters, we assume  $R = 1.4$  m,  $a = 0.67$  m [representing  $(ab)^{1/2}$  for a shaped tokamak],  $B_0 = 10$  T,  $T_e(0) = T_i(0) = 30$  keV [volume average 10 keV], and  $n_e(0) = n_i(0) = 10^{21}$  m $^{-3}$  [volume average  $5 \times 10^{20}$  m $^{-3}$ ]. The alpha particles are described by a gaussian radial distribution with  $n_\alpha(0) = 2 \times 10^{19}$  m $^{-3}$ . The slowing-down distribution yields  $T_\alpha \approx 1$  MeV, with the Maxwellian  $T_\alpha$  taken to be the same for comparison. The real mode frequency is  $\omega_{(0,-2)} = 4.05 \times 10^6$  sec $^{-1}$ . The (0,-1) mode has a much weaker growth rate than the (0,-2) mode. However, the inclusion of toroidicity or noncircularity effects may reduce the (0,-2) growth rate by introducing an Alfvén resonance through coupling to the continuum of the (0,-1) mode.

Toroidicity can also induce a new class of global low- $n$  discrete eigenmodes, with frequencies that lie within gaps in the shear Alfvén continuum

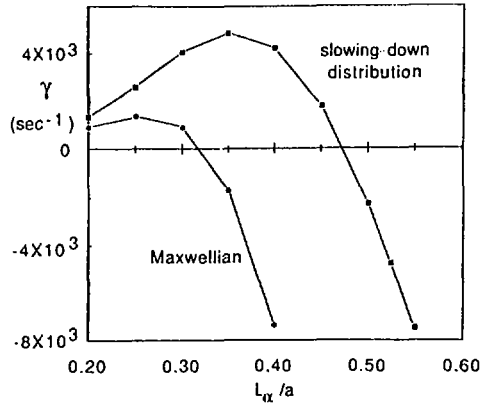


FIG. 5. Growth rate  $\gamma$  of axisymmetric  $(0, -2)$  global Alfvén eigenmode for CIT parameters versus the density gradient scale length  $L_{\alpha}$ , for 1 MeV slowing-down and Maxwellian alpha particles.

[11]. These toroidicity-induced shear Alfvén eigenmodes can be destabilized by inverse Landau interaction with energetic particles. The growth rate for such a toroidal gap mode due to coupling between the  $(-1, -1)$  and  $(-1, -2)$  modes was estimated to be approximately an order of magnitude larger than that for the most unstable cylindrical global Alfvén eigenmode,  $(0, -2)$ , described previously.

#### 4. CONCLUSIONS

The following picture emerges of the effects of energetic particles on tokamak stability. At moderately high energies, characteristic of neutral-beam-injected ions or medium energy alpha particles (for example [11],  $T_{\perp\alpha}/T_i < 150$ ), resonant destabilization of macroscopic MHD modes such as ballooning is to be expected when the beta value of the hot particle trapped component exceeds a modest threshold. In particular, flat  $q$  and peaked pressure profiles that will be characteristic of low edge  $q$  ignited plasmas with alpha particle driven sawtoothing are susceptible to instability; hence, sawtooth-free operation is desirable if the trapped alpha resonance effects cannot be stabilized. Increasing the plasma electron temperature ( $T_e > 40$  keV) can also degrade stability; this feature could provide an automatic burn control mechanism. The destabilizing effects of moderately energetic particles can be avoided with the use of "sloshing" distributions that are pressure-weighted on the small major radius side; however, these drift-reversed hot particles tend to drive a purely growing continuum instability, with growth rates comparable to MHD rates.

At higher energies – typically 500 keV for PDX-like parameters or a few MeV for reactor parameters – the usual MHD modes are stabilized. The energetic particles can permit access to the high-beta second regime of ballooning stability, although fairly high auxiliary heating power may be required during the dynamic process. Also, second stability is more stringent for off-midplane modes. In the nonresonant limit, the energetic particles do tend to stabilize low-beta resistive ballooning modes.

At these high energies, however, the energetic particles interact with the shear Alfvén continuum to produce a new unstable discrete gap mode with no threshold, as well as to resonantly destabilize the low- $n$  toroidicity-induced gap eigenmode. Moreover, for the parameters of the proposed Compact Ignition Tokamak, the birth distribution of alpha particles is expected to be narrow enough to lead to destabilization of the global Alfvén modes. Thus, although the MHD modes can be suppressed at high energies, subtler instabilities related to Alfvén waves are predicted, whose nonlinear and experimental consequences warrant scrutiny.

## ACKNOWLEDGMENTS

This work was supported in part by the U.S. Department of Energy under Contract No. DE-FG05-80ET-53088 with The University of Texas and Contract No. DE-AC05-84OR-21400 with Martin Marietta Energy Systems, Inc., and Massachusetts Institute of Technology.

## REFERENCES

- [1] CHEN, L., WHITE, R.B., CHENG, C.Z., ROMANELLI, F., WEILAND, J., HAY, R., VAN DAM, J.W., ROSENBLUTH, M.N., TSAI, S.T., BARNES, D.C., in *Plasma Physics and Controlled Nuclear Fusion Research 1984 (Proc. 10th Int. Conf. London, 1984)*, Vol. 2, IAEA, Vienna (1985) 59.
- [2] SPONG, D.A., SIGMAR, D.J., TSANG, K.T., RAMOS, J.J., HASTINGS, D.E., COOPER, W.A., *Effects of Isotropic Alpha Populations on Tokamak Ballooning Stability*, Rep. ORNL-TM-10200, Oak Ridge National Lab., TN (1986).
- [3] STOTLER, D.P., *The Effect of Energetic Particles on Stability of Mirror and Tokamak Plasmas (PhD Thesis)*, Rep. IFSR-238, Inst. for Fusion Studies, Texas Univ., Austin (1986).
- [4] STOTLER, D.P., BERK, H.L., *The Effects of Sloshing Energetic Particles on Ballooning Modes in Tokamaks*, Rep. IFSR-259, Inst. for Fusion Studies, Texas Univ., Austin (1986).
- [5] NAITOU, H., VAN DAM, J.W., BARNES, D.C., *Energetic Particle Stabilization of Ballooning Modes in a Finite-Aspect-Ratio Tokamak*, Rep. IPPJ-797, Inst. of Plasma Physics, Nagoya Univ. (1986).
- [6] FU, G.Y., VAN DAM, J.W., ROSENBLUTH, M.N., *Effects of Ballooning Instability on Tokamak Confinement*, Rep. IFSR-254, Inst. for Fusion Studies, Texas Univ., Austin (1986).

- [7] LLOBET, X., BERK, H.L., ROSENBLUTH, M.N., Finite Pressure Ballooning Mode Stability in Toroidal Equilibrium, Rep. IFSR-263, Inst. for Fusion Studies, Texas Univ., Austin (1986).
- [8] DOMINGUEZ, N., Stability of Ballooning Modes in Tokamaks with Energetic Particles (PhD Thesis), Rep. IFSR-245, Inst. for Fusion Studies, Texas Univ., Austin (1986).
- [9] VAN DAM, J.W., ROSENBLUTH, M.N., in Sherwood Annual Controlled Fusion Theory Conference (Proc. Conf. Madison, WI, 1985), Wisconsin Univ., Madison (1985) Paper 1C6.
- [10] LI, Y.M., MAHAJAN, S.M., ROSS, D.W., Destabilization of Global Alfvén Eigenmodes and Kinetic Alfvén Waves by Alpha Particles in a Tokamak Plasma, Rep. FRCR-276, Texas Univ., Austin (1985)
- [11] CHENG, C.Z., CHANCE, M.S., Phys. Fluids **29** (1986) 3695.
- [12] SPONG, D.A., SIGMAR, D.J., COOPER, W.A., HASTINGS, D.E., TSANG, K.T., Phys. Fluids **28** (1985) 2494.



## DISCUSSION

### ON PAPERS IAEA-CN-47/E-II-2-1 TO E-II-2-3

J.A. WESSON: Do you still accept your original interpretation of the fishbone activity observed on PDX?

L. CHEN: Since for PDX parameters,  $\bar{\omega}_{dh} \geq \omega_R$ , ideal MHD approximation remains valid.

J.A. WESSON: Further, do you have any understanding of the observation of fishbone instabilities on JET which should be stable according to theory?

L. CHEN: No. Our prediction is based on the assumption that the equilibria in JET are more or less similar to those in PDX. If this is not the case, as suggested by your sawtooth theory, we need to re-examine the situation for JET.

J.A. WESSON: A final point — would quasi-interchange  $m = 1$  behaviour have fishbone stability different from the  $m = 1$  kink behaviour which you assumed?

L. CHEN: We have not carried out detailed analyses and so I can only speculate. Since the eigenmode structures and the singular layer properties are different, I would say that this is the case.

Mingsheng CHU: Can the fishbone excitation process which you described be operative at the  $q = 2$  surface? If so, what is the signature of such a mode in the non-linear regime?

L. CHEN: If I stretch the argument, I could regard modes localized at about  $m/n = q = 2$  as either ideal ballooning modes or resistive interchange modes. Since these modes are radially localized and break the third invariant of energetic trapped particles, the instabilities would definitely lead to local flattening of hot particles through instability induced outward diffusion.

K. ITOH: When the stability of the modes in the presence of alpha particles is estimated, the result depends on the assumption regarding the source distribution in real space and in velocity space. What assumption is made and which model is used for the conclusion that there is alpha driven instability?

My second question concerns the excitation of high  $k_{\perp} \sim \omega_p/c$  modes. The convection to the high  $k$ -axis in the  $k$ -space corresponds to the condensation near the rational surface. Can global modes excite  $k_{\perp} \sim \omega_p/c$  modes on every magnetic surface, and do you need many high  $m$ -modes?

L. CHEN: For alpha induced fishbones, the alpha velocity space distribution is taken to be sufficiently smooth and the modes are therefore essentially driven by the real space gradients. Our results are estimated on the basis of transport code simulations of alpha particle distributions.

Regarding your second question, strictly speaking, propagation to high  $k$  corresponds to mode behaviours as  $\exp(it|r-r_s|)$  (i.e.  $k \propto t$ ), and condensation around mode rational surfaces occurs if dissipations are introduced.



# NONLINEAR TOROIDAL PLASMA DYNAMICS BY REDUCED FLUID MODELS

M. KOTSCHENREUTHER, A. AYDEMIR, R. CARRERA,  
R.D. HAZELTINE, J.D. MEISS, P.J. MORRISON  
Institute for Fusion Studies,  
The University of Texas at Austin,  
Austin, Texas,  
United States of America

## Abstract

NONLINEAR TOROIDAL PLASMA DYNAMICS BY REDUCED FLUID MODELS.

Fluid models are presented which generalize reduced MHD by allowing for compressibility, Finite Larmor Radius, and long mean free path in toroidal geometry. The Hamiltonian structure of the models leads to a generalized energy principle for determining linear and nonlinear MHD stability of equilibria with flows and Finite Larmor Radius effects. Neoclassical effects from the long mean free path lead to new dissipative terms giving rotation damping, bootstrap currents and the Ware pinch. Rotation damping from non-ambipolar transport in stellarators can lead to self-consistent plasma currents which strongly reduce or "heal" steady-state magnetic stochasticity (e.g., from coil errors or Pfirsch-Schlüter currents). The bootstrap current in tokamaks causes the growth of nonlinear magnetic islands in the Rutherford regime. Thus, otherwise stable moderate mode number islands can potentially overlap, with serious detriment to confinement.

## INTRODUCTION

We present models that generalize reduced MHD by allowing for compressibility, Finite Larmor Radius, and long mean free path. The Hamiltonian structure of the models leads to a significantly generalized energy principle. Applications include linear and nonlinear instabilities and results regarding self-consistent magnetic stochasticity.

### 1. MORE REALISTIC FLUID MODELS

A. Conventional high  $\beta$  reduced MHD[1] contains three fields: the poloidal flux function  $\psi$ , a velocity stream function  $\phi$ , and pressure  $p$ . To allow for compressible flows, we add parallel velocity. Previous Alfvénic normalizations are used[1]. FLR terms enter proportional to a parameter  $\delta$ , defined so that the normalized diamagnetic velocity  $(cT/neB)\hat{z} \times \nabla n/\epsilon v_A$  is equal to  $\delta \hat{z} \times \nabla p$ . We also define  $[Q_1, Q_2] = \hat{z} \cdot \nabla Q_1 \times \nabla Q_2$ ,  $\nabla_{\parallel} Q = \frac{\partial Q}{\partial z} - [\psi, Q]$ ,  $F = \phi + k\delta p$ ,  $W = \nabla_{\perp}^2 F$ ,  $J = \nabla_{\perp}^2 \psi$ , with  $k = T_i/T_e$ . The conserved energy is

$$H = \frac{1}{2} \int (|\nabla\psi|^2 + |\nabla F|^2 + \left(\frac{1+k}{2}\right) p^2 + v^2) \quad (1)$$

We therefore write the four-field model with the terms needed for energy conservation on the left, and higher order FLR terms needed to be Hamiltonian on the right.

$$\begin{aligned} \dot{W} + [F, W] - \delta k \nabla \cdot [p, \nabla F] + \nabla_{\parallel} J + (1+k)[h, p] \\ = (k\delta\beta/2) \{ -2\delta(1+k)\nabla_{\perp}^2 [h, p] - \nabla_{\perp}^2 \nabla_{\parallel} (v + 2\delta J) \\ + k\delta\nabla^2 [p + 2\beta h, W] \} \end{aligned} \quad (2)$$

$$\dot{\psi} + \nabla_{\parallel} F - \delta(1+k)\nabla_{\parallel} p + k\delta^2\beta\nabla_{\parallel} W = 0 \quad (3)$$

$$\dot{p} + [F, p] + \beta\nabla_{\parallel} (v + 2\delta J) - 2\beta[h, F - (1+k)\delta p] = k\delta^2\beta[p + 2\beta h, W] \quad (4)$$

$$\begin{aligned} \dot{v} + [F - kp, v] + \frac{1}{2}(1+k)\nabla_{\parallel} p = -k\delta [v, 2\beta h + k\delta^2\beta\nabla_{\perp}^2 p - 2\delta\beta W] \\ + \frac{1}{2}k\delta\beta\nabla_{\parallel} W \end{aligned} \quad (5)$$

where  $h$  gives the effects of curvature;  $h$  is the normalized distance in the direction outward from the torus.

B. In modern tokamaks the collisional mean free path exceeds the device size. Nonetheless, fluid equations can be rigorously derived to describe the region near a rational surface. The calculation uses kinetic theory together with a systematic two-scale expansion in the parallel gradients, and is similar in spirit to previous MHD analysis by Glasser et al. and Kotschenreuther et al. For simplicity we use an aspect ratio expansion and plateau collisionality. For maximum generality, we include FLR effects, parallel compressibility, resistive flux diffusion in the inner layer, semicollisionality, rotation damping of parallel velocity, nonlinear convection and nonlinear modifications of the equilibrium field. A maximal ordering to systematically include all the above, in which all quantities are ordered in terms of  $\epsilon$ , is:  $\Delta r \sim \rho_p$ ,  $\rho_p/r \sim \epsilon^2$ ,  $\omega \sim \epsilon^2 v_i/R$ ,  $\beta \sim \epsilon^2$ ,  $B_p/B \sim \epsilon$ ,  $\nu_e R/v_e \sim \epsilon$ ,  $\sqrt{m_e/m_i} \sim \epsilon$ , where  $\Delta r$ ,  $r$ ,  $v_i$ , and  $\rho_p$  are the layer width, minor radius, ion thermal velocity and poloidal gyroradius.

The final fluid equations have non-dissipative and dissipative terms usually found in slab models, but also additional dissipative terms giving rotation damping, bootstrap currents, and the Ware pinch; similar effects were previously found by Callen and Shaing[2]. The dissipation-free terms are, in fact, the same as those on the left sides of Eqs. (2)–(5), but with  $h = 0$  (also, the terms on the right do not occur—they are higher order). The new neoclassical terms in Eqs. (2) and (5) are

$$\dot{W} + \dots = -\nu \frac{\partial}{\partial r} \left( \frac{\partial F}{\partial r} + \Theta v \right) \quad (6)$$

$$\dot{v} + \dots = -\Theta\nu \left( \frac{\partial F}{\partial r} + \Theta'v \right) \quad (7)$$

For an axisymmetric tokamak with nearly circular surfaces,  $\nu = \sqrt{\pi\beta_i q}$ ,  $\theta = \theta' =$  the ratio of poloidal to toroidal field. We have general expressions for non-circular non-symmetric geometries, which are omitted due to space.

The vorticity is damped at a rate  $\nu$ , and the parallel velocity is damped at a rate  $\theta\theta'\nu \sim \epsilon^2\nu$ . For moderate  $\beta$ , the rotation damping term is much larger than the usual inertial term in Eq. (2). For axisymmetry the damping terms tend to equilibrate both  $F$  and  $v$  to satisfy  $v = -\theta^{-1}\partial F/\partial r$ , as in equilibrium neoclassical theory. The toroidal angular momentum is conserved by the damping terms for axisymmetry. In a stellarator,  $|\theta'| > |\theta|$ . Then the damping terms tend to make both  $F$  and  $v$  vanish. This also is the condition in equilibrium neoclassical theory, where the ions are electrostatically confined.

The Ohms' Law and pressure evolution, Eqs. (3) and (4), have neoclassical dissipative terms

$$\dot{\psi} + \dots = \eta \left[ J + \alpha \frac{\partial}{\partial r} (1+k)p - \frac{\alpha}{\delta} \left( \frac{\partial F}{\partial r} + \Theta v \right) \right] \quad (8)$$

$$\dot{p} + \dots = 2\beta\alpha\eta \frac{\partial}{\partial r} \left[ J + \alpha \frac{\partial}{\partial r} (1+k)p - \frac{\alpha}{\delta} \left( \frac{\partial F}{\partial r} + \Theta v \right) \right] \quad (9)$$

For equilibrated ion flows, these give a bootstrap current and Ware pinch in agreement with equilibrium neoclassical theory. For plateau collisionality,  $\alpha \sim \epsilon\nu_e/R\nu_e$ .

## 2. ENERGY PRINCIPLES FOR NONLINEAR STABILITY

Here we present generalizations of the ideal MHD energy principle,  $\delta W$ , for fluid and kinetic models, that can handle equilibrium flow and FLR effects.

Consider a noncanonical Hamiltonian system with field variable  $f(z, t)$ . Functionals called Casimirs exist for such systems, which are constants of the motion. (For example, in the Vlasov equation with distribution function  $f$ ,  $\int dx dv G(f)$  is constant for any function  $G$ .) Denote such a Casimir by  $C[f]$ , and denote the Hamiltonian by  $H[f]$ . It has previously been shown [3,4] that for each Casimir  $C$ , an equilibrium can be found by solving  $\frac{\delta H[f]}{\delta f} = \frac{\delta C[f]}{\delta f}$ , where  $\delta/\delta f$  means functional differentiation with respect to  $f$ . Consider perturbations  $\delta f$  away from  $f_0$ . We have

$$\begin{aligned} C[f_0 + \delta f] - C[f_0] &= \int dz \frac{\delta C}{\delta f} \delta f \\ &+ \frac{1}{2} \int dz \frac{\delta^2 C}{\delta f^2} \delta f^2 + \text{Higher order terms} \end{aligned} \quad (10)$$

$$\begin{aligned}
H[f_0 + \delta f] - H[f_0] &= \int dz \frac{\delta H}{\delta f} \delta f \\
&+ \frac{1}{2} \int dz \frac{\delta^2 H}{\delta f^2} \delta f^2 + \text{Higher order terms} \quad (11)
\end{aligned}$$

Now we can obtain the change in energy from a perturbation  $\delta f$ . Since the system is constrained by  $C(f) = \text{constant}$ , the only accessible perturbations are those where the left side of Eq. (10) vanishes. Then by the equilibrium condition we have that the change in  $H$  at constant Casimir  $C$ ,  $\Delta H|_c$ , is

$$\Delta H|_c = \frac{1}{2} \int dz \frac{\delta^2(H - C)}{\delta f^2} \delta f^2 + \text{Higher order terms}$$

and we define  $F = H - C$  to be the free energy for accessible perturbations. As expected, the perturbed energy is second order in  $\delta f$ . Also note that the energy released or absorbed to create an allowable perturbation  $\delta f$  depends on the equilibrium through  $C$ .

If  $\delta^2 F$  is positive definite, then all accessible small perturbations  $\delta f$  increase  $H$ . Since  $H$  is conserved, no small perturbation can grow indefinitely, and we have both linear and nonlinear stability for small  $\delta f$ . (Technically this only implies formal stability, but the step from formal to nonlinear stability is usually straightforward[3,4].)

Note that we have not considered the linearized equations of motion to come to this conclusion. The linearized equations depend on both  $H$  and the Poisson bracket. The latter can be quite complicated for noncanonical systems.

If  $\delta^2 F$  is indefinite, then either there is a linear instability or a linearly stable negative energy wave (or direction in function space). It is not possible to determine which without considering the Poisson bracket. Nonetheless, note that a linearly stable negative energy wave can lead to serious nonlinear instabilities. For example, explosive instabilities are possible in Hamiltonian systems with three interacting waves with resonant frequencies. More complicated nonlinear phenomena are also possible in continuous media; these are currently under investigation. The important point is that when  $\delta^2 F$  is indefinite, an instability of some kind is likely.

Negative energy waves can also be found in simple cases by applying the Brillouin-Laue condition  $\omega \partial \epsilon / \partial \omega < 0$ . We can show that this condition must agree with  $\delta^2 F$ . However,  $\epsilon$  can only be easily defined in uniform homogeneous media. Dielectric response theory in non-homogeneous media is very lengthy or intractable. The free energy functional  $\delta^2 F$  is far more practical in such cases.

Thus, we believe that  $\delta^2 F$  is a better tool than linear spectral theory to find the total instability potential of many configurations.

As an example we consider reduced low  $\beta$  MHD with poloidal flow. Suppose we wish to consider stability of cylindrically symmetric equilibria to perturbations with a given helicity. Let  $\chi$  be the relevant helical flux,  $\chi = \psi - r^2/2q_0$ . The Casimirs are  $\int H(\psi)dx$  and  $\int UG(\psi)$ , for arbitrary functions  $H$  and  $G$ . The free energy  $F$  is

$$F = \int \left| \nabla_{\perp} \left( \chi + \frac{r^2}{2q_0} \right) \right|^2 + |\nabla\phi|^2 + H(\chi) + UG(\chi) dx \quad (12)$$

Equilibria are given by  $\nabla_{\perp}^2 (\chi + r^2/2q_0) = H'(\chi) + \nabla_{\perp}^2 GG'$ ,  $\phi = G(\chi)$ . To examine stability, take the second variation and rearrange terms to get

$$\begin{aligned} \delta^2 F = \int & \left( |\nabla\delta\phi - \nabla G'\delta\chi|^2 + |\nabla\delta\chi|^2 (1 - G'^2) \right. \\ & \left. + \delta\chi^2 [G''\nabla^2 G + H'' + G'\nabla \cdot G''\nabla\chi] \right) dx \end{aligned} \quad (13)$$

An instability or negative energy wave exists if  $\delta^2 F$  can be made negative. To minimize  $\delta^2 F$ , choose  $\delta\phi$  to make the first term vanish. The minimizing  $\delta\chi$  can be found by standard techniques, e.g., solve the relevant Eulers equation, or for an approximate answer, insert trial functions and vary their parameters, etc.

For equilibria without flow,  $G = 0$ , the Eulers equation is equivalent to the small aspect ratio  $\delta w$  result for ideal kinks; the second term gives the stabilizing influence of line bending, and the  $H''$  term gives the destabilizing influence of current gradients. We see that the nonlinear stability with flow can be found by a similar Eulers equation; no qualitatively new features arise in the mathematical analysis given Eq. (13).

### 3. APPLICATIONS

A. Large self-consistent plasma currents can arise in magnetic stochasticity and islands when the neoclassical transport is not intrinsically ambipolar. Here we consider only steady-state stochasticity (from non-axisymmetric equilibrium Pfirsch-Schlüter currents or coils).

Let us estimate the size of the self-consistent parallel currents and fields from radial electron diffusion in stochasticity. Resonant magnetic perturbations  $\delta B_r = \delta B_{\text{ind}} + \delta B_{\text{ext}}$  arise on an integrable background field  $B$ , due to both an external agent (i.e. field coils or Pfirsch-Schlüter currents) and the induced plasma response. The flux average radial electron current from parallel motion in the stochasticity is  $\langle j_r^e \rangle = \langle \delta j_{\parallel} \delta B_r / B \rangle$ . Breaking this into the various helicities, which we label by perpendicular wavenumber  $k$ ,  $\langle j_r^e \rangle = \sum_k \langle \delta j_{\parallel}^{-k} \delta B_r^k / B \rangle$ . The motion of electrons in a stochastic field is only correlated with the resonant harmonic near its respective rational surface; call the distance  $\Delta x_c$ . Thus, at a given radius, only terms from

nearly rational surfaces contribute. Denote the typical spacing between the rational surfaces by  $\lambda$ ; then  $\Delta x_c/\lambda$  harmonics contribute at a given point, and if all resonant harmonics have roughly the same amplitude we have  $\langle j_r^e \rangle \sim (\Delta x_c/\lambda) \delta B^k/B \delta j_{\parallel}^{-k}$ . The induced magnetic perturbation can be simply computed using the "constant  $\psi$ " approximation, which here implies  $(\Delta'/k) \delta B_{\text{ind}}^k = (4\pi/c) \int dx \delta j_{\parallel}^k \sim (4\pi/c) \delta j_{\parallel}^k \Delta x_c$ . Self-consistency is important when  $\delta B_{\text{ind}} \gtrsim \delta B_r$ , which gives the criterion

$$\left( \frac{\delta B^k}{B} \right)^2 < \frac{4\pi}{c} \frac{\lambda \langle j_r^e \rangle k_{\perp}}{B \Delta'} \quad (14)$$

A neoclassical ion current arises because the magnetic stochasticity changes the radial electric field. Equal radial electron and ion current occurs. For typical reactor parameters and ion transport levels consistent with the Lawson criterion, self-consistency is important for  $\delta B/B \sim 10^{-2}$ , which can cause very large overlapping islands.

More detailed analysis of both the single helicity and multihelicity cases reveals that the self-consistent currents cause the resonant perturbation to be shielded out, and thus islands and stochasticity are "healed" in steady state if the inequality in (13) is satisfied.

B. The bootstrap current term in Ohm's Law can cause magnetic islands to grow in the Rutherford regime. For sufficiently large islands, the vorticity equation implies  $\nabla_{\parallel} J = 0$ , and  $J$  is a flux function, so as in previous analysis the current can be found by taking the flux average of Ohm's Law. Also, the pressure becomes a flux function because of parallel convection by sound waves. The pressure profile is found as in Appendix A of Ref. 6.

We obtain the following evolution equation for  $\Delta x$ , the island width

$$\frac{K_1}{\eta} \frac{d\Delta x}{dt} = \Delta' + k_2 \frac{S' \alpha}{\Delta x} \frac{dp}{dx} \quad (15)$$

where  $K_1 \simeq 1.6$ ,  $k_2 \simeq 6$ , and  $S' = q^2/r(dq/dr)$ . For small islands the bootstrap current term dominates and the island grows. For  $\Delta' < 0$ , the steady-state island width is given by  $\Delta x = \frac{K_2 s' \alpha (dP/dx)}{\Delta'}$ .

This is similar to previous results for unstable interchanges[5,6]. Thus, as in that case, island overlap always occurs if islands up to sufficiently high mode numbers are considered[6]. For typical parameters and  $\beta \sim 1\%$ , island overlap occurs for islands with  $m \sim 5 - 10$ .

One must keep in mind that the above calculation is only valid for single helicity islands; the dynamics may change considerably as overlap is approached. If islands significantly overlap, the stochastic diffusion can be crudely estimated from the quasilinear formula; for  $\beta \gtrsim 1\%$ , the confinement

deterioration is significant for current and future devices and rapidly worsens with increasing  $\beta$ .

C. We find that the shear Alfvén resonant mode is destabilized by gradients in the equilibrium  $\omega_*$ -profile. Significantly, its growth rate dominates the tearing mode for either large  $\omega_*$  or low shear and depends only weakly on the resistivity,  $\gamma \propto \eta^{1/4}$ . Thus, it should predominate in reactors. The mode's stability is independent of  $\Delta'$ .

D. Numerical studies of the  $m = 1$  tearing mode show that it continues exponential growth well into the nonlinear regime. We have an analytic theory explaining this. Space does not allow a full discussion of this, but the primary reason for the rapid growth of the  $m = 1$  mode is that its island size depends linearly on the magnetic flux perturbation.

### ACKNOWLEDGEMENTS

This work was supported by USDOE, Contract No. DE-FG05-80ET-53088.

### REFERENCES

- [1] STRAUSS, H.R., *Phys. Fluids* **19** (1976) 134.
- [2] CALLEN, J.D., SHAIN, K.C., *Bull. Am. Phys. Soc.* **30** (1985) 1424.
- [3] HOLM, D.D., MARSDEN, J.E., RATIU, T., WEINSTEIN, A., *Phys. Rep.* **123** (1985) 1.
- [4] HAZELTINE, R.D., HOLM, D.D., MARSDEN, J.E., MORRISON, P.J., in *Plasma Physics (Proc. Int. Conf. Lausanne, 1984)*, Centre de recherches en physique des plasmas, Ecole polytechnique fédérale de Lausanne, Lausanne, Switzerland (1984).
- [5] KOTSCHENREUTER, M., HAZELTINE, R.D., MORRISON, P.J., *Phys. Fluids* **28** (1985) 294.
- [6] CARY, J.R., KOTSCHENREUTHER, M., *Phys. Fluids* **28** (1985) 1392.



# NEOCLASSICAL MHD EQUATIONS, INSTABILITIES AND TRANSPORT IN TOKAMAKS\*

J.D. CALLEN, W.X. QU<sup>1</sup>, K.D. SIEBERT<sup>2</sup>

University of Wisconsin,  
Madison, Wisconsin

B.A. CARRERAS, K.C. SHAIN, D.A. SPONG

Oak Ridge National Laboratory,  
Oak Ridge, Tennessee

United States of America

## Abstract

### NEOCLASSICAL MHD EQUATIONS, INSTABILITIES AND TRANSPORT IN TOKAMAKS.

The reduced equations of resistive MHD are extended for tokamaks into the experimentally relevant banana-plateau collisionality regime by adding parallel viscous stress effects. The resultant neoclassical MHD equations include: (1) rapid ( $\sim \nu$ ) viscous damping of poloidal ion flows; (2) the trapped particle effects on the electrical conductivity and bootstrap current contributions to Ohm's law; (3) an enhanced (by  $B^2/B\hat{\rho}$ ) perpendicular dielectric constant; and (4) all neoclassical transport effects. The types of neoclassical MHD instabilities that occur are analogous to the resistive-g, tearing and rippling modes of resistive MHD, but more virulent. Low mode number tearing type modes evolve into the usual nonlinear stage of resistive tearing modes. Turbulent transport due to medium mode number neoclassical MHD instabilities is estimated and shown to lead to energy confinement scalings similar to experimental results. Finally, the total transport in neoclassical MHD is shown to be comprised of equilibrium and transient Coulomb collisional effects (classical and neoclassical), convection-driven turbulent transport and magnetic flutter effects.

## 1. INTRODUCTION

Resistive magnetohydrodynamic (MHD) models have proven to be very successful [1] in describing many macroscopic phenomena in tokamak discharges (e.g., major disruptions, Mirnov oscillations and anomalous skin penetration). Also, a resistive MHD based model of anomalous transport due to medium mode number ( $n \geq 10$ ) resistive ballooning modes correlates well with the finite  $\beta$

---

\* Research supported by the United States Department of Energy under Contract No. DE-FG02-86ER5318 (Univ. Wisconsin) and Contract No. DE-AC05-84OR21400 (ORNL/Martin Marietta Energy Systems, Inc.).

<sup>1</sup> Permanent address: Southwestern Institute of Physics, Leshan, Sichuan, China.

<sup>2</sup> Present address: Mission Research Corporation, Santa Barbara, CA, USA.

ISX-B experiments [2]. Further, the energy confinement scaling in tokamaks has been found [3] to be best described in terms of dimensionless parameters derived from resistive MHD [4].

The resistive MHD model is, however, only valid in a collisional or short mean-free path ( $\lambda \ll R_0 q$ , Pfirsch-Schlüter) regime, whereas tokamaks operate in a long mean-free path ( $\lambda \gg R_0 q$ , banana-plateau) regime. In this work we extend the reduced equations [5] of resistive MHD into the tokamak-relevant banana-plateau collisionality regime by adding the parallel viscous stress effects (Section 2). The resultant "neoclassical MHD" equations (Section 3) are the appropriate Braginskii [6] type equations for a tokamak plasma. The neoclassical MHD equations include all neoclassical transport effects in equilibrium (Section 4) and an enhanced dielectric constant (Section 5). Neoclassical MHD instabilities (Section 6) and the transport they induce (Section 7), together with the implied energy confinement scaling (Section 8) and the overall transport fluxes (Section 9), are also discussed. Section 10 summarizes the impact of neoclassical MHD on our understanding of resistive MHD type phenomena in tokamaks.

## 2. VISCIOUS FORCES IN A TOKAMAK

The viscous stress tensor  $\underline{\pi}$  has parallel [ $\pi_{\parallel} \sim n_0 \nabla V$ ], cross or gyroviscous [ $\pi_x \sim n_{3,4} \underline{B} \times \nabla V$ ] and perpendicular [ $\pi_{\perp} \sim n_{1,2} (\nabla V)_{\perp}$ ] components in a magnetized plasma [6]. In analogy with the heat flow  $\underline{q}$ , the parallel stress ( $n_0 \sim \nu \lambda^2$ ) dominates the cross-stress ( $n_{3,4} \sim \nu \rho \lambda \sim \rho \nu_T$ ) by one order in the gyroradius expansion and the perpendicular stress ( $n_{1,2} \sim \nu \rho^2$ ) by two orders. The dominant, parallel stress can be written in the usual anisotropic-pressure (CGL) form for all collisionality regimes:  $\underline{\pi}_{\parallel} = (p_{\parallel} - p_{\perp})(\underline{b}\underline{b} - \underline{I}/3)$  in which  $\underline{b} = \underline{B}/B$  is a unit vector along the magnetic field direction.

The pressure anisotropy caused by flows in the plasma has been derived previously in the collisional regime [7]. For incompressible flows it can be written as  $p_{\parallel} - p_{\perp} = -3n_0(\underline{V} \cdot \nabla \ln B)$ , which indicates the magnetic pumping rather than diffusive character of the parallel viscous stress [8]. For arbitrary collisionality it can be written, to lowest order in an aspect ratio expansion, as

$$p_{\parallel} - p_{\perp} \approx - \frac{mn\mu \langle B^2 \rangle}{\langle (\underline{b} \cdot \nabla B)^2 \rangle} (\underline{V} \cdot \nabla \ln B), \quad \underline{\pi}_{\parallel} \equiv (p_{\parallel} - p_{\perp})(\underline{b}\underline{b} - \underline{I}/3) \quad (1)$$

in which  $\langle \rangle$  denotes the flux surface average. Here,  $\mu$  is the frequency for viscous damping of flows in the  $\nabla B$  direction. Its static value for electron and ion plasma components in a  $Z = 1$  plasma is [9]<sup>3</sup>

<sup>3</sup> However, the normalization of  $\mu$  is different; there,  $\mu$  has the units of Braginskii's  $\eta_0$  [6], whereas here,  $\mu$  has units of frequency.

$$\mu_e = \frac{2.3 \epsilon^{1/2} v_e}{(1+1.07 v_{*e}^{1/2} + 1.02 v_{*e})(1+1.07 v_{*e} \epsilon^{3/2})} \quad (2)$$

$$\mu_i = \frac{0.66 \epsilon^{1/2} v_i}{(1+1.03 v_{*i}^{1/2} + 0.31 v_{*i})(1+0.66 v_{*i} \epsilon^{3/2})}$$

Here,  $v_* = v \epsilon^{-3/2} R_0 q / v_T$  is the collisionality parameter that is unity at the transition from the banana to plateau collisionality regime. In the banana collisionality regime ( $v_* \ll 1$ ),  $\mu \sim \epsilon^{1/2} v$ , which reflects the viscous damping of parallel flows carried by circulating particles through collisions with the  $\epsilon^{1/2}$  fraction of immobile trapped particles. The time-varying form of the viscous damping frequency in the banana collisionality regime is derived in reference [10].

The dominant viscous force  $\underline{\nabla} \cdot \underline{\pi}_{||}$  and its parallel (to  $\underline{B}$ ) component are given by

$$\underline{\nabla} \cdot \underline{\pi}_{||} = (p_{||} - p_{\perp}) [(\underline{b} \cdot \underline{\nabla}) \underline{b} - \underline{b} (\underline{b} \cdot \underline{\nabla}) \wedge nB] + \underline{b} (\underline{b} \cdot \underline{\nabla}) (p_{||} - p_{\perp}) - \underline{\nabla} (p_{||} - p_{\perp}) / 3 \quad (3)$$

$$\underline{B} \cdot \underline{\nabla} \cdot \underline{\pi}_{||} = - (p_{||} - p_{\perp}) (\underline{b} \cdot \underline{\nabla}) B + (2/3) (\underline{B} \cdot \underline{\nabla}) (p_{||} - p_{\perp}) \quad (4)$$

$$\langle \underline{B} \cdot \underline{\nabla} \cdot \underline{\pi}_{||} \rangle = mn \mu U_{\theta} \langle B^2 \rangle, \quad U_{\theta} = \underline{V} \cdot \underline{\nabla} \theta / (\underline{B} \cdot \underline{\nabla} \theta) = V_{\theta} / B_{\theta} \quad (5)$$

### 3. NEOCLASSICAL MHD EQUATIONS

The neoclassical MHD equations [8] result from adding the parallel and cross viscous stress effects to the usual reduced equations of resistive MHD [5]. The usual assumptions are made:  $T = \text{constant}$  (but  $T_e \neq T_i$ ); a small gyroradius expansion ( $\delta \sim \rho / l \ll 1$ ); a twistable but incompressible magnetic field ( $\partial \underline{B} / \partial t \neq 0$ , but  $\partial B / \partial t = 0$  -- valid for low  $\beta$ ); and axisymmetric magnetic field geometry  $\underline{B} = I \underline{\nabla} \zeta + \underline{\nabla} \zeta \times \underline{\nabla} \psi$  with  $I(\psi) = R B_{\zeta}$ ,  $|\underline{\nabla} \zeta| = 1/R$  and  $\underline{B} \times \underline{\nabla} \psi / B^2 = R^2 \underline{\nabla} \zeta - \underline{I} B / B^2$ . In these plasma approximations an electron-ion plasma is governed by density and momentum conservation equations for each plasma species:

$$\partial n / \partial t + \underline{\nabla} \cdot n \underline{V} = 0 \quad (6)$$

$$mn \, d\underline{V} / dt = nq(\underline{E} + c^{-1} \underline{V} \times \underline{B}) - \underline{\nabla} p - \underline{R} - \underline{\nabla} \cdot \underline{\pi} \quad (7)$$

where  $\underline{R} = nq(J_{\perp} / \sigma_{\perp} + J_{||} / \sigma_{||})$  is the interspecies frictional force.

The perpendicular components of Eq. (7) can be solved iteratively in the small gyroradius expansion to yield ( $\underline{E} = - \underline{\nabla} \phi - c^{-1} \partial \underline{A} / \partial t$  with  $\underline{A} = - \psi \underline{\nabla} \zeta$ )

$$\underline{V}_{\perp} = \frac{c}{B^2} \underline{B} \times [ \underline{\nabla} (\phi + \frac{T}{q} \ln n) + \frac{1}{nq} (mn \frac{d\underline{V}_{\perp}}{dt} + \underline{R} + \underline{\nabla} \cdot \underline{\pi}) ] + \frac{|\underline{\nabla} \zeta|^2}{B^2} \underline{\nabla} \psi \frac{\partial \psi}{\partial t} \quad (8)$$

$$\underline{J}_\perp = (c/B^2) \underline{B} \times [\underline{\nabla}P + \rho_m d\underline{V}_\perp/dt + \sum_S \underline{\nabla} \cdot \underline{\pi}_S] \quad (9)$$

Here, the perpendicular flow  $\underline{V}_\perp$  has first order (in  $\delta$ )  $\underline{B} \times \underline{\nabla} \phi$  and diamagnetic flows, and second order polarization drift, friction and viscous force driven flows. The last  $(\partial\psi/\partial t)$  term is a small ( $\sim \delta^2$ ) "grid velocity" contribution arising from the vector potential part of  $\underline{E} \times \underline{B}$ . Since the lowest order flows are derivable from a potential,  $\underline{V}$  is incompressible to lowest order [ $\underline{\nabla} \cdot \underline{V} \sim \delta^2$ ]. Also, the poloidal flow velocity in Eq. (5) can now be written as  $U_\theta = V_\parallel/B + (cI/B^2)(\partial/\partial\psi)[\phi + (T/q)\ln n] + \mathcal{O}(\delta^2)$ . The perpendicular current  $\underline{J}_\perp$  has similar contributions, but is missing the  $\underline{E} \times \underline{B}$  and friction driven terms because these flows are ambipolar. The viscous force effects contribute to  $\underline{J}_\perp$  because, while they lead (to order  $\delta^2$ ) to only ambipolar flows in equilibrium, they are in general nonambipolar [11].

The parallel flows are determined from the sum and electron component (with  $d/dt \ll v_e$ ) of the parallel momentum balances[8]:

$$\rho_m (\partial/\partial t + \underline{V}_E \cdot \underline{\nabla})(V_{\parallel i} B) = - (\underline{B} \cdot \underline{\nabla})P - \underline{B} \cdot \underline{\nabla} \cdot \sum_S \underline{\pi}_S \quad (10)$$

$$0 = - n_e e (\underline{E} \cdot \underline{B}) - (\underline{B} \cdot \underline{\nabla})p_e + n_e e J_{\parallel B} / \sigma_{\parallel} - \underline{B} \cdot \underline{\nabla} \cdot \underline{\pi}_{ne} \quad (11)$$

Here,  $\underline{V}_E = (c/B^2) \underline{B} \times \underline{\nabla} \phi$  is the potential part of the  $\underline{E} \times \underline{B}$  flow velocity. It is the only order  $\delta$  flow which enters the convective derivative on the left of Eq. (10) because the diamagnetic part of this convective derivative is cancelled by  $\underline{B} \cdot \underline{\nabla} \cdot \underline{\pi}_x$  [8,12].

The neoclassical MHD equations are time evolution equations for the density, perpendicular and parallel plasma flows and the magnetic flux. They are obtained from the preceding equations as follows. The density conservation equation for electrons is utilized with  $\underline{\nabla} \cdot n \underline{V}_{ne} = (\underline{B} \cdot \underline{\nabla})(n V_{ne}/B) = (\underline{B} \cdot \underline{\nabla})(n V_{\parallel i}/B - J_{\parallel}/eB)$  and  $\underline{V}_{\perp e}$  as defined in Eq. (8). The perpendicular flow evolution equation results from  $0 = \underline{\nabla} \cdot \underline{J} = (\underline{B} \cdot \underline{\nabla})(J_{\parallel}/B) + \underline{\nabla} \cdot \underline{J}_\perp$  with  $\underline{J}_\perp$  as given in Eq. (9). The parallel flow evolution equation is given in Eq. (10). Finally, the magnetic flux evolution equation is obtained from the Ohm's law with  $\underline{E} = - \underline{\nabla} \phi + c^{-1} (\partial\psi/\partial t) \underline{\nabla} \zeta$ . The neoclassical MHD equations can thus be written as

$$\partial n/\partial t + \underline{\nabla} \cdot n \underline{V}_{\perp e} + (\underline{B} \cdot \underline{\nabla})(n V_{\parallel i}/B - J_{\parallel}/eB) = 0 \quad (12)$$

$$- \underline{\nabla} \cdot (c\rho_m/B^2) \underline{B} \times d\underline{V}_{\perp i}/dt = (\underline{B} \cdot \underline{\nabla})(J_{\parallel}/B) + \underline{\nabla} \cdot [(c/B^2) \underline{B} \times (\underline{\nabla}P + \underline{\nabla} \cdot \sum_S \underline{\pi}_S)] \quad (13)$$

$$\rho_m d(V_{\parallel i} B)/dt = - (\underline{B} \cdot \underline{\nabla})P - \underline{B} \cdot \underline{\nabla} \cdot \sum_S \underline{\pi}_S \quad (14)$$

$$- \frac{I}{cR^2} \frac{\partial\psi}{\partial t} = - \frac{J_{\parallel} B}{\sigma_{\parallel}} - (\underline{B} \cdot \underline{\nabla})(\phi - \frac{T_e}{e} \ln n) + \frac{1}{ne} \underline{B} \cdot \underline{\nabla} \cdot \underline{\pi}_{ne} \quad (15)$$

where  $d/dt = \partial/\partial t + \underline{V}_E \cdot \underline{\nabla}$  and  $J_{\parallel}/B = - (cR^2/4\pi I) \underline{\nabla} \cdot (\underline{\nabla} \psi/R^2) + \mathcal{O}(\epsilon^2)$ . The terms involving the divergence of the parallel viscous stress

in Eqs (12,8) and (13) can be simplified using  $\nabla \cdot (B^{-2} \underline{B} \times \nabla \cdot \underline{\pi}_{||}) = \nabla \cdot (B^{-2} (p_{||} - p_{\perp}) \underline{b} \times \nabla B + (2/3B) \underline{b} \times \nabla (p_{||} - p_{\perp}) - (p_{||} - p_{\perp}) (4\pi/cB^2) \underline{J}_{||}) \approx \nabla \cdot [B^{-2} (p_{||} - p_{\perp}) \underline{b} \times \nabla B]$ , where in the last approximation finite  $\beta$  and small pressure anisotropy terms are neglected compared to similar isotropic pressure terms in Eqs (12) and (13). If desired, perpendicular viscosity effects can be added to these equations by replacing  $\underline{\pi}_{||}$  by  $\underline{\pi}_{||} + \underline{\pi}_{\perp}$ .

The neoclassical MHD equations simplify to the usual reduced resistive MHD equations [5] in the limit of small parallel viscous stress  $\underline{\pi}_{||}$  ( $\mu \rightarrow 0$  for  $\lambda \ll R_0 q$ ), since then the last term in each of Eqs (8), (13)-(15) becomes negligible. They can be shown to satisfy an energy conservation relation. This is obtained by multiplying Eqs (12)-(15) by the factors  $(T_e + T_i) \ln n$ ,  $(\phi + (T_i/e) \ln n)$ ,  $V_{||i}/B$  and  $J_{||}/B$ , integrating over all space, neglecting surface terms for simplicity and summing the resulting equations to yield (correct to order  $\delta^2$ )

$$\frac{\partial}{\partial t} \int d^3x \left[ \frac{\rho_m}{2} (V_{||i}^2 + V_{||e}^2) + \frac{B_0^2}{8\pi} + P \ln n \right] = - \int d^3x \left[ \frac{J_{||}^2}{\sigma_{||}} + \frac{J_{\perp}^2}{\sigma_{\perp}} + \sum_s \underline{V}_s \cdot \nabla \cdot \underline{\pi}_{||s} \right] \quad (16)$$

Neoclassical MHD adds to the comparable energy conservation relation for resistive MHD [13] the parallel flow energy term  $\rho_m V_{||i}^2/2$  and the parallel viscous dissipation  $\sum_s \underline{V}_s \cdot \nabla \cdot \underline{\pi}_{||s}$  which, for the form of  $\langle \underline{B} \cdot \nabla \cdot \underline{\pi}_{||} \rangle$  given in Eq.(5), becomes  $m_n \mu U_{\theta}^2 \langle B^2 \rangle$  and indicates the viscous dissipation due to poloidal flow against the parallel viscosity -- neoclassical transport. The cross-viscosity  $\underline{\pi}_{\perp}$  is dissipationless [6,14] and so does not enter Eq.(16). The various dissipation terms on the right of Eq.(16) could be removed [13] by adding temperature evolution equations for electrons and ions.

#### 4. NEOCLASSICAL MHD EQUILIBRIUM

In equilibrium ( $d/dt \ll \mu_i$ )  $P=P(\psi)$ ,  $U_{\theta}=U_{\theta}(\psi)$  and the total parallel momentum balance Eq.(14) is  $0 = \langle \underline{B} \cdot \nabla \cdot \sum_s \underline{\pi}_{||s} \rangle = m_i n_i \mu_i U_{\theta i} \langle B^2 \rangle$ . Thus, the parallel viscous stress damps the poloidal ion flow to zero [9], which causes the ion flow to be toroidal:  $U_{\theta i 0} = 0$ ,  $V_{||i 0} = -cI(\partial/\partial\psi) [\phi_0 + (T_i/e) \ln n_0]$ ,  $\underline{V}_0 = \Omega_0 R^2 \underline{\nabla} \zeta$ ,  $\Omega_0(\psi) = -c(\partial/\partial\psi) [\phi_0 + (T_i/e) \ln n_0]$ . (If  $\underline{V}_i$  effects were included, there would be a small, residual poloidal ion flow.) The predominance of electron-ion friction over electron viscosity causes the lowest order Ohm's law to be  $\langle J_{||} B \rangle / \sigma_{||} = \langle E_{||}^A B \rangle$  and hence a poloidal electron flow  $U_{\theta e} = [-(cI/ne)(dP/d\psi) + (e/m_e v_e) \langle E_{||}^A B \rangle] / (1 + \mu_e/v_e) \langle B^2 \rangle$ , where  $E_{||}^A$  is the transformer-induced  $\underline{E}$  field. The parallel viscous force  $\langle \underline{B} \cdot \nabla \cdot \underline{\pi}_{||e} \rangle$  on this poloidal electron flow induces the bootstrap current and trapped-particle conductivity modification [ $\sigma_{||eff} = \sigma_{||} / (1 + \mu_e/v_e)$ ] contributions to the parallel Ohm's law [9]. Also, the radial flux driven by the electron viscous force,  $\langle n \underline{\nabla} \psi \cdot (c/eB^2) \underline{B} \times \nabla \cdot \underline{\pi}_{||e} \rangle$ , yields [8] the neoclassical

diffusive fluxes ( $D^{nc} \sim \nu_e \rho_e^2 q^2 + \mu_e \rho_e^2 \theta^2$ ) and the neoclassical pinch velocity,  $\sim (\mu_e / \nu_e) c \langle E_{\parallel}^A B \rangle I(\psi) / |\nabla\psi| \langle B^2 \rangle$ . Thus, the equilibrium limit of the neoclassical MHD equations includes all known neoclassical effects.

## 5. DIELECTRIC PROPERTIES

The perpendicular dielectric constant can be inferred by noting from the divergence of Ampere's law that  $\nabla \cdot \underline{J}_{\perp} = -(1/4\pi) \nabla \cdot \underline{\epsilon}_{\perp} \cdot (\partial \underline{E}_{\perp} / \partial t)$ . In resistive MHD the  $\underline{J}_{\perp}$  induced by the polarization drift, or perpendicular flow inertia [cf. Eqs (9), (13)] leads to the dielectric constant  $\epsilon_{\perp} \approx 1 + c^2 / v_A^2$ , with  $v_A = B / (4\pi \rho_m)^{1/2}$ . In neoclassical MHD the  $\underline{J}_{\perp}$  induced by the viscous force [cf. Eqs (9), (13)] introduces a parallel flow inertia term [8], which is effectively an additional polarization drift and leads to a perpendicular dielectric constant for radial (or  $\nabla\psi$ ) charge imbalances given by  $\epsilon_{\perp} = 1 + (c^2 / v_{A\theta}^2) (\mu_i / (\mu_i - i\bar{\omega}))$ , with  $v_{A\theta} = B_{\theta} / (4\pi \rho_m)^{1/2}$ . (There is also a smaller, Pfirsch-Schlüter contribution,  $\sim c^2 q^2 / v_A^2$ , which we neglect here.) For slow processes ( $-i\bar{\omega} = d/dt \ll \mu_i$ ) this dielectric constant is  $B^2 / B_{\theta} - 10^2$ , larger than the resistive MHD one and reflects the additional inertial effects due to the poloidal flow damping.

## 6. NEOCLASSICAL MHD INSTABILITIES

The types of instabilities obtained from the neoclassical MHD equations are analogous to the standard resistive MHD instabilities [15]: resistive-g, tearing and rippling. The pressure-gradient-driven neoclassical MHD instabilities [10,16] are found to have growth rates  $\gamma_{\mu}$  and resistive layer widths  $\delta_{\mu}$ :

$$\gamma_{\mu} = \frac{n^{2/3}}{\tau_{A\theta} S_{\theta}^{1/3}} \left[ \left( \frac{\mu_e}{\nu_e} \right)^{1/2} \left( \frac{\beta_{\theta}}{2r_p} \right) \right]^{2/3}, \quad \delta_{\mu} = \frac{r / (rdq/dr)^{1/2}}{2^{1/2} n^{1/3} S_{\theta}^{1/3}} \left[ \left( \frac{\mu_e}{\nu_e} \right)^2 \left( \frac{\beta_{\theta}}{2r_p} \right) \right]^{1/6} \quad (17)$$

where  $\beta_{\theta} = 8\pi P_0 / B_{\theta}^2$ ,  $1/r_p = rd \ln P_0 / dr$ ,  $S_{\theta} = \tau_R / \tau_{A\theta}$ ,  $\tau_R = 4\pi \sigma_n r^2 / c^2$ , and  $\tau_{A\theta} = (4\pi \rho_m)^{1/2} R_0 q / B_{\theta}$ . These new modes are analogous to resistive-g modes [15], except that they are more virulent in that they [16]: (1) depend on the parallel electron viscous damping rate  $\mu_e$ , which in neoclassical MHD predominates over the magnetic field curvature in providing access to the expansion free energy, and (2) have growth rates and resistive layer widths that are larger by  $(\mu_e / \nu_e)^{1/3} (B / B_{\theta})^{2/3} \sim 5$  and depend only on the poloidal magnetic field  $B_{\theta}$ , because of the larger,  $B_{\theta}$  dependent dielectric constant in neoclassical MHD. Including the modifications due to diamagnetic drift effects [10,16] yields a growth rate  $\gamma \sim \gamma_{\mu} / (1 + \omega_{\mu}^2 / \gamma_{\mu}^2)$  and a resistive layer width  $\delta \sim \delta_{\mu} / (1 + \omega_{\mu}^2 / \gamma_{\mu}^2)^{1/2}$ .

Neoclassical MHD tearing instabilities [17] have access to both the current profile free energy through  $\Delta'$  and to the

expansion free energy through the bootstrap current. For  $\beta_{\theta} \mu_e / \nu_e \gg S_{\theta}^{-2/5}$ , they have growth rates and resistive layer widths approximately equal to those given in Eq.(17) above (i.e. the  $\Delta'$  dependence is very weak in this limit) and so are primarily pressure-gradient-driven modes in tokamaks. In their nonlinear evolution [18], the neoclassical MHD tearing modes first grow exponentially in time. They next enter a  $w \sim \psi^{3/2} \sim t^{1/2}$  growth regime where the bootstrap current contribution is important [18,19]. For  $\Delta' > 0$ , they ultimately enter the Rutherford growth regime [20] where the bootstrap current contribution is negligible,  $w \sim t$  and ultimate saturation is achieved if  $\Delta'(w_{max}) = 0$ , or disruption occurs if two islands of different helicity overlap [1]. Thus, low mode number tearing type neoclassical MHD instabilities with  $\Delta' > 0$  eventually evolve according to standard resistive MHD nonlinear theory. For higher mode numbers with  $\Delta' < 0$ , individual neoclassical MHD modes would saturate at the end of a  $w \sim t^{1/2}$  growth regime, but then the plasma becomes turbulent.

New, rippling-type neoclassical MHD instabilities are possible for  $\nu_e \sim 1$  through density perturbation effects in the effective parallel electrical conductivity  $\sigma_{\parallel \text{eff}} = \sigma_{\parallel} / (1 + \mu_e / \nu_e)$ .

The neoclassical MHD instabilities are all purely growing in a toroidal  $\mathbf{E}_0 \times \mathbf{B}$  rest frame ( $U_{\theta i 0} = 0$ ) and have a laboratory frame frequency [16],  $\omega_E = -nc \, d\phi_0 / d\psi \approx - (nq/r)(c/B)(d\phi_0/dr)$ . Since in tokamak experiments, one often finds [21]  $(n_e/T_e)(d\phi_0/dr) \sim -dn_e/dr$ , these modes would usually be observed experimentally to be moving in the electron diamagnetic drift direction.

## 7. INSTABILITY - INDUCED TRANSPORT

The turbulent transport induced by medium mode number ( $n=3-30$ ) neoclassical MHD instabilities can be estimated from mixing length type turbulence arguments. (This procedure is analogous to, but more physical than, scale length invariance arguments [4]. While it properly predicts the dominant scalings, more precise estimates [22] of the turbulence and transport coefficients are larger by effective Reynolds number type factors  $\sim 10$ .) The radial flow, density and magnetic field fluctuation levels estimated from mixing length arguments are

$$\bar{v}_{1x} \sim \gamma_{\mu} \delta_{\mu}, \quad \frac{\bar{n}}{n} \sim \frac{\delta_{\mu}}{n_0} \frac{dn_0}{dr}, \quad \frac{\bar{B}_x}{B} \sim \left( \frac{\gamma_{\mu} \delta_{\mu}^2}{4\pi\sigma_{\parallel}/c^2} \right) \left( \frac{k_{\theta} \delta_{\mu}^2}{L_S} \right) \quad (18)$$

In the Direct-Interaction-Approximation,  $D \sim \Sigma \bar{v}_x^2 / (\gamma_{\mu} + k_x^2 D)$ , which in the strong turbulence limit ( $\gamma_{\mu} < k_x^2 D$ ) yields (for  $k_x \sim 1/\delta_{\mu}$ )  $D \sim (\Sigma \bar{v}_x^2 / k_x^2)^{1/2} \sim C_0 \gamma_{\mu} \delta_{\mu}^2$ , in which  $C_0$  is a dimensionless spectrum sum. Similarly, the magnetic field diffusion coefficient  $D_m \sim \langle \Delta x^2 \rangle / \Delta t \sim \Sigma (\bar{B}_x/B)^2 / k_x^2 D_m$ , which yields [2]  $D_m \sim C_1 \delta_{\mu} (\bar{B}_x/B)$ , with  $C_1$  being another spectrum sum. To calculate the spectrum coefficients  $C_0, C_1$ , one must go beyond the mixing length arguments

and do a two-point correlation theory (cf. [22,23]) to determine the spectrum. While this has not yet been done, we can anticipate  $C_0, C_1 \gg 1$ .

The anomalous electron heat conduction induced by the magnetic field diffusion can be estimated [24] as  $\chi_e \sim v_{Te} D_m$ . The resultant estimates for the particle and electron heat conduction coefficients are similar to those derived by Carreras, Diamond et al. [2] for resistive ballooning modes, but are somewhat larger and are, in contrast, valid for arbitrarily small values of  $\beta_\theta$ . They can be written as

$$D \sim C_0 D_\eta \left( \frac{\mu_e \beta_\theta}{v_e} \right) \left| \frac{r_q}{r_p} \right|, \quad \chi_e \sim C_1 D_\eta \left( \frac{\mu_e \beta_\theta}{v_e} \right)^2 \left( \frac{m_i}{m_e} \right)^{1/2} \left| \frac{r_q}{r_p} \right|^{3/2} \left( \frac{2T_e}{T_e + T_i} \right)^{1/2} \quad (19)$$

in which  $\left| r_q/r_p \right| = \left| d \ln P_0 / d \ln q \right|$  and  $D_\eta = c^2 / 4\pi \sigma_{\parallel} \eta_n / \mu_0$  (in mks) is the coefficient for magnetic field line diffusion in a resistive plasma. [Since in the present theory the temperature is held constant, the pressure gradient scale length in Eqs (17,19) is rigorously just the density gradient scale length.]

The particle diffusion induced by neoclassical MHD turbulence is proportional to neoclassical diffusion ( $D \sim C_0 \mu_e \rho_\theta^2 \sim C_0 D^{nc}$ ), but exceeds it by the factor  $C_0$ . The induced impurity diffusion and ion heat conduction coefficients should also be comparable [ $D_{imp} \sim D$ ,  $\chi_i \sim (5/2)D$ ]. The turbulence-induced electron heat conduction is, however, much larger [ $\chi_e/D \sim (C_1/C_0)(\mu_e \beta_\theta / v_e)(m_i/m_e)^{1/2} \sim 5-10$ ], and comparable to that observed experimentally.

## 8. CONFINEMENT SCALING

For ohmically heated plasmas, since the  $\chi_e$  given in Eq.(19) is proportional to  $D_\eta \beta_\theta^2$ , the ohmic power balance leads to a unique prediction for  $\beta_\theta$  of  $(m_e/m_i)^{1/6} (\mu_e/v_e)^{-2/3} \leq 0.3$ , which is similar to experimental observations. For the transport determining  $r/a > 1/2$  region of ohmically heated plasmas where  $v_{*e} \geq 1$ , we have  $\mu_e/v_e \sim \epsilon^{1/2}/v_{*e}$ . Under these conditions the ohmic power balance yields (with  $\tau_E \sim a^2/4\chi_e$ ) the prediction

$$\tau_E \sim n_e^{-13/14} a^{4/7} R_0^{-15/7} q^{5/7} B_\theta^{-1/7} \quad (20)$$

in which we used the often observed experimental scaling  $Z_{eff} \sim 1/n_e$ . This energy confinement scaling (and magnitude for  $C_1 \sim 10$ ) is reasonably close to the neo-Alcator scaling  $\tau_E \sim n_e a R_0^2 q^{3/4}$ . For hotter, auxiliary heated plasmas which have  $v_{*e} \ll 1$  over most of the plasma,  $\mu_e/v_e \sim \epsilon^{1/2}$  and the power balance yields the ultimate ( $P_{aux} \gg P_{OH}$ ) scaling  $\tau_E \sim P_{aux}^{-1/3} n_e^{-1/3} B_\theta^{8/3}$ . In the transition from ohmic to auxiliary heating, where  $\mu_e/v_e \sim \epsilon^{1/2}/v_{*e}$ , one finds  $\tau_E \sim P_{aux}^{-5/7}$ . These various scalings are in reasonable agreement with experimental observations.

## 9. OVERALL TRANSPORT BEHAVIOUR

The flux-surface-averaged radial particle flux ( $\sim \delta^2$ ) is

$$\Gamma_{\psi} = \langle n \underline{V} \cdot \underline{\nabla} \psi \rangle = \langle n_0 \underline{V}_2 \cdot \underline{\nabla} \psi \rangle + \langle \tilde{n}_1 \tilde{\underline{V}}_1 \cdot \underline{\nabla} \psi \rangle + \langle (\tilde{\underline{E}}_1 \cdot \underline{\nabla} \psi) n_0 \tilde{\underline{V}}_{11} / B \rangle \quad (21)$$

Here, the three terms indicate, respectively, the transport due to Coulomb collisions (classical and neoclassical),  $\tilde{\underline{E}}_1 \times \underline{B}_0$  convection-driven turbulence and "magnetic flutter" [25]. (The  $\underline{V}_2$  term can conceivably include fluctuation driven terms as well.) The analogous radial heat flux  $q_{\psi} = \langle \underline{q} \cdot \underline{\nabla} \psi \rangle$  also has these three types of contributions.

The neoclassical contributions are usually derived in equilibrium. For rapid transients ( $d/dt \gtrsim v_i$ ), the poloidal ion flow must be determined from Eqs (5), (14) and leads to additional transport fluxes with velocity  $\underline{V}_{\psi} \sim (\mu_e / \Omega_{\theta e}) (U_{\theta i} \underline{B})$ . These effects are nonambipolar and lead to transient ( $\Delta t \sim v_i^{-1}$ ) changes in the equilibrium potential  $\phi_0(\psi)$  and electron and ion heat conduction. They should be taken into account in modelling transient effects and could be important for "fast time-scale" transport effects in tokamaks.

The  $\langle \tilde{n}_1 \tilde{\underline{V}}_1 \cdot \underline{\nabla} \psi \rangle$  contribution is predominantly the usual  $\tilde{\underline{E}}_1 \times \underline{B}_0$  convection driven transport. Since the neoclassical MHD instabilities are purely growing,  $\tilde{n}$  and  $\tilde{\underline{V}}_1$  are in phase and the turbulent transport can be calculated as indicated in Section 7.

The last contribution to the fluxes is caused by magnetic fluctuations. To lowest order, it yields ambipolar particle fluxes since [26], from Ampere's law,  $\tilde{\underline{J}}_{\parallel} = (c/4\pi) \underline{b}_0 \cdot \underline{\nabla} \times \tilde{\underline{B}}$ , so that  $\langle (\tilde{\underline{E}}_1 \cdot \underline{\nabla} \psi) \tilde{\underline{J}}_{\parallel} / B \rangle \approx 0$ . However, it does lead to a heat flux contribution which is predominantly that due to electrons and which has been estimated in Eq.(19).

## 10. SUMMARY

The fluidlike resistive MHD theory has been extended for tokamaks into the experimentally relevant banana-plateau collisionality regime. The resultant neoclassical MHD equations include the reduced equations of resistive MHD and all equilibrium and transient neoclassical effects, including a perpendicular dielectric constant that depends on the poloidal magnetic field  $B_{\theta}$ . Neoclassical MHD instabilities are similar to resistive MHD ones, but more virulent. Low mode number tearing-type modes evolve into the usual nonlinear regime governed by regular resistive MHD. Thus, the previous good correlation of these fluidlike theories with tokamak discharge phenomenology [1] is preserved. Higher mode number ( $n \sim 3-30$ ) neoclassical MHD instabilities lead to anomalous transport estimates which correlate reasonably well with tokamak experimental results -- primarily because they depend on only the poloidal magnetic field  $B_{\theta}$ . A neoclassical MHD computer code

similar to those in references [2,5,22,23] has been written. The code works, has been debugged, and is beginning to be used to explore the linear and nonlinear behavior of the neoclassical MHD equations more comprehensively and precisely.

## REFERENCES

- [1] CALLEN, J.D., et al., in *Plasma Physics and Controlled Nuclear Fusion Research 1978* (Proc. 7th Int. Conf. Innsbruck, 1978), Vol. 1, IAEA, Vienna (1979) 425;  
FURTH, H.P., *Phys. Fluids* **28** (1985) 1595.
- [2] CARRERAS, B.A., et al., *Phys. Rev. Lett.* **50** (1983) 503.
- [3] CORDEY, J.G., et al., these Proceedings, Vol. 1, p. 99.
- [4] THOMAS, P.R., in *Controlled Fusion and Plasma Heating* (Proc. 13th Europ. Conf. Schliersee, 1986), European Physical Society (1986).
- [4] CONNOR, J.W., TAYLOR, J.B., *Phys. Fluids* **27** (1984) 2676.
- [5] STRAUSS, H.R., *Phys. Fluids* **19** (1976) 134;  
WADDELL, B.V., et al., *Phys. Fluids* **22** (1979) 896.
- [6] BRAGINSKII, S.I., "Transport processes in a plasma", *Reviews of Plasma Physics* (LEONTOVICH, M.A., Ed.), Vol. 1, Consultants Bureau, New York (1965) 205.
- [7] GRIMM, R.C., JOHNSON, J.L., *Plasma Phys.* **14** (1972) 617.
- [8] CALLEN, J.D., SHAIN, K.C., Rep. UWPR-85-8, University of Wisconsin (1986).
- [9] HIRSHMAN, S.P., SIGMAR, D.J., *Nucl. Fusion* **21** (1981) 1079;  
HIRSHMAN, S.P., *Phys. Fluids* **21** (1978) 1295.
- [10] SHAIN, K.C., CALLEN, J.D., *Phys. Fluids* **28** (1985) 1859.
- [11] HIRSHMAN, S.P., *Nucl. Fusion* **18** (1978) 917.
- [12] HSU, C.T., et al., *Phys. Fluids* **29** (1986) 1480.
- [13] DRAKE, J.F., ANTONSEN, T.M., Jr., *Phys. Fluids* **27** (1984) 898.
- [14] SIEBERT, K.D., Ph.D. Thesis, Univ. of Wisconsin, 1986.
- [15] FURTH, H.P., et al., *Phys. Fluids* **6** (1963) 459.
- [16] CALLEN, J.D., SHAIN, K.C., *Phys. Fluids* **28** (1985) 1845;  
CONNOR, J.W., CHEN, L., *Phys. Fluids* **28** (1985) 2001.
- [17] QU, W.X., CALLEN, J.D., Rep. UWPR-85-2, University of Wisconsin (1985).
- [18] QU, W.X., CALLEN, J.D., Rep. UWPR-85-5, University of Wisconsin (1985).
- [19] CARRERA, R., et al., *Phys. Fluids* **29** (1986) 899.
- [20] RUTHERFORD, P.H., *Phys. Fluids* **16** (1971) 1903.
- [21] HALLOCK, G.A., et al., *Phys. Rev. Lett.* **56** (1986) 1248.
- [22] CARRERAS, B.A., et al., Theory of resistive pressure-gradient-driven turbulence, to be published.
- [23] TERRY, P.W., et al., *Phys. Fluids* **29** (1986) 2501.
- [24] RECHESTER, A.B., ROSENBLUTH, M.N., *Phys. Rev. Lett.* **40** (1978) 38.
- [25] CALLEN, J.D., *Phys. Rev. Lett.* **39** (1977) 1540.
- [26] MANHEIMER, W.M., COOK, I., *Comments Plasma Phys.* **5** (1979) 9;  
WALTZ, R.E., *Phys. Fluids* **25** (1982) 1269;  
KOTSCHENREUTHER, M., Ph.D. Thesis, Princeton Univ., 1982.

**I. PLASMA EDGE MICROINSTABILITY  
WITH UP-DOWN ASYMMETRY**  
**II. THEORY OF COLLISIONAL TEARING MODES  
FOR ARBITRARY LARMOR RADII**

A. ROGISTER, G. HASSELBERG  
Euratom-KFA Association,  
Institut für Plasmaphysik,  
Kernforschungsanlage Jülich GmbH,  
Jülich, Federal Republic of Germany

**Abstract**

- I. PLASMA EDGE MICROINSTABILITY WITH UP-DOWN ASYMMETRY.  
II. THEORY OF COLLISIONAL TEARING MODES FOR ARBITRARY LARMOR RADII.

The linear theory of the rippling instability in a torus permits the occurrence, at the edge of tokamaks, of density fluctuation spectra with up-down asymmetries to be anticipated; for low  $k_{\theta}$ , the waves propagate in the electron diamagnetic direction with a common phase velocity  $v_{ph} = (1 + 1.71 \eta_e) v_{De}$ . These predictions are supported by experimental results from TEXT. The limitations of the present theory are discussed and additional experiments are proposed. A simple differential formulation is given of the collisional tearing problem for arbitrary values of the ratio width of the resistive layer to the ion Larmor radius without having recourse to any approximation (e.g. the 'constant  $\psi$  approximation'). The technique used is that of a Fourier transform of generalized functions; the most significant mathematical step has been to transpose the boundary conditions from geometrical space to k-space.

**I. PLASMA EDGE MICROINSTABILITY  
WITH UP-DOWN ASYMMETRY**

**1. INTRODUCTION**

The rippling instability [1, 2] is efficiently suppressed, in the cylindrical model, by the diamagnetic drifts [3, 4]. In toroidal geometry, we have found that an instability window reappears owing to the curvature and to the field gradient. The general mathematical analysis has been presented elsewhere [5, 6]. Our purpose here is (1) to outline the conclusions, but also the approximations, of the calculation; (2) to compare the theoretical and experimental results; (3) to identify the necessary extensions of the theory; (4) to suggest complementary experimental investigations.

## 2. OUTLINE OF THEORY, COMPARISON WITH EXPERIMENTAL RESULTS AND DISCUSSION

### 2.1. Theoretical results and their limitation

The theoretical results simplify appreciably, although they remain essentially correct, if we consider the parameter  $\eta = (d \ln T/dr)/(d \ln N/dr)$  to be large compared to unity. The results may be summarized as follows:

(1) The mode frequency is given by

$$\omega_0 = (1 + 1.71 \eta_e) \omega_e^* \quad (\text{I-1})$$

where  $\omega_e^* = -k_\theta c T_e / |e| B L_N$  is the electron diamagnetic frequency ( $k_\theta = m/r$  is the poloidal mode number and  $L_N = (d \ln N/d r)^{-1}$  is the density gradient length scale).

(2) The growth rate is given by

$$\gamma \tau_e = 0.24 \mu A^{-1/3} |\xi_s^2 L_s / L_T|^{2/3} - k_\parallel^2 \chi_{1,e} \tau_e / 1.5N \quad (\text{I-2})$$

where  $\tau_e$  is Braginskii's collision time,  $\mu = m_e/m_i$ ,  $\xi_s = U_\parallel/c_i$  is the streaming parameter ( $c_i = \sqrt{T_i/m_i}$  is the ion thermal velocity),  $L_s$  is the shear length,  $L_T = L_n/\eta$ ,  $k_\parallel = \vec{k} \cdot \vec{B}/B$  is the parallel component of the mode number, and  $\chi_{1,e}$  is the parallel electron thermal conductivity. The instability only occurs in a window defined approximately by

$$0.13/q^2 \leq \lambda^2 < 0.30 \quad (\text{I-3})$$

within which the quantity  $A = -1.59 + 12.25 q^2 \lambda^2 / (1 - 3.25 \lambda^2)$  is positive.  $\lambda \equiv c_i/qR\omega_0$  is the ratio of the distance travelled by a thermal ion in one wave period to the connection length  $qR$ ; the first term originates from ion inertia and gyroviscosity, and the second term from the radial component of the magnetic drifts (the mode is, thus, stable in a cylinder).

(3) The density fluctuation spectrum

$$|n_{k_\theta, k_r}|^2 \propto \left( 1 + \sin \Theta \frac{k_r L_N}{k_\theta R} \frac{3.17 + 1.95 \lambda^2}{1 - 3.25 \lambda^2} \right)^2 \exp(-k_r^2 a_i^2 / \mathcal{E}) \quad (\text{I-4})$$

is to be contrasted with the potential fluctuation spectrum:

$$|\phi_{k_\theta, k_r}|^2 \propto \exp(-k_r^2 a_i^2 / \mathcal{E}) \quad (\text{I-5})$$

Here,  $\mathcal{E} = 0.41A^{-2/3} |\xi_s L_T / L_s|^{2/3}$ ;  $a_i = c_i/\Omega_i$  is the ion Larmor radius.

The following assumptions have been made (in addition to  $\eta \gg 1$ ) in deriving these results: (i)  $k_r \gg k_\theta$  and, more precisely,  $k_r L_N \sim k_\theta R$  — as appropriate to rippling modes; (ii)  $\omega_0 \gg \gamma$ , i.e. 'weak instability', (iii)  $T_i(r) = T_e(r)$  and  $\beta \rightarrow 0$  — i.e. negligible kinetic pressure compared to magnetic pressure — as appropriate to the edge plasma.

## 2.2. Comparison with experimental results

An up-down asymmetry of the density fluctuation spectrum has been observed in TEXT, the Texas Experimental Tokamak [7]. Both the experimental and the theoretical asymmetries reverse (even if this does not appear clearly from formula (I-4)) with the plasma current. We consider the parameters of the TEXT discharge described in [8] at the normalized radius  $r/a = 0.8$ :  $c_i = 1.0 \times 10^7 \text{ cm} \cdot \text{s}^{-1}$ ;  $a_i = 0.052 \text{ cm}$ ;  $\xi_s = 0.67$  (derived by assuming  $q = 1$  on axis and Spitzer resistivity);  $N = 1.2 \times 10^{13} \text{ cm}^{-3}$ ;  $T_e = T_i = 100 \text{ eV}$ ;  $\eta = 1$ , but the theoretical results remain essentially valid;  $L_s = 116 \text{ cm}$ ;  $L_N = 6.5 \text{ cm}$ ;  $\omega_e^* = 3.7 \times 10^3 \text{ cycles} \cdot \text{s}^{-1}$ ;  $\tau_e = 4.2 \times 10^{-7} \text{ s}$  (assuming  $Z_{\text{edge}} = 4$ );  $q = 2.33$ . We conclude:

(1) The phase velocity of the modes is

$$v_{\text{ph}} = 2.71 v_{\text{De}} \quad (\text{I-6})$$

where  $v_{\text{De}} = \omega_e^*/k_\theta$  is the electron diamagnetic velocity, in close agreement with the experimental result  $v_{\text{ph}} \approx 3v_{\text{De}}$  (we note that plasma rotation can probably be ruled out in these experiments [7]).

(2) The instability window, Eq. (I-3), implies that the linearly unstable mode numbers are in the range

$$8 < m \leq 28 \quad \text{or} \quad 0.37 \text{ cm}^{-1} < k_\theta \leq 1.30 \text{ cm}^{-1} \quad (\text{I-7})$$

Although the destabilizing term in Eq. (I-2) vanishes at the above lower limit (where  $A \rightarrow \infty$ ) and becomes infinite at the upper limit (where  $A \rightarrow 0$ , see Section 2.3), the results of the linear theory disagree mildly with the experimental finding that the spectrum maximum occurs between 2 and 4.5  $\text{cm}^{-1}$ . This, as well as the fact that asymmetric modes have been observed at poloidal wavenumbers as high as 13  $\text{cm}^{-1}$ , could result from a cascading process from the long to the short wavelengths of the spectrum.

## 2.3. Discussion and necessary theoretical improvement

The divergence of the destabilizing term at the upper limit of the instability window (Eq. (I-7)) could not be anticipated. It is, of course, unphysical and implies

the breakdown of the approximation  $\omega_0 \gg \gamma$  (Section 2.1), but suggests a probably very large growth rate  $\gamma \sim \omega_0 \sim 3 \times 10^5 \text{ s}^{-1}$ ! This quite strong instability will, however, be limited to a narrow range of mode numbers for the following reason. The second and the first terms in Eq. (I-2) have a ratio of  $1.19 \text{ A} \cdot \text{m}^2$  (we use the expression for  $\Xi$  in evaluating  $k_{\parallel}^2$ ); although it can be shown that parallel electron heat conduction does not stabilize the rippling modes but only reduces their growth rates [9] — as in the resistive MHD approximation [2] — this large value implies a rapid fall-off of  $\gamma$  away from that value of  $m$  for which  $A = 0$ .

#### 2.4. Proposed additional experiments

(1) Equation (I-5) shows that, within the limits of the theoretical approximations, the spectrum of the potential fluctuations is symmetric. This point could be investigated with Langmuir probes.

(2) If the source of edge turbulence has such a narrow bandwidth as discussed in the preceding section, it might be possible to use selective stabilizing means. Does a magnetic separatrix perhaps play such a role? Is there possibly a connection between edge localized modes [10], which grow out of a quiet background level in less than  $20 \mu\text{s}$ , and the toroidal rippling instability which could have growth rates as large as  $3 \times 10^5 \text{ s}^{-1}$  in a narrow  $k_{\theta}$  bandwidth?

#### REFERENCES

- [1] FURTH, H.P., KILLEEN, J., ROSENBLUTH, M.N., *Phys. Fluids* **6** (1963) 459.
- [2] CARRERAS, B.A., GAFFNEY, P.W., HICKS, H.R., CALLEN, J.D., *Phys. Fluids* **25** (1982) 1231.
- [3] COPPI, B., *Phys. Fluids* **8** (1965) 2273.
- [4] ROGISTER, A., *Plasma Phys. Controll. Fusion* **26** (1984) 1063.
- [5] ROGISTER, A., *Plasma Phys. Controll. Fusion* **28** (1986) 547.
- [6] ROGISTER, A., *Nucl. Fusion* **27** (1987) 325.
- [7] BROWN, D.L., PEEBLES, W.A., LUHMANN, N.C., Jr., SAVAGE, R.L., Jr., *Phys. Rev. Lett.* **54** (1985) 689.
- [8] RITZ, C.P., BRAVENEC, R.V., BENGTON, R.D., et al., *Edge Diagnostics and Transport in the TEXT Tokamak*, Rep. Univ. of Texas (1986).
- [9] AMEIN, W.H., ROGISTER, A., *Plasma Phys. Controll. Fusion* **28** (1986) 1511.
- [10] KEILHACKER, M., et al., *Plasma Phys. Controll. Fusion* **26** (1984) 49.

## II. THEORY OF COLLISIONAL TEARING MODES FOR ARBITRARY LARMOR RADII

### 1. INTRODUCTION

With the parameters achieved in present day tokamak plasmas where the width of the resistive layer of tearing modes ( $\Delta$ ) is of the order of — and often less than — the ion Larmor radius ( $a_i$ ),

(i) the electrons can effectively be described by the fluid equations;

(ii) only a Vlasov description is justified for the ions since the relevant radial length scales are not larger than the particle Larmor radius of the particles and their periodic drift ( $\sim qa_i$ ) away from the magnetic surfaces; the parallel fluid equations also break down because  $\lambda_{mf} \gg c_i/\omega$ .

In the cylindrical limit, the introduction of the Fourier transform and of the notion of generalized functions [1] leads to an elegant *differential* formulation of the tearing problem — directly amenable to numerical treatment — for *arbitrary* values of the ratio  $\Delta/a_i$  without — which is worth noting — having to introduce the ‘constant  $\psi$  approximation’. The theory thus applies to the 1/1 mode as well and, in particular, to the neutral MHD mode; it has, in this respect, a broader scope than previous works by Crew et al. [2] and Cowley et al. [3] and is easier to handle than their integral formulation. The present work is, however, restricted to the regime which Drake et al. [4] call ‘collisional’ ( $C > 1$ ) but we hope that it can be extended to other regimes. In TEXTOR, tearing modes are just at the edge of collisionality with  $C \approx 1/m$ .

### 2. ANALYTICAL FORMULATION OF THE PROBLEM

#### 2.1. The ion and electron responses

Straightforward solution of the ion gyrokinetic equation in the parameter range of interest yields the following results:

$$(zn - \phi)_k = [(\tau z + 1)(\Gamma_0 - 1) + \eta_i k^2 \Gamma_0] \phi_k \equiv zf(k) \phi_k \quad (\text{II-1})$$

The Fourier transform (F.T.) is defined by

$$\phi(\xi) = \int_{-\infty}^{\infty} dk \exp(ik\xi) \phi_k$$

where  $\xi$  is the normalized distance ( $= x/a_i$ ) from the mode rational surface; in addition to the definitions introduced in (I), we have set  $\Gamma_0 = \exp(-k^2) I_0(k^2)$ ,

$\tau = T_e/T_i$  and  $z = \omega/\omega_c^*$ , where  $\omega$  is the wave frequency;  $r$  is the radius of the rational surface where the resistive layer is localized.

The electron fluid equations, taking proper account of the projection of the thermal force and of the electron heat flux along the total (static plus perturbed) magnetic field, are given by

$$zn - \phi = -i(\theta\xi/Dz) (\xi\phi + z\alpha\psi) [(t-z) + 1.07i\theta\xi^2(1-z)/z] \quad (\text{II-2})$$

Here,

$$D = 1 + 4.03i (\theta\xi^2/z) - 1.07(\theta\xi^2/z)^2$$

$$\theta = (k_{\parallel} a_i c_e)^2 \tau_e / 0.51 \omega_c^* (\equiv 1/C\tau)$$

$$\alpha = \beta_i L_S^2 / L_N^2, \quad k_{\parallel} = m\xi a_i / r L_S, \quad \beta_i = 4\pi N T_i / B^2 \quad \text{and} \quad t = 1 + 1.71\eta_e$$

The electrostatic potential  $\Phi$  and the parallel component of the electromagnetic potential  $A_{\parallel}$  associated with the wave have been normalized according to

$$\phi = (e_i \Phi / T_e), \quad \psi = (A_{\parallel} L_N / B a_i L_S \beta_i) \quad (\text{II-3})$$

In the limit of high collisionality ( $C \gg 1$ ), the F.T. of Eq. (II-2) is easily combined with Eq. (II-1) to yield:

$$f(k)\phi_k = i\theta (t-z) z^{-2} (\phi_k'' - iz\alpha\psi_k')$$

where the prime stands for  $\partial/\partial k$ . Upon F.T., Ampère's law becomes:

$$k^2\psi_k = \tau\theta(t-z)z^{-1} (\phi_k' - iz\alpha\psi_k)$$

Thus, since  $f(k) \propto k^2$  for small  $k$ 's and we look for odd  $\phi$ , even  $\psi$ , solutions,

$$\phi_k = (i/\tau z) [f^{-1}(k) I_k' + C_1 \delta'(k)] \quad (\text{II-4})$$

$$I_k'' - (f'/f) I_k' - z^2 [(\tau\alpha/k^2) - i/\theta(t-z)] f I_k = -C_1 f''(0) \delta(k) \quad (\text{II-5})$$

where  $I_k \equiv k^2\psi_k$  is the F.T. of the normalized parallel current density  $k_{\parallel} a_i J_{\parallel} / \omega_i^* N e_i$ .

## 2.2. The boundary conditions

For the purpose of this analysis, the hydromagnetic solution which holds in the outer layers can, in the neighbourhood of the resistive layer, be cast in the symmetric/antisymmetric form:

$$\psi_H = \psi_\infty + |\xi| \Delta\psi'_\infty/2, \quad \phi_H = -\alpha z \psi_H/\xi \quad (\text{II-6})$$

where  $\Delta\psi'_\infty$  is the jump of  $\psi'_H$  across the resistive layer. We have

$$\Delta\psi'_\infty = \int_{-\infty}^{\infty} d\xi \partial^2 \psi / \partial \xi^2 = -2\pi \int_{-\infty}^{\infty} dk \delta(k) I_k = -2\pi \lim_{k \rightarrow 0} I_k \quad (\text{II-7})$$

$$[\phi]_{-\infty}^{\infty} = -\alpha z \Delta\psi'_\infty = -(2\pi/\tau z) \lim_{k \rightarrow 0} [(k/f) I'_k - C_1 \delta(k)] \quad (\text{II-8})$$

Solving Eq. (II-5) in the neighbourhood of  $k = 0$  shows that  $\lim_{k \rightarrow 0} (k/f) I_k = -\alpha \tau z^2 \lim_{k \rightarrow 0} I_k$ . Thus  $C_1 = 0$ . We have

$$[\xi^2 \partial \phi / \partial \xi]_0^{\infty} = \alpha z \psi_\infty = (\tau z)^{-1} \lim_{\xi \rightarrow \infty} \int_{-\infty}^{\infty} dk e^{ik\xi} (k I'_k / f)''$$

The last expression where one eliminates  $I'_k/f$  through Eq. (II-5) is non-zero only if  $I_k''''$  behaves like a Dirac function as  $k \rightarrow 0$ ;  $I_k''''$  has thus a discontinuity. Since  $I_k$  is even, we finally obtain:

$$\psi_\infty = 2 (I_k''')_0^+ / \alpha \tau z^2 f''(0) \quad (\text{II-9})$$

The problem has thus been reduced to solving the differential equation (II-5) subject to the boundary conditions (II-7, 9). To illustrate the procedure leading to (II-9), one can consider the function  $\phi(\xi) = \tan^{-1} \xi$ .

### 3. ANALYTICAL AND NUMERICAL SOLUTIONS

#### 3.1. The limiting case $\Delta/a_1 \rightarrow \infty$

Here  $f(k) \equiv f''(0) k^2/2 = -z^{-1}(s + \tau z)k^2$ , where  $s = 1 + \eta_i$ . Equation (II-5) can be reduced to Kummer's differential equation for the confluent hypergeometric function [5]  $\omega(a, -1/2, Ak^2) = \exp(Ak^2/2) I_k$ , where the parameters  $A$  and  $a$  are defined by

$$A^2 = iz(s + \tau z)/\theta(t-z), \quad \text{Re} A > 0 \quad (\text{II-10})$$

$$a = -[1 + \alpha \tau z(s + \tau z)/A]/4$$

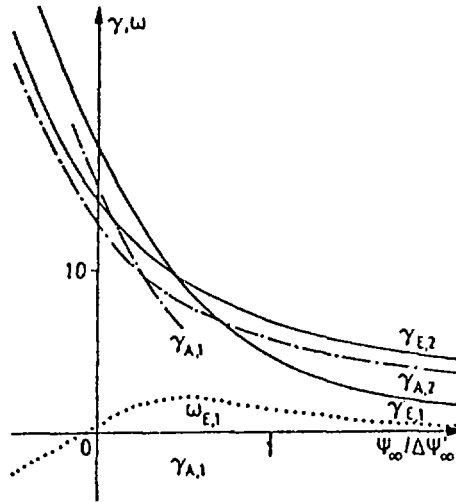


FIG. 1. Growth rates and frequencies of the 1/1 tearing mode as functions of  $\psi_\infty/\Delta\psi'_\infty$ . — and . . . : exact results; - - - - : approximate ones from the finite Larmor radius expansion; (1) with  $(L_N, L_T) = (58, 29)$  cm, i.e.  $\omega_c^* = 4.7 \times 10^3$  cycles  $\cdot$  s $^{-1}$ ; (2) with  $(L_N, L_T) = (\infty, \infty)$ .

Convergence of  $I_k$  as  $k \rightarrow \infty$  selects the solution  $\omega(a, -1/2, Ak^2) = U(a, -1/2, Ak^2)$ . The ratio  $(I_k''/I_k)_0$  is, thus, obtained from Eq. (13.1.3) of Ref. [5]. There, it follows that

$$\psi_\infty/\Delta\psi'_\infty = [8A^{3/2}/\pi\alpha\tau z(s + \tau z)] [\Gamma(a + 3/2)/\Gamma(a)] \quad (\text{II-11})$$

where  $\text{Re}A^{1/2} > 0$  since the principal branch of  $U$  is given by  $-\pi < \arg Ak^2 \leq \pi$  and we consider positive  $k$ 's.  $\Gamma$  is the gamma function. Introducing  $\lambda/\epsilon = i\theta\alpha\tau(t-z)$ ,  $\lambda^2 = -\alpha\tau z(s + \tau z)$ , (thus  $A^2 = \lambda\epsilon$ ),  $\hat{\lambda} = \lambda/\epsilon^{1/2}$ , and  $\lambda_H = -\pi\psi_\infty/\Delta\psi'_\infty$  we recover the dispersion relation by Coppi et al. [6]. For the MHD neutral mode ( $\psi_\infty = 0$ ) we obtain  $a = 0$ , i.e.  $z(s + \tau z)(t-z) = i/\alpha^2\tau^2\theta$ .

### 3.2. The case of arbitrary $\Delta/a$ ,

We consider a typical TEXTOR discharge (shot 19730,  $B = 2$  T,  $T_{e0} = T_{i0} = 850$  eV,  $N_0 = 4.92 \times 10^{13}$  cm $^{-3}$ ,  $Z = 2$ ,  $I_p = 334$  kA,  $R = 175$  cm,  $a = 46$  cm,  $q_a = 3.6$ ) for which the current density profile and thus  $L_S(r)$  is known [7]:  $J \approx J_0 [1 - (r/a)^2]^2$ ,  $J_0 = 220$  A  $\cdot$  cm $^{-2}$ ,  $q_0 = 0.83$ . We calculate the eigenvalues of the 1/1 tearing mode ( $r = 16$  cm) for different values of  $\psi_\infty/\Delta\psi'_\infty$  for two sets  $(L_N, L_T)$ . The results are given in Fig. 1. We note that, with the finite Larmor radius expansion the unstable solution becomes unbounded for  $\psi_\infty/\Delta\psi'_\infty \approx 0.5$

if  $\omega_e^* = 4.7 \times 10^3 \text{ cycles} \cdot \text{s}^{-1}$ . The curves obviously show that the finiteness of the ratio  $\Delta/a_i$  cannot explain an eventual stabilization of the mode following temperature crashes in TEXTOR. If such a stabilization occurs, it must result from the change in  $\psi_\infty/\Delta\psi'_\infty$ . A simple calculation which expands on the 'g' term in the MHD cylindrical equation and assumes a pressure and a (frozen) current profile  $\propto [1 - (r^2/a^2)]^{p(0)}$  indicates that this ratio changes sign when  $p = -j/6\beta_\theta(q = 1)$ , i.e. a moderately hollow pressure profile stabilizes the mode.

## REFERENCES

- [1] LIGHTHILL, M.J., *Fourier Analysis and Generalised Functions*, Cambridge University Press (1962).
- [2] CREW, G.B., ANTONSEN, T.M., Jr., COPPI, B., *Nucl. Fusion* **22** (1982) 41.
- [3] COWLEY, S.C., KULSRUD, R.M., HAHM, T.S., *Linear Stability of Tearing Modes*, Rep. PPPL-2262, Plasma Physics Lab., Princeton Univ., NJ (1986).
- [4] DRAKE, J.F., ANTONSEN, T.M., Jr., HASSAM, A.B., GLADD, N.T., *Phys. Fluids* **26** (1983) 2509.
- [5] ABRAMOWITZ, M., STEGUN, I.A. (Eds), *Handbook of Mathematical Functions*, Dover, New York (1965) 504.
- [6] COPPI, B., GALVÃO, R., PELLAT, R., ROSENBLUTH, M., RUTHERFORD, P., *Fiz. Plazmy* **2** (1976) 961.
- [7] SOLTWISCH, H., STODIEK, W. MANICKAM, J., SCHLÜTER, J., *these Proceedings*, Vol. 1, p. 263.



## EDGE PLASMA OSCILLATIONS IN THE H-MODE: EFFECT OR CAUSE?

S.I. KRASHENINNIKOV, A.S. KUKUSHKIN,  
V.A. POZHAROV  
I.V. Kurchatov Institute of Atomic Energy,  
Moscow, Union of Soviet Socialist Republics

### Abstract

#### EDGE PLASMA OSCILLATIONS IN THE H-MODE: EFFECT OR CAUSE?

A model for self-sustained oscillations in a dense divertor plasma which provides a unified explanation for both improved plasma confinement and non-steady edge phenomena in the H-mode is further developed.

### INTRODUCTION

This paper discusses the behaviour of a dense divertor plasma. The recently emerging interest in this subject is connected both with experiments on existing tokamaks, which led to the discovery of the H-modes and with divertor studies aiming at tokamak reactor design. Recently, it was shown [1, 2] that under certain conditions in the divertor plasma, self-sustained oscillations due to peculiarities of the interaction between the plasma and the neutral gas formed upon its neutralization on the divertor target may develop. The results of further advancing the theoretical model of the oscillations are given, and good agreement between the 2-D numerical simulation and a simple analytical model is shown, in Section 1 of the paper. The effect of the self-sustained oscillations on the bulk plasma parameters is addressed in Section 2. The oscillations are shown to lead, for ASDEX parameters, to a strong modulation of the neutral flow into the main chamber,  $\Gamma_N^s$ . In view of the fact that the edge plasma parameters, which apparently exert a strong influence on the global energy confinement time  $\tau_E$ , are to a great extent determined by the flow  $\Gamma_N^s$ , it may be expected that the modulations  $\Gamma_N^s$  will cause variations in  $\tau_E$  and trigger the H-mode. In this way, the non-steady edge phenomena accompanying the H-mode [3, 4] are also provided with a natural explanation:

#### 1. SELF-SUSTAINED OSCILLATIONS IN A DIVERTOR PLASMA

According to experimental data and numerical results [5], the energy and particle fluxes flowing within the scrape-off layer towards the target are localized

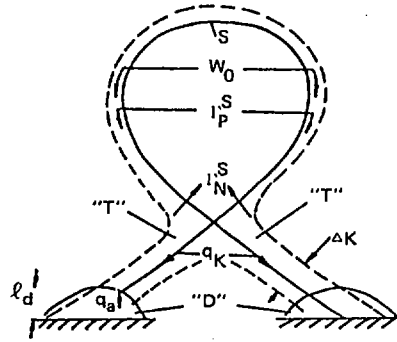


FIG. 1. Geometry of the problem.

in a rather narrow hot 'core', which is surrounded by a relatively cold and rarefied plasma (Fig. 1). We shall particularly be concerned with conditions where the ionization length for neutral particles leaving the target,  $\ell_d$ , is less than the core width,  $\Delta_k$ , i.e. the neutrals are localized in the core [1, 2]. In this case, the plasma flow entering the scrape-off layer,  $\Gamma_p$ , becomes much weaker than the plasma flow onto the target,  $\Gamma_d$ , and plays no significant part. An estimate of the particle localization factor,  $\xi_k = \ell_d/\Delta_k$ , can be obtained from the following equations of balance of particles and energy in the recycling zone (the D-zone, Fig. 1):

$$K_I(T_d)n_d N_d \ell_d - \alpha n_d c_d \sin \psi = 0 \quad (1)$$

$$D_d N_d / \ell_d - K_I(T_d)n_d N_d \ell_d = 0 \quad (2)$$

$$q_0 = j_d(\beta T_d + E_d) \equiv \alpha n_d c_d \sin \psi (\beta T_d + E_d) \quad (3)$$

where  $n_d$ ,  $N_d$  and  $T_d$  are the plasma and neutral density and temperature in the D-zone;  $q_0$  is the energy flux entering the D-zone;  $\psi \ll 1$  is the angle between the magnetic field lines and the target plane;  $D_d = T_d/MK_{cx}(T_d)n_d$ ;  $E_d$  is the energy loss per ionized atom in the D-zone;  $M$  is the mass of the atom;  $K_{cx}$ ,  $K_I$  are charge exchange and ionization rates, respectively;  $\alpha$  and  $\beta$  are factors correcting for the deviation of plasma fluid velocity in the D-zone from the sound speed  $c_d$ , and for the conditions of convective energy transport to the target, respectively.

The  $q_0$  value is related to the power,  $W_0$ , entering the scrape-off layer of a tokamak with a  $k_0$ -null divertor:  $W_0 = 4\pi k_0 q_0 R \Delta_k$ ,  $R$  being the major radius. Then, we find from Eqs (1)–(3):

$$\xi_k = 4\pi\alpha k_0 v_d c_d e_d R \sin \psi / W_0 (K_{cx}^d K_I^d)^{1/2} \quad (4)$$

where  $\epsilon_d = \beta T_d + E_d$ ;  $v_d = (T_d/M)^{1/2}$ ;  $K_{cx,I}^d = K_{cx,I}(T_d)$ . The dependence  $\xi_k^*(T_d) = \xi_k W_0 M_H^{3/4} / (R\alpha k_0)$  is shown in Fig. 2 (here,  $W_0$  is in MW,  $R$  being in m). It is easily seen that a heavier filling gas and a single-null divertor do facilitate the localization ( $\xi_k < 1$ ) condition  $W_0 \gtrsim 14 \alpha k_0 \sin \psi R / M_H^{3/4}$  ( $5 \text{ eV} \leq T_d \leq 15 \text{ eV}$ ). This yields the following estimate for ASDEX:  $W_0 \gtrsim 0.7 \text{ MW}$  ( $k_0 = 1$ ,  $M_H = 2$ ,  $\sin \psi \approx 0.1$ ,  $\alpha \approx 0.5$ ). For  $\xi_k < 1$ , particle exchange between the core and the surrounding cool plasma is reduced and can be neglected in a first approximation. Then the basic parameter, besides  $q_0$ , determining the steady state distribution of the core plasma parameters along the magnetic field is the core averaged number of particles  $\tilde{N}$  (ions plus neutrals). It has already been shown [1, 2] that the dependence of the plasma parameters on  $\tilde{N}$  for sufficiently high  $q_0$  values may be ambiguous and discontinuous, and that particle exchange between core and cool plasma causes variations in  $\tilde{N}$  and leads to the self-sustained oscillations, involving transitions between the stable branches of the one-dimensional steady states (OSS). A quasi-stationary theory of the variations in  $\tilde{N}$ , developed in Ref. [2], does not allow us to consider the transitions between the different OSS branches which are accompanied by particle redistribution between the recycling region (the D-zone) and the rest of the core (the T-zone, Fig. 1) because that theory assumes equality of the plasma pressures,  $P_0$  and  $P_T$ , in the D- and T-zones. Provided that the pressure difference between the two zones is small, the plasma fluid velocity,  $v_0$ , in the transition zone between the D- and T-zones depends on the longitudinal viscosity  $\eta(T_d)$  of the plasma:

$$v_0 = (P_T - P_D)z_0 / \eta(T_d) \quad (5)$$

where

$$z_0 = [q_0(\gamma_e/\kappa_e(T_d) + \gamma_i/\kappa_i(T_d)) / 2 T_d \sin \psi]^{-1} \\ \cong (d \ln n/dz)^{-1} \cong (d \ln T/dz)^{-1}$$

is the characteristic scale-length for the variation in the plasma fluid velocity;  $\kappa_e$  and  $\kappa_i$  are the electron and ion heat conductivities along the magnetic field;  $\gamma_e$  and  $\gamma_i$  are the relative amounts of total power as transported by electrons and ions, respectively.

The pressure  $P_T$  can be expressed as  $P_T = (5/7)\tilde{N}_T T_S$  [2], where  $\tilde{N}_T$  is a T-zone contribution to  $\tilde{N}$ ;  $T_S = (7/2)(q_0 L T_d^{5/2} \sin \psi)^{2/7} [(\gamma_e/\kappa_e(T_d))^{2/7} + (\gamma_i/\kappa_i(T_d))^{2/7}]$  is the total (ion and electron) temperature at the separatrix,  $L$  being the length of the magnetic field line in the core. The pressure  $P_D$  can be found together with  $\tilde{N}_D$  – a D-zone contribution to the  $\tilde{N}$  – from the steady state equations (1) to (3) since the relaxation times of the plasma parameters in the D-zone are roughly proportional to  $(K_I^d n_d)^{-1}$  and small:

$$P_D = q_0 T_d / \alpha c_d \mathcal{E}_d \sin \psi \quad (6)$$

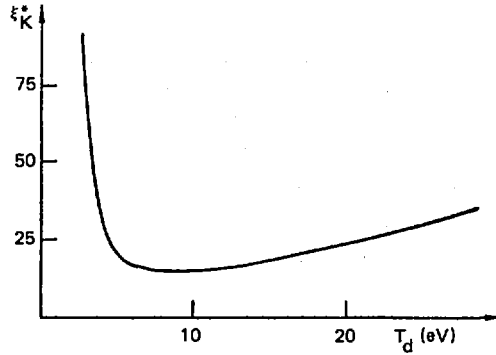


FIG. 2. Reduced parameter of neutral localization in the core,  $\xi_k^*$ , versus plasma temperature at the target.

$$\tilde{N}_D = v_d / (K_{cx}^d K_I^d)^{1/2} L \sin \psi \quad (7)$$

We use the diffusion approach to treat the particle exchange between core and cool plasma, which is mainly caused by neutral component transport [2]. Taking the  $N(x, z)$  dependence to be  $N = N_d(x) \exp(-z/\ell_d(x))$  and using the  $\tau$ -approximation along the  $x$ -coordinate, we obtain from Eqs (5–7):

$$\frac{d\tilde{N}_T}{dt} = -\nu_{\parallel}(T_d)(\tilde{N}_T - \Phi(T_d)) \quad (8)$$

$$\frac{d\tilde{N}}{dt} \equiv \frac{d}{dt}(\tilde{N}_T + \tilde{N}_D(T_d)) = \tilde{N}_D(T_d) G_1(T_d, T_*) \quad (9)$$

where  $T_*$  is the cool plasma temperature at the target, and

$$\Phi(T_d) = 7q_0 T_d / 5\alpha T_s c_d \mathcal{E}_d \sin \psi$$

$$\nu_{\parallel}(T_d) = (5/7)^2 T_s^2 z_0(T_d) \Phi(T_d) / T_d \eta(T_d)$$

$$G_1(T_d, T_*) = 4(\alpha \sin \psi)^2 c_d v_d \mathcal{E}_d (K_I^d / c_{cx}^d)^{1/2} \times [v_* / K_I^* - v_d / K_I^d] / q_0 \Delta_k^2$$

$$v_* = (T_* / M)^{1/2} \text{ and } K_I^* = K_I(T_*)$$

Note that  $G_1 > 0$  for  $T_d > T_*$  and  $G_1 < 0$  for  $T_d < T_*$  (we shall not consider the range of extremely high temperatures). The system of Eqs (8) and (9)

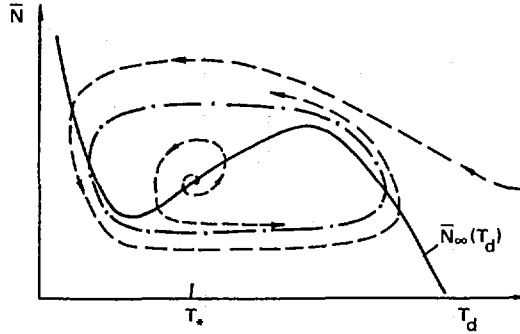


FIG. 3. 'Phase portrait' of self-sustained oscillations.

allows us to study all phases of self-sustained oscillations. Linearizing Eqs (8) and (9) around the steady-state solution,  $T_d = T_*$ ,  $\tilde{N}_T = \Phi(T_*)$ , we obtain the following instability criterion:

$$\left\{ \frac{dF(T_d)}{d \ln T_d} - \frac{\nu_{\perp}}{\nu_{\parallel}} \tilde{N}_D(T_d) \right\} \Big|_{T_d = T_*} > 0 \quad (10)$$

where  $F(T_d) = \Phi(T_d) + \tilde{N}_D(T_d)$  and  $\nu_{\perp} = \partial G_{\perp} / \partial \ln T_d > 0$ . Note that the inequality (10) is somewhat more stringent than the instability condition for the OSS branch,  $dF/dT_d > 0$  [1]. The behaviour of the solution to Eqs (8) and (9) in the  $(\tilde{N}, T_d)$  phase space obeys the equation

$$\frac{d\tilde{N}}{dT_d} = - \frac{\xi_D(T_d) \tilde{N}_D(T_d)}{T_d} \frac{\tilde{N}_D(T_d) G_{\perp}(T_d, T_*) / \nu_{\parallel}(T_d)}{\tilde{N} - \tilde{N}_{\infty}(T_d)} \quad (11)$$

where

$$\xi_D(T_d) = -d \ln \tilde{N}_D / d \ln T_d > 0$$

$$\tilde{N}_{\infty}(T_d) = F(T_d) - \tilde{N}_D(T_d) G_{\perp}(T_d, T_*) / \nu_{\parallel}(T_d)$$

In case of an unstable equilibrium, the phase trajectories tend to a stable limiting cycle (Fig. 3). Figure 4 shows the results of a numerical solution to Eqs (8) and (9) and of a 2-D numerical simulation of the INTOR divertor plasma. The simulation was carried out in conditions similar to those used in Refs [1, 2], but with a fluid description of the neutral component [6]. The sharp drops in  $T_d(t)$  correspond to transitions between the different OSS branches

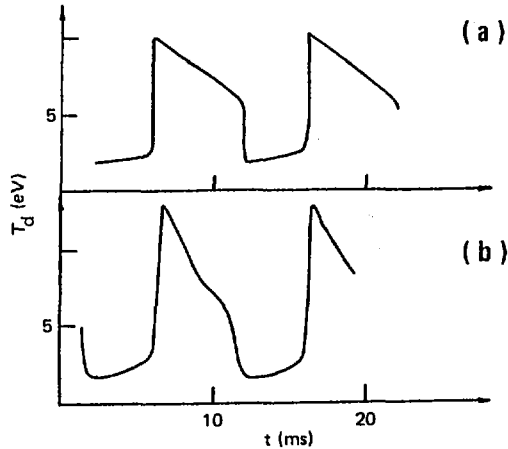


FIG. 4. Temporal evolution of plasma temperature at the sheath during oscillations obtained from analytical model (a) and 2-D computation (b).

( $\nu_{\perp}/\nu_{\parallel} \ll 1$ ). The good agreement between patterns (a) and (b) in Fig. 4 justifies the application of this simple model to an analysis of the effect of the processes in the divertor upon the bulk plasma.

## 2. SELF-SUSTAINED OSCILLATIONS AND THE OCCURRENCE OF H-MODES

As follows from the theory of tearing modes, the profiles of current density  $j(r)$ , and hence of the electron temperature  $T_e(r)$  (assuming  $j \propto T_e^{3/2}$ ), are of a rather peculiar kind [7–9]. Thus, it is desirable to have a  $j(r)$  profile with a sharp drop just beyond the  $q = 2$  resonant surface in order to stabilize the most dangerous  $m/n = 2/1$  mode [8]. The T-10 experiments on electron cyclotron heating [10] apparently confirm this conclusion. An analysis of TFTR experiments also leads the author of Ref. [9] to infer a strong dependence of  $\tau_E$  on the  $T_e(r)$  profile, at the column periphery.

The temperature profile satisfies the heat conduction equation,

$$\frac{1}{r} \frac{\partial}{\partial r} \left( \kappa_{\perp} r \frac{\partial T_e}{\partial r} \right) + Q_h - Q_r - Q_{ei} = 0 \quad (12)$$

where  $Q_h$ ,  $Q_r$ ,  $Q_{ei}$  are the power densities of heating, radiative losses and electron-ion energy exchange, respectively;  $\kappa_{\perp}$  is the cross-field thermal conductivity of the plasma. It follows from Eq. (12) that, for low values of  $Q_r$  and  $Q_{ei}$ , the

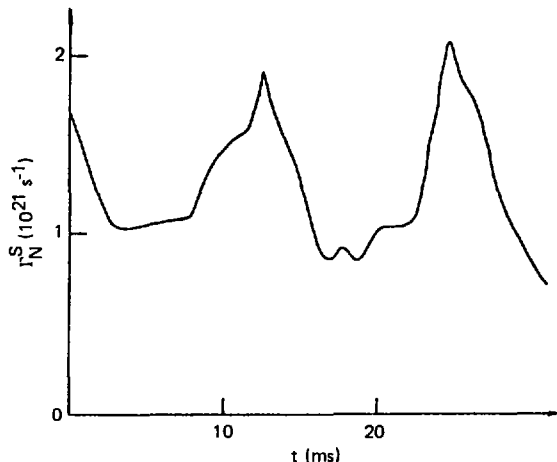


FIG. 5. Modulation of neutral influx into main plasma by self-sustained oscillations in the divertor (2-D modelling, ASDEX, single-null divertor, deuterium).

$T_e(r)$  profiles necessary for 2/1 mode stabilization and hence leading to high  $\tau_E$  could be realized. However, an increase in  $Q_r$  and  $Q_{ei}$  increases the second derivative,  $d^2 T_e/dr^2$ , and finally leads to 2/1 mode destabilization and deterioration of  $\tau_E$ .  $Q_r$  is determined by the level of impurity content, wall sputtering by charge exchange neutrals being one of the main channels of impurity input into diverted discharges [11]. Apart from this effect, the neutrals give rise to charge exchange energy losses from the ion component, lowering the ion temperature and increasing  $Q_{ei}$ . Thus,  $\tau_E$  may depend strongly on the neutral influx,  $\Gamma_N$ , into the main tokamak chamber. In steady state operation, the flow  $\Gamma_N^s$  is constant and  $\Gamma_N^s = \Gamma_p^s$ . If the plasma confinement is poor,  $\Gamma_p^s$  is high (we assume  $\tau_p \propto \tau_E$ ) so that the high energy losses from electrons make the optimum  $T_e(r)$  profile impossible.

The self-sustained oscillations in the divertor plasma modulate  $\Gamma_N^s$ . Figure 5 shows the pattern of  $\Gamma_N^s(t)$  variation as obtained from 2-D modelling, making use of a Monte Carlo technique for the treatment of neutrals, for ASDEX parameters (single-null divertor, deuterium,  $W_0 = 2.5$  MW). Note that, for  $W_0 = 2.5$  MW, double-null divertor and hydrogen as filling gas, no oscillations were observed in the simulation. During time intervals when  $\Gamma_N^s$  is reduced, the impurity influx and charge exchange losses are small, and the  $T_e(r)$  profile could shift to optimum, thus improving the confinement.

Let us now see to what extent the dependences of the self-sustained oscillation thresholds, of power  $W_0$  and plasma density at the separatrix,  $n_s$ , on the sort of filling gas (H, D) and on the divertor geometry (single-null, double-null:  $k_0 = 1, 2$ ) match the corresponding dependences of the conditions for the occurrence of the H-modes. Let us first find the threshold values of  $q_0$

from Eq. (10) and then relate them to the values of  $W_0$  and  $n_s$ . If  $\nu_{\perp}/\nu_{\parallel} > 1$ , then, considering that  $q_0 \Delta_k \propto W_0/k_0$  and  $L \propto 1/k_0$ , the inequality (10) can be written as

$$W_0/\tilde{W}_0 \gtrsim k_0^{3/2}/M_H \hat{\kappa}_{\parallel}^{1/2} \quad (13)$$

where  $\hat{\kappa}_{\parallel} = (1 \text{ to } M_H^{-1/2})$ , depending on the relative contributions of electrons and ions to the energy flow along the magnetic field in the T-region;  $M_H$  is the atomic mass in amu,  $W_0$  is a normalization constant. For  $\nu_{\perp}/\nu_{\parallel} < 1$ , the inequality (10) can be represented in the following form:

$$q_0 > q_0^{\text{th}} \propto k_0 \hat{\kappa}_{\parallel}^{2/5}/M_H^{21/20} \quad (14)$$

Note that, for  $q_0 \approx q_0^{\text{th}}$ , the temperature  $T_d$  is about 10 eV. To relate  $q_0$  to  $W_0$ , we should examine the energy balance in the T-zone:

$$\nabla_{\perp} \kappa_{\perp} \nabla_{\perp} T + \nabla_{\parallel} \kappa_{\parallel} \nabla_{\parallel} T = 0 \quad (15)$$

Hence, assuming  $\kappa_{\perp} = \hat{\kappa}_{\perp} n^b T^c$  and taking account of the pressure constancy along a field line and of the boundary conditions at the sheath (3) and at the separatrix,  $\kappa_{\perp} T_s/\Delta_k = W_0 (2\pi)^2 a R$  ( $a$  is the minor radius), we obtain, after extensive calculations, the following condition for the onset of self-sustained oscillation:

$$\frac{W_0}{\tilde{W}_0} \gtrsim \left\{ \hat{\kappa}_{\perp} \frac{k_0^{b+2} M_H^b \hat{\kappa}_{\parallel}^{b+2}}{(\hat{\kappa}_{\parallel}^{3/5} M_H^{21/20})^{5b+6c+9}} \right\}^{1/2} \quad (16)$$

The minimum plasma density at the separatrix is only determined by the threshold value of  $q_0$  and is independent of the  $\kappa_{\perp}$  scaling:

$$n_s/\tilde{n}_s \gtrsim k_0 \hat{\kappa}_{\parallel}^{4/7}/M_H^{1/4} \quad (17)$$

For various scalings, such as T-11, Alcator, Bohm-like and  $\kappa_{\perp} \propto n$  scalings, Eq. (16) yields results that are rather close to each other:

$$W_0/\tilde{W}_0 \gtrsim k_0^{(1 \text{ to } 1.5)}/M_H^{(0.8 \text{ to } 1.25)} \quad (18)$$

Thus, the functional dependences (13), (17) and (18) of the oscillation thresholds on the atomic mass of the filling gas and on the divertor configuration are in agreement with the corresponding conditions for the onset of the H-modes [12].

The set of the three main factors – (a) the effect of edge plasma parameters on global plasma confinement; (b) the important role of neutral influx into the main plasma,  $\Gamma_N^s$ , in the energy balance of the plasma edge; (c) buildup, in certain conditions, of self-sustained oscillations modulating  $\Gamma_N^s$  – enables us to propose the following model for H-mode onset in a diverted tokamak discharge: in the L-mode, the power  $W_0$  is below the threshold value, (13) and (18), and the divertor acts steadily. Plasma confinement is poor; the strong flow  $\Gamma_N^s$  cools the plasma edge down, inhibiting the formation of optimum plasma parameter profiles, in particular around the  $q = 2$  surface. With  $W_0$  increasing beyond the threshold value, self-sustained oscillations are triggered in the divertor. In the appropriate phase of the oscillations, when the  $\Gamma_N^s$  flow decreases, the energy losses from the plasma edge are reduced, the plasma profiles are rearranged, and  $\tau_E$  rises. Further development of the oscillation leads to an increase in  $\Gamma_N^s$ , causing edge cooling and lowering of  $\tau_E$ . The power  $W_0$  released into the scrape-off layer increases sharply, ensuring ionization of the neutrals and limiting further increase in  $\Gamma_N^s$  and edge cooling. In the next oscillation phase,  $\Gamma_N^s$  decreases again, etc. As a result, the good plasma confinement in the H-mode is accompanied by regular bursts of  $H_\alpha$  line radiation, together with MHD activity, reducing  $\tau_E$  and giving rise to an enhanced power release into the scrape-off layer. Note that, in this model, the edge plasma oscillations are the primary cause of the onset, not a feature, of the H-mode.

The proposed model is, of course, still of a qualitative character; further studies are necessary to refine and check the model. In particular, the effect of enhanced particle and energy release into the scrape-off layer upon the oscillation dynamics is not quite clear. Nevertheless, the theory provides a unified explanation for both the improvement of plasma confinement and the non-steady edge phenomena in the H-mode. A number of coincidences are hardly attributable to simple chance, such as: (a) the closeness of the threshold  $W_0$  values for onset of the H-mode [12] and the buildup of self-sustained oscillations (the above presented example of modelling ASDEX with SN and DN divertor configurations); (b) the similar types of dependence of these thresholds on the sort of filling gas and on the divertor geometry, [12] as well as Eqs (13) and (18); (c) the agreement between the period of the oscillations (Fig. 5) and the characteristic time interval between  $H_\alpha$  spikes in the H-mode [3, 4]; (d) the important role played by neutral recycling at the plasma edge in the H-mode onset, which is pointed out in the bulk of the experimental papers (remember the difficulties in producing the H-mode in open divertor geometry [4], where the neutrals can penetrate more effectively into the main plasma).

#### ACKNOWLEDGEMENT

The authors are grateful to Dr. A.M. Stefanovskij for discussion of the subject.

## REFERENCES

- [1] KRASHENINNIKOV, S.I., et al., in *Controlled Fusion and Plasma Physics (Proc. 12th Europ. Conf. Budapest, 1985)*, Part II, European Physical Society (1985) 500.
- [2] KRASHENINNIKOV, S.I., et al., *Self-Sustained Oscillations in the Divertor Plasma*, Preprint IAE-4235/6, Moscow, 1985.
- [3] KEILHACKER, M., et al., *Nucl. Fusion* **25** (1985) 1045.
- [4] KAYE, S.M., et al., *J. Nucl. Mater.* **121** (1984) 115.
- [5] INTOR GROUP, *International Tokamak Reactor, Phase Two A, Part II (Rep. Int. Workshop Vienna, 1984 and 1985)*, IAEA, Vienna (1986).
- [6] KRASHENINNIKOV, S.I., POZHAROV, V.A., *Fluid Description of Neutral Component in Divertor Plasmas*, Preprint IAE-4173/6, Moscow, 1985 (in Russian).
- [7] GLASSER, A.H., et al., *Phys. Rev. Lett.* **38** (1977) 234.
- [8] BOGOMOLOV, L.M., et al., *Kink- and Tearing-Mode Stability Conditions in the Tokamak*, Preprint IAE-3827/6, Moscow, 1983 (in Russian).
- [9] FURTH, H.P., in *Controlled Fusion and Plasma Physics (Proc. 12th Europ. Conf. Budapest, 1985)*, Part II, European Physical Society (1985) 980.
- [10] ALIKAEV, V.V., et al., in *Plasma Physics and Controlled Nuclear Fusion Research 1984 (Proc. 10th Int. Conf. London, 1984)*, Vol. 1, IAEA, Vienna (1985) 419.
- [11] STAUDENMAIER, G.J., *Vac. Sci. Technol.*, A **3** (1985) 1091.
- [12] WAGNER, F., et al., *Nucl. Fusion* **25** (1985) 1490.

# MAGNETIC ISLANDS AND CHAOS INDUCED BY HEAT FLOW

P.H. REBUT, M. BRUSATI, M. HUGON, P. LALLIA  
JET Joint Undertaking,  
Abingdon, Oxfordshire,  
United Kingdom

## Abstract

### MAGNETIC ISLANDS AND CHAOS INDUCED BY HEAT FLOW.

A theoretical model is presented which treats the problem of confinement degradation in tokamaks with increasing input power. It is shown that, when full account is taken of the magnetic field line topology, the adiabatic invariance conditions and the particle motion equations in the guiding centre approximation permit the heat flow to be related with the level of magnetic perturbation associated with large ( $M \sim 15$ ) poloidal mode numbers. It is shown that substantial power can be transported across the plasma by low level magnetic fluctuations. One possible mechanism for the self-sustainment of the magnetic islands is investigated.

## 1. INTRODUCTION

The degradation of confinement in tokamaks when a substantial amount of heating power is applied is generally ascribed to anomalously high electron losses.

In this paper we show how low-level broad-band magnetic perturbations ( $\bar{B}/B_0 \sim 3 \times 10^{-4}$ ) associated with large poloidal mode numbers ( $M \sim 15$ ) are sufficient to account for the losses observed experimentally. To achieve this result it is necessary to take full account of the topological properties of the magnetic field lines.

The calculations are carried out for low collisionality plasmas in steady state regime, neglecting curvature and finite Larmor radius effects. The low collisionality assumption is justified by present experimental conditions; for typical JET parameters [1] the electron mean free path ( $\leq 10^{-4}$  m) is much longer than the plasma toroidal length ( $\sim 20$  m).

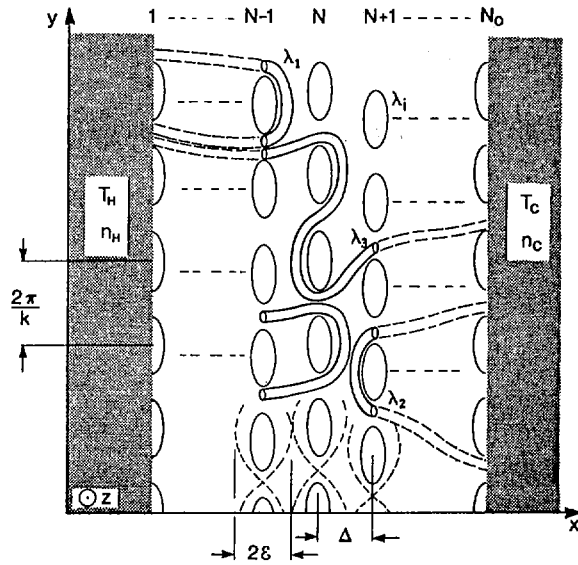


FIG. 1. Schematic diagram of the slab model.

## 2. MAGNETIC TOPOLOGY

The magnetic field in a slab geometry (Fig 1) is described by the components of the vector potential  $\underline{A}(x,y,z)$ :

$$\begin{aligned}
 A_x &= 0 \\
 A_y &= B_z x \\
 (1) \quad A_z &= \frac{B_{O'}}{2} x^2 + A \sum_{N=0}^{N_0} \cos k \left( y + \frac{Nz}{kR} \right) \\
 \underline{B} &= \underline{\nabla} \times \underline{A} \\
 \epsilon^2 &= -\frac{4A}{B_{O'}}; \quad \gamma = \frac{2\epsilon}{\Delta}
 \end{aligned}$$

In toroidal geometry:

$$B_{O'} = \frac{r}{R} B_z \frac{q'}{q^2}$$

where  $q'$  is the shear term,  $\epsilon$  the virtual island half-width and  $\gamma$  the overlapping parameter of the different chains of magnetic islands;  $\frac{2\pi}{k}$  and  $2\pi R$  are the periodicities in the  $y$  and  $z$  directions, respectively. Eq. (1) corresponds to  $N_0$  chains of magnetic islands [2].

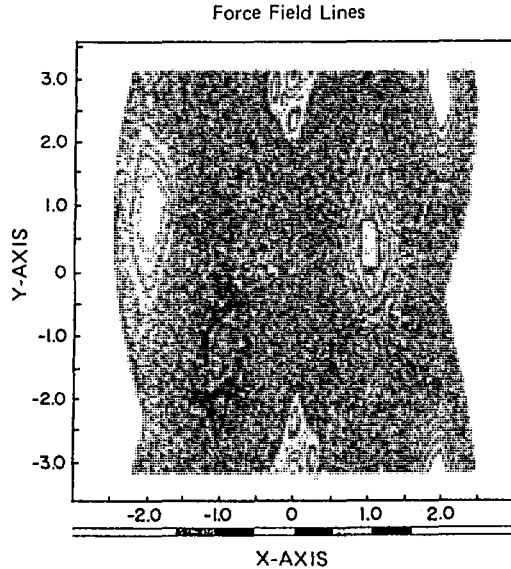


FIG. 2. Poincaré map computed for the field distribution of Eq. (1), with  $\gamma = 1.0$ . Satellites (secondary islands) are visible around the main magnetic island structures.

The different chains of islands can be mapped into each other through a translation by  $\Delta$  (distance between two chains of islands) and a rotation due to the shear. Consequently, they are all equivalent and the full slab topology can be deduced from the detailed knowledge of the properties of a single chain of islands. In Fig. 2 the  $(x,y)$  Poincaré map is shown for five chains of islands with an overlapping parameter  $\gamma = 1.0$ . The onset of stochasticity affecting neighbouring chains of islands occurs at values of  $\gamma \geq \gamma_c = .8$ . For  $.8 \leq \gamma \leq 1.5$ , islands with closed magnetic surfaces are embedded in a chaotic region.

With reference to Fig. 1, the normalised cross-sectional area  $\sigma$  of the tube of flux associated with a chaotic field line and crossing one chain of islands is given by:

$$(2) \quad \sigma(\gamma) = \frac{2}{S} \iint \frac{B_x(\gamma)}{B_z} H(B_x) H_{\text{cross}} \, dy \, dz \quad ; \quad S = \int dy \, dz$$

where  $H_{\text{cross}} = \begin{cases} 1 & \text{when the field line crosses the island chain} \\ \emptyset & \text{otherwise.} \end{cases}$

Similarly,  $H(B_x)$  is the Heaviside function for  $B_x$ .

Following the same formalism, we can define the fraction  $\alpha(\gamma)$  of the flux tube which crosses the next chain of islands

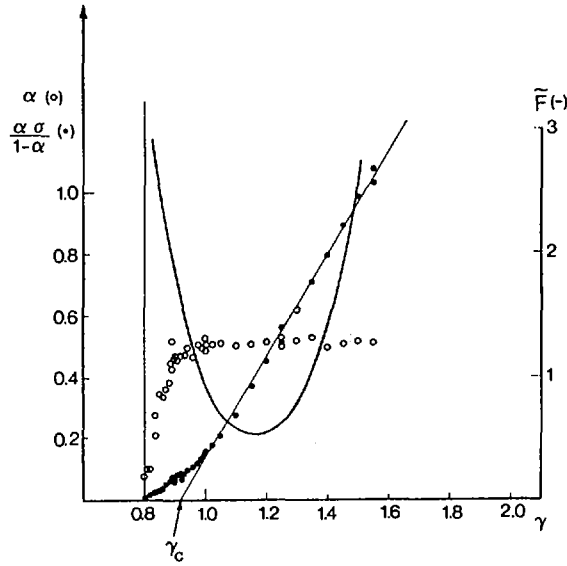


FIG. 3. Plots of  $\alpha$ ,  $\alpha, \sigma/(1-\alpha)$  and  $\tilde{F}$  as a function of the overlapping parameter  $\gamma$ .

and the normalised cross-section of the island. Results of numerical computations are shown in Fig. 3 for  $\alpha$  and the quantity  $\frac{\alpha \sigma}{1-\alpha}$ .

The behaviour of the field lines in the chaotic zone corresponds to a diffusion process through neighbouring chains of islands according to an equation of the type:

$$(3) \quad L_0 \frac{\partial F}{\partial L} = \frac{1}{2} \Delta^2 \frac{\partial^2 F}{\partial x^2} \quad ; \quad L_0 = \frac{S_c(\gamma)}{\sigma(\gamma)} \frac{2\pi R q^2}{M q' \Delta} \quad (\alpha = \frac{1}{2})$$

where  $F(L, x)$  is the probability of finding a field line at  $x$  after a path length  $L$ , and  $L_0$  is the required path length for a field line to cross an island chain; and where  $S_c(\gamma)$  is the cross-sectional area of the chaotic region (normalised).

### 3. PARTICLE MOTION

The following equations are written in a reference frame in which the magnetic islands are at rest and where  $\phi$  is the electric potential which ensures the plasma quasi-neutrality. The electric field satisfies the symmetry invariance of the magnetic field.

Taking into account the constancy of the magnetic field in the chosen frame, the particle adiabatic invariants are:

$$(4) \quad \begin{aligned} U_{\perp} &= \frac{1}{2} m w_{\perp}^2 \\ U_{\parallel} &= \frac{1}{2} m w_{\parallel}^2 + q\phi \end{aligned}$$

where subscripts  $\perp$ ,  $\parallel$  refer to the field lines. The motion equations in the guiding centre approximation are:

$$(5) \quad \frac{dr}{dt} = \frac{\underline{w} \cdot \underline{B}}{|\underline{B}|^2} \underline{B} + \underline{v}_0$$

They correspond to a motion along the field lines and a perpendicular drift with velocity  $\underline{v}_0 = \frac{\underline{E} \times \underline{B}}{|\underline{B}|^2}$ , where  $\underline{E} = -\underline{\nabla}\phi$  is the electric field.

From conservation of the number of guiding centres, the total current  $\underline{j}_g$  associated with them satisfies the equation:

$$(6) \quad \underline{\nabla} \cdot \underline{j}_g = \underline{\nabla} \cdot (\underline{j}_{eg} + \underline{j}_{ig}) = \underline{\nabla} \cdot [j_{\parallel g} \underline{e}_{\parallel} + (q_i n_i + q_e n_e) \underline{v}_0] = 0$$

when perpendicular diffusion is neglected.

In conditions of quasi-neutrality and taking into account that the parallel plasma current  $j_{\parallel}$  equals  $j_{\parallel g}$ , we have:

$$(7) \quad \underline{\nabla} \cdot (j_{\parallel} \underline{e}_{\parallel}) = 0$$

Defining a scalar  $\lambda$  by:  $j_{\parallel} \underline{e}_{\parallel} = \lambda \underline{B}$

we get:

$$(8) \quad \underline{B} \cdot \underline{\nabla} \lambda = 0$$

Eq.(8) shows that the parameter  $\lambda$  is constant on every field line. In particular,  $\lambda$  is constant on a magnetic surface.

When the parallel resistivity  $\eta_{\parallel}$  is taken into account,  $\lambda$  is defined by:

$$(9) \quad \lambda \int_0^L \eta_{\parallel} dl = L \frac{1}{B} \frac{V}{2\pi R}$$

where  $L$  is the field line path and  $V$  is the loop voltage. Eq.(9) can be solved using Eq.(3).

A particular case arises from Eq.(8), when all field lines behave similarly; in this case,  $\lambda$  is single valued over the whole region [3].

In the chaotic region, field lines with different paths have different values of  $\lambda$ , which depend also on the boundary conditions. At a given location, an average value  $\lambda_{ch}$  can be

defined statistically over three classes of field lines: field lines connected to each boundary ( $\lambda_1, \lambda_2$ ) and linking both boundaries ( $\lambda_3$ ). On the contrary, the field lines in the magnetic islands remain localised and have in general a different  $\lambda_i$  (Fig. 1). The guiding centre trajectories can be calculated simply by referring to pseudo field line equations.

In the particular case when  $\phi = \phi(x) = -E_0 x$ , the guiding centre equations become:

$$(10) \quad \begin{aligned} \frac{dX}{dt} &= w_{\parallel} \frac{B_x}{B_z} \\ \frac{dY}{dt} &= -w_{\parallel} \frac{B'_0}{B_z} X \end{aligned}$$

where  $X = x + \frac{E_0}{B'_0 w_{\parallel}}$ ,  $Y = y$ . For a given  $w_{\parallel}$  the guiding centre trajectories have the same behaviour as the field lines and the topological properties summarised in section 2 apply to the particle motion.

The effect of the electric field is smallest for fast particles; when  $E_0/B'_0 w_{\parallel} < \Delta$ , particles follow closely the field lines, while drift effects dominate when  $E_0/B'_0 w_{\parallel} > \Delta$  (slow particles).

#### 4. PARTICLE AND ENERGY FLOW

To maintain temperature and density gradients as particles are crossing the various chains of islands, suitable sources and sinks have to be introduced at the boundaries of the slab. These will be schematically represented by hot and cold "seas" of particles with Maxwellian velocity distributions  $F_H$  and  $F_C$ , respectively, at temperatures and densities  $T_H, n_H$  and  $T_C, n_C$  (Fig. 1).

Taking into account the symmetry properties of the magnetic islands and the adiabatic invariants (Eq.(4)), it can be shown by recurrence analysis that the electron flow  $\Psi$  through  $N_0$  chains of islands is given by:

$$(11) \quad \Psi = \frac{\alpha \sigma}{N_0(1-\alpha)+1} \left[ n_H \sqrt{\frac{2KT_H}{\pi m_e}} \exp\left(-\frac{q_e \phi_0}{KT_H}\right) - n_C \sqrt{\frac{2KT_C}{\pi m_e}} \right] l M \frac{q'}{q^2} \Delta^2$$

where  $\phi_0$  ( $\phi_0 = E_0 N_0 \Delta$ ) is the potential difference between the hot and the cold sea and  $l$  is the slab dimension in the  $y$ -direction.

In order to maintain quasi-neutrality conditions, the electron flow has to equal the ion flow. Assuming similar temperatures for electrons and ions we get:

$$(12) \quad \exp\left(-\frac{q_e \phi_0}{KT_H}\right) = \frac{n_c}{n_H} \left(\frac{T_c}{T_H}\right)^{1/2} + \left(\frac{m_e}{m_i}\right)^{1/2}$$

In the approximation  $(m_e/m_i)^{1/2} \approx 0$ :

$$(13) \quad E_0 = \frac{KT_H}{q_e} \left( \frac{\nabla_x n}{n_H} + \frac{1}{2} \frac{\nabla_x T}{T_H} \right)$$

which shows that the velocity  $v_0$  of the chosen reference frame follows the diamagnetic velocity of the electrons, a result already obtained for microtearing modes [4].

Similarly, the heat flows are given by:

$$(14a) \quad P_{\text{Heat}_{e^-}} = \frac{\alpha \sigma}{N_0(1-\alpha)+1} n_c \sqrt{\frac{8KT_c}{\pi m_e}} (KT_H - KT_c) 1M \frac{q'}{q^2} \Delta^2$$

$$(14b) \quad P_{\text{Heat}_{i^+}} = \frac{\alpha \sigma}{N_0(1-\alpha)+1} n_{iH} \sqrt{\frac{8KT_{iH}}{\pi m_i}} KT_{iH} 1M \frac{q'}{q^2} \Delta^2$$

The electron distribution function in the chaotic region at the Nth chain of islands is:

$$(15) \quad F_N = F_H(w_{II}) + \frac{N}{N_0} (F_C(w_{II}) - F_H(w_{II})) H\left[\frac{1}{2} m_e w^2 - \left(\frac{N_0 - N}{N_0}\right) q_e \phi_0\right]$$

which shows a linear combination of the Maxwellian distribution functions describing the hot and cold "seas".

## 5. SELF-SUSTAINMENT OF THE PERTURBATION

The necessary condition for self-sustainment is found through the determination of the relative difference  $\rho = (\lambda_{ch} - \lambda_i) / \langle \lambda \rangle$  between the values of  $\lambda$  associated to the chaotic zone and to the islands respectively. In the presence of perturbations with a range  $(\Delta M)$  of poloidal mode numbers around an average value  $\bar{M}$ , such as  $(\Delta M) / \bar{M} = \mu$ , the mean separation  $\Delta$  between chains of islands in toroidal geometry is:

$$(16) \quad \Delta = \frac{3}{2\mu} \cdot \frac{1}{\bar{M}^2} \cdot \frac{q^2}{q'} ; \quad q = \frac{rB_z}{RB_p}$$

Ampère's equation and the definition of the overlapping parameter  $\gamma$  leads to the relation:

$$(17) \quad 2\mu \cdot \bar{M} \cdot \rho = \bar{F}(\gamma) \cdot \frac{B_z}{\mu_0 \cdot jR}$$

where  $j$  is the average current parallel to the magnetic field at the minor radius  $r$  and where  $\bar{F}(\gamma)$  depends on the shape and

cross-section of the islands. As shown in Fig. 3,  $\bar{F}(\gamma)$  has a minimum close to 0.5 for  $\gamma \sim 1.1 - 1.2$ .

Then, by using the safety factor  $q_0$  and current density  $j_0$  on the axis of a Tokamak, we get the necessary condition of self-sustainment of the perturbation:

$$(18) \quad 8\mu \cdot \frac{\bar{M}}{q_0} \cdot \frac{\delta j}{j_0} > 1 \quad \delta j = j_{ch} - j_i$$

where  $\delta j$  is the default of current inside the islands with respect to the chaotic region.

Substituting Eq.(16) into Eq.(14a), the electron heat flow can be written as:

$$(19) \quad P_{Heat_{e^-}} = \frac{\alpha \sigma (2\pi r KVT)}{1-\alpha} \left(\frac{3}{2\mu}\right)^3 \frac{1}{\bar{M}^5} \left(\frac{q^2}{q'}\right)^2 n_c v_c ; v_c = \sqrt{\frac{8KT_c}{\pi m_e}}$$

Eq.(19) shows that the heat flow is strongly dependent on the average poloidal mode number  $\bar{M}$  which defines the number  $N_0$  of chains to be crossed, and on the temperature and density of the cold "sea". Around the separatrix in X-point discharges,  $q$  and consequently  $\bar{M}$  go to infinity, implying that  $P_{Heat_{e^-}}$  go to zero.

However, the transport in this region could be explained by other phenomena (neoclassical limit, MHD instabilities).

Combining Eq.(17) with Eq.(19) leads to:

$$(20) \quad \rho = \frac{1}{2} \left(\frac{1}{2\mu}\right)^{2/5} \left(\frac{1}{3}\right)^{3/5} \bar{F}(\gamma) \cdot \left(\frac{1-\alpha}{\alpha \sigma}\right)^{1/5} \cdot \frac{j_0 q_0}{jq} \cdot \left(q q'^2 \frac{P_{Heat_{e^-}}}{2\pi r n_c v_c KVT}\right)^{1/5}$$

The minimum value of  $\rho$  occurs at  $\gamma = 1.2$ .

By reference to Section 3, the average electrical resistivity  $\eta$  along a field line depends upon the relative length of its path in the different plasma regions including the two "seas" and on the local distribution function given by Eq.(15). In case of "infinite seas" the current density in the chaotic zone can be written as:

$$(21) \quad j_{ch} = \frac{Nj_c + (N_0 - N)j_H}{N_0} = \frac{V}{2\pi R \eta_{ch}}$$

As  $\eta \propto T^{-3/2}$ ,  $j_{ch}$  is larger than the current density of a plasma with temperature  $T_{ch} = \frac{N_0}{N T_c + (N_0 - N) T_H}$ . The determination of  $j_i$ , the current density in the islands, requires to calculate the local distribution function by integrating the particle trajectories including the  $\underline{E} \times \underline{B}$  drift.

For small temperature and density differences between the hot and the cold sea, it can be shown that

$$(22) \quad \rho = \nu \frac{(T_H - T_C)^2}{T_{ch}^2}$$

where  $\nu$  is a numerical coefficient, the value of which depends on the details of the collision and on the relative value of the radial electric field. Using Spitzer conductivity and a Krook collisional model,  $\nu$  is found to be in the range 0.1 - 0.3. A rough estimate of  $(T_H - T_C)/T_{ch}$  based on the relative plasma volumes at high and low temperatures leads to a self-consistent  $\rho$  value of a few percent.

It must be noted that a full treatment should take into account the ion Larmor radius when it is only marginally smaller than the island size. We should also remark that the crash of a sawteeth can also contribute to  $\rho$  as the current expelled from the central region of the plasma should flow preferably in the chaotic zone.

Preliminary comparison with JET experimental results has been carried out. Inserting JET data into Eq.(20) for  $q = 1.5$  we get  $\rho = \frac{\delta_j}{j} > 2.5 \times 10^{-2}$  and a band of  $M$  numbers extending from 10 to 20. The corresponding magnetic perturbation  $B/B_p$  has an amplitude of  $3 \cdot 10^{-4}$  and the chains of islands are separated by a distance  $\Delta \sim 10^{-2}m$ , i.e. only a few times larger than the ion Larmor radius. From Eq.(22) with  $\nu = 0.3$ ,  $(T_H - T_C)/T_{ch} \sim 0.3$  and the number of chains of islands between the two "seas" would be in the range 15 to 20.

## 6. CONCLUSION

The topology of magnetic field lines is a dominant feature affecting the properties of magnetically confined plasmas. An equilibrium could exist ( $\gamma \sim 1.2$ ) between undestroyed magnetic islands and chaotic regions.

This topology may be the key feature which explains the "anomalous" confinement in tokamaks, by allowing transport along field lines linking different regions of the plasma. This transport is affected by the plasma density and temperature at the edge. The reverse field pinch configuration could represent an extreme case of this model.

The current perturbation and then the topology may be self-sustained by the difference of resistivity between chaotic zone and islands, resulting from the field line path and the presence of hot electrons in the chaotic zone. The islands have a phase velocity close to the electron diamagnetic velocity.

Other effects, not taken into account so far, like finite ion Larmor radius, perpendicular diffusion and field curvature, could play an important role in the self-sustainment of such a topology.

When the model is applied to JET, the observed heat fluxes can be accounted for by perturbation levels in the magnetic field  $\tilde{B}/B_p \approx 3 \cdot 10^{-4}$  and in the current  $\delta_j/j \approx 3\%$ , corresponding to average poloidal mode number  $\bar{M} \approx 15$ .

#### ACKNOWLEDGEMENTS

We acknowledge the contribution of A. Samain, who is working along similar lines at Cadarache (CEA).

#### REFERENCES

- [1] JET TEAM (presented by P.H. Rebut), these Proceedings, Vol. 1, p. 31.  
CORDEY, J.G., et al., these Proceedings, Vol. 1, p. 99.
- [2] REBUT, P.H., HUGON, M., in Plasma Physics and Controlled Nuclear Fusion Research 1984 (Proc. 10th Int. Conf. London, 1984), Vol. 2, IAEA, Vienna (1985) 197.
- [3] TAYLOR, J.B., Phys. Rev. Lett. **33** (1974) 19.
- [4] SAMAIN, A., Plasma Phys. Contr. Fusion **26** (1984) 5.

# INCOMPLETE THERMALIZATION AND ENHANCED TRANSPORT IN TOKAMAK PLASMAS

S.-I. ITOH

Institute for Fusion Theory,  
Hiroshima University,  
Hiroshima

K. ITOH

Plasma Physics Laboratory,  
Kyoto University,  
Kyoto

Japan

## Abstract

### INCOMPLETE THERMALIZATION AND ENHANCED TRANSPORT IN TOKAMAK PLASMAS.

Plasma transport in the presence of unthermalized particles is analysed. During intensive heating a high energy tail develops and the spatial loss of fast particles affects the global energy balance. The paper examines the anomalous transport of electrons in the tail current operation of Ohmic discharges, the effect of the spatial loss on RF current drive, and the ion confinement in ICRF heating plasmas. Experimental results show that the tail current operation of Ohmic plasmas reduces the anomalous loss. On the other hand, the fast particle losses put an upper limit to the efficient heating and current drive. The small amount of fast particle loss (such as ripple loss) annihilates the RF enhancement of the fusion reactivity. In this case, the order of magnitude of the global confinement time is between that of the bulk particle confinement time and that of the slowing-down time. Effects of incomplete thermalization in real space are also discussed.

## 1. INTRODUCTION

Recently, alternative operation in tokamaks has attracted attention. For instance, enhancement of the fusion reaction rate by taking advantage of the non-Maxwellian ion component has been discussed. Various methods of intensive heating, current drive, current profile control, and slide-away discharge using a highly conductive plasma have been applied in order to extend the attainable parameter regime. The formation and sustainment of the tail components are key issues in the realization of these operations.

If spatial loss of tail components occurs, the thermalization of the tail becomes incomplete. Mechanisms of incomplete thermalization put a limit to the extension of plasma parameters and affect global confinement. In an

investigation of the conditions of alternative operation methods and the achievable plasma regime, we have examined mechanisms of the limitation of the tail development.

We analyse electron tail operation of Ohmic discharges in the low density regime and discuss the possibility of reduction of anomalous transport. Concerning RF-induced ion tail development, we report on serious constraints due to direct tail loss for the input power and the reaction enhancement. The reduction of the current drive efficiency is also examined.

## 2. TAIL OPERATION OF OHMIC PLASMA

A model of magnetic braiding [1-3] is employed for the electron loss mechanism, using the velocity dependent diffusion coefficient  $D = |u|D_0$  ( $u = v/v_e$ ,  $D_0 = Cv_e\delta^2/qR$ ,  $C$  being a numerical coefficient,  $q$  the safety factor,  $v_e$  the electron thermal velocity and  $R$  the major radius). For application to low density plasma, a correction to the collisionless skin depth is taken into account, i.e. the smaller quantity of  $c/\omega_p$  and  $1/Rk_{\parallel}^{\prime}$  is indicated by  $\delta$ ; we simply have  $\delta^2 = c^2/\omega_p^2 (1 + n_c/n)$ . To determine the velocity distribution function, we first solve the one-dimensional Fokker-Planck equation for steady state:

$$\frac{\partial}{\partial u} \left\{ -\frac{eE}{mv_e} f + \nu g \left( \frac{\partial f}{\partial u} + uf \right) \right\} - \frac{|u|}{\tau_0} f + S = 0 \quad (1)$$

where  $E$  is the DC electric field,  $\nu$  is the collision frequency at  $v_e$ ,  $g = 1/(3\sqrt{\pi} + |u|^3)$ ,  $\tau_0 = a^2/D_0$  and  $S$  is the source of cold electrons. We have  $f = f_{\text{bulk}} + f_{\text{tail}}$  and  $f_{\text{tail}}(u) \cong 10\sqrt{2}\epsilon \exp(-1/4\epsilon - u^2/2\epsilon\nu\tau_0) f(0)$  in the small  $\epsilon$  limit ( $\epsilon \equiv eE/\nu mv_e$ ). The tail current is given by  $J_{\text{tail}} = -ev_e \int uf_{\text{tail}} du$ .

The spatial profiles are determined by the radial transport equation  $\nabla \cdot \vec{q} + \vec{E} \cdot \vec{J} = 0$ , where  $\vec{q} = -nD_0\nabla T_e$  and  $E = \text{const}$ . The boundary conditions are  $q(0) = 1$ ,  $J' = 0$  for  $r < r_1$  ( $q(r_1) = 1$ ) and  $J = 0$  for  $r > r_2$  ( $q(r_2) = 2$ ) [4, 5]. The density profile is assumed to be parabolic. This model has been used successfully to explain the results for ordinary Ohmic discharges. Our analysis includes the tail component following the bulk distribution according to Eq. (1). The plasma current profile is obtained from the transport equation

$$\begin{aligned} J_{\text{bulk}} &= \frac{2\alpha B}{\mu_0 R} h(x) \\ &= \frac{2\alpha B}{\mu_0 R} \frac{J_0(x) Y_0(x_2) - Y_0(x) J_0(x_2)}{J_0(x_1) Y_0(x_2) - Y_0(x_1) J_0(x_2)} \end{aligned} \quad (2a)$$

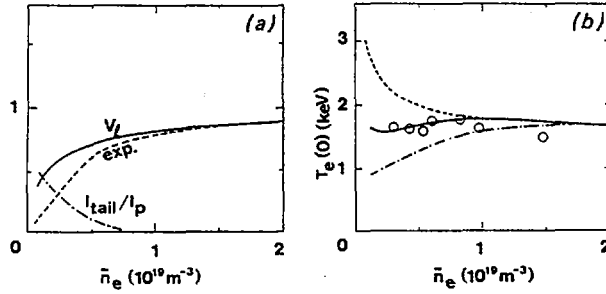


FIG. 1. Low density OH discharge for PLT parameters:  $R = 1.35$  m,  $a = 0.4$  m,  $B = 3.1$  T,  $I_p = 0.25$  MA,  $Z_{\text{eff}} = 2$  and  $n_c = 10^{18}$  m $^{-3}$ .

(a) One-turn voltage (solid line for theory, dashed line for experiment;  $V_l$  is given in volts) and tail current normalized to  $I_p$  versus  $\bar{n}_e$ .

(b)  $T_e(0)$  versus  $\bar{n}_e$ . The solid line indicates the present model and the open circles are experimental values. For explanation of dashed line and dashed-dotted line see text.

$$J_{\text{tail}} = \frac{2B}{\mu_0 R} \frac{(1-\alpha)\epsilon}{\epsilon(0)} \exp\left\{-\frac{1}{4}\epsilon + \frac{1}{4}\epsilon(0)\right\} \quad (2b)$$

where  $x = \mu r$ ,  $\mu^2 = 77.4\sqrt{\pi} R \epsilon_0 R^2 / m_e Z_{\text{eff}} \ln \Lambda c^2$ ,  $\epsilon = \epsilon(0)h^{2/3}$ ,  $\sigma(0)E = 2\alpha B / \mu_0 R$ ,  $\sigma$  is the electrical conductivity at  $T_e$ ,  $x_{1,2} = \mu r_{1,2}$  and  $\alpha \equiv J_{\text{bulk}}^{(0)} / J(0)$ . The eigenvalues  $E$  and  $\alpha$  are obtained numerically. Figure 1 shows the density dependence of the loop voltage,  $V_l = 2\pi R E$ ,  $I_{\text{tail}}/I_p$  and  $T_e(0)$ . A recent PLT experiment has been simulated [6]. The numerical coefficient  $C$  for  $D_0$  is given by adjusting  $V_l$  to the experiment at  $\bar{n} = 2 \times 10^{19}$  m $^{-3}$ . The solid lines indicate the results of our analysis. Figure 1 (b) also shows the results of a model which neglects the tail (dashed line) and of a model without  $\delta$ -correction ( $n_c = 0$ , dashed-dotted line). These two models do not explain the  $n$ -dependence of  $T_e$ ; the confinement time is longer than that expected from Alcator scaling. Our model seems to fit the experimental results in the range of  $\bar{n} > 5 \times 10^{18}$  m $^{-3}$ . However, for  $\bar{n} < 5 \times 10^{18}$  m $^{-3}$  there is still a discrepancy; theory predicts  $V_l \propto \sqrt{\bar{n}}$ , but the experiment shows  $V_l \propto n$ . It is not only the magnetic braiding model which gives this proportionality of  $V_l$ ; other models, such as that for the collisionless trapped particle mode [4], also give  $V_l \propto \sqrt{\bar{n}}$  in the low density limit. Experimental observation shows a further reduction of  $V_l$  and thermal conductivity [6, 7]. This fact raises questions regarding further experiments, for instance whether anomalous electron loss can be reduced by sustainment of the beam current (to make the bulk electrons current-free as in the Astron-Spherator configuration [8, 9]).

## 3. ION TAIL GENERATION BY RF WAVES

We investigate the effect of the high energy particle loss by examining the minority ion cyclotron resonance heating. The Fokker-Planck equation, with RF heating and particle loss, may be written as

$$\frac{\partial f}{\partial t} = C(f) + K(f) - \lambda f + S$$

where  $C(f)$  is the collision term and  $\lambda$  is the spatial loss, assumed to have the form  $\lambda = |u|^s/\tau_0$  ( $u = v/v_T$ ,  $v_T$  being the thermal velocity at background temperature). For simplicity, we use the linearized collision operator, assume isotropic distribution, and write [10, 11]:

$$K(f) = \frac{\partial \left( K v^2 \frac{\partial f}{\partial v} \right)}{\partial v \cdot v^2}$$

The absorbed RF power is given by  $P_{rf} = 3mKn$ .

In the high heating limit,  $\xi \equiv P_{rf}\tau_s/3nT_e \gg 1$  (with  $\tau_s$  the slowing-down time by electrons), the ion tail develops and the characteristic tail temperature is given by  $\xi T_e$ . In this limit, the tail distribution is approximately given by

$$f_{\text{tail}} \approx \exp \left( -\frac{u^2}{\xi} - \frac{2}{s+2} \frac{v_T}{\sqrt{K}\tau_0} u^{s/2+1} \right) \quad (3)$$

If the index  $s$  is greater than 2, the tail distribution decays much faster than the Gaussian distribution for  $u > u_c$ . The cut-off velocity  $u_c$  is approximately given as  $u_c \approx (\tau_0/\tau_s \xi)^{1/(s-2)}$ . The loss rate  $\eta$  is calculated as

$$\eta = P_{\text{loss}}/P_{rf} = \int \lambda f w d\vec{v} / \int w K(f) d\vec{v} \quad (w = mv^2/2)$$

In the weak loss limit, we have

$$\eta \approx (2\ell!/\sqrt{\pi}) \cdot \tau_s \xi^{s/2} / \tau_0$$

(if  $s$  is odd and  $s = 2\ell + 1$ ). The loss becomes appreciable for  $\xi > (\tau_0/\tau_s)^{2/s}$ .

We solve the Fokker-Planck equation numerically. Considering ripple loss [12], we take  $s = 7$ . The power contributing to bulk heating is given as  $P_{\text{bulk}} = \int C(f) w d\vec{v}$ . In the range of  $\xi \approx O(10^2)$  and  $\tau_0/\tau_s \approx O(10^4)$ , the bulk

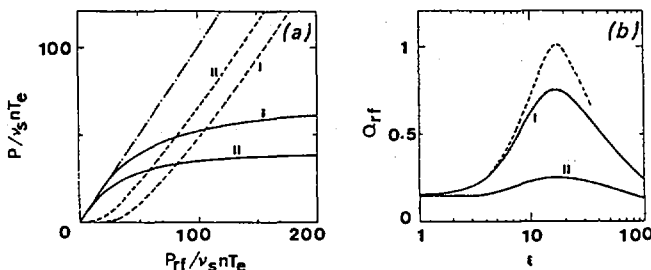


FIG. 2. Power partition and power amplification factor for  $s = 7$ .

(a)  $P_{loss}$  (dashed line) and  $P_{bulk}$  (solid line) for  $\tau_0/\tau_s = 10^5$  (I) and  $\tau_0/\tau_s = 10^3$  (II). The dashed-dotted line is for  $P = P_{rf}$ .

(b)  $Q_{rf}$  versus  $\xi$  for  $\tau_0/\tau_s = 10^5$  (I) and  $\tau_0/\tau_s = 10^3$  (II). The dashed line is for  $\tau_s/\tau_0 = 0$  (no spatial loss).

heating rate,  $P_{bulk}/P_{rf} = 1 - \eta$ , is approximately given by  $1 - \eta \approx 3\xi^{-0.86}(\tau_0/\tau_s)^{0.12}$  for  $s = 7$ . Figure 2(a) shows the partition of the absorbed power as a function of the heating density for the cases of  $\tau_0/\tau_s = 10^5$  and  $\tau_0/\tau_s = 10^3$ . Although the spatial loss is negligibly small for thermal particles,  $P_{loss}$  exceeds  $P_{bulk}$  for  $\xi > \xi_c$ .  $\xi_c \approx 20$  for  $\tau_0/\tau_s = 10^3$  and  $\xi_c \approx 35$  for  $\tau_0/\tau_s = 10^5$ . It is also noted that if  $\xi$  exceeds  $\xi_c$  the power transferred to bulk particles saturates and the increment of the heating power enhances only the fast ion loss.

The deterioration of the tail confinement affects the fusion reaction rate. The fusion reaction with the background tritons can be calculated assuming that the minority deuterons are heated. For the estimate we employ the Duane formula for D-T reactions [13]. In the calculation of the average reactivity  $\langle \sigma v \rangle$  we use the power amplification factor,  $Q_{rf} = P_{fusion}/P_{rf} = w_f n_T n_D \langle \sigma v \rangle / P_{rf}$  ( $w_f = 22.4$  MeV). Figure 2(b) illustrates  $Q_{rf}$  as a function of  $\xi$  for  $T_e = 6$  keV;  $\tau_s/\tau_0$  is chosen to be 0,  $10^{-5}$  and  $10^{-3}$ . The enhancement of the reactivity is annihilated by the small amount of the fast particle loss.

We note that the estimated loss rate  $\eta$  is the upper limit (see Fig. 2). The spatial loss  $\lambda$  starts to decrease in the high energy limit because the  $\nabla B$  drift becomes large for energetic particles. For particles  $w > w_H$  ( $w_H$  satisfies the relation  $\Omega_H(w_H) = \nu_{eff}(w_H)$ ,  $\Omega_H$  being the poloidal rotation by  $\nabla B$  drift),  $s = -0.5$  holds. In this case,  $\eta$  saturates for large  $\xi$ , and  $P_{loss}/P_{rf}$  scales as  $(\tau_s/\tau_0)^{0.7}$ .

#### 4. EFFECT ON RF CURRENT DRIVE EFFICIENCY

The efficiency of the RF current drive is limited by the spatial loss. If we write the loss term as  $|u|f/\tau_0$  (see Section 2), Eq. (1) reduces to

$$C(f) + K(f) - |u|f/\tau_0 + S = 0$$

where  $K(f) = \nabla \cdot \tilde{R} \nabla f$  ( $\tilde{R}$  being the driving term due to the RF momentum absorption). For high energy particles, the RF force compensates the spatial loss of the momentum.

If the RF driving term extends to the region of high phase velocity and  $K(f)$  is written as  $K \cong \tilde{R} \partial^2 f / \partial u^2$ , the asymptotic form of the tail distribution is given as

$$f_{\text{tail}} \approx \exp(\nu_e / \tilde{R} u - 2u^{3/2} / 3 \sqrt{\tau_0 \tilde{R}})$$

The tail distribution decays exponentially in the presence of spatial loss. The energy limit of the tail electrons is estimated as  $u_c \approx (\nu_e / \tilde{R})^{0.2} (\nu_e \tau_0)^{0.2}$ . For  $u > u_c$ ,  $f$  decays quickly. As the power level increases, the critical velocity slows down and the sustained current normalized to the RF power decreases.

When  $u_c$  approaches unity, the current drive efficiency becomes very low.

This process imposes an upper limit on the sustained current for a given value of  $\nu_e \tau_0$ .

## 5. SUMMARY AND DISCUSSION

The confinement of a tokamak plasma with unthermalized particles has been investigated. The role of the tail component appears to be different for OH plasma and ICH plasma. In OH plasma, the generation of highly conductive and high energy electrons reduces the electric field. The confinement is not deteriorated by selective loss of fast electrons; the experimental results show a reduction of bulk transport. In contrast, in ICH plasma the high energy ion mode ( $\xi > 10$ ) is largely affected by selective loss of energetic particles. In the density limit of the high heating regime the order of magnitude of the global confinement time is between the order of magnitude of the collision time and the order of magnitude of the bulk diffusion time. The lowering of the current drive efficiency is also discussed.

The processes discussed in this paper are the phenomena associated with incomplete thermalization in velocity space. Incomplete thermalization also occurs in real space where it is accompanied by thermoelectric effects. The electron temperature is usually considered to be constant on the magnetic surface. Temperature inhomogeneity along the field lines appears in the disruption phase [14] and/or near the plasma periphery where local cooling takes place owing to interaction with external materials. In this situation the heat flux along the field lines completes the thermalization, and this flux can enhance the cross-field plasma losses. These processes illustrate the importance of incomplete thermalization in global confinement.

## ACKNOWLEDGEMENTS

The authors wish to thank Dr. A. Fukuyama for many useful comments and discussions. Continuous encouragement by Profs. K. Nishikawa, A. Iiyoshi and K. Uo is also acknowledged.

This work was partly supported by a Grant in Aid for Scientific Research and a Grant in Aid for Fusion Research of the Ministry of Education of Japan.

## REFERENCES

- [1] OHKAWA, T., *Phys. Lett.*, A **67** (1978) 35.
- [2] RECHESTER, A.B., ROSENBLUTH, M.N., *Phys. Rev. Lett.* **40** (1978) 38.
- [3] KADOMTSEV, B.B., POGUTSE, O.P., in *Plasma Physics and Controlled Nuclear Fusion Research 1984* (Proc. 10th Int. Conf. London, 1984), Vol. 2, IAEA, Vienna (1985) 69.
- [4] PERKINS, F.W., in *Heating in Toroidal Plasmas* (Proc. 4th Int. Symp. Rome, 1984), Vol. 2, Int. School of Plasma Physics, Varenna (1984) 977.
- [5] ITOH, K., ITOH, S.-I., PERKINS, F.W., *Res. Rep. HIFT-121*, Hiroshima University (1986); *Comments Plasma Phys. Controll. Fusion* **10** (1986) 103.
- [6] CHU, T.K., et al., *Plasma Confinement in Toroidal Discharges Sustained by a Highly Conducting Plasma Current*, preprint, Princeton University, 1985.
- [7] FUSSMANN, G., BECKER, G., BEHRINGER, K., et al., in *Plasma Physics and Controlled Nuclear Fusion Research 1982* (Proc. 9th Int. Conf. Baltimore, 1982), Vol. 3, IAEA, Vienna (1983) 295.
- [8] YOSHIKAWA, S., CHRISTOFILOS, N.C., in *Plasma Physics and Controlled Nuclear Fusion Research 1971* (Proc. 4th Int. Conf. Madison, 1971), Vol. 2, IAEA, Vienna (1971) 357.
- [9] MOHRI, A., NARIHARA, K., YOMITA, Y., et al., in *Plasma Physics and Controlled Nuclear Fusion Research 1984* (Proc. 10th Int. Conf. London, 1984), Vol. 3, IAEA, Vienna (1985) 395.
- [10] STIX, T.H., *Nucl. Fusion* **15** (1975) 737.
- [11] FUKUYAMA, A., et al., these Proceedings, Vol. 1, p.627.
- [12] KOVRIZHNYKH, L.M., *Nucl. Fusion* **24** (1984) 851.
- [13] BOOK, D.L., *NRL Plasma Formulary*, Office of Naval Research (1978) 36.
- [14] ITOH, K., ITOH, S.-I., *Phys. Lett.*, A **109** (1985) 31.



# EFFECT OF QUASI-LINEAR EVOLUTION OF THE MINORITY ION DISTRIBUTION FUNCTION ON THE WAVE DISPERSION AND ABSORPTION AND ON THE THERMONUCLEAR REACTION RATE

A.V. LONGINOV, S.S. PAVLOV, K.N. STEPANOV  
Kharkov Institute of Physics and Technology,  
Ukrainian SSR Academy of Sciences,  
Kharkov,  
Union of Soviet Socialist Republics

## Abstract

EFFECT OF QUASI-LINEAR EVOLUTION OF THE MINORITY ION DISTRIBUTION FUNCTION ON THE WAVE DISPERSION AND ABSORPTION AND ON THE THERMONUCLEAR REACTION RATE.

The effect of the quasi-linear (QL) evolution of the minority ion distribution function caused by slow (ion cyclotron) wave absorption at minority ion resonances,  $\omega \approx \omega'_c$  or  $\omega \approx 2\omega'_c$ , on the dispersion and damping of the slow waves is considered. The conversion of the slow waves (SW) propagating from the low magnetic field side into shorter wavelength SW and the opacity zone found between conversion and ion cyclotron resonance points existing for minority ion densities in excess of the critical density are shown to disappear at large SW amplitudes. This is due to the high energy tail 'cut-off' for minority ions as a result of quasi-linear diffusion of resonant ions in the velocity space, perpendicular to the magnetic field. If the opacity zone disappears and the zone  $\omega \approx 2\omega'_c$  is accessible, it is possible to heat the plasma in powerful regimes with the help of SW excited on the low magnetic field side, either directly or by using fast wave conversion into SW. — It is also shown that SW accessibility of the cyclotron resonance zone for minority ions allows one to reach the two-component reactor regime (resonance  $\omega = \omega_{cd}$  for the deuteron minority in the tritium plasma and resonance  $\omega = 2\omega_{ct}$  for the triton minority in the deuterium plasma). In the former, somewhat more efficient regime (d-minority in the t-plasma), the Q-factor reaches values of  $Q \approx 1.5-2.5$  at  $T = 5-10$  keV; moreover, the energy confinement time can be reduced by more than an order of magnitude, and the specific power of the d-t reaction increases three to five times over a conventional regime with  $n_d = n_t$ .

## 1. INTRODUCTION

In the region  $\omega \sim \omega_{ci}$ , along with long wavelength ( $k_{\perp}\rho_i \sim v_{Ti}/v_A \ll 1$ ) fast magnetosonic waves (FMSW), short wavelength ( $k_{\perp}\rho_i \sim 1$ ) ion cyclotron (slow) waves (SW) are employed for plasma heating and current drive [1-13]. The waves can be excited either directly by an external antenna [2, 3] or by conversion effects [2, 4-12]. SW can be absorbed by minority ions at  $\omega = 2\omega'_c$

[2, 7-15] if their density does not exceed a critical value,  $n' < n'_{cr}$  [1, 7]. For  $n' > n'_{cr}$ , a SW propagating from the low magnetic field side converts into a wave with a shorter wavelength that propagates backwards, i.e. down in the magnetic field. In this case, the opacity zone appears between the conversion point and the minority ion cyclotron resonance (MICR) zone, and, hence, the SW cannot reach the MICR zone.

At the same time, at high SW power levels, quasi-linear deformation of the minority ion distribution function (MIDF) due to SW cyclotron absorption by these ions may cause a substantially decreased ion contribution to the RF current as compared with the linear case, because of the sharp tail cutoff of the distribution function [8, 11]

This paper shows that the strong influence of quasi-linear effects on SW dispersion may take the opacity region disappear and the SW reach the MICR zone  $\omega = \ell\omega'_c$  ( $\ell = 1$  or  $\ell = 2$ ), even for  $n' \gg n'_{cr}$ . This enables one to employ the resonance for SW in powerful regimes. These effects may also be used to create a two-component reactor. An analysis of the parameters of such an RF reactor is presented in this paper.

## 2. EFFECT OF MINORITY ION HEATING ON SW PROPAGATION

### 2.1. Formulation of the problem

Consider a dispersion equation for SW in the range  $\omega \approx \ell\omega'_c$ . The distribution functions of the bulk ions and electrons are assumed to be Maxwellian, with  $T_e = T_i = T$ . We determine the MIDF  $f'_0(v_{\perp}, v_{\parallel})$ , averaged over the magnetic surface  $r = \text{const}$ , from the quasi-linear kinetic equation accounting for the collisions with bulk ions and electrons. The dispersion equation relating the perpendicular and the parallel refractive indices  $N_{\perp} = k_{\perp}c/\omega$  and  $N_{\parallel} = k_{\parallel}c/\omega$  has the form [1]:

$$(\varepsilon_1 + \varepsilon')N_{\perp}^4 + \varepsilon_3[(N_{\parallel}^2 - \varepsilon_1 - \varepsilon')N_{\perp}^2 - \varepsilon_2^2] = 0 \quad (1)$$

$$\varepsilon_1 = 1 + \frac{\omega_{pe}^2}{\omega_{ce}^2} + \frac{2\omega_{pi}^2}{K_{\perp}^2 V_{Ti}^2} \left[ 1 - \sum_{n=-\infty}^{\infty} A_n(x) \frac{\omega}{\omega - n\omega_{ci}} \right] \quad (2)$$

$$\varepsilon_2 = -\frac{\omega_{pe}^2}{\omega|\omega_{ce}|} - \frac{\omega_{pi}^2}{\omega^2} \sum_{n=-\infty}^{\infty} A'_n(x) \frac{\omega}{\omega - n\omega_{ci}}$$

$$A_n(x) = e^{-x} I_n(x), \quad A'_n = \frac{dA_n}{dx}, \quad x = \frac{1}{2} K_{\perp}^2 \varrho_i^2, \quad \varrho_i = \frac{V_{Ti}}{\omega_{ci}}$$

$$\begin{aligned} \varepsilon_3 &= \frac{2\omega_{pe}^2}{K_{\parallel}^2 v_{Te}^2} \left[ 1 + i\sqrt{\pi} Z e W(Z e) \right] \quad \left( Z e = \frac{\omega}{K_{\parallel} v_{Te}} \right) \\ \varepsilon'_1 &= -\frac{2i\pi^{3/2}\omega_p'^2\omega}{v_{T\perp}' K_{\perp}^2 K_{\parallel}} W(Z'_{\perp}) \int_0^{\infty} J_{\ell}^2 \left( \frac{K_{\perp} v_{\perp}}{\omega_{c\ell}'} \right) \frac{\partial f'_0(v_{\perp})}{\partial v_{\perp}} dv_{\perp} \quad (3) \\ W(Z) &= e^{-Z^2} \left( 1 + \frac{2i}{\sqrt{\pi}} \int_0^Z e^{t^2} dt \right), \quad Z'_{\perp} = \frac{\omega - \ell\omega_c}{K_{\parallel} v_{T\perp}'}, \quad v_{T\perp}' = \sqrt{\frac{2T_{\perp}'}{m'}} \\ \omega_{ci} &= \frac{e_i B}{m_i c}, \quad \omega_c' = \frac{e' B}{m' c}, \quad \omega_{p\alpha} = \left( \frac{4\pi e_{\alpha}^2 n_{\alpha}}{m_{\alpha}} \right)^{1/2}, \quad \omega_p' = \left( \frac{4\pi e'^2 n'}{m'} \right)^{1/2} \end{aligned}$$

where  $e_{\alpha}$ ,  $m_{\alpha}$ ,  $n_{\alpha}$  and  $e'$ ,  $m'$ ,  $n'$  are the charges, masses and densities of the bulk electrons ( $\alpha = e$ ) and ions ( $\alpha = i$ ) and the minority ions ( $n' \ll n_i$ ).

The MIDF is approximated by a product

$$f'_0(v_{\perp}, v_{\parallel}) = f'_0(v_{\perp}) f'_0(v_{\parallel})$$

where

$$\begin{aligned} f'_0(v_{\parallel}) &= (1/\sqrt{\pi} v_{T\parallel}') \exp(-v_{\parallel}^2/v_{T\parallel}'^2) \\ v_{T\parallel}' &= \sqrt{\frac{2T_{\parallel}'}{m'}}, \quad T_{\parallel}' \gg T \end{aligned}$$

(in the following, the difference between  $T_{\parallel}$  and  $T$  is not significant). Averaging the kinetic equation over the magnetic surface, we assume the SW electric field  $E_r$  and  $k_{\perp}$  to be slightly varying in the range  $\omega \approx \ell\omega_c'$  ( $k_{\perp} = k_{\perp}^0 = k_{\perp}$  ( $Z'_{\perp} = 0$ ) = const), which corresponds to weak damping of SW,  $\text{Im}k_{\perp} \ll k_{\perp}$ ,  $\int \text{Im}k_{\perp} dR \ll 1$ . We also assume that the QL diffusion changes only  $v_{\perp}$  so that  $\langle v_{\perp}^2 \rangle \gg \langle v_{\parallel}^2 \rangle$  and neglected the angular scattering of minority ions. (This is true for heavy ions,  $m' \gg m_i$ ; for  $m' \sim m_i$  the scattering may change  $f'_0$  to a certain extent.) Then, in the steady case, the kinetic equation for  $f'_0(v_{\perp})$  reduces to

$$(D_i + D_e + D_{RF}) \frac{df'_0}{d\mu} + (F_i + F_e) f'_0 = 0 \quad (4)$$

$$D_i = \frac{1}{2u^3} \Psi(u), \quad D_e = \frac{1}{2u^3} \frac{m'}{m_e} \Psi(u \sqrt{m_e/m_i})$$

$$F_i = \frac{m'}{m_i} \frac{\Psi(u)}{u^2}, \quad F_e = \frac{m'}{m_e} \Psi(u \sqrt{m_e/m_i}) \frac{1}{u^2}$$

$$\varphi(u) = \frac{4}{\sqrt{\pi}} \int_0^u e^{-u^2} u^2 du, \quad u = \frac{v_{\perp}}{v_{Ti}} \quad (5)$$

$$D_{RF} = \xi^2 \frac{j_{\perp}^2(\lambda_0 u)}{\lambda_0^2 u^2}, \quad \lambda_0 = K_{\perp}^0 \rho_i \frac{\omega_{ci}}{\omega_c^i}$$

$$\xi^2 = \frac{\ell v_{Ti}}{8\pi e_i^2 n_i L \omega_c^i} \frac{R}{r} E_r^2, \quad E_r^2 = \frac{16\pi}{\omega} \frac{P_{RF}}{|d\epsilon_1/dK_{\perp}|} \quad (6)$$

Here,  $L = 15$  is the Coulomb logarithm, and  $P_{RF}$  is the SW power flux density. The solution to Eq. (4) is

$$f_0'(u) = C \exp\left(-\int_0^u A(u) du\right) \quad (7)$$

$$A(u) = u \frac{F_e + F_i}{D_i + D_e + D_{RF}} \quad (8)$$

where  $C$  is determined from the condition

$$2\pi v_{Ti}^2 \int_0^{\infty} f_0'(u) u du = 1$$

Equation (7) is used to derive the specific RF power (averaged over the magnetic surface) which is absorbed by minority ions, the fraction of the energy transferred from these minority ions to ions  $p_i$  and to electrons  $p_e$  ( $p_e + p_i = 1$ ), the ratio of the average transverse energy of the minority ions to the transverse energy of bulk ions,  $W_{\perp}$ , and the contribution of resonance ions to the dielectric permeability  $\epsilon'$ :

$$\langle P \rangle_{RF} = 3\sqrt{\frac{\pi}{2}} \frac{T n_i}{\tau_i} \frac{n_i'}{n_i} \left(\frac{\epsilon'}{\epsilon_i}\right)^2 F(\lambda_0, \xi^2) \quad (9)$$

$$F(\lambda_0, \xi^2) = \frac{m_i}{m'} \frac{\int_0^{\infty} \exp\left(-\int_0^u A du\right) D_{RF} A u^2 du}{\int_0^{\infty} \exp\left(-\int_0^u A du\right) u du} \quad (10)$$

$$\tau_i = \frac{3}{4} \frac{T^{3/2} m_i^{1/2}}{\sqrt{\pi} e_i^4 n_i L}$$

$$\rho_i = \frac{\int_0^{\infty} \exp(-\int_0^u A du) (F_i - D_i A) u^2 du}{\int_0^{\infty} \exp(-\int_0^u A du) D_{RF} A u^2 du} \quad (11)$$

$$W_{\perp} = \frac{m'_i \langle v_{\perp}^2 \rangle}{m_i v_{Ti}^2} = \frac{m'_i \int_0^{\infty} \exp(-\int_0^u A du) u^3 du}{m_i \int_0^{\infty} \exp(-\int_0^u A du) u du} \quad (12)$$

$$\mathcal{E}'(Z'_l) = i \frac{2\sqrt{\kappa'} \omega_p^2 \omega}{\omega_c'^2 k_{\parallel} v_T'} \Phi(\kappa_{\perp} g_i, \lambda_0, \xi^2) W(Z'_l) \quad (13)$$

$$\Phi = \frac{\int_0^{\infty} J_l^2(\lambda u) \exp(-\int_0^u A du) A du}{\lambda^2 \int_0^{\infty} \exp(-\int_0^u A du) u du}, \quad \lambda = \kappa_{\perp} g_i \frac{\omega_{ci}}{\omega_c'} \quad (14)$$

The damping coefficient is proportional to  $\exp(-Z_l'^2) \Phi$ ; it differs from zero in the narrow range where  $|Z_l'| \leq 1$ . The resonance surface  $\omega = \ell \omega_c'$  is assumed to be located at  $R = R_0$  so that  $Z_l' = (\omega/k_{\parallel} v_T') (R - R_0)/R_0$ .

## 2.2. Accessibility of $\omega = \ell \omega_c'$ zone at high $n'$ values

Consider the accessibility condition of the zone  $\omega = \ell \omega_c'$  at  $n' > n'_{cr}$  for  $|\epsilon_3| \gg N_{\parallel}^2$  when Eq. (1) reduces to

$$\epsilon_1 + \epsilon' - N_{\parallel}^2 = 0 \quad (15)$$

where  $\epsilon_1$  can be taken at the surface  $\omega = \ell \omega_c'$  and  $\epsilon'$  is determined by formula (13).

As an example, let us take a  ${}^7\text{Li}$  impurity in a deuterium plasma ( $N_{\parallel}^2 = 9$ ,  $n_e = n_d = 7 \times 10^{13} \text{ cm}^{-3}$ ,  $T = 1 \text{ keV}$ ,  $\omega = 2\omega_c'$ ,  $\omega/\omega_{cd} = 1.7$ ,  $\lambda_0 = 0.9\sqrt{2}$ ,  $\lambda_0$  being weakly dependent on  $N_{\parallel}^2$ ,  $n_i$  and  $T$ , if  $N_A^2 = \omega_{pi}^2/\omega_{ci}^2 \gg N_{\parallel}^2$ ,  $1 + \omega_{pe}^2/\omega_{ce}^2$ ). It can be seen from Fig. 1 that for high powers (large  $\xi^2$ ) a distribution function is formed with a pronounced effect of tail cutoff in the range where  $D_{RF} \rightarrow 0$ . Figure 2 shows that, as  $\xi^2$  grows, the function  $\Phi$  and, hence, the values of  $\epsilon'$  for sufficiently large  $k_{\perp} \rho_i$  become very small.

Figure 3 demonstrates a graphic solution to Eq. (15). Here, for  $\xi^2 = 0$ ,  $T' = T_d$ ,  $Z'_2 = 1$  the function  $\epsilon'$  is represented by Curve 1 for  $n' = n_1 < n'_{cr}$ , Curve 2 for  $n' = n_2 = n'_{cr}$  and Curve 3 for  $n' = n_3 > n'_{cr}$ . As is seen in Fig. 3, for  $n' = n_1$  at  $Z'_2 > 0$  ( $\text{Re } \epsilon' < 0$ ), we have positive roots  $k_1$  and  $k_2$  for all  $Z'_2 > 0$ ; for  $n' = n_2$ , the roots  $k_1$  and  $k_2$  merge, producing the conversion region at  $Z'_2 \approx 1$ ; for  $n' = n_3$ , positive roots  $k_1$  and  $k_2$  for  $Z'_2 = 1$  are absent, which is

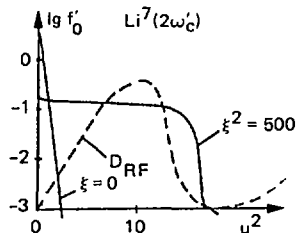


FIG. 1.  $D_{RF}$  and  $\lg f'_0$  versus  $u^2$  for  ${}^7\text{Li}$  minority ions at  $\omega = 2\omega'_c$  for various  $\xi^2$ .

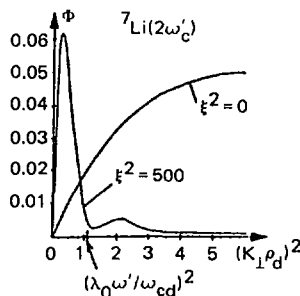


FIG. 2.  $\Phi(k_{\perp}\rho_d)$  versus  $k_{\perp}^2\rho_d^2$ .

indicative of the presence of an opacity zone (obviously, positive roots appear for  $Z'_2 \gg 1$ ). Thus, the MICR zone can be reached for  $T' = T_d$  only at  $n' < n'_{cr}$ , where the values of  $n'_{cr}$  may be very small, especially for large differences  $\omega'_c - \omega_{cd}$  and small  $N_{\parallel}^0$  (see also [2, 8]).

It can be shown that in the case of  $n' = n'_3 > n'_{cr}$  and a strongly deformed Li ion distribution function ( $\xi^2 = 500$ , Fig. 1) due to a substantial decrease in the function (see Fig. 2) for  $k_{\perp}^0\rho_d = \lambda_0\omega'_c/\omega = 1.17$  (the same value as in a pure d-plasma) at  $Z'_2 \approx 1$  (and hence, throughout the range  $Z'_2 > 0$ ), we have two roots of Eq. (15),  $k_1 \approx k_{10}$  and  $k_2$ , even for  $T'_{\parallel} = T$  (see Fig. 3, broken curves).

In Fig. 4, the solutions to Eq. (1) for  $\xi^2 = 0$  ( $T' = T$ ) and  $\xi^2 = 500$  are presented, showing that for  $\xi^2 = 500$  and  $n' > n'_{cr}$ , the solutions to the dispersion equation are close to each other for  $n' \ll n'_{cr}$ ,  $\xi^2 = 0$  and  $n' \gg n'_{cr}$ ,  $\xi^2 = 500$ .

The opacity zone for SW propagating from the low magnetic field side appears also for the resonance  $\omega = \omega'_c$ , e.g. in a d-plasma with a  ${}^3\text{He}$  impurity. For  $\omega = \omega_{c^3\text{He}}$  ( $\omega/\omega_{cd} = 4/3$ ) one has  $k_{\perp}^0\rho_d = 2,3$ ;  $\lambda_0 = 1.7$ . Since  $\lambda_0$  is high, a significant transport of  ${}^3\text{He}$  ions through the zeros of  $D_{RF}$  occurs due to the diffusion in deuterium, but still the tail cutoff caused by decreased  $D_{RF}(u)$  is distinct (Fig. 5). The function  $\Phi(k_{\perp}\rho_d)$  for  ${}^3\text{He}$  is shown in Fig. 6, and the

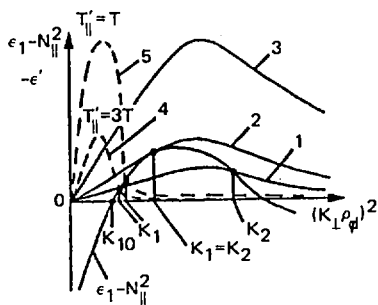


FIG. 3. Graphical solution of Eq. (15) at  $\omega \approx 2\omega'_c$  ( $Z'_2 \sim 1$ ) for  ${}^7\text{Li}$  minority ions in d-plasma. The root  $k_{10}$  corresponds to pure d-plasma ( $\omega/\omega_{cd} = 12/7$ ,  $k_{\perp} \rho_d = 0.77$ ).

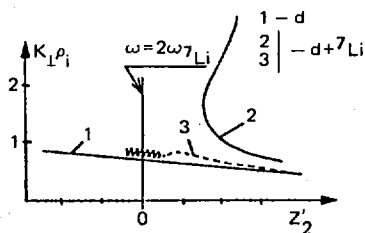


FIG. 4.  $k_{\perp} \rho_d$  versus  $Z'_2$  obtained from Eq. (1):  ${}^7\text{Li}$  minority ions in d-plasma,  $\omega \approx 2\omega'_c$ ,  $n_e = 7 \times 10^{13} \text{ cm}^{-3}$ ,  $T = 1 \text{ keV}$ ,  $N_{\parallel} = 3$ ,  $B_0 = 3T$ . Curves 2 ( $T' = T$ ) and 3 ( $\xi^2 = 500$ ) correspond to d +  ${}^7\text{Li}$  (6%)-plasma, Curve 1 refers to pure d-plasma. Shaded area shows maximum cyclotron SW absorption.

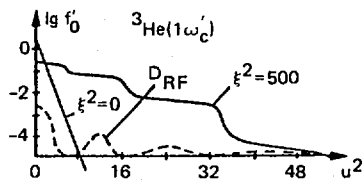


FIG. 5.  $D_{\text{RF}}$  and  $\lg f'_0$  versus  $u^2$  for d-plasma with  ${}^3\text{He}$  minority ions at  $\omega = \omega'_c$  for  $\xi^2$  at  $\lambda_0 = 1.75$ .

solution to Eq. (1) is in Fig. 7 for  $N_{\parallel} = 3$ ,  $n_e = 7 \times 10^{13} \text{ cm}^{-3}$ ,  $B_0 = 3T$ ,  $T = 1 \text{ keV}$  ( $\xi^2 = 500$  for Curve 3,  $\xi^2 = 0$  for Curves 1 ( $n' < n'_{\text{cr}}$ ) and 2 ( $n' > n'_{\text{cr}}$ )). The high value of  $\lambda_0 = 1.7$  limits the  ${}^3\text{He}$  ion energies and, consequently, the  ${}^3\text{He}$  ion pressure. This effect can be employed in high RF power experiments with bulk ion heating.

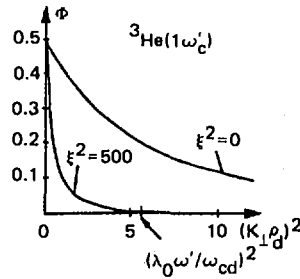


FIG. 6.  $\Phi(k_{\perp}\rho_d)$  versus  $k_{\perp}^2\rho_d^2$  ( $d$ -plasma with  ${}^3\text{He}$  minority ions at  $\omega = \omega'_c$ ,  $\lambda_0 = 1.75$ ).

To achieve the regime where the resonance  $\omega = \lambda\omega'_c$  is accessible at  $n' > n'_{cr}$ , it is necessary for the SW specific power flux to exceed the value

$$P_{RF} \gg P_{min} \sim \mathcal{R} r \langle \rho \rangle_{RF} \quad (16)$$

For  $P_{RF} < P_{min}$ , a stable steady state with accessible MICR zone is not possible.

When condition (16) is satisfied, two stable steady solutions to the above set of equations are possible, corresponding to Curve 2 (A regime) and to Curve 3 (B regime) of Fig. 4.

Which of the two regimes will materialize depends on the initial conditions. As an example, two temporal diagrams are presented in Fig. 7, showing how different regimes are realized. If the density  $n'$  ceases to increase before the value  $n' = n'_{cr}$  is reached where condition (16) holds, the B regime may well exist as a steady state. For  $n' > n'_{cr}$ , the RF power flux is not sufficient to maintain the B regime, and return to the A regime will occur. (Note that such a scheme of  ${}^{22}\text{Ne}$  isotope puffing was realized in ICF heating in T-10 [10].

### 3. TWO-COMPONENT THERMONUCLEAR REACTOR USING ICR HEATING WITH SLOW WAVES

#### 3.1. Formulation of the problem

In a two-component reactor [13-15], where in the  $d(t)$ -plasma, the non-equilibrium distribution function of minority ions  $t(d)$  is maintained with the help of external power sources, an important problem is to achieve a high power multiplication factor  $Q$ . In this context, it is most useful to employ  $\delta$ -function-type distributions,  $f'_0 \propto \delta(E - E_0)$ , with  $E = E_0$  corresponding to maximum  $Q$ .

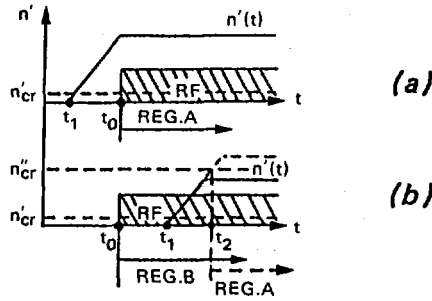


FIG. 7. Time behaviour of ion impurity puffing showing possibility of achieving A regime (cyclotron resonance zone for minority ions is not accessible to SW) and B regime (cyclotron resonance zone is accessible to SW).

For example, for  $T_i \leq 1$  keV and  $T_e \geq 40$  keV,

$$Q_{\max} = \frac{(\sigma v_{\alpha}^2)_{\max} m_{\beta} E_{\Delta}}{4\pi e^4 L} \quad E_{\Delta} = 22.4 \text{ MeV}, \quad \alpha = t(d) \\ \beta = d(t)$$

whence it follows that, for  $\alpha = d$ ,  $Q_{\max} = 8.2$  and for  $\alpha = t$ , we obtain  $Q_{\max} = 5.5$ . The distribution function of the d-ions for deuterium atoms injected into the t-plasma is similar to a  $\delta$ -function [14, 15]. In ICR heating of d-ions in the t-plasma with FMSW,  $f'_0 \propto \exp(-\alpha E)$  differs from the  $\delta$ -function essentially; therefore, the Q-factor is substantially lower [13].

Plateau formation due to high power SW and the MIDF tail cutoff provides a rather good approximation to the  $\delta$ -function, enabling high enough Q-values to be reached. Tail cutoff leads to a limitation of the impurity ion transverse pressure, permitting an increase of the specific thermonuclear power.

Regimes with absorption at the fundamental cyclotron frequency of deuterium minority ions in the t-plasma (1dt regime) and with absorption at the second harmonic of tritium minority ions in the d-plasma (2td regime) can be implemented with the help of high power SW.

Consider the following basic parameters  $Q$ ,  $p_{TN}$  and  $\tau'_E$ .

- (i) The Q-factor is the ratio of the specific power of the thermonuclear reaction accounting for neutron capture in the lithium blanket,  $p_{TN}$ , to the specific power required to maintain the non-Maxwellian distribution of minority ions and to heat the bulk plasma  $\langle p \rangle_{RF}$ ,

$$Q = p_{TN} / \langle p \rangle_{RF} \quad (17)$$

$$p_{TN} = n_d n_e \langle \sigma v \rangle_{RF} E_{\Delta} = n'_t n_e \langle \sigma v \rangle_{RF} E_{\Delta} \quad (18)$$

$$\langle \sigma v \rangle_{RF} = \frac{2}{\sqrt{\pi}} \frac{V_{Ti}}{\int u f'_0 du} \int_0^\infty f'_0(u) du \int_0^\infty e^{-u'^2} u' du' \int_0^1 \sigma[y(u, u')] y(u, u') (u' + u - u'd) \quad (19)$$

where  $y = (u' + u - |u' - u|t + |u - u'|)$ ,  $\sigma$  is the  $d + t$  reaction cross-section at relative velocity,  $\langle \sigma v \rangle_{RF}$  is the value of  $\sigma v$  averaged over the distribution functions of bulk particles with a Maxwellian distribution of temperature  $T$  and of the resonant minority ions. With (19), we obtain

$$Q = \frac{\langle \sigma v \rangle_{RF} E_\Delta T^{1/2} m_i^{1/2}}{\sqrt{8} \pi e^4 L F(\lambda_0, \xi^2)} \quad (20)$$

- (ii) The maximum value  $p_{TN} = p_{max}$ , which is reached for  $n_i$  and  $n'$  corresponding to the limiting plasma pressure  $p_L = \max(n_e + n_i + n'W_L)T = \beta_{max} B_0^2/8$  determined by the equilibrium and stability conditions

$$n_i = \frac{p_L}{4T}, \quad n' = \frac{2n_i}{1+W_L} \quad (21)$$

is given by

$$p_{max} = \frac{\langle \sigma v \rangle_{RF} E_\Delta}{8(1+W_L)T^2} p_L^2 \equiv \eta p_L^2 \quad (22)$$

In a conventional reactor ( $n_t = n_d = 0.5 n_e$ ):

$$p_{max}^{(o)} = \frac{\langle \sigma v \rangle_o E_\Delta}{16T^2} \equiv \eta_o p_L^2 \quad (p_L = 2n_e T) \quad (23)$$

- (iii) The energy confinement time  $\tau_E$  in the steady regime is given by

$$\tau_E' \equiv \frac{(n_e + n_i + n')T}{\langle p \rangle_{RF} + p_\alpha} \quad (24)$$

where  $p_\alpha = 3.5 p_{TN}/22.4 = 0.156 p_{TN}$  is the specific power heating the plasma by  $\alpha$ -particle deceleration. Assuming  $n'$  to be optimum (21) and Coulomb collisions to be the main source of energy losses for fast ions, we obtain

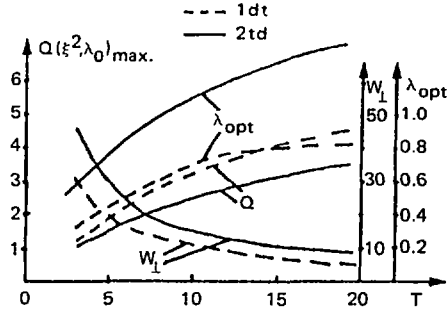


FIG. 8. Maximum  $Q(\xi^2, \lambda_0)$ ,  $W_{\perp}$  and  $\lambda_{\text{opt}}$  versus  $T$  for 1dt and 2dt regimes.

$$\tau_E' = \frac{2n_i(3+W_{\perp})T}{(1+W_{\perp})(\langle p \rangle_{RF} + 0.156\rho_{TN})} = \frac{12.8(3+W_{\perp})Qn_iT}{(1+W_{\perp})\rho_{TN}(6.4+Q)} \quad (25)$$

We now introduce a parameter

$$\alpha = \tau_E^0 / \tau_E' \quad (26)$$

where  $\tau_E^0 = 12.6 n_e T / p_{TN}^0$  is the energy confinement time in a conventional reactor ( $n_d = n_t$ ;  $T_t = T_d = T$ ) and a parameter  $\alpha_{\min} = \tau_{E\min}^0 / \tau_E'$  where  $\tau_{E\min}^0 = 12.6 n_e T_{\text{opt}} / p_{TN}^0$  is the minimum value of  $\tau_E^0$  for given  $p_{\max}$  ( $T = T_{\text{opt}}$  corresponds to the maximum  $\langle \sigma v \rangle_0 / T^2$ ). The parameter  $\alpha$  describes the decrease in  $\tau_E'$  compared to  $\tau_E^0$  at the same values of  $T$ , and the parameter  $\alpha_{\min}$  corresponds to the case where the thermal conductivity does not depend on  $T$  and the value of  $T = T_{\text{opt}}$  for a conventional reactor regime is chosen for minimum  $\tau_E^0$  at fixed  $p_{\perp}$ . From (24) and (25), it follows that

$$\alpha(T') = \frac{4}{3+W_{\perp}} \frac{\langle \sigma v \rangle_{RF}}{\langle \sigma v \rangle_0} \frac{6.4+Q}{Q}, \quad (T'=T) \quad (27)$$

$$\alpha_{\min}(T') = \frac{4}{3+W_{\perp}} \frac{6.4+Q}{Q} \frac{\langle \sigma v \rangle_{RF}}{T'^2} \frac{1}{(\langle \sigma v \rangle_0 / T^2)_{\max}} \quad (28)$$

where  $T'$  is the plasma temperature in a two-component reactor.

### 3.2. Q-factor optimization

In accordance with (20), the Q-factor depends on  $\lambda_0$  and  $\xi^2$ . Figure 8 shows Q as a function of  $T'$ ; for given  $T'$  the values of  $\lambda_0$  and  $\xi^2$  are chosen

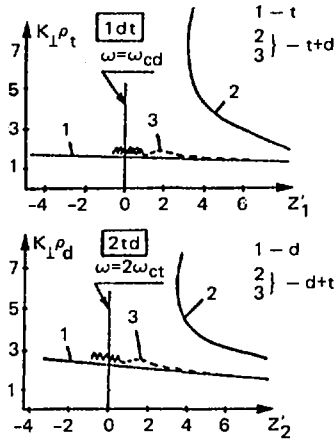


FIG. 9.  $k_{\perp}\rho_i$  versus  $Z'_l$  in the resonance region  $\omega = \omega'_c$  for 1dt regime (Curve 1: pure d-plasma, Curve 2: (t + d 15%)-plasma (A regime,  $\xi^2 = 150$ ), Curve 3: (t + d 15%)-plasma (B regime,  $\xi^2 = 150$ ) and for 2td regime (Curve 1: pure d-plasma, Curves 2 and 3: (d + t, 25%)-plasma,  $\xi^2 = 500$ );  $n_i = 10^{14} \text{ cm}^{-3}$ ,  $B_0 = 5T$ ,  $N_{\parallel} = 3$ .

such as to maximize  $Q$  which has maximum at  $\lambda_0 = \lambda_{\text{opt}}$  (Fig. 8). As is seen in Fig. 8, the  $Q$ -values for the 1dt regime are higher than for the 2td regime. Moreover, the latter has higher  $W_{\perp}$  values.  $\lambda_{\text{opt}}$  increases as  $T$  rises. It follows from (21) and the curve for  $W_{\perp}(T)$  that the optimum minority ion concentration is relatively high (10–30%).

### 3.3. Accessibility of cyclotron resonance region for d-ions in t-plasma and for t-ions in d-plasma

Although, to achieve the maximum  $Q$ -factor, one has to choose the optimum value for  $\lambda_0$ , the possibility of changing  $\lambda_0$  is, in reality, rather limited. (This can, e.g., be done by varying  $N_{\parallel}^2$  or using an additional ion impurity ( $^3\text{He}$  in the 1dt regime or  $\text{H}^+$  in the 2td regime)). Therefore, we shall below consider the simple case where the parameter  $\lambda_0$  corresponds to a value in the zone  $\omega = \omega_{\text{cd}}$  in pure t-plasma or to a value in the resonant zone  $\omega = 2\omega_{\text{ct}}$  in pure d-plasma. Obviously, such a situation prevails for low impurity concentrations ( $n' < n'_{\text{cr}}$ ) or high impurity concentrations in the B regime.

In Figure 9,  $k_{\perp}\rho_d$  versus  $Z'_l$  is plotted for pure d-plasma in the region  $\omega = \frac{4}{3}\omega_{\text{cd}}$  (resonance  $\omega = 2\omega'_c$  for t) and for pure t-plasma in the range  $\omega = \frac{3}{2}\omega_{\text{ct}}$  (resonance  $\omega = \omega'_c$  for d). As can be seen in Fig. 9, the values  $k_{\perp}^0\rho_i = 2.3$  ( $\lambda_0 = 3.45$ ) and  $k_{\perp}^0\rho_i = 1.76$  ( $\lambda_0 = 1.17$ ) are well in excess of the optimum values, especially for the 2td regime (see Fig. 8). A numerical analysis of the dispersion equation (1) shows that the MICR zone is only accessible at  $\xi^2 \rightarrow 0$  for low impurity ion concentrations ( $n'/n_i < 1\%$ ).

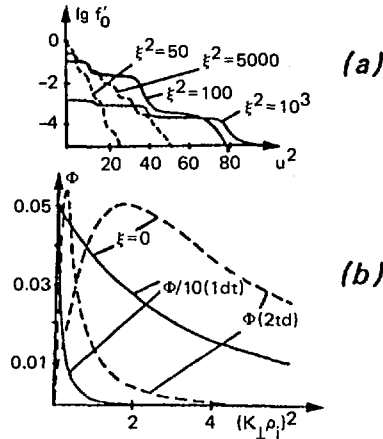


FIG. 10. (a)  $\lg f'_0$  versus  $u^2$ , (b)  $\Phi$  versus  $k_{\perp}^2 \rho_i^2$  for various  $\xi^2$  (solid line: 1dt regime,  $\lambda_0 = 3.45$ ; dotted line: 2dt regime,  $\lambda_0 = 1.14$ ).

Let us discuss the possibility of realizing the B regime at high impurity ion concentrations. As an example, Fig. 10 shows distribution functions  $f'_0(u)$  and functions  $\Phi(k_{\perp} \rho_i)$  for  $\lambda_0 = 1.17$  (1dt) and  $\lambda_0 = 3.45$  (2dt). It can be seen from Fig. 10 that the impurity ion contribution to the RF current is reduced by a factor of 200, only because of the decrease in  $\Phi(k_{\perp} \rho_i)$  at  $k_{\perp} \rho_i = \lambda_0 \omega_c / \omega_{ci}$  (the additional decrease in the minority ion RF current in the range  $Z_i \approx 1$  is due to the increase in  $T_{\parallel}^i$ ). The behaviour of  $k_{\perp} \rho_i$  in the B regime (see Fig. 9, broken line) is obtained from the solution to Eq. (1) taking into account  $\Phi(k_{\perp} \rho_i)$  (Fig. 10). Thus, because of a significant QL evolution of the MIDF, the  $Z_i^i$ -dependence of  $k_{\perp} \rho_i$  is close to the  $Z_i^i$  dependence of  $k_{\perp} \rho_i$  for  $n' \rightarrow 0$ , even for  $n' \gg n'_{cr}$ .

### 3.4. Analysis of reactor parameters

*1dt regime.* Temperature dependences of reactor parameters are shown in Fig. 11 for  $\lambda_0 = 1.17$ . The parameter  $\xi^2$  is chosen for maximum Q; therefore, the values of  $\eta$ ,  $\alpha$  and  $\alpha_{min}$  in Fig. 11 are somewhat lower than the corresponding optimized values. The Q-factor is now lower than at  $\lambda_0 = \lambda_{opt}$ . For  $T > 10$  keV,  $Q = 3-4$ , but in this region  $p_{TN} \approx p_{TN}^0$ , and we have lower  $\epsilon \tau_E$  ( $\alpha \approx \alpha_{min} \approx 3-10$ ). The principal advantages of this two-component regime are found at  $T \leq 10$  keV where  $\eta/\eta_0 \sim 3-5$  and  $\alpha > \alpha_{min} \geq 10$  though Q is not very high here,  $Q = 1.5-2.4$ . This region is of interest in view of its application in a hybrid reactor where the Q-factor can be increased five to ten times owing to the energy release in the uranium blanket [16] as well as in the neutron sources. In the region  $T = 5-10$  keV, the optimum concentration of deuterons is 14-25%.

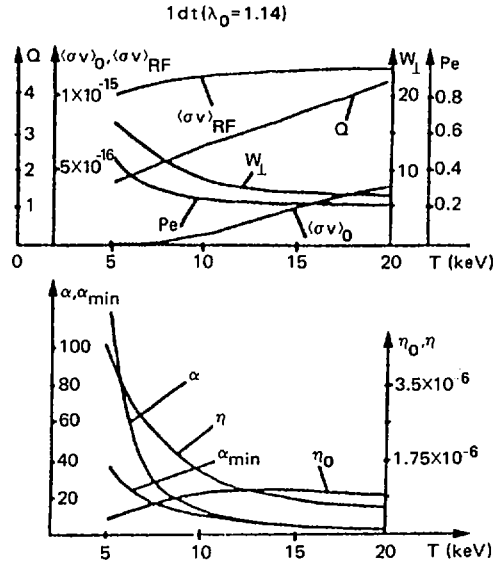


FIG. 11.  $\langle\sigma v\rangle_{RF}$ ,  $Q$ ,  $W_L$ ,  $p_e$ ,  $\alpha$ ,  $\alpha_{min}$  and  $\eta$  versus temperature for 1dt regime ( $\lambda_0 = 1.14$ ) and  $\langle\sigma v\rangle_0$  and  $\eta_0$  versus temperature for conventional regime.

*2td regime.* In this case, the parameters of the two-component reactor, e.g. Q-factor, are somewhat lower than for the 1td regime. This is, in particular, due to the high value of the parameter  $\lambda_0 = 3.45$ .

## REFERENCES

- [1] LONGINOV, A.V., STEPANOV, K.N., in Proc. All-Union Meeting Gorky, 1982, Inst. Prikl. Fiz. AN SSSR, Gorky (1983) 105.
- [2] LONGINOV, A.V., Zh. Tekh. Fiz. **42** (1972) 1591.
- [3] ONO, M., STIX, T.H., WONG, K.L., HORTON, R., in Heating in Toroidal Plasmas (Proc. 2nd Joint Varenna-Grenoble Int. Symp. Como, 1980), Vol. 1, CEC, Brussels (1980) 593.
- [4] KLIMA, R., LONGINOV, A.V., STEPANOV, K.N., Nucl. Fusion **15** (1975) 1157.
- [5] PERKINS, F., Nucl. Fusion **17** (1977) 1197.
- [6] SCHARER, J.E., MacVEY, B.D., MAU, T.K., in Theoretical and Experimental Aspects of Heating in Toroidal Plasmas (Proc. 3rd Int. Meeting Grenoble, 1976), Vol. 1 (1976) 79.
- [7] LONGINOV, A.V., STEPANOV, K.N., in Plasma Heating in Toroidal Systems (Proc. 4th Int. Symp. Rome, 1984), Vol. 1, (1984) 486.
- [8] LONGINOV, A.V., PAVLOV, S.S., STEPANOV, K.N., in Controlled Fusion and Plasma Physics (Proc. 12th Europ. Conf. Budapest, 1985), Part II, European Physical Society (1985) 132.

- [9] ALIKAEV, V.V., BEREZOVSKIY, E.L., VASIN, N.A., et al., *ibid.*, p. 156.
- [10] TFR GROUP, *ibid.*, p. 112.
- [11] LONGINOV, A.V., PAVLOV, S.S., STEPANOV, K.N., in *Controlled Fusion and Plasma Heating (Proc. 13th Europ. Conf. Schliersee, 1986)*, European Physical Society (1986) 107.
- [12] LONGINOV, A.V., PAVLOV, S.S., STEPANOV, K.N., *ibid.*, p. 141.
- [13] STIX, T.H., *Nucl. Fusion* **15** (1975) 737.
- [14] DAWSON, J.M., FURTH, H.P., TENNEY, F.H., *Phys. Rev. Lett.* **26** (1971) 1156.
- [15] PISTUNOVICH, V.I., *At. Ehnerg.* **35** (1973) 11.
- [16] KADOMTSEV, B.B., ORLOV, V.V., *Itogi Nauki i Tekhniki, Fizika Plazmy*, Vol. 6, Moscow (1985) 5 (in Russian).



## EFFECT OF x-POINT LOCATION ON EDGE CONFINEMENT IN DIVERTED TOKAMAKS

T. OHKAWA, F.L. HINTON  
GA Technologies Inc.,  
San Diego, California,  
United States of America

### Abstract

EFFECT OF x-POINT LOCATION ON EDGE CONFINEMENT IN DIVERTED TOKAMAKS.

The edge mirror physics mode in a diverted tokamak is shown to have good confinement properties. This mode is possible only if the x-point is located away from the outboard median plane so that a trapped ion population can exist near the separatrix. The H-mode has been found experimentally only in this case.

### 1. EDGE MIRROR PHYSICS

When the ion collisionality near the separatrix is low, the confinement properties of the edge region are essentially the same as in a mirror device [1,2]. Loss regions in velocity space exist, analogous to loss cones in mirrors, for ions inside the separatrix, as well as outside. These loss regions correspond to collisionless drift orbits which cross the separatrix, allowing ions to escape into the divertor. Small angle Coulomb scattering into these loss regions is the primary loss mechanism when the effective collision frequency is smaller than the bounce frequency and when turbulence is suppressed. All energy leaving the central region must pass through the edge, when charge exchange losses in the core are negligible. The edge region, within a few ion banana widths of the separatrix, is thus in series with the core or central region for ion energy transport. The edge can therefore form an effective barrier to energy flow in the ion channel.

The energy transport out of the edge region is purely convective, since energy is lost only when ions escape. Confinement is then simply particle confinement, just as when a plasma is surrounded by vacuum. Since electrons cannot escape in this manner from as far inside the separatrix as ions can, a negative radial electric field must be present, to partially hold the ions back. For ambipolarity, an anomalous value of the electron mobility is required, which is related, via the Einstein relation, to a diffusivity comparable to the ion thermal diffusivity, which is therefore comparable to the empirical electron thermal diffusivity, on the order of  $1 \text{ m}^2\text{sec}^{-1}$ .

When ions and electrons diffuse through the electric field in this region, the ions do work against the field, which does work on the electrons, so that thermal energy is transferred from ions to electrons. Thus, the electron thermal confinement is coupled to that of the ions. The global energy confinement time is proportional to the edge temperature, which can be kept high by keeping the neutral density low, as we shall now show.

The edge confinement time  $\tau_0$  is the time for an ion to scatter into a loss region, or roughly  $\tau_0 = \tau_{ii}\epsilon$ , where  $\tau_{ii}$  is the ion collision time and  $\epsilon$  is the inverse aspect ratio. Since the thickness of the edge layer is roughly an ion banana width, the volume of the edge region is  $V_0 = S\epsilon^{1/2}\rho_{ip}$ , where  $S$  is the plasma surface area and  $\rho_{ip}$  is the ion poloidal gyroradius. Assuming that the edge layer thickness is much smaller than the plasma radius, and assuming no confinement in the core, the confinement time is given by

$$\frac{nV}{\tau} = \Gamma = \frac{nV_0}{\tau_0}$$

where  $V \sim Sa/2$  is the plasma volume and  $\Gamma$  is the particle flux. Hence,

$$\tau \sim \tau_{ii} \frac{a}{2\rho_{ip}} \epsilon^{1/2}$$

or, using  $\epsilon = 1/3$ ,

$$n\tau = 1.5 \times 10^9 (T_i/e) I$$

For a given density, the confinement time is proportional to the edge temperature and to the current. For  $T_i = 1.5 \times 10^3$  eV and  $I = 5 \times 10^5$  Amp, for example, we have

$$n\tau \sim 10^{18} \text{ m}^{-3}\text{sec}$$

which is roughly the total confinement observed in H-mode experiments [3,4]. For an ignition device, with  $I = 10^7$  Amp and  $T_i = 2 \times 10^4$  eV, we obtain

$$n\tau \sim 3 \times 10^{20} \text{ m}^{-3}\text{sec}$$

Note that ignition occurs even without the benefit of core confinement.

The power throughput is

$$P = \frac{3nTV_0}{\tau_0}$$

or

$$P = 4.3 \times 10^{-28} n^2 V / I$$

which is independent of edge temperature. For  $V = 4 \text{ m}^3$  and  $I = 4 \times 10^5 \text{ Amp}$ , we have

$$P = 4.3 \times 10^5 (n \times 10^{-19})^2 \text{ watt}$$

which is roughly the heating power in the H-mode experiments. The heating power determines the density and not the temperature.

The particle throughput determines the temperature. Since the mirror loss is convective, the power throughput is related to the particle throughput  $\Gamma$  by

$$P = 3\Gamma T$$

If the beam fueling is insignificant, the particle flux is given by

$$\Gamma = S n_o v_o$$

where  $n_o$  is the neutral density outside the plasma,  $v_o$  is the average velocity of the neutral atoms, and it is assumed that the neutral atoms are ionized and heated before they are lost. The edge temperature is then given by

$$T/e = 4.4 \times 10^{-10} \frac{an^2}{In_o v_o}$$

For a given minor radius, plasma density, current, and neutral velocity, the edge temperature is inversely proportional to the neutral density. For  $a = 0.4$  m,  $I = 4 \times 10^5$  Amp,  $n = 3 \times 10^{19} \text{ m}^{-3}$ , and  $v_o = 10^3 \text{ m-sec}^{-1}$  we have  $T/e = 4 \times 10^{20} n_o^{-1}$ . An edge temperature of 1keV corresponds to about  $1 \times 10^{-5}$  torr of neutral atom pressure.

If there is fueling only from neutral beams, the temperature must rise to 1/3 the beam energy. This would be the ideal situation, with beam fueling, and only a small neutral density at the edge, so that the edge could be heated to increase the confinement time.

The edge temperature can be kept high if there is negligible cooling of ions by neutral atoms in the recycling process. One condition for this is that charge exchange does not dominate the ion energy losses in the edge. The charge exchange time  $\tau_{cx}$  is given by

$$\tau_{cx} = \frac{1}{n_o^* \sigma_{cx} v_i}$$

where  $n_o^*$  is the neutral density in the plasma,  $\sigma_{cx}$  is the charge exchange cross section, and  $v_i$  is the ion thermal velocity. The condition that the charge exchange time is longer than the mirror loss time,  $\tau_{cx} > \tau_0$ , is

$$n_o^*/n < \frac{1.85 \times 10^{-16}}{\sigma_{cx}} (T/e)^2$$

For  $\sigma_{cx} = 10^{-19} \text{ m}^2$ , and  $T/e = 10^3$  v, we have

$$n_o^*/n < 1.85 \times 10^{-3}$$

For  $n = 2 \times 10^{19} \text{ m}^{-3}$  and  $n_o^* < 3.7 \times 10^{16} \text{ m}^{-3}$ , for example, this condition is satisfied.

Another condition for no cooling of ions in the edge by recycling is that the cold ions created by ionization in the edge are scattered into the loss regions before they are heated by the hot ions. The neutral atoms coming into the plasma edge are ionized by electron impact within a mean free path

$$\lambda_o = \frac{v_o}{n \sigma_{ion} v_e}$$

where  $\sigma_{\text{ion}}$  is the ionization cross-section and  $v_e$  is the electron thermal velocity. The cold ions produced by ionization are typically heated to a velocity  $v_c$  before they are scattered into the loss regions, where  $v_c$  is such that the ion banana width at that velocity equals the distance between their birth location and the separatrix. We estimate this distance to be about one ionization mean free path and obtain

$$\epsilon^{1/2} \frac{v_c}{\Omega_{\text{ip}}} \sim \lambda_o$$

where  $\Omega_{\text{ip}}$  is the ion poloidal gyrofrequency. For ion energy losses to be small, we want the velocity  $v_c$  to be less than the ion thermal velocity,  $v_c < v_i$ . This is the same as the condition that the mean free path be shorter than the ion banana width,

$$\lambda_o < \epsilon^{1/2} \rho_{\text{ip}}$$

For  $B_p = 0.2T$ ,  $T = 10^3$  eV,  $v_o = 10^3$  m · sec<sup>-1</sup>, and  $\sigma_{\text{ion}} = 10^{-21}$  m<sup>2</sup> we have  $n > 6 \times 10^{18}$  m<sup>-3</sup>. For the experimental parameters, therefore, the neutral density is attenuated in the edge region, and the cold ions are lost before they cool the edge.

Good mirror confinement at the edge is obtained in a window of the edge density. A high density shortens the mirror confinement, while at low density, the cold ions produced by the recycling process cool the edge. At sufficiently low density, charge exchange becomes the dominant loss.

The position of the x-point on the separatrix plays an important role in the mirror confinement. (We assume single-null operation, for simplicity.) It is necessary that a trapped-ion population exist, near the separatrix. But this requires that the effective collision frequency divided by bounce frequency,  $\nu_{*i} \equiv \nu_{ii}/(\omega_b \epsilon)$ , be small compared with unity. The bounce frequency  $\omega_b$  becomes very small for ions which pass near the x-point, since for them,

$$\omega_b \sim \epsilon^{1/2} v_i / R q_\psi$$

where  $q_\psi$  is the MHD safety factor, which becomes infinite at the separatrix. Such ions cannot be considered to be trapped long enough to contribute to the mirror confinement at the edge. Only those ions with turning points sufficiently close to the median plane, which are never

close to the x-point, play a role in the mirror confinement process. This restriction is effectively eliminated if the x-point is near the minimum major radius side of the separatrix, as in a "D" shape. In the other extreme case, when the x-point is on the outboard median plane, as in the JT-60 design, the trapped ion population is effectively eliminated near the separatrix. The beneficial effects of the mirror confined edge region would not be expected to be present in the latter case.

## 2. THE TRANSITION FROM A COLLISIONAL EDGE PLASMA TO A COLLISIONLESS ONE

The foregoing assumes a high enough edge ion temperature for the collisionality to be low,  $\nu_{*i} < 1$ . A threshold amount of power was needed to cause a transition from the L-mode to the H-mode in ASDEX [3], which was also a transition from  $\nu_{*i} > 1$  to  $\nu_{*i} < 1$ . In single null operation, the threshold power depended upon the location of the x-point, and was lower when the x-point was in the direction of the ion grad-B drift. A theoretical model which attempted to explain this was given previously [5], and the results will now be summarized.

We begin by considering the high-collisionality regime, since that is more appropriate for the L-mode. With single-null divertor operation, if the ion grad-B drift is toward the x-point, the Pfirsch-Schlüter parallel ion heat flow is away from the x-point. This heat flow adds to the parallel heat flow due to the lower temperature in the divertor, to give the net heat flow. The net heat flow into the divertor must equal the ion heat flow out of the plasma edge, assuming there are no other energy losses. The Pfirsch-Schlüter heat flow thus reduces the net heat flow into the divertor chamber, for the same ion temperature gradient  $\partial T_i / \partial r$ . Or, if the heat flow is given, the ion temperature gradient must be larger, due to the toroidal effect. We assume that a threshold  $\partial T_i / \partial r$  is required for the H-mode, which may be understood in terms of the need for the ions to be hot enough in the edge to be in the low collisionality regime. Then the threshold heating power for the H-mode is lower with this x-point location, than when the ion grad-B drift is away from the x-point. This effect has been clearly seen experimentally in ASDEX [6].

With double-null operation, the ion grad-B drift direction should not matter, because the effects of the two nulls cancel. Also, at higher heating power, the ion grad-B drift direction should not matter, because the ion loss occurs through banana orbit excursions, and is not

sensitive to null location. These predictions are also in agreement with experiment [6].

The location of the x-point thus plays an important role in the L- to H-mode transition. The favorable locations are above the median plane when the ion grad-B drift is up, and below the median plane, when the ion grad-B drift is down. An x-point on the median plane, as in the JT-60 design, would be expected to have no effect, favorable or unfavorable, just as with symmetric double null operation. In this case, the power threshold for the H-mode would be expected to be higher than with the favorable location.

### 3. SUMMARY

When the edge plasma is governed by the mirror physics we have described, confinement in a divertor tokamak has the following properties.

- (1) The global energy confinement time is proportional to the edge temperature and to the current, for a given density.
- (2) The edge density is determined by the heating power.
- (3) The edge temperature is determined by the particle throughput.
- (4) If the edge density is not too low, excessive cooling of the edge plasma by recycling can be avoided.

The edge mirror physics mode is possible only if the x-point is located away from the outboard median plane, so that a trapped ion population can exist near the separatrix. The transition from a collisional edge plasma to a collisionless one requires a lower heating power when the x-point is located away from the median plane, in the direction of the ion grad-B drift.

### REFERENCES

- [1] HINTON, F.L., CHU, M.S., Nucl. Fusion 25 (1985) 345.
- [2] OHKAWA, T., Combined confinement system applied to tokamaks (to be published in Kakuyugo Kenkyu).
- [3] WAGNER, F., et al., Phys. Rev. Lett. 49 (1982) 1408.
- [4] FONCK, R.J., et al., in Heating in Toroidal Plasmas (Proc. 4th Int. Symp. Rome, 1984), Vol. 1 (1984) 37.
- [5] HINTON, F.L., Nucl. Fusion 25 (1985) 1457.
- [6] WAGNER, F., et al., Nucl. Fusion 25 (1985) 1490.



**Session C**

**OPEN CONFINEMENT SYSTEMS**

## **Chairman of Session**

**Session C-I**

**D.D. RYUTOV**

**USSR**

*Papers C-I-4-1 and C-I-4-2*

*were presented by R. Itatani as Rapporteur*

**Session C-II (Posters)**

## TMX-U TANDEM MIRROR THERMAL BARRIER EXPERIMENTS\*

T.C. SIMONEN, S.L. ALLEN, D.E. BALDWIN, J.D. BARTER<sup>1</sup>,  
 L.V. BERZINS<sup>2</sup>, M.R. CARTER<sup>2</sup>, T.A. CASPER,  
 J.F. CLAUSER, F.H. COENSGEN, D.L. CORRELL,  
 W.F. CUMMINS, C.C. DAMM, G. DIMONTE<sup>1</sup>, B.H. FAILOR<sup>2</sup>,  
 S. FALABELLA<sup>2</sup>, J.H. FOOTE, T.K. FOWLER, A.H. FUTCH,  
 R.K. GOODMAN, D.P. GRUBB, D. HILL, E.B. HOOPER,  
 R.S. HORNADY, R.D. HORTON<sup>1</sup>, W.L. HSU<sup>3</sup>, B. HUFF<sup>1</sup>,  
 A.L. HUNT, R.A. JAMES, C.J. LASNIER<sup>4</sup>, C.A. LEAVITT<sup>1</sup>,  
 W.H. MEYER, J.M. MOLLER, A.W. MOLVIK, W.E. NEXSEN,  
 D.E. PERKINS, W.L. PICKLES, P.A. PINCOSY<sup>1</sup>,  
 G.D. PORTER, P. POULSEN, D.B. RESS, M. SHIHO<sup>5</sup>,  
 E.H. SILVER, B.W. STALLARD, W.C. TURNER,  
 R.D. WOOD, T.L. YU<sup>6</sup>  
 Lawrence Livermore National Laboratory,  
 University of California,  
 Livermore, California,  
 United States of America

### Abstract

#### TMX-U TANDEM MIRROR THERMAL BARRIER EXPERIMENTS.

Thermal barrier experiments have been carried out in the Tandem Mirror Experiment-Upgrade (TMX-U). Measurements of nonambipolar and ambipolar radial transport show that these transport processes, as well as end losses, can be controlled at modest densities and durations. Central cell heating methods using ion cyclotron heating and neutral beam injection have been demonstrated. Potential measurements with recently developed methods indicate that deep thermal barriers can be established.

### 1. INTRODUCTION

This paper describes thermal barrier experiments from the Tandem Mirror Experiment-Upgrade (TMX-U) using new heating systems and improved diagnostics aimed at improving our understanding of how tandem mirrors work. We can operate TMX-U

---

\* Work performed under the auspices of the United States Department of Energy by the Lawrence Livermore National Laboratory, under Contract No. W-7405-ENG-48.

<sup>1</sup> TRW, Inc., Redondo Beach, CA, USA.

<sup>2</sup> University of California, Davis, CA, USA.

<sup>3</sup> Sandia National Laboratories, Livermore, CA, USA.

<sup>4</sup> University of Maryland, College Park, MD, USA.

<sup>5</sup> Japan Atomic Energy Research Institute, Naka-machi, Naka-gun, Ibaraki-ken, Japan.

<sup>6</sup> Johns Hopkins University, Baltimore, MD, USA.

as a standard tandem mirror at densities near  $10^{13}$   $\text{cm}^{-3}$  and ion temperatures of 2 keV with 4 ms energy confinement time. However, we have concentrated our experiments on the thermal barrier mode which could scale to a reactor. In this mode, three processes limit the central-cell density. First is nonambipolar radial transport, second is ambipolar transport, and third is the loss of end plugging. When those three loss processes are controlled, the central-cell density increases at the ionization rate up to a maximum line averaged value of 1 to  $3 \times 10^{12}$   $\text{cm}^{-3}$ .

The purpose of the program of measurements presented here has been to improve our understanding of the above three processes in order to continue increasing the density toward the  $10^{13}$   $\text{cm}^{-3}$  theoretical maximum. Because of changes in funding priorities, for the present we will not be able to complete this program on TMX-U, but the work will be continued on the other tandem mirror facilities elsewhere, such as GAMMA-10, TARA and Phaedrus. However, we have made considerable progress, especially in understanding and controlling radial transport, which was of considerable concern in the past. Section 2 describes this work. The remaining sections deal with two topics related to understanding and controlling end losses. Section 3 summarizes our progress on central-cell heating and fueling by ICH and neutral beams, which ultimately control barrier filling. Section 4 describes our recent measurements of thermal barrier axial potential profiles.

TMX-U employs minimum-B, thermal barrier end plugs [1,2]. The 0.3 T nonaxisymmetric central cell is 8 m long, and is currently operated with a 24 cm radius limiter. The heating systems operate for a 75 ms duration. Ten of the 24 neutral injectors are located in the central cell and operate at either 2 or 20 kV. A total of fourteen 20 kV beams are used in the end plug as sloshing beams ( $47^\circ$  and  $40^\circ$ ) and as pump beams ( $18^\circ$  and  $24^\circ$ ). Two 200 kW, 28 GHz gyrotrons are used in each end cell. Two 200 kW transmitters drive separate ICH antennas at each end of the central cell, between which  $\text{D}_2$  gas is injected to provide fueling. The end-wall plasma potential control (PPC) plates [3] can operate either grounded or floating.

## 2. RADIAL TRANSPORT AND PARTICLE ACCOUNTABILITY

In TMX-U, nonambipolar radial transport is driven by the central-cell potential [4]. Recent experiments with grounded end walls indicate that the nonambipolar radial current depends on the plug sloshing beam current in addition to the plasma potential. (The two terms are comparable.) A portion of the sloshing ion loss is radial. To compare the central-cell transport with resonant neoclassical theory, we evaluate its nonambipolar confinement time by using regression analysis to

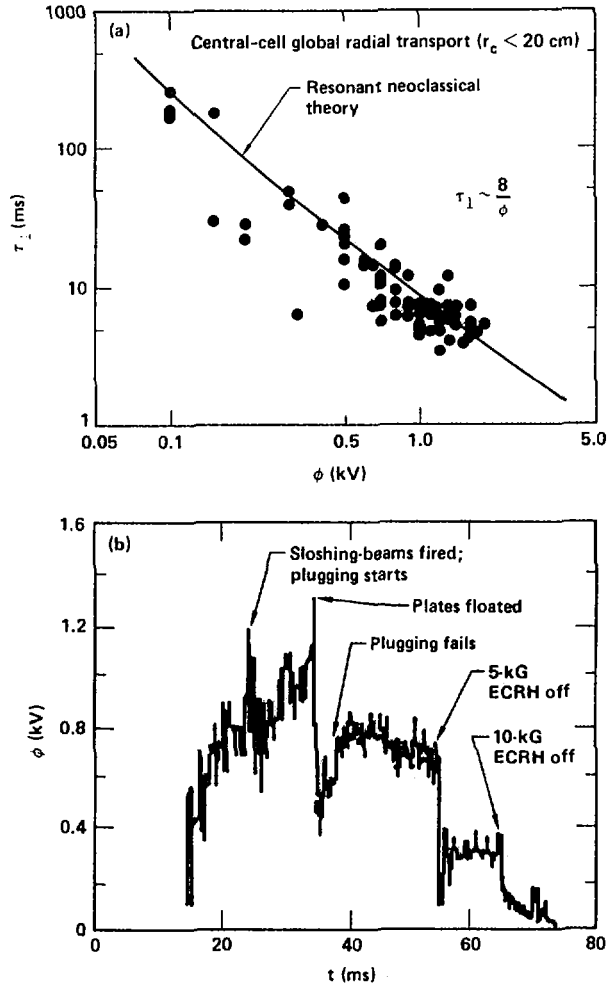


FIG. 1. (a) Variation of radial average central-cell nonambipolar radial transport time with plasma potential shows agreement with neoclassical theory. (b) Thallium ion beam probe measurements of the central-cell potential show a sharp decrease when the end walls are floated.

subtract the inferred radial sloshing ion current from the total measured net current. In Fig. 1a, the variation of  $\tau_{1, \text{LNA}}^{\text{CC}}$  with potential is compared with the theoretical prediction at  $r = 20$  cm, assuming  $T_{ic} \sim \phi/4$ . Good agreement is found in this radially averaged confinement time.

Nonambipolar transport has been significantly decreased by electrically floating segmented end PPC plates [3]. During plasma operation, the 26 plates on each end charge to a negative potential of 1 to 3 kV negative through  $10^4$  ohm resistors to grounds. Potential measurements have now demonstrated that the

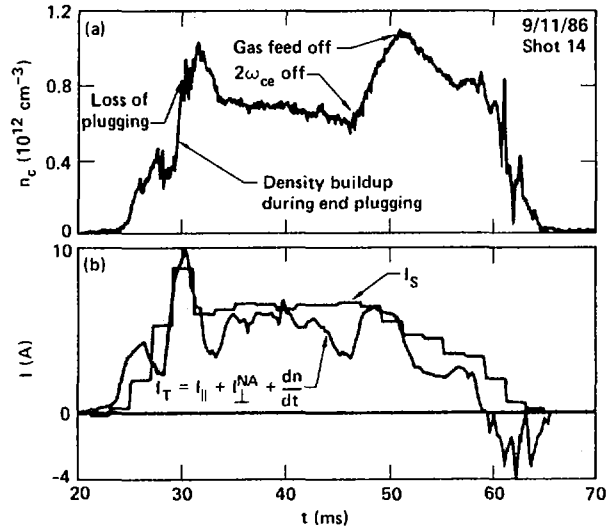


FIG. 2. Measurements of (a) central-cell density and (b) ionization current  $I_s$  and total measured loss current  $I_T$ . These measurements show that TMX-U can operate with small ambipolar losses.

end-wall plates reduce the central-cell plasma potential, confirming the conclusion deduced from the effect of the plates on the nonambipolar radial ion transport [1,3]. Figure 1b shows the time history of the central-cell potential during a discharge in which the plates were floated during plugging. The potential on-axis dropped from 1.1 to 0.5 kV with the plates floating. The plates usually drop twice as much below ground. In this shot, plugging failed 3 ms later and the potential partially recovered.

Since radial transport can occur independently in the central cell and the end cells, a low PPC plate net current does not guarantee small nonambipolar radial transport in the central cell nor does it indicate low ambipolar transport. Consequently, particle accountability is used to evaluate the amount of ambipolar radial transport in the plasma; here we consider the core of the plasma ( $r < 10$  cm). The ion particle balance equation is:

$$\frac{qdN}{dt} = I_s - I_{\parallel} - I_{\perp}^{NA} - I_{\perp}^A$$

where  $I_s$  is the core ionization source current determined from an absolutely calibrated imaging high-speed H-alpha camera system [5],  $I_{\parallel}$  is the axial ion loss current obtained from an array of Faraday cups,  $I_{\perp}^{NA}$  is the nonambipolar loss current measured by the end-wall PPC plates, and  $I_{\perp}^A$  is the residual (ambipolar) current required to balance the equation. Results of our measurements are shown in Fig. 2, which shows (a) the

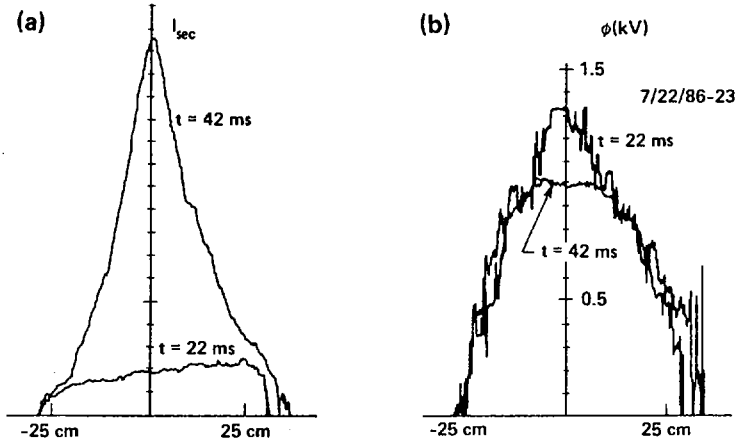


FIG. 3. Thallium ion-beam probe central-cell radial profiles of (a) secondary current (proportional to  $n_e \langle \sigma_v \rangle$ ) and (b) plasma potential. At 22 ms the plasma is plugged, but with large ambipolar transport, and at 42 ms the plasma is not plugged and ambipolar transport is small.

central-cell density and (b) a comparison between the measured core source  $I_s$  and the sum of the terms:  $I_T = (qdN/dt + I_I^{NA} + I_{||})$ . Between 25 to 30 ms, we have achieved plasma conditions with small axial losses and the PPC plates were floated ( $10^4$  ohms) to reduce nonambipolar radial losses. The total particle confinement time under these conditions is 10 ms. During this plugged period (25-30 ms) the density rises and is the main contribution to  $I_T$ . Later in this shot, we observe a discrepancy indicative of some ambipolar transport, which is reduced when the  $2\omega_{ce}$  electron cyclotron heating (ECH) is turned off. Under usual operating conditions,  $I_s$  and  $I_T$  agree to better than a factor of two, implying that ambipolar losses are no greater than the sum of the other losses. However, under some conditions of central-cell fueling and heating rates, we observe larger amounts of ambipolar transport usually accompanied by 2 to 7 kHz fluctuations.

Figure 3 shows the central-cell radial "density" (thallium ionization current) and potential profiles with and without significant ambipolar radial transport. At 22 ms, the measured (H-alpha) ambipolar transport is large and the radial "density" profile is flat. During this time the axial ion end losses are plugged and the radial potential profile is peaked. Later, at 42 ms, the measured ambipolar radial transport is small and the "density" profile is strongly peaked. At this time, axial plugging is weak and the potential profile is nearly constant in the plasma core. Such peaked density profiles are also measured during plugging, when the central-cell density increases.

### 3. CENTRAL-CELL HEATING AND FUELING

End plugging requires that the passing-ion thermal barrier collisional filling rate be reduced below the pumping rate. The filling rate should be reduced by ICH of the passing ions and by reducing the passing-ion density at the plug mirrors through anisotropic trapping in the central cell. Our previous experiments used gas fueling 2.25 m west of the central-cell midplane and a double half-turn loop 1.26 m west of the midplane. These resulted in efficient perpendicular heating of mirror-trapped ions to 2 keV but did not heat ions entering the west plug. Present experiments use a more symmetrical arrangement, with gas fueling near the central-cell midplane (0.25 m east) and double half-turn antennas toward both ends of the central cell. The ICH frequencies are selected for resonance between each antenna and the gas box so that newly ionized particles must pass through an ICH resonance before reaching an end cell. The increase in the parallel ion temperature with ICH power is similar at both ends, as shown in Fig. 4a. Using this ICH configuration, we increased the central-cell density to  $3 \times 10^{12} \text{ cm}^{-3}$  as shown in Fig. 4b. In this shot,  $T_{ec} = 90 \text{ eV}$  and  $T_{ic} = 160 \text{ eV}$ . During this operation, we achieved long axial and nonambipolar confinement times; however, low-frequency fluctuations driven by the ICH limited the ambipolar confinement time to 2 ms.

With 20 kV extraction voltage, the ten central-cell neutral beams inject 2.5 MW of power for heating and beta studies. These experiments were carried out in the standard tandem mirror operating mode rather than the thermal-barrier mode. At densities above  $10^{12} \text{ cm}^{-3}$ , the beam coupling to the low-energy ions increases, as indicated by the increase in  $T_{ii}$  shown in Fig. 5a. The average ion perpendicular energy for this operation was 2 keV. The average plasma beta increases to 6% at higher density and is limited by beam power.

With 2 kV extraction, low-energy neutral injection (LENI), the ten injectors are designed to fuel the central-cell plasma at densities above  $3 \times 10^{12} \text{ cm}^{-3}$  without gas fueling. Buildup calculations using the TREQ code predict that density buildup will require 170 atom-amp incident and 10 ms particle confinement time. In the experiments to date, the incident LENI beam current and particle confinement time are each a factor of 2 to 3 less than these levels, except for periods shorter than the required 20 ms buildup time. As a consequence, the density of the trapped beam ions increases to only  $4 \times 10^{11} \text{ cm}^{-3}$  with LENI beam injection. Thallium beam probe density measurements (Fig. 5b) and diamagnetic loop measurements (Fig. 5c) indicate that this could be a promising method of fueling the plasma core with modest energy ions. The emphasis of our present work is to understand and improve confinement while increasing the LENI beam current so that a higher plasma density can be sustained with the LENI beam system.

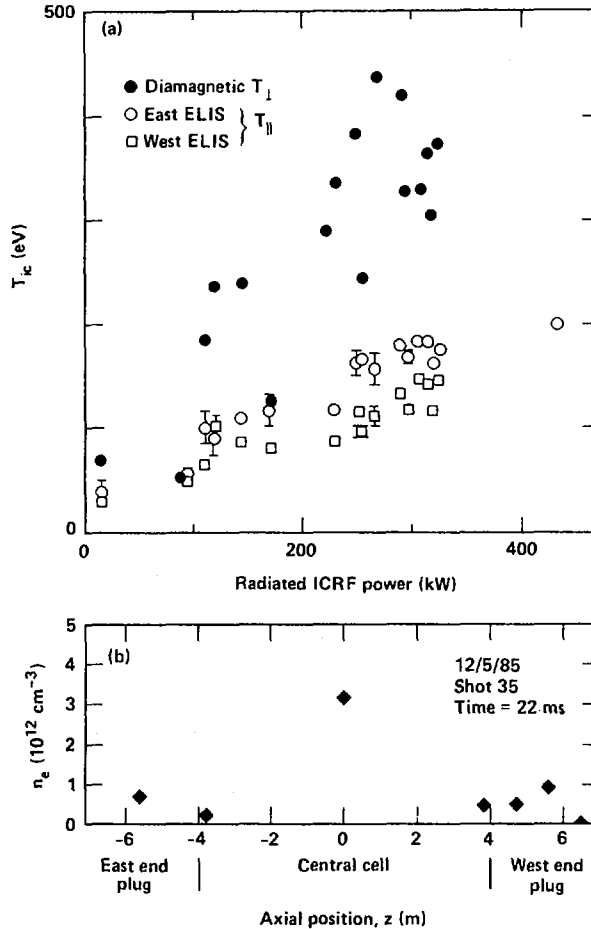


FIG. 4. (a) Measurements of ICRF heating with diamagnetic loop and end-loss spectrometer (ELIS). (b) Axial density profile during high density plugging using ICRF.

A very important question for tandem mirrors concerns the electron temperature that can be achieved with open field line geometry. Central-cell electron temperatures have reached 280 eV. As shown in Fig. 6, this temperature can be strongly correlated with the stored end-cell diamagnetic energy. The achievement of these electron temperatures is significant because it indicates the absence of very strong electron power losses along open field lines.

#### 4. AXIAL CONFINEMENT AND PLASMA POTENTIAL MEASUREMENTS

Past measurements of TMX-U axial plasma potential profiles were obtained during experiments with single-ended plugging.

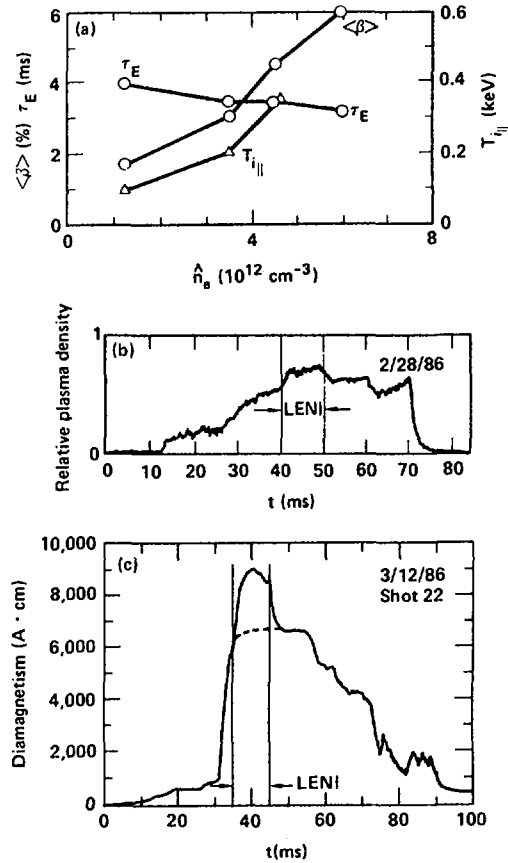


FIG. 5. Results of central-cell neutral-beam injection: (a) Average beta  $\langle\beta\rangle$ , parallel ion temperature  $T_{i\parallel}$  and diamagnetic energy confinement time  $\tau_E$ , as a function of on-axis electron density; 20 kV beams without strong end plugging are used. (b) With 2 kV LENI beams, the thallium ion-beam probe measures a small but encouraging increase in density. (c) The diamagnetic loop indicates an increase in the central-cell energy.

More recently, we have developed several new methods using particle beam probing to measure plasma potential in different axial locations with improved energy and temporal resolution and with redundancy. We conclude that thermal barriers as large as 0.75 kV are present in TMX-U.

We are currently carrying out measurements under various TMX-U operating conditions. An example of our recent thermal barrier region potential measurements is shown in Fig. 7. Figure 7a shows the thermal barrier potential measurements as a function of time. These are made by measuring the reflection energy of a  $24^\circ$  hydrogen pump beam with an end-loss ion spectrometer (ELIS) [6]. In this shot, the thermal barrier

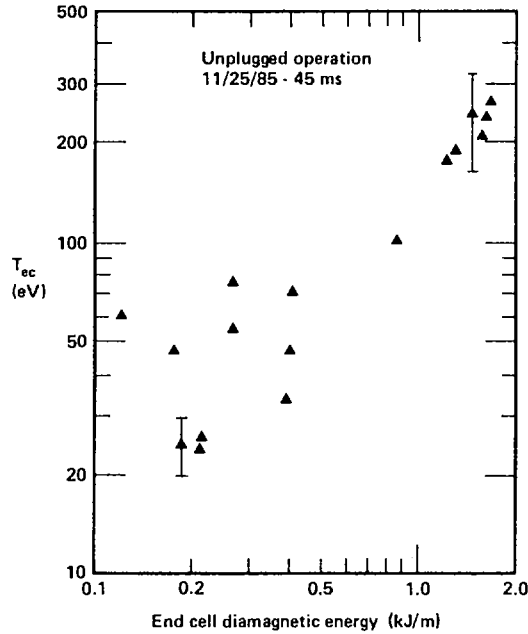


FIG. 6. High central-cell electron temperature measured by Thomson scattering, correlated with end-cell diamagnetic energy (or ECH power).

depth reaches 0.75 kV at 44 ms. The PPC end plates are grounded in this operation. Note that the thermal barrier depth rapidly decreases when the  $2 \omega_{ce}$  ECH is turned off. These measurements are localized along magnetic field lines, as indicated by the pump neutral beam footprints shown in Fig. 7b. Using these footprints to estimate spatial locations of the potential measurements, we have constructed the axial potential profile shown in Fig. 7c. The solid circle is measured with a thallium ion beam probe at  $z = 0$ . The solid square is from the centroid of the transmitted  $6F-18^\circ$  beam measurements and the open squares are from the energy spread in the transmitted signal assuming a monotonic decreasing potential. The solid diamond is from the centroid of the reflected  $2A-24^\circ$  pump beam and is arbitrarily located at the end-cell midplane. The barrier could be even deeper, since atoms ionized at that location would be trapped and not detected. The open diamonds are obtained from the centroid of the transmitted signal and are plotted symmetrically around the potential minimum. The bar indicates the ELIS energy range between the minimum energy detected and the energy of the maximum current. The open triangle is the calculated potential that provides the measured 13 ms axial confinement time. The measured barrier depth is 0.75 kV, much larger than the  $\pm 0.1$  kV uncertainties of this data.

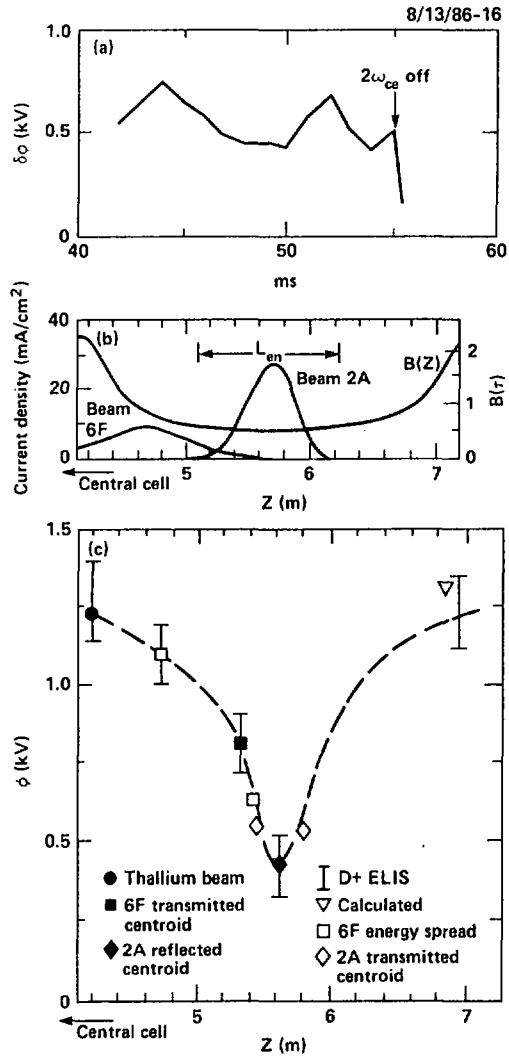


FIG. 7. (a) Simultaneous plasma potential measurements in the TMX-U thermal barrier region. (b) Axial locations of pump beam intersections with plasma and measured hot electron  $1/e$  diamagnetic length. (c) Axial potential profile constructed at 44 ms. The rise in the potential at 6.8 m is not measured directly by the ELIS but is indicated by the lack of density at the outer sloshing-ion turning point.

## 5. CONCLUSIONS

Thermal barrier experiments have been carried out in the TMX-U tandem mirror experiment. Measurements of nonambipolar and ambipolar radial transport show that these processes, as well as end losses, can be controlled at modest densities and durations. Central-cell heating methods using ICH and neutral-

beam injection have been demonstrated. Potential measurements with several recently developed methods indicate that deep (0.75 kV) thermal barriers can be established. These results provide encouragement to the prospect that the tandem mirror could be developed into an attractive reactor concept.

## REFERENCES

- [1] SIMONEN, T.C., et al., in Plasma Physics and Controlled Nuclear Fusion Research 1984 (Proc. 10th Int. Conf. London, 1984), Vol. 2, IAEA, Vienna (1985) 255.
- [2] GRUBB, D.P., et al., Phys. Rev. Lett. **53** (1984) 783.
- [3] HOOPER, E.B., et al., Phys. Fluids **27** (1984) 2264.
- [4] HOOPER, E.B., et al., Phys. Fluids **28** (1985) 3609.
- [5] ALLEN, S., et al., Rev. Sci. Instrum. **57** (1986) 2072.
- [6] FOOTE, J.H., Rev. Sci. Instrum. **57** (1986) 1786.

## DISCUSSION

T. CHO: With regard to the thermal barrier operation with  $3 \times 10^{12} \text{ cm}^{-3}$  in the central cell, I would like to ask the following. Is the ratio of the hot mirror trapped electron density to the total density consistent with the previous theory of thermal barrier potential formation?

T.C. SIMONEN: The ratio of mirror trapped electrons to total electrons was not measured during this operation. Under similar conditions we have determined this ratio to be about 40%. However, since the determination of it is very model-dependent, the uncertainties are as large as a factor of two. We cannot say with certainty whether this ratio is less than in the theory of thermal barrier potential formation.

T.N. TODD: You referred to central cell heating by ICH and 20 kV neutral-beam heating. What is the incremental energy confinement time, considering only the central cell energy and power input?

T.C. SIMONEN: The incremental central cell energy increase depends on the location of the gas puffing. For off-midplane gas puffing the increase is about 10 eV/kW. For midplane gas puffing the increase is about 1 eV/kW.

R.J. HAWRYLUK: What is the incremental confinement time with the application of auxiliary heating to the central cell?

T.C. SIMONEN: Depending on the location of gas puffing, the incremental central cell energy confinement time is 3 ms for off-midplane gas puffing, and 0.3 ms for midplane gas puffing.



## STUDIES OF POTENTIAL FORMATION AND TRANSPORT IN THE TANDEM MIRROR GAMMA 10

T. CHO, M. ICHIMURA, M. INUTAKE, K. ISHII,  
A. ITAKURA, I. KATANUMA, Y. KIWAMOTO, A. MASE,  
S. MIYOSHI, Y. NAKASHIMA, T. SAITO, K. SAWADA,  
D. TSUBOUCHI, N. YAMAGUCHI, K. YATSU

Plasma Research Centre,  
University of Tsukuba,  
Ibaraki-ken, Japan

### Abstract

STUDIES OF POTENTIAL FORMATION AND TRANSPORT IN THE TANDEM MIRROR GAMMA 10.

Experimental studies have been carried out on axial and radial transport in the tandem mirror GAMMA 10. It has been demonstrated that contributions of the thermal barrier enhance the selective heating of plug electrons and therefore increase the attainable ion confining potential, supporting strong plugging at both ends. The axial confinement time has reached 0.4 s for a central cell density of  $3 \times 10^{12} \text{ cm}^{-3}$ . The barrier decay mechanism has been found to be classical, so that the pumping requirements for steady state operation can be reduced by decreasing the collisionality of passing ions and local ionizations. Non-ambipolar radial transport has been observed to be consistent with neoclassical theory. The associated confinement time  $\tau_{\perp}^{NA}$  can be increased above 1 s by properly terminating the end plates.

### 1. THE GAMMA 10 DEVICE

GAMMA 10 is a thermal barrier tandem mirror with inboard minimum-B anchors flanking the central solenoid (see Fig. 1). At each end of the axisymmetric mirror cell an electron repelling thermal barrier potential dip and an ion confining plug potential hill are created by a combination of sloshing ion and hot and warm electron populations. To reduce resonant radial transport, the magnetic configuration is effectively axisymmetrized so that the drift orbits of confined ions form concentric circles in the central cell midplane [1-3]. At each end of the machine, radially and azimuthally segmented plates with resistors of  $1 \text{ M}\Omega$  are provided which terminate the loss fluxes of the plasma. The base pressure is kept below  $7 \times 10^{-6} \text{ Pa}$  and the pressure rise is limited to less than  $7 \times 10^{-5} \text{ Pa}$  during the plasma shot.

Key diagnostics in tandem mirrors are measurements of the potentials at cardinal points and of losses to the ends. The potentials  $\Phi_c$  at the central cell and  $\Phi_B$  at the thermal barrier midplane are directly measured with  $\text{Au}^0$  beam probes [4]. The amount of end losses and the plug potential  $\Phi_p$  are determined with radially scannable end loss analysers of a multigridded structure.

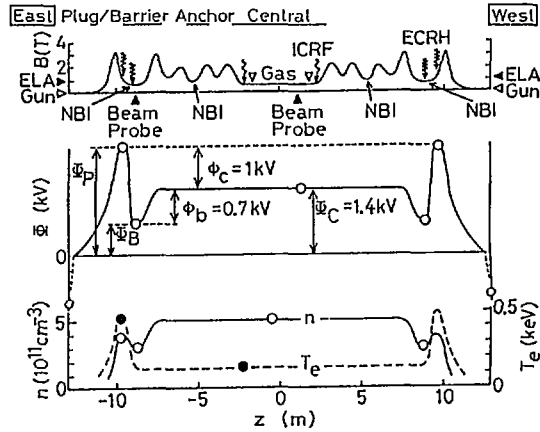


FIG. 1. GAMMA 10: Axial profiles of magnetic field strength and locations of heating sources and key diagnostics (top); potential distribution (middle); density and temperature profiles (bottom). ELA is end loss analysis.

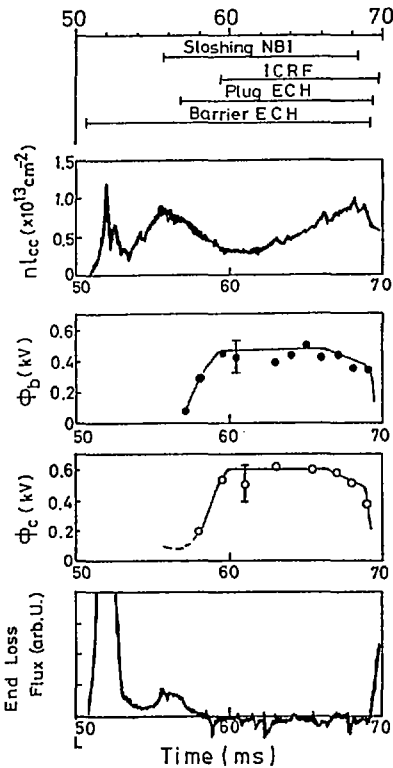


FIG. 2. Time evolution of central cell line density  $n_{lcc}$ , barrier depth  $\phi_b$ , confining potential  $\phi_c$  and end loss flux.

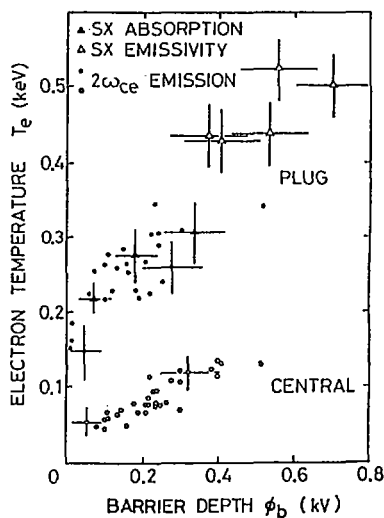


FIG. 3. Electron temperature as a function of thermal barrier depth  $\phi_b$ . The temperature  $T_{ep}$  at the plug is measured with the soft-X-ray absorption method ( $\blacktriangle$ ), the soft-X-ray emissivity method ( $\triangle$ ) and cyclotron emission at  $2\omega_{ce}$  ( $\bullet$ ). The temperature  $T_{ec}$  at the central cell is measured with  $2\omega_{ce}$  cyclotron emission at  $2\omega_{ce}$  ( $\circ$ ).

## 2. AXIAL TRANSPORT

### 2.1. Potential formation and plugging

The axially confining potential profile is created by a combination of neutral beams injected at  $41^\circ$  (25 kV, 70 A<sub>drain</sub>, two modules) and 28 GHz gyrotron power (<140 kW, four modules). The fast ion population forms the basis of the density distribution, with pitch-angle distribution peaking at  $41^\circ$ . The temperature of the hot electrons at the thermal barrier cells has been successfully controlled to below about 50 keV, as theoretically required by the flute stability criterion. The technique is based on relativistic detuning of overheated electrons according to the  $2\omega_{ce}$  ECH resonance condition; a spatially limited microwave beam power is injected dominantly in the x-mode [5].

On application of  $\omega_{ce}$  ECH at the 1 T point of the plug, the potentials  $\Phi_c$ ,  $\Phi_B$  and  $\Phi_p$  increase until the thermal barrier distribution  $\Phi_B < \Phi_c < \Phi_p$  is formed, while the potential of each end plate decreases. Figure 2 shows the time evolution of the potentials, the end losses and the line density at the central cell. A substantial reduction of the end losses (i.e. plugging) is observed in connection with the formation of the ion confining potential,  $\phi_c = \Phi_p - \Phi_c$ . A large confining potential is created when the thermal barrier depth,  $\phi_b = \Phi_c - \Phi_B$ , is large. The plugging becomes weaker when  $\phi_c$  decreases as  $\phi_b$  decays.

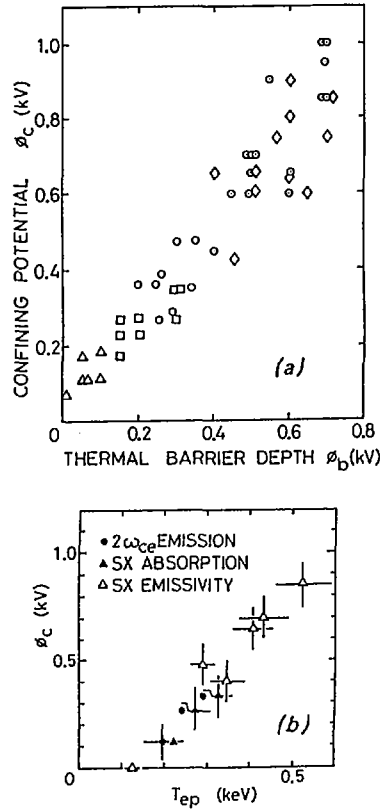


FIG. 4. (a) Confining potential  $\phi_c$  as a function of  $\phi_b$  for  $\omega_{ce}$  ECH powers of 20 kW ( $\Delta$ ), 40 kW ( $\square$ ) and 70 kW ( $\circ$ ), with other parameters kept unchanged and with  $n_{lcc} \sim 1 \times 10^{13} \text{ cm}^{-2}$ . The plots marked by  $\blacklozenge$  and  $\odot$  are those obtained with slightly lower density and in better vacuum conditions. (b) Confining potential  $\phi_c$  as a function of plug electron temperature  $T_{ep}$ , determined from cyclotron emission ( $\bullet$ ), the X-ray absorption method ( $\blacktriangle$ ) and the X-ray emissivity method ( $\triangle$ ).

Among the heating sources applied to the GAMMA 10 plasma,  $\omega_{ce}$  ECH has a dominant effect on the formation of the electron velocity distribution and therefore on the potential profile. The x-mode microwave beam, obliquely injected from the high field side, illuminates the 1 T resonant surface over a half-power width of about 5 cm. More than 90% absorption is estimated for one pass through the resonant surface according to microwave attenuation measurements. The electron temperature  $T_{ep}$ , determined at the plug from the soft-X-ray spectrum and the cyclotron emission, increases with increasing power of  $\omega_{ce}$  ECH. At the same time,  $T_{ep}$  is significantly influenced by the thermal barrier depth, as shown in Fig. 3. The electron temperature  $T_{ec}$  at the central cell does not increase so much as  $T_{ep}$  during the formation of the thermal barrier. This feature represents a reduction of thermal conduction across the thermal barrier.

The maximum attainable confining potential  $\phi_c$  increases with increasing  $\phi_b$ , as shown in Fig. 4(a). Here the  $\omega_{ce}$  ECH power is varied, with the plasma density kept nearly constant for the plots indicated by  $\Delta$ ,  $\square$  and  $\circ$ . The increase of  $\phi_c$  is well correlated with the increase in  $T_{ep}$ , as shown in Fig. 4(b). An advantage of the installation of the thermal barrier is the efficient creation of a confining potential. In the presence of the thermal barrier, the confining potential can be established with a plug density  $n_p$  lower than the central cell density  $n_c$ . It has been observed that the axial particle confinement time  $\tau_1$ , defined as the total number of ions confined in a core flux tube ( $r_c < 10$  cm at the central cell midplane) divided by the end loss fluxes, is in agreement with the theoretical prediction of the Pastukhov scaling formula [3]. For an ICRF heated plasma of  $T_{i\perp} = 1.7$  keV and  $T_{i\parallel} = (0.2-0.3)$  keV,  $\tau_1 = 0.4$  s has been obtained at  $n_c = 3 \times 10^{12}$  cm $^{-3}$ .

The observed depth  $\phi_b$  of the thermal barrier potential is normally larger than  $T_{ec} \ln [n_c/(n_b - n_{bh})]$ . One possible explanation for this, derived from our Fokker-Planck code simulation [6], is that the velocity distribution of low energy electrons at the barrier is distorted from Maxwellian under strong  $2\omega_{ce}$  ECH fields so that the density of the mirror trapped electrons is larger than the measured hot electron density  $n_{bh}$ . The simulation predicts an effective reduction of the thermal electron density by a factor of 1.5-1.8. Experimental evidence from the energy analysis of end loss electrons suggests the production of an abundant population of mirror trapped warm electrons.

## 2.2. Thermal barrier duration

In examinations of the feasibility of steady state operation of tandem mirror reactors, one of the fundamental problems is the evaluation of the decay rate of the thermal barrier potential. Collisional trapping of passing ions from the central cell

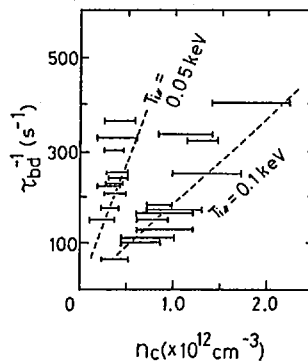


FIG. 5. Duration of thermal barrier,  $\tau_{bd}$ , plotted as a function of central cell density  $n_c$ . The dotted lines are best fits to the data of two cases, with  $T_{i\parallel} = 0.05$  keV,  $n_b = (3-6) \times 10^{11}$  cm $^{-3}$ , and  $T_{i\parallel} = 0.1$  keV,  $n_b = \sim 7 \times 10^{11}$  cm $^{-3}$ .

and local ionizations are conceivable classical processes which tend to weaken the potential dip. Without pumping, the decay rate, or equivalently the required pumping rate for steady state operation, is related to the duration of the barrier potential. In Fig. 5, the inverse of the observed duration of the thermal barrier,  $\tau_{bd}^{-1}$ , is plotted as a function of the central cell density  $n_c$  for different passing ion temperatures,  $T_{i||} = 0.05$  keV and 0.1 keV, and barrier densities,  $n_b = (3-6) \times 10^{11} \text{ cm}^{-3}$  and about  $7 \times 10^{11} \text{ cm}^{-3}$ . These values can be represented by a fitting equation

$$\tau_{bd}^{-1} = 6.0 \times 10^{-12} n_c T_{i||}^{-3/2}$$

This expression is in very good agreement with the theoretically predicted collisional barrier filling rate of passing ions,

$$\nu_b = (3.2-6.4) \times 10^{-12} n_c T_{i||}^{-3/2}$$

derived from the classical Futch-LoDestro formula. Also, it has been observed that  $\tau_{bd}^{-1}$  increases linearly with  $n_b T_{i||}^{-3/2}$  for relatively low  $n_b$  if  $n_c$  is kept nearly constant. These observations indicate that the decay of the thermal barrier is mainly due to classical processes. The required rate for barrier pumping can be reduced by decreasing the collisionality of the passing ions and by reducing the local neutral density.

### 3. RADIAL TRANSPORT

Radial transport inherent in an open system is of a non-ambipolar nature, as predicted by neoclassical theory, which means that the quadrupole magnetic field causes enhanced radial transport of ions in relation to electrons. The charge balance condition requires an excess flow of electrons to the ends. Since the non-ambipolar particle flux is measurable in terms of a net current flowing into the end plates, the associated confinement time  $\tau_{\perp}^{NA}$  can be determined in a similar manner as  $\tau_{||}$  [7].

When the end plates are forced to be short-circuited to the machine wall, an empirical relation of  $\tau_{\perp}^{NA} \propto \Phi_c^{-1}$  is obtained [3]. The observed  $\Phi_c^{-1}$  dependence is consistent with that predicted by neoclassical theory, but the value of  $\tau_{\perp}^{NA}$  is smaller by a factor of two to three.

On the other hand, in the normal mode of operation of GAMMA 10, the end plates are terminated by resistors of 1 M $\Omega$ . Measurements of  $\tau_{\perp}^{NA}$  have been made for different resistances  $R_{EP}$  grounding each segment of the plates to the machine (see Fig. 6). As  $R_{EP}$  is increased from 1  $\Omega$  to 1.135 M $\Omega$ ,  $\tau_{\perp}^{NA}$  increases from about 10 ms to above 1 s, and the central cell potential  $\Phi_c$  decreases from 2 kV to 0.6 kV, allowing for a change in  $n_c$  of within a factor of three. In the relatively narrow range of  $\Phi_c$  observed,  $\tau_{\perp}^{NA}$  is proportional to  $\Phi_c^{-\alpha}$ , with  $\alpha$  varying from 1 to 2 for  $R_{EP} < 135 \text{ k}\Omega$ . When  $R_{EP} = 1.135 \text{ M}\Omega$ ,  $\tau_{\perp}^{NA}$  is poorly correlated with  $\Phi_c$ , but a clear correlation between  $\tau_{\perp}^{NA}$  and  $n_c^2$  is observed. A full theoretical explanation is

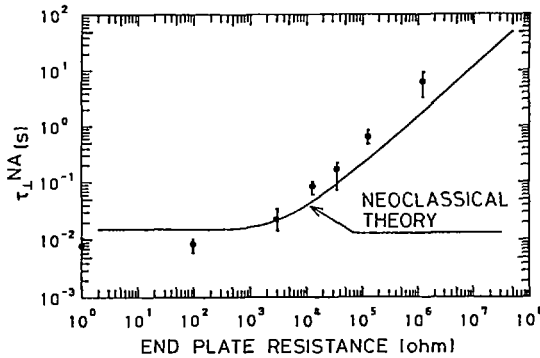


FIG. 6. Non-ambipolar confinement time,  $\tau_{\perp}^{NA}$ , as a function of termination resistance of each end plate segment. The black circles represent the experimental data and the solid line indicates the result of neoclassical calculations.

not available yet, but it can be said that this correlation is favourable for increasing the plasma density. A neoclassical calculation has been carried out with a simplified model in which the end plates form one plate which is grounded to the machine through a variable resistance. The radial profile of the potential is self-consistently calculated by using previously determined neoclassical transport coefficients. The result of the calculation is shown by the solid line in Fig. 6. The good agreement between the theoretical and experimental results indicates the validity of the neoclassical treatment of radial transport in GAMMA 10. These results also indicate that non-ambipolar radial transport can be effectively suppressed in GAMMA 10 by increasing the terminating impedance of the end plates.

#### 4. CONCLUSION

Efficient formation of a confining potential in connection with a thermal barrier has been realized. The confinement time is improved by more than two orders of magnitude over that of a single mirror. It has been confirmed that the axial particle confinement time is in good agreement with the Pastukhov scaling formula. The observed duration of the thermal barrier indicates that the barrier pumping requirements for steady state operation can be determined from classical scaling, including collisional and ionization processes. The non-ambipolar radial transport is observed to be consistent with neoclassical theory.

#### REFERENCES

- [1] MIYOSHI, S., et al., Selected Lectures Presented at Spring College on Fusion Energy, Trieste, 1981, International Centre for Theoretical Physics, Trieste (1982) 239.

- [2] CHO, T., ICHIMURA, M., INUTAKE, M., et al., in Plasma Physics and Controlled Nuclear Fusion Research 1984 (Proc. 10th Int. Conf. London, 1984), Vol. 2, IAEA, Vienna (1985) 275.
- [3] INUTAKE, M., et al., Phys. Rev. Lett. **55** (1985) 939.
- [4] ISHII, K., et al., Rev. Sci. Instrum. **56** (1985) 1053.
- [5] KIWAMOTO, Y., et al., Phys. Fluids **29** (1986).
- [6] KATANUMA, I., et al., Phys. Fluids **29** (1986) 4138.
- [7] HOOPER, E.B., et al., Phys. Fluids **28** (1985) 3609.

## DISCUSSION

R.S. POST: I would like to ask two questions. First, referring to what you said about confinement times, could you say whether  $\tau = 0.4$  s corresponds to particle confinement or energy confinement? Second, if you take the quoted values for  $\tau_{p\parallel}$  and  $\tau_{p\perp}$  together, does that give you an energy confinement time consistent with the measured values?

Y. KIWAMOTO: The quoted value of  $\tau = 0.4$  s corresponds to the particle confinement time.

The energy confinement time  $\tau_{Ei}$  was estimated from the decay time,  $\tau_{Decay}^{DM}$ , of the central cell diamagnetism after turning off the low power ICRH. We subtracted the charge exchange rate  $1/\tau_{cx}$  from the decay rate  $1/\tau_{Decay}^{DM}$ , since the charge exchange process ultimately poses minimal technical problems.

The neutral density, which was obtained from both the  $H_{\alpha}$  measurement and the neutral pressure measurement, has been consistently used in the evaluations of  $\tau_p$  and  $\tau_{Ei}$ .

T.C. SIMONEN: You describe new results at a density of  $8 \times 10^{12}$  cm<sup>-3</sup>. What was the duration of the strong axial confinement and how did you start and operate these plasma experiments?

Y. KIWAMOTO: The startup and operation sequence is somewhat different from the standard mode. The magnitude of the central cell magnetic field is 55% of the standard value and the central cell plasma is sustained by ICRF. The duration of strong plugging is 10 ms, which corresponds to the width of the plug ECH pulse.

## RECENT RESULTS FROM THE TARA TANDEM MIRROR AND THE CONSTANCE-B MIRROR\*

R.S. POST, K. BRAU, J. CASEY, X. CHEN,  
J. COLEMAN, H.R. GARNER, M. GERVER,  
S. GOLOVATO, D. GOODMAN, W. GUSS, S. HIROE<sup>1</sup>,  
S. HOKIN, S. HORNE, J. IRBY, J. KESNER, B. LANE,  
T. MORAN, L. PÓCS<sup>2</sup>, E. SEVILLANO, D. SMATLAK,  
D.K. SMITH, J. SULLIVAN, R.P. TORTI, X.Z. YAO<sup>3</sup>  
Plasma Fusion Center,  
Massachusetts Institute of Technology,  
Cambridge, Massachusetts,  
United States of America

### Abstract

#### RECENT RESULTS FROM THE TARA TANDEM MIRROR AND THE CONSTANCE-B MIRROR.

The Tara tandem mirror program has studied anchor and ponderomotive stabilization, axicell plugging with ECH and ICRF, sloshing ion buildup in the axicells, and halo formation and stabilization by an axisymmetric divertor. Central cell plasma parameters achieved by midplane fueling and slow wave ICRF heating from a local magnetic hill are  $\beta = 1.2\%$ ,  $n_e = 3 \times 10^{12} \text{ cm}^{-3}$ . The plasma is stabilized both by anchor ion  $\beta$  and by ponderomotive stabilization with the central cell ICRF in combination with a magnetic divertor, realizing a completely axisymmetric configuration. Anchor ICRF creates non-Boltzmann potential plugging of central cell ions. Neutral beam injection establishes a sloshing ion distribution for a cold dense cell stream; the hot ion confinement is classical and dominated by electron drag. Axicell ECH plugging experiments lead to near total reduction in endloss, but also to a decrease in the central cell density, indicating increased radial losses. Single ended ECH plugging shows no increase in opposite endloss. Single-ended plugging with axicell ICRF produces 50% reduction in ion endloss, with about half of the reflected ions observed in the opposite endloss. In the Constance-B quadrupole mirror the hot electron pressure profile is peaked off-axis and has the shape of a baseball seam.

---

\* Funded by the United States Department of Energy, under Contract No. DE-AC02-78ET51013.

<sup>1</sup> Oak Ridge National Laboratory, Oak Ridge, TN, USA.

<sup>2</sup> Central Research Institute for Physics, Budapest, Hungary.

<sup>3</sup> Institute of Physics, Beijing, China.

## Central Cell Startup

ICRF heating and midplane gas fueling on a magnetic hill are used to create the startup plasma<sup>1,2</sup> (fig. 1). Figure 2 is a plot of the axial density profile with slot antenna heating only indicating the presence of mirror-trapped ions in the two central cell magnetic wells. Assuming flat temperature profiles, and measured parabolic density profiles typical on-axis parameters in the magnetic well closest to the slot antenna are  $n_{e0} = 3 - 4 \times 10^{12} \text{cm}^{-3}$ ,  $T_{i\perp} = 700 \text{ eV}$ ,  $T_{i\parallel} = 150 \text{ eV}$ , and  $T_e = 60 - 80 \text{ eV}$ .

Stability of the central cell plasma to flute-like fluctuations is obtained by creating average minimum-B with an ICRF heated anchor plasma, or by the use of high power central cell ICRF heating. In discharges where the anchor ICRF is terminated well before the slot antenna, the central cell plasma remains stable at sufficient slot antenna power, which suggests ponderomotive stabilization. The anchor ICRF creates non-Boltzmann potentials<sup>3,4</sup> that plug the central cell stream.

In fig. 3 the central cell diamagnetism and line density, and total endloss currents are plotted for a discharge where the anchor ICRF is off at 20 msec and back on at 40 msec. During anchor ICRF the total ion endloss is reduced, while the total net current indicates increased ion radial transport. Assuming the rise in central cell density to be caused by reflected ions, the reflected current is about 10 A, in agreement with the drop in ion endloss in the core ( $r < a/2$ ) plasma. Ions reflected near the edge are subject to substantial radial losses and thus do not contribute to the central cell density rise. Pressure rises are observed in the transition region between the axicell and anchor, where the ion radial drifts are largest. These losses maintain a low density in the transition and are an example of passive pumping.<sup>5</sup>

## Axicell Sloshing Ion Formation by Neutral Beam Injection

Three Berkeley-type injectors per axicell together provide 70 A atomic on target at about 11 kV average energy. The 40° injection angle results in a sloshing ion distribution peaked at a mirror ratio of about 2.4. A doubling of the density can be observed throughout the machine under conditions of low central cell ICRF power and high gas feed, which produces a cold, dense plasma stream to the plug. Figure 4 shows the data

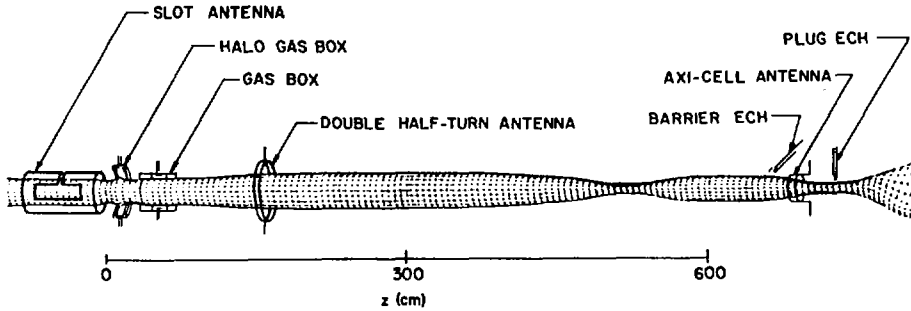


FIG. 1. Schematic of Tara magnetic geometry, heating and fueling systems for north central cell and axicell, and part of south central cell (anchors not shown). Tara is symmetric about midplane divertor except for central gas box and slot antenna.

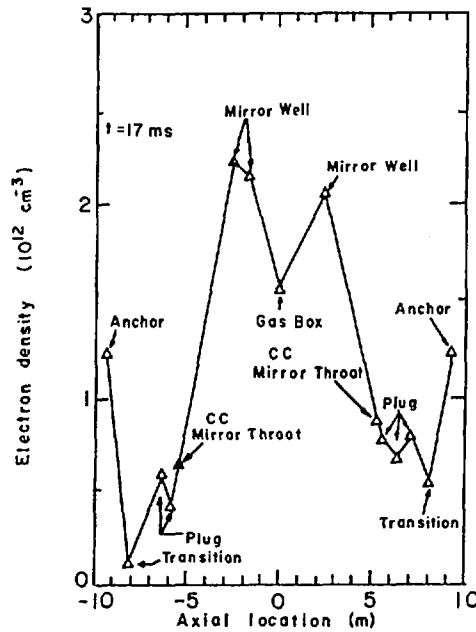


FIG. 2. Axial profile of line averaged central cell density during slot antenna heating.

from a particular shot. The diamagnetism and line density at the plug midplane increase; the mirror peak line density also increases because of the higher ionization rate due to increased  $T_e$ . An energetic ( $> 600$  eV) ion component is observed in the endloss current. The ion confinement can be calculated from the interferometer and endloss data. From the decay

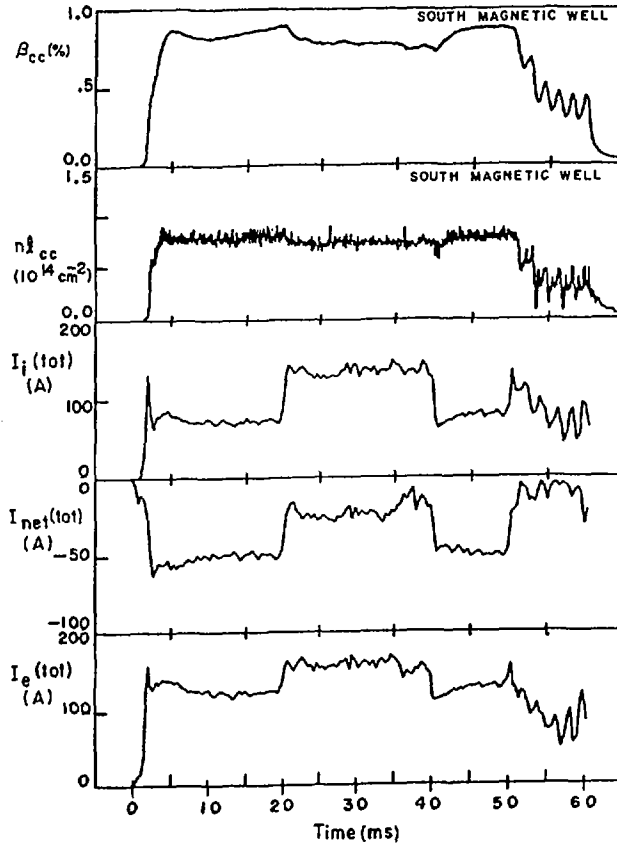


FIG. 3. Central cell  $\beta$  and density, total ion, net, and electron endloss currents for a discharge with central cell slot antenna heating. Anchor RF on from 0 to 20 ms and 40 to 55 ms.

of the diamagnetic loop signal after beam turnoff and endloss measurements of the potential we conclude that  $T_e \sim 20\text{eV}$  and that sloshing ion confinement is nearly classical and is dominated by electron drag. Under conditions given above of higher central cell heating power and lower gas feed the sloshing ion buildup is much lower than expected based on  $T_e$ , the measured edge neutral gas pressure and target density, and assuming classical confinement.

### End Plugging with Gyrotron Heating

Each axicell is equipped with two gyrotron ECH systems at 28 GHz, for fundamental and second harmonic heating. Each antenna typically

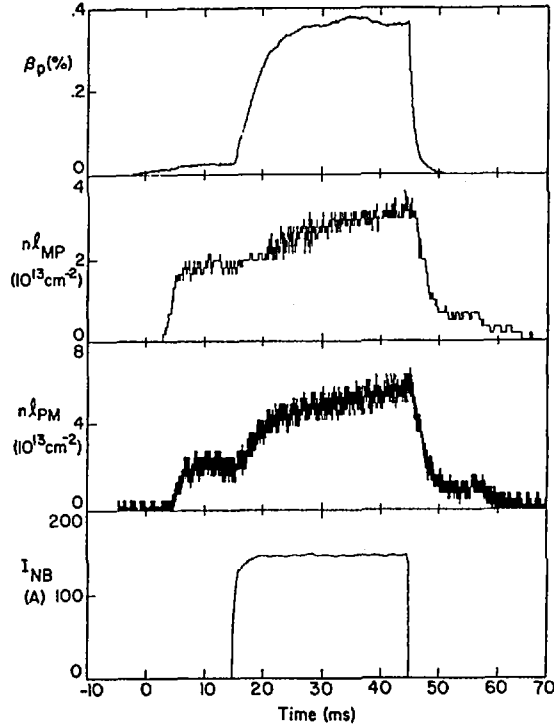


FIG. 4. (Bottom to top traces) Injected neutral beam current in south axicell, line density in south axicell midplane and south mirror throat,  $\beta$  at south axicell midplane. The part of fluctuation in line density signal due to bit noise can be seen from signal at 60 ms.

radiates 50 kW for pulse lengths up to 75 ms. In the following discussion of thermal and potential barrier generation by ECH, end plugging is defined as an increase in the ratio of the central cell mirror throat density to the ion endloss current. Figure 5 is a plot of experimental data for a "single-ended" plugging shot, with ICRF in one anchor to provide MHD stability, and the barrier ( $2\omega_{ce}$ ) and plug ( $\omega_{ce}$ ) gyrotrons in the opposite end on at 10 and 25 ms, respectively. Immediately after initiation of the plug gyrotron there is a sharp reduction of the north endloss current, and a rise in  $\tau_{||}$ . The reflected ion current (about 50 A for the core) is not observed either in the opposite endloss current or as a rise in the central cell density. This result is consistent with radial losses in either the axicell or the central cell. The plug potential, as measured by endloss analyzers, increases on both the plugged and unplugged ends of the machine from 200 V before the ECH to 275 V during the plugging. This potential is

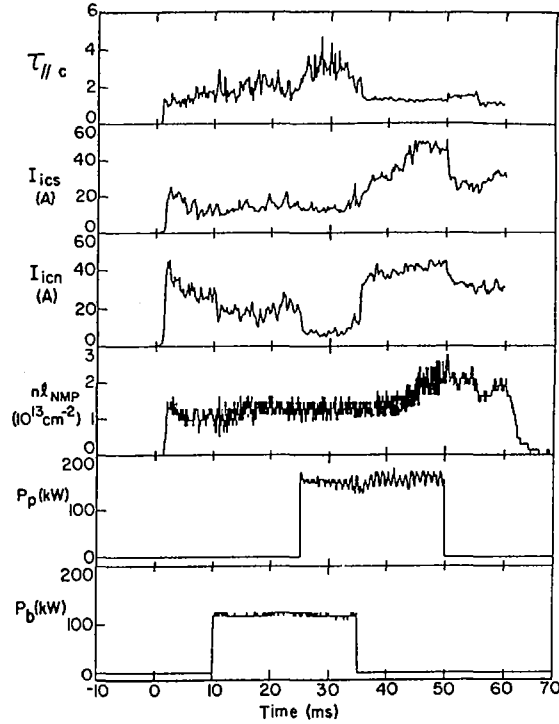


FIG. 5. (Bottom to top traces) Barrier and plug gyrotron powers, north mirror throat density, south and north ion core endless currents, and core parallel confinement time, during single-ended ECH plugging experiment.

non-Boltzmann since the axicell density is below the central cell density. The rapid drop in axicell  $\beta$  at barrier turnoff implies an electron energy of  $\sim 5$  keV, assuming classical scattering.

Plugging occurs independently of neutral beam injection. The axicell midplane density is typically 30% of the mirror peak, indicating some mechanism which removes the low energy ions trapped in the negative potential at the midplane. The density at the 10 kG point drops sharply during plugging, which is consistent with a Boltzmann-factor reduction of the outgoing stream at the high potential region. The potential formation is consistent with a theoretical analysis of strong ECH diffusion, similar to the treatment by Cohen<sup>6</sup> assuming an anomalous radial ion transport at the barrier. To achieve plugging normally requires both  $\omega_{ce}$  and  $2\omega_{ce}$  heating. Plugging is observed for on-axis central cell densities of  $1 - 3 \times 10^{12} \text{cm}^{-3}$ . Also characteristic of plugging is a flattening of

the endloss profile. This transport is ambipolar, in contrast to TMX-U results.<sup>7</sup> In a typical double-ended plugging experiment (data not shown), with barrier and plug gyrotrons on at 20 and 25 ms, respectively, the central cell north throat interferometer rises by about 20% during the first ms after application of the plug ECH, then drops abruptly to 60% of its initial value. The central cell density drops by a factor of two. In this case the increased radial particle loss rate more than compensates the improvement in axial confinement. The initial rise in the north mirror throat density indicates plugging by the north axicell ECH; then as the central cell stream to the anchor is cut off, the anchor ion  $\beta$  drops nearly to zero, and a loss of MHD stability ensues.

### End Plugging with Axicell ICRF

ICRF heating has been used in the north axicell to study the trapping and heating of the central cell stream in order to improve the neutral beam target plasma, as well as to provide plugging by potential formation. Unlike ICRF plugging in the quadrupole anchors plugging in the axicell avoids the problems of neoclassical radial transport. The antenna is located near the R=2 point on the outboard side of the R=4 mirror. The RF is normally excited at the midplane ion cyclotron frequency, which produces the largest increase in density and diamagnetism. The potential plugging by the ICRF is produced over the range  $0.9 < \omega/\omega_{ci} < 1.2$  at the midplane. For constant central cell conditions, the plugging, as measured by the reduction in ion losses out of the north end, increases roughly as the square root of axicell ICRF power.

In a shot with no ICRF plasma in the anchors (fig. 6) the ion loss out of the north end is reduced by 50% across the entire profile during application of axicell ICRF. The line density in the north central cell mirror peak increases by 42%, showing that the ions are reflected from the north axicell. The plug potential (not shown) increases by 100 V during the ICRF, with the pre-ICRF parallel ion temperature,  $T_{i||}=120$  eV. This would be expected to reduce the ion end loss by approximately  $\exp(-\Delta\Phi/T_{i||}) = 0.43$ , which is consistent with the observed end loss reduction of 50%. About 55% of the reflected ion current is unaccounted for in the axial losses out the other end, indicating that additional radial losses are occurring when the axicell ICRF is applied.

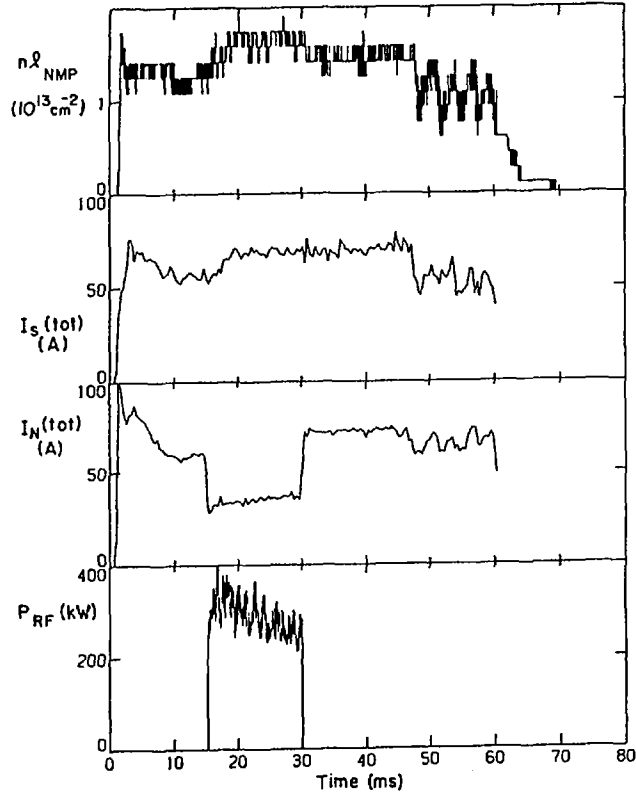


FIG. 6. (Bottom to top traces) North axicell ICRF power, mirror throat density, north and south ion endloss for single-ended ICRF plugging discharge.

## Magnetic Divertor

A magnetic flux divertor was recently installed at the central cell midplane to provide stability to  $m=1$  fluctuations<sup>8</sup> and to create a dense "halo" plasma.<sup>9</sup> Up to 20% of the magnetic flux can be diverted around an internal coil.<sup>10</sup> During end plugged operation the gas fueling requirements of the well confined core plasma should drop by an order of magnitude with respect to the flow-confined edge. By diverting this edge plasma into a separate chamber the two regions can be fueled independently. Gas is injected at four azimuthal positions in the divertor using a system identical to the central cell.<sup>11</sup> Plasma which intercepts the internal ring supports and current leads (total area  $4.3 \text{ cm}^2$ ) causes recycling of  $\sim 6\%$  of the calculated classical flow loss, and provides an additional fueling source.

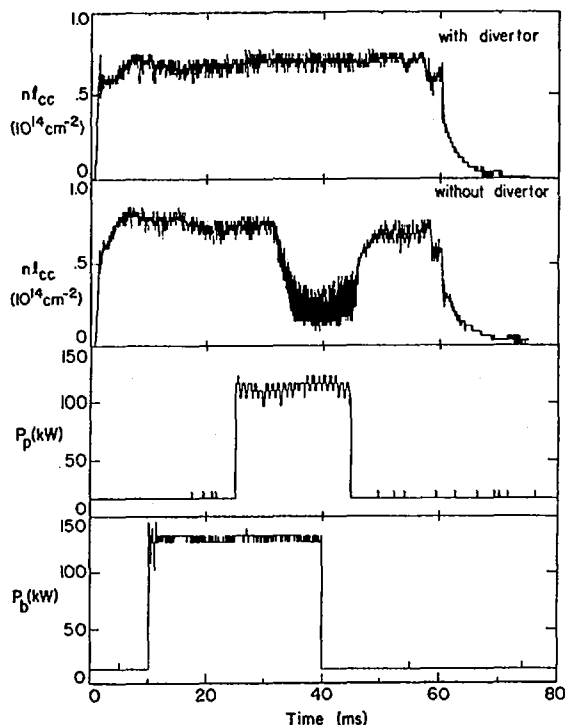


FIG. 7. Comparison of axicell ECH induced fluctuations in central cell density for cases with and without axisymmetric divertor.

The halo power is supplied by edge heating from the ICRF antennas. In the divertor the density peaks at  $n_e \sim 3 \times 10^{11} \text{ cm}^{-3}$  with a half-width of 0.5 cm, which maps to a 2 cm thick annulus in the magnetic wells. The electron temperature is 30–40 eV across the profile. About 25% of the gas injected in the divertor appears as ionization of the core, indicating good plasma shielding. Stabilization of  $m=1$  fluctuations by the divertor during axicell ECH has been observed. Figure 7 illustrates the response of the central cell plasma density to the axicell ECH both with and without the divertor, at a central cell fueling rate of 28 torr-l/sec.

### Constance-B

In the Constance-B experiment the equilibrium, stability, and confinement of hot electrons in a minimum-B mirror with a large radial well depth have been studied. Up to 4 kW of 10.5 GHz ECRH power is used

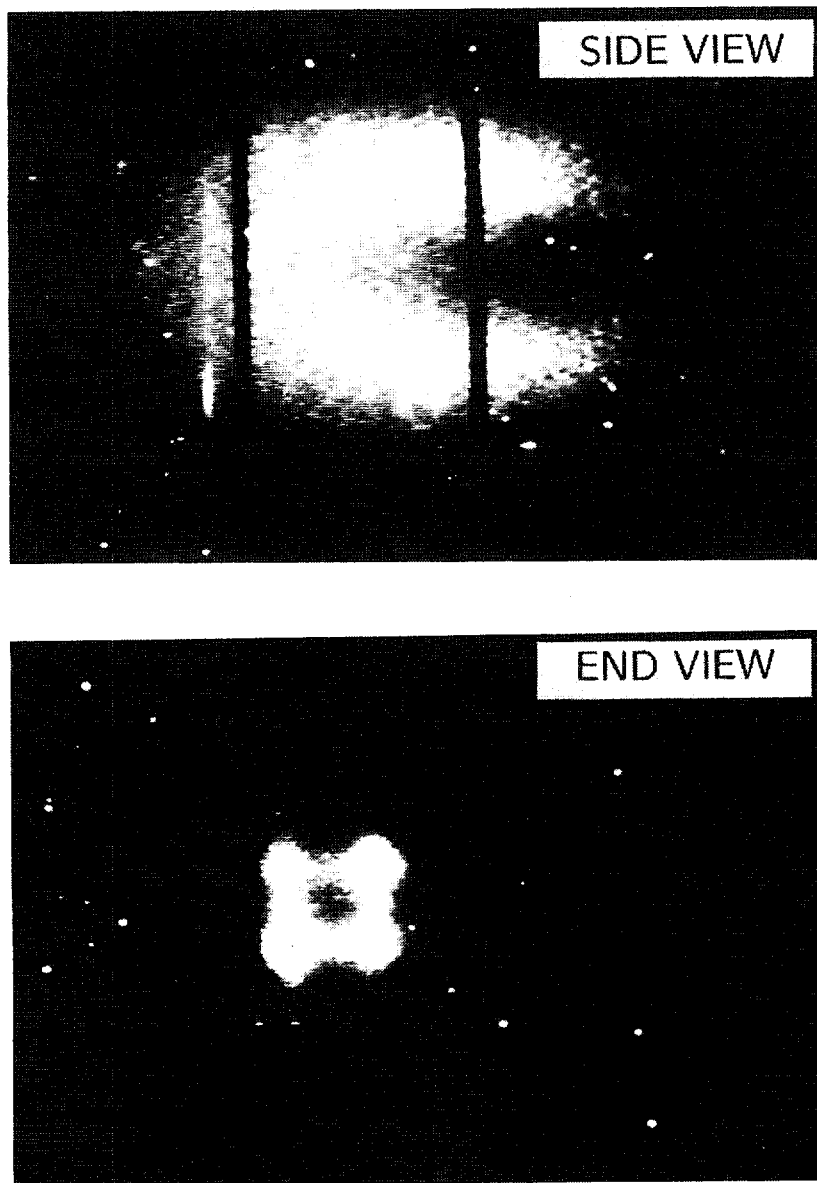


FIG. 8. Visible light photographs of Constance-B hot electron distribution.

to create plasmas with  $\beta > 30\%$ ,  $T_{eh} = 450 \text{ keV}$ ,  $n_{eh} = 2 \times 10^{11} \text{ cm}^{-3}$ , and  $n_{ec} = 2 \times 10^{11} \text{ cm}^{-3}$ . Visible light and x-ray pinhole photographs have revealed that the hot electron pressure profile is peaked off-axis and has the shape of a baseball seam. This curve coincides with the drift surface of the deeply-trapped electrons (fig. 8). The plasma is MHD stable both during ECRH and in the afterglow when only hot electrons are present. The stability of the afterglow plasma contrasts with EBT results,<sup>12</sup> that stabilizing mechanisms other than cold plasma are important.

RF diffusion of hot ( $E > 50 \text{ keV}$ ) electrons has been studied by means of x-ray and endloss measurements. The RF-induced endloss exceeds collisional losses by factors of 10–1000. The ratio of the two losses scales as  $P_{rf}^2$ . This is due in part to the increase in field strength, for which a linear scaling with  $P_{rf}$  has been measured, and in part to the change in plasma parameters produced by the larger powers. These hot electrons are heated up to well above the adiabatic barrier to diffusion, which is calculated to be at  $E=20 \text{ keV}$  for the electric field strength of  $15 \text{ V/cm}$  measured outside the plasma. The rf-induced endloss is maximum when the nonrelativistic ECRH resonance is near the mirror peak.

## REFERENCES

- [1] POST, R.S., GERVER, M., KESNER, J., IRBY, J.H., LANE, B.G., et al., in Plasma Physics and Controlled Nuclear Fusion Research, 1984 (Proc. 10th Int. Conf. London, 1984), Vol. 2, IAEA, Vienna (1983) 285.
- [2] POST, R.S., BRAU, K., GOLOVATO, S., SEVILLANO, E., SMITH, D.K., et al., to be published in Nucl. Fusion.
- [3] SMITH, D.K., BRAU, K., GOODRICH P., IRBY, J., MAUEL, M., et al., Phys. Fluids **29** (1986) 902.
- [4] HERSHKOWITZ, N., NELSON, B.A., JOHNSON, J., FERRON, J.R., PERSING, H., et al., Phys. Rev. Lett. **55** (1985) 947.
- [5] KESNER, J., Comments Plasma Phys. Controll. Fusion **4** (1979) 123.
- [6] COHEN, R.H., Phys. Fluids **26** (1983) 2774.
- [7] HOOPER, E.B., Jr., COHEN, R.H., CORRELL, D.L., GILMORE, J.M., GRUBB, D.P., Phys. Fluids **28** (1985) 3609.
- [8] KESNER, J., LANE, B., POST, R.S., Stabilization of MHD Modes in an Axisymmetric Plasma Column Through the Use of a Magnetic Divertor, Rep. MIT/PFC/JA-86-53, Massachusetts Inst. of Tech., Cambridge (1986); to be published in Nucl. Fusion.
- [9] POST, R.S., HORNE, S., BRAU, K., CASEY, J., GOLOVATO, S., et al., presented at 1986 AVS Meeting, Baltimore, MD, USA.

- [10] POST, R.S., BRAU, K., CASEY J., COLEMAN, J., GOLOVATO, S., et al., "The Tara Tandem Mirror Experiment", in *Plasma-Surface Interactions in Controlled Fusion Devices* (Proc. 7th Int. Conf. Princeton, NJ, 1986).
- [11] BRAU, K., GOODRICH, P., POST, R.S., SEVILLANO, E., *J. Vac. Sci. Technol.*, A 4 (1986) 1079.
- [12] HIROE, S., WILGEN, J.B., BAITY, F.W., BERRY, L.A., COLCHIN, R.J., et al., *Phys. Fluids* 27 (1984) 1019.

## DISCUSSION

T. KAWABE: You showed us a new scheme for stabilizing the MHD mode in a pure axisymmetric mirror by use of a divertor coil with ponderomotive force. I think it is important to use a mirror confined plasma or small power reactor as a neutron source. My question is whether this new concept is scalable to the fusion condition or not.

R.S. POST: The answer to that rests in the precise position of the separatrix in the pressure profile. Presently, we believe that the separatrix is located at  $\sim 10\%$  of the peak pressure. Rough estimates indicate that associate support losses would be acceptable. For a neutron source, one could consider a superconducting ring, as in the Levitron or FM-1. In that case there would be no support losses, but adequate shielding would be required.

N. HERSHKOWITZ: Could you compare the plasma parameters with and without this magnetic divertor and perhaps comment on possible changes in ponderomotive stability when the divertor is turned on.

R.S. POST: When the divertor is switched on, we can operate at  $\sim 40\%$  lower gas feed rate. The electron and ion temperature rise by about the same factor, all other conditions being the same.

The ponderomotive stabilization may well be affected by the divertor due to changes in the edge profile. This is an issue we are currently studying, but we do not have any results yet.

T. CHO: With regard to thermal barrier operation in TARA with plugging but without NBI, do you have any idea how one can explain the sustainment mechanism of the thermal barrier against barrier filling by passing ions?

R.S. POST: We assume that the loss or barrier pumping is by anomalous radial transport. The rates required to pump the barrier can be consistent with the measured rates.

# STABILIZATION OF MHD MODES IN AN AXISYMMETRIC MAGNETIC MIRROR BY APPLIED RF WAVES AND INITIAL RESULTS OF PHAEDRUS-B

R.A. BREUN, P. BROOKER, D. BROUCHOUS, J. BROWNING,  
G. BUTZ, J. CONRAD, E. DALES, J. FERRON, R. GOULDING,  
N. HERSHKOWITZ, T. INTRATOR, C. LITWIN, R. MAJESKI,  
S. MEASSICK, B. NELSON, L. PERANICH, H. PERSING,  
J. RADTKE, D. ROBERTS, G. SEVERN, D. SING, Enyao WANG  
Nuclear Engineering Department,  
University of Wisconsin,  
Madison, Wisconsin

D.A. D'IPPOLITO, J.R. MYRA, G.L. FRANCIS  
Science Applications International,  
Boulder, Colorado

United States of America

## Abstract

STABILIZATION OF MHD MODES IN AN AXISYMMETRIC MAGNETIC MIRROR BY APPLIED RF WAVES AND INITIAL RESULTS OF PHAEDRUS-B.

Phaedrus was operated as a three-cell axisymmetric tandem mirror with dual half-turn end cell antennas at the end cell midplanes. The device was converted to a five-cell tandem mirror (Phaedrus-B) with quadrupole end cells by adding choke coils at the ends of the central cell and dual half-turn antennas throughout the device. The axisymmetric Phaedrus operation achieved enhanced axial plugging which improved the central cell density to  $n = 1 \times 10^{13} \text{ cm}^{-3}$ , the peak plasma beta to 13% and  $n\tau_p$  to  $3 \times 10^{10} \text{ cm}^{-3}$ . The MHD stability was enhanced by radial ponderomotive force using ICRF at 1.3, 1.7 and 4  $\Omega_i$ . A kinetic theory of RF stabilization has been developed which includes the effects of RF sideband modes. The results suggest that RF far fields 'lean' on the device walls and RF near fields 'lean' on the antennas. The results were found to be sensitive to the antenna  $k_z$  spectrum. Thermal barrier potential dips were identified without active barrier pumping. Low frequency fluctuations were found to be sensitive to the phasing of the central cell antennas. Plugging was enhanced by the presence of end cell RF which was resonant only in the central cell.

## 1. INTRODUCTION

The Phaedrus Tandem mirror uses RF near the ion cyclotron frequency (ICRF) to achieve: MHD stability by radial ponderomotive force, electrostatic ion plugging in the end cells, end cell fueling, and ion and electron heating[1,2,3]. Phaedrus can be operated with quadrupole end cells or with

axisymmetric end cells and so has many operating modes. Here we report Phaedrus operation as an axisymmetric three-cell device, with MHD stability provided entirely by externally applied RF electric fields[1]. Our original experiments[1,2] employed RF frequencies slightly larger than the local ion cyclotron frequency (i.e.  $\omega \approx \Omega_i$ ). This paper presents results of recent experiments which demonstrate that stabilization does not require  $\omega$  to be nearly equal to  $\Omega_i$ . Stability has been enhanced by RF at 1.3, 1.7 or 4  $\Omega_i$ . In addition, the use of axisymmetric end cell antennas resulted in stable plasmas with central cell densities as high as  $10^{13} \text{ cm}^{-3}$ .

A theoretical treatment has been developed which shows that the self-consistent interaction of the RF with the plasma results in sideband mode coupling terms which tend to reduce the stabilizing effects of the RF.

During the first half of 1985, Phaedrus was upgraded from a three-cell device to a five-cell device by inserting 1 T choke coils at each end of the central cell. New central cell antennas were added to allow control of the spectrum of the ICRF axial wavenumber  $k_z$  and the azimuthal mode number. This device, Phaedrus-B, was designed to provide thermal barriers in the choke coil end cell transitions without the presence of hot ECH produced electrons and to further improve the understanding of ICRF. This paper presents the first results of Phaedrus-B which demonstrate the presence of thermal barrier potential wells and axial density dips in the transition, achieved without the presence of active barrier pumping. The new antenna set has resulted in increased plasma density. Effects of antenna phasing on plasma stability and of operation of additional end cell antennas at lower frequencies are also presented.

## 2. RF STABILIZATION EXPERIMENTS IN THE AXISYMMETRIC CONFIGURATION

The stabilizing effects in these experiments are due primarily to the radial ponderomotive force  $F_p$  of the ICRF on the plasma.  $F_p$  can be written:

$$F_p = \frac{-e^2}{4m_i} \left[ \frac{\nabla_r E_+^2}{(\omega - \Omega_i)\Omega_i} + \frac{\nabla_r E_-^2}{(\omega + \Omega_i)\Omega_i} + \frac{m_i}{m_e} \frac{\nabla_r E_z^2}{\omega^2} \right] \quad (1)$$

where  $E_+$  is the left circularly polarized field (which rotates with the ions),  $E_-$  is the right circularly polarized field, and  $E_z$  is the field parallel to the magnetic field. Eq.(1) is appropriate for a cold plasma, i.e.  $\omega - \Omega_i \gg k v_i$  and  $\omega \gg k v_e$ , where  $v_i$  and  $v_e$  are the ion and electron thermal velocity, respectively. If  $\omega \approx \Omega_i$ , the term which depends on  $E_+$  is

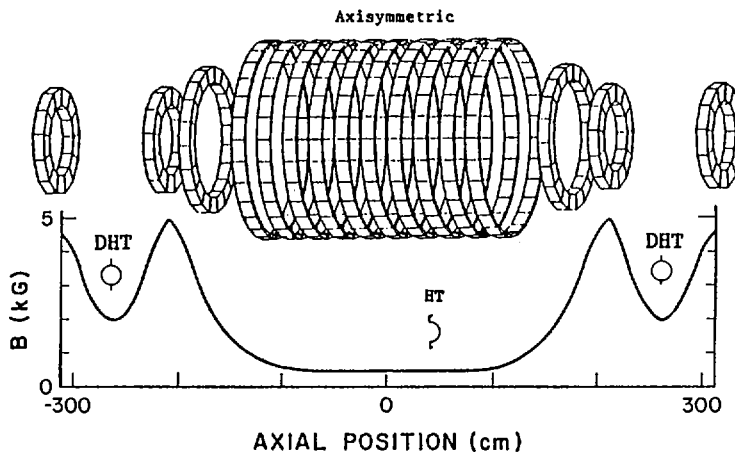


FIG. 1. Schematic of magnetic field coils and axial magnetic field profile for axisymmetric three-cell operation, illustrating the placement of the dual half-turn (DHT) antennas in the end cells and of the half-turn antenna (HT) in the central cell.

important. This term comes from the force on the ions. It changes sign with  $\omega - \Omega_i$  and may be responsible for the abrupt change in stability reported previously[1]. The terms which depend on  $E_r$  and  $E_z$  are due primarily to the force on electrons. In Phaedrus the  $E_r$  term becomes the largest contributor to  $F_p$  when  $\omega$  is not close to  $\Omega_i$ . The sign of  $F_p$  depends on the direction of the radial electric field gradients. Data from all experiments are consistent with the gradient directions required for stabilization. The only propagating wave for the Phaedrus plasma parameters is the azimuthal mode number  $\ell = 1$  fast magnetosonic wave. For this mode, radial  $E_r$  and  $E_z$  profiles peak on the edge of the plasma while  $E_r$  profiles peak on axis. Measurements of the RF magnetic field profiles in the plasma are consistent with this description.

The axisymmetric configuration of the Phaedrus tandem mirror is given schematically in Fig. 1. Unlike in previous experiments, which used line antennas in the end cells, dual half-turn antennas were operated at the end cell midplanes. As shown in Fig. 2, application of RF to the end cell antennas resulted in enhanced axial confinement and a factor of 3 increase in the central cell density. In the central cell the ion temperature  $T_i \approx 40$  eV, the electron temperature  $T_e \approx 20$  eV, the peak plasma density was  $n = 1 \times 10^{13} \text{ cm}^{-3}$ , the peak plasma beta was 13 percent and  $n\tau_p = 3 \times 10^{10} \text{ cm}^{-3} \cdot \text{s}$  was measured, where  $\tau_p$  is the axial particle confinement time. (In other experiments a plasma beta of 11 percent was achieved at  $n = 1 \times 10^{12} \text{ cm}^{-3}$  and  $T_i = 550$  eV.) An  $\ell = +1$  fast wave at the

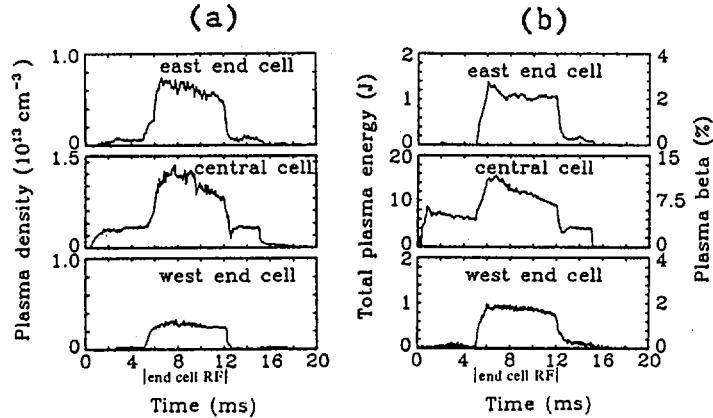


FIG. 2. Plasma density (a) and energy density (b) versus time in each cell for axisymmetric three-cell operation. End cell RF is on from 5 to 12 ms; central cell RF is on from 0 to 15 ms.

end cell RF frequency (approximately 4 times the central cell ion cyclotron frequency) was observed in the central cell. This wave was observed to enhance central cell stability. Fig. 3 gives line density as a function of time. Note the reduction in the fluctuation level when the end cell RF was turned on in one end cell at 5 ms. Application of RF to only one end cell does not make significant changes in central cell plasma parameters. In other experiments[4] the stability of plasma produced by RF with  $\omega \leq \Omega_i$  was enhanced by application of RF at either  $1.3 \Omega_i$  or  $1.7 \Omega_i$  in the central cell.

### 3. THEORY

A theory describing the nonlinear interaction of RF waves with low frequency MHD modes has been developed[5,6] and applied to model the recent RF stabilization experiments in Phaedrus. The nonlinear RF coupling term which enters the ballooning equation has been calculated, including the effect of both the RF wave driven by the antenna and the RF sidebands generated by beating with the MHD wave. An important analytic result[6] was obtained for  $m = 1$  rigid shift interchange modes: the ICRF stabilization vanishes as the antenna and conducting walls are removed from the proximity of the plasma. This suggests that the plasma cannot "lean" on the high-frequency fields themselves but only on the rigid structures which support them.

In a numerical study the fast wave eigenmodes of a diffuse cylindrical plasma column and the near-field pattern corresponding to the  $\ell = 1$  Phaedrus antenna are calculated for

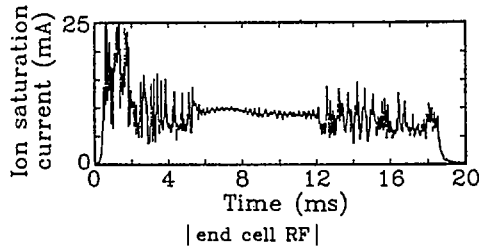


FIG. 3. Probe ion saturation current versus time. One end cell RF system is turned on at 5 ms and turned off at 13 ms.

typical experimental parameters. For simplicity, in the numerical work we assume  $E = 0$  (valid everywhere except within an electron skin depth of the plasma edge where  $E$  is highly evanescent), and the model is applied only in the  $z$  regime where the RF frequency  $\omega$  is greater than the ion cyclotron frequency  $\Omega_i$ , in order to avoid the shear-Alfvén resonance. The critical RF field (or antenna current) for  $m = 1$  interchange stability is calculated using a rigid shift MHD trial function and the numerically determined RF wave and sideband wave profiles.

For far-field fast wave stabilization (eigenmode "leaning" on a conducting wall), the analytic prediction that the stabilizing effect vanishes as the wall moves out to infinity has been verified numerically. It has been found that the degree of stabilization is sensitive to the conducting wall position and that an optimal wall position exists. Even at the optimal position the ponderomotive and sideband terms tend to cancel to a large degree for  $m = 1$  MHD stability, thereby diminishing the effect of the far field compared with estimates based on balancing the equilibrium ponderomotive force with the curvature drive. For near-field stabilization (fields "leaning" on an antenna), the results depend sensitively on the radial profile of the applied waves and on the  $k_z$  spectrum of the antenna (due to the presence of main wave and sideband resonances). Our results suggest that an antenna design which primarily drives the near-field amplitudes just below the  $k_z$  required for fast wave propagation is advantageous for stability. Applied to Phaedrus, the model predicts critical RF fields for both far- and near-field stabilization on the order of 20 V/cm (peak fields) and antenna currents consistent with those used in the experiments.

Further generalizations of the model would be useful to obtain a more detailed understanding of the experiment. First is the inclusion of the  $E$  terms. Order of magnitude estimates based on the full theoretical model[6], with  $E$  estimated from McVey's antenna coupling code[7], indicate that the nonlinear terms due to this component can be comparable to the

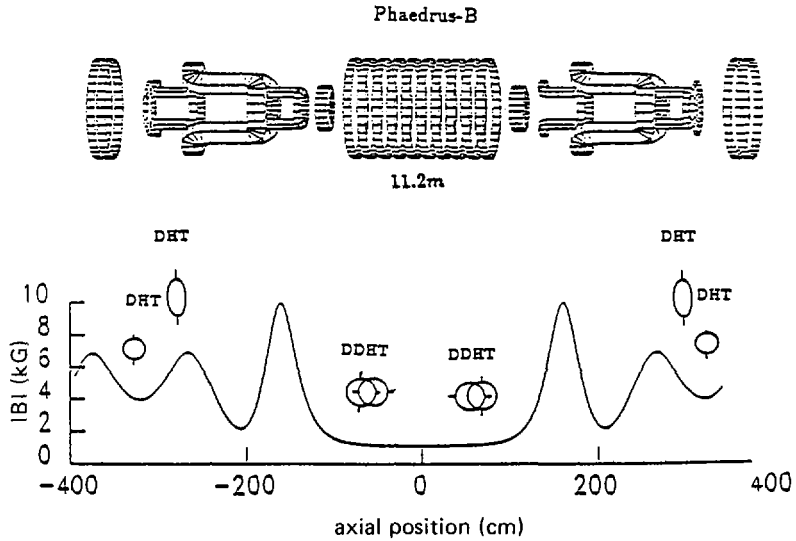


FIG. 4. Schematic of magnetic field coils and axial magnetic field profile for Phaedrus-B, illustrating the placement of the four double half-turn (DHT) antennas in the end cells and the two double dual half-turn (DDHT) antennas in the central cell.

contribution of the other components at the plasma edge. Further work is in progress on this problem. Second, the observed transition to instability[1] as  $\omega$  drops below  $\Omega_i$  is not addressed in the present calculation. In order to treat this problem rigorously, a physical mechanism to resolve the shear-Alfvén resonance must be introduced into the model. Despite these omissions, the results obtained here indicate that basic consistency between theory and experiment has already been achieved, and that RF stabilization is a promising tool for enhancing the performance of future experiments.

#### 4. PHAEDRUS-B

Recently, Phaedrus was upgraded to Phaedrus-B, a five-cell device, by elongating the machine 1.2 m and inserting 1 T choke coils at the ends of the central cell (see Fig. 4). Overall, magnetic fields were increased throughout the machine. In addition, two double dual half-turn antennas were installed in the central cell (at  $z = \pm 50$  cm) and two dual half-turn antennas were installed in each end cell (at  $z = \pm 300$  cm and  $z = \pm 322$  cm). The antennas have normally been operated with  $\omega$  close to the local ion cyclotron frequency, with the exception of the off-midplane antennas in the end cells. Use of the new antenna set resulted in  $n$  as high as  $8 \times 10^{12} \text{ cm}^{-3}$  without end

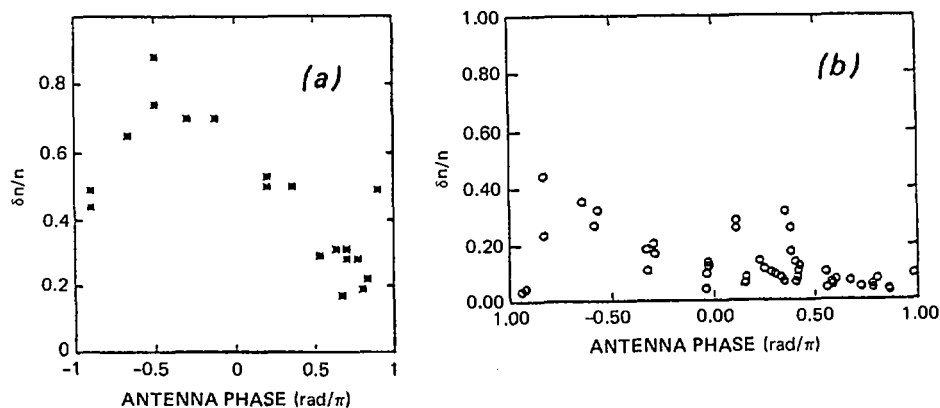


FIG. 5. Langmuir probe ion saturation current fluctuations versus relative antenna phase. MHD activity is a strong function of antenna phasing at (a)  $\omega/\Omega_i = 0.8$  and (b)  $\omega/\Omega_i = 1.0$ .

plugging.  $T$  increased from 20 eV to  $> 60$  eV. Excitation of slow waves in the west end cell, at half the end cell  $\Omega_i$ , resulted in a significant reduction in the net west ion end loss current.

The central cell antennas (at  $\pm 50$  cm) allow control of the spectrum of the ICRF wavenumber and the azimuthal mode number, through the relative antenna phase. The dominant propagating wave (with  $\omega > \Omega_i$ ) is a magnetosonic  $\ell = +1$  fast wave. By adjusting the relative phase of the two dual half-turn antennas (located at  $\pm 50$  cm) it is possible to approximately cancel out this mode (because the central cell antenna separation is 1 m, comparable to the central cell parallel wavelength of the  $\ell = +1$  mode). As shown in Fig. 5, the relative density fluctuation level depends on the antenna phase and varies from an on-axis value as high as 60 percent to as low as 5 percent. Antenna phasing affects stability because RF stabilization is sensitive to the radial electric field profiles. The antenna phase difference determines the axial wavenumber and the azimuthal mode number spectrum of the antenna set. This affects the radial profile of the RF fields through the plasma response to the antenna spectrum. Computations of the RF fields show that the average radial  $E_r$  field is most altered by the antenna phasing. For  $\phi = 0.75\pi$  in Fig. 5, the gradients provide a stabilizing contribution, while for  $\phi = -0.75\pi$  the contribution is approximately neutral. It should also be noted that the contribution from side-band mode coupling is also sensitive to the  $k_z$  spectrum.

When the dual half-turn antennas at the midplane of each end cell are excited, the central cell density ( $n$ ) can increase by a factor of two. The axial density profile is shown in Fig. 6. The maximum end cell density resulting from

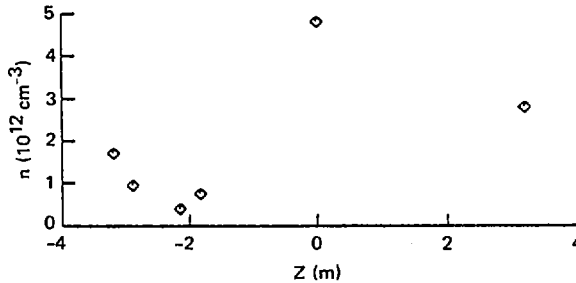


FIG. 6. Axial density profile in Phaedrus-B for operation with resonant end cell and central cell RF. Only a single dual half-turn antenna at  $z = -50$  cm is excited in the central cell.

RF trapping in the end cells is never more than 60 percent of  $n_c$ . This is a feature of RF enhanced end cell plugging[8]. Also, the density in the thermal barrier region is as low as  $0.5 \times 10^{12} \text{ cm}^{-3}$  or approximately  $0.1 n_c$ . Direct measurements of the barrier and central cell plasma<sup>c</sup> potential indicate that thermal barrier potentials are present in the choke coil end cell transition cell. The barrier potential is measured to be approximately 80 V more negative than the central cell value of 110 V. The reduction in density in the thermal barrier (shown in Fig. 6) is then consistent with a Boltzmann relation, i.e.  $e\Delta\phi \approx T \ln(n_c/n_b)$ , where  $\Delta\phi$  is the change in plasma potential and  $n_b$  is the barrier density.

Studies of the trapping and pumping mechanisms occurring in the thermal barrier cell indicate that RF trapping is the largest contributor to barrier fueling. Barrier fueling by neutrals is not found to be as large. The total neutral pressure in the region is low ( $< 1 \times 10^{-6}$  Torr), and an order of magnitude increase in hydrogen pressure, produced by local gas puffing, only doubles the local plasma density. In addition, the increased rate of fueling of the trapped ion population with the addition of gas into the thermal barrier is found to be accompanied by an increase in barrier limiter current. This indicates that a passive pumping mechanism, which produces a radial loss of locally trapped ions, is present. The thermal barrier cell in Phaedrus-B is circular at one end and elliptical at the other, so it is a non-omnigenous mirror cell having trapped ion drift surfaces which differ from the magnetic flux surfaces. Transport associated with non-omnigenous cells has been proposed as a passive pumping technique to pump thermal barriers[9].

Good plugging of central cell end loss has been observed on operation of a second RF ("beach") antenna in the west end cell ( $z = 300$ ) at approximately half the end cell midplane  $\Omega_c$ . An ion cyclotron resonance at this frequency exists only near the end of the central cell, at  $R = 2$ . Slow waves launched by

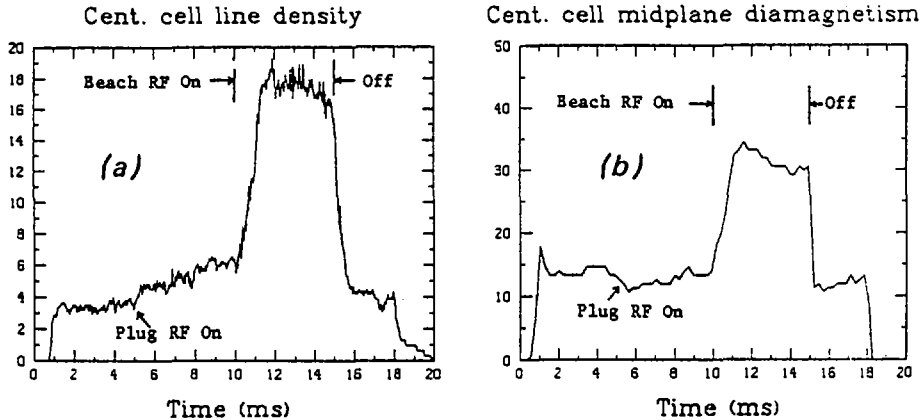


FIG. 7. Symmetric use of the beach antennas produces large increases in (a) central cell density and (b) central cell midplane diamagnetism. Peak density in (a) is  $(6-7) \times 10^{12} \text{ cm}^{-3}$ . Peak beta in (b) is 1.5%.

the low frequency antenna propagate through the thermal barrier region to the resonance where the wave is strongly damped. Symmetric use of such antennas can produce a 300 percent increase in central cell density, with a 250 percent increase in diamagnetism, for a 40 percent increase in total ICRF power (see Fig. 7).

#### ACKNOWLEDGEMENTS

This work was supported by the United States Department of Energy, under Contracts Nos DE-AC02-78ET51015 and DE-AC03-76ET53057.

#### REFERENCES

- [1] FERRON, J.R., et al., Phys. Rev. Lett. **51** (1983) 1955.
- [2] HERSHKOWITZ, N., et al., in Plasma Physics and Controlled Nuclear Fusion Research 1984 (Proc. 10th Int. Conf. London, 1984), Vol. 2, IAEA, Vienna (1985) 265.
- [3] PHAEDRUS GROUP, Nucl. Fusion **25** (1985) 1213.
- [4] FERRON, J.R., et al., Interchange stabilization of an axisymmetric single cell mirror using high frequency electric fields, to be published in Phys. Fluids.
- [5] MYRA, J.R., D'IPPOLITO, D.A., Nucl. Fusion **26** (1986) 361.
- [6] D'IPPOLITO, D.A., MYRA, J.R., Phys. Fluids **29** (1986) 2594.
- [7] McVEY, B., Rep. PFC RR-84-12, Massachusetts Inst. of Tech., Cambridge (1984).
- [8] HERSHKOWITZ, N., et al., Phys. Rev. Lett. **55** 9 (1985) 947.
- [9] KESNER, J., Comments Plasma Phys. Controll. Fusion **5** (1979) 123.



# AXISYMMETRIC MIRROR PLASMA PRODUCED, HEATED AND STABILIZED BY ICRF ONLY

R. ITATANI, H. TAKENO, Y. YASAKA  
Department of Electronics,  
Kyoto University,  
Kyoto, Japan

## Abstract

AXISYMMETRIC MIRROR PLASMA PRODUCED, HEATED AND STABILIZED BY ICRF ONLY.

The HIEI device is an axisymmetric single mirror machine in which radiofrequency (RF) stabilization and heating have been investigated. It is shown that the MHD stable plasma can be started up and sustained by selecting the azimuthal mode of the applied ICRF. The mechanism of stabilization is identified as the RF ponderomotive force due to the radial gradient of the RF field. With a combination of RF production and stabilization by the  $m = \pm 2$  RF mode and heating by the  $m = \pm 1$  mode, a stable plasma with ion temperatures above 100 eV can be produced and sustained.

## 1. INTRODUCTION

Non-axisymmetric MHD anchors have been predicted to give rise to resonant radial diffusion. Radiofrequency (RF) stabilization of MHD instabilities offers the possibility of operating a tandem mirror in a purely axisymmetric mode, i.e. with a simpler and more compact configuration. The HIEI device is an axisymmetric single mirror machine in which the effectiveness of RF stabilization has been demonstrated [1-4]. This paper describes a method by which high temperature plasma is started up, heated, stabilized and sustained by ICRF only, with RF mode control. The mechanism of RF stabilization is also discussed.

## 2. RF PLASMA PRODUCTION AND STABILIZATION

The HIEI device has a mirror length of 1.2 m, a maximum magnetic field  $B_M$  of 1.1 T, a mirror ratio  $R$  of 1.4 to 4, and a plasma radius of  $\approx 4.5$  cm. Two RF antenna systems are installed; one system is located at the midplane, for plasma production and stabilization, and the other is placed at one of the throats, for heating. Each antenna consists of four elements aligned axially with  $90^\circ$  spacing in the azimuthal direction. By adjusting the phase and amplitude of the RF current in each antenna element, the RF fields of the  $m = 0, +1, -1, \pm 1$  and  $\pm 2$  azimuthal modes can be selectively established.

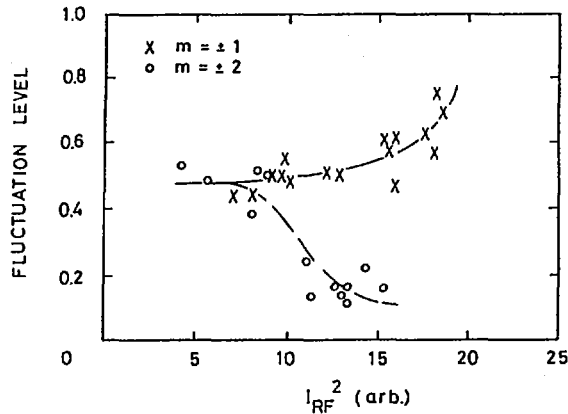


FIG. 1. Fluctuation level of the flute instabilities as a function of the squared RF current in the mid-plane antenna for the  $m = \pm 2$  (circles) and  $m = \pm 1$  (crosses) RF modes.  $R = 2.3$ , the radius of the magnetic field line curvature  $R_c = 4.3$  m, and  $\omega/\omega_{ci} = 2.3$ .

The plasma is produced by hydrogen gas puffing from a gas box; an RF pulse from the midplane antenna follows. In order to eliminate the line tying effect, no startup gun is used. The end-free plasma is sustained for the duration of the RF pulse of up to 10 ms. Figure 1 shows the fluctuation level of the plasma versus the mid-plane antenna current  $I_{RF}$  for the  $m = \pm 1$  and  $m = \pm 2$  RF modes. The ratio of radiofrequency to the local ion cyclotron frequency is  $\omega/\omega_{ci} = 2.3-2.6$ . For low  $I_{RF}$  the fluctuation level is nearly the same in both RF modes. With a correlation measurement, the fluctuation has been identified as the flute mode, with a frequency of 6–10 kHz, and the azimuthal mode  $m = 1$ . For higher  $I_{RF}$  the flute mode is further destabilized when the  $I_{RF}$  of the  $m = \pm 1$  mode increases. In some shots the plasma density decreases to near zero, even during the RF pulse. In contrast, when the  $I_{RF}$  of the  $m = \pm 2$  mode is increased, the flute instability can be stabilized and the plasma with a fluctuation level of less than 10% can be sustained for the whole duration of the RF pulse. The plasma density for the  $m = \pm 2$  RF mode is  $n \approx 1.2 \times 10^{12}$  cm $^{-3}$  at  $r \approx 2$  cm, which is twice as large as that for the  $m = \pm 1$  RF mode. Since gas ionization is mainly caused by the axial electric field of the antenna near-field, the plasma production rate is insensitive to the RF mode number  $m$ . This is supported by the fact that with low values of  $I_{RF}$  both the fluctuation level and the plasma density are almost the same for the  $m = \pm 1$  and  $m = \pm 2$  RF modes. From a measurement of the profile of the RF magnetic field, it is found that the radial gradient of the RF field for the  $m = \pm 2$  mode is much larger than that for the  $m = \pm 1$  mode. The large difference in stability for the two RF modes observed for higher  $I_{RF}$  is attributed to the difference in the radial gradient scale length  $l_B$  of the perpendicular RF magnetic field  $B_{\perp}$ .

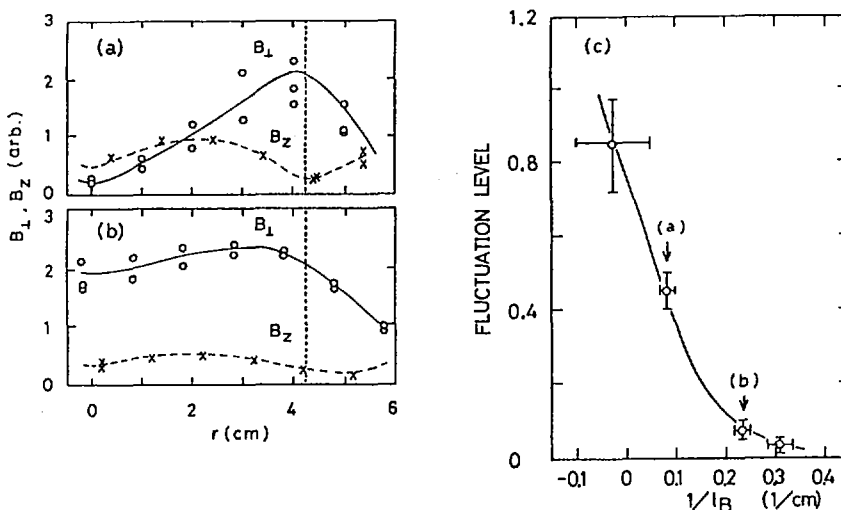


FIG. 2. Measured radial profiles of the perpendicular ( $B_{\perp}$ ) and axial ( $B_z$ ) components of RF magnetic fields for (a) the  $m = \pm 2$  RF mode and (b) the  $m = \pm 1$  RF mode. (c) Fluctuation level of the flute instability versus the reciprocal of the radial gradient scale length  $\ell_B$  of  $B_{\perp}$ .

The midplane antenna is then used to generate a mixture of the  $m = \pm 1$  and  $m = \pm 2$  RF modes. The change in the ratio of the modes results in a change in  $\ell_B$ . The measured radial profiles of  $B_{\perp}$  and  $B_z$  are shown in Fig. 2, with (a) the  $m = \pm 2$  RF mode dominant and (b) the  $m = \pm 1$  RF mode dominant. The fluctuation level of the flute instability is plotted in (c) as a function of the reciprocal of  $\ell_B$  for  $B_{\perp} \approx 5$  G. The values of  $\ell_B$  corresponding to (a) and (b) are indicated by arrows. For lower values of  $\ell_B^{-1}$ , the  $m = \pm 1$  mode component is larger than the  $m = \pm 2$  mode component, and vice versa for higher values of  $\ell_B^{-1}$ . It can be seen that the fluctuation level decreases smoothly with a shortening of  $\ell_B$ .

The radial ponderomotive force for ions, due to linearly polarized RF fields and in adiabatic conditions, is roughly given by

$$F_p \approx -(e^2/2m_i) E_{\perp}^2/\ell_E (\omega^2 - \omega_{ci}^2) \quad (1)$$

where  $m_i$  is the ion mass,  $E_{\perp}$  is the perpendicular RF electric field and  $\ell_E$  is the radial scale length of  $E_{\perp}$ . For stabilization of the flute mode, it is required that this force oppose the effective gravity  $G$ , which is equal to  $e(T_i + T_e)/R_c$ , with  $R_c$  being the radius of the field line curvature. Since the functional dependences of  $B_r$  and  $B_{\theta}$  on  $r$  are, respectively, the same as those of  $E_{\theta}$  and  $E_r$ , provided  $E_z$  is small,

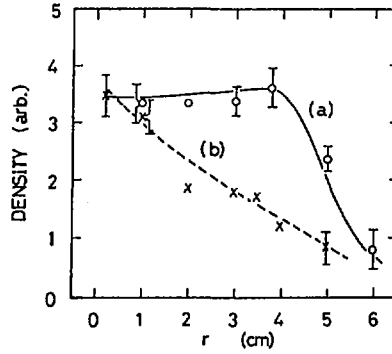


FIG. 3. Radial density profiles for different  $l_B$  values of RF fields corresponding to points (a) and (b) in Fig. 2.

we can use the value of  $l_B$  as the radial scale length of  $E_{\perp}$  ( $l_E \approx l_B$ ). For  $l_B^{-1} \geq 0.15 \text{ cm}^{-1}$  in Fig. 2(c),  $F_p/G \geq 2.1$  is obtained from Eq. (1). Thus, the result presented in Fig. 2(c) is in good agreement with Eq. (1). In previous experiments [2, 4] it was observed that the fluctuation level of the flute mode decreased when  $B_{\perp}$  was increased. These results indicate that the stabilization mechanism can be attributed to the RF ponderomotive force for ions.

The ponderomotive effect on electrons is negligible because  $E_{\perp}$  is estimated to be almost linearly polarized and the electrons are collisional. Side-band coupling effects [5] are also calculated to be small compared with the ponderomotive effect because  $\omega$  is far from  $\omega_{ci}$  and the plasma radius is small enough for side-band waves to be cut off [6].

Figure 3 shows a comparison of the density profiles for different  $l_B$  values corresponding to points (a) and (b) in Fig. 2. The density profile of curve (a) in Fig. 3 is almost flat over the radius of the gas box (made of insulator material). When the flute fluctuation level is high, the density decreases rapidly towards the outside, as shown by curve (b). In the steady state, the ionization current  $I_i$  is equal to  $I_{\perp} + I_{\parallel}$  (radial and parallel total loss current), provided non-ambipolar loss is negligible [7]. The particle confinement time is  $\tau_p = eN/I_i$ , with  $\tau_p^{-1} = \tau_{\perp}^{-1} + \tau_{\parallel}^{-1}$ , where  $\tau_{\perp} = eN/I_{\perp}$ ,  $\tau_{\parallel} = eN/I_{\parallel}$ , and  $N$  is the total particle number. The value of  $I_i$  is considered to be almost the same for cases (a) and (b) in Fig. 3 because the production rate is insensitive to the RF mode number, as discussed before. The value of  $N$  over the radius of the gas box for (a) is 1.9 times larger than that for (b). This means that  $\tau_p$  for (a) is larger than  $\tau_p$  for (b) by a factor of two. End-loss measurements of  $I_{\parallel}$  show that  $\tau_{\parallel}$  for (a) is smaller than  $\tau_{\parallel}$  for (b). Therefore, the increase of  $\tau_p$  for (a) should be due to the improvement of  $\tau_{\perp}$ . We see that the RF mode with a larger radial gradient stabilizes the flute instability, which results in an improvement of radial confinement.

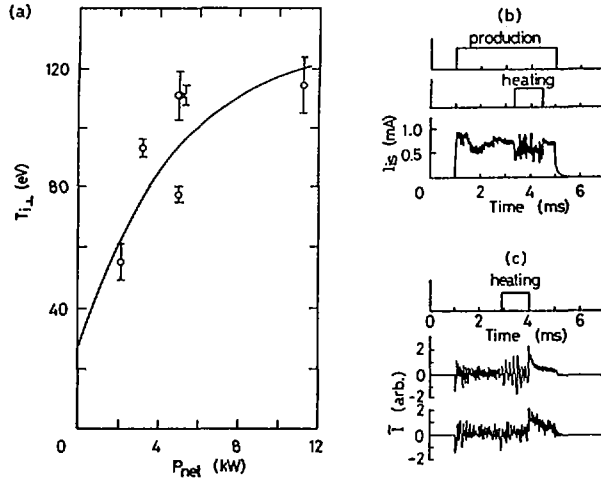


FIG. 4. Results of slow wave heating. (a) Perpendicular ion temperature at  $r = 2$  cm as a function of net RF power of the  $m = \pm 1$  mode from the throat antenna. (b) Time evolution of the ion saturation current to a Langmuir probe at  $r = 3$  cm. (c) AC components of the probe current for the midplane antenna currents of 58 A (upper trace) and 67 A (lower trace).

### 3. HEATING OF RF PRODUCED PLASMA

We performed additional ion heating with the throat antenna which excited slow waves of the  $m = +1$ ,  $m = -1$  or  $m = \pm 1$  modes. The throat antenna was energized 2 ms after switching on the midplane antenna. The plasma produced by the  $m = \pm 2$  RF mode from the midplane antenna was stable and had parameters of  $n \approx 0.5 \times 10^{12} \text{ cm}^{-3}$ ,  $T_e \approx 17 \text{ eV}$ ,  $T_{i\perp} \approx 20 \text{ eV}$  and  $T_{i\parallel} \approx 10 \text{ eV}$ .  $T_{i\perp}$  and  $T_{i\parallel}$  were measured with a movable multigrad energy analyser of 6 mm dia and an end-loss analyser, respectively. The value of  $\omega/\omega_{ci}$  varied from 1.0 to 0.7 along the throat antenna element. Figure 4(a) shows  $T_{i\perp}$  at  $r = 2$  cm versus the coupled RF power from the throat antenna. The value of  $T_{i\perp}$  increases from 20 eV to about 120 eV;  $T_{i\parallel}$  averaged over the radius is about 80 eV. At these temperatures the charge exchange time is estimated to be about 20  $\mu\text{s}$  because of the small volume and the low pumping speed of HIEI. This results in an apparent saturation of  $T_{i\perp}$ . Calculations of power balance equations combined with neutral pressure balance equations are consistent with the results presented in Fig. 4(a).

During the application of heating, the fluctuation level is sometimes increased, as shown in Fig. 4(b). It is likely that the flute mode becomes unstable owing to the increase of  $T_i$ . This may occur when the effective gravity, increased by ion heating, exceeds the stabilizing ponderomotive force created by the  $m = \pm 2$  RF at the midplane. In fact, this fluctuation is stabilized when the RF current in the midplane

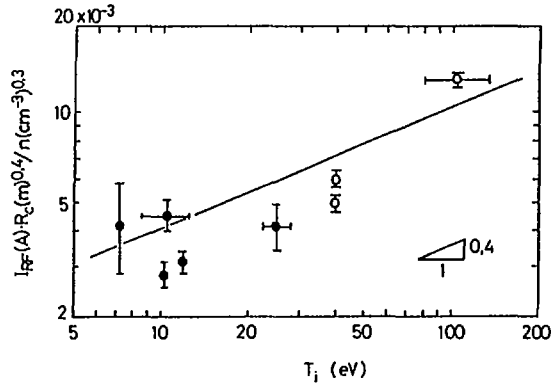


FIG. 5. Extension of the empirical scaling law. Previous results are indicated by black circles and the results for higher  $T_i$  values by white circles.

antenna is increased. This is demonstrated in Fig. 4(c), where  $I_{RF}$  for the lower trace is larger than  $I_{RF}$  for the upper trace.

As found previously with an empirical scaling law, the  $I_{RF}$  required for flute stabilization is proportional to  $n^{0.3 \pm 0.05} G^{0.4 \pm 0.1}$  for plasmas with  $T_i$  up to 25 eV [4]. The scaling is shown by the straight line in Fig. 5, together with previous experimental points (black circles). The results for plasmas with higher  $T_i$  (white circles) lie on this line, showing the extension of the scaling law for  $T_i$  as high as 100 eV.

#### 4. CONCLUSIONS

In the axisymmetric mirror HIEI it has been shown that the MHD stable plasma can be started up and sustained by selecting the azimuthal mode number of the applied ICRF. The mechanism of stabilization is identified as the RF ponderomotive force due to the radial gradient of the RF field.

With a combination of RF production and stabilization by the midplane antenna and heating by the throat antenna, a plasma with  $T_i \approx 100$  eV has been started up, stabilized, heated and sustained by ICRF only.

#### REFERENCES

- [1] YASAKA, Y., et al., in Plasma Physics (Proc. Int. Conf. Nagoya, 1980), Vol. 1, Fusion Research Association of Japan, Nagoya (1980) 327.
- [2] INUTAKE, M., ITATANI, R., et al., in Plasma Physics and Controlled Nuclear Fusion Research 1982 (Proc. 9th Int. Conf. Baltimore, 1982), Vol. 1, IAEA, Vienna (1983) 545.

- [3] OKAMURA, S., ITATANI, R., et al., in Plasma Physics and Controlled Nuclear Fusion Reserach 1984 (Proc. 10th Int. Conf. London, 1984), Vol. 1, IAEA, Vienna (1985) 337.
- [4] YASAKA, Y., ITATANI, R., Nucl. Fusion **24** (1984) 445; **25** (1985) 29.
- [5] D'IPPOLITO, D., MYRA, J., Rep. SAIC-85/1922, Science Applications, Inc., Pleasanton, CA (1986).
- [6] YASAKA, Y., ITATANI, R., Phys. Rev. Lett. **56** (1986) 2811.
- [7] INUTAKE, M., et al., Phys. Rev. Lett. **55** (1985) 939.



## DISCUSSION

ON PAPERS IAEA-CN-47/C-I-4-1 AND C-I-4-2

T. KAWABE: I think your work on the stabilization of the flute mode by RF ponderomotive forces is important for the creation of a neutron source by burning D-T plasma confined in an axisymmetric mirror. At present, the plasma temperature is of the order of 100 eV. What action should we take, in your opinion, to acquire more confidence in the use of this method for fusion conditions as in the Fusion Engineering Facility?

R. ITATANI: The scaling law we derived shows that the required RF current is proportional to approximately  $n^{0.3}(\tau_{||}/R)^{0.4}$ . We have already performed a check-up to  $4 \times 10^{14} \text{ cm}^{-3}$  in plasma density. However, the effective gravity (which is proportional to  $\tau_{||}/R$ ) should be increased so as to obtain a confirmation of the scaling law. The radius of curvature of the magnetic field lines is already of the same order as that in the FEF. It is necessary to test the scaling law, using plasmas of higher temperature, as high as 1 keV or 10 keV. Also, studies of the energy flow of applied RF should be performed so as to enable a proper choice of the RF mode to be made.



## A TANDEM MIRROR MODELLING CODE\*

W.M. NEVINS, B.M. BOGHOSIAN, R.H. COHEN,  
W.F. CUMMINS, P.F. DUBOIS, A. FRIEDMAN,  
L.L. LoDESTRO, Y. MATSUDA, L.D. PEARLSTEIN,  
G.D. PORTER, M.E. RENSINK, T.D. ROGNLIEN,  
G.R. SMITH, J.J. STEWART

Lawrence Livermore National Laboratory,  
University of California,  
Livermore, California

M. PHILLIPS  
Grumman Aerospace Corp.,  
Princeton, New Jersey

United States of America

### Abstract

#### A TANDEM MIRROR MODELLING CODE.

The paper describes a computer code that models the time evolution of tandem mirror plasma and power deposition by radiofrequency (rf) fields within the plasma. Rate equations for seven groups of particles are integrated in time. The effects of axial variations in the potential are included. An analytic model for rf-heated electron populations is described. Code predictions are compared with data from the TMX-U experiment. Power deposition profiles for electron cyclotron resonant heating in TMX-U are shown. A full-wave solution for ion cyclotron heating fields is displayed, and the ponderomotive forces are evaluated.

## 1. INTRODUCTION

This paper describes comprehensive modeling of tandem mirrors, focusing on our code MERTH (Mirror Equilibrium Radial Transport and Heating). MERTH includes physics packages together with a command language interpreter that provides a convenient user interface. The MERTH physics packages described here include a transport package, a ray-tracing package, and an ion cyclotron heating package. MERTH also contains a mapping package that provides self-consistent axial profiles of density and temperature, and a MHD equilibrium package that describes the magnetic field geometry. MERTH physics packages can easily exchange information and use consistent models of the magnetic field and the axial and radial profiles of density and temperature.

---

\* Work performed under the auspices of the United States Department of Energy, under Contract No. W-7405-ENG-48.

## 2. RATE EQUATIONS

The transport package in MERTH, called TREQ (Tandem mirror Rate Equations), solves for the potential in five axial regions (central cell, inboard mirror, thermal barrier, plug, and end wall) and solves rate equations for seven groups of particles (thermal electrons and ions, central-cell and end-cell beam ions, barrier-trapped ions, magnetically trapped electrons in the end cell, and plug-trapped electrons). For each group of particles in a thermal barrier tandem mirror, we describe particle and energy balance with a system of zero-dimensional rate equations. Axial coupling exists between particle groups because the bounce orbits of two or more particle groups may pass through any one axial region. The axial profiles of the particle and energy density for thermal electrons and ions depend on the potential in each axial region. Rate equations for the thermal electrons and ions that employ these self-consistent axial profiles are formulated in section 2.1. An analytic model of the effect of electron cyclotron resonant heating (ECRH) on the electrons in the plug cell of a thermal barrier tandem mirror is described in section 2.2.

Calculations with this transport package indicate a strong coupling of the plasma densities in the various axial regions of the device. In section 2.3 this coupling is shown to be in qualitative agreement with Tandem Mirror Experiment-Upgrade (TMX-U) observations.

### 2.1. Thermal Particle Rate Equations

On the most fundamental level, particles in a tandem mirror obey a bounce-averaged Fokker-Planck equation. To reduce this equation for each group of particles into a system of rate equations for the number of particles,  $N_g$ , and the total energy,  $E_g$ , we assume a functional form for the distribution of each particle group that involves two parameters, and take the particle and energy moments of the bounce-averaged kinetic equation. For example, we assume that the thermal central-cell electrons have a nearly Maxwellian distribution in  $\epsilon$  and  $\mu$ ,

$$f_e(\epsilon) = n_o^{(e)} \left( \frac{m_e}{2\pi T_e} \right)^{3/2} \left\{ \exp\left(-\frac{\epsilon}{T_e}\right) - \exp\left[-\frac{\epsilon_{loss}^{(e)}(\mu)}{T_e} + \alpha_e \left( \frac{\epsilon - \epsilon_{loss}^{(e)}(\mu)}{T_e} \right) \right] \right\} \quad (2.1)$$

where  $\epsilon_{loss}^{(e)}(\mu)$  is the loss boundary for the thermal central-cell electrons. The two parameters used to fit the total particle and energy content of this group of particles are then  $n_o^{(e)}$  and  $T_e$ . A third parameter,  $\alpha_e$ , which measures the width of the boundary layer near the loss cone over which the distribution function departs significantly from a Maxwellian, is held fixed with a value of order unity.

The thermal barrier tandem mirror is modeled as a sequence of connected square wells. The particle and energy content of group  $g$  may then be expressed in terms of  $n_o^{(g)}$  and  $T_g$  as

$$N_g = n_o^{(g)} \sum_j \frac{L_j}{B_j} a_j^{(g)}(q_g\{\phi\}/T_g), \quad E_g = \frac{3}{2} n_o^{(g)} T_g \sum_j \frac{L_j}{B_j} c_j^{(g)}(q_g\{\phi\}/T_g) \quad (2.2)$$

where  $j$  labels regions,  $L_j$  is the length of the  $j^{\text{th}}$  region,  $B_j$  is the magnetic induction in the  $j^{\text{th}}$  region. The symbol  $\{\phi\}$  is used to indicate that  $a_j^{(g)}(q_g\{\phi\}/T_g)$  and  $c_j^{(g)}(q_g\{\phi\}/T_g)$  depend on the values of the potential  $\phi$  in all regions. For particle groups with nearly Maxwellian distributions, the functions  $a_j^{(g)}(q_g\{\phi\}/T_g)$  and  $c_j^{(g)}(q_g\{\phi\}/T_g)$ —which involve moments of the distribution function over a known region of phase space—may be expressed in terms of error functions and Dawson's integral [1].

The particle and energy moments of the kinetic equation yield equations that describe the rate of change for the number and energy content of each group of particles,

$$\dot{N}_g = \dot{N}_g|_{cl} + \frac{q_g n_o^{(g)}}{T_g} \sum_{j,k} \frac{L_j}{B_j} b_{jk}^{(g)}(q_g\{\phi\}/T_g) (\dot{\phi}_j - \dot{\phi}_k) \quad (2.3)$$

with a similar equation for the rate of change of the energy. The final term in Eq. (2.3) describes the transfer of particles from one group to another because of the motion of separatrices between groups of particles. The term  $\dot{N}_g|_{cl}$  represents sources and sinks of particles that are due to classical processes such as ionization, charge exchange, collisional coupling between groups of particles, and radial transport. Radial transport is modeled by a phenomenological loss rate proportional to the central-cell potential.

Evaluating the source/sink term in Eq. (2.3),  $\dot{N}_g|_{cl}$ , requires knowing the density of each group of particles in each axial region. These densities may be expressed in terms of  $n_o^{(g)}$ ,  $T_g$ , and  $\{\phi\}$  by taking the appropriate moment of the distribution function defined in Eq. (2.1). Equation (2.3) for  $N_g$  is integrated in time by the TREQ package, while the parameters  $n_o^{(g)}$  and  $T_g$ , as well as the potentials  $\{\phi\}$ , are obtained by enforcing Eqs. (2.2), and quasineutrality in each region as constraints at each time level. The entire set is solved using the differential-algebraic equation package DASSL [2].

## 2.2 Hot-Electron Physics

Electron cyclotron resonant heating (ECRH) is used in the plug cell of a thermal barrier tandem mirror to heat electrons, and to assist in the formation of the barrier and plugging potentials. ECRH is applied at both the plug and barrier locations. The ECRH is typically strong enough to render the electron distribution function far from Maxwellian.

We have developed approximate forms for the hot-electron distribution function in the strong-ECRH limit by assuming that the coefficients of collisional and rf diffusion are slowly varying. For fundamental heating at the plug, with weaker

second-harmonic heating at the barrier, the non-relativistic Fokker-Planck equation for plug electrons can be written approximately in the form

$$\frac{\partial}{\partial x} \hat{\nu} \frac{\partial f}{\partial x} + \frac{\partial}{\partial y} \hat{D}_p \frac{\partial f}{\partial y} = 0$$

where  $x$  and  $y$  are the parallel energies at the plug and the inner mirror, respectively, normalized to the central-cell electron temperature  $T_e$ ;  $\hat{D}_p(x, y)$  is the diffusion coefficient for plug ECRH in these variables; and  $\hat{\nu}(x, y)$  is a sum of collisional and barrier-ECRH diffusion coefficients. The separatrix dividing passing from magnetically trapped electrons is a portion of the line  $y = 0$ ; in the limit where passing (from the central cell) electrons are constrained to be Maxwellian (long solenoid approximation),  $f$  must vary as  $\exp(-\rho x)$ , where  $\rho = R_{mp}/(R_{mp} - 1)$  on that separatrix. Here,  $R_{mp}$  is the mirror ratio from the inner mirror to the plug. One may verify *a posteriori* or observe from relativistic Fokker-Planck code results that  $f$  varies most rapidly near the intersection of the passing, magnetically trapped, and potential-trapped regions, over an energy scale that is short compared with the variation of  $\hat{D}_p$  and  $\hat{\nu}$ . Treating  $\hat{\nu}/\hat{D}_p$  as slowly varying and rescaling variables to  $X = \rho(x - x_0)$  and  $Y = \rho(\hat{\nu}/\hat{D}_p)^{1/2}(y - y_0)$ , where  $x_0$  and  $y_0$  are the coordinates of the aforementioned intersection, reduces the Fokker-Planck equation locally to Laplace's equation in  $X$  and  $Y$ . Extending the domain to all  $X, Y$  and requiring that  $f$  be finite at infinity (validity requires that the hot-electron flux into the  $v_\perp$  axis in the plug is small compared with its maximum value on the passing separatrix), we find  $f \propto \text{Im}\{Z[(X + iY)^{1/2}]\}$ , where  $Z$  is the plasma dispersion function. A similar result is obtained for electrons confined to the barrier region. Here the boundary condition on the line  $v_\parallel = 0$  at the plug is obtained from the plug solution. The overall solution compares well to results from the bounce-averaged Fokker-Planck code SMOKE as shown in Fig. 1, where level surfaces of the distribution function are plotted. We are developing a model for TREQ based on this analytic solution.

The remainder of this section describes a number of features common to the analytic and Fokker-Planck solutions that are qualitatively incorporated in a cruder end-cell electron model that is now operational in TREQ. The combination of rf diffusion and collisions provides an efficient means of transport from low to high parallel velocity for passing electrons. This process leads to heating of central-cell electrons, and to enhanced electron end loss and thus high overall machine potentials. The enhancement of end loss over the purely collisional level (from the entire machine) is modest when the ECRH is weak enough, so the passing electrons are Maxwellian, but can become substantial when the ECRH is strong enough to dominate over collisions for passing electrons. In the latter case, for a fixed potential profile, the hot-electron end-loss rate is limited by the rate at which barrier electrons are replenished by collisional scattering of central-cell electrons into the passing region. Thus TREQ and Fokker-Planck calculations both show that as the ECRH level is increased, the overall electron end-loss rate varies from the collisional (Pastukhov [3]) rate for climbing the potential hill to the end wall, to the collisional rate for merely climbing the solenoid-to-barrier potential.

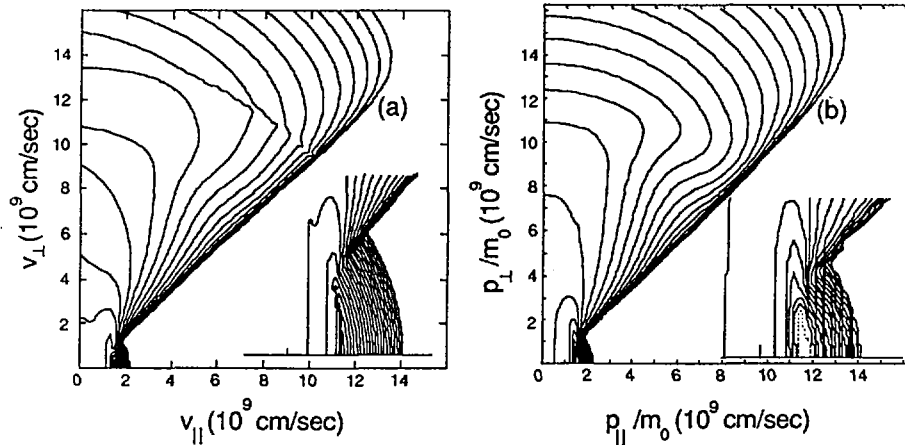


FIG. 1. Comparison of (a) analytic and (b) Fokker-Planck distributions at the plug (no free parameters). Inserts are enlargements of the region near the passing-trapped separatrix.

ECRH heating provides a large inventory of hot electrons, the size of which depends on the strength of the plug and barrier ECRH; hence, TREQ calculates barrier depths and plugging potentials that are sensitive to the ECRH levels.

The distribution function contains two potential drives for instability. The first arises because a distribution function, which is monotonically decreasing up the  $v_{\perp}$  axis in the barrier, maps in the plug to a boundary condition that is inverted (increasing with  $v_{\parallel}$ ) on the separatrix bounding the potential-trapped region. For strong plug ECRH, the plug distribution then has a peak near the maximum  $v_{\parallel}$  point on the separatrix. This distribution yields a density that can be a nonmonotone function of the plug-to-barrier potential. This nonmonotonic density can result in multiple roots for the potential, leading to root jumping and hysteresis in TREQ solutions as other parameters (e.g., ECRH power, density) vary. This behavior is suggestive of the loss of plugging observed in the TMX-U experiment. We also speculate that this bump-on-tail distribution can be micro-unstable. An option in the TREQ model that fills in the plug distribution, simulating but overestimating the effect of quasilinear diffusion, leads to a lower plugging potential. However, the potential can still be a locally sensitive function of parameters.

The second possible instability drive comes from the increasing of the distribution function with  $v_{\perp}$  at finite  $v_{\parallel}$  in the barrier. Instability can arise because of the inverted energy population. For these cases, the absorption of power from the barrier ECRH is found to be negative in both TREQ and Fokker-Planck studies.

### 2.3. Comparison of TREQ modeling with TMX-U

An important feature of the transport package within MERTH is the ability to model the coupling of the plasma densities in various axial regions of a thermal-barrier tandem mirror. The ionization current that is injected in the central cell

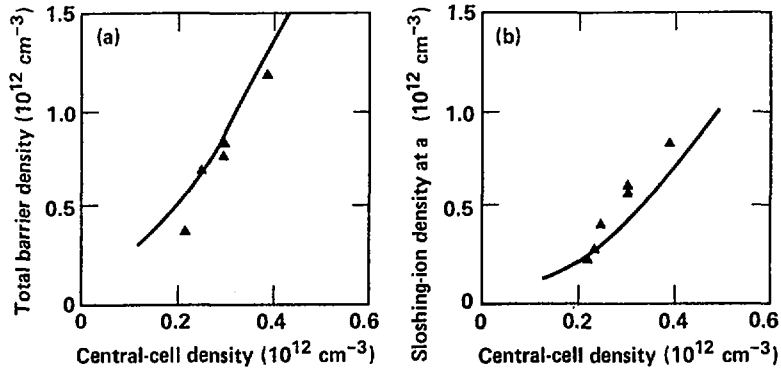


FIG. 2. Variation of (a) the total density at the midplane of the barrier, and (b) the sloshing ion density at the turning point with the central-cell density. The triangles are data from the TMX-U experiment in which the central-cell density was varied by varying the fueling rate, and the lines are the result of a TREQ simulation of these experiments. These experiments were done under conditions of good axial confinement, so the end-loss currents were small compared with other loss mechanisms.

of a tandem mirror creates a plasma in that cell. Some of these ions, the passing ions, lie in the region of phase space that permits their transit into the anchor cells of the device. Scattering of these passing ions produces a warm ion population that is trapped in the thermal barrier. In turn, these cold locally trapped ions are a target for the neutral beams that provide the sloshing ion population. Hence these three ion populations—central cell, barrier-trapped, and sloshing—are all coupled. Figure 2(a) shows the dependence of the total density at the thermal-barrier midplane; Fig. 2(b) shows the dependence of the sloshing-ion density on the central-cell density. The solid triangles are data obtained in TMX-U by varying the central-cell gas-fueling rate and keeping all other machine parameters fixed. The solid lines are the results of the TREQ modeling of these experiments. Good agreement exists between the experimental results and the model. The data presented in Fig. 2 were obtained in the strong plugging mode in which the axial ion losses were small compared with the radial losses. Hence, the results are insensitive to the plugging model, i.e., the anchor electron model.

### 3. ELECTRON CYCLOTRON HEATING

Propagation and absorption of waves in the electron-cyclotron frequency range are modeled by tracing bundles of rays and calculating the power deposited in the plasma. We describe here some features of our computational model, and we show results for one of the microwave-launching systems in TMX-U.

The equilibrium magnetic field is derived from a vacuum field that is calculated from a realistic coil set, together with a paraxial, low- $\beta$  approximation of plasma diamagnetism. Inclusion of diamagnetism leads to cyclotron resonance shifts that affect both ray trajectories and power absorption. The electron den-

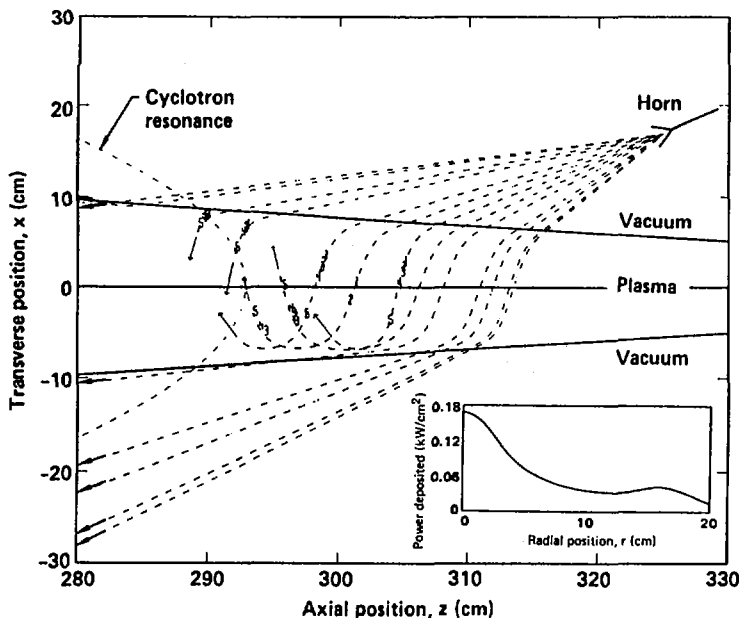


FIG. 3. Selected rays, launched by an 18 GHz horn in TMX-U. This  $xz$ -plane shows projections of 13 rays and cross-sections of both the plasma (bounded by vacuum) and the cyclotron resonance surface. The numbers 1, 2, 3, 4 and 5 along the rays indicate, respectively, where 20, 40, 60, 80 and 99% of the power has been absorbed. The peak values of density and temperature (on the magnetic axis  $x = y = 0$ ) are  $\hat{n} = 10^{12} \text{ cm}^{-3}$  and  $\hat{T}_e = 0.1 \text{ keV}$ .

sity and temperature are assumed to depend only on the radial magnetic flux coordinate and are therefore uniform along field lines and around the azimuth of the elliptical flux surfaces.

The power absorption calculation assumes a Maxwellian electron distribution and yields a power deposition profile that is a function of both the radial and azimuthal flux coordinates. We can thus assess the azimuthal asymmetry of the deposition that is due to launching microwaves toward one side of the plasma. Averaging the deposition profile over azimuth, which presumably occurs in experiments after an  $\mathbf{E} \times \mathbf{B}$  rotation time, yields a radial deposition profile for one-dimensional calculations of axial and radial transport.

We report here the ray trajectories and radial deposition profile for the 18-GHz heating system in the central cell of TMX-U. We model one of the four horns included in the system. The reported values of power deposition are proportional to the 10 kW of incident power that we assume enters the plasma in the extraordinary mode.

Figure 3 shows a view of the ray bundle impinging on the plasma and being absorbed. Only 13 of the 121 rays are shown, the central ray and 12 rays with the maximum divergence angle of  $20^\circ$ . Note the strong refraction that tends to trap the power and guide it down the field until absorption occurs near the

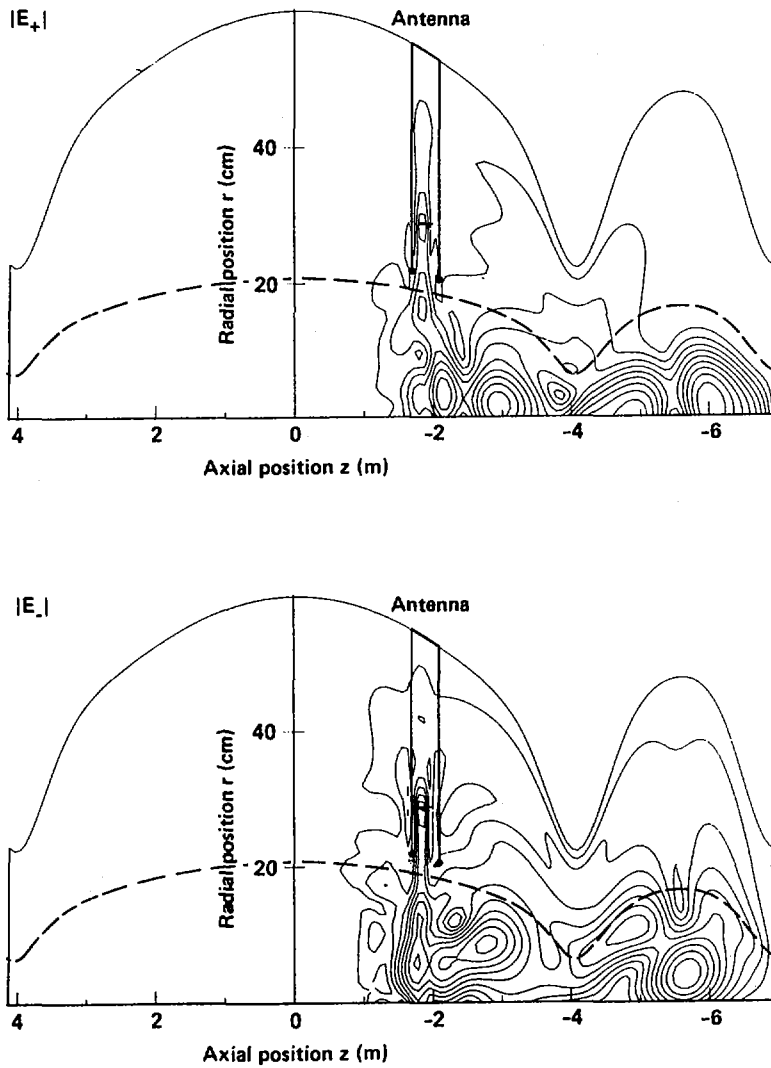


FIG. 4. Contours of the absolute values of the electric field strength in the  $E_+$  and  $E_-$  components in TMX-U, when the east antenna is excited. Contour levels have linear spacing and are separated by 1.2 V/m (for  $|E_+|$ ) and 0.6 V/m (for  $|E_-|$ ) per ampere of total current in the two drive elements. Note the greatly enlarged scales used on the radial (vertical) axes compared with the axial (horizontal) axes. The location of the antenna current elements is indicated. The dashed curve is a contour of constant plasma density at 0.1 f. We model only the central cell (between the inner mirrors at  $z = \pm 4$  m) and the east end cell ( $-7 \text{ m} < z < -4 \text{ m}$ ). Note that  $z$  increases from right to left.

cyclotron resonance. The inset shows the corresponding radial deposition profile. The deposition near radial position  $r = 0$  is four times that given by a uniform-deposition estimate, because the horn illuminates only a narrow swath near the  $y = 0$  plane. Integrating over  $r$ , we find that over 80% of the incident power is absorbed in the plasma and that over 30% is absorbed in the core ( $r < 10$  cm).

#### 4. ION CYCLOTRON HEATING

Propagation and absorption of applied ion-cyclotron waves are investigated by calculating the global wave structure of ion-cyclotron frequency fields in axisymmetric mirrors. Simpler, eikonal methods are not applicable to the mirror machines of interest because wavelengths in the plasma are comparable to density and magnetic-field scale lengths. We use the GARFIELD code to solve for the electromagnetic field in an axisymmetric region containing a plasma and surrounded by conducting walls. The plasma is described by the cold-plasma dispersion relation with a small collision term to simulate absorption. Further details on GARFIELD can be found in Ref. [4].

We apply GARFIELD to the TMX-U experiment. The axial magnetic field profile generated by the actual coil set is modeled by a number of filamentary current loops of appropriate radii and axial locations. Radial density profiles have exponential forms suggested by measurements, and axial ion density profiles model a mirror-trapped population plus a (constant) passing population. Antennas are modeled by one or more azimuthal current loops. For instance, opposed half-turn loop antennas with a shield are simulated by two drive currents for the main straps and six image-current elements representing the shield. These latter currents are estimated using a finite-element antenna code.

Calculated contours of the left and right circularly polarized components of the electromagnetic field,  $|E_+|$  and  $|E_-|$  respectively, are shown in Fig. 4 for the TMX-U central cell and the east end cell, with excitation of the east antenna at  $\omega = 1.03 \Omega_{i0}$ , where  $\Omega_{i0} \equiv \Omega_i(z = 0)$ . The cyclotron frequency  $\Omega_i$  at the antenna is such that  $\omega < \Omega_i$ . The peak density is  $\hat{n} = 2 \times 10^{12} \text{ cm}^{-3}$ . Of the spectrum of azimuthal modes excited by the antennas, only  $m = -1$  for  $E_+$  and  $m = +1$  for  $E_-$  are large in the plasma core near  $r = 0$ .

In TMX-U, the  $E_+$  component propagates where  $\Omega_i > \omega$  and is absorbed at the cyclotron resonance near  $z = -1$  m. Reflection of this component from the inner mirror causes a standing-wave pattern between the antenna and mirror. The  $E_-$  component is not absorbed by ions, but it is nevertheless absent for  $z > -1$  m because it is cut off there; however, at higher density,  $\hat{n} = 5 \times 10^{12} \text{ cm}^{-3}$ , this component propagates into the other half of the central cell. The wave fields external to the plasma are probably related to modes discussed by Paoloni [5]. Those fields, rather than the fields in the plasma, excite standing waves in the end cell, which might heat electrons by transit-time pumping or cause anomalous ion diffusion.

Ponderomotive forces of sufficient magnitude and appropriate spatial variation can affect plasma stability. Figure 5 shows the radial variation of these forces

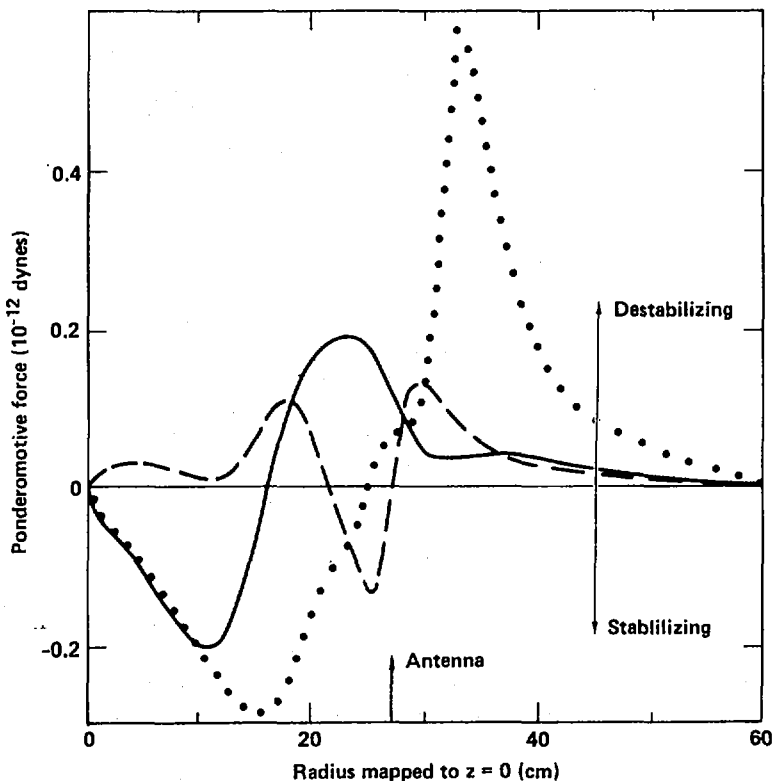


FIG. 5. Magnitude and radial variation of the ponderomotive force in the TMX-U central cell, with east and west antennas each excited at  $\omega = 1.5 \Omega_{i0}$  with a 2 kA current. The force is plotted against a normalized radius  $r[B(z)/B(0)]^{1/2}$ . The three axial locations are at the midplane ( $z = 0$ ), where  $\omega/\Omega_i = 1.5$  (solid curve); at the west antenna ( $z = 1.1$  m), where  $\omega/\Omega_i = 1.385$  (dashed curve); and at the east antenna ( $z = -1.85$  m), where  $\omega/\Omega_i = 1.21$  (dotted curve).

at three axial locations in the central cell of TMX-U. The east and west antennas (located at  $z = -1.85$  m and 1.1 m) were both driven at  $\omega = 1.5 \Omega_{i0}$  with a current of 2 kA. Differences in the radial force profiles at the two antenna locations are due to the different values of  $\omega/\Omega_i$  at those locations. As expected, the forces are generally negative, i. e. stabilizing, inside the antenna current loops.

## REFERENCES

- [1] GAUTSCHI, M., in Handbook of Mathematical Functions (ABRAMOWITZ, M., STEGUN, I.A., Eds), U.S. Government Printing Office, Washington, D.C. (1972) 295.
- [2] PETZOLD, L.R., in Scientific Computing (Proc. 10th World Congress on Systems Simulation and Scientific Computing, 1982), North Holland, Amsterdam (1982) 65.
- [3] PASTUKHOV, V.P., Nucl. Fusion **14** (1974) 3.
- [4] PHILLIPS, M.W., TODD, A.M.M., Comput. Phys. Commun. **40** (1986) 65.
- [5] PAOLONI, F.J., Phys. Fluids **18** (1975) 640.

## DRIFT PUMPING OF TANDEM MIRROR THERMAL BARRIERS\*

D.E. BALDWIN, J.A. BYERS, Y.J. CHEN, T.B. KAISER  
Lawrence Livermore National Laboratory,  
University of California,  
Livermore, California,  
United States of America

### Abstract

#### DRIFT PUMPING OF TANDEM MIRROR THERMAL BARRIERS.

Drift pumping is a means of selectively removing low energy ions from the thermal barrier of a tandem mirror by induced radial transport. The paper determines the conditions for, and the properties of, transport induced by externally applied low frequency waves resonating with the trapped-ion azimuthal drift frequency. Considerations that are discussed include conditions necessary for stochasticity, derivation of the local diffusion coefficient, and computation of the perturbed fields throughout the plasma for a model based on TMX-U profiles with and without a throttle-coil geometry.

### 1. INTRODUCTION AND OVERVIEW

A thermal barrier in a tandem mirror is a negative dip in potential between the central cell and the confining plug potential [1], as illustrated in Fig. 1. The barrier energetically separates plug electrons from central-cell thermal electrons, permitting a higher plug temperature and potential with a reduced plug-to-central-cell density ratio. The potential profile is generated by the space charge of magnetically trapped, energetic ion and electron plug populations. Maintenance of the profile requires control of these particle distributions and of the local thermal densities.

The thermal ion accumulation in the barrier must be prevented. The process of removing thermal ions as they are trapped by collisions and ionization is called "pumping" of the thermal barrier. There are two possible channels for pumping: heating out of the barrier, and radial transport to the surface. Current experiments use a version of the first: i.e. charge exchange on injected neutral beams converts barrier-trapped ions to energetic untrapped ions or to magnetically trapped ions--a process prohibitively inefficient at reactor energies. As an alternative, we describe a method for inducing the radial transport of barrier-trapped ions, using appropriate externally

---

\* Work performed under the auspices of the United States Department of Energy, under Contract No. W-7405-ENG-48.

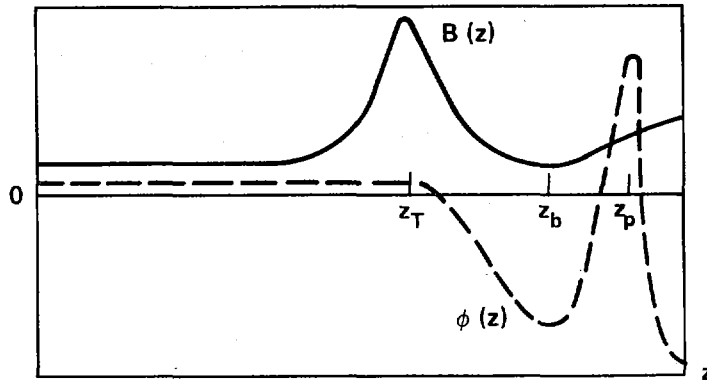


FIG. 1. Typical thermal-barrier-plug axial profiles of magnetic field  $B(z)$  and potential  $\phi(z)$ .

applied radio-frequency (rf) fields. At the plasma surface, the ions would then be lost by axial flow. To minimize enhancement of the ion barrier-trapping rate, we adopt drift frequencies that preserve the cyclotron and bounce adiabatic invariants, suggesting the name "drift pumping".

The idea of expulsion of a certain class of ions by waves resonant with their drift frequency is reminiscent of the expulsion of energetic beam-injected ions from a tokamak by fishbone oscillations [2]. The difference here is that the rf fields responsible would be externally driven.

A suitable rf drift-pump field must satisfy several constraints. The perturbed fields must cause particle displacements off the density-level surfaces as the latter are convected by the moving flux. In the Lagrangian frame, this motion requires perturbations having either parallel electric fields, magnetic compression, or line curvature. The motion must either be irreversible for diffusion to occur, or must convect ions to the surface. The former condition implies a stochastic motion of trapped ions in the combined equilibrium and rf fields; either motion sets restrictions on the applied spectrum, dependent on the equilibrium. The pump fields must have low azimuthal mode number and adequate penetration to induce transport more or less uniformly across the column. This requirement is fairly well satisfied, given the low frequencies required and the short Alfvén penetration time. Although drift frequencies in the central cell will in general differ from those in the plug, the pump fields must not penetrate too strongly into the plug cell in order not to excessively enhance ion transport there. The degree of penetration depends in some detail on the magnetic geometry, and this issue could be a determining one in selecting one pump configuration over another.

Drift pumping also offers the possibility of pumping impurities--a process very difficult to accomplish with charge exchange. To the degree that drift frequencies are determined by  $E \times B$  drifts, impurities would be as easily pumped as ions. Were magnetic drifts to dominate, the impurity drift frequencies would differ owing to their charge-to-mass ratios; for narrow bandwidth, resonance with a fuel-ion pump would be lost. It would not be practical to impose a separate set of frequencies for each impurity. Therefore, the preferred situation for pumping impurities is one in which the drift frequency of particles trapped in the barrier region is dominated by electric fields.

To the extent that  $E \times B$  drifts do dominate, thermal electrons would be transported along with ions. This is in potential conflict with the requirements of a gridless direct convertor in a reactor [3] for which the total electron transport must be small. However, in the barrier itself, the large (>80%) hot electron density is dominated by magnetic drifts having quite different frequency (and possibly sign). These electrons would not transport in drift-pump fields resonating with the  $E \times B$  frequency, and the charge separation in the particles lost to the direct convertor is thereby preserved.

## 2. LINEARIZED PARTICLE DRIFT EQUATIONS

We choose a gauge such that the electric field can be written

$$\underline{E} = -c^{-1} \dot{\underline{\xi}} \times \underline{B} - \nabla \chi \quad (1)$$

where the dot denotes differentiation with respect to time,  $\dot{\underline{\xi}} \cdot \underline{B} = 0$ , and

$$\dot{\underline{B}} = \nabla \times (\dot{\underline{\xi}} \times \underline{B}) \quad (2)$$

In this gauge, because  $\nabla \cdot (\underline{\xi} \times \underline{B}) \neq 0$ ,  $\chi$  is generally not the electrostatic potential. Linearization of Eqs (1 and 2) is direct, with  $\underline{\xi}$ ,  $\chi \rightarrow \tilde{\underline{\xi}}$ ,  $\tilde{\chi}$ .  $\dot{\underline{\xi}}$  is the velocity frame in which  $\psi$ ,  $\theta$  do not change, i.e.  $\dot{\psi} + \dot{\underline{\xi}} \cdot \nabla \psi = \dot{\theta} + \dot{\underline{\xi}} \cdot \nabla \theta = 0$ .

With this choice of gauge, the adiabatic invariant for bounce motion of a particle of energy  $\epsilon$  and magnetic moment  $\mu$  (per unit mass) is given by

$$J = \oint ds [2(\epsilon - \mu B - \frac{q}{m} \chi)]^{1/2} \quad (3)$$

where  $s$  measures distance along a field line.  $J$  is conserved for the frequencies assumed (below the bounce frequency), leading to Hamiltonian equations for the particle flux coordinates

$$\frac{d\psi}{dt} = -\frac{mc}{q} \frac{\partial K}{\partial \theta} \quad (4a)$$

$$\frac{d\theta}{dt} = \frac{mc}{q} \frac{\partial K}{\partial \psi} \quad (4b)$$

$K(\psi, \theta, J, t)$  is defined by the constancy in  $J$  in time-dependent fields

$$J = \oint ds \{2[K(\psi, \theta, J, t) - V(\psi, \theta, s, t)]\}^{1/2} = \text{constant} \quad (5)$$

where

$$V = \mu B(\psi, \theta, s, t) + \frac{q}{m} \chi(\psi, \theta, s, t)$$

is the effective potential for parallel bounce motion.

The fields can be linearized into equilibrium and small time-varying components. The Hamiltonian can likewise be linearized by linearizing Eq. (5), holding  $J$  constant. We generate a Lagrangian linearization, e.g.  $V \rightarrow V_0 + \tilde{V}^L$ , where  $\tilde{V}^L$  is related to its Eulerian counterpart  $\tilde{V}$  by

$$\hat{V}^L = \tilde{V} + \tilde{\xi} \cdot \nabla V_0 \quad (6)$$

by adding to the displacement  $\tilde{\xi}$  a component parallel to  $\underline{b}$ ,

$$\xi_{\parallel} = \int^s ds \tilde{\xi} \cdot \underline{\kappa} \quad (7)$$

where  $\underline{\kappa} = \underline{b} \cdot \nabla \underline{b}$  is the equilibrium line curvature. This gives

$$\tilde{\kappa} = \frac{1}{\tau_B} \oint \frac{ds}{v_{\parallel}} \tilde{V}^L \quad (8)$$

where  $\tau_B = \oint \frac{ds}{v_{\parallel}}$  and  $v_{\parallel} = [2(\epsilon - V_0)]^{1/2}$ . A feature of the gauge and displacement chosen is that the parallel electric field is given by  $\underline{b} \cdot \nabla \chi$ . In particular, when  $\tilde{E}_{\parallel}^L = 0$ , owing to high parallel conductivity,  $\tilde{\chi}^L$  is independent of  $s$ . We

subsequently discard the zero subscript on equilibrium quantities. Equation (8) is equivalent to that obtained by Antonsen et al. [4] for particle motion in low-frequency waves.

For equilibria independent of  $\theta$ , the linearized equations of motion are

$$\frac{d\psi}{dt} = - \frac{mc}{q} \frac{\partial \tilde{K}}{\partial \theta} \quad (9)$$

and

$$\frac{d\theta}{dt} = \omega_D + \frac{mc}{q} \frac{\partial \tilde{K}}{\partial \psi} \quad (10)$$

where

$$\omega_D(\psi) = \frac{mc}{q} \frac{\partial K}{\partial \psi} \quad (11)$$

is the bounce-averaged equilibrium drift frequency.

### 3. CONDITIONS FOR DIFFUSIVE TRANSPORT

Drift pumping employs rf fields resonating with  $\omega_D$ .

Convective loss in a small-amplitude, single-frequency pump field requires an  $\omega_D$  that is nearly linear in  $\psi$ , which we assume generally not to occur. Diffusive loss relies on an irreversible element in Eqs (9 through 11). This could arise from collisions, which in practice are too infrequent, or from properties of the particle motion in more complex applied spectra. A rf source having sufficient continuous bandwidth to cover a practical range of  $\omega_D$  is less electrically efficient than one of the same spread but having a number of discrete frequencies, each generated by high-Q resonant circuits. Particle motion in these latter fields is stochastic only when the resonance overlap condition is satisfied. Under this condition, using Eq. (8), the resulting diffusion coefficient is given by

$$D_\psi = \int_0^\infty dt' \left\langle \frac{\partial \psi(t)}{\partial t} \frac{\partial \psi(t+t')}{\partial t} \right\rangle = \left( \frac{mc}{q} \right)^2 \int_0^\infty dt' \left\langle \frac{\partial \tilde{K}(t)}{\partial \theta} \frac{\partial \tilde{K}(t+t')}{\partial \theta} \right\rangle \quad (12)$$

If we limit the rf field to azimuthal mode number  $\ell = 1$  with multiple frequencies,

$$\bar{K} = \cos \theta \sum_n \bar{K}_n \cos (\omega_n t + \delta_n) \quad (13)$$

then

$$D_\psi = \frac{\pi}{8} \left(\frac{mc}{q}\right)^2 \sum_n \bar{K}_n^2 \delta (\omega_D(\psi) - \omega_n)$$

When  $\bar{K}_n$  and  $\omega_n$  are slowly varying with  $n$ ,

$$D_\psi = \frac{\pi}{8} \left(\frac{mc}{q}\right)^2 \frac{\bar{K}_n^2}{\delta\omega_n} \Big|_{\omega_n = \omega_D(\psi)}$$

Following the analysis of Ref. [5], the condition for resonance overlap requires that the amplitude of particle motion in the vicinity of one resonance,  $\Delta\psi_n$ , satisfy

$$\left| \Delta\psi_n \right| > \frac{1}{3} \delta\psi_n$$

where  $\delta\psi_n$  is the separation between adjacent resonances. When  $\Delta\psi_n$  is expressed in terms of the locally resonant component of the perturbed Hamiltonian, this becomes

$$\delta\omega_n < 6 \left( \frac{mc}{2q} \left| \bar{K}_n \frac{d\omega_D}{d\psi} \right| \right)^{1/2} \quad (14)$$

If the number of applied frequencies  $N$  is increased by reducing  $\delta\omega_n$  and  $\bar{K}_n$ , while preserving the total bandwidth  $-N\delta\omega_n$  and the total power  $-N\bar{K}_n^2$ , the diffusion coefficient given by Eq. (12) is unchanged, while the stochasticity condition given by Eq. (14) becomes better satisfied.

#### 4. CHARACTERISTICS OF CONSTANT-J PUMPING

Transporting a particle to the surface by drift pumping requires that successive frequency components be resonant with  $\omega_D = \omega_D(\psi)$ , where  $\omega_D$  is to be computed at constant  $J$ . While transporting, a particle's kinetic energy and pitch angle will change.

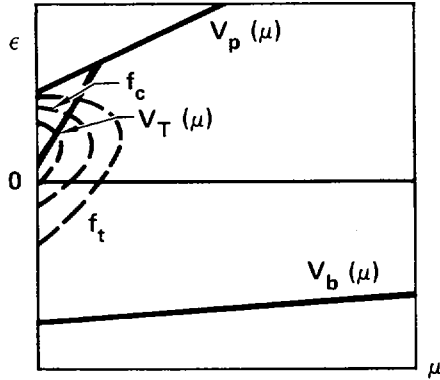


FIG. 2. Typical separatrices between passing and trapped ions at fixed  $\psi$ .

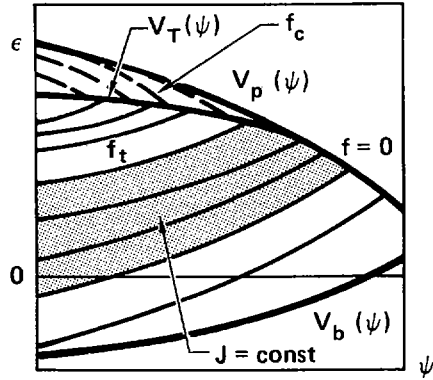


FIG. 3. Typical separatrices between passing and trapped ions at fixed  $\mu$ .

To picture the process, assume a throttle-coil magnetic configuration having negatively biased endwalls, giving rise to the on-axis profiles illustrated in Fig. 1. Off-axis, assume that the potential retains a similar shape but decreases in magnitude to zero at the surface, i.e.  $\phi(\psi, z) = \phi_1(\psi) \phi_2(z)$ .

First, construct a familiar  $\epsilon$ - $\mu$  diagram for the barrier region at a fixed  $\psi$ , as shown in Fig. 2. Note the separatrices defined by  $V_\sigma = B_\sigma + q\chi_\sigma/m$ . Respectively,  $\sigma = T, b, p$ , describe ions of vanishing parallel velocity at the throttle coil  $z_T$ , the barrier  $z_b$ , and the plug location  $z_p$ . For  $\epsilon > V_p$  (except at very large  $\mu$ ), ions are unconfined and the distribution vanishes along  $\epsilon = V_p$ . For  $V_p > \epsilon > V_T$ , ions pass from the central cell and are confined by the plug potential; their distribution is Maxwellian at central-cell density and temperature for that  $\psi$ -value. For  $\epsilon < V_T$ , ions are trapped between the throttle coil and the plug potential, and the trapped distribution must equal the passing distribution along  $\epsilon = V_T$ . Such a figure exists for each  $\psi$ , with the contribution of potential smaller in magnitude at larger  $\psi$ .

Because  $\mu$  is nearly constant (affected only by collisions), we construct  $\epsilon$  -  $\psi$  diagrams at constant  $\mu$ , as shown in Fig. 3. The separatrices here have variation due to  $\chi(\psi)$  and also  $B(\psi)$  (which we neglect). The central-cell distribution  $f_c$  vanishes along  $\epsilon = V_p(\psi)$ ; for  $\epsilon < V_p$ ,  $f_c$  decreases with both increasing  $\epsilon$  and  $\psi$ .

The trapped-region distribution  $f_t$  is to be obtained by solution of a diffusion equation competing drift pumping with ionization and collisional trapping across  $\epsilon = V_T$  (as well as

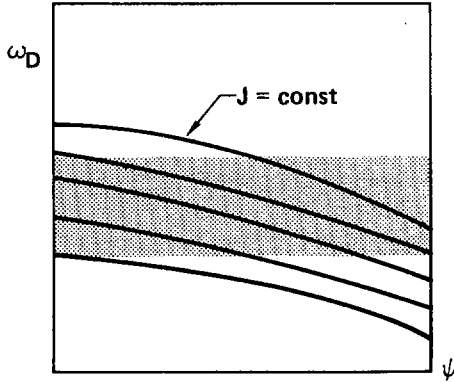


FIG. 4. Typical variation of  $\omega_D(\psi)$  at fixed  $\mu, J$ .

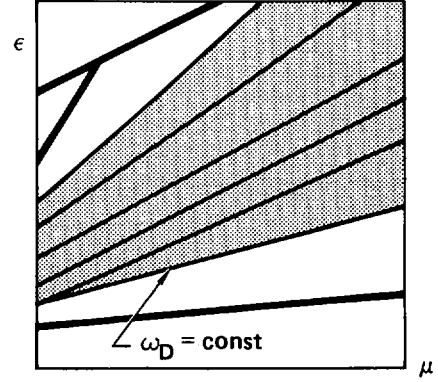


FIG. 5. Typical level surfaces of  $\omega_D(\epsilon, \mu)$  at fixed  $\psi$ .

from adjacent  $\mu$ -values). As a diffusion problem,  $f_t$  is prescribed along the broken boundary formed by the two separatrices  $\epsilon = V_T$  and  $\epsilon = V_p$ :  $f_t = f_c$  along the  $V_T$  portion, and  $f_t = 0$  along the  $V_p$  portion. Owing to  $J$  conservation, the rf diffusion reduces to one dimension, i.e. the constant- $J$  surfaces in Fig. 3, which must be constructed numerically for general  $B$  and  $\chi$ .  $J$  surfaces intersecting the  $\epsilon = V_p$  boundary lead to true loss of trapped particles; those that intersect the  $\epsilon = V_T$  boundary enhance trapping. In the strong-pumping limit in which drift diffusion dominates collisions, there is a limiting form to  $f_t$ : on the former  $J$  surfaces,  $f_t$  vanishes; on the latter,  $f_t$  has its value on the surface. This limiting form will give the minimum attainable trapped-ion density for the profiles assumed; collisions will only increase it.

Whether the motion along the  $J$ -surfaces is irreversible depends on the profile and the applied spectrum. Figure 4 illustrates profiles of  $\omega_D$  at constant  $J$ ; and Fig. 5 contours of  $\omega_D$  in  $\epsilon - \mu$  for fixed  $\psi$ . A selected band of rf frequencies covers a band in  $\omega_D$  and in  $\epsilon - \mu$ , e.g. as shown shaded in Figs 4 and 5. The band of  $J$ -values that will be resonant can be read off of Fig. 4, giving the surfaces in Fig. 3 along which diffusion will occur, provided the stochasticity condition [Eq. (14)] is satisfied.

## 5. EXAMPLE: PUMP FIELDS IN PARAXIAL QUADRUPOLE GEOMETRY

As an example, we calculate the pump fields in a low beta quadrupole configuration for which paraxial field lines are given by

$$\begin{aligned} x &= \sqrt{2\psi} \sigma(z) \cos \theta \\ y &= \sqrt{2\psi} \tau(z) \sin \theta \end{aligned} \quad (15)$$

where  $\sigma, \tau$  are the fanning factors. We limit ourselves to incompressible perturbations generated by a coil set external to the plasma and we neglect the effects of potentials. For this case it is convenient in Eq. (4a) to write

$$\frac{\partial K}{\partial \theta} = \frac{1}{\tau_B} \oint \frac{ds}{v_{\parallel}} (v_{\parallel}^2 + \mu B) \mathbb{H} \quad (16)$$

where  $\mathbb{H} = B^{-1} \underline{b} \times \nabla \psi \cdot \underline{\kappa}$  is the geodesic curvature. Then, in the paraxial approximation, linearization gives

$$\frac{\partial \tilde{K}}{\partial \theta} = \frac{1}{\tau_B} \oint \frac{ds}{v_{\parallel}} (v_{\parallel}^2 + \mu B) \tilde{\mathbb{H}} \quad (17)$$

For rigid  $l = 1$  displacements,

$$\tilde{\mathbb{H}} = \tilde{\xi}_{x\parallel} \frac{\partial x}{\partial \theta} + \tilde{\xi}_{y\parallel} \frac{\partial y}{\partial \theta} \quad (18)$$

where the prime denotes differentiation with respect to  $z$ , and the  $n$ th frequency component is given by

$$\tilde{\mathbb{H}}_n = -\sqrt{2\psi} [\sigma(\sigma u_n)_{\parallel} \sin \theta + \tau(\tau v_n)_{\parallel} \cos \theta] \quad (19)$$

The expression for the diffusion coefficient becomes

$$D_{\psi} = \frac{\pi \psi}{4} \left( \frac{mc}{q} \right)^2 \frac{1}{\delta \omega_n} \left[ \frac{(\overline{v_{\parallel}^2 + \mu B} \sigma(\sigma u_n)_{\parallel})^2}{(\overline{v_{\parallel}^2 + \mu B} \tau(\tau v_n)_{\parallel})^2} \right] \quad (20)$$

where the overbar denotes the bounce average. For symmetrically arranged pump coils, we have  $\sigma(z) = \tau(-z)$ . Then, with appropriate source terms, the equation for line-bending perturbations becomes

$$\begin{aligned} \frac{d}{dz} \left[ (B\sigma^2 + 1) \frac{du}{dz} \right] + \left[ \omega^2 \frac{\rho \sigma^2}{B} - 2 \frac{\langle p \rangle}{B} \sigma \sigma_{\parallel} \right] u \\ = - \frac{d}{dz} [\tilde{B}_x (\sigma + \tau)] \end{aligned} \quad (21)$$

where  $\langle p \rangle = \langle p_{\perp} + p_{\parallel} \rangle / 2$  is the flux-averaged pressure.

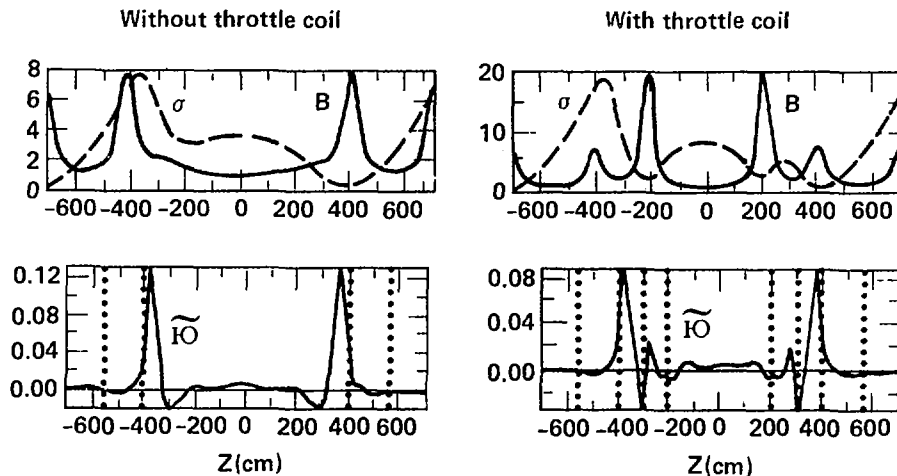


FIG. 6. Typical axial profiles of  $B$ ,  $\sigma$  and  $\theta = \pi/4$ , for TMX-U geometry with and without throttle coils. The perturbation coils generating  $\tilde{B}_x$  and  $\tilde{B}_y$  are at  $z = 390$  cm and  $z = -390$  cm without throttle coil, and at  $z = 300$  cm and  $z = -300$  cm with throttle coil. Vertical dotted lines in the lower figures mark extrema of  $B$ .

Generally, even though  $\tilde{B}_x$  is localized in  $z$ , the function  $u$  has sizable amplitude throughout the plasma column. However, when there is a choke coil or a thin fan between the perturbing coils and the central cell, so that  $\sigma = \tau = 1/\sqrt{B}$  in the central cell,  $\tilde{\theta}$  is small there. Figure 6 shows profiles of  $\tilde{\theta}$  for the TMX-U geometry without and with a throttle coil. In each case the perturbation coil has been placed at the location of the thin fan, as illustrated in the figure.

## 6. OTHER TOPICS

We have also considered creation of electrostatic perturbations by using modulation of biased segments of the endwall, and by using modulation of power inputs to the plasma, such as by ECRH. The analysis of these perturbations is similar to that of trapped particle modes [6]. Although some localization to the barrier is possible, we find considerable penetration of perturbations into the central cell. Such techniques would generate effective pumps only if the ions in the central cell did not exhibit the same drift resonances as those in the barrier.

Drift pumping of an axisymmetric geometry is found to be more difficult than one having equilibrium geodesic line curvature. First, the geodesic curvature increases the flux

displacements of particles relative to an axisymmetric geometry with the same  $B(z)$  profile. Second, the thin fans of a quadrupole geometry permit tight coupling between perturbation coils and the plasma. An experimental test of drift pumping must compete the induced diffusion with collisional trapping. Therefore, a near-term test in a relatively collisional machine would be more easily carried out if the device had an asymmetric geometry.

### REFERENCES

- [1] BALDWIN, D.E., LOGAN, B.G., Phys. Rev. Lett. **43** (1979) 131.
- [2] McGUIRE, K., et al., Phys. Rev. Lett. **50** (1983) 891.
- [3] LOGAN, B.G., et al., in Plasma Physics and Controlled Nuclear Fusion Research 1984 (Proc. 10th Int. Conf. London, 1984), Vol. 3, IAEA, Vienna (1985) 335.
- [4] ANTONSEN, T.M., Jr., LEE, Y.C., Phys. Fluids **25** (1982) 132.
- [5] LICHTENBERG, A.J., LIEBERMAN, M.A., Regular and Stochastic Motion, Springer-Verlag, New York (1983) Ch.4.
- [6] BERK, H.L., ROSENBLUTH, M.N., WONG, H.V., ANTONSEN, T.M., Jr., BALDWIN, D.E., Fiz. Plazmy **9** (1983) 176; Sov. J. Plasma Phys. **9** (1983) 108.



## STABILIZATION OF FLUTE INSTABILITY IN AXIALLY SYMMETRIC MIRROR MACHINES

I.A. KOTEL'NIKOV, G.V. ROSLYAKOV,  
D.D. RYUTOV, G.V. STUPAKOV  
Institute of Nuclear Physics,  
Siberian Branch of the  
USSR Academy of Sciences,  
Novosibirsk, Union of Soviet Socialist Republics

### Abstract

#### STABILIZATION OF FLUTE INSTABILITY IN AXIALLY SYMMETRIC MIRROR MACHINES.

Axially symmetric tandem mirrors have a number of important advantages over axially non-symmetric ones, but attempts to create them have foundered on the serious difficulty of stabilizing the flute oscillations excited in them because of the — on average — unfavourable curvature of the magnetic field lines. The paper describes new results of studies on two methods of achieving stabilization in axisymmetric mirror machines by using, first, a non-paraxial magnetic field and, second, sloshing ions in a paraxial mirror machine. The overall conclusion of the paper is that there is some prospect of creating an MHD stable axisymmetric mirror machine with 'natural' geometry (i.e. with a single-connected plasma which does not contain conductors within it).

### 1. INTRODUCTION

At present the main method of stabilizing plasma flute instability in open traps is to create a magnetic well using multipole windings. However, the disruption of the axial symmetry of the plasma which inevitably follows from this procedure produces a number of undesirable effects, notably an increase in transverse transport [1] and distortion of plasma equilibrium on long sections of the homogeneous field [2]. Consequently, a number of suggestions have been made recently regarding the possibility of stabilizing flute perturbations within axisymmetric magnetic configurations [3-10]<sup>1</sup>. Most of these suggestions are based on the use of systems with non-single-connected plasma [4, 6, 9] and cusps [5, 7]. The transition to a non-single-connected plasma is, however, accompanied by certain technical difficulties, the main one being a reduction in plasma thickness (which carries with it the danger of micro-instability excitation); as far as the use of cusps is concerned, it should be noted that their operation will depend largely on the behaviour of the hot plasma near the magnetic field zero point, a question which has so far been the subject of little experimental study.

<sup>1</sup> This paper considers devices with a long plasma particle free path, concentrating mainly on tandem mirrors; for systems with a short free path, an effective mechanism for stabilization (namely, the plasma flow beyond the mirror) has long been known [11, 12].

References [3, 8, 10] dealt with plasma stabilization within the framework of 'natural' open trap geometry. Timofeev [3] suggested stabilizing the plasma entirely by kinetic effects similar to finite Lamor radius (FLR) effects. This approach seems promising, but the possible role of fluctuations with negative energy which can appear in systems with fast ion drift is still not fully understood. In Ref. [8] Hinton and Rosenbluth made a detailed study of a possibility which had frequently been raised earlier, namely that of stabilizing a plasma by creating in it a population of 'sloshing' ions having a turning point in a region of favourable curvature of the field lines; however, the technical requirements for the injection system (injection energy  $\sim 40$  MeV) for the magnetic field configurations examined in Ref. [8] turned out to be extremely demanding. In Ref. [10] Kesner suggested installing a conducting casing near the plasma surface to achieve stability, but in this case stabilization — if achieved at all — occurs only at high plasma pressure and when the plasma has a high degree of anisotropy.

The above short summary of work on MHD stabilization of axisymmetric traps indicates that, although there are a number of interesting proposals, the problem is far from resolved. The present paper examines a further two possibilities for creating an axisymmetric MHD stabilizer for open (mainly tandem) traps.

The first possibility is the use of a stabilizer in the form of a non-paraxial mirror machine in which the transverse dimension of the plasma is comparable with the distance between the mirrors. We show that large scale flute oscillations can be made stable in such a device, while small scale fluctuations can be stabilized by the FLR effect. It may even be conceivable that complete stabilization is not necessary since a certain level of MHD activity at high modes will not result in excessively fast plasma losses. The essential point is that stabilization should occur within the 'natural' open trap geometry and should not require transition to a non-single-connected plasma.

The second possibility lies in the use of sloshing ions. We demonstrate that, by optimizing the shape of the magnetic field and using drift pumping [13], the injection energy requirements can be lowered significantly (by comparison with the predictions in Ref. [8]), which greatly improves the prospects for this stabilization method.

## 2. MHD STABILITY IN A NON-PARAXIAL MIRROR MACHINE

### 2.1. Model of plasma as an ideal gas

We shall consider the mirror machine to be part of a tandem mirror with a long central cell whose presence ensures the stability of all flute modes (except the global mode  $m = 1$ ) because of FLR effects [10].

FLR effects in the long homogeneous section of a central mirror machine exert no influence on the rigid body displacement of the plasma in this section. Such

displacement is due to the homogeneous electric field to which the potential perturbation of the following form corresponds:

$$\varphi = \text{const } \sqrt{\psi} \cos \theta \quad (1)$$

where  $\theta$  is the azimuthal angle. In a flute perturbation the potential  $\varphi$  is constant along the field lines, and so in a finite mirror machine the potential will also be given by Eq. (1). In this case the potential perturbation energy is defined by the equation:

$$\delta W = A \int \left[ p'U' + \gamma \frac{p}{U} U'^2 \right] \psi d\psi \quad (2)$$

where

$$U = \int \frac{d\ell}{B} \quad (3)$$

is the specific volume of the flux tube (integration is performed with respect to the field line between infinitely strong mirrors),  $\psi$  is the magnetic flux inside a given magnetic surface,  $p$  is the pressure,  $A > 0$  is a constant which does not need to be considered further, and the prime indicates differentiation with respect to  $\psi$ .

If the plasma transverse dimension is small compared with the scale of the change in the magnetic field, then we have the inequality  $|p'|/p \gg U'/U$  and the last term in expression (2) can be neglected. Performing an integration by parts in the first term and taking into account that  $\psi U'' \rightarrow 0$ , in the paraxial region, we obtain the following for a 'thin' plasma:

$$\delta W = -AU' \Big|_{\psi=0} \int p d\psi < 0 \quad (4)$$

It is well known that on the magnetic axis (at  $\psi = 0$ ) the derivative  $U'$  is positive (see Ref. [14], for example), in other words that a 'thin' plasma proves to be universally — and independently of the pressure profile  $p(\psi)$  — unstable in relation to the global mode [4].

The last term in Eq. (2), which plays a stabilizing role, becomes crucial at distances from the axis of the order of the length of a finite mirror machine. Thus, if it is possible to stabilize the global mode at all, this can only be done if the plasma is 'thick' (and the paraxial approximation is no longer valid).

Integrating the first term in Eq. (2) by parts we obtain

$$\delta W = A \int p F(\psi) \psi d\psi \quad (5)$$

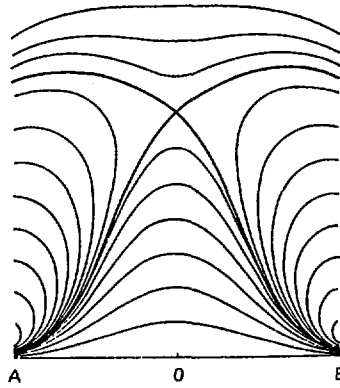


FIG. 1. Magnetic field lines of two 'point' mirror coils located at points A and B. Bold line denotes separatrix passing through the magnetic field zero point. Point O is equidistant from points A and B.

where

$$F(\psi) \equiv \gamma \frac{\psi}{U} U'^2 - (\psi U')' \quad (6)$$

To prove the existence of stable pressure profiles it is enough to show that a range of values of  $\psi$  exists in which  $F(\psi) > 0$ . For small  $\psi$ ,  $F(\psi) \approx -U'(0)$  and, in accordance with what was said above,  $F(\psi) > 0$ . As the distance from the magnetic axis increases, the plasma confinement region is usually bounded by the separatrix passing through the magnetic field zero point (points) (see Fig. 1 for an example). It is a simple matter to demonstrate that, as the distance to the separatrix decreases,  $U$  increases according to the law

$$U \propto \ln \frac{1}{|\psi_s - \psi|} \quad (7)$$

where  $\psi_s$  is the magnetic flux enclosed within the separatrix. Using Eq. (7), we find that, for  $\psi \rightarrow \psi_s$ ,  $F(\psi) \approx -a(\psi - \psi_s)^{-2}$ , with  $a > 0$ , in other words  $F(\psi) < 0$  here also. Hence, steady states can only exist at intermediate  $\psi$  values, in a certain ring region. It is worth noting that if such a region (stability ring) exists, then any pressure distribution inside it will be stable (with respect to the global mode).

Magnetic field configurations in which a stability ring exists are far from common. The magnetic field of the two point coils whose field lines are shown in Fig. 1 does not possess this property, for example; the function  $F(\psi)$  for this field

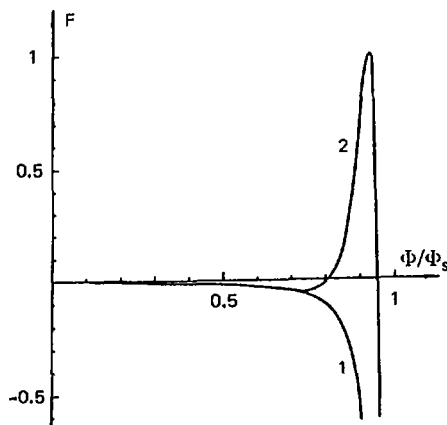


FIG. 2. Graph of function  $F(\Phi)$  (in arbitrary units) given by expression (6). Curve (1) corresponds to field of the point coils, and curve (2) to superposition of this field and the homogeneous field,  $\Delta B = 0.06B_*$ .

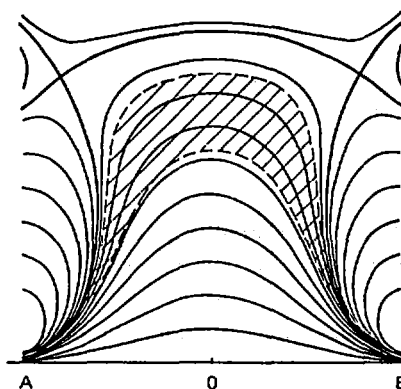


FIG. 3. Force lines of superposition of field of the two point coils and the homogeneous field,  $\Delta B = 0.06B_*$ . Separatrix is indicated by bold line.

is shown in Fig. 2. If a homogeneous field  $\Delta B$  directed along the coil axis is superimposed on this field, then a stability ring occurs in the range of values

$$0.023 B_* < \Delta B < 0.20 B_*$$

where  $B_*$  is the field at the point 0 in Fig. 1. For  $\Delta B = 6 \times 10^{-2} B_*$ , a graph of the function  $F(\psi)$  and the field lines are illustrated in Figs 2 and 3, respectively. Figure 4 presents graphs of the functions  $U(\psi)$  and  $B_0(\psi)$  ( $B_0$  is the field in the equatorial plane of the mirror machine) for this field.

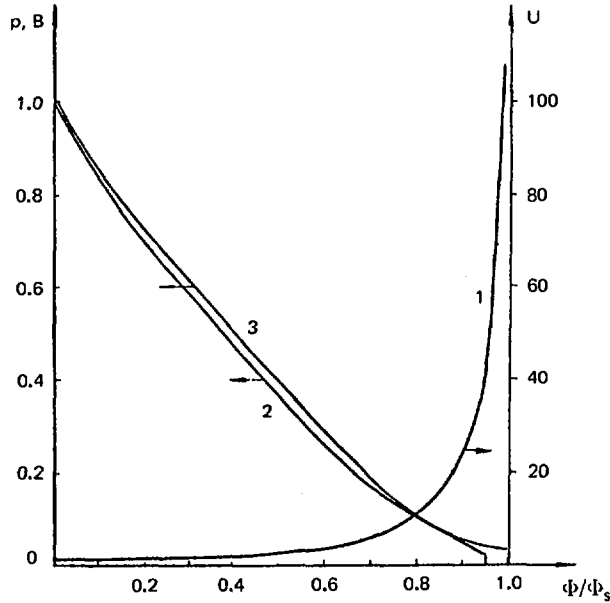


FIG. 4. Graphs of the dependences  $U(\Phi)$  (curve (1)),  $B(\Phi)$  (curve (2)) and  $p(\Phi) \propto U^{-0.87}$  (curve (3)) for the field shown in Fig. 3. The dependences  $p(\Phi)$  and  $B(\Phi)$  are normalized to their values on the trap axis,  $U(\Phi)$  is given in arbitrary units.

By creating a plasma in the stability ring, we ensure a certain MHD stability margin which enables a certain quantity of plasma to be placed also in the paraxial region of the outermost mirror cells. Thus for the magnetic configuration illustrated in Fig. 3, a numerical calculation indicates that for pressure distributions of the form

$$p = \begin{cases} p_a (U/U_a)^{-\alpha}, & \psi < \psi^* \\ 0, & \psi > \psi^* \end{cases} \quad (8)$$

where  $\psi^*$  is the magnetic flux corresponding to the outer boundary of the stability ring, and the index 'a' relates to the values  $p$  and  $U$  on the magnetic axis, there is stability at  $\alpha < 0.87$  (the maximum pressure profile, corresponding to  $\alpha = 0.87$ , is shown in Fig. 4).

## 2.2. Kinetic energy principle

Above we have used the energy principle in an ideal magnetohydrodynamic model in order to study stability. More appropriate for collisionless plasma is the Kruskal-Oberman energy principle [15], which is not limited by the isotropic

pressure approximation and enables the equilibrium stability of anisotropic plasma to be studied also.

Let us first consider the new contribution that the Kruskal–Oberman energy principle makes to the problem of isotropic plasma stability examined in the preceding section. Using the Kruskal–Oberman energy expression changes the shape of the function  $F(\psi)$  entering into integral (5). It is possible to show, however, that this function is, as usual, negative both for small  $\psi$  and for  $\psi \rightarrow \psi_s$ . Consequently, as before, the steady states — if they exist — form a stability ring, and this ring will be wider than the one that results from magnetohydrodynamics, for the familiar reason that the Kruskal–Oberman energy principle predicts better plasma stability than magnetohydrodynamics with the adiabatic index  $\gamma = 5/3$ . However, as the numerical calculations show, the widening of the stability ring that results from switching to the Kruskal–Oberman energy principle is not large.

Let us now look at the question of the stability of a plasma with a strongly anisotropic distribution function. This situation is of less interest from the practical point of view for two reasons: first, the creation of strongly anisotropic distributions in characteristic thermonuclear reactor conditions requires extremely high injection energies; and, secondly, such distributions are more susceptible to micro-instabilities. We shall none the less consider such distributions also, since they can be created in existing small scale devices with low electron temperature<sup>2</sup>.

Let us begin with a plasma with  $p_{\parallel} = 0$ . It occupies the equatorial plane of the trap ( $z = 0$ ). For the plasma to be stable in relation to displacements along the field line, the magnetic field should have a ‘longitudinal’ minimum at  $z = 0$ . It can be shown that the condition for the existence of this minimum has the following form [16]:

$$2 \left( \frac{dB_0}{dr} \right)^2 > \frac{B_0}{r} \frac{d}{dr} r \frac{dB_0}{dr} \quad (9)$$

where  $B_0(r) \equiv B_z|_{z=0}$  is the magnetic field in the equatorial plane.

Let us clarify the question of whether it is possible to achieve stability in such a system in relation to all flute modes. The expression for the flute perturbation energy in a disc plasma has the following form [21]:

$$\delta W = -A \int d\psi r^2 \xi^2 \left[ B'_0 W'_{\perp} - 2 \frac{W_{\perp}}{B_0} B_0'^2 \right] \quad (10)$$

where  $W_{\perp}$  is the energy per unit plasma area,  $\xi$  is the radial displacement component in the flute perturbation and  $A$  is the positive constant. It can be seen from expression (10) that the outer plasma boundary can only be stable if it is located in

<sup>2</sup> A low electron temperature enables the injection energy  $E_{inj}$  to be reduced since the condition  $E_{inj} \gg (m_i/m_e)^{1/3} T_e$  has to be satisfied in order to obtain narrow angular distributions.

the region where  $dB_0/dr > 0$ . Two possibilities should now be considered: (1)  $B_0$  increases monotonically from the axis itself to the outer plasma boundary; (2) there is a minimum (minima) in the intermediate space. In the first case inequality (15) definitely ceases to be valid near the axis (at  $r \rightarrow 0$ )<sup>3</sup>, in other words the paraxial region is empty and the plasma has an inner boundary where  $\partial W_{\perp}/\partial r < 0$ . But because of the condition  $dB_0/dr > 0$  the inner boundary is unstable, and hence absolute stability is impossible in the first case. Turning to the second case, let us look at the vicinity of the  $B_0$  minimum nearest to the outer plasma boundary. In the vicinity of the minimum, where the  $dB_0/dr$  derivative is sufficiently small, inequality (9) clearly does not hold, in other words, the region around the minimum is empty and the plasma has an inner boundary located outside the minimum. However, this boundary is then unstable. We have thus demonstrated that absolute stability is impossible for a disc plasma.

Let us check, therefore, whether it is not possible for such a plasma to be stable to the global mode. This condition is obtained if the displacement  $\xi$  corresponding to the disruption of the potential (1) is substituted in Eq. (10), thus producing:

$$\delta W = \text{const} \int d\psi \frac{W_{\perp}}{B_0^2} \frac{\partial}{\partial \psi} \psi \frac{\partial B_0}{\partial \psi} \quad (11)$$

Consequently, it is essential for stability that the following inequality be satisfied at the same time as Eq. (9) at one point at least on the radius.

$$\frac{d}{dr} \frac{\Phi}{rB_0} \frac{dB_0}{dr} > 0 \quad (12)$$

It is easy to verify that inequalities (9) and (12) cannot be reconciled in the paraxial region. However, they may be satisfied simultaneously at finite distances from the axis. In the magnetic field shown in Fig. 3, for example, this happens in the interval  $0.49 r_s < r < 0.83 r_s$ , where  $r_s$  is the radius of the separatrix.

We can also examine the opposite extreme case where the transverse component of the particle velocity in the equatorial plane is very small (extreme case of tangential injection). The mirror ratio in this case is considered to be so large that these particles are still retained within the trap, stopping in the region of the very strong field in the mirror. For global mode stability it is necessary for the following condition to be satisfied on at least one magnetic surface [17]:

$$\frac{d}{d\psi} \frac{\psi}{\ell^3} \frac{d\ell}{d\psi} > 0 \quad (13)$$

<sup>3</sup> It should be recalled that near the axis  $B_0 = C_1 + C_2 r^2$ .

where  $\ell$  is the length of the field line between the mirrors. This condition is not fulfilled anywhere for the magnetic field shown in Fig. 3, so that this case offers no advantages over that of the isotropic plasma where there is a wide stability ring in the same field.

### 3. STABILIZATION OF FLUTE PERTURBATIONS IN A PARAXIAL MIRROR MACHINE BY MEANS OF SLOSHING IONS

MHD stability of a plasma in a paraxial axisymmetric mirror machine can be achieved if a group of sloshing ions is introduced into the system and the magnetic field profile is selected in such a way that the turning point and, consequently, the pressure peak of such ions are located in the region where the curvature of the field lines is favourable. This method of stabilizing flute fluctuations by means of sloshing ions is fairly self-evident but the evaluations conducted earlier did not reveal all its capabilities. It was found in Ref. [8] that to stabilize the system it is necessary to form a population of sloshing ions with an extremely small angle straggling similar to that of helium ions of 50 MeV energy during injection into a plasma with an electron temperature  $T_e = 50$  keV (ions with so much energy are scattered much more slowly than they are slowed down by electrons).

Below we show that optimizing the magnetic field profile can make MHD stabilization by means of sloshing ions a more realistic possibility.

#### 3.1. Stability condition

To determine whether a given system is stable with respect to flute perturbations, it is sufficient in a paraxial approximation to examine the case of a plasma with a sharp boundary, when the pressure is constant over its cross-section. Then, in accordance with the Rosenbluth-Longmire criterion [18], an axisymmetric configuration is stable if

$$I = \int_{-L}^L P a^3 \frac{d^2 a}{dz^2} dz > 0 \quad (14)$$

where  $a = a(z)$  is the boundary field line equation and  $d^2 a/dz^2$  is its curvature. The sum of the longitudinal and transverse pressure  $P = p_{\parallel} + p_{\perp}$  is a function of the magnetic field induction  $B$  (see Ref. [19], for example) which in a paraxial approximation is proportional to  $a^{-2}$ ; hence it can be considered that  $P = P(a)$ . Integration in Eq. (14) is performed along the  $z$ -axis of the trap for the region occupied by the plasma. At the boundary of this region  $z = \pm L$ , the function  $P(a)$  goes to zero while the magnetic field, which can be considered symmetrical relative to the  $z = 0$  plane

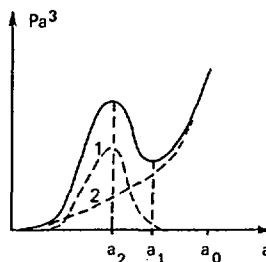


FIG. 5. Qualitative form of the function  $Pa^3$  when criterion (16) is satisfied. Dashed line depicts contributions of isotropic plasma (1) and sloshing ions (2).

without limiting its generality, reaches a maximum. Having performed an integration by parts in Eq. (1):

$$I = - \int_{-L}^L dz \left( \frac{da}{dz} \right)^2 \frac{d}{da} [Pa^3] \quad (15)$$

it is not difficult to establish that, if the function

$$g(a) = \frac{d}{da} [Pa^3]$$

is of fixed sign and, as in the case of isotropic plasma, positive, then  $I > 0$ . The system may be stable,  $I > 0$ , only if  $g(a)$  is negative in a certain interval. In this case a local minimum appears in the graph of the function  $Pa^3$  (Fig. 5). This is precisely the situation that arises if a population of sloshing ions with a sufficiently small angle straggling is created. The points  $a = a_1$  and  $a = a_2$ , where  $g(a) = 0$ , isolate on the field line the section  $a_1 < a(z) < a_2$ , in which  $g(a) < 0$  and which makes a stabilizing (positive) contribution to the integral (15). By reducing the length of this section  $\ell = z_2 - z_1$  at fixed values  $a(z_1) = a_1$  and  $a(z_2) = a_2$  and thereby increasing here the angle of inclination of the field line  $|da/dz|$  (but none the less remaining within the framework of the paraxial approximation), it is possible to satisfy the stability criterion  $I > 0$  even at a very small (in absolute terms) negative value of the minimum  $g(a)$ . Thus the question of MHD stabilization by means of sloshing ions boils down to ascertaining the conditions at which

$$\min_a g(a) < 0 \quad (16)$$

It should be noted that the stabilization boundary

$$\min_a g(a) = 0$$

corresponds to such a small peak value on the  $Pa^3$  function graph that the local maximum and minimum run together, and at the point of convergence  $a_1 = a_2$  an inflection forms, i.e.

$$g(a_1) = 0, \quad \left. \frac{dg}{da} \right|_{a=a_1} = 0 \quad (17)$$

With regard to the stabilization boundary found in Ref. [8], it corresponds to a large peak value such that  $P(a_1)a_1^3 \sim P(a_0)a_0^3$ , where  $a_0$  is the plasma radius at the magnetic field minimum.

### 3.2. Fast ion distribution function

A population of sloshing ions is formed by injecting monoenergetic particles with a very small initial angle straggling and then slowing them down on electrons; because of the large energy  $E_0$  of the injected particles this slowing down takes place much more quickly than slowing down and scattering due to plasma ions. Assuming that a major part of the plasma volume  $V$  is allotted to the long homogeneous central part of the trap, we can write the kinetic equation for the sloshing ion distribution function  $f(V, \theta)$  in this part of the trap in the following form:

$$\begin{aligned} \frac{\partial f}{\partial t} = & \frac{1}{\tau_{ei} v^2} \frac{\partial}{\partial v} (v^3 + v_c^3) f + \frac{v_0^3}{\tau_{ii} v^3} \frac{\partial^2 f}{\partial \theta^2} \\ & - \frac{f}{\tau_*} + \frac{Q \delta(v-v_0)}{4\pi V \sin \theta_0 v^2} [\delta(\theta-\theta_0) + \delta(\theta+\theta_0)] \end{aligned} \quad (18)$$

where the penultimate term describes the reduction in sloshing ions as a result of either external pumping (see below) or of charge exchange with the neutral atoms present in the plasma;  $\theta_0$  is the injection angle (reckoned from the system axis);  $Q$  is the injection power;

$$\tau_{ei} = \frac{3}{4} \frac{M}{\sqrt{2\pi}} \frac{M}{\sqrt{m_e}} \frac{T_e^{3/2}}{Z^2 \Lambda e^4 n}$$

is the slowing down time of ions with charge  $Z$  and mass  $M$  due to electrons:

$$\tau_{ii} = \frac{M^2 v_0^3}{2\pi Z^2 \Lambda e^4 n}$$

is the scattering time (due to ions),  $\Lambda$  is the Coulomb logarithm;  $v_0 = (2E_0/M)^{1/2}$  and  $v_c = (3\pi^{1/2} m_e/4M)^{1/3} (2T_e/m_e)^{1/2}$  are the initial and critical velocities of injected ions respectively (at  $v = v_c$  the velocities of their scattering and slowing down

due to electrons are comparable);  $E_0$  is the injection energy. Assuming for the sake of simplicity that  $\tau_* = \text{const}$ , it is a simple matter to find a steady state solution for Eq. (18):

$$f = \frac{Q \tau_{ei} (v^3 + v_c^3)^{-1}}{4\pi^{3/2} V E_0 \sin \theta_0 \Delta\theta} \left[ e^{-\left(\frac{\theta - \theta_0}{\Delta\theta}\right)^2} + e^{-\left(\frac{\theta - \pi + \theta_0}{\Delta\theta}\right)^2} \right] \left( \frac{v^3 + v_c^3}{v_0^3 + v_c^3} \right)^{\frac{\tau_{ei}}{3\tau_*}} \quad (19)$$

where

$$\Delta\theta = \Delta\theta_0 \left( \frac{v_0^3}{v_c^3} \ln \frac{1 + v_c^3/v^3}{1 + v_c^3/v_0^3} \right)^{1/2}$$

$$\Delta\theta_0 = \frac{2}{3} \left( \frac{v_c^3}{v_0^3} \right)^{1/2}$$

### 3.3. Stabilization condition at $\tau \gg \tau_{ei}$

Let us first examine the case where the lifetime of the fast ions is not long enough to allow them to be converted by charge exchange into neutral atoms, i.e.  $\tau_{ei} \ll \tau_*$ . In such a case, as we shall see, the minimum injection energy at which it is possible to achieve stabilization by sloshing ions is several times higher than the energy

$$E_c = \frac{Mv_c^3}{2} = 14.8 \left( \frac{M}{m_H} \right)^{1/3} T_e$$

(where  $m_H$  is the proton mass) at which slowing down due to electrons and ions is comparable.

Having performed calculations similar to those in Ref. [20] (see also Ref. [8]), it is possible to obtain the function  $Pa^3$  and, using correlation (17), to determine the injection energy and power at which flute perturbation stability can be ensured.

As has already been shown, the system is stable if the function  $Pa^3$  is non-monotonic and if there is a marked contribution from the spike created by sloshing ions against a background of a monotonically increasing contribution from the isotropic plasma  $2p_0a^3$  (see the dashed line in Fig. 5). Of course, the greater the isotropic plasma pressure is, the greater must be the power  $Q$  and (or) the injection energy  $E_0$  in order to ensure stability (the spike becomes higher as  $Q$  increases and narrower as  $E_0$  increases). If the injection energy is not high enough, the function

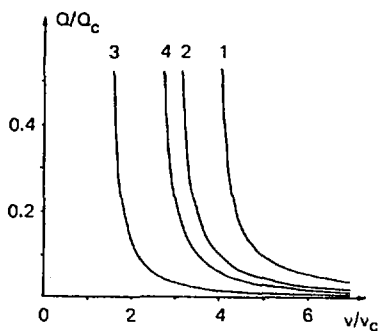


FIG. 6. Graph of dependence of injection power on initial velocity of particles injected at angles:  
 1 -  $\tau_* \gg \tau_{ei}$ , for the optimal magnetic field;  
 2 -  $\tau_* \gg \tau_{ei}$ , result of Ref. [8];  
 3 -  $\tau_* = 0.5 \tau_{ei}$ , pumping of sloshing ions from additional short mirror cell;  
 4 -  $\tau_* = 0.5 \tau_{ei}$ , pumping from long mirror cell.

$Pa^3$  becomes monotonic even if the isotropic plasma contribution is ignored. Hence stabilization can only be achieved if the injection energy is greater than a certain critical value  $E_*$ .

Calculations (the details of which can be found in Ref. [21]) show that the dependence of the injection power required for stabilization on the injected particle velocity has the form:

$$Q = \frac{Vp_0}{\tau_{ei}} \frac{33.2 \sin^{1/2} \cdot 2\theta_0 (v_c/v_0)^{9/4}}{1 - 11.8 \operatorname{ctg} \theta_0 (v_c/v_0)^{3/2}} \quad (20)$$

To compare Eq. (20) with the results of Ref. [8], which are for helium injection into an isothermal deuterium plasma, we shall assume that  $\theta_0 = \arcsin \sqrt{6/7}$  as in Ref. [8] and will express  $Q$  in dimensionless form in terms of  $Q/Q_c$ .

$$Q_c = \frac{3}{2} \frac{p_0 V}{\tau_c} \left\{ \left( \frac{T_i}{T_e} \right)^{3/2} \left( \frac{Z}{2} \right)^2 \left( \frac{4m_H}{M} \right) \left( \frac{m_i}{2m_H} \right)^{1/2} \right\} \lg R$$

where, neglecting ambipolar effects, the multiplier in front of the braces is, with an accuracy up to the numerical coefficient, equal to the energy flow through the mirrors, the combination in the braces is equal to unity for helium injection into an isothermal deuterium plasma,  $m_H$  is the proton mass,

$$\tau_c = \tau_{ei} \left( \frac{T_i}{T_e} \right)^{3/2} \frac{(2m_i m_e)^{1/2}}{M} Z^2 \lg R$$

is the scattering time into the loss cone for ions of the main plasma component which have a unit charge and mass  $m_i$ . As a result, we obtain

$$\frac{Q}{Q_c} = \frac{0.86 (v_c/v_0)^{9/4}}{1 - (2.85 v_c/v_0)^{3/2}} \quad (21)$$

It is very important that at a  $v_0$  value 1.5 to 2 times greater than the minimum injected ion velocity  $v_* = \sqrt{2E_*/M} = 2.85 v_c$ , at which stabilization by sloshing ions is still possible ( $Q \rightarrow \infty$  at  $v \rightarrow v_*$ ), the injection power derived from relation (13) decreases much more quickly ( $Q \propto v_0^{-9/4}$ ) as  $v_0$  increases than follows from the calculation performed in Ref. [8] ( $Q \propto v_0^{-3/4}$ ). Equation (21) and the corresponding dependence

$$\left. \frac{Q}{Q_c} \right|_{[8]} = \frac{0.022}{(v_0/3.81 v_c)^{3/4} - 1} \quad (22)$$

obtained in Ref. [8] are plotted in Fig. 6. A comparison of Eqs (21) and (22) shows that the minimum velocity  $v_*$  of injected ions can be reduced by a factor of 1.34, and hence the injection energy  $E_*$  by a factor of 1.8.

#### 4. FURTHER REDUCTION OF MINIMUM INJECTION ENERGY

Since the minimum injection energy  $E_*$  is still very high, it would be advantageous to find a way of reducing it further. This can be achieved by changing to a system of two mirror cells — one long and the other short (but such that the paraxial approximation in it still applies). We shall consider that tangential injection is only performed into the long mirror cell, the injection angle  $\theta_0$  corresponding to the turning point of the fast ions at the magnetic field maximum in the mirror which separates the two mirror cells (1 in Fig. 7). Under these conditions only those fast ions whose pitch angle has decreased compared with  $\theta_0$  (because of scattering) can penetrate the short mirror cell. In this case the fast particle angular distribution

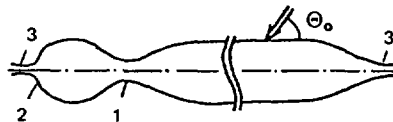


FIG. 7. Two-mirror cell system. Outer mirrors 3 are stronger than intermediate mirror 1. Arrow indicates injection of fast particles. Angle of inclination of field lines to system axis is not given to scale (in reality, it is less) and in the stabilizing section 2 the inclination is much greater than in the remaining part of trap.

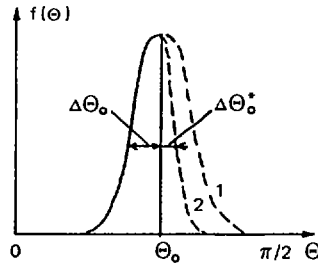


FIG. 8. Fast ion angular distribution function in short mirror cell reduced to magnetic field in centre of long mirror cell. Curve 1 corresponds to the absence of pumping ( $\tau_* \gg \tau_{ei}$ ), curve 2 to pumping whose time  $\tau_*$  satisfies conditions (23) and (24).

function in the short mirror cell will have the form shown by the solid line in Fig. 8, which ensures the existence of a section with negative values of the function  $g(a)$  even at large  $\Delta\theta_0$  values (i.e. at low injection energies). The appearance of this segment makes it possible to stabilize the flute instability by creating a section with a sharply increasing magnetic field in the outer mirror of the short mirror cell (2 in Fig. 7).

Collisions in the short mirror cell will, of course, cause blurring of the right hand boundary of the fast particle distribution function in Fig. 8 and a reduction in the stabilizing effect. To prevent this from happening, some mechanism for pumping out trapped fast particles must be introduced in the short mirror cell. The most suitable one is the drift pumping mechanism [13] associated with the use of a small axially non-symmetric perturbation of the magnetic field oscillating at a frequency close to that of the drift revolution of the fast particles around the magnetic axis. The advantage of this pumping method is that, because of the considerable difference between the drift frequencies of the three populations of ions — fast trapped, fast passing (i.e. fast ions with  $\theta < \theta_0$ ) and slow — it is possible to achieve selective pumping of the first population without losing the second and third.

The substantial (of the order of  $\Delta\theta_0$ ) time for the blurring of the right hand boundary of the fast particle distribution function is equal by order of magnitude to the scattering time for such particles at the angle  $\Delta\theta_0$  (the scattering corresponds by order of magnitude to their slowing-down time due to electrons  $\tau_{ei}$ ). For this reason, the characteristic 'pumping time' should satisfy the condition

$$\tau_* \ll \tau_{ei} \quad (23)$$

Given condition (23) the width of the right hand boundary of the peak in Fig. 8 can be calculated from the equation

$$\Delta\theta_* \sim \Delta\theta_0 \sqrt{\tau_*/\tau_{ei}}$$

while the power  $Q_*$  lost from the system together with the pumped out particles can be evaluated from the equation

$$Q_* \sim \frac{\Delta\theta_0}{\Delta\theta_*} \frac{V_*}{V} Q$$

where  $V_*$  is the volume of the short mirror cell. To ensure that pumping particles out of the short mirror cell does not lead to a significant reduction in the number of fast particles in the system, it is necessary for the condition  $Q_* < Q$  to be satisfied as this limits the permissible pumping time to below:

$$\tau_* > \tau_{ei} \left( \frac{V_*}{V} \right)^2 \quad (24)$$

Hence, for the minimum attainable  $\Delta\theta_*$  value, we have:  $\Delta\theta_* \sim \Delta\theta_0 V_*/V$ . Thus, when the volume of the short mirror cell is sufficiently small, it really is possible to increase substantially the steepness of the right hand slope of the fast particle angular distribution and thereby to reduce injection energy.

The results of quantitative calculations of the dependence  $Q(v_0)$  (for details see Ref. [21]) are given in Fig. 6 (curve 3).

Another method of reducing  $E_*$  is to pump sloshing ions out of the long mirror cell. A natural mechanism for such pumping may be losses due to the charge exchange of fast ions in the residual gas penetrating the plasma. Naturally, because of the pumping of ions directly out of the long mirror cell, the injection power has to be increased in order to achieve stabilization, but under these conditions it is no longer necessary to have an additional mirror cell. The dependence  $Q(v_0)$  for such a case is shown by curve 4 in Fig. 6.

## REFERENCES

- [1] RYUTOV, D.D., STUPAKOV, G.V., *Pis'ma Zh. Ehksp. Teor. Fiz.* **26** (1977) 186.
- [2] STUPAKOV, G.V., *Fiz. Plazmy* **5** (1979) 871.
- [3] TIMOFEEV, A.V., *Pis'ma Zh. Ehksp. Teor. Fiz.* **29** (1979) 277.
- [4] ARSENIN, V.V., *Fiz. Plazmy* **5** (1979) 1293.
- [5] LOGAN, B.G., *Comments Plasma Phys. Controll. Fusion* **6** (1980) 199.
- [6] ARSENIN, V.V., *Fiz. Plazmy* **8** (1982) 484.
- [7] DIMOV, G.I., Prepr. No. 82-150, Nuclear Physics Institute, Siberian Dept. USSR Acad. Sci., Novosibirsk (1982).
- [8] HINTON, F.L., ROSENBLUTH, M.N., *Nucl. Fusion* **22** (1982) 1547.
- [9] ARSENIN, V.V., *Pis'ma Zh. Ehksp. Teor. Fiz.* **37** (1983) 534.
- [10] KESNER, J., *Nucl. Fusion* **25** (1985) 275.
- [11] MIRNOV, V.V., RYUTOV, D.D., *Pis'ma Zh. Tekh. Fiz.* **5** (1979) 678.
- [12] NAGORNYI, V.P., RYUTOV, D.D., STUPAKOV, G.V., *Nucl. Fusion* **24** (1984) 1421.

- [13] BALDWIN, D., in Mirror-Based and Field-Reversed Approaches to Magnetic Fusion (Proc. Workshop Varenna, 1983), Vol. 1, International School of Plasma Physics (1984) 109.
- [14] MOROZOV, A.I., SOLOV'EV, L.S., Voprosy Teorii Plazmy, Vol. 2 (LEONTOVICH, M.A., Ed.), Gosatomizdat, Moscow (1963) 3.
- [15] KRUSKAL, M.O., OBERMAN, C.R., Phys. Fluids **1** (1958) 275.
- [16] ARSENIN, V.V., in Plasma Physics (Proc. Int. Conf. Lausanne, 1984), Vol. 1, CEC, Brussels (1985) 206.
- [17] RYUTOV, D.D., STUPAKOV, G.V., Prepr. No. 85-146, Nuclear Physics Institute, Siberian Dept. USSR Acad. Sci., Novosibirsk (1985).
- [18] ROSENBLUTH, M.N., LONGMIRE, C., Ann. Phys. **1** (1957) 120.
- [19] RYUTOV, D.D., STUPAKOV, G.V., in Voprosy Teorii Plazmy, Vol. 13 (KADOMTSEV, B.B., Ed.), Atomizdat, Moscow (1983) 74.
- [20] KOTEL'NIKOV, I.A., RYUTOV, D.D., Fiz. Plazmy **11** (1985) 1155.
- [21] KOTEL'NIKOV, I.A., ROSLYAKOV, G.V., RYUTOV, D.D., Prepr. No. 86-31, Nuclear Physics Institute, Siberian Dept. USSR Acad. Sci., Novosibirsk (1986).



## PROGRESS IN PLASMA HEATING WITH POWERFUL ELECTRON BEAMS IN OPEN SYSTEMS

A.V. ARZHANNIKOV, V.T. ASTRELIN, A.P. AVROROV,  
B.N. BREJZMAN, A.V. BURDAKOV, V.S. BURMASOV,  
V.V. CHIKUNOV, I.V. KANDAUROV, V.A. KAPITONOV,  
A.D. KHIL'CHENKO, B.A. KNYAZEV, V.S. KOJDAN,  
V.V. KONYUKHOV, Eh.P. KRUGLYAKOV, S.V. LEBEDEV,  
K.I. MEKLER, O.I. MESHKOV, V.V. POSTUPAEV,  
D.D. RYUTOV, A.L. SANIN, M.A. SHCHEGLOV,  
S.L. SINITSKIJ, S.G. VOROPAEV, L.N. VYACHESLAVOV  
Institute of Nuclear Physics,  
Siberian Branch of the  
USSR Academy of Sciences,  
Novosibirsk, Union of Soviet Socialist Republics

### Abstract

PROGRESS IN PLASMA HEATING WITH POWERFUL ELECTRON BEAMS IN OPEN SYSTEMS.

Investigations of the effects of plasma heating with REB are reported. The plasma heating problem is an important part of the research programme designed to investigate the possibility of building a multimirror fusion reactor. Asymmetry of the distribution function along the system axis is observed and investigated on the INAR machine. It was shown that high energy electrons are created even at large distances ( $\sim 7$  m) from the point of REB injection into the plasma (GOL-1). A new machine for investigating REB interaction with plasma (GOL-M) is described, and the first experimental results are reported. It is shown that the interaction efficiency increases with the magnetic field strength up to the largest fields obtained in experiments (4.5 T on GOL-M, 7 T on INAR). The practical results obtained in generating REB of microsecond duration (3–4  $\mu$ s) on a plane diode (U-1 machine) is discussed. A beam energy content of 130 kJ is obtained. After compression (in a 10 T field) the REB energy content is 100 kJ. In the final section of the paper, a method is proposed for increasing the duration and energy content of the beam.

### 1. INTRODUCTION

The plasma heating experiments with powerful relativistic electron beams (REB) carried out at the Institute of Nuclear Physics of the USSR Academy of Sciences (Siberian Division) are directed towards the development of a method for rapid heating of dense plasma in elongated open systems with magnetic confinement. The heating is designed to take place in two stages whereby the beam gives up the larger part of its energy in a plasma with a density of  $10^{15}$  cm<sup>-3</sup> in the central part of the trap, after which the energy is transmitted through two-particle collisions to

a denser plasma ( $n \sim 10^{17} \text{ cm}^{-3}$ ) adjacent to the ends. A multimirror magnetic system is to be used to confine the dense plasma. The ultimate purpose of the present stage is to build the GOL-3 machine [1]. Our paper presents the results of work carried out under this programme quite recently.

Section 2 reports the results of experiments on the INAR device. Here, attention is concentrated on phenomena occurring in the immediate neighbourhood of the beam injection point ( $z \leq 1 \text{ m}$ ), and in a magnetic field up to 7 T. Section 3 presents the results of experiments on the GOL-1 machine. Thanks to the comparatively great length of this device ( $L = 7.5 \text{ m}$ ), it is possible to distinguish between effects occurring at the entrance to the machine and those distributed over its length. In Section 4 we describe the modernized GOL-M device and give the results of initial experiments on it with magnetic fields of up to 4.5 T.

The final two sections (Sections 5 and 6) are devoted to work aimed at developing a technology for generating REB of microsecond duration for heating plasma in machines of the next generation. Section 5 deals with beam generation on a plane diode followed by magnetic compression of the beam. Section 6 describes a possible scheme for enhancing energy content and beam duration by successive reduction of a number of band-shaped beams from different generators onto a single "magnetic path", followed by transformation of the beam from the band shape to a circular cross-section.

## 2. EXPERIMENTS ON THE INAR DEVICE

A new series of experiments has been carried out on INAR to investigate collective heating of plasma electrons by the stream instability, with the accent on phenomena occurring close to the point of beam injection into the plasma. In earlier experiments [1-5] it was shown that over the first metre from the injection point the diamagnetism falls off sharply (by several factors) and then continues to drop more slowly; the beam energy is imparted largely to the high-energy "tails" of the electron distribution function; and with time the diamagnetism tends to even out over the length of the machine.

In the experiments described here we obtained a direct recording of the directional movement of "hot" plasma electrons from the entrance to the outlet of the machine. The geometry of the experiment set up to determine the directional motion of hot electrons by small angle laser scattering is shown in Fig. 1. The relativistic beam and the laser radiation propagate along the  $x$  and  $z$  axes respectively, and the radiation scattered at an angle of  $\phi = 8^\circ$  is recorded in a solid angle  $\Omega = \sin \phi d\phi \psi$ . Since the azimuthal angle region is symmetrical relative to the  $y$  axis, a contribution to the useful signal is made by electrons having both positive and negative velocity projections onto the direction of REB motion. The signals from such electrons can be separated by measuring separately the power of the radiation scattered in directions bounded by the angles  $\psi_1$  and  $\psi_2$ . (The spectral range of the

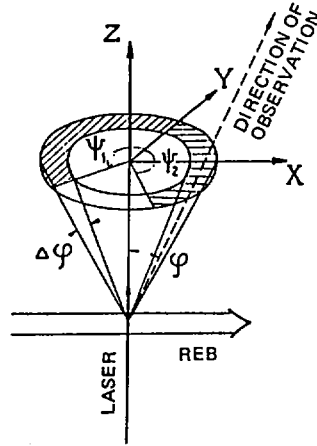


FIG. 1. Geometry of experiment designed to record anisotropy of electron distribution function on INAR by Thomson scattering method.  $\Omega = \sin \phi \Delta\psi$  is the solid angle of measurement;  $\psi_1 + \psi_2 = 135^\circ$ .

scattered radiation is localized on one side of the centre of the laser line.) Measurements of this kind for the 0.3–1.5 keV electron energy region gave a ratio of radiation intensities  $I_+/I_- = 3 \pm 1$  for radiation scattered by electrons moving along the REB and in the reverse direction. Thus, we observe a stream of fast electrons from the point of REB entry into the plasma in the direction of beam propagation.

The undoubted fact that the hot electron distribution function is strongly asymmetrical (showing a “forward-backward” shape) indicates that heat transport takes place at a velocity of the same order as the thermal velocity of these electrons. The “secondary” instabilities which in theory might develop in a flux of this kind (see Ref. [6], for example) do not lead to any substantial slowing-down of the electrons, as predicted in Ref. [6].

A special experiment was set up to test the asymmetrical nature of the electron distribution function. Earlier the plasma had been produced by a discharge ignited between an annular electrode located in the centre of the discharge chamber and the end foils of the magnetic mirror trap. In the present experiment, on the other hand, the annular electrode was surrounded by a thin foil (normally 9  $\mu\text{m}$  of aluminium). In this way the preliminary plasma was produced by a direct discharge between the central and the two end electrodes. The plasma parameters were the same in both parts of the discharge. The plasma density, as before, was  $1.5 \times 10^{15} \text{ cm}^{-3}$  and the thickness of the foil was such that the REB passed through it without any appreciable change in the angular and energy characteristics; at the same time the foil was opaque to “hot” plasma electrons.

In these circumstances the diamagnetic signals in the region from the beam inlet to the "internal" foil remained virtually unchanged whereas in the second part of the machine they were considerably reduced. This form of signal behaviour points to the presence of an electron flux from the trap inlet.

In another series of experiments we considered how the plasma energy content is affected by increasing the REB energy content and enhancing the longitudinal magnetic field. In order to increase the energy content and the beam duration, the beam generator was modernized. As a result the REB duration increased from 70 ns at the base and 30 ns at half-height to 100 ns and 60 ns, respectively. The current generated by the accelerator also increased and the energy content of the beam was doubled. Where this beam was injected into a plasma with a density of  $1 \times 10^{15} \text{ cm}^{-3}$  we observed an increase in the plasma pressure measured by diamagnetic probes which was proportional to the growth of the REB energy content — i.e. the plasma pressure was approximately doubled. Preliminary laser measurements have indicated both an increase in the temperature of the main plasma electron component and an increased energy content in the "tails" of the distribution function. In these experiments, in contrast to earlier ones, the signals from laser scattering could be observed directly during the time of beam passage through the plasma. The experiments suggest that the increase in REB energy content (duration and current) does in fact lead to an increase in plasma energy content.

In order to examine the processes which occur when the REB interacts with plasma in a strong magnetic field (up to 7 T), we set up a magnetic discharge system with new geometry. A magnetic field up to 8 T at the mirrors and 7 T in the homogeneous part of the system was produced by a solenoid 1 m in length. A pre-plasma 3 cm in diameter was formed by a pulsed Penning discharge. The plasma parameters were measured with a Michelson interferometer ( $\lambda = 3.30 \mu\text{m}$ ), a system for scattering the rays emitted by a ruby laser at  $90^\circ$ , and diamagnetic probes. The plasma density varied from  $10^{15} \text{ cm}^{-3}$  to  $10^{16} \text{ cm}^{-3}$ . The beam current rose to 35 kA and the current density was  $10 \text{ kA} \cdot \text{cm}^{-2}$ .

In one series of experiments with plasma density of  $(3-5) \times 10^{15} \text{ cm}^{-3}$  we found an increase in the diamagnetic signals ( $nT_{\perp S}$ ) by factors of 2 to 2.5 when the external magnetic field strength was increased from 1 to 7 T.

### 3. EXPERIMENTS ON THE GOL-1 DEVICE

The great length of the GOL-1 machine (7.5 m) makes it possible to elucidate certain characteristics of the beam-plasma interaction which are difficult to investigate on machines of shorter length. The length factor becomes particularly important when we wish to study fine interaction effects such as non-equilibrium of the plasma electron distribution function following REB heating of the plasma.

In order to gain a better understanding of the physics of the beam-plasma interaction, we must not only establish the fact of non-equilibrium of the distribution function, but also find an answer to the question where the electrons of the "tail" are produced and determine whether "hot" electron generation is an effect distributed over the length of the trap or whether these electrons are produced near the point of REB injection into the plasma. The pulsed target method [7] was used to study REB interaction with the plasma in GOL-1, the essence of which consists in determining the "hot" electron parameters from the characteristic radiation excited by these electrons in the plasma, with pulsed injection into the plasma of various gases (in the experiments we used Ne, Ar, Kr and Xe, which were injected into the vacuum chamber at a distance  $z = 650$  cm from the point of REB injection into the plasma). For a plasma density of  $n_e = 4.5 \times 10^{14} \text{cm}^{-3}$  and an REB current density of  $j_b \approx 2 \text{ kA} \cdot \text{cm}^{-2}$  (total current  $I_b = 60 \text{ kA}$ , electron energy  $E_e \approx 0.5 \text{ MeV}$ , initial angular scatter  $\sqrt{\theta_0^2} = 18^\circ$ , beam duration at half-height  $\tau_b \approx 40 \text{ ns}$ ), we have succeeded in establishing the following by means of the pulsed target method:

1. At  $z = 650$  cm from the point of REB injection into the plasma, the "hot" electrons of the "tail" have a density of  $n_e^* = (0.7 \pm 0.2) \times 10^{12} \text{ cm}^{-3}$  and an average energy  $\epsilon^* = 45 \pm 20 \text{ keV}$ ;
2. Electrons with the above parameters were formed directly at the observation point, i.e.  $z = 650$  cm from the REB injection point.  
This conclusion is based on the good correlation between the times of beam arrival, and the appearance of the diamagnetic signal and the characteristic X-radiation;
3. As the angular scatter of the REB increases, the energy content of the "hot" electron group decreases; moreover, the increase in the angular scatter leads on the whole to a decrease in the density of the "tail" electrons (roughly according to the law  $n_e^* \sim 1/\theta^2$ ), leaving the average energy of these electrons virtually unchanged.

In a theoretical paper which appeared quite recently [8] we find evaluations for the effective energy  $\epsilon^*$  of the "tail" electrons:

$$\frac{\epsilon^*}{T} \sim 2 \omega_{pe} t \left( \frac{\omega_{Be}}{\omega_{pe}} \right)^2$$

(where  $T$  is the temperature of the plasma "core", and  $t$  is the REB duration), and for the density of the electrons responsible for the absorption of Langmuir waves:

$$n_e^* \sim n_e \frac{\Gamma_b}{\omega_{pe}} \sim n_b \frac{mc^2}{mc^2 + E} \frac{1}{\theta^2}$$

The parameters of the "tails" obtained experimentally are in reasonable agreement with theoretical evaluations.

For the conditions we have described, the distribution of diamagnetism over the length of the system is strongly inhomogeneous and is in reasonable agreement with a relationship of the form

$$W_{\perp}(z) \sim \left( \theta_0^3 + \frac{z}{\ell} \right)^{-2/3}$$

where  $\theta_0$  is the initial angular scatter of the beam,  $z$  is the distance between the anode foil and the point of REB injection, and  $\ell$  is the relaxation length (see Refs [9,10] for more details).

As we have already indicated, the theoretical evaluations of Brejzman and Erofeev [8] predict an increase in the density of "hot" electrons with decreasing angular scatter. This has also been confirmed experimentally [11]. Thus we may assume that the inhomogeneous distribution of diamagnetism is most likely due to inhomogeneity in the density distribution of "hot" electrons over the length of the system.

#### 4. THE GOL-M DEVICE

Since the beginning of 1986 a new machine has been operating at the Institute of Nuclear Physics: the GOL-M, designed for continued research into the interaction of powerful REB with plasma in strong magnetic fields (up to  $B = 6$  T). This device can also be used for engineering experiments on various components of the large multimirror system called GOL-3, which is being built at the Institute, and for developing new methods of diagnostics which can be used in strong pulsed magnetic fields. Figure 2 shows a diagram of this machine, which consists of the following elements:

- (1) An REB generator (1) with a beam current of  $I_b \approx 100$  kA, electron energy  $E_b \approx 0.5$  MeV, beam duration (at half-height)  $\tau_b \approx 120$  ns and energy of the beam injected into the plasma  $Q = 3.5-4$  kJ;
- (2) A system for producing a magnetic field, consisting of a solenoid (2) with a total length of 7.5 m and maximum magnetic field strength 6 T and two autonomous end mirrors (3) with maximum magnetic field strength up to 12 T. The period of the magnetic field, both at the mirrors and at the solenoid, is about 11 ms. The transverse component of the magnetic field at the solenoid is suppressed to a level  $B_{\perp}/B \approx 10^{-3}$  while high transparency of the solenoid is conserved;

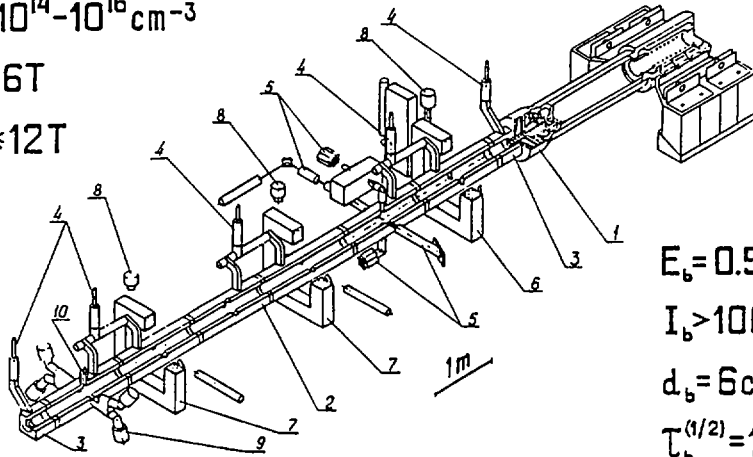
With these new parameters, then, we carried out experiments on magnetic beam compression which were in fact a continuation of the work described in Refs [11, 13,

## GOL-M

$$n_p = 10^{14} - 10^{16} \text{ cm}^{-3}$$

$$B_0 = 6 \text{ T}$$

$$B_m \leq 12 \text{ T}$$



$$E_b = 0.5 \text{ MeV}$$

$$I_b > 100 \text{ kA}$$

$$d_b = 6 \text{ cm}$$

$$\tau_b^{(1/2)} = 120 \text{ ns}$$

FIG. 2. Diagram of GOL-M device:

- 1 — diode of REB generator
- 2 — solenoid section
- 3 — end magnetic mirrors
- 4 — current lead-in
- 5 — ruby laser and system for recording Thomson scattering
- 6 — nine-channel Michelson interferometer ( $\lambda_g = 3.39 \mu\text{m}$ )
- 7 — single-channel interferometer
- 8 — cooled interferometer detectors (Ge-Au,  $T = 77 \text{ K}$ )
- 9 — four-channel X-ray crystal spectrometer
- 10 — valve for pulse target shaping

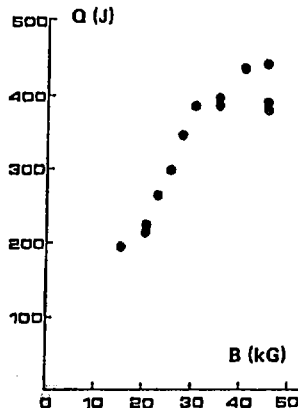


FIG. 3. Energy content of plasma after REB heating as a function of magnetic field (GOL-M):  
 $n_e \approx 10^{15} \text{ cm}^{-3}$ ,  $j_b = 2.7 \pm 0.3 \text{ kA} \cdot \text{cm}^{-2}$ ,  $d_b = 6 \text{ cm}$ .

- (3) A vacuum chamber constructed of quartz tubes 108 mm in diameter, the ends of which are pneumatically sealed. Two methods of producing the pre-plasma have been tried: an oscillating discharge of the Penning type and a direct discharge. In the density region  $n_e \sim 10^{15} \text{ cm}^{-3}$ , with a column diameter of 8 cm, the direct discharge gives better reproducibility of plasma parameters.

The results of the preliminary experiments suggest that the effectiveness of the interaction is enhanced by increasing the magnetic field strength. Experiments were carried out at  $n_e \sim 10^{15} \text{ cm}^{-3}$ ,  $T_{e0} \approx 1 \text{ eV}$ , transverse plasma dimension  $d = 8 \text{ cm}$ , and beam current density  $j_b = 2.7 \pm 0.3 \text{ kA} \cdot \text{cm}^{-2}$ . The initial angular scatter of the REB in the plasma is  $\sqrt{\theta_0^2} \approx 20^\circ$ . Figure 3 shows experimental results for the efficiency of the REB-plasma interaction as a function of magnetic field strength. Each point in this figure represents a calculation of total plasma energy content:

$$Q = \frac{3}{2} \int_0^L n_e T_{\perp} S \, dZ$$

The measured temperature of the plasma electrons after heating is  $\sim 10 \text{ eV}$ , which is in agreement with the  $T_e$  evaluation for the case of plasma heating by reverse current. An evaluation of  $T_e$  from diamagnetic measurements gives a considerably higher value. Thus, we find the results obtained earlier on INAR and GOL-1 confirmed in stronger magnetic fields as well: when a high current REB interacts with plasma, a non-equilibrium distribution function prevails. A substantial part of the energy imparted by the beam to the plasma is given up in the "tails".

## 5. NEW EXPERIMENTS DESIGNED TO PRODUCE A MICROSECOND ELECTRON BEAM IN THE U-1 MACHINE

The U-1 electron accelerator is an LC-generator which produces a high voltage pulse; this passes through the main discharge gap to a plane graphite cathode (1) 21.5 cm in diameter, located in the diode chamber (Fig. 4). At the diode a longitudinal magnetic field of 0.5 T is set up. The electron beam is extracted from the diode through an anode foil (2).

The beam parameters were higher than those quoted in Ref. [11], firstly because an extra LC-generator was installed parallel to the one already in place [12] and secondly because of the new design of the accelerator diode chamber which made it possible to reduce current leakage. As a result, the energy content of the beam extracted from the diode — which in this case was recorded by a graphite calorimeter [9] located just after the anode foil (2) — was raised to 130 kJ. The voltage on the diode was 1 MV, the current 60 kA, and the duration at the base  $4 \mu\text{s}$  (Fig. 5(a)).

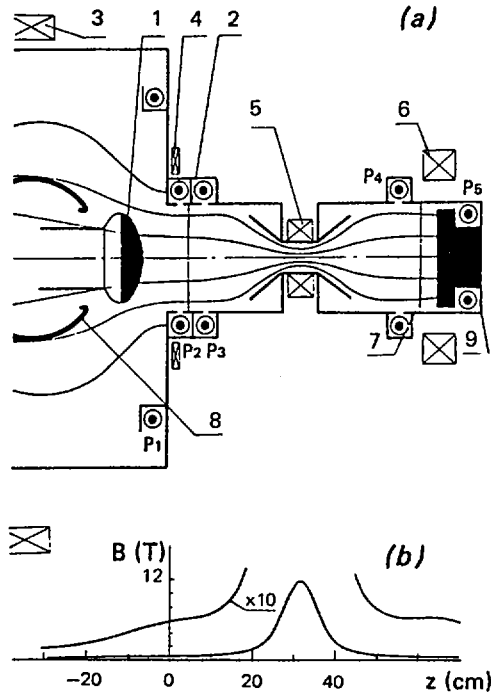


FIG. 4. (a) Experimental layout: 1 — cathode; 2 — anode foil; 3, 4, 5 and 6 — magnetic system coils; 7 — foil; 8 — cathode holder. (b) Distribution of magnetic induction along device axis.

14]. In these experiments the energy content of the initial beam  $Q_1$ , received by the collector after foil 2, was 110 kJ (Fig. 5(b)). The distance between the cathode and the anode foil was 9 cm. The anode foil was dacron a few tens of microns thick covered with aluminium on both sides. The beam compression was done with a magnetic field of mirror configuration [15] (0.5 T at the anode foil and 10 T at the mirror). The distance between foils 2 and 7 was 55 cm. The pressure in the compression chamber could be varied from  $10^{-5}$  to 1 torr. The Rogowski coils  $P_2$  and  $P_5$  measured the beam current at the inlet,  $I_2$ , and at the outlet,  $I_5$ , of the compression chamber. Coils  $P_3$  and  $P_4$  recorded the total current made up of the beam current and the inverse current in the plasma being formed. Coil  $P_1$  recorded the diode current. The energy content of the beam,  $Q_2$ , after passing through the magnetic mirror was measured by the graphite calorimeter (9), and also from the integral  $\int UI_5 dt$ .

The experiments showed that the beam is transported most effectively ( $\eta = Q_2/Q_1 \approx 90\%$ ) through the magnetic mirror when the gas pressure in the compression chamber is  $10^{-4}$  torr. If this condition is satisfied, the beam in the compression chamber is neutralized in relation to the space charge, but no current

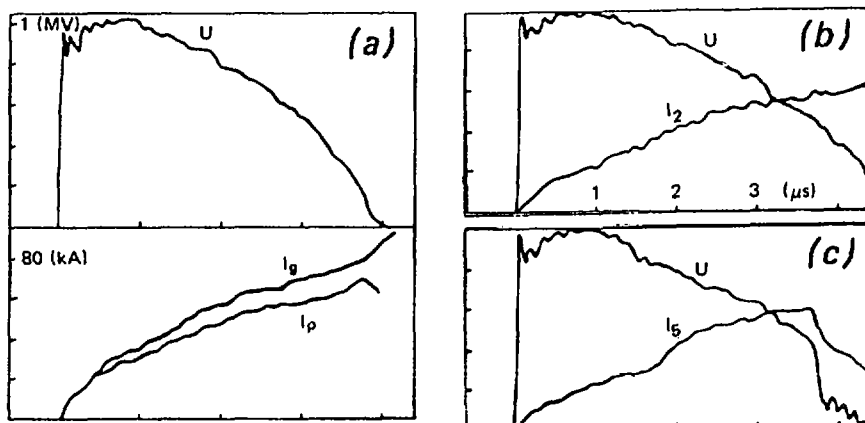


FIG. 5. Oscillograms of diode voltage  $U$  and current  $I$ :

- (a) Beam is received by calorimeter 9 installed in place of the compression chamber:  $I_g$  — generator current,  $I_p$  — beam current;  
 (b) Beam is received by collector placed immediately after anode foil 2;  $I_2$  is current recorded by coil P2;  
 (c) Beam passes through compression system:  $I_5$  is the current recorded by coil P5.

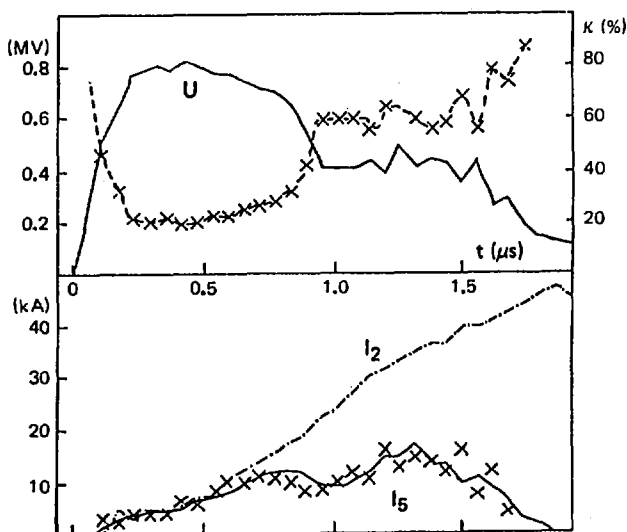


FIG. 6. Diode voltage  $U$  and current at inlet ( $I_2$ ) and outlet ( $I_5$ ) of compression chamber when the beam is injected into compression chamber through  $30\ \mu\text{m}$  Al foil. Calculated values of the beam reflection coefficient  $\kappa$  and of the current which should be passing through mirror are indicated by crosses ( $d = 8.5\ \text{cm}$ ).

compensation has yet been observed. As a result of these experiments, we obtained a compressed beam with a diameter of 4 cm, energy content  $Q_2 = 100$  kJ and current density  $5 \text{ kA} \cdot \text{cm}^{-2}$ . The corresponding oscillograms are shown in Fig. 5(c). There is some reduction of energy content with beam compression owing to the earlier shorting out of the diode.

Experiments were carried out to investigate how the angular scatter of the initial beam affects the operation of the diode with REV injection into a magnetic mirror. Replacement of the dacron anode foil by an aluminium layer with a thickness of  $10 \mu\text{m}$  increases the number of electrons reflected from the mirror. These electrons oscillate through the anode foil, losing energy in it, which results in earlier plasma formation at the anode and accelerates the shorting of the diode. Increasing the thickness of the foil to  $30 \mu\text{m}$  of aluminium puts the diode into an "impedance collapse" regime in which the voltage on the diode falls off very sharply (Fig. 6) but the rate of current rise increases [16]. At the beginning of the pulse the diode is cut off by the space charge from the reflected and oscillating electrons, and then, after the formation of plasma at the anode, moves into a collapse regime which also explains the observed five-fold decrease of diode impedance. With a thin anode foil, when the number of reflected oscillating electrons is small, there is practically no influence of the compression system on the diode and the beam can be compressed with great efficiency.

## 6. BAND BEAMS: THE U-2 DEVICE

In order to increase the energy content of the plasma, Voropaev and co-workers [13] suggested injecting through the ends of the machine a series of electron beams generated successively in a number of separate diodes. These are initially generated as band beams and are cast onto a single "magnetic track"; subsequently, they are converted into ordinary cylindrical beams by an appropriate manipulation of the magnetic flux. The scheme used for successive injection of two beams into the plasma is shown in Fig. 7. In the vacuum magneto-insulated diodes D1 and D2 ( $B_z = 0.5$  T), band beams with a  $4 \times 140$  cm cross-section are generated in turn at an electron current of  $j \sim 0.1 \text{ kA} \cdot \text{cm}^{-2}$ . The thin band beams are transported in narrow channels K1, K2 and K3 with conducting walls even without neutralization, because with this type of beam and channel cross-section the potential sag due to the characteristic space charge of the beam electrons is not very large. In cases where the switching field  $B_x = 0$ , the magnetic flux in channel K3 contains about half of the magnetic fluxes in channels K1 and K2. By switching on the magnetic field  $B_x$  we can transfer virtually all the magnetic flux from transport channel K1 to channel K3 (in one specific calculation variant  $B_x \approx 0.1 B_z$ ). When the sign of  $B_x$  is reversed, the flux from channel K2 is transferred to channel K3.

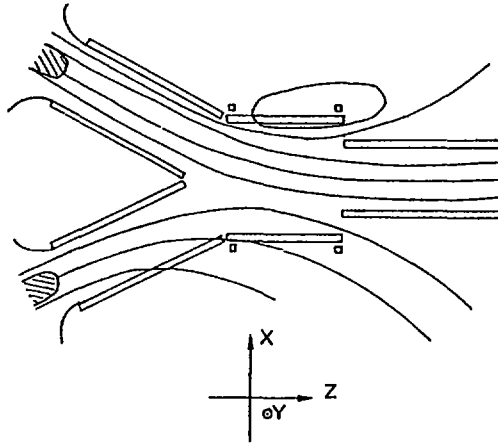


FIG. 7. Layout for successive injection of band shaped REB into the plasma.  $D_1$  and  $D_2$  are the vacuum magneto-insulated diodes,  $K_1$ ,  $K_2$  and  $K_3$  are the beam transport channels.

#### U-2 GENERATOR

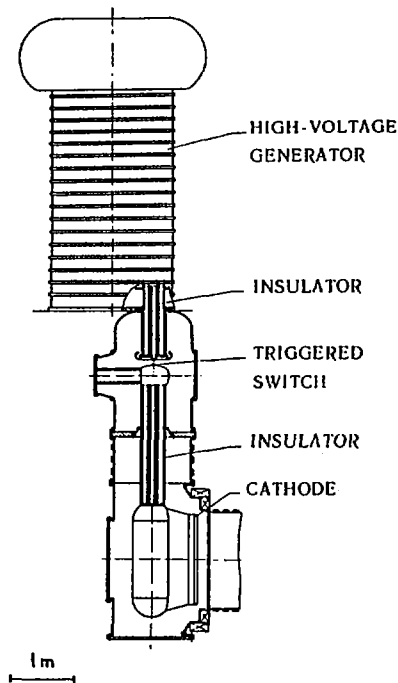


FIG. 8. Layout of the U-2 generator: 1 — high voltage generator, 2 and 4 — insulators, 3 — spark gap switch, 5 — cathode.

Thus, transport channel K3 will receive first the beam from diode D1 and then the beam from diode D2. With further propagation of the beam in the transport channel K3, the flux cross-section of the guiding magnetic field undergoes a twenty-fold area compression as it approaches the plasma trap, and at the same time the shape changes to circular from being strongly elongated along the y co-ordinate. Similar changes also occur in the beam cross-section. It is assumed that charge neutralization of the REB occurs as an effect of the ions.

One of the main difficulties in providing for the transport of a band beam without axial symmetry is that the transverse cross-section shape of the beam can change as a result of the drift movement of the electrons in crossed electrical and magnetic fields. In order to keep the shape of the beam cross-section unchanged during its movement in a homogeneous magnetic field, we must satisfy the condition that the constant density level lines of the beam current should coincide with the lines of electron motion in a plane perpendicular to the vector of the guiding magnetic field [17]. Analytical and numerical calculations have made it possible to find a broad class of such equilibria. It has emerged that, for the case where the beam is symmetrical in the channel and uniform in cross-section, the ratio of the beam width to the channel width can — in an equilibrium configuration — be unambiguously established at 3/4. The gap between the beam and the conducting wall, which accordingly, for this case, has to be 1/8 of the channel width, can be considered acceptable from the standpoint of insulating the electron flux from the metal in magnetic fields with  $B_z \geq 0.5$  T.

The U-2 facility is being built at the Institute of Nuclear Physics for experimental investigations of the generation, switching and transport of large band beams. The structure of one large band-shaped REB generator is shown in Fig. 8. LC-generator (1) generates a voltage pulse with a rise time of 12  $\mu$ s and a no-load amplitude of up to 1.7 MV. This pulse passes via insulator (2) to the controlled gas discharge gap (3). When this operates, the voltage from the next insulator (4) is transferred to vacuum diode (5). The beam cross-section has a length of about 140 cm and its width can be selected in the range from 4 to 12 cm.

At the present time the experiments being carried out on the U-2 devices are designed to study generator operation at equivalent active load with a resistance of about 20 ohms. The tests have indicated great reliability of generator operation with an on-load energy output of more than 100 kJ within about 10 ms.

## 7. SUMMARY OF MAIN RESULTS

- (1) Direct measurements have shown (on INAR) that heat transport by hot plasma electrons takes place at a velocity of the same order as the thermal velocity of the electrons. This is an important fact to know if we wish to devise a method of "two-stage" plasma heating.

- (2) It has been established (on GOL-1) that in the REB-plasma interaction hot electrons are formed even at large distances ( $\sim 7$  m) from the point of REB injection into the plasma.
- (3) The tendency observed earlier towards increased plasma heating efficiency with increasing field strength continues right up to the largest fields obtained in present experimental work (4.5 T on GOL-M and 7 T on INAR).
- (4) On the U-1 device, REB parameters have reached the following values: electron energy 1 MeV, pulse length 3–4  $\mu$ s, energy content before beam compression 130 kJ. After compression in a 10 T field the energy content is 100 kJ and the current density 5 kA  $\cdot$  cm $^{-2}$ .

### REFERENCES

- [1] KOIDAN, V.S., KRUGLYAKOV, E.P., RYUTOV, D.D., in High Power Electron and Ion Beam Research and Technology (Proc. 4th Int. Conf. Palaiseau, France, 1981) 531.
- [2] ARZHANNIKOV, A.V., BURDAKOV, A.V., KOJDAN, V.S. et al., *Pis'ma Zh. Ehksp. Teor. Fiz.* **27** (1978) 173.
- [3] ARZHANNIKOV, A.V., BURDAKOV, A.V., BURMASOV, V.S., et al., in High Power Electron and Ion Beam Research and Technology (Proc. 3rd Int. Conf. Novosibirsk, 1979) 29.
- [4] ARZHANNIKOV, A.V., BURDAKOV, A.V., KOIDAN, V.S., VYACHESLAVOV, L.N., *Phys. Scr.* **T2/2** (1982) 303.
- [5] ARZHANNIKOV, A.V., BURDAKOV, A.V., KOIDAN, V.S., et al., in Plasma Physics (Proc. Int. Conf. Lausanne, 1984), Vol. 1, Invited Papers (1984) 285.
- [6] RYUTOV, D.D., SAGDEEV, R.Z., *Zh. Ehksp. Teor. Fiz.* **58** (1970) 739.
- [7] KRUGLYAKOV, E.P., LUK'YANOV, V.N., PODYMINOGIN, A.A., in *Diagnostika Plazmy*, No. 5, Ehnergoatomizdat, Moscow (1986) 85.
- [8] BREJZMAN, B.N., EROFEEV, V.I., *Fiz. Plazmy* **11** (1985) 387.
- [9] BREJZMAN, B.N., KRUGLYAKOV, E.P., in Phenomena in Ionized Gases (Proc. 1st Int. Conf. Minsk, 1981), Vol. 1, Invited Papers (1981) 93.
- [10] BURMASOV, V.S., KHILCHENKO, A.D., KORNILOV, V.A., et al., in Controlled Fusion and Plasma Physics (Proc. 10th Europ. Conf. Moscow, 1981), Vol. 1 (1981) paper C-2.
- [11] ARZHANNIKOV, A.V., BREJZMAN, B.N., BURDAKOV, A.V., et al., in Plasma Physics and Controlled Nuclear Fusion Research 1984 (Proc. 10th Int. Conf. London, 1984), Vol. 2, IAEA, Vienna (1985) 347.
- [12] VOROPAEV, S.G., LEBEDEV, S.V., CHIKUNOV, V.V., SHCHEGLOV, M.A., *Pis'ma Zh. Ehksp. Teor. Fiz.* **11** (1985) 267.
- [13] VOROPAEV, S.G., KNYAZEVA, B.A., KOJDAN, V.S. et al., in Engineering Problems of Fusion Reactors (Proc. 3rd All-Union Conf. Leningrad, 1984), Vol. 1, Moscow (1984) 298 (in Russian).
- [14] CHIKUNOV, V.V., KNYAZEVA, B.A., KOIDAN, V.S., et al., in Controlled Fusion and Plasma Physics (Proc. 12th Europ. Conf. Budapest, 1985), Vol. 9F (1985) 508.
- [15] VOROPAEV, S.G., GORBOVSKIY, A.I., KNYAZEVA, B.A. et al., *Voprosy atomnoj nauki i tekhniki (Problems of Atomic Science and Technology)*, Ser. termoyad. sintez (Nuclear Fusion Series), Vol. 2 (1986) 25.
- [16] VOROPAEV, S.G., KNYAZEVA, B.A., KOJDAN, V.S., et al., Preprint 86-82, Institute of Nuclear Physics, Academy of Sciences of the USSR, Siberian Branch, Novosibirsk (1986).
- [17] ASTRELIN, V.T., EROFEEV, V.I., in Summaries of Papers Presented at 6th All-Union Symp. High-Current Electronics, Vol. 1, Tomsk (1986) 160.

# ENHANCEMENT OF RADIAL TRANSPORT BY COLLECTIVE PROCESSES

D.L. EGGLESTON, J.D. CRAWFORD,  
T.M. O'NEIL, J.H. MALMBERG  
Physics Department,  
University of California, San Diego,  
La Jolla, California,  
United States of America

## Abstract

### ENHANCEMENT OF RADIAL TRANSPORT BY COLLECTIVE PROCESSES.

The paper shows how collective effects can enhance the radial transport produced when nonaxisymmetric fields are applied to a nominally cylindrical pure electron plasma. Both linear and nonlinear collective effects are considered and experimental demonstrations of each effect given. In the linear case, the field asymmetry drives an asymmetric plasma mode and the mode field produces additional transport. In the nonlinear case, the field asymmetry can either excite daughter modes via a decay instability or drive a mode by induced particle scattering. Since the physical basis for these processes is quite general, they may be relevant for understanding nonambipolar transport in other rotating plasma systems such as tandem mirrors.

## 1. Introduction

This paper shows how collective effects can enhance the radial transport produced when nonaxisymmetric fields are applied to a cylindrical pure electron plasma. This enhancement may be produced by either linear or nonlinear collective effects and both cases are observed experimentally. Because the physical basis for these processes is quite general, they may be relevant for understanding nonambipolar transport in other rotating plasma systems such as tandem mirrors.

It is well known that the presence of nonaxisymmetric fields produces radial ion transport in tandem mirrors [1]. Such fields also produce radial transport in pure electron plasmas. The transport problem may be viewed as having two parts. The first part is the determination of the self-consistent fields in the plasma and the second part is the determination of the transport of particles in those fields. The point of this paper is that the first part of the problem is nontrivial. In a rotating plasma the field asymmetry may act as a pump for various collective processes and thus excite large asymmetric mode fields in the plasma. This collective enhancement of the field asymmetry results in enhanced radial transport.

## 2. Theory

The simplest case is that of a linear resonance between an external field asymmetry with a Fourier component  $e^{i(l\theta + kz - \omega t)}$  and a standing wave in the

plasma column. This requires that  $\omega$ ,  $k$ , and  $l$  of the field asymmetry satisfy the dispersion relation for the mode of interest. For confinement considerations, it is of particular interest to note that a mode can occur which propagates backwards on the rotating column so that it has zero frequency in the laboratory frame. Such a mode can be driven to large amplitude by a static field asymmetry and the large mode field can then produce enhanced transport [2].

It is important to consider nonlinear generalizations [3,4] of this linear process, since a zero frequency eigenmode will not generally appear in a bounded plasma for arbitrarily chosen values of density, magnetic field strength, column length, etc. The simplest generalization merely replaces the linear resonance with a resonant three-wave interaction in which the field asymmetry acts as a pump which drives two daughter modes via the decay instability. For a static field asymmetry, the daughter modes must have frequencies that satisfy the resonance condition  $\omega_1 + \omega_2 \approx 0$ .

In a second generalization, one of the daughter modes is in effect replaced by resonant particles. The field asymmetry nonlinearly excites the remaining mode through induced scattering off of these particles (i.e. nonlinear Landau growth). For finite columns, which necessarily have discrete frequencies, this second mechanism can occur more generally than the decay instability because the resonance condition  $\omega_1 + \omega_2 \approx 0$  is not required. These two processes are not exhaustive (higher order analogues are obvious), but are illustrative of the kind of nonlinear effects that can degrade plasma confinement.

### 3. Experiment

We have experimentally studied the collective enhancement of radial transport in a pure electron plasma device [5]. The extremely long confinement times [6] of these devices make them especially suitable for controlled studies of induced radial transport. Radial confinement is provided by a uniform axial magnetic field while the axial confinement is provided by electrostatic potentials. Typical parameters are  $n_e \approx 10^7 \text{ cm}^{-3}$ ,  $T_e \approx 1 \text{ eV}$ ,  $B_0 = 350 \text{ G}$ , and a plasma lifetime exceeding  $10^5$  axial bounce times.

Our device is shown schematically in figure 1a and our basic experimental sequence is a modification of techniques described in detail elsewhere [5,6]. The cylindrical conducting wall of the device is divided into rings of various lengths and two of the rings (S1, S2) are divided azimuthally as well. Rings G1 and G3 are normally held at a large negative potential and the remaining rings are grounded. To start a cycle, ring G1 is switched to ground potential, allowing electrons from a negatively biased spiral filament to fill the device. Ring G1 is then returned to a negative potential, thus producing a confined plasma sample. After the procedures described below are completed, the electrons are dumped by grounding ring G3. Electrons are collected either by a radially moveable probe (giving the line integrated density at a particular radius) or by a plate (giving the total number of remaining electrons).

To demonstrate the collective enhancement of transport by a linear resonance we proceed as follows [7]. After the electrons are confined we apply a nonaxisymmetric electrostatic perturbation by placing a signal of frequency  $\omega$  on the two  $180^\circ$  azimuthal sectors of ring S1 in a push-pull fashion. Ring S2 is used to monitor the plasma for nonaxisymmetric modes. By applying

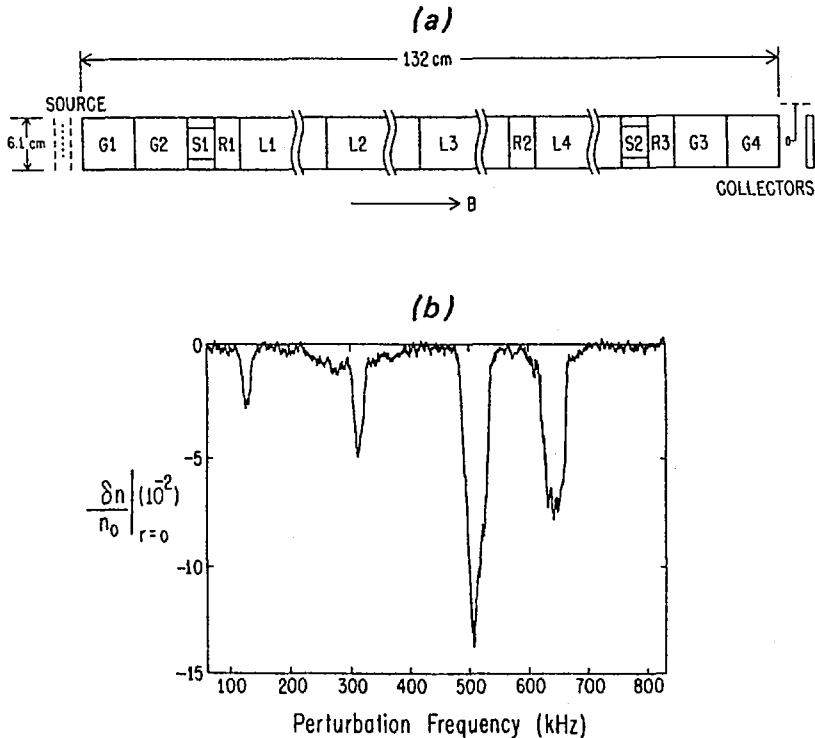


FIG. 1. (a) Schematic of experimental device.

(b) Normalized central density change due to the application of an electrostatic field asymmetry of variable frequency. The radial transport is enhanced at normal mode frequencies.

this perturbation only on alternate machine cycles and analyzing the change in signal on the collectors, one may obtain, for example, the density change  $\delta n(r)$  due to the applied field asymmetry. Figure 1b shows the perturbation-induced density change at the center of the plasma as a function of applied frequency. At the frequencies where normal modes are excited (as indicated by the detector on S2) we also find an enhanced level of radial transport as reflected in the increase of the magnitude of  $\delta n$ .

We have also observed enhancement of transport by nonlinear collective effects. Here we present an example of an induced scattering instability driven by a static field asymmetry. For such an instability a single growing mode should be observed and in this case the mode is an  $l=0$ ,  $k=\pi/L$  plasma wave, where  $L$  is the length of the plasma column. The wave becomes unstable when a threshold condition is exceeded and eventually saturates after growing 40-50 dB. Three features of this instability identify it as due to induced scattering: 1) The threshold condition, in addition to depending on

the mode damping, depends on the amplitude of the applied asymmetry. 2) The presence of the instability is associated with an enhanced level of radial transport. This is significant since an azimuthally symmetric wave ( $l=0$ ) does not by itself produce a radial drift of particles. 3) The instability does not require any particular tuning of conditions but appears over a broad range of plasma parameters.

According to theory [4], the time evolution of the observed mode is governed by the equation

$$\frac{dA_m}{dt} = \left[ -|\gamma_m| + \Gamma |A_e|^2 \right] A_m \quad (1)$$

where  $\gamma_m$  is the linear mode damping rate,  $A_m$  and  $A_e$  are the mode and field asymmetry amplitudes, and  $\Gamma$  is the beat-resonant coupling coefficient.<sup>1</sup> When the bracketed term is positive, the mode is unstable and grows exponentially. Since any real plasma device will have small asymmetries due to construction imperfections,  $A_e$  is always nonzero. In our experiments, these small asymmetries are sometimes large enough to exceed the threshold condition and the instability appears as soon as the plasma is captured. Such a case is shown by curve *a* in figure 2. The wave starts to grow immediately after the injection gate is closed ( $t \approx 1$  ms).<sup>2</sup> We may prevent the mode growth, in accordance with equation (1), by increasing the value of  $|\gamma_m|$ . One way to do this is by placing a resistive load between a ring within the containment volume (e.g. L3) and ground. Wall currents induced by the wave flow through this load and dissipate the wave energy. This creates additional mode damping beyond that produced by wave-particle effects. The stabilizing effect of such an addition is shown by curves *b* and *c* in figure 2. In curve *b* the plasma remains stable until the resistive load is removed at the time indicated by the lower arrow. In curve *c* the instability is quenched by the addition of the resistive load at the time indicated by the upper arrow.

Equation (1) also predicts that a stable plasma will be destabilized by increasing the magnitude of the field asymmetry. To demonstrate this effect we adjust the injection conditions to create a stable plasma (i.e. a plasma where the mode Landau damping is large enough to prevent the spontaneous growth shown in figure 2). We drive the  $l=0$  mode by applying a short (50  $\mu$ s) tone burst at the mode frequency to ring R3. At the same time we apply a static field asymmetry to the plasma by placing voltages on the 180° sector probes of S1 and S2. Figure 3 shows the mode amplitude versus time, with the voltage applied to the sector probes as a parameter. As the asymmetry amplitude increases, the mode becomes more lightly damped and finally becomes unstable.

The rate of loss of plasma particles due to radial transport is increased by as much as a factor of twelve when the instability is present. Preliminary measurements show that the loss rate increases with the amplitude of both the unstable mode and the field asymmetry. These results agree with theoretical expectations.

<sup>1</sup> In what follows we assume  $\Gamma$  is positive. The requirements for this to be true are discussed in reference [4].

<sup>2</sup> The large signal observed from  $t \approx 0-1$  ms is broadband noise due to the plasma injection and should be ignored in this context.

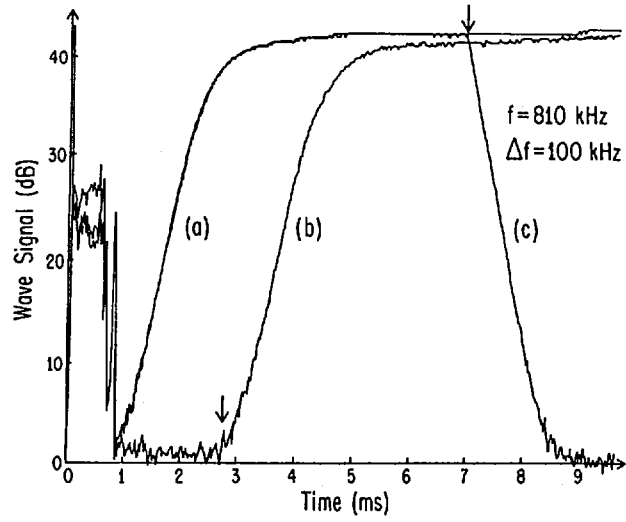


FIG. 2. Control of induced scattering instability by varying the mode damping rate.

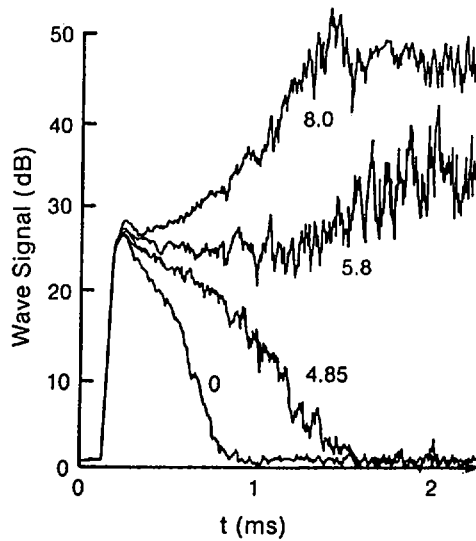


FIG. 3. Time evolution of a launched  $l = 0$  mode with field asymmetry magnitude as a parameter. The mode is destabilized as the field asymmetry magnitude is increased.

As stated above, this instability occurs over a wide range of plasma parameters. This is consistent with expectations for an induced scattering instability. In contrast, the linear resonance and the decay instability both have frequency matching conditions which, in general, would only be satisfied for certain sets of plasma parameters. Because of this, the induced scattering process may be more important for enhancing radial transport than either the linear resonance or the decay instability.

#### 4. Conclusion

We have shown how linear and nonlinear collective effects can enhance radial transport in a rotating plasma subject to nonaxisymmetric fields. Although our work involves transport in a pure electron plasma, similar processes may affect the transport in other confinement devices. Processes analogous to our linear collective enhancement have been considered for both toroidal devices [8] and tandem mirrors [9]. To our knowledge, however, there have been no studies of nonlinear collective enhancement in such devices.

#### Acknowledgments

This work was supported by DOE Grant DEFG 03-86ER53199 and NSF Grant PHY83-06077.

#### REFERENCES

- [1] RYUTOV, D.D., STUPAKOV, G.V., *Sov. Phys. Dokl.* **23** (1978) 412.
- [2] KEINIGS, R., *Phys. Fluids* **24** (1981) 860.
- [3] CRAWFORD, J.D., O'NEIL, T.M., MALMBERG, J.H., *Phys. Rev. Lett.* **54** (1985) 697.
- [4] CRAWFORD, J.D., O'NEIL, T.M., Nonlinear collective processes and the confinement of a pure electron plasma, submitted to *Phys. Fluids*.
- [5] MALMBERG, J.H., DeGRASSIE, J.S., *Phys. Rev. Lett.* **35** (1975) 577.
- [6] DRISCOLL, C.F., MALMBERG, J.H., *Phys. Rev. Lett.* **50** (1983) 167.
- [7] EGGLESTON, D.L., O'NEIL, T.M., MALMBERG, J.H., *Phys. Rev. Lett.* **53** (1984) 982.
- [8] STRINGER, T.E., *Phys. Rev. Lett.* **22** (1969) 770.
- [9] LEE, X.S., MYRA, J.R., CATTO, P.J., *Phys. Fluids* **27** (1984) 2248.

# RADIOFREQUENCY PLUGGING AND TANDEM MIRROR EXPERIMENTS IN A CUSP-ANCHORED MIRROR DEVICE

T. SATO, R. KUMAZAWA, S. OKAMURA, K. ADATI,  
T. AOKI, H. FUJITA, S. HIDEKUMA, T. KAWAMOTO,  
H. MASUMOTO, K. NISHIMURA, T. HATORI, K. TAKAYAMA<sup>1</sup>  
Institute of Plasma Physics,  
Nagoya University,  
Nagoya, Japan

H.R. GARNER, H.D. PRICE<sup>2</sup>, A.M. HOWALD, B.J. LEIKIND,  
H. IKEZI, P.B. PARKS, P. ANDREWS  
GA Technologies, Inc.,  
San Diego, California,  
United States of America

## Abstract

RADIOFREQUENCY PLUGGING AND TANDEM MIRROR EXPERIMENTS IN A CUSP-ANCHORED MIRROR DEVICE.

The paper covers three experimental topics: (1) An empirical scaling relation for the radio-frequency plug potential (ponderomotive potential) has been obtained and the maximum plug potential measured is 1 kV. (2) A negative potential mode produced with ICRF power only has been discovered and its equilibrium is investigated. (3) The MHD stability condition in a cusp-anchored mirror plasma has been obtained experimentally.

## 1. INTRODUCTION

The RFC-XX-M device has a linear, axisymmetric, MHD stable configuration, which is a simple mirror (central section) terminated by spindle cusps with radio-frequency (RF) plugging. RF plugging is one of the important possible means of suppressing end losses in open-ended systems. Preferential RF plugging [1] is especially useful for keeping the confinement region free of impurities. MHD stability in RFC-XX-M is ensured by the axisymmetric cusp anchor which can prevent anomalous perpendicular transport. It is valuable to compare the ambipolar potential plugging in this axisymmetric device with other, non-axisymmetric tandem mirror devices. Experiments on ambipolar potential plugging have been carried out since 1982, in a Japan-USA co-operative effort.

<sup>1</sup> Tokai University, Hiratsuka 259-12, Japan.

<sup>2</sup> Physics International, San Francisco, CA, USA.

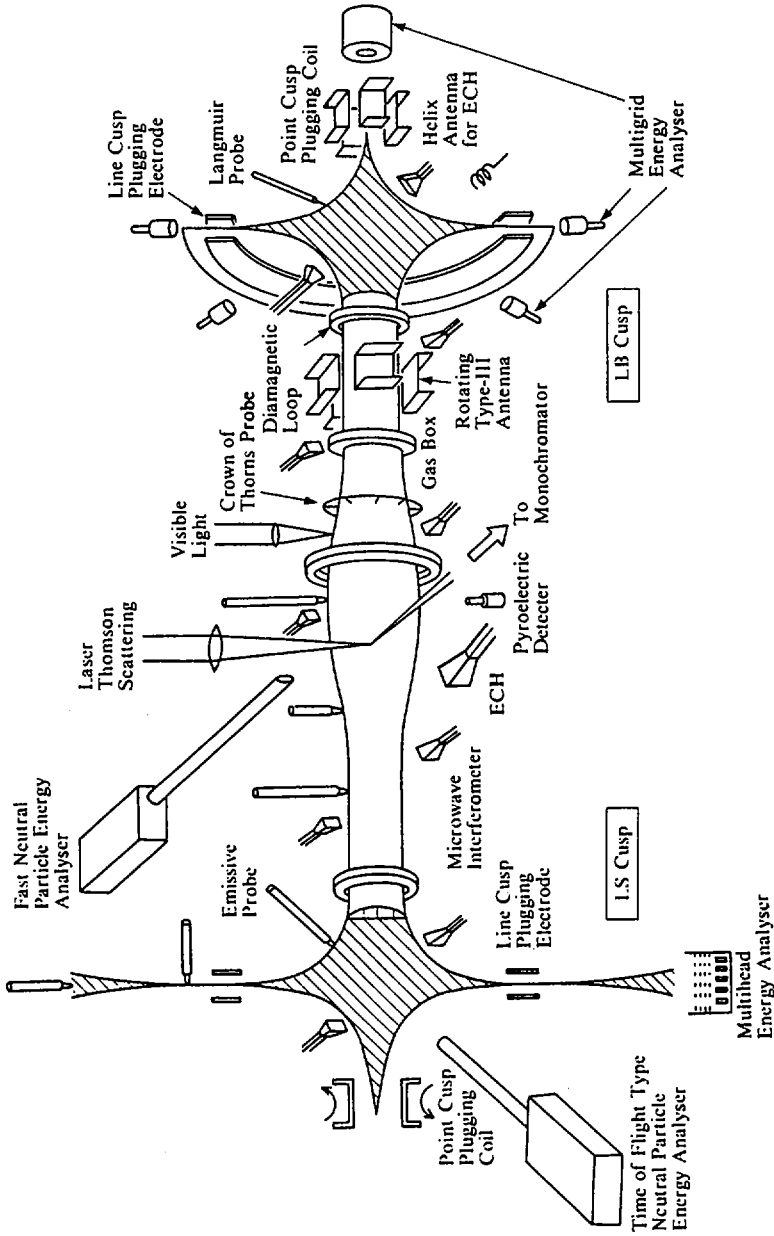


FIG. 1. Schematic drawing and diagnostic system of RFC-XX-M.

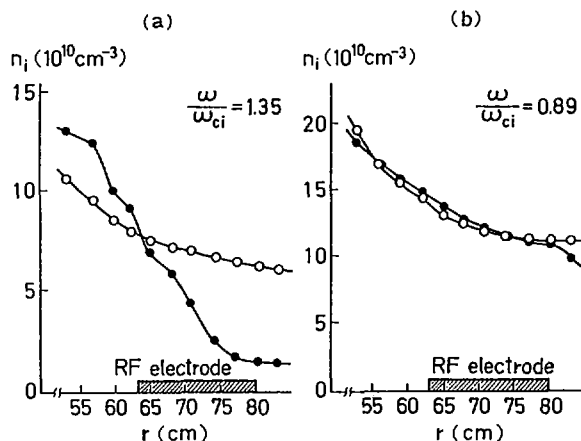


FIG. 2. Ion density distribution along the magnetic lines of force in the plug section. (a)  $\omega/\omega_{ci} = 1.35$ ,  $(\omega_{pi}/\omega_{ci})^2 = 14$ ,  $V_{rf} = 4$  kV,  $\psi = 0.8$  kV. (b)  $\omega/\omega_{ci} = 0.89$ ,  $(\omega_{pi}/\omega_{ci})^2 = 12$ ,  $V_{rf} = 4$  kV,  $\psi = 0$  kV.  $\circ$  — without RF plugging,  $\bullet$  — with RF plugging.

## 2. RADIOFREQUENCY PLUGGING

In 1984, at the London Conference [2] we reported that the energy confinement time due to the end loss of ICRH-sustained plasma is improved to about 10 ms by RF plugging and that the RF plug potential is produced for frequencies above the local ion cyclotron frequency at the line cusp. In this paper, we confirm the effect of RF plugging by measuring the ion density distribution along the magnetic lines of force in the plug section, and we obtain an empirical scaling relation for the RF plug potential in a broad range of plasma parameters.

A schematic diagram of RFC-XX-M is shown in Fig. 1. The distance between field-null points is 3 m. The magnetic field strength at full excitation is 2.1 T at the line cusp, 0.35 T at the central mirror midplane, and 0.97 T at the mirror throat. A rotating (phase) Nagoya type-III antenna is located in the mirror throat for plasma production and is driven by two 0.4 MW RF oscillators ( $f = 7$  MHz). For RF plugging, a pair of ring electrodes is installed in each line cusp and connected to a 1 MW RF oscillator ( $f = 24.5$  MHz).

The ion density distribution along the magnetic field lines in the plug section is measured by a movable Langmuir probe. Figure 2(a) shows that the ion density distribution has a very steep gradient under the RF electrodes when the applied RF frequency,  $\omega$ , is greater than the local ion cyclotron frequency,  $\omega_{ci}$ , under the RF electrodes. This suggests that an RF plug potential exists under the RF electrodes. In fact, the RF plug potential,  $\psi$ , measured by a method discussed later, is 0.8 kV.

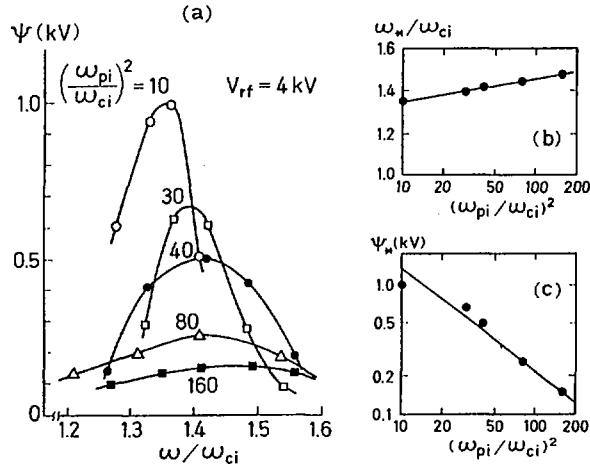


FIG. 3. (a) RF plug potential  $\psi$  versus  $\omega/\omega_{ci}$  for  $V_{rf} = 4$  kV, as a parameter of  $(\omega_{pi}/\omega_{ci})^2$ . (b) Dependence of the optimum frequency  $\omega_*/\omega_{ci}$  on  $(\omega_{pi}/\omega_{ci})^2$ . (c)  $\psi_*$  versus  $(\omega_{pi}/\omega_{ci})^2$  when  $\omega = \omega_*$ .

In the case of  $\omega/\omega_{ci} = 0.89$  ( $< 1$ ), however, no RF plug potential is produced and consequently the ion density distribution is almost the same as in the case without RF plugging, as shown in Fig. 2(b).

The RF plug potential is measured by means of multi-grid energy analysers (MGAs) located on the two end walls of the line cusp. In this experiment, the RF plugging is applied to either the LS line cusp or the LB line cusp of RFC-XX-M. In the ion energy analysis the RF plug potential is determined from the difference between the plug-side MGA and the non-plug-side MGA. Details are described in Ref. [2].

The RF plug potential is plotted in Fig. 3(a) as a function of  $\omega/\omega_{ci}$ . The parameter is the normalized plasma density,  $(\omega_{pi}/\omega_{ci})^2$ , where  $\omega_{pi}$  is the ion plasma frequency evaluated by using the density under the RF electrodes. The optimum value of  $\omega/\omega_{ci}$ , where  $\psi$  reaches its maximum value  $\psi_*$ , varies with  $(\omega_{pi}/\omega_{ci})^2$ . This optimum frequency, referred to as  $\omega_*/\omega_{ci}$ , is plotted in Fig. 3(b) as a function of  $(\omega_{pi}/\omega_{ci})^2$ . It shifts from 1.35 to 1.5 as  $(\omega_{pi}/\omega_{ci})^2$  increases from 10 to 160. This is consistent with the dispersion relation of the eigenmode of the ion Bernstein wave in the plug region [3]. Figure 3(c) shows the dependence of  $\psi_*$  on  $(\omega_{pi}/\omega_{ci})^2$  in the case of the applied RF voltage  $V_{rf} = 4$  kV. The value of  $\psi_*$  reaches 1 kV for  $(\omega_{pi}/\omega_{ci})^2 = 10$  and is proportional to  $(\omega_{pi}/\omega_{ci})^{-1.6}$ . This result is similar to that obtained in the TPD-III device [4] and agrees with theoretical expectations [5]. The dependence of  $\psi_*$  on the plug RF voltage is shown in Fig. 4 for  $\omega/\omega_{ci} = 1.41$  and

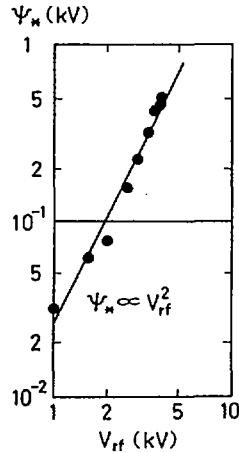


FIG. 4. Dependence of  $\psi_*$  on  $V_{rf}$  for  $\omega/\omega_{ci} = 1.41$  and  $(\omega_{pi}/\omega_{ci})^2 = 40$ .

$(\omega_{pi}/\omega_{ci})^2 = 40$ . The results indicate that  $\psi_*$  is approximately proportional to the square of  $V_{rf}$ . These relations can be unified and expressed in the following equation, with the frequency chosen to be equal to  $\omega_*$

$$\psi_* \text{ [kV]} = 4.7 E_{rf}^2 \text{ [kV/cm]} (\omega_{pi}/\omega_{ci})^{-1.6} \quad (1)$$

where  $E_{rf} = V_{rf}/d$  and  $d$  is the separation of the RF electrodes.

We can conclude from these results that: (i) the RF field penetrates into the line cusp plasma by coupling with the eigenmode of the ion Bernstein wave, (ii) the penetrating RF electric field produces an RF plug potential (ponderomotive potential) as expressed by Eq. (1), and (iii) the potential operates to suppress the ion loss flux through the line cusp.

### 3. NEGATIVE POTENTIAL MODE

In 1984, a new plasma equilibrium was discovered in RFC-XX-M. We call this the negative potential mode (n-mode) because end-loss analysers indicate the plasma potential to be near zero, and because measurements of the negative potential and the probe floating potential show a deep (negative) barrier between the central cell and the cusp end cell. Heavy ion beam probe measurements of the central cell plasma potential show it to be much lower than in the normal mode, and measurements of plasma rotation using a carbon tracer indicate that the central cell plasma potential

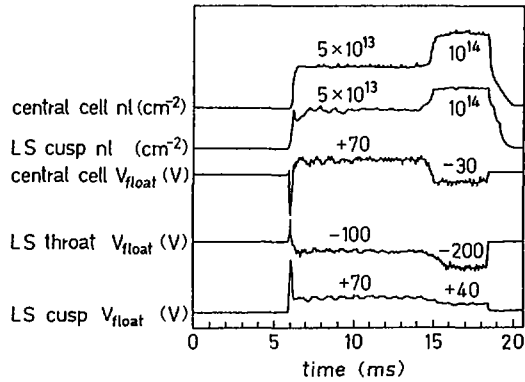


FIG. 5. Line density and floating potential as functions of time at various axial locations. A small gas puff in the central cell is responsible for the changes at 14 ms.

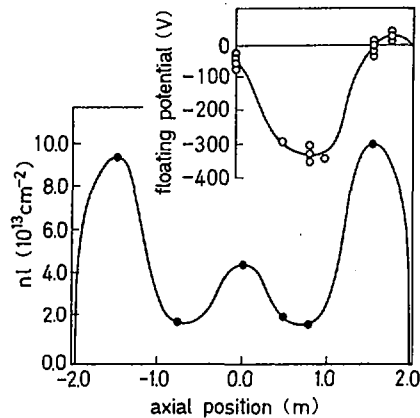


FIG. 6. Axial floating potential profile and line density profile, showing the presence of a potential barrier between the central cell and the cusp end-cells.

is near zero. The n-mode is a tandem mirror operating mode which is sustained by ICRF only, for up to 150 ms (limited by the ICRF power supply).

The line density and floating potential as functions of time are shown for a typical shot in Fig. 5. For this shot the plasma starts out slightly negative and is driven further negative by a small gas puff in the central cell at 14 ms. It is also possible to adjust the RF phasing and fuelling so as to achieve a transition from a normal mode plasma to the n-mode plasma during a single shot. The two modes have very different axial and radial profiles and confinement properties.

The axial density profile and the floating potential profile in the n-mode are shown in Fig. 6. The cusp end-cell densities are high because of the fuelling there, the central cell is fuelled by ions trapped by ICRF or collisions, and the density in the barrier is low because it is located on a magnetic anti-well. Floating potentials as large as  $-500$  V have been measured on the anti-well. The radial density profile is highly peaked on axis, and the electron temperature profile is flat at about 20 eV. The potential barrier is largest near the plasma edge where the density is low and the  $E_{\parallel}$  fields are high.

The global particle and energy confinement time is less than 1 ms. The measured central cell confinement time exceeds 1 ms and is possibly longer than the shot duration (up to 150 ms).

Scaling studies indicate that the mode is sensitive to internal RF fields (i.e. the phasing of the rotating Nagoya type-III antenna), the gas puff location and timing, and the wall conditions. The potentials of the central cell and the barrier are insensitive to the RF power (less than  $P_{rf}^{0.5}$ ). The mode can be formed as long as the fast wave can propagate (high plasma density), and a region of strong  $E_{\parallel}$  exists between the midplane and the field maximum at the end of the central cell. Gas fuelling is done primarily in the cusp end-cells to prevent cold ions from filling in the barrier regions.

We have used the computer code GARFIELD [6] to calculate the  $E_{\parallel}$  RF fields in the plasma. Using this code together with a new analytic model, a relationship between the density variation and the potential variation is obtained which corresponds to the experimentally measured profiles. Model ion distribution functions have been constructed, with the main features of the expected actual distribution functions in the strong ICRH limit [7]. Since these are functions of the invariant energy and magnetic moment, parallel pressure balance is guaranteed. The Boltzmann equation fails under these conditions and the anisotropic electron pressure driven by the  $E_{\parallel}$  RF fields must be taken into account. This model predicts barrier potentials much greater than the perpendicular electron temperature, as have been observed experimentally.

#### 4. MHD STABILIZATION BY THE CUSP ANCHOR

The mirror plasma in RFC-XX-M is quite stable in the usual operational modes, such as the normal mode, the RF plug mode, the normal tandem mode and the negative potential mode [8]. To verify the effect of the cusp anchor, an MHD instability is intentionally generated by reducing the cusp plasma pressure with respect to the mirror plasma pressure. In the normal mode, gas is puffed into the central section only. By adjusting the gas pressure, the ratio of the density in the cusp region to the density in the central section can be changed. When the ratio is less than a critical value, MHD instability occurs, as shown in Fig. 7(a). During the instability, the diamagnetic loop signal and the microwave interferometer signal show a sawtooth type relaxation oscillation, the repetition time of which is about 0.5 ms. The signal

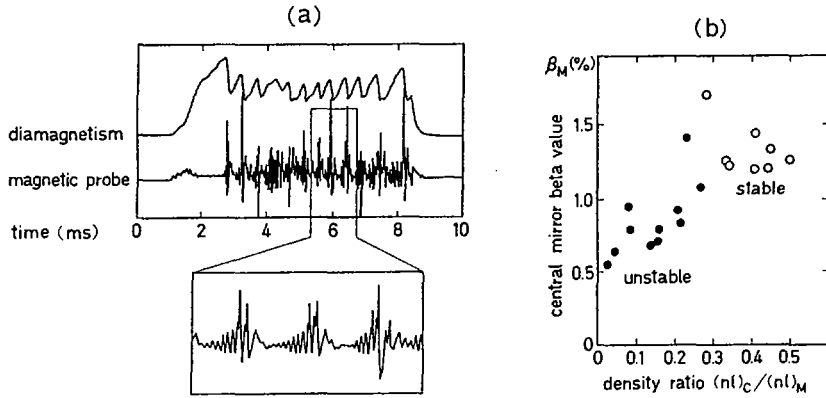


FIG. 7. (a) Typical example of MHD instability. (b) Stable and unstable shots for various settings of the beta value of the central mirror plasma and the ratio of the cusp plasma line density to the mirror plasma line density,  $(nl)_C/(nl)_M$ .

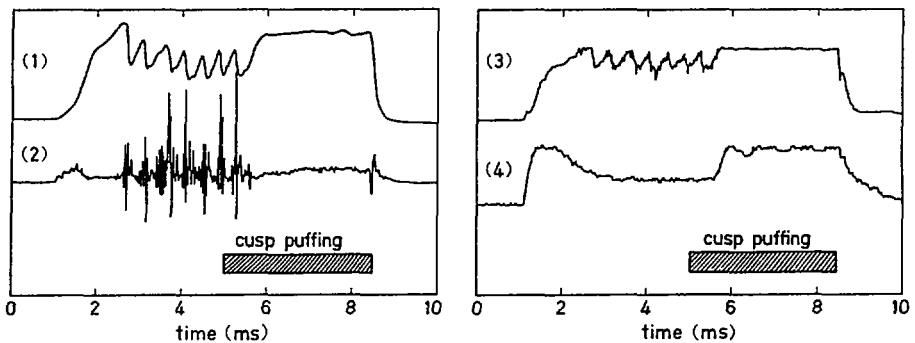


FIG. 8. Stabilization of MHD instability by gas injection into the cusp region. The traces are for (1) central mirror diamagnetism, (2) magnetic probe signal, (3) central mirror line density and (4) cusp line density.

of the MHD fluctuation is detected by a magnetic probe placed at the outer boundary and by the crown-of-thorns probe shown in Fig. 1. The fluctuation shows an exponentially growing oscillation, with a frequency of about 30 kHz, and rotates in the direction of the ion diamagnetic current with an azimuthal mode number 1. When the amplitude reaches a threshold level, the diamagnetic loop signal and the microwave interferometer signal begin to decay sharply and reach their minimum values within 100  $\mu$ s. At that time, the MHD fluctuation has its maximum amplitude and then disappears.

In Fig. 7(b), stable and unstable shots are plotted for various settings of the beta value of the central mirror plasma and the ratio of the cusp plasma line density ( $n\ell_C$ ) to the mirror plasma line density ( $n\ell_M$ ). This figure shows that the mirror plasma is stable when the line density ratio is larger than 0.27. In this experiment, the ion temperature of the mirror plasma and the cusp plasma is measured. From this measurement the critical pressure ratio corresponding to the line density ratio can be estimated as 0.13, which means that the cusp plasma, whose pressure is only 1/8 of the mirror plasma pressure, ensures MHD stability of the mirror plasma.

The plasma pressure in the cusp region is sustained by the outgoing ICRF wave launched at the mirror throat and thus it is possible to raise the cusp pressure simply by additional fuelling in the cusp region. An example of stabilization of MHD instabilities is shown in Fig. 8. During the unstable state, a small amount of gas is injected into the cusp region. The cusp plasma density increases and the instability is stabilized when the density ratio exceeds the above-mentioned critical value.

A cusp anchor is very attractive from the point of view of axisymmetry, small plasma volume and strong good curvature.

### ACKNOWLEDGEMENTS

The authors wish to express their gratitude to Professor H. Kakahana, the former director of the Institute of Plasma Physics of the Nagoya University, to Drs T. Ohkawa and R.L. Freeman from GA Technologies Inc., and to Dr. R.E. Price from the United States Department of Energy, for their encouragement.

This work was supported in part by the United States Department of Energy, under Contract No. DE-AT03-83SF11713.

### REFERENCES

- [1] HIDEKUMA, S., et al., *Phys. Rev. Lett.* **33** (1974) 1537.
- [2] OKAMURA, S., et al., in *Plasma Physics and Controlled Nuclear Fusion Research 1984* (Proc. 10th Int. Conf. London, 1984), Vol. 2, IAEA, Vienna (1985) 337.
- [3] CHAUDRY, M.B., et al., *J. Phys. Soc. Jpn.* **51** (1982) 2666.
- [4] HIROE, S., et al., *Phys. Fluids* **21** (1978) 676.
- [5] HATORI, T., *Phys. Fluids* **28** (1985) 219.
- [6] PHILLIPS, M.W., TODD, A.M.M., *Comput. Phys. Commun.* **40** (1986) 65.
- [7] PARKS, P.B., et al., in *Sherwood Controlled Fusion Theory Conference* (Proc. Conf. New York, 1986), Paper 3D-2 (1986).
- [8] PRICE, H., et al., *Bull. Am. Phys. Soc.* **30** (1985) 1493.



**Session D**

**ALTERNATIVE AND SUPPORTING SYSTEMS**

## Chairmen of Sessions

<b>Session D-I</b>	<b>L.M. KOVRIZHNYKH</b>	<b>USSR</b>
<b>Session D-II</b>	<b>T. UCHIDA</b>	<b>Japan</b>
<b>Session D-III</b>	<b>G. GRIEGER</b>	<b>Germany, Fed. Rep.</b>
<b>Session D-IV</b>	<b>F.L. RIBE</b>	<b>USA</b>

*Papers D-IV-1-1 and D-IV-1-2  
were presented by B.L. Wright as Rapporteur*

*Papers D-IV-2-1 and D-IV-2-2  
were presented by T. Ishimura as Rapporteur*

*Papers D-IV-5-1 and D-IV-5-2  
were presented by S. Denus as Rapporteur*

### **Session D-V (Posters)**

## STUDIES ON CURRENTLESS HELIOTRON E PLASMA

K. UO, A. IYOSHI, T. OBIKI, S. MORIMOTO, O. MOTOJIMA, M. SATO, S. SUDO, F. SANO, T. MUTOH, K. AKAISHI, M. NAKASUGA, K. KONDO, K. HANATANI, H. ZUSHI, S. BESSHOU, H. KANEKO, T. MIZUUCHI, H. OKADA, Y. TAKEIRI, N. NODA, I. OHTAKE, Y. IJIRI, M. IIMA, T. KAWABATA, T. SENJU, K. YAGUCHI, T. BABA, S. KOBAYASHI, R. TAKAHASHI, M. MURAKAMI<sup>1</sup>, H.C. HOWE<sup>1</sup>, D.L. HILLIS<sup>1</sup>, P.K. MIODUSZEWSKI<sup>1</sup>, G.H. NEILSON<sup>1</sup>, J. RICE<sup>2</sup>, J. TERRY<sup>2</sup>, E. MARMAR<sup>2</sup>, T. YAMASHINA<sup>3</sup>, T. HINO<sup>3</sup>, H. MINAGAWA<sup>3</sup>, T. ODA<sup>4</sup>, M. HAMAMOTO<sup>5</sup>, T. OHGO<sup>6</sup>, Y. SAKAMOTO<sup>7</sup>, H. AMEMIYA<sup>7</sup>, K. OKAZAKI<sup>7</sup>, H. OYAMA<sup>7</sup>, S. KATO<sup>7</sup>, A. AMEMIYA<sup>8</sup>, H. SUGAI<sup>9</sup>, S. URANO<sup>9</sup>, K. UCHINO<sup>10</sup>, T. KOGA<sup>10</sup>, K. MURAOKA<sup>10</sup>, M. AKAZAKI<sup>10</sup>, M. MAEDA<sup>11</sup>, S. MORITA<sup>12</sup>

Plasma Physics Laboratory,  
Kyoto University,  
Gokasho, Uji, Kyoto,  
Japan

### Abstract

#### STUDIES ON CURRENTLESS HELIOTRON E PLASMA.

Three kinds of heating, i.e. electron cyclotron resonance heating (ECRH), ion cyclotron frequency range heating (ICRF), and neutral beam injection heating (NBI) have been applied to heat the Heliotron E plasma. There has been particular interest in studies of confinement scaling, particle and impurity control, high beta properties, and high energy drift orbit dynamics. At a magnetic field of  $B_h = 1.9$  T, the central chord averaged ion temperature reached more than 1.2 keV with NBI and more than 1.6 keV with ICRF at low densities ( $\bar{n}_e = 2 \times 10^{13} \text{ cm}^{-3}$  in NBI and  $\bar{n}_e = 0.5 \times 10^{13} \text{ cm}^{-3}$  in ICRF). The central electron temperature  $T_e(0)$  of ECRH plasmas scales as  $T_e(0) \propto (P_{rf} / \bar{n}_e)^{0.41}$ , where  $P_{rf}$  is the ECRH power injected. The observed  $\tau_E(a)$  scaling of NBI plasmas is:  $\tau_E(a) \propto P_{heat}^{-0.64} \bar{n}_e^{0.54}$ , which shows a positive density dependence of the energy confinement time. This density dependence partially offsets the negative power dependence. In the case of long pulse ECRH + NBI produced plasmas, a

<sup>1</sup> Oak Ridge National Laboratory, Oak Ridge, TN, USA.

<sup>2</sup> Plasma Fusion Center, Massachusetts Inst. of Tech., Cambridge, MA, USA.

<sup>3</sup> Department of Nuclear Engineering, Hokkaido University, Sapporo, Japan.

<sup>4</sup> Department of Applied Physics, Hiroshima University, Higashi-Hiroshima, Japan.

<sup>5</sup> Department of Applied Physics, Oita University, Oita, Japan.

<sup>6</sup> Physics Department, Fukuoka University of Education, Munakata, Japan.

<sup>7</sup> Institute of Physical and Chemical Research, Saitama, Japan.

<sup>8</sup> Department of Nuclear Engineering, Nagoya University, Nagoya, Japan.

<sup>9</sup> Department of Electrical Engineering, Nagoya University, Nagoya, Japan.

<sup>10</sup> Department of Energy Conversion, Kyushu University, Fukuoka, Japan.

<sup>11</sup> Department of Electrical Engineering, Kyushu University, Fukuoka, Japan.

<sup>12</sup> Institute of Plasma Physics, Nagoya University, Nagoya, Japan.

small ECRH power added to the NBI plasma was found to pump out impurities. A wall carbonization technique was also found effective in reducing iron impurities and thus contributed to raising the stored energy with extended pulse length. In addition, the topology of drift orbits modified by the presence of a radial electric field was examined numerically.

## 1. INTRODUCTION

The recent Heliotron E experiments have emphasized studies of heating and confinement of currentless plasmas, and are also concentrated on particle and impurity control, aiming at long-pulse operation. The currentless plasma is first initiated by ECRH (53.2 GHz, <500 kW) and is additionally heated by NBI (3 beam-lines, <4 MW through the ports) [1] or ICRF (26 MHz, 2 MW) [2]. This paper discusses the behavior of ECRH and ECRH+NBI heated plasmas with special reference to the mechanisms that control the energy transport. Results of ICRF are reported in another paper of this IAEA conference [3].

## 2. ECRH EXPERIMENTS

The 53.2 GHz microwave power was injected into the Heliotron E vacuum vessel with the  $TE_{02}$  and  $HE_{11}$  modes. The resonant magnetic field is 1.9 T. The resonance position is adjusted to the position of the plasma center. The microwave (rf) power injected was varied from 160 kW to 500 kW by increasing the number of gyrotrons (up to 3 gyrotrons) [2]. Figure 1 shows a typical example of the temporal development of line-averaged electron density, electron and ion temperatures, bolometric loss, and soft X-ray intensity. These parameters become constant from the early phase of the rf pulse. The flat top time is much longer than the confinement time estimated from the decay of electron and ion temperatures. This result shows that a steady-state plasma is maintained by ECRH. A temporal increase of impurities has never been observed. The relevant studies of impurity behavior are described in section 4. The gross energy confinement time estimated from the electron decay time is 14 ms.

Figure 2 shows the profiles of  $T_e(r)$ ,  $n_e(r)$ ,  $T_i(r)$ , the absorbed rf power density  $P_{abs}(r)$ , and the integrated rf power  $P_{int}(r)$ . The density is  $\bar{n}_e = 2.5 \times 10^{13} \text{ cm}^{-3}$ . The electron density

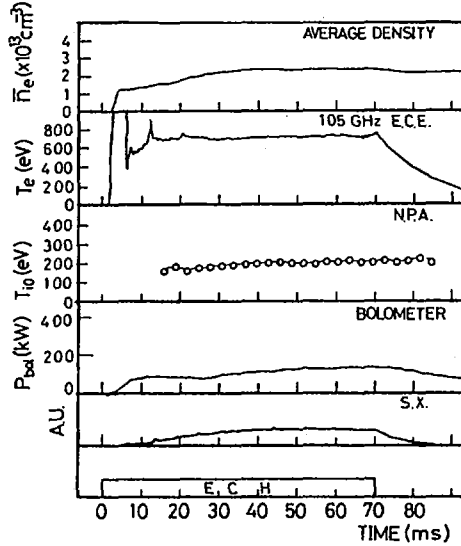


FIG. 1. Temporal behavior of  $\bar{n}_e$ ,  $T_e(0)$ ,  $T_i^{ch}(\theta=0)$ ,  $P_{bol}$ , S.X. at  $B_h = 1.9$  T.  $P_{rf} = 500$  kW with  $D_2$  gas.

profile is flat or slightly hollow at this density. However, in the lower density plasmas, the hollow profile becomes more typical. The rf energy-deposition profile,  $P_{abs}(r)$ , was measured from the electron energy decay time. It was assumed that the energy confinement time did not change immediately after the rf-power had been turned off. The total rf absorption efficiency,  $P_{int}(a)/P_{rf}$ , was about 50 to 70%. It depends on the electron density and temperature. From one third to half of the absorbed rf power was deposited inside the  $\bar{a}/2$  radius. The deposition profile was found to be flatter than expected from a single-pass, ray-tracing calculation for the  $TE_{02}$  mode injection.

The central electron temperature  $T_e(0)$  scaling is shown in Fig. 3.  $T_e(0)$  was measured with a laser-Thomson-scattering system. It scales as  $T_e(0) \propto (P_{rf}/\bar{n}_e)^{0.41 \pm 0.1}$ , where  $P_{rf}$  is the ECRH power injected. The heating rate becomes smaller as  $P_{rf}/\bar{n}_e$  increases. The collisionality of electrons near the plasma center is in the plateau regime. On the other hand, it is in the localized particle (ripple-trapped-particle) regime in the region from around  $\bar{r} = 0.3\bar{a}$  to  $\bar{r} = 0.8\bar{a}$ .

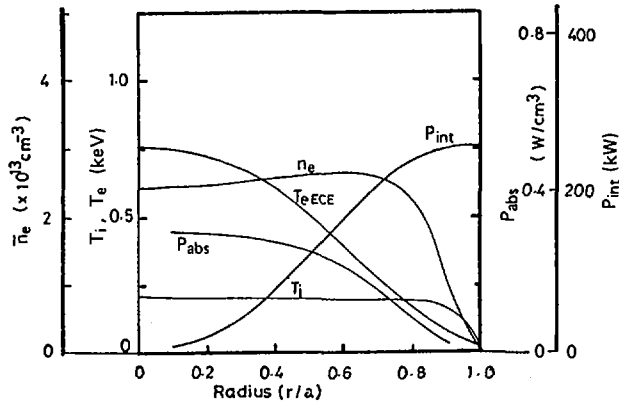


FIG. 2. Radial profiles of  $T_e(r)$ ,  $T_i(r)$ ,  $n_e(r)$ , and absorbed rf power density  $P_{abs}(r)$ .  $P_{int}(r)$  is the integrated rf power.  $\bar{n}_e = 2.5 \times 10^{13} \text{ cm}^{-3}$  at  $B_h = 1.9 \text{ T}$ .  $P_{rf} = 500 \text{ kW}$  with  $D_2$  gas.

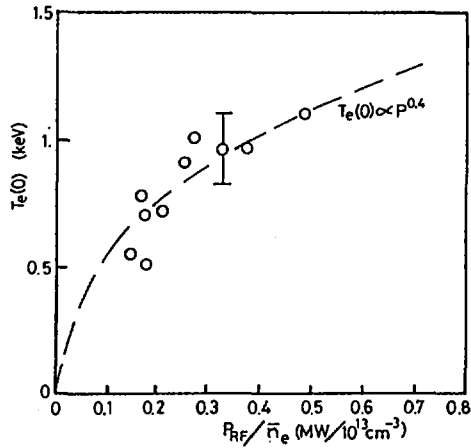


FIG. 3. Central temperature is shown for  $P_{rf}/\bar{n}_e$ .  $B_h = 1.9 \text{ T}$ ,  $P_{rf} = 150\text{--}500 \text{ kW}$ , and  $\bar{n}_e = 1.0\text{--}2.5 \times 10^{13} \text{ cm}^{-3}$ .

### 3. NBI EXPERIMENTS

The first phase of the NBI experiment in the Heliotron E device, which was reported previously [1], focused on the ion-heating efficiency achievable for the medium injection power level of  $P_{inj} < 2 \text{ MW}$ . The encouraging results led to the second-phase experiment (from 1984) using much higher injection power up

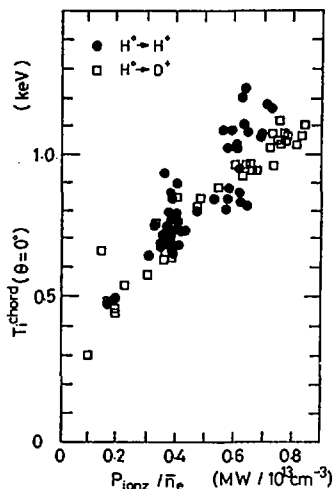


FIG. 4. Dependence of  $T_i^{\text{ch}}(\theta=0)$  on  $P_{\text{ionz}}/\bar{n}_e$ .  $P_{\text{ionz}}$  is the initially ionized neutral beam power injected through the ports.

to 4 MW. One of three beam lines was replaced. Its injection angle was changed from  $62^\circ$  to  $90^\circ$ . The second-phase study now in progress is also marked by an evolving understanding obtained with a variety of operational tools such as impurity injection [5], pellet fueling [6], pump-limiter [7], and in-situ carbon coating [8, 9]. The ion heating efficiency of the second-phase experiment ( $B_h=1.9$  T) is shown in Fig. 4. Within the experimental error bars, it is the same as that of the first-phase experiment (Fig. 1 of the previous report [1]), though the injection angle was changed to perpendicular. With an injected power of 3.5 MW, Heliotron E was able to achieve ion and electron temperatures of  $T_i^{\text{ch}}(\theta=0) > 1.2$  keV and  $T_e(0) > 0.7$  keV at the line-averaged densities of  $\bar{n}_e = 2\text{--}3 \times 10^{13}$  cm $^{-3}$ . Here  $T_i^{\text{ch}}(\theta=0)$  is the central-chord averaged ion temperature measured by a neutral particle analyzer. The central ion temperature is estimated to be higher by a factor of 1.2 to 1.3 than this value. The data base obtained from 1985 to 1986 includes the whole operating regime in density ( $\bar{n}_e = 1.5\text{--}9 \times 10^{13}$  cm $^{-3}$ ) and injection power  $P_{\text{inj}} = 0\text{--}3.5$  MW at two different magnetic fields ( $B_h = 1.9$  and 0.94 T). The global energy confinement time  $\tau_E(a)$ , defined as  $\tau_E(a) = W_p(a)/P_{\text{heat}}(a)$ , is 8–20 ms.  $W_p(a)$  is the total plasma internal energy and  $P_{\text{heat}}(a)$  is the heating power calculated by an orbit following Monte-Carlo-code [10] ( $P_{\text{heat}}(a) = P_b^e(a) +$

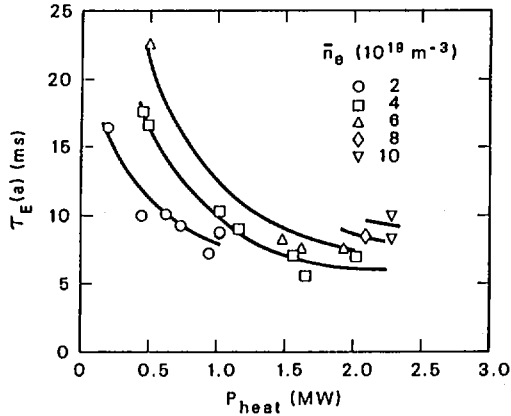


FIG. 5. Dependence of energy confinement time  $\tau_E(a)$  on NBI heating power.

$P_b^i(a) = P_{inj} - P_{shine-through} - P_{cx} - P_{orbit}$ ). As shown in Fig. 5, the confinement time was observed to scale as  $\tau_E(a) \propto P_{heat}(a)^\alpha \bar{n}_e^\beta$ , where  $\alpha = -0.64 \pm 0.15$  and  $\beta = 0.54 \pm 0.15$ . Although the  $\tau_E(a)$  dependence on the heating power  $P_{heat}(a)$  is similar to that observed in tokamaks (L-mode), the positive density dependence partially offsets the negative power dependence. Since  $\bar{n}_e \propto P_{inj}$  experimentally, the value of  $\tau_E(a)$  appears roughly constant at high injection power. For this data base, the local energy balance has been studied using the ORNL-developed transport/data analysis code, PROCTR [11]. A relatively large uncertainty exists in these studies, which is the level of thermal neutrals and the resulting loss of fast ions due to charge exchange process. To improve the accuracy of the neutral-density estimation, the laser-induced fluorescence using Balmer alpha transition is measured [12]. In the case of low power and low density, the convective loss can be dominant in the ion power balance at  $\bar{r} = 2\bar{a}/3$ . As the power and density are increased, the electron conductive loss becomes dominant in the over-all energy balance. A comparison was made between the experimentally inferred energy transport loss rate and the corresponding neoclassical rate (including the helical ripple and radial potential [13]). The inferred experimental electron energy transport coefficient is close to the neoclassical value at very low heating power. However, it increases to a substantially greater value than the neoclassical rate at high heating power.

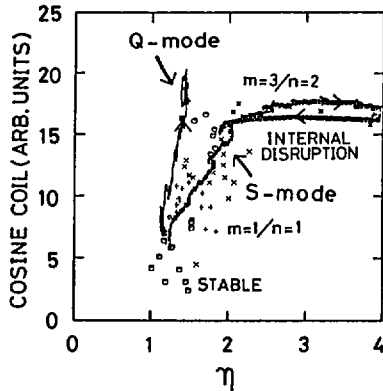


FIG. 6. Cosine coil signal versus density profile peaking parameter  $\eta$ .  $\eta \propto \bar{n}_e(\text{central chord}) / \bar{n}_e(\text{peripheral chord})$ .

The ion loss rate is in the neoclassical range within a factor of 3 at all heating powers [22].

In addition to the transport study, MHD activity has been analyzed to explore the stability map for several operational modes ( $B_n = 0.94$  T). Figure 6 shows a plot of a cosine-coil signal against the density-profile peaking parameter  $\eta (= \bar{n}_e(\text{center chord}) / \bar{n}_e(\text{peripheral chord}))$ . The cosine-coil signal is a measure of the beta value and the pressure profile. The NBI plasma initially lies in the stable-plasma region of low beta and flat density profile. With a temporal increase in beta followed by an increase in injection power, the plasma treads two different paths. The first path can be called the stable path (Q mode) [14], since no MHD instabilities have been observed. Along this path, the profile was kept broad by additional gas fueling. The MHD beta limit is not reached yet. The second path (S mode) is chosen by a condition where the pressure profile becomes peaked with less or no gas puffing. Pellet injection usually causes the density profile to be more peaked. This produces the S mode plasma. The initially observed instability of the S mode is the  $m=1/n=1$  mode, and thereafter as predicted from MHD theory the  $m=3/n=2$  mode dominates with increases in beta and peaking parameter  $\eta$  [15]. The  $m=3/n=2$  mode leads to an internal disruption. In this moment, the density (pressure) profile changes from a peaked one (unstable) to a broader one (stable). These observations suggest that the MHD beta limit in S mode is observed in the case of peaked profiles.

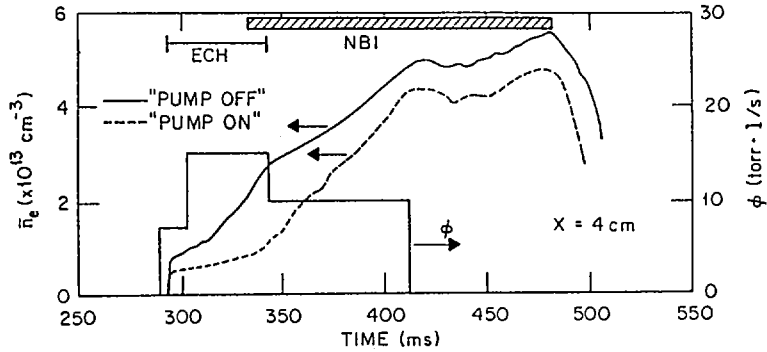


FIG. 7. Electron density  $\bar{n}_e$  and gas puff program: before activation of the limiter pumps (OFF) and after activation (ON). The NBI power of 3.2 MW was injected through the ports. The limiter was inserted 4 cm inside the last closed flux surface.

#### 4. LONG PULSE PLASMA PRODUCTION AND RELATED PARTICLE AND IMPURITY CONTROL

Long-pulse ECH+NBI plasma production has been achieved so far with careful gas-puffing control. Gas-puffing control is closely related to the particle- and impurity-transport behavior. One approach to active particle control is pellet fueling [6]. A sharp rise in density due to pellet fueling provides an encouraging prospect for particle control and a resultant improvement in particle confinement. Both the electron and ion temperatures recovered to the levels of the pre-pellet phase in about 30 ms. Since the injecting power does not change, this means the improvement of energy confinement as density increases. Another approach for particle control is the utilization of a pump-limiter [7]. Figure 7 shows the global effects of the pump-limiter on the core-plasma density. The gas flow rate,  $\phi$  [torr l/s], and neutral beam power were identical both before and after the activation of the gettering-pump of the pump limiter. A clear density drop was observed after the gettering-pump was activated, when the limiter was located 4 cm inside the last closed flux surface.

For long-pulse operation, impurity contamination of the plasma is a large problem due to the enhanced radiation loss. The main impurity species in neutral beam heated Heliotron E plasmas are iron, chromium, nickel (the material of the wall, YUS 170 stainless steel), titanium (the gettering material), oxygen, and

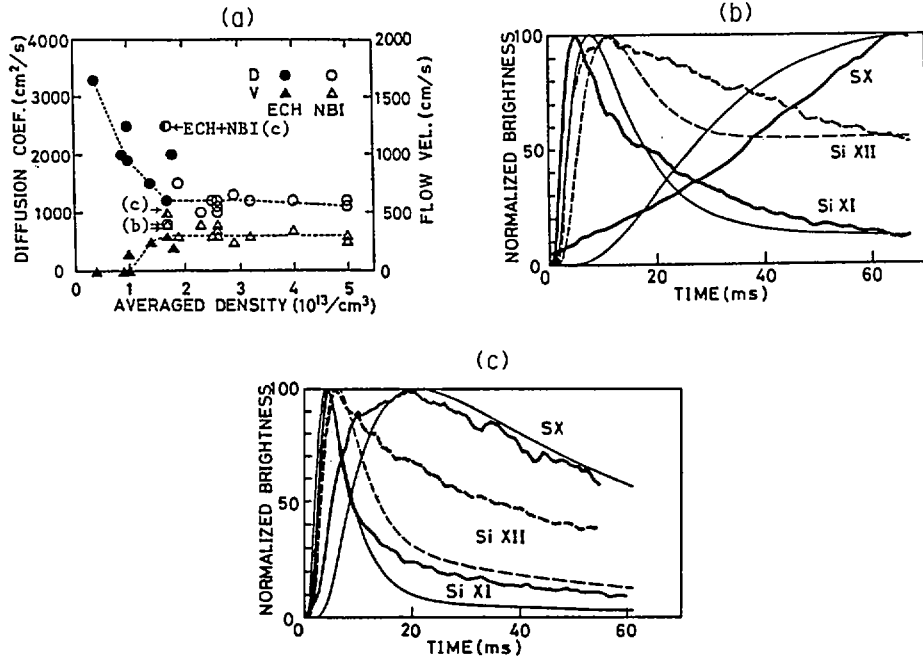


FIG. 8. (a) Transport properties analysed by simulation fitting. Diffusion coefficient  $D$  and flow velocity  $V$  as a function of  $\bar{n}_e$ . Dashed lines show the density dependence observed in well controlled shots. The cases (b) and (c) below are pointed. (b) In NBI plasma ( $T_e(0) \sim 400$  eV), the linear increase of SX at the central chord shows impurity accumulation. The code predicts the probable values of  $D \sim 800$  cm<sup>2</sup>·s<sup>-1</sup> and  $V \sim 400$  cm·s<sup>-1</sup> (fine lines). (c) NBI plasma with overlapped ECRH ( $T_e(0) \sim 450$  eV) shows shorter impurity confinement time. The SX signal increases more rapidly due to enhanced transport ( $D \sim 2500$  cm<sup>2</sup>·s<sup>-1</sup>,  $V \sim 500$  cm·s<sup>-1</sup>) than the previous case (b), but it decays.

carbon. At high densities ( $\bar{n}_e > 6 \times 10^{13}$  cm<sup>-3</sup>), a substantial contribution to the radiation loss from the iron impurity was observed in the spectroscopic measurements. The impurity problem is solved essentially by suppressing the impurity influx, e.g., by wall carbonization. However, the impurity contamination process is closely related to the impurity transport. In order to study these transport mechanisms, the laser blow-off technique has been used to inject trace impurities such as silicon into the ECRH+NBI plasmas [5]. Figure 8(a) shows the values of  $D$  (diffusion coefficient) and  $V$  (inward flow velocity at the plasma surface), evaluated by a 1-D numerical simulation code. The horizontal axis is the line-averaged density. With well-controlled operation, gas puffing was successfully applied to provide a steady-state, long-pulse NBI plasma. This aims at

achieving a temporally constant density phase with adequate gas puffing. The comparison between ECRH and NBI plasmas yielded a new aspect of impurity transport. In NBI plasmas with a density of  $1.7 \times 10^{13} \text{ cm}^{-3}$ , where the control of the gas puffing is difficult, impurity accumulation was observed as shown in Fig. 8(b) (see the trace for SX). The corresponding data points are shown in Fig. 8(a). The confinement time of injected silicon was 900 ms. When the ECH pulse was applied to the NBI plasma, the impurity density showed a simple decay with a time constant of 60 ms (Fig. 8(c)). This means that the impurities in NBI plasmas were pumped out by applying the ECRH power.

A local measurement of iron atom densities was made using a coaxial laser-induced fluorescence spectroscopic system [16]. The temporal and spatial measurements for NBI plasmas have revealed that the locations of the iron sources are broader than the width of the divertor trace of the chamber [21]. This suggests that a correlation is present between charge exchange neutral fluxes and fluorescence intensities for low-density plasmas ( $\bar{n}_e = 2-3 \times 10^{13} \text{ cm}^{-3}$ ). The obtained results reveal that the release of iron atoms from the surface of the chamber can be interpreted as being due to sputtering by charge-exchange neutrals.

The impurity fluxes in the plasma edge region were also examined using a surface analysis station with an "in-situ" AUGER electron spectroscopic system [17]. The dominant impurity species deposited on the  $\alpha$ -S<sub>1</sub> probe was iron when the probe surface was directly exposed to the plasma ( $\bar{n}_e = 2-3 \times 10^{13} \text{ cm}^{-3}$ ). The amount of deposited iron atoms increased with increasing neutral beam power. There was a correlation between this amount and the bolometer signal as well as with the brightness of multiply ionized iron ions. Since the low-temperature edge plasma ( $T_e < 10 \text{ eV}$ ) can not assume a principal role in sputtering of iron atoms, the higher-energy particles such as charge exchange neutrals (and fast ions on loss orbits) are considered to be responsible for releasing the iron atoms. This result was consistent with the observation obtained from the laser-induced fluorescence measurement. However, it should be noted that those two measurements have been made locally in poloidal and toroidal positions. It is necessary to continue the experiments to investigate whether the impurity sources are local or not.

The carbonization (in-situ carbon coating) technique has been established in tokamaks to reduce metal-impurity contents.

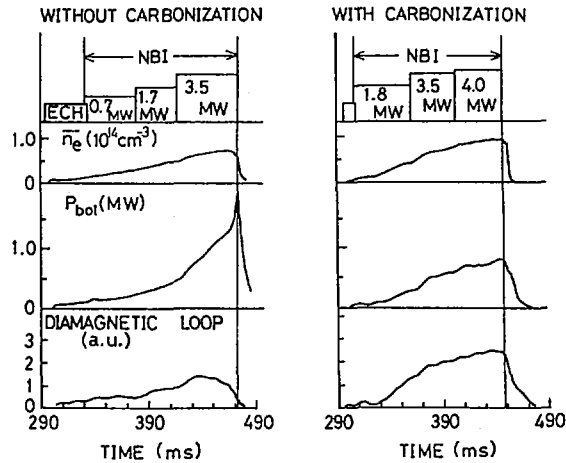


FIG. 9. Time behavior of  $\bar{n}_e$ , bolometric signal  $P_{bol}$ , and a diamagnetic loop signal in NBI heated plasmas with and without carbonization. Heating scheme is shown at the top.

This is a method to make thin carbon films on the surfaces of all in-vessel components, thus providing an environment for metal-impurity free plasma [8,9]. In Heliotron E, the carbonization has been conducted with a DC glow discharge in a methane/hydrogen mixture with wall at room temperature. The coating rate was 200 Å/hour. After the carbonization (300-500 Å), the NBI pulse length (at densities over  $\bar{n}_e=10^{14} \text{ cm}^{-3}$ ) could be extended while keeping temperatures almost constant. The radiation intensity from the iron impurity (e.g., Fe XVI) was reduced by more than a factor of 10 compared to the intensity before carbonization. The total bolometric loss [18] was also reduced by a factor of 2-3. This was a primary reason that the long-pulse operation became possible with high-power NBI and RF. Figure 9 shows typical time behavior of  $n_e$ ,  $P_{bol}$  and a diamagnetic-loop signal in NBI heated plasmas with and without carbonization. Without carbonization, the radiation loss, especially in low-field operation, increased continuously during the heating pulse, which was typical in low-field operation. The stored energy decreased in the later half of the pulse. With carbonization, the radiation intensity became stationary at the end of the heating pulse. The stored energy measured increased continuously. A higher averaged-beta value was obtained. An additional result with the carbonization was the shift of achievable density to higher values due to the strongly enhanced recycling on the carbonized surfaces. The

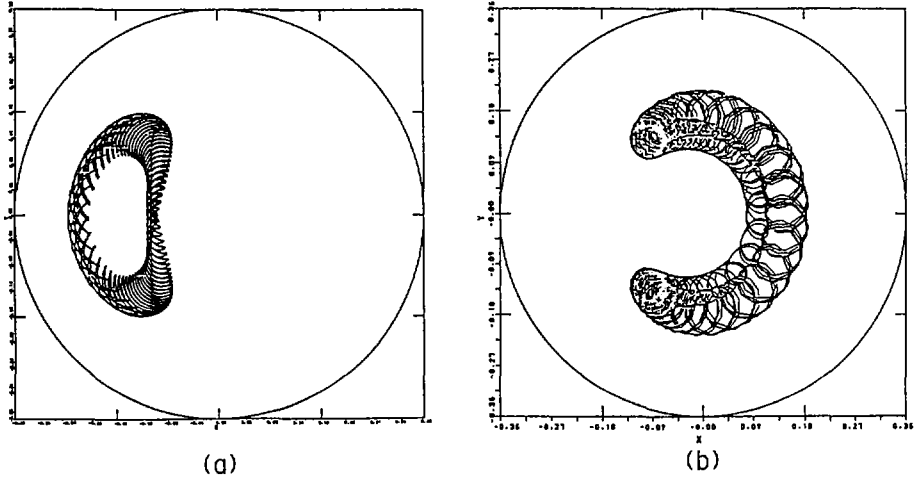


FIG. 10. Two different types of the resonant orbits confirmed numerically in Heliotron E. (a) Resonant superbanana orbit. (b) Resonant banana orbit.

highest density so far is  $\bar{n}_e = 1.8 \times 10^{14} \text{ cm}^{-3}$  at  $B_h = 1.9 \text{ T}$  in pellet-aided gas fueled operation.

## 5. DRIFT ORBIT CALCULATION

Recent neutral beam injection experiments on the WVII-A stellarator suggested that the electric potential  $\phi$  plays key roles in both confinement and heating of the plasma [19]. It is interesting to know under what conditions (sign, magnitude and profile of  $\phi$ ) the confinement of the ion orbits in Heliotron E is improved or deteriorated by the  $E_r$  field. To answer this question, calculations have been carried out by using a newly developed orbit following code. In order to reduce the computing time, this code uses the "field splitting" algorithm [20], which decomposes the fully 3D field quantities into helically symmetric (2D) and symmetry-breaking (3D) parts. The  $E_r$  field is calculated from the potential which is constant on 3D magnetic surface;  $\vec{E} = -\nabla\phi(\psi)$ ,  $2\pi\psi = \int \vec{B} \cdot d\vec{S}$  being the toroidal flux. Two different types of resonance were confirmed numerically. One is the "helical resonance" ( $\Omega_h + \Omega_{E \times B} = 0$ ) and the other is the "toroidal resonance" ( $\tau_{v_{||}}/R + \Omega_{E \times B} = 0$ ). Near these conditions, resonant super banana (Fig. 10(a)) and resonant banana orbits (Fig. 10(b)), which cannot be found without an  $E_r$  field, were obtained. If the  $E_r$  field is strong enough (off resonance), the

electric potential improves the confinement of helically trapped particles. Another notable effect of the  $E_r$  field is that it induces additional collisionless detrapping.

#### ACKNOWLEDGMENTS

It is a pleasure to acknowledge the other members of the Laboratory whose dedicated efforts have enabled us to conduct these experiments. We are grateful to Drs. M. Wakatani and K. Itoh for stimulating discussions. The US participants were supported by the US Department of Energy Contract No. DE-AC05-84OR21400 and DE-AC02-78ET51013.

#### REFERENCES

- [1] UO, K., HELIOTRON E GROUP, in Plasma Physics and Controlled Nuclear Fusion Research 1984 (Proc. 10th Int. Conf. London, 1984), Vol. 2, IAEA, Vienna (1985) 383.
- [2] IYOSHI, A., HELIOTRON E GROUP, *ibid.*, Vol. 1, p. 453.
- [3] MUTOH, T., HELIOTRON E GROUP, Paper IAEA-CN-47/D-III-2, these Proceedings, Vol. 2.
- [4] UO, K., HELIOTRON E GROUP, Nucl. Fusion **24** (1984) 1551.
- [5] RICE, J.E., TERRY, J.L., MARMAR, E.S., MOTOJIMA, O., HELIOTRON E GROUP, Nucl. Fusion **24** (1984) 1205.
- [6] SUDO, S., HELIOTRON E GROUP, Nucl. Fusion **25** (1985) 95.
- [7] HILLIS, D.L., et al., in Plasma-Surface Interactions in Controlled Fusion Devices (Proc. 7th Int. Conf. Princeton, NJ, 1986), to appear in J. Nucl. Mater.
- [8] WINTER, J., *ibid.*
- [9] NODA, N., HORI, Y., MASAI, K., et al., *ibid.*
- [10] HANATANI, K., et al., Nucl. Fusion **25** (1985) 259.
- [11] HOWE, H.C., Physics Models in Tokamak Transport Code PROCTR, Rep. ORNL/TM-9537, Oak Ridge National Laboratory (1985).
- [12] OKANO, D., et al., in Plasma-Surface Interactions in Controlled Fusion Devices (Proc. 7th Int. Conf. Princeton, NJ, 1986), to appear in J. Nucl. Mater.
- [13] HASTINGS, D.E., HOULBERG, W.A., SHAING, K.C., Nucl. Fusion **25** (1985) 445.
- [14] MOTOJIMA, O., HELIOTRON E GROUP, Nucl. Fusion **25** (1985) 1783.
- [15] WAKATANI, M., et al., Paper IAEA-CN-47/D-V-3, these Proceedings, Vol. 2.
- [16] KONDO, K., HELIOTRON E GROUP, in Plasma-Surface Interactions in Controlled Fusion Devices (Proc. 7th Int. Conf. Princeton, NJ, 1986), to appear in J. Nucl. Mater.
- [17] MIZUUCHI, T., HELIOTRON E GROUP, *ibid.*
- [18] BESSHOU, S., MORIMOTO, S., MOTOJIMA, O., et al., Nucl. Fusion **26** (1986) 114.
- [19] GRIEGER, G., WVII-A TEAM, Plasma Phys. Controll. Fusion **28** (1986) 43.
- [20] HANATANI, K., UO, K., in 3-D MHD Studies (Proc. US-Japan Workshop Oak Ridge, TN, 1984) (1984) 7.
- [21] MOTOJIMA, O., MIZUUCHI, T., BESSHOU, S., IYOSHI, A., UO, K., et al., Nucl. Mater. **128&129** (1984) 524.
- [22] SANO, F., OBIKI, T., MOTOJIMA, O., SASAKI, A., HANATANI, K., et al., Nucl. Fusion **24** (1984) 1103.

## DISCUSSION

K. LACKNER: In your ECRH heating experiments, did you change the power deposition profile by varying  $B_0$ ? If so, how did the  $T_e$  profile respond? For example, did you observe 'profile consistency', such as in tokamaks, or adjustment of the  $T_e$  to the power deposition profile, as in the Wendelstein VII-A stellarator?

K. UO: Yes, we did change  $B_0$ . The central temperature  $T_e(0)$  is about 1 keV, if  $\omega_{ce}$  is on the magnetic axis ( $B_0 = 1.90$  T). It decreases to 0.6 keV when  $B_0$  is reduced on 1.84 T, while the temperature at the half-radius  $T_e(a/2)$  increases from 0.7 keV to 0.85 keV. The 'profile consistency' is now under study by measurement of the electron energy transport, and more details will be available later on.

O.S. PAVLICHENKO: Did you try to measure any unidirectional current during your NBI heating experiments, or do you consider that your plasma was really currentless?

K. UO: In the cases of unidirectional NBI and ECRH, we observed a small amount of current — less than 1 kA.

## PLASMA CONFINEMENT IN THE WENDELSTEIN VII-A STELLARATOR

H. WOBIG, H. MAASSBERG, H. RENNER,  
W VII-A TEAM<sup>1</sup>, ECRH GROUP<sup>2</sup>, NI GROUP<sup>3</sup>  
Euratom-IPP Association,  
Max-Planck-Institut für Plasmaphysik,  
Garching, Federal Republic of Germany

### Abstract

#### PLASMA CONFINEMENT IN THE WENDELSTEIN VII-A STELLARATOR.

The confinement behaviour of the W VII-A stellarator depends on the magnetic field structure, the heating method as well as the plasma properties. At low (m,n) rational numbers of the rotational transform,  $\epsilon = m/n$ , strongly deteriorated confinement is observed which is explained by island formation and ergodization of magnetic surfaces. It is only in the close vicinity of these fundamental resonances,  $\epsilon = \frac{1}{2}$  and  $\frac{1}{3}$ , where the most stable magnetic surfaces are expected, that optimum confinement is found. It is sensitively dependent on both the edge value of  $\epsilon$  and on small additional shear. It is only for these optimum confinement conditions that the particle and energy transport is analysed in the paper. — The ion energy transport in W VII-A is found to be in rather good agreement with neoclassical theory. In detail, in case of NBI heating, large radial electric fields are built up by the fast ions, strongly improving the confinement of thermal ions. Collisional slowing down of the ions originating from the NBI is found. For ECF heated discharges, the observed radial electric fields are comparable with neoclassical estimates (by means of the ambipolarity condition). For the central part of the plasma, the particle fluxes are explained in terms of neoclassical transport; at outer radii, strongly enhanced particle transport must be concluded. ECF heated discharges, especially with low density, indicate neoclassical electron heat conduction in the central part; in the edge region, however, the electron energy confinement must be described by anomalous transport.

### I. Introduction

Experiments in the low shear stellarator W VII-A exhibit a critical dependence of the plasma confinement on the structure of the magnetic field. At particular values of the external rotational transform ( $t_0 = \frac{1}{2}$  and  $\frac{1}{3}$ ), the confinement is deteriorated whereas in the close neighbourhood of these values confinement time and energy content are maximum (Figure 1). Both energy and particle balance at optimum confinement have been studied in "currentless" plasmas generated by NBI and ECRH and will be discussed in the subsequent sections. The residual current (1-2 kA) observed under these conditions does not contribute to the heating power.

<sup>1</sup> G. Cattanei, D. Dorst, A. Elsner, V. Erckmann, U. Gasparino, G. Grieger, P. Grigull, H. Hacker, H.J. Hartfuß, J. Häckel, R. Jaenicke, J. Junker, M. Kick, H. Kroiss, G. Kuehner, H. Maaßberg, C. Mahn, G. Müller, W. Ohlendorf, F. Rau, H. Renner, H. Ringler, F. Sardei, M. Tutter, A. Weller, H. Wobig, E. Würsching, M. Zippe.

<sup>2</sup> W. Kasperek, G.A. Müller, P.G. Schüller, M. Thumm, R. Wilhelm (Institut für Plasmaforschung, Univ. Stuttgart).

<sup>3</sup> R. Freudenberger, W. Ott, F.P. Penningsfeld, E. Speth.

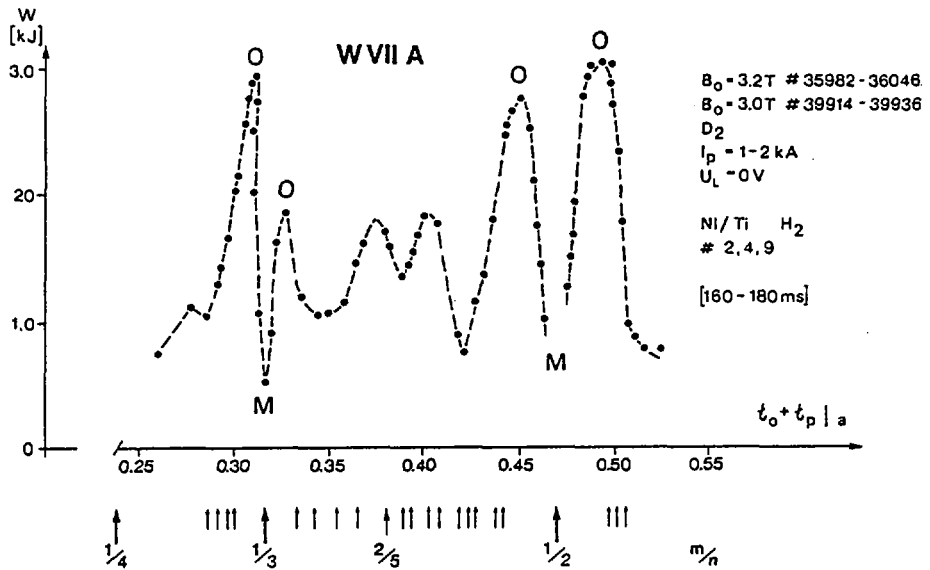


FIG. 1. Total plasma energy in W VII-A as a function of rotational transform at plasma edge,  $t_a = t_0 + t_{p|a}$ . Heating by neutral beam injection. O indicates regions of optimum confinement, M are states of minimum confinement.

In NBI heated plasmas (Section II), the main topics are ion energy balance, the role of the radial electric field and the heating mechanism, where in contrast to earlier assumptions /1/ the classical slowing down mechanism could be verified. Particle transport is discussed in Section III. ECR heated plasmas offer a better chance to analyse the electron energy balance (Section IV) than NBI heated plasmas. In ECR heated plasmas, the electron transport in the bulk of the plasma can be explained by neoclassical effects, in the boundary regions, however, anomalous transport has to be assumed. In the minima of confinement ( $t_0 = \frac{1}{2}$  and  $\frac{1}{3}$ ), the most plausible explanation for the enhanced losses is island formation in the magnetic field structure and stochasticity caused by external perturbations. This effect will be discussed in Section V.

## II. NBI heating

The slowing down of the fast ions originating from the nearly perpendicular ( $84^\circ$ ) neutral beam injection had been experimentally proved to be collisional both for stationary conditions and after switching off the injectors /2/. This was demonstrated by neutron flux measurements of D-D reactions in case of  $D^0$  injection into a  $D^+$  target plasma as well as by the charge exchange diagnostic. Both the absolute value of the stationary neutron production as well as the transient neutron flux after the  $D^0$  injection switched off were found to be in rather good agreement with simplified Fokker-Planck estimates based on the assumption of only collisional interaction (Coulomb scattering) /3/. Additionally, the measured time decay of high energetic CX neutrals after switching

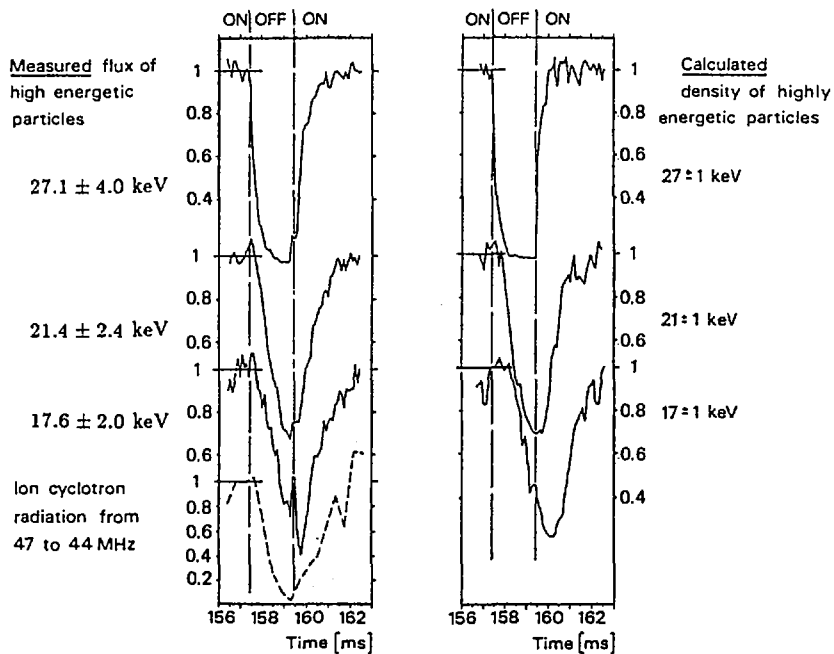


FIG. 2. Charge exchange fluxes measured (on the left) and simulated (on the right) versus time for phase of all neutral beam injectors switched off.

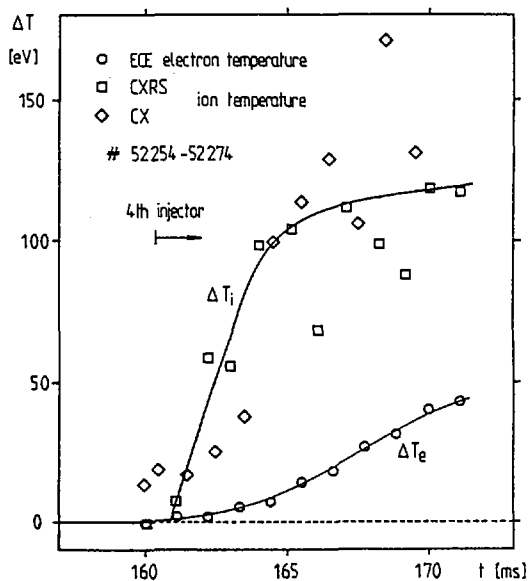


FIG. 3. Ion and electron temperature increase,  $\Delta T$ , versus time after fourth neutral beam injector is switched on ( $T_i \approx 650$  eV and  $T_e \approx 500$  eV).

off the NBI could be reproduced by Monte Carlo simulation on the basis of only collisional slowing down (see Figure 2). The ion distributions were estimated to be highly anisotropic /4/ due to the high power NBI. By means of linear stability analysis /5/, these ion distributions were found to be stable against low harmonic ion cyclotron instabilities (ion Bernstein modes) for stationary conditions. Unstable lower hybrid modes are expected to smooth the ion distribution function near the injection velocities but having negligible effect on the energy transfer.

Only in the transient phase after switching on the injectors, the radiation close to the low ion cyclotron harmonics (ICE) measured by a probe in the limiter shadow was strongly increased. From the stability analysis of the transient ion distributions after switching on the NBI, low harmonic ion Bernstein modes were found to be strongly unstable. Although these distributions were calculated on the basis of collisional slowing down, strong instability is expected leading to preferential ion heating. This prediction is consistent both with a measured delay of the neutron flux increase and with the strong increase of the ion temperature immediately after switch on of an additional beam. This temperature increase,  $\Delta T_i$  (see Figure 3), is in rather good agreement with the assumption that the absorbed NBI power of the additional beam given by the diamagnetic signal is only transferred to the ions; direct electron heating is rather small ( $\Delta T_e \ll \Delta T_i$ ). For collisional slowing down, however, preferential electron heating should be expected for the initial phase since high energetic ions are mainly slowed down by electrons.

From the measured Doppler shift of impurity lines connected with poloidal plasma rotation, radial electric fields up to 1 kV/cm were deduced. The toroidal plasma rotation,  $v_\theta$ , was found to be not larger than the poloidal one:  $v_\theta \gg v_\psi/A$  where  $A$  is the aspect ratio ( $A = 20$  for W VII-A); this result is quite different to tokamak cases /6, 7/. Without radial electric fields, the fast ion loss rate is quite high due to the nearly perpendicular injection and the small plasma radius in W VII-A ( $r_n \leq 10$  cm) leading to only poor heating efficiency. It was clearly shown by Monte Carlo calculations (ODIN code, /8/) that the fraction of fast ion losses can be significantly reduced by radial electric fields which, on the other hand, are built up by the loss of such fast ions /9/. Due to the strong radial electric fields deduced from the measured poloidal plasma rotation the heating efficiencies for both co- and counter-injection (which are analogously defined with respect to the rotational transform  $\iota$ ) are strongly improved. For both injection cases which are experimentally realized by changing all magnetic field directions, similar confinement properties were found. However, in case of counter-injection, higher electric fields,  $E_r$ , were observed than for co-injection. This is consistent with the condition  $E_r + v_{\parallel} B r/R \simeq const$  which can be derived for strong radial electric fields from the kinetic equation (poloidal component of  $(\vec{v}_{\parallel} + \vec{v}_D) \cdot \nabla f \simeq const$ ) describing the partial compensation of the  $\nabla B$ -drift effects.

The connection of fast ion losses with the global confinement properties was demonstrated by measuring the Fe sputtering by means of laser induced fluorescence (LIF). By Monte Carlo calculations with electric fields included, the fast ion flux distribution onto the stainless steel vacuum vessel was estimated leading to Fe densities which are within a factor of 2 in agreement with the LIF measurements. Figure 4 shows the time behaviour of the Fe sputtering (upper plot) which is equivalent to the orbit loss rate for a discharge in which the rotational transform was transiently shifted over the deteriorated confinement regime from the optimum confinement below to the one above  $\iota \simeq \frac{1}{2}$ . This shift of the external rotational transform leads to a strong decrease in the energy content,  $W$  (middle plot), within the deteriorated confinement regime. The corresponding

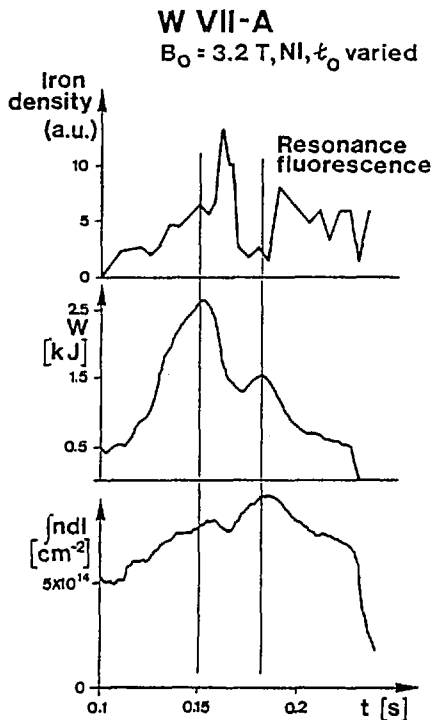


FIG. 4. Iron sputtering, total energy content and line density versus time. For these discharges, external rotational transform was shifted from optimum confinement below (line on left) to the one above  $\epsilon \approx \frac{1}{2}$  (line on right).

decrease of line density,  $\int n dl$  (lower plot), is partially compensated by higher neutral gas influx due to the increased recycling. The stronger neutral gas production is confirmed by an increase of the  $H_{\alpha}$  signal. Then, both the energy as well as the particle confinement times are significantly reduced close to the rational value  $\epsilon = \frac{1}{2}$  which is connected with an increase of fast ion losses leading to a reduced NBI heating efficiency and the strong decrease of the energy content. For degraded confinement properties, this flux of fast ions onto the vacuum vessel is up to 20% of the total influx of NBI neutrals (the fraction of transmitted neutrals is typically between 30% and 60% depending on line density). Consequently, fast ion losses can contribute significantly to the particle transport. Furthermore, the poloidal plasma rotation was found to be smaller within the  $t$ -range of deteriorated confinement. These experimental findings confirm the correlation between radial electric fields and the confinement properties of the fast ions. Although the fraction of fast ions is relative small (typically  $< 10\%$ ), the fast ion loss contributes significantly to the particle fluxes. Consequently, the radial electric fields are mainly determined by the fast ion loss rate to satisfy the ambipolarity condition of the particle fluxes.

### III. Particle transport

Since in general detailed information about the particle sources is not available (especially the neutral gas distribution within the torus is largely unknown), the analysis of particle transport has to be based on some reasonable assumptions. This situation is different to the energy analysis where profiles of heating power deposition and radiated power are known, at least to some extent. However, both particle transport and heat conduction are strongly correlated in all transport theories of interest.

In the early phase of W VII-A operation with only ohmic heating, detailed energy transport studies were carried out leading to the electron thermal conductivity /9/:  $\chi_e^{\text{OH}} \propto n_e^{-1} \cdot T_e^{-2/3}$  (see Section IV). Only for the case of ohmically heated helium discharges the particle diffusion coefficient could be derived from the measured ionization rates /10/. The radial behaviour was found to be similar to the electron thermal conductivity, but the absolute value was about one order of magnitude smaller:  $D^{\text{OH}} \simeq 0.1 \cdot \chi_e^{\text{OH}}$ . The flattening of the density profiles at outer radii which is typical for all discharges in W VII-A and the increased particle sources due to neutral gas ionization lead to strongly enhanced particle transport as it is described by the  $n$  and  $T$  dependence of the anomalous diffusion coefficient  $D^{\text{OH}}$ . Contrary to the electron heat conduction, the anomalous flux,  $\Gamma^{\text{AN}} \simeq -D^{\text{OH}} \cdot n'_r$ , is less than or of the same order of magnitude as the neoclassical particle flux in the central part of the plasma. The transport coefficients of the thermal ions are mainly determined by the values of the plateau collisionality regime which without radial electric fields strongly exceed the electron transport coefficients.

In case of the strong neutral beam heating in W VII-A, the beam particle deposition is the main particle source in the central region of the plasma column leading to the nearly linear density increase during the duration of the NBI heating ( $\leq 200$  ms) for good confinement conditions. The beam particle deposition, however, is not known accurately enough since the ionization profiles of the charge exchange generated thermal neutrals cannot be determined up to now; the transport of these neutrals is mainly determined by CX collisions quite similar to the problem of neutral gas influx. Assuming that all these neutrals are ionized, a lower limit of the particle confinement time can be estimated. In doing this, particle confinement times of typically more than 100 ms were found for the central plasma region. These very good confinement properties were confirmed by pellet injection experiments where all the additional particles were confined for the rest of the discharge duration ( $\leq 100$  ms). Only in the case of an additional ECF pulse, these particle confinement properties seem to be degraded /11/. For the other cases, the experimentally deduced particle fluxes are of the same order of magnitude as the neoclassical electron transport in the bulk part of the plasma within the uncertainty of the particle sources. However, already in the maximum gradient region the anomalous transport becomes dominant.

ECF sustained discharges at higher densities where the ions are effectively heated by electron collisions can be analyzed on the basis of the neoclassical formalism since the ion distribution functions are close to Maxwellians. As the ions are in the plateau collisionality regime, their transport coefficients are reduced by a suitable radial electric field in order to satisfy the ambipolarity condition. On the basis of measured profiles of density and temperatures, the local radial electric field is calculated by means of the ambipolarity condition of only the neoclassical fluxes  $\Gamma_i^{\text{NC}} = \Gamma_e^{\text{NC}}$  consisting of Pfirsch-Schlüter and plateau regime contributions /12/. The calculated radial electric fields are in good agreement with the values deduced from the Doppler shift of impurity lines for

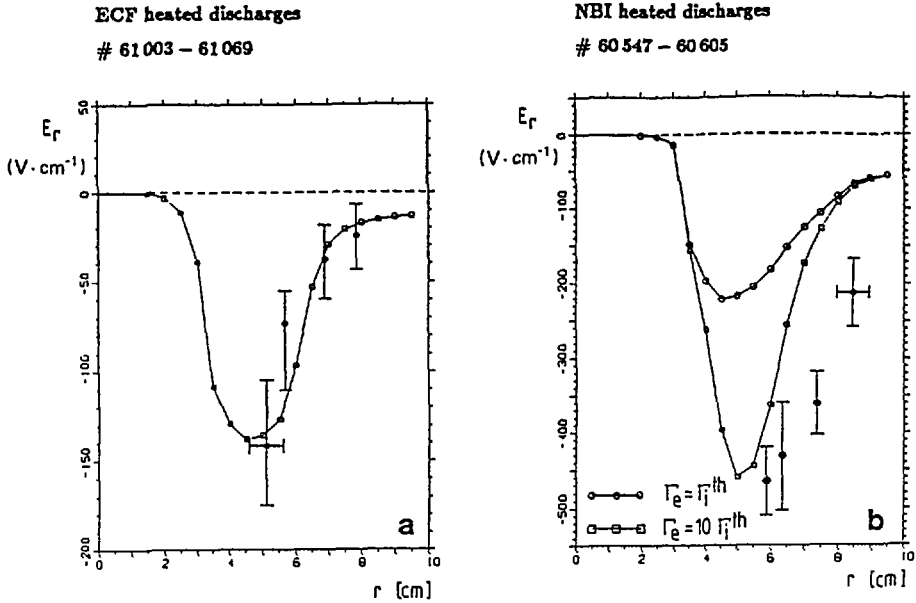


FIG. 5. Radial electric fields measured (dots) and calculated versus plasma radius for ECF and NBI heated discharges, plots (a) and (b), respectively.

the case of ECF heated discharges (s. Figure 5a); however, it must be mentioned that the measured values are obtained at radii where the *anomalous* transport is dominant. Furthermore, on the basis of measured profiles it is impossible to satisfy the continuity equation with only neoclassical fluxes at outer radii.

In order to get a consistent description, the total particle flux density is modeled by:  $\Gamma = \Gamma^{NC} + \Gamma^{AN}$  where  $\Gamma^{NC}$  is the neoclassical term consisting of Pfirsch-Schlüter and plateau regime contributions and  $\Gamma^{AN}$  the *anomalous* term derived from the ohmically heated discharges ( $\Gamma^{AN} \approx -D^{OH} \cdot n'_r$ ). In the plasma boundary region, the *anomalous* term exceeds the neoclassical term by orders of magnitude. Up to now, no proven picture exists for these *anomalous* fluxes, however, it is believed that both the *anomalous* particle transport and the *anomalous* electron heat conduction are caused by convective transport. This hypothesis of convective transport based on  $\mathbf{E} \times \mathbf{B}$ -drift is in agreement with the experimental experience. Then, the *anomalous* transport of electrons and ions is ambipolar on their own:  $\Gamma_i^{AN} = \Gamma_e^{AN}$ . With this assumption, the radial electric fields have to be determined by the balance of the neoclassical fluxes (mainly of the plateau regime contributions) with the fast ion losses included in case of neutral beam heating. Then, neoclassical theory may be used to estimate the radial electric fields and the ion heat conduction. The basis of the neoclassical formalism is the expansion of the distribution functions starting from Maxwellians. For estimating the radial electric fields, experimental values of density and temperature have to be used to define the local Maxwellians. On this basis, the analysis of the ECF heated discharges supports the hypothesis of the ambipolarity of the *anomalous* fluxes.

In case of strong neutral beam heating, however, the highly anisotropic ion distributions violate the basic assumption of distribution functions being close to Maxwellians. For this case, the observed radial electric fields are much larger than those estimated with the assumption of only thermal ions (s. Figure 5b) supporting the conclusion that the radial electric fields are mainly generated by the fast ions. The thermal ion heat conduction is strongly reduced by the electric fields in both cases. Only with this reduction of the ion heat conductivity coefficients, the ion energy balance could be satisfied for both the high density ECF as well as the NBI heated discharges /13/. However, as the neutral gas density and thus the CX losses are largely unknown, the ion energy balance is not conclusive at outer radii.

Finally, the influence of the anomalous particle transport on the ion energy balance is discussed shortly. At outer radii, the dominant anomalous flux is related to the ionization of neutral gas:  $div \Gamma_i^{AN} \approx \langle \sigma v \rangle_e n_e n_0$  where  $\langle \sigma v \rangle_e$  is the ionization rate due to electron collisions. The contribution to the ion heat conduction  $Q_i$  is given by  $\frac{3}{2} T_i \Gamma_i^{AN}$  and less than the charge exchange ion energy loss by the factor  $\langle \sigma v \rangle_e / \langle \sigma v \rangle_{CX}$  where  $\langle \sigma v \rangle_{CX}$  is the charge exchange rate coefficient; this factor is typically of the order of 0.3 at outer radii. Consequently, anomalous transport is of minor importance for the ion energy balance which may be significantly influenced by CX losses at outer radii.

#### IV. Electron heat conduction

Local analysis of electron thermal conduction was made for OH- discharges, NBI-heated discharges and ECRH-discharges. The transport coefficient was obtained from the measured profiles with the power deposition profile taken from the current density profile (OH) or from numerical calculations (NBI).

In the analysis of ohmically heated discharges one has to avoid strong effects of current driven MHD instabilities which significantly deteriorate the confinement. In the region outside the  $q = 1$  surface, when strong tearing modes are absent, the local thermal conductivity,  $\chi_e$ , has been evaluated from local measurements of density, temperature and radiative power. Within the main field range  $B_0 = 2.5 - 3.5 T$ , an experimental thermal conductivity  $\chi_e^{OH} \approx 3.8 \cdot 10^{18} \cdot n_e^{-1} \cdot T_e^{-2/3} [cm^2/s]$  was found depending on the density  $n_e [cm^{-3}]$  and  $T_e [eV]$ , see /9/.

The analysis of electron heat losses during currentless operation with NBI was more difficult since the separation of electron heat conduction is hampered by the uncertainties of the heating power deposition, the strong coupling of electrons and ions at densities  $n_e \sim 10^{14} cm^{-3}$ , the radiative losses, and the nonstationary conditions due to the strong particle input flux. However, there are strong indications that neoclassical thermal conductivity alone is not sufficient to model the discharge.

ECF sustained discharges seem to be more suited for analysing the electron energy transport. The wave energy is transferred directly to the electrons. Other loss channels such as electron ion coupling and radiation play a minor role. Consequently, the dependence of the heat conduction on various parameters ( $B$ ,  $n_e$ ,  $t$ ,  $T_e$ ) could be studied. Launching the rf power with different modes of irradiation (TE02, HE11 at  $\alpha$ -mode or  $x$ -mode) and for off-axis resonance conditions, strong variation of the power deposition profiles and the electron temperature profiles have been obtained /14/. Furthermore, a power modulation technique has been applied. Analysing the generated heat waves across the plasma, the local conductivity coefficients could be derived from the time dependent temperature profiles /15/.

A coupled system of equations for the energy balance of electrons and ions was solved to fit the experimental density and temperature profiles /16/. The steady state TEMPL code models the electron thermal conductivity by a sum of the axisymmetric neoclassical part, the magnetic ripple dependent neoclassical part and the anomalous part. Especially in the boundary, enhanced electron energy transport seems to be necessary to fit the flat temperature profiles. The anomalous transport coefficient was assumed to follow the same scaling as in ohmically heated discharges.

So far, at  $\epsilon$ -values with optimum confinement good agreement of experimental data with the neoclassical model is concluded for the central part of the plasma. Especially at higher temperature (low collisionality) and large magnetic ripple at higher  $\epsilon$ , ripple effects become dominant. In the boundary region where the density and temperature are small, enhanced losses have to be assumed. Atomic processes, perturbations of the magnetic surfaces or drift instabilities may be responsible for the enhanced loss. However, the dependence of the anomalous heat conduction  $\chi_e^{(H)} \sim C \cdot n_e^{-1} \cdot T_e^{-2/3}$  restricts its influence more and more to the boundary the higher the energy density of the plasma grows. The anomalous transport used to fit the currentless ECF heated discharges is following the empirical scaling for OH discharges assuming the coefficient  $C$  to be proportional to  $B$ . If in both cases the same loss process occurs, this suggests that current driven instabilities are not responsible for the anomaly.

## V. Destruction of magnetic surfaces

At particular values of the rotational transform,  $\epsilon = \frac{1}{2}, \frac{1}{3}, \frac{2}{5}, \dots$ , confinement is deteriorated, which indicates that around these low-order rational values of  $\epsilon$  magnetic surfaces may be destroyed by symmetry breaking perturbation fields. This effect occurs in currentless operation obtained by various heating methods (NBI, ECRH) and seems to appear independently on the plasma pressure. The experimental results suggest that the perturbation breaks the five fold symmetry of the configuration and therefore can be explained by field errors coming from the coil system. Numerical calculations have indeed shown that current leads to the helix create a local perturbation field of 10 – 20 G, which gives rise to island formation on rational surfaces. The largest islands occur at  $\epsilon = \frac{1}{2}$ , three smaller islands at  $\epsilon = \frac{1}{3}$  and five islands at  $\epsilon = \frac{2}{5}$ . Islands are also found at  $\epsilon = \frac{3}{7}$  and  $\epsilon = \frac{3}{8}$ . Other perturbations which are caused by misalignment of the coils and magnetic material may also exist and lead to larger islands as calculated above.

The plasma confinement shows pronounced minima around  $\epsilon = \frac{1}{2}, \frac{1}{3}, \frac{2}{5}$  and  $\frac{2}{3}$ ; in close proximity of  $\epsilon = \frac{1}{2}$  and  $\epsilon = \frac{1}{3}$ , however, the confinement is maximum (Figure 1). This effect can be understood on the basis of island formation by a general external, time independent field  $\mathbf{B}_1$ . The Fourier spectrum of this field may contain several harmonics with decreasing amplitude. Then, every harmonic generates a chain of primary islands on a rational surface with  $\epsilon = \frac{m}{n}$  ( $n$  = toroidal mode number,  $m$  = poloidal mode number). In the neighbourhood  $\epsilon = \frac{1}{2}$  or  $\frac{1}{3}$  or any other low  $(m, n)$  rational surface only large  $(m, n)$  rational surfaces exist, which is a general result of number theory. Therefore only high harmonics of  $\mathbf{B}_1$ , or nonlinear interaction of low harmonics can create islands in the vicinity of  $\epsilon = \frac{1}{2}$  or  $\frac{1}{3}$ . The size of these islands, in general, will be small.

In order to study the behaviour of small shear stellarators under the influence of an external perturbation  $\mathbf{B}_1$ , the mapping technique developed by J. Greene /17/ was applied /18/. In general the perturbation  $\mathbf{B}_1$  leads to a perturbed twist map  $T$  of the

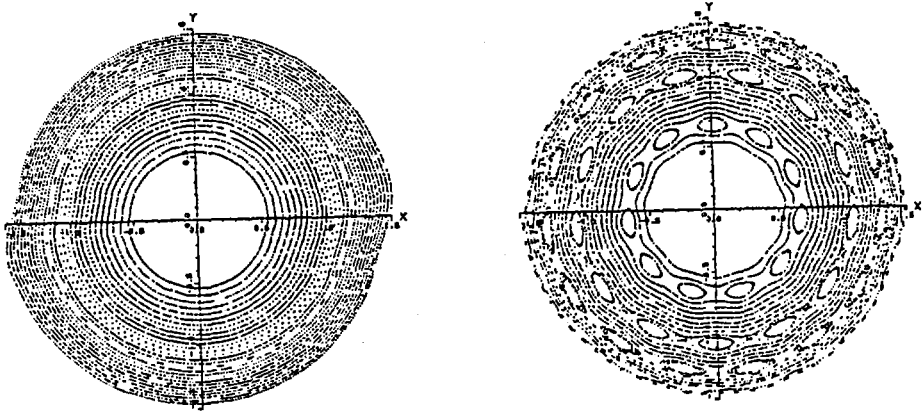


FIG. 6. Poincaré plots of magnetic surfaces for the same perturbation function with nearly undisturbed magnetic surfaces ( $0.47 < \epsilon < 0.49$ , left) and island formation ( $0.45 < \epsilon < 0.47$ , right).

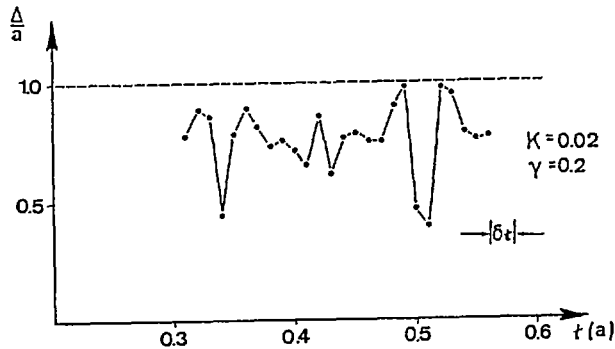


FIG. 7. Effective plasma radius,  $\Delta$ , as a function of external rotational transform,  $t(a)$ .  $K$  and  $\gamma$  are parameters describing perturbation.

poloidal plane onto itself. Written in the magnetic coordinates  $\psi, \theta$  of the unperturbed field  $\mathbf{B}_0$  the twist map can be derived from a generating function

$$S(\psi_1, \theta_0) = \psi_1 \theta_0 + 2\pi \int^{\psi_1} \epsilon(\psi) d\psi + h(\psi_1, \theta_0)$$

and yields  $T : (\psi_0, \theta_0) \rightarrow (\psi_1, \theta_1)$ . Iteration of  $T$  generates the desired Poincaré plot. The effect of the perturbation field  $\mathbf{B}_1$  is described by the function  $h(\psi_1, \theta_0)$  and various analytical perturbation functions  $h(\psi_1, \theta_0)$  have been investigated. Variation of the rotational transform  $\epsilon_0 + \epsilon, \psi$  with a fixed perturbation  $h(\psi_1, \theta_0)$  always shows the same pattern: The vicinity of  $\epsilon = \frac{1}{2}$  or  $\frac{1}{3}$  ((O) in Fig. 1) is the most stable against island formation and destruction. The feature is independent of the particular choice of  $h(\psi_1, \theta_0)$ . With increasing amplitude of  $h$  the neighbourhood of  $\epsilon = \frac{1}{2}$  or  $\frac{1}{3}$  is the last one to be destroyed. Figure 6 compares the region at  $\epsilon = 0.47 - 0.49$  with  $\epsilon = 0.45 - 0.47$  under the same perturbation.

The size of the islands has been computed /18/ from the residues and the sum of all island widths was subtracted from the plasma radius  $a$ , thus defining an effective plasma radius,  $\Delta$ . This effective plasma radius is plotted vs  $\epsilon(a)$  in Figure 7. One sees that the effective plasma radius vs  $\epsilon(a)$  exhibits a similar pattern as the measured plasma energy.

These considerations are of pure geometric nature, the plasma may react in different ways on the presence of islands. Plasma currents and electric fields will be modified by islands leading to enhanced convective losses. But also neoclassical particle losses will be enhanced as has been shown by Boozer and White /19/ for tokamaks. It has to be expected that due to islands and field ergodization also the energy transport of electrons will be strongly enhanced, therefore, the confinement in W VII-A based on neoclassical effects will exhibit a similar dependence on  $\epsilon_0$  as the effective plasma radius,  $\Delta$ . A Monte Carlo code addressing this effect is in preparation.

## VI. The effect of shear

Experimentally the influence of shear on confinement was extensively studied starting from a nearly shearless magnetic configuration /20/ with  $\delta\epsilon/\epsilon \approx 10^{-2}$  and varying the shear up to  $\delta\epsilon/\epsilon = \pm 0.2$ . Shear was introduced externally by operating the 2 sets of the helical windings with unbalanced currents (Torsatron mode /21/) and internally by a small induced toroidal current and the inhomogeneous distribution of the residual plasma current including effects of the plasma pressure. Mainly around  $\epsilon = \frac{1}{2}$  the effect of shear was investigated.

In the ECR-heated plasmas ( $B = 2.5$  T,  $n \approx 10^{13}$  cm $^{-3}$ ) the negative shear resulting from 4 kA induced toroidal current improves the confinement at  $\epsilon = \frac{1}{2}$  but leads to no further improvement in the region of optimum confinement (O). At higher plasma density ( $n = 2 - 4 \times 10^{13}$  cm $^{-3}$ ), however, 2 kA plasma current provides optimum conditions, whereas 4 kA reduce the confinement everywhere to the level of  $\epsilon = \frac{1}{2}$ . At this density the bootstrap current may already modify the  $\epsilon$ -profile, therefore the exact shear is not known. Numerical studies indicate that strong shear reduces the island widths but due to islands overlapping ergodization of the region in between islands occurs. Consequently moderate shear may reduce the influence of a single island at the fundamental resonance but a strong shear deteriorates confinement by island overlapping.

A small positive external shear seems to be more favourable for high  $\beta$  plasmas ( $\beta(0) \leq 1\%$ ). The residual plasma current which roughly grows proportional with plasma pressure and which probably is related to the bootstrap current leads to further positive shear. Starting from negative external shear the current density profile of the residual current which in case of the bootstrap current is peaked in the maximum gradient region may compensate the shear locally to zero, which could lead to large islands. After a rapid loss of plasma the build-up of the plasma pressure and the pressure driven current would start again and thus lead to relaxation oscillations. Consistent with this idea, strongly unstable conditions were observed for the negative external shear case during increase of the plasma energy. These experiments support the picture of island formation and ergodization of the magnetic surfaces as the reason for deteriorating the confinement.

## VII. Summary and conclusions

As demonstrated, plasma confinement in W VII-A depends very sensitively on the structure of the magnetic field which is determined by the particular value of the rotational transform and the magnitude of the shear. The effect appears with all heating

methods if the shear is small enough. The strong dependence of the confinement on the values of  $t_0$  and shear can be understood on the basis of magnetic surface destruction by external symmetry breaking field errors among which some helix joints could be identified. Close to the fundamental resonance  $\iota = \frac{1}{2}$  and  $\iota = \frac{1}{3}$  only high Fourier harmonics of the perturbation field may create small islands. This explains why this region is the most stable against any kind of external perturbations. Since external perturbations are maximum at the plasma boundary, this also explains the experimental finding that confinement is deteriorated in particular if the resonant  $\iota = \frac{1}{2}$  - surface is close to the plasma boundary. Small variations of the  $\iota$ -profile during the discharge, either caused by pressure effects or by small induced currents, may shift the plasma from optimum confinement (O) to minimum confinement (M). Therefore in the experiment a careful control of the edge values of the rotational transform and the shear is necessary to achieve optimum plasma parameters. The conclusion for future stellarator experiments with low shear is that modifications of the  $\iota$ -profile with increasing plasma pressure be as small as possible and external symmetry breaking field errors be avoided or minimized.

For optimum conditions of ECR-heated currentless plasmas the electron thermal conductivity in the central part of the plasma column can be described by neoclassical theory including effects of helical ripple. In the edge region an anomalous transport coefficient, assumed to be the same as in ohmically heated discharges, is necessary to fit the experimental data. Because of the uncertainties of the exact power deposition profile, this hypothesis has to be considered with caution, so far, however, no contradiction did arise. A conclusion from these results is that the anomalous thermal conductivity, which exists in all tokamaks, is not caused by the ohmic heating current. Due to the  $T_e^{-2/3}$ -scaling of the anomalous conductivity its influence in future high temperature experiments is expected to be small. The effect of the anomaly will be shifted more and more towards the plasma boundary. A temperature independent thermal conductivity  $\chi_c \sim 1/n$  did not provide a good fit to the experimental data.

In ECR-heated plasmas neoclassical ambipolarity condition explains the measured  $E$ -field. Anomalous particle transport - if ambipolar - does not change this result. In NBI-heated plasmas high energetic particle losses drive the observed radial electric field which improves the confinement of the thermal ions in the plateau regime. This beneficial effect is predicted by neoclassical theory and it is particularly effective in large aspect ratio devices as W VII-A ( $A = 20$ ).

Particle transport in the plasma center is comparable with neoclassical predictions, if one takes into account the uncertainties of the particles sources. In the boundary region, however, strongly enhanced particle losses (possibly by convective mechanisms) have to be concluded.

## REFERENCES

- [1] W VII-A TEAM, NI GROUP, in Plasma Physics and Controlled Nuclear Fusion Research 1980 (Proc. 8th Int. Conf. Brussels, 1980), Vol. 1, IAEA, Vienna (1981) 185.
- [2] W VII-A TEAM, NI GROUP, in Plasma Physics and Controlled Nuclear Fusion Research 1984 (Proc. 10th Int. Conf. London, 1984), Vol. 2, IAEA, Vienna (1985) 371.
- [3] WELLER, A., MAASSBERG, H., Neutron Flux Measurements at the Wendelstein VII-A Stellarator, Rep. IPP-2/278, Max-Planck-Institut für Plasmaphysik, Garching (1985).
- [4] MAASSBERG, H., Rep. IPP-2/281, Max-Planck-Institut für Plasmaphysik, Garching (1986).

- [5] MAASSBERG, H., HELLBERG, M.A., Rep. IPP-2/282, Max-Planck-Institut für Plasma-physik, Garching (1985).
- [6] ISLER, R.C., et al., Nucl. Fusion **26** (1986) 391.
- [7] STACEY, W.M., Jr., SIGMAR, D.J., Phys. Fluids **27** (1984) 2076.
- [8] PENNINGSFELD, F.P., OTT, W., SPETH, E., in Controlled Fusion and Plasma Physics (Proc. 12th Europ. Conf. Budapest, 1985), Vol. 9 F, Pt. 1, European Physical Society (1985) 397.
- [9] GRIEGER, G., et al., Plasma Phys. Controll. Fusion **28** (1986) 43.
- [10] W VII-A TEAM, in Controlled Fusion and Plasma Physics (Proc. 9th Europ. Conf. Oxford, 1979) paper A2.4.
- [11] RINGLER, H., et al., IAEA-CN-47/D-V-1, these Proceedings, Vol. 2.
- [12] MAASSBERG, H., et al., Controlled Fusion and Plasma Physics (Proc. 12 Europ. Conf. Budapest, 1985), Vol. 9F, Pt. 1, European Physical Society (1985) 389.
- [13] W VII-A TEAM, NI TEAM, in Fifth International Workshop on Stellarators (Proc. IAEA Tech. Comm. Mtg on Plasma Confinement and Heating in Stellarators, Schloss Ringberg, 1984), Vol. 1, EUR-9618-EN, CEC, Brussels (1984) 219.
- [14] ERCKMANN, V., et al., Plasma Phys. Controll. Fusion **28** (1986) 1277.
- [15] HARTFUSS, J., et al. Nucl. Fusion **26** (1986) 678.
- [16] WOBIG, H., W VII-A TEAM in Controlled Fusion and Plasma Heating (Proc. 13th Europ. Conf. Schliersee, 1986), Vol. 1, European Physical Society (1986) 291.
- [17] GREENE, J., J. Math. Phys. **20** (1973) 1183.
- [18] WOBIG, H., Magnetic Surfaces and Localized Perturbations in the Wendelstein VII-A Stellarator, Rep. IPP-2/283, Max-Planck-Institut für Plasmaphysik, Garching (1986).
- [19] BOOZER, A.H., WHITE, R.B., Phys. Rev. Lett. **49** (1982) 786.
- [20] RENNER, H., W VII-A TEAM, in Controlled Fusion and Plasma Heating (Proc. 13th Europ. Conf. Schliersee, 1986), Vol. 1, European Physical Society (1986) 287.
- [21] HARMEYER, E., et al., Wendelstein VII-A in Torsatron Mode, Rep. IPP-2/275, Max-Planck-Institut für Plasmaphysik, Garching (1985).

## DISCUSSION

K. ITOH: If the improvement in the confinement time in NBI plasma achieved by eliminating OH current is attributed to the stabilization of the tearing mode, why is this improvement not observed in the ECH plasma? Since the reduction in the drift parameter,  $\chi \propto I/n$ , is prominent in the low density case, one might expect the decrease in the anomaly to be greater in the ECH plasma.

H. RENNER: The improvement in confinement in NBI heated plasmas was observed at high density. ERC heated plasmas operate at lower density whereas in OH plasmas no strong effect by tearing modes was observed. Improvement in confinement of ECR heated as compared with low density OH plasmas is only marginal. It is not as large as expected from the drift parameter scaling.

K. ITOH: I have another question. Did you observe that the electron temperature profile was peaked, indicating the islands on the periphery in the discharges, the rotational transform of which correspond to the minima of  $\tau_E$ ?

H. RENNER: Yes, the observed electron temperature profile is more peaked under these conditions. The effect, however, depends on the amount of shear.

S.M. HAMBERGER: Do you have any views on the origin or nature of the instability responsible for the anomalous heat transport during ECRH operation of the W VII-A stellarator?

H. RENNER: Fluctuations in density have been observed between 50 kHz and 1 MHz. These could be drift wave oscillations, but a detailed comparison of theory and experiment has not been made, since the diagnostic equipment does not enable us to investigate an extended k-range.

## PHYSICS STUDIES FOR ADVANCED STELLARATORS

W. DOMMASCHK, F. HERRNEGGER, W. LOTZ, P. MERKEL,  
J. NÜHRENBURG, A. SCHLÜTER, U. SCHWENN, R. ZILLE  
IPP-Euratom Association,  
Max-Planck Institut für Plasmaphysik,  
Garching, Federal Republic of Germany

### Abstract

#### PHYSICS STUDIES FOR ADVANCED STELLARATORS.

In the Helias class of stellarators, a value of  $\langle \beta \rangle = 0.09$  can be achieved which is stable with respect to resistive interchange modes. Accordingly, the parallel current density is strongly reduced,  $\langle j_{\parallel}^2/j_{\perp}^2 \rangle < 1/2$ , the shear of the configuration is virtually unaffected by  $\beta$ , and the change in rotational transform is moderate. The self-consistent reduction of  $\beta$  due to resonances at rational values of the rotational transform is taken into account: the pressure driven current density varies smoothly through zero at rational  $\iota$ . — Helias vacuum fields are studied in two ways: i) the NESTOR code obtains the vacuum field which has the Helias boundary as the outermost flux surface; this procedure allows island sizes and basic features of modular coils to be studied; ii) representation of Helias configurations with Dommaschk potentials leads to more realistic coil studies. — Neoclassical energy confinement times of Helias configurations are obtained by Monte Carlo simulation of a monoenergetic guiding centre test distribution subject to pitch angle scattering. Preliminary results indicate that, with an electric potential of the order of the particle energy, ion confinement in the long mean free path region improves to about  $10^2$  collision times.

## 1. INTRODUCTION

Advanced stellarators, exploiting favourable properties of stellarator configurational space, are candidates for viable stellarator fusion reactors. Two important confinement questions in stellarators are the  $\beta$ -value which can be achieved in a stable way and the neoclassical energy transport. Results pertaining to these issues are obtained for Helias [1] configurations.

Three aspects of the equilibrium properties of stellarators are well described by today's 3D flux-variable based codes [2, 3, 4] supplemented by evaluation of the parallel current density [5]. The Shafranov shift yields the simple equilibrium- $\beta$  estimate  $\iota^2/A$  ( $\iota$  rotational transform,  $A$  aspect ratio). In advanced stellarators this limit is overcome by reduction of

the parallel current density; W VII-AS [6] and Helias rely on this principle. The rotational transform profile depends on  $\beta$  for genuine stellarator equilibria with identically vanishing net toroidal current; for advanced stellarators this dependence is smaller than for stellarators of the  $\ell = 2$  type [1, 7]. Near a resonant surface, i.e. a rational value of rotational transform, a finite pressure gradient drives a diverging parallel current density which is of particular importance in devices with sizeable rotational transform per period,  $\iota_p$ , as e.g. Helias [8], and can be eliminated by pressure profile flattening near the resonance [9]. A fourth aspect is the size of the islands occurring at rational  $\iota$  in finite  $\beta$  equilibria and constitutes the main risk in the assessment of equilibrium properties because its computational treatment has still to be developed [10].

The MHD stability behaviour of stellarators without net toroidal current through each magnetic surface is completely different from that found in tokamaks. The modes are purely pressure-driven and probably only the resonant ones are dangerous. Fixed- and free-boundary modes are of the same nature and the growth rates of unstable modes increase with increasing mode number [11, 12]. This behaviour leads to the conjecture that local ideal modes are formally the most unstable ones. Evaluation of Mercier modes and ballooning modes has shown that Mercier modes are observed first as  $\beta$  is increased [13]. An even more stringent condition on  $\beta$  is obtained from the resistive interchange criterion [14] which endangers not only the second stability regime of tokamaks [15] but also those stellarators which rely on shear and strong Shafranov shift as e.g. ATF [16]. This criterion has been used while finding the Helias class of stellarators and provides a natural means for pressure profile flattening [9]. The resistive interchange criterion is, for the case of vanishing net toroidal current, identical with the applicability condition of a sufficient stability criterion [17] and with the stability condition of peeling modes [18], which adds significance to its use for selecting finite- $\beta$  stellarators. Moreover, it has been shown [19] that island growth (as a function of  $\beta$ ) is connected with resistive instability.

Neoclassical energy transport in stellarators with long mean free path has been successfully simulated by Monte Carlo methods [20–22]. A calculation of an energy confinement time with the help of a monoenergetic guiding centre test distribution subject to pitch angle scattering and energy relaxation in a prescribed electric potential is performed for Helias configurations.

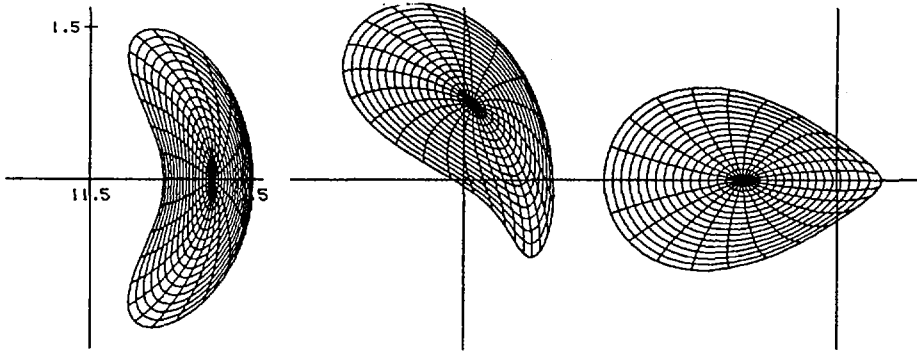


FIG. 1. Flux surface cross-sections at  $V = 0, \pi/2, \pi$  of a Helias equilibrium with  $N = 5, A = 11.5, R_{0,1} = 0.8, Z_{0,1} = 0.4, \Delta_{1,0} = 0.1, \Delta_0 = 0.07, \Delta_{2,0} = 0.05, \Delta_{1,-1} = 0.39, \Delta_{2,-1} = 0.24, \Delta_{2,-2} = 0.07$ .

## 2. $\beta$ -VALUES IN HELIAS

In continuation of Helias stability studies [1], a configuration with five periods and aspect ratio 11.5 has been identified in which a  $\beta$ -value of  $\langle \beta \rangle \approx 0.09$  is marginally stable against resistive interchange modes. Figure 1 shows the flux surface geometry of this configuration.

Figure 2a shows the rotational transform profile of the vacuum and the finite- $\beta$  case. Figure 2b shows the corresponding pressure profile,  $-dp/ds$ , which exhibits the flattening around the  $\iota_p = \frac{1}{8}$  resonance resulting in a  $\beta$  value which is about 10% smaller than it would be without taking this resonance into account.

Figure 3a shows the vacuum field solution obtained with the NESTOR code [23]. Comparison of island thickness and the width of the pressure profile flattening yields comparable numbers and clearly shows the need for refined 3D codes which can compute the island size as a function of  $\beta$ . Given this lack of knowledge one would prefer configurations in which both the size of the vacuum field islands and the width of the pressure profile flattening are small. This is the case for Helias configurations which stay below  $\iota_p = \frac{1}{7}$ , as is shown in Fig.3. An alternative to these moderate-shear cases would be to avoid resonances of this order by considering finite- $\beta$  equilibria with very small shear. Such Helias equilibria have also been found and will be discussed elsewhere.

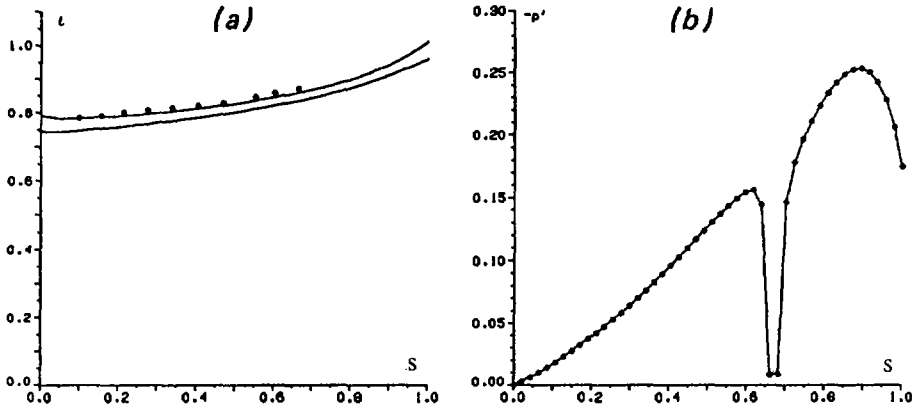


FIG. 2. (a) Three  $\iota$ -profiles: circles are obtained from result of Fig. 3(a), upper line is result obtained with MOMCON [4] for  $\beta = 0$  case, lower line is result for  $\langle \beta \rangle = 0.09$ ; (b) corresponding profile  $-p'(s)$ . Radial label  $s$  is square root of normalized toroidal flux.

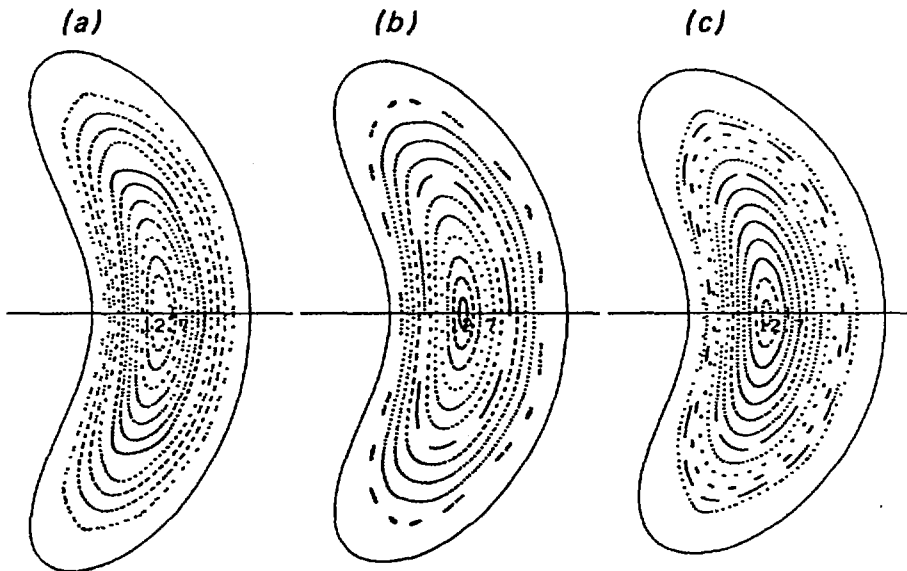


FIG. 3. Poincaré plots of Helias vacuum fields with surface parameters as given in Fig. 1, except for  $\Delta_{l,-l} = 0.39, 0.3336, 0.284$ .

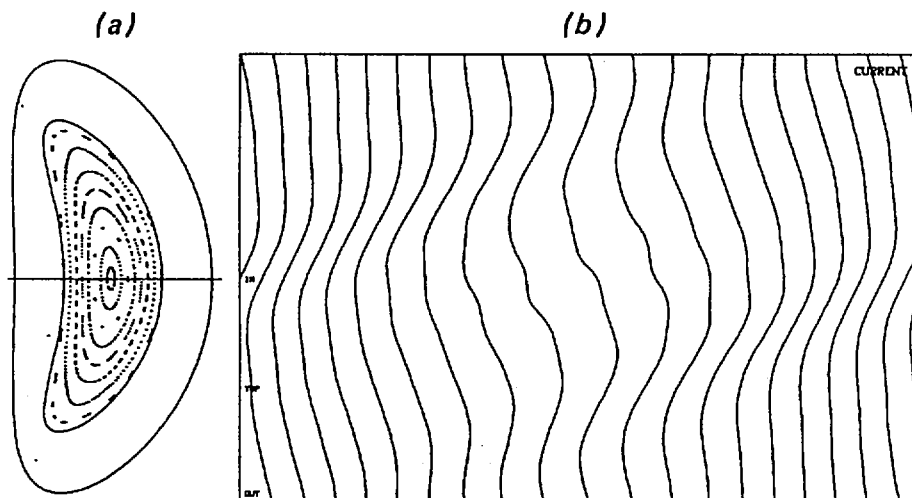


FIG. 4. (a) A Helias boundary (at  $V = 0$ ) with parameters of Fig. 1, except for  $A = 12$ ,  $\Delta_{2,-1} = 0.12$ ,  $\Delta_{2,-2} = 0.1$ , magnetic surfaces of approximate solution to boundary value problem with Dommaschk potentials, and outer surface on which modular coils are calculated; (b) line currents, ordinate being poloidal parameter, abscissa  $0 < V < 2\pi$ .

### 3. MODULAR COIL STUDIES FOR HELIAS

A Helias version with less indentation than that of Fig.1, but still allowing  $\langle \beta \rangle \approx 0.05$ , was used to solve a boundary value problem with Dommaschk potentials [24]. The result allows the computation of modular coils for this configuration on a surrounding surface, see Fig.4a. Fig.4b shows line currents which do not look more complicated than the corresponding result for WVII-AS [6].

### 4. MONTE CARLO SIMULATION OF ENERGY CONFINEMENT IN HELIAS

Monte Carlo methods developed previously [20, 21] for calculating neoclassical heat conductivity in stellarators have been generalized to the calculation of energy confinement times [22]. This generalization allows one to treat not only the cases of large ratio  $Q_\rho$  of plasma radius  $a$  to gyroradius  $\rho$  in which a local transport coefficient can be calculated ( $Q_\rho \gtrsim 500$ ), but also cases in which the gyroradius is too large for a strictly local transport coefficient to exist ( $Q_\rho < 500$ ). An electric field  $F$  is included in the

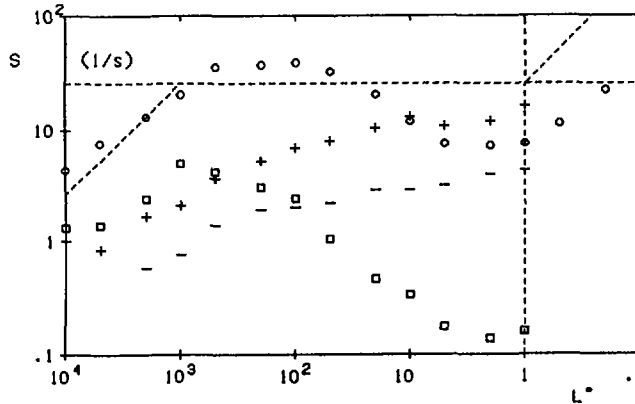


FIG. 5. Loss rates of ions and electrons as functions of normalized mean free path in Helias, parameters as in Fig. 1, except for  $\Delta_{1,-1} = 0.29$ ,  $\beta = 0$ .  $\circ$  Ion loss without electric field; +, - ion losses with  $e\phi/E = \pm 1$ ;  $\square$  electron loss.

form of an electric potential  $\phi$  which is constant on magnetic surfaces,  $F = \phi_0 2\tau/a^2$ , and a monoenergetic test particle distribution with energy  $E$  is used. With the help of  $L_c = \pi R_0/\iota$  ( $R_0$  major torus radius), so that  $L_c$  is half the connection length, and of the plateau transport value  $S_P = 3.6\nu/Q_\rho^2 \nu \pi R_0$  [ $\nu = (2E/m)^{1/2}$ ] the results can be described in a dimensionless  $S^*(L^*)$  diagram, where  $S^* = S/S_P$ ,  $L^* = \Lambda/L_c$  and  $S(\Lambda)$  is the actual loss rate as a function of mean free path  $\Lambda$ . For electrons  $S$  is obtained from the relation  $S = D/(a/2.4)^2$  and  $D$  is the computed local transport coefficient. Results which were obtained for Helias [25] show that for  $Q_\rho = 100$  and  $|e\phi_0/E| = 1$  the ion loss rate is only a weak function of mean free path in the range  $1 < L^* < 10^3$ , while the electrons are in the  $\nu^{-1}$ -regime, see Fig.5 where the ordinate corresponds to  $B_0 = 3$  T,  $R_0 = 5$  m, and 4 keV deuterons and electrons. These results can be interpreted as energy losses corresponding to  $\tau_E \gtrsim 200$  msec. The mean free paths of the two species are approximately equal.

## 5. CONCLUSION

The MHD, modular coil, and transport properties of the Helias configurations discussed above are promising so that further research is justified. With respect to the MHD problems, the finite- $\beta$  structure of isolated regions and the analysis of global MHD modes appear to be the most

important issues; the coil calculations have to be subjected to engineering constraints; the transport calculations need to be refined, in particular with respect to the quasineutrality problem. Thus, for an experimental program, substantial improvement of the computational tools is needed.

### ACKNOWLEDGEMENT

We are indebted to our colleagues at the Oak Ridge National Laboratory, in particular to S.P. Hirshman, R.H. Fowler, J.A. Rome, and J.F. Lyon for providing us with the MOMCON code and the initial version of their Monte Carlo transport code.

### REFERENCES

- [1] NÜHRENBERG, J., ZILLE, R., *Phys. Letters* **114A** (1986) 129.
- [2] BAUER, F., BETANCOURT, O., GARABEDIAN, P., *A Computational Method in Plasma Physics* (Springer, Berlin, 1978); *Magnetohydrodynamic Equilibrium and Stability of Stellarators* (Springer, Berlin 1984).
- [3] SCHWENN, U., 5th Int. Workshop on Stellarators, Schloß Ringberg 1984, Comm. EC., EUR 9618 EN, I, 377.
- [4] HIRSHMAN, S.P., LEE, D.K., *Comput. Phys. Comm.* **39** (1986) 161.
- [5] GROSSMANN, R., NÜHRENBERG, J., *Proc. ICPP 1984*, I, 117.
- [6] BROSSMANN, U. et al., *Plasma Physics and Contr. Nucl. Fusion Research 1982, Ninth Conf. Proc., Nucl. Fusion, Supplement 1983*, III, 141.
- [7] HENDER, T.C. et al., *Nucl. Fusion* **25** (1985) 1463.
- [8] BOOZER, A.H. et al., *Plasma Physics and Contr. Nucl. Fusion Research 1982, Ninth Conf. Proc., Nucl. Fusion, Supplement 1983*, III, 129.
- [9] HIRSHMAN, S.P., NÜHRENBERG, J., ZILLE, R., 8th Europhysics Conf. on Comp. Physics 1986, ECA Vol. **10D** (1986) 157.
- [10] REIMAN, A., GREENSIDE, H., *Proc. 8th Europhysics Conf. on Comp. Physics 1986, Comput. Phys. Comm.* 1986.
- [11] MERKEL, P., NÜHRENBERG, J., GRUBER, R., TROYON, F., *Nucl. Fusion* **23** (1983) 1061.
- [12] HERRNEGGER, F., 8th Europhysics Conf. on Comp. Physics 1986, ECA Vol. **10D** (1986) 153.

- [13] NÜHRENBERG, J., ZILLE, R., Proc. 12th Eur. Conf. on Contr. Fusion and Plasma Physics (Budapest, 1985), EPS, Budapest 1985, Vol. 9F, I, 445.
- [14] GLASSER, A.H., GREENE, J.M., JOHNSON, J.L., Phys. Fluids 18 (1975) 875.
- [15] CORREA-RESTREPO, D., Pl. Phys. and Contr. Fusion 27 (1985) 565.
- [16] NÜHRENBERG, J., ZILLE, R., Proc. 5th Int. Workshop on Stellarators (Schloß Ringberg, 1984), Comm. EC, EUR 9618 EN, I, 339.
- [17] LORTZ, W., REBHAN, E., SPIES, G., Nucl. Fusion 11 (1971) 583.
- [18] LORTZ, D., Nucl. Fusion 15 (1975) 49.
- [19] CARY, J.R., KOTSCHENREUTHER, M., Phys. Fluids 28 (1985) 1392.
- [20] BOOZER, A.H., KUO-PETRAVIC, G., Phys. Fluids 24 (1981) 851.
- [21] FOWLER, R.H., ROME, J.A., LYON, J.F., Phys. Fluids 28 (1985) 338.
- [22] DOMMASCHK, W., LOTZ, W., NÜHRENBERG, J., Nucl. Fusion 24 (1984) 794; LOTZ, W., NÜHRENBERG, J., SCHLÜTER, A., J. Comput. Physics (1986).
- [23] MERKEL, P., J. Comput. Physics 65 (1986).
- [24] DOMMASCHK, W., Comput. Phys. Comm. 40 (1986) 203.
- [25] LOTZ, W., 8th Europhysics Conf. on Comp. Physics 1986, ECA Vol. 10D (1986) 105; IPP Annual Report 1985, p.142.

## DISCUSSION

B. COPPI: Why did you devote special attention to resistive interchange modes, given the fact that they tend to become stable at high temperature as a result of the effects of ion-ion collisions?

J. NÜHRENBERG: Previous work has shown that the stability limit for ballooning modes proper is higher than the Mercier limit, which is close to the resistive interchange limits for HELIAS. Thus, the resistive interchange criterion may be used as a simple means to achieve complete stability with respect to fixed boundary MHD modes. In addition,  $\beta$ -iteration towards marginal stability with respect to this criterion is very convenient for elimination of the pressure driven singular currents near rational values of rotational transform. Finally, this criterion is well suited for minimizing the parallel current density, which is the origin of a deterioration in the quality of the flux surfaces with increasing  $\beta$ .

## TRANSPORT THEORY IN STELLARATORS\*

K.C. SHAIN, S.P. HIRSHMAN,  
C.O. BEASLEY, Jr., E.C. CRUME, Jr.  
Oak Ridge National Laboratory

W.I. VAN RIJ  
Computing and Telecommunications Division,  
Martin Marietta Energy Systems, Inc.

Oak Ridge, Tennessee,  
United States of America

### Abstract

#### TRANSPORT THEORY IN STELLARATORS.

A comprehensive numerical treatment has been developed for analysing neoclassical transport in general three-dimensional plasmas. It is used to study the assumptions underlying previous analytic approximations and to develop accurate formulae for transport coefficients in stellarators. In the plateau regime, a resonant enhancement factor for diffusion that agrees with analytic results is found. In the lower collisionality regimes, the structure of the particle distribution function in phase space is computed to examine the validity of boundary conditions employed in analytic calculations. A diffusion coefficient  $D$  in the collisionless detrapping regime is computed and found to have the form  $D \approx \nu \epsilon_i^{3/2} G(\epsilon_h, \epsilon_i) T^2 / (M^2 \Omega^2 r^2 \Omega_E^2)$ . Here,  $G(\epsilon_h, \epsilon_i)$  is a weak function of  $\epsilon_h$  and  $\epsilon_i$ , in contrast with previous analytic results. A resonance between parallel and  $\mathbf{E} \times \mathbf{B}$  motions, which is neglected in bounce-averaged theories, is found to increase (decrease) diffusion in the  $\nu$  ( $1/\nu$  or plateau) regime. The improved transport properties of configurations with helical wells localized at the inside of the torus, which have been previously noted for the  $1/\nu$  regime, are found to persist into the lower collisionality regimes. This tendency is confirmed by comparison with Monte Carlo results.

### 1. INTRODUCTION

The parameters such as rotational transform  $\iota$ , number of field periods  $m$ , inverse aspect ratio  $\epsilon_t$ , and helical modulation  $\epsilon_h$  for different types of stellarators (e.g., torsatron, heliac, heliotron) can vary widely. The stellarator transport coefficients obtained by analytically solving the bounce-averaged drift kinetic equation [1] may be invalid for realistic values of these parameters. To relax the approximations associated with bounce-averaging (e.g.,  $J$ -conservation), a numerical code is used to solve

---

\* Research sponsored by the Office of Fusion Energy, United States Department of Energy, under Contract No. DE-AC05-84OR21400 with Martin Marietta Energy Systems, Inc., and under Contract No. DE-FG05-80ET-53088 with the University of Texas.

the linearized drift kinetic equation for the particle distribution function [2]. Transport fluxes are then calculated by taking appropriate moments of the particle distribution. We use the code to study the assumptions underlying previous analytic approximations and to develop accurate formulas for transport coefficients in stellarators.

## 2. DRIFT KINETIC EQUATION SOLVER (DKES)

The DKES code solves the linearized drift kinetic equation [2]

$$\mathbf{v} \cdot \nabla f_1 + \dot{\alpha} \frac{\partial f_1}{\partial \alpha} - C(f_1) = S \quad (1)$$

where  $f_1$  is the deviation of the particle distribution from the Maxwellian  $f_M$ ,  $\mathbf{v} = v \cos \alpha \hat{n} + E_\rho \nabla \rho \times \hat{n} / \langle B^2 \rangle$ ,  $\hat{n} = \mathbf{B} / B$ ,  $v_{\parallel} / v = \cos \alpha$ ,  $\dot{\alpha} = -(v/2)(\sin \alpha) \mathbf{B} \cdot \nabla (1/B)$ ,  $S = f_M [-\mathbf{v}_d \cdot \nabla \rho (A_1 + K A_2) - B v \cos \alpha A_3]$ ,  $A_1 = n'/n - 3T'/2T - eE_\rho/T$ ,  $A_2 = T'/T$ ,  $A_3 = -e(\mathbf{E} \cdot \mathbf{B})/T \langle B^2 \rangle$ ,  $\mathbf{v}_d = -\hat{n} \times [e\mathbf{E} - (Mv_{\perp}^2/2)\nabla \ln B] / M\Omega + (v_{\parallel}^2/\Omega) [\nabla \times \hat{n} - (\hat{n} \cdot \nabla \times \hat{n})\hat{n}]$ ,  $E_\rho = -d\Phi/d\rho$  with  $\Phi$  the electrostatic potential,  $\rho$  is the radial flux coordinate, the angle brackets denote the flux surface average, and  $K = Mv^2/2T$ . To obtain Eq. (1), we have neglected  $\nabla B$  and curvature drift terms in  $\mathbf{v} \cdot \nabla f_1$ , so the transport phenomena associated with resonant superbanana orbits are ignored. However, we do include the poloidal  $\mathbf{E} \times \mathbf{B}$  drift to describe the effect of the collisionless detrapping due to helically trapped particle orbits. In this code a pitch angle scattering operator is used for  $C(f_1)$ . Equation (1) is solved in terms of Fourier-Legendre series for  $f_1$  at a fixed value of normalized energy  $K$ , and neoclassical fluxes are calculated by taking the appropriate moments of  $f_1$ . The DKES code can be employed to calculate neoclassical fluxes for any toroidal device once the Fourier decomposition of  $B$  is known. A numerical code has been developed to Fourier analyze  $B$  in Boozer coordinates for realistic finite- $\beta$  toroidal equilibria [3].

## 3. RESULTS AND DISCUSSION

Numerical calculations for stellarators are carried out by using a truncated magnetic field spectrum  $B = B_0 [1 - \epsilon_t \cos \theta - \epsilon_h \cos(\ell\theta - m\zeta)]$ , where  $B_0$  is the magnetic field strength on the axis,  $\epsilon_t$  ( $\epsilon_h$ ) is the dominant toroidal (helical) magnetic field harmonic, and  $\ell$  ( $m$ ) is the poloidal (toroidal) mode number. One should not use the values of diffusion coefficients shown in the paper to estimate the confinement time without determining electric field and flow velocity. In Fig. 1, we show the diffusion coefficient  $D$  versus  $\nu/\omega_t$ , where  $\nu$  is the collision frequency and  $\omega_t$  is the transit frequency for an ATF torsatron (Fig. 1a) with  $\epsilon_t = 0.12$ ,  $\epsilon_h = 0.14$ ,  $\ell = 2$ ,  $m = 12$ , and  $\iota = 0.68$  and for a stellarator (Fig. 1b) with  $\epsilon_t = 0.1$ ,  $\epsilon_h = 0.075$ ,  $\ell = 2$ ,  $m = 5$ , and  $\iota = 1.8$ . Also shown is  $D$  for the equivalent symmetric configuration (with  $\epsilon_h = 0$  for the same  $\epsilon_t$ ,  $\iota$ , and  $B_0$ ).

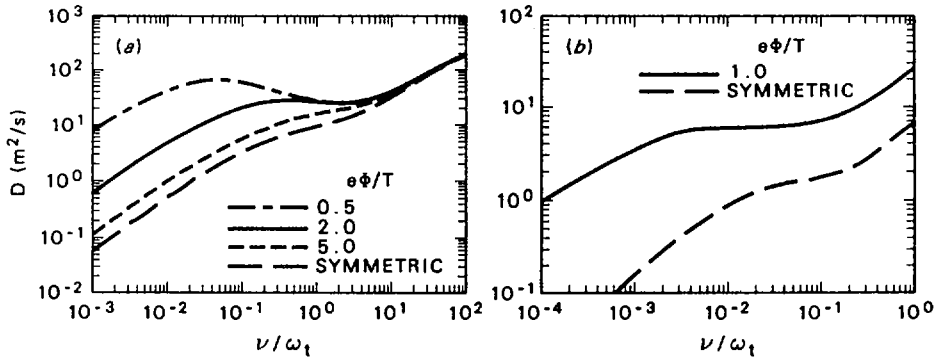


FIG. 1. Diffusion coefficient  $D$  versus  $\nu_h/\omega_t$  for two torsatron devices and their equivalent symmetric configurations. (a) ATF, an  $\ell = 2$ ,  $m = 12$ ,  $\nu = 0.68$  torsatron, with no significant resonant enhancement of  $D$  in the plateau and Pfirsch-Schlüter regimes. (b) A model  $\ell = 2$ ,  $m = 5$ ,  $\nu = 1.8$  stellarator, with resonant enhancement of  $D$  in the plateau and Pfirsch-Schlüter regimes.

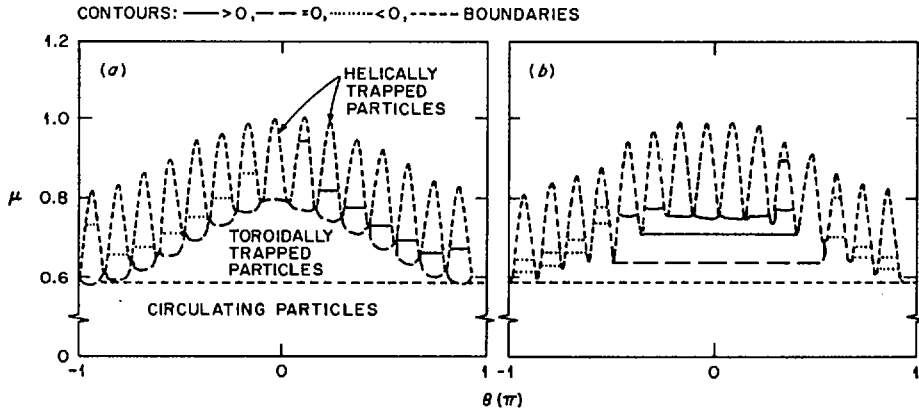


FIG. 2. Contours of  $f_1$  in  $(\mu, \theta)$  space for a fixed magnetic field line: typical characteristics for (a)  $1/\nu$  and (b)  $\nu$  regimes.

Figure 1a demonstrates the well-known fact that the electric field can reduce the diffusion coefficient in the low collisionality regime. The ratio of the diffusion coefficients for the stellarator and its equivalent symmetric configuration is  $D_s/D_e \simeq 5$  in the Pfirsch-Schlüter regime and  $D_s/D_e \simeq 4$  in the plateau regime for the device shown in Fig. 1b. However, there is no significant resonant enhancement in the plateau and Pfirsch-Schlüter regimes in ATF. The results shown in Fig. 1b agree with the analytic calculations of  $D_s/D_e = 1 + \ell^2 (\tau_{\ell m}/\tau_{10})^2 (\epsilon_h/\epsilon_t)^2 \simeq 4.7$  in the Pfirsch-Schlüter regime [4] and  $D_s/D_e = 1 + \ell^2 (\tau_{\ell m}/\tau_{10}) (\epsilon_h/\epsilon_t)^2 \simeq 3.8$  in the plateau regime [5], with  $\tau_{\ell m} (\equiv \omega_t^{-1} |\ell - m/\nu|^{-1})$  the resonant transit time.

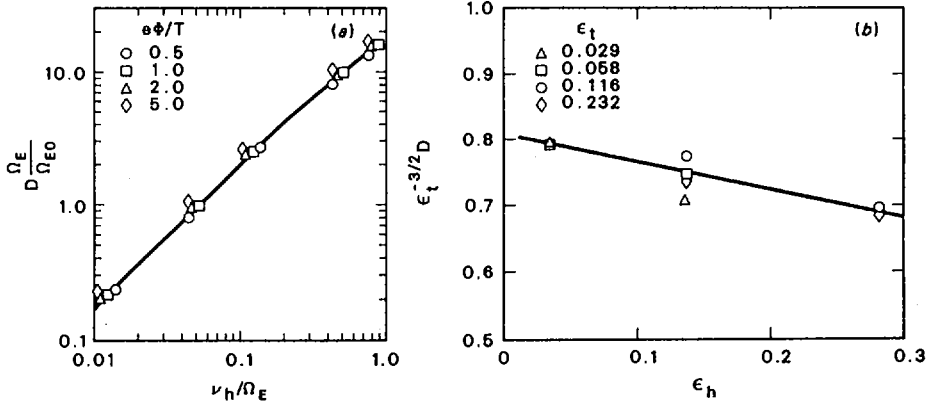


FIG. 3. (a) Electric field and collision frequency and (b) geometric scaling of the diffusion coefficient in the  $\nu$  regime.  $\Omega_{E0} \equiv \Omega_E(e\Phi/T = 1)$ .

The ratio  $D_s/D_e$  can be greater than unity if  $\tau_{\ell m}/\tau_{10} > 1$  and/or  $\epsilon_h > \epsilon_t$ . In the case of Fig. 1b,  $\tau_{\ell m}/\tau_{10} = 1.28$ , so that there is a resonant enhancement of transport due to a finite value of  $\iota/m$ . This shows that resonances should be avoided to minimize the stellarator transport. We note that the helical contribution to the diffusion coefficient cannot be obtained by solving the bounce-averaged drift kinetic equation.

In the low collisionality regime ( $\nu_h \equiv \nu/\epsilon_h \ll \omega_{th}$ , the transit frequency of helically trapped particles), analytic calculations assume that the particle distribution function  $f_1$  is constant along the magnetic field line to lowest order in  $\nu_h/\omega_{th}$ . Figure 2 shows the contours of  $f_1$  in  $(\mu, \theta)$  space for a fixed magnetic field line in an  $\ell = 2, m = 12$  torsatron, where  $\mu$  is the magnetic moment and  $\theta$  measures the distance along the field line. In both the  $1/\nu$  (Fig. 2a) and  $\nu$  (Fig. 2b) regimes, the numerically computed  $f_1$  is nearly constant along the field line for fixed  $\mu$  within individual helical wells. Note that  $f_1$  vanishes at the helical trapping boundary in the  $1/\nu$  regime, but not in the  $\nu$  regime, as is evidenced by nonzero contours in the toroidal well. This shows that the boundary conditions employed in some analytic calculations [1] in the  $\nu$  regime are inappropriate. Note also that in both regimes  $f_1$  varies slowly from one helical well to the next for helically trapped particles, since particles trapped in one helical well cannot communicate with those trapped in the next well. These characteristics of  $f_1$  are not sensitive to the geometric parameters.

It is difficult to calculate transport coefficients analytically in the  $\nu$  regime because of the complicated boundary conditions for the kinetic equation. In particular, one needs to impose  $\sum J_i \partial f_i^T / \partial \mu = \sum J_i \partial f_i^h / \partial \mu$  at the boundary  $\mu = \mu_h$  between helically and toroidally trapped distributions. Here,  $J_i$  is the longitudinal invariant in the  $i$ th helical well, and  $f_i^T (f_i^h)$  is the toroidally (helically) trapped distribution. In Fig. 3, we show the diffusion coefficient scaling obtained using the DKES code

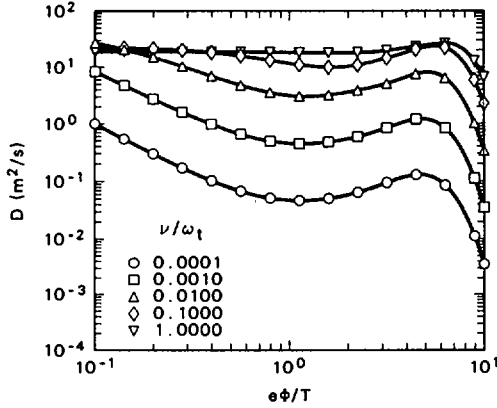


FIG. 4. Diffusion coefficient  $D$  versus  $e\Phi/T$  for various collision frequencies.

for an  $\ell = 2$ ,  $m = 12$  stellarator. From Fig. 3a, which shows the electric field and collision frequency scalings, we conclude that  $D \propto \nu/\Omega_E^2$ , where  $\Omega_E$  is the  $\mathbf{E} \times \mathbf{B}$  drift frequency. The geometric scaling shown in Fig. 3b is obtained by systematically varying  $\epsilon_t$  and  $\epsilon_h$ . We find that  $D$  is not very sensitive to the value of  $\epsilon_h$  within the accuracy of the code and that  $D$  is roughly proportional to  $\epsilon_t^{3/2}$ . The weak  $\epsilon_h$  dependence is also observed in results obtained from a Monte Carlo code [6]. This scaling can be understood heuristically from the following random walk argument. In the  $\nu$  regime, the step size  $\Delta r$  is determined by the helically trapped particles and is  $\Delta r \simeq v_{dr}/\Omega_E \simeq \epsilon_t T / (M\Omega r\Omega_E)$ , where  $v_{dr}$  is the radial drift velocity and  $r$  is the local minor radius. The diffusion coefficient  $D \sim f(\Delta r)^2/\Delta t \sim \nu(\Delta r)^2/f$ , where  $\Delta t \sim (\nu/f^2)^{-1}$  is assumed and  $f$  is the fraction of particles that participate in the transport process. The scaling obtained from the DKES results indicates that  $f \sim \sqrt{\epsilon_t}G^{-1}(\epsilon_h, \epsilon_t)$  where  $G$  is a weak function of  $\epsilon_h$  and  $\epsilon_t$ . Thus we obtain  $D \sim \nu\epsilon_t^{3/2}G(\epsilon_h, \epsilon_t)T^2/(M^2\Omega^2r^2\Omega_E^2)$ . Note that this scaling differs from those given in Refs. [1, 7, 8] for the  $\nu$  regime, showing a weaker dependence on  $\epsilon_h$  than found previously.

We find a resonance effect for the diffusion coefficient in large aspect ratio stellarators when the condition  $v_{||} - E_p/B_\theta \simeq 0$  is satisfied, where  $B_\theta$  is the poloidal magnetic field strength. A similar effect was also observed in [6,9]. In Fig. 4, we show  $D$  versus  $e\Phi/T$  at various collision frequencies for an  $\iota = 0.35$ ,  $\epsilon_t = 0.037$ ,  $\epsilon_h = 0.022$ ,  $\ell = 2$ ,  $m = 12$  stellarator. For these parameters the effect of the resonance becomes important for  $e\Phi/T \sim 5.5$  where  $D$  has a local maximum. For the high collision frequency case,  $D$  is not independent of  $\Phi$ , as it would be in the absence of the resonance, but decreases substantially for  $e\Phi/T > 5.5$ .

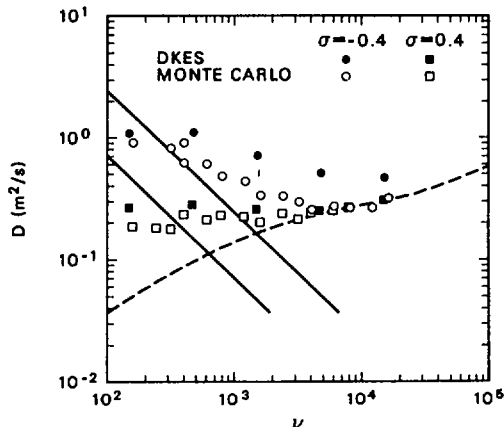


FIG. 5. Diffusion coefficient  $D$  versus  $\nu$  for a  $\sigma$ -optimized configuration. Both DKES results and Monte Carlo results are shown. The solid lines are asymptotic limits of  $1/\nu$  diffusion coefficients for  $\sigma = \pm 0.4$ . The dashed line is the diffusion coefficient of the equivalent tokamak.

The DKES code can be used to calculate diffusion coefficients for a stellarator with a complicated magnetic field spectrum. As an example, we show in Fig. 5 the results obtained for  $\sigma$ -optimized configurations [10] with  $B = B_0[1 - \epsilon_t \cos \theta + (\sigma \epsilon_h/2) \cos(\theta - 12\zeta) - \epsilon_h \cos(2\theta - 12\zeta) + (\sigma \epsilon_h/2) \cos(3\theta - 12\zeta)] = B_0[1 - \epsilon_t \cos \theta - \epsilon_h(1 - \sigma \cos \theta) \cos(2\theta - 12\zeta)]$ . The  $\sigma = 0.4$  configuration for  $e\Phi/T = 1$ , which reduces the helical ripple on the outside of the stellarator, has better confinement than the  $\sigma = -0.4$  configuration, in agreement with other calculations [10]. We also compare DKES results with Monte Carlo results [6] in Fig. 5. In the low collisionality regime, agreement between the two computations is good. The discrepancy between the results in the plateau regime for  $\sigma = -0.4$  is not understood.

## CONCLUSIONS

We find that analytic results obtained using the bounce-averaged kinetic equation are generally inappropriate for stellarator configurations. For example, resonant enhancement of diffusion coefficients in the plateau regime cannot be treated using the averaged kinetic equation. From the numerically computed contours of the particle distribution  $f_1$  in phase space, it is found that  $f_1$  does not vanish at the helical trapping boundary ( $\kappa^2 = 1$ ) in the  $\nu$  regime. That casts doubt on the validity of certain analytic results obtained by assuming  $f_1 = 0$  for  $\kappa^2 \geq 1$ , where  $\kappa^2 \simeq \langle \cos^2 \alpha \rangle$  is the well-depth parameter. A transport scaling for an  $\ell = 2$ ,  $m = 12$  stellarator is inferred from the DKES code results in the  $\nu$  regime by systematically varying geometric and physical parameters. It has the form

$D \simeq \nu \epsilon_t^{3/2} G(\epsilon_h, \epsilon_t) T^2 / (M^2 \Omega^2 r^2 \Omega_E^2)$ . The function  $G$  depends weakly on  $\epsilon_t$  and  $\epsilon_h$ . If the resonance condition  $v_{||} - E_\rho / B_\theta \simeq 0$  is satisfied, the diffusion coefficient is modified significantly by the electric field.

## REFERENCES

- [1] KOVRIZHNYKH, L.M., Nucl. Fusion **24** (1984) 851.
- [2] HIRSHMAN, S.P., SHAINING, K.C., VAN RIJ, W.I., BEASLEY, C.O., Jr., CRUME, E.C., Jr., Phys. Fluids **29** (1986) 2951.
- [3] BEASLEY, C.O., Jr., ROME, J.A., ATTENBERGER, S.E., HIRSHMAN, S.P., Rep. ORNL/TM-10222, Oak Ridge National Lab. (1986).
- [4] BOOZER, A.H., Phys. Fluids **24** (1981) 1999.
- [5] SHAINING, K.C., HIRSHMAN, S.P., CALLEN, J.D., Phys. Fluids **29** (1986) 521; SOLANO, E., SHAINING, K.C., Phys. Fluids **30** (1987) 462.
- [6] BEIDLER, C.D., personal communication, 1986.
- [7] GALEEV, A.A., SAGDEEV, R.Z., Usp. Fiz. Nauk **99** (1969) 528.
- [8] MYNICK, H.E., Phys. Fluids **26** (1983) 2609.
- [9] MAASSBERG, H., in Fifth International Workshop on Stellarators (Proc. IAEA Tech. Comm. Mtg on Plasma Confinement and Heating in Stellarators, Schloss Ringberg), EUR-9618-EN, Vol. 2, CEC, Directorate-General XII — Fusion Programme, Brussels (1984) 507.
- [10] MYNICK, H.E., CHU, T.K., BOOZER, A.H., Phys. Rev. Lett. **48** (1982) 322.
- [11] BEIDLER, C.D., HITCHON, W.N.G., personal communication, 1986.



## RESULTS FROM HBTX WITH IMPROVED CONFINEMENT

B. ALPER, V. ANTONI<sup>1</sup>, M.K. BEVIR, H.A.B. BODIN,  
C.A. BUNTING, P.G. CAROLAN, J. CUNNANE<sup>2</sup>, D.E. EVANS,  
A.R. FIELD<sup>3</sup>, S.J. GEE<sup>4</sup>, C.G. GIMBLETT, R. HAYDEN<sup>2</sup>,  
T.R. JARBOE<sup>5</sup>, P. KIRBY, A. MANLEY<sup>3</sup>, A.A. NEWTON,  
P.G. NOONAN, A. PATEL<sup>3</sup>, R.S. PEASE, M.G. RUSBRIDGE<sup>4</sup>,  
K.P. SCHNEIDER<sup>4</sup>, D.P. STOREY<sup>6</sup>, H.Y.W. TSUI,  
S. WHITFIELD<sup>7</sup>, P.D. WILCOCK  
Euratom-UKAEA Fusion Association,  
Culham Laboratory,  
Abingdon, Oxfordshire, United Kingdom

### Abstract

#### RESULTS FROM HBTX WITH IMPROVED CONFINEMENT.

In the HBTX Reversed Field Pinch ( $R/a = 0.8 \text{ m}/0.25 \text{ m}$ ), the resistance has been decreased by reducing field errors and, by using wall loading to increase the density, there is a fivefold increase in  $\tau_E$ . The resistance decreases with the size of the edge region, defined by field errors and limiters, and the resistivity anomaly might be explained in terms of helicity transport and dissipation, where field lines intersect material objects. From 200 to 450 eV,  $T_i \sim T_e$ ; plasma rotation in  $\phi$  and  $\theta$  is observed but this cannot account for the anomalous ion heating. The on axis value of  $T_e$  increases with  $I_\phi$  up to 430 kA, but slower than linearly and  $\beta_\theta$  falls with  $I_\phi$ , from  $\sim 20\%$  at 80 kA to  $\sim 10\%$  at 220 kA and more slowly thereafter, possibly saturating. With deep reversal a rotating  $m = 1$ ,  $n = 6$  helical structure is interpreted as Taylor's second relaxed state.

### 1. INTRODUCTION

This paper describes results on plasma resistivity and confinement, radiation, ion heating, scaling, and fluctuations from HBTX1B, an improved version of HBTX1A [1], and simulations with a 3D single fluid incompressible MHD code.

<sup>1</sup> Istituto Gas Ionizzati, Consiglio Nazionale delle Ricerche, Padua, Italy.

<sup>2</sup> University College, Cork, Ireland.

<sup>3</sup> Royal Holloway and Bedford New College, University of London, UK.

<sup>4</sup> UMIST, Manchester, UK.

<sup>5</sup> Los Alamos National Laboratory, NM, USA.

<sup>6</sup> University of Hull, UK.

<sup>7</sup> Imperial College of Science and Technology, University of London, UK.

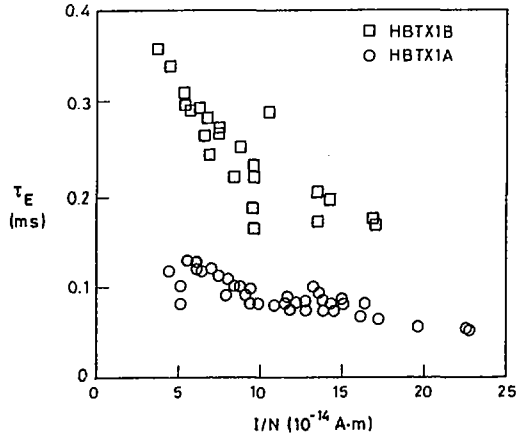


FIG. 1. Energy confinement time as a function of  $I/N$  in HBTX1B with improved magnetic geometry and density control using wall loading, compared with that observed previously in HBTX1A. Current varies from 190 to 230 kA. ( $\tau_E$  is calculated from profiles similar to those of Fig. 3.)

## 2. FIELD ERRORS AND EQUILIBRIUM

Field errors due to windings ripple and port distortions have been reduced from 0.2% to 0.01% (equivalent error flux area normalised to liner surface area) using a new windings former with one toroidal gap. This gives a reduction in resistance by a factor  $\sim 1.5-2$ . The equilibrium displacement, typically  $\sim 3$  cm, contributes an equivalent error of 1.5%, compensated by a steady  $B_v$  up to 8 mT, to give a further twofold reduction in resistance to  $\sim 150$   $\mu\text{ohm}$  at 200 kA. Neither  $T_e$  nor  $\beta_\theta$  vary significantly with  $B_v$  or field error reduction. In conditions where both current and density (using wall loading) are sustained there is an overall improvement in  $\tau_E$  by up to 5 to 0.35 ms. Figure 1 shows  $\tau_E$  vs  $I/N$  for HBTX1A and HBTX1B.

## 3. RESISTANCE ANOMALY

The resistivity calculated from the global resistance  $\Omega = V_\phi / I_\phi$  (where  $V_\phi$  is the loop volts) using helicity balance exceeds the Spitzer value for the observed  $T_e$  and spectroscopic  $Z_{\text{eff}}$  by a factor  $\sim 3$  at high density ( $I/N \sim 4 \times 10^{-4}$  A.m), rising

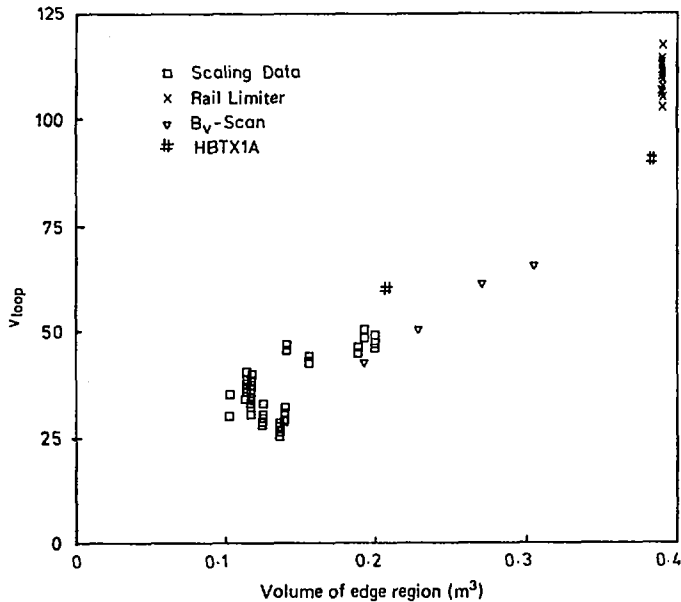


FIG. 2. Loop voltage as a function of edge region size, determined by field errors, equilibrium displacement, or limiters. Data from HBTX1A and HBTX1B.

to more than ten as  $n_e$  is reduced. This analysis takes account of experimentally estimated radial profiles of  $T_e$ ,  $n_e$ , ion species and  $Z_{eff}$ . Moreover,  $\alpha$  is almost independent of  $T_e$ , eg between 200 and 450 eV at  $I = 220$  kA.

As seen in Fig. 2,  $V_{loop}$  increases with the size of the edge region, which was varied by reducing field errors, by changing the equilibrium using  $B_v$  and, most strikingly, when a rail limiter was inserted 5 cm into the plasma. In the latter case  $V_{loop}$  increased from 30 V to 115 V at constant  $I$  [2]. These observations have been interpreted in terms of helicity dissipation in the edge region either close to the walls or at the actual boundary where field lines intersect physical surfaces.

The helicity balance equation, in the steady state, can be written in the form

$$V_{loop} \phi = \int_{\text{Bulk plasma}} \vec{E} \cdot \vec{B} \, d^3x + \int_{\text{Edge plasma}} \vec{E} \cdot \vec{B} \, d^3x$$

$$\text{or} \quad V_{\ell} = I_{\phi} \Omega_{sp} + E_{\text{edge}} (\theta/\pi a^2) V_{\text{edge}}$$

The injection term (LHS) is balanced by ohmic dissipation in the bulk plasma ( $\propto I_{\phi} \Omega_{sp}$ ), together with additional dissipation in the edge region ( $\propto E_{\text{edge}} V_{\text{edge}}$ );  $V_{\text{edge}}$  is the volume of the edge region defined by field errors and limiters and  $E_{\text{edge}}$  is the equivalent time and volume averaged electric field in this region. It is found that  $E_{\text{edge}}$  is approximately constant at  $27 \pm 7$  volts-m<sup>-1</sup> for all the conditions shown in Fig.2.

When helicity is dissipated at physical boundaries where  $\vec{B} \cdot \vec{n} \neq 0$ , the helicity balance equation is

$$V_{\ell} \phi = \int_{\text{plasma}} \vec{E} \cdot \vec{B} d^3x + \int_{\text{surface}} \chi \vec{B} \cdot \vec{n} d^2x = I_{\phi} \Omega_{sp} \phi + \Delta\chi B_{\text{edge}} A$$

$$\text{or} \quad V_{\ell} = I_{\phi} \Omega_{sp} + \Delta\chi (\theta/\pi a^2) A$$

Here,  $\Delta\chi$  is the electric potential difference between the physical surfaces where field lines enter and leave the plasma and  $A$  is the projected area of such surfaces normal to the field lines. Additional power input, which appears as the resistance anomaly, is required to compensate for the energy loss associated with the helicity transport needed to balance its dissipation at the boundary.

Studies with a small carbon limiter (5 cm wide) inserted progressively up to 6 cm into the plasma confirm that the increase in loop voltage  $\Delta V$  is proportional to the flux intercepted and  $\Delta V$  scales linearly to the rail limiter data. No increase in oxygen or metal impurities was observed. The rise in  $Z_{\text{eff}}$  from the measured increase in carbon makes an estimated 10-20% contribution to  $\Delta V$ .

It is the helicity transport, by fluctuations of the form  $\langle \tilde{u} \wedge \tilde{B} \rangle$ , which couples the edge region to the bulk plasma. Because the system is a relaxed state the loop voltage associated with the edge region acts in addition to the Spitzer loop voltage and appears as an anomalous resistance.

According to both of these models, when field errors are eliminated, the resistance would be that derived using helicity balance from Spitzer resistivity including impurities.

Probe measurements indicate that the carbon tile limiters together (8% surface coverage) must draw 10-40 kA electron

current and that the edge is active with 100 amp, 10  $\mu$ sec spikes.

#### 4. FIELD CONTROL

In matched mode start-up over 7 ms, the planned RFX [3] value scaled for HBTX, current termination occurs before reversal, but constant- $\theta$  (ramping) yields standard plasmas. From a comparison at risetimes at which both modes could be used, the risetime dependent term in the volt seconds using ramping is a factor of two smaller, indicating a useful reduction for long risetimes. Controlled rundown at constant- $\theta$  [4] forestalls abrupt termination until the current falls to 10-20% of its maximum value.

The voltages on the plasma surface during sustainment were scanned through those calculated to minimise dynamo activity ( $V_\phi \sim -10$  volts,  $V_\theta \sim -6$  volts). Fluctuations were reduced as  $V_\phi$  varied from +50 volts (flat top) to -50 volts, most markedly from +50 volts to 0 (which yielded only a modest reduction in  $\tau_{\text{pulse}}$ ). A significant effect was observed using a multichord spectrometer which views the whole plasma volume, with a typically two fold decrease in  $\bar{B}/B$  from edge coils. Previously [5] a similar effect was strongest when  $V_\phi < 0$ .

#### 5. IMPURITIES

The impurity concentration, typically 1-2% low Z and 0.1% metals, is as in HBTX1A [1]. Impurity transport was studied by fitting C V profiles calculated with a 1D code (see [6]) for different transport coefficients to observations from a 20 chord surface barrier diode (SBD) array. Profiles of  $T_e(r)$  were determined from CV line intensity ratios from the cluster near 40Å and the 2271Å line, measured by the SBD array and a 20 chord visible spectrometer respectively, which view the same volume. A collisional-radiative computation shows that in HBTX this ratio is almost linear in  $T_e$  and virtually independent of  $n_e$ , whose profile is measured with a 3-chord interferometer. Computed CV distributions with diffusion at 100 and 150  $\text{m}^2\text{s}^{-1}$  are compared with measurements in Fig.3, for the  $T_e(r)$  and  $n_e(r)$  profiles indicated. A value of  $n_e \tau_{\text{imp}} \approx 10^{16} \text{ m}^{-3} \text{ s}$  is deduced, comparable with  $n_e \tau_E$  for the plasma as a whole.

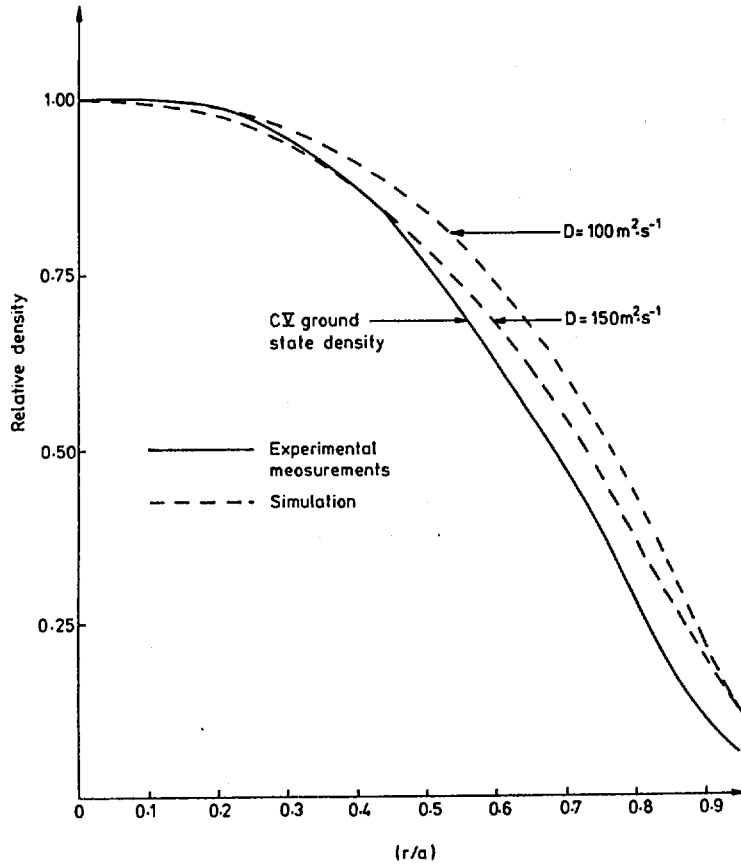


FIG. 3. Relative density of C V as a function of normalised radius at 200 kA; the experimental curve is compared with simulation (dashed line) for two values of diffusion coefficient. Density and temperature profiles estimated from experiment were used as follows:

$$n_e = (n_{e0} - n_{e0}) [1 - (r/a)^2]^{0.5} + n_{ea}, \quad T_e = (T_{e0} - T_{ea}) [1 - (r/a)^2]^{0.25} + T_{ea}.$$

The total radiation during sustainment, measured by a three chord absolutely calibrated bolometer, is typically  $\sim 4\%$   $P_{\text{ohmic}}$ . Radiation is insignificant in the power balance for the plasma as a whole and for the edge, although it rises towards the walls and can show poloidal asymmetries. There is no radiation cooled mantle controlling the edge temperature as in the Tokamak.

## 6. ION HEATING

The value of  $T_i$  from NPA data tracks  $T_e$  within 20% from 200 eV to 450 eV. The ions are heated anomalously since in an ion

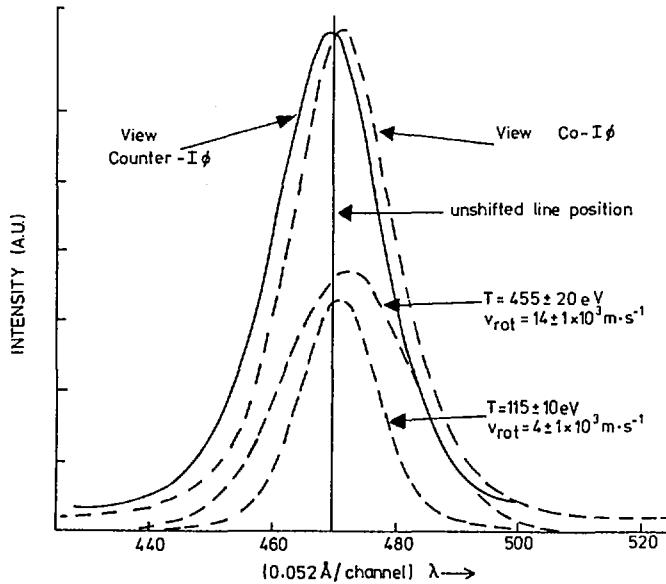


FIG. 4. Experimental spectrum of the CV 2271 Å line viewed through opposing tangential ports in horizontal toroidal plane. Separation is due to red (view co- $I_\phi$ ) and blue (view counter- $I_\phi$ ). Doppler shifts correspond to an ion velocity in  $I_\phi$ -direction. Lower curves are two Gaussians whose sum, convolved with instrument function, fits experimental red shifted spectrum.

energy confinement time  $\approx 0.3$  ms electron-ion collisions, taking into account impurities, only raise  $T_i$  to less than  $1/10 T_e$ .

A visible Doppler spectrometer with OMA and twin quartz fibre inputs, viewing the plasma simultaneously in opposing tangential directions, measures time integrated deuterium and impurity ion temperatures and rotational velocities. Spectra of a CV (2271) line viewed through opposing tangential ports in the horizontal toroidal plane are shown in Fig. 4. They appear to be composite and can be fitted with 1% accuracy by the weighted sum of a pair of gaussians, one having  $T_i = 455 \pm 20$  eV and shifted by  $v_\phi = 1.4 \pm 1 \times 10^4$  ms $^{-1}$ , the other having  $T_i = 115 \pm 10$  eV and  $v_\phi = 4 \pm 1 \times 10^3$  ms $^{-1}$ . The ratio of the hot to the cold components is  $\sim 1.7 \pm 0.2$ . The velocities are in the direction of the toroidal ion current. These results suggest the existence of rotational shear. Temperatures measured in the poloidal plane tend to be 10-20% lower than those measured toroidally; the velocity, also in the direction of the poloidal ion current, is 2-3 times smaller. Although values of  $v_\phi$  up to

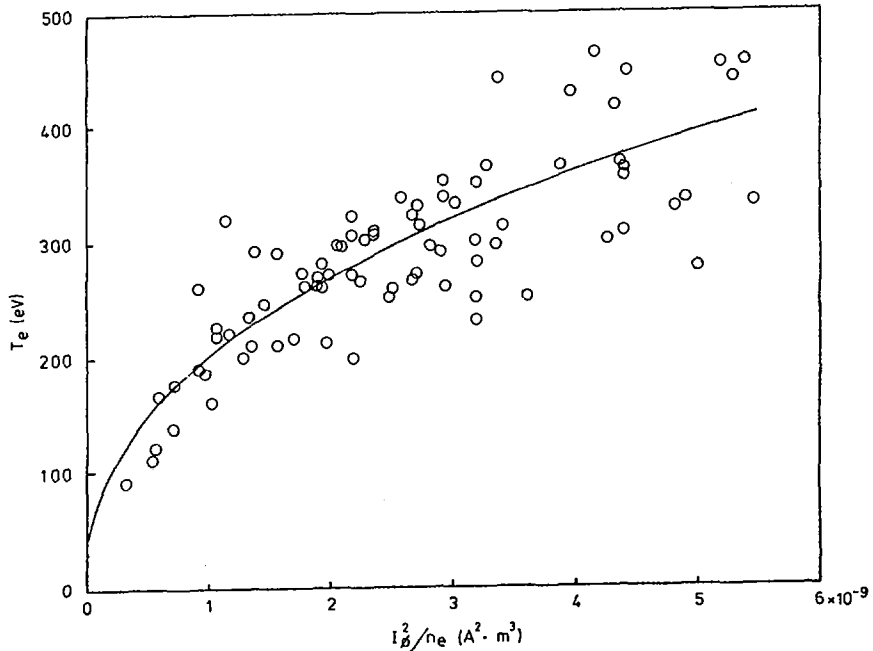


FIG. 5. Electron temperature  $T_e$  as a function of  $I_p^2/n_e$  for currents between 80 and 430 kA. Best fit curve is shown through points.

$4 \times 10^4$  ms $^{-1}$  have been observed and the carbon ions can get significant energy directly from the applied electric field this effect appears insufficient to explain the deuteron temperatures.

## 7. SCALING

The variation of  $T_e$ ,  $\beta_\theta$  and  $\tau_E$  with  $I$  from 80 kA to 435 kA ( $F = -0.1$  and  $\theta = 1.4$ ) has been studied. The density is controlled by preloading the carbon tiles, to give a five fold increase to  $\sim 5 \times 10^{19}$  m $^{-3}$  sustained for 5 ms; typically  $I/N \sim 5 \times 10^{-14}$  A.m.

The observed  $T_e$  vs  $I$  dependence might be interpreted on the basis of a linear 1 eV/kA variation (see [7][8]) but in this work it is more complicated with evidence for a linear variation at lower current and some flattening off at higher values. At 220 kA a density scan yielded  $T_e \approx n_e^{-0.6}$ . A maximum likelihood fit to all the data yields  $T_e \approx 10^{0.78} n_e^{-0.55}$ .

This fit implies some reduction of  $\beta_\theta$  with current which can be deduced from Fig.5 in which  $T_e$  is plotted against  $I^2/n$ . A constant  $\beta_\theta$ , i.e.  $T_e = I$  at fixed  $I/N$ , corresponds to a line of constant slope; a better fit is obtained by the curve. The variation is most pronounced at low currents, and  $\beta_\theta$  falls from  $> 20\%$  at 80 kA to  $\sim 10\%$  at 220 kA and more slowly thereafter. (Profiles similar to those in Fig.3 are used). When the data is corrected for the observed profile broadening with increasing current and replotted vs. Lundquist number there is some indication for saturation.

The value of  $\tau_E$  rises with current at low values but thereafter it is hard to identify a clear trend and there is a wide spread in the data; at high currents the optimum  $B_V$  could not be used and there was only limited conditioning. The Lawson parameter increases strongly with  $I_\phi$  as observed elsewhere.

According to theories of transport due to resistive fluid turbulence, when g-modes dominate [9]  $\beta_\theta \sim \text{constant}$  and  $n_e \tau_E \propto I^{2.5}$ . If tearing modes dominate [10],  $\beta_\theta \sim I^{-1/3}$  and  $n_e \tau_E \propto I^{1.67}$ . Experimental uncertainty makes it difficult to say which, if either, model fits HBTX1B data. The value of  $\tau_E$  is based on the global resistance, and therefore depends on the non-ohmic contribution due to the edge effects (Section 3) which involves factors not taken into account in the theories. It might be appropriate to deduct this part which would increase  $\tau_E$  to  $\sim 1$  ms.

## 8. FLUCTUATIONS

Fluctuations are detected by internal poloidal and toroidal arrays of edge coils. With  $\theta = 1.4$ ,  $F = -0.1$ , HBTX1B is similar to HBTX1A with  $\delta/B = 1-2\%$ , dominant poloidal modes  $m=0,1$  resonant inside the reversal surface, and a wide range of toroidal modes with  $|n| = 8-17$  peaking at 10-12. These modes rotate in the same sense as the plasma ion current with toroidal speed  $v_\phi = 5 \times 10^4 \text{ ms}^{-1}$  and poloidal speed  $v_\theta = 3 \times 10^4 \text{ ms}^{-1}$ , which may be compared with the CV rotation (Section 6).

With deep reversal,  $F < -0.35$  and  $\theta > 1.6$ ,  $\delta/B = 5-10\%$ , and there is a dominant single rotating  $m=1$  structure resonant outside the reversal surface, always with  $n=6$ , and  $v_\phi \sim 2-7 \times 10^4 \text{ ms}^{-1}$  which has been interpreted as Taylor's (second)  $m=1$

helical minimum energy state ( $n=4$  for HBTX1B). Since  $\theta$  has not saturated the plasma is evidently not fully relaxed.

With deep reversal, sawtooth-like fluctuations are seen in the  $m=0$   $\tilde{B}$  signals and in the soft X-ray emission detected by the SBDs.  $\phi$  Toroidal flux and  $I$  are observed to oscillate and there are associated field profile changes seen by means of an insertable magnetic probe. The global parameters such as  $n_e$  and  $\eta^k$  are more influenced by changes in  $F$  (which characterises the plasma edge) than by  $\theta$ , which is an average quantity, indicating that the outer region plays an important role. With deep reversal both  $n_e$  and  $\eta^k$  are higher and more prone to variation.

Fine-scale fluctuations are observed on the SBD that have a transverse correlation length of the order of 0.1 minor radius and are consistent with density fluctuations due to motion of particles along magnetic field lines.

## 9. 3D SIMULATIONS

Numerical simulation has been performed using a single-fluid, incompressible MHD code in cylindrical geometry [11]. Plasma parameters are specified in terms of the Lundquist number  $S$  and the normalised radial profile of the resistivity. As it evolves the fluid exhibits both spontaneous field reversal and sustainment. If  $S = 10^4$  and resistivity increases towards the wall, as in HBTX, the  $F$ - $\theta$  variation is in good agreement with curves modelled by the MBFM to fit experiment. The code also displays field fluctuations, defined as departures from axisymmetry, which are about 10% for  $S=10^2$  and fall as  $S$  is increased to about 4% at  $S=10^4$ . For uniform resistivity and  $S=10^3$  the energy spectrum of fluctuations in radial field  $B_r$  is dominated by two low order toroidal  $m=1$  modes during sustainment, similar to experiment.

The relative strengths of the individual terms in the axisymmetric part of the poloidal component of Ohm's law,  $(\vec{v} \times \vec{B})_\theta = v_r B_\phi - v_\phi B_r$  responsible for sustaining the reversal have been evaluated for uniform resistivity and  $S=10^3$ ;  $\langle v_r B_\phi \rangle$  provides the dominant emf balancing resistive diffusion.  $\phi_r$  The computed profile of  $\mu = J_\parallel / B$  corresponds well with experiment.

## 10. THIN SHELL OPERATION

A new shell assembly has been constructed with a  $B_V$  time constant of 2 ms (compared with 80 ms at present). MHD instabilities with a resistive wall have been studied theoretically [12] and tearing modes, which can lead to magnetic islands, are stabilised by toroidal rotation at  $\sim 10^2$ - $10^3$   $\text{ms}^{-1}$ , smaller than observed. Ideal modes are not stabilised by rotation and lock to the wall, but parallel viscosity and non-linear relaxation may play a role. Qualitatively, if the wall time constant exceeds the relaxation time continuously growing modes may not occur. The centre limb of iron core will be encased in a conducting bandage to minimise the possible effects of shift and tilt modes.

## 11. CONCLUSIONS

- (i) In HBTX1B improved magnetic geometry and density control have yielded a fivefold increase in  $\tau_E$  compared with HBTX1A in sustained density and current conditions.
- (ii) The resistance increases with the size of the edge region, varied by changing field errors,  $B_V$  and the limiter configuration; it is postulated that anomalous resistivity can be explained in terms of an additional contribution to the loop voltage from helicity transport in the plasma and dissipation where field lines intersect physical obstructions at the edge.
- (iii) Radiation is unimportant in the energy balance even at the edge although it increases towards the walls.
- (iv) From 200 to 450 eV  $T_i = T_e \pm 20\%$ , but the ions are not heated by collisions. Tangential CV measurements show  $T(CV) \sim T_i$  and rotation velocities  $v_\theta, v_\phi$  in the direction of the ion current up to  $\sim 4 \times 10^4 \text{ms}^{-1}$ .
- (v)  $T_e$  increases as  $I^n$  with  $0.5 < n < 1$ ;  $\beta_\theta$  decreases with  $I$ , from 20% at 80 kA to  $\sim 10\%$  at 220 kA and slowly thereafter, possibly saturating with increasing  $S$ .
- (vi) For  $F=-0.1$  modes with  $m=1$ ,  $|n|=8-17$  rotate with  $v_\theta \approx v_\phi = 5 \times 10^4 \text{ms}^{-1}$ ; at deep reversal a rotating helical  $m=1$  structure with  $n \sim 6$  is interpreted as Taylor's second relaxed state.
- (vii) Several aspects of RFP behaviour can be simulated by a 3-D single fluid incompressible code.

## REFERENCES

- [1] CAROLAN, P.G., et al., in Plasma Physics and Controlled Nuclear Fusion Research 1984 (Proc. 10th Int. Conf. London, 1984), Vol. 2, IAEA, Vienna (1985) 449.
- [2] JARBOE, T.R., ALPER, B., submitted to Phys. Fluids.
- [3] MALESANI, G., ROSTAGNI, G., paper presented at The RFX Experiment (14th Symp. Fusion Technology, Avignon, 1986).
- [4] NEWTON, A.A., NOONAN, P.G., Nucl. Instrum. Methods Plasma Res. A **425** (1986) 167.
- [5] ROBINSON, D.C., KING, R.E., in Plasma Physics and Controlled Nuclear Fusion Research (Proc. 3rd Int. Conf. Novosibirsk, 1968), Vol. 1, IAEA, Vienna (1969) 263.
- [6] BEHRINGER, K.H., et al., Nucl. Fusion **26** (1986) 751.
- [7] TAMANO, T., in Plasma Physics and Controlled Nuclear Fusion Research (Proc 10th Int. Conf. London, 1984), Vol. 2, IAEA, Vienna (1985) 43.
- [8] BAKER, D.A., et al., *ibid.*, p. 439.
- [9] CONNOR, J.W., TAYLOR, J.B., Phys. Fluids **27** (1984) 2676.
- [10] AN, Z.G., et al., in Plasma Physics and Controlled Nuclear Fusion Research 1984 (Proc. 10th Int. Conf. London, 1984), Vol. 2, IAEA, Vienna (1985) 231.
- [11] KIRBY, P., in Computational Physics (Proc. 8th Europ. Conf. Bad Eibsee, 1986), Vol. 10D, European Physical Society (1986) 23.
- [12] GIMBLETT, C.G., Nucl. Fusion **26** (1986) 617.

## DISCUSSION

H. TOYAMA: Is there any difference between the  $\beta$  scaling of the deep reversal and that of the standard reversal?

H.A.B. BODIN: We did not make any scaling studies with deep reversal since there was increased plasma-wall interaction and some risks to the integrity of the liner at high currents.

M. HAINES: How can you explain ion heating by rotation? Surely only *sheared* rotation will lead to viscous heating.

H.A.B. BODIN: The rotation is sheared. The two fitted Gaussians for C V contained in the figures with  $T = 455$  eV and  $T = 115$  eV have *different* rotation speeds —  $14 \times 10^3$  m·s<sup>-1</sup> and  $4 \times 10^3$  m·s<sup>-1</sup>, respectively.

T. OHKAWA: What is your definition of the 'edge region'? After all, inserting the limiter further or retracting the conducting shell further both increase the edge volume.

H.A.B. BODIN: The edge region is defined by the radial distance from the inner surface of the rail limiter or standard carbon tiles to the inner surface of the *liner*. For field errors and equilibrium cases, an equivalent 'edge volume' representing the size of the region where flux tubes due to field errors or displacement intersect the liner is used. The position of the shell does not enter into it when the shell and liner are separate structures.

It should be noted that two ways of looking at this are described in my paper. The one I discussed orally is in terms of the edge volume (above). The second, now

preferred, is in terms of the projected area of inserted objects normal to the field lines (approximately  $\beta_\theta$  near the wall). It should be mentioned as well that one of two theories based on this second approach predicts a value of the change in loop voltage when objects are inserted in rough agreement with observation without fitted parameters.



## EXPERIMENTAL AND THEORETICAL STUDIES OF THE STP-3(M) REVERSED FIELD PINCH IN THE HIGH CURRENT DENSITY REGIME

K. SATO, T. AMANO, Z.X. CHEN<sup>1</sup>, H. ARIMOTO,  
S. YAMADA, A. NAGATA<sup>2</sup>, K. YOKOYAMA<sup>3</sup>, Y. KAMADA<sup>4</sup>,  
A. MATSUOKA<sup>5</sup>, S. MASAMUNE<sup>6</sup>, H. SHINDO<sup>2</sup>, K. SAITO<sup>3</sup>,  
H. MURATA<sup>5</sup>, H. OSHIYAMA, S. SHIINA, T. TAMARU  
Institute of Plasma Physics,  
Nagoya University,  
Nagoya, Japan

### Abstract

EXPERIMENTAL AND THEORETICAL STUDIES OF THE STP-3(M) REVERSED FIELD PINCH IN THE HIGH CURRENT DENSITY REGIME.

Reversed field pinch experiments are carried out, with a high current density of up to  $7 \text{ MA} \cdot \text{m}^{-2}$ . The electron temperature is nearly proportional to the current density. The self-organizing action and its effect on plasma confinement are investigated experimentally and theoretically. The typical RFP behaviour is essentially the same in the entire current density region of 2 to  $7 \text{ MA} \cdot \text{m}^{-2}$ . In the high current density regime, the magnetic fluctuation level decreases slightly and plasma-wall interaction caused by the dynamo action sets in.

### 1. INTRODUCTION

In this paper, the results of experimental and theoretical studies on the self-organizing action of an RFP plasma [1] and its effect in the high current density regime are presented. These studies are very important in realizing a compact and simple RFP reactor [2] with high power density.

The experiments are carried out in STP-3(M) [3], which has a stainless steel liner ( $R/a = 0.5/0.1 \text{ m}$ ) with molybdenum limiters. Its load assemblies and electric power source are designed so that the plasma current can be driven up to 350 kA, which corresponds to a current density of  $15 \text{ MA} \cdot \text{m}^{-2}$ . So far, the maximum plasma current density and plasma lifetime attained are  $7 \text{ MA} \cdot \text{m}^{-2}$  (170 kA) and 3.1 ms, respectively. STP-3(M) has no vertical field coils for

<sup>1</sup> Institute of Plasma Physics, Hefei, China.

<sup>2</sup> Faculty of Engineering, Hiroshima University, Higashi-Hiroshima 724, Japan.

<sup>3</sup> Department of Physics, College of Science and Technology, Nihon University, Tokyo 101, Japan.

<sup>4</sup> Department of Nuclear Engineering, University of Tokyo, Tokyo 113, Japan.

<sup>5</sup> College of Technology, Gunma University, Gunma 376, Japan.

<sup>6</sup> Department of Electrical Engineering, Kyoto Institute of Technology, Kyoto 606, Japan.

plasma position control. Equilibrium is maintained by a conducting shell, which is a double shell structure for the purpose of reducing the field errors. The outward displacement of the plasma column is kept within 6 mm during the entire plasma lifetime. In the quiescent phase, the fluctuation level  $\delta B/B$  is 0.5–2% and the electron temperature is 120–300 eV, with a plasma current of 50–100 kA.

To simulate MHD phenomena in STP-3(M), a three-dimensional semi-implicit compressible code has been developed. By using this code, the mechanism of the self-organizing effect and its effect on the diffusion are studied.

## 2. SELF-ORGANIZING EFFECT

Typical waveforms of the characteristic parameters of the STP-3(M) plasma are shown in Fig. 1. The electron temperature ( $T_e$ ) and the electron density ( $n_e$ ) are measured by Thomson scattering, and the conductivity temperature ( $T_{e\sigma}$ ) is estimated by assuming  $Z_{\text{eff}} = 1$  and the geometrical factor to be equal to 4. The fluctuation level is high (5–10%) up to the end of the current rise phase. In this phase, the toroidal flux increases. In the current decay, or flat-top, phase, the fluctuation level decreases to 0.5–1%, and the electron temperature increases above 100 eV, which indicates improved confinement in this phase.

The field reversal ratio ( $F$ ) and the pinch parameter ( $\theta$ ) are kept constant after the setting up of the RFP configuration. This is the result of the self-organization which accompanies the generation of toroidal flux. The self-organizing effect is sensitive to the magnetic Reynolds number ( $S$ ). In the low  $S$  case, the  $F$  and  $\theta$  values move along wide trajectories in the  $F$ – $\theta$  diagram. On the other hand, in the high  $S$  case, the trajectory tends to stay, for a long time, at a particular point in the  $F$ – $\theta$  diagram, as is shown in Fig. 1(e). The  $\theta$ -value in STP-3(M) is about 1.7–2.0. The  $F$ – $\theta$  diagram for high input power is shown in Fig. 2. The ratio of the amplitude of the helical fluctuation to that of the symmetric fluctuation does not depend on the volt-seconds stored in the plasma. These experimental results imply that the helical equilibrium of an RFP plasma with finite pressure is not always described by Taylor's theory.

To investigate the mechanism of the self-organizing effect, magnetic probes of various kinds and flux loops located at toroidal positions are used. A poloidal array of coils is installed behind the limiters at four poloidal locations in the meridional planes. A toroidal array of coils is set up between the liner and the shell.

The fluctuation propagates toroidally in the anti-plasma-current direction. Poloidally, it propagates in the direction of the electron diamagnetic drift with respect to the outer toroidal magnetic field. The screw of the observed fluctuation always coincides with that of the magnetic line of force inside the reversal

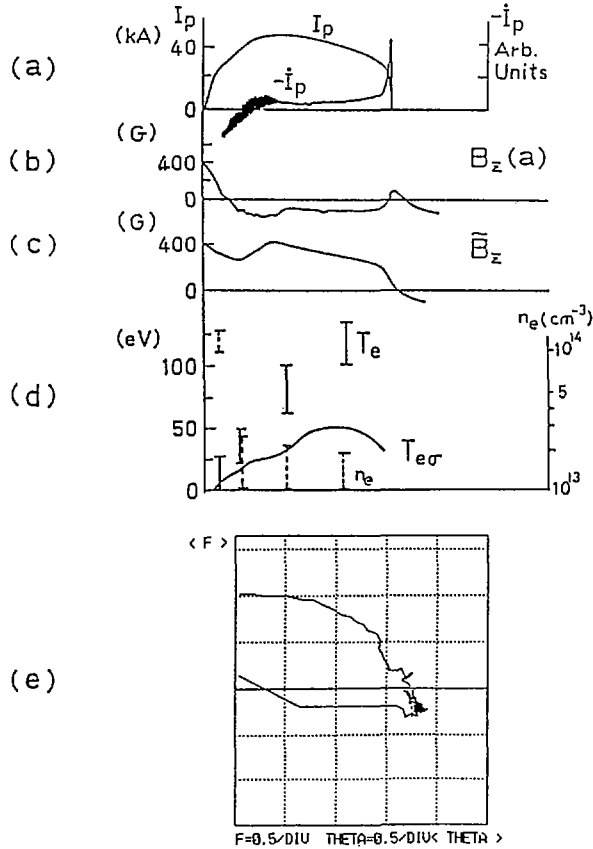


FIG. 1. Typical waveforms of characteristic STP-3(M) plasma parameters: (a) plasma current and its time derivative; (b) toroidal magnetic field at wall; (c) averaged toroidal magnetic field; (d) electron temperature, conductivity temperature and electron density; (e)  $F$ - $\theta$  diagram.

surface, and the fluctuations always propagate in the anti-plasma-current direction. Furthermore, the poloidal plasma flow inside the reversal surface is found by measuring the Doppler shifts of the impurity lines [4]. All the observed fluctuations, such as those of the toroidal flux, visible light emission and density at the edge propagate in the direction of the electron current flow [5, 6]. From these observations, we conclude that plasma flow along the magnetic field lines exists and propagates in the same direction as the fluctuation.

The results of mode analysis made by using FFT show that the dominant poloidal mode number ( $m$ ) is  $m = 1$ ;  $m = 0$  and  $m = 2$  modes are also observed. The dominant toroidal mode numbers ( $n$ ) are 9 to 13. The time evolution of the toroidal flux in the quiescent phase is shown in Fig. 3, together with those

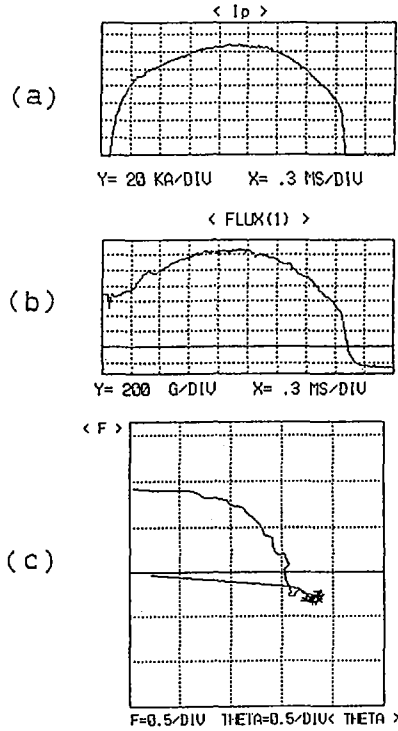


FIG. 2.  $F$ - $\theta$  diagram for high input power: (a) plasma current; (b) toroidal magnetic flux; (c)  $F$ - $\theta$  diagram.

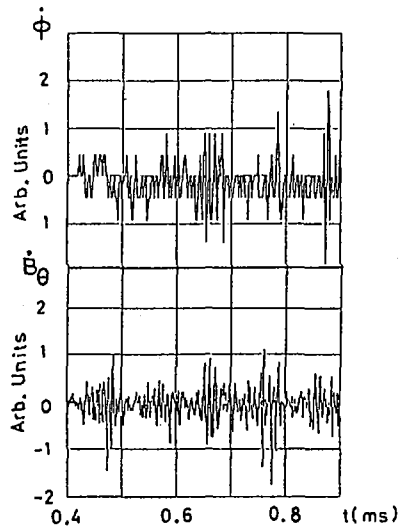


FIG. 3. Time evolutions of toroidal flux and poloidal magnetic fluctuation in quiescent phase.

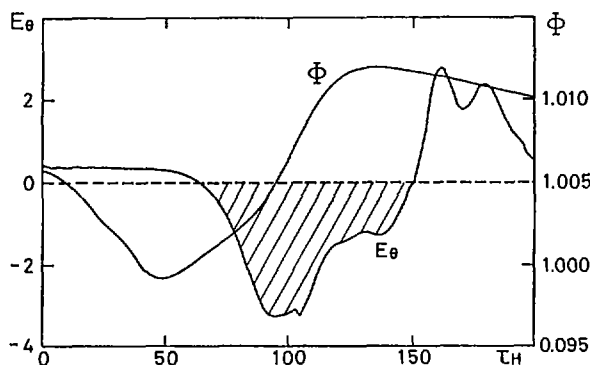


FIG. 4.  $E_\theta$  at reverse field surface and toroidal flux inside reverse field surface versus time.  $E_\theta$  is negative in shaded region.

of the poloidal magnetic fluctuation. Toroidal flux enhancement is observed as a discrete event, and a growing sinusoidal oscillation usually appears in the  $B_\theta$  signal, which is composed of  $m = 0, 1, 2$  modes. These experimental results indicate that the mechanism of self-organizing action is due to coupling with helical modes having  $m = 1, n = 9$  to 13.

To simulate the non-linear evolution of MHD fluctuations, two resistive MHD codes (incompressible and compressible) solving primitive MHD equations in cylindrical co-ordinates  $(\gamma, \theta, Z)$  have been developed. Both codes use finite difference in  $r$  and spectral representation in  $\theta$  and  $z$ . Fifty to one hundred  $(m, n)$  modes with multi-helicity are taken into account. The compressible code uses a semi-implicit method in order to avoid the short time steps due to compressional Alfvén modes. As to tokamak disruption simulation, the two codes give essentially the same results as the reduced MHD model. By comparing the results of five different codes, Aydemir et al. [7] have shown that compressible codes predict field reversal maintenance while incompressible codes do not, for a configuration with an aspect ratio of  $R/a = 1$  and  $S = 10^3$ . Using a force-free paramagnetic field model as initial configuration, our codes lead to the same conclusion: the compressible code predicts appearance and maintenance of field reversal while the incompressible code does not.

By considering a more realistic configuration with  $R/a = 5$ , and starting from an initial finite beta Robinson equilibrium, a series of simulations has been done in which the  $S$  number ranges from  $10^4$  to  $10^6$ . Axial flux conservation and constant toroidal current were used as boundary conditions. It was observed that field reversal was maintained, even in the incompressible case, in contrast to the  $R/a = 1$  case.

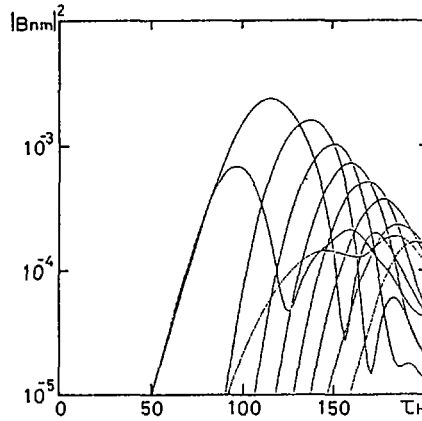


FIG. 5. Magnetic field energy of ten dominant modes versus time. The  $(m,n)$  numbers of each mode are  $(1,-10)$ ,  $(1,-11)$ ,  $(1,-12)$ ,  $(1,-13)$ ,  $(1,-9)$ ,  $(1,-14)$ ,  $(1,-15)$ ,  $(1,-16)$ ,  $(0,-1)$ ,  $(1,-17)$  in the order of decreasing maximum amplitudes.

Figure 4 shows the time history of toroidal field flux  $\Phi$  (inside the field reversed surface) and poloidal electric field  $E_\theta$  measured at the field reversal surface for the case of  $S = 10^5$ ,  $\beta = 8\%$ . The  $F$  and  $\theta$  values are 2 and  $-0.23$ , respectively. Beta was kept constant by introducing a diffusion term into the pressure equation. 58 modes were considered. A reverse field configuration was maintained throughout the simulation, up to  $t = 200 \tau_H$ . Negative  $E_\theta$  (shaded region) corresponds to toroidal flux enhancement. For other  $S$  values ( $10^4$ ,  $10^6$ ) and  $\beta$  values (5%), similar trends were observed. Figure 5 shows the magnetic energy of ten dominant modes:  $(1,-10)$ ,  $(1,-11)$ ,  $(1,-12)$ ,  $(1,-13)$ ,  $(1,-9)$ ,  $(1,-14)$ ,  $(1,-15)$ ,  $(1,-16)$ ,  $(0,-1)$ ,  $(1,-17)$  in order of decreasing maximum amplitudes. During the simulation, the central safety factor,  $q(0)$ , was less than 0.1 for most of the time; therefore, all modes except  $(1,-9)$  are resonant modes. The total fluctuating magnetic field energy was about 1% of the equilibrium field energy.

### 3. EFFECT OF SELF-ORGANIZATION ON PLASMA-WALL INTERACTION

To study the relationship between plasma-wall interaction and self-organization, the electron saturation current ( $I_s^-$ ) in the edge region measured by double probes, visible line radiation of metal impurities and the toroidal flux are measured in the same plane. The results of the measurements are shown in Fig. 6. Except for the initial phase before setting up the RFP configuration, the large pulsed peaks in the line radiation and in  $I_s^-$  were synchronous with

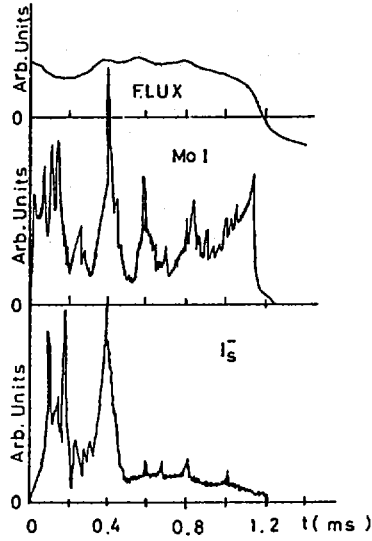


FIG. 6. Time evolutions of electron saturation current ( $I_s^-$ ) in edge region, visible line radiation (MoI) and toroidal magnetic flux.

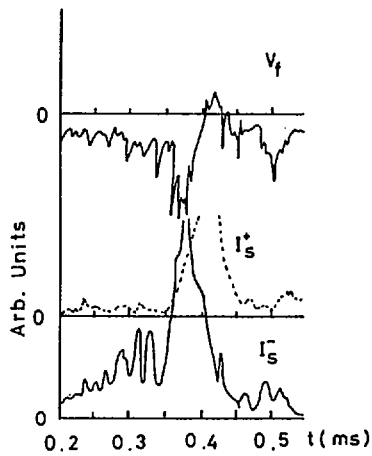


FIG. 7. Time histories of  $I_s^-$ , ion saturation current ( $I_s^+$ ) and floating potential ( $V_f$ ) measured at nearly the same position.

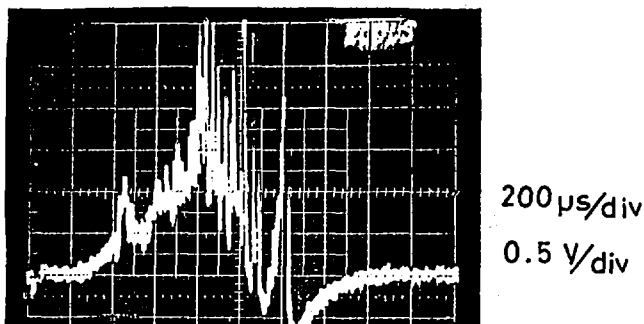


FIG. 8. Typical waveform of soft X-ray measured by surface barrier diode (SBD).

toroidal flux enhancement. These facts show that self-organization enhances the plasma-wall interaction. As the current density increases, the plasma-wall interaction due to self-organization becomes more and more conspicuous.

To study the origin of the metal impurities,  $I_s^-$ , the ion saturation current ( $I_s^+$ ) and the floating potential ( $V_f$ ) are measured at nearly the same positions by triple probes installed behind the limiters. The time evolutions of  $I_s^-$ ,  $I_s^+$  and  $V_f$  are shown in Fig. 7.  $I_s^-$  and  $I_s^+$  start increasing simultaneously at the time of flux enhancement, but  $I_s^-$  varies more rapidly than  $I_s^+$ . As a result we found that the floating potential assumes increasingly negative values first and then returns to zero. The peak value of  $I_s^+$  is nearly equal to that of  $I_s^-$ . These facts indicate that electrons and ions are emitted from the plasma towards the wall, by the self-organizing action.

The soft X-rays measured by a surface barrier diode (SBD) are shown in Fig. 8. There is a slowly changing and a pulsive signal. The occurrence of the latter coincides with toroidal flux enhancement. By using collimators, it is confirmed that almost the entire pulsive soft X-ray activity occurs at the wall. This is consistent with the results obtained from the triple probes. Furthermore, the electron energy is estimated by an absorber method using Be foils. The energy of the slowly changing signal is about 150–300 eV, which is in good agreement with the results of Thomson scattering. The latter signal has an energy of 2 to 8 keV, on the assumption that the electrons collide with the vacuum vessel. This shows that high energy electrons and ions are emitted from the plasma towards the wall by the self-organizing effect and metal impurity influx is caused by these impinging high energy ions.

#### 4. HIGH CURRENT DENSITY OPERATION

High current density operation ( $\geq 4 \text{ MA} \cdot \text{m}^{-2}$ ,  $\geq 100 \text{ kA}$ ) is carried out in STP-3(M). The typical RFP behaviour for high current density is basically the

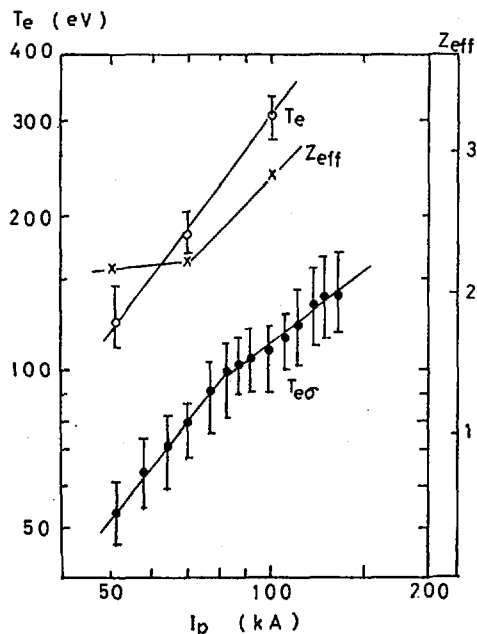


FIG. 9. Relation between electron temperatures ( $T_e$ ,  $T_{e\sigma}$ ) and plasma current for round top operation.

same as in the low current density regime. With increasing plasma current, the self-organizing action sets in, and the corresponding plasma-wall interaction is intensified.

The relationship between electron temperature ( $T_e$ ,  $T_{e\sigma}$ ) and plasma current in the case of round top operation is shown in Fig. 9, together with  $Z_{eff}(T_e/T_{e\sigma})$ . The electron temperature,  $T_e$ , is nearly proportional to the plasma current. On the other hand, the conductivity temperature ( $T_{e\sigma}$ ) shows a tendency to saturate above a plasma current of about 100 kA ( $3.7 \text{ MA} \cdot \text{m}^{-2}$ ). Accordingly,  $Z_{eff}$  increases gradually as the plasma current increases. Since the magnetic fluctuation level decreases slightly, the increment in  $Z_{eff}$  seems to be caused by the influx of metal impurities due to the self-organizing effect. Preliminary bolometer measurements of the radiation power emitted by the plasma support these statements.

## 5. CONCLUSIONS

The self-organizing action and its effect on RFP plasma confinement were studied experimentally and theoretically. It was found that self-organization

is caused by coupling with helical instabilities having  $m = 1$ ,  $n = 9-13$  modes inside the reversal surface and that it enhances plasma-wall interaction. It was confirmed that the dominant process of metal impurity release is caused by ion sputtering. The typical RFP behaviour for high current density is basically the same as that for low current density, except for the increase in plasma-wall interaction. To attain a high current density in RFP, it is important to suppress the plasma-wall interaction caused by the self-organizing action.

### REFERENCES

- [1] TAYLOR, J.B., Phys. Rev. Lett. **33** (1974) 139.
- [2] HAGENSON, R.L., KRAKOWSKI, R.A., Compact Reversed Field Pinch Reactors (CRFPR): Sensitivity Study and Design-Point Determination, Rep. LA-9389-MS, Los Alamos National Laboratory, NM (1982).
- [3] SATO, K.I., Nucl. Fusion **25** (1985) 1301.
- [4] ARIMOTO, H., et al., submitted to Nucl. Fusion.
- [5] ARIMOTO, H., et al., J. Phys. Soc. Jpn. **54** (1985) 1232.
- [6] MATSUOKA, A., et al., to be published in J. Phys. Soc. Jpn.
- [7] AYDEMIR, A.Y., et al., Phys. Fluids **28** (1985) 898.

### DISCUSSION

R.S. PEASE: How do you propose to reduce the undesirable plasma-wall interaction?

K. SATO: The plasma-wall interaction (PWI) due to the dynamo process seems to depend on  $I/N$ , where  $I$  is the plasma current and  $N$  is the line density. With increasing  $I/N$ , PWI increases in reversed field pinches. In STP-3(M), the operating region of  $I/N$  is above  $10^{-13}$  A-m, which is ten times larger than in other machines. In order to decrease the PWI, it is necessary to operate in a regime of low  $I/N$ . We will therefore try to decrease the PWI using carbonization.

## REVERSED FIELD PINCH EXPERIMENTS IN ZT-40M AND ZT-P

K.F. SCHOENBERG, G.A. WURDEN, P.G. WEBER, J.C. INGRAHAM,  
C.P. MUNSON, D.A. BAKER, C.J. BUCHENAUER, L.C. BURKHARDT,  
T.E. CAYTON, J.N. DiMARCO, J.N. DOWNING, R.M. ERICKSON,  
P.R. FORMAN, A. HABERSTICH, R.B. HOWELL, F.C. JAHODA,  
R.S. MASSEY, G. MILLER, R.W. MOSES, Jr., R.A. NEBEL,  
J.A. PHILLIPS, M.M. PICKRELL, A.E. SCHOFIELD, R.G. WATT,  
D.M. WELDON, K.A. WERLEY

Los Alamos National Laboratory,  
Los Alamos, New Mexico,  
United States of America

### Abstract

#### REVERSED FIELD PINCH EXPERIMENTS IN ZT-40M AND ZT-P.

Key experimental research on the Los Alamos ZT-40M and ZT-P Reversed Field Pinch (RFP) experiments is summarized. Fuelling of an RFP by pellet injection has been successfully demonstrated on ZT-40M. When employed with programmed gas injection, the fuelling effectiveness noticeably increases and demonstrates the potential for density control in next-generation RFP devices. The exploration of Oscillating Field Current Drive (OFCD), as a mechanism to provide steady-state RFP operation by low frequency field modulation, is under experimental investigation. Initial results have shown that the amplitude of the plasma current is dependent on the field modulation phase, as predicted by theory. However, the data suggest that the current drive response is presently offset by increased plasma resistance due to modulation enhanced plasma-wall interactions. The use of wall carbonization has been tested for controlling metal impurity influx during OFCD and standard discharges. During normal operation, significant reductions in metallic and oxygen impurities were noted, with a concomitant decrease in the plasma  $Z_{\text{eff}}$ . However, wall carbonization was less effective during OFCD discharges because of its shortened life under the high power load conditions. For certain modes of ZT-40M operation, energetic ion plasmas are obtained, and the observed increase in plasma ion energy can significantly contribute to the total plasma beta. Investigation of ramped current start-up has allowed RFP formation at reduced voltages, and scaling results project acceptable volt-second consumption for future, larger devices. The ZT-P experiment is being used to study design issues, such as dynamic equilibrium control, field error effects, and high current density scaling, for the Los Alamos ZT-H experiment.

### INTRODUCTION

In the last two years, the Reversed Field Pinch (RFP) effort at the Los Alamos National Laboratory has been devoted to conducting research on the ZT-40M[1] and ZT-P[2] experiments, and to developing the design of the high current Los Alamos ZT-H[3] experiment. This paper summarizes key experimental work associated with ZT-40M and ZT-P. It is organized into six

sections: 1. Density control by programmed gas and pellet injection; 2. Steady-state current sustainment by Oscillating Field Current Drive; 3. Impurity control by wall carbonization; 4. Energetic ion plasma experiments; 5. RFP start-up; and 6. ZT-P operations.

## 1. DENSITY CONTROL

Recent experiments on ZT-40M have successfully demonstrated the first pellet refueling of a reversed field pinch (RFP). The four-barrel pneumatic pellet injector, used on Alcator C [4], was modified for ZT-40M operation to inject cylindrical hydrogen or deuterium pellets with radii up to 0.7 mm at velocities of 150 to 800  $\text{m}\cdot\text{s}^{-1}$ . Injection along the major radius at velocities exceeding 400  $\text{m}\cdot\text{s}^{-1}$  into discharges with  $I_\phi = 100$  to 250 kA,  $\bar{n}_e = 1$  to  $8 \times 10^{19} \text{m}^{-3}$  and  $T_e(0) = 100$  to 300 eV, typically resulted in a density increase of  $2 \times 10^{19} \text{m}^{-3}$ . Still photographs taken from above show full penetration for low density discharges, with some toroidal curvature of the trajectory. Data from an array of  $D_\alpha$  monitors and from side photographs show poloidal curvature of the trajectory, with the pellet typically approaching only to 0.1 m of the minor axis ( $a = 0.2$  m). These deflections are attributed to preferential ablation of the pellet by electrons moving along field lines. As a result of the deflections, density profile peaking has not been observed. Also, because the particle confinement time is comparable to the ablation time, only 40 to 60% of the pellet is seen in the plasma particle inventory.

Figure 1(a) shows data from a two-chord FIR interferometer (impact parameters 0 and 0.12 m) for a pellet which curved strongly and remained at  $r > 0.12$  m. This is to be compared to a pellet which penetrated close to the major radius [Fig. 1(b)]. Both pellets initially traveled at 500  $\text{m}\cdot\text{s}^{-1}$  into 230 kA discharges. The electron temperature on axis, measured by Thomson scattering, and ion temperatures, measured by Doppler broadening of impurity lines and a time-of-flight neutral particle spectrometer, decrease sharply at the density rise, and recover as the density decays so that the plasma  $\beta$  is maintained roughly constant. The largest absolute density increase yet observed is shown in Fig. 1(c). Four almost simultaneous pellets were injected into a discharge where the current was ramped from 100 kA to 180 kA in 10 milliseconds. The injection resulted in a six-fold density increase of  $8 \times 10^{19} \text{m}^{-3}$ .

Noticeable improvements in the effectiveness of both pellet injection and gas puffing have been observed when the two techniques are combined. Figure 1(f) shows the density traces for an  $I_\phi = 200$  kA discharge with four pellets, and a sustained total gas puff of 180 torr·l/sec from three piezo-electric

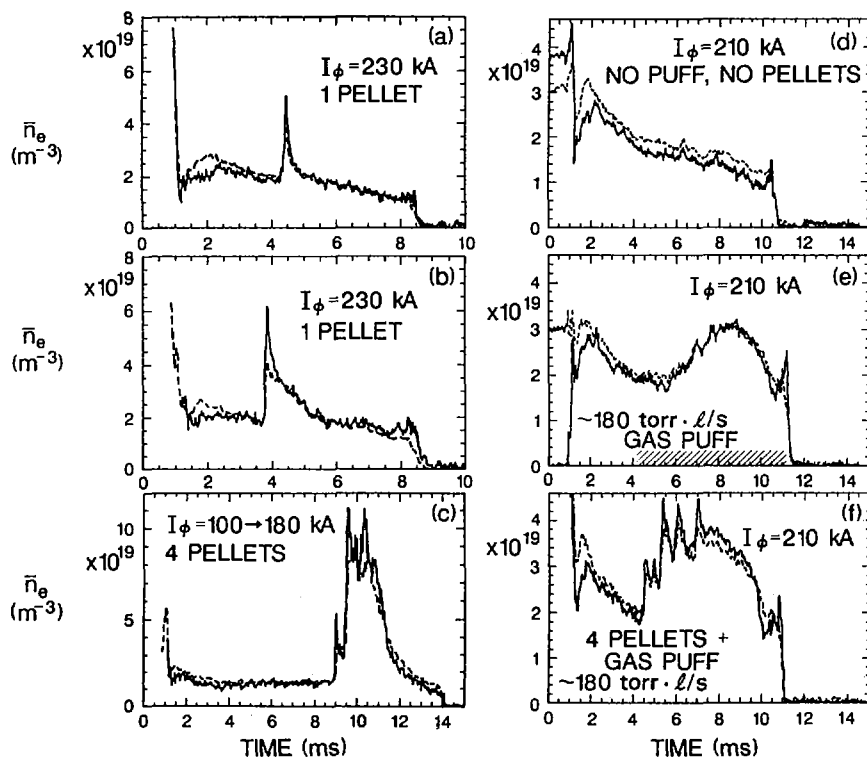


FIG. 1. Mean chordal density as a function of time for density control discharges. The dashed and solid curves denote the  $r = 0$  and  $r = 0.12$  m impact parameters, respectively.

valves around the torus. Figure 1(d) and 1(e) show a comparable discharge without and with gas puffing, respectively. The improved performance with combined gas puffing and pellet injection is hypothesized to result from an increased neutral density in the plasma edge due to strong gas puffing, which suppresses the energetic plasma electrons responsible for the preferential ablation. The data demonstrate the ability to produce a substantial density increase for many particle confinement times over a considerable discharge duration, and demonstrate the potential for density control in future long pulse RFP devices.

## 2. OSCILLATING FIELD CURRENT DRIVE

Steady-state current sustainment by Oscillating Field Current Drive (OFCD) employs a technique in which the toroidal and poloidal magnetic fields at the plasma surface are modulated

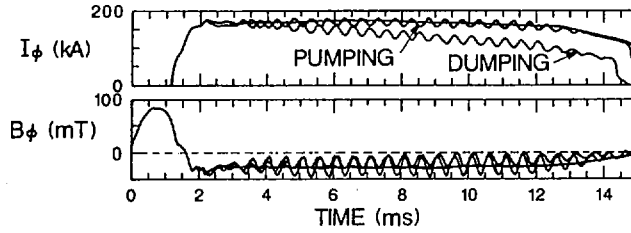


FIG. 2. Plasma current ( $I_\phi$ ) and toroidal magnetic field at the plasma edge ( $B_\phi(a)$ ) for one non-modulated and two OFCD discharges.

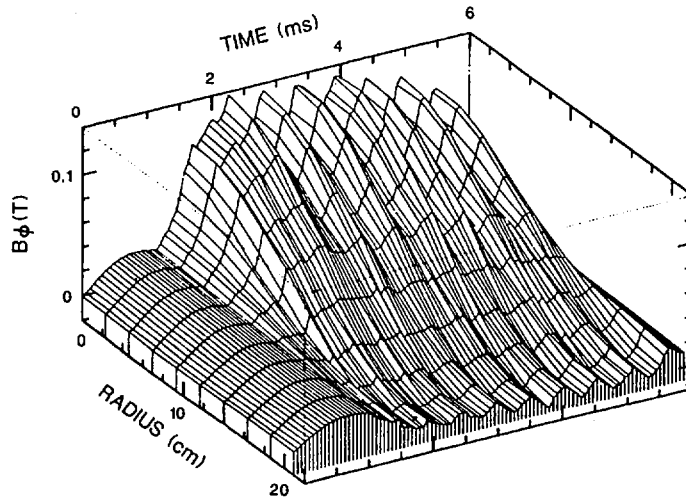


FIG. 3. Time dependent, spatial toroidal magnetic field profile during an OFCD pumping discharge.

in quadrature at audiofrequencies [5,6]. The non-linear coupling of these modulations by the plasma is predicted to provide steady-state maintenance of the mean magnetic fields and hence the plasma current. Because this technique is technologically simple, non-invasive, and scales well to high temperature, high density plasmas[6], the possibility exists for a relatively simple current drive system in future large RFP devices. In addition, OFCD may be applicable to other toroidal confinement systems, provided appropriate "relaxation" mechanisms exist[7,8].

An experimental program was initiated on ZT-40M to assess this current drive technique. Figure 2 illustrates three comparative discharges. The non-modulated curve displays a

nominally flat-topped 180 kA discharge. The modulated traces display the results of applying sinusoidal voltage components to the toroidal and poloidal field circuits, but with different relative phases. For the "pumping" trace, the applied  $\tilde{V}_\theta$  and  $\tilde{V}_\phi$  measured at the plasma edge were driven in quadrature. The "dumping" trace was obtained by changing the driving phase of  $\tilde{V}_\theta$  with respect to  $\tilde{V}_\phi$  by  $\pi$ .

The experimental results were compared with 0-D simulations that use the F- $\theta$  trajectory ( $F = B_\phi(a)/\langle B_\phi \rangle$ ,  $\theta = B_\theta(a)/\langle B_\phi \rangle$ ) and plasma inductance calculated from the Modified Bessel Function Model (MBFM)[6]. The general dependence of discharge behavior on driving phase is in agreement with the 0-D simulations. In addition, internal magnetic field probes have been employed to measure the RFP magnetic field profiles during modulation. The time dependent toroidal field profile for a 50 kA discharge is shown in Fig. 3. The 15% oscillation of  $B_\phi(0)$  on axis is in phase with the plasma current, and  $180^\circ$  out of phase with respect to  $B_\phi$  at the plasma edge. This phase relationship is also in agreement with the MBFM calculation when the model is supplied with the externally measured magnetic fields. Comparisons of the data with 1-D MHD simulations are discussed in Ref. [9].

The strong agreement between the MBFM simulation predictions and the data is encouraging in that it indicates a plasma response necessary for current drive. The data, however, suggest that the failure to increase the current under high power "pumping" conditions is due to an increased plasma resistance resulting from modulation enhanced plasma-wall interactions. For example, during the pumping discharge illustrated in Fig. 2, the 0-D model calculated that a 10 to 15 per cent increase in the bulk plasma resistivity and resistance is necessary to match the experimental results. This is of the same order as the expected OFCD current enhancement, assuming the resistance was not directly affected by the applied modulations. Although investigation of techniques to reduce the wall interactions on ZT-40M is continuing, an unambiguous demonstration of OFCD may require the substantially improved performance characteristics, in terms of plasma resistivity and wall protection, anticipated for ZT-H.

### 3. IMPURITY CONTROL

ZT-40M has typically operated without limiters, or with limiters whose scrape-off lengths are short compared to the connection lengths between the limiters. As a result, the degree of metal contamination in the plasma has been high enough to account for most of the radiated power and for the spectroscopically determined  $Z_{\text{eff}}$ [10]. Because the metal influx

from the Inconel wall[11] increases strongly with the ratio of plasma current to electron inventory ( $I/N$ ), a number of methods, including pulsed discharge cleaning, gas puffing, pellet injection, and wall carbonization, have been used to maintain an appropriately high density at a given current.

Wall carbonization[12] entails depositing thin layers of carbon on the Inconel vacuum liner with the intent of substituting a low-Z wall material for some higher-Z elements. Depending on the wall carbonization method, one can either generate a metal carbide layer or a layer of carbon whose structure is a function of the deposition procedure[12]. With the method utilized on ZT-40M[13], approximately 40 monolayers of carbon were deposited. The carbon layer was presumably not the very hard structure that can be obtained at elevated temperatures[12].

Reversed field pinch discharges were obtained almost immediately after carbonization and showed significant differences in impurity content. Specifically, C III emission implied an increase in carbon from 0.06 % with a metal wall to 1-2 % after carbonization. The reduction in metal impurities was approximately a factor of two, assuming self-similar profiles, and both metals and oxygen were at the low end of their historical range. Soft x-ray fluxes, which are sensitive to metal impurities, were also lower. Due to the increased density, electron temperatures measured on axis by Thomson scattering showed a reduction from 360 to 200 eV for discharges with carbonization compared to the metal wall case. However, the plasma resistivity was nearly the same[13], implying a reduction in  $Z_{\text{eff}}$  assuming the resistivity behaves classically.

The beneficial impurity control effects of carbonization on ZT-40M are relatively short-lived. Spectroscopy indicates an e-folding time of 30-60 discharges for the carbon level to decrease and the metal influx to increase. This effect was further accelerated on the liner segment that lies under the gap in the shell and during OFCD discharges, implying that a large power flux will remove the layer more rapidly. However, in future RFP devices such as ZT-H, a combination of an effective limiter set and carbonization at higher wall temperatures is expected to improve the effectiveness of this impurity control technique.

#### 4. ENERGETIC ION PLASMAS

Normally, ZT-40M operates in a regime where the inferred ion temperatures are approximately equal to the electron temperature. However, during low density ramped current discharges, OFCD discharges, or high- $\theta$  flat-topped discharges,

enhanced ion heating during the discharge is apparent. For example, in discharges where the plasma current was ramped from 100 to 200 kA with  $T_e(o) \sim 300$  to 400 eV and  $\bar{n}_e \sim 1.8 \times 10^{19} \text{ m}^{-3}$ , inferred ion temperatures exceeded  $T_e$  by at least a factor of two.

Measurements of ion energies in ZT-40M were made using Doppler broadening of light impurity ions (CV, NVI, OVII)[14], a Time-Of-Flight (TOF) charge exchange neutral particle spectrometer, measured deposition profiles in silicone samples exposed to the plasma[11], and neutron production. Absolute neutron yield was obtained from a post-shot arsenic activation detector[15], while the time resolved neutron rate was obtained from a  $\gamma$ -insensitive ZnS(Ag) proton recoil detector, as well as a  ${}^6\text{LiI}$  scintillator.

A TOF neutron spectrometer, from Phillips Petroleum Company[16], has indicated that the measured neutron flux corresponds to 2.5 MeV D-D neutrons, but with insufficient statistics to resolve a spectral width or shift. For the ion impurity inferred temperatures, the thermal characteristics of the high energy deuterons are also unresolved. However, a thermal deuterium ion distribution with  $T_i > T_e$  is consistent with neutral energy spectra ( $\leq 2$  keV) measured by the TOF charge exchange spectrometer. The enhanced ion heating observed, during energetic ion discharges, may be sufficient to maintain a constant  $\beta_{\text{TOTAL}}$ , in spite of the slow decrease of  $\beta_e$  with I/N which was previously reported[17,18].

## 5. RFP START-UP

Studies on ZT-40M have addressed start-up methods in order to assess their use in the design of high current (multi-mega-ampere) RFP devices. The standard matched mode start-up, in which the toroidal flux is kept constant, has been successful for RFP experiments, but presents problems for future high current devices. For example, a fast matched mode start-up requires the use of high loop voltage, while a slow start suffers from a long duration before field reversal, resulting in increased energy losses and resistive V·s consumption.

The ramped mode[1,19] uses a fast, low-current, matched mode RFP formation followed by a slow ramp to the final high current. These ramped discharges have allowed successful RFP start-up at reduced voltages, and their scaling results project acceptable V·s consumption for initiating discharges in ZT-H[3,19], the next-generation RFP experiment at Los Alamos.

A survey of ramped mode start-up as a function of ramping rate was made to determine its physical characteristics for use in scaling to high currents. It was found that the bulk plasma

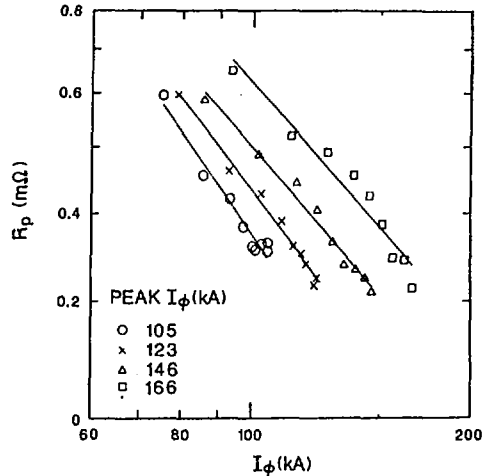


FIG. 4. Calculated bulk plasma resistance ( $R_p$ ) as a function of the instantaneous current during a ramped discharge. Each curve corresponds to a different ramping rate for a duration of 11 ms. The curves are labelled by the peak value of  $I_\phi$  measured at the end of the ramp.

resistance  $R_p$ , as deduced using the 0-D model[6], increased with the ramping rate (Fig. 4.). This result may be attributed to an increased  $Z_{eff}$ , due to enhanced wall loading and impurity release accompanying the faster ramping rates. The increased resistance may also be due to the increased dynamo activity needed for the large rate of toroidal flux generation during the faster ramps. Since the dynamo plays a prominent role during ramped start-up, ramping provides a valuable experimental basis for improving the understanding of RFP discharges[20,21,22].

## 6. ZT-P OPERATIONS

The ZT-P experiment[2] was designed as a prototype for the ZT-H experiment. ZT-P utilizes an air-core poloidal field system to drive the plasma current and provide plasma equilibrium with intrinsically low magnetic field errors. ZT-P began operation in October 1984 and obtained its first RFP plasma discharge in January 1985. To date, ZT-P has investigated ramped RFP plasma start-up and air-core RFP equilibrium control by passive field programming, using both flat-topped and decaying current discharges. For these discharges, which have been run up to 60 kA ( $\langle j \rangle \sim 5 \text{ MA/m}^2$ ) for durations up to 1.2 ms, spectroscopic measurements indicate a hot ( $T_e \geq 70 \text{ eV}$ ) and relatively low-Z plasma. Ongoing ZT-P experiments are continuing to investigate ZT-H design issues,

including dynamic RFP equilibrium control in an air-core system, as well as the effects of imposed field errors on performance. High current density RFP scaling is also being studied using recently fielded 2-color interferometry and Thomson scattering systems.

#### ACKNOWLEDGMENTS

The authors gratefully acknowledge the contributions to this work by visiting staff members, including Dr. Zensho Yoshida, Dr. Shunjiro Shinohara, Dr. Sadao Masamune, Ms. Elizabeth Nilles, and Dr. Klaus Buchl. We are also grateful to the Los Alamos RFP operations team for their assistance and cooperation. This work was supported by the U.S. Department of Energy.

#### **REFERENCES**

- [1] BAKER, D.A., BUCHENAUER, C.J., BURKHARDT, L.C., et al., in Plasma Physics and Controlled Nuclear Fusion Research 1984 (Proc. 10th Int. Conf. London, 1984), Vol. 2, IAEA, Vienna (1985) 439.
- [2] SCHOENBERG, K.F., et al., ZT-P: An Advanced Air Core Reversed Field Pinch Prototype, Rep. LA-10593-MS, Los Alamos National Lab. (1986).
- [3] THULLEN, P., SCHOENBERG, K.F. (Eds), ZT-H Reversed Field Pinch Experiment, Rep. LA-UR-84-2602, Los Alamos National Lab. (1985).
- [4] GREENWALD, M., GWINN, D., MILORA, S., et al., Phys. Rev. Lett. **53** (1984) 352.
- [5] BEVIR, M.K., GRAY, J.W., Proceedings of the Reversed Field Pinch Theory Workshop, Rep. LA-8944-C, Los Alamos National Lab. (1981) 176.
- [6] SCHOENBERG, K.F., GRIBBLE, R.F., BAKER, D.A., J. Appl. Phys. **56** (1984) 2519; Rep. LA-9161-MS, Los Alamos National Lab. (1984).
- [7] BELLAN, P.M., Tokamak applications of helicity injection, Los Alamos Current Drive Workshop 5/86, personal communication.
- [8] HOGAN, J.T., OFCD studies at ORNL, Los Alamos Current Drive Workshop 5/86, personal communication.
- [9] NEBEL, R.A., et al., Paper IAEA-CN-47/D-V-12, these Proceedings, Vol. 2.
- [10] WEBER, P.G., Phys. Fluids **28** (1985) 3136.
- [11] BASTASZ, R.R., CAYTON, T.E., J. Nucl. Mater., to be published.
- [12] WINTER, J., WAELBROECK, F., WIENHOLD, P., et al., J. Nucl. Mater. **122&123** (1984) 1187.
- [13] CAYTON, T.E., DOWNING, J.N., WEBER, P.G., et al., J. Nucl. Mater., to be published.
- [14] HOWELL, R.B., NAGAYAMA, Y., Phys. Fluids **28** (1985) 743.
- [15] JACOBS, E.L., BONAPARTE, S.D., THATCHER, P.D., Nucl. Instrum. Methods **213** (1983) 387.
- [16] WALKER, S.E., PRESZLER, A.M., MILLARD, W.A., Rev. Sci. Instrum. **57** (1986) 1740.
- [17] WURDEN, G.A., WELDON, D.M., WEBER, P.G., et al., Bull. Am. Phys. Soc. **30** (1985) 1402.
- [18] ALPER, B., EVANS, D.E., STOREY, D.P., TSUI, H., Bull. Am. Phys. Soc. **30** (1985) 1406.

- [19] PHILLIPS, J.A., et al., Observations on Ramped Current Operations in ZT-40M, Rep. LA-10060-MS, Los Alamos National Lab. (1984).
- [20] CARAMANA, E.J., BAKER, D.A., Nucl. Fusion **24** (1984) 423.
- [21] CARAMANA, E.J., SCHNACK, D.D., Phys. Fluids **29** (1986) 3023.
- [22] HOWELL, R.B., INGRAHAM, J.C., WURDEN, G.A., WEBER, P.G., BUCHENAUER, C.J., Rep. LA-UR-86-1727, Los Alamos National Lab. (1986), submitted to Phys. Fluids.

## EXPERIMENTAL STUDIES OF REVERSED FIELD PINCH IN REPUTE-1 AND ULTRA-LOW-q DISCHARGE

N. ASAKURA<sup>1</sup>, A. FUJISAWA<sup>1</sup>, T. FUJITA, Y. FUKUDA,  
H. HATTORI, N. INOUE, S. ISHIDA, K. ITAMI, Y. IWATA, H. JI<sup>1</sup>,  
Y. KAMADA, K. KUSANO<sup>2</sup>, S. MATSUZUKA<sup>1</sup>, K. MIYAMOTO<sup>1</sup>,  
J. MORIKAWA, C.P. MUNSON<sup>3</sup>, Y. MURAKAMI, Y. NAGAYAMA<sup>1</sup>,  
H. NIHEI, S. ONODERA<sup>1</sup>, M.T. SAITO, T. SATO<sup>2</sup>, S. SHINOHARA<sup>1</sup>,  
H. TOYAMA<sup>1</sup>, Y. UEDA<sup>1</sup>, M. UTUMI, H. YAMADA,  
K. YAMAGISHI<sup>1</sup>, Z. YOSHIDA  
Department of Nuclear Engineering,  
Faculty of Engineering,  
University of Tokyo,  
Tokyo, Japan

### Abstract

#### EXPERIMENTAL STUDIES OF REVERSED FIELD PINCH IN REPUTE-1 AND ULTRA-LOW-q DISCHARGE.

The general behaviour and the relaxation process of the RFP plasma in the REPUTE-1 experiment are described. The RFP plasma is formed in the resistive shell, with a time constant of 1 ms; the maximum discharge duration is 2.5 ms, at present. The dynamics of the relaxation phenomena is studied by inserting magnetic probes. It is observed that the current density profile and the  $\lambda(r) = \mu_0 \vec{j} \cdot \vec{B} / B^2$  profile become peaked and the safety factor  $q_0$  on axis decreases during the current sustainment phase. Then,  $q_0$  recovery takes place in a time of the order of several tens of the Alfvén transit time and the toroidal current density flattens; this process is repeated. These observations and the results of resistive MHD simulation correspond to each other satisfactorily. Stable toroidal discharges in an ultra-low-q (ULQ) regime, i.e.  $1/2 \leq q_a < 1$ , have been realized and sustained for a much longer time than the characteristic MHD time. An ULQ equilibrium is set up through MHD relaxation, promoted by an  $m = 1$  global kink instability and characterized by a  $dq/dr < 0$  profile. A class of  $dq/dr < 0$  equilibria is shown to be stable against low  $n$  kink modes, by using an energy principle.

### 1. DEVICE

REPUTE-1 (Reversed Field Pinch, University of Tokyo Experiment) is a reversed field pinch (RFP) device with a major radius  $R$  of 82 cm, a minor radius  $a_p$  of 20 cm and a flux swing of the iron core transformer  $\phi$  of 1.6 V·s [1, 2]. The vacuum chamber of Inconel bellows is surrounded by a 5 mm thick stainless steel

<sup>1</sup> Department of Physics, Faculty of Science, University of Tokyo, Tokyo, Japan.

<sup>2</sup> Institute for Fusion Theory, Hiroshima University, Hiroshima, Japan.

<sup>3</sup> Los Alamos National Laboratory, Los Alamos, NM, USA.

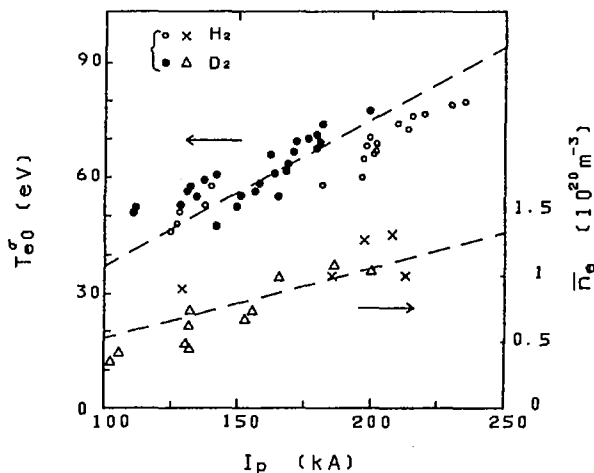


FIG. 1. Dependence of  $\bar{n}_e$  and  $T_{e0}^\sigma$  (under the assumption of  $Z_{\text{eff}} = 1$  and modified Bessel function model) on plasma current  $I_p$  ( $\Theta = 1.6$ – $1.8$ ) for optimized conditions. Filling pressure is about 3.2 mtorr.

shell with a time constant of 1 ms for vertical field penetration. The equilibrium field is applied externally by vertical field coils wound outside the toroidal field coils. The rise time of the plasma current is 0.5 or 1 ms. This device is also used for ultra-low-q discharge experiments.

## 2. RFP EXPERIMENT IN REPUTE-1

### 2.1. Parameters of RFP plasma in REPUTE-1

Experiments have been carried out in the  $I_p < 240$  kA range of plasma current. The RFP plasma is formed in the resistive shell with a 1 ms time constant; the maximum discharge duration is 2.5 ms, at present. An enhancement of the  $m = 1$  MHD perturbation and a deviation of the externally applied vertical field from the value required for equilibrium are observed before discharge termination. The line averaged electron density,  $\bar{n}_e$ , measured by a  $\text{CO}_2$  laser interferometer at the current flat-top, and the conductivity electron temperature  $T_{e0}^\sigma$  on axis increase approximately linearly with the plasma current in optimized conditions ( $\bar{n}_e \sim 1.0 \times 10^{14} \text{ cm}^{-3}$ ,  $T_{e0}^\sigma \sim 80 \text{ eV}$  at  $I_p = 200$  kA, on the assumption of  $Z_{\text{eff}} = 1$ ; see Fig. 1). The O V line is burnt through during current flat-top. The ion temperature  $T_i$ , measured by a time of flight method, is about 80 eV at 200 kA. The time variation of the plasma parameters of a typical RFP discharge, in the case of a high pinch parameter  $\Theta$ , is shown in Fig. 2.

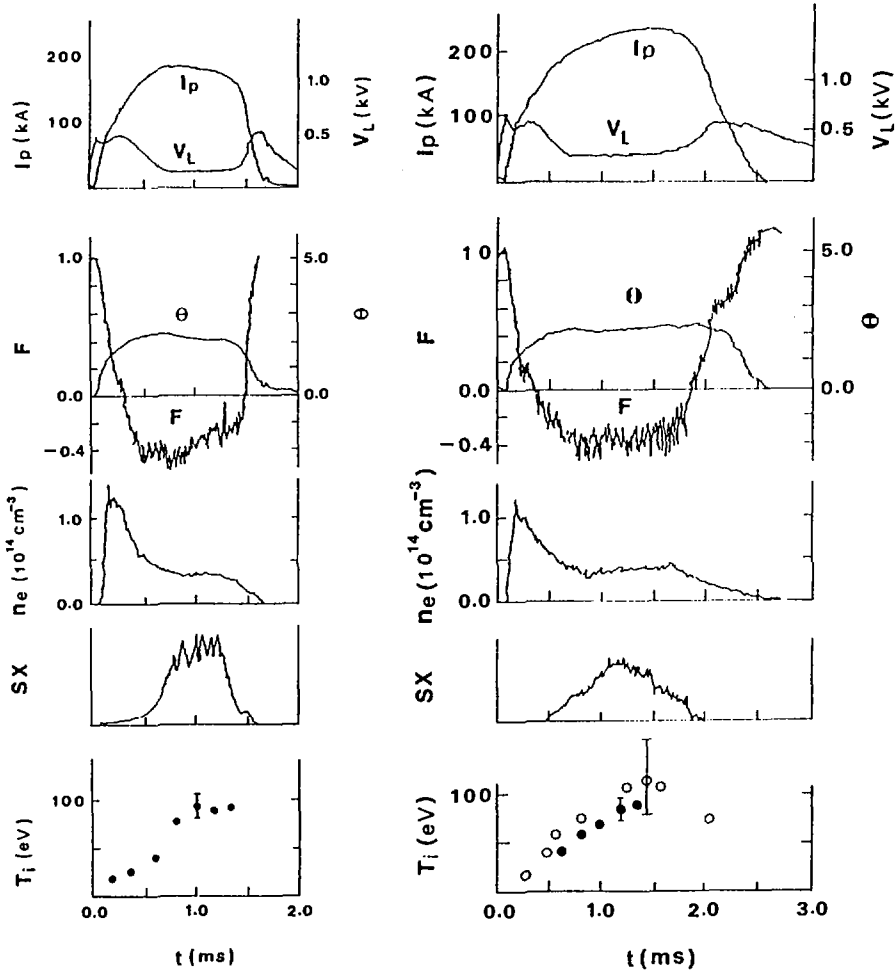


FIG. 2. Time variation of loop voltage  $V_L$ , plasma current  $I_p$ , pinch parameter  $\Theta$ , reversal ratio  $F$ , line averaged electron density  $\bar{n}_e$ , relative intensity of soft X-ray  $SX$  along horizontal line measured by surface barrier diode ORTEC CR-017-050-100 with  $4 \mu\text{m}$  thick polypropylene filter, ion temperature  $T_i$  measured by time of flight method (closed circles) and by Doppler broadening of  $O V$  line ( $278 \text{ nm}$ , open circles) in typical RFP discharges.

## 2.2. Relaxation process in RFP plasma

The internal distribution of the magnetic fields and field fluctuations of the poloidal and toroidal fields during current flat-top is measured in detail by using inserted magnetic probes in order to study the dynamics of the relaxation phenomena in the range of  $I_p < 130 \text{ kA}$ . The magnetic fields in the toroidal and poloidal directions are measured simultaneously at six radial points  $3.4 \text{ cm}$  apart from each other.

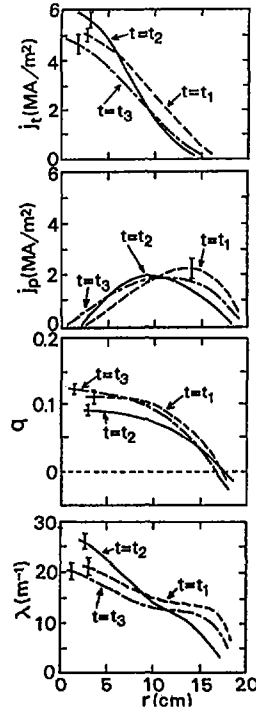


FIG. 3. Time evolution of toroidal and poloidal current densities,  $j_t(r)$  and  $j_p(r)$ , safety factor  $q(r)$  and  $\lambda(r)$  parameter estimated from magnetic probe measurements at different times  $t_1 = 0.56$  ms,  $t_2 = 0.66$  ms and  $t_3 = 0.70$  ms for  $\Theta \approx 1.9$  operation.

External magnetic probes and an array of surface barrier diodes without filter for VUV measurement are also used. A large amplitude oscillation of the poloidal field with mode numbers  $m = 0$  and  $m = 1$  is observed when the pinch parameter  $\Theta$  exceeds about 1.75. Figure 3 shows the time evolution of the toroidal and poloidal current densities,  $j_t(r)$ ,  $j_p(r)$ , the safety factor  $q(r)$  and  $\lambda(r)$  parameter defined by  $\lambda(r) = \mu_0 \vec{j} \cdot \vec{B} / B^2$ , estimated from magnetic probe measurement and plotted at different times  $t_1 = 0.56$  ms,  $t_2 = 0.66$  ms and  $t_3 = 0.70$  ms from the start of the discharge ( $\Theta \approx 1.9$ ). The safety factor on axis,  $q_0$ , becomes lower, because of the peaking of the current density profile ( $t_1 = 0.56$  ms  $\rightarrow$   $t_2 = 0.66$  ms); the  $m = 1$  fluctuation of the VUV signal becomes large. Then,  $q_0$  recovery takes place in a time ( $< 40 \mu\text{s}$ ) of several tens of the Alfvén transit time,  $\tau_A$  and the toroidal current density flattens. The RFP plasma reaches a more relaxed state as is seen from the  $\lambda(r)$  profile at  $t_3 = 0.70$  ms as the  $q_0$  value recovers (increases); this process is repeated (Fig. 4). While the  $q_0$  value recovers, toroidal flux is generated. These observations and the results of a resistive MHD simulation [3–5] show good correspondence to each other, and these experimental results could be explained by non-linear, driven reconnection of a global (non-resonant) helical mode. A lower limit of

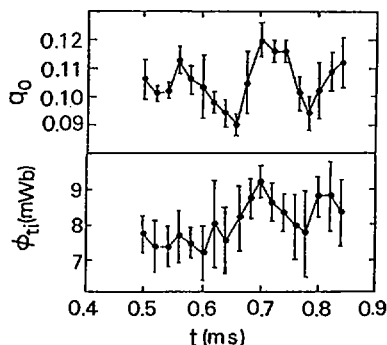


FIG. 4. Time variation of safety factor on axis,  $q_0$ , and toroidal flux  $\phi_{t1}$  calculated from magnetic field profile.

the  $q_0$  value exists at  $\sim 0.095$ , and the  $q_0$  value after recovery exceeds 0.11–0.12, in most cases. The observed dominant mode is  $(m,n)=(1,9)$ . These results are consistent with the stability limit of an ideal internal  $m = 1$  kink mode. We observe an increase in the ion saturation current of the Langmuir probe at the plasma edge, at the time of  $q_0$  recovery. This suggests that the plasma energy loss is enhanced by the reconnection process.

### 3. ULQ DISCHARGE

We shall now describe the observation of stable ultra-low- $q$  equilibria. The ultra-low- $q$  (ULQ) regime, i.e.  $0 < q_a < 1$ , studied here lies in the parameter region intermediate between tokamak and RFP. Z-pinch discharges as were studied extensively in the old days belong to the ULQ discharge. Their equilibria were, however, destabilized by kink instabilities in the characteristic MHD time-scale (about the Alfvén time) [6].

We have realized stable toroidal discharges against a global kink mode with  $q_a \sim 1/2$ , through the relaxation phenomena. The basic idea of the production of ULQ equilibria has been proven experimentally in REPUTE-1 [7]; TORIUT-6 ( $R/a = 0.33/0.05$  m) was constructed for the specific purpose of ULQ experiments. Figure 5 shows typical ULQ discharges on TORIUT-6 in different two operational schemes. In the discharge of Fig. 5(a), the plasma is raised to the MHD excited state by the current spike in the startup phase. Then, it experiences an MHD relaxation associated with a global kink mode  $((m,n) = (1,3))$  and enters a quasi-stable phase analogous to the quiescent phase of an RFP, where the amplitude of the poloidal field fluctuation at the wall is less than 2% of the equilibrium field. An ion density pumpout phenomenon is also observed simultaneously with the relaxation. The magnetic Reynolds number,  $S$ , is estimated to be around  $5 \times 10^{13}$ , during ULQ

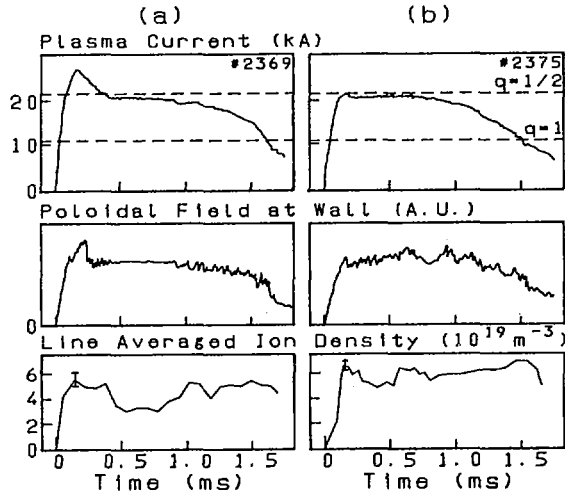


FIG. 5. Plasma current, poloidal field at wall and line averaged ion density measured by a neutral beam probe for ULQ discharges on TORIUT-6: (a) set up through MHD relaxation, (b) without relaxation.

quiescence. After a period of a quasi-stable state for  $600 \mu\text{s}$ , another global kink instability ( $(m,n) = (1,2)$ ) is excited and degrades the plasma. Obvious differences from the other discharge without current spike can be seen as is shown in Fig. 5(b). The fluctuation of the magnetic field is much larger than in the former case, and the  $(1,2)$  kink instability appears in an early phase of the discharge. The plasma is not stable against MHD modes throughout the discharge.

The toroidal current density and the  $q$ -profiles derived from the local field measurements by inserted probes are shown in Fig. 6 for the same discharges as are illustrated in Fig. 5. When the stable ULQ state is set up at  $t = 466 \mu\text{s}$ , the current profile is hollow in the central region, and  $dq/dr$  is negative and  $q$  lies between two rational values, i.e.  $1/3$  and  $1/2$  (see Fig. 6(a)). The poloidal field decreases around the edge of the plasma and in the vacuum region, which indicates that the volume current does not flow behind the limiter. The  $dq/dr < 0$  state is maintained for around  $600 \mu\text{s}$  and no instabilities are observed to degrade the plasma within that scale. However, the magnetic field diffusion ( $\tau_R \approx 200 \mu\text{s}$  in these experiments) slowly deforms the field structure to the state with  $dq/dr > 0$ , where the global modes are destabilized. On the other hand, while the  $dq/dr$  is a little negative in the initial phase by the skin effect of the current penetration, the stable ULQ equilibrium cannot be formed without the spire of the current (see Figs 5(b) and 6(b)). We can conclude from the comparison between two shots that whether the relaxation takes place or not makes a fundamental difference in equilibria.

Linear stability against ideal MHD modes is studied numerically by the energy principle. A class of  $dq/dr < 0$  ULQ equilibria is shown to be stable against low- $n$

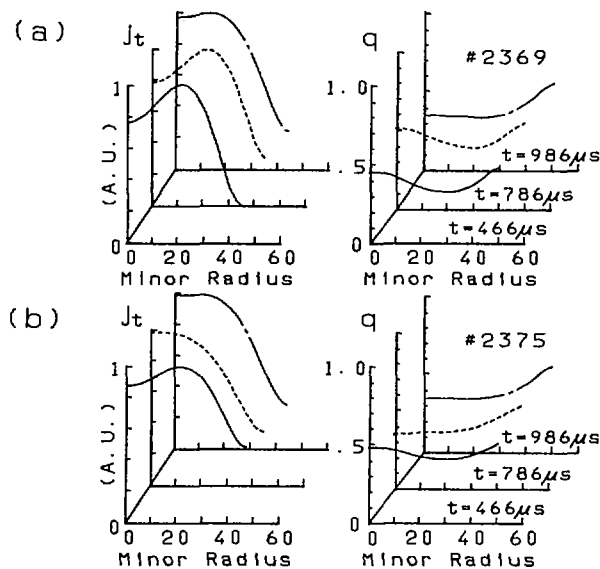


FIG. 6. Toroidal current density and  $q$ -profile evolution. Figures (a) and (b) correspond to discharges (a) and (b) of Fig. 5, respectively. Unit of minor radius is mm.

kink modes. The maximum beta limited by kink mode stability is about 5%. A preliminary estimate of the average toroidal beta is typically around 2% in TORIUT-6 experiments. The global mode stability is robust enough to permit a certain vacuum region between the plasma and the wall (typically, the radius ratio  $\sim 1.1$ ). Local modes are destabilized in the ULQ equilibrium because of the existence of the pitch minimum. They are, however, fairly localized in the pitch minimum region, and their growth rate is by an order of magnitude smaller than those of the internal kink modes.

The setting up of ULQ equilibrium is simulated and analysed by a 3-D MHD code and contrasted with the self-reversal mechanism of RFP and the sawtooth activity in a tokamak. It is concluded that the non-linear growth of the global helical kink instability and the driven reconnection lead to a stable  $dq/dr < 0$  state in the ULQ region. This relaxation process occurs in the relatively high  $S$  regime ( $> 10^3$ ). In the low  $S$  regime, the evolution is dominated by magnetic field diffusion, and no  $dq/dr < 0$  state is attained. Experiments and MHD simulation have led to a consistent and comprehensible picture of ULQ physics in terms of MHD relaxation.

## REFERENCES

- [1] MIYAMOTO, K., INOUE, N., Nucl. Fusion **25** (1985) 1303.
- [2] ASAKURA, N., FUJITA, T., HATTORI, K., INOUE, N., ISHIDA, S., et al., Plasma Phys. Controll. Fusion **28** (1985) 805.

- [3] SCHNACK, D.D., CANAMARA, E.J., NEBEL, R.A., Phys. Fluids **28** (1985) 321.
- [4] SATO, T., KUSANO, K., Phys. Rev. Lett. **54** (1985) 808.
- [5] KUSANO, K., SATO, T., Nucl. Fusion **26** (1986) 1051.
- [6] FURTH, H.P., Phys. Fluids **28** (1985) 1595.
- [7] YOSHIDA, Z., et al., J. Phys. Soc. Jpn. **55** (1986) 389.

## DISCUSSION

T. TAMANO: I should like to ask two questions. First, ultra-low- $q$  discharges last longer than RFP discharges. Do you have any explanation for that? Second, did you observe that the  $m = 1$ ,  $n = 10$  mode appeared and disappeared according to the change in  $q(0)$ ?

K. MIYAMOTO: RFP plasmas are likely to be unstable for high  $n$  modes and are sensitive to the effect of local error fields. Ultra-low- $q$  plasmas have a strong toroidal field compared to the poloidal field and may withstand the local perturbations.

In reply to your second question, although  $n = q$  is the dominant mode, there are several different  $n$  modes. We did not study the differences in mode spectrum for the change in  $q(0)$  in detail, but in any case we did not observe any big difference in fluctuation modes for the  $q(10)$  change during a discharge.

## HEATING AND CONFINEMENT STUDIES IN REVERSED FIELD PINCHES

V. ANTONI, A. BUFFA, L. CARRARO, S. COSTA,  
P. De SIMONE, G. FLOR, F. FLORA, L. GABELLIERI,  
M. GIUBBILEI, L. GIUDICOTTI, P. INNOCENTE,  
K. JAIN<sup>1</sup>, P. MARTIN, S. MARTINI, D. MERLIN,  
S. ORTOLANI, R. PACCAGNELLA, M.E. PUIATTI,  
B. SASS<sup>2</sup>, P. SCARIN, H. SORENSEN<sup>2</sup>, M. VALISA,  
K. WEISBERG<sup>2</sup>, S. ZAGO, E. ZILLI

Associazione Euratom-ENEA-CNR,  
Istituto Gas Ionizzati,  
Consiglio Nazionale delle Ricerche,  
Padua, Italy

### Abstract

#### HEATING AND CONFINEMENT STUDIES IN REVERSED FIELD PINCHES.

A possible interpretation of the large resistivity anomaly factors characteristic of the low density regime is related with an increase of  $Z_{\text{eff}}$  in the plasma edge region, leading to an enhanced dynamo contribution to the apparent on-axis resistivity. The natural tendency of the discharge to evolve towards a low density, high  $I/N$  regime is counteracted by pellet injection, resulting in higher beta discharges. The sustainment of the RFP distribution can be interpreted as the outcome of periodical relaxation processes which counteract the resistive diffusion. Resistive  $m=1$  instabilities are a probable mechanism underlying relaxation; they set a limit to  $q$  on axis of about  $\frac{2}{3} a/R$ . The expected plasma performance in the RFX experiment is discussed.

### 1. INTRODUCTION

During 1985-1986, the experiments on Reversed Field Pinches (RFP) in ETA-BETA II have been aimed at a more detailed study of the physics phenomena underlying plasma heating and confinement as well as sustainment of the configuration. Since the 1984 IAEA conference [1], more detailed measurements have been carried out, with spatial resolution of plasma density, temperature, impurities, fluctuations and mean magnetic field [2, 3]. From these measurements it has

<sup>1</sup> Institute for Plasma Research, Gandhinagar, Ahmedabad, India.

<sup>2</sup> Risø National Laboratory, Roskilde, Denmark.

become clear that the RFP behaviour is strongly related with the continuous relaxation process and the consequent sustainment of the magnetic field profiles. In particular, distinct progress has been made in the following areas:

- (a) *Density dependence of heating and confinement:* The confinement degradation observed in the low density regime [4] has been interpreted as being due to the enhanced dissipation associated with the RFP profile sustainment when larger  $Z_{\text{eff}}$  values are present in the plasma edge region [5]. These studies have stressed even more the importance of density sustainment. First results of pellet injection are reported in this paper.
- (b) *MHD stability and  $q$ -limits of the mean magnetic field profiles.* During the sustainment phase, regular oscillations of the on-axis safety factor  $q(0)$  of about  $\frac{2}{3} a/R$  have been measured [3] and the MHD stability analysis shows that this limit on  $q(0)$  is related with  $m = 1$  tearing modes resonant inside the region of toroidal field reversal [6].

Finally, beta limits and confinement scaling are briefly discussed and the expected parameters of the RFX experiment [7, 8] under construction at Padua are given.

## 2. DENSITY DEPENDENCE OF HEATING AND CONFINEMENT

### 2.1. Resistivity anomaly factor

On ETA-BETA II, it has been observed [2, 4] that the low density regime (with an  $I/N$  ratio of  $\geq 10^{-14}$  A·m, where  $N$  is the cross-section integrated density) is associated with a degraded confinement time, although it is characterized by high electron temperatures. This confinement degradation is associated with a decrease of beta and with a strong increase of the on-axis resistivity anomaly factor, defined as

$$Z_{\text{eff}}^*(0) = \eta^*(0)/\eta_{\text{Spitzer}, Z=1}(0)$$

where  $\eta^*(0)$  is the resistivity derived from Ohm's law on axis,  $\eta^*(0) = V_{\text{loop}}/(2\pi R J_{\phi}(0))$ . The values of  $Z_{\text{eff}}^*(0)$  may exceed 15 in some cases and show a clear correlation with the  $I/N$  parameter [4]. With the assumption of a uniform effective ion charge  $Z_{\text{eff}}$ , the highest  $Z_{\text{eff}}^*(0)$  can be accounted for only marginally and by assuming the highest possible estimates for the ion charge  $Z_{\text{eff}}$  [4], even by computing the on-axis resistivity from a helicity balance as  $\eta^k(0) = \Phi V_{\text{loop}} / \int_V \eta \vec{J} \cdot \vec{B} dv$  (where  $\tilde{\eta}(r)$  is the resistivity normalized to the on-axis value).

On the other hand, we have recently considered the effect of a non-uniform  $Z_{\text{eff}}$  and we find that large resistivity anomaly factors can be associated with increased dissipation in the outer plasma region connected with a hollow profile of the ion effective charge [5]. From the line emission profile of the dominant impurity ions

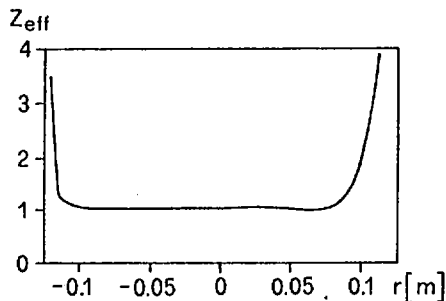


FIG. 1. Experimental profile of ion effective charge.

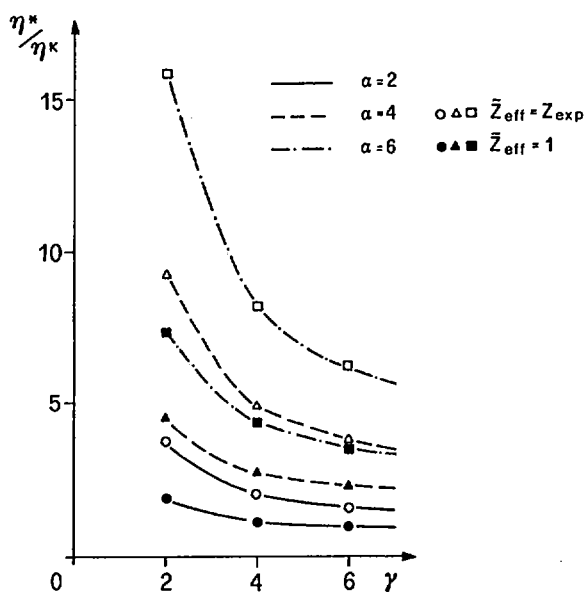


FIG. 2. Comparison of the  $\eta^*(0)/\eta^k(0)$  values corresponding to the experimental  $\bar{Z}_{eff}$  profile and those with  $\bar{Z}_{eff} = 1$  ( $\bar{Z}_{eff}(r) = Z_{eff}(r)/Z_{eff}(0)$ ) for several  $J$  and  $T_e$  profiles.

(oxygen) measured in ETA-BETA II [5] the radial profile of the ion effective charge can be derived and is indeed found to be hollow, as shown in Fig. 1. The corresponding values of the  $\eta^*(0)/\eta^k(0)$  ratio are shown for several current density and electron temperature profiles in Fig. 2. The current density profiles are described by  $\mu = \mu_0(J_1/B)$ , with  $\mu/\mu(0) = 1 - (r/a)^\alpha$  (see Section 3), and the expression  $T_e/T_e(0) = 1 - (r/a)^\gamma$  is used to study the effect of different  $T_e$  profiles. It can be

seen that for typical values of  $\alpha$  and  $\gamma$  (between 2 and 4 as deduced from the experimental profiles [2, 3]), the  $\eta^*(0)/\eta^k$  ratio ranges between 3 and 10. To highlight the effect of a non-uniform  $Z_{\text{eff}}$ , the results obtained with  $Z_{\text{eff}} = \text{const}$  are also reported. The apparent resistivity on axis,  $\eta^*(0)$ , is higher by a factor of about two for the experimental  $Z_{\text{eff}}$  profile. Since the corresponding average ion charge is small (about 1.2), the difference found is practically only due to the profile shape. Thus the  $\eta^*(0)/\eta^k(0)$  enhancement due to a hollow  $Z_{\text{eff}}$  profile could explain the observed discrepancies between  $Z_{\text{eff}}^*(0)$  and the estimated global ion charge, particularly at high  $I/N$  [2, 4]. In fact, to sustain the current density distribution in a pinch characterized by a relatively high ion charge (i.e. a highly resistive plasma) in the outer region, a higher loop voltage must be applied so that the enhanced dissipation of helicity can be balanced by a higher external input via the dynamo process. This results in an increase of the apparent resistivity on axis.

It can therefore be concluded that, in general, the impurity content in an RFP is of fundamental importance in the determination of the plasma behaviour, both in the high density regime and in the low density regime [9]. At high density the impurities have a direct influence on the upper limit for the electron density (or, more precisely, the lower limit for  $I/N$ ) beyond which radiation losses dominate the plasma power balance [9, 10]. Although radiation is much lower in the low density regime, the ion effective charge increases, owing to the density decrease and probably the increase of impurities, and enhances the dissipation in the outer region of the plasma. Hence the sustainment of the RFP requires a stronger dynamo activity, which in turn is associated with enhanced transport and confinement degradation. This interpretation clearly stresses the importance of operating at high density. First results with pellet injection are presented in the following section.

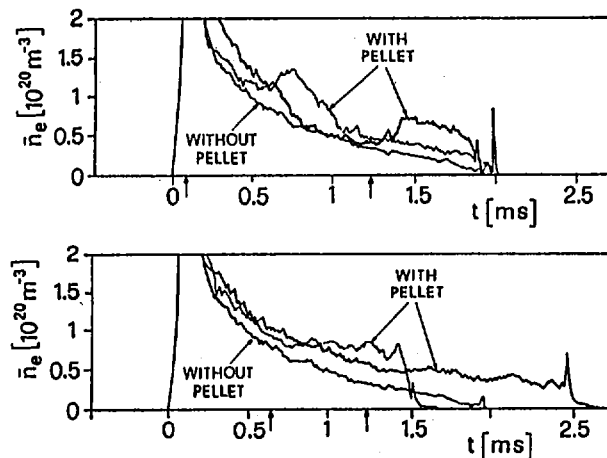


FIG. 3. Line averaged density versus time for various discharges with and without pellet injection. The arrows indicate the time at which the pellet is injected.

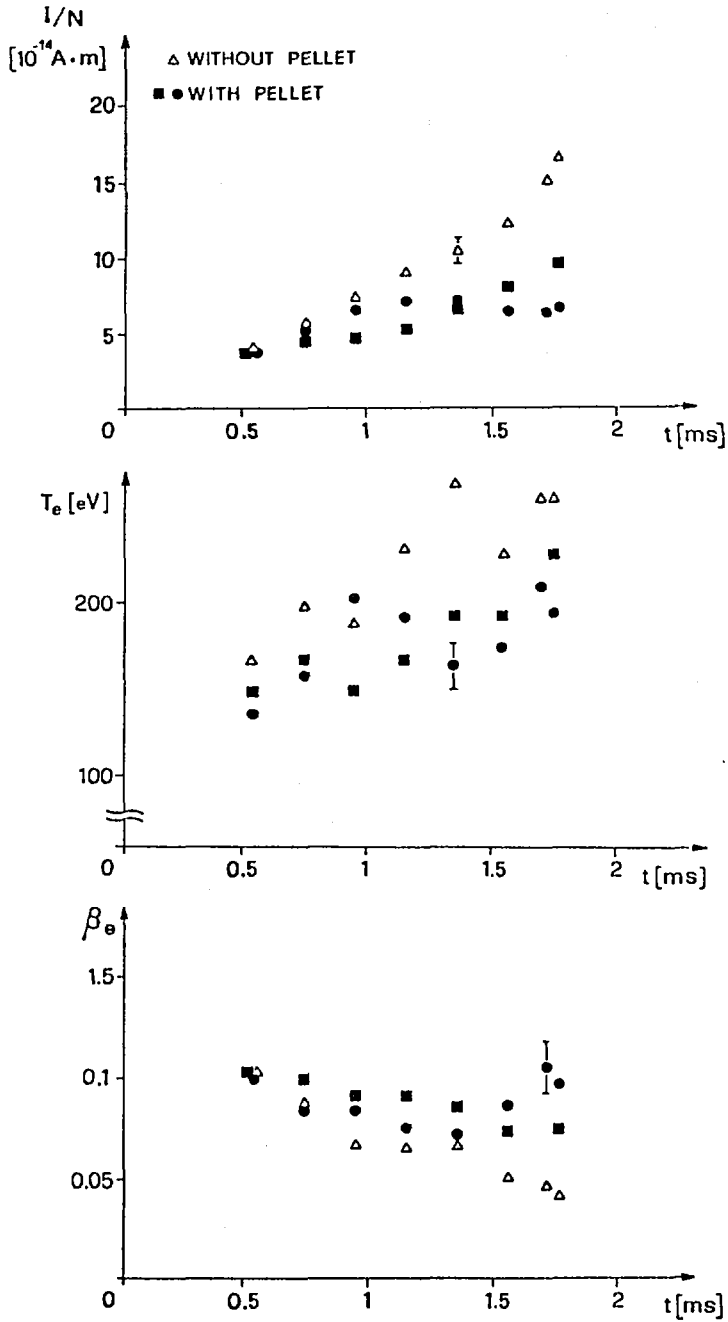


FIG. 4. Time evolution of  $I/N$ ,  $T_e$  from SXR pulse height analysis and  $\beta_e$  for three typical sets of discharges, with and without pellet injection. Each point is averaged over many discharges and over  $200 \mu\text{s}$  time intervals.

## 2.2. Pellet injection results

Single deuterium pellets with velocities of about 100 m/s and a mass of about  $10^{19}$  molecules have been injected in ETA-BETA II for the first time, with an injector system developed at Risø National Laboratory [11]. The pellet is completely ablated during the pulse. Figure 3 shows some examples of the line integrated density versus time, with and without pellet injection. It is seen that the time evolution of the density is significantly altered by this technique. In some cases this leads to densities higher than  $5 \times 10^{19} \text{ m}^{-3}$  which are maintained throughout the pulse. In this way the natural tendency of the discharge to evolve towards a high I/N regime can be somewhat controlled and counteracted (see Fig. 4). The change in density behaviour is coupled with a change in the electron temperature; this is also shown in Fig. 4 for two typical sets of discharges, with and without pellet injection. Of course, higher densities correspond to lower temperatures. However, as shown in Fig. 4, when the density is sustained, beta is also sustained. Thus, these preliminary results are a further proof of the interdependence between I/N,  $\beta$  and  $\tau_E$  previously found [2, 4]. Moreover, it appears now possible to escape from the high I/N regime.

## 3. MHD STABILITY AND q-LIMITS OF THE MEAN MAGNETIC FIELD PROFILES

The processes underlying the sustainment of the RFP distribution ('dynamo' mechanism) are not well understood at present. However, under consideration is the effect of the magnetic fluctuations and in particular of that portion of the spectrum which is interpreted as being due to MHD activity. Actually, it has been found recently [3] that a periodical activity comes from the turbulent background fluctuations that are always present in RFPs with amplitudes of about 1% in present experiments. This process is related with a substantial redistribution of currents in the plasma, resulting in a cyclic flattening of the current density profile which would otherwise tend to peak on axis. It has also been found that the experimental profiles can be well described by the expression  $\mu(r) = \mu(0)[1-(r/a)^\alpha]$  [12] and that the process results in a periodical oscillation of  $\mu(0)$  or equivalently of the on-axis safety factor  $q(0) = 2/(R\mu(0))$  [3].

An MHD stability analysis for current driven modes of these profiles has been performed over a wide range of  $\alpha$  and  $\mu(0)$  [6]. The most severe boundaries for stability are due to  $m=1$  resistive modes; they are plotted in Fig. 5 in terms of the values of  $q$  on axis and  $q$  at the wall. Also shown are experimental values of  $q(a)$  and  $q(0)$  for typical RFP distributions. The mean field experimental distributions lie in the stable region below the uniform  $\mu$ -curve corresponding to Taylor's fully relaxed states; they are close to the  $m=1$  resistive internal (i.e. resonant inside the toroidal field reversal surface) tearing mode boundary. Hence a lower limit on  $q(0)$ , associated with the destabilization of these  $m=1$  modes, can be identified as

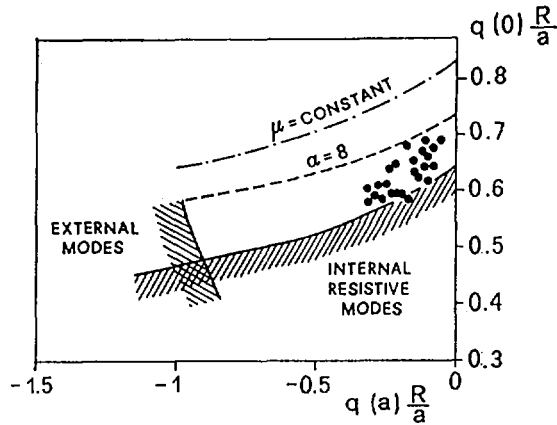


FIG. 5. Stability diagram for  $m=1$  modes in the plane  $q(a)R/a - q(0)R/a$ ; the dots indicate experimental configurations. Also shown are the curve for the fully relaxed  $\mu = \text{const}$  states with  $\theta$  in the range 1.2-1.56, and the curve for our model with  $\alpha=8$ .

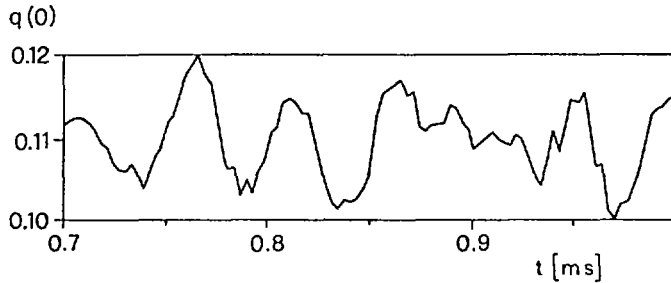


FIG. 6. Time evolution of the experimental value of  $q$  on axis.

$q(0) > \frac{2}{3} a/R$ . This limit is slightly dependent on the  $\mu$ -profile (varying between about  $\frac{2}{3} a/R$  for  $\alpha = 3.9$  and about  $\frac{1}{2} a/R$  for  $\alpha = 2.7$ ) and imposes an upper limit on the on-axis current density  $J(0)$  when  $J(0) < 3B(0)/\mu_0 a$  [12]. Generally, the experimental magnetic field profiles are stable for current driven modes, but resistive diffusion tends to destabilize the configuration by peaking the current distribution on axis and thus leading to lower  $q(0)$ . The excited internal current driven instabilities lead to a redistribution of the current density profile and thus the stable configuration of the initial tearing mode is recovered; this process is repeated in a cyclic way [13]. In this sense the experimental mean field profiles, although they are not fully relaxed, represent the outcome of periodical relaxation processes which counteract the diffusion process. This mechanism can explain quite well the periodical oscillations of  $q(0)$  experimentally found in ETA-BETA II [3] around 0.11 ( $\sim \frac{2}{3} a/R$ ), as shown in Fig. 6.

TABLE I. PLASMA PARAMETERS  
EXPECTED FOR RFX<sup>a</sup>

	(a)	(b)
a (m)	0.5	0.5
R (m)	2	2
I (MA)	2	2
I/N ( $10^{-14}$ A·m)	4	4
$Z_{eff}^*$	4	4
$\langle n \rangle$ ( $10^{20}$ m <sup>-3</sup> )	0.6	0.6
$\beta_\theta$ (%)	10	4.6
T(0) (keV)	1.8	0.9
$\tau_E$ (ms)	47	7
$\langle n \rangle \tau_E$ ( $10^{18}$ m <sup>-3</sup> ·s)	3	0.5
$\beta_\theta \tau_E$ (ms)	4.7	0.3

<sup>a</sup> Scaling with  $\beta = \text{const}$  (a) and  $\beta = I^{-1/3}$  (b).

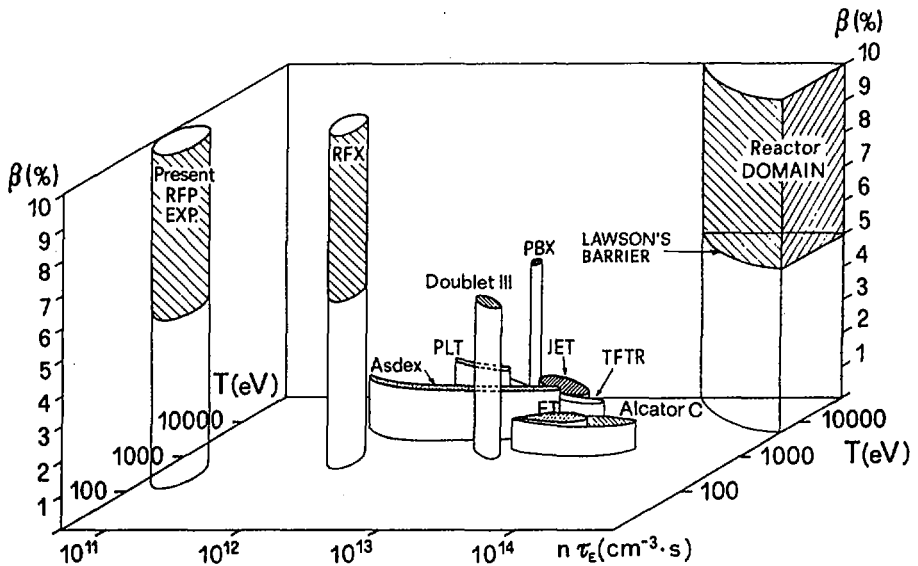


FIG. 7. Three-dimensional version of Lawson's diagram, including the beta values achieved in the present experiment and those expected in RFX.

#### 4. BETA LIMITS AND CONFINEMENT SCALING TO RFX

A simple estimate of the ideal MHD beta limits can be obtained by computing the pressure gradient which marginally satisfies the Suydam's criterion for the  $\mu$ -profiles considered in Section 3. It is found that the tearing mode stable profiles can support average beta values of the order of 30%.

However, in present experiments, beta values of only about 10% (well below the ideal MHD limit) are achieved. Thus, the experimental beta values can be interpreted as the outcome of competing processes of relaxation and transport acting against Ohmic heating. Two sets of plasma parameters as expected for RFX are listed in Table I, according to two different scalings [7]. The value of  $\beta_0 \tau_E$ , which can be of the order of 1 ms in RFX, is of particular interest. Indeed, the beta values should be considered when comparing various approaches to magnetic fusion. Figure 7 shows a three-dimensional version of the usual Lawson's diagram. A vertical axis is added to represent beta, and a beta value of 5% is set as the minimum for a fusion reactor to be of practical interest.

The main goal of RFP research and in particular of the RFX experiment is to demonstrate at higher currents the possibility of confinement of a relatively high beta plasma produced solely by Ohmic heating.

#### ACKNOWLEDGEMENTS

The authors wish to acknowledge the essential contribution of E. Baseggio in the operation of the pellet injector and of ETA-BETA II. The valuable help of G. Mella with the vacuum system and the technical support of I. Dalla Libera, I. Molon, E. Perdon and A. Tamiazzo is also gratefully acknowledged.

#### REFERENCES

- [1] ANTONI, V., et al., in *Plasma Physics and Controlled Nuclear Fusion Research 1984* (Proc. 10th Int. Conf. London, 1984), Vol. 2, IAEA, Vienna (1985) 487.
- [2] BUFFA, A., et al., in *Controlled Fusion and Plasma Heating* (Proc. 13th Europ. Conf. Schliersee, 1986), Vol. 1, European Physical Society (1986) 349.
- [3] ANTONI, V., et al., *ibid.*, p. 337.
- [4] ALPER, B., MARTINI, S., ORTOLANI, S., *Nucl. Fusion* **26** (1986) 1256.
- [5] GABELLIERI, L., et al., *Enhanced Dynamo Contribution to the Resistivity of a RFP due to Non-uniform Effective Charge Profiles*, Internal Rep. 86/03, Istituto Gas Ionizzati, Padua (1986).
- [6] ANTONI, V., MERLIN, D., ORTOLANI, S., PACCAGNELLA, R., *Nucl. Fusion* **26** (1986) 1711.
- [7] ANTONI, V., MARTINI, S., ORTOLANI, S., in *Controlled Fusion and Plasma Heating* (Proc. 13th Europ. Conf. Schliersee, 1986), Vol. 1, European Physical Society (1986) 385.
- [8] MALESANI, G., ROSTAGNI, G., "The RFX experiment", *Fusion Technology* (Proc. 14th Symp. Avignon, 1986), Pergamon Press, Oxford (1987).

- [9] ORTOLANI, S., ROSAGNI, G., Nucl. Instrum. Methods **207** (1983) 35.
- [10] COSTA, S., De ANGELIS, R., ORTOLANI, S., PUIATTI, M.E., Nucl. Fusion **22** (1982) 1301.
- [11] SORENSEN, H., et al., "D<sub>2</sub> pellet injector for the Reversed Field Pinch Eta-Beta II in Padova", Fusion Technology (Proc. 14th Symp. Avignon, 1986), Pergamon Press, Oxford (1987).
- [12] ORTOLANI, S., in *Mirror-Based and Field-Reversed Approaches to Magnetic Fusion* (Proc. Workshop Varenna, 1983), Int. School of Plasma Physics (1984) 513.
- [13] ORTOLANI, S., in *Twenty Years of Plasma Physics* (Proc. ICTP Commemorative Meeting Trieste, 1984), World Scientific Publishing, Singapore (1985) 75.

## DISCUSSION

H.A.B. BODIN: I am puzzled by the curve in Fig. 1 showing that  $Z_{\text{eff}}$  rises at the edge. This seems to imply high impurity confinement times or  $n\tau$  values at the edge, so that the ions reach stages where they can contribute to  $Z_{\text{eff}}$ ; this also suggests slow impurity transport, otherwise the highly excited ions would be dominant in the middle, giving higher  $Z_{\text{eff}}$  there.

S. ORTOLANI: Actually, the hollow  $Z_{\text{eff}}$  profile is due to the short particle confinement time, which prevents higher ionization stages being reached and which results in  $Z_{\text{eff}}$  values close to one in the centre and relatively higher in the outer region where the plasma electron density is lower.

A.A. NEWTON: You drew attention to the constancy of beta with time and under a variety of conditions. Several experiments have shown beta to be about 10%, including the pellet injection in ZT-40M, and this now extends over a wide range of parameters and Lundquist numbers. Does your cyclic model of diffusion, instability and relaxation lead to a beta prediction?

S. ORTOLANI: The cyclic model of relaxation enables us to view the beta values as the result of the counteracting actions of relaxation (and associated transport) and diffusion (heating). The model therefore suggests saturation at the beta value at which this balance is achieved. So far, however, there is no quantitative prediction for the beta values.

K. MIYAMOTO: If I understood you correctly, the  $m = 1$  resistive modes are responsible for the MHD associated with the relaxation process. However, the growth time for resistive instability is of the order of 1 ms. The fluctuation period of  $q(0)$  is shorter than the growth time. I would think that the ideal internal kink mode could be responsible for the MHD activity associated with the relaxation process.

S. ORTOLANI: The MHD stability analysis shows that as  $q(0)$  decreases and the current density profile becomes more peaked, the first modes to be destabilized are the  $m = 1$  tearing modes. However, for lower  $q(0)$  and more peaked current density distributions — as obtained at higher  $\theta$  values — ideal internal kink modes are also found, as described in Ref. [6]. A quantitative comparison with the experimental

time-scales of the observed oscillations depends upon the relevant layer thickness which enters into the process.

B. COPPI: Do you have a theoretical explanation for the observed near-constancy of beta as  $n$  is increased?

S. ORTOLANI: When the density is sustained by pellet injection, the temperature decreases, but the resulting beta values are higher than those obtained without pellet injection. More precisely, beta remains high and does not decrease with time. This is an experimental result and I do not have an exact theoretical explanation.



# RESULTS FROM THE REVERSED FIELD PINCH EXPERIMENT ON TPE-1RM15 WITH A PROGRAMMED VERTICAL FIELD

T. SHIMADA, Y. HIRANO, Y. YAGI,  
A.A. NEWTON<sup>1</sup>, K. OGAWA  
Electrotechnical Laboratory,  
Sakura-mura, Niihari-gun, Ibaraki-ken,  
Japan

## Abstract

RESULTS FROM THE REVERSED FIELD PINCH EXPERIMENT ON TPE-1RM15 WITH A PROGRAMMED VERTICAL FIELD.

The TPE-1RM15 is a new moderate size machine with  $R = 0.7$  m and  $a = 0.135$  m, operating as a Reversed Field Pinch (RFP) at a current of up to 200 kA and a pulse duration of 8 ms. A DC vertical field,  $B_{vdc}$ , is used to centre the plasma toroidal equilibrium in a thick shell, and plasma formation is assisted by a pulse cancellation field produced by coils inside the shell. During the flat-top phase at  $I_p = 135$  kA, there is an optimum in  $B_{vdc}$  equal to 7.7 mT, and  $T_{e0} \sim 600$  eV and  $n_{e0} \sim 2 \times 10^{19} \text{ m}^{-3}$  are obtained by Thomson scattering. The temperature is confirmed by analysis of the soft-X-ray spectrum measured with a SiLi detector. In these conditions the helicity resistivity on axis shows an anomaly factor of four,  $V_{loop} = 30$  V,  $\beta_p \sim 10\%$ ,  $\tau_E \sim 0.2$  ms and  $1/N \sim 25 \times 10^{-14} \text{ A}\cdot\text{m}$ . The DC vertical field is varied over a wide range and  $T_{e0} \sim 400$  eV at  $B_{vdc} = 0$ .

## 1. INTRODUCTION

The TPE-1RM15, which succeeds TPE-1RM [1], is a new moderate size machine with  $R = 0.7$  m and  $a = 0.135$  m, operating as a Reversed Field Pinch (RFP) at a current of up to 200 kA and a pulse duration of 8 ms. Recent RFP experiments on various machines [2-4], including TPE-1RM, show that reduction of magnetic field errors and control of plasma equilibrium are essential for good RFP discharges.

Our objectives in the TPE-1RM15 experiment are as follows:

- (a) To establish a technological and physical basis for obtaining and maintaining a stable RFP configuration;

---

<sup>1</sup> Euratom-UKAEA Fusion Association, Culham Laboratory, Abingdon, Oxfordshire, UK.

- (b) To demonstrate that temperatures in the range of  $T_e = 0.5\text{--}1$  keV and confinement times of up to 0.5 ms can be realized at high beta by Ohmic heating alone;
- (c) To determine the scaling laws of temperature, beta and confinement time with current and density; and to establish a benchmark at a moderate radius.

To realize these objectives, the following items were included in the design of the experiment:

- Minimization of error fields arising from coils, current feeders, cuts in the conducting shell and supporting structures;
- Control of the plasma equilibrium by two kinds of vertical fields, namely the DC vertical field,  $B_{\text{vdc}}$ , for aligning the outer magnetic flux surface with the limiters during the flat top, and the control vertical field,  $B_{\text{vcv}}$ , for reducing the error field at the shell gap;
- Transient cancellation of the DC vertical field at the set-up in order to facilitate plasma formation;
- Possibility of access for profile measurement of various plasma parameters.

The experiment has been successfully performed with vertical field control, and high electron temperatures ( $T_{e0} \sim 600$  eV) have been obtained at  $I_p = 135$  kA. The loop voltage has been reduced by a factor of two. The results show the importance of plasma positioning by the DC vertical field.

## 2. THE DEVICE

The heart of the new device [5] is an air core solenoid of 0.8 V·s, pulsed by a 1.0 MJ capacitor bank so that the plasma current and the magnetizing current rise simultaneously. The experiment starts with a slow current rise (2 ms) and early reversal of the toroidal field (0.5 ms). A power crowbar bank maintains a flat top for 3–4 ms, followed by slow decay. A sudden termination of the discharge usually occurs at 7–8 ms.

Equilibrium and stability are achieved with a 25 mm thick copper shell of 0.162 m inner radius. The vacuum vessel and the limiters (0.135 m inner radius) are made of stainless steel. Because of the surface currents the poloidal field outside the shell would be that of a ring, and therefore a control vertical field,  $B_{\text{vcv}}$ , produced by a pair of coils, is used to suppress the vertical component at the two shell gaps. The control vertical field is driven by start and power crowbar banks to match the time dependence of the plasma current. The same coils produce a DC vertical field,  $B_{\text{vdc}}$ , which is applied 2 s before the discharge to centre the plasma during the flat top. The shell gap fields, measured by coils across the gap on an inner surface of the shell, are  $\leq 5$  mT during the flat top; the normalized gap flux,  $\phi_g/I_a$ , is  $\leq 2$  mWb/MA·m, which is the flux used in medium-sized machines.

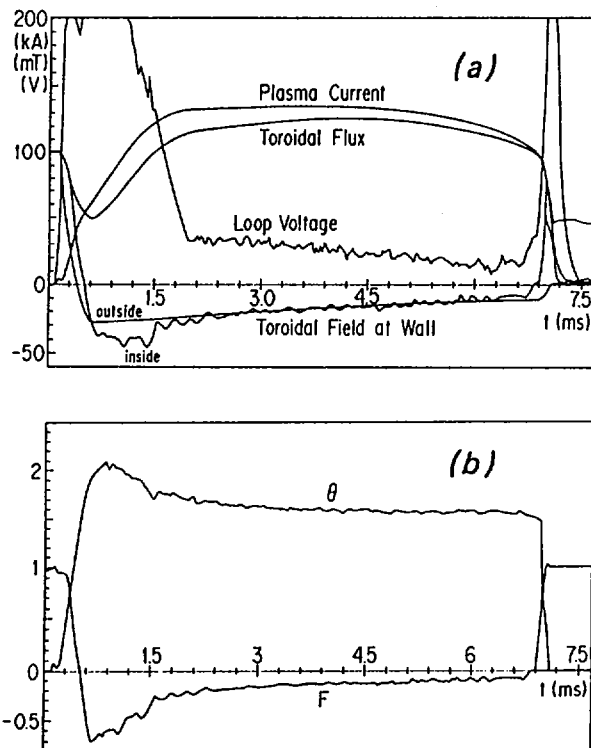


FIG. 1. (a) Typical waveforms with an optimum DC vertical field (7.7 mT) and with optimum cancellation of the error field in the flat-top case with  $I_p = 135$  kA. Filling gas  $D_2$ , pressure  $P_0 = 4$  mtorr, initial toroidal field  $B_0 = 100$  mT.

(b) Time variations of the pinch parameter  $\theta$  and the reversal parameter  $F$ , under the same conditions as in (a).

Since the DC vertical field would inhibit the growth of ionization, a pulse cancellation field,  $B_{vpc}$ , produced by coils inside the shell, is applied for 2 ms shortly before the start of the discharge. In this way, the plasma can be formed with filling pressures,  $P_0$ , of  $\geq 4$  mtorr and with  $B_{vdc} \leq 10$  mT.

In this early period, the pulse cancellation field produces an additional vertical field in the shell gap; this is reduced to  $< 30$  mT by pulsed saddle coils placed across the gaps.

### 3. PLASMA PARAMETERS

Typical discharge waveforms, the pinch parameter  $\theta$  and the reversal parameter  $F$  are shown in Fig. 1. The  $\theta$ -value stays nearly constant (1.6–1.5) and the  $F$ -value

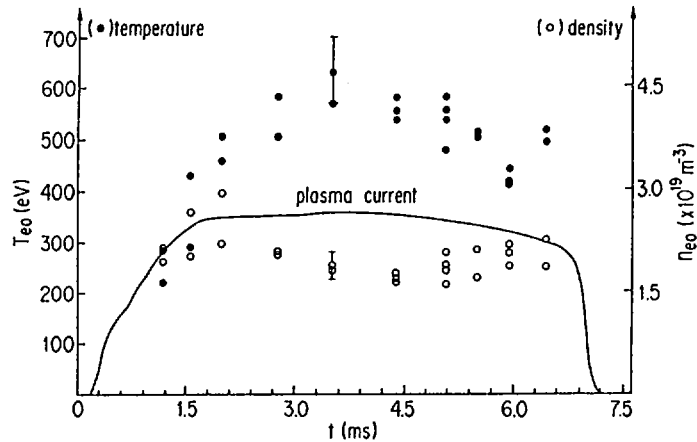


FIG. 2. Time variations of electron temperature and density measured by Thomson scattering, under the same conditions as in Fig. 1(a).

decays slowly from  $-0.2$  to  $-0.1$ . A low loop voltage (20–30 V) is obtained during the flat-top phase at  $I_p = 135$  kA when the optimum DC vertical field is applied.

The electron temperature and density are measured by Thomson scattering (Fig. 2). The temperature rises 1 ms after the current rise and reaches 500–600 eV, where it remains constant for 3 ms near current maximum; the decay is slow at first and more rapid near current termination. Simultaneous soft-X-ray measurements with a SiLi detector between 2.4 ms and 5.4 ms also give a high electron temperature (about 570 eV); this agrees fairly well with the above measurements.

In the current rise and flat-top phases the electron velocity distribution is well fitted by a Maxwellian, but there are about a factor of two more electrons of 2 keV in the current decay phase.

After the current rise phase the plasma density is constant at  $n_{e0} \sim 2 \times 10^{19} \text{ m}^{-3}$ . The reproducibility of the line radiation of iron (225.9 nm) and soft X-rays measured with a surface barrier diode is fairly good.

If we make the usual assumption of equal ion and electron temperatures and a parabolic pressure profile,  $\beta_p \sim 10\%$  and  $\tau_E \sim 0.2$  ms. The estimated helicity resistivity on axis,  $\eta_0^k$ , using the modified Bessel function model (MBFM), gives an anomaly factor of four when calculated with the measured electron temperature and  $Z=1$ .

The value of  $I/N$  is about  $25 \times 10^{-14} \text{ A}\cdot\text{m}$ , assuming a parabolic density profile, and corresponds to a high Lundquist number  $S$ .

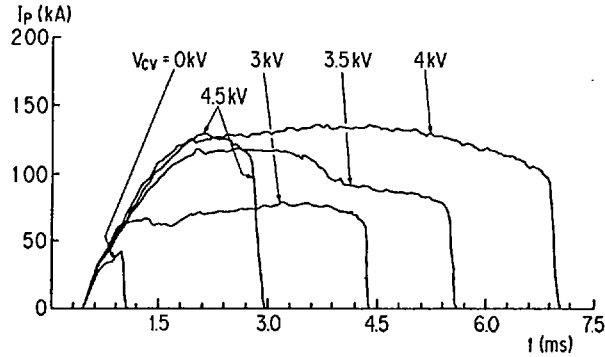


FIG. 3. Variation of plasma current waveforms with different control vertical fields cancelling the error field at the shell gap, from no cancellation (0 kV), through optimum cancellation (4 kV), to over-cancellation (4.5 kV).  $B_0 = 50$  mT,  $p_0 = 3.5$  mtorr ( $D_2$ ), with the same bank conditions, except for the control vertical field.

#### 4. SHELL GAP ERROR FIELD

A problem in connection with the conducting shell is the fact that the induced surface currents inside and outside of the shell produce an error field at the gap (cut). This error field is compensated by the control vertical field as described above. The plasma behaviour is very sensitive to the measured Br signal at the gaps; this can be seen in Fig. 3, which shows the plasma current waveforms with different control vertical fields. If the cancellation of the error field is insufficient, the discharge pulse is considerably shortened. With optimum cancellation, the discharge pulse lasts 8 ms.

#### 5. VARIATION OF THE DC VERTICAL FIELD

When plasma equilibrium is maintained by the conducting shell alone, the minor radius,  $r_p$ , of the outward toroidal shift of the plasma,  $\Delta$ , is reduced. Since the conductivity of the shell is finite, the effective distance between the plasma and the shell grows with time; this causes an additional shift of the plasma and a further reduction of  $r_p$ . For positioning of the plasma column, a DC vertical field is applied which can control the extent of toroidal shift. Figures 4 and 5 show the dependence of the electron temperature, density, plasma resistance ( $R_p$ ) and energy confinement time on the DC vertical field in the current flat-top phase. In these experiments the plasma current is maintained in a flat top at around 135 kA for 3–5 ms.

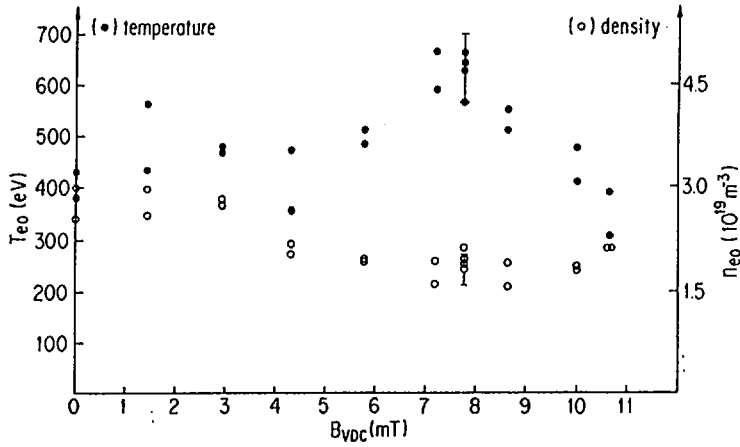


FIG. 4. Dependence of electron density and temperature on the DC vertical field. Flat-top cases with  $I_p \sim 135$  kA, 3.45 ms after start of plasma current.

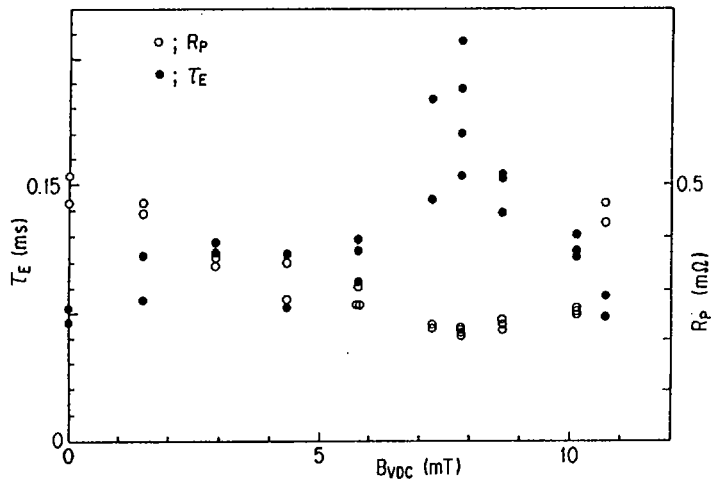


FIG. 5. Dependence of energy confinement time and plasma resistance on the DC vertical field. Flat-top cases with  $I_p \sim 135$  kA, 3.45 ms after start of plasma current.

The plasma resistance is at a minimum and the electron temperature is at a maximum around  $B_{VDC} = 7.7$  mT. When the effect of the penetration of the surface current into the shell is considered, this value agrees well with that calculated from Shafranov's formula for  $\Delta \sim 0$ . The ratio of the mean energy resistivity to the value  $\eta_0$  on axis, calculated using Spitzer's formula ( $Z=1$ ), decreases gradually with the

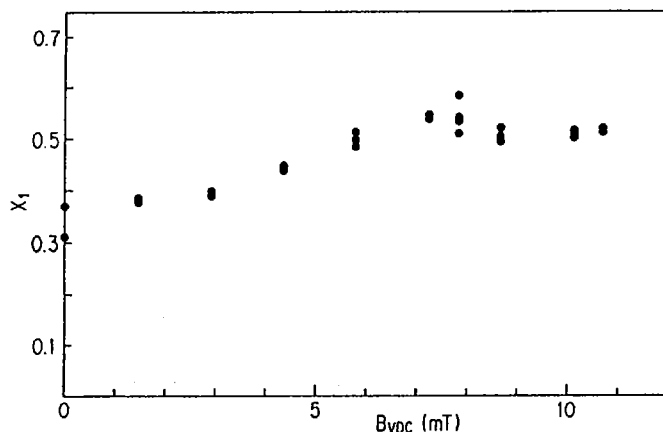


FIG. 6. Dependence of  $X_1$  (the point where  $\mu$  in the MBFM begins to decrease) on the DC vertical field. Flat-top cases with  $I_p \sim 135$  kA, 3.45 ms after start of plasma current.

vertical field from 20 to 15 at the optimum  $B_{vdc}$ . The energy confinement time  $\tau_E$  peaks at the optimum  $B_{vdc}$  and the plasma resistance  $R_p$  decreases by more than a factor of two. The value of  $X_1$ , which is the point where  $\mu$  in the MBFM begins to decrease, increases from 0.35 to 0.55 (see Fig. 6), showing that the volume of relaxed plasma increases as the optimum  $B_{vdc}$  is approached.

## 6. DISCUSSION

The improvement in the plasma properties, especially in the energy confinement time, when a vertical field is used for control of plasma equilibrium is striking. This has been observed on HBTX1A [2] and HBTX1B [6], as well as on TPE-1RM15, even though the aspect ratio of TPE-1RM15 is larger (5.2 compared with 3.2 on HBTX1). It is interesting to compare the results for TPE-1RM15 ( $B_{vdc} = 0$ ) with those for ETA-BETA-II which has similar dimensions ( $R = 0.65$  m,  $a = 0.125$  m) and a similar current range (100 – 180 kA). The value of  $I/N$  is a factor of two to ten higher in TPE-1RM15, but  $\beta_p$  and  $\tau_E$  are essentially the same [7]. The value of  $Z_{eff}^*$  is about three-quarters of that expected from the trend with  $I/N$  as reported for ETA-BETA-II [8]. When a vertical field is used,  $\beta_p$  is only marginally increased, which indicates a strong tendency for  $\beta_p$  to remain constant as  $I/N$  is varied by an order of magnitude. In TPE-1RM15, with the use of a vertical field,  $\tau_E$  is increased by more than a factor of two, mainly because of the low loop voltage, although  $Z_{eff}^*$

is unchanged. The fact that  $\eta_0^k/\eta_0 \sim 4$  is also unchanged implies that the contribution due to impurities is also constant. According to the observed FE II line radiation, the optimum positioning of the plasma column by the vertical field corresponds to less plasma-wall interaction, which may result in a low recycling level and low plasma density (see Fig. 4). With  $\beta_p$  constant, the low density gives a high electron temperature, which could be responsible for the observed low loop voltage in the optimum condition.

An alternative explanation is that the dissipation of helicity in the outer plasma regions is increased when the plasma is not centred and that more poloidal flux intersects the wall [6]. The estimated variation of the anomalous loop voltage with the DC vertical field closely follows the observed loop voltage. The variation of  $X_1$  with  $B_{vdc}$  indicates that more helicity dissipation can be expected without a DC vertical field.

The increase in the number of electrons with an energy three to four times larger than  $T_{e0}$  suggests that energetic particles are better contained with a slowly decaying current.

## 7. CONCLUSIONS

Reversed field pinches were obtained in the new TPE-1RM15 machine when the toroidal equilibrium was corrected by a DC vertical field. Cancellation of this field by coils inside the shell for a short time (2 ms) permits plasma formation over a wide range of filling pressures ( $\geq 4$  mtorr) and vertical field ( $\leq 10$  mT).

In all cases the pulse duration is very sensitive to the shell gap error. When this is minimized, the pulse length is about 8 ms.

During the flat-top phase at  $T_p = 135$  kA, the electron temperature remains constant at  $T_{e0} \sim 600$  eV for 3–5 ms,  $n_{e0} \sim 2 \times 10^{19} \text{ m}^{-3}$ ,  $\beta_p \sim 10\%$  and  $\tau_E \sim 0.2$  ms, with the usual assumptions and with an optimum DC vertical field of 7.7 mT. With no DC vertical field,  $T_{e0}$  and  $\tau_E$  are reduced to about 400 eV and 0.08 ms, respectively. The variation of the loop voltage with the DC vertical field follows that of the electron temperature, consistent with a resistance anomaly factor of four.

The TPE-1RM15 is operated at very large  $I/N$  ( $25 \times 10^{-14} \text{ A}\cdot\text{m}$ ), but significant degradation of  $\beta_p$  and  $\tau_E$  is not observed.

The importance of positioning the RFP plasma in the vacuum vessel and of cancellation of the shell gap error field, even for a machine with a large aspect ratio, is clearly shown by the results presented.

## ACKNOWLEDGEMENTS

This work was supported by the Atomic Energy Bureau, Science and Technology Agency (STA), Japan. One of the authors is grateful for the hospitality of the Electrotechnical Laboratory and for the support of STA.

## REFERENCES

- [1] HIRANO, Y., MAEJIMA, Y., OGAWA, K., et al., in Plasma Physics and Controlled Nuclear Fusion Research 1984 (Proc. 10th Int. Conf. London, 1984), Vol. 2, IAEA, Vienna (1985) 475.
- [2] CAROLAN, P.G., ALPER, B., BODIN, H.A.B., et al., *ibid.*, p. 449.
- [3] BAKER, D.A., BUCHENAUER, C.J., BURKHARDT, L.C., et al., *ibid.*, p. 439.
- [4] NOONAN, P.G., TSUI, H., NEWTON, A.A., Plasma Phys. Contr. Fusion **27** (1985) 1307.
- [5] SHIMADA, T., HIRANO, Y., YAGI, Y., et al., in Fusion Technology (Proc. 14th Symp. Avignon, 1986), Pergamon Press, Oxford, to be published.
- [6] ALPER, B., ANTONI, V., BEVIR, M.K., et al., Paper IAEA-CN-47/D-II-1, these Proceedings, Vol. 2.
- [7] ALPER, B., MARTINI, S., Electron Temperature Studies on ETA-BETA-2, Rep. IGI-85/04, Istituto Gas Ionizzati, Consiglio Nazionale delle Ricerche, Padua (1985).
- [8] ALPER, A., ANTONI, V., BASSAM, M., et al., in Controlled Fusion and Plasma Physics (Proc. 12th Europ. Conf. Budapest, 1985), Vol. 9F, Part 1, European Physical Society (1985) 578.

## DISCUSSION

T. TAMANO: Allow me to congratulate you on the good initial results. You have constructed a scaled-up device with a design philosophy very similar to the previous one, and, further, you have obtained almost the same temperature and density with an improved confinement time. Could you comment on the size scaling?

T. SHIMADA: Thank you. The equilibrium control reduces the outer volume and this may lead to a reduction of the anomalous component of the loop voltage, as suggested by another RFP experiment. One consequence of this reduction is a higher energy confinement time. However, it is too early to comment on the size scaling.

S. ORTOLANI: As you have stressed, the densities at which you operate are rather low ( $N_{e0} \approx 2 \times 10^{19} \text{ m}^{-3}$ ). Have you tried to operate at higher densities or is there something that prevents it?

T. SHIMADA: The density is determined by recycling. In our device it is low because of the all-metal vessel. In principle, there is nothing to prevent higher densities being obtained with, say, gas puffing or pellet injection.

The good magnetic field configuration allows us to operate at a higher I/N ratio than in any previous experiment and so we obtain high temperatures.



# PLASMA HEATING IN STELLARATOR/TORSATRONS AND TOKAMAKS BY ION CYCLOTRON WAVES

E.F. JAEGER, D.B. BATCHELOR

Oak Ridge National Laboratory,  
Oak Ridge, Tennessee

K. IMRE, H. WEITZNER

Courant Institute of Mathematical Sciences,  
New York University,  
New York, New York

United States of America

## Abstract

### PLASMA HEATING IN STELLARATOR/TORSATRONS AND TOKAMAKS BY ION CYCLOTRON WAVES.

High power ion cyclotron heating experiments are currently planned for the Heliotron-E device in Kyoto and for the ATF torsatron at Oak Ridge National Laboratory. Reliable solutions for the radiofrequency fields and wave absorption are needed to optimize antenna designs and heating scenarios as well as to determine heating profiles and tail formation for the interpretation of confinement experiments. The complicated field structure in torsatrons makes a number of approximations commonly used in studying ICRH in tokamaks of questionable validity. For example, in tokamaks the cyclotron resonance and ion-ion hybrid resonance layers are, to a good approximation, vertical sections and small changes of frequency or field B result in small shifts in their locations. However, in a torsatron a saddle point in B occurs near the magnetic axis so that resonance and cut-off layers occur on two sheets oriented either horizontally or vertically. Small changes of frequency therefore can cause radical changes in the resonance cut-off topology. This phenomenon has been investigated by performing two-dimensional calculations of the wave fields and heating profiles in a cold plasma model. The effects of finite temperature in this geometry have also been investigated by calculating cyclotron damping and mode conversion in a slab having a non-monotonic B profile. Resonances and cut-offs therefore exist in pairs, and by adjusting the wave frequency they can be made to merge together and to annihilate in pairs. In large tokamaks and stellarator/torsatrons the well known geometrical optics approximation may apply and in certain regimes of configuration space the system is approximately perpendicularly stratified. In such regions near cyclotron harmonic resonances, geometrical optics fails and boundary layer expansion techniques are employed to obtain a wave equation whose solutions match the geometrical optics solutions. In this manner, energy absorption, wave reflection, and mode conversion for fundamental, second and third harmonic and ion-ion hybrid resonances are studied for incident fast waves and incident Bernstein waves.

## 1. FULL WAVE CALCULATIONS IN 2 DIMENSIONS

We consider a model torsatron equilibrium which is straight and helically symmetric. That is, all equilibrium quantities depend on  $r$  and  $\phi = \theta - kz$ . We introduce axial

and poloidal flux functions  $\psi(r, \phi)\chi(r, \phi)$  and use the Bessel function model for  $\psi$ . The density is assumed to be a function of  $\psi$ . In these coordinates the equilibrium is independent of  $z$  so that the wave fields can be Fourier analyzed with respect to  $z$ . We take the limit of zero electron mass and set  $E_{\parallel} = 0$ . Then the projection of the  $\vec{\nabla}\psi \times \vec{B}$  vector wave equation in the  $\nabla\psi$  direction and in the  $\nabla\psi \times \vec{B}$  directions gives two coupled pde's for  $E_{\theta}$  and  $E_r$ . The full equations are given in Ref. [1].

Two models have been used for the plasma current response. Most calculations were done using the cold plasma conductivity with an ad hoc collision frequency used to resolve the cyclotron resonance. To test the sensitivity of the results to the use of collisions to broaden the cyclotron resonance we have also done calculations using the warm plasma conductivity tensor. For these, the  $k_{\perp}\rho_i = 0$  limit was taken and where  $k_{\parallel}$  appears in the plasma dispersion function,  $k_z$  was used.

Figure 1 shows contours of equal power deposition for three different frequencies, giving different topologies of the minority cyclotron, ion-ion hybrid and cut-off layers. Figure 2 shows the radial heating profiles for the three frequencies of Fig. 1. The plasma parameters were chosen relevant to ATF:  $l = 2$ ,  $m = 12$ ,  $a_{\text{coil}} = 54$  cm,

$$n_e(0) = 4 \times 10^{13} \text{ cm}^{-3}, \quad B(0) = 20 \text{ kG}, \quad n_{\text{scrape-off}} = 4 \times 10^{11} \text{ cm}^{-3},$$

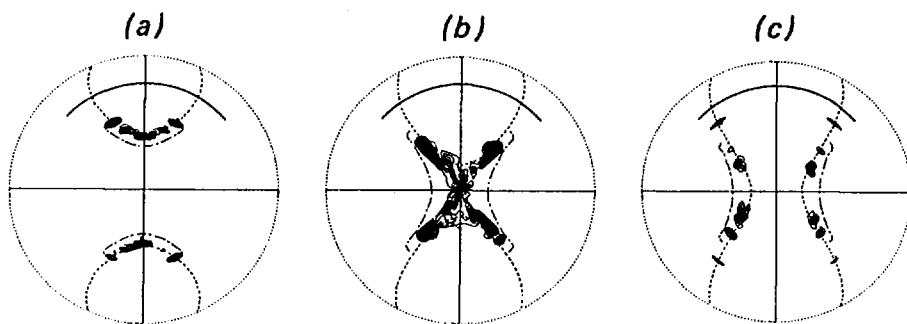


FIG. 1. Two-dimensional full wave calculation for ATF, showing contours of constant power deposition  $\dot{W}(r, \phi)$  for (a)  $f = 28$  MHz, (b)  $f = 30$  MHz, and (c)  $f = 31$  MHz.

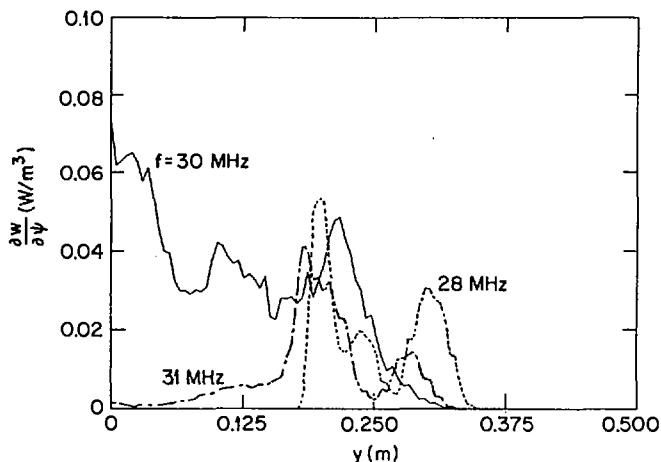


FIG. 2. Flux surface average of the power absorbed  $\langle \dot{W} \rangle_\psi$  for the cases shown in Fig. 1.

$k_z = N_T/R_T$ , where  $R_T = 210$  cm and the toroidal mode number  $N_T = 8$ . The antenna current was an approximately 1/4 turn circular loop in the  $\theta$ -direction at  $r = 42.4$  cm. For the calculations in Fig. 1 the fluctuating plasma wave current was obtained from the warm plasma conductivity model with  $T_e = T_i = 1$  keV. As expected when using the cold plasma model with collisional broadening, the total power absorbed is independent of  $\nu/\omega$  for sufficiently small  $\nu$ . Similarly, we find that in the warm plasma conductivity model at small  $T_i$  the total absorption or antenna loading is independent of  $T_i$  and agrees with that predicted by the collisional model. The power deposition patterns are also very similar for the two conductivity models, except that collisional absorption away from resonance layers (for example due to cavity modes) is absent in the warm plasma conductivity model. In Fig. 1a ( $f = 28$  MHz) a vertical chord through the center of the antenna intersects the minority cyclotron resonance and the ion-ion hybrid resonance twice. In Fig. 1b ( $f = 30$  MHz) the topology has changed such that the hybrid resonances have moved to the side and a vertical chord intersects the minority cyclotron resonance twice but does not cross the hybrid resonances. In Fig. 1c ( $f = 31$  MHz), both resonance layers are at the side so that neither is directly in front of the antenna. From Fig. 2 we see that the heating is much greater for the 30 MHz case and the profile is much more center peaked. Thus a frequency variation of 3% causes a radical change in loading and power deposition profile. Obviously, the coupling to Bernstein modes will be much different for the three cases.

A striking feature of these 2-D calculations is that the power deposition lies on localized island structures lying on flux surfaces rather than being smoothly spread over the resonance surfaces. This phenomenon has been seen in a number of previous 2-D calculations for tokamaks [2,3,4]. Hellsten et al. [5] have developed a theory of these structures based on a Frobenius type expansion of the wave equation in the vicinity of possible singular layers. Other suggestions have been made that these structures along the  $\psi$  surfaces are in fact the result of cavity modes or reflect the constancy of  $n_e$  on  $\psi$  or are perhaps merely numerical artifacts. We have studied these heating structures in detail in tokamak geometry and find them to be quite insensitive to the wall and antenna location and also to the fineness of the numerical grid. In addition, the islands persist if the density is taken constant. This strongly suggests that they are not due to cavity modes, density contours or numerics. The islands do however depend on the quantities appearing in Hellsten's eigenvalue equation, namely  $f$ ,  $n_e$ ,  $B k_z$ ,  $\nu$ . However, having solved the eigenvalue equation, we are not able to obtain any systematic agreement on the location and shape of the islands observed in the 2-D calculations. The theory of Hellsten et al. is an ideal theory ( $\nu = 0$ ) which relies on the self-adjointness of the  $\theta$  eigenvalue problem. Indeed, the system has no periodic solutions for real  $r$  when  $\nu \neq 0$ . We conjecture that by introducing  $\nu$  sufficient to resolve the resonance in our mesh, we eliminate the singularity revealed by the Frobenius expansion and thereby modify the problem so that detailed agreement is no longer obtained.

## 2. ONE-DIMENSIONAL FULL WAVE SOLUTIONS IN WARM PLASMA

Some insight into the effect of finite temperature for this system can be obtained from an idealized model in which a wave propagates across a magnetized plasma slab [ $\vec{B} = B(x)\hat{z}$ ] where the plasma parameters  $n_e(x)$ ,  $T_e(x)$ ,  $T_i(x)$ ,  $B(x)$  are those of a vertical chord through the axis of the 2-D model above (the profiles are approximately parabolic). Our calculation is similar to Ref. [6] in that the unperturbed distribution function includes diamagnetic drifts and the associated anisotropy to second order in Larmor radius. The Vlasov equation is expanded to second order in gyroradius retaining all  $x$ -dependence of  $B$  and  $p = n_e T$ . This gives a plasma current operator of the form:

$$\vec{j}(x) = (\sigma^0 + \rho^1 + \tau^2) \cdot \vec{E} + [\sigma^1 + \rho^2]_U \cdot \frac{\partial \vec{E}}{\partial x} \\ + \frac{\partial}{\partial x} ([\sigma^1 + \rho^2]_L \cdot \vec{E}) + \frac{\partial}{\partial x} (\sigma^2 \cdot \frac{\partial \vec{E}}{\partial x})$$

Full expressions for the  $\sigma$ ,  $\rho$  and  $\tau$  tensors can be found in Refs [6-7]. The electric field parallel to  $\vec{B}$  is retained to include collisionless damping of the ion Bernstein wave. The resulting sixth order wave equation is solved as a 2-point boundary value problem by finite differencing. A vacuum region is included at the edge of the plasma and vanishing of transverse  $E$  is imposed as a boundary condition at the wall.

In order to interpret the solutions with respect to local power deposition, it is necessary to use Poynting's theorem and separate  $\text{Re} \{ \vec{E}^* \cdot \vec{j} \}$  into a part  $P$  representing local dissipation and a part  $\vec{v} \cdot \vec{Q}$  where  $\vec{Q}$  is the kinetic wave energy flux. There is no unique way to make this separation and a number of different choices appear in the literature. We use the definitions:

$$P_s = \frac{1}{2} \text{Re} \left\{ \vec{E}^+ \cdot \left( \sigma_\rho - \frac{1}{2} \frac{\sigma_Q}{\partial x} \right)_H \cdot \vec{E} + \vec{E}^+ \cdot \sigma_{QA} \cdot \frac{\partial \vec{E}}{\partial x} + \vec{E}^+ \cdot \frac{\partial}{\partial x} \left( \sigma_H^2 \cdot \frac{\partial \vec{E}}{\partial x} \right) \right\}$$

$$Q_s = \frac{1}{2} \text{Re} \left\{ \vec{E}^+ \cdot \frac{\sigma_{QH}}{2} \cdot \vec{E} + \vec{E}^+ \cdot \sigma_A^2 \cdot \frac{\partial \vec{E}}{\partial x} \right\}$$

These forms for  $P_s$  and  $Q_s$  reduce to the correct forms for local power dissipation and kinetic flux in the WKB limit when a single wave is present in the system. Also the total absorbed power as determined by integrating  $\Sigma P_s$  over the plasma volume agrees to high accuracy with that obtained by integrating  $\text{Re} \{ \vec{E}^* \cdot \vec{j}_{\text{ext}} \}$  over the antenna current distribution. When using the definitions given in Ref. [6] we find local regions of negative  $P_e$  associated with transit time magnetic pumping on the fast wave and Landau damping on the Bernstein wave. With our forms the regions of negative TTMP are eliminated and negative Landau damping is reduced. At small  $k_{\parallel}$  we do see negative oscillations on  $P_e$  associated with cross-terms between fast wave and Bernstein wave (e.g.,  $\vec{E}_{\text{fast}} \cdot \sigma \cdot \vec{E}_{\text{Bernstein}}$ ). Our definition is similar to that given in Ref. [8], although in that work the terms associated with diamagnetic drifts are not retained in  $\vec{j}$  nor in  $P_s, Q_s$ .

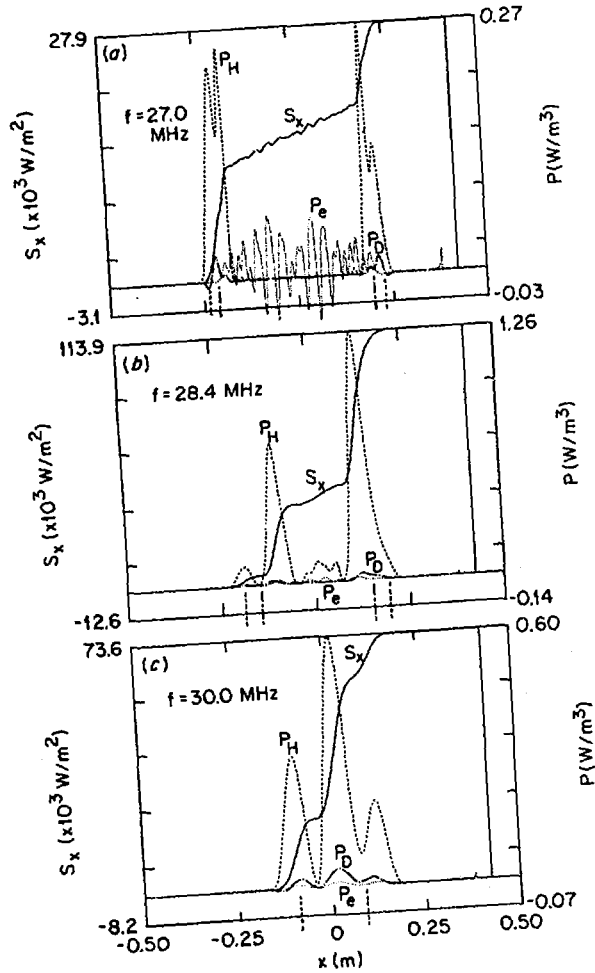


FIG. 3. Model 1-D stellarator calculation for ATF, showing total energy flux,  $S_x$ , and power absorbed by electrons,  $P_e$ , minority hydrogen,  $P_H$ , and majority deuterium,  $P_D$ , for (a)  $f = 27$  MHz, (b)  $f = 28.4$  MHz and (c)  $f = 30$  MHz.

Figure 3 shows spatial profiles of total power flux,  $S = S_{EM} + \sum S_{\alpha}$ , and local power deposition  $P_{\alpha}$  for each of the plasma species. The antenna is at  $x = 40$  cm on the right, so  $S_x$  represents the net wave power flowing to the left. The plasma parameters are similar to those used in the 2-D calculations:  $n_e = 40 \times 10^{13} \text{ cm}^{-3}$ ,  $B(0) = 20 \text{ kG}$ ,  $T_e = 1.5 \text{ keV}$ ,  $T_H = 1.5 \text{ keV}$ ,  $T_D = 1.5 \text{ keV}$ ,  $k_z = 1300 \text{ cm}^{-1}$ . In Fig. 4a, for  $f = 27$  MHz, the resonances are widely separated, but the minority cyclotron resonances are relatively near to the associated hybrid resonances. One clearly sees Bernstein

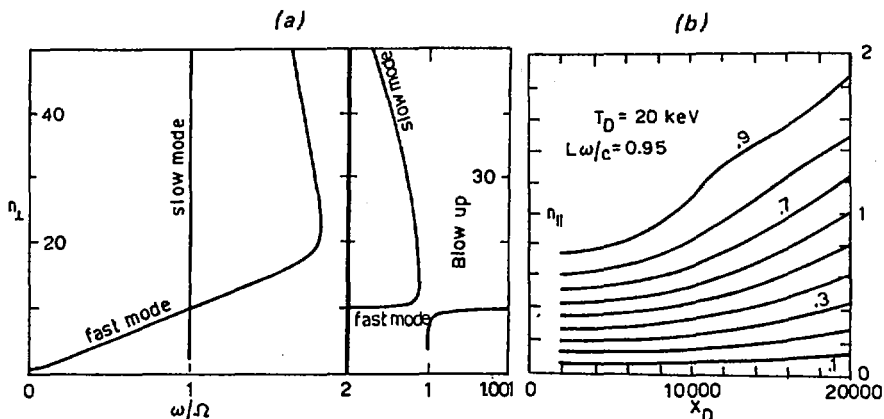


FIG. 4. (a) Dispersion relation for the fast and slow modes near the fundamental ion resonance. (b) Absorption contours for the slow mode incidence in the plane of  $X = \omega_p^2/\omega^2$  and  $n_1 = k_1 \omega/c$ . For instance, a deuterium plasma with  $B_0 = 3$  T,  $T = 5$  keV, and the characteristic equilibrium gradient length  $L = 100$  cm.

modes generated which are trapped and must be absorbed between the two resonance pairs. The Bernstein modes do not propagate at the plasma edge where  $\Omega_{ci} < \omega$ . In Fig. 4b,  $f = 28.4$  MHz, the hybrid resonances have moved closer together and the separation between the hybrid and minority cyclotron resonance has increased. This frequency, which corresponds to one fast wavelength between hybrid resonances, gives maximum absorption except when high Q cavity resonances are present. In Fig. 4c,  $f = 30$  MHz, the hybrid resonances have come together at the center and disappeared. Two minority cyclotron resonances do remain, however. One sees center peaked minority heating and also some majority heating. However, electron heating associated with Bernstein modes has disappeared.

### 3. GEOMETRICAL OPTICS APPLIED TO CYCLOTRON RESONANCES IN A PERPENDICULARLY STRATIFIED MEDIUM

In an approximately perpendicularly stratified plasma in which the geometrical optics approximation generally applies, special techniques are needed near cyclotron harmonic resonances. We apply a boundary layer expansion method and find a wave equation valid there whose solutions connect to the geometrical optics solution away from resonance. In this manner we study pure fundamental cyclotron resonance, pure second harmonic and pure third harmonic resonances, and ion-ion hybrid resonance of a minority fundamental resonance

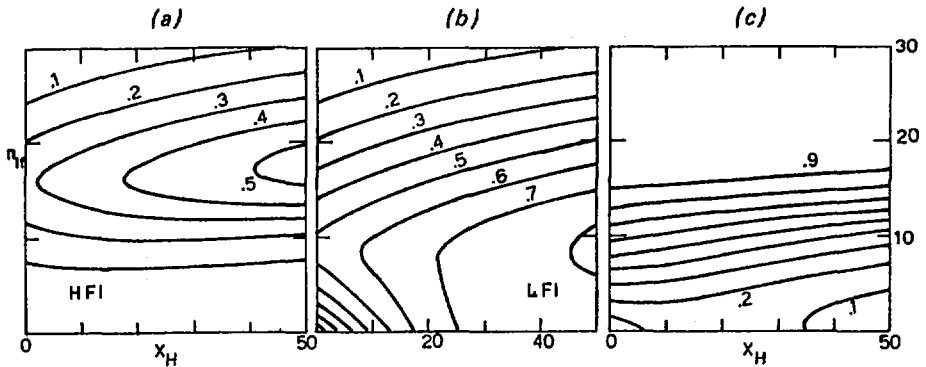


FIG. 5. Absorption contours for (a) fast wave incident on the high field side, (b) fast wave incident on the low field side, and (c) Bernstein mode incidence for the H-D hybrid resonance, where  $T_H = T_D = 5$  keV,  $X_D = 500$  and  $L\omega/c = 1$ , corresponding to a plasma with  $n_D = 4 \times 10^{14}$  cm $^{-3}$ ,  $B_0 = 4$  T and  $L = 40$  cm.

species with majority second harmonic resonant species. In all but the pure fundamental resonance case, incident waves may be either fast wave from the high field side or fast wave from the low field side, or an ion Bernstein wave from the appropriate side. In the pure fundamental resonance a fast wave may be incident from either side or a slow wave may be incident from the high field side. We characterize the wave propagation in terms of energy flux transmission and reflection coefficients, energy flux absorption, and energy flux mode conversion and/or reflected wave mode conversion coefficients.

We can obtain a wide class of exact results. The fast wave propagates on both sides of the resonance and the transmission coefficients for low or high field side incidence are equal and are given by the geometrical optics result and by an explicit formula. No fast wave is reflected when a fast wave is incident from the high field side. We extend the reciprocity theorems of Chiu and Mau [9] and show that the mode conversion transmission coefficients and the mode conversion reflection coefficients are independent of incident wave type.

We may use the explicit formulas for the transmission coefficient to isolate those cases for which the coefficient is much less than one and consequently plasma heating is possible. By numerical calculation we may determine the range of values of  $n_{\parallel}$  in which significant energy absorption

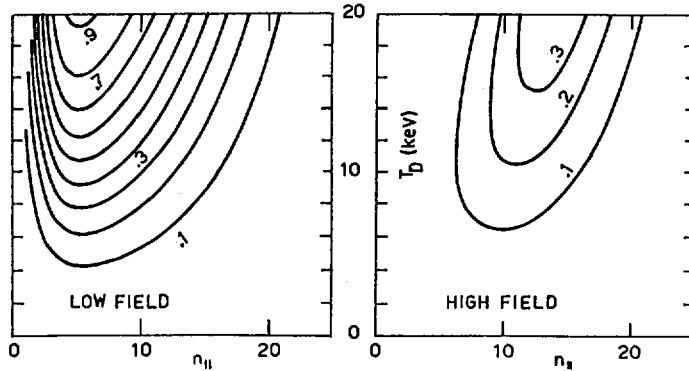


FIG. 6. Absorption contours for the third harmonic resonance for  $X_D = 2000$  and  $L\omega/c = 1$ , in the  $(n_{\parallel}, T)$  plane, corresponding to a deuterium plasma with  $n_D = 5 \times 10^{14} \text{ cm}^{-3}$ ,  $B_0 = 3 \text{ T}$  and  $L = 40 \text{ cm}$ .

occurs. Generally, the heating is more efficient as the density and/or temperature increase. We show in Fig. 4 wave propagation properties at fundamental resonance. In Fig. 4a the dispersion relation is given with both the fast waves and the slow waves present. The slow wave is clearly accessible from the high field side. In Fig. 4b the strong absorption of the slow wave is evident. In fusion plasmas the fast wave is only very weakly absorbed. Figure 5 considers pure second harmonic resonance as well as the effect of the addition of small concentrations of a fundamental harmonic resonant species. The fundamental resonant species reduces the transmission coefficient of the fast wave, and a moderate value of  $n_{\parallel}$  leads to effective energy absorption. Incident ion Bernstein waves are also typically well absorbed for such  $n_{\parallel}$ . Finally, a pure third harmonic resonant fast wave has an extremely small transmission coefficient so that addition of a moderate  $n_{\parallel}$  yields a substantial energy absorption. We show such results in Fig. 6.

#### 4. CONCLUSIONS

Because of the presence of the saddle point in B found in torsatrons the detailed behavior of ICRH is expected to be quite different than in tokamaks. This makes calculations and interpretation of experiments more difficult but may also give flexibility in tailoring the heating profiles or the effects on different species. The long VB scale length at

the center may be used to advantage. Note the large value of central ion heating in Fig. 3c even though no hybrid resonance is present. A very critical unresolved question is the confinement of energetic tails produced by ICRH. When geometrical optics applies in a perpendicularly stratified plasma we exhibit a wide range of effective wave energy absorption at fundamental, second and third harmonic resonances.

#### ACKNOWLEDGMENTS

Research sponsored by the Office of Fusion Energy, U.S. Department of Energy, under Contract No. DE-AC05-84OR21400 with Martin Marietta Energy Systems, Inc., and by U.S. Department of Energy Grant Nos. DE-FG02-86ER53223 and DE-FG02-86ER53233.

#### REFERENCES

- [1] JAEGER, E.F., WEITZNER, H., BATCHELOR, D.B., ICRF Heating in a Straight Helically Symmetric Stellarator, Rep. ORNL-TM-10223, Oak Ridge National Lab. (1986).
- [2] VILLARD, L., APPERT, K., GRUBER, R., VACLAVIK, J., Comput. Phys. Rep. 4 (1986) 95.
- [3] FUKUYAMA, A., OKAZAKI, N., GOTO, A., ITOH, S.-I., ITOH, K., Nucl. Fusion 26 (1986) 151.
- [4] ITOH, K., ITOH, S., FUKUYAMA, A., Nucl. Fusion 24 (1984) 13.
- [5] HELLSTEN, T., TENNFORS, E., in Controlled Fusion and Plasma Physics (Proc. 9th Europ. Conf. Oxford, 1979), UKAEA, Culham Lab., Abingdon, Oxfordshire (1979) 355; Phys. Scr. 30 (1984) 341.
- [6] MARTIN, T., VACLAVIK, J., Dielectric Tensor Operator of a Nonuniformly Magnetized Inhomogeneous Plasma, Rep. LRP-259/85, Ecole polytechnique fédérale de Lausanne (1985).
- [7] JAEGER, E.F., BATCHELOR, D.B., WEITZNER, H., Global Ion Cyclotron Waves in a Parallely Stratified One-Dimensional Warm Plasma, Rep. ORNL-TM-0224, Oak Ridge National Lab. (1987).
- [8] FUKUYAMA, A., ITOH, K., ITOH, S.I., Comput. Phys. Rep. 4 (1986) 137.
- [9] CHIU, S.C., MAU, T.K., Nucl. Fusion 23 (1983) 1613.

#### DISCUSSION

F.L. RIBE: Could you describe the various types of calculations that you used? I should also like to ask about the RF eigenmodes in the stellarator system.

H. WEITZNER: Three types of codes are described in the paper: they relate to a full-wave, three-dimensional cold plasma model; a perpendicularly stratified medium, including a Vlasov equation expanded through  $(k_{\perp}\rho_i)^2$ ; and a boundary layer expansion of the Vlasov equation near the resonance layers.

Regarding your second point, eigenmodes associated with the plasma and cavity have been found, but they are not the origin of the effect shown in Fig. 1 of my paper.

## ICRF HEATING OF CURRENTLESS PLASMA IN HELIOTRON E

T. MUTOH, O. MOTOJIMA, M. SATO, H. OKADA,  
H. ZUSHI, K. KONDO, N. NODA, H. KANEKO,  
T. MIZUUCHI, S. BESSHOU, F. SANO, S. SUDO,  
Y. TAKEIRI, K. AKAISHI, T. KAWABATA, Y. IJIRI,  
K. ITOH, S. MORIMOTO, A. IYOSHI, K. UO  
Plasma Physics Laboratory,  
Kyoto University,  
Gokasho, Uji, Kyoto, Japan

### Abstract

#### ICRF HEATING OF CURRENTLESS PLASMA IN HELIOTRON E.

High power and long pulse ICRF heating of a currentless plasma is carried out in Heliotron E. Three kinds of wave mode are studied in a wide range of plasma parameters. Fast wave (minority heating), ion Bernstein wave and slow wave (ion cyclotron wave) heatings are performed by using the same antenna system, while gas species, electron density and magnetic field strength are varied. With the fast wave heating, the ion temperature increases from 200 eV to 650 eV at an electron density of  $2.2 \times 10^{19} \text{ m}^{-3}$ . The duration of effective heating is, however, limited to less than 50 ms, because of the rapid increase in radiation loss power. Carbonization of the vacuum chamber reduces the radiation loss power to about 30%, and then the plasma which has been initiated by an ECH pulse is effectively heated and sustained by ICRF pulse for 100 ms only. The behaviour of the antenna loading resistance is studied in comparison with a theoretical analysis. The fundamental cavity mode is clearly identified. — With ion Bernstein wave heating, the ion energy spectrum has a two component form. The effective ion temperature in the perpendicular direction increases quickly during the ICRF pulse of a frequency of  $4 \omega_{cD}$ . With slow wave heating, the ion temperature increases up to 1.6 keV at an electron density of  $0.6 \times 10^{19} \text{ m}^{-3}$ . The heating efficiency depends strongly on the electron density.

### 1. INTRODUCTION

The ICRF method of ion and electron heating has been investigated in Heliotron E since 1984 [1, 2]. The previous, first phase experiment [3] was the first trial of ICRF fast wave heating in a fully toroidal device with current-free operation. Heating characteristics and cavity mode excitation were studied, and agreement with theoretical predictions was observed [3]. The available heating pulse length and power were, however, restricted to less than 15 ms and 1 MW, because of the limitation of the RF power source. In the present, second phase experiment, the available pulse length was extended to 200 ms, and the number of installed antenna loops and RF generators was doubled.

There were three modes of ICRF heating in Heliotron E: Fast wave (minority) heating has been extensively carried out in a medium density

( $\bar{n}_e \geq 1.5 \times 10^{19} \text{ m}^{-3}$ )  $\text{D}_2$  plasma. Ion Bernstein wave heating was carried out at the fourth harmonic ion cyclotron frequency in a low density ( $\bar{n}_e \approx 1.0 \times 10^{19} \text{ m}^{-3}$ )  $\text{D}_2$  plasma, and slow wave (ion cyclotron wave) heating was carried out in a low density ( $\bar{n}_e < 1.0 \times 10^{19} \text{ m}^{-3}$ )  $\text{H}_2$  plasma. Direct excitation of an electrostatic wave (IBW) may have occurred, because of the incompleteness of the electrostatic shielding on the plasma boundary in the direction of the magnetic field.

## 2. FAST WAVE HEATING AND CAVITY MODE OBSERVATION

The eight antenna loops were fed by two generators at different frequencies. All antenna loops were installed on the high field side inside the vacuum chamber. Figure 1 shows a picture of the minor cross-section of the toroid in the feedthrough section. The shapes of the cyclotron resonance layers are quite different from those of usual tokamaks. Normally, the magnetic field strength on axis was 1.9 T, which was determined by the ECH gyrotron frequency (53.2 GHz). The ICRF frequencies (26.7 and 28.2 MHz) correspond to the proton cyclotron frequencies at 1.75 T and 1.85 T, respectively. For the case at 26.7 MHz, the left hand cut-off and the two-ion hybrid resonance layers are located near the axis as shown in Fig. 1, when the minority proton fraction is around 10–15%.

Figure 2(a) shows typical time traces of plasma parameters without carbonization. The target plasma was produced and heated by an ECH pulse of about 300 kW, and, after that, the plasma was heated by an ECH pulse (150 kW) and an ICRF pulse (1.5 MW). The electron density increased from  $1.5$  to  $2.2 \times 10^{19} \text{ m}^{-3}$  during the

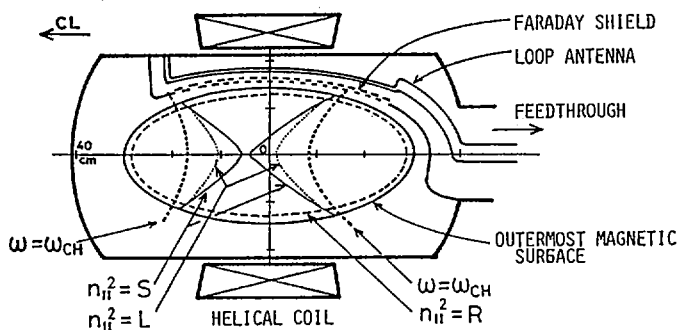


FIG. 1. Geometries of proton cyclotron resonance surface ( $\omega = \omega_{CH} = 2\omega_{CD}$ ), left hand cut-off ( $n_1^2 = L$ ) surface, two-ion hybrid resonance ( $n_1^2 = S$ ) surface, and right hand cut-off ( $n_1^2 = R$ ) surface of the fast wave in heliotron minor cross-section. Antennas are placed on high field side of plasma. ( $|B|_{r=0} = 1.9 \text{ T}$ ,  $n_H/n_H + n_D = 0.15$ ,  $n_e(0) = 4 \times 10^{19} \text{ m}^{-3}$ , frequency = 26.7 MHz.)

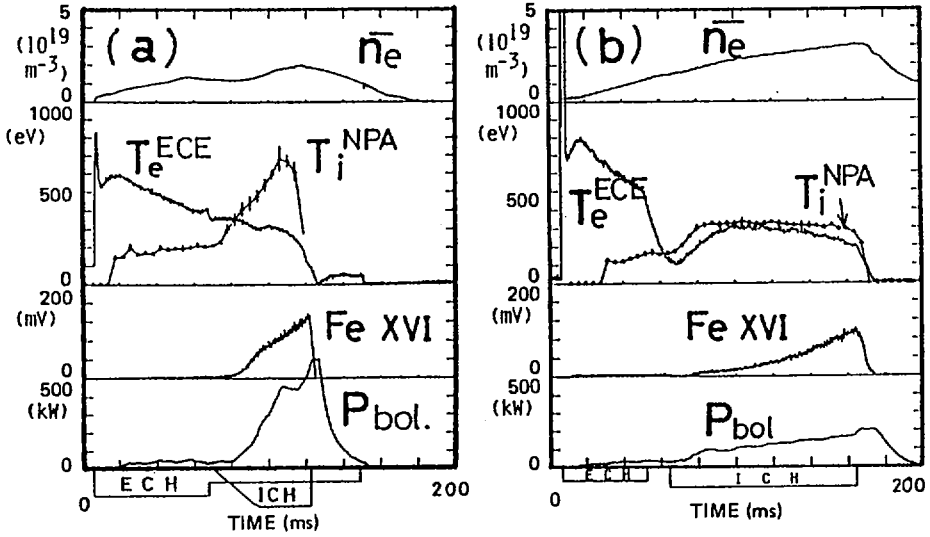


FIG. 2. Temporal evolution of electron density, electron temperature measured by electron cyclotron emission, central chord ion temperature measured by charge exchange neutral particle analyser, impurity line intensity of Fe XVI and bolometric loss power. ECH and ICRF pulses are also shown. (a) without carbonization in ECH+ICRF mode ( $n_H/n_D + n_H = 0.2-0.3$ ,  $P_{RF} = 1.5 \text{ MW}$ ), (b) with carbonization in ICRF sustained mode. ( $n_H/n_D + n_H = 0.1-0.2$ ,  $P_{RF} = 700 \text{ kW}$ ).

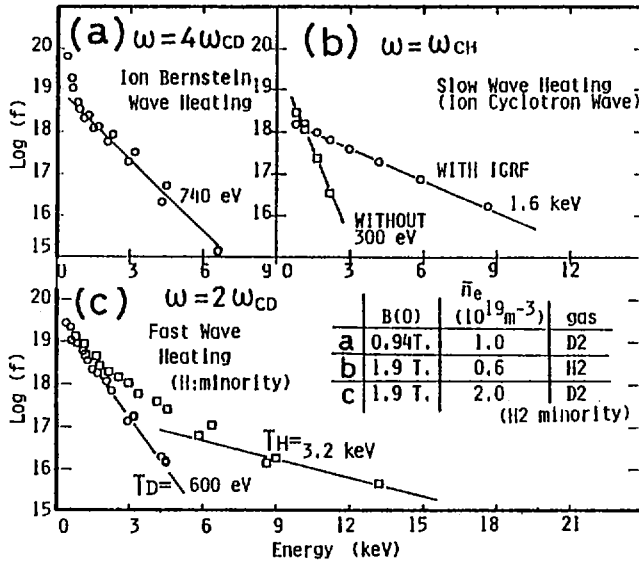


FIG. 3. Ion energy distributions for perpendicular component: (a) ion Bernstein wave heating mode ( $P_{RF} = 400 \text{ kW}$ ), (b) slow wave heating mode ( $P_{RF} = 400 \text{ kW}$ ), (c) fast wave heating mode ( $P_{RF} = 1.5 \text{ MW}$ )

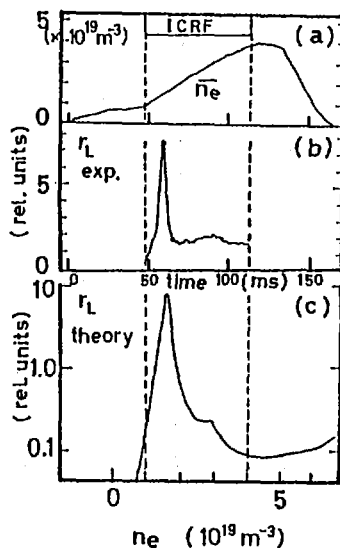


FIG. 4. Comparison between measured loading resistance of an antenna loop (b) and theoretical result [4] (c); (a) shows temporal evolution of electron density.

ICRF pulse without additional gas puffing. The ion temperature of the majority deuterium increased from 200 eV to 650 eV. During the ICRF pulse, the bolometric signal and the impurity spectrum line intensities for Fe, O and Ti increased rapidly, and the electron temperature decreased gradually. The duration of effective heating was limited to less than 50 ms, and the heating efficiency of the ICRF pulse was also reduced. The ion energy spectra which were measured by a perpendicular neutral particle analyser (NPA) are shown in Fig. 3(c). The temperature of the high energy tail of minority protons increased almost linearly with the ICRF power, and no particular deterioration of the tail confinement was observed in the range of  $E < 15$  keV. These phenomena are similar to those seen in minority heating experiments in usual tokamaks.

After carbonization of the vacuum chamber, the bolometric loss decreased to about 30%, and the impurity line intensities were also reduced. Figure 2(b) shows time tracers of the ICRF sustained plasma parameters. In this case, the ECH pulse produced a seed plasma, and then the plasma was heated by the ICRF pulse only. The electron density was not controlled by additional gas puffing during the ICRF pulse. It increased from  $1.5$  to  $3.1 \times 10^{19} \text{ m}^{-3}$  by enhanced influx from the wall surface. Ion and electron temperatures were sustained at a level of 300 to 350 eV. From the time traces of these temperatures, it seems that the ICRF power initially heated the ions and then transfer of the energy to the electrons occurred by collisions. The bolometric signal increased slowly, and, finally, radiation loss terminated the plasma sustainment. The main improvement brought about by carbonization was that

the duration of effective heating increased from 50 to 100 ms as is shown in Figs 2(a) and (b).

Recently, the structures of the excited wave were analysed theoretically and numerically in a 2-D straight heliotron configuration model by Fukuyama et al. [4]. Figure 4 shows a comparison between the measured antenna loading resistance and the analytical result of Ref. [4]. In this case, the density increased almost linearly with time; therefore, the measured loading resistance could easily be compared with the analytical results. The first sharp peak coincides well with the calculated position of the fundamental cavity mode ( $m = 0$ ), with  $\lambda_r$  equal to half the helical pitch length. Theory had predicted that the half-width of the peak is inversely proportional to the damping rate of the wave. In the case of pure deuterium plasma, a higher and narrower peak appeared, and it split into three or four sharper fine structure lines. On the other hand, in the case of a high proton ratio ( $> 5\%$ ) plasma, this peak became lower and wider as the proton ratio increased. This observation of the antenna loading peak suggests that the fast wave propagates to the centre of the plasma for  $n_e > 1.0 \times 10^{19} \text{ m}^{-3}$  and that the absorption rate is enhanced by the introduction of minority protons.

### 3. ION BERNSTEIN WAVE HEATING AND SLOW WAVE (ION CYCLOTRON WAVE) HEATING

Recently, ion Bernstein wave heating has been tested in several tokamaks [5]. In Heliotron E, ion Bernstein wave heating was applied for the first time. By using the same antenna system, ICRF power coupled to the plasma when the frequency was the fourth harmonic of the central ion cyclotron frequency. The target plasma was produced by a second harmonic ECH pulse at  $|B| = 0.94 \text{ T}$ , and the electron density was about  $1 \times 10^{13} \text{ cm}^{-3}$ . The ion temperature, which was measured by the perpendicular NPA, quickly increased from 100 eV to 700 eV during less than 5 ms. The ion energy spectrum is shown in Fig. 3(a). The spectrum shows a two component form, which implies that the heated ions are not well thermalized.

Slow wave heating has been an efficient ion heating method for stellarators [6] and heliotrons [3, 7]. In Fig. 5(a), time traces of various plasma parameters for slow wave heating are shown. The electron density was kept to a low level of less than  $6 \times 10^{18} \text{ m}^{-3}$  during the ICRF pulse of 400 kW. The ion temperature, which was measured by the perpendicular NPA, increased from 300 eV to 1.6 keV. The ion energy spectrum is shown in Fig. 3(b). The electron temperature stayed around 1.0 keV and varied almost independently from that of the ions since the energy transfer between electrons and ions was negligibly small in this parameter range. The radiation loss had an effect on the electrons only.

In this heating mode, the ion temperature strongly correlated with the electron density. The most effective heating was obtained at an electron density of  $(5-6) \times 10^{18} \text{ m}^{-3}$ . Even a slight increase in density, for example, up to

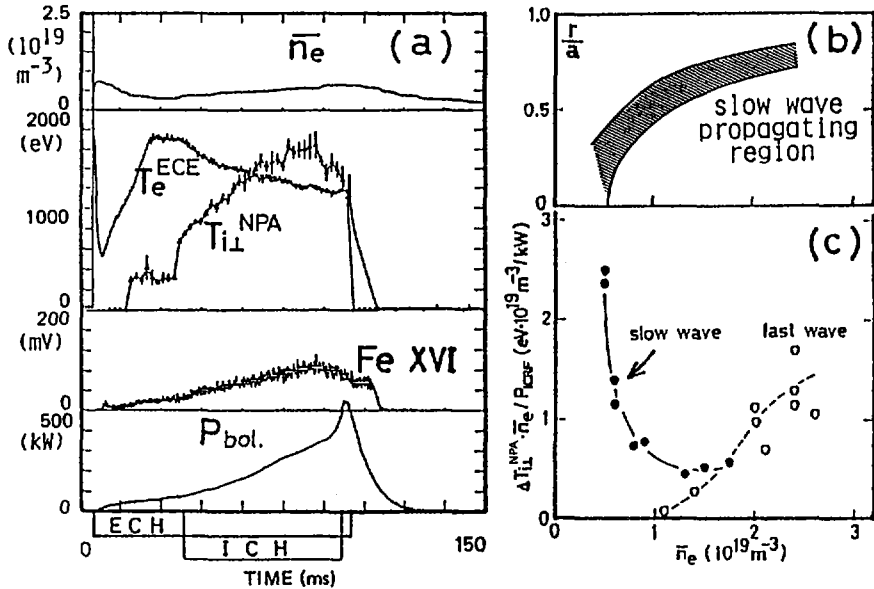


FIG. 5. (a) Temporal evolution of plasma parameters in slow wave heating mode. Parameters are the same as in Fig. 2 (frequency = 26.7 MHz,  $|B|_{r=0} = 1.9$  T, 100%  $H_2$ ); (b) positional shift of slow wave propagating region on short axis of minor cross-section versus electron density ( $n_e(r)$ ): parabolic,  $k_{\perp} = 26$   $m^{-1}$ ); (c) dependence of ion energy increments, normalized by RF power, on line averaged density. Data for fast and slow wave heating are shown.

$\bar{n}_e = 8 \times 10^{18} \text{ m}^{-3}$ , could reduce the heating efficiency for the central ion temperature by about 50%. This phenomenon can be explained by a position change of the slow wave propagating region as the density increases [3]. In Figs 5(b) and (c), the ion heating efficiency and the position of the slow wave propagating region are shown versus electron density. For slow wave heating, it was very essential to heat the central region in order to obtain high ion heating efficiency.

#### 4. SUMMARY

Fast, ion Bernstein and slow wave heating experiments were carried out on Heliotron E. For fast wave heating, the ion temperature increased up to 650 eV at an electron density of  $2.2 \times 10^{19} \text{ m}^{-3}$  and an input ICRF power of 1.5 MW. The duration of effective heating was limited to about 50 ms by radiation loss. With carbonization of the chamber wall, the effective heating time increased to longer than 100 ms. This may be due to the reduction of the iron impurity influx. Then, the ICRF pulse became able to sustain the plasma for 100 ms without an ECH pulse. The

behaviour of the antenna loading resistance with changing plasma density was studied by comparison with theoretical predictions. The good agreement confirms that a cavity mode was excited in the heliotron plasma.

These results suggest the effectiveness of the fast wave heating for heliotron plasmas.

With ion Bernstein wave heating, the perpendicular ion temperature increased from 100 eV to 700 eV at an electron density of  $1.0 \times 10^{19} \text{ m}^{-3}$  and an ICRF power of 400 kW, but the ions were not well thermalized.

With slow wave heating, the ion temperature increased up to 1.6 keV, as determined by the perpendicular NPA measurement at an electron density of  $6 \times 10^{18} \text{ m}^{-3}$  and an ICRF power of 400 kW. The heating characteristics depended strongly on the electron density and were explained by a positional shift of the slow wave propagating region. The ion heating efficiencies of fast and slow wave heating are shown in Fig. 5(c). The dependences on the electron density are consistent with theoretical predictions.

## REFERENCES

- [1] UO, K., et al., in Plasma Physics and Controlled Nuclear Fusion Research 1984 (Proc. 10th Int. Conf. London, 1984), Vol. 2, IAEA, Vienna (1985) 383.
- [2] IYOSHI, A., *ibid.*, Vol. 1, p. 453.
- [3] MUTOH, T., et al., Nucl. Fusion **24** (1984) 1003.
- [4] FUKUYAMA, A., et al., Nucl. Fusion **26** (1986) 151.
- [5] ONO, M., et al., Phys. Rev. Lett. **54** (1985) 2239.
- [6] BROWN, I.G., et al., Phys. Fluids **12** (1969) 1318.
- [7] IYOSHI, A., et al., Nucl. Fusion **14** (1974) 789.

## DISCUSSION

L. KOVRIZHNYKH: According to your Fig. 2, the ion temperature increases monotonically during the HF pulse. Does this mean that the ion energy lifetime is more than the duration of the HF pulse?

T. MUTOH: The ion energy confinement time was of the order of 10 ms. hence the time-scale for the ion temperature variation for the slow wave mode was longer than that time. Our understanding is that the power deposition profile gradually changed during the ICRF pulse. The changes in  $n_e(r)$  and temperatures probably relate to this mechanism.

R.J. GOLDSTON: You can now support similar plasmas with ICH and NBI on Heliotron E. Would you compare the energy confinement time or the heating efficiency in the two cases?

T. MUTOH: We have not yet estimated the absorbed power of ICRF heating so we cannot make an accurate comparison. Roughly speaking, heating efficiencies

were almost the same for NBI and ICRF within a factor of 1.5. The power dependences of the gross energy confinement time in both cases were around  $\propto p^{-0.5}$ , given the same electron density.

S. SHINOHARA: In the case of the ion Bernstein wave, is there any possibility that other waves such as the fast magnetosonic wave can propagate in the plasma and heat the ions? And what in your opinion is the fraction of the wave power carried by the ion Bernstein wave? It seems to me that in the Heliotron E device, because of the magnetic field geometry and antenna current direction, it is rather difficult for the ion Bernstein wave to propagate, as compared with the case of the tokamak with low field side excitation, in which the antenna current is parallel to the toroidal magnetic field.

T. MUTOH: At fourth harmonic frequency, fast wave damping was negligibly small. The absorbed power in the plasma column was therefore mainly due to the ion Bernstein wave. But the fast wave was excited simultaneously, so the excited wave structure was probably a combination of the fast wave and the ion Bernstein wave.

## I. ELECTRON CYCLOTRON RESONANCE PLASMA HEATING BY ORDINARY WAVES IN THE L-2 STELLARATOR

E.D. ANDRYUKHINA, D.K. AKULINA, G.M. BATANOV,  
V.A. BATYUK, M.S. BEREZHETSKIJ, M.A. BLOKH,  
G.S. VORONOV, S.E. GREBENSHCHIKOV, S.I. DOLGAEV,  
N.P. DONSKAYA, K.S. DYABILIN, L.M. KOVRIZHNYKH,  
L.V. KOLIK, N.F. LARIONOVA, K.M. LIKIN,  
A.I. MESHCHERYAKOV, P.E. MOROZ, S.N. POPOV,  
A.E. PETROV, V.I. ROSHCHIN, A.V. SAPOZHNIKOV,  
K.A. SARKSYAN, N.N. SKVORTSOVA, I.S. SBITNIKOVA,  
A.D. SMIRNOVA, V.N. SUKHODOL'SKIJ,  
M.F. TERNOVSKAYA, O.I. FEDYANIN, S.I. FEDORENKO,  
Yu.V. KHOLNOV, M.G. SHATS, I.S. SHPIGEL'  
Institute of General Physics,  
Academy of Sciences of the USSR

## II. FAST WAVE EIGENMODES IN THE L-2 STELLARATOR DURING ICR PLASMA HEATING

V.A. BATYUK, S.E. GREBENSHCHIKOV,  
A.I. MESHCHERYAKOV, P.E. MOROZ,  
I.S. SBITNIKOVA, I.S. SHPIGEL'  
Institute of General Physics,  
Academy of Sciences of the USSR

Moscow, Union of Soviet Socialist Republics

### Abstract

I. ELECTRON CYCLOTRON RESONANCE PLASMA HEATING BY ORDINARY WAVES IN THE L-2 STELLARATOR.

II. FAST WAVE EIGENMODES IN THE L-2 STELLARATOR DURING ICR PLASMA HEATING.

Experimental results on electron cyclotron resonance plasma heating (ECRH) by ordinary waves ( $\vec{E} \parallel \vec{B}$ ) in the L-2 stellarator are presented. Microwave radiation ( $f = 37.5$  GHz,  $P = 100$  kW) is launched into the plasma in the form of a Gaussian beam from the weak field side. The heating is observed to be in resonance with the magnetic field. The electron temperature increases by a factor of two (up to 0.6 to 0.7 keV) at a plasma density of  $10^{13}$  cm $^{-3}$ , the heating efficiency being 5 to 6 eV·kW $^{-1}$ . The ion energy distributions are non-thermal during ECR heating. — Experimental results on propagation and damping of waves and excitation of eigenmodes during ICR plasma heating in the L-2 stellarator are presented and explained theoretically. In the theoretical model, plasma and magnetic field inhomogeneities and the presence of an Alfvén resonance are included. The experimental results are in good agreement with the calculations.

# I. ELECTRON CYCLOTRON RESONANCE PLASMA HEATING BY ORDINARY WAVES IN THE L-2 STELLARATOR

## 1. Introduction

The experiments were carried out in the L-2 stellarator [1] ( $R = 100$  cm,  $a_p = 11.5$  cm,  $\ell = 2$ ,  $m = 14$ ). Microwave power taken from a gyrotron with  $f = 37.5$  GHz,  $P_0 = 100$  kW and a pulse duration of  $\leq 7 \times 10^{-3}$  s, was launched into the machine through a system of two lenses in the form of a linearly polarized Gaussian beam with  $\vec{E} \parallel \vec{B}$ , a beam divergence of 0.02, and a beam diameter of about 6 cm, the ordinary wave containing 99% of the total power. The target plasma was produced by Ohmic discharges at relatively low levels of plasma current and Ohmic power ( $I_p = 12-13$  kA,  $P_{OH} = 20-25$  kW,  $\bar{n}_e \approx 7.5 \times 10^{12}$  cm $^{-3}$ ,  $T_e(0) \approx 0.35$  keV,  $T_i(0) \approx 70$  eV, hydrogen). To reduce the impurity content and the radiative losses (RL), a graphite limiter was placed at the magnetic surface with  $\bar{r} = 9$  cm.

## 2. Results

Figure 1 shows the time histories of plasma current  $I_p$ , resistive component of loop voltage  $U$ , radiative loss power  $P_{rad}$  and mean electron density  $\bar{n}_e$  during a heating pulse when the resonance condition  $\omega_0 = \omega_{ce}$  is fulfilled in the plasma centre. When the ECR power is switched on, the plasma current starts decreasing more slowly than before, and the loop voltage has a characteristic drop, i.e. it decreases by a factor of about two at the end of the pulse, and the plasma conductivity increases by about 2.5 times. During this process,  $\bar{n}_e$  changes by no more than 10%, and  $P_{rad}$  increases by 5 to 8 kW, reaching 18 to 20 kW at the end of the pulse.

The electron temperature at the centre,  $T_e(0)$ , as measured by Thomson scattering, soft X-ray PHA spectrometry and foils, increases from 0.35 keV to 0.6–0.7 keV, and the main temperature variation occurs during 1.5 to 2 ms after switching on the microwave power. The electron distribution function is Maxwellian. Figure 2 shows the energy spectra of the charge exchange atoms for Ohmic and ECR heating. In contrast to the case of Ohmic heating, non-Maxwellian ion distributions with a tail of high energy particles are observed during ECRH. If we, conventionally, divide the available energy range into two parts,  $E_1 = 0.2 - 0.5$  keV and  $E_2 = 0.5 - 1.5$  keV, we can derive the effective temperatures for these ranges:  $T_i^{(1)}$  (bulk ions) and  $T_i^{(2)}$  (tail). The time histories of  $T_i^{(1)}$  and  $T_i^{(2)}$  are presented in Fig. 3. When we switch on the ECR power, the energy distribution is deformed rapidly during about 1 ms, i.e.  $T_i^{(1)}$  rises from 70 to 90 eV and  $T_i^{(2)}$  increases to about 150 eV, while  $T_i^{(1)} = T_i^{(2)}$  before ECR heating. The spatial profile of  $T_i^{(1)}$  is relatively flat in both cases.

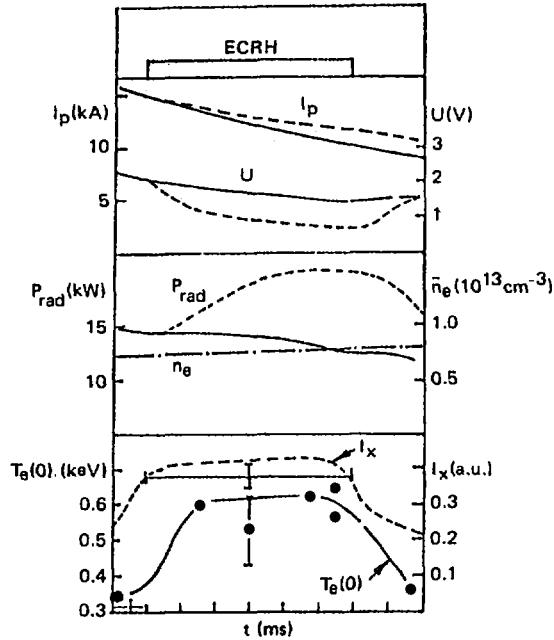


FIG. 1. Time dependences of  $I_p$ ,  $U$ ,  $P_{rad}$  and  $\bar{n}_e$  during ECR heating pulse (— OH, - - OH + ECRH) and of central electron temperature,  $T_e(0)$ : (●: Thomson scattering, +: soft X-ray spectra,  $I_x$ : ratio of X-ray fluxes passing through Be filters of thickness  $25 \mu\text{m}$  and  $50 \mu\text{m}$ ).

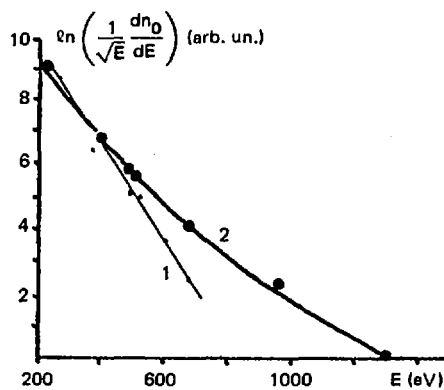


FIG. 2. Energy spectra of charge exchange neutral atoms (1: OH, 2: OH + ECRH).

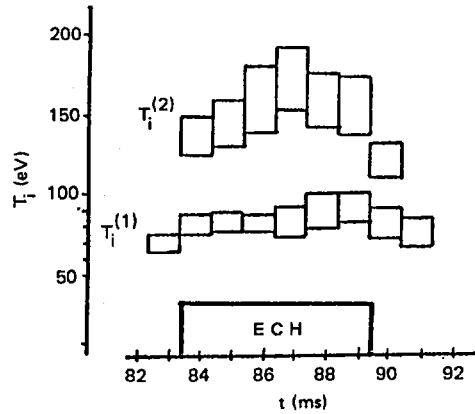


FIG. 3. Time dependence of ion temperatures  $T_i^{(1)}$  and  $T_i^{(2)}$  during ECRH pulse.

To determine the efficiency of ECR heating, we measured the absorption of microwave power by using two methods: measuring the power passing through the plasma near the launching point and analysing the plasma energy loss channels related to radiation and thermal conductivity, the main part of the thermoconductive flux being deposited at the limiter. These methods yield approximately the same value of absorbed power, i.e. 0.5 to 0.6 of  $P_0$ .

### 3. Discussion

(a) The Ohmic heating power during ECRH is low ( $P_{OH} \approx 10 \text{ kW} \approx 0.15-0.2 P_0$ ) and is not essential in the plasma energy balance.

(b) The plasma conductivity increases continuously during the heating pulse while  $T_e(0)$  rises for 1.5 to 2 ms only. This fact indicates that the electron temperature profile broadens during heating since no increase in the effective plasma charge was observed spectroscopically. The increase in conductivity could be due to current drive or to an increase in the number of runaway electrons. When, however, the directions of current and magnetic field were reversed, no changes in  $I_p(t)$  and  $U(t)$  were observed. On the other hand, according to the X-ray spectra in the range of 2 to 40 keV and from the estimates carried out, no increase in the number of runaways takes place.

(c) The increase in ion temperature at  $T_e/T_i = 7-8$  and the non-thermal ion energy distributions indicate that ion heating is due to a non-linear mechanism rather than to Coulomb collisions.

(d) Microwave absorption was numerically calculated by using ray tracing (31 rays), in geometrical optics approximation, in the real geometry of the L-2 magnetic field. It was shown that the maximum absorption of about 40% takes place for

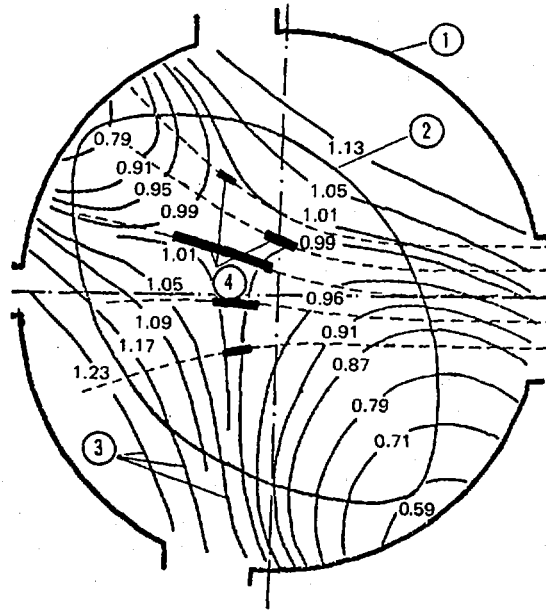


FIG. 4. Structure of magnetic field module  $|B|$  (3), ray traces (dashed lines) and absorption regions (4) at cross-section where microwave power is launched, vacuum vessel (1), and the last closed magnetic surface (2); torus major axis is at left hand side.

$\bar{n}_e(0) = 10^{13} \text{ cm}^{-3}$ ,  $T_e(0) \approx 0.4 \text{ keV}$ , and with resonance conditions at the plasma centre. Figure 4 shows the ray traces calculated under the above mentioned conditions; also shown are the absorption regions and the structure of  $|B|$ . Microwave absorption is localized within the saddle shaped region of  $|B|$ , where  $d \ln B/dr$  is minimum. The results of the calculations are in good agreement with the experimental ones.

(e) Just as in the previous experiments [2, 3], the heating efficiency decreases by a factor of three when the magnetic field changes by  $\pm 5\%$ , which is due to the specific structure of the magnetic field in the L-2 stellarator.

(f) The other important parameters are: plasma energy  $W \sim 120 \text{ J}$ , global energy lifetime  $\approx 2 \text{ ms}$ ,  $\beta(0) \approx 0.16\%$ , and ECR heating efficiency  $5-6 \text{ eV} \cdot \text{kW}^{-1}$  per  $10^{13} \text{ cm}^{-3}$ .

## REFERENCES

- [1] ANDRYUKHINA, E.D., et al., Preprint No. 154, Lebedev Institute, Moscow (1977).
- [2] ANDRYUKHINA, E.D., in Plasma Physics and Controlled Nuclear Fusion Research 1984 (Proc. 10th Int. Conf. London, 1984), Vol. 2, IAEA, Vienna (1985) 409.
- [3] ANDRYUKHINA, E.D., et al., Pis'ma Zh. Ehksp. Teor. Fiz. **40** (1984) 377.

## II. FAST WAVE EIGENMODES IN THE L-2 STELLARATOR DURING ICR PLASMA HEATING

In the experiments on ICR heating ( $\omega = \Omega_i$  of hydrogen plasmas in the L-2 stellarator [1], the heating efficiency was rather high. The present experiments, studying wave propagation in the ICR heating regime of a hydrogen plasma, were carried out for plasma densities of  $n_0 \equiv n_e(0) \lesssim 4 \times 10^{13} \text{ cm}^{-3}$  and a magnetic field of  $B_0 \approx 12 \text{ kG}$  at the axis. The antenna was a bent loop whose central part — without Faraday screen — was moved close to the plasma. The longitudinal component of the radiofrequency magnetic field was measured by magnetic probes placed along the torus at different distances from the antenna. The eigenmodes of the fast magnetosonic waves corresponding to waves with  $k_{\parallel} = \ell/R_0$ , where  $\ell$  is an integer and  $R_0$  is the major radius of the torus, were observed as spikes of the radiofrequency amplitude when the plasma density was changed. The experimental dependence of  $k_{\parallel}$  on  $n_0$  for the eigenmodes is shown in Fig. 5(a). The character of wave propagation changed essentially (Fig. 5(b)) when the magnetic field  $B_0$  became close to  $B_c$ , which corresponds to the resonance condition  $\omega = \Omega_i$  at the plasma centre, i.e. when the longitudinal damping length,  $\lambda_D$ , was less than the torus

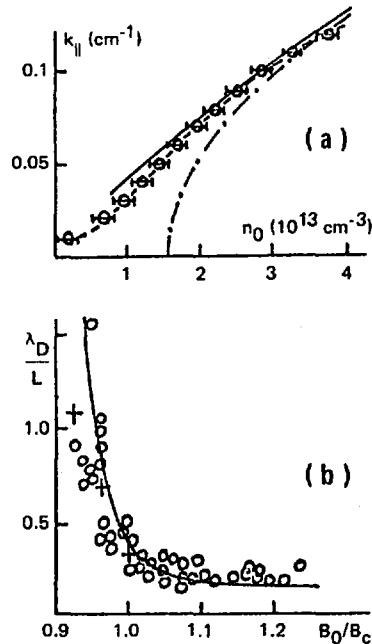


FIG. 5. Theoretical and experimental dependence of (a)  $k_{\parallel}$  on  $n_0$  and (b) relative damping length,  $\lambda_D/L$ , on  $B_0/B_c$ .

perimeter,  $L = 2\pi R_0$ . These dependences can neither be explained by collisional nor by cyclotron absorption of fast magnetosonic waves. Calculations allowing for the presence of a resonance surface with  $\epsilon_1 = n_i^2$  in the plasma show that the strong damping and the observed wave dispersion may be due to Alfvén resonance.

To determine the quality factor  $Q$  and the damping length  $\lambda_D$ , we have calculated the dependences of the loading resistance of the antenna  $R_{km}$  on  $B_0/B_c$  for various  $k_{\parallel}$  ( $n_0 = \text{const}$ ) for the  $m = 1$  mode. The values of  $Q$  and  $\lambda_D$  were estimated from  $Q = (2\delta)^{-1}$  and  $\lambda_D = 2Qv_g/\omega$ . Here,  $\delta$  is the ratio of the half-width-at-half-maximum of the peak of  $R_{km}$  to the value of  $B_0/B_c$  at the maximum, and  $v_g$  is the longitudinal component of the mean group velocity. Using the dependences of  $R_{km}$  on  $k_{\parallel}$  for various  $n_0$  ( $B_0 = B_c$ ), we could find the  $k_{\parallel}^*$  that corresponds to the maximum of  $R_{km}$ , by analogy with the eigenmodes. The results of the calculations are shown by the solid lines in Figs 5(a) and (b). If the Alfvén resonance is taken into account, the results of the calculations differ essentially from those of Ref. [2] (dash-dotted line in Fig. 5(a)), especially for low plasma densities, the results of [2] having been obtained for a homogeneous magnetic field. The calculations are in good agreement with the experimental results.

## REFERENCES

- [1] BATYUK, V.A., et al., in *Controlled Fusion and Plasma Physics* (Proc. 11th Europ. Conf. Aachen, 1983), Vol. 7D, Part 1, European Physical Society (1983).
- [2] KOVRIZHNYKH, L.M., MOROZ, P.E., *Zh. Tekh. Fiz.* **54** (1984) 649.

## DISCUSSION

H. WOBIG: You reported a confinement time of 2 ms in ECR heated plasmas. How did the confinement time change when you applied the ECRH power to the ohmically heated target?

L.M. KOVRIZHNYKH: When the high microwave frequency power is applied, the confinement time decreases slightly. But the reason for this may not only be the degradation of confinement due to input of the power; it may also be a direct result of an increase in electron temperature.

A.C. RIVIERE: You have described some anomalous ion heating during ECRH. Do you believe that this is due to the connection of the EC wave to the electron Bernstein wave at the upper hybrid resonance, leading to a parametric decay instability?

L.M. KOVRIZHNYKH: Yes, it is possible; but the exact mechanism underlying the ion heating is not yet known.



## PLASMA POTENTIAL AND CONFINEMENT IN THE NAGOYA BUMPY TORUS (NBT-1M)

H. IKEGAMI, M. HOSOKAWA, H. IGUCHI, T. SHOJI,  
T. KAMIMURA, H. SANUKI, K. TAKASUGI, F. TSUBOI,  
T. TAKEUCHI, A. KOMORI<sup>1</sup>, K. KADOTA, J. FUJITA,  
C. HONDA<sup>2</sup>, M. YOKOO<sup>2</sup>, M. MAEDA<sup>2</sup>, K. MURAOKA<sup>1</sup>,  
T. YUYAMA<sup>3</sup>, T. MICHISHITA<sup>3</sup>, H. KUBO<sup>3</sup>, M. FUJIWARA  
Institute of Plasma Physics,  
Nagoya University,  
Nagoya, Japan

### Abstract

PLASMA POTENTIAL AND CONFINEMENT IN THE NAGOYA BUMPY TORUS (NBT-1M).

There are two critical issues to be confirmed for the bumpy torus concept to be established. One is the average minimum-B configuration produced by the hot electron rings that stabilizes MHD instabilities to which bumpy torus plasmas are susceptible. The other is confinement scaling, especially confinement enhanced with the radial electric field. — With increased microwave power input of 90 kW into one mirror sector, which is equivalent to a total input of 2.16 MW to the bumpy torus NBT-1M, gradient B reversal is not achieved. The hot electron ring beta is observed to remain at a level of several per cent, i.e. almost at the same level as in the case of 30 kW total input power, although more than one order of magnitude increase is detected in the diamagnetic loop signal and the hard X-ray intensity. — The plasma space potential is found to be controlled by energetic electrons generated in the second harmonic electron cyclotron resonance zone and by their loss mechanism. The potential profile is little influenced by the transport of the core plasma for the present NBT-1M plasma parameters, but because of the potential produced by the energetic electrons, neoclassical transport models can be applied to the core plasma. — As to confinement scaling, the effect of the radial electric field is studied with the use of high power ECH and ICH, for the purpose of controlling the polarity of the radial electric field and the collisionality. No drastic improvement is observed, regardless of the sign of the electrostatic potential (well or hill) with respect to the plasma edge. The observed energy confinement times agree, however, with the prediction from neoclassical transport theory.

### 1. INTRODUCTION

The Nagoya Bumpy Torus (NBT-1M) [1] is composed of 24 simple mirrors connected end to end into a torus with a major radius of 1.4 m and an average aspect ratio of approximately 10. The plasmas are produced and heated by a combination of microwave power (18 GHz and 28 GHz) for ECH and RF power (7–9 MHz) for ICH. The MHD instabilities to which simple mirror plasmas are susceptible, could

<sup>1</sup> Graduate School of Engineering Sciences, Kyushu University, Fukuoka, Japan.

<sup>2</sup> Faculty of Engineering, Kyushu University, Fukuoka, Japan.

<sup>3</sup> College of General Education, Kyoto University, Kyoto, Japan.

be stabilized by the average minimum-B configuration produced by a hot electron ring, which is generated by electron cyclotron heating (ECH) in the midplane of each mirror sector; in addition, the hot electron ring beta is considered to control the maximum beta of the toroidal core plasma.

Neoclassical theory [2] predicts an electron energy confinement time  $\tau_E$  given by

$$\tau_E/\tau_{ei} = 1.3(R/a)^2 (1 + \nu^2/\Omega^2) (e\phi_0/T_e)^2 \quad (1)$$

where  $\Omega$  is the poloidal precessional frequency dominated by  $\vec{E} \times \vec{B}$  drift over  $\nabla B$  drift,  $\phi_0$  is the electrostatic potential at the plasma centre with respect to the plasma edge, and  $\tau_{ei}$ ,  $R$ ,  $a$  are the electron collision time, the major radius and the average plasma radius, respectively.

## 2. GRADIENT B REVERSAL BY HOT ELECTRON RING

The most critical issue for the bumpy torus concept is whether the hot electron ring can produce the average minimum-B configuration for the stabilization of MHD instabilities. The ring beta must then be large enough to push out the local magnetic field to reverse  $\nabla_{\perp} B$  in the outer edge of the ring.

With a microwave power of 3 kW at 18 GHz fed into each mirror sector, the plasma magnetic field at the ring location was measured by the Zeeman splitting of lithium beam atoms excited by plasma electrons, and the ring beta was observed to reach several per cent which was too small to reverse  $\nabla_{\perp} B$ . So the microwave power was increased up to 90 kW at 28 GHz fed into a single mirror sector. For the measurement, to enhance the fluorescence signal intensity, sodium beam atoms were excited by a scanning dye laser as shown in Fig. 1(a), and Zeeman splittings were detected [3]. The microwave power input of 90 kW per mirror sector was equivalent to a total power input of 2.16 MW, and, according to the 30 times greater input power compared with the previous cases, both the ring energy detected by the diamagnetic loops and the line integrated hard X-ray signals were observed to increase more than one order of magnitude. However, as is seen in Fig. 1(b), the change in the magnetic field intensity was detected to remain always at the level of several per cent and no reversal of  $\nabla_{\perp} B$  was ever observed.

It should be noted that even in this case the NBT plasma was observed to be MHD stable. Several explanations for the observed stability [4], such as shear of  $\vec{E} \times \vec{B}$  poloidal drift, line tying, charge uncovering, etc., are proposed.

## 3. EFFECT OF RADIAL ELECTRIC FIELD ON CONFINEMENT

The confinement properties and their relationship with the plasma potential in an ECH plasma have been studied by using a high power 28 GHz pulse gyrotron

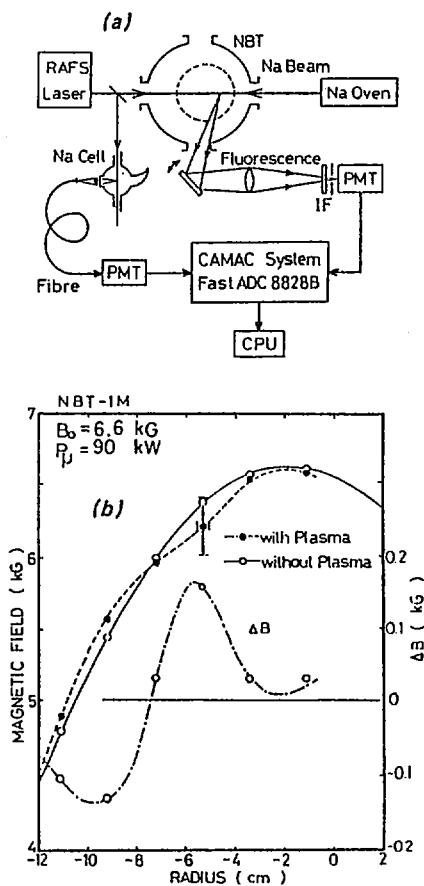


FIG. 1. (a) Schematic diagram of local magnetic field measurement with sodium beam, Zeeman fluorescence spectroscopy induced by rapid frequency scanning dye laser.

(b) Magnetic field modification by hot electron ring generated with 90 kW (28 GHz, 50 ms) microwave power. Measurement was made 5 ms after 28 GHz power turnoff.

(200 kW/75 ms). The initial plasma is produced by 18 GHz microwave power (4–26 kW), and a 28 GHz pulse is superimposed, when the initial plasma reaches almost a steady state.

Figure 2(a) shows the typical time evolution of several plasma parameters, together with the time sequence of the superimposed microwave power. Both plasma density and ring stored energy increase gradually with the applied 28 GHz power, but the  $n_e f(T_e)$  signal shows a sharp rise, which may indicate that the electrons in the core plasma are heated rapidly. From a comparison of  $n_e$  and  $n_e f(T_e)$ , the core electron temperature is estimated to remain nearly constant during the duration of the

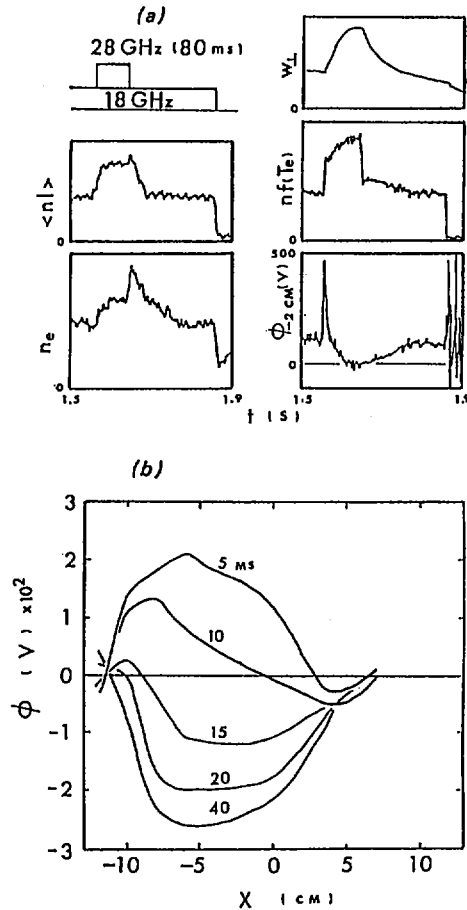


FIG. 2. (a) Time evolution of plasma parameters associated with superposition of 110 kW (28 GHz) microwave pulse on plasma produced by 26 kW (18 GHz) microwave source. Line integrated density,  $\langle n_l \rangle$ , from 75 GHz interferometer; central electron density,  $n_e$ , from lithium neutral beam probe; ring stored energy,  $W_L$ , from diamagnetic loop; sum of doubly ionized caesium beam currents on split plate detectors,  $n_f(T_e)$ ; central plasma space potential,  $\phi$ , determined by heavy ion beam probe.

(b) Time evolution of radial potential profile after 160 kW (28 GHz) pulse front superposed on plasma produced by 4 kW (18 GHz) source in magnetic field of 6.6 kG.

28 GHz power. Thomson scattering revealed that the electron distribution was non-Maxwellian and the average energy was 100 to 150 eV. An additional slow increase and decay of the  $n_f(T_e)$  signals after the rapid change, at 'on' and 'off' of the 28 GHz pulse, will be due to ionization by slowly produced energetic electrons.

It is also found in Fig. 2(a) that the plasma potential is controlled by the energetic electrons rather than by the core plasma. The time evolution of the radial potential profiles is shown in Fig. 2(b), where it takes 20 ms before the potential forms

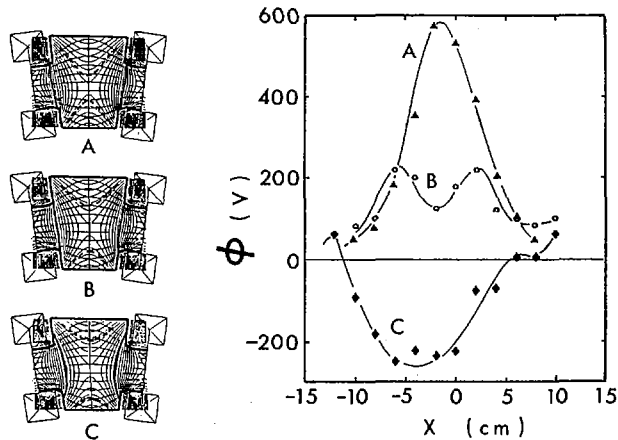


FIG. 3. Electron cyclotron resonance configuration in mirror sector, where solid and dashed lines indicate fundamental and second harmonic electron cyclotron resonance zones. Corresponding to three cases [A (5.2 kG), B (5.9 kG), C (6.9 kG)], each with different magnetic field intensity, space potential profiles are shown. Plasmas are produced with combination of 160 kW (28 GHz) and 4 kW (18 GHz) for preionization.

a well depth of 200 to 250 V; thereafter it remains constant until the 28 GHz power is turned off. The characteristic time-scale of this potential well formation is much longer than the core plasma confinement time, indicating that the potential well formation is related to the energetic electrons rather than to the core plasma electrons.

The mechanism of potential formation was further examined by varying the electron cyclotron resonance zone (the energy deposition profiles), i.e. by varying the magnetic field strength. In Fig. 3, the radial profiles of the space potential are shown in three cases with different magnetic field strengths. In the case of a lower magnetic field, where the second electron cyclotron resonance zone is located in the core plasma region, the potential profile is peaked at the centre, which indicates that energetic electrons are efficiently generated in the central area where the second ECR zone gets closer to the lower magnetic field. With increasing magnetic field, the peak splits apart in radial direction, and between the two separate peaks there is a potential well. When the second harmonic ECR zone is properly separated in the midplane, a hot electron ring is most effectively generated there, encircling the core plasma. The energetic electrons not only control the core plasma stability, but also have a profound effect on the core plasma placed in the potential produced in this way.

It is important to recognize that if we assume the potential profile to be the result of ambipolar diffusion of the core plasma, the observed direction of the radial electric field is contrary to the prediction of neoclassical transport theory. Because of the potential produced by the energetic electrons, the neoclassical transport model can be applied to the core plasma, but the core plasma itself will have little effect on the potential, for the present core plasma parameters.

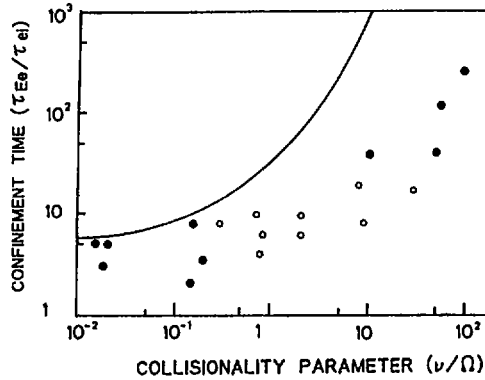


FIG. 4. Electron energy confinement time normalized by electron-ion collision time versus collisionality  $\nu/\Omega$ . Closed and open circles are for RF and ECH plasmas, respectively. Solid curve is given by neoclassical transport theory [5].

Studies were made on the confinement scaling of the core plasma by using ECH and ICH, varying the value of collisionality  $\nu/\Omega$  over a wide range. The energy confinement time was estimated from density, temperature, and volume of the core plasma, divided by the input power, on the assumption that the fraction of the absorbed power is 30% and constant.

In an ECH plasma ( $n_e \sim 10^{12} \text{ cm}^{-3}$ ,  $T_e \sim 100 \text{ eV}$ ) of standard NBT-1M operation, the collisionality was in the intermediate regime  $1 < \nu/\Omega < 10$ , and the energy confinement was estimated to be in the range of three to ten times the electron-ion collision time. The potential profile was observed to have a typical negative well.

In a high density ICH plasma ( $n_e \sim 10^{13} \text{ cm}^{-3}$ ,  $T_e \sim 10 \text{ eV}$ ), the electrons were collisional,  $10 < \nu/\Omega < 100$ , and the ratio  $\tau_{Ee}/\tau_{ei}$  ranged between 30 and 300, in a peaked positive potential ( $\phi_0 \sim 500 \text{ V}$ ). In a low density RF plasma ( $n_e \sim 10^{10} \text{ cm}^{-3}$ ,  $T_e \sim 30 \text{ eV}$ ) and low magnetic field, to which no ECH was applied, no energetic electrons were supposed to be generated. The collisionality was in the range  $0.02 < \nu/\Omega < 1$ , with a positive hill potential generated; however, no clear improvement of confinement was observed.

The comparison with neoclassical transport theory [5] is summarized in Fig. 4, where the experimental values show reasonable agreement with theory.

#### 4. CONCLUSIONS

With an increased microwave power input of 90 kW into one mirror sector, which is equivalent to a total input of 2.16 MW into the bumpy torus NBT-1M, no gradient B reversal has ever been achieved. The hot electron ring beta was always observed to remain at a level of several per cent, i.e. at almost the same level as in

the case of 30 kW total input power, although a more than one order of magnitude increase was detected in the diamagnetic loop signal and the hard X-ray intensity. There must be some mechanism at work that levels off the ring beta to such a low level as several per cent.

The plasma space potential is determined by the generation of energetic electrons in the second harmonic electron cyclotron resonance zone and by their loss mechanism. The potential profile may be little influenced by the transport of the core plasma under the present NBT-1M plasma parameters, but the potential produced in this way may have a profound effect on core plasma transport.

On the assumption that the absorbed power is a constant fraction of 30% of the input power, the volume averaged energy confinement time shows reasonable agreement with the prediction of neoclassical transport theory, regardless of the sign of the potential, and is estimated to be three to ten times the electron-ion collision time, for a collisionality of  $\nu/\Omega = 0.02-10$ .

## REFERENCES

- [1] FUJIWARA, M., et al., in Plasma Physics and Controlled Nuclear Fusion Research 1980 (Proc. 8th Int. Conf. Brussels, 1980), Vol. 2, IAEA, Vienna (1981) 845; in Plasma Physics and Controlled Nuclear Fusion Research 1982 (Proc. 9th Int. Conf. Baltimore, 1982), Vol. 2, IAEA, Vienna (1983) 197; in Plasma Physics and Controlled Nuclear Fusion Research 1984 (Proc. 10th Int. Conf. London, 1984), Vol. 2, IAEA, Vienna (1985) 551.
- [2] JAEGER, E.F., et al., Phys. Rev. Lett. **40** (1978) 866.
- [3] HONDA, C., et al., Jpn. J. Appl. Phys. **24** (1985) 1402.
- [4] SANUKI, H., CHEN, F., Phys. Fluids **28** (1985) 3567.
- [5] HASTINGS, D., KAMIMURA, T., J. Comput. Phys. **61** (1985) 286.

## DISCUSSION

H. WEITZNER: How would you compare your observation of the non-reversal of  $\nabla_{\perp}B$  with the EBT results?

H. IKEGAMI: I don't think that the reversal of  $\nabla_{\perp}B$  has ever been achieved with EBT at Oak Ridge. Whether the non-reversal of  $\nabla_{\perp}B$  is due to the canted mirror asymmetry, or to the nature of the hot electron ring itself, is not yet clear and requires further research.

J.D. CALLEN: If I understand correctly, you increased the ECH power input in one cavity from 3 to 90 kW, and the stored energy in the hot electron ring went up by about a factor of ten. Theoretically, the  $\Delta B$  would increase by a similar factor unless the ring increased in size by a corresponding factor. Since  $\Delta B$  apparently did not increase, could you say whether the ring increased in its radial or axial extent?

H. IKEGAMI: When the ECH power was changed from 3 to 90 kW, the microwave frequency was also changed, from 18 to 28 GHz, so it is for the magnetic field intensity to provide the ECH resonance, and in order to give the same  $\Delta B/B$ , the hot electron energy density must have increased by a factor of 2.4, at least. The rest of the increment factor may be attributed to some expansion and spread of the ring in a radial direction, especially towards the wall.

K. ITOH: The asymmetry of the potential profile persists during the change in the sign of the potential. Does this mean the existence of the large convective cells, and does it degrade the confinement?

H. IKEGAMI: In a system like the bumpy torus, there are several unfavourable mechanisms, besides the asymmetry, causing deterioration of the confinement. For example, the resonant cancellation in the poloidal precession,  $\Omega_{\nabla B} + \Omega_{\text{EXB}} \approx 0$ , may change the bumpy torus to almost a simple torus, as you may have observed in Fig. 2(b). The convective cells you mention may develop from any discrepancy between the equipotential surface and the constant  $|B|$  surface.

## EFFECTS ON EQUILIBRIUM AND STABILITY OF HIGH BETA RF HEATED PLASMAS IN THE URAGAN-3 TORSATRON

V.L. BEREZHNYJ, N.T. BESEDIN, M.P. VASIL'EV, V.S. VOJTSENYA,  
E.D. VOLKOV, Ya.F. VOLKOV, S.P. GUBAREV, Yu.V. GUTAREV,  
A.G. DIKIJ, V.M. ZAIKIND, G.V. ZELENIN, V.K. KONOVALOV,  
V.I. KONONENKO, V.D. KOTSUBANOV, B.V. KRAVCHIN, A.E. KULAGA,  
Yu.K. KUZNETSOV, G.G. LESNIYAKOV, A.P. LITVINOV, Yu.K. MIRONOV,  
N.I. NAZAROV, O.S. PAVLICHENKO, V.K. PASHNEV, N.F. PEREPEL'KIN,  
V.V. PLYUSNIN, G.N. POLAKOVA, N.P. PONOMARENKO, T.Yu. RANYUK,  
L.N. REMEZ, K.S. RUBTSOV, S.I. SOLODOVCHENKO, A.I. SKIBENKO,  
A.S. SLAVNIJ, I.S. SUSHKO, V.S. TARAN, V.T. TOLOK, T.O. TORYAK,  
I.P. FOMIN, A.N. SHAPOVAL, O.M. SHVETS, A.F. SHTAN'

Institute of Physics and Technology,  
Ukrainian Academy of Sciences,  
Kharkov,  
Union of Soviet Socialist Republics

### Abstract

#### EFFECTS ON EQUILIBRIUM AND STABILITY OF HIGH BETA RF HEATED PLASMAS IN THE URAGAN-3 TORSATRON.

Systematic studies of currentless plasma produced in the URAGAN-3 torsatron by RF heating at  $\omega \lesssim \omega_{\text{Hi}}$  have led to the discovery of three types of discharge. The first type (called D-discharges) was encountered on working with bare, stainless steel, helical frame antennas. They were characterized by rather high densities ( $n_e(0) \leq 2 \times 10^{13} \text{ cm}^{-3}$ ), moderate temperatures ( $T_i(0) \leq 0.3 \text{ keV}$ ,  $T_e(0) \leq 0.23 \text{ keV}$ ) and a short pulse duration ( $\Delta t \approx 3$  to  $4 \text{ ms}$ ) due to progressive degradation of the electron and ion temperatures. The second type (called Q-discharges) was obtained when the antenna was coated by TiN. These discharges were characterized by long pulse duration ( $\Delta t \approx 50 \text{ ms}$ ), lower electron densities ( $n_e(0) \leq 4 \times 10^{12} \text{ cm}^{-3}$ ) and higher temperatures ( $T_i \leq 1.1 \text{ keV}$ ,  $T_e \leq 0.3 \text{ keV}$ ). The third type of discharge (called QR-discharges) was encountered when the magnetic configuration axis was shifted outwards by the transverse magnetic field. These discharges were characterized by relaxation oscillations of the plasma parameters, similar to those of the high- $\beta$  S-regime of Heliotron E.

### 1. INTRODUCTION

Currentless plasma production and heating by RF waves in the ion cyclotron and Alfvén resonance regions have been studied in the URAGAN-3 torsatron during the last four years [1-5]. RF waves are excited in a plasma by helical frame antennas (without Faraday screen) with a specially chosen spectrum of toroidal and poloidal wavenumbers. Such antennas provide gas ionization and subsequent plasma heating via a 'mode relay race' mechanism [2]. Plasma with an electron density of  $n_e(0) \leq 2 \times 10^{13} \text{ cm}^{-3}$ , an ion temperature of  $T_i(0) \leq 300 \text{ eV}$  and an electron

temperature of  $T_e(0) \leq 270$  eV was obtained in URAGAN-3 for a confining field of  $B_0 \approx 0.92$  T with an RF radiated power of 0.6 MW [4]. Such parameters were sustained for no longer than 3–4 ms, because of progressive electron and ion temperature degradation [4, 5]. Plasma radiative cooling by metal impurities from a stainless steel (SS) RF antenna was considered to be a probable reason for the temperature degradation.

To study the role of the antenna material, a titanium nitride (TiN) coated antenna was installed in URAGAN-3 in autumn 1985. Quasi-stationary discharges of a duration determined by the RF pulse length ( $t \leq 50$  ms) were obtained with this antenna, and a plasma with a  $\beta$ -value close to the critical one, from the view of equilibrium, was produced at moderate RF power ( $\leq 0.6$  MW).

In this paper, results of studies of the effects of a plasma with maximum  $\bar{\beta} = 0.6\%$  on equilibrium and stability in URAGAN-3 are presented.

## 2. EXPERIMENTAL TECHNIQUES

The URAGAN-3 torsatron design is described in Ref. [1]. It consists of a magnetic system installed inside a large (volume  $\approx 70$  m<sup>3</sup>) vacuum chamber with diagnostic ports.

The magnetic configuration is produced by one  $\ell = 3$ ,  $m = 9$  helical winding set wound on the torus with a major radius of  $R = 100$  cm and a minor radius of  $a_h = 26$  cm, according to the winding law

$$\phi = -\frac{1}{3}(\theta - 0.2 \sin \theta - 0.01 \sin 2\theta)$$

and by two circular coils ( $R \approx 150$  cm,  $\Delta z = \pm 50$  cm) containing compensating and correcting windings which produce a vertical magnetic field ( $B_{\perp}$ ).

Two frame antennas (length = 70 cm, width  $\approx 20$  cm) were placed near the toroidal surface with a minor radius  $r_a \approx 10$ –12 cm inside the helical winding at the low field side. Antennas were fed by separate RF generators (5.3 MHz, 2 MW, 50 ms) with a two step RF pulse. Most experiments were performed at a constant gas ( $H_2$ ) inlet into the evacuated vacuum chamber and after extensive inside surface cleaning by RF discharges at a low magnetic field [3].

## 3. MAGNETIC FIELD CONFIGURATION

Magnetic field configuration studies performed since 1981 by the electron beam mapping technique showed that the region of nested magnetic surfaces is smaller than was predicted by calculations. Substantial improvement in the configuration took place after introducing a 9% imbalance in the vertical field coil currents. This suggests the possible presence of an additional radial error field.

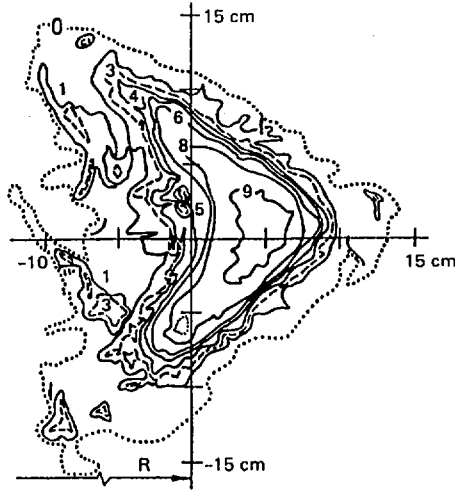


FIG. 1. Flux surfaces in URAGAN-3 measured by stationary electron emitter and grid. Surfaces with different magnetic field line transits  $N$  have the following numbers: (1):  $N = 10 \pm 2$ , (3):  $N = 20 \pm 5$ , (4):  $N = 30 \pm 5$ , (5):  $N = 40 \pm 5$ , (6):  $N = 50 \pm 5$ , (8):  $N = 70 \pm 5$ , (9):  $N = 100 \pm 10$ . Regime 0 ( $B_{\perp}/B_0 = +0.77\%$ ).

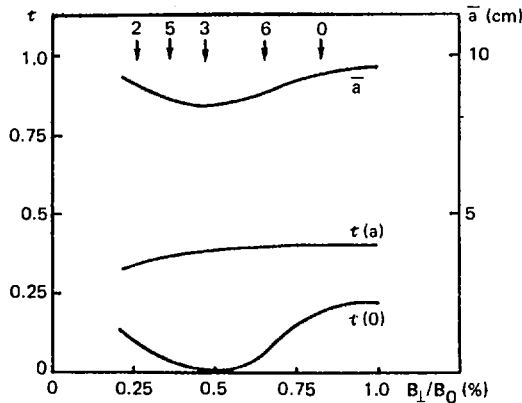


FIG. 2. URAGAN-3 magnetic configuration parameters as functions of vertical magnetic field  $B_{\perp}$  (results of numerical calculation). Numbers near arrows are the numbers of regimes used.

Construction and alignment errors in the massive magnetic system were possible reasons for this situation. The magnetic system alignment for URAGAN-3 was verified by a novel technique developed in co-operation with ORNL [6]. Measurements by this technique showed that the vertical field coil was shifted by about 1 cm relative to the axis of the helical coil set. This shift was eliminated by displacing the vertical field coil set. After coil alignment, the flux surfaces in URAGAN-3 were studied by a novel technique [7]. These studies showed that coil

alignment resulted in some improvement of the configuration although the radius of the last closed surface remained smaller than the calculated value. Helical field coil shape studies showed local misalignment within the helical coil set itself. Flux surface calculations including the data of helical coil shape studies showed that these local misalignments probably were the reason for the observed flux surface destruction in URAGAN-3.

Experimentally mapped flux surfaces in the optimum regime of URAGAN-3 after coil alignment are shown in Fig. 1. The general diagnosis of the magnetic field configuration in URAGAN-3 is as follows: the nested flux surface region (average radius about 9 cm) is surrounded by an ergodic magnetic layer (radial width 3 to 4 cm), where the magnetic field lines go round the torus one to ten times. The magnetic field configuration in URAGAN-3 can be changed by varying the vertical magnetic field,  $B_{\perp}$ . The main effects of  $B_{\perp}$  variation are a shift of the magnetic axis and a change in the central rotational transform,  $\iota(0)$ , the outer transform  $\iota(a)$  remaining practically unchanged (Fig. 2). This possibility of machine design was used in equilibrium and stability studies and proved to be very useful.

#### 4. PLASMA BEHAVIOUR IN Q-DISCHARGES

RF discharges with quasi-stationary behaviour of plasma parameters (Q-discharges) were encountered when one of the two installed SS antennas was replaced by a TiN coated antenna. With this RF activated TiN antenna and after the usual RF discharge cleaning, discharges without temperature degradation during a time of up to 50 ms were obtained and studied.

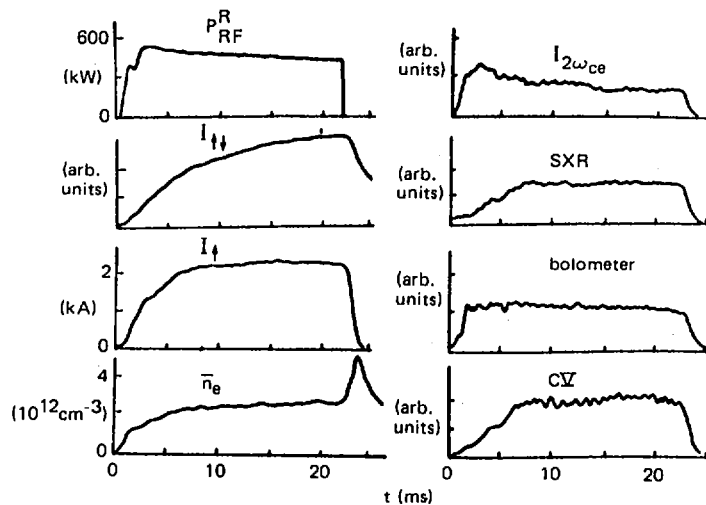


FIG. 3. Plasma parameter behaviour in Q-discharge ( $B_0 = 0.43$  T,  $B_{\perp}/B_0 = +0.36\%$ ).

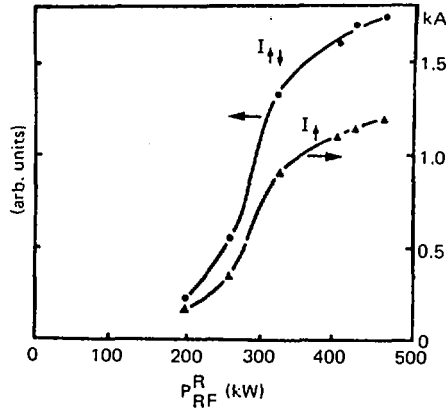


FIG. 4. Dependence of unidirectional ( $I_{\uparrow}$ ) and bidirectional ( $I_{\uparrow\downarrow}$ ) currents on RF power,  $P_{RF}^R$  ( $B_0 = 0.43$  T,  $B_{\perp}/B_0 = +0.77\%$ ).

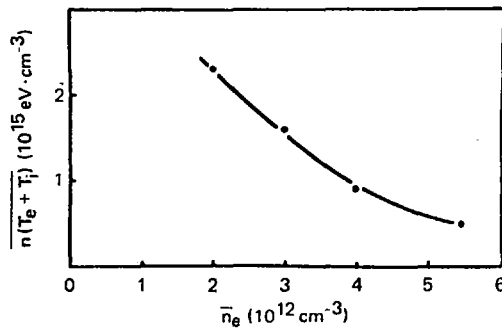


FIG. 5. Dependence of plasma pressure on electron density ( $B_0 = 0.43$  T,  $B_{\perp}/B_0 = +0.36\%$ ,  $P_{RF}^R = 450$  kW).

Figure 3 shows the time behaviour of the plasma parameters in a Q-discharge. Here,  $P_{RF}^R$  is the RF radiated power,  $I_{\uparrow\downarrow}$  is the bidirectional current measured by a saddle-type magnetic winding [3],  $I_{\uparrow}$  is the unidirectional current measured by a Rogowski coil,  $\bar{n}_e$  is the electron density averaged over the vertical chord and measured by a 2 mm interferometer, SXR is the soft X-ray diode detector signal, 'bolometer' refers to the pyroelectric detector signal, C V is the intensity of the C V spectral line,  $I_{2\omega_{ce}}$  is the intensity of the plasma radiation at  $2\omega_{ce}$ . The important features of these 'currentless' discharges were quasi-stationary, longitudinal unidirectional ( $I_{\uparrow}$ ) and bidirectional (dipole,  $I_{\uparrow\downarrow}$ ) currents. Both current directions changed with the poloidal magnetic field direction of the helical winding. The current increased with increasing RF power (Fig. 4). It was shown earlier [3] that the value

TABLE I. RESULTS OF MEASUREMENTS

Regime 3 ( $P_{RF}^R = 500$  kW),  $t = 12.5$  ms.

$B_0$ (T)	$\bar{n}_e$ ( $\text{cm}^{-3}$ )	$\bar{p}$ ( $\text{eV} \cdot \text{cm}^{-3}$ )	$T_{i\perp}$ (eV)	$T_{i\parallel}$ (eV)	$T_e^{sc}$ (eV)	$T_e 2\omega_{ce}$ (eV)	$\overline{n(T_e + T_i)}$ ( $\text{eV} \cdot \text{cm}^{-3}$ )
0.43 +0.48	$2 \times 10^{12}$	$2.5 \times 10^{15}$	980	930	250	270	$2.4 \times 10^{15}$

of the bidirectional current in RF produced plasmas in URAGAN-3 is in good agreement with the current value as calculated from a simple analytical model of MHD plasma equilibrium in a stellarator (Pfirsch-Schlüter current). This conclusion allowed us to use measurements of the dipole current poloidal magnetic flux for estimating the average plasma pressure  $\bar{p} = n(T_i + T_e)$  and the parameter  $\bar{\beta} = 8\pi \bar{p}/B_0^2$ .

For a given value of antenna radiated RF power, the plasma pressure depended on a few parameters: confining and vertical magnetic field values and hydrogen pressure. A decrease in hydrogen pressure resulted in a decrease of the electron density and a simultaneous increase in plasma pressure (Fig. 5), showing a strong increase in plasma temperature.

In these experiments with a confining magnetic field,  $B_0 = 0.43$  T, and one active antenna ( $P_{RF}^R \leq 0.55$  MW), a plasma with  $\bar{p} = 2.6 \times 10^{15}$   $\text{eV} \cdot \text{cm}^{-3}$  and  $\bar{\beta} = 0.6\%$  was obtained at an electron density of  $\bar{n}_e = 2.1 \times 10^{12}$   $\text{cm}^{-3}$ . The fact that the keV range of the average plasma temperature  $T_e + T_i$  was reached was confirmed by independent measurements of the plasma temperatures. The ion temperature was measured by two charge exchange neutral energy analysers measuring the longitudinal and transverse neutral fluxes in the equatorial plane of the torsatron. The electron temperature was measured by laser scattering at  $R = 103$  cm of the equatorial plane and by second harmonic electron cyclotron radiation. Vertical scanning of the transverse neutral flux showed that  $T_i$  did not change very much. Measurement of the  $2\omega_{ce}$  spectrum showed that the  $T_e(r)$  profile was close to the parabolic profile. Table I shows the results of these measurements. The average plasma pressure  $\overline{n(T_e + T_i)}$  was calculated on the assumption that the electron density and temperature distributions were parabolic and the ion temperature profile was homogeneous; it was found to be  $2.4 \times 10^{15}$   $\text{eV} \cdot \text{cm}^{-3}$ . Comparisons of this kind allowed us to conclude that the description of the dipole equilibrium current chosen represents the experimental situation rather well up to values of  $\bar{\beta} = 0.6\%$ , thereby permitting the use of dipole current measurements in order to measure  $\bar{p}$  and  $\bar{\beta}$ .

The theory of finite  $\beta$  plasma equilibrium in a stellarator [8] predicts two main effects: (1) shift of magnetic surfaces and (2) destruction of magnetic surfaces in the

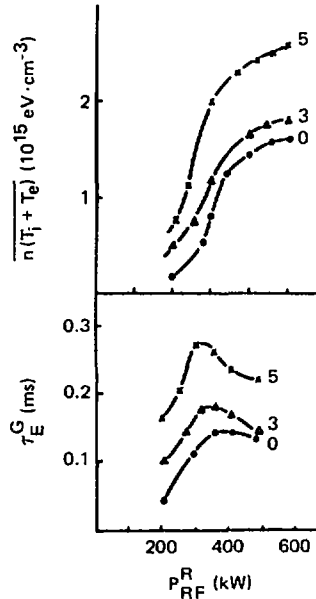


FIG. 6. Dependences of plasma pressure and global energy confinement time on RF power,  $P_{RF}^R$ , for different vertical fields ( $B_0 = 0.43$  T, 0:  $B_{\perp}/B_0 = +0.77\%$ , 3:  $B_{\perp}/B_0 = +0.48\%$ , 5:  $B_{\perp}/B_0 = +0.36\%$ ).

pre-separatrix region. The shift of the magnetic surfaces can be eliminated by using a transverse magnetic field so that destruction of magnetic surfaces and related confinement degradation should be the main effect of high  $\beta$  plasma equilibrium [9]. A conventional rough estimate of the critical beta,  $\beta_c = \epsilon^2(a) a/R$ , for the URAGAN-3 yields a value of 1.4%.

MHD calculations for URAGAN-3 show that, for  $\beta \geq 0.2\beta_c$ , we may expect a pronounced shift of the magnetic surfaces and a plasma pressure effect due to the transverse magnetic field. These expectations were confirmed by measurements of the plasma pressure dependence on the transverse magnetic field  $B_t$  (Fig. 6): we see that the maximum plasma energy content is obtained for the inward shifted vacuum magnetic configuration.

It was interesting to find out whether energy confinement degradation would occur at beta values attained in URAGAN-3. As a confinement factor of merit, one can use the value of the global energy confinement time:

$$\tau_E^G = \frac{3/2 \overline{n(T_e + T_i)} V}{P_{RF}^A}$$

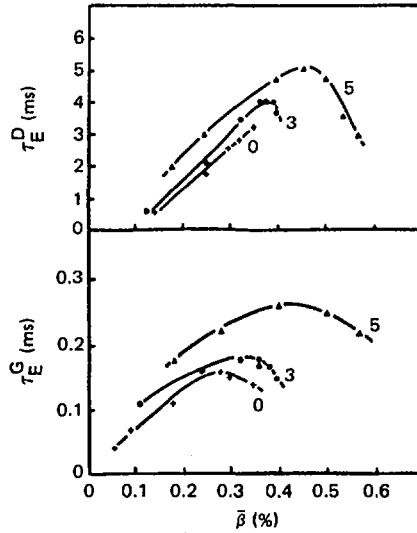


FIG. 7. Energy decay time,  $\tau_E^D$ , and global energy confinement time,  $\tau_E^G$ , versus  $\bar{\beta}$  (same conditions as for Fig. 6).

where  $P_{RF}^A$  is the absorbed RF power and  $V$  the plasma volume. Assuming that the total antenna radiated power is absorbed by the plasma ( $P_{RF}^A = P_{RF}^R$ ) and  $V = 1.7 \times 10^5 \text{ cm}^{-3}$  ( $\bar{a} = 9 \text{ cm}$ ), we calculated  $\tau_E^G$  as shown in Fig. 6. We see saturation and degradation of  $\tau_E^G$  with increasing radiated RF power. Energy confinement degradation in experiments with additional RF plasma heating is a common feature in tokamaks. Therefore, to check this option, we measured the energy decay time  $\tau_E^D$ :

$$\tau_E^D = - \frac{W}{\dot{W}}$$

with

$$W = \frac{3}{2} n (T_e + T_i) \cdot V$$

0.2 ms after switching off the RF power. As to the RF power, it was not a parameter of importance for  $\tau_E^D$ ; we have plotted the dependence of  $\tau_E^D$  on average beta at the moment of the  $\tau_E^D$  calculation (Fig. 7). This figure also shows  $\tau_E^G$  at the end of the RF pulse. From this figure, we see a qualitative similarity between  $\tau_E^G = f_1(\bar{\beta})$  and  $\tau_E^D = f_2(\bar{\beta})$  and a strong quantitative difference between their values which could be

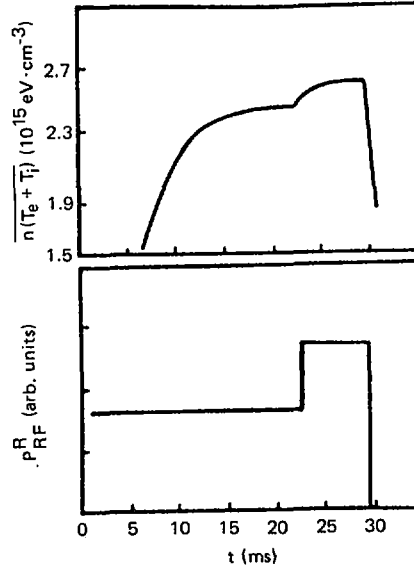


FIG. 8. Plasma pressure increase after step-like RF power increase ( $B_0 = 0.43$  T,  $B_{\perp}/B_0 = +0.36\%$ ,  $P_{RF}^R = 350$  kW,  $\Delta P_{RF}^R = 70$  kW,  $\tau_E^B = 2.7$  ms,  $\tau_E^D = 3.5$  ms).

considered to be evidence for the negative influence RF power has on energy confinement. To verify this conclusion, we measured the plasma energy buildup time,  $\tau_E^B$ , which describes the time behaviour of the plasma energy increase  $\Delta W(t)$  with a step-like increase of the absorbed power  $\Delta P_{RF}^A$ :

$$\Delta W(t) = \Delta P_{RF}^A \tau_E^B \left[ 1 - \exp\left(-\frac{t}{\tau_E^B}\right) \right]$$

Figure 8 shows typical data for  $\Delta W(t)/V$ , confirming the time behaviour as predicted by Eq. (1). The general conclusion resulting from the available data on  $\tau_E^B$  and  $\tau_E^D$  is:

$$\tau_E^B \approx \tau_E^G$$

This means that the transition times,  $\tau_E^B$  and  $\tau_E^G$ , represent the plasma energy confinement time  $\tau_{ED}$ . The observed strong difference between  $\tau_E^G$  and  $\tau_E^B \approx \tau_E^D$  is the result of a large difference between radiated and absorbed RF powers ( $P_{RF}^R \gg P_{RF}^A$ ). This conclusion will need some explanation, in the future. At any rate, a beta soft saturation at  $\bar{\beta} = 0.5\beta_c$ , which results from the energy confinement degradation appearing for  $\bar{\beta} \geq 0.3$ , is evident for URAGAN-3 plasmas.

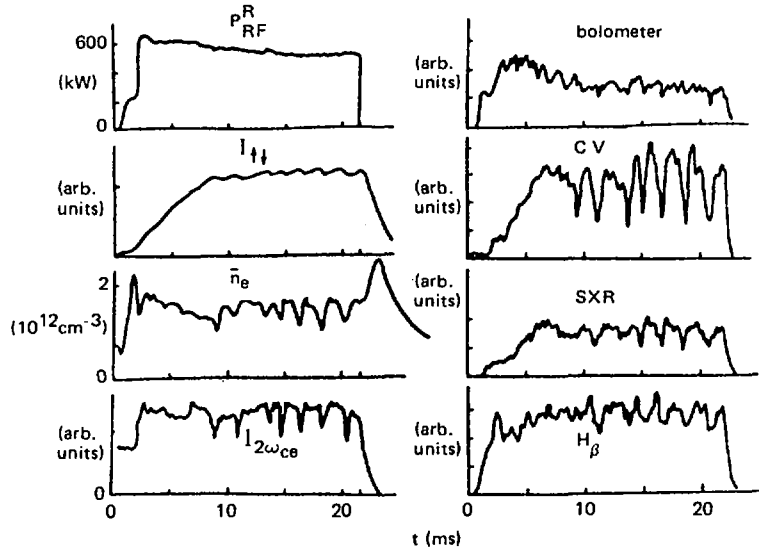


FIG. 9. Plasma parameter behaviour in QR-discharge ( $B_0 = 0.43 T$ ,  $B_\perp/B_0 = +0.48\%$ ).

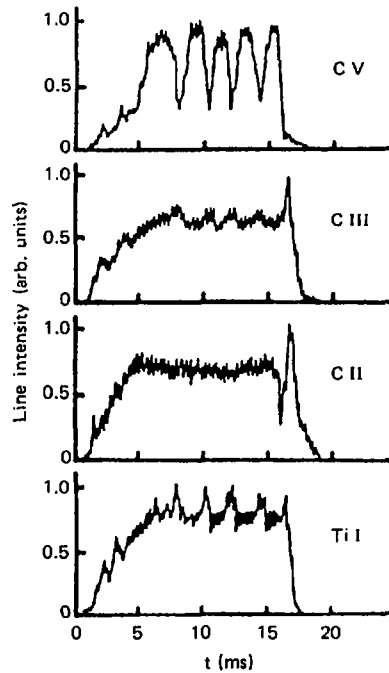


FIG. 10. Time behaviour of carbon ion and titanium atom spectral lines ( $B_0 = 0.43 T$ ,  $B_\perp/B_0 = +0.77\%$ ,  $P_{RF}^R = 400 kW$ ).

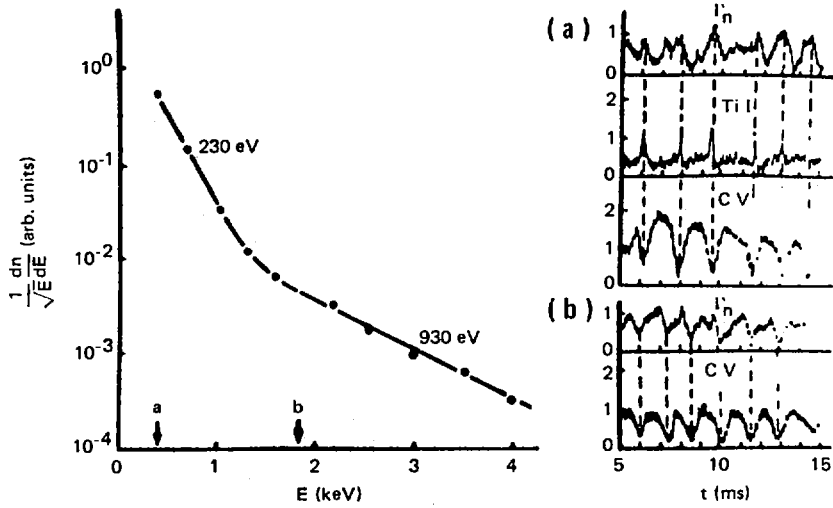


FIG. 11. Time behaviour of longitudinal neutral flux  $\Gamma_n$ , for different neutral energies shown by arrows in typical energy spectrum. Oscillograms of C V (plasma centre) and Ti N (near antenna) are also shown.

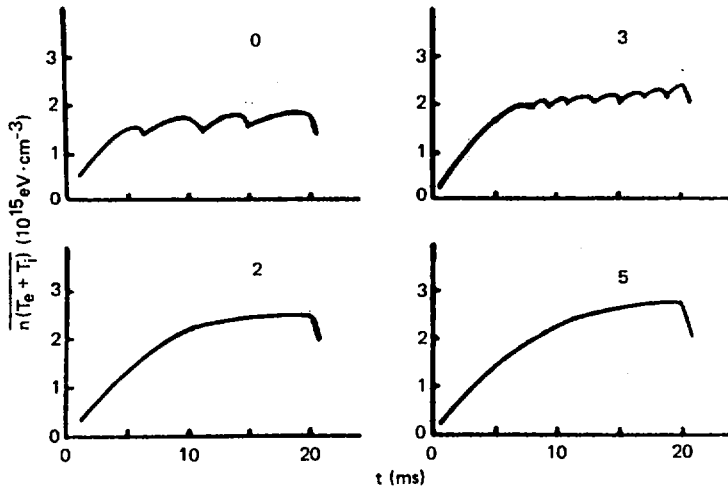


FIG. 12. Time behaviour of plasma pressure for different vertical field values ( $B_0 = 0.43$  T,  $P_{RF}^R = 450$  kW). Regime numbers from Fig. 2.

## 5. RELAXATION OSCILLATIONS IN A HIGH $\beta$ PLASMA

All Q-discharges showed pronounced ( $\sim 10\%$ ) plasma parameter fluctuations in the frequency range of 1 to 30 kHz. In regimes with the vertical field  $B_1/B_0 \geq +0.5\%$  and  $\bar{\beta} > 0.3\%$ , new types of discharge, called the QR-discharges and characterized by the occurrence of relaxation oscillations, were encountered (Fig. 9). For most values of the plasma parameters, these oscillations were of disruptive nature, but for plasma parameters revealing radial localization (impurity ions), the oscillation shape changed (Fig. 10). On some signals related to the periphery localized parameters (Ti I emission near the antenna,  $H_\beta$  emission in the diverted flux) positive spikes were observed before the disruptions. This implies that the perturbation propagated from the centre to the periphery of the discharge. The change in shape of the relaxation oscillation for energetic neutrals with neutral energy variation (Fig. 11) and its correlation with the shape of spatially localized parameters (C V, Ti I) allowed us to conclude that the high energy neutrals of the energy distribution presented in this figure characterize the plasma central zone and its temperature. Low energy neutrals yield information on the ion temperature in the ergodic magnetic layer.

The pattern of relaxation oscillations changed with the value of the vertical magnetic field  $B_\perp$ : discharges with lower  $B_\perp$  values were more stable, in spite of the increase in plasma pressure (Fig. 12).

## 6. CONCLUSIONS

After coating the RF antenna with a TiN layer, a quasi-stationary, high temperature ( $T_i \geq 1$  keV) plasma with  $\bar{\beta} = 0.5\beta_c$  has been obtained in URAGAN-3. In this plasma a bidirectional current with all features of the Pfirsch-Schlüter equilibrium current and a unidirectional current proportional to the plasma pressure are flowing.

The observed relaxation oscillations appear similar to those of the high  $\beta$  S-regime of Heliotron E [10]. However, in URAGAN-3, in addition to the pressure gradient, the unidirectional current can also be a driving force for the tearing mode instability.

The observed soft saturation of  $\beta$  with the increase of the RF power results from energy confinement degradation for  $\bar{\beta} > 0.3\beta_c$ . To which of the effects — equilibrium, stability or peculiarity of transport — the observed  $\tau_E$  degradation is related is a question to be elucidated in our future experiments on the URAGAN-3 torsatron.

## REFERENCES

- [1] ARSEN'EV, A.V., et al., in Plasma Physics and Controlled Nuclear Fusion Research 1982 (Proc. 9th Int. Conf. Baltimore, 1982), Vol. 2, IAEA, Vienna (1983) 227.

- [2] SHVETS, O.M., et al., in Heating in Toroidal Plasmas (Proc. 4th Int. Symp. Rome, 1984), Vol. 1, CEC (1984) 513.
- [3] BAKAEV, V.V., et al., in Plasma Physics and Controlled Nuclear Fusion Research (Proc. 10th Int. Conf. London, 1984), Vol. 2, IAEA, Vienna (1985) 397.
- [4] PAVLICHENKO, O.S., paper presented at US-USSR Stellarator Workshop, Oak Ridge (1985).
- [5] NAZAROV, N.I., et al., in Controlled Fusion and Plasma Heating (Proc. 13th Europ. Conf. Schliersee, 1986), Vol. 1, European Physical Society (1986) 192.
- [6] COLCHIN, R.J., et al., Rev. Sci. Instrum. **57** (1986) 1233.
- [7] GEORGIEVSKIJ, A.V., et al., in Controlled Fusion and Plasma Physics (Proc. 12th Europ. Conf. Budapest, 1985), Vol. 1, European Physical Society (1985) 68.
- [8] SHAFRANOV, V.D., Voprosy teorii plazmy (Problems of Plasma Theory), Vol. 2 (1963) 92 (in Russian).
- [9] GORBACHEV, N.S., KUZNETSOV, Yu.K., PINOS, I.B., Nucl. Fusion **20** (1980) 341.
- [10] HARRIS, J.H., et al., Phys. Rev. Lett. **53** (1984) 2242.



## EXPERIMENTAL AND THEORETICAL STUDIES OF TOROIDAL HELIACS

B.D. BLACKWELL, R.L. DEWAR, H.J. GARDNER,  
S.M. HAMBERGER, L.E. SHARP, X.H. SHI,  
C.F. VANCE, D.F. ZHOU<sup>1</sup>  
Australian National University,  
Canberra, Australia

### Abstract

#### EXPERIMENTAL AND THEORETICAL STUDIES OF TOROIDAL HELIACS.

Experimental results are given for the small heliac SHEILA whose rotational transform profile can be varied by an  $l = 1$  helical current around the central ring. Introducing low order resonances adversely affects the confinement, as predicted. The mode structure of an electrostatic fluctuation is shown to resonate with the helical field geometry. Computations presented for a large heliac demonstrate how both  $|B|$  ripple and toroidal effects can be greatly reduced by judicious choice of coil geometry. Results are presented for stability against ideal interchange and ballooning modes of free-boundary helically symmetric equilibria obtained from a new equilibrium code. Plasma shifts are found to be stabilizing.

### 1. Experiments on Prototype Heliac SHEILA

Further detailed work has confirmed the results of initial experiments on SHEILA (Table I) reported earlier [1] which demonstrated the existence of well-defined, low- $\beta$ , long mean-free-path equilibria via the coincidence of the experimentally measured isobaric surfaces ( $n_e T_e = \text{const}$ ) and the computed helical flux surfaces. For typical plasma conditions ( $\bar{n}_e \sim 1-5 \times 10^{18} / \text{m}^3$ ,  $T_e \sim 10 \text{ eV}$ ,  $B \sim 0.2 \text{ T}$ ),  $\beta \lesssim 10^{-4}$ , and only small oscillatory currents are used in plasma production. Thus the flux surfaces are, to a good approximation, those of the vacuum field computed from actual conductor geometries and currents.

The subsequent addition of an  $l = 1$  helical winding around the ring, as suggested by Harris *et al.* [2], has allowed a wide measure of control over rotational transform  $\iota(\psi)$ , shear  $\Delta\iota/\iota(0)$  and magnetic well  $W(\psi) = 1 - V'(\psi)/V'(0)$ . Fig. 1 shows some examples for various ratios of helix to ring current  $C \equiv I_h/I_c$ . Notice that for  $C \leq -0.1$  the magnetic well is very small, while the shear is large, and that for  $C \sim 0.125$  the shear vanishes while the well deepens. Another important feature is the presence of the resonance  $\iota/N = 1/2$ , ( $\iota = 1.5$ ) for  $0.09 \lesssim C \lesssim 0.125$ , which leads to island formation.

<sup>1</sup> On leave from the Institute of Plasma Physics, Hefei, China.

TABLE I. COMPARISON OF EXPERIMENTAL RESULTS FOR SHEILA AND H-1

	SHEILA	H-1
No. of field periods $N$	3	3
No. of toroidal coils $N_T$	24	36
Mean radius of toroidal coils $r_c$ (m)	0.065	0.383
Helical excursion $\rho$ (m)	0.025	0.22
Major radius $R_o$ (m)	0.19	1.0
Mean minor plasma radius $\langle a \rangle$	0.03	0.20
Max. field $B$ (T)	0.4	0.2 1.0
Duration (s)	0.04	$\infty$  1
Max. ring current $I_c$ (kAT)	28	500
Max. vertical field $B_v$ (T)	0.04	0.1
Radius of control helix $r_h$ (m)	0.014	0.10
$\epsilon(0) \epsilon(a)$	1.2 1.35	1.1 1.18
Well depth $W$	3%	3%
Dia. of vacuum enclosure(m)	0.6	3.8

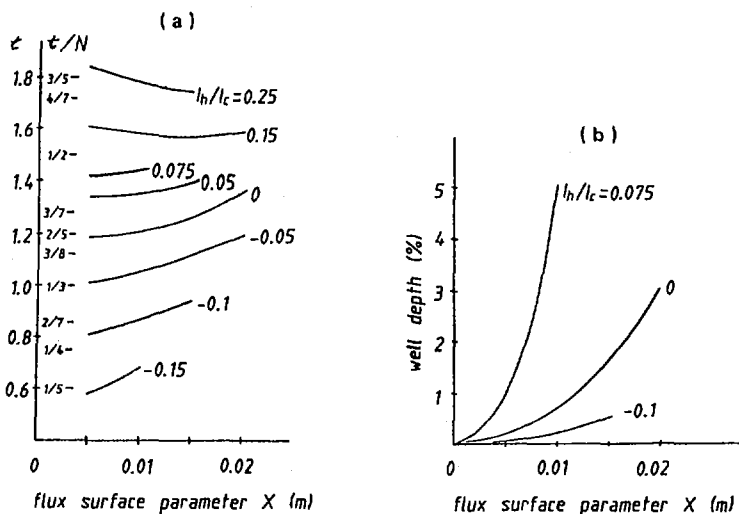


FIG. 1. Rotational transform  $\epsilon$  (a) and well depth (b) for different values of  $C \equiv I_h/I_c$  on the SHEILA heliac. The flux surfaces are identified by the parameter  $X$ , defined as the distance between the magnetic axis and the surface at  $\phi = 0$ ,  $z = 0$ , for increasing  $R$ .

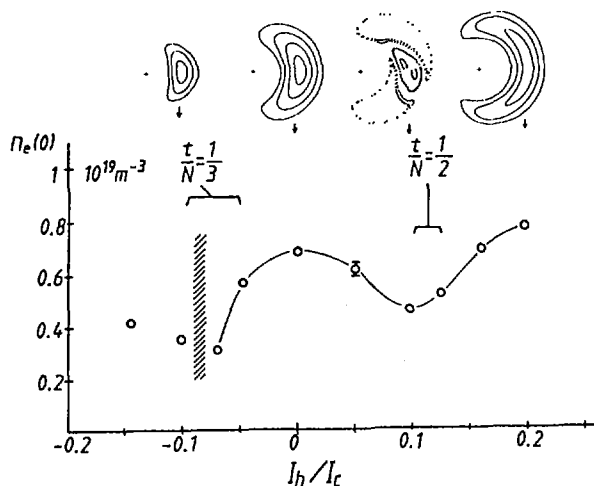


FIG. 2. Dependence of central electron density on helical winding current. Representative vacuum magnetic surfaces at  $\phi = 0$  are shown for some values of  $C$ .

Initial experimental observations obtained when the configuration is progressively changed clearly show the adverse effects of the resonances on particle confinement. For example, Fig. 2 shows the dependence on  $C$  of central electron density for the same r.f. input and gas conditions, with vertical field adjusted for optimum particle confinement time.

At  $C = 0.1$ , computation shows that the  $1/2$  resonance causes the helical surfaces to bifurcate, while experimentally the particle confinement time is clearly reduced. As  $C \rightarrow -0.07$ , where the  $\nu/N = 1/3$  resonance is located near mid-radius, the confinement again falls. For conditions corresponding to the shaded region, no plasma can be formed. We attribute this to the effect of stray fields on the  $1/3$  resonance.

For some conditions ( $c_s/\omega_{ci} \lesssim a$ ) a single mode of quasi-electrostatic oscillation frequency at  $\sim 10$  kHz and amplitude  $\tilde{n}_e/n_e \sim 10^{-1}$  appears, provisionally identified as a dissipative drift wave. Although it has only slight effect on confinement, its structure (obtained using large arrays of electrostatic probes located on a given flux surface) can be used to provide an independent check on the magnetic geometry in the helical plasma frame. For example, Fig. 3 shows (for  $C = 0$ ) the dependence of its phase on position in the magnetic field-line coordinate system  $(\psi, \vartheta, \phi)$  [3,5], suggesting a wave field of the form  $\xi = \xi_0 \cos(m\vartheta - n\phi)$ .

The propagation clearly shows  $m = 3, n = 5$ , which is resonant with the helical rotational transform ( $\nu_h \equiv N - \nu$ ) of  $5/3$  in the region of maximum

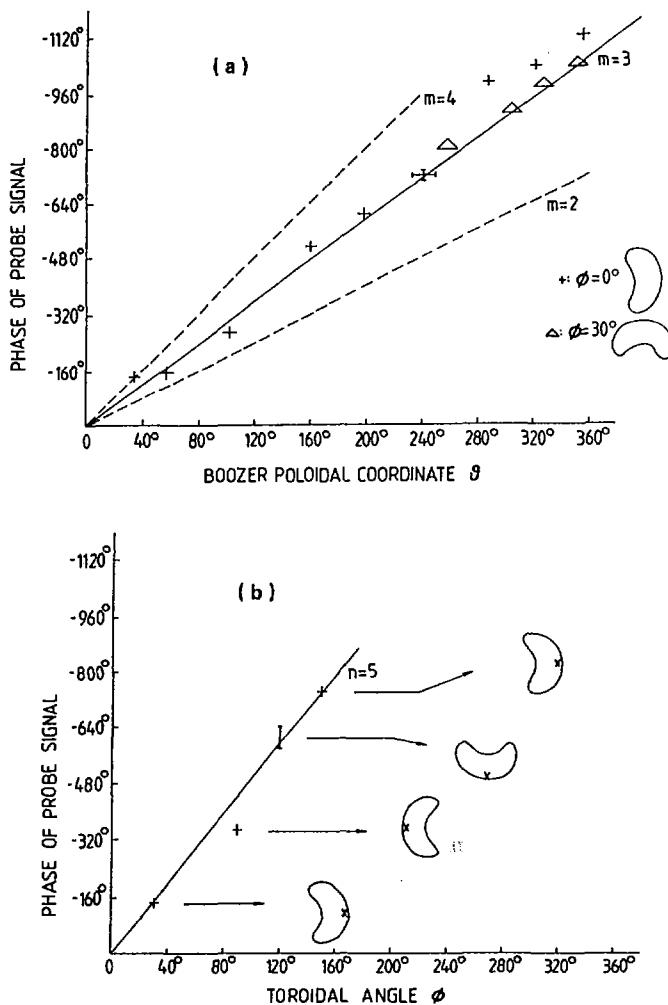


FIG. 3. Phase of the electrostatic mode versus (a) the magnetic poloidal coordinate,  $\vartheta$ , and (b) the toroidal coordinate  $\phi$ .

wave-field, where  $\epsilon \simeq 1.33$ . Varying the ion mass confirms that the toroidal phase velocity  $\approx c_s$ , while varying  $\epsilon$  produces the expected changes in both mode number and frequency.

## 2. Optimization of the Magnetic Structure of H-1

Extensive calculations made during the process of optimization of the design of the much larger heliac, H-1 (under construction, see Table I) have

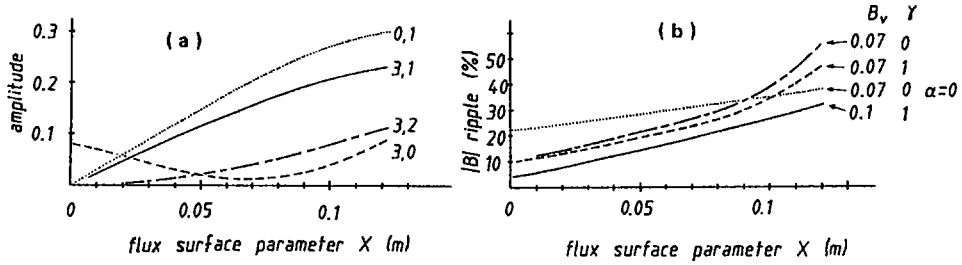


FIG. 4. (a) Amplitudes  $\delta_{m,n}$  of the Jacobian harmonics versus  $X$  (as defined in Fig. 1). The case illustrated has  $\alpha = 0.3$ ,  $\gamma = 1$ ,  $B_v = 0.1$  T. (b) Ripple amplitude  $((B_{max} - B_{min})/(B_{max} + B_{min}))$  for different values of vertical field and index. The azimuthally equispaced toroidal coil case ( $\alpha = 0$ ) is shown for comparison.

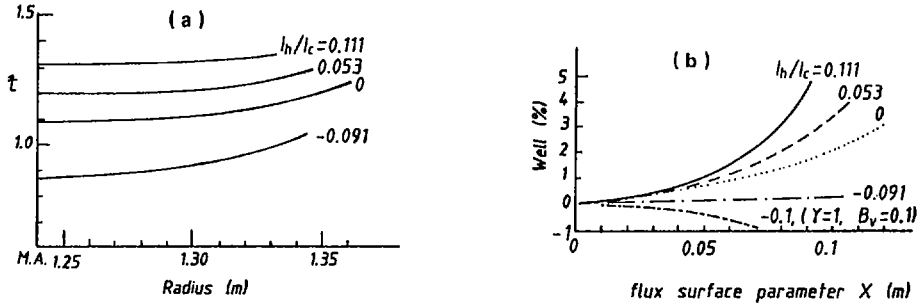


FIG. 5. Rotational transform (a) and well depth (b) for various values of  $C$ . Except where noted,  $\alpha = 0.3$ ,  $B_v = 0.07$  and  $\gamma = 0$ . M.A. is magnetic axis.

confirmed the suggestion [4] that strong toroidal effects associated with a low aspect ratio device can be greatly reduced by azimuthal redistribution of the coils. Using the prescription

$$\phi = \phi' - \alpha \frac{\sin N \phi'}{N}, \quad \phi' = \frac{2\pi(j - \frac{1}{2})}{N_T}, \quad j = 1, 2, \dots, N$$

with  $\alpha$  a constant (taken here as 0.3), we have been able to markedly reduce the global  $1/R$  variation in  $|B|$ . This has the consequential advantage of reducing both the variation in surface cross-sectional shape with toroidal angle and the total magnetic ripple. The Jacobian harmonic  $\delta_{3,0}$  which governs the Pfirsch-Schlüter currents due to toroidicity [5] is also considerably reduced, e.g. by a factor  $\sim 5$  at mid-radius (see Fig. 4a).

The choice of rotational transform per period  $t/N \simeq 0.379$  (a "noble ratio") and low shear (Fig. 5a) conveniently avoids the worst low order

resonances, particularly those like (3,2) which can be pressure driven directly via  $\delta_{3,2}$ . An additional improvement in magnetic ripple can be achieved if the applied vertical field  $B_v$  is made to vary with major radius as  $B_v(R) \propto (R_0/R)^\gamma$ , and its magnitude adjusted to centre the magnetic surfaces with respect to the minor axis. For an index  $\gamma = 1$  and  $B_v(R_0) = 0.1B_T$ , the  $|\mathbf{B}|$  ripple on the magnetic axis is reduced (Fig. 4b) from 10% to 4% and, at an outer surface, from 55% to 32%, at the expense of a reduction in well depth and an increase in the poloidal variation in surface shape. The harmonics of the Jacobian for this case (Fig. 4a) show the component  $\delta_{3,0}$ , which corresponds to the  $1/R$  variation of  $1/B^2$  over one helical period, to be everywhere less than 7.5%. The local  $1/R$  variation, which contributes to  $\delta_{0,1}$ , is more difficult to control as it is linked to the toroidal curvature (in a current-free region) by  $\nabla \times \mathbf{B} = 0$ . By judicious adjustment of the vertical field index and magnitude, a compromise can be achieved between these two extremes.

Excitation of the helical control winding gives access to a wide range of magnetic configurations: Fig. 5 shows its effect on  $\epsilon$  and  $W$  profiles, once again demonstrating the possibility of comparing low shear, deep well configurations with moderate shear, antiwell configurations.

### 3. Stability Studies of Free-Boundary Equilibria

As a complement to the 3-D field-line-tracing studies, we have studied the finite- $\beta$  stability properties of SHEILA in the helically symmetric limit. A new code, FEQ2.5(FR), which models free-boundary heliac equilibria, has been developed. The fixed-boundary inverse-equilibrium code FEQ2.5 [6] has been combined with an iterative technique using the Green's function,  $G$ , for the helical Grad-Shafranov equation:

$$\nabla \cdot (K \nabla G) = \frac{-4\pi}{r} \delta(r - r_0) \delta(\zeta - \zeta_0) \quad (1)$$

where  $\zeta = \phi - hz$ ,  $h$  is the helical pitch,  $K = h^2/(1 + h^2r^2)$  and  $(r, \phi, z)$  are the usual cylindrical coordinates. One solution for  $G$  is

$$G(r, \zeta | r_0, \zeta_0) = \frac{2}{h^2} [\ln(r_<) + \frac{1}{2} h^2 r_<^2] - 4rr_0 \sum_{n=1}^{\infty} I'_n(nhr_<) K'_n(nhr_>) \cos[n(\zeta - \zeta_0)] \quad (2)$$

with  $r_< = \min(r, r_0)$ ,  $r_> = \max(r, r_0)$ .

The code FEQ2.5(FR), which is described in detail in [7], assumes that the vacuum helical flux function of the external coil system may be expanded as a Fourier-Bessel series:

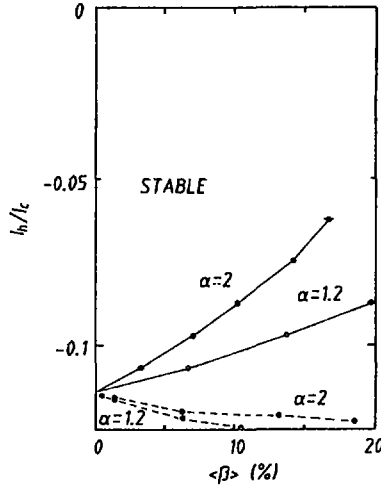


FIG. 6. Critical  $\langle\beta\rangle$  for stability against ideal interchange and ballooning modes for helically symmetric, net-current-free SHEILA fixed-boundary (solid lines) and free-boundary (broken lines) equilibria. The pressure profiles have the form  $p \propto \psi^\alpha$ . The plasma is stable above the curves and unstable below.

$$\psi_i = a_1 \ln(r) + a_2 r^2 / 2 + r \sum_{n=1}^{\infty} b_n I'_n(nhr) \cos(n\zeta) + r \sum_{n=1}^{\infty} c_n K'_n(nhr) \cos(n\zeta) \quad (3)$$

For a typical helically symmetric heliac, consisting of a helical solenoid which carries a wholly azimuthal current, which is up-down symmetric and which encloses the  $z$ -axis and a number of helical windings, the series of Eq. 3 is certainly valid inside the inner tangent cylinder to the solenoid, and outside the largest radius,  $r_h$ , of the helical windings. For circular cross-section solenoids the series can also be shown to converge *throughout* the region interior to the solenoid, but outside  $r = r_h$  when the displacement of the solenoid satisfies certain conditions [8].

It is possible to construct a stability diagram for the SHEILA heliac using the current in the extra helical coil as a parameter with which to deform the shape of the outer flux surface. This is shown in Fig. 6, where the plasma elongation and indentation increases moving up the vertical axis. When the plasma boundary is fixed to its vacuum shape, we confirm the high critical  $\langle\beta\rangle$  to Mercier and ballooning instabilities predicted by others [6,9] with a stronger dependence on the pressure profile than that noted by [6]. The limiting point at zero  $\langle\beta\rangle$  corresponds to the appearance (with decreasing elongation and indentation) of a magnetic hill close to, but not

exactly at, the magnetic axis. When the plasma boundary is allowed to move, it shifts away from the  $z$ -axis and broadens. The increase in helical aspect ratio is sufficient to ensure Mercier stability for all those configurations for which there is a transition to instability at finite pressure. In other words, any zero-pressure configuration with a uniform magnetic well across the plasma will remain Mercier-stable as  $\langle\beta\rangle$  is increased.

## REFERENCES

- [1] BLACKWELL, B.D., HAMBERGER, S.M., SHARP, L.E., SHI, X.H., Nucl. Fusion **25** (1985) 1485.
- [2] HARRIS, J.H., CANTRELL, J.L., HENDER, T.C., CARRERAS, B.A., MORRIS, R.N., Nucl. Fusion **25** (1985) 623.
- [3] BOOZER, A.H., Phys. Fluids **23** (1980) 904.
- [4] CARY, J., KOTSCHENREUTHER, M., in Fifth International Workshop on Stellarators (Proc. IAEA Tech. Comm. Mtg on Plasma Confinement and Heating in Stellarators, Schloss Ringberg, 1984), Vol. 1, CEC, Directorate-General XII — Fusion Programme, Brussels (1984) 291.
- [5] REIMAN, A.H., BOOZER, A.H., Phys. Fluids **27** (1984) 2446.
- [6] MONTICELLO, D.A., et al., Phys. Fluids **27** (1984) 1248.
- [7] GARDNER, H.J., The free boundary equilibrium problem for helically symmetric plasmas, PhD Thesis, Australian National University, Canberra, 1986.  
GARDNER, H.J., DEWAR, R.L., SY, W.N.-C., The Free Boundary Equilibrium Problem for Helically Symmetric Plasmas, Rep. ANU/TPP-86/02, Australian National University, Canberra (1986); submitted to J. Comput. Phys.
- [8] DEWAR, R.L., GARDNER, H.J., The Eigenfunction Expansion for the Helical Solenoid, Rep. ANU/TPP-86/03, Australian National University, Canberra (1986).
- [9] MERKEL, P., NÜHRENBERG, J., GRUBER, R., TROYON, F., Nucl. Fusion **23** (1983) 1061.

## DISCUSSION

F.L. RIBE: I would like to ask three questions. First, can you control the resonance with the helical windings; second, why do you not choose  $N = 4$  instead of  $N = 3$ ; and third, what are your plans for heating your device?

S.M. HAMBERGER: The helical winding current controls the position of the low order resonances: When one is inside the confinement region, the plasma density falls. Notice that the shear is low where the one-half resonance is important and fairly high for the one-third resonance.

The answer to your second question is that we prefer  $N = 3$  for several reasons. Firstly, the larger number of toroidal coils per period reduces magnetic ripple near the outside and improves the flux surfaces. Secondly,  $N = 3$  provides a more convenient experimental layout. The suggestion that, with  $N = 3$ , resonances cannot be avoided is not correct, provided careful design is used.

Finally, it is intended to use RF heating only, using frequencies in the ICR region. The actual method has not yet been decided. ECRH will be used if suitable gyrotrons become available to us.

# HELICITY CONSERVATION AND ENERGY CONFINEMENT IN CTX SPHEROMAKS\*

B.L. WRIGHT, C.W. BARNES, J.C. FERNANDEZ,  
I. HENINS, H.W. HOIDA, T.R. JARBOE, S.O. KNOX,  
G.J. MARKLIN, R.M. MAYO<sup>1</sup>, D.A. PLATTS  
Los Alamos National Laboratory,  
University of California,  
Los Alamos, New Mexico,  
United States of America

## Abstract

### HELICITY CONSERVATION AND ENERGY CONFINEMENT IN CTX SPHEROMAKS.

Results are reported for the CTX spheromak experiment with a flux conserver of 0.67 m radius. The measured currents in the mesh allow a non-perturbing determination of the equilibrium current profile. Analysis of magnetic data shows that injected magnetic helicity is conserved. A mode of operation has been encountered in which periodic decreases in the helicity content of sustained spheromaks are correlated with the quiescence of current-driven instabilities. Increase of the spheromak radius from 0.40 m to 0.67 m has not led to an increase in energy confinement. Attempts to resolve this issue, including the use of a conducting core and applied bias fields, are discussed.

## 1. INTRODUCTION

In the CTX experiment at Los Alamos, magnetized coaxial electrodes are used for the formation and sustainment of spheromak plasmas that are stably confined in an oblate conducting shell called a flux conserver [1]. The electrode configuration is that of a Marshall gun with a solenoid mounted inside the inner electrode to provide an axial magnetic field. Because this applied flux is linked with the injected azimuthal flux, the gun is a source of magnetic helicity. The source and flux conserver are on a common axis and are separated by a short cylindrical section with a conducting wall. Plasma contact with surfaces is reduced and diagnostic access is improved by constructing the flux conserver from a mesh of 12.7 mm diameter copper bars at an approximately 50 mm spacing. As reported previously [1,2], the spheromak field configuration can be sustained in CTX over many resistive decay times by the continuous injection of magnetic helicity from the coaxial source. This prior work was performed in a 0.40 m radius flux conserver and resulted in the achievement of a core temperature in excess of 100 eV [3]. We now report on helicity balance and confinement results using a larger, 0.67 m radius, flux conserver.

\* Work performed under the auspices of the United States Department of Energy.

<sup>1</sup> Department of Nuclear Engineering, Purdue University, West Lafayette, IN, USA.

## 2. DIAGNOSTIC TECHNIQUES

The principal diagnostics in use on the CTX experiment are: over 35 Rogowski loops that measure currents flowing in the mesh of the flux conserver, an 8-chord quadrature interferometer for midplane density profiles, multipoint Thomson scattering for  $T_e$  near the magnetic axis, two steerable gold foil bolometers, a Lyman- $\alpha$  monitor, a selection of VUV instruments for impurity concentration studies, two polychromators for impurity ion Doppler broadening, and a double Langmuir probe to measure conditions at the plasma edge.

An important feature of recent CTX work is our ability to use Rogowski loop measurements of the toroidal equilibrium currents flowing in the hoops of the mesh flux conserver to infer the internal profiles of  $\vec{j}$  and  $\vec{B}$  [4]. This technique, which eliminates the need for perturbing internal magnetic probes, is based on fitting the hoop current data to computed axisymmetric force-free equilibria defined by  $\nabla \times \vec{B} = \lambda \vec{B}$ , where the scalar  $\lambda$  is considered to be a linear function of the normalized poloidal flux,  $\psi$ :  $\lambda(\psi) = \lambda[1 + \alpha(2\psi - 1)]$ . Figure 1 shows the current density profiles of three such equilibria. The fitted parameter  $\alpha$  determines whether  $j/B$  increases ( $\alpha > 0$ ) or decreases ( $\alpha < 0$ ) toward the magnetic axis.

The evolution of a typical CTX spheromak discharge has two phases: the sustainment phase when magnetic helicity is injected to build up and maintain the spheromak fields, and the resistive decay phase that begins when the helicity source is turned off.

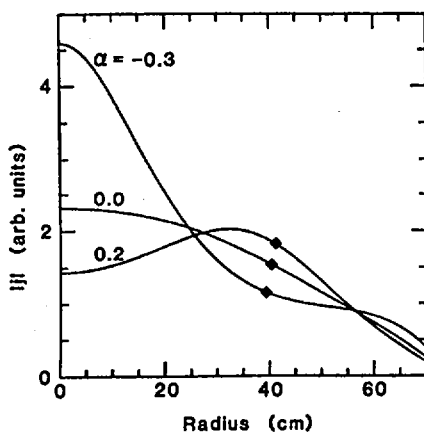


FIG. 1. Magnitude of the plasma current density versus radius in the midplane of the 0.67 m radius flux conserver for three values of the profile parameter  $\alpha$ . Solid diamonds indicate the radius of the magnetic axis.

During sustainment, the enhancement of current on the outer flux surfaces, which are connected with the coaxial electrodes, results in an observed value of  $\alpha$  in the vicinity of  $-0.3$ . The spheromak poloidal current is typically 5 times the source current. During decay, the spheromak is isolated from the electrodes and the lower resistivity of the core plasma near the magnetic axis results in peaking of the current profile. The measured  $\alpha$  becomes increasingly positive, reaching 0.6 to 1.0 toward the end of the decay. Our analysis of the Rogowski loop data is supported by the appearance of saturated rotating magnetic distortions under conditions for which the inferred  $q(\psi)$  profile predicts the instability of nonresonant internal kink modes [2,4].

### 3. HELICITY BALANCE AND RELAXATION IN SUSTAINED SPHEROMAKS

A recent analysis of magnetic helicity balance in CTX [5] gives compelling evidence for the existence and importance of relaxation processes that minimize magnetic energy on time scales much shorter than the resistive diffusion time scale for loss of the magnetic helicity. The significance of such processes for the formation and evolution of RFP and spheromak equilibria has long been recognized [6]. Though equilibria that are close to the fully relaxed state have been observed in many experiments, a key issue is also whether the relatively rapid relaxation process is accompanied by any helicity loss. This issue has been examined by comparing CTX data with the following model:

$$\frac{\partial K}{\partial t} = -\frac{K}{\tau_K} + 2V_g \dot{\phi}_g$$

where  $K$  is the helicity of the spheromak equilibrium,  $\tau_K$  is its characteristic resistive decay time,  $\dot{\phi}_g$  is the applied source axial magnetic flux, and  $V_g$  is the electric potential across the coaxial source electrodes measuring the rate of generation of linking azimuthal flux. The term  $2V_g \dot{\phi}_g$  gives the rate of magnetic helicity injection for our source. Thus the model tests whether helicity injected by the source is conserved as it is incorporated into the spheromak equilibrium. One result of this study is shown in Fig. 2 where the increase in helicity of the spheromak equilibrium,  $\Delta K$ , after time  $\Delta t = 50 \mu s$ , is compared with the injected helicity,  $\int_0^{\Delta t} 2V_g \dot{\phi}_g dt$ , over a range of values of  $V_g$  and  $\dot{\phi}_g$ . These data represent the early phase of sustained CTX discharges during which  $K$  is growing and resistive loss of helicity is unimportant ( $\Delta t \ll \tau_K$ ). They show that, within the  $\pm 12\%$  uncertainty of the data, the injected helicity is conserved during the formation of a relaxed spheromak equilibrium. The full model, with  $\tau_K$  included as an unknown, constant parameter, gives good fits to both sustained and decaying phases of CTX discharges [5]. The values of  $\tau_K$  so determined agree with estimates of the plasma resistivity.

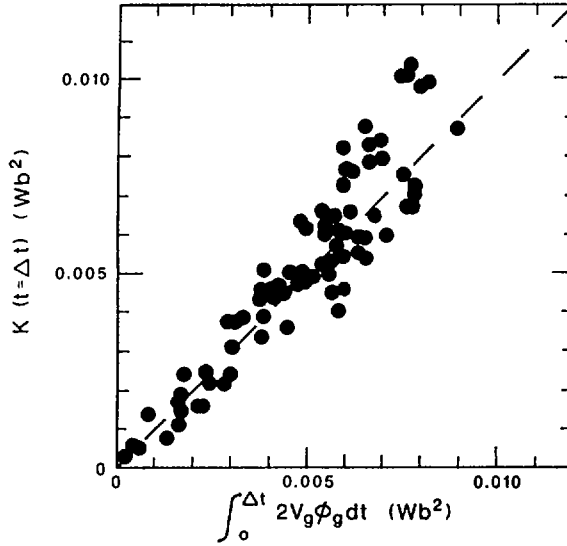


FIG. 2. Comparison of the magnetic helicity content of the CTX spheromak with the magnetic helicity injected by the source after a short time  $\Delta t$ .

During sustainment, the model is valid in spite of strong relaxation processes that produce a sustained spheromak field profile ( $\alpha = -0.3$ ) departing from the fully relaxed state ( $\alpha = 0$ ) by only 3% in magnetic energy.

The study of helicity conservation on CTX referred to above did not identify the specific relaxation mechanism that dissipates excess injected magnetic energy and maintains a constant ratio of poloidal and toroidal spheromak fluxes during the sustainment phase. This phase is characterized by prominent oscillations ( $\Delta B/B \sim 0.1$ ) associated with rotating saturated  $n = 1$  kink modes. The modes arise because of the unrelaxed condition of the driven  $q$ -profile, with  $q \approx 1$  on the magnetic axis. Evidence for a connection between  $n = 1$  modes and helicity injection on CTX has now appeared with the implementation of circuitry to achieve constant-current discharges with  $I_{\text{tor}}$  as high as 700 kA sustained for up to 2.0 ms. In this mode of operation we have observed cyclic variations in the plasma toroidal current, as illustrated in Fig. 3a. Corresponding variations in the relative amplitude of the  $n = 1$  oscillations (as seen in  $B_{\text{pol}}$  at the wall) are shown in Fig. 3b. We note that although the helicity injection rate is constant,  $I_{\text{tor}}$  and the spheromak helicity decrease during the quiescent intervals (when  $\Delta B_{\text{pol}}$  is small) and increase when the  $n = 1$  oscillations are active. These findings support the view that  $n = 1$  modes play a role in the assimilation of injected

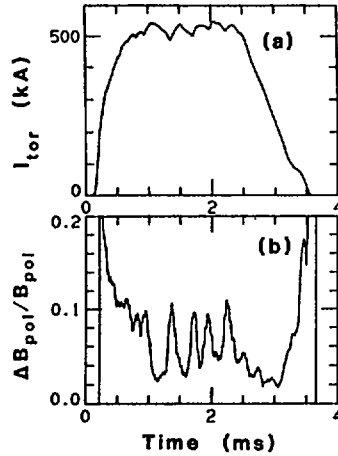


FIG. 3. (a) Cyclic variations in the toroidal plasma current during sustainment. The rate of helicity injection was constant within  $\pm 20\%$  until the source was turned off at 2.5 ms.

(b) Corresponding variations in the rms level of  $n = 1$  perturbations of the poloidal magnetic field at the wall normalized to the equilibrium value.

Both (a) and (b) have been filtered to average over the individual  $n = 1$  oscillations.

helicity by the spheromak. In terms of the helicity balance model with 100% conservation, the observed variations in  $K$  would imply a spheromak resistivity (as represented by  $1/\tau_K$ ) that is periodically increased by a factor sufficiently large that its time-average value is about twice that measured for decaying spheromaks ( $V_g = 0$ ) under the same conditions. Because this conclusion seems unlikely, we are looking into other explanations. For example, it could be that the assumption of a linear relation between  $\lambda$  and  $\psi$  is not valid during this process, but this possibility alone cannot account for the observed variation of  $K$ . It is therefore likely that the transfer of helicity from the source to the spheromak is periodically interrupted by decreases in  $n = 1$  mode activity. One expects that such a process would be accompanied by noticeable profile changes. However, as determined from our analysis, the parameter  $\alpha$  does not show large variations. In general, a current distribution that is somewhat more peaked toward the outside is indicated during quiescent periods.

#### 4. CTX CONFINEMENT

Although encouraging results had been obtained in CTX with the 0.40 m diameter flux conserver, a 0-D energy balance analysis [7] showed that ionization of the background fill gas to replace rapid plasma particle losses ( $\tau_p \approx 0.17$  ms) was the dominant electron energy loss mechanism of decaying spheromaks.

TABLE I. CTX SPHEROMAK PARAMETERS FOR TWO SIZES OF THE FLUX CONSERVER

$R_{fc}$ (m)	0.40	0.67
$B_{peak}$ (kG)	$2.9 \pm 0.3$	$4.9 \pm 0.6$
$I_{tor}$ (kA)	$191 \pm 20$	$471 \pm 58$
$n_e$ ( $10^{13} \text{ cm}^{-3}$ )	$6.0 \pm 1.2$	$5.5 \pm 1.0$
$j/n_e$ ( $10^{-14} \text{ A}\cdot\text{m}$ )	$2.0 \pm .2$	$2.1 \pm .2$
$T_{core}$ (eV)	$90 \pm 10$	$80 \pm 10$
$\langle\beta\rangle_{vol}$ (%)	$7.0 \pm 1.5$	$1.8 \pm 0.3$
$\tau_{B^2}$ ( $\mu\text{s}$ )	$240 \pm 60$	$840 \pm 100$
$\tau_E$ ( $\mu\text{s}$ )	$24 \pm 4$	$22 \pm 3$
$\tau_{Alfvén}$ ( $\mu\text{s}$ )	0.19	0.17
$S$ ( $10^4$ )	2.7	7.3

Indeed, low impurity levels had been achieved by rapid particle pumpout rather than by direct burnthrough. With the aim of exploring a more relevant regime for confinement studies with higher  $T_e$ ,  $\tau_p$  and  $S$ , the 0.67 m radius flux conserver was installed and the helicity source radius was increased from 0.15 m to 0.28 m. Table I shows a comparison of the parameters achieved for decaying spheromaks at both sizes. The data represent averages of a selection of shots chosen for best simultaneous confinement and temperature. The temperature  $T_{core}$  is the value of  $T_e$  obtained from Thomson scattering in the core region near the magnetic axis. The other parameters listed correspond to the time of the Thomson scattering pulse. Values of  $\beta$  are based on the assumption  $T_i = T_e$ . For the Alfvén time,  $\tau_A$ , we use  $\lambda^{-1}$  as a characteristic length. The data are for decaying spheromaks, but  $T_e$  from Thomson scattering and the level of impurity radiation show no significant difference between sustained and decaying phases. Although the magnetic energy loss time,  $\tau_{B^2}$ , has increased as  $R$  (indicating no change in average plasma resistivity), no significant change has occurred in the plasma energy loss time,  $\tau_E$ , and the achievable plasma  $\beta$  has correspondingly decreased. The achievement of record spheromak currents ( $I_{tor} = 1 \text{ MA}$ ) and of values of space-averaged  $j/n_e$  as high as  $3 \times 10^{-14} \text{ A}\cdot\text{m}$  (sufficient to burn through low- $Z$  impurities) has not succeeded in raising  $T_e$

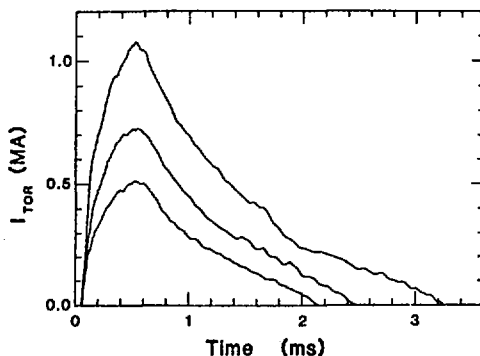


FIG. 4. Toroidal plasma current waveforms for a high-current mode of CTX operation.

significantly. Examples of high current CTX operation are shown in Fig. 4. Because  $\tau_p$  has increased with size, we may be faced with a new energy  $p_{\text{loss}}$  process involving strong thermal conduction or convection.

In order to reach such a conclusion, it is first necessary to characterize energy losses from impurity radiation. A steerable gold foil bolometer was initially used to look from the source end of the experiment along various paths. It showed that there exists a large region, including the magnetic axis, from which, during the decaying phase, the radiated energy density can be as low as 20% of the local initial magnetic energy density at the start of the decay. However, relaxation dynamics may be transferring magnetic energy outward without local dissipation. We have recently extended the range of our bolometer scans (with a second steerable instrument) to include the outer flux surfaces near the geometric axis so that the total radiative loss can be determined. Though the conditions obtained during this study have not been our best in terms of decaying spheromak lifetime, we find that, during the decaying phase, an upper bound for the total radiated energy is 45% of the total available magnetic energy. Our analysis is verified by the observation of nearly complete conversion of field energy to radiation under conditions of high impurity concentration (e.g. just after a vacuum opening or with the introduction of large amounts of argon). The observed general trend, both for sustained and decaying phases, is a reduction in the radiated energy fraction with increased time-averaged  $j/n$ . However, we recognize that impurity radiation can dominate the global dynamics of spheromak evolution through its local effects on the plasma resistivity even though the net radiated power is small. Ion heating above the classical rate may also be significant in the energy balance. Doppler broadening measurements of C-III, O-IV and O-V radiation show ion temperatures of these

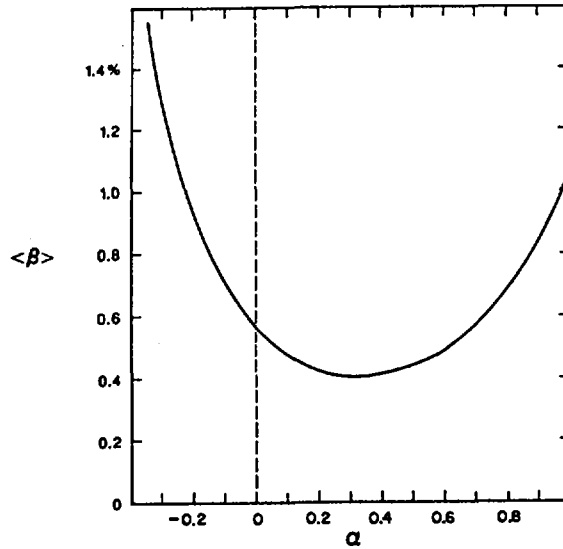


FIG. 5. Volume-averaged plasma beta at marginal stability (Mercier criterion) versus the CTX profile parameter  $\alpha$ .

impurities that are  $5 \times T_e$  during sustainment and  $2 \times T_e$  during the decay phase. We are looking for a current-driven instability (e.g. the electrostatic ion cyclotron instability) which could produce these temperature differences.

Because of the low shear of spheromak equilibria, the predicted threshold in  $\beta$  for the onset of pressure-driven modes is low. Figure 5 shows the result of recent calculations using the Mercier criterion for the marginal stability of CTX equilibria described by the parameter  $\alpha$ . It appears likely that these ideal modes are active in all spheromak discharges. In order to see whether pressure-driven modes were determining  $\tau_E$ , we attempted to raise the critical  $\beta$  for instability by modifying the  $q$ -profile. We inserted a 0.15 m radius copper cylinder, with a hemispherical cap, along the geometric axis of CTX. The resultant configuration was like that used at Osaka for the stabilization of disruptive instabilities on CTCC-1 [8]. Figure 6 shows theoretically how the volume-averaged  $\beta$  at the instability threshold is raised with increasing insertion,  $L$ . At  $L = 0.50$  m in CTX, the axial current measured in the cylinder was only 5% of the spheromak poloidal current. However, even with peak  $j/n_e$  as high as  $3 \times 10^{-14}$  A·m, the electron temperature of decaying spheromaks as measured by Thomson scattering was lower than before. Insertion of the cylinder also increased the radiated energy density near the magnetic axis to 50% of the local magnetic energy density. The global

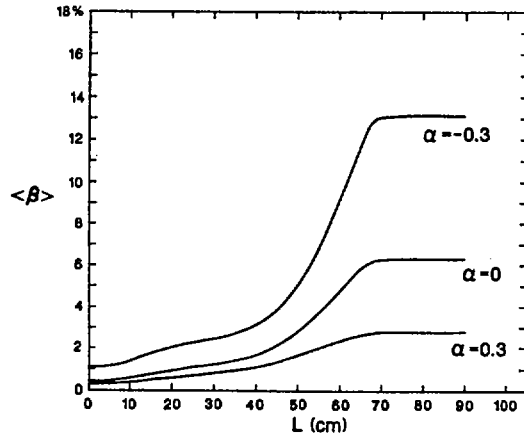


FIG. 6. Volume-averaged plasma beta versus the insertion length of a conducting cylinder of 0.15 m radius in CTX for three values of  $\alpha$ .

energy fraction radiated during decay was 70%. Thus, changes in the contribution of impurity radiation to the energy balance may have obscured the effects of modifying the q-profile.

## 5. STUDIES WITH APPLIED BIAS FIELD

During CTX discharges the flux conserver acts as the plasma limiter. In addition, as magnetic flux is lost through the copper hoops because of their resistivity, an increasing fraction of the spheromak's magnetic field passes outside the mesh boundary [7]. As a result, the edge plasma is cold, with  $T_e = 5$  to 10 eV, as measured by the Langmuir probe. To vary the edge conditions and thus study their effect on confinement, coils located outside the CTX vacuum tank were used to apply an external bias field, parallel to the spheromak geometric axis [9]. With the sign of the applied field such as to push the spheromak flux surfaces inward, the plasma density was increased and Lyman- $\alpha$  emission was reduced. A "global" particle confinement time inferred from the ratio of these chord-averaged measurements thus increased with the application of bias field. It decreased for bias of the opposite sign. These results show the sensitivity of particle confinement to separatrix geometry. The effects of bias field on global energy confinement were found to be more complex. Under some conditions with applied bias, a quiescent phase occurred during spheromak decay accompanied by reduced current flow to the flux conserver and increased magnetic field decay time. The inferred increase in energy confinement time from this reduction in edge effects could be as large as a factor of 2. We are now testing the effectiveness of a strongly mirrored bias field using a pair of

coils inside the CTX tank. This configuration can more completely disengage the equilibrium fields of decaying spheromaks from the flux conserver, but, as observed on CTCC-1 [10], it also lowers the applied flux at which the spheromak undergoes a  $180^\circ$  rotation of its axis during formation.

### REFERENCES

- [1] JARBOE, T.R., et al., Phys. Rev. Lett. **51** (1983) 39.
- [2] JARBOE, T.R., et al., in Plasma Physics and Controlled Nuclear Fusion Research 1984 (Proc. 10th Int. Conf. London, 1984), Vol. 2, IAEA, Vienna (1985) 501.
- [3] JARBOE, T.R., et al., Phys. Fluids **27** (1984) 13.
- [4] KNOX, S.O., et al., Phys. Rev. Lett. **56** (1986) 842.
- [5] BARNES, C.W., et al., Phys. Fluids **29** (1986) 3415.
- [6] TAYLOR, J.B., Rev. Mod. Phys. **58** (1986) 741.
- [7] BARNES, C.W., et al., Nucl. Fusion **25** (1985) 1657.
- [8] NAGATA, N., et al., in Plasma Physics and Controlled Nuclear Fusion Research 1984 (Proc. 10th Int. Conf. London, 1984), Vol. 2, IAEA, Vienna (1985) 655.
- [9] BARNES, C.W., et al., Phys. Fluids **28** (1985) 3443.
- [10] SATOMI, N., et al., Paper IAEA-CN-47/D-IV-1-2, these Proceedings, Vol. 2.

## CONFINEMENT EXPERIMENTS AND SIMULATION ON THE CTCC-I SPHEROMAK

N. SATOMI, S. GOTO, Y. HONDA, Y. KATO,  
M. NAGATA, M. NISHIKAWA, A. OZAKI,  
T. TAKAISHI, T. UYAMA, K. WATANABE  
Faculty of Engineering,  
Osaka University,  
Suita, Osaka

T. SATO, T. HAYASHI  
Institute for Fusion Theory,  
Hiroshima University,  
Higashisenda-cho, Naka-ku, Hiroshima  
Japan

### Abstract

#### CONFINEMENT EXPERIMENTS AND SIMULATION ON THE CTCC-I SPHEROMAK.

The CTCC-I spheromak is confined in a metal flux conserver so that external global (tilt and/or shift) instabilities can be prevented. However, the plasma in close contact with the solid wall, hence, the plasma-wall interaction, which is a drawback of the flux conserver method, directly affects the confinement. The formation of a detached spheromak is studied both experimentally and numerically to find a method of improving the present spheromak confinement. The internal instabilities, especially the tilting instability, of the detached spheromak are studied by a full 3-D MHD simulation code. The experiment of spheromak detachment from the solid wall is attempted in two ways, by applying the external magnetic field through conductive and through resistive walls. Numerically, a fairly stable detached configuration for the tilting instability is found for  $L/a = 1.0$ , where  $L$  is the height of the flux conserver and  $a$  is the radius. No tilting mode is excited, even if the external flux applied is more than 60% of the internal flux. Experimentally, the formation of the detached spheromak is demonstrated, although still in the initial phase.

### 1. INTRODUCTION

Basically there are two experimental approaches in spheromak research. One is to confine a spheromak plasma by an external field pressure (vertical field), notably the Princeton S-1, and the other by a conducting wall, notably the Osaka CTCC-I and the LANL CTX. The former spheromak has an isolated space between the separatrix and the rigid wall while it is always globally (tilt and/or shift) unstable. In contrast, the latter can be globally stable while the plasma is in close contact with the rigid wall. From the standpoint of MHD confinement, globally unstable configurations do not satisfy the necessary

condition for the confinement vessel. From the standpoint of particle confinement, however, the closeness of plasma and the wall is, in several ways, detrimental to confinement.

The Osaka group has, for many years, been conducting extensive research into the flux conserver (FC) confined spheromak. The main results of previous work are described in the literature [1, 2]. The experiments can be roughly divided into three phases: In the first phase, efforts are primarily focused on the creation of a well shaped, long lived spheromak by using, for example, titanium coating, spheroidal vessel and highly conductive material. The typical lifetime is 1 ms (the present record is 1.3 ms), with  $n = (3-5) \times 10^{13} \text{ cm}^{-3}$  and  $T_e = 20-30 \text{ eV}$ . The second phase is more closely related to an understanding of physical processes, namely, the internal MHD instability and associated MHD relaxation.

With these achievements, we attempt to detach the plasma (separatrix) from the wall so that the plasma-wall interaction, which is a real drawback of the flux conserver method, can be reduced. The attempt is carried out both experimentally and numerically. First, by means of a 3-D MHD simulation, the internal MHD instabilities including the  $n = 1$  (tilt),  $n = 2$  and  $n = 3$  instabilities, are studied in detail. Then, a simulation model is developed which is capable of studying the detachment of the separatrix by externally applying a magnetic flux through the FC wall. By this model the internal instabilities, in particular the tilting instability, of the detached spheromak are studied.

Secondly, experiments of spheromak detachment from the FC wall are attempted in two ways: The first attempt is to apply an external flux through a wall of relatively high conductivity from external coils surrounding the flux conserver before the co-axial gun is fired. The second method is to apply an external flux through a wall of relatively low conductivity, together with the firing of the co-axial gun.

In the following section, we describe some typical experimental data which may show the difference in lifetime, depending on the vessel conditions and the experimental devices used for the present detachment experiment. In Section 3, the simulation model and results are described, and in Section 4 the present status of the experimental results is presented. Finally, conclusions are given in Section 5.

## 2. DESCRIPTION OF CTCC-I SPHEROMAK FEATURES AND DETACHED MODE EXPERIMENT

In the CTCC-I experiments, the spheromaks are produced by a magnetized co-axial plasma gun and confined in a metal FC. Typical poloidal magnetic field measured at the symmetry axis is 2 kG. Assuming the forcefree minimum energy state, the total toroidal and poloidal currents are estimated to be 90 kA and

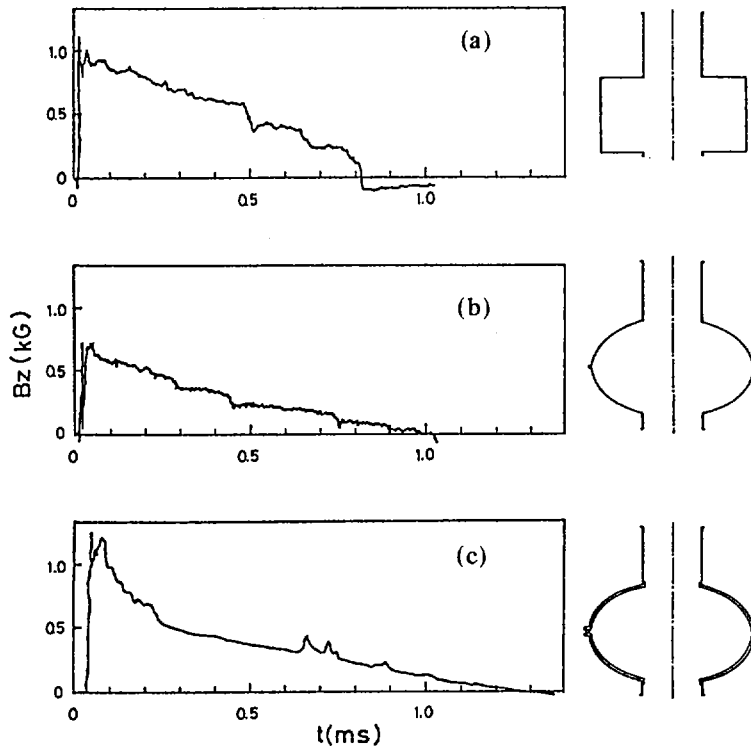


FIG. 1. Temporal evolution of magnetic field in CTCC-I spheromak obtained with various flux conservers.

140 kA, respectively. The initial plasma produced without impurity control (titanium coating on the FC inner wall) is radiation dominated, and the plasma exhibits a quiet exponential decay of 0.2 ms.

The cylindrical FC (1.5 mm thick copper) has been used from the start of our spheromak experiment. By using this FC, the maximum configuration lifetime of 0.8 ms was attained when the impurity control, the titanium coating, and the central conductor were applied as is shown in Fig. 1 (a). The effects of FC geometry, shape and wall thickness on plasma confinement were studied. The FCs shown in Figs 1 (b) and 1 (c) both have oblate spheroidal shapes; the first FC consists of 1.5 mm thick copper, and the second FC of 15 mm thick aluminium. As is shown in Fig. 1 (b), plasma confinement was improved by using the spheroidal FC to attain a maximum lifetime of 1.0 ms; this indicates that the vessel shape plays an important role in the confinement. The wall thickness is also thought to be significant for the confinement since the magnetic field lines in the plasma would escape through an FC wall of finite conductivity, i.e. flux loss would take

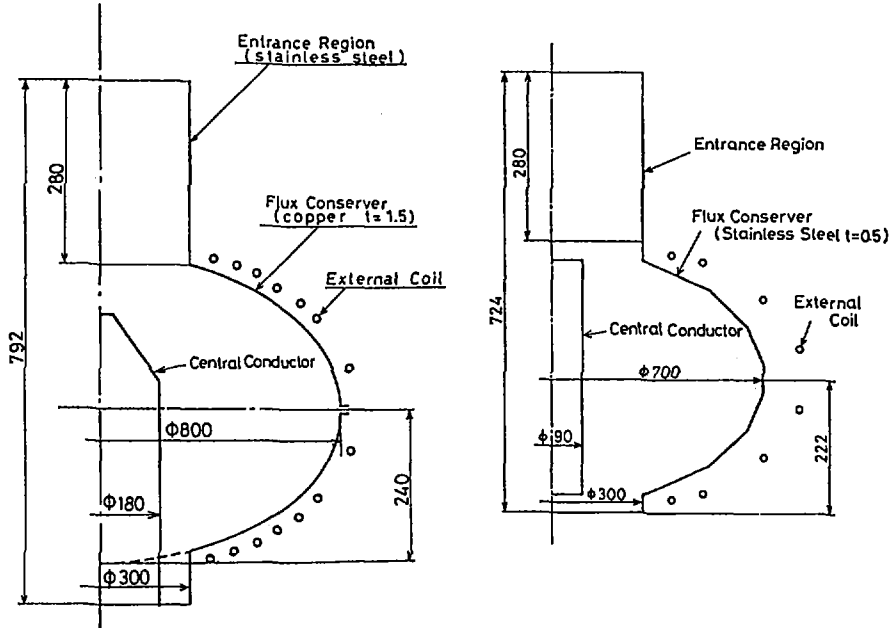


FIG. 2. Flux conservers used in detached mode experiment.

place during long confinement. This was confirmed in the experiment which used a thick wall FC, where the lifetime was extended up to 1.3 ms as is shown in Fig. 1 (c). It was in the long lived CTCC-I spheromak, a stepwise MHD activity of the magnetic field in association with the internal MHD instability during resistive plasma decay [1, 2] was observed.

To study the detached spheromak, two types of FC with external coil as shown in Fig. 2 are used. The first type is made of highly conductive metal (1.5 mm thick copper); the major and minor semi-axes are 0.4 m and 0.24 m long. As external coils, fourteen copper conductors (8 mm diameter) connected in series are installed on the FC, spaced 3 cm from it by ceramic insulators. By using this FC, the spheromak is formed in the presence of an external bias flux so as to detach the separatrix. The second type consists of 0.5 mm thick stainless steel, where the major and minor semi-axes are 0.35 m and 0.21 m long. In this case, eight conductors (10 mm diameter) connected in series are used as external coils. They are supported on the frame surrounding the FC. The rise-time of the coil current is about 60  $\mu$ s, and the decay time can be varied in the range of 0.5 to 2.0 ms. The maximum coil current is 10 kA. In the second experimental scheme, a pulsed vertical field is applied through the resistive FC to detach the separatrix, after a spheromak has been produced in the FC without external field.

### 3. SIMULATION STUDY OF DETACHED SPHEROMAK FOR MHD INSTABILITIES

The principal aim of the present simulation study is to provide guidance to planning and designing the detached mode experiment.

Before carrying out the detached analysis, let us examine the internal MHD instabilities of spheromaks in an FC. To extract the general features of the problem as thoroughly as possible, we adopt a simple geometry for the FC. The FC is assumed to be drum shaped, with radius  $a$  and height  $L$ . The spheromak equilibria to be studied are obtained by solving the Grad-Shafranov equations, where the toroidal current and the plasma pressure are assumed to be proportional to  $\psi^\lambda$  ( $\psi$  is the poloidal flux) and 0, respectively, and the total toroidal current is fixed to a certain value. Thus, the initial equilibria are represented by two parameters only,  $L/a$  and  $\lambda$ . Plugging the equilibria obtained in this way into the full 3-D MHD simulation code as initial conditions [3], we shall study the behaviour of the MHD instabilities.

The growth rates of the three most dangerous modes, i.e.  $m/n = 1/1$ ,  $1/2$  and  $1/3$ , are examined as functions of  $L/a$  and  $\lambda$ . The general tendency for all these modes is to become more unstable for larger  $L/a$  and larger  $\lambda$ . There is a threshold for  $L/a$  below which a mode becomes stable. Since we are here mainly concerned with the tilt mode ( $m/n = 1/1$ ), we show the growth rates of the  $1/1$  mode for three  $\lambda$  values ( $\lambda = 1.5, 2.0$  and  $3.0$ ) as functions of  $L/a$  in Fig. 3. Although not shown here, all modes are stable for  $L/a = 1.0$ . As can be seen from this figure, the threshold values lie in the range  $L/a = 1.0$  to  $1.3$  for

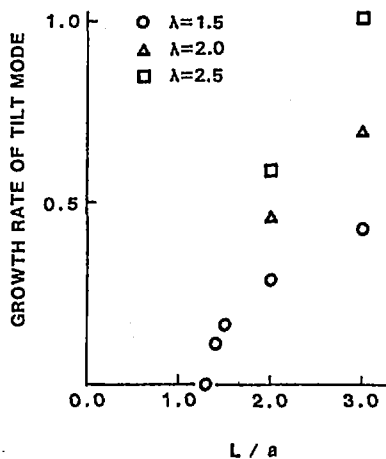


FIG. 3. Growth rates of tilting mode,  $m/n = 1/-1$ , for  $\lambda = 1.5, 2.0, 2.0, 2.5$  ( $I \propto \psi^\lambda$ ) as a function of elongation,  $L/a$ , where  $L$  and  $a$  are height and radius of flux conserver.

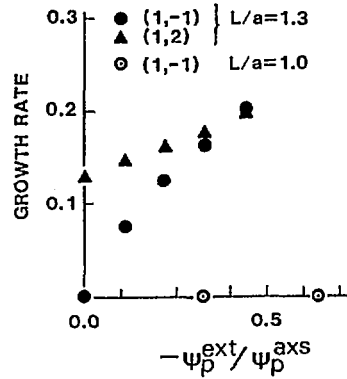


FIG. 4. Growth rate of tilting mode and helical kink mode as a function of external flux normalized by internal plasma flux.

$\lambda = 1.5$  to  $3.0$ . A discrepancy is observed between our numerical and the analytical result [4], which may, however, be attributed to the difference in the equilibria. The equilibrium in [4] is the Bessel function model, while ours assumes  $\psi^\lambda$ .

With this result in mind, we proceed to the detached mode. As an initial condition, we use an equilibrium obtained by solving the Grad-Shafranov equations. On choosing the equilibrium, we dynamically supply an external flux through the FC wall. In the actual simulation run, the magnitude of the on-wall magnetic field parallel to the wall is changed with time whereby the magnetic pressure on the wall pushes the plasma inwards and, subsequently, the external field is brought inside the FC. When a certain amount of external flux has been brought inside and the separatrix is detached from the wall, we impose a tilting perturbation on the system and make the 3-D simulation code run.

The growth rate of the tilt mode as a function of the external flux relative to the spheromak flux is plotted in Fig. 4. The filled circles correspond to the  $\lambda = 1.5$  and  $L/a = 1.3$  case, and the dot-in-open circles refer to the  $\lambda = 1.5$  and  $L/a = 1.0$  case. The filled circles indicate that the growth rate increases drastically as the external flux increases. Considering that the original spheromak is tilt stable, it is evident that the external flux destabilizes the tilt mode. For comparison, the growth rate of the  $1/2$  mode is shown by the triangles, showing a slightly increasing tendency as the external flux increases, which is, however, substantially smaller than for the tilt mode. The slight increase may be attributed to the change in the spheromak configuration due to the intrusion of external flux. Incidentally, the  $1/3$  mode was always stable in this example. In Fig. 5 we show an example of a spheromak that is non-linearly deformed by  $n = 1$  and  $n = 2$  instabilities.

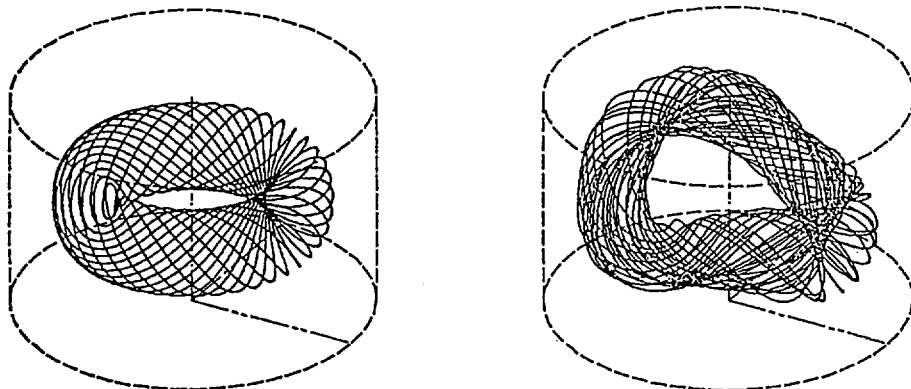


FIG. 5. Magnetic field line trajectories in initial and developed ( $n = 1$  and  $n = 2$  mode) spheromak phases.

Interestingly enough, the tilt mode was not excited in the  $L/a = 1.0$  case, even if the intrusion of external flux exceeded 60% of the internal flux. From these simulation results we can, therefore, conclude that certainly the external flux contributes to destabilization but that there exists a realistic, detached mode condition that can absolutely prevent the tilting instability. The condition is that the shape of the FC should be as oblate as possible, most favourably  $L/a = 1.0$ . The encouraging results of this simulation study led to planning the detached mode experiment. This will be discussed in the following section.

## 4. EXPERIMENTAL RESULTS

### 4.1. Bias flux experiment

The experiments presented here were carried out by the bias flux mode, i.e. the spheromaks were formed in the presence of bias flux [5, 6]. The spheromak plasma becomes tilt unstable within 0.1 ms if the bias flux exceeds a certain critical value, 0.75 mWb, as is shown in Fig. 6(a). Here, the bias flux inside the FC is estimated by using the measured bias magnetic field without spheromak formation. The magnetic field shows rapid decay after the onset of tilting, and during this decay the density increases slightly, thus indicating increased plasma-wall interaction. The O V ( $630 \text{ \AA}$ ) line radiation is only observed in the early phase while this radiation increases gradually in the period of 0.2 to 0.3 ms in the case of the long lived spheromak obtained without bias flux. When external flux of the amount of this critical bias flux is applied, the spheromak suffers from tilting instabilities in 30% of all the discharge shots. When a bias flux of 3 mWb is used, tilting is always observed. The tilting growth rate depends on the

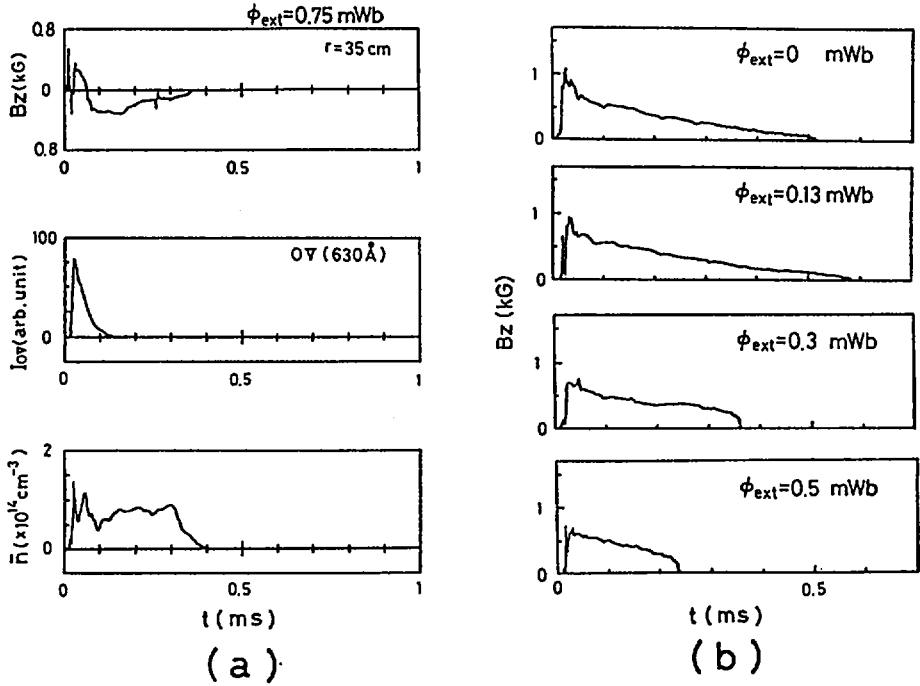


FIG. 6. Typical data in bias flux experiment:

(a) Time evolutions of magnetic field,  $O V$  line radiation and density without central conductor; (b) time evolutions of magnetic field for various bias fluxes with central conductor ( $d = 18$  cm).

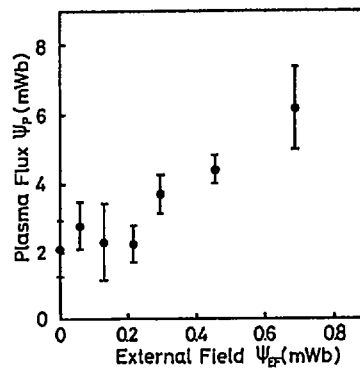


FIG. 7. Internal plasma flux at termination onset time of discharge as a function of external flux.

amount of bias flux; for a bias flux of 0.75 mWb, it takes 50 to 60  $\mu\text{s}$  to complete the tilting. This feature is, at least qualitatively, in agreement with the previous numerical result.

To stabilize this tilting as observed in the formation phase, we used a central conductor. Figure 6(b) shows the results of the experiment with an 18 cm diameter central conductor for various applied bias fluxes: 0.13, 0.3 and 0.5 mWb. In the small bias flux case (0.13 mWb), the plasma is not, within the reproducibility of the discharge, affected by the external field. These results indicate that the initial tilting is not observed for an external field of less than 0.5 mWb, but termination of the discharge is always observed and the time after which termination sets in becomes shorter as the amount of the bias flux increases. When a bias flux higher than 0.5 mWb was applied, the plasma could not be injected into the FC, and no spheromak formation took place, because of the small annular space between the central conductor and the entrance tube of the FC. The internal flux of the plasma at the time when the termination of the discharge is observed is shown in Fig. 7 as a function of the amount of applied bias flux. This indicates that the flux ratio at the onset time of the termination is about 10%.

#### 4.2. Pulsed vertical field experiment

In this experiment, an external vertical field with a rise-time of about 60  $\mu\text{s}$  was applied through the resistive wall after gun firing. The typical delay time of the external coil discharge described here is 5  $\mu\text{s}$ . The experiments presented here were carried out without titanium coating. So, the plasma is radiation dominated, and the lifetime of the configuration is 100 to 150  $\mu\text{s}$  in the present experiment, while the lifetime of the previous plasma in the experiment with cylindrical FC was, typically, 200 to 300  $\mu\text{s}$ .

Figure 8 shows typical poloidal and toroidal magnetic fields, measured simultaneously at five radial positions in the midplane, without and with external field. The radial position of the magnetic axis is estimated to be  $r = 22$  cm if force-free minimum energy is assumed. In Fig. 8(a), the poloidal magnetic field at  $r = 23$  cm changes from positive to negative, gradually in time, i.e. the magnetic axis of this plasma shifts outwards, probably because of flux loss through the resistive wall. In most of the discharges, the poloidal magnetic field at  $r = 23$  cm is rather large throughout the discharge; thus, the spheromak configuration in the resistive FC is far away from the force-free minimum energy state. The global behaviour of the measured magnetic field does not change markedly even if an external field is applied. It is, however, remarkable that, when the external field is applied, the toroidal magnetic field near the FC, for example at  $r = 32$  cm, becomes very small as is shown in Fig. 8(b). The  $B_t$  signal at  $r = 35$  cm is an error field caused by the effect of the observation hole on the FC. Figure 9 shows the toroidal magnetic field at  $r = 32$  cm and the ratio of the toroidal fields at two positions,  $r = 32$  cm and  $r = 23$  cm, as a

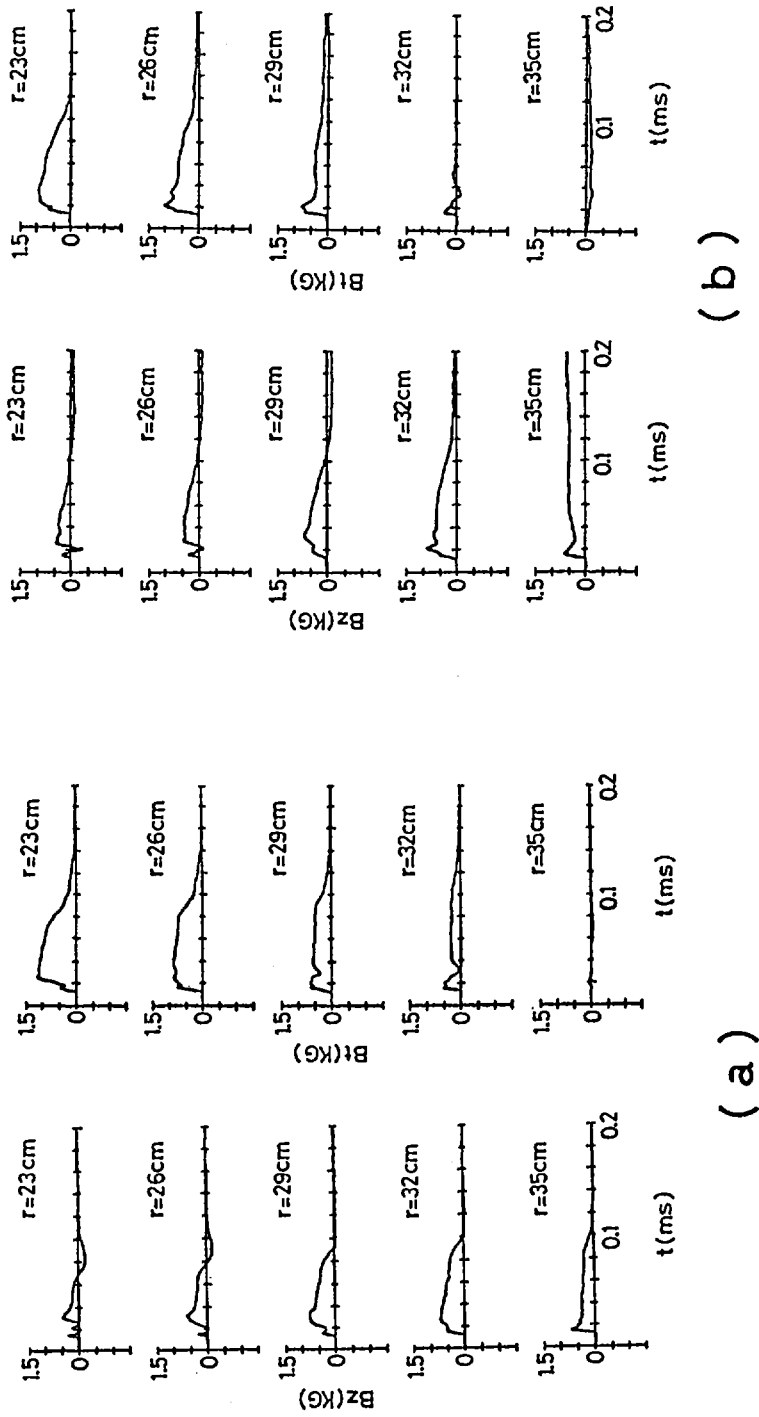


FIG. 8. Time evolution of poloidal and toroidal magnetic fields measured at five different radii, without external field (a) and with external field (b).

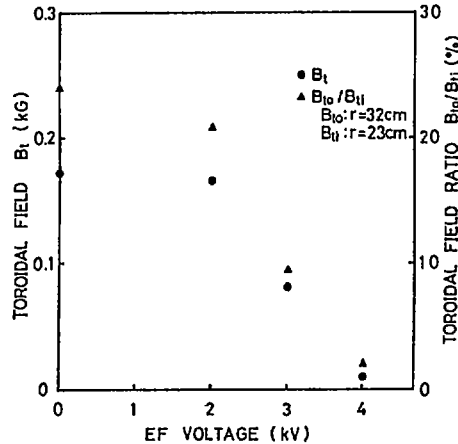


FIG. 9. Toroidal field  $B_t(r = 32 \text{ cm})$  and toroidal field ratio  $B_{t0}(r = 32 \text{ cm})/B_{t1}(r = 23 \text{ cm})$  as a function of charging voltage of external field coil source.

function of the charging voltage of the power source for the external field. This indicates that the separatrix of the spheromak is detached by about 2 to 3 cm from the FC wall when a rather high external field is applied. There is no evidence of tilting in the present detached spheromak.

## 5. CONCLUSIONS

The numerical simulations have shown that the external magnetic flux brought inside the FC acts to destabilize the tilt mode, but that if the shape of the FC is sufficiently oblate (e.g.  $L/a \approx 1.0$ ), we can realize a tilt stable, well detached spheromak. Although the results reached so far are still only preliminary, the experiments are in good agreement with the simulations, for example, as far as the tendency of tilt destabilization in proportion to the external flux is concerned.

## REFERENCES

- [1] NAGATA, M., et al., in Plasma Physics and Controlled Nuclear Fusion Research 1984 (Proc. 10th Int. Conf. London, 1984), Vol. 2, IAEA, Vienna (1985) 655.
- [2] SATOMI, N., et al., in Advances in Compact Torus Research (Proc. Tech. Comm. Mtg. Sydney, 1985) (1985) 203.
- [3] HAYASHI, T., SATO, T., Phys. Fluids **28** (1985) 3654.
- [4] FIN, J.M., MANHEIMER, W.M., Phys. Fluids **24** (1981) 1336;  
BONDESON, A., et al., Phys. Fluids **24** (1981) 1682.
- [5] BARNES, C.W., et al., in Compact Toroids (Proc. 7th Int. Conf. Santa Fe, NM, 1985), Los Alamos National Lab., to be published.
- [6] SATOMI, N., et al., in Compact Toroids (Proc. US-Japan Workshop, Seattle, 1985) (1985) 41.



# FIELD REVERSED CONFIGURATION TRANSPORT

## *Theory and measurements of flux, energy, and particle lifetimes\**

A.L. HOFFMAN, J.T. SLOUGH, L.C. STEINHAUER  
Spectra Technology, Inc.,  
Bellevue, Washington

N.A. KRALL, S. HAMASAKI  
JAYCOR,  
San Diego, California  
United States of America

### Abstract

FIELD REVERSED CONFIGURATION TRANSPORT: THEORY AND MEASUREMENTS OF FLUX, ENERGY, AND PARTICLE LIFETIMES.

Experimental flux, energy, and particle lifetimes are reported for a wide range of conditions in the slow risetime TRX-2 field reversed theta pinch. The measurements have been compared with theoretical estimates based on low frequency drift waves and trapped particle waves in the peculiar FRC geometry. These estimates give reasonable agreement with the measured lifetimes and, for the first time, model the anomalous flux loss rates.

### 1. INTRODUCTION

The first detailed description of field reversed configuration (FRC) transport was given by Hamasaki and Krall [1], and subsequently by Tuszewski and Linford [2], who modelled particle transport across the separatrix and subsequent flow along open field lines. The model was based on classical transport plus localized lower hybrid drift (LHD) microturbulence, and it successfully predicted the  $R^2/\rho_{i0}$  particle lifetime scaling seen between the FRX-B [3] and FRX-C [4] experiments ( $R$  is the radius of the magnetic field null and  $\rho_{i0}$  is the ion gyroradius in the external field  $B_0$ ; the ion temperature is assumed to be uniform throughout the FRC). Localized LHD microturbulence is weak near the field null, however, and the LHD-based model cannot account for the fact that the flux loss rates are more rapid than the classical ones [5]. Comparisons with later experiments also showed deviations from the LHD-predicted scaling dependences, even for particle lifetimes [4, 6].

In this paper we describe flux, energy and particle lifetime measurements in the TRX series of experiments, particularly in TRX-2, which is a slow, multiturn field

---

\* Work supported by the United States Department of Energy.

TABLE I. SUMMARY OF OPERATING CONDITIONS OF TRX EXPERIMENTS

Device	Measurements						Point model scaling		Pseudo 2-D code $\tau_a$ ( $\mu$ s)		
	$P_0$ (mtorr)	$B_c$ (kG)	$T_i$ (eV)	$r_i$ (cm)	$\xi$ (cm)	$\tau_a$ ( $\mu$ s)	$\tau_{Ep}$ ( $\mu$ s)	$\tau_N$ ( $\mu$ s)		$\tau_a$ ( $\mu$ s)	
TRX-1 ( $r_c = 12.5$ cm)	10	8	450	6.3	45	75	45	75	52	42	48
	15	7.5	350	7.0	52	85	68	100	73	76	
	20	9	300	4.2	53	35	30	55	37	30	
TRX-2 ( $r_c = 12.1$ cm)	3	7	500	4.8	51	20	21	50	22	15	20
	6-8	14	750	3.8	33	20	13	20	21	17	
	7	13.5	900	4.6	29	27	21	29	24	19	
	10	13	550	4.4	33	30	24	37	32	28	
	10-12	12.5	475	4.1	38	30	25	35	32	28	
	10	10.5	550	4.8	41	25	23	35	30	25	
	10	8.5	400	5.2	41	32	27	85	40	34	
FRX-B ( $r_c = 12.5$ cm)	12	10	400	4.7	40	40	34	65	40*	34*	36
	12	4.5	225	7.0	63	57	62	130	69	54	
	15	7.0	225	5.3	60	68	47	87	61	56	
	20	5.5	150	5.6	66	85	53	80	78	73	
	17	6.5	300	5.4	70	50	52	39	46	36	
FRX-C ( $r_c = 25$ cm)	5	8	800	9.0	130	250	60	67	61	56	320
	20	7	250	10.0	150	180	135	155	202	320	

\* Reference point for point model scaling.

reversed theta pinch utilizing programmed formation [7, 8]. TRX-2 has been operated over a wide range of experimental conditions (fill pressures varying from 3 to 20 mtorr  $D_2$  and magnetic fields varying from 5 to 15 kG) and provides scaling information for ion temperatures varying between 75 eV and 800 eV, and electron densities varying from  $2 \times 10^{15} \text{ cm}^{-3}$  to  $8 \times 10^{15} \text{ cm}^{-3}$ . The measured lifetime scaling dependences show the same deviations from LHD-based calculations as noted previously. The new computations which are presented here and which are based on low frequency drift and trapped particle waves give better agreement with the measured lifetimes.

## 2. EXPERIMENTAL METHODOLOGY

TRX-2 is a multiturn version of the previous TRX-1 device [9], with coils of radius  $r_c = 12 \text{ cm}$ . Trigger and plug coils are used to achieve programmed formation [7, 10], and microwave pre-preionization is utilized, together with a z-discharge, to permit operation at fill pressures as low as 3 mtorr. The results presented here are only for 'well formed' FRCs, by which we mean symmetrical and untorn FRCs (monotonically decreasing diamagnetism from the centre to the ends) well separated from the end mirrors. Even with this selection, there was a scatter of about a factor of two in the lifetime data for shots run under nominally identical conditions [11].

The experimental lifetimes were determined from the decay rates of  $\phi_p$ ,  $E_p$  and  $N$ . An exponential fit was made for a time period at least as long as 0.4 of the measured lifetime. Details of the data reduction procedure are given in Ref. [11].

## 3. LIFETIME MEASUREMENTS

Most of the lifetime measurements on TRX-2 were obtained for one of the eleven conditions listed in Table I. Each point represents the average over at least three shots. The changes in separatrix radius  $r_s$  for shots with the same fill pressure  $p_0$  and external magnetic field reflect either different initial bias fields or different amounts of flux retention.  $\ell_s$  is the full separatrix length and  $T_i$  is the total temperature obtained from pressure balance and the measured electron density and magnetic field. On the basis of previous FRC measurements, it was assumed that  $T_e$  equalled  $T_i$  for total temperatures below 200 eV and that  $T_e$  scaled up to 150 eV as the total temperature increased.

Several experimental averages from TRX-1 plus one condition from FRX-B and two conditions from FRX-C are also listed in Table I [4]. We have examined scaling dependences for the TRX data and found correlations with  $r_s$  and  $\rho_{i0}$ . To a first approximation, all lifetime data appeared to scale with the parameter  $r_s/\rho_{i0}^{1/2}$ . This scaling is shown in Figs 1-3 for the points listed in Table I. These averaged data generally show a closer fit than the individual TRX measurements.

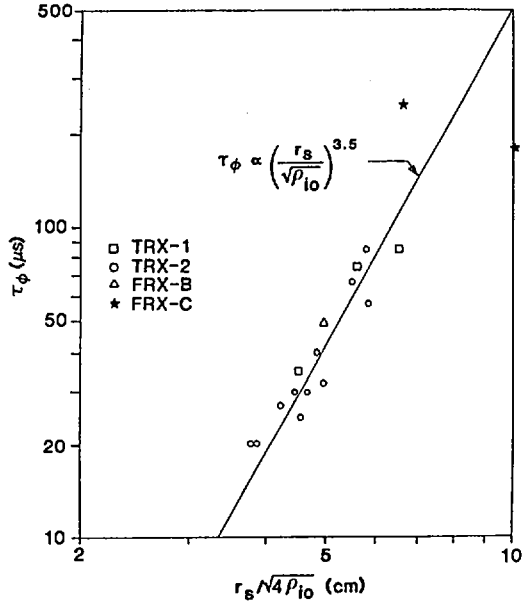


FIG. 1. Flux lifetime measurements.

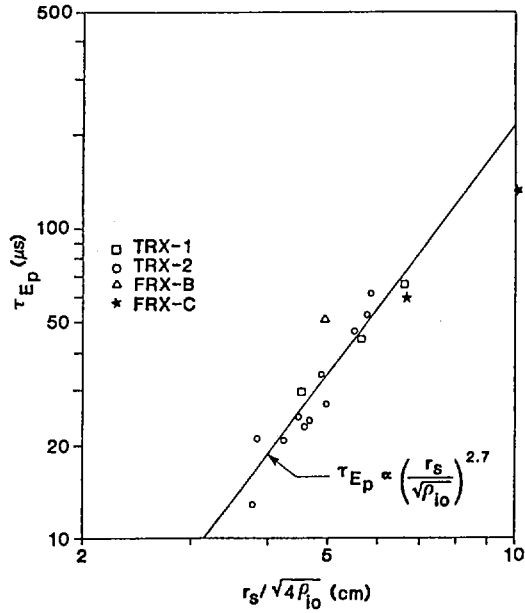


FIG. 2. Energy lifetime measurements.

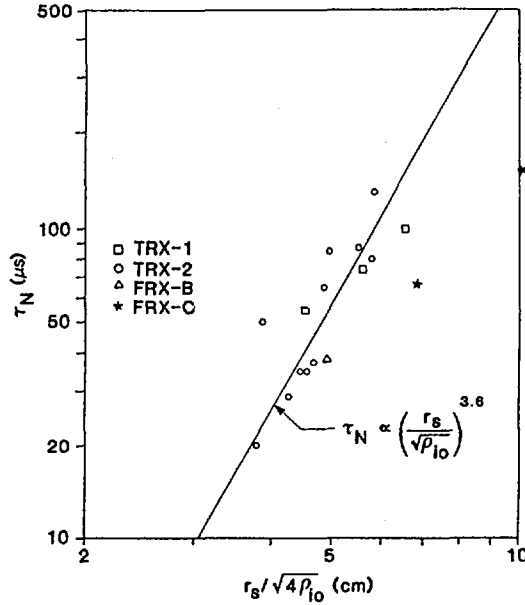


FIG. 3. Particle lifetime measurements.

The flux lifetime measurements indicate best the average FRC cross-field-line transport since they do not depend directly on open field line effects or bulk losses of energy. The data for the small machines (TRX and FRX-B) show very strong  $r_s/\rho_{i0}^{1/2}$  dependence,

$$\tau_{\phi} (\mu\text{s}) = 0.012 \left[ \frac{r_s}{\rho_{i0}^{1/2}} \right]^{3.5}$$

where the dimensions are given in centimetres. On the basis of a constant plasma resistivity  $\eta$  and a calculated flux lifetime of the form  $\tau_{\phi\text{RR}} = (\mu_0/\eta)a^2$  ( $a$  is a characteristic length equal to  $r_s/4$ ) [5], the effective flux diffusion coefficient can be written as

$$\left[ \frac{\eta}{\mu_0} \right]_{\perp} (\text{m}^2 \cdot \text{s}^{-1}) \approx 43 \left[ \frac{\rho_{i0}}{a} \right]^{1.5}$$

For typical values of  $a/\rho_{i0} = 5$ , the flux diffusion coefficient has a value of about  $4 \text{ m}^2 \cdot \text{s}^{-1}$ .

The flux lifetime measurements from the larger FRX-C machine show some deviation from the TRX scaling. The 5 mtorr data point is above the TRX scaling curve; this may be indicative of a flattening of the magnetic field profile near the field null, which is expected to occur when the flux lifetime exceeds the particle lifetime. A low electron temperature could contribute to the 20 mtorr data point being below the TRX scaling.

The energy lifetime  $\tau_{E_p}$  is seen to scale approximately as  $(r_s/\rho_{io}^{1/2})^{2.7}$ . The energy lifetime is determined by several loss processes, including particle losses, ion and electron thermal losses, and radiation. The TRX energy lifetime scaling shown in Fig. 2 is weaker than the corresponding particle lifetime scaling shown in Fig. 3. This may be indicative of radiative losses becoming relatively more important as the FRC size increases and the relative thermal and particle loss rates are lowered.

The TRX particle lifetime data show the same scaling tendency as the flux lifetime, although there is considerably more scatter. However, the scaling from the  $r_c = 12.5$  cm FRX-B machine to the  $r_c = 25$  cm FRX-C machine indicates an additional dependence on  $r_c$ . This is indicative of the fact that  $x_s \equiv r_s/r_c$  is, independent of  $r_s$  alone, an important parameter for particle loss. Particle loss rates are strongly influenced by the density gradients near the separatrix, and hence by the density gradients on  $x_s$ . The  $r_s$  portion of the TRX scaling shown in Fig. 3 could be written equally well as  $x_s^{1.6} r_s^2$ , which would better fit the FRX-B and FRX-C measurements where  $x_s$  was approximately 0.4. On TRX,  $x_s$  was varied from 0.3 to about 0.6.

#### 4. LOW FREQUENCY DRIFT WAVE THEORY

The experimental measurements indicate a resistivity dependence on the effective drift parameter ( $v_E/v_i \propto \rho_{io}/a$ ), but the detailed form of this dependence is inconsistent with localized LHD predictions. Thus, low frequency electromagnetic drift waves and trapped particle waves have been investigated theoretically with the aim of finding a possible explanation for the observed FRC transport behaviour.

TABLE II. COMPARISON OF PARAMETERS FOR FRCs AND TOKAMAKS

	FRX-C (5 mtorr)	FRX-C (20 mtorr)	TRX-1	TFTR/JET
$a_p$	10 cm	10 cm	6.2 cm	82 cm
$\rho_i$	0.45 cm	0.22 cm	0.33 cm	0.1 cm
$\beta$ ( $r = 0$ )	$\infty$	$\infty$	$\infty$	$0.2 \times 10^{-2}$
$\beta$ ( $r = a_p$ )	0.54	0.66	0.66	$0.17 \times 10^{-2}$
$\nu_{ee}/\omega^*$	$3/ka_i$	$100/ka_i$	$15/ka_i$	$0.07/ka_i$

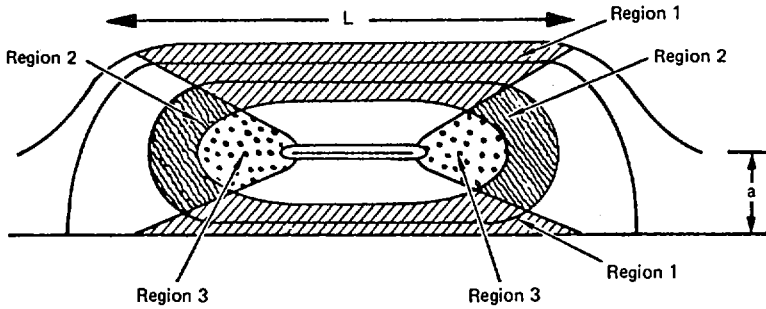


FIG. 4. Stability regions of field reversed configurations.

Low frequency stability has been explored for a variety of systems, and basic equations have been derived for a wide range of parameters and geometry [12, 13]. These equations have been adapted in order to derive a dispersion relation for low frequency waves in a slab plasma with parameters relevant to current FRCs. There are substantial differences between this case and previous applications, including the wide variation of internal beta in the FRC (from  $< 1$  at the separatrix to infinite at the magnetic null) as well as the similarity of the characteristic distances along and across the magnetic field, which can make  $\omega/k_{\parallel}$  comparable to or smaller than the ion thermal velocity. Besides the geometry, key parameters such as  $\beta$ ,  $a_p/\rho_i$  (plasma size divided by local ion gyroradius) and collisionality determine the parameter range of theoretical studies. The parameters of the FRC are compared with those of more widely studied tokamak experiments in Table II, where  $a_p$  is the plasma radius ( $r_s$  for FRCs),  $\nu_{ee}$  is the electron-electron collision frequency (detrapping frequency), and  $\omega^*$  is the diamagnetic drift frequency.

Solution of the dispersion relation shows that three separate regions of instability exist, which are indicated in Fig. 4. A plasma with straight magnetic field lines and a length (parallel to  $B_0$ ) much greater than  $l_n = (dn/ndx)^{-1}$  is similar to the straight region near the FRC separatrix (region 1 in Fig. 4) and can be unstable to a high beta, electromagnetic version of the familiar drift dissipative instabilities, with  $\omega_r \approx -\omega^*$ ,  $\omega_i \approx \nu/\beta$ , and  $\delta B \gg \delta E$ , depending on the length of the region. A plasma with magnetic mirrors and a length (along  $B_0$ ) not much greater than  $l_n$  is similar to the curved end of the FRC (region 2) and can be unstable to an electrostatic trapped particle instability,  $\omega_r \approx \omega_i \approx \omega^*(\nu/\omega^*)^{1/2}$ . The interior high beta ( $> 1$ ) end region (region 3) can be unstable to an electromagnetic trapped particle mode with  $\omega_r \approx \omega_i \approx 0.2\omega^*/k^2\rho_i^2$  and  $\delta B \gg \delta E$ . This mode is distinct from any mode studied in previous applications. Because of the electromagnetic nature of the internal trapped particle mode, differential ion-electron energy loss is possible. Although the slab model lacks some specific features of FRC geometry, these results give strong indications of high beta trapped particle instabilities in FRCs.

Estimates have been made of the transport due to these instabilities. Two of them have  $\delta B \gg \delta E$  and are dominated by stochastic effects, which can be described using the usual theories for magnetic field line diffusion [14]. The mean free path is assumed to be longer than  $L \equiv k_{\perp}^{-1}$  and the saturated field is small, such that  $b = \delta B/B$  is less than  $L$  divided by the perpendicular correlation distance. For quasi-linear flow  $\langle nv_r \rangle \approx \delta \langle nv_r \rangle \delta B/B$ , the anomalous resistivity is  $\eta \approx \langle v_r \rangle B/cJ$ , and with the usual saturation fluctuation levels the magnitude and scaling of  $\tau_{\phi}$ ,  $\tau_{E_p}$ , and  $\tau_N$  can be estimated. A fairly crude point model analysis, based only on low frequency drift waves, gives the scaling as  $\tau_{E_p} \approx a^3 b^2 / T^{3/2}$ ,  $\tau_{\phi} \approx \tau_N \approx a^2 B/T$ , where a weak dependence on  $L$  is suppressed.

The above scaling is normalized to the conditions for TRX-2 (12 mtorr, 10 kG,  $r_s = 4.7$  cm) and the scaling results are compared in Table I with the experimental measurements for flux and energy lifetimes. The proper transport in regions 1, 2 and 3 is also included in a pseudo 2-D transport model, and the calculated flux lifetimes are indicated in Table I for several conditions.

## 5. SUMMARY AND CONCLUSIONS

The theoretical predictions for low frequency drift waves agree well with all measurements, except for the 5 mtorr flux lifetime and the 20 mtorr energy lifetime of FRX-C. However, as mentioned previously, the 20 mtorr FRX-C plasma is relatively cold, and classical loss processes plus radiation may be dominant. The 5 mtorr flux loss is anomalously high, even compared with the TRX empirical scaling, and warrants further experimental and theoretical attention.

The scaling results obtained empirically and those based on the LHD model and the low frequency drift wave model are summarized in Table III. Because of the high beta nature of the FRC the  $\rho_{i0} \propto T_i^{1/2}/B_e$  portion of the scaling has been written as  $n^{-1/2}$ . The parameter  $s$ , given in the LHD particle scaling, is defined in Ref. [7] as approximately the number of ion gyroradii between  $R$  and  $r_s$ . Because of small  $s$  and influences of the open field line loss rate on the FRC pressure profile, it is difficult

TABLE III. SUMMARY OF EMPIRICAL AND THEORETICAL SCALING

	Experiment	LHD (classical) model	Low frequency drift wave model
$\tau_{\phi}$	$n^{0.9} r_s^{3.5}$	$T_e^{3/2} r_s^2$	$n^{0.5} T^{-0.5} r_s^2$
$\tau_E$	$n^{0.7} r_s^{2.7}$	—	$n^1 T^{-0.5} r_s^3$
$\tau_N$	$n^{0.9} x_s^{1.6} r_s^2$	$T^{-1/2} [1 + s/3]^3$	$n^{0.5} T^{-0.5} r_s^2$

to evaluate the appropriateness of new resistivity models. The low frequency drift wave model, however, is the first explicit theoretical model which reproduces both the flux and the energy/particle lifetimes in FRCs. This strongly suggests that low frequency drift and trapped particle instabilities are an important component of FRC transport physics. A new FRC experiment with large  $s$  (LSX) is being constructed, which should provide additional transport information over a much wider and more reactor relevant range.

## REFERENCES

- [1] HAMASAKI, S., KRALL, N.A., in Plasma Science (Proc. IEEE Int. Conf. Montreal, 1979), IEEE, New York (1979) 143.
- [2] TUSZEWSKI, M., LINFORD, R.K., Phys. Fluids **25** (1982) 765.
- [3] ARMSTRONG, W.T., et al., Phys. Fluids **24** (1981) 2068.
- [4] SIEMON, R.E., et al., Fusion Technol. **9** (1986) 13.
- [5] HOFFMAN, A.L., et al., Appl. Phys. Lett. **42** (1982) 31.
- [6] STEINHAUER, L.C., et al., Phys. Fluids **28** (1984) 888.
- [7] SLOUGH, J.T., et al., Nucl. Fusion **24** (1984) 1537.
- [8] HOFFMAN, A.L., et al., Fusion Technol. **9** (1986) 48.
- [9] ARMSTRONG, W.T., et al., Phys. Fluids **25** (1982) 2121.
- [10] BELKOV, V.V., et al., "Suppression of losses in a compact torus with programmed shaping of the magnetic structure", Plasma Physics and Controlled Nuclear Fusion Research 1982 (Proc. 9th Int. Conf. Baltimore, 1982), Vol. 2, IAEA, Vienna (1983) 343.
- [11] HOFFMAN, A.L., SLOUGH, J.T., to be published.
- [12] KRALL, N.A., Advances in Plasma Physics, Vol. 1 (SIMON, A., THOMPSON, W.B., Eds), Interscience, New York (1968) 153.
- [13] MANHEIMER, W.M., An Introduction to Trapped Particle Instability in Tokamaks, Rep. TID-27157, National Technical Information Service, Springfield, VA (1977).
- [14] LIEWER, P.C., Nucl. Fusion **25** (1985) 543.



## SLOW FORMATION AND STABILIZATION OF FRC PLASMAS

S. OKADA, Y. ITO, M. KAKO, R.E. CHRIEN<sup>1</sup>, S. OHI,  
S. GOTO, T. ISHIMURA, H. ITÔ  
Plasma Physics Laboratory,  
Osaka University,  
Osaka

T. TAKAHASHI, M. OHARA, S. SHIMAMURA,  
M. MACHIDA<sup>2</sup>, Y. NOGI  
College of Science and Technology,  
Nihon University, Tokyo

Japan

### Abstract

#### SLOW FORMATION AND STABILIZATION OF FRC PLASMAS.

In preliminary experiments of slow FRC plasma formation, the effects of an auxiliary axial current on the formation and containment of FRC plasma in the NUCTE device at Nihon University were studied. By applying the axial current before the main compression, the bias field is amplified so as to satisfy the forcefree equilibrium condition. For larger values of the axial current ( $> 4$  kA), the lifetime of the plasma becomes short. When the axial current is applied to the FRC plasma after the main compression, the upper limit of the current not destroying the FRC was found to be given by the condition that the safety factor  $q$  on the separatrix is larger than unity. The onset time of the  $n = 2$  rotational instability was delayed by the application of the axial current. This suggests that the axial current is effective in improving the plasma lifetime.

FRC plasma stabilization experiments were done on the OCT device at Osaka University. The modification of the multipole field from a straight to a helical configuration resulted in a drastic decrease of the threshold strength for suppressing the  $n = 2$  rotational instability. This agrees qualitatively with previous experiments on the NUCTE device but the dependence of the threshold on the pitch angle of the helical field seems to be different from the previous value. The rotational angular velocity of the FRC plasma was determined from the Doppler shift of the  $H_{\beta}$  line emitted from charge exchange neutrals produced by the injection of an intense, pulsed neutral beam. The measured angular velocity of  $4 \times 10^5$  rad·s<sup>-1</sup> is lower than the real frequency of  $7 \times 10^5$  rad·s<sup>-1</sup> of the  $n = 2$  mode deduced from the interferometry signal. If the ideal MHD

<sup>1</sup> On leave from Los Alamos National Laboratory, USA.

<sup>2</sup> On leave from Universidade Estadual de Campinas, Brazil.

approximation were valid, the two values should agree with one another. Therefore, the above discrepancy implies that ion kinetic effects are important for the  $n = 2$  rotational instability.

## 1. INTRODUCTION

To construct a large scale machine producing FRC plasmas with a long lifetime, many improvements are necessary in the plasma formation technique. Slow formation with axial current is considered to be one of the possible improvements. In the NUCTE experiments at Nihon University, effects of the axial current on the formation and containment of FRC plasma were investigated.

Suppression of the  $n = 2$  rotational instability excited in FRC plasmas has already been achieved by applying multipole fields; there remain, however, unsolved problems on the details of the suppression mechanisms. In the OCT experiments at Osaka University, these problems were investigated.

## 2. EFFECTS OF AXIAL CURRENT ON THE FORMATION AND CONTAINMENT OF FRC PLASMA

The application of an axial current is proposed for a successful formation of the FRC. In the formation phase, three effects are expected: heating of the embedded plasma in the bias field, amplification of the initial bias flux, and control of the plasma expansion to the wall by the azimuthal field. In the confinement phase, the current heats the cold plasma near the separatrix so that an improvement of the plasma confinement properties is expected.

The FRC plasma is generated by using the theta pinch device NUCTE II, which has a 1.7 m long, 16 cm bore coil. Deuterium gas is filled into a 14 cm bore discharge tube at 12 mtorr. When the negative bias field reaches  $-630$  G, the compression field is applied to the plasma preheated by the axial current  $I_{z1}$  as is shown in Fig. 1. The rise-time, maximum strength and e-folding time of the compression field are  $2 \mu\text{s}$ , 12 kG and  $65 \mu\text{s}$ , respectively. Another current  $I_{z2}$  is applied to the plasma in order to investigate its effects on the FRC plasma. The parameters of the produced plasma without application of the  $I_{z2}$  are described elsewhere [1].

### 2.1. Amplification of the negative bias flux

When the axial current  $I_{z2}$  is applied before the main compression, it flows through the well ionized plasma immersed in the bias field and induces paramagnetic effects so as to increase the axial bias field. The axial field is measured

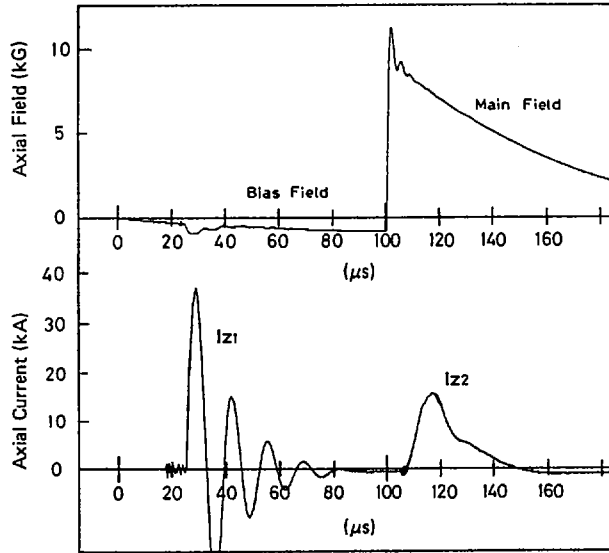


FIG. 1. Time sequence of discharge.

by a magnetic probe located at the centre of the discharge tube. As is seen in Fig. 2, the bias field just before the main compression increases with the axial current. The solid line in the figure shows the bias field as a function of  $I_{z2}$  which is calculated on the assumption of the forcefree current profile having boundary conditions  $B_z = -630$  G and  $B_\theta = \mu_0 I_z / 2\pi r_w$  at the tube wall  $r_w$ . The experimental results agree well with the theoretical prediction. This means that the bias flux is amplified by the axial current.

## 2.2. Disturbance in the FRC formation

It is an interesting problem whether the axial current disturbs the FRC or not. A similar problem of spheromak formation was already examined in MS-1 experiments at the University of Maryland [2]. The FRC is formed in our experiment; the lifetime is, however, strongly affected by the magnitude of the current. The lifetime which is obtained from the e-folding time of  $\pi r_s^2$  ( $r_s$  is the separatrix radius of the FRC) becomes short for a current above 4 kA. On the other hand, when the current is higher than 10 kA, the number of trapped particles in the plasma is found to decrease. Here, we have used the method of estimation of line mass density by analysing the radial oscillation of the plasma [3].

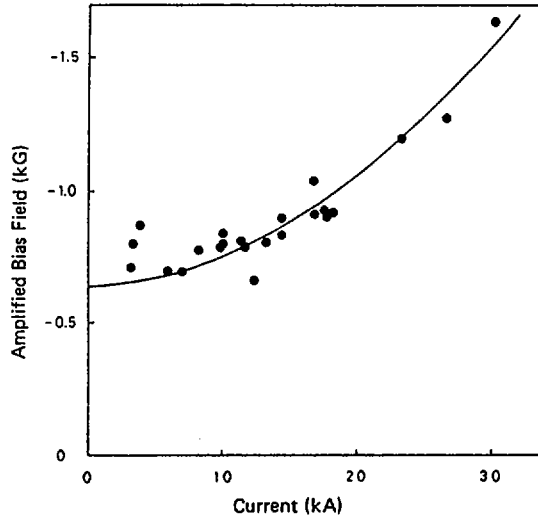


FIG. 2. Bias field strength versus axial current.

### 2.3. Effect of current flowing on the separatrix surface

In this experiment, the axial current is applied to the FRC after the formation to avoid a disturbance in the formation phase. We find that there is a limit for the current not to destroy the FRC. This limit is given by the following condition:

$$q = \frac{2\pi r_s B_e}{\mu_0 \ell_p I_z / 2\pi r_s} > 1 \quad (1)$$

where  $\ell_p$  and  $B_e$  are the separatrix length and the axial field strength at the outside of the separatrix, respectively. The destruction of FRC can be seen from the end of the trajectory in the  $B_e$ - $I_z$  diagram of Fig. 3, where  $\ell_p$  is assumed to be equal to half the coil length. The ratio of Joule energy generated by the current to the loss of internal plasma energy can be obtained from the equation

$$\beta = \frac{I_z^2 R}{W/\tau_e} = \frac{I_z^2 \ell_p \eta_s / 2\pi r_s \delta}{(3/2)\pi r_s^2 \ell_p \langle p \rangle / \tau_e} \quad (2)$$

where  $\tau_e$ ,  $\eta_s$ ,  $\delta$  and  $\langle p \rangle$  are the energy confinement time of the plasma, the resistivity of the plasma near  $r_s$ , the depth of the current path on the separatrix, and the average pressure of the plasma, respectively. The ratio calculated by

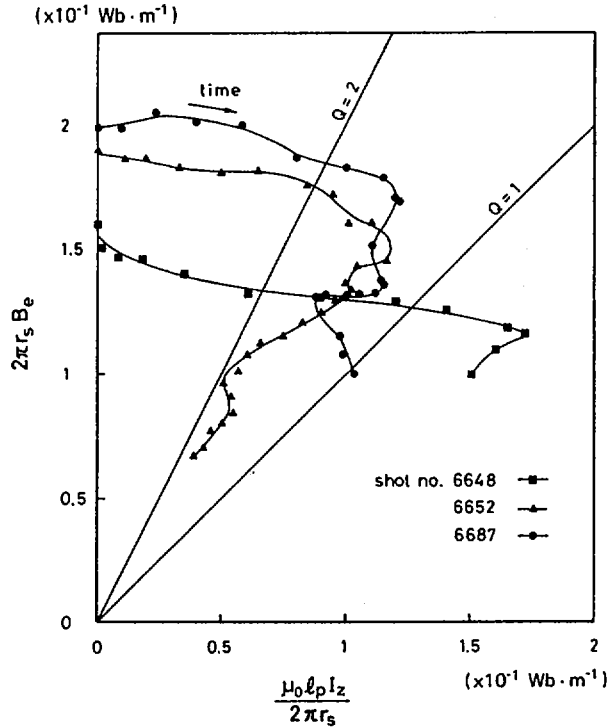


FIG. 3.  $B_e - I_z$  diagram. Termination of trajectory means that the cross-section  $S$  of the initial plasma column decreases to  $S/e$ . Times:  $21 \mu\text{s}$  (shot No. 6648),  $24 \mu\text{s}$  (shot No. 6687), and  $31 \mu\text{s}$  (shot No. 6652).

using the plasma parameters at  $25 \mu\text{s}$  after the formation of the FRC is 0.1–0.2, in optimum current conditions. The onset time of the  $n = 2$  instability, which is determined by inspecting the photodiode signals, is delayed by the application of the current. We consider this to be one indication for the improvement of confinement because there is a prospect for a rotational instability which occurs when some portion of the confined particles is lost [4, 5].

### 3. ROTATIONAL INSTABILITY AND MULTIPOLE FIELD SUPPRESSION

Recent experimental studies on FRC plasmas in many laboratories have established that the  $n = 2$  rotational instability ( $n$  is the toroidal mode number) can be completely suppressed by applying a multipole magnetic field to the

plasma [6]. On the basis of ideal MHD theory, the threshold field strength  $B_{s,c}$  necessary to suppress the instability was obtained as

$$B_{s,c} = \frac{1}{2\sqrt{m-1}} |\Omega| r_s \sqrt{\mu_0 \rho} \quad (3)$$

where  $2m$  is the order of the multipole field,  $\mu_0$  the permeability of the vacuum, and  $\Omega$ ,  $r_s$  and  $\rho$  the rotational angular velocity, the radius, and the mass density of the plasma column, respectively [7]. In many cases, the reported experimental thresholds have amounted to 25–50% of the theoretical predictions. Furthermore, it has been reported that a helical multipole suppresses the instability more effectively than a straight multipole [1]. However, experiments carried out by another group have yielded results there are contradictory to those noted above [8]. Later, the helical multipole field stabilization experiments were repeated to verify that helical stabilization was more effective. Next, we addressed one of the most important issues when we compared theoretical and experimental stabilization thresholds. The experimental measurements of the rotational angular velocity  $\Omega$  were regarded as ambiguous because the velocities were not measured directly but estimated from the observed real frequency of the instability or from the Doppler shift of an impurity line (usually, the C V line). Since the rotational angular velocity  $\Omega$  is the most important physical quantity affecting the rotational instability, direct measurements of  $\Omega$  are of vital importance. In our experiment, we measured the ion velocity distribution to determine the rotational angular velocity  $\Omega$ , together with the ion temperature  $T_i$ , by using the beam probe spectroscopic technique which we had developed previously [9].

### 3.1. Suppression of $n = 2$ instability by a helical quadrupole field

In this experiment, the hydrogen FRC plasma is translated into a stainless steel vessel with an inner diameter of 30 cm and is confined for  $\sim 100 \mu\text{s}$  between mirror fields separated by a distance of  $\sim 130$  cm. The plasma parameters in the confinement region are typically as follows: ion temperature  $T_i \leq 80$  eV, plasma density  $n \cong 4 \times 10^{14} \text{ cm}^{-3}$ ,  $r_s \approx 8$  cm, and plasma length  $l_p \approx 90$  cm. The axial magnetic field outside the separatrix radius is about 1.5 kG at  $r_s \approx 7.5$  cm. The straight or helical winding coil was set just outside the vessel between the mirror coils. The distortion  $\Delta r$  of the plasma column caused by the instability was determined from the cyclic deviation of the interferometry signal, which measured the integrated density,  $\int n d\ell$ , along the diameter at the midplane. From many interferograms, each of which shows the time history of  $\int n d\ell$  for one shot, we obtained a plot of the relative distortion  $\Delta r/r_s$  versus the multipole field strength. The results are shown in Fig. 4 for straight ( $\alpha = 0$ ) and

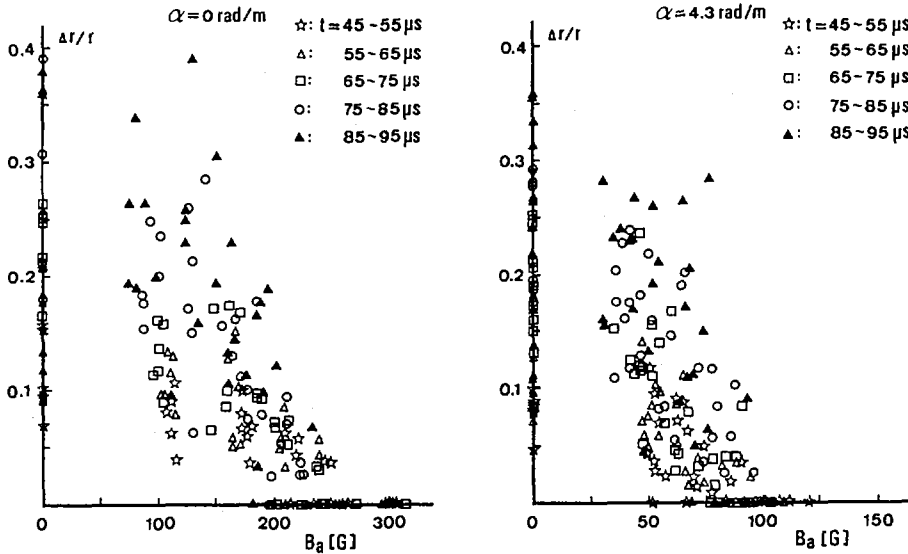


FIG. 4. Relative distortion  $\Delta r/r$  of plasma column plotted against quadrupole field strength  $B_a$  on plasma surface for straight ( $\alpha = 0$ ) and helical ( $\alpha = 4.3 \text{ rad}\cdot\text{m}^{-1}$ ) cases.

helical ( $\alpha = 4.3 \text{ rad/m}$ ) quadrupole fields, where  $B_a$  is the maximum multipole field strength on the plasma surface, which is equal to twice the field strength  $B_s$ , in the absence of plasma. In the straight multipole field case, the experimental stability threshold  $B_{a,\text{th}}$  is 250 G, while the theoretical threshold  $2B_{s,c}$  is estimated to be 275 G, by using the value of  $\Omega$  measured by beam probe spectroscopy. The threshold in the helical multipole field case is 100 G. This result agrees with the previous observation on the NUCTE device that the threshold of the helical field is smaller than that of the straight field. However, in the previous experiment, the straight multipole field was only able to partly suppress the instability so that a modification from straight to helical multipoles was definitely important. This suggests that the effect of the helical multipole field depends not only on the pitch  $\alpha$  but on the other plasma parameters, as well.

### 3.2. Rotational angular velocity of the FRC plasma

To generate charge exchange neutrals, intense pulsed hydrogen beams produced by a Z-pinch type beam source were injected into the plasma along the diameter of the midplane. The parameters of the probing beam at the observation point ( $r = 7 \text{ cm}$ ) are: energy  $E_b \approx 400 \text{ eV}$ , density  $n_b \approx 3 \times 10^{12} \text{ cm}^{-3}$ , and pulse width  $\Delta t_b \leq 2 \mu\text{s}$ . The rotational angular velocity  $\Omega$  and ion tempera-

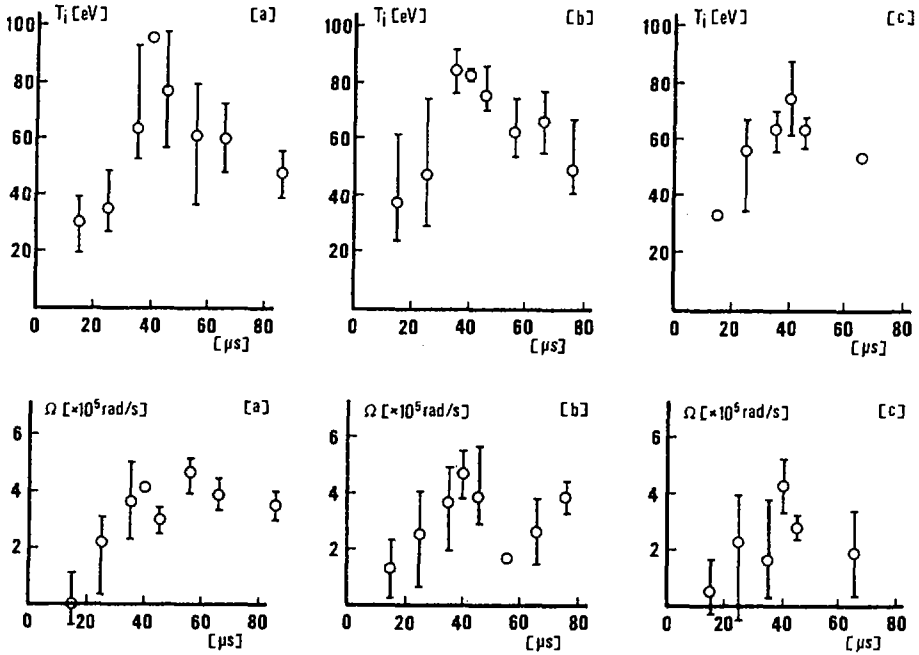


FIG. 5. Time evolution of ion temperature  $T_i$  and rotational angular velocity  $\Omega$  for quadrupole field strength  $B_a = 0$  (a),  $B_a \approx 83$  G (b), and  $B_a \approx 134$  G (c) at  $r_s = 7.5$  cm.

ture  $T_i$  were estimated from the respective Doppler shift and the broadening of the  $H\beta$  line emitted by the charge exchange neutrals. In Fig. 5, the time development of  $T_i$  and  $\Omega$  is shown for the cases of  $B_a = 0$  (a),  $B_a \approx 83$  G at  $r_s = 7.5$  cm (b), and  $B_a \approx 134$  G at  $r_s = 7.5$  cm (c), where  $B_a$  is the strength of the helical quadrupole field of  $\alpha = 4.3$  rad  $\cdot$  m $^{-1}$  used to suppress the instability. The temperature increase from 30 eV to 80 eV up to 40  $\mu$ s probably results from the relaxation of the kinetic to thermal energy of the plasma translated by reflection from the mirrors because the macroscopic motion of the plasma ceases around 40  $\mu$ s. The observed value  $\Omega$  at  $t \geq 40$   $\mu$ s. is  $\sim 4 \times 10^5$  rad  $\cdot$  s $^{-1}$  (a) and  $\sim (2-4) \times 10^5$  rad  $\cdot$  s $^{-1}$  (b and c), where the direction of the rotation agrees with the ion diamagnetic drift. The angular frequency  $\omega_{Te}$  of the instability is estimated to be  $\sim 7 \times 10^5$  rad  $\cdot$  s $^{-1}$  from the time history of  $f n d\ell$ . If the ideal MHD approximation were valid,  $\Omega$  and  $\omega_{Te}$  should agree with each other. Therefore, the apparent discrepancy between the two values indicates the importance of the ion kinetic effects on the  $n = 2$  mode. The ratio  $\Omega_{Te}/\omega$  obtained here agrees well with computer simulation results by Harned using a hybrid code, which includes both resonant ion and finite ion Larmor radius effects [10]. The ion diamagnetic angular frequency  $\Omega^*$  ( $= |(T_i/eBr)(1/n)(dn/dr)|$ ) was estimated to be  $\sim 4 \times 10^5$  rad  $\cdot$  s $^{-1}$ , on the

assumption of a rigid rotor equilibrium. Thus, the ratio  $\Omega/\Omega^*$  is about unity at the onset time of the instability ( $t \approx 40 \mu\text{s}$ ). When a quadrupole field is applied to the plasma (b and c), the ions continue rotating, although  $\Omega$  is slightly reduced to  $\sim(2-4) \times 10^5 \text{ rad} \cdot \text{s}^{-1}$ .

#### 4. CONCLUSIONS

The effects of an axial current on formation and confinement of FRC plasmas were investigated. Preliminary results showed an amplification of the bias flux and a delay of the onset time of the rotational instability. These effects are desirable for the formation of the FRC, using a slowly rising compression field. However, the lifetime becomes short when the axial current is too high. Further investigation is necessary to utilize the flux amplification effect in the formation phase in order to increase the trapped flux.

The helical multipole field was shown to be more effective in suppressing the  $n = 2$  rotational instability than the straight field. This agrees with previous results; the dependence of the threshold field strength on the pitch angle  $\alpha$  seems, however, to be different from the previous one. The rotational angular velocity, which was estimated from the Doppler shift of the  $H\beta$  line emission from the charge exchange neutrals, was smaller than the frequency of the  $n = 2$  mode. This suggests the importance of the ion kinetic effects on the  $n = 2$  mode.

#### REFERENCES

- [1] SHIMAMURA, S., NOGI, Y., *Fusion Technol.* **9** (1986) 69.
- [2] GOLDENBAUM, G., IRBY, J., CHONG, Y., HART, G., *Phys. Rev. Lett.* **44** (1980) 393.
- [3] NIBLETT, G., GREEN, T., *Proc. Phys. Soc.* **74** (1959) 737.
- [4] BARNES, D., SEYLER, C., in *Compact Toruses and Energetic Particle Injection* (Proc. US-Japan Joint Symp. Princeton, 1979), Plasma Physics Lab., Princeton Univ., NJ (1979) 110.
- [5] HARNED, D., HEWETT, D., *Nucl. Fusion* **24** (1984) 201.
- [6] OHI, S., et al., *Phys. Rev. Lett.* **51** (1983) 1042.
- [7] ISHIMURA, T., *Phys. Fluids* **27** (1984) 2139.
- [8] REJ, D.J., et al., *Phys. Fluids* **29** (1986) 2648.
- [9] ITO, Y., et al., *J. Appl. Phys.* **58** (1985) 1752.
- [10] HARNED, D.S., *Phys. Fluids* **26** (1983) 1320.



## **DISCUSSION**

ON PAPERS IAEA-CN-47/D-IV-2-1 AND D-IV-2-2

M.G. HAINES: Can you tell us more about the physics of the suppression of rotation in the FRC?

T. ISHIMURA: By using multipole fields we can suppress the deformation of the plasma column due to rotation. The multipole field exerts magnetic pressure on the surface of the plasma column and, if the column deforms, the pressure is stronger at the part of it which bulges, and further deformation is then suppressed.



## HIGH BETA PLASMA CONFINEMENT WITH NEAR-NEOCLASSICAL TRANSPORT IN TPE-2\*

K. HAYASE, I. HIROTA, H. KIYAMA, S. KIYAMA, Y. MAEJIMA,  
Y. SATO, S. TAKEDA, E. YAHAGI, M. KITO, K. KOYAMA  
Electrotechnical Laboratory,  
Sakura-mura, Niihari-gun,  
Ibaraki-ken, Japan

### Abstract

#### HIGH BETA PLASMA CONFINEMENT WITH NEAR-NEOCLASSICAL TRANSPORT IN TPE-2.

The stability and the energy confinement of a high  $\beta$  tokamak-like plasma are studied experimentally at  $\beta_t = 0.02-0.1$  and  $q_a = 1-4$  in ETL-TPE-2. Plasmas with  $\beta_t \approx 0.1$ ,  $\beta_p \approx 1$  and  $q_a \approx 1.3$  are stably confined at  $\bar{T} = 30-400$  eV and  $\bar{n}_e = 1 \times 10^{20}$  to  $10^{21}$  m<sup>-3</sup>. The volume averaged toroidal beta,  $\beta_t$ , obtained so far increases with decreasing  $q_a$ . The maximum value of  $\beta_t$  tends to exceed the Troyon limit. The global energy confinement time,  $\tau_E$ , is a few milliseconds at  $q_a \leq 1.5$  and  $\beta_p \approx 1$ . The scaling with electron density and poloidal field is found to be close to neoclassical. The evolution of the  $q_\psi$  profile shows that it may be self-organized by the relaxation process. The current density profile is nearly flat. A flat current profile is essential to good, stable confinement of a high  $\beta$  plasma with low  $q_a$ .

### 1. INTRODUCTION

High  $\beta$  confinement and stability of a screw pinch plasma are studied experimentally in ETL-TPE-2. TPE-2 is a toroidal screw pinch device with elongated cross-section ( $b/a = 21$  cm/13 cm,  $\kappa = 1.6$ ) and small aspect ratio ( $A = 3.0$ ) [1, 2]. The device is capable of producing and setting up a high  $\beta$  tokamak-like plasma by a fast pulsed discharge. The operating parameters are flexible so that we can vary the initial values of  $\beta_t$ ,  $q_a$ ,  $\bar{n}_e$ , etc., over a wide range. We can also choose the plasma current operation mode: constant, ramping or decaying. Stable confinement of a plasma with  $\beta_t \approx 0.1$  was reported in the previous conference [3]. The maximum value of  $\beta_t$  that can be stably confined in the tokamak is suggested by ballooning mode theory [4, 5]. In tokamaks, high power auxiliary heating is necessary for operation in a high  $\beta$  region. In a screw pinch with high power implosion heating, however, high  $\beta$  operation is much easier to obtain than in a tokamak.

The main objective of the present experimental study is to explore the stability and the energy transport of high  $\beta$  plasmas around the theoretical limit. The impurity

---

\* Supported by the Atomic Energy Bureau, Science and Technology Agency, Prime Minister's Office, Tokyo, Japan.

TABLE I. TPE-2 PARAMETER RANGE

Toroidal field, $B_t$ (T)	0.6–0.75 (flat-top: $\sim 0.6$ ms)
Plasma current, $I_p$ (kA)	40–175 (programmable)
Safety factor, $q_a$	1.3–4.0
D <sub>2</sub> filling pressure, $p$ (Pa, mtorr)	0.16–1.13 Pa (1.2–8.5 mtorr)
Electron density <sup>a</sup> , $\bar{n}_e$ (m <sup>-3</sup> )	$1 \times 10^{20}$ to $10^{21}$
Temperature <sup>b</sup> , $\bar{T}$ (eV)	30–400

<sup>a</sup> CO<sub>2</sub> and He–Ne laser interferometers.

<sup>b</sup>  $T_e$ : conductivity, Thomson scattering and soft X-rays.

$T_i$ : C V Doppler broadening.

reduction and the optimum setting-up of a confining configuration enabled us to operate it with  $q_a \approx 1.3$  and  $\beta_p \approx 1$  ( $\bar{\beta}_t \approx 0.1$ ), where  $q_a$  is the safety factor at the periphery of the plasma column in cylindrical approximation. We show that high  $\beta$  ( $\bar{\beta}_t \leq 0.1$ ) plasma can be stably confined at  $q_a$  ( $1.3 \leq q_a < 2$ ) with near-neoclassical transport. We also discuss the characteristic features of the  $q_\psi$  profile (the safety factor defined on each flux surface), which is formed by the self-relaxation process in the screw pinch configuration.

## 2. SETTING-UP

The initial  $\bar{\beta}_t$  and  $\beta_p$  values are controlled by preheating and the filling pressure,  $p$ . We can easily achieve that  $\beta_p > 1$  is fulfilled in this device. The fast implosion heated plasma ( $T_i \gg T_e$ ) is further heated by Ohmic current in the confinement stage. When the Ohmic input overcomes the conduction and radiation losses, the total plasma energy increases.

The operating range of parameters in the experiment is listed in Table I. We investigate the initial parameter ( $q_a$ ,  $\beta_p$  and  $\bar{n}_e$ ) dependences of the discharge. So far, a discharge with an initial  $q_a$  lower than 2 is not stable and is characterized by large fluctuations of the magnetic and radiation signals and by a high toroidal one-turn voltage,  $V_p$ . A stable low  $q_a$  discharge ( $q_a < 2$ ) can only be attained by ramping the plasma current over a long time, where  $q_a$  starts at  $\sim 2.5$  and decreases as low as 1.3. A discharge with a  $q_a$  higher than 3 is very quiescent. A highly diamagnetic ( $\beta_p > 2$ ) plasma is produced in the initial stage. However, the following Ohmic heating is not sufficient to maintain it, and  $\beta_p$  relaxes to  $\sim 1$ . The high density operation with  $p > 8$  mtorr is accompanied by strong radiation and conduction losses and high  $V_p$ , even for  $q_a > 2$ . Experiments are carried out mainly with an initial  $q_a$  of  $\sim 2.5$  and  $p < 5$  mtorr, both in constant and ramp current modes.

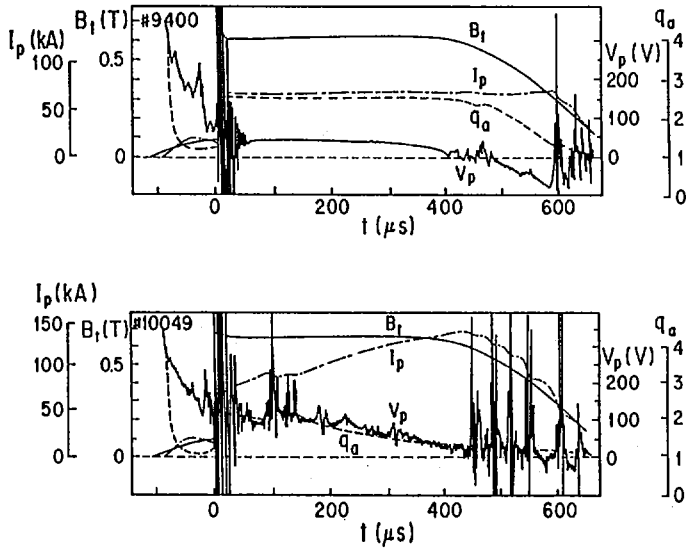


FIG. 1. Typical discharges. Upper and lower diagrams show  $B_t$ ,  $I_p$ ,  $V_p$  and  $q_a$  in the constant and ramp operations of current, respectively.

In Fig. 1, we show typical waveforms of discharges in constant and ramp current modes with an initial  $q_a$  of  $\sim 2.5$  and  $\beta_p$  less than 1, at 2.5 mtorr. The plasma current,  $I_p$ , is sustained for 600  $\mu\text{s}$  in the constant current mode. In the ramp current mode, the plasma current builds up from 60 to 140 kA within 400  $\mu\text{s}$ , and  $q_a$  reaches 1.3. When  $q_a$  passes through 2, some spikes in the  $V_p$  signal and a small dip in the  $I_p$  signal appear. The low  $q_a$  discharge ( $q_a < 2$ ) has been operated in tokamaks with unusual discharge conditions, for example in Ref. [6].  $\beta_t$  is low ( $\beta_t < 0.01$ ) with a low electron density ( $\bar{n}_e \sim 10^{19} \text{ m}^{-3}$ ).

The ion temperature,  $T_i$ , is 200 to 400 eV, from C V Doppler broadening in the initial stage. It decreases gradually by equipartition among ions and electrons. The radius of the high  $T_i$  core is one-half to one-third of the vessel radius. On the other hand, the initially low electron temperature continues increasing by energy transfer from the ions and by Ohmic heating and, finally, is nearly equal to the ion temperature. The electron temperature on axis,  $T_e$ , obtained from conductivity and Thomson scattering at 400 to 450  $\mu\text{s}$  after the start of the main discharge at  $I_p \approx 120$  kA is shown as a function of the filling pressure in Fig. 2. In deriving  $T_e$  from the plasma conductivity, we have assumed  $Z_{\text{eff}} = 1$  and classical resistivity as well as an appropriate radial distribution of the temperature. The electron density,  $\bar{n}_e$ , from the interferometer measurement is proportional to the filling gas pressure and is roughly constant during the discharge.

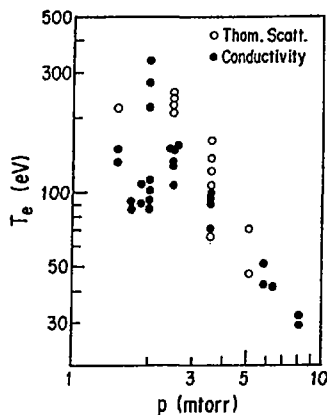


FIG. 2. Electron temperature  $T_e$  on axis from plasma conductivity and Thomson scattering as a function of filling pressure  $p$  at 400–450  $\mu$ s ( $I_p \approx 120$  kA).

### 3. BETA

The  $\bar{\beta}_t$  value is measured by magnetic analysis [7, 8]. The initial  $\bar{\beta}_t$  is determined by preheating and implosion heating. In the same conditions, the value is larger at a higher filling pressure. It does not depend on the plasma current. The maximum value of the initial  $\bar{\beta}_t$  can be varied up to 0.08. The corresponding  $\beta_p$  is given by  $\sim 6\bar{\beta}_t q_a^2$ . In Fig. 3, we show the temporal variation of  $\bar{\beta}_t$  in the constant current ( $q_a \approx 2.5$ ) and ramp current ( $q_a = 2.5-1.3$ ) modes as a function of the filling pressure. The dependence on the filling pressure is weak except for the values in the early stage. The energy of the plasma increases when the Ohmic input is larger than the loss. This is more significant when the plasma current is ramped up. In this case, the final  $\bar{\beta}_t$  reaches  $\sim 0.1$  at 500  $\mu$ s when the toroidal field begins to decay. The value of  $\beta_p$  increases to  $\sim 1$  and is kept constant even if it is initially lower than 1, regardless of the  $q_a$  value.

By changing the preheating condition, the initial  $\beta_p$  and  $\bar{\beta}_t$  are raised to higher than 2 and 0.07, respectively. The temporal behaviour of  $\bar{\beta}_t$  and  $\beta_p$  in the constant and decaying current modes is shown in Fig. 4. In both cases,  $\beta_p$  relaxes to  $\sim 1$ , as the high  $\beta_p$  state cannot be sustained by Ohmic heating alone. In the decaying current case,  $\beta_p > 1$  is kept for more than 300  $\mu$ s. The value  $\bar{\beta}_t$  decays with a time constant of  $\sim 100$   $\mu$ s in both cases and then reaches the same level as that of the low initial  $\bar{\beta}_t$  case. Hence, the energy confinement time may be  $\sim 100$   $\mu$ s in the early stage. The relatively poor energy confinement is not due to high  $\beta_p$  since it is the same in the low initial  $\beta_p$  ( $\beta_p < 1$ ) case.

The experimental values of  $\bar{\beta}_t$  are compared with the values from ballooning mode theory [4, 5]. The operating region for Figs 3 and 4 is shown in the  $\bar{\beta}_t$  and

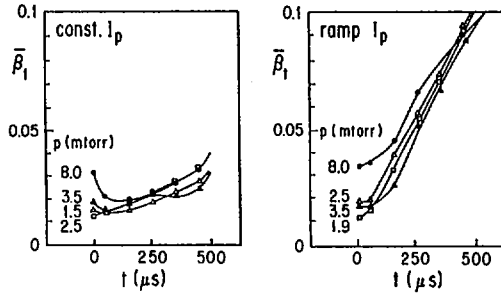


FIG. 3. Temporal variations of  $\bar{\beta}_t$  in constant (left,  $q_a \approx 2.5$ ) and ramp (right,  $q_a$  from 2.5 to 1.3) operations of current.

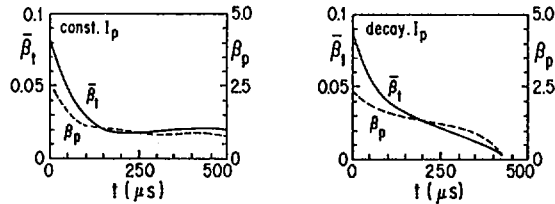


FIG. 4. Temporal variations of  $\bar{\beta}_t$  and  $\beta_p$  with high initial value of  $\beta_p$  ( $\sim 2$ ). Left hand figure shows case of constant current ( $q_a \approx 2.7$ ); right hand figure is case of decaying current ( $q_a$  from 2.3 to 3.4).

$1/q_a$  space, compared to the Troyon limit in Fig. 5. In the ramp mode,  $\bar{\beta}_t$  increases from below to above the limit. In the constant current mode,  $\bar{\beta}_t$  lies just below or around the limit. In the high initial  $\beta_p$  case, however, the initial  $\bar{\beta}_t$  is far above the limit, and then the value decreases to below or around that value.

#### 4. HIGH BETA STABILITY

To investigate the MHD stability of a high  $\beta$  discharge, we observe the fluctuations in the magnetic loops, the one turn voltage loops, visible radiation, etc. The kink mode is observed around the integer  $q_a$  values, and a certain amount of plasma energy is lost when  $q_a$  crosses  $\sim 2$  transiently in the ramp current mode.

Two 3-D plots of the poloidal field on the wall surface in the outer half of the poloidal plane are shown in Fig. 6. The distortion of the surface field is not very large, except for  $q_a$  larger than 2.5. A low level fluctuation is observed, and it is larger for smaller  $q_a$ . The small fluctuations for low  $q_a$  are not correlated well on the plasma surface, in the poloidal and toroidal directions [9]. There are less temporal

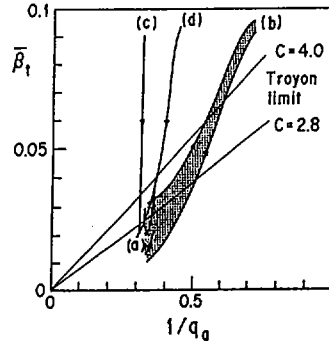


FIG. 5. Operating region of  $\beta_p$ . (a) and (b) correspond to left and right hand parts of Fig. 3, respectively. (c) and (d) correspond to left and right hand parts of Fig. 4, respectively. Troyon limit is shown by two lines,  $C = 4$  and  $C = 2.8$ .

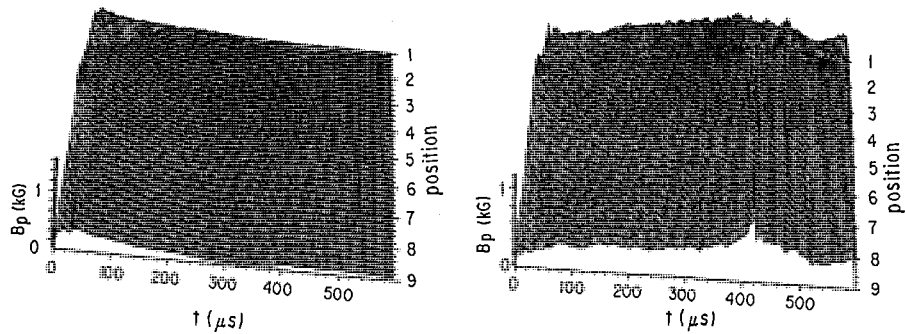


FIG. 6. 3-D plots of poloidal field in outer half-plane of poloidal surface. Left and right hand figures are cases of slowly decaying and ramp modes, respectively.  $q_a$  starts at 2.5 in both cases. Position number indicates top (1) to bottom (9). Plasma is strongly unstable ( $q_a \leq 1$ ) after 400  $\mu\text{s}$  in ramp mode.

( $\sim 10 \mu\text{s}$ ) and spatial ( $\sim \pi/4$ ) correlations in such magnetic fluctuations on the surface. As the surface mode is stabilized by the conducting shell, a kink may occur in the interior. A significant change in the internal  $q_\psi$  profile is only seen for  $q_a \approx 2$  or  $\leq 1$ , as will be shown in the next section. This behaviour does not depend on  $\beta_p$ , even if it is large ( $\beta_p \geq 1$ ). Fluctuation of the soft X-ray radiation from the interior is also observed. No fluctuation characteristic of high  $\beta_p$  is, however, detected. Then, these fluctuations are considered to originate from an internal kink or a tearing of higher toroidal mode number in the edge plasma region. No ballooning mode has been observed, as yet.

Therefore, plasma with  $\beta_p \geq 1$  is grossly stable if  $q_a$  is chosen appropriately. The level of fluctuation changes with the discharge. If it is low, the confinement is

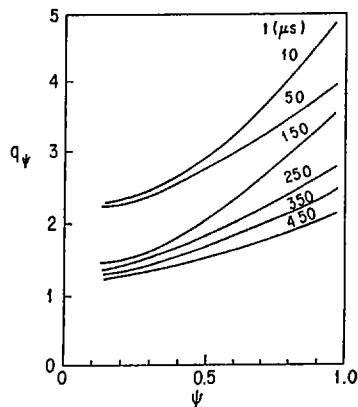


FIG. 7. Time evolution of  $q_\psi$  profile in ramp mode. It changes rapidly at 50–150  $\mu\text{s}$  by crossing  $q_a \approx 2$ . Profiles at 50  $\mu\text{s}$  and after 250  $\mu\text{s}$  are similar to one another.

better and  $\bar{\beta}_t$  increases more with time by Ohmic heating. Hence, it is important for confinement of high  $\bar{\beta}_t$  plasma to choose  $q_a$  and to control the equilibrium configuration in a precise manner.

## 5. RELAXATION OF THE $q_\psi$ PROFILE

The shape of the  $q_\psi$  profile is essential for the stability of a high  $\beta_t$  and low  $q_a$  plasma. In TPE-2, the flux profile and, hence, the  $q_\psi$  profile are calculated from the poloidal field distribution on the wall [7]. The temporal evolution of the  $q_\psi$  profile is shown for the ramp mode in Fig. 7. We see that the profiles are independent of  $q_a$  (i.e. the plasma current) in the quasi-steady state. The profile is disturbed by an MHD instability during the transition through  $q_a \approx 2$ . The profiles are similar to each other before and after the transition. For the constant current mode, the profile remains unchanged except in the early stage. We can say that the current density distribution relaxes to a self-organized state. The ratio of axial to peripheral  $q_\psi$  is around 1.8. The toroidal current density profile calculated from the  $q_\psi$  profile is nearly flat over the plasma cross-section. By assuming a parabolic plasma pressure profile, the poloidal current distribution is calculated for the case of  $\beta_p \sim 1$ . The plasma is diamagnetic near the axis.

This type of profile seems essential for the stability of a high  $\beta$  plasma. If the configuration deviates substantially from this, the transition through  $q_a \approx 2$  is not successful. In this case, the discharge is accompanied by a high one turn voltage, with a spike, and large fluctuations in the peripheral magnetic field, the visible and the X-ray radiations. Hence, setting up the configuration in the production stage, which is nearly the same as that in the equilibrium stage, is important for the good confinement of a high  $\beta$  plasma.

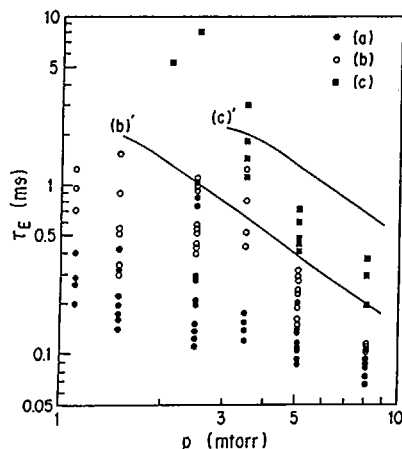


FIG. 8. Global energy confinement time  $\tau_E$  as a function of filling pressure. Values change greatly shot by shot, because of irreproducible electron density. (a) and (b) show values at 100  $\mu$ s and  $\sim 300$   $\mu$ s, respectively, in constant mode ( $I_p \approx 70$  kA). (c) shows the case at  $\sim 300$   $\mu$ s in ramp mode ( $I_p \approx 120$  kA). Lines (b)' and (c)' show results of numerical simulations for (b) and (c), respectively.

## 6. ENERGY CONFINEMENT

The global energy confinement time  $\tau_E$  is evaluated from  $\tau_E = W_p / (V_p I_p - dW_p/dt)$ . The plasma energy  $W_p$  is calculated from  $\bar{\beta}_i$ . The radiation loss has been greatly reduced to less than one-third of the total loss although the older screw pinch and belt pinch were dominated by the radiation loss [10].

The dependence of  $\tau_E$  on the filling pressure and plasma current is measured (see Fig. 8). In the early stage,  $\tau_E$  is  $\sim 100$   $\mu$ s but increases gradually to more than a few milliseconds. The enhancement of energy confinement in the later stage may be due to the self-relaxation and improvement of the equilibrium configuration as described in the previous section. Following the establishment of the configuration, the plasma energy is considered to be better confined and increased. If the ideal configuration is set up in the production stage, then, 100  $\mu$ s later,  $\tau_E$  is already high. The value  $\tau_E$  tends to be larger for higher  $\bar{\beta}_i$ .

As to scaling,  $\tau_E$  decreases with increasing filling pressure and with decreasing plasma current. As the electron density is approximately proportional to the filling pressure, the dependence is similar to neoclassical, in the collision dominated regime. To check this in greater detail, a numerical simulation is carried out, where neo-Alcator scaling is assumed for the electron transport [11]. The assumption of neoclassical ion transport can explain the experimental results. We indicate the energy confinement time from the simulations in the same figure. The experimental values are close to the neoclassical ones in the well confined discharges.

## 7. CONCLUSIONS

The experimental results are summarized as follows:

A stable discharge at  $\beta_p \approx 1$ ,  $q_a \approx 1.3$  and  $\beta_t \approx 0.1$  is established. Energy transport here is near-neoclassical. A high  $\beta_p$  ( $\sim 2$ ) discharge can be realized without noticeable instability but is not sustained by Ohmic heating alone. No ballooning mode has been clearly observed in the high  $\beta_p$  operation. Relaxation and self-organization of the  $q_\psi$  profile are observed. The current density is nearly flat over the cross-section, and the plasma is diamagnetic in the central region. This profile is essential to good, stable confinement in a high  $\beta$  tokamak configuration.

## ACKNOWLEDGEMENTS

The authors are grateful to Drs H. Ashida and H. Sugimoto for useful discussions on high  $\beta$  theory.

## REFERENCES

- [1] TAKEDA, S., et al., in Fusion Technology (Proc. 9th Symp. Garmisch-Partenkirchen, 1976), Pergamon Press, Oxford (1976) 1943.
- [2] SATO, Y., et al., in Fusion Technology (Proc. 11th Symp. London, 1980), Pergamon Press, Oxford (1980) 1563.
- [3] KIYAMA, S., et al., in Plasma Physics and Controlled Nuclear Fusion Research 1984 (Proc. 10th Int. Conf. London, 1984), Vol. 1, IAEA, Vienna (1985) 393.
- [4] SYKES, A., et al., in Controlled Fusion and Plasma Physics (Proc. 11th Europ. Conf. Aachen, 1983), Vol. 2, European Physical Society (1983) 363.
- [5] TROYON, F., et al., Plasma Phys. Contr. Fusion **26** (1984) 209.
- [6] TFR GROUP, Nucl. Fusion **24** (1984) 784.
- [7] KIYAMA, S., et al., Bull. Electrotechn. Lab. **50** (1986) 95.
- [8] HAYASE, K., et al., Bull. Electrotechn. Lab. **47** (1983) 129.
- [9] HAYASE, K., et al., Bull. Electrotechn. Lab. **50** (1986) 137.
- [10] BECKER, G., et al., Nucl. Fusion **18** (1978) 1653.
- [11] KIYAMA, H., et al., Bull. Electrotechn. Lab. **50** (1986) 122.



## Z-PINCH EXPERIMENTS AND THEORY

M.G. HAINES, A.E. DANGOR, A. FOLKERSKI,  
P. BALDOCK, C.D. CHALLIS<sup>1</sup>, P. CHOI, M. COPPINS,  
C. DEENEY, M.B. FAVRE-DOMINGUEZ<sup>2</sup>, E. FIGURA,  
J.D. SETHIAN<sup>3</sup>

The Blackett Laboratory,  
Imperial College of Science and Technology,  
London, United Kingdom

### Abstract

#### Z-PINCH EXPERIMENTS AND THEORY.

The paper presents a report of density and temperature measurements performed in three Z-pinch experiments. In the compressional pinch, a stable pinch is formed by shock compression. The density profile and line density (about  $10^{19} \text{ m}^{-1}$ ) are maintained even after current reversal. The temperature (about 130 eV) agrees with the Bennett relation, but the decay is more rapid. In the gas-embedded pinch, pressure equilibrium is obtained by preheating a laser-initiated filament in hydrogen at about 1 bar. During the preheat phase, expansion of the plasma column generates a shock in the surrounding neutral gas. The equilibrium is destroyed by a deformation of the plasma column into a radially expanding spiral. The results from two experiments ( $I \sim 1.5 \times 10^{12} \text{ A}\cdot\text{s}^{-1}$  and  $4.5 \times 10^{12} \text{ A}\cdot\text{s}^{-1}$ ) show different scalings of the duration of equilibrium with pressure. In the gas puff pinch, where an annular gas jet is ionized and imploded, short lived (about 5 ns) 'hot spots' ( $n_e = 10^{27} \text{ m}^{-3}$ ,  $T_e \sim 600 \text{ eV}$ ) of submillimetre dimensions are observed to occur at intervals of 50 ns. Simultaneously, a plasma of high temperature (about 5 keV) and low density is detected. The 'hot spots' and the surrounding plasma are observed only when a longer lived (about 50 ns) electron beam (about 10 kA and 10 kV) is present. Self-similar profiles for an ohmically heated pinch in pressure equilibrium have been calculated. Numerical solutions of the linear MHD eigenvalue equation are obtained for a variety of equilibria. A minimum energy state corresponding to a helical current flow is found to exist. Initial results for the stabilization due to a large ion Larmor radius are presented.

Three types of Z-pinch experiments, and analytical and computational investigations in the Z-pinch area have been performed at the Imperial College of Science and Technology.

### 1. COMPRESSIONAL PINCH

The experimental details of the apparatus used are described in Ref. [1]. The Marx generator and the pulse-forming line provide a current pulse of about 130 kA,

<sup>1</sup> JET Joint Undertaking, Abingdon, Oxfordshire, UK.

<sup>2</sup> Pontificia Universidad de Chile, Santiago, Chile.

<sup>3</sup> Naval Research Laboratory, Washington, D.C., USA.

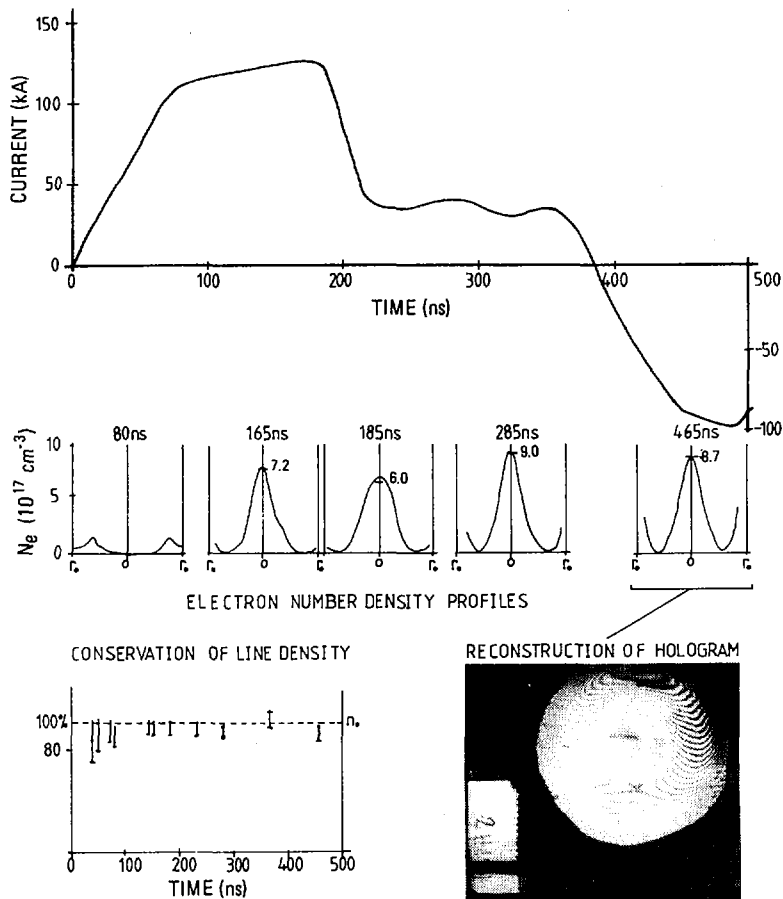


FIG. 1. Current waveform and number density profiles in the compressional pinch (1 torr hydrogen).

of some 200 ns duration and 50 ns rise time. The quartz pinch tube is 50 mm long and 20 mm in diameter. Filling pressures of 300 mtorr to 2 torr of hydrogen are used. The discharge collapses to about one-third of the tube radius, in agreement with the slug model [2], and then remains generally stable for some 500 ns.

Figure 1 shows the current waveform and the time resolved number density profiles obtained by end-on pulsed ruby laser interferometry at 1 torr pressure. The measured line density,  $N = 2 \times 10^{19} \text{ m}^{-1}$ , in the central column remains constant for more than 500 ns and agrees with the initial filling pressure. At  $t \sim 200$  ns, additional plasma is generated at the wall; at about the same time there is a considerable drop in the current measured in the external circuit. This behaviour is compatible with the assumption of an internal crowbar occurring at this instant. Conservation of

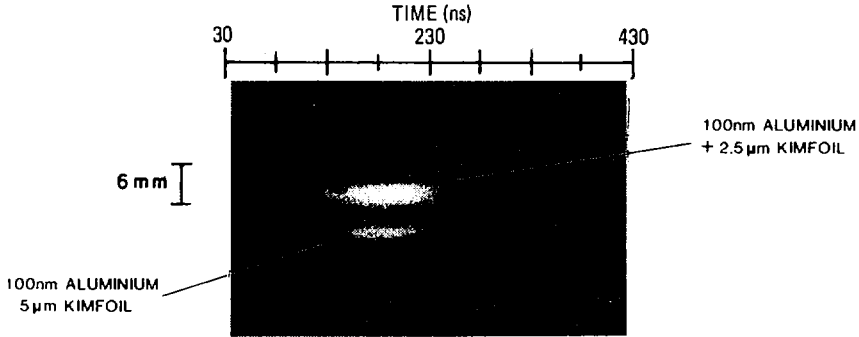


FIG. 2. Time-resolved X-ray images, end-on, from two pinholes (1 torr  $H_2$ , 132 kA).

the magnetic flux after this period can explain the continuation of equilibrium after current reversal. A similar behaviour and a constant line density are observed at 2 torr.

Figure 2 shows streak photographs of two end-on X-ray images of the discharge obtained simultaneously, using two pinhole cameras with different absorbers. The hot phase lasts about 100 ns and the measured temperature is  $250 \pm 200$  eV. Experiments with different absorbers will improve the precision of this measurement.

The Bennett relation with  $T_e = T_i$ ,  $I = 130$  kA and  $N = 2 \times 10^{19} \text{ m}^{-1}$  yields  $T_e \approx 130$  eV. The ions are magnetized with  $\omega\tau_{ii} \approx 1.8$ , and the ratio of the ion Larmor radius to the pinch radius is  $a_i/a \approx 0.13$ . At 130 eV, the MHD instability growth time ( $\tau_{\text{MHD}} \approx \text{radius/ion thermal speed}$ ) is 25 ns and the thermal ion transit time from centre to electrode along the axis is 225 ns. The axial heat loss calculated according to Haines [3] is about  $42 \text{ MJ} \cdot \text{s}^{-1}$ ; with a heat content of 62 J, this yields a decay time for temperature of about  $1 \mu\text{s}$ . If the observed duration of the stable phase,  $> 500$  ns, is interpreted as an inductive decay with  $\tau = L/R = 200$  ns, then the resistance  $R$  is  $0.06 \Omega$ . With a thickness of 2 mm, this gives for the wall plasma a temperature of more than 4 eV.

## 2. GAS-EMBEDDED PINCH

In the compressional pinch a high temperature is achieved by dynamic compression. With the gas-embedded configuration the aim is to start with a high density plasma and to heat it under conditions of pressure balance. Equating the rate of increase of internal energy to the rate of Joule heating, using the Bennett relation and the transverse Spitzer resistivity, we obtain [4]:

$$\frac{dI}{dt} = 2.7 \times 10^{-3} \frac{\sqrt{n}}{aT} \log e \Lambda \quad (\text{A} \cdot \text{s}^{-1})$$

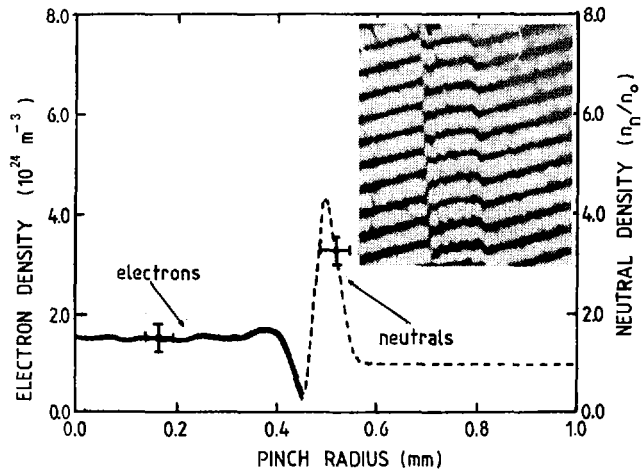


FIG. 3. Number density profiles during preheating in the gas-embedded pinch at  $p = 0.3$  bar.

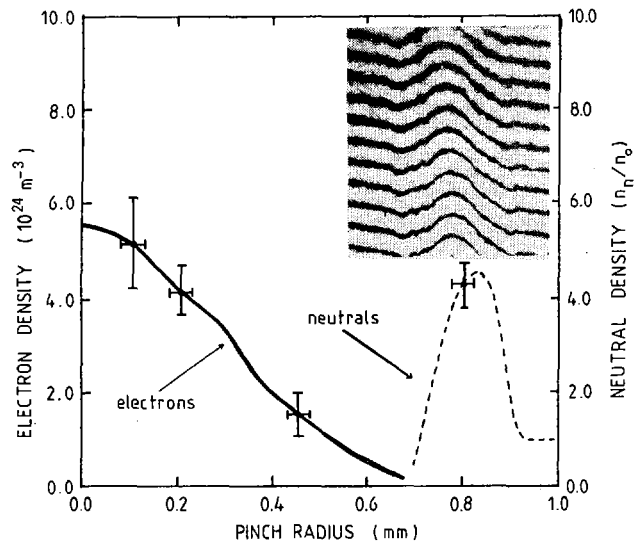


FIG. 4. Number density profiles during the equilibrium phase at  $p = 0.3$  bar.

where  $n$  is the number density in  $\text{m}^{-3}$ ,  $T$  is the temperature in eV, and  $a$  is the radius in m. With the available  $dI/dt$  of  $2 \times 10^{12} \text{ A}\cdot\text{s}^{-1}$ , the plasma channel must be preheated if pressure balance is to be achieved.

The earlier low current experiment was described previously [1, 4]. First, a narrow channel of ionization is formed by a laser beam in hydrogen at  $p = 1$  bar. A current of 6 kA is used to preheat the plasma for about 60 ns and then the main current is switched on. In the low current apparatus,  $dI/dt$  is limited to  $1.5 \times 10^{12} \text{ A}\cdot\text{s}^{-1}$  and  $I_{\text{peak}}$  is 50 kA. In the high current apparatus the corresponding figures are  $4.5 \times 10^{12} \text{ A}\cdot\text{s}^{-1}$  and 150 kA. Side-on pulsed laser Schlieren photography and interferometry are used to examine the plasma.

Three phases are distinguished. In the first phase, the preheating phase, the plasma column expands from an initial radius of  $100 \mu\text{m}$  with a radial velocity of about  $1.7 \times 10^4 \text{ m}\cdot\text{s}^{-1}$ , which drives a cylindrical shock wave in the neutral gas. Figure 3 shows density profiles obtained by Abel inversion from an interferogram taken during preheating. In the outward propagating shock, the initial step in neutral gas density is a factor of four, as expected for a strong shock. The electron number density profile is flat.

The second phase, the equilibrium phase, begins when the main current is switched on. During this time,  $r = 400 \mu\text{m}$  and the column is heated in radial equilibrium; no further expansion occurs. Figure 4 shows that the electron density becomes peaked on axis. The equilibrium phase terminates when a spiral configuration rapidly develops. The pressure dependence of the duration of the equilibrium phase is:

	$p = 0.3$ bar	$p = 1.0$ bar
Low current apparatus	40 ns	15 ns
High current apparatus	12 ns	27 ns

The behaviour in the low current case does not agree with MHD expectations. It should be mentioned that the length of the discharge is 40 mm in the low current case and 13 mm in the high current case. During the equilibrium phase the electron line density increases by a factor of two, which indicates an accretion of plasma resulting from the radial diffusion of neutrals into the plasma. In the low current apparatus at 0.33 bar the electron temperature was measured by X-ray absorber techniques [5]. A value of  $70 \pm 5$  eV was obtained, while the Bennett relation with  $T_e = T_i$  gives for 20 kA and  $N = 2 \times 10^{12} \text{ m}^{-1}$  a value of 30 eV.

The third phase has the configuration of a spiral. Optical framing photographs and Schlieren exposures indicate that the spiral grows from the axis. Interferometric measurements clearly show that the perturbation begins on the axis (Fig. 5). When the perturbation reaches the surface, the overall diameter of the plasma increases rapidly. The growth time  $r/\dot{r}$  in the low and high current cases is measured as 12 ns and 9 ns at 1 bar, and as 14 ns and 5 ns at 0.3 bar. The ratio of the pitch of the spiral

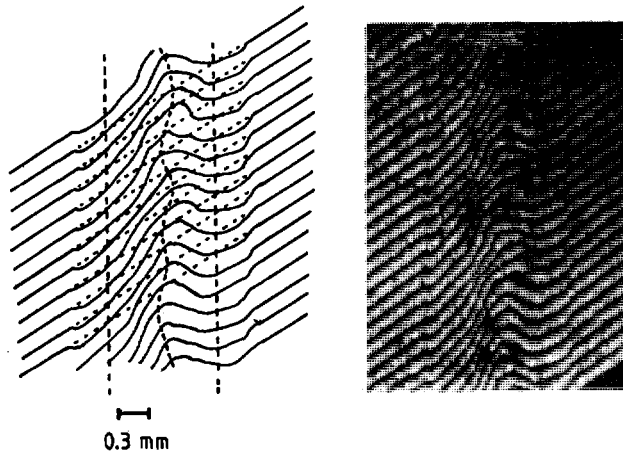


FIG. 5. Interferogram showing how the spiral begins to grow from the axis ( $p = 1$  bar).

to the radius of the pinch (in equilibrium),  $\lambda/a$ , is 4 in the low current case and 2 in the high current case. A single-turn coil positioned coaxially with the pinch and close to the ground electrode is used to measure the axial magnetic field due to the azimuthal component of the helical current. This is done on the high current apparatus only. It is found that the onset of  $B_z$  at  $p = 0.3$  bar occurs at  $I = 25$  kA, while at  $p = 1$  bar it occurs at  $I = 75$  kA. The direction of  $B_z$  is always from cathode to anode, but it has not been possible to reverse the polarity of the discharge. The helical configuration, which terminates the attempt to heat the pinch under pressure equilibrium, is itself relatively stable, and the spiral remains inside an overall cylindrical envelope.

### 3. GAS PUFF Z-PINCH

A hollow cylindrical shell of gas is formed by supersonic gas injection. When a large current (about 300 kA) is applied, the hollow shell collapses onto the axis and a hot plasma is formed. Normally, argon is used, but some experiments have been carried out with neon and other gases. The apparatus is described in Refs [1, 6].

Optical streak measurements of velocity give the kinetic energy as 250–300 J with a mass of 400  $\mu\text{g}$ .

Time-resolved streak photographs of two pinhole X-ray cameras, taken simultaneously with different absorbers, show short-lived 'hot spots' on the axis, as well as anode emission of longer duration which is ascribed to the incidence of electron beams. Figure 6 shows on a common time axis the  $dI/dt$  trace, the hard-X-ray signal from the PIN diode looking at the anode, and the soft-X-ray signal from the X-ray

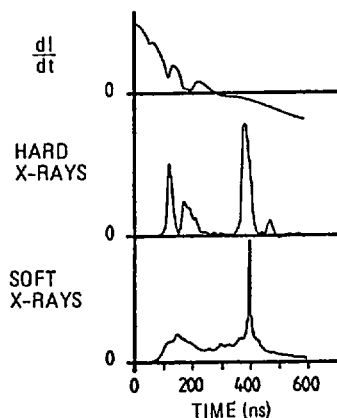


FIG. 6. Time-correlated signals, showing  $dI/dt$  ( $\dot{I}$ ), hard X-rays from the anode and soft X-rays from the plasma in the gas puff pinch.

diode looking at the body of the discharge. The 'hot spots' are about  $100 \mu\text{m}$  in diameter and  $300\text{--}500 \mu\text{m}$  long, and are observed both in time-resolved and time-integrated X-ray images. They occur randomly along the axis and last  $< 5 \text{ ns}$ ; they occur in bursts at intervals of  $30\text{--}100 \text{ ns}$ . Spectra taken with a PET crystal spectrometer ( $\lambda = 3.7\text{--}4.3 \text{ \AA}$ ) are consistent with the hot spots having  $n_e \approx 10^{27} \text{ m}^{-3}$  and  $T_e \approx 600 \text{ eV}$ . Measurements using collimated PIN diodes with appropriate absorbers show that the hot spots are surrounded by plasma of higher temperature. If the radiation is due to bremsstrahlung, then the temperature of this hot plasma is about  $5 \text{ keV}$ . The hot spots are always preceded by electron beams, but not all beams are followed by hot spots. The intensity and angular distribution of the X-rays from the anode indicate electron beams with  $I \approx 10 \text{ kA}$  and electrons of about  $10 \text{ keV}$ .

There are two classes of beams. Beams occurring early in the discharge are always associated with peaks in the  $\dot{I}$  signal. These beams may be due to large inductive fields producing runaways, and they are not followed by hot spots. Later in the discharge, beams occur when the  $\dot{I}$  signal is fairly smooth, presumably owing to an internal crowbar, and these beams are followed by hot spots.

#### 4. THEORETICAL INVESTIGATIONS

##### 4.1. Self-similar profiles

To preserve pressure balance during the heating of a Z-pinch, the current must rise according to a particular prescription, the 'Haines-Hammel curve' [7, 8]. It is found that this imposes a restriction on the possible equilibrium profiles. Figure 7 shows self-similar profiles computed under this restriction. The inclusion of radial ion thermal conduction gives rise to a small finite pressure at the edge.

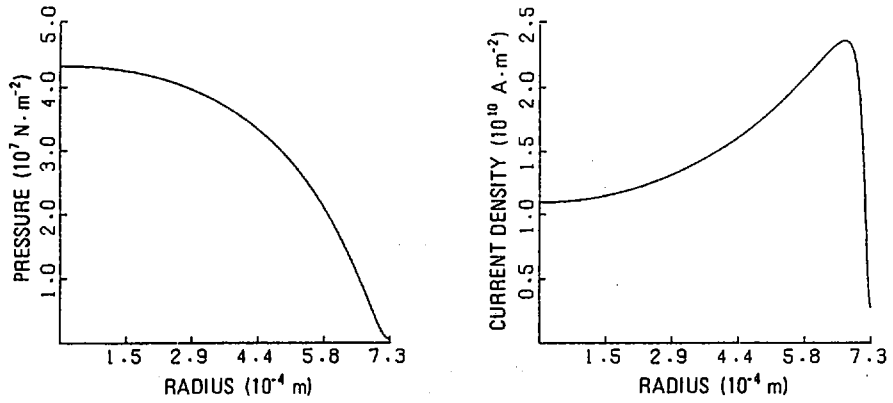


FIG. 7. Computed profiles of pressure and current density for a self-similar case with ion thermal conductions.

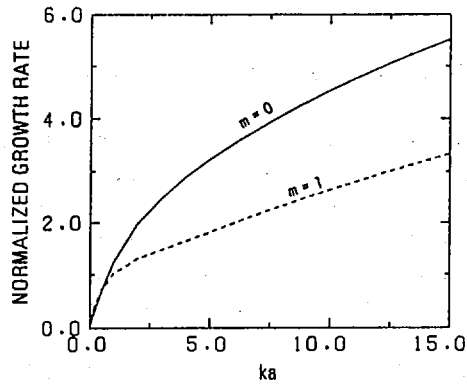


FIG. 8. MHD growth rates normalized in terms of thermal ion radial transit time ( $k$  is axial wavelength,  $a$  is pinch radius).

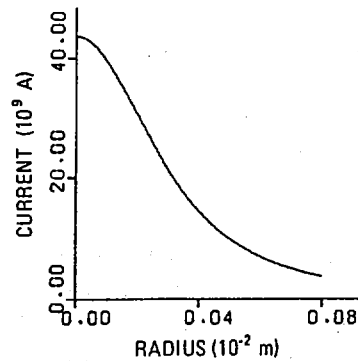


FIG. 9. Current density ( $\text{A} \cdot \text{m}^{-2}$ ) profile for an equilibrium marginally stable to the  $m=0$  mode.

#### 4.2. Ideal MHD stability

The 1-D shooting code developed by C. Davies at the Imperial College of Science and Technology has been used to obtain numerical solutions of the ideal MHD linear eigenvalue equation for a variety of equilibria satisfying pressure balance. Figure 8 shows the growth rates of the  $m = 0$  and  $m = 1$  modes when a uniform current distribution is assumed. The  $m = 0$  mode grows faster over almost the whole range of  $ka$ . Figure 9 shows an equilibrium current profile peaked on axis, which is stable to  $m \geq 2$  modes, marginally stable to the  $m = 0$  mode [9], but unstable to the  $m = 1$  mode. The  $m = 1$  eigenmode is peaked on axis and has a predicted growth time of 7.3 ns, which agrees with the experiment. It is to be noted that the experimental electron density peaks on axis before the development of the spiral, but the current density could not be measured.

#### 4.3. Minimum energy states

The gas-embedded pinches transform into helical structures with  $\lambda/a \sim 4$ . Linear MHD predicts the highest growth rates in the limit of  $\lambda \rightarrow 0$ . Minimum energy states with helical configurations have been sought. If one assumes: (i) a cylindrical bulk plasma, (ii) a helical current path on the surface, (iii) a vacuum surrounding the plasma, (iv) a perfectly conducting wall, and (v) conservation of magnetic flux and entropy, then a minimum energy state is found with  $9.9 \geq \lambda/a \geq 6.5$ , the precise value depending on the wall radius. In the more realistic case of a uniform current density and with the wavelength of the helical current paths being independent of radius, a value of  $\lambda/a \equiv 9.0$  is found. A lower value is obtained if a centrally peaked current distribution is assumed.

#### 4.4. Large ion Larmor radius effects

Our linear initial value code for Hall fluid instabilities [10] has been modified to treat ions as an ensemble of particles, as described earlier [1]. Preliminary results for  $m = 0$  internal modes have been obtained for various values of  $\epsilon$  (the ratio of average ion Larmor radius to pinch radius). For  $\epsilon = 0.3$ , a considerable reduction in the growth rate by up to a factor of five has been found, but definitive results could not be obtained so far because of numerical problems in the scheme.

### REFERENCES

- [1] HAINES, M.G., DANGOR, A.E., FOLKIERSKI, A., et al., "Z-pinch experiments and theory", Plasma Physics and Controlled Nuclear Fusion Research 1984 (Proc. 10th Int. Conf. London, 1984), Vol. 2, IAEA, Vienna (1985) 647.
- [2] POTTER, D.E., Nucl. Fusion **18** (1978) 813.
- [3] HAINES, M.G., Proc. Phys. Soc. **77** (1961) 643.

- [4] DANGOR, A.E., et al., Phys. Rev., A **27** (1983) 2751.
- [5] FAVRE-DOMINGUEZ, M.B., Experimental investigation of gas-embedded Z-pinch, PhD Thesis, Imperial College, Univ. of London, 1985.
- [6] CHALLIS, C.D., X-ray observations of an annular gas-puff Z-pinch, PhD Thesis, Imperial College, Univ. of London, 1986.
- [7] HAINES, M.G., Proc. Phys. Soc. **76** (1960) 249.
- [8] HAMMEL, J.E., Rep. LA-6203-MS, Los Alamos Scientific Lab., NM (1976).
- [9] KADOMTSEV, B.B., in Reviews of Plasma Physics, Vol. 2, Consultants Bureau, New York (1966).
- [10] COPPINS, M., et al., Phys. Fluids **27** (1984) 2886.

## DISCUSSION

B.P. LEHNERT: Just a short comment. In the theoretical analysis of our EXTRAP pinch experiments we also found that large Larmor radius effects<sup>1</sup> contribute significantly to the stability of the Z-pinch; this is in agreement with your results. I think that a relevant analysis of high beta systems cannot be based on MHD theory alone but must, at least in part, be extended to include kinetic effects.

A. SEN: In your compressional Z-pinch experiments did you estimate the size of betatron orbits and can you say something about their role in the stabilization of the pinch?

M.G. HAINES: The size of the betatron orbits, or what we call singular orbits, is approximately  $\sqrt{a_i a}$ , where  $a_i$  is the mean ion Larmor radius and  $a$  the pinch radius. For our compressional Z-pinch, where  $a_i/a$  is 0.13, the singular orbits occupy a region of radius 0.36  $a$  from the axis. We believe that they play an important role in the stabilization of the pinch. As stated in the paper, a considerable reduction in the growth rate of the  $m = 0$  mode has been found in a kinetic simulation with  $a_i/a$  up to 0.3.

---

<sup>1</sup> LEHNERT, B.P., Comments Plasma Phys. Controll. Fusion **9** (1985) 91.

## INVESTIGATION OF PLASMA DYNAMICS AND EMISSION IN A DENSE PLASMA FOCUS

K. HIRANO, T. YAMAMOTO, K. SHIMODA,  
Y. OKABE, K. WAKABAYASHI  
Department of Electronic Engineering,  
Gunma University,  
Kiryu, Gunma

M. YOKOYAMA, Y. YAMAMOTO, Y. YAMADA,  
Y. KITAGAWA, M. YAMANAKA  
Institute of Laser Engineering,  
Osaka University,  
Suita, Osaka  
Japan

### Abstract

#### INVESTIGATION OF PLASMA DYNAMICS AND EMISSION IN A DENSE PLASMA FOCUS.

The heating mechanism of plasma in a plasma focus discharge is investigated through correlation between plasma dynamics and emission of neutrons, X-rays and charged particles. Various measurements are carried out by using a Mach-Zehnder interferometer, a time resolved soft X-ray camera, and a Thomson parabola ion analyser. High energy deuterons are measured by nuclear activation techniques. The target used in the measurement, consisting of two semi-circles (aluminium and carbon), determines the mean energy of the deuterons, from the  $^{13}\text{N}/^{28}\text{Al}$  ratio. The ion temperature and the kinetic energy, from the D-D/D- $^3\text{He}$  yield ratio, are obtained by using an equimolecular  $\text{D}_2$ - $^3\text{He}$  mixture. The neutron emission region and the neutron intensity distribution are determined by using a neutron pinhole camera. The experimental results show that the plasma emits soft X-rays in three successive phases: the maximum compression, plasma disruption and decay phases. Immediately after disruption, emission of neutrons, soft X-rays and charged particles is observed. The energy distribution of the deuteron beam produced by the plasma focus is obtained.

### 1. INTRODUCTION

The plasma focus is considered to be one of the most efficient pulsed neutron, X-ray and charged particle sources [1]. Moreover, recent developments in plasma focus research suggest the possibility of a breakeven reactor [2]. However, the mechanism of these emissions is not fully understood, in spite of investigations performed from various points of view.

After the initial breakdown along the insulator surface, the filling gas  $D_2$  is snowploughed by the current sheet which is driven by the electromagnetic force. When the current reaches the end of the inner electrode, the current collapses radially and forms a plasma column. The length of the plasma column extends axially in time. Then, the column is disrupted by the growth of the  $m = 0$  instabilities. After the disruption, neutron, X-ray and ion emissions are observed.

The aim of the present study is to precisely investigate the correlation between the dynamic behaviour of a focused plasma and the emission and to clarify the heating mechanism of the plasma.

## 2. APPARATUS

The experiments were carried out by using two Mather type plasma focus devices with which capacitor banks of  $4.24 \mu\text{F}$ , 65 kV and  $40 \mu\text{F}$ , 30 kV were employed [3].

The macroscopic behaviour of the plasma was observed by a Mach-Zehnder interferometer and a time resolved soft X-ray pinhole camera. The light source for the interferometer was an  $N_2$  laser whose light pulse width (FWHM) was less than 1 ns. A microchannel plate (MCP) (Hamamatsu Photonics F2223-11P) was employed as an image sensor of the pinhole camera. The effective exposure time of the camera was 1.5 ns [4]. The soft X-ray emission was also recorded with a PIN photodiode.

A Thomson parabola analyser was used to measure the charged particle beam generated by the focused plasma in the downstream direction with respect to the discharge current. Deflection fields of up to 5 kG and  $5 \text{ kV}\cdot\text{cm}^{-1}$ , respectively, can be applied. A time resolved measurement of the ion beam was carried out by developing a detector consisting of MCP with multianode. A method of calibrating the electron multiplication factor of the MCP for charged particles was developed [5].

We obtained the ion temperature and the kinetic energy from the  $D-D/D-^3\text{He}$  yield ratio by using a  $D_2-^3\text{He}$  mixture. The  $D(d,n)^3\text{He}$  reaction yield was determined from the neutron yield measured by a silver activation counter, while the  $^3\text{He}(d,n)^4\text{He}$  reaction yield was determined by an analysis of the  $\gamma$ -decay spectrum induced by the  $^{63}\text{Cu}(p,n)^{63}\text{Zn}$  reaction (the threshold is 4.21 MeV). Such a mixture gas method was reported by Gullickson et al. [6].

Moreover, we used a neutron time of flight detector to obtain a maximum neutron yield of  $1.2 \times 10^9$  in 60 ns and a silicon PIN (250  $\mu\text{m}$  thick) detector to determine the ion generation time, which agrees with the 10 ns pulse duration of hard X-rays. The spatial distribution of neutron emission was also measured by a neutron pinhole camera, consisting of a paraffin pinhole and a detector [7].

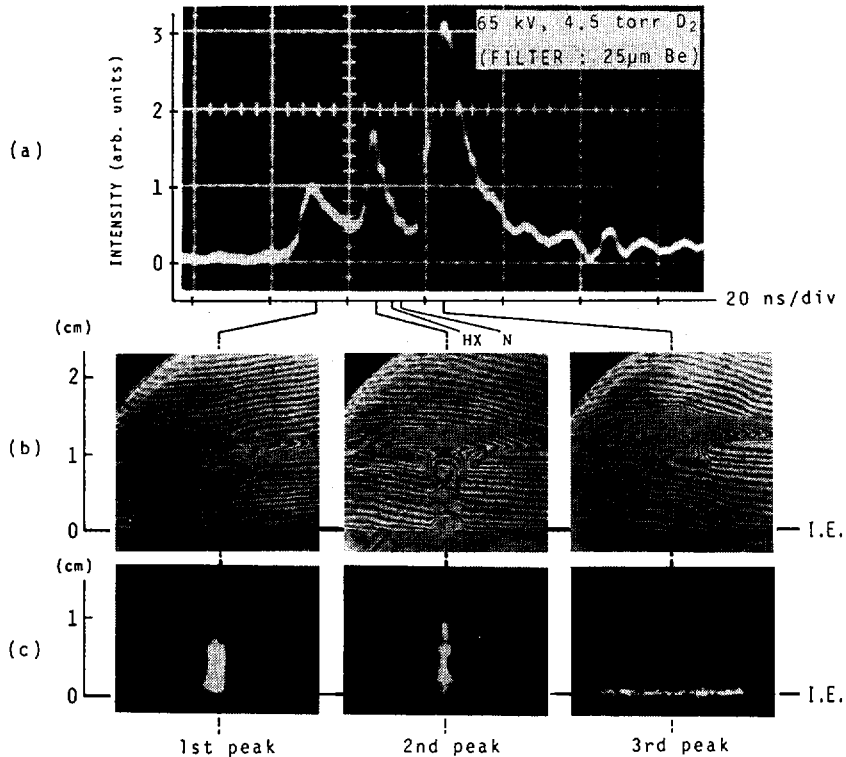


FIG. 1. Time correlation between emission of soft X-rays and macroscopic plasma behaviour. Soft X-ray signal is obtained by the PIN photodiode detector (a), framing interferograms (b), time resolved soft X-ray images (c). Inner electrode face is designated by I.E.

### 3. EXPERIMENTAL RESULTS AND DISCUSSION

A typical example for soft X-ray signal obtained by one of the PIN photodiodes is shown in Fig. 1 (a). Obviously, the soft X-ray signal has three peaks with good reproducibility. The peaks of hard X-rays and neutrons are pointed out by HX and N in this figure, respectively. Figures 1 (b) and (c) show interferograms and soft X-ray images taken at each peak of the soft X-ray signal in (a). It is observed that soft X-ray emission starts before maximum compression and continues for a relatively long time (60–70 ns), whereas hard X-rays and neutrons are emitted in single pulses. The first peak corresponds approximately to maximum compression as is seen from Figs 1 (b) and (c). In this phase, the soft X-rays are emitted nearly uniformly from the collapsed plasma column. The second peak coincides with the time when the plasma column is disrupted by the growth of the  $m = 0$  instabilities. At this instant, it is recognized that the plasma column is partly disrupted as is shown in Fig. 1 (b),

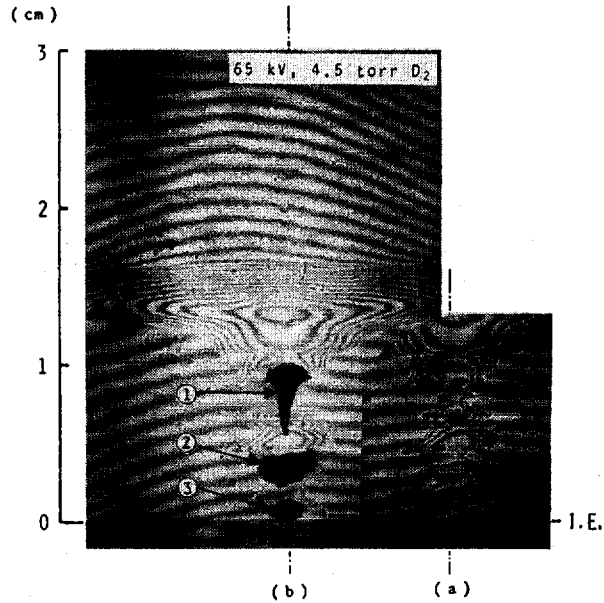


FIG. 2. Interferogram (a) and schematic drawing of soft X-ray images overlapping interferogram (b). Inner electrode face is labelled I.E.

and dense plasmas which are confirmed by the numbers of shifted fringes are seen at both sides of the disrupted region. At the third peak, we cannot recognize the plasma column up to 1 cm above the inner electrode face. In this phase, soft X-rays are only emitted from the inner electrode face. The peaks of the hard X-ray and neutron signals appear immediately after the second peak of the soft X-ray signal. This fact suggests that the second peak is closely related to the most interesting phenomena in the plasma focus discharge. Soft X-ray images, with sufficient intensity, could only be taken in the vicinity of each peak.

Figure 2 shows an example for the interferograms and soft X-ray images immediately before disruption. In this interferogram, extremely developed  $m = 0$  instabilities appear in the plasma column. A filamentary structure and a high intensity spot can be seen on the electrode axis in the soft X-ray image. The fringe shifts in the interferogram are proportional to the electron density,  $n_e$ . On the other hand, the intensity of the soft X-rays produced by the bremsstrahlung corresponds to  $n_e^2 T^{1/2}$ , where  $T_e$  is electron temperature. The region has a higher  $T_e$ , if intense soft X-rays are generated from the region with lower electron density. In Fig. 2(b), region ① shows a rather high  $n_e$ , and so the intense X-rays are ascribed to the higher  $n_e$ . There are two or more fringes between the lateral face and the axis of the plasma column at ①. It is, therefore, assumed that an extremely intense spot of the soft X-rays at ② is produced by high temperature electrons

since the plasma has a low density in this region. The regions ① and ② may be origins of anomalous resistivity.

A deuteron beam produced by a single shot of the plasma focus was recorded after energy analysis with the Thomson parabola analyser. An example for deuteron tracks registered on a CN film after etching is shown in Fig. 3(a). Tracks of the same width as the multianode were counted by using a microscope. The deuterons collected on the CN film are shown in Fig. 3(b). The width of each curve on the energy axis ( $\Delta E_d$ ) is calculated by taking energy borne by an equivalent width of the multianodes into account. The analog signals which were obtained simultaneously by the multianode are shown in Fig. 3(c). The signals are caused by ions which are produced at the same time and the same location, but have different energy, and so we can determine the energies which correspond to each signal. Integrating the curves in Fig. 3(b) across the beam width, we obtain the number of ions collected in each area, i.e. an energy distribution function as is shown in Fig. 4. Two vertical axes are used, corresponding to an ion count per anode of an area 0.5 mm  $\times$  8 mm and an ion count per keV and steradian.

From the ratio of the activated products  $^{13}\text{N}$  and  $^{28}\text{Al}$  obtained from the target, we calculated the mean deuteron energies as 1.5 MeV at 1.5 torr and 1.4 MeV at 5 torr, which shows that the mean energy depends weakly on the filling pressure although the beam intensity is very sensitive to it. No copper activation was observed, which indicates that deuterons above 4 MeV are very few.

To study the correlation between neutrons and energetic deuterons, we measured the deuteron temperature and kinetic energy by using a  $\text{D}_2\text{-}^3\text{He}$  mixture gas, where the pressure dependence of the neutron yields was the same as in pure deuterium gas. The results are listed in Table I, where we estimated the deuteron temperature  $T_i$  from a pure thermonuclear model and the deuteron kinetic energy  $E_d$  from a pure beam-target model.  $T_i = 11$  keV at 1.5 torr is much higher than the neutron time of flight (3 keV), which implies that the thermonuclear model is not applicable at the low pressure.

In the low pressure regime, optical and ion pinhole images indicate that the deuterons are produced by the plasma diode. This plasma diode plays the role of an opening switch interrupting the current with a very short rise-time, which may induce a high accelerating voltage across the plasma diode. We estimate the accelerating voltage  $V_p$  given by

$$V_p = V - L\dot{I}$$

where  $V$  is the voltage across the electrodes,  $L$  the inductance in the discharge, and  $I$  the discharge current. The inductance is assumed to be constant (40 nH in our device), during the interruption. We assume  $\Delta I$  equal to three-quarters of the total current, and to be 480 kA, dropping off in 5 ns, as is determined from the hard X-ray emission time, so that

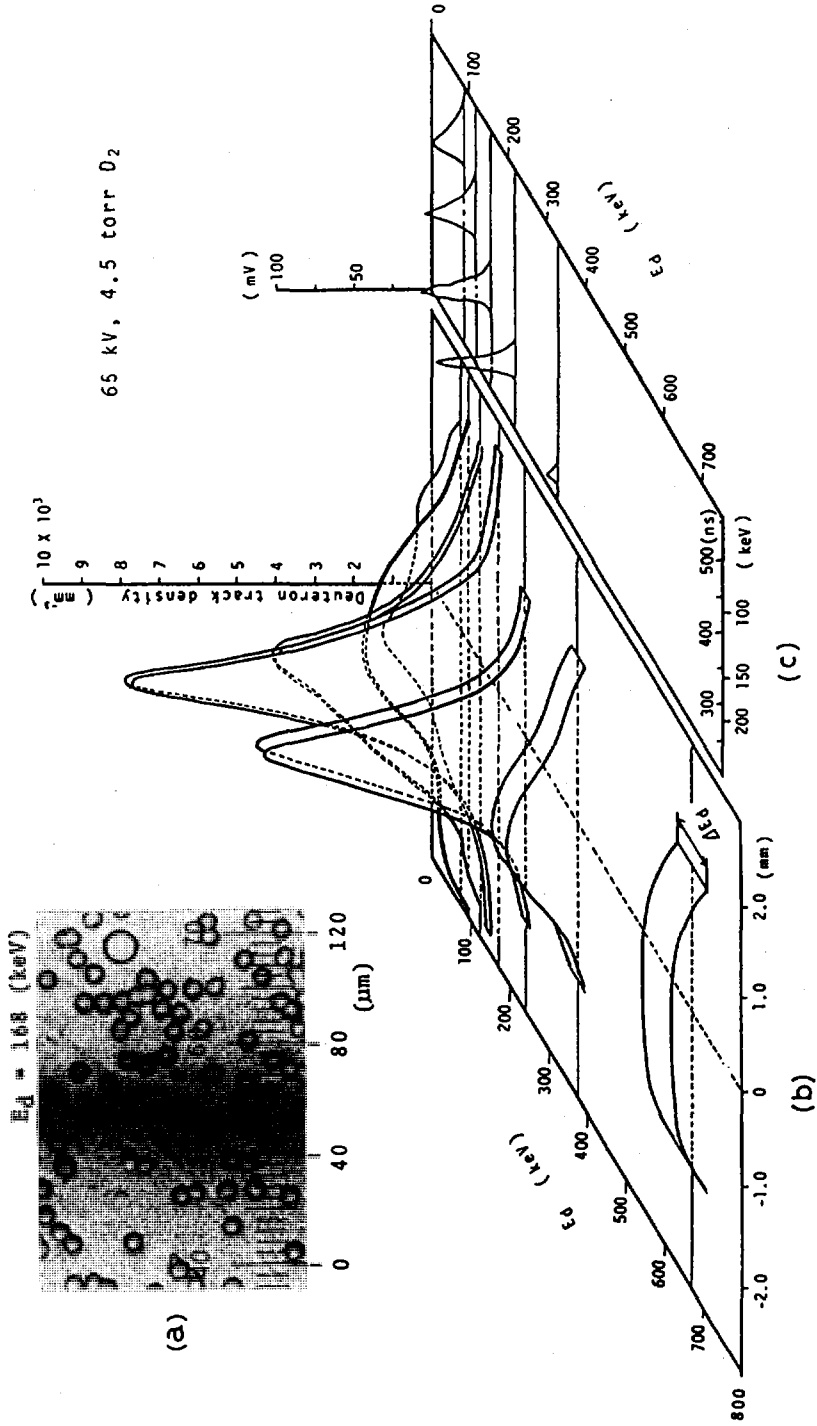


FIG. 3. Example of deuteron track (a), distribution of ion tracks registered in each domain of CN film (b), and energy analysed deuteron signals (c). Circle in (a) shows diameter of microchannel.

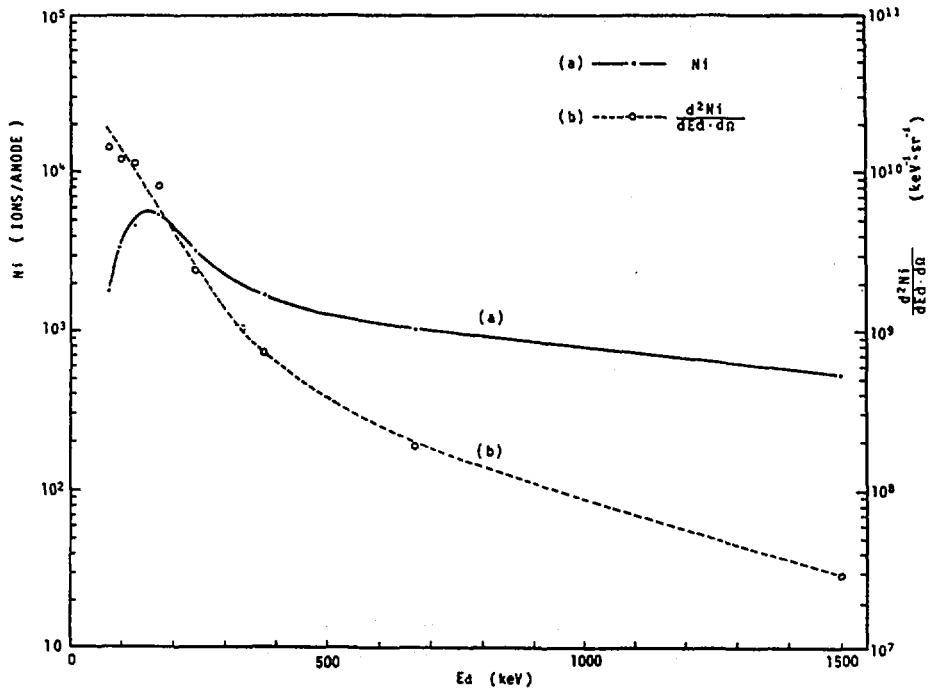


FIG. 4. Energy distribution of deuterons obtained by integrating tracks in Fig. 3 (b).

$$V_p \approx -L\Delta I/\Delta t = 3.8 \text{ MV}$$

This voltage is consistent with the observed deuteron energy.

The plasma diode was formed above the anode surface, but no dense pinch was formed in this regime. This suggests the possibility of current interruption due to the enhancement of radiative loss caused by high Z impurities such as tantalum from the anode tip [8].

To determine the location of the neutron emission region in the focus pinch column, we first measured the axial intensity distribution of the neutron emission by using a horizontal paraffin slit (1 cm X 10 cm X 5 cm) as neutron collimator. Then, we measured the radial intensity distribution of the neutron emission by using a vertical paraffin slit (10 cm X 0.5 X 50 cm).

As is seen in Fig. 5, the highest density of neutrons is located up to 2 cm above the anode tip with a maximum radius of 0.5 cm; emission takes place within a conical angle of  $44^\circ \pm 10^\circ$ , where the top of the cone is located at the anode tip [9].

TABLE I. ION TEMPERATURE  $T_i$  AND DEUTERON KINETIC ENERGY  $E_d$   
*Second column refers to equiatomic case, whose data are not so different from equimolecular case (first column)*

$D_2 + {}^3\text{He}$	D-D neutrons D- ${}^3\text{He}$ protons	$T_i$ (keV) (thermonuclear model)	$E_d$ (keV) (beam acceleration model)
4 torr (1:1)	14	5.0	42
4 torr (1:2)	13	5.2	43
1.5 torr (1:1)	3	11	74

#### 4. CONCLUSIONS

From the experimental results we conclude the following:

- (1) Soft X-rays are emitted for a rather long period from the collapse phase up to the disruption of the plasma column, whereas the hard X-rays whose appearance coincides with the emission of the electron beam consist of a narrow pulse.
- (2) Typically, the soft X-ray signal had three successive peaks. According to the interferometric observation, three soft X-ray signal peaks correspond to the instant of (i) maximum compression, (ii) disruption and (iii) the decay phase of the plasma column. This was also confirmed by the time resolved soft X-ray pinhole camera.
- (3) The soft X-rays emitted from the disrupted region were less intense than those of the unstable phase. The peak of the voltage spike appeared in this phase. According to a previous paper, the generation of the voltage spike can be ascribed to a rapid increase in plasma resistance rather than to a rapid increase in plasma inductance [10]. This means that the electrons in the disrupted region can be heated further, for example, by turbulent heating. The plasma has, however, a low electron density in this region, as is shown by interferometric observation, and, thus, emission of the soft X-rays is not intense in spite of the higher electron temperature. Therefore, the high resistivity generated in this region provides an intense electric field and the field accelerates ions up to a sufficient energy to produce neutrons.
- (4) A Thomson ion analyser in which an MCP was employed as an ion detector was developed. A method of calibrating the electron multiplication factor of the MCP for charged particles was established. By using the Thomson ion analyser, the energy distribution of the deuteron beam produced by the plasma focus device was obtained.

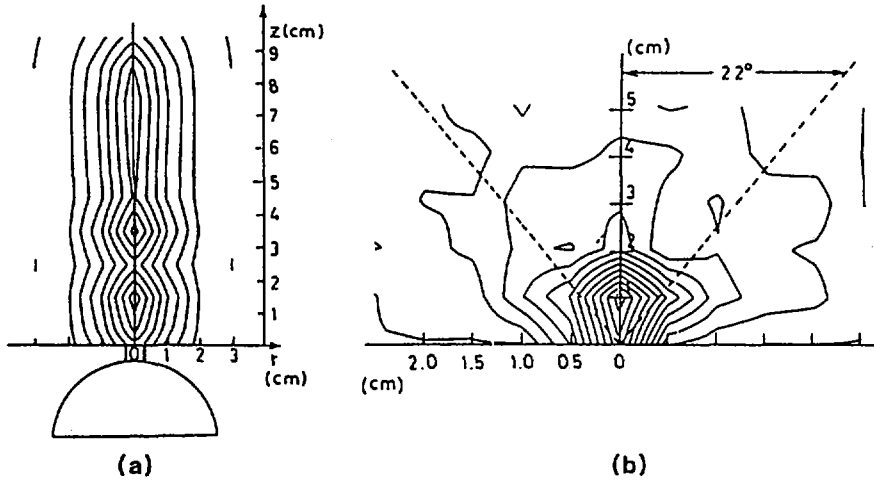


FIG. 5. Isointensity contour display of neutron source by using (a) single collimator and (b) double collimators.

(5) We estimate the neutron yield using a pure beam target model as

$$Y_b = n_d n \sigma v A L t$$

where  $n_d$  and  $n$  are the deuteron beam and target densities,  $\sigma$  is a reaction cross-section,  $v$  is the beam velocity,  $A$  and  $L$  are the target plasma cross-section and length, and  $t$  is the production duration. For 74 keV deuterons directed into a cold gas target of 1.5 torr,  $\sigma = 10^{-26} \text{ cm}^2$ ,  $v = 2.7 \times 10^8 \text{ cm} \cdot \text{s}^{-1}$ ,  $n_d \cong 8.8 \times 10^{16} \text{ cm}^{-3}$  (from experimental results),  $A \approx \pi \times 10^{-2} \text{ cm}^2$ ,  $t \approx 60 \text{ ns}$ , and  $L = vt = 16 \text{ cm}$ , which agrees with the results of the neutron pinhole camera measurement. The neutron yield is then  $5.1 \times 10^8$ . Since the measured average neutron yield was  $7.0 \times 10^8$ , the neutron production mechanism at low pressure is explained by the beam target model. Note that not the deuterons above 330 keV, but the deuterons  $\lesssim 74 \text{ keV}$ , contribute to the neutron yield.

(6) The highest density of neutrons is located up to 2 cm above the anode tip with maximum radius of 0.5 cm and emission is within a cone angle of  $44^\circ \pm 10^\circ$ , where the top of the cone is located at the anode tip.

## REFERENCES

- [1] GULLICKSON, R.L., SAHLIN, H.L., *J. Appl. Phys.* **49** (1978) 1099.
- [2] HEROLD, H., HAYD, A., in *Plasma Focus Research (Proc. 3rd Int. Workshop Stuttgart, 1983)*, IPF-83-6, Institut für Plasmaforschung der Universität Stuttgart (1983) 131.

- [3] HIRANO, K., YAMAMOTO, T., SHIMODA, K., et al., in *Plasma Physics and Controlled Nuclear Fusion Research 1984* (Proc. 10th Int. Conf. London, 1984), Vol. 2, IAEA, Vienna (1985) 569.
- [4] HIRANO, K., YAMAMOTO, T., SHIMODA, K., TAGAYA, Y., *Jpn. J. Appl. Phys.* **24** (1985) 1514.
- [5] HIRANO, K., YAMAMOTO, T., OKABE, Y., SHIMODA, K., to be published in *Rev. Sci. Instrum.*
- [6] GULLICKSON, R.L., LUCE, J.S., SAHLIN, H.L., *J. Appl. Phys.* **48** (1977) 3718.
- [7] YAMAMOTO, Y., KISODA, A., YAMADA, A., NIKI, H., KITAGAWA, Y., YAMANAKA, M., YOKOYAMA, M., YAMANAKA, C., *Jpn. J. Appl. Phys.* **23** (1984) 1410.
- [8] YAMADA, Y., KITAGAWA, Y., YOKOYAMA, M., *J. Appl. Phys.* **58** (1985) 188.
- [9] YAMAMOTO, Y., KISODA, A., YAMADA, A., NIKI, H., KITAGAWA, Y., YAMANAKA, M., YOKOYAMA, M., YAMANAKA, C., *J. High Temp. Soc.* **11** (1985) 113.
- [10] YAMAMOTO, T., SHIMODA, K., HIRANO, K., *Jpn. J. Appl. Phys.* **24** (1985) 324.

# INVESTIGATION OF COLLAPSE, PINCH DYNAMICS AND FAST PARTICLE EMISSION IN A PLASMA FOCUS DISCHARGE

S. CZEKAJ, S. DENUS, A. KASPERCZUK,  
R. MIKLASZEWSKI, M. PADUCH, T. PISARCZYK,  
S. SLEDZIŃSKI, A. SZYDŁOWSKI, Z. WERESZCZYŃSKI  
Institute of Plasma Physics and Laser Microfusion,  
Warsaw, Poland

## Abstract

INVESTIGATION OF COLLAPSE, PINCH DYNAMICS AND FAST PARTICLE EMISSION IN A PLASMA FOCUS DISCHARGE.

The experimental results of investigations into the plasma focus (PF) phenomenon are presented. Interferometry was used on two devices, PF-360 and PF-150. The emission of fast particles was studied on the PF-150 device only. The dynamics of the collapse and the pinch works differently in the two devices. It seems that it is due to different geometry and circuit parameters. It was found in the PF-150 device that the emission characteristics of relatively slow D ions (within the energy range of 50–1000 keV) and of very fast ones (of energy above 1 MeV) are quite different.

## 1. THE COLLAPSE AND THE PINCH DYNAMICS

Experimental investigations were carried out on the PF-150 (60 kJ) and the PF-360 (100–170 kJ) plasma focus devices by means of laser interferometry [1–3]. Thus, we could compare two facilities with energies differing by a factor of two to three. Unfortunately, the characteristics of the condenser bank used (lower inductance of the larger device) does not allow a simple scaling of the plasma dynamics to be performed because of the difference in the dimensionless parameters relating to the plasma and circuit characteristic times [4].

Essential differences in plasma sheath dynamics and pinch behaviour have been observed [2–3]. In this paper, we present an attempt to explain the nature of these differences on the basis of classical MHD theory. The interesting question is whether these differences are due to a difference in energy in the condenser bank or whether they are the consequence of different electrode geometries and circuit parameters. A characteristic feature of plasma sheath dynamics in the collapse phase are the MHD instabilities, which are not observed in the PF-150 device. Some explanations for this phenomenon were presented in Refs [2, 3]. The second difference which has important consequences is the curvature radius of the plasma sheath just before the sheath

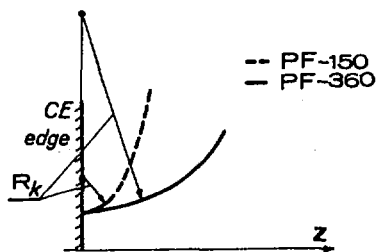


FIG. 1. Shape of plasma sheath.

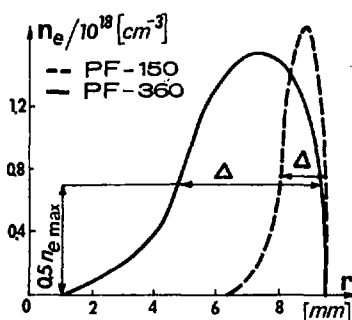


FIG. 2. Structure of plasma sheath ( $n_e$  is the electron density).

arrives at the axis. This radius in the PF-360 device is about eight to nine times longer than that in the PF-150 device (Fig. 1).

The greater thickness of the plasma sheath is an immediate consequence of this fact. It agrees well with theoretical prediction:

$$\Delta \approx \sqrt{\frac{R_k r}{\rho/\rho_0}}$$

where  $\Delta$  is the thickness of the sheath,  $R$  is the curvature radius,  $r$  the actual radius of the sheath, and  $\rho/\rho_0$  the compression ratio. This formula is based on Bernoulli's law; it is valid in the late, collapse phase and differs essentially from Gureev's formula [5].

Greater sheath thickness with virtually the same plasma density (Fig. 2) implies a greater amount of plasma inside and, then, a greater radius of the plasma column in the PF-360 device.

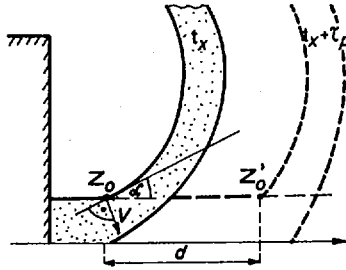


FIG. 3. Pinch formation geometry.

The difference in the curvature radii of the plasma sheath also affects the character of the MHD instabilities in the pinch phase. Let us estimate the axial plasma pressure gradient during the process of pinch formation. Let the pressure rise-time in the  $z = z_0$  plane be given by (Fig. 3):

$$\tau_p \approx \frac{\Delta}{v \cos \alpha}$$

During this period, the point  $z$  moves towards  $z_0$ , leading to

$$z'_0 - z_0 = d = \tau_p u$$

where  $u$  is the rate of pinch formation. From simple geometrical considerations, we obtain:

$$u = \frac{v}{\sin \alpha}$$

Then, the characteristic length of the pressure gradient is as follows:

$$d \approx \frac{\Delta}{v \cos \alpha} \frac{v}{\sin \alpha} = \frac{2\Delta}{\sin 2\alpha}$$

Thus, the pressure gradient along the axis may be estimated to be

$$\nabla p \approx \frac{1}{d} \approx \frac{\sin 2\alpha}{2\Delta}$$

When the sheath has a small curvature radius (PF-150 device), the thickness  $\Delta$  of the plasma sheath is also small, and the angle  $\alpha$  is large; high pressure gradients



FIG. 4. MHD pinch instability in PF-150.

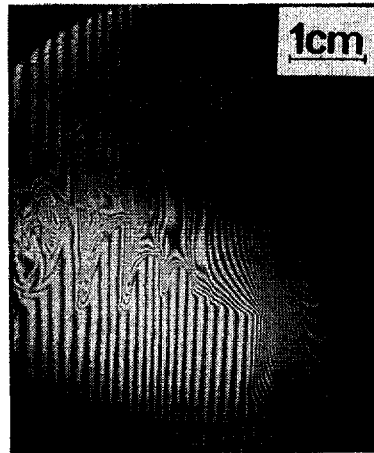


FIG. 5. MHD pinch instability in PF-360.

develop during pinch formation, and an intense plasma outflow from the pinch is observed. As a consequence of this outflow, there is a fast developing flute in the pinch which leads to a break of the column, as is shown in Fig. 4. In the PF-360 device, where the plasma sheath curvature radius is greater, weak plasma outflow along the pinch axis and classical MHD instabilities were observed (Fig. 5). The important role of the sheath curvature radius was confirmed in an experiment with an additional axial magnetic field  $B_z$  applied in the PF-150 device [6]. The rise in  $B_z$  caused an increase in curvature radius and sheath thickness and, in addition, changed the character of the MHD instabilities.

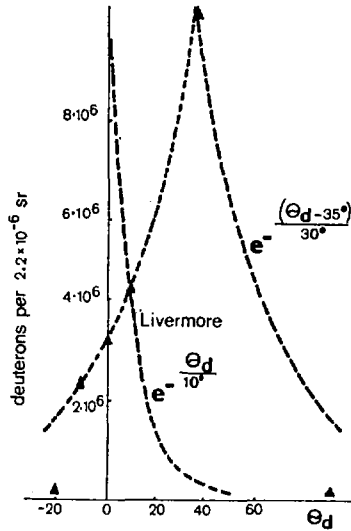


FIG. 6. Angular distribution of ions in PF-150 obtained from track number on pinhole images.

## 2. FAST PARTICLE EMISSION

Two methods were applied to obtain the angular distribution of the fast  $D^+$  ions. The first method was based on counting the numbers of tracks in the pinhole images (along the whole area). This method is time consuming and very cumbersome, but yields the angular distribution of relatively slow deuterons (Fig. 6). In the second method, the track detector plates were located inside the discharge chamber along a semicircle (22 cm radius) around the inner electrode face. To prevent the detector plates from being damaged by the plasma and the waves in the ionized gas, a metallic shield with drilled holes (1 mm in diameter) was placed in front of the detector plates so that the detectors registered only deuterons which passed through the holes. To avoid track saturation effects, we covered the detectors with either mylar or Al foils of different thicknesses. Up to now, only angular distributions of very fast deuterons which penetrated 9  $\mu\text{m}$  thick Al foils ( $E_d > 900$  keV) have been obtained (Fig. 7). A comparison of the angular distributions as obtained by the first and by the second method seems to show that deuterons of lower energy have a broader angular spectrum. The angular distributions achieved by the second method are very similar to those obtained with a carbon target activation technique in other laboratories [7–8]. It should, however, be noted that, by using an activation technique, one can only register  $D^+$  ions with energies above 700 keV.

The energetic distributions of deuterons were studied by means of a Thomson spectrometer and an ion collector. In certain spectra (Fig. 8) two components can be distinguished: within the energy range 0.15 to 1 MeV, the shape of the spectrum is

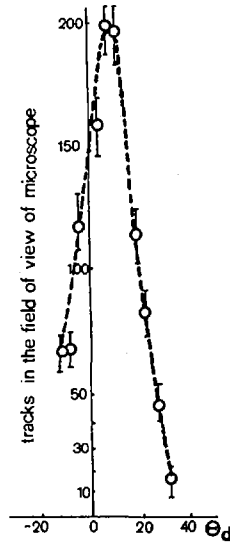


FIG. 7. Angular ion distribution obtained with metal semi-ring located in front of detector.

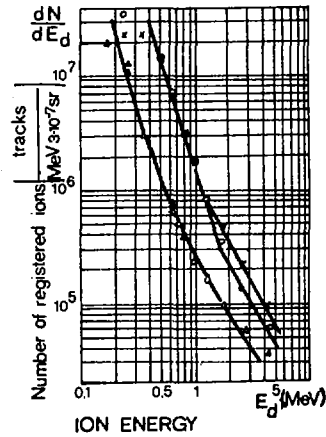


FIG. 8. Deuteron spectra registered by Thomson spectrometer in PF-150.

well approximated by the formula  $f(E_d) \propto E_d^{-3}$ , while above 1 MeV this function is given by  $f(E_d) \propto E_d^{-2}$ . It was confirmed that the apparent maximum of the spectrum in the low energy range ( $< 300$  keV) is due to the effect of an interaction between the registered ions and molecules of the  $D_2$  gas filling the discharge chamber. The maxima of the spectra obtained with the ion collector were more and more shifted

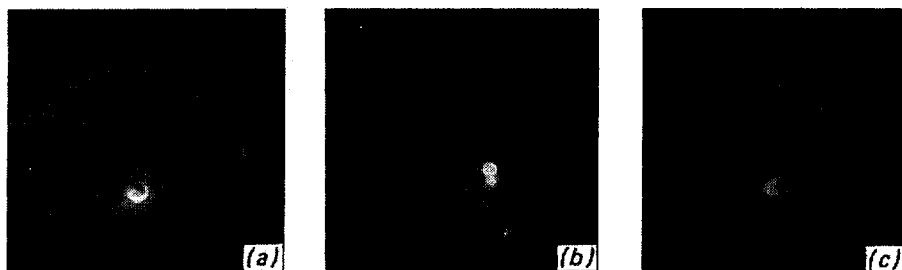


FIG. 9. Pinhole images of ion source in PF-150 device: (a) ions passing through pinhole straightforward hitting the detector, (b) track detector covered with  $1 \mu\text{m}$  mylar foil, (c) track detector covered with  $9 \mu\text{m}$  Al foil.

towards the low energy side as the thickness of the gas layer along the ion path became smaller.

The ion emission source was determined with the set of three pinhole cameras [9–10] located at angles of  $0^\circ$ ,  $9^\circ$  and  $11^\circ$  with respect to the electrode axis. Ion source images created by pinholes were recorded by the plates of a dielectric track detector. By covering the pinholes with foils of various thicknesses, we could obtain the images of ions with various energies. In this way, we found that very slow ions ( $E_d > 50 \text{ keV}$ ) are emitted from a large area around the inner electrode and, probably, also from the converging plasma sheath. Very fast ions ( $E_d > 900 \text{ keV}$ ) are emitted from hot spots which are located near the central electrode axis (Fig. 9).

A schematic of view of the experimental set-up for measurements of the fast electron energy spectrum is presented in Fig. 10. A magnetic spectrometer was used to measure the fast electron energies. The electron beam deflected by the B field was recorded on a KODAK X-ray film of RAR type. A photograph of the exposed film and its densitogram is shown in Fig. 10, as well. The maximum energy of the electrons was about 1 MeV. The fine structure of the energy spectrum is evident. One also sees several distinctly marked components of the electron beam. In the bulk of electrons of continuous energy distribution, intense groups of monoenergetic electrons seem to appear.

### 3. SUMMARY

Essential differences in the pinch behaviour in PF-150 (50 kJ) and PF-360 (100 to 170 kJ) were observed. It was shown that these differences are connected with a difference in the plasma sheath curvature radius in a late phase of the collapse. Since the plasma sheath curvature radius depends on the electrode geometry, one can

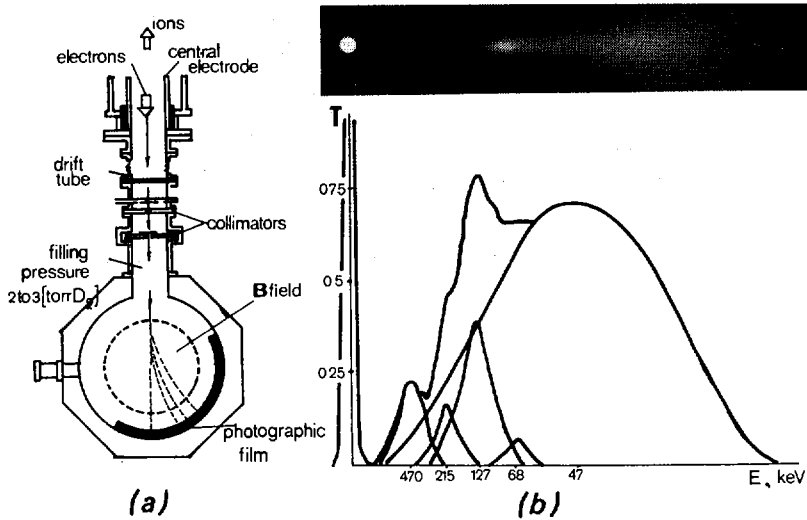


FIG. 10. Scheme of experimental arrangement for electron beam registration (a) and electron beam spectrum (b).

change the pinch properties by changing this geometry. The emission characteristics of relatively slow  $D^+$  ions ( $E_d > 50$  keV) are quite different from the characteristics of very fast ions ( $E_d > 900$  keV). Fast electrons with energies of up to 1 MeV were registered. The fine structure of the fast electron spectrum was observed.

## REFERENCES

- [1] JERZYKIEWICZ, A., et al., in *Plasma Physics and Controlled Nuclear Fusion Research 1984* (Proc. 10th Int. Conf. London, 1984), Vol. 2, IAEA, Vienna (1985) 591.
- [2] CZEKAJ, S., et al., in *Controlled Fusion and Plasma Physics* (Proc. 12th Europ. Conf. Budapest, 1985), Vol. 9F, Part I, European Physical Society (1985) 550.
- [3] CZEKAJ, S., et al., in *Plasma Focus and Z-Pinch Research* (Proc. 4th Int. Workshop Warsaw, 1985) 122.
- [4] IMSHENNIK, V.S., FILIPPOV, N.V., FILIPPOVA, T.I., *Nucl. Fusion* **13** (1973) 929.
- [5] CZEKAJ, S., et al., Rep. No. 4/81, Institute of Plasma Physics and Laser Microfusion, Warsaw (1981).
- [6] GUREEV, K.G., *Fiz. Plasmy* **4** (1978) 304.
- [7] GULLICKSON, R.L., SAHLIN, H.L., *J. Appl. Phys.* **49** (1978) 1099.
- [8] STEINMETZ, K., Rep. Plasmabericht 1/8 (Nov. 1980).
- [9] CZEKAJ, S., DENUS, S., SZYDŁOWSKI, A., in *Controlled Fusion and Plasma Physics* (Proc. 11th Europ. Conf. Aachen, 1983), Vol. 1, European Physical Society (1983) 539.
- [10] CZEKAJ, S., DENUS, S., SZYDŁOWSKI, A., *Atomkernenerg. Kerntech.* **44** (1984) 189.

## DISCUSSION

### ON PAPERS IAEA-CN-47/D-IV-5-1 AND D-IV-5-2

K. SATO: Could you comment on future prospects for this kind of plasma focus device, especially in terms of a future neutron source as well as a plasma fusion machine?

S. DENUS: Plasma focus has an optimistic scaling law for thermonuclear neutron production, according to which the neutron yield per shot is proportional to the condenser bank energy when squared or to the current when cubed (or even raised to a higher power). This scaling law has now been confirmed by experiments up to a bank energy of about 400 to 500 kJ. An answer to your question can be given when this scaling law, or a modified version of it, is confirmed by plasma focus experiments performed at higher energy levels equal to one to two or even more megajoules. As far as I know, these experiments are being planned, including in Poland.



## IMPURITY BEHAVIOUR IN THE WENDELSTEIN VII-A STELLARATOR

H. RINGLER, F. SARDEI, A. WELLER,  
W VII-A TEAM<sup>1</sup>,  
ECRH GROUP<sup>2</sup>, NI GROUP<sup>3</sup>  
Euratom-IPP Association,  
Max-Planck-Institut für Plasmaphysik,  
Garching, Federal Republic of Germany

### Abstract

#### IMPURITY BEHAVIOUR IN THE WENDELSTEIN VII-A STELLARATOR.

Plasma buildup and heating of net-current-free plasmas by ECRH (70 GHz) and further heating by NBI are successfully demonstrated at  $B_0 = 2.5$  T. Impurity transport studies are carried out. In NBI sustained discharges, neoclassical behaviour is found for impurities, similar to that in discharges starting from OH target plasmas reported earlier. During combined application of ECRH and NBI heating aluminium introduced by laser ablation is lost much faster than would be expected neoclassically. The electron line density, which increases linearly with time during NBI, levels off during the additional ECRH pulse and then remains constant. A similar degradation in impurity confinement is observed in pure ECRH discharges.

#### Impurity Confinement

In the W VII-A stellarator high radiation losses due to impurity accumulation were observed for NBI-heated, "currentless" plasma discharges created by ohmic heating /1/. The impurity transport study presented here refers to "currentless" plasmas created by ECRH with a 70 GHz gyrotron at  $B_0 = 2.5$  T with  $\epsilon_0 \lesssim 0.5$ . Three main types of discharges were investigated:

- a) NBI-sustained discharges at an input power level of 750 kW,  
 $\bar{n}_e \approx 3.7 - 5.5 \times 10^{13} \text{ cm}^{-3}$ ,  $T_e(o) \approx 400 \text{ eV}$ ,  $T_i(o) \approx 600 \text{ eV}$ .
- b) EC-sustained discharges at 70 GHz with a power of 150 kW,  
 $\bar{n}_e \approx 1.7 - 2.7 \times 10^{13} \text{ cm}^{-3}$ ,  $T_e(o) \approx 900 - 1400 \text{ eV}$ ,  
 $T_i(o) \approx 100 - 300 \text{ eV}$ .

<sup>1</sup> G. Cattanei, D. Dorst, A. Elsner, V. Ereckmann, U. Gasparino, G. Grieger, P. Grigull, H. Hacker, H.J. Hartfuß, H. Jäckel, R. Jaenicke, J. Junker, M. Kick, H. Kroiss, G. Kuehner, H. Maaßberg, C. Mahn, G. Müller, W. Ohlendorf, F. Rau, H. Renner, H. Ringler, F. Sardei, M. Tutter, A. Weller, H. Wobig, E. Würsching, M. Zippe.

<sup>2</sup> W. Kasperek, G.A. Müller, P.G. Schüller, M. Thumm, R. Wilhelm (Institut für Plasmaforschung, Univ. Stuttgart).

<sup>3</sup> K. Freudenberger, W. Ott, F.P. Penningsfeld, E. Speth.

- c) NBI-sustained discharges with additional ECR heating during part of the discharge,  $\bar{n}_e \approx 4 \times 10^{13} \text{ cm}^{-3}$ , ( $n_e(o)$  close to the cutoff density),  $T_e(o) \approx 500 \text{ eV}$ ,  $T_i(o) \approx 600 \text{ eV}$ .

As in previous transport studies, both Al trace impurities injected by the laser blow-off technique and intrinsic impurities were considered. The simulations were done with the SITAR code /1/.

- a) For NBI-sustained discharges starting from an ECRH target plasma, the measured Al radiation is reproduced reasonably well by neoclassical transport simulations using experimental profiles for  $n_e$  and  $T_e$ . In particular, good agreement is found for the time evolution and the absolute intensity of the central Al XII + Al XIII radiation from soft X-ray measurements and of line-averaged intensities from six Al ionization states. According to neoclassical expectations, the measurements show Al accumulation at the plasma center and no evidence of appreciable losses during the time of the discharge.

For the intrinsic impurities (predominantly oxygen in W VII-A) good agreement of soft X-ray measurements and neoclassical calculations was obtained by assuming in the calculations, in addition to a 1 % oxygen contamination of the neutral beam, which constitutes an oxygen deposition of  $\approx 2 \times 10^{18} \text{ s}^{-1}$ , an oxygen influx from the walls increasing from  $1 \times 10^{18}$  to  $7 \times 10^{18} \text{ s}^{-1}$  during the discharge.

- b) In contrast to the NBI-sustained discharges, for pure ECRH discharges the Al XII + Al XIII radiation from soft X-ray measurements (Fig. 1a) and the single line radiation from six ionization states Al VIII - Al XIII could not be reproduced by the neoclassical model (Fig. 1b). The main discrepancy concerns the fast loss of Al from the plasma center after 80 ms as indicated by the decrease of the central Al XII + Al XIII radiation and of the corresponding line radiation, which cannot be explained by atomic processes ( $n_e$ ,  $T_e \approx \text{constant}$  in time). Furthermore, the time scale for the Al penetration into the plasma center is much shorter than in the neoclassical simulations. The fast loss of Al could be simulated, however, by an additional diffusivity  $D_{\text{anom}} = 3 \times 10^3 \text{ cm}^2 \cdot \text{s}^{-1}$ , constant in space and time. An additional inward velocity  $v_{\text{anom}} = 3 \times 10^3 \times r/a \text{ cm} \cdot \text{s}^{-1}$ , linearly decreasing to zero during the ECRH pulse, was used to accelerate the Al penetration and to fit the absolute level of the central radiation approximately (Fig. 1c).
- c) The discharges heated jointly by NBI and ECR differ from the purely NBI-heated discharges in that for the former an

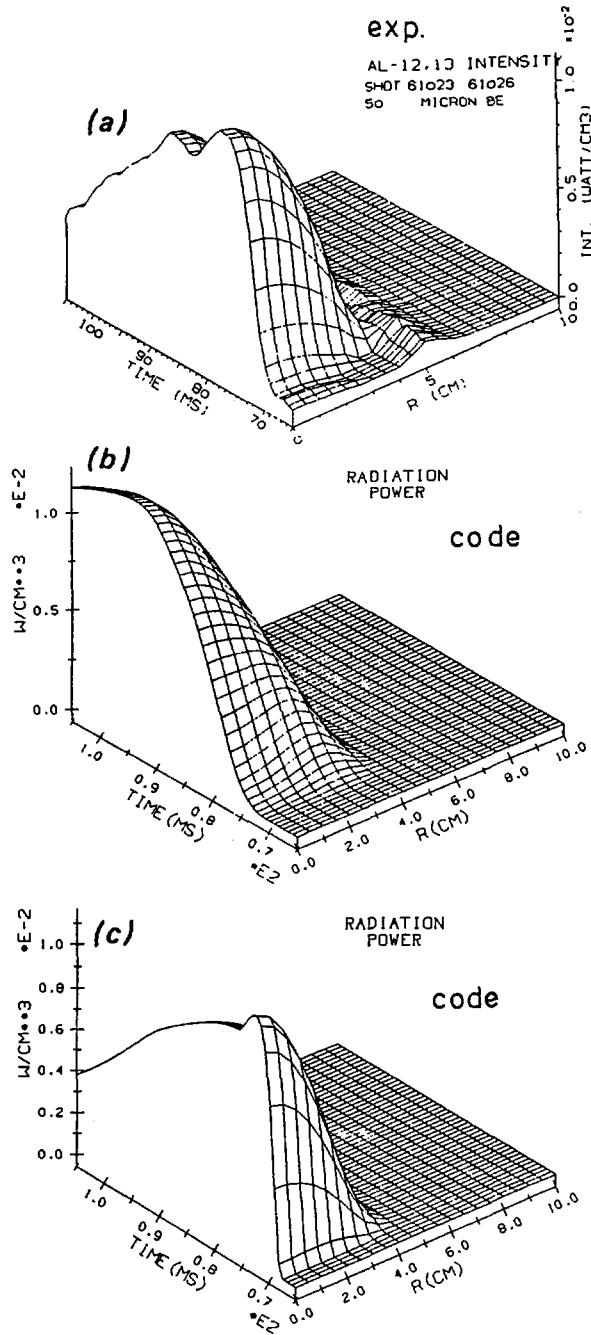


FIG. 1. (a) Evolution of Al XII + Al XIII radiation power from soft X-ray measurements after Al injection into an EC sustained discharge;  
(b) code simulation with neoclassical transport fluxes;  
(c) code simulation with additional anomalous diffusivity and inward velocity.

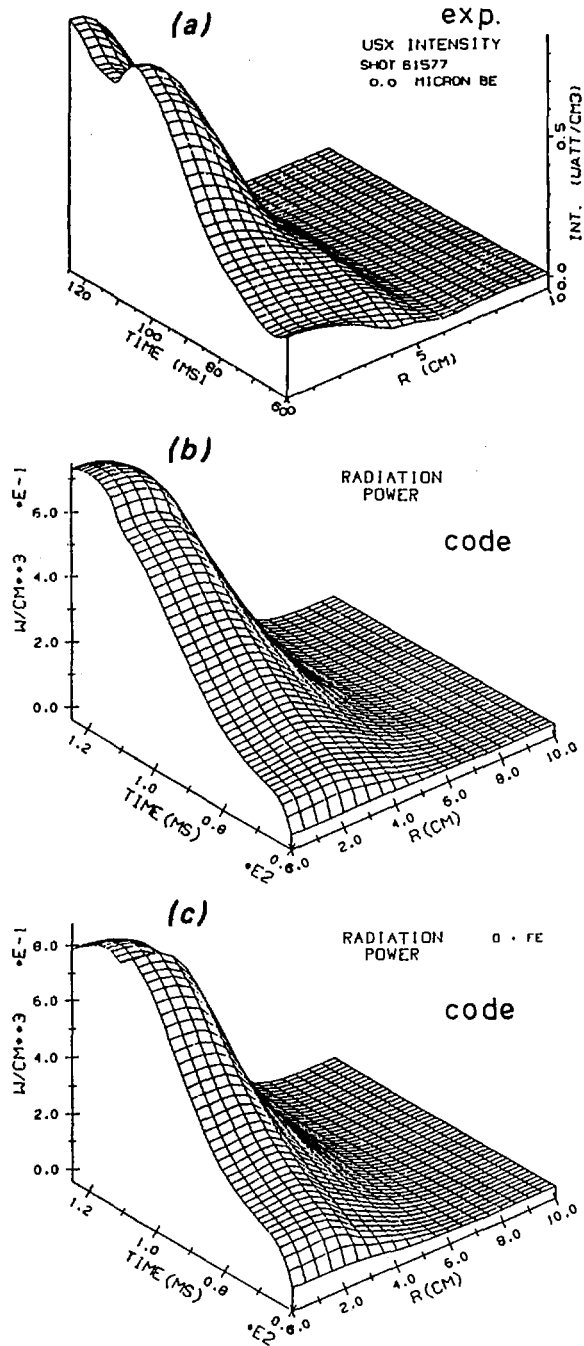


FIG. 2. (a) Evolution of soft X-radiation for an NBI + EC heated discharge;  
 (b) code simulation with oxygen impurities and neoclassical + anomalous transport;  
 (c) same as (b), but with additional Fe impurities.

additional 150 kW ECRH pulse was switched on for  $\approx 50$  ms during the discharge. During this time interval a flattening of the density evolution is typically observed (see Fig. 5). This flattening may be explained by a deterioration of the particle confinement during the ECRH pulse or by a reduced penetration of recycled neutrals due to edge deposition of ECRH power, which is discussed later in this paper. The interpretation of reduced particle confinement is supported by the observed evolution of the Al radiation from soft X and single-line radiation measurements, which indicate a fast loss of Al from the plasma center, in contradiction to neoclassical theory. The time scale for the decay of the radiation and the values of  $D_{anom}$  required to simulate it with the code were about the same as for pure ECRH discharges, with the anomalous impurity behaviour extending throughout the gradient region.

The soft X-radiation from the intrinsic impurities for this discharge type is shown in Fig.2a. In a previous paper [2] it was shown that the increase of the central radiation could be reproduced reasonably well by pure neoclassical transport with oxygen impurities from 1 % beam contamination and from wall influx rising from  $2 \times 10^{18}$  to  $5 \times 10^{18} \text{ s}^{-1}$  during the discharge. However, if the same anomalous behaviour is assumed for the intrinsic impurities as for the ablated Al during its escaping phase from the plasma center, i.e. if the same  $D_{anom}$  is added while keeping the wall influx unaltered, then the central oxygen radiation drops to unacceptably small intensities. In this case, the measured radiation could only be reproduced if the oxygen influx at the plasma edge was raised by almost an order of magnitude with respect to the values assumed for the neoclassical simulations. However, only about 10 % of this impurity influx contributes to the increase of the central oxygen density. The remaining 90 % circulates, after ionization, back to the wall, thus keeping the impurity gradients at the plasma edge higher than in the neoclassical case.

In this picture of enhanced transport the typical neoclassical impurity accumulation is strongly reduced. That is, for a given central radiation level the impurity density at the edge can be maintained at a substantially higher level than in the neoclassical picture. This may facilitate impurity removal from the plasma edge. A further consequence of this model is that the plasma particle outflux to the walls, which is linearly related to the oxygen desorption rate, would also have to be increased by about an order of magnitude with respect to the neoclassical transport case.

Unfortunately, the experimental information available on the edge plasma of these discharges was not sufficient to decide

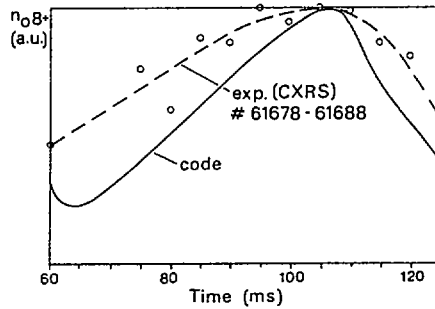


FIG. 3. Central  $O^{8+}$  density (activity units) versus time from active CXRS measurements in comparison with code calculations.

whether the high oxygen influx is a reasonable assumption. On the other hand, the code calculations show that the higher oxygen density at the plasma edge resulting from the increased oxygen influx would still be too small to give an observable increase of the bolometer signal. Uncertainties would also arise in checking the simulations with spectroscopic measurements of the lower oxygen ionization states. In fact, the enhanced transport would lead to an outward shift of the higher ionization states, thus decreasing the density of the lower states with respect to their values at coronal equilibrium. This would compensate to a large extent the density increase due to the higher fluxes at the edge.

Concerning the possibility of an impurity flow reversal mechanism associated with the ECR heating process /3/, it is not yet clear at present whether or not the required additional poloidal electric field was sufficiently high for the W VII-A discharges discussed here to create outward drift contributions compensating to a large extent the neoclassical inward drift. However, even if this were the case, the outward drift would have essentially the same consequences as the assumed enhanced diffusion with respect to the high impurity sources required to maintain the central radiation level.

The evolution of the OVII + OVIII radiation resulting from the code calculations discussed is shown in Fig. 2b. At the late stage of the discharge, a drop of the measured soft X-radiation is observed (Fig. 2a), in evident contrast to the simulation, which shows a steep increase of the OVII + OVIII radiation. Such an increase of oxygen radiation is essentially a consequence of the  $T_e$  drop ( $\Delta T_e = 140$  eV within 10 ms) observed after switching off the ECRH pulse. In order to reduce the discrepancy, additional high-Z material was included in the simulations for this discharge type (Fig. 2c).

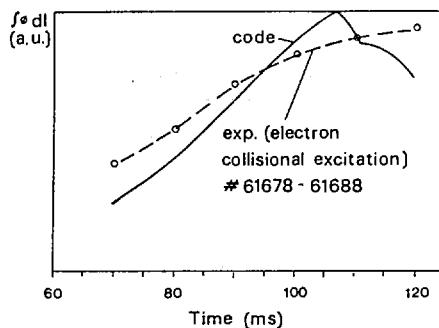


FIG. 4. Flux of O VIII (2976 Å) line intensity (activity units) versus time from electron excitation in comparison with code calculations.

Such impurities could originate from, for example, sputtering of plasma ions at the vacuum vessel (Fe, Cr) and sputtering at the limiter and NI beam dump plates (Mo)/4,5,6/. By assuming a Fe wall influx of 4 % of the oxygen influx, the measured central radiation could be qualitatively reproduced.

For the same discharge type, the evolution of the  $O^{8+}$  density has been measured by CX recombination spectroscopy (active signal) /2/. On the other hand, the passive signal, obtained with the diagnostic beam off, yields a flux which is proportional to the  $O^{7+}$  density /2/. The time histories of both signals are reproduced reasonably well by the simulations (Figs. 3,4). In particular, the decrease of the  $O^{8+}$  density related to the  $T_e$  drop observed after switching off the ECRH pulse is clearly confirmed by the CX recombination measurements.

### Electron Confinement

As shown above, Al introduced by laser ablation into a combined NBI and ECRH discharge is lost faster than neoclassically. (Similar results are reported for Si from the Heliotron E experiment /7/.) Using the same transport coefficients for the oxygen transport to model the total radiation requires an increased oxygen influx from the walls.

In this section the confinement behaviour of the background plasma, protons and electrons during this phase will be discussed.

Starting from ECRH target plasmas NBI leads to density increases of  $\dot{N}_e \approx 0.5 - 2 \times 10^{20} \text{ s}^{-1}$ , as in NBI discharges starting from OH target plasmas, which can be explained by the total particle

influx from the neutral beams (ECRH switched off after transition phase). There is no saturation of the density increase during the injection phase, which leads to particle confinement times in the  $\tau_p \approx 100$  ms range. Impurity transport and particle confinement show no difference from those measured earlier /1/.

With an additional ECRH pulse during NBI, however, the line density increase levels off and stays constant, with a significant increase in the  $H_\alpha$  signal. An influence of ECRH on the time evolution of the density has also been observed in tokamaks /8,9/. At electron densities  $n_{e0}$  well below  $n_{e,crit.}$ , core heating is observed, while for  $n_{e0}$  approaching  $n_{e,crit.}$ , edge heating is seen from ECE /10/, but even for  $n_{e0} > n_{e,crit.}$  during ECRH  $\int n_e dl$  stays constant. Two possible explanations for this behaviour have been given /8/:

- a) In addition to impurity confinement, the electron confinement is also decreased, or
- b) the gas flux from the walls is ionized by ECRH power outside the last closed flux surface, reducing the gas flux penetrating through the scrape off layer and thus allowing constant density with electron confinement still unchanged.

So far, no clear-cut experimental proof for either one of these explanations can be given. In this position a discussion of both possibilities in a more or less phenomenological way seems appropriate.

- a) - Looking at the time history of the  $H_\alpha$  signal there is increased recycling (or loss of particles) even in the early ECRH target phase, when NBI starts and external fluxes are switched off (Fig. 5), with no density increase. After ECRH shut-off the density increases strongly with a sharp drop in the  $H_\alpha$  signal. With the second ECRH pulse applied later in the discharge  $\int n_e dl$  stays constant and  $H_\alpha$  increases, this being followed by a drop and a corresponding density increase after the ECRH is switched off again.

- At the line density under consideration ( $5.7 \times 10^{14} \text{ cm}^{-2}$ ) a large fraction of the beam particles  $20 \times 10^{19} \text{ s}^{-1}$  (63 % of the NB power) hit the molybdenum beam dump. Owing to a surface temperature of  $\approx 400^\circ\text{C}$  all beam particles are expected to be released from the beam dump during the 100 ms interval of injection /11/ and used to refuel the plasma.

The source of fast ions, produced mainly by CX, amounts to  $12 \times 10^{19} \text{ s}^{-1}$ . Only a source of Selectrons  $\approx 7 \times 10^{19} \text{ s}^{-1}$  is estimated to lead to particle production, with 1/3 of the halo neutrals assumed to be reionized in addition to 1/3 of

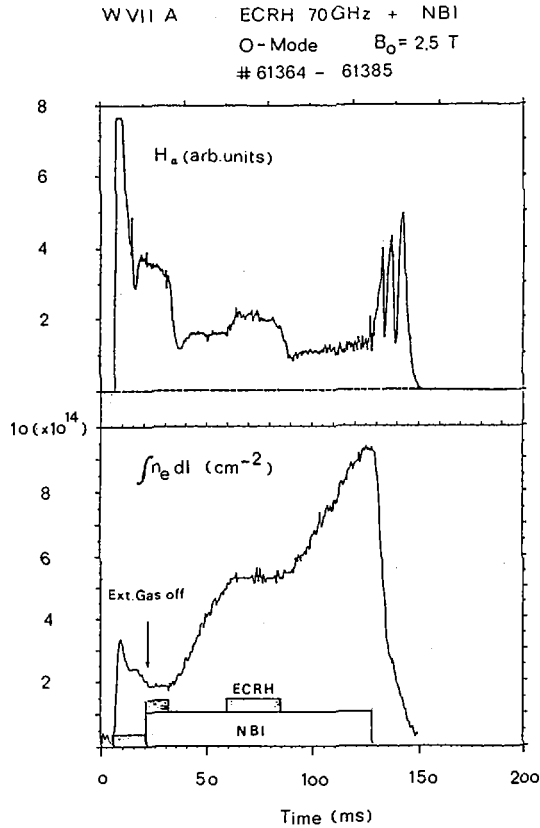


FIG. 5.  $H_\alpha$  signal and line integrated electron density versus time.  $H_\alpha$  signal taken at position of ICRH antenna.

the flux of fast ions which is created by proton and electron collision rather than by charge exchange.

A flux of  $10 \times 10^{19} \text{ s}^{-1}$  fast ions is lost via orbit losses (ODIN code calculations, including electric fields), is deposited in the SS wall of the vacuum vessel and is not released during the injection interval /9/. The reflux from the wall and limiter due to plasma losses with an expected particle confinement time of  $\tau_p \approx 100$  ms during the pure NBI phase and a recycling coefficient of 0.7

( $N_{e,\text{total}} = 8.4 \times 10^{18}$ ) is also small compared with the flux from the beam dump, which thus appears to be the main particle source.

- Now, if during the  $\dot{N}_e \approx 0$  phase with ECRH applied a particle confinement time of  $\tau_p \approx 100$  ms were to be maintained, a

flux of  $2.5 \times 10^{19} \text{ s}^{-1}$  particles would be sufficient, which is of the order of the flux of particles directly produced by the beam.

The ECRH power would therefore have to decouple the large hydrogen flux out of the beam dump from the plasma almost completely.

Density profiles during and after ECRH, however, show little change and thus do not support this explanation. In addition, the ionization length by electron collisions for thermal hydrogen atoms released at the beam dump is long enough to penetrate into the non-ergodic region, where particles are confined on flux surfaces. This would hold even for electron densities up to  $10^{12} \text{ cm}^{-3}$  within the ergodic region, because  $\langle \sigma v \rangle$  is only weakly dependent on temperature.

It is therefore not very likely that the neutral flux from the outside is strongly reduced by ECRH.

- b) - Poloidal plasma rotation shows no change during the ECRH pulse, so radial electric fields which are associated with the rotation still indicate good confinement.
- By application of an additional external gas flux  $\int n_e dl$  can be made to increase again during ECRH, which, however, would also be true with reduced particle confinement.

### Conclusion

The technique of an additional ECRH pulse applied to a NBI-sustained discharge has some very interesting aspects:

- Stationary discharges can be maintained with good energy confinement at tolerable radiation levels, whereas without additional ECRH pulse the density increases linearly with time along with high radiation losses due to impurity accumulation.
- There is experimental evidence that the electron particle confinement also deteriorates.
- For the ablated Al a faster loss of impurities from the central region is observed.

## REFERENCES

- [1] W VII-A TEAM, NI GROUP, Nucl. Fusion **25** (1985) 1593.
- [2] KICK, M., RINGLER, H., SARDEI, F., WELLER, A., et al., in Controlled Fusion and Plasma Heating (Proc. 13th Europ. Conf. Schliersee, 1986), Vol. 10c, Part I, European Physical Society (1986) 319.
- [3] STACEY, W.M., The Effect of Poloidal Electric Fields on Impurity Asymmetries and Transport in Tokamaks, Rep. GTFR 63, Georgia Institute of Technology Fusion Research (1986).
- [4] W VII-A TEAM, NI GROUP, in Fifth International Workshop on Stellarators (Proc. IAEA Tech. Comm. Mtg on Plasma Confinement and Heating in Stellarators, Schloss Ringberg), Vol. 1, CEC, Directorate-General XII — Fusion Programme, Brussels (1984) 259.
- [5] BOGEN, P., SCHWEER, B., RINGLER, H., OTT, W., J. Nucl. Mater. **111&112** (1982) 67.
- [6] WELLER, A., Measurements of the Radiation Energy Distribution in the Soft X-Ray Region in the Wendelstein VII-A Stellarator, Rep. IPP 2/277, Max-Planck-Institut für Plasmaphysik, Garching (1985).
- [7] UO, K., paper IAEA-CN-47/D-I-1, these Proceedings, Vol. 2.
- [8] ALIKAEV, V.V., et al., in Plasma Physics and Controlled Nuclear Fusion Research 1984 (Proc. 10th Int. Conf. London, 1984), Vol. 1, IAEA, Vienna (1985) 419.
- [9] FOM ECRH TEAM, TFR GROUP, in Controlled Fusion and Plasma Physics (Proc. 12th Europ. Conf. Budapest, 1985), Vol. 12, European Physical Society (1985) 60.
- [10] ERCKMANN, V., et al., Plasma Phys. **28** (1986) 1277.
- [11] MOELLER, W., SCHERZER, B., private communication, 1986.



# STABLE ACCESS TO SECOND STABILITY REGIME IN LARGE-ASPECT-RATIO TORSATRON/HELIOTRON CONFIGURATIONS\*

B.A. CARRERAS, L. GARCIA  
Fusion Energy Division,  
Oak Ridge National Laboratory,  
Oak Ridge, Tennessee

L.A. CHARLTON, J.A. HOLMES, V.E. LYNCH  
Computing and Telecommunications Division,  
Martin Marietta Energy Systems, Inc.,  
Oak Ridge, Tennessee

P.H. DIAMOND  
Institute for Fusion Studies,  
The University of Texas at Austin,  
Austin, Texas

United States of America

## Abstract

### STABLE ACCESS TO SECOND STABILITY REGIME IN LARGE-ASPECT-RATIO TORSATRON/HELIOTRON CONFIGURATIONS.

Shear stabilization caused by beta-induced modification of the transform profile can give stable access to the second stability regime for Heliotron configurations to which an external toroidal field is added. This stabilization mechanism is effective for free boundary and fixed boundary modes. The existence of resistive instabilities and their implications for anomalous transport are also discussed. Saturated resistive pressure-gradient-driven turbulence is studied, and an accurate saturation criterion is proposed. The resulting predicted pressure diffusivity scales in a similar way as the mixing length estimate, but it is significantly larger in magnitude.

### 1. EFFECT OF TOROIDAL FIELD COILS ON THE STABILITY OF HELIOTRON CONFIGURATIONS

Two alternative routes to the second stability regime are possible for torsatron devices. One, for small-aspect-ratio configurations, relies on the deepening of the magnetic well with increasing  $\beta$ . This  $\beta$  self-stabilization mechanism [1] has been studied in detail for some configurations [2], and

---

\* Research sponsored by the Office of Fusion Energy, United States Department of Energy, under Contract No. DE-AC05-85OR21400 with Martin Marietta Energy Systems, Inc., and under Contract No. DE-FG05-80ET-53088 with the University of Texas.

the ATF device [3,4] has been designed to explore it. The second alternative, for higher aspect ratio configurations, relies on the increase of shear with increasing  $\beta$ . This stabilization mechanism should be able to eliminate the most unstable modes in Heliotron-type configurations and permit the achievement of high- $\beta$  plasmas.

If one relies on the increase of shear with  $\beta$ , it is necessary to allow the equilibrium to relax to a true stellarator (zero-current) equilibrium and let the transform profile change accordingly. Therefore, slow heating and long pulses are essential in gaining access to the second stability regime for this type of configuration. It is also important to select the transform profile in a way that places the most unstable surfaces in the high-shear region. This can be done for the Heliotron E configuration [5] by using toroidal field coils [6].

The studies presented in this paper are based on the stellarator expansion approach [7] to the equilibrium and stability of three-dimensional (3-D) configurations. For planar axis configurations, the stellarator expansion compares favorably with 3-D calculations [2,8]. Therefore, it is a useful approach for magnetohydrodynamic (MHD) studies. Details of the equations and numerical methods used for the calculations presented here can be found in Ref. [9]. For fixed-boundary calculations, the equilibrium equations are solved by the RSTEQ code and the linear stability equations by the full implicit FAR code. The latter solves the MHD equations for stellarator configurations derived by extending the stellarator expansion to the dynamical evolution problem [10]. Free-boundary stability has been studied using the STEP code described in Ref. [11]. This code uses a  $\delta W$  approach, with an optional conducting wall that can be placed at any distance from the plasma. This free-boundary code is a modified version of the tokamak MHD equilibrium and stability code PEST [12], which uses the stellarator expansion.

To study the effect of an additional toroidal field ( $B_T$ ), we have added 19 circular toroidal field coils to the standard helical coil Heliotron E model [6]. They are located at the beginning of each field period, and their radius is  $a_T = 0.59$  m. The addition of this toroidal field to that generated by the helical coils ( $B_0$ ) reduces the rotational transform  $\iota$  and increases the plasma minor radius. In general, we have assumed that a limiter is used to keep the plasma aspect ratio constant. The reduction of  $\iota$  results in an increase in the magnetic axis shift at finite  $\beta$ . The larger shift gives a deeper magnetic well. This affects the plasma core stability but not the stability at the  $\iota = 1$  surface.

The stability properties of the  $n = 1$  internal mode are very sensitive to the magnitude of the added toroidal field. When the added toroidal field is 15% of the total field, the  $n = 1$  internal mode is stable for all  $\beta$  values considered. As in the case of the standard Heliotron E configuration, the dominant component of the  $n = 1$  mode is the ( $m = 1; n = 1$ ). This component, for  $\beta$  values near the threshold ( $\beta_0 \gtrsim 3\%$  for  $B_T/B_0 \leq 10\%$ ), is very localized radially. It is then reasonable to assume that the stability properties of the  $n = 1$  mode depend mostly on local quantities at the  $\iota = 1$  surface. For a constant  $\beta$  value and increasing  $B_T/B_0$ , the linear growth rate decreases, the shear increases, and  $V''$  becomes increasingly positive. Therefore, since the overall effect is stabilizing, the shear stabilization is the dominant effect. As the  $n = 1$  internal mode is stabilized by the effect

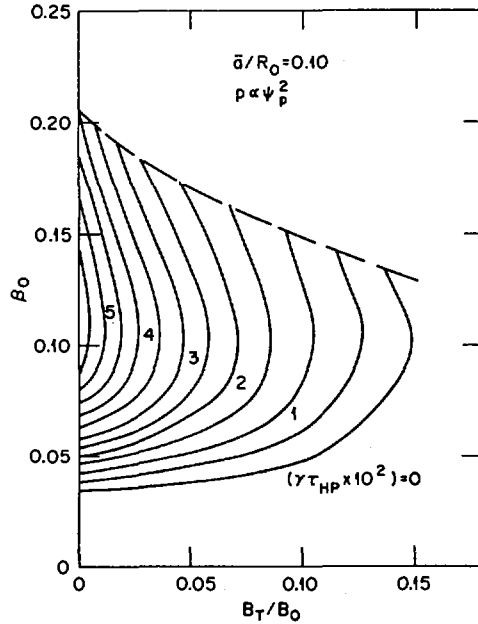


FIG. 1. Fixed boundary stability:  
Constant linear growth rate contour plots.

of the added toroidal field, the critical stability  $\beta$  for this mode becomes higher. All these effects are summarized in Fig. 1, where lines of constant  $n = 1$  linear growth rate in the  $\beta - B_T$  plane have been plotted. This figure also shows the critical equilibrium  $\beta$  contour (dotted line). For  $B_T/B_0 \gtrsim 0.15$ , the  $\beta$  limitation is due only to equilibrium failure. In this situation, peak  $\beta$  well above 10% could be achieved in the Heliotron E device.

The results shown in Fig. 1 are for a strongly unstable pressure profile,  $p \propto \psi^2$ . For more favorable profiles, the toroidal field required to stabilize the  $n = 1$  mode is much smaller. For instance, for the  $p \propto \psi^3$  pressure profile, only a 5% increase of the toroidal field is required. In this case, even higher values of  $\beta$  could be attained in the Heliotron E device.

Internal pressure-driven modes, when they are unstable, have growth rates that increase with  $n$ . Therefore, higher  $n$  modes have higher growth rates than the  $n = 1$  mode. However, the numerical results show that their linear instability threshold is close to the  $n = 1$  mode threshold. We have studied the stability of Heliotron E plasmas to  $n = 2$  modes with varying toroidal fields. The marginal stability contours in the  $\beta - B_T$  plane are nearly identical to those for the  $n = 1$  mode. Therefore, the calculated marginal stability contours for the  $n = 1$  mode can be taken as the marginal stability contours for all  $n$  modes.

We can also see from Fig. 1 that the self-stabilization effect can be strong enough to totally stabilize the  $n = 1$  mode and not merely reduce

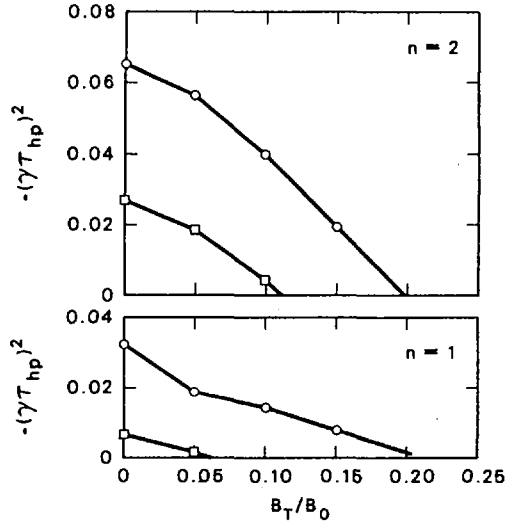


FIG. 2. Free boundary stability:  
Linear growth rates for fixed  $\beta_0 = 8\%$ .

its linear growth rate. The cause for the  $\beta$  self-stabilization effect is the same as for the added toroidal field. As  $\beta$  increases, the transform changes to maintain zero current in each flux surface. In doing so, the transform at the magnetic axis increases, that at the plasma edge decreases, and the whole profile changes. This change produces an increase of the shear at the  $\iota = 1$  surface. As in the case of the addition of a toroidal field,  $V''$  stays positive at the  $\iota = 1$  surface and increases with  $\beta$ . Therefore, the second stability region in Heliotron-type configurations is again due to shear stabilization and not to the deepening of the magnetic well.

Let us now consider stability to external modes. As the conducting wall is moved away from the plasma, the  $n = 1$  linear growth rate increases, particularly at high  $\beta$  ( $\beta_0 > 6\%$ ). The eigenmode structure also changes, becoming less localized and more like a kink mode. The qualitative effect of removing the conducting wall is very similar to that observed for a shifted-in ATF-type configuration [13].

The effect of the added toroidal field on the free-boundary modes is analogous to the effect on the internal modes (Fig. 2). There is a stabilization of the internal modes with increasing  $B_T/B_0$ . However, somewhat larger values of  $B_T/B_0$  are required for full stabilization when the conducting wall is absent. In Fig. 2, the result for the linear growth rate without the conducting wall (open circles) is contrasted with the case with the conducting wall at a distance of half the plasma radius (open squares). The marginal points for the latter are very close to those for the internal modes. This situation is probably the most relevant one for the experiment. Therefore, the conclusions drawn from internal mode stability are not modified by the most realistic assumptions on the position of the conducting wall.

## 2. EFFECT ON CONFINEMENT OF THE RESISTIVE PRESSURE-GRADIENT-DRIVEN TURBULENCE

For configurations relying on shear stabilization to access high  $\beta$ , a question remains: resistive mode stability and its implications for confinement. The resistive interchange in particular is believed to be a potential cause of anomalous transport [14] in devices with average unfavorable curvature, which is the case for the torsatron near the plasma edge. Thus, it is important to consider the effects of resistive pressure-gradient-driven turbulence.

Previous work on the theory of resistive pressure-gradient-driven turbulence has consisted primarily of the application of mixing length arguments [15] and dimensional analysis techniques [16]. Mixing length arguments, such as  $D = \gamma/k_z^2$ , attempt to relate the properties of fully evolved turbulence to the characteristic scales of the underlying linear instability by semiquantitatively balancing nonlinearity with the linear drive. Dimensional analysis techniques use the scale transformation symmetries of the basic, nonlinear equations. Both yield similar results for predicted fluctuation levels, diffusivities, etc. These predictions are in quantitative agreement with the results of numerical simulations performed for relatively high resistivity and high velocity. The agreement was particularly good for predicted scalings with  $\beta_p$  and  $dp_0/dr$ . However, when compared directly with experimental results, the predicted thermal diffusivities were, in general, too small to explain the observed phenomena.

There are several deficiencies in the theoretical underpinnings of the mixing length and dimensional analysis approaches. First, mixing length predictions are derived from a heuristic procedure of balancing nonlinearity with linear drive. In particular, no genuine saturation criterion based on considerations of energetics is satisfied or even established. Second, the dimensional analysis approach, as implemented in Ref. [16], omits the effects of dissipation and the role of scales dominated by dissipative damping. The omission of damping, which is analogous to the lack of a well-defined saturation criterion, explains why the (zero damping) mixing length predictions agree with those of dimensional analysis.

The simple model of the resistive interchange instability used in this paper contains the main physics properties of the instability, while taking the average pressure gradient as the only source of free energy. The model consists of two equations:

$$\frac{dU}{dt} = -\frac{1}{\eta\rho_m} \nabla_{\parallel}^{(0)2} \phi + \frac{1}{\rho_m} \hat{z} \cdot \left[ \vec{\nabla} \Omega \times \vec{\nabla} \tilde{p} \right] + \mu \nabla_{\perp}^2 U \quad (1)$$

$$\frac{d\tilde{p}}{dt} = \chi_{\perp} \nabla_{\perp}^2 \tilde{p} - \frac{1}{r} \frac{\partial \phi}{\partial \theta} \frac{dp_0}{dr} \quad (2)$$

Here  $\nabla_{\parallel}^{(0)}$  means that only the equilibrium magnetic field is included in the parallel derivative (electrostatic approximation). A detailed analysis of this model is given in Ref. [17]. The fluid viscosity  $\mu$  and thermal diffusivity  $\chi_{\perp}$  are retained in the analysis and calculations. The viscosity and thermal diffusivity guarantee the existence of a stable large- $m$  dissipation range, which serves as an energy sink. In the numerical calculation

the electromagnetic model is considered, and the pressure gradient is held fixed, thus avoiding possible confusion of quasi-linear and nonlinear effects. Sufficient large- $m$  resolution is retained, and the existence of a saturated state is demonstrated by well-converged numerical calculations.

The resistive pressure-gradient-driven turbulence saturates by the mechanism of nonlinear transfer of energy from large to small scales. An analytical theory of such a process requires a renormalized two-point theory of the fluctuation spectrum to describe the nonlinear coupling of the low- $m$  energy-containing region to the large- $m$  dissipation range. In the case when a few low- $m$  modes dominate the energy spectrum, an alternative, more tractable calculation is to determine the energy outflow from the low- $m$  modes required for saturation. Such a tactic is implemented by deriving low- $m$  renormalized response equations and then determining the level of diffusion, representative of the spectrum-averaged rate of coupling to smaller scales, required for low- $m$  saturation. The latter method is used in this paper.

The calculation of energy outflow from low- $m$  modes is only meaningful if there is sufficient large- $m$  dissipation so that a saturated state is attainable. Dissipation in both the vorticity and pressure evolution equations is required for a nontrivial stationary state ( $dp_0/dr \neq 0$ ). A related requirement is that viscous dissipation and resistive diffusion are required in the vorticity evolution equation. The need for viscous dissipation is a consequence of the fact that nonlinear transfer to large  $m$  ultimately couples to modes with  $m$  numbers for which  $m/r > W_m^{(0)}$ . Such  $m$  numbers correspond to modes in the fast interchange regime, with (ideal) growth rates for which resistive field line diffusion is dynamically irrelevant. Thus, substantial viscous dissipation is required for the necessary stabilization of short-wavelength interchange modes.

Renormalized response equations, which describe the nonlinear dynamics of resistive pressure-gradient-driven modes in the presence of turbulence, can be derived [17]. For long-wavelength modes, a saturation condition is established by setting the time derivative terms to zero. Then,

$$\mu \nabla_{\perp}^2 U_{\vec{k}} - \vec{\nabla}_{\perp} \mu_{xx} \cdot \vec{\nabla}_{\perp} U_{\vec{k}} = \frac{1}{\eta \rho_m} k_{\perp}^2 \phi_{\vec{k}} - \frac{i}{\rho_m} \frac{d\Omega}{dr} k_y \tilde{p}_{\vec{k}} \quad (3)$$

$$-\chi_{\perp} \nabla_{\perp}^2 \tilde{p}_{\vec{k}} - \vec{\nabla}_{\perp} D_{xx} \vec{\nabla}_{\perp} \tilde{p}_{\vec{k}} = -i \frac{dp_0}{dr} k_y \phi_{\vec{k}} \quad (4)$$

where the nonlinear diffusion and viscosity coefficients are

$$D_{xx} = \sum_{m', n'} \left( \frac{m'}{r} \right) \langle \phi^2 \rangle_{\vec{k}', \Gamma_{2\vec{k}''}^{-1}} \quad (5)$$

$$\mu_{xx} = \sum_{m', n'} \left( \frac{m}{m''} \right)^2 \left( \frac{m'}{r} \right)^2 \langle \phi^2 \rangle_{\vec{k}', \Gamma_{1\vec{k}''}^{-1}} \quad (6)$$

Here,  $\Gamma_{1\vec{k}''}$  and  $\Gamma_{2\vec{k}''}$  are the propagators for the "beat mode"  $\vec{k}''$ . They can be approximated by the decorrelation rate, which corresponds to the

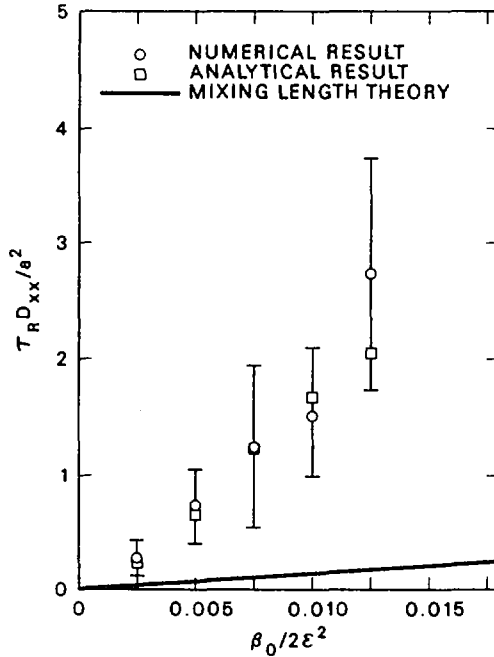


FIG. 3. Nonlinear diffusion coefficient.

characteristic rate of nonlinear interaction for resistive pressure-gradient-driven turbulence.

Assuming that there is a known relationship between  $\mu_{xx}$  and  $D_{xx}$ , Eqs. (3) and (4) define an eigenvalue problem. An approximate analytical solution valid for low  $m$  and low resistivity is

$$D_{xx} \simeq \gamma_m^{(0)} W_m^{(0)2} \Lambda^2 \quad (7)$$

where  $\gamma_m^{(0)}$  is the linear growth rate and  $W_m^{(0)}$  the linear mode width in absence of collisional dissipation. The factor  $\Lambda$ ,

$$\Lambda \equiv \frac{2}{3\pi} \ln \left[ \frac{\beta_0}{2\epsilon^2} \frac{a^2}{L_p r_c} \left( \frac{r}{m} \right)^4 \frac{64S^2}{\tau_R^2 (\mu + \mu_{xx}) (\chi_{\perp} + D_{xx})} \right] \quad (8)$$

is an enhancement factor over the mixing length theory prediction.

The main properties of the nonlinear diffusion coefficient  $D_{xx}$  are as follows. (1) The scaling with  $\beta$  is very close to linear, as in the mixing length prediction (Fig. 3). (2) The nonlinear  $D_{xx}$  is about an order of magnitude larger than the mixing length result due to the  $\Lambda^2$  factor (Fig. 3). (3) The correction factor gives a weak dependence on  $m$ , close to  $m^{-1}$ . (4) The dependence on  $\mu$  and  $\chi_{\perp}$  is weak for realistic values of these parameters. Once the relation between the coefficients  $D_{xx}$  and  $\mu_{xx}$

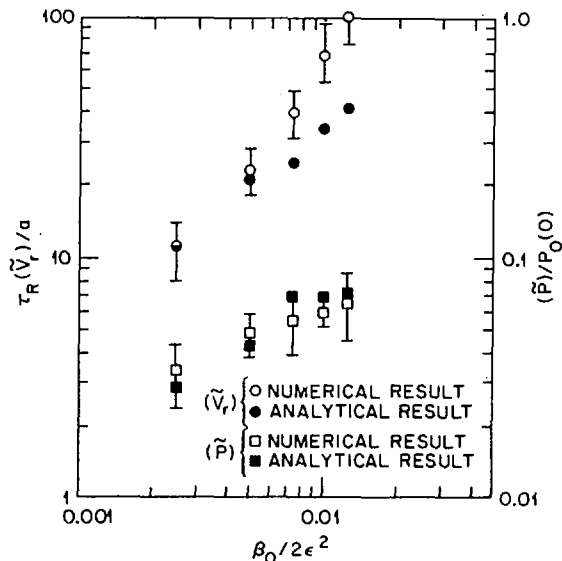


FIG. 4. Comparison between analytic and numerical results for saturation levels.

is known, we can estimate the turbulence level at saturation and the main physics parameters characterizing the turbulent state. In this way, we find that the mean square radial velocity and the rms pressure fluctuation are

$$\langle \tilde{V}_r^2 \rangle^{\frac{1}{2}} \cong \gamma_{\langle m \rangle}^{(0)} W_{\langle m \rangle}^{(0)} \Lambda^{\frac{5}{6}} \quad (9)$$

$$\langle \tilde{p}^2 \rangle^{\frac{1}{2}} \cong \left| \frac{dp_0}{dr} \right| W_{\langle m \rangle}^{(0)} \Lambda^{\frac{7}{6}} \quad (10)$$

The characteristic nonlinear width of the velocity fluctuation is  $\Delta_m \cong W_m^{(0)} \Lambda^{\frac{1}{6}}$ , and the decorrelation rate is  $\Delta\omega_m \cong \gamma_m^{(0)} \Lambda^{\frac{5}{6}}$ .

The nonlinear stability of a sequence of equilibria with different values of  $\beta_0/2\epsilon^2$  has been numerically studied. The values of the  $V_r$  and  $\tilde{p}$  fluctuations at saturation are given in Fig. 4. These values have been calculated by averaging over time, and the error bar corresponds to one standard deviation. The analytical results are calculated with Eqs. (9) and (10). The values for  $\langle m^2 \rangle$  used in those equations are taken from the numerical results. The scaling with  $\beta$  is very well reproduced by the analytical model, and the agreement shown in Fig. 4 is good. The importance of the logarithmic factor modifying the mixing length is clear.

The losses caused by the induced electron heat conductivity can be estimated by modifying the result of Ref. [14]. Using the nonlinear width  $\Delta$  and the decorrelation rate  $\Delta\omega_m$  instead of the linear width and linear growth rate, the calculated  $\chi_e$  is

$$\chi_e \cong \epsilon \left( \frac{L_q^2}{r_c L_p} \right)^{\frac{3}{2}} \beta_p^{\frac{3}{2}} v_{te} a \frac{1}{S} \Lambda^{\frac{3}{2}} \quad (11)$$

The enhancement of  $\chi_e$  at finite  $\beta$  can be up to an order of magnitude.

## REFERENCES

- [1] MIKHAILOVSKII, A.B., SHAFRANOV, V.D., *Zh. Eksp. Teor. Fiz.* **66** (1984) 190; *Sov. Phys. — JETP* **66** (1974) 88.
- [2] CARRERAS, B.A., et al., *Phys. Fluids* **26** (1983) 3569.
- [3] LYON, J.F., CARRERAS, B.A., et al., *Fusion Technol.* **10** (1986) 179.
- [4] CARRERAS, B.A., HICKS, H.R., HOLMES, J.A., LYNCH, V.E., NEILSON, G.H., *Nucl. Fusion* **24** (1984) 1347.
- [5] UO, K., *Plasma Phys.* **13** (1971) 243.
- [6] CARRERAS, B.A., GARCIA, L., LYNCH, V.E., *Phys. Fluids* **29** (1986) 3356.
- [7] GREENE, J.M., JOHNSON, J.L., *Phys. Fluids* **4** (1961) 875.
- [8] HERRNEGGER, F., MERKEL, P., JOHNSON, J.L., *J. Comput. Phys.* **66** (1986) 445.
- [9] LYNCH, V.E., CARRERAS, B.A., CHARLTON, L.A., HENDER, T.C., GARCIA, L., et al., *J. Comput. Phys.* **66** (1986) 411.
- [10] STRAUSS, H.R., *Plasma Phys.* **22** (1980) 733.
- [11] ANANIA, G., JOHNSON, J.L., *Phys. Fluids* **26** (1983) 3070.
- [12] JOHNSON, J.L., et al., *J. Comput. Phys.* **32** (1979) 212.
- [13] HENDER, T.C., et al., *Nucl. Fusion* **25** (1985) 1463.
- [14] SHANG, K.C., CARRERAS, B.A., *Phys. Fluids* **28** (1985) 2027.
- [15] AN, Z.G., et al., in *Plasma Physics and Controlled Nuclear Fusion Research 1984* (Proc. 10th Int. Conf. London, 1984), Vol. 2, IAEA, Vienna (1985) 231.
- [16] CONNOR, J.W., TAYLOR, J.B., *ibid.*, p. 13.
- [17] CARRERAS, B.A., GARCIA, L., DIAMOND, P.H., *Theory of Resistive Pressure-Gradient-Driven Turbulence*, Rep. ORNL/TM-10150, Oak Ridge National Lab. (1986).



## THREE-DIMENSIONAL MHD STUDIES OF IDEAL AND RESISTIVE INTERCHANGE MODES IN HELIOTRON CONFIGURATIONS

M. WAKATANI, K. ICHIGUCHI, H. SUGAMA, K. ITOH  
 Plasma Physics Laboratory,  
 Kyoto University,  
 Kyoto, Japan

A. HASEGAWA<sup>1</sup>  
 AT&T Bell Laboratories,  
 Murray Hill, New Jersey,  
 United States of America

J. TODOROKI, H. NAITOU  
 Institute of Plasma Physics,  
 Nagoya University,  
 Nagoya, Japan

### Abstract

#### THREE-DIMENSIONAL MHD STUDIES OF IDEAL AND RESISTIVE INTERCHANGE MODES IN HELIOTRON CONFIGURATIONS.

In Heliotron E high beta experiments, the highest average beta value,  $\bar{\beta} = 2\%$ , is obtained for a flat profile,  $\beta(0)/\bar{\beta} \leq 1.5$ , while pressure driven instabilities are observed for peaked profiles. The beta value at the magnetic axis is denoted by  $\beta(0)$ . By measuring density fluctuations and soft X-ray fluctuations, sawtooth oscillations accompanied by an  $m = 1/n = 1$  mode are observed for  $\beta(0)/\bar{\beta} \approx 2.5-3$ ; an internal disruption accompanied by an  $m = 3/n = 2$  mode is observed for  $\beta(0)/\bar{\beta} \geq 3-4$ . These fluctuations are well explained in terms of non-linear evolution of the resistive interchange mode (G mode) under the assumption of multi-helicity. — Transport analysis of Heliotron E predicts anomalous transport in the edge region; a candidate for explaining the transport is G mode turbulence. Model equations including the electron temperature Larmor radius effect are derived. The linear growth of the G mode with the electron diamagnetic frequency is examined, and three-dimensional non-linear calculations of density and potential fluctuations are performed to obtain a saturated state for a fixed background density profile in the electrostatic approximation. — To improve the beta limit of heliotron configurations in the context of ideal MHD, the effect of an additional vertical field applied to shift the magnetic axis, on the ideal interchange instabilities, is studied by two approaches: three-dimensional MHD equilibrium and stability code (BETA code) calculations and H-ERATO code calculations, which are a modification of the ERATO code for tokamaks, based on the assumption of the averaging method for stellarator fields. According to the BETA code, the  $m = 1/n = 1$  internal mode is completely stabilized by the outward shift of the magnetic axis for  $\beta \leq 5-6\%$  in heliotron configurations. The MHD equilibria for the H-ERATO code are calculated by a code which is able to optimize the pressure profile according to the Mercier criterion and the local

<sup>1</sup> Co-operative research supported by the United States Department of Energy, under Contract No. DE-F40580ET53088.

ballooning stability. This study shows that stability against the low mode number interchange instability is correlated with the local mode stability in the Heliotron E case. Improvement of the beta limit by the additional vertical field is also confirmed by the H-ERATO code.

## 1. $m = 3/n = 2$ RESISTIVE INTERCHANGE MODE DRIVEN INTERNAL DISRUPTION

A recent high beta experiment in Heliotron E reveals that the density fluctuations as measured by the FIR laser and correlated with the internal disruption have a spatial structure which is not explained by the  $m = 1/n = 1$  mode only [1]. In the paper discussing the first high beta plasma confinement, both the pressure driven sawtooth oscillation and the internal disruption in the soft X-ray signals were related to the  $m = 1/n = 1$  mode, where  $\beta(0)/\bar{\beta} \approx 2.5-3$  and  $3.6\% \geq \beta(0) \geq 2\%$  [2]. After the neutral beam injection power has increased from 2 MW to 4 MW, the density profile peaking is enhanced in the case of weak or no gas puffing. When density fluctuations with  $m = 3/n = 2$  mode structure were observed for  $\beta(0)/\bar{\beta} \geq 3-4$  and  $\beta(0) \geq 2\%$ , internal disruption or flattening of the density profile occurred successively. To examine the relationship between  $m = 3/n = 2$  and  $m = 1/n = 1$  modes, we extend the numerical studies of the non-linear evolution of the  $m = 1/n = 1$  resistive interchange mode in Ref. [3] to multi-helicity calculations. Line integrals of the pressure profile are compared with the experimental observation of the density fluctuations, by assuming uniform temperature.

For a peaked profile, the linear growth of the  $m = 3/n = 2$  mode is faster than that of the  $m = 1/n = 1$  mode [4]. Thus, the non-linear behaviour of the  $m = 3/n = 2$  mode becomes dominant for the pressure profile  $p = p_0 (1-r^2)^4$  and  $\beta(0) = 3\%$ , as is shown in Fig. 1. Here, the magnetic Reynolds number  $S$  is assumed to be  $5 \times 10^3$ ; twenty modes given by the mode selection rule introduced in the multi-helicity non-linear tearing mode calculation are included [5]. Figure 2 demonstrates the relative density fluctuations at  $T = 288$ , normalized by the poloidal Alfvén transit time, and the density profile along the  $\theta = 0^\circ$  line, where  $\theta$  is a poloidal angle. The peaked density profile is dominantly flattened by the non-linear evolution of the  $m = 3/n = 2$  mode. Figure 2 agrees with the experimental data of Ref. [1].

Thus, the internal disruption caused by the  $m = 3/n = 2$  resistive interchange mode resonant at the  $\iota = 2/3$  surface limits the central beta value for highly peaked pressure profiles in Heliotron E. The beta limit is, however, improved by tailoring the pressure profile to obtain broad profiles [6].

## 2. FINITE LARMOR RADIUS (FLR) EFFECTS ON G MODE

In setting up the FLR-MHD equations, the FLR terms are introduced through both the ion pressure and the electron pressure gradients [7]. The former FLR effect

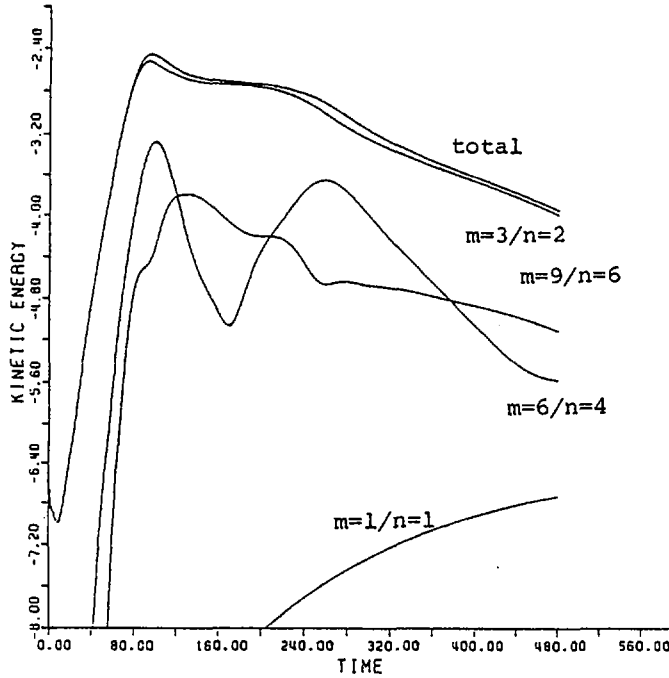


FIG. 1. Evolution of kinetic energy of multi-helicity G mode for strongly peaked pressure profile in H-E.

was examined in the case of an ideal interchange mode in Heliotron E; a destabilizing effect of FLR was pointed out [8]. Here, we are interested in the latter FLR effect on the G mode. Reduced MHD equations including the parallel electron pressure gradient in Ohm's law, which introduces the electron diamagnetic frequency, can be derived on the basis of the stellarator expansion and an averaging method [9].

In the electrostatic limit, Ohm's law yields

$$\mathbf{j}_{\parallel} = \frac{\epsilon}{\nu} \nabla_{\parallel} (\varphi - n) \quad (1)$$

where  $\mathbf{j}_{\parallel}$ ,  $\varphi$  and  $n$  are the parallel current normalized by the sound velocity,  $\mathbf{j}_{\parallel}/n_0 e C_s$ , the normalized electrostatic potential  $e\varphi/T$  and the normalized density  $n/n_0$ , respectively. The temperature  $T$  is assumed to be constant,  $\nu$  is the normalized collision frequency, and  $\epsilon = a/R$ . By using Eq. (1), the continuity equation is written as

$$\frac{\partial n}{\partial t} - [n, \varphi] = \frac{\epsilon^2}{\nu} \nabla_{\parallel} (n - \varphi) \quad (2)$$

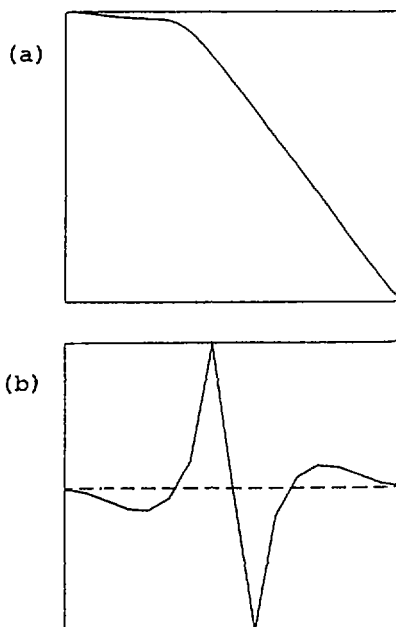


FIG. 2. (a) Density profile along  $\theta = 0^\circ$  line and (b) line density fluctuation profile at  $T = 288$ .

and the equation of motion is reduced to

$$\frac{\partial}{\partial t} \nabla_{\perp}^2 \varphi - [\nabla_{\perp}^2 \varphi, \varphi] = \frac{\epsilon}{\rho^2} [\Omega, n] + \frac{\epsilon^2}{\nu \rho^2} \nabla_{\parallel}^2 (n - \varphi) \quad (3)$$

where the perpendicular length is normalized by  $a$ , the parallel length is normalized by  $R$ , and the time is normalized by  $\omega_{ci}(\rho/a)^2 t$ . Here,  $\rho$  is Larmor radius measured by the electron temperature and  $\omega_{ci}$  is the ion cyclotron frequency. The brackets are Poisson brackets. The curvature term,  $\Omega$ , is given by

$$\Omega = N\epsilon/\ell \left\{ \frac{1}{2} r^2 \iota(r) + \int_0^r r \iota(r) dr \right\}$$

where  $\ell$  is the pole number and  $N$  the pitch number. When the curvature term is neglected, Eqs (2) and (3) become the model equation derived by Hasegawa and Wakatani [10, 11] for resistive drift wave turbulence. A cylindrical plasma model is employed and the rotational transform is assumed as  $\iota = 0.51 + 1.69r^{2.5}$ . Figure 3 shows a linear mode structure of the G mode of  $m = 1/n = 1$ , including the electron diamagnetic effect for  $\nu = 10^{-3}$  and  $\rho/a = 0.02$ . The potential and density pertur-

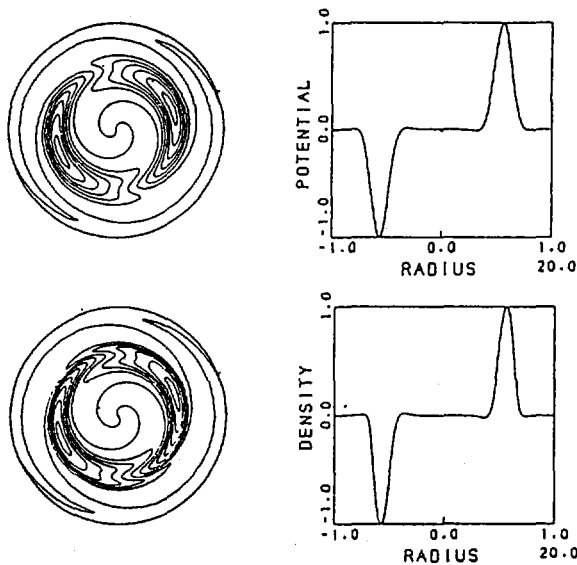


FIG. 3. Linear mode structure of G mode including FLR effect with  $m=1/n=1$ .

bations become close to the Boltzmann relation  $n \approx \varphi$  and show diamagnetic rotation with an angular frequency of  $\omega_r = 0.6445$ . The growth rate is  $\omega_i = 2.222$  and approximately scales like  $\nu^{1/2}$ . Non-linear calculations for the G mode turbulence described by Eqs (2) and (3) are performed under the assumption of a fixed background density profile. When low mode resonant surfaces such as  $\iota = 1$  and  $\iota = 2/3$  exist inside the plasma, no saturation of density and potential fluctuations was obtained without quasi-linear flattening of the background density profile in the present calculation using 59 modes. For a configuration with  $\iota = 0.68 + 0.27r^2$  and  $n(r) = n_0 \{0.7\exp(-2r^2) + 0.3\}$ , a saturated turbulent state was obtained by adding a small diffusion term on the right hand side of Eq. (2) for the fixed background density profile. The wavenumber spectrum is broad, and the average fluctuation level is  $\bar{n}/n_0 \approx 0.06$ .

### 3. BETA LIMIT IMPROVEMENT OF HELIOTRONS

The problem of MHD equilibrium and stability in fully three-dimensional geometry can be treated numerically by applying the classical variational principle of MHD. This is implemented in the BETA code [12]. Stability against the  $m = 1/n = 1$  internal mode is investigated in an H-E model configuration for currentless equilibria [13]. The beta limit in the first stability region is  $\bar{\beta} \approx 2\%$ , which is consistent with the maximum beta value obtained for H-E. For  $\bar{\beta} \geq 5\%$ , a second

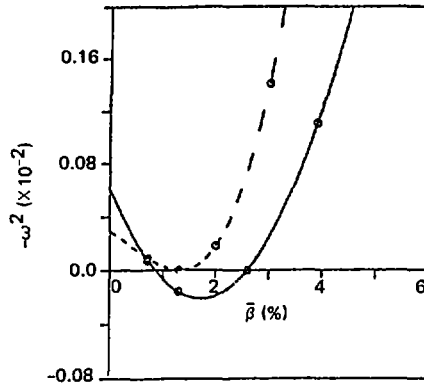


FIG. 4. Eigenvalue of  $m = 1/n = 1$  mode versus average beta in H-DR. Solid line shows case of standard configuration; dashed line shows case of outward magnetic axis shift.

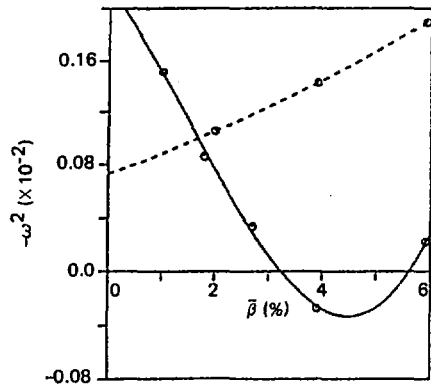


FIG. 5. Eigenvalue of  $m = 1/n = 1$  mode versus average beta in H-H. Solid line shows case of standard configuration; dashed line shows case of outward magnetic axis shift.

stability region appears. Stability against the same mode was examined for H-E currentless equilibria modified by an additional vertical field. By introducing about 15% shift of magnetic axis with respect to the averaged radius, the  $m = 1/n = 1$  internal mode is completely stabilized. The same stability examination was also tried for other heliotrons  $p = p_0 (1 - r^2)^2$  in the straight approximation other heliotrons: Heliotron DR(H-DR) and Heliotron H(H-H). H-DR has  $R/\bar{a} \approx 14$  and  $l = 2/N = 15$ , where  $\iota(0) \approx 0.8$  and  $\iota(a) \approx 1.3$ . The first stability beta limit of 0.8% is smaller than that of H-E (see Fig. 4). Here, negative  $-\omega^2$  corresponds to instability. By applying an additional vertical field to shift the magnetic axis outside, the  $m = 1/n = 1$  internal mode disappears (as is shown in Fig. 4).

It is well known that the  $m = 1/n = 1$  internal mode becomes dangerous when the  $\iota = 1$  surface is inside the plasma. When it is removed into the outer region, an

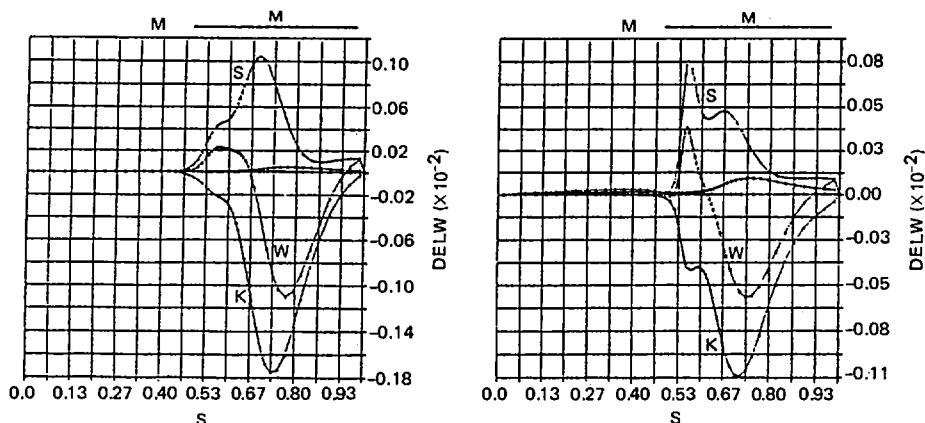


FIG. 6. Distributions of destabilizing potential energy (K), dominant stabilizing potential energy (S) and total potential energy (W) for  $n = 1$  mode (left) and  $n = 2$  mode (right). M designates regions violating Mercier criterion.

example of an  $\ell = 2$  torsatron is the ATF. On the other hand, an example of a heliotron with rotational transform larger than unity,  $\iota(0) \approx 1.2$  and  $\iota(a) \approx 1.6$ , is H-H; it also has  $\ell = 2/N = 15$  and  $R/\bar{a} \approx 14$ . In Fig. 5, the first stability beta limit is  $\bar{\beta} = 3.2\%$ , which is determined by the non-resonant mode of  $m = 1/n = 1$ . H-H is more stable than H-E. This may be due to the removal of the  $\iota = 1$  surface. The stabilization by the outward shift of the magnetic axis also works in H-H, as is shown by the dashed line in Fig. 5.

Thus, the BETA code predicts that the most dangerous mode in heliotron configurations can be suppressed by appropriately shifting the magnetic axis outside. The stabilizing mechanism is magnetic well formation by the finite beta effect.

We have developed a new formulation of the averaging method on the basis of an asymptotic expansion of the MHD equations with a co-ordinate transformation technique [14]. The H-APPOLO and H-ERATO codes have been developed for equilibrium and stability analyses, respectively. H-APPOLO calculates free boundary currentless equilibria, tests the ballooning and Mercier criteria on each magnetic surface, and is able to produce an optimized pressure profile for local modes. H-ERATO is the helical torus version of the ERATO stability code for tokamaks designed to test low  $n$  global mode stability [15].

First, the low  $n$  mode stability of H-E free boundary currentless equilibria is examined. A beta limit smaller than  $\bar{\beta} = 2\%$  is given by the  $n = 1$  mode localized around the  $\iota = 1$  surface, when the pressure gradient on this surface is substantial. When the pressure profile becomes flatter or the peak of the pressure gradient is moved outside, the  $m = 2/n = 3$  internal mode or the  $m = 1/n = 2$  free boundary mode becomes unstable so as to limit the beta value. In H-E, it seems that the pressure profile favourable to Mercier and ballooning stabilities is also favourable to the low  $n$  global modes. Figure 6 shows that the Mercier stability is violated near the

unstable region of the global modes with  $n = 1$  and  $n = 2$  for a peaked pressure profile of  $\bar{\beta} = 2\%$ .

Therefore, first, pressure profile optimization with respect to the local mode is carried out in the H-APPOLO code; then the result is put into the H-ERATO code to check the stability against  $n = 1, 2, 3$  modes. When the additional vertical field is chosen so as to shift the magnetic axis outward as is done in the BETA code study, self-stabilization occurs, or the magnetic axis is shifted significantly by the finite beta effect, and a magnetic well is created around the central region. The pressure gradient in the central region increases as a result of pressure profile optimization, and a plasma with  $\bar{\beta} = 2.5\%$  is easily obtained; it is stable against the  $n = 1, 2, 3$  modes. As was discussed in Section 1, this kind of peaked pressure profile is, however, unstable with respect to the resistive interchange mode; internal disruption may occur in H-E before self-stabilization is expected to take place. To enter the stable region with a highly peaked profile, a high beta plasma of high temperature will be required.

## REFERENCES

- [1] ZUSHI, H., et al., submitted to Nucl. Fusion.
- [2] HARRIS, J.H., et al., Phys. Rev. Lett. **53** (1984) 2242.
- [3] WAKATANI, M., SHIRAI, H., YAMAGIWA, M., Nucl. Fusion **24** (1984) 1407.
- [4] YAMAGIWA, M., WAKATANI, M., NAKAMURA, Y., J. Phys. Soc. Jpn. **54** (1985) 15.
- [5] HICKS, H.R., et al., 3-D Nonlinear Calculations of Resistive Tearing Modes, Rep. ORNL/TM-7132, Oak Ridge National Laboratory (1981).
- [6] WAKATANI, M., IEEE Trans. Plasma Sci. **PS-9** (1981) 243.
- [7] HASEGAWA, A., WAKATANI, M., Phys. Fluids **26** (1983) 2770.
- [8] WAKATANI, M., SUGAMA, H., HASEGAWA, A., Phys. Fluids **29** (1986) 905.
- [9] YAGI, M., HASEGAWA, A., WAKATANI, M., submitted to J. Phys. Soc. Jpn.
- [10] HASEGAWA, A., WAKATANI, M., Phys. Rev. Lett. **50** (1983) 682.
- [11] WAKATANI, M., HASEGAWA, A., Phys. Fluids **27** (1984) 305.
- [12] BAUER, F., BETANCOURT, O., GARABEDIAN, P., Magnetohydrodynamic Equilibrium and Stability of Stellarators, Springer, New York (1984).
- [13] WAKATANI, M., ICHIGUCHI, K., BAUER, F., BETANCOURT, O., GARABEDIAN, P.R., to be published in Nucl. Fusion.
- [14] TODOROKI, J., to be published in J. Phys. Soc. Jpn.
- [15] GRUBER, R., RAPPAZ, J., Finite Element Methods in Linear Ideal Magnetohydrodynamics, Springer, New York (1985).

# SELF-CONSISTENT RADIAL ELECTRIC FIELD EVALUATIONS FOR THE TJ-II HELIAC

J. GUASP  
Asociación Euratom-JEN,  
Junta de Energía Nuclear,  
Madrid, Spain

## Abstract

### SELF-CONSISTENT RADIAL ELECTRIC FIELD EVALUATIONS FOR THE TJ-II HELIAC.

Confinement times and self-consistent ambipolar radial electric field values have been calculated by using the model introduced by K. Shaing et al. for helically trapped fluxes, together with the contribution of the 'corner' ripple term that, with a hypothesis of additivity, is taken from the banana plateau rippled expressions. The behaviour of the confinement times and of the self-consistent radial electric fields for the expected TJ-II conditions is discussed, as well as the three root situations appearing for the electric field.

TJ-II is a four-period helical axis stellarator of heliac type to be built at JEN [1, 2]; it has 1.5 m major radius, 0.20 m average plasma radius and an average toroidal magnetic field of 1 T.

Former confinement time and transport coefficient evaluations were done by using the Kovrizhnykh model [3, 4] with a simplified treatment for the corner ripple term; the results were presented elsewhere [5]. In this study, a different model based on a model by K. Shaing et al. [6, 7] is used together with a more realistic treatment for the corner ripple term [8].

To apply the model, we approximate the magnetic field intensity for TJ-II by the expression:

$$B = B_0 [1 - \epsilon_T \cos \theta - \epsilon_h \cos (\theta + m\varphi) - \delta \cos m\varphi] \quad (1)$$

where  $m = 4$  and  $\epsilon_T$  and  $\epsilon_h$  are toroidal and helical magnetic field modulations and  $\delta$  is the ripple due to the variation in position of the helically placed TF coil centres (the so-called 'corner' ripple) [1], which reflects one of the main differences between TJ-II and other stellarators, from the transport point of view.

For this work we have evaluated the parameters  $\epsilon_T$ ,  $\epsilon_h$ ,  $\delta$  and the radial dependence by means of a series expansion around the helical magnetic axis and by adjusting the resulting coefficients with the real surface average field intensity for TJ-II. This gives, for the usual references case (circular coil current 95 kA, helical coil current 219 kA, rotational transform at axis  $\iota_0 = 1.46$ ),  $\epsilon_T = 0.104$ ,  $\epsilon_h = 0.109$ ,

$B_0 = 0.866$  and  $\delta = 0.107$  for the case of no TF coil current modulation, while for a modulation factor of 15% the ripple reduces to  $\delta = 0.01$ . Other current settings produce different values for  $\epsilon_T$ ,  $\epsilon_h$  and  $\delta$ ; in this study we have limited the calculations to the 'reference' case quoted.

More exact studies considering a greater number of Fourier harmonics for the field in Boozer co-ordinates and solving the drift kinetic equation are also under way [9, 10].

To apply the quoted models to field expression (1), we suppose the additivity of the fluxes to the 'corner' ripple terms and the remaining terms. In this way, the total particle flux could be divided into three parts:

$$\Gamma^a = \Gamma_{nc}^a + \Gamma_{ht}^a + \Gamma_{ns}^a \quad (2)$$

the index  $a$  corresponding to electrons and ions and similar expressions governing the heat fluxes. The first part in (2),  $\Gamma_{nc}$ , corresponds to the usual complete axisymmetric neoclassical flux given by Hinton and Hazeltine [11].

The second term,  $\Gamma_{ht}$ , is the helically trapped contribution for a stellarator field with the magnetic field given by the three first terms of Eq. (1), and we use for this flux contribution the expressions given by the Shaing model (formulas (7) of Ref. [6] or (4) to (12) of [7]), where a strong dependence on the electric field appears.

The last term in the flux expression (2),  $\Gamma_{ns}$ , corresponds to the non-axisymmetric corner ripple, whose expression has been taken from Ref. [8] (formulas (40) and (41), valid for the banana plateau regime, retaining only the ripple dependent part, both for the electric field dependent term and for the ambipolar part.

The self-consistent radial electric field can be obtained by setting equal the total electron and ion particle fluxes:

$$\Gamma^e(\Phi') = \Gamma^i(\Phi') \quad (3)$$

which, as will be confirmed later, may lead to multiple simultaneous roots for the electric potential  $\Phi$ , in many cases [7].

Once the fluxes are obtained, different confinement times [3] and 'effective' diffusion or conductivity coefficients may be evaluated. In all cases, we calculate the fluxes at a radial point where the electron density is half the central value and suppose parabolic profiles of density and temperatures for the dependence on the average radius.

In this way, Fig. 1 gives the dependence of the global energy confinement time,  $\tau_E$ , on the central electron temperature for a central density of  $n_0 = 2 \times 10^{19} \text{ m}^{-3}$  and an electron to ion temperature ratio of  $T_e(0)/T_i(0) = 3.33$ , which corresponds to the estimated energy balance situation for 400 kW ECRH injection in TJ-II. In this figure, three different values for the radial electric field are plotted, corresponding to a ratio between the electric potential and the central electronic temperature of  $e\Phi/T_e(0) = +1, 0, -1$ . The influence of the electric field is very important at high

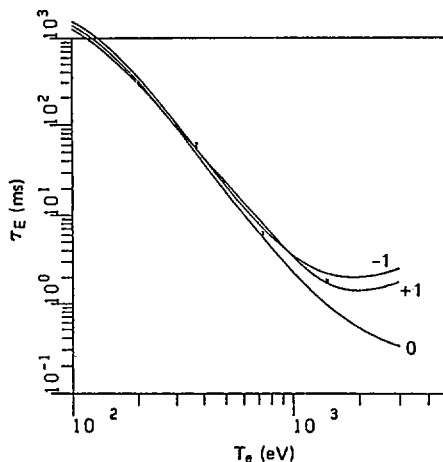


FIG. 1. Global energy confinement time versus central electron temperature for typical TJ-II ECRH situation ( $n_0 = 2 \times 10^{19} \text{ m}^{-3}$ ,  $T_e(0)/T_i(0) = 3.33$ ). Electric potential  $\Phi$  normalized to  $T_e(0)$ .

electron temperatures and more sensitive to the potential value than to the sign; thus, for  $T_e(0) = 770 \text{ eV}$ ,  $\tau_E$  can change by 43% for the quoted potential variation, but the alteration decreases to 10% at 300 eV.

Figure 2 shows the temperature dependence of  $\tau_E$  for the same case; but for a self-consistent radial electric field as determined by Eq. (3), it is clear that a threefold root appears above 625 eV and remains up to 1020 eV; the root corresponding to a lower  $\tau_E$  value has a moderate negative electric potential (Fig. 3). It is the ion root accessible from the low temperature region, while the upper  $\tau_E$  value root corresponds to a high positive electric potential. It is the electron root accessible from the high temperature region; as usual, the intermediate root corresponds to a low field, generally positive, and represents an unstable situation. When the temperature increases, the first and last roots approach each other, and finally, at 1020 eV, coalesce and disappear, leaving only the electron root with high field and  $\tau_E$  values (8.7 ms,  $e\Phi/T_e(0) = +2.15$ ).

A rough global energy balance, taking in account transport, bremsstrahlung losses and electron to ion energy transfer, yields an equilibrium central electron temperature of about 750 eV with a  $\tau_E$  value, for the ion root (that which is accessible from low temperature), of 4.85 ms and an electric potential of  $e\Phi/T_e(0) = -0.175$ . These confinement time values are of the same order of magnitude as those calculated previously by means of the Kovrizhnykh model [5].

The behaviour, as a function of  $T_e$ , of the three self-consistent electric potential roots is shown in Fig. 3. In addition, the dependence of the electron and ion fluxes on the electric potential for the quoted case and a  $T_e(0)$  value of 770 eV is represented by Fig. 4, showing the pronouncedly peaked shape at null field of the

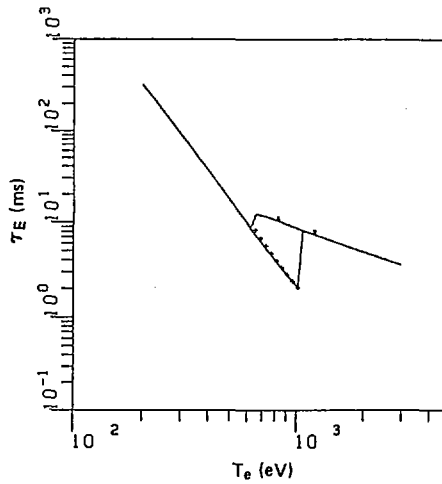


FIG. 2. Same as Fig. 1, but with self-consistent electric potential.

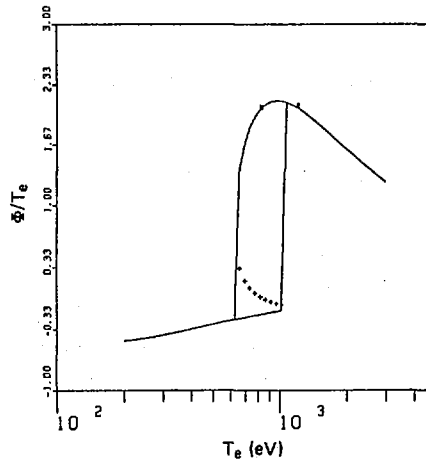


FIG. 3. Dependence of self-consistent electric potential on  $T_e(0)$  (same case as Fig. 1).

ion flux and the smoother behaviour of  $\Gamma^e$ ; in this case, the two fluxes intersect at three points, corresponding to the three roots discussed previously. A change in temperature shifts the curves so that two of the roots coalesce and disappear, restoring a single root situation [7].

The dependence on 'corner' ripple has also been studied, showing an increase in  $\tau_E$  with a modulation factor which is only appreciable for high temperatures, because of the presence of the ripple term in the banana plateau regime. For a TF coil current modulation factor of 15%, the increase for the former case at

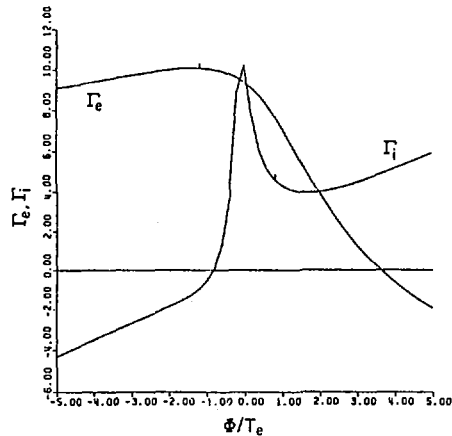


FIG. 4. Variation of electron and ion particle fluxes with electric potential (case of Fig. 1 for  $T_e(0) = 770$  eV). Fluxes in  $10^{19} \text{ m}^{-2} \cdot \text{s}^{-1}$ .

$T_e(0) = 750$  eV is only by 2%, while at 1100 eV where the electron root is alone the increase is almost by a factor of 3 (23.5 against 8.1 ms without modulation); in addition, the region of three roots shifts slightly towards lower temperatures.

The dependence on density and the electron to ion temperature ratio has also been studied, giving the usual increase in density for the ion root, which is less important, but a visible increase for the electron root and a shift of the three root region towards higher temperatures. On the other hand, an increase in the  $T_e/T_i$  ratio can totally alter the root topology, with a disappearance of the multiple root region for values greater than 3.6 [3]; in this case, the single electric field root shifts smoothly from the ion to the electron value, with small changes in the  $\tau_E$  values. In contrast, a decrease in the temperature ratio produces smooth changes in the root topology and very slight changes in the  $\tau_E$  values for each individual root, but extends the width of the three root region without modification of the starting bifurcation temperature. For example, a decrease in  $T_e/T_i$  from 3.3 to 2.7 brings the upper limit of the three root region from 1020 eV up to 1945 eV, maintaining the starting point at around 625 eV.

Calculations with this model for other TJ-II configurations and heating scenarios (NB injection, in particular) are now under way, as is a more detailed, global energy balance analysis.

## REFERENCES

- [1] TJ-II GROUP, ATF DESIGN TEAM, in Controlled Fusion and Plasma Physics (Proc. 12th Europ. Conf. Budapest, 1985), Vol. 9F, European Physical Society (1985) 441.
- [2] TJ-II GROUP, ATF DESIGN TEAM, *ibid.*, p. 433.

- [3] KOVRIZHNYKH, L.M., Nucl. Fusion **24** (1984) 435.
- [4] KOVRIZHNYKH, L.M., Nucl. Fusion **24** (1984) 851.
- [5] GUASP, J., in Controlled Fusion and Plasma Heating (Proc. 13th Europ. Conf. Schliersee, 1985), Vol. 10F, Part I, European Physical Society (1986) 299.
- [6] SHAING, K.C., Phys. Fluids **27** (1984) 1567,
- [7] HASTINGS, D.E., HOULBERG, W.A., SHAING, K.C., Nucl. Fusion **25** (1985) 445.
- [8] SHAING, K.C., HIRSHMAN, S.P., CALLEN, J.D., Phys. Fluids **29** (1986) 521.
- [9] SOLANO, E.R., ROME, J.J., LYON, J.F., HIRSHMAN, S.P., Paper 7S9, presented at American Physical Society Meeting San Diego, CA, Nov. 1985.
- [10] SOLANO, E.R., SHAING, K.C., submitted to Phys. Fluids.
- [11] HINTON, F.L., HAZELTINE, R.D., Rev. Mod. Phys. **48** (1976) 239.

## EVOLUTION, RELAXATION AND TRANSPORT IN SPHEROMAKS AND REVERSED FIELD PINCHES\*

R.Y. DAGAZIAN, J.P. DAHLBURG<sup>1</sup>, G. DOOLEN,  
G.J. MARKLIN, A.A. MIRIN<sup>2</sup>, J.P. MONDT,  
D. MONTGOMERY<sup>3</sup>, A.G. SGRO, L. TURNER, J. WEILAND<sup>4</sup>  
Los Alamos National Laboratory,  
University of California,  
Los Alamos, New Mexico,  
United States of America

### Abstract

EVOLUTION, RELAXATION AND TRANSPORT IN SPHEROMAKS AND REVERSED FIELD PINCHES.

The strongly nonlinear dynamics present in spheromaks and reversed field pinches, which offer the promise of compact, ohmically heated reactors, have been studied by various computational and analytical methods. This has resulted in new insight into the significance of minimum energy states and of transport mechanisms that limit the confinement. The paper reports on the following investigations: (1) Exploration of the tendency of plasmas to oscillate about or to approach relaxed states, using simulations of a decaying spheromak and of a low-S, magnetized, self-reversing Z-pinch. (2) Finding of finite-beta relaxed MHD states with Hall terms. (3) Presenting details of the structure of three-dimensional states relevant to spheromak helicity injection. (4) Investigation of transport due to either thermal convection or steep temperature gradients.

The resistive evolution of a decaying spheromak initially in a constant  $J/B$  (minimum-energy) equilibrium is calculated. A spatially varying resistivity  $\eta(\psi)$  [for which  $\eta$  (magnetic axis)  $< \eta$  (wall)] causes evolution away from the minimum energy state that concentrates the current near the magnetic axis in a manner similar to the RFP and other confinement schemes. After sufficient current peaking (when  $q$  falls below  $1/2$  everywhere), the plasma becomes unstable to a mode having toroidal mode number  $n=2$  (Fig. 1a), the plasma distorts into a nonaxisymmetric  $n=2$  configuration, and the unstable mode saturates (Fig. 1b,c).

---

\* Work performed under the auspices of the United States Department of Energy.

<sup>1</sup> United States Naval Research Laboratory, Washington, D.C. 20375, USA.

<sup>2</sup> National Magnetic Fusion Energy Computer Center, Lawrence Livermore National Laboratory, Livermore, CA 94550, USA.

<sup>3</sup> Department of Physics and Astronomy, Dartmouth College, Hanover, NH 03755, USA.

<sup>4</sup> Chalmers Institute of Technology, Göteborg, Sweden.

The shift away from axisymmetry is large. The value of  $\delta B/B$  at the boundary is about 10%, in agreement with the measurement of this quantity on the CTX experiment, and the magnetic axis moves about halfway to the wall. The nonaxisymmetric equilibrium is initially stable and the plasma profiles then change, due to diffusion. Eventually, the plasma becomes unstable again (Fig. 1d), a new magnetic axis is formed (Fig. 1e), the old one is pushed out toward the wall, and the plasma approaches the axisymmetric ( $n=0$ ) minimum energy state again (Fig. 1f). Since the expulsion of the old axis also involves expulsion of the plasma near the old axis, this would presumably have the effect of a convective cooling of the plasma. Thus, superimposed on the overall decay of the spheromak is an oscillation between an axisymmetric equilibrium and an equilibrium with  $n=2$  structure. In Fig. 2a,  $\tau_x/\tau_{B2}$ , the ratio of the oscillation time to the configuration lifetime, is plotted as a function of  $S$  and three regions are indicated. In the large  $S$  region (region I),  $\tau_x \sim 1.5 \tau_{B2}$ . The lifetime of the decaying phase of the experiment is typically several magnetic decay times, so that more than one or two complete relaxation oscillations are unlikely. It is possible that only the first part of one oscillation will be observed. In fact, the reconnection which drives the magnetic axis to the wall may terminate the discharge. For intermediate  $S$  (region II),  $\tau_x$  can be considerably smaller than  $\tau_{B2}$ , so several oscillations may occur. For very small  $S$  (region III), diffusion will dominate, resulting in a smooth decay and no oscillations. It is not clear how small  $S$  would have to be before the oscillations become undetectable. For high  $S$ , the energy loss concomitant with the magnetic axis expulsion would be considerably reduced, since there would be at most one oscillation. Only  $n=0$  and  $n=2$  activity is exhibited by 3D code simulations. When  $n=1, 3$  or  $4$  modes are present, they decay while  $n=2$  grows and saturates. The predominance of closed flux surfaces minimizes possible heat loss along stochastic field lines. The numerical results qualitatively agree with experimental data.

The nature of 3D minimum energy states is analyzed by examining a configuration in which an unstable magnetized Z-pinch is used to supply helicity through a long cylindrical entrance region ( $D = L = 40$  cm) to sustain a spheromak in a flux conserver ( $D = 80$  cm,  $L = 40$  cm), as illustrated in Fig. 2c. In the entrance region, which has no net magnetic flux, the minimum energy state has a helical  $m=1$  structure varying as  $\exp[i(\theta + kz)]$  with  $k = 6.25 \text{ m}^{-1}$  and  $\lambda_{ER} = 15.6 \text{ m}^{-1}$  ( $\lambda = \mu_0 j_{||} / B$ ). The minimum energy state in the flux conserver is the usual axisymmetric ( $m=0$ ) spheromak configuration with  $\lambda_s = 13.2 \text{ m}^{-1}$ . The  $\lambda$  value of the z-pinch is the ratio of the current to the external flux,  $\lambda_{zP} = \mu_0 I / \Phi$ . If  $\lambda_{zP} > \lambda_{ER}$  the z-pinch will become kink unstable and will feed helicity into the entrance region and on into the spheromak since helicity flows towards regions of lower  $\lambda$ , and the spheromak can be maintained in steady state against resistive dissipation. This

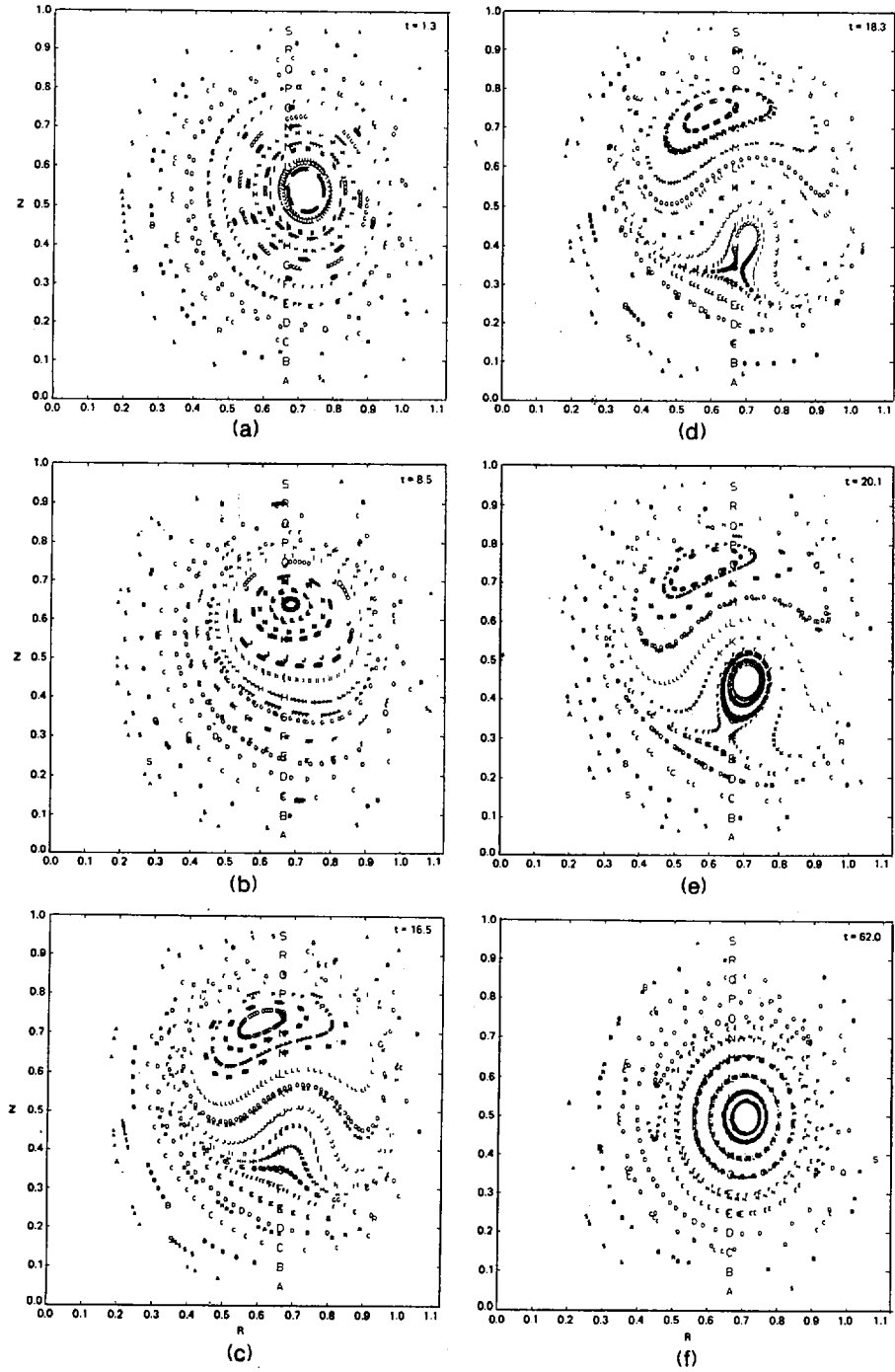


FIG. 1. Magnetic field puncture plots at various times.

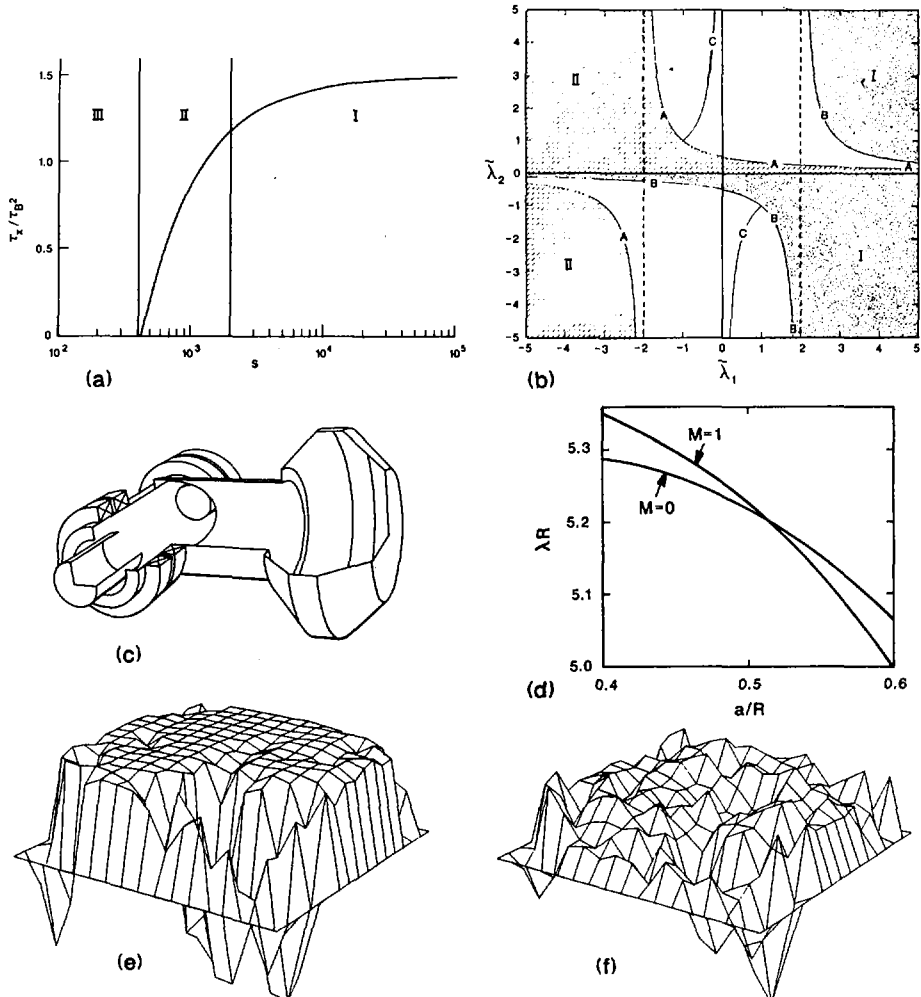


FIG. 2. (a) Plot of  $\tau_x/\tau_B^2$  versus  $S$ . For large  $S$  (region I),  $\tau_x$  is comparable to the plasma lifetime and at most one or two complete oscillations (and possibly the first part of one oscillation) will be observed. For intermediate  $S$  (region II), several oscillations are likely. For small  $S$  (region III), the plasma is diffusion dominated and never evolves far from the minimum energy state, so that no oscillations occur.

(b) Character of the eigenvalues,  $\mu$ , as a function of the values of  $\tilde{\lambda}_1$  and  $\tilde{\lambda}_2$ . In the shaded regions, labelled I and II, the eigenvalues are real. In the clear regions, the eigenvalues are complex. In particular, the eigenvalues are imaginary on the hyperbolas labelled C. They are degenerate on the hyperbolas labelled A or B. Previously studied force-free magnetic field configurations correspond to the domain of the  $\tilde{\lambda}_2 = 0$  axis.

(c) Shape of the flux conserver.

(d) Eigenvalues of the  $m = 0$  and  $m = 1$  minimum energy states plotted as a function of  $a/R$ , the radius of the entrance region over the radius of the flux conserver.

(e) Three-dimensional perspective plots of the alignment cosine and for a relaxed Z-pinch state [1].

(f) Same as (e) for  $\lambda = j\mathbf{B}/B^2$ .

equilibrium is difficult to calculate because there is no overall symmetry and the fields are fully 3-dimensional. We attack this problem by separately computing global solutions to  $\nabla \times \underline{B}_m = \lambda_m \underline{B}_m$  for the  $m = 0$  and  $m = 1$  modes in a conducting boundary which includes the flux conserver and the entrance region, but not the z-pinch. The eigenvalues  $\lambda_m$  are computed as functions of  $a/R$ , the radius of the entrance region over the radius of the flux conserver, and are plotted in Fig. 2d. At  $a/R \sim .5$  the  $m = 0$  and  $m = 1$  eigenvalues are equal, so the two solutions  $\underline{B}_0$  and  $\underline{B}_1$  can be added in any linear combination, resulting in a fully 3-dimensional solution to  $\nabla \times \underline{B} = \lambda \underline{B}$ . The structure of the fields can then be studied by examining the properties of this 3D minimum energy state. Flux surface plots obtained by field line tracing show a helical structure in the entrance region and a toroidal structure in the flux conserver, as expected. If the amplitude of the  $m = 1$  component is small compared to the  $m = 0$ , most of the volume of the flux conserver has good magnetic surfaces which resemble a slightly tilted spheromak. When the amplitudes are equal, however, as they usually are in experiments, the field is highly stochastic and there are only a few good surfaces near the magnetic axis of the tilted and distorted spheromak.

A conservative rule of thumb for MHD computation is that one grid point (or expansion coefficient, or finite element) is required per unit Lundquist number  $S$  for each spatial dimension, in order to guarantee well-resolved dissipation scales for MHD computation. This estimate probably cannot be exceeded by more than an order of magnitude. Thus, an affordable (on the Cray I or Cray II)  $64^3$  3D code probably cannot fully resolve nonlinear Z-pinch dynamics at  $S > 1000$ . This limitation restricts computations to  $S$  of a few hundred. Fortunately, it has turned out that several experimentally significant effects can be seen from the equations of incompressible, resistive MHD at such  $S$  values. Among those are relaxation toward a force-free state and spontaneous reversal of the toroidal component of the magnetic field at the wall. We are currently performing 3D MHD computations with a pseudospectral code in which the equations of resistive, incompressible, non-viscous MHD are solved inside a 3D region with a square  $(x,y)$  poloidal boundary and periodic boundary conditions in the toroidal  $(Z)$  direction. The poloidal boundary is rigid, perfectly conducting, and free-slip. A net magnetic flux crosses every plane of constant  $Z$ . Non-equilibrium initial  $Z$  current profiles evolve through several tens of poloidal Alfvén transit times; typical runs require 10 hours of CRAY-II time. Considerable small-scale turbulence results (low "m", high "n") and the dissipation spectra are not always fully resolved. The ratio of the total energy to the magnetic helicity decreases monotonically. The kinetic energy rises from nearly zero to a few percent of the magnetic energy and then falls again. Since the current density and the magnetic field obey different boundary conditions, a

turbulent boundary layer persists near the wall. Over the interior of the plasma, a nearly force-free state results. The flatter profile of  $\mathbf{j} \cdot \mathbf{B} / jB = \cos \theta$ , as compared with that of  $\lambda = \mathbf{j} \cdot \mathbf{B} / B^2$  in a poloidal cross-section (Fig. 2e,f) suggests [1] that the relaxed state is better characterized as "force free" than as "minimum energy" (for which  $\lambda$  as well as  $\cos \theta$  would be constant).

We have studied magnetic relaxation derived from a new variational principle obtained from incompressible MHD, modified to include the Hall term in Ohm's law [2] (referred to as HMHD). The Hall term breaks the symmetry of ideal MHD under the gauge transformation associated with the cross-helicity invariant ( $\int \mathbf{v} \cdot \mathbf{B} d^3 r$ ). However, we found that in ideal HMHD, a new quantity, the hybrid helicity, is conserved instead. This hybrid helicity represents the self-linkage or knottedness of a generalized vorticity,  $\mathcal{Q} = e\mathbf{B}/mc + \nabla \times \mathbf{v}$ . The conservation results from  $\mathcal{Q}$ 's being "frozen" to the fluid motion according to  $\partial \mathcal{Q} / \partial t = \nabla \times (\mathbf{v} \times \mathcal{Q})$ . The aforementioned variational principle is a consequence of the hypothesis that when dissipative effects are present, the total (kinetic plus magnetic) energy,  $W$ , decays more readily than do the (ideally conserved) magnetic and hybrid helicities,  $K$  and  $X$ , respectively. We then suppose that  $W$  decays to the minimum value compatible with the initial values of the two helicities, the magnetic flux and the fluid vorticity flux. Hence we arrive at the principle  $\delta \int (\lambda_1 K + \lambda_2 X - W) = 0$ . Thus the Lagrange multiplier parameter space is expanded to 2-D (namely,  $\lambda_1$  and  $\lambda_2$ ). The two Euler equations that result couple the behavior of the magnetic field to that of the fluid vorticity field. The solution for each field can be expressed as the sum of two eigenvectors of the curl operator with eigenvalues,  $\tilde{\mu}$ , that are possibly complex (Fig. 2b). As a result of this coupling, we found that the relaxed magnetic field configuration need not be force-free if the fluid vorticity is nonzero, leading to the existence of relaxed magnetic field configurations with finite plasma beta. Our results are enticing for further explorations. Can fusion-worthy relaxed magnetic field configurations that confine significant plasma pressure be achieved in the Hall regime? By virtue of the relaxation process that couples magnetic field to fluid vorticity, are there new methods of current drive, possibly mechanical in origin, that can be used to sustain a fusion plasma? Can vorticity be used to stabilize such a plasma? When Hall effects are present, is the concept of magnetic reconnection appropriately replaced by the concept of reconnection of the generalized vorticity?

The theory of Rayleigh-Benard thermal convection in ordinary fluids is employed as a prototype for studying plasma convection resulting from small-scale g-mode fluctuations. For well behaved strongly magnetized plasmas, situations of strong turbulence are unlikely and a quasi-linear theory as expounded

here may be adequate in describing basic physical processes. The physical model that we employ is that of one-fluid resistive MHD augmented by collisional tensor viscosity and simple thermal conductivity. The existence of stationary states for resistive modes in this model has been proven [3]. The basic situation is that of a diffuse cylindrical pinch with weak density variation over the bulk of the plasma so that temperature convection is the dominant nonlinear saturation mechanism for the fast resistive interchange. This mode is chosen to work with because a) it is the usual resistive g-mode of RFP's and underlies resistive ballooning; b) its stationary eigenfunctions die off quickly with distance from the resonant surface so that the analysis is relatively simple. The anomalous confinement time can be written as  $\tau = 4\sqrt{2}a^2\mu_0(m_e/m_i)^{1/2}/(\eta\beta N)$ , where  $a$  is the plasma characteristic dimension,  $\eta$  the plasma resistivity,  $\beta$  the kinetic to magnetic energy ratio,  $N$  the Nusselt number, and  $m_e$  and  $m_i$  the electron and ion mass, respectively.

Edge plasmas are characterized by steep temperature gradients and, in discharges with gas puffing, much smaller density gradients. In reversed field pinches the large plasma current prompts an investigation of enhanced transport due to current-convective instabilities. The mode structure of such linear instabilities which are resonant in different regions may overlap [4]. The present work consists of a two-fluid treatment of the resultant second-order mode coupling and transport. In view of the short  $k_{\perp}$ , time-scales slower than the resistive diffusion rate across a perpendicular wave length are considered, and  $k_{\parallel}^2 \lambda_{mfp}^2 \ll k_{\perp}^2 \rho_s^2$  is assumed, where  $\rho_s$  is the thermal ion Larmor radius at the electron temperature and  $\lambda_{mfp}$  is the electron mean free path parallel to the magnetic field. Then, magnetic islands are short-lived on time-scales of interest, whereas the perturbation in the parallel current density dominates all other electromagnetic effects. The model consists of the parallel component of the inertialess Ohm's law including electron pressure and parallel thermal force effects, and the electron energy equation including parallel electron thermal conductivity and compressibility, the drift heat flux and parallel thermal forces. Ohmic heating rates are typically slow compared with the relevant nonlinear rates. The parallel component of Ohm's law eliminates the current perturbation, whilst the electron temperature disturbance is coupled back to the electrostatic potential through the ion vorticity equation, obtained from ion force balance with lowest-order finite Larmor radius effects and quasi-neutrality in the usual manner. The resultant heat diffusion coefficient is roughly  $D = (cT_e/eB) \kappa V$ , where  $\kappa \approx \rho_s/l_T$  and  $V \approx v_{e\parallel}/C_s$  are the normalized inverse temperature gradient scale length and parallel electron drift velocity, respectively. It was also found that on time-scales short compared with viscous damping, thermal solitary vortices can exist even in the presence of shear and parallel thermal diffusion. If such vortices are attractors of the

nonlinear dynamics, nonlinear steepening balancing dispersion may further enhance the heat loss associated with current-carrying edge plasmas.

Although the thermal convective mode and the current convective mode may effect the confinement properties of some regions, it is not implied that they determine the global confinement time. Rather, the global confinement time will be determined by regions having good flux surfaces and nearly classical cross-field thermal conduction.

#### REFERENCES

- [1] DAHLBURG, J.P., MONTGOMERY, D., DOOLEN, G.D., TURNER, L., Phys. Rev. Lett. 57 (1986) 428.
- [2] TURNER, L., IEEE Trans. Plasma Sci. (Dec. 1986).
- [3] DAGAZIAN, R.Y., PARIS, R.B., Phys. Fluids 29 (1986) 3.
- [4] MONDT, J.P., GOEDERT, J., Phys. Fluids 28 (1985) 1816.

# EXPERIMENTS WITH A FULLY TOROIDAL EXTRAP Z-PINCH

J.R. DRAKE, J.E. ENINGER, B.P. LEHNERT  
 Department of Plasma Physics and Fusion Research,  
 Royal Institute of Technology,  
 Stockholm, Sweden

## Abstract

### EXPERIMENTS WITH A FULLY TOROIDAL EXTRAP Z-PINCH.

In the Extrap plasma confinement scheme, a Z-pinch is produced along the null of an octupole field generated by currents in external conductors. In the paper, studies of the discharge startup process in a fully toroidal configuration are described. Startup involves first breaking down a toroidal discharge and then driving up the current in order to reach the pinch parameter regime. Current densities of  $2 \times 10^6 \text{ A} \cdot \text{m}^{-2}$  have been achieved. The estimated plasma density is  $6 \times 10^{20} \text{ m}^{-3}$ , and the temperature is about 4 eV. These parameters correspond to pinch conditions.

## 1. INTRODUCTION

An Extrap Z-pinch is a high beta discharge where the current channel has a characteristic non-circular cross-section achieved by bounding the discharge by a magnetic separatrix [1-3]. The configuration is produced by generating the discharge along the magnetic field null line of an octupole magnetic field. In a toroidal configuration, the vacuum octupole field is produced by parallel currents in four rings. The discharge current is located in the vicinity of the octupole null and is antiparallel to the ring current. A schematic representation of the configuration is shown in Fig. 1.

A series of linear and toroidal sector experiments have shown that a globally stable pinch equilibrium can be achieved. Theoretical studies indicate that the stability of the configuration can depend on the imposed octupole field [1,4,5], the effects of the separatrix on the pressure profile [6], finite Larmor radius effects [1,6] and large Larmor radius effects [7].

The next step in the investigation of this scheme is a fully toroidal experiment and the device T1 has been constructed for these studies. The goals of the experiments are; 1) development of discharge startup procedures, 2) achievement of equilibrium and 3) studies of stability and confinement. In this report we present the results of studies of discharge startup.

## 2. DESCRIPTION OF THE EXTRAP T1 EXPERIMENTAL APPARATUS

The Extrap T1 apparatus, shown schematically in Fig. 2, consists of a stainless steel toroidal vacuum vessel with a 0.20 m x 0.25 m rectangular

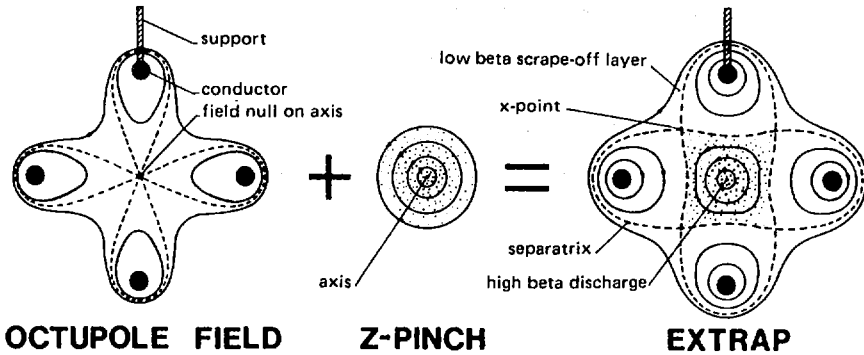


FIG. 1. Extrap Z-pinch configuration results when Z-pinch is generated along vacuum octupole magnetic field axis produced by currents in four conductors. Self-field of discharge, together with octupole field, generates configuration where pinch discharge region is surrounded by separatrix field line segments defined by four X-point field nulls. High beta pinch is located inside region defined by nulls; low beta plasma, contained by vacuum field, is located outside this region.

cross-section. The vessel is divided mechanically and electrically into two halves; this allows for easy assembly and disassembly as well as flexibility in the circuit configuration. Each half is further divided into four sections which are separated by polyethylene insulated gaps. In the present experiments the gaps are shorted to provide a return path for the ring current so that the ring circuit, which produces the octupole field, is decoupled from the Ohmic heating discharge circuit. The four rings, located at  $(R, \theta, z) = (450 \pm 30 \text{ mm}, \theta, 0)$  and  $(R, \theta, z) = (450 \text{ mm}, \theta, \pm 30 \text{ mm})$ , are made of 10-mm diameter chrome-copper. The rings are supported mechanically at 50-mm intervals by radial spokes machined into 4-mm thick stainless steel plates. These support frames also connect the rings electrically around the circumference. The rings are driven in parallel by a 12-mF, 8-kV capacitor bank through a current limiting 20- $\mu\text{H}$  inductance which can be shorted out by an ignitron switch during an experimental pulse in order to increase the rate of rise of the ring current. The ring system is designed for currents up to 100 kA in each ring. The 2  $\mu\text{H}$  inductance connected in the gap at the vacuum vessel is essential for achieving a uniform plasma breakdown and a closed toroidal current channel.

The plasma current is induced through a 0.5-Vs iron-core transformer driven by two 24- $\mu\text{F}$ , 30-kV capacitor banks feeding a common two-turn primary. Two separate banks having different resistors in series permits a soft start up of a low current ( $< 1 \text{ kA}$ ) predischage. The time constant of the predischage is 200  $\mu\text{s}$ . The predischage is followed by a second high current, 60- $\mu\text{s}$  pulse to build up the discharge.

The rings are uninsulated from the plasma except at the two breaks in the vacuum vessel where there are 100-mm long, 45-mm diameter ceramic tubes inserted inside the rings to provide insulation of the ring gaps.

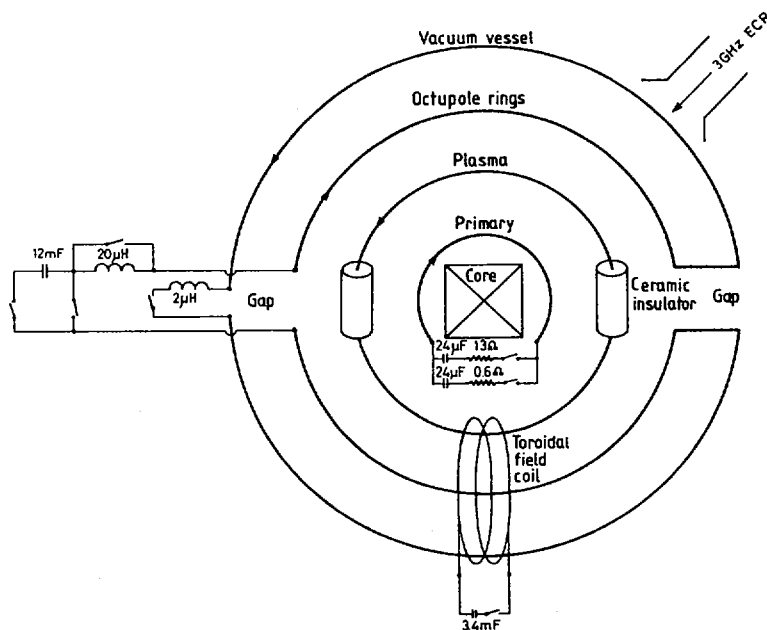


FIG. 2. Schematic diagram of toroidal Extrap experiment.

### 3. DISCHARGE STARTUP

Experience has shown that it is difficult to achieve toroidal Extrap discharges. This is of course expected as the desired discharge is perpendicular to the vacuum octupole magnetic field. The particle  $\vec{E} \times \vec{B}$  drifts hinder breakdown when the toroidal electric field is applied.

In linear Extrap experiments, discharges have been produced using electrodes placed on the linear axis where the octupole field is zero. With electrodes, breakdown is easily achieved. Initially, the current channel is centered on the axis and is very thin. Breakdown occurs in the region where the magnitude of the magnetic field is sufficiently small so that the  $\vec{E} \times \vec{B}$  drift has no effect on the electron trajectory and the breakdown conditions are then similar to the well known Townsend conditions [3].

In principle, breakdown could be achieved in the toroidal configuration in a similar fashion. Ionization would be limited to a small region close to the toroidal axis where the octupole field is small. When the ionization rate exceeds the loss rate, breakdown would result [8].

However, it is difficult to achieve breakdown in this fashion on the fast time scale desired for the Extrap discharge. In the linear experiments, fully developed Extrap discharges exhibited good global stability but the initial thin

discharge located in the weak octupole field region was observed to be globally unstable. With electrodes it was possible to drive the discharge current up to a level where full ionization was achieved in a few microseconds. The current channel expanded into the region where the octupole field was stronger and those stabilizing features, which characterize the Extrap configuration, became effective before the global instabilities destroyed the young pinch.

Two approaches to discharge startup in the toroidal experiment T1 have been studied. The primary approach, to be discussed in detail later in this report, incorporates a weak toroidal field which expedites breakdown by improving the electron containment in the region of the octupole field null.

### 3.1 STARTUP WITHOUT A TOROIDAL B FIELD

A second approach, which has also been the subject of preliminary investigations, involves using the ring currents which produce the octupole field as the primary circuit for inducing the discharge. First the discharge is broken down at a gap in the rings. At this stage the plasma current is not fully toroidal and this discharge current is driven directly by the voltage applied at the gap. The plasma circuit does not include an induced EMF. However the  $\mathbf{J} \times \mathbf{B}$  force on the plasma current drives the discharge away from the gap, on both sides of the gap, so that the plasma discharge sector becomes a larger and larger fraction of the full torus. When the two ends of the discharge meet at the antigap,  $180^\circ$  from the gap, the plasma discharge becomes fully toroidal forming a closed loop secondary and the plasma current is then driven by the induced EMF applied by driving the ring current at the gap.

This approach to achieving breakdown is not as clean as the approach where breakdown is achieved along the toroidal magnetic null without contact with the rings. When the rings also function as electrodes during breakdown, impurities are introduced which can of course affect the energy balance throughout the discharge. The advantages of this approach are that no toroidal field is required and very high power inputs can be achieved giving a fully toroidal, fully ionized discharge on a fast time scale.

In the experiments performed to date, the discharge has propagated to the antigap when ring gap voltages of the order of 2 kV have been applied. The propagation velocity of the ionization front is about  $5 \times 10^4 \text{ ms}^{-1}$  which is consistent with earlier studies of moving ionization fronts [9]. After about 30  $\mu\text{s}$  the two ends of the discharge meet at the antigap,  $180^\circ$  from the gap. However, induced toroidal discharges have not been achieved. The problem is that the current magnitude necessary to drive the discharge to the antigap exceeds the stability limit and the discharge goes globally unstable before forming a toroidal pinch discharge.

### 3.2 STARTUP WITH A TOROIDAL B FIELD

We now turn to the discharge startup studies that have been carried out incorporating a toroidal magnetic field. The toroidal discharge is produced

directly along the octupole field null. Discharge startup involves first breaking down the neutral fill gas near the toroidal axis thus forming a secondary for the Ohmic heating primary circuit. The discharge starts on the axis because the octupole field hinders breakdown elsewhere. An ECR source provides necessary preionization. A loop voltage of 2 kV is needed for breakdown. The current is then driven up thus increasing the Ohmic power input so that the plasma pressure builds up. The startup phase is complete when the discharge parameters are in the pinch regime. In general this means that the pinch pressure is balanced by the magnetic field produced by the discharge current.

The two basic requirements for achieving a pinch discharge are sufficient discharge current for confinement and sufficient power input for burning through the radiation barrier. The confinement requirement is expressed in the Bennett relation which is a global expression for the force balance in the form

$$I^2 = 16 \pi N_e kT / \mu_0 \quad (1)$$

where  $N_e$  is the electron line density,  $T$  is the temperature and  $I$  is the discharge current.

During the buildup phase the dominant power loss is radiation and the power balance becomes

$$I^2 \eta = N_e N_H R_H \quad (2)$$

where  $\eta(T)$  is the resistivity,  $N_H$  is the neutral hydrogen line density and  $R_H(T)$  is the radiation power factor. If light impurities are present, the power balance can be dominated by impurity radiation. In reversed field pinch discharges, which operate in a similar regime, burn-through of light impurities requires discharge currents such that [10]

$$I / N > 1 \times 10^{-14} \text{ Am} \quad (3)$$

These expressions can be used to establish operational regime curves for filling pressure and discharge current. We assume that the discharge is permeable to neutral gas so that  $N_H$  is determined by the filling pressure and that the plasma density is also equal to the filling density. The cross-sectional area of the discharge is determined by the aspect ratio of the octupole rings and the ratio of the discharge current to the ring current. However, the dependence on this current ratio is weak so a constant cross-sectional area can be used for calculational purposes. In Fig. 3 we show curves of the filling pressure versus discharge current derived from the Bennett relation and the power balance for several temperatures. The operational regime of the buildup studies carried out to date is also shown in Fig. 3. For these studies, the toroidal field strength was 0.1 T. In a tokamak mode, a requirement of

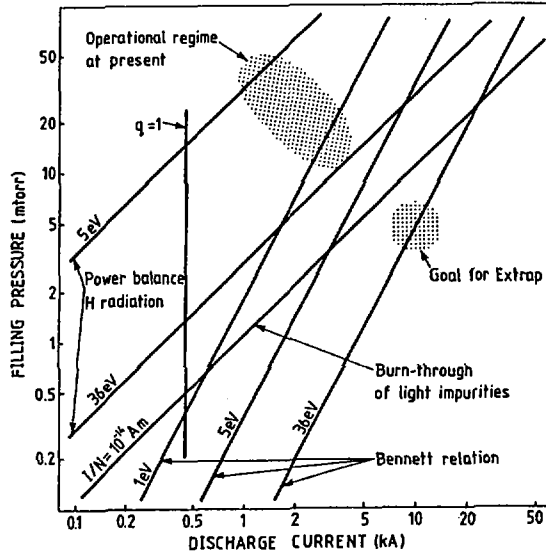


FIG. 3. Operational regime curves of filling pressure and discharge current. Limits imposed by Bennett relation and radiation losses are shown.

$q = 1$  would limit the discharge current to 440 A for the given aspect ratio. As can be seen, discharge currents of up to about 4 kA have been achieved so far. In the present device the desired operational regime requires currents exceeding 10 kA. The limitation in the present series of experiments is difficulty in raising the octupole field, in the presence of the discharge, due to breakdown at the ring gap.

Magnetic probes have been used to measure the magnetic field profiles in the discharge current channel. In Fig. 4 we show a measured profile of the poloidal field due to the discharge current alone. The vacuum octupole field has been subtracted. This profile has been used to calculate a current distribution which is also shown. Characteristic parameters for this discharge are given in Table I.

#### 4. SUMMARY

The discharge parameters shown in Fig. 3 and Table I indicate that the discharge is in the pinch regime. Current densities of  $2 \times 10^6 \text{ Am}^{-2}$  have been achieved. The estimated plasma density is  $6 \times 10^{20} \text{ m}^{-3}$  and the temperature is about 4 eV. These parameters correspond to pinch conditions. The pinch is cold and the power balance can be assumed to be dominated by radiation losses. However, the pinch is well developed and well positioned near the minor axis. In Fig. 5 we show an open shutter photograph of the discharge showing that the pinch boundary is well defined.

TABLE I. CHARACTERISTIC DISCHARGE PARAMETERS

Major radius (m)	0.45
Total ring current (kA)	10
Toroidal magnetic field (T)	0.1
Filling density, $n_H$ ( $10^{20} \text{ m}^{-3}$ )	6
Discharge cross-section ( $10^{-3} \text{ m}^2$ )	1
Total discharge current (kA)	3
$I/N_H$ ( $10^{-15} \text{ A}\cdot\text{m}$ )	5
Loop voltage (V)	700
Calculated electron temperature (eV)	4
Calculated electron density ( $10^{20} \text{ m}^{-3}$ )	6
Alfvén transit time, $a/v_A$ ( $\mu\text{s}$ )	1
Discharge pulse duration ( $\mu\text{s}$ )	60

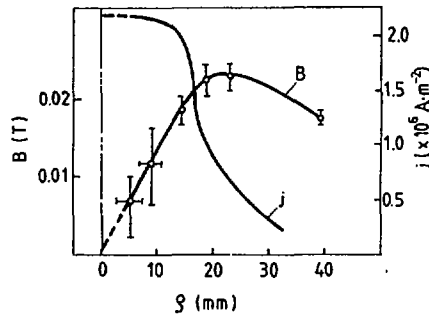


FIG. 4. Measured profiles of poloidal magnetic field strength produced by discharge current. Coordinate  $\rho$  is radial distance from discharge axis which is about 5 mm outside geometric minor axis for the four rings. With given vacuum octupole field, X-point is at  $\rho = 18$  mm. Profile of corresponding current density is also shown.

In the next series of experiments, the discharge current and octupole field strength will be increased. A vertical magnetic field necessary for controlling the equilibrium position of the pinch at the higher current levels will be implemented. The goal is to maintain equilibrium at the higher currents and achieve higher temperatures.

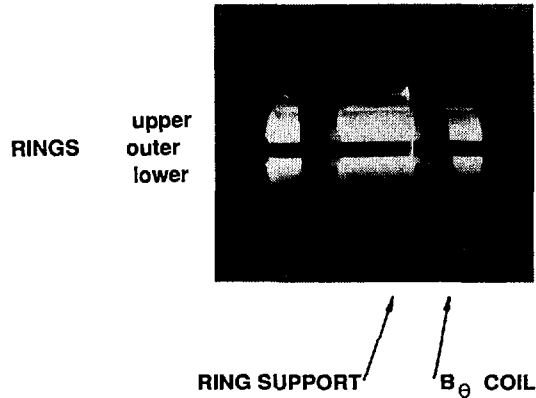


FIG. 5. Open shutter photograph of discharge taken through a 100 mm diameter window in vacuum vessel outer wall.

### ACKNOWLEDGEMENTS

The authors wish to thank the academic and technical staffs of the Department for their contributions and the effort that has been made to design, construct and run the Extrap experiment.

This work has been supported by the European Communities under an association contract between Euratom and Sweden through the Swedish Energy Research Commission, Project Number 4210014/2.

### REFERENCES

- [1] LEHNERT, B., *Phys. Scr.* **10** (1974) 139; **16** (1977) 147.
- [2] DRAKE, J.R., HELLSTEN, T., LANDBERG, R., LEHNERT, B., WILNER, B., in *Plasma Physics and Controlled Nuclear Fusion Research 1980* (Proc. 8th Int. Conf. Brussels, 1980), Vol. 2, IAEA, Vienna (1981) 717.
- [3] DRAKE, J.R., *Plasma Phys.* **26** (1984) 387.
- [4] WAHLBERG, C., ARORA, A.K., RING, R., *Plasma Phys. Controll. Fusion* **26** (1984) 1261.
- [5] BRYNOLF, J., RING, R., WAHLBERG, C., *Plasma Phys. Controll. Fusion* **27** (1985) 1255.
- [6] HELLSTEN, T., *Nucl. Fusion* **22** (1982) 565.
- [7] LEHNERT, B., *Comments Plasma Phys. Controll. Fusion* **9** (1985) 91.
- [8] TENDLER, M., Peculiarities in the Start-up Process in a Toroidal Extrap, Rep. TRITA-PFU-86-08, Royal Institute of Technology, Stockholm (to be published in *Europhys. Lett.*).
- [9] ENINGER, J.E., in *Phenomena in Ionized Gases* (Proc. 7th Int. Conf. Belgrade, 1966), Vol. 1 (1966) 520.
- [10] COSTA, S., De ANGELIS, R., ORTOLANI, S., PUIATTI, M.E., *Nucl. Fusion* **22** (1982) 1301.

## CHARACTERISTICS OF REVERSED FIELD PINCH PLASMAS WITH A RESISTIVE SHELL

T. TAMANO, W.D. BARD, T. CARLSTROM, C. CHU,  
R.R. GOFORTH, Y. KONDOH<sup>1</sup>, R.J. La HAYE, P. LEE,  
E.J. NILLES<sup>2</sup>, M.T. SAITO, M.J. SCHAFFER, P.L. TAYLOR  
GA Technologies Inc.,  
San Diego, California,  
United States of America

### Abstract

#### CHARACTERISTICS OF REVERSED FIELD PINCH PLASMAS WITH A RESISTIVE SHELL.

Reversed field pinch plasmas in a resistive shell were investigated in the OHTE device. The discharges were sustained over 10 ms — much longer than the resistive shell time of 1.5 ms. Global plasma characteristics, such as plasma temperature, density, resistance and magnetic fluctuations, were very similar to those obtained with the previous highly conducting shell. A new type of toroidally localized kink instability, called the 'slinky' mode, was found. It grew initially with a growth time of approximately the resistive shell time, as predicted by the linear MHD theories, but self-healing was usually observed after a few milliseconds. This indicates that a highly conducting shell may not be required for a reversed field pinch and suggests that linear plasma stability is not always necessary in a confinement system.

Remarkable progress has been made in recent years in the field of reversed field pinch (RFP) and OHTE helical pinch [1-5]. Discharges have been sustained for over 10 ms and improvement of both the plasma temperature and the Lawson parameter has been observed as the plasma current increased. The pinch devices have been operated with a conducting shell surrounding the plasma that has a time constant much longer than the duration of the plasma discharges. The linear MHD theories predict that RFP plasmas are unstable with a resistive shell and that unstable modes grow on the resistive shell time-scale  $\tau_s = \mu_0 \sigma b w / 2$ , where  $\sigma$ ,  $b$  and  $w$  are the electrical conductivity of the shell, the minor radius and the thickness of the shell, respectively [6-8]. In the future devices, the discharge duration will be much longer than the resistive shell time. Therefore, it is important to study plasma behavior in a resistive shell. For this reason, the OHTE conducting shell was replaced by the resistive shell in the early spring of 1985 and experiments have been carried out with the resistive shell since then [9].

<sup>1</sup> Present address: Department of Electronic Engineering, Gunma University, Kiryu, Gunma, Japan.

<sup>2</sup> Present address: Department of Physics, University of Wisconsin, Madison, WI 53706, USA.

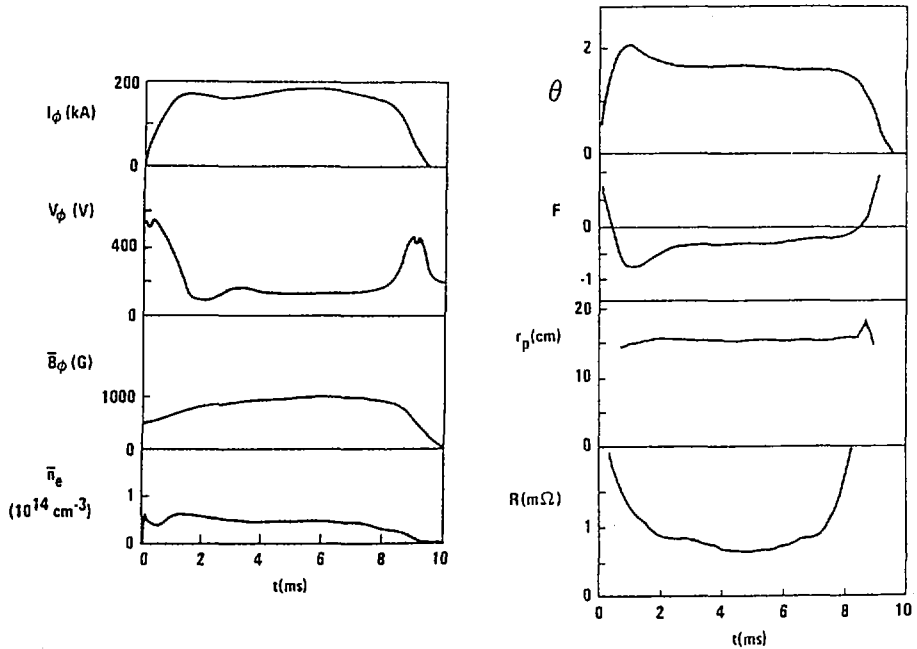


FIG. 1. Waveforms of plasma current  $I_\phi$ , loop voltage  $V_\phi$ , average toroidal field  $\bar{B}_\phi$  inside the liner, line-average electron density  $\bar{n}_e$ , pinch parameter  $\theta$ , reversal parameter  $F$ , plasma radius  $r_p$  from the truncated Bessel function model, and plasma resistance  $R$ .

The OHTE device has a major radius of 1.24 m and a minor radius of 0.183 m to the inside surface of graphite tiles that completely cover the inside of the stainless-steel bellows plasma chamber. The resistive shell has a minor radius of 0.200 m. The resistive shell is made of brass with a thickness of 0.8 mm, bonded to a 13.2 mm thick plastic composite. The electrical resistivity of the brass is  $6 \times 10^{-8} \Omega \cdot \text{m}$ . The shell has a single gap in the toroidal direction and is poloidally continuous. The resistive shell time is 1.5 ms while the shell time of the old aluminum shell (14 mm thick) was 25 ms. The characteristic time of the plasma chamber for vertical field penetration is 0.1 ms. The copper helical windings occupy half the volume between the minor radii of 0.215 m and 0.255 m.

This OHTE device with the resistive shell was operated in the reversed field pinch mode. Reversed field pinch discharges were routinely produced for durations much longer than the resistive shell time. The longest discharge produced had a reversed field duration of 11.3 ms, corresponding to a factor 7.5 times the shell time constant.

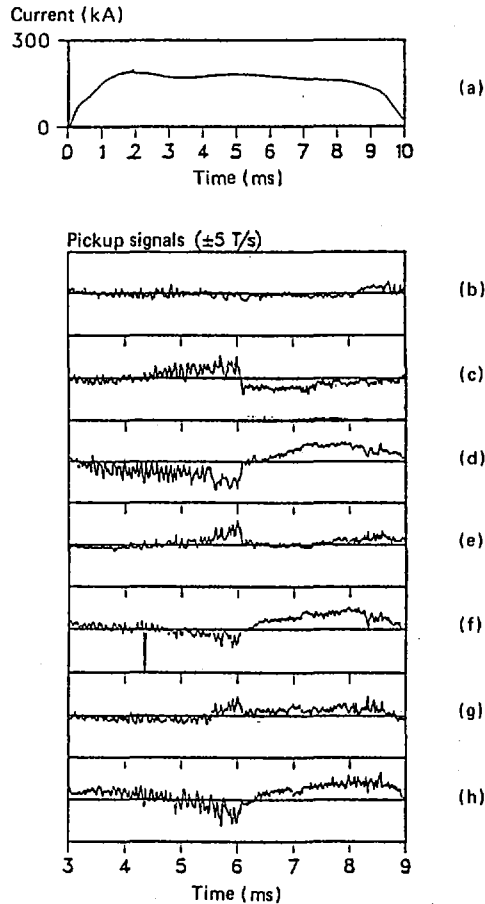


FIG. 2. Typical plasma current waveforms (a) and magnetic pickup loop signals  $\dot{B}_r$ : top  $78.50^\circ$  (b), top  $146.25^\circ$  (c), top  $157.50^\circ$  (d), outside  $140.625^\circ$  (e), outside  $151.875^\circ$  (f), bottom  $135.00^\circ$  (g) and bottom  $146.25^\circ$  (h).

An example of waveforms from a single discharge is shown in Fig. 1. The plasma current,  $I_\phi$ , has a broad peak with a value of 185 kA at 5.7 ms. The one-turn voltage,  $V_\phi$ , at the peak is 123 V. The average toroidal field,  $\bar{B}_\phi$ , inside the plasma chamber is about 1 kG. The average electron density,  $\bar{n}_e$ , measured with an infra-red laser interferometer, is nearly steady and is  $4.4 \times 10^{13} \text{ cm}^{-3}$  at the current peak. The magnitude and time behavior of the line-average density are similar to those previously obtained with the conducting shell. The central electron temperature measured at 4 ms is  $178 \pm 45$  eV, which is also in good agreement with the results of 1 eV/kA obtained in the conducting shell experiments.

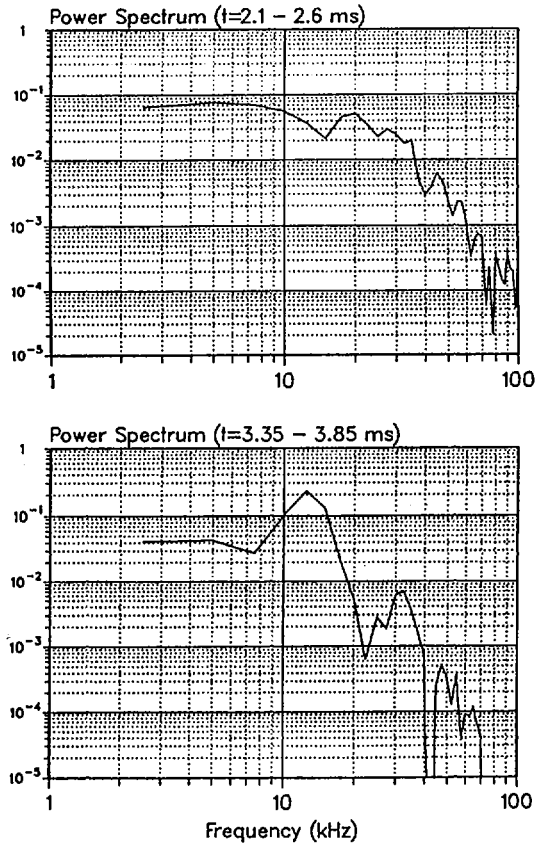


FIG. 3. Examples of frequency power spectra before the development of the slinky mode ( $t = 2.1-2.6$  ms) and near its maximum amplitude ( $t = 3.35-3.85$  ms).

The pinch parameter  $\Theta = B_{\theta}(a)/\bar{B}_{\phi}$ , the reversal parameter  $F = B_{\phi}(a)/\bar{B}_{\phi}$ , the equivalent plasma radius  $r_p$  derived by use of a truncated Bessel function model and the plasma resistance are also very close to those with the conducting shell, and the resistance follows the previous  $I_{\phi}^{-3/2}$  scaling. The rapid rise in the plasma resistance late in time is correlated with the mismatch in the equilibrium vertical field provided by the pre-programmed external coil currents, and the lack of precise equilibrium control appears to be a primary cause for the plasma termination.

High frequency magnetic fluctuations measured just inside the resistive shell for components of  $B_{\phi}$  with  $m = 0$  and  $m = -1$  generally have frequency spectra and amplitudes very similar to

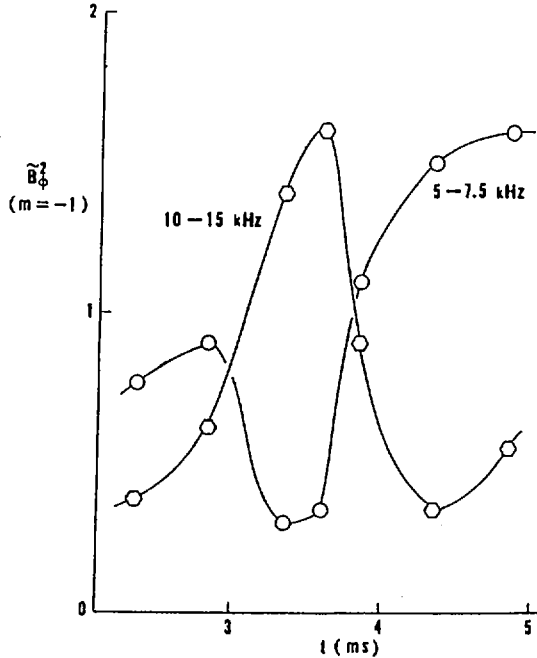


FIG. 4. Time behavior of average power spectra,  $\tilde{B}_\phi^2$ , for the  $m = -1$  mode with  $5 \text{ kHz} \leq f \leq 7.5 \text{ kHz}$  and  $10 \text{ kHz} \leq f \leq 15 \text{ kHz}$ .

those observed in the conducting shell. It appears that the replacement of the conducting shell by the resistive shell does not seem to affect the internal resistive kink mode (tearing mode) with high toroidal mode numbers  $n$ , as expected by the linear MHD stability theories. On the other hand, kink instabilities with low  $n$  predicted by the linear theories for the resistive shell case are not observed.

In order to investigate detailed MHD behavior of the plasmas with the resistive shell, an array of 128 pickup loops, 32 toroidally by 4 poloidally, was installed over the outer surface of the helical coils at a minor radius of 0.255 m. Each pickup loop spans  $11.25^\circ$  toroidally by  $90^\circ$  poloidally, and together they cover the entire torus. The pickup loops are sensitive to radial magnetic fluxes.

Figure 2 shows a typical plasma current waveform and the magnetic loop signals at about 180 kA. Most of the pickup loop signals are reasonably quiet, as represented by the top pickup loop signal  $\tilde{B}_r$  at the toroidal location of  $78.50^\circ$  (Fig. 2b).

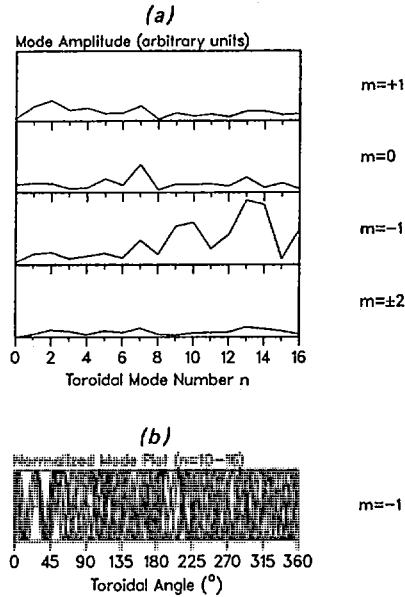


FIG. 5. (a) Mode amplitudes for  $m = +1, 0, -1$  and  $\pm 2$ , versus toroidal mode number. (b) Phases of the  $m = -1$  modes with  $10 \leq n \leq 16$ , as a function of toroidal angle  $\phi$ .

Figures 2c through 2h show the  $\dot{B}_r$  signals of the top pickup loops at  $146.25^{\circ}$  and  $157.50^{\circ}$ ; the outside pickup loops at  $140.625^{\circ}$  and  $151.875^{\circ}$ ; and the bottom pickup loops at  $135.00^{\circ}$  and  $146.25^{\circ}$ , respectively. These exhibit a local kink instability starting at about 4 ms into the discharge with a growth time of about 1 ms (i.e., resistive shell time). Its toroidal extent is limited to approximately one period and its toroidal period ( $\sim 0.5$  m long) corresponds to  $n \sim 16$ . It has the same helical handedness as internal magnetic field lines. The plasma shape with this mode is analogous to the kink when the spring toy "slinky" is twisted. Thus, we have named it the "slinky" mode.

An interesting and important feature of the slinky mode is that it suddenly stops growing, as seen at 6 ms in the example, and self-heals. Apparently, slinky modes arise randomly in time and toroidal position. As its amplitude increases, the mode also expands spatially in the toroidal direction, but a sudden rearrangement of the plasma prevents it from growing further beyond one or two periods, and the slinky mode decays away after the rearrangement.

The plasma high frequency oscillations seen also have characteristic mode numbers  $n \sim 16$ . The spectra of  $m = -1$  high frequency oscillations measured by a pickup loop inside the shell indicate development of a peak between  $10 \sim 20$  kHz when a slinky mode is growing nearby. Figures 3a and 3b show the spectra obtained from another shot before the development of the slinky mode (2.1 ~ 2.6 ms) and near its maximum amplitude (3.35 ~ 3.85 ms). Figure 4 illustrates the time behavior of average power spectra,  $B_z^2$ , for the  $m = -1$  mode with  $5 \text{ kHz} < f < 7.5 \text{ kHz}$  and  $10 \text{ kHz} < f < 15 \text{ kHz}$ . It indicates the power in 10-15 kHz started decreasing soon after the plasma rearrangement, which occurred at 3.6 ms in this case.

The Fourier analysis of the 128 pickup coil signals shows that  $m = -1$  is the dominant mode when a slinky mode exists, as shown in Fig. 5a. The analysis of  $n$  mode numbers indicates that the dominant modes are  $10 < n < 16$ . However, because of the finite number of pickup coils, modes with  $16 < n < 22$  could also have contributed. It turns out that the several  $m = -1$  modes with adjacent  $n$ -mode numbers around 16 form a slinky mode if they all add up at one location. Indeed, Fig. 5b confirms that all the  $m = -1$  with  $n$  values mentioned above are adding up near  $\phi = 35^\circ$ , where the slinky mode is located. This leads to the following explanation: Typical RFP plasmas are unstable against  $m = -1$  resistive internal kink modes with  $n \gtrsim 10$ . The modes with very high  $n$  numbers may be stable because of the magnetic shear. Thus, the  $m = -1$  modes with  $10 \lesssim n \lesssim 22$  may become all unstable and grow with the resistive shell time-scale. Under a certain condition, they all lock together and add up at one location, forming a slinky mode. However, the phase locking is suddenly lost and after that the modes no longer add up. This is likely due to mixing of field lines through the slinky region, so the plasma finds a way to get to the relaxed state.

In summary, the results with the resistive shell are very similar to those with the conducting shell, except for the observation of the slinky mode, which grows with the resistive shell time-scale and then self-heals. This indicates that a highly conducting shell may not be required for a reversed field pinch and suggests that linear plasma stability is not always necessary in a confinement system.

#### ACKNOWLEDGEMENT

This work was supported by the United States Department of Energy, under Contract No. DE-FG03-86ER53228.

## REFERENCES

- [1] TAMANO, T., et al., in *Plasma Physics and Controlled Nuclear Fusion Research 1984* (Proc. 10th Int. Conf. London, 1984), Vol. 1, IAEA, Vienna (1985) 431.
- [2] BAKER, D.A., et al., *ibid.*, p. 439.
- [3] CAROLAN, P.G., et al., *ibid.*, p. 449.
- [4] HIRANO, Y., et al., *ibid.*, p. 475.
- [5] ANTONI, V., et al., *ibid.*, p. 487.
- [6] GOEDBLOED, J.P., et al., *Nucl. Fusion* **12** (1972) 649.
- [7] TANAKA, M., et al., *Nucl. Fusion* **12** (1972) 119.
- [8] NALESSO, G.F., COSTA, S., *Nucl. Fusion* **20** (1980) 443.
- [9] GOFORTH, R.R., et al., *Nucl. Fusion* **26** (1986) 515.

# ENERGY CONFINEMENT AND NONLINEAR TEARING MODE DYNAMICS IN A HIGH CURRENT REVERSED FIELD PINCH

Z.G. AN<sup>1</sup>, P.H. DIAMOND, T.S. HAHM,  
G.S. LEE<sup>2</sup>, B.D. SCOTT  
Institute for Fusion Studies,  
The University of Texas at Austin,  
Austin, Texas

B.A. CARRERAS, L. GARCIA,  
J.A. HOLMES, V.E. LYNCH  
Oak Ridge National Laboratory,  
Oak Ridge, Tennessee

United States of America

## Abstract

ENERGY CONFINEMENT AND NONLINEAR TEARING MODE DYNAMICS IN A HIGH CURRENT REVERSED FIELD PINCH.

Energy confinement and nonlinear tearing mode dynamics in RFP plasmas are discussed. The observed broadening of the  $m = 1$  mode spectrum and the role of  $m = 1$  interaction with the  $m = 0$  mode in this process are examined. Magnetic fluctuation levels are found to be insensitive to resistivity. Developments in the theory of resistive pressure gradient driven turbulence are reported, and ion temperature gradient driven modes are identified as a possible loss mechanism at higher current. Pellet injection is proposed as a means of improving energy confinement in RFP plasmas.

## 1. NONLINEAR TEARING MODE DYNAMICS

The dynamics of  $m = 1$  tearing modes has been linked to relaxation and configuration maintenance in Reversed Field Pinch (RFP) plasmas. [1] In previous work [2,3], the basic theory of MHD turbulence in current-carrying plasma was developed and used to describe the nonlinear interaction of  $m = 1$  tearing modes in RFP. In particular, a new, nonlinear saturation mechanism based on 'cascading' to small scales initiated by the generation of  $m = 2$  current sheets was proposed and used to estimate  $\langle B_z \rangle$  evolution (i.e. field-reversal) rates using quasilinear theory. Here, further

<sup>1</sup> Present address: Center for Nonlinear Studies, Los Alamos National Laboratory, NM, USA.

Permanent address: Department of Physics, Beijing University, Beijing, China.

<sup>2</sup> Present address: Oak Ridge National Laboratory, TN, USA.

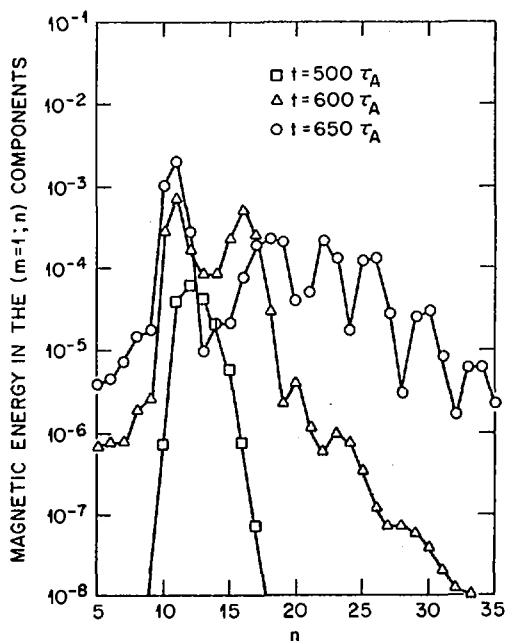


FIG. 1. Evolution of the  $n$ -spectrum of  $m = 1$  modes in time.

detailed studies of the saturation and relaxation mechanisms are summarized. Attention is focussed on the broadening of the  $m = 1$  spectrum in toroidal mode-number  $n$  and radius, the role of nonlinear interaction with the  $m = 0$ ,  $n = 1$  mode in this process, and on what the nonlinear dynamics imply about magnetic fluctuation levels. Throughout this paper, frequent reference is made to the results of nonlinear, numerical calculations. These computations, which utilize the reduced MHD (RMHD) equations for RFP [4] unless otherwise indicated, should be viewed as a means for elucidation of basic physical processes and not as 'simulations' of RFP plasmas.

Initially, tearing modes with  $m = 1$ ,  $10 < n < 20$  are destabilized by resistive diffusion away from the Taylor state. However, in the course of nonlinear evolution, the  $m = 1$  spectrum broadens, as  $m = 1$  modes with  $20 < n < 40$  are generated. At the same time, the radial extent of the turbulent zone broadens to encompass the region from the axis to reversal surface. Figures 1 and 2 illustrate these features of  $m = 1$  mode evolution.

The broadening of the  $m = 1$  spectrum discussed above is a consequence of quasilinear 'mode competition' and nonlinear interaction. However, comparison of quasilinear numerical calculations, which retain  $m = 1$  and  $m = 0$ ,  $n = 0$  evolution only, with corresponding full nonlinear calculations indicates that nonlinear coupling processes are dominant (Fig. 3).

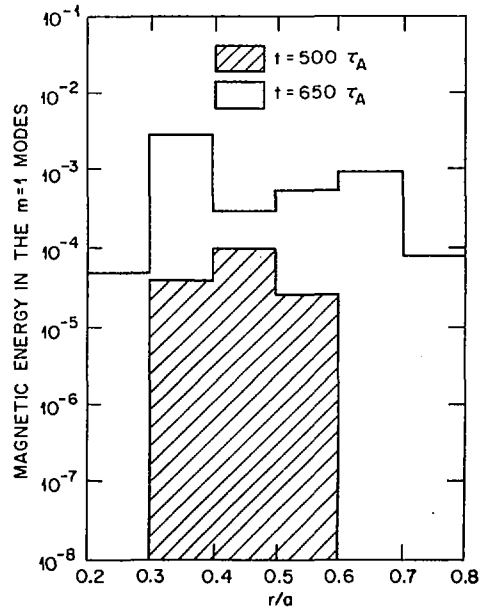


FIG. 2. Evolution of the  $m = 1$  mode spectrum in radius.

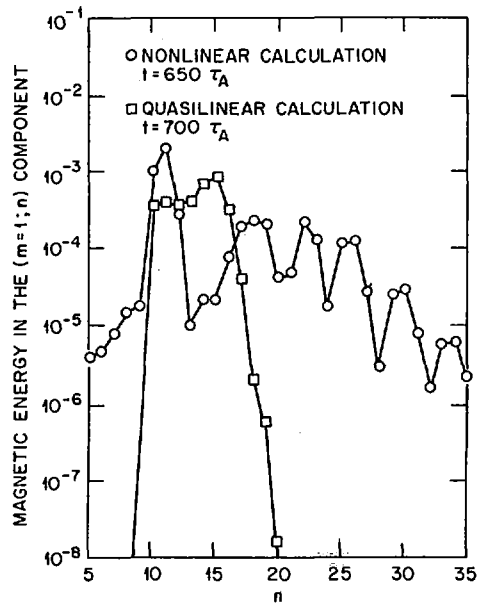
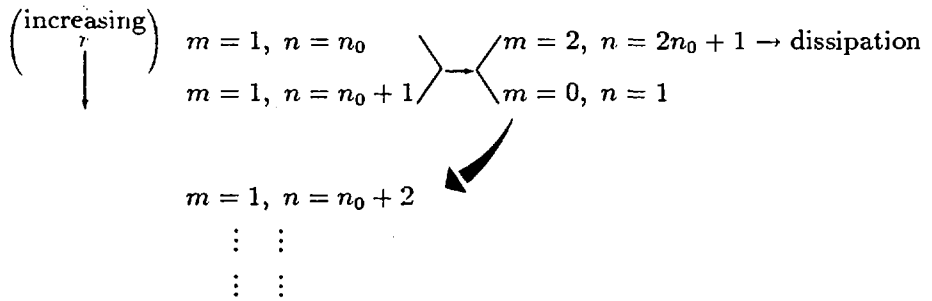


FIG. 3. Comparison of quasilinear and nonlinear effects in the evolution of the  $m = 1$  mode spectrum.

Indeed, the  $m = 1$  spectrum is strongly affected by nonlinear interaction with the  $m = 0, n = 1$  mode. This is because neighboring  $m = 1, n = n_0; m = 1, n = n_0 + 1$  modes beat together to drive  $m = 0, n = 1$  and  $m = 2, n = 2n_0 + 1$  modes. The  $m = 2, n = 2n_0 + 1$  mode is a localized, stable, driven current sheet which transfers  $m = 1$  energy to small scale dissipation. In contrast, the driven  $m = 0, n = 1$  mode is global, with stability maintained by strong magnetic shear at the reversal surface. It back-reacts with the  $m = 1, n = n_0 + 1$  to drive the  $m = 1, n = n_0 + 2$ . As a result, the  $m = 1$  spectrum broadens. The radial spreading of the turbulent zone is, in turn, a consequence of the generation of  $m = 1$  modes with progressively lower resonant  $q(r_s)$  values. This process of nonlinear mode competition can thus be represented as:



and has been observed experimentally. Indeed, the  $m = 1$  spectrum evolution indicated by the nonlinear calculations (Fig. 4) is in good, qualitative agreement with results from the HBTX1-A RFP [5].

Theoretical insight into the role of the  $m = 0$  mode in  $m = 1$  dynamics may be gained by utilizing the previously derived energy spectrum equations [3] for MHD turbulence in current-carrying plasma. In particular, the  $m = 0, n = 1$  is driven by coherent scattering from  $m = 1, n = n_0$  off  $m = 1, n = n_0 + 1$ . Similarly, the  $m = 1, n = n_0 + 2$  is driven by incoherent emission from the beating of  $m = 1, n = n_0 + 1$  with  $m = 0, n = 1$ . These two nonlinear interaction processes appear in the mode energy ( $E$ ) evolution equations as:

$$\frac{\partial}{\partial t} E_{n=n_0}^{m=1} \cong \int dx \sum_{m',n'} \Delta'_{m'',n''} \frac{\delta(x'')}{\Delta\omega_{m'',n''}} I(m = 1, n = n_0; m' = 1, n' = n_0 + 1) \tag{1}$$

$$\frac{\partial}{\partial t} E_{n=n_0+2}^{m=1} \cong - \int dx \sum_{\substack{m',n' \\ m'',n''}} \frac{\Delta'_{1,n_0+2}}{\Delta\omega_{1,n_0+2}} \delta(x) I(m' = 1, n' = n_0 + 1; m'' = 0, n'' = 1) \tag{2}$$

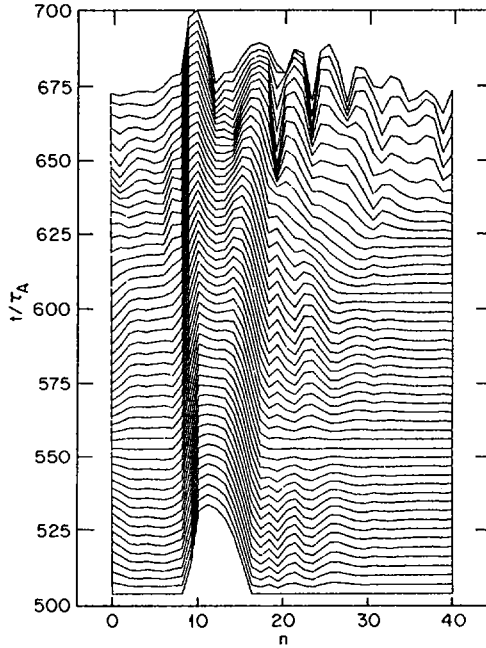


FIG. 4. Time evolution of the  $m = 1$  spectrum.  
(Compare with Fig. 19 of Ref. [5].)

respectively, where

$$I(\mathbf{r}, \mathbf{s}) = \left\langle (\nabla_{\perp} \hat{A}_{\perp})^2 \right\rangle_{\mathbf{r}} \left\langle (\nabla_{\mathbf{r}} \hat{\phi})^2 \right\rangle_{\mathbf{s}} + \left\langle (\nabla_{\perp} \hat{\phi})^2 \right\rangle_{\mathbf{r}} \left\langle (\nabla_{\mathbf{r}} \hat{A}_{\parallel})^2 \right\rangle_{\mathbf{s}}$$

Here,  $\Delta'$  is the MHD stability parameter,  $\Delta\omega_k$  is the nonlinear decorrelation rate,  $\hat{\phi}$  is the electrostatic potential and  $\hat{A}_{\parallel}$  is the parallel component of the vector potential (i.e.  $\hat{A}_{\parallel} \simeq \hat{A}_z$  in the core,  $\hat{A}_{\parallel} \simeq \hat{A}_{\theta}$  at the reversal surface). It is important to note that  $\Delta'_{m=0} < 0$ ,  $\Delta'_{m=2} < 0$  and  $\Delta'_{m=1} < 0$  for  $20 < n < 40$ , i.e. the  $m = 1$  modes with higher  $n$ 's are nonlinearly driven. As a consequence of the global character of the  $m = 0$  mode (i.e. Fig. 5),  $m = 1$  interaction with  $m = 0$  is stronger than with  $m = 2$ , discussed previously. However, it is clear from Eqs. (1,2) that the nonlinear interaction terms are of opposite sign, so that cancellation would result if an  $n$ -summation were performed. This result, which follows from energy conservation, indicates that the principal role of interaction with the  $m = 0$ ,  $n = 1$  mode is to *redistribute*  $m = 1$  mode energy among different  $n$ 's. However, since the  $m = 1$ ,  $n = n_0$  spectrum broadens, the  $m'' = 2$ ,  $n'' = 2n_0 + 1$  driven mode spectrum also broadens, thus facilitating net  $m = 1$  damping via nonlinear coupling to smaller scales. Hence, the  $m = 0$ ,  $n = 1$  interaction

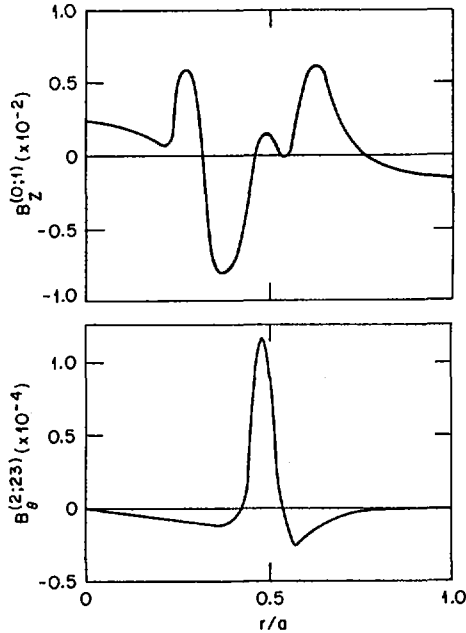


FIG. 5. Comparison of the  $m = 0$  and  $m = 2$  radial eigenfunctions.

also serves to accelerate the true nonlinear saturation mechanism. Indeed, the slow decay of the  $E(m)$  spectrum (Fig. 6) is consistent with the notion of cascade to small scales. Finally, it should be noted that reconnection associated with the driven  $m = 0$ ,  $n = 1$  mode serves to 'lock-in' the reversed  $\langle B_z(r) \rangle$  quasilinearly generated by  $m = 1$  kink modes [3].

The scaling of saturated  $m = 1$  mode magnetic fluctuation levels with magnetic Reynolds number  $S = (\tau_R/\tau_A)$  is of considerable interest. Previous work [3], which predicted a weak dependence of  $(\hat{B}/B)_{m=1}$  on  $S$ , was based on an assumed balance of linear  $m = 1$  growth with nonlinear coupling to  $m = 2$ . However, the results of the numerical calculations indicate that  $(\hat{B}_r/B)_{m=1}$  is *virtually independent of  $S$*  (Fig. 7)! Hence, despite the robust character of  $m = 1$  modes, the linear growth rate is apparently *not* a good approximation for the instability drive in the nonlinear regime. Recently [6], the closure theory for MHD turbulence in current-carrying plasma was extended to include a treatment of the driving term

$$- \int dx \langle \hat{\phi} \nabla_{\perp} \hat{A}_{\parallel} \rangle_{\mathbf{k}} \langle J \rangle$$

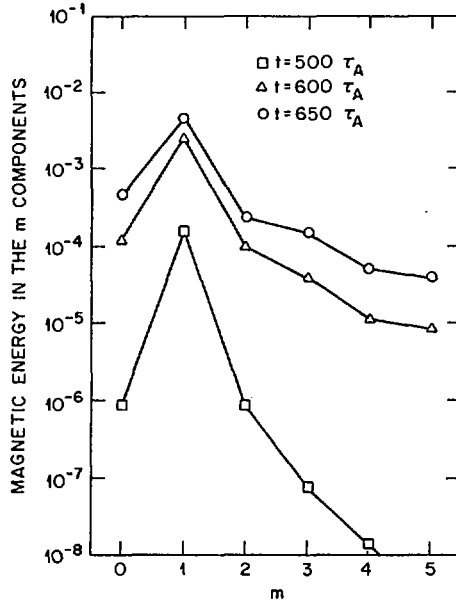


FIG. 6. Mode energy spectrum as a function of  $m$ .

This energy source term depends on the cross-correlation  $\langle \hat{\phi} \nabla_{\perp} \hat{A}_{\parallel} \rangle_{\mathbf{k}}$  which is, in turn, determined by the closure equation:

$$\begin{aligned} \frac{\partial}{\partial t} \langle \hat{\phi} \nabla_{\perp} \hat{A}_{\parallel} \rangle_{\mathbf{k}} &= \left( a_{\mathbf{k}} + \frac{\nabla_{\perp}^2}{S} \right) \langle \hat{\phi} \nabla_{\perp} \hat{A}_{\parallel} \rangle_{\mathbf{k}} \\ &= \langle (\nabla_{\perp} \hat{A}_{\parallel}) \nabla_{\perp}^{-2} (\nabla_{\perp} \hat{A}_{\parallel}) \rangle_{\mathbf{k}} - k_{\parallel} k_{\perp} \left( \langle \hat{A}_{\parallel}^2 \rangle_{\mathbf{k}} - \langle \hat{\phi}^2 \rangle_{\mathbf{k}} \right) \end{aligned} \quad (3)$$

where

$$a_{\mathbf{k}} = \sum_{\mathbf{k}'} \Delta'_{\mathbf{k}''} \frac{\delta(x'')}{\Delta \omega_{\mathbf{k}''}} \langle (\nabla_{\perp} \hat{A}_{\parallel})^2 \rangle_{\mathbf{k}'} \quad (4)$$

Equation (3) represents an extension of mean-field-electrodynamics [7] to inhomogeneous, current-carrying plasmas. During nonlinear evolution,  $a_{\mathbf{k}} > \|\nabla_{\perp}^2/S\|$  and thus the solution for the driving term does not scale with  $S$ . Alternatively, nonlinear interaction rather than resistive diffusion determines the phase-shift between  $\hat{\phi}$  and  $\nabla_{\perp} \hat{A}_{\parallel}$ . These conclusions are supported by scale transformation analysis of the basic nonlinear equations, in the limit of negligible inertia (i.e.  $\mathbf{B} \cdot \nabla J_{\parallel} \approx 0$ ). A further assumption, required to properly treat the multiplicity of scales inherent in tearing modes, is that  $\hat{J}_{\parallel} \sim (\Delta'/w) \hat{A}_{\parallel}$ , where  $w$  is the radial scale factor ultimately determined by dimensional analysis.

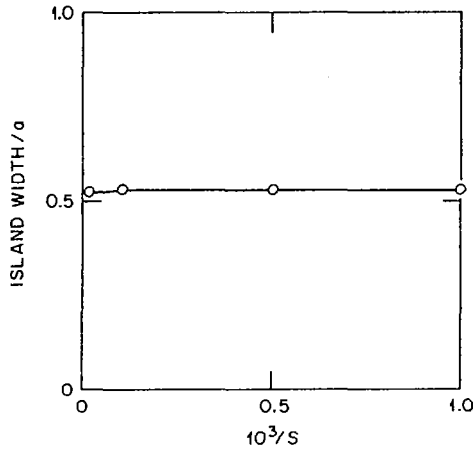


FIG. 7.  $m = 1$ ,  $n = 10$  mode island width ( $\omega_i$ ) plotted versus  $S^{-1}$ .

Investigations of high temperature tearing mode dynamics utilizing RMHD with additional temperature and density evolution equations indicate that the nonlinear evolution of even a *single* tearing mode may depart significantly from expectations based on linear theory. In particular, finite-sized islands were initialized and allowed to evolve. Results indicate that even if the underlying mode is linearly stable [8], the island need only be weakly nonlinear ( $W_I^2 > L_s^2 \omega_{*e} / \chi_{\parallel} k_{\perp}^2$ , where  $W_I$  is the island width,  $\omega_{*e} = k_{\perp} \rho_s c_s / L_T$ ,  $\chi_{\parallel} = v_{Te}^2 / \nu_{e,e}$ ) in order that flattening of temperature along field lines causes the islands to grow under the influence of  $\Delta'$  [9]. Thus, the nonlinear interaction mechanisms and their consequences discussed above may be expected to persist into higher temperature regimes, even if linear theory predicts stability there.

## 2. Energy Confinement

Energy confinement in RFP plasmas is determined by a combination of tearing mode and microinstability induced loss mechanisms. Foremost amongst the latter is resistive pressure gradient driven turbulence (RPGDT) due to resistive interchange modes. Previous work [3] predicted that magnetic fluctuations associated with RPGDT drive stochastic magnetic field induced transport with thermal diffusivity  $\chi_E \sim (\epsilon / a q')^3 \beta_{\vartheta}^{3/2} v_{Te} a / S$ . Balancing such losses with Ohmic heating yielded the scaling relations  $T_e \sim I_p^2 / N$ , where  $N$  is the line-averaged density, and  $\beta_{\vartheta} \sim (r q' / \epsilon) (m_e / m_i)^{1/6} \sim 10\%$ . These results were derived using heuristic mixing-length arguments. However, recent theoretical and computational

studies of RPGDT [10,11] indicate that while heuristic approaches may be adequate for predicting scalings, they do not accurately predict fluctuation levels. In particular, the thermal diffusivity is enhanced beyond the previous result according to  $\chi_E = \chi_E^{(0)} \Lambda^{3/2}$ , where  $\Lambda$  [11] is a logarithmic function of  $\beta_\theta$ ,  $S$ , etc. For typical RFP parameters,  $\chi_E/\chi_E^{(0)} \sim 10!$  As a consequence, the new results predict a slow degradation of  $\beta_\theta$  as  $I_p$  increases. Finally, when the diamagnetic frequency  $\omega_{*e}$  exceeds the characteristic MHD frequency (i.e. growth rate) for RPGDT,  $\chi_E$  is modified according to [12]:

$$\chi_E = \chi_E^{(0)} / \left(1 + \overline{(\omega_{*e}/\gamma)^2}\right)^{1/4} \quad (5)$$

where the bar denotes a spectrum average. Thus, steep density gradients tend to quench RPGDT losses.

The RPGDT model is, of course, based on resistive MHD. However, at temperatures expected in future high current RFP experiments, the conditions required for the applicability of resistive MHD will be violated. In particular, the rather flat density profiles and strong ion heating (via equilibration, proportional to  $n^2$ , and anomalous processes) present in RFP plasmas make it quite possible that  $\eta_i = d\ln T_i/d\ln n$  exceeds the threshold  $\eta_{i,crit} \sim 1.5$  for the onset of another type of pressure gradient driven turbulence, namely that produced by ion temperature gradient driven ( $\eta_i$ )-modes. Ion temperature gradient driven modes [13] are insensitive to electron collisionality, with growth rates  $\gamma \sim [(1+\eta_i)/\tau] |nq'| \rho_s c_s / r$  increasing with shear and mode widths  $\Delta x \sim [(1+\eta_i)/\tau]^{1/2} \rho_s$ . Here  $\tau = T_e/T_i$  and  $\rho_s = c_s/\Omega_i$ . Moreover, inclusion of non-adiabatic electron dynamics allows coupling of the  $\eta_i$ -mode to the resistive interchange mode [14]. This coupling acts to enhance instability in all parameter regimes. Indeed, solution of the eigenmode equation for the coupled system reveals a smooth spectrum of roots from the pure RPGDT limit (non-adiabatic electron) to the pure  $\eta_i$ -mode (adiabatic electron) limit. At higher temperatures (i.e.  $k_{\parallel}^2 v_{Te}^2 / \omega \nu > 1$ ) the  $\eta_i$ -mode character dominates. In particular,  $\eta_i$ -modes are broader and more robust than semi-collisional resistive interchange modes. Results from renormalized turbulence theory [15] indicate that the resulting ion thermal diffusivity is given by

$$\chi_i = |c(\text{Re})|^2 \bar{n} \frac{|q'|}{r} \rho_s^2 c_s \left(\frac{1+\eta_i}{\tau}\right)^2 \quad (6)$$

where  $c(\text{Re}) \sim \ell n(1+\eta_i)$  and  $\bar{n}$  is the average toroidal mode number. It follows that for ZT-40 parameters, the predicted energy confinement time is  $\tau_E \sim .5 \text{msec}$ . Balancing with Ohmic heating (for  $T_e \sim T_i$ ) yields the scaling relations  $T \sim I_p/N^{1/4}$  and  $\beta_\theta \sim N^{3/4}/I_p$ . Hence,  $\beta_\theta$  may be expected to degrade with current (for  $N \sim I_p$ ) if  $\eta_i$ -modes are excited.

The implications of the various studies of RFP thermal transport can be summarized as follows. In the core, magnetic fluctuations driven by  $m = 1$  tearing modes dominate. Since  $\hat{B}/B$  remains constant as  $I_p$  increases, central confinement is always poor. Nearer the edge, RPGDT and  $\eta_i$ -modes control the local transport. Results indicate that *both* mechanisms result in the degradation of  $\beta_\theta$  as  $I_p$  increases. Thus, the implications appear quite pessimistic at first glance. However, it is important to recall that steep density gradients tend to suppress  $\eta_i$ -modes ( $\eta_i < \eta_{i,crit}$ ) and to quench RPGDT losses via diamagnetic effects (Eq. (5)). Hence, improving particle confinement and steepening the density profile may be expected to result in improved energy confinement! Thus, *pellet injection* is suggested as a potentially viable mechanism for improving RFP performance at high currents.

### ACKNOWLEDGMENT

This research was supported by the Office of Fusion Energy, U.S.D.O.E., under Contract No. DE-FG05-80ET-53088 with The University of Texas and Contract No. DE-AC05-84OR21400 with Martin Marietta Energy Systems, Inc.

### REFERENCES

- [1] WATT, R.G., NEBEL, R.A., Phys. Fluids **26** (1983) 1168.
- [2] DIAMOND, P.H., et al., Phys. Fluids **27** (1984) 1449.
- [3] AN, Z.G., et al., in Plasma Physics and Controlled Nuclear Fusion Research 1984 (Proc. 10th Int. Conf. London, 1984), Vol. 2, IAEA, Vienna (1985) 231.
- [4] STRAUSS, H.R., Phys. Fluids **27** (1984) 2580.
- [5] HUTCHINSON, I.H., et al., Nucl. Fusion **24** (1984) 59.
- [6] LEE, G.S., PhD Thesis, The University of Texas at Austin, 1986.
- [7] MOFFATT, H.K., Magnetic Field Generation in Electrically Conducting Fluids, Cambridge Univ. Press (1978).
- [8] DRAKE, J.F., et al., Phys. Fluid **26** (1983) 2509.
- [9] SCOTT, B.D., et al., Phys. Rev. Lett. **54** (1985) 1027.
- [10] CARRERAS, B.A., et al., Rep. No. 247, Institute for Fusion Studies, Texas Univ. (1986); to be published in Phys. Fluids.
- [11] CARRERAS, B.A., et al., Paper IAEA-CN-47/D-V-2, these Proceedings, Vol. 2.
- [12] DIAMOND, P.H., et al., Phys. Fluids **28** (1985) 1116.
- [13] COPPI, B., et al., Phys. Fluids **10** (1967) 582.
- [14] AN, Z.G., et al., in Compact Toroids (Proc. 7th Int. Conf. Santa Fe, NM, 1985), Los Alamos National Lab., NM.
- [15] LEE, G.S., DIAMOND, P.H., Phys. Fluids **29** (1986).

## THEORETICAL AND EXPERIMENTAL STUDIES OF FIELD REVERSED CONFIGURATIONS\*

D.C. BARNES

Science Applications International Corporation,  
Austin, Texas, United States of America

W.T. ARMSTRONG, E.J. CARAMANA, R.E. CHRIEN,  
W.N. HUGRASS, H.R. LEWIS, R.K. LINFORD, K.M. LING,  
K.F. McKENNA, D.J. REJ, J.L. SCHWARZMEIER,  
R.E. SIEMON, M.M. TUSZEWSKI, K.A. WERLEY  
Los Alamos National Laboratory,  
Los Alamos, New Mexico, United States of America

D.S. HARNED

Courant Institute, New York University,  
New York, N.Y., United States of America

S. OKADA

Osaka University,  
Osaka, Japan

C.E. SEYLER

Cornell University,  
Ithaca, N.Y., United States of America

D.E. SHUMAKER

National Magnetic Fusion Computer Center,  
Livermore, California, United States of America

H. TUCZEK

Essen University,  
Essen, Federal Republic of Germany

G. VLASES, R.D. BROOKS, Z.A. PIETRZYK,  
K.D. HAHN, D. LOTZ, R. RAMEN, J. WIGHT  
University of Washington,  
Seattle, Washington, United States of America

### Abstract

#### THEORETICAL AND EXPERIMENTAL STUDIES OF FIELD REVERSED CONFIGURATIONS.

Important new Field Reversed Configuration (FRC) results are presented. A kinetic ion model is used to calculate the growth rate of the internal tilting mode, including exact ion orbits in a self-consistent, axisymmetric FRC. Previous calculations, which used the MHD mode as a trial function,

---

\* Work supported by the United States Department of Energy.

are extended to determine the kinetic eigenfunction consistently. A regularity condition must be imposed on the solution at the internal field null (0-point). This condition is derived for an appropriate choice of the independent variable. The new results on kinetic stabilization in present experiments show kinetic modifications of the tilt mode and reductions in growth rate for large  $s$  comparable to those found in previous studies. — Transport calculations using both 1½-D and 1½-D models show that experimentally observed transport exceeds classical expectations by roughly one order of magnitude. — The FRX-C/T formation region has been enlarged in diameter by 50%, and quasi-steady cusp coils have been installed to compare tearing and non-tearing formation. FRCs with significantly larger poloidal flux ( $\leq 8$  mWb) and  $s$  ( $\leq 4$ ) have been formed. However, their flux confinement was degraded compared with earlier FRX-C results. — Initial results from the Coaxial Slow Source (CSS) are reported and compared with numerical modeling. A long 'annular FRC' is formed at lower voltages and is maintained for 30 to 60  $\mu$ s. Flux builds up to levels of 7 to 10 mWb with a flux confinement time of about 15  $\mu$ s.

### KINETIC STABILITY CALCULATIONS

A long-standing question concerning FRC observations has been the lack of experimental observation of the internal tilt mode, even though MHD calculations predict a virulent instability. In the Los Alamos FRX-C experiment, for example, FRCs show no evidence of the internal tilt mode for the transport-determined lifetime of up to 300  $\mu$ s, which is over an order of magnitude larger than the MHD growth time. Profile effects [1], nonlinear effects [2] and finite Larmor radius [3,4] theory do not explain the stability. Recent Vlasov-fluid model computations [5] show that large orbit ions have a strong stabilizing effect on the tilt mode. In the present computation, a dispersion functional (quadratic form) [6] is constructed, which includes exact ion orbits in a self-consistent 2-D FRC equilibrium. Efficient use of data generated by a Monte Carlo sampling of particle orbits makes the calculation feasible numerically. For a representative FRC equilibrium, the kinetic value of the growth rate has been calculated vs.  $s$  (Fig. 1), where  $s$  measures the number of local ion Larmor radii from the field null to the separatrix. Values of  $s$  in present experiments for cases that optimize confinement are in the range of 1 to 2. In initial calculations, which used the MHD eigenmode as a trial function in the kinetic dispersion functional, the growth rate for  $s \leq 2.0$  is less than the MHD value by more than a factor of 10. When  $s$  increases to about 7, the growth rate increases to about one half of the MHD value.

In the stabilized regime ( $s \leq 2$ ) strong kinetic effects may cause the kinetic mode to differ significantly from the MHD mode. The effect of this variation on the growth rate is investigated by extending the previous calculations so that the kinetic eigenmode is determined self-consistently along with the eigenfrequency. As described previously [5], the field-line displacement  $\xi$  is represented in terms of a single function  $\xi_z(\psi)$ , where  $\psi$  is the magnetic flux and  $\xi_z$  the axial displacement. An approximation of  $\xi_z$  was first determined by

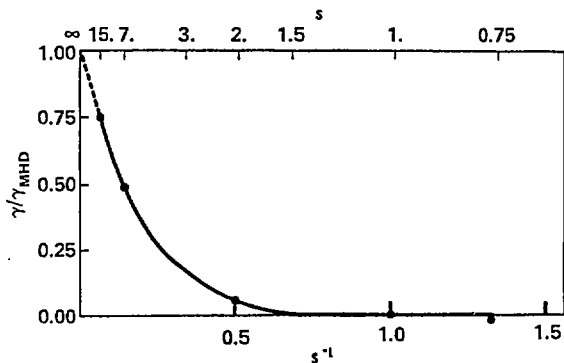


FIG. 1. Variation of normalized kinetic growth rate with system size parameter  $s$ . As  $s \rightarrow 0$ , mode becomes kinetically stabilized. As  $s \rightarrow \infty$ , kinetic growth rate approaches MHD growth rate. Points obtained numerically are indicated. Lower scale indicates  $s^{-1}$  as the abscissa, the upper  $s$  (increasing to left).

expanding  $\zeta_z$  in terms of a finite basis set of functions of  $\psi$ , then requiring the variation of the dispersion functional with respect to the conjugate expansion coefficients to vanish. However, this procedure led to very inaccurate results. This inaccuracy appears to have been caused by admixture of a component of the singular solution of the integro-differential normal mode equation near the o-point, which is a singular point of the magnetic flux coordinates. It has proven to be effective to consider the regularity problem in terms of an independent variable  $\rho$  instead of  $\psi$ . The variable  $\rho$  is a radius-like coordinate defined by  $\rho = \sqrt{\psi - \psi_0}$ , where  $\psi_0$  is the value of  $\psi$  at the o-point. The requirement that the magnetic field and current density be nonsingular at the o-point implies that  $\zeta_z$  be twice differentiable with respect to  $\psi$ . In terms of  $\rho$ , this condition means that the first and third derivatives of  $\zeta_z$  with respect to  $\rho$  vanish at  $\rho = 0$ .

Results have been obtained by imposing this regularity condition and the condition that  $\zeta_z$  vanish at the separatrix onto the basis of B-splines over a uniform  $\rho$  mesh. That is, linear combinations of the B-splines which satisfy these boundary conditions are first formed; then  $\zeta_z$  is represented as a linear combination of these resulting basis elements, the coefficients of which are determined by the variational procedure. Figure 2 shows a comparison of the kinetic mode with the previously determined MHD mode for an MHD-like case ( $s = 15$ ). For this approximation, the range of  $\rho$  from the o-point to the separatrix was divided into 9 uniform intervals. Even for this large  $s$  case, there is a modification of the mode near the o-point where kinetic effects dominate. The mode also develops an imaginary part (phase is chosen to make  $\zeta_z$  real at the o-point), so that there is a twisting of the tilt as position varies across the

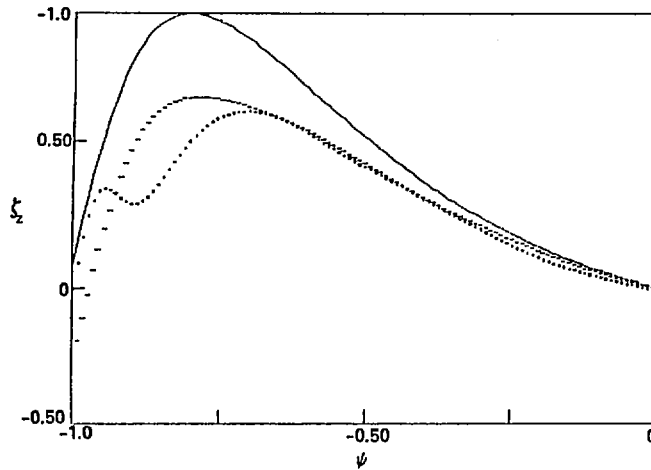


FIG. 2. Comparison of MHD eigenmode (solid curve) with real (dashed curve) and imaginary (dotted curve) parts of kinetic mode for  $s = 15$ . Normalization is such that area under magnitude of kinetic mode is same as MHD mode and max of MHD mode is unity.

flux surfaces. The growth rate determined with this self-consistent mode is 0.76 of the MHD value, compared to 0.75 obtained using the MHD mode as a trial function. Calculations of the self-consistent mode in the kinetically stabilized regime are now being completed.

#### FRC TRANSPORT CALCULATIONS

Transport simulations of FRCs were performed using both 1-1/2-D [7] and 1-1/4-D [8,9] transport codes. The 1-1/2-D code alternates between an 2-D equilibrium and a 1-D transport calculation, and includes Braginskii and lower-hybrid drift (LHD) transport coefficients. The 1-1/4-D code refers to a 1-D FRC model with some 2-D effects. This latter code describes radial transport in both the closed and open field line regions, while incorporating such effects as axial contraction of the separatrix, flux surface averaging and axial streaming and conduction along open field lines. By multiplying the classical collision frequencies by appropriate factors, the confinement times for the FRX-C experiment can be duplicated to within 10% by both transport codes. The 1-1/2-D code predicts that for the 20 mtorr case the e-i collision frequency must be increased by a factor of about 4.5 at the o-point while only a factor of one at the separatrix. For the 5 mtorr case the resistivity anomaly factor at the o-point is 11. Ion thermal conduction is approximately classical, while the electron thermal conductivity is strongly anomalous. For example, in the 5 mtorr case, the electron thermal conductivity is 22 times classical. For both

the 5 and 20 mtorr cases only half of the LHD anomalous resistivity is used. Comparison of the 1-1/4-D code with the 1-1/2-D code has been done for the case of thermal conduction being the only transport mechanism, and the agreement is good. Simulations of the FRX-C experiment with the 1-1/4-D code predict for 20 mtorr:  $\kappa_i = \kappa_{cl}$ ,  $\kappa_e = 6.5 * \kappa_{cl}$ ,  $\eta = 5.2 * \eta_{cl}$ ; and for 5 mtorr:  $\kappa_i = \kappa_{cl}$ ,  $\kappa_e = 36 * \kappa_{cl}$ ,  $\eta = 9 * \eta_{cl}$ . In the 20 mtorr case, electron-ion equilibration dominates and holds  $T_i = T_e$ . In the 5 mtorr case, ions on the open field lines are collisionless thereby permitting  $T_i$  to remain high for the discharge duration. It is unclear whether the difference between the 5 and 20 mtorr cases is due to some transport scaling or whether the plasma is exhibiting completely different transport physics regimes.

## STUDIES OF TEARING AND NON-TEARING FORMATION IN LSM

### A. Introduction

The FRX-C/T device[10] has been modified by enlarging the diameter of the FRC formation region by 50%. This larger formation region (termed LSM for Large Source Modification) will be more suitable for future translation and adiabatic compression experiments; it has to date been used (without translation) to study the processes governing FRC formation. An important experimental objective is to achieve the maximum possible trapped poloidal flux  $\phi_p$  in the larger source (corresponding to maximum  $s$ ) in order to obtain optimum confinement and to look for the tilt instability. Improved FRC formation in small (0.2 → 0.3 m) diameter devices has been reported when field line tearing and reconnection is avoided[11,12]. Installation of quasi-steady cusp coils on LSM has permitted comparisons of tearing and non-tearing formation in a larger device which are reported here. It was found that larger-radius FRCs (up to 0.21 m), with increased values of the inferred  $\phi_p$  ( $\leq 8$  mWb) and  $s$  ( $\leq 4$ ), could be formed in LSM. However, their flux confinement, in both tearing and non-tearing operation, was degraded compared with that obtained in earlier FRX-C experiments[13,14].

### B. Description of Experiment

The measurements were obtained with the formation geometry and magnetic characteristics listed in Table I. The plasma was created in an initial 10 mtorr static fill of deuterium gas (except for 2 mtorr results in section E.). The preionization method consisted of an initial seed ionization produced by a 10 MHz generator coupled to antennas at each end of the coil, followed by full ionization produced by a 175 kHz ringing  $\vartheta$ -pinch discharge. The capacitor bank energies and voltages were unchanged from earlier FRX-C operation. Thus the azimuthal electric field at the quartz tube during field-reversal was decreased from 37 kV/m in FRX-C to 28 kV/m in LSM. Another significant change was the decrease in  $\vartheta$ -pinch coil elongation

TABLE I. CHARACTERISTICS OF LSM

<u>Formation Geometry</u>	
$\varphi$ -Pinch Coil Length (overall)	2.01 m
Coil Central Diameter (1.4 m long)	0.76 m
Passive Mirror Diam. (0.3 m each end)	0.68 m
Magnetic Mirror Ratio (on axis)	1.20
Quartz Chamber I.D.	0.60 m
<u>Magnetic Fields</u>	
Main Field Swing (vacuum)	0.6 T
Main Field Rise Time ( $\tau/4$ )	6.7 $\mu$ s
Main Field Decay Time (L/R)	500 $\mu$ s
$\varphi$ -Preionization Field Amplitude	0.08 T
Bias Field (maximum)	0.13 T
Cusp Field (maximum on axis)	0.30 T
Cusp Field Rise Time ( $\tau/4$ )	4 ms

(length between mirror peaks to central diameter ratio) from 3.6 to 2.1, which tended to reduce the FRC elongation and increase the influence of the mirror fields on the FRC equilibrium. The passive mirror ratio of 1.20 was sufficient to prevent FRCs from drifting axially out of the coil following formation (a mirror ratio of 1.11 was found to be inadequate).

### C. Tearing versus Non-Tearing Formation

After performing initial tests of tearing formation, cusp coils were installed at each end of the  $\varphi$ -pinch coil to permit direct comparison of tearing and non-tearing formation. The two formation techniques are illustrated by the 2-D MHD simulations[15] shown in Fig. 3. The simulations indicated that cusp field strength  $B_{\text{cusp}} \geq 0.05 \rightarrow 0.10$  T was needed to avoid tearing and ejection of part of the plasma at each end. This transition was qualitatively confirmed by a large reduction in visible light observed at the end during non-tearing formation.

Cusp fields were found to enhance flux trapping. This enhancement was particularly noticeable at weak bias field  $B_b$  ( $B_b < 0.08$  T) for which the "zero-crossing" flux,  $\phi_{zc} = \phi(B_w=0)$ , was increased by 1.3  $\rightarrow$  2.5 times that obtained with  $B_{\text{cusp}} = 0$ .

The use of cusp coils was observed to improve the symmetry (about the axial midplane) of FRC formation. One way to quantify the improved symmetry was to observe the maximum axial speed of the FRCs separatrix volume. The corresponding axial kinetic energy decreased monotonically from 28 J to 8 J as  $B_{\text{cusp}}$  was increased from 0 to 0.2  $\rightarrow$  0.3 T. The observed improvement in formation symmetry was consistent with the transition from tearing to non-tearing formation as predicted by the simulations.

The axial contraction tended to be stronger for non-tearing formation. The strength of the axial contraction was estimated using the minimum elongation  $\epsilon_{\text{min}}$  defined as the ratio of the

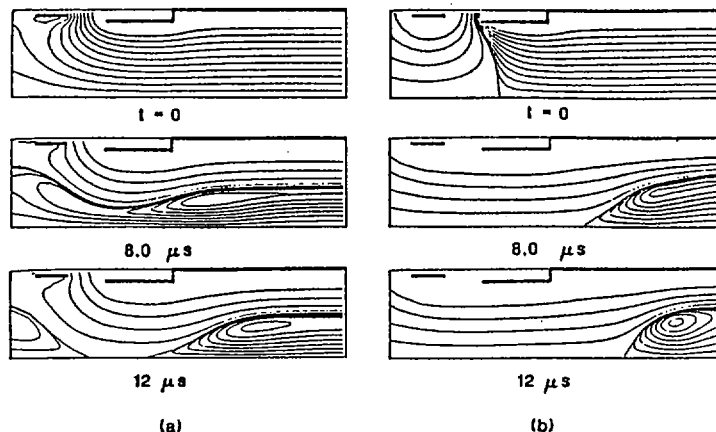


FIG. 3. Configuration of LSM formation region showing simulations of (a) tearing and (b) non-tearing formation. In tearing formation, closed field lines tear and reconnect under passive mirrors after main field has risen. In non-tearing formation, cusp coil fields drive preformed FRC separatrix inwards in axial direction shortly after field reversal, thereby preventing tearing.

(FWHM) length of the FRC measured using an axial array of interferometers to the maximum diameter inferred from the separatrix radius profile. The  $\epsilon_{\min}$  values were  $1.2 \rightarrow 1.8$  without tearing and  $2.0 \rightarrow 3.5$  with tearing (for  $B_b = 0.07 \rightarrow 0.09$  T). The axial contraction also took place earlier without tearing.

For the formation conditions which optimized confinement, larger  $\varphi_p$  values could be retained in the equilibrium FRC with non-tearing formation. An example of the parameters of one of the best FRCs formed using non-tearing formation is shown in Fig. 4. The largest average  $\varphi_p$  values ( $5.8 \pm 0.6$  mWb, where the error estimates denote standard deviations) were obtained for  $B_{\text{cusp}} = 0.2 \rightarrow 0.3$  T and  $B_b = 0.08 \rightarrow 0.09$  T ("cusp on" condition). When  $B_{\text{cusp}} = 0$  ("cusp off" condition),  $\varphi_p$  was lower ( $2.3 \pm 0.5$  mWb for  $B_b = 0.065 \rightarrow 0.075$  T). However, larger  $\varphi_p$  with tearing formation ( $3.5 \pm 0.6$  mWb) could be obtained under similar conditions before the cusp coils were installed ("no cusp" condition). Thus it appeared that the currents induced in the cusp hardware were detrimental to the tearing formation process.

Corresponding to the larger  $\varphi_p$ , larger values of  $s$  (up to 4) were also attained with non-tearing formation. In the "cusp on" condition,  $s$  values of  $2.7 \pm 0.4$  were observed at  $30 \mu\text{s}$  after field-reversal. In the "cusp off" condition, the  $s$  values were  $1.9 \pm 0.4$ . Both  $\varphi_p$  and  $s$  were inferred from external measurements assuming a typical diffuse profile[14] that matched FRX-C data. Further work is needed to determine the most appropriate profile for LSM conditions.

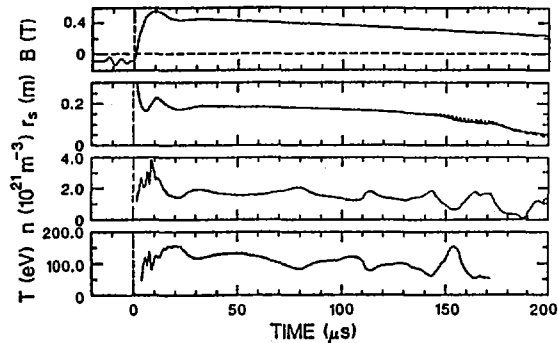


FIG. 4. Time evolution of external magnetic field, separatrix radius, average density, and average temperature  $((T_i + T_e)/2)$  for one of the best FRCs formed without tearing. Equilibrium ( $t = 30 \mu\text{s}$ ) is characterized by  $x_s = 0.50$ ,  $\phi_p = 6.7 \text{ mWb}$ , and  $s = 3.0$ . Confinement times ( $t = 30 - 100 \mu\text{s}$ ):  $\tau_\phi = 130 \mu\text{s}$ ,  $\tau_N = 250 \mu\text{s}$ , and  $\tau_E = 85 \mu\text{s}$ .

#### D. FRC Confinement

The confinement times of flux ( $\tau_\phi$ ), particles ( $\tau_N$ ), and energy ( $\tau_E$ ) were determined over an interval from the start of the axial equilibrium ( $t = 30 \mu\text{s}$ ) to the appearance of the  $n=2$  mode ( $t = 70 \pm 10 \mu\text{s}$ ). When no  $n=2$  oscillations occurred, the time the separatrix radius began to decay more rapidly was chosen to end the interval.

The flux confinement of FRCs produced in LSM was, on average, degraded compared with that observed in earlier FRX-C experiments. Similar average  $\tau_\phi$  values were observed for "cusp on" ( $\tau_\phi = 58 \pm 40 \mu\text{s}$ ) and "cusp off" ( $\tau_\phi = 50 \pm 22 \mu\text{s}$ ) conditions. Somewhat better average flux confinement was observed during tearing formation in the "no cusp" condition ( $\tau_\phi = 110 \pm 45 \mu\text{s}$ ). The maximum  $\tau_\phi$  was about  $200 \mu\text{s}$ . The absence of  $T_e$  measurements prevented detailed comparisons with classical flux confinement predictions. However, the resistivity anomaly with respect to the classical resistivity of a 100 eV plasma (assuming a rigid rotor FRC profile) was in the range  $15 - 60$ . This was significantly larger than the resistivity anomaly ( $3 - 7$ ) measured in FRX-C[13,14].

The particle confinement in LSM improved with  $\tau_\phi$  ( $\tau_N \approx 1.2\tau_\phi$ ). For those FRCs with greater than average  $\tau_\phi$  values,  $\tau_N$  was, on average, a factor of two smaller than the predictions of a transport theory based on lower hybrid drift turbulence[16]. The global energy confinement times[17] scaled with  $\tau_N$  ( $\tau_E \approx \tau_N/2$ ) in a manner consistent with an energy balance dominated by particle convection.

#### E. Low Fill Pressure Operation

A data run at 2 mtorr was conducted in which hotter ( $T_e + T_i \leq 0.8 \text{ keV}$ ) and less dense ( $\bar{n} \approx 5 \times 10^{20} \text{ m}^{-3}$ ) FRCs were formed. The best confinement,  $\tau_\phi = (75 \pm 35) \mu\text{s}$ , could only be

achieved with non-tearing formation ( $B_{\text{cusp}} \approx 0.25 \text{ T}$ ) and weak bias ( $B_{\text{b}} \approx 0.04 \text{ T}$ ). Tearing formation at 2 mtorr resulted in poor confinement with  $\tau < 35 \mu\text{s}$  for any  $B_{\text{b}}$ . For non-tearing formation strong axial  $\phi$  contractions were observed and the equilibrium values of  $\phi_{\text{p}}$  ( $= 2.6 \pm 0.3 \text{ mWb}$ ) and  $s$  ( $\approx 1.0$ ) were smaller than those inferred at 10 mtorr because of the lower  $B_{\text{b}}$  and higher  $T_{\text{i}}$ .

#### F. Discussion

LSM experiments (and formation simulations) have shown several advantages in the use of auxiliary quasi-steady cusp coils for FRC formation. First, cusp fields in sufficient strength permit FRC formation without field line tearing and reconnection driven by mirror fields. This eliminates the necessity for those mirror fields during formation. Second, non-tearing formation is more symmetric, resulting in less axial speed. Third, FRCs with larger  $\phi_{\text{p}}$  and  $s$  can be formed in the non-tearing mode. Fourth, FRC formation was possible at low (2 mtorr) fill pressure with non-tearing formation. These advantages were attained in LSM without the complexity of rapidly pulsed auxiliary coils and precise timing necessary for "balloon"[11] or "programmed"[12] formation modes.

Flux confinement was degraded in LSM compared with earlier tearing formation results in FRX-C, independent of the formation mode used. The degraded confinement is not presently understood. Some possible explanations are poor formation, low  $T_{\text{e}}$ , FRC elongations that are too small (either transiently or in equilibrium), interaction with mirror fields, and instability to the tilt mode. The possibility of low  $T_{\text{e}}$  will be tested by Thomson scattering measurements. Elongation and mirror effects can be ameliorated by a change in coil geometry (e. g. a 0.70 m diam. coil without passive mirrors) or by translation experiments using the FRX-C/T translation region. We have attempted to identify tilt instability by searching for  $m=1, n=1$  magnetic perturbations ( $B_{\phi}$ ) outside the quartz vacuum chamber. No evidence for the tilt mode has been detected by this method (but it is not clear whether the probe sensitivities ( $10^{-3} \text{ T}$ ) are adequate to detect the largely internal mode predicted by linear theory). It is also worth noting that formation at low bias field or fill pressure resulted in FRCs with the same range of  $s$  as in FRX-C and yet continued to show lower  $\tau_{\phi}$  values. This indicates that formation or equilibrium problems are more likely than tilt instability to be responsible for the degraded flux confinement.

#### LOW VOLTAGE GENERATION OF ANNULAR FRC'S IN THE CSS DEVICE

The conventional modified  $\psi$ -pinch method of forming FRCs, as exemplified by the FRX-C device, requires flux insertion on Alfvén time scales, with concomitant high-voltage technology. We report here on early results with a system called the Coaxial

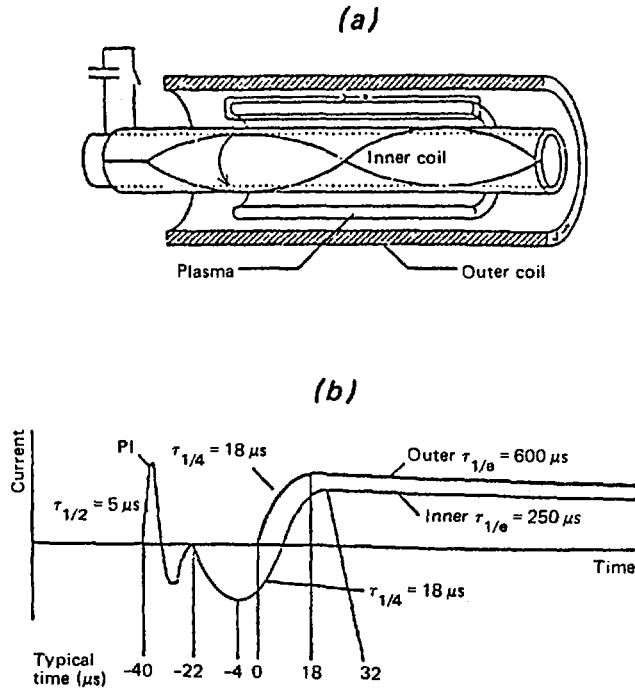


FIG. 5. (a) Schematic of CSS; (b) CSS timing.

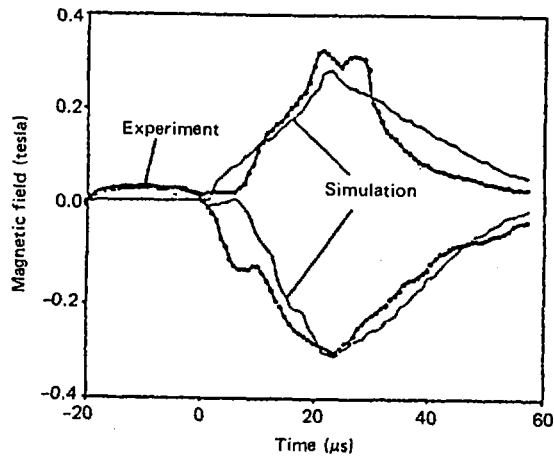


FIG. 6.  $B_z$  at midplane adjacent to inner (below) and outer (above) coils.

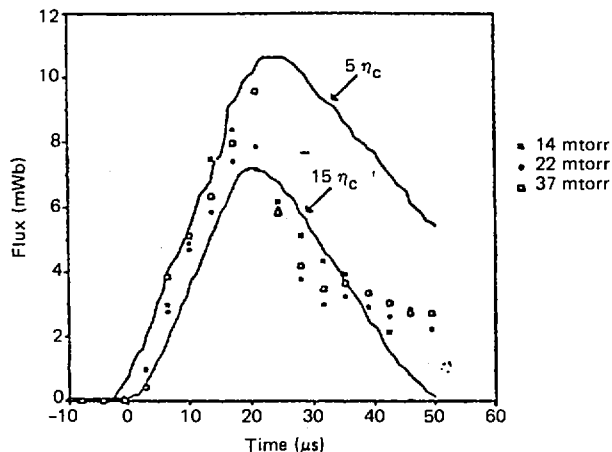


FIG. 7. Flux within separatrix measured and predicted on the basis of resistivities shown.

Slow Source (CSS) [18], which is designed to form "annular FRCs" (Fig. 5a) at low voltage, with flux build-up on diffusive time scales. In an optimized system, the flux inside the inner coil goes to zero as the inner coil current reaches its maximum (3rd-1/4 cycle, Fig. 5b) so that no flux links both coils and the plasmoid can, in principle, be translated into a simple cylindrical chamber, and coalesce into a true compact toroid. The CSS coils are 95 cm long and have radii of 7 and 21 cm. The loop voltage is typically 1.25-2 kV, with stored energies up to 25 kJ and an effective system rise time of 30  $\mu$ s. Deuterium fill pressures used range from 10 to 50 mtorr. Design of the device and experiment interpolation have been aided by the use of calculations based on a 2-D resistive MHD code coupled to a vacuum field solver [19]. The principal results of the initial testing phase of the program are as follows:

- The field reversed configuration, characterized by oppositely directed  $B_z$  fields at the inner and outer walls, is established quickly after start of the outer coil current, for all fill pressures examined. It lasts from 30 to 60  $\mu$ s, depending on coil voltage ratio and fill pressure (Fig. 6).
- The flux within the separatrix increases for approximately 25  $\mu$ s, to values of 7-10 mWb, depending on charging voltage and fairly independent of fill pressure. Figure 7 shows a comparison of experiment and simulation.
- The plasma radial position can be controlled by choice of coil voltage ratio. The length remains long under most cases, with X-points near the coil ends, similar to simulation plots of Fig. 8.

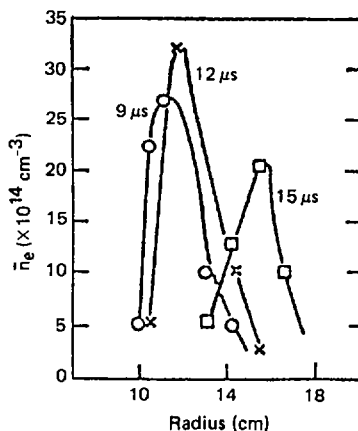


FIG. 8. Calculated flux contours.

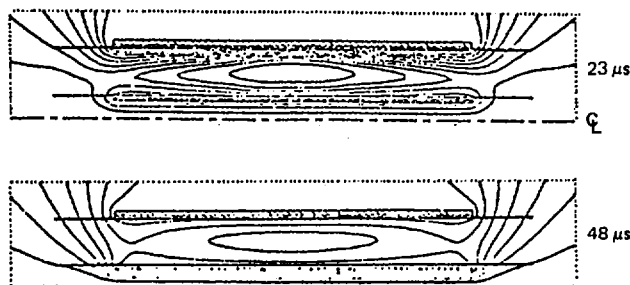


FIG. 9. Holographically determined electron density.

- Density profiles are measured holographically, as illustrated in Fig. 9. Pressure balance total temperatures range from 50 eV at  $P_o = 50$  mtorr to about 200 eV at  $P_o = 10$  mtorr.
- The flux lifetime is on the order of 15  $\mu$ s, nearly independent of  $P_o$ , and thus  $T_e + T_i$ . This suggests the presence of an anomalous, drift-parameter dependent, effective resistivity as is seen in conventional FRCs, although low  $T_e$  values resulting from radiation barriers may play a role as well.

In conclusion, slow flux buildup to FRX-C like levels has been achieved on long time scales, and at about 1/50th of the FRX-C loop voltage. Efforts are now concentrating on improving plasma lifetime.

## REFERENCES

- [1] SCHWARZMEIER, J.L., BARNES, D.C., HEWETT, D.W., SEYLER, C.E., SHESTAKOV, A.I., SPENCER, R.L., Phys. Fluids **26** (1983) 1295.
- [2] SCHNACK, D.D., BARNES, D.C., AYDEMIR, A.H., ANDERSON, D.V., submitted to Phys. Rev. Lett.
- [3] SEYLER, C.E., BARNES, D.C., Phys. Fluids **25** (1981) 1989.
- [4] SCHWARZMEIER, J.L., SEYLER, C.E., Phys. Fluids **27** (1984) 2151.
- [5] BARNES, D.C., SCHWARZMEIER, J.L., LEWIS, H.R., SEYLER, C.E., Phys. Fluids **29** (1986) 2616.
- [6] LEWIS, H.R., BARNES, D.C., SCHWARZMEIER, J.L., SEYLER, C.E., Phys. Fluids **28** (1985) 2546.
- [7] SHUMAKER, D.E., Rep. UCRL-94433, Lawrence Livermore National Lab.; submitted to J. Comput. Phys.
- [8] CARAMANA, E.J., Phys. Fluids **28** (1985) 3557.
- [9] WERLEY, K.A., Rep. LA-UR-86-642, Los Alamos National Lab.; submitted to Phys. Fluids.
- [10] REJ, D.J., et al., Phys. Fluids **29** (1986) 852.
- [11] BELIKOV, V.V., et al., in Plasma Physics and Controlled Nuclear Fusion Research 1982 (Proc. 9th Int. Conf. Baltimore, 1982), Vol. 2, IAEA, Vienna (1983) 343.
- [12] SLOUGH, J.T., et al., Nucl. Fusion **24** (1984) 1537.
- [13] TUSZEWSKI, M., et al., Phys. Fluids **25** (1982) 1696.
- [14] SIEMON, R.E., et al., Fusion Technol. **9** (1986) 13.
- [15] MILROY, R.D., BRACKBILL, J.U., Phys. Fluids **25** (1982) 775.
- [16] TUSZEWSKI, M., LINFORD, R.K., Phys. Fluids **25** (1982) 765.
- [17] REJ, D.J., TUSZEWSKI, M., Phys. Fluids **27** (1984) 1514.
- [18] VLASES, G.C., et al., Bull. Am. Phys. Soc. **29** (1984) 1369.
- [19] BARNES, D.C., SCHNACK, D.D., Bull. Am. Phys. Soc. **30** (1985) 1514.



# EXPERIMENT ON RELATIVISTIC ELECTRON BEAM RING CORE SPHERATOR

K. NARIHARA, T. TOMITA, S. KUBO, M. HASEGAWA<sup>1</sup>,  
M. MATSUI, T. TSUZUKI, A. MOHRI  
Institute of Plasma Physics,  
Nagoya University,  
Nagoya, Japan

## Abstract

EXPERIMENT ON RELATIVISTIC ELECTRON BEAM RING CORE SPHERATOR.

Intense relativistic electron beam (REB) rings with a peak current of 30 kA and a lifetime of 40 ms are realized in SPAC-VII by using a novel REB injector improved in impurity reduction and REB trapping efficiency. A very quiescent phase at a fluctuation level  $|\hat{B}_p/B_p|$  as low as  $10^{-5}$  continues for more than 15 ms at a ring current of 20 kA. There, the activity of velocity anisotropy instabilities becomes very weak, owing to the strong decrease of the acceleration field induced by the current decay. The RF produced plasma is demonstrated to be confined around the ring with a particle confinement time of about 1 ms.

## 1. INTRODUCTION

It has been shown [1] that a magnetic configuration such as spherator (Astron-Spherator [2] or REB Ring Core Spherator [1]) can be formed by injecting a pulsed, intense relativistic electron beam (REB) into the toroidal device SPAC-VII. This configuration has marked features that distinguish it from ordinary tokamak. No sawtooth oscillations occur although the  $q$ -value varies from less than 1 at the centre to 3 to 4 in the outer confinement region. The current profile peaks more sharply than that of a tokamak but no MHD-like instabilities are present. Owing to the strong vertical field necessary for ring equilibrium, a toroidal magnetic configuration with a deep magnetic well, together with high shear, is formed. Therefore, high  $\beta$  plasma may, in principle, be confined. For example, the stability criteria for both Mercier's condition and ballooning modes lead to a  $\beta$ -limit above 20%, excluding kink modes which have not been observed in the experiment.

The experiments on SPAC-VII were carried out in an attempt to solve the following key problems in order to improve the chances for an REB ring core

---

<sup>1</sup> Mitsubishi Electric Corporation, Tokyo 100, Japan.

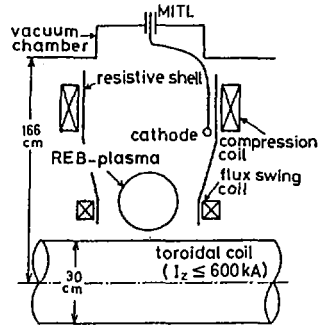


FIG. 1. Schematic drawing of ring formation section of toroidal device SPAC-VII.

spherator to function as a fusion plasma container: (i) effective formation of a long lived, high current REB ring, (ii) conditions for achieving a stable REB ring and (iii) clarifying the characteristics of a confined plasma.

## 2. FORMATION OF INTENSE LONG LIVED REB RING

The ring formation section is drawn schematically in Fig. 1. To generate an REB (normally, of 900 keV, 30 kA, 700 ns), a high voltage pulse was sent on a 7 m long transmission line from a Marx generator to an REB injector installed inside the formation section. The toroidal field produced by a current in a central conductor was 3 kG at a major radius of  $R = 30$  cm; the vertical magnetic field was pre-programmed to control the orbital motion of the injected REB and the equilibrium position of the formed ring.

To achieve high current REB rings, the trapping efficiency of the injected REB was substantially improved by developing a new injector system. A cathode of conical shape was placed near the side wall at  $R = 58$  cm and connected to a metallic rod attached to the end of the transmission line (Fig. 1). Both the cathode and the rod were immersed in a gun produced plasma before the pulse was imposed. The rod worked as a magnetically insulated transmission line (MITL) with the plasma operating as the outer conductor. This is an extension of the plasma anode method [3]. Owing to the small cross-section of the rod MITL and the action of the electromagnetic fields around the injector, a bombardment of the injected REB by the injector after circulating around the torus was prevented to such an extent that the loss in injected REB as well as the resulting release of metallic impurities were substantially reduced.

A factor which limits the attainable ring current is the deceleration of injected electrons by an electric field induced by the rising ring current [4]. Injection of an REB with higher energy is, therefore, favourable in order to

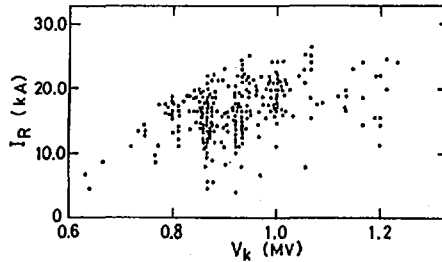


FIG. 2. Ring current versus cathode voltage.

maintain sufficient kinetic momentum of the beam electrons in the ring. In Fig. 2, the ring current  $I_R$  is plotted versus the acceleration voltage  $V_k$  for different conditions. The upper envelope of  $I_R$  increases with  $V_k$  up to  $V_k^L \sim 1\text{MV}$ , but saturates in the range  $V_k < V_k^L$ , where electric breakdown is observed around the injector. The voltage  $V_k^L$  was increased with the new injector so that REB injection became possible at higher beam energy without encountering a fatal impurity problem.

When the new injector was used, the intensity of the bremsstrahlung X-rays decreased by more than one order of magnitude compared with the case of the old injectors. To find out the origin of residual impurities, different materials (C, Ti, Ta, Mo) were attached on the wall and/or used for the cathode, and impurity lines were diagnosed spectroscopically. The residual impurities were mainly released from the wall and not from the cathode. These concentrations were evaluated in the plasma by comparing X-ray intensities before and after argon gas puffing. The relation  $X \propto \sum_z n_z Z^2$  was used, where  $X$  is the intensity and  $n_z$  the density of particles with atomic number  $Z$ . Thus, it was found that  $n_z Z^2 / n_e < 20$ . This means that further reduction of the impurities is necessary in order to attain better plasma confinement and a longer lifetime of the REB ring.

### 3. STABILITY OF REB RING

Frequently, REB rings are accompanied by two kinds of instabilities (Fig. 3(a)): one is characterized by stepwise current drops and the other one by a train of short pulse increments in line emission, X-rays and diamagnetic signals [5]. When the former instability occurred, the ring position moved inward so as to retain equilibrium. This instability is, as yet, beyond control but seems to be related to the strength of the toroidal field. An externally applied  $m = 1$  dominant error field  $B_{er}$  triggered the instability when the ratio  $B_{er}/B_T$  reached a threshold value.

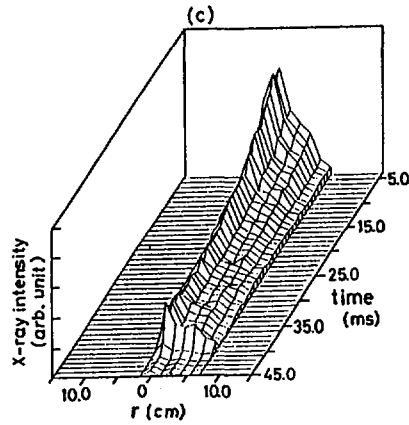
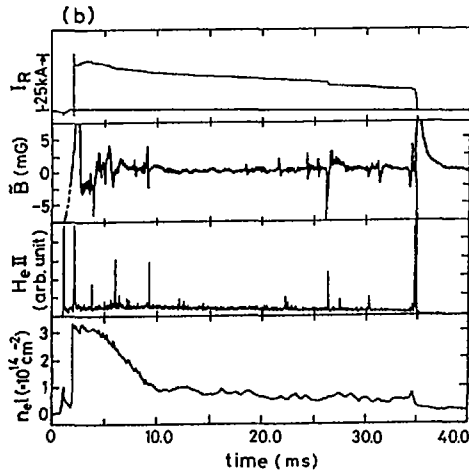
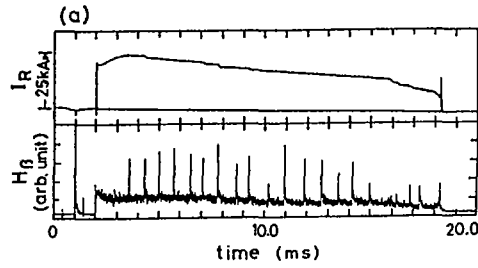


FIG. 3. (a) Traces exhibiting typical instabilities observed in REB ring. Ring current  $I_R$  and  $H_\beta$  radiation. (b) Behaviour of REB ring with REB injected into helium plasma. Ring current,  $I_R$ ; fluctuation of poloidal magnetic field,  $B$ ; He II radiation; and electron line density,  $n_e \ell$ . (c) Time evolution of minor radius profile of X-ray emissivity.

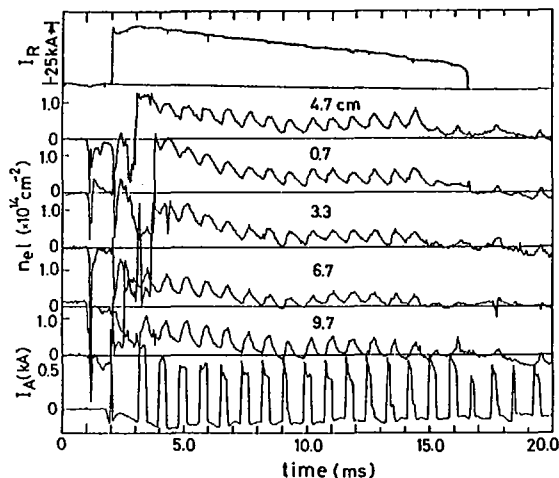


FIG. 4. Time evolution of electron line densities along different chords during RF power application. Distance between ring centre and each chord is indicated. For reference, RF antenna current,  $I_A$ , and ring current,  $I_R$ , are shown.

The latter instability, arising with pulsive signals, is in many respects similar to tail anisotropy instabilities observed in tokamak plasmas with suprathreshold or runaway electrons: However, the plasma, in this experiment, is in the  $\omega_{pe} > \omega_{ce}$  regime, in contrast to the tokamak case,  $\omega_{pe} < \omega_{ce}$ . The repetition rate of the pulsive signals became higher for faster current decay. This fact suggests that the beam electrons were accelerated by the electric field induced by the decay of the self-magnetic ring flux.

When the REB was injected into a helium plasma with a lower neutral particle concentration, the lifetime of the ring was extended to 40 ms or more; it decayed exponentially with a time constant of 50 ms (Fig. 3(b)). It was noted that a very quiescent phase continued for 15 ms, while the fluctuation level of the poloidal field,  $|B_p/B_p|$ , was as low as  $10^{-5}$ . The kinetic instabilities caused by the velocity anisotropy to be noticed in Fig. 3(a) disappeared, in this case, because of the weak acceleration of the tail electrons (if present). The profile of the X-ray emissivity, which reflected the profile of the REB electrons, maintained its peaked shape during such a long decay phase (Fig. 3(c)).

#### 4. PLASMA CONFINEMENT

The electron density profile measured with a five channel HCN laser interferometer system [6] shows that the plasma electrons produced in the REB ring region diffused towards the wall. To examine the particle confinement properties in greater detail, a pulsed RF (100 kW, 3.7 MHz, 0.2 ms pulse width with 25% duty) was applied to a one-third turn antenna set in the toroidal direction. Figure 4 shows the line integrated electron densities  $n_e l$  at five different chords

during the RF pulse train. The decay rate of  $n_e \ell$  at the centre was lower than that at the periphery, which indicates that the central region had better particle confinement than the periphery. The global electron confinement times estimated from these data are 1 ms for a ring current of  $I_R = 20$  kA and 0.5 ms for  $I_R = 12$  kA. From the spectroscopic data, the electron temperature was estimated to be lower than 10 eV. For the present plasma parameters ( $n_e = 5 \times 10^{12} \text{ cm}^{-3}$ ,  $T_e \sim 10$  eV,  $B_T = 3$  kG,  $R/a = 3$ ), the classical diffusion time is about 10 ms, which is about ten times longer than the observed value.

## REFERENCES

- [1] MOHRI, A., NARIHARA, K., TOMITA, Y., HASEGAWA, M., KUBO, S., TSUZUKI, T., KOBATA, T., FLEISCHMANN, H.H., in *Plasma Physics and Controlled Nuclear Fusion Research 1984* (Proc. 10th Int. Conf. London, 1984), Vol. 3, IAEA, Vienna (1985) 395.
- [2] YOSHIKAWA, S., CHRISTOFILOS, N.C., in *Plasma Physics and Controlled Nuclear Fusion Research 1971* (Proc. 4th Int. Conf. Madison, 1971), Vol. 2, IAEA, Vienna (1971) 375.
- [3] MOHRI, A., NARIHARA, K., TSUZUKI, T., KUBOTA, Y., TOMITA, Y., IKUTA, K., MASUZAKI, M., in *Plasma Physics and Controlled Nuclear Fusion Research 1978* (Proc. 7th Int. Conf. Innsbruck, 1979), Vol. 3, IAEA, Vienna (1979) 311.
- [4] NARIHARA, K., *Jpn. J. Appl. Phys.* **20** (1981) L683.
- [5] TOMITA, Y., NARIHARA, K., KUBO, S., TSUZUKI, T., MATSUI, M., MOHRI, A., in *High-Power Particle Beams* (Proc. 6th Int. Conf. Kobe, 1986) (1986) 399.
- [6] KUBO, S., NARIHARA, K., TOMITA, Y., TSUZUKI, T., MOHRI, A., in *Controlled Fusion and Plasma Heating* (Proc. 13th Europ. Conf. Schliersee, 1986), Vol. 1, European Physical Society (1986) 364.

## THREE-DIMENSIONAL MHD STUDIES OF THE MAGNETIC ENERGY RELAXATION PROCESSES

T. SATO, K. KUSANO  
Institute for Fusion Theory,  
Hiroshima University,  
Higashisenda-machi, Naka-ku, Hiroshima

R. HORIUCHI  
Science Project Corporation,  
Kuchita-minami, Asakita-ku, Hiroshima

Japan

### Abstract

#### THREE-DIMENSIONAL MHD STUDIES OF THE MAGNETIC ENERGY RELAXATION PROCESSES.

A unified theory of MHD relaxation is presented. Driven reconnection is found to be the only fundamental process governing the relaxation. The MHD relaxation is categorized into two types, i.e. 'global' relaxation, where the global magnetic topology is changed, and 'local' relaxation, where the topology remains the same. Global relaxation is associated with 'total' reconnection, which is reconnection of antiparallel fields. It is proved that local magnetic helicity vanishes at the reconnection point of total reconnection; thus, total helicity is conserved. Local relaxation, on the other hand, is associated with 'partial' reconnection, which is reconnection of obliquely intersecting fields. Helicity is, therefore, not zero at the reconnection point of partial reconnection; thus, total helicity is not conserved.

### 1. INTRODUCTION

The frozen-in principle is the basis of magnetic confinement in closed systems, e.g. stellarators, tokamaks, spheromaks, and FRCs. An ideal plasma can forever be confined within a closed magnetic surface. This is true, regardless of whether the configuration is ideally stable or unstable since the magnetic topology remains unchanged even locally against an ideal instability.

There are two ways a confined plasma can escape from a closed magnetic surface. One is slippage between the plasma and the magnetic surface or percolation of the plasma through the magnetic surface. This occurs without any change of the magnetic topology, neither globally nor locally. The other way is break of the magnetic surface. The first process may simply be called a 'diffusion' and the other one a 'reconnection' process. In both processes, 'resistivity' is the key parameter, whether it is classical or anomalous.

In this paper we survey the roles of the reconnection process in a magneto-hydrodynamic (MHD) plasma and propose a unified view of MHD confinement.

## 2. TOKAMAK-TYPE RELAXATION AND RFP-TYPE RELAXATION

We first assume that the diffusion process defined above is a sufficiently slow process on our time-scale of interest, i.e. on the MHD time-scale. Hence, the percolative escape of the plasma through a magnetic surface is negligible. In other words, unless a magnetic surface is broken by reconnection, the plasma confined by magnetic surface remains confined forever. Secondly, we assume that the effect of the diamagnetic current is negligible compared to that of the force-free current, i.e. the pressure effect is negligible.

On these assumptions, let us consider a force-free equilibrium confined by a closed conducting wall. If the equilibrium concerned is ideally stable, it can be a good candidate for magnetic confinement geometry. The so-called minimum energy state under a realistic constraint, notably, the constancy of the total magnetic helicity [1-4], is one of the ideally stable states. In other words, if the energy level of the initial equilibrium is higher than that of the minimum energy state, the equilibrium is ideally unstable, subject to a current driven (kink) instability [2-4].

According to the above definition of the minimum energy state, i.e. that the state is ideally stable, the tokamak configuration with an on-axis  $q$ -value larger than one and the RFP configuration can both be minimum energy states. The tokamak configuration with  $q_{\text{axis}} < 1$  and the RFP configuration in the setting-up phase are, however, both ideally kink-unstable. Therefore, they are not the minimum energy state. Thus, they tend to relax towards the corresponding minimum energy states. We notice an essential difference between the two relaxations: the initial and final tokamak configurations are 'topologically' identical, although some minor 'geometrical' difference may exist. In contrast, the initial and final RFP configurations are 'topologically' different.

## 3. PARTIAL AND TOTAL RECONNECTION

Let us here consider the physical reason for and the physical significance of the difference between the two relaxations. Of course, magnetic reconnection takes place in both relaxations. Therefore, some significant difference between the two reconnection processes must exist. As can be seen in Fig. 1, the initial and final topologies of the reduced field  $B^*$  are different. Here, the reduced part  $B^*$  is defined by  $B^* = B - B_H$ , where  $B$  is the true field and  $B_H$  is the resonant ( $n = 1$ ) helical field. When we express  $B = B_p \hat{\theta} + B_t \hat{\phi}$  and  $B_H = q B_p \hat{\theta} + B_t \hat{\phi}$ , where  $\hat{\theta}$  is the poloidal and  $\hat{\phi}$  the toroidal unit vector, we have  $B^* = (1-q) B_p \hat{\theta}$ . To see the topologies of the true fields we must, therefore, add the helical part  $B_H$  to  $B^*$ . Then, it turns out that the final topology is generally the same as the initial one, in the usual tokamak operation.

The above argument indicates that reconnection involved in the tokamak relaxation is 'partial' reconnection. 'Partial' means that only a fraction of the total magnetic

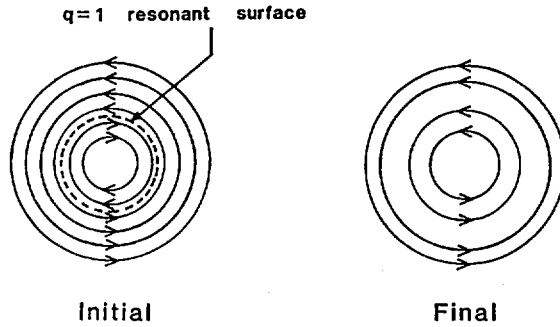


FIG. 1. Topologies of reduced field component of tokamak field,  $B^* = B - B_H$ , where  $B$  is tokamak field and  $B_H$  is resonant helical field of  $q = 1$ , before and after reconnection is triggered by  $m = 1/n = 1$  kink mode.

field takes part in the reconnection. More specifically, when a magnetic component exists perpendicular to the reconnection plane ( $B_H$  in the present example), i.e. when oblique field lines reconnect with each other, we speak of a 'partial' reconnection. Incidentally, it is also interesting to note that the  $m = 1/n = 1$  kink instability relevant to the tokamak relaxation is a resonant (non-global) instability. When antiparallel fields reconnect we shall, on the other hand, call this phenomenon a 'total' reconnection.

In the RFP relaxation, the global topology changes during the relaxation process. Since the  $m = 1$  kink instability relevant to the relaxation in this case is a global (non-resonant) instability, the entire plasma is deformed by the global flow induced by the global instability, and, consequently, non-linear driven reconnection takes place at certain places whereby the magnetic topology is globally changed [2-4]. This strongly suggests that the relevant reconnection process must be the 'total' rather than the 'partial' process.

Let us prove that the Taylor-type relaxation (which is accompanied by a global topological change) is caused by 'total' reconnection. As was mentioned previously, 'total' reconnection should not have a magnetic field component perpendicular to the reconnection plane. The previous simulation of RFP self-reversal strongly supports this hypothesis. Here we reproduce one example of Ref. [4], in Fig. 2. This figure shows that the reconnection point is more or less coincident with a point on the demarcation circle between the positive and negative toroidal fields, i.e. on the null toroidal field circle. Another evidence is that reconnection takes place at the null points of local magnetic helicity as is shown in Fig. 3 reproduced from Ref. [3]. Let us discuss this point analytically in the next section.

#### 4. HELICITY CONSERVATION IN TOTAL RECONNECTION

Without loss of generality, we can define the reconnection plane to be the  $x$ - $y$  plane, in rectangular co-ordinates  $(x, y, z)$ . Then, at the reconnection point, the mag-

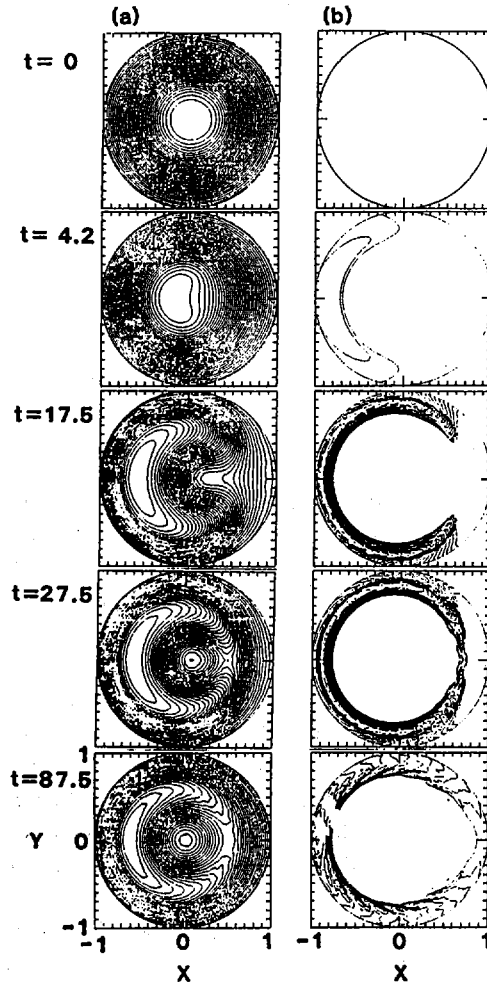


FIG. 2. Contours of helical flux (a) and negative toroidal field (b) at different times for single helicity simulation in RFP setting-up phase.

netic field  $\mathbf{B}$  has only the z-component  $B_z$ , i.e.  $\mathbf{B} = B_z \hat{z}$ . Thus, the local magnetic helicity  $K_x$  at the reconnection point is given by

$$K_x = \vec{\mathbf{A}} \cdot \vec{\mathbf{B}} = A_z B_z \quad (1)$$

Using the simulation result that the local helicity is zero at the (non-linearly formed) reconnection point, we may conclude that

$$B_z = 0 \quad (2)$$

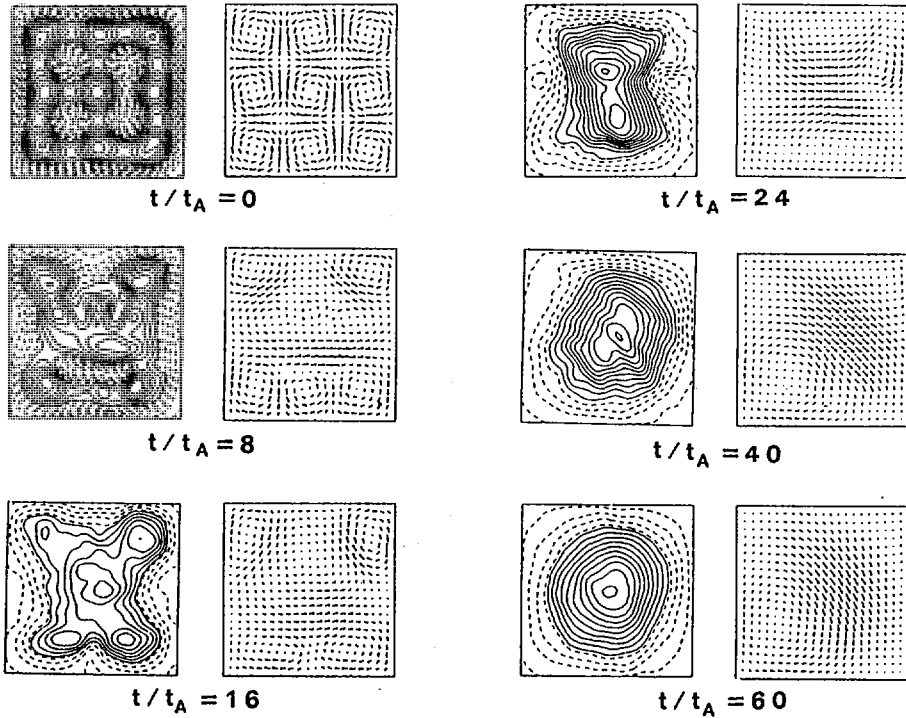


FIG. 3. Contour maps of magnetic helicity density and poloidal magnetic field lines of force in poloidal plane at six different times.

Thus, we can reach two important conclusions: non-linear driven reconnection as observed in Refs [2-4] is 'total' reconnection, and 'total' reconnection occurs at the 'zero' helicity point. Conversely speaking, since Taylor relaxation assumes 'total' reconnection resulting in a true topology change, the magnetic helicity does not decay at the reconnection point; hence, the total helicity is conserved.

## 5. GLOBAL AND LOCAL RELAXATION

We have seen above that there are two classes of MHD relaxation: one is associated with 'partial' reconnection and no global topology change occurs in the magnetic field. Tokamak relaxation generally corresponds to this class. The other class is associated with 'total' reconnection, and the magnetic topology is changed globally. The RFP (Taylor-type) relaxation corresponds to this class. We here propose to call the former class 'local relaxation' and the latter class 'global relaxation'.

## 6. NECESSITY OF DRIVEN RECONNECTION IN MHD RELAXATION

In what follows we shall discuss the time-scale of the MHD relaxation since this is the essential point in this relaxation process. The MHD relaxation should be defined as the process which evolves on the MHD time-scale,  $t_{A0}$  (i.e. the Alfvén time-scale). Thus, the energy decay process associated with the resistive (diffusion) time-scale,  $t_{R0}$ , should be excluded from MHD relaxation. The key issue to be resolved is, therefore, whether there exists a fundamental process leading to magnetic energy dissipation on the MHD time-scale, not on the resistive time-scale. Since the only mechanism causing magnetic energy dissipation is resistive diffusion (Ohmic heating), it appears at a glance that the answer is no. We may suppose here that the tearing mode instability is a candidate. Certainly, the tearing mode instability accelerates dissipation and reduces the time-scale substantially. But still the time-scale (the inverse of the growth rate) is largely dependent on the resistivity (proportional to  $S^{3/5}$ ,  $S$  being the magnetic Reynolds number). Therefore, when resistivity is infinitesimally small, the tearing time-scale is infinitely large compared to the MHD time-scale. Thus, the tearing mode can be excluded from the MHD relaxation defined at present.

Reconnection is unavoidable in the relaxation. Therefore, the above question can be rephrased as whether there exists fast reconnection that evolves on the Alfvén time-scale, or not. There is one reconnection meeting this condition: ‘driven’ reconnection [5, 6]. Here, we reproduce some results that represent the general features of ‘driven’ reconnection. Figure 4(a) shows the temporal evolution of the electric fields at the reconnection point (reconnection rate) for different resistivities with fixed driving force (driving flow speed); Fig. 4(b) shows this evolution for different driving forces with fixed resistivity. As can be clearly seen in these figures, the rise-time and the saturation value are independent of the resistivity (Fig. 4(a)) but largely dependent on the driving force (Fig. 4(b)). We further note that the time-scale is of the order of the MHD time-scale. The only dependence of the driven reconnection process on the resistivity is the onset time of reconnection (Fig. 4(a)). These features are observed consistently in quite different simulation processes [4, 7].

These features of driven reconnection can be physically explained as follows: Driven reconnection essentially requires ‘compressibility’ for its onset since a converging flow is necessary [8]. The essential point of driven reconnection is that the local characteristic spatial scale (scale of the current profile) is narrowed at the flow converging point (or line), i.e. current peaking takes place there. Let the magnitude of the converging flow, the initial spatial characteristic scale and the narrowed spatial scale be designated by  $V$ ,  $L$  and  $d$ , respectively. Then,

$$T_R = \mu_0 d^2 / \eta = T_{R0} (d/L)^2 \quad (3)$$

where  $T_{R0} = \mu_0 L^2 / \eta$ ,  $\eta$  is the resistivity and  $\mu_0$  is the vacuum permeability. It can be roughly said that driven reconnection is triggered when the local diffusion speed,  $V_R$ , reaches the converging (driving) flow speed

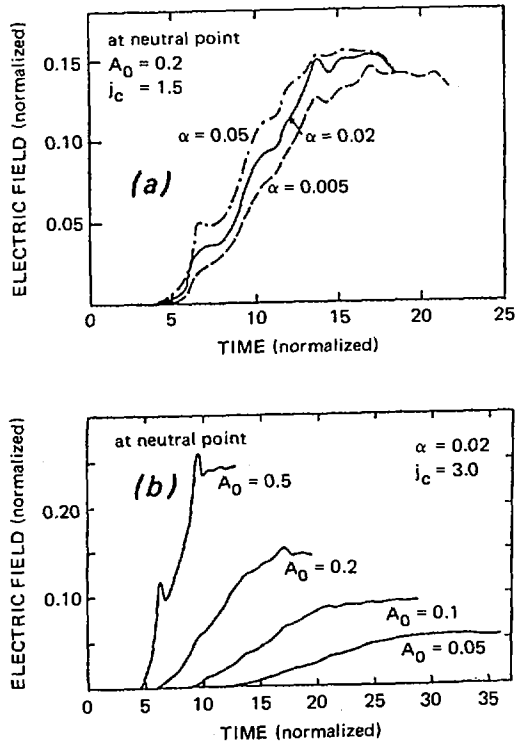


FIG. 4. (a) Development of neutral point electric fields for three different resistivity coefficients  $\alpha$ . (b) Development of neutral point electric fields for four different input fluxes  $A_0$ .

$$V = V_R \equiv d/T_R \quad (4)$$

From (3) and (4), we obtain

$$d/L = (V_{A0}/V)S^{-1} \quad (5)$$

where  $V_{A0} = L/T_{A0}$  and  $S = T_{R0}/T_{A0}$ . Since the reconnection rate  $A$  is represented by  $V/V_{A0}$  ( $V_{A0}$  is the Alfvén speed defined by the initial values), it is, as a matter of fact, independent of resistivity. Specifically, when the induction electric field associated with the plasma motion penetrates into the reconnection (X) point, driven reconnection starts, and the magnitude of the electric field is independent of the resistivity. Resistivity only takes part in the determination of the time (penetration time) during which the induction electric field penetrates through the diffusion layer  $d$ . Since, usually,  $V/V_{A0} \sim O(10^{-2})$  and  $S > 10^4$ , we have  $d/L > 10^{-2}$ . Therefore, the penetration time,  $d/V_R = d/V$ , is, at most, of the order of the Alfvén transit time  $T_{A0}$ . This indicates that the delay time of the reconnection onset is given

by  $T_R$ , which is proportional to resistivity, but is limited by the Alfvén transit time,  $T_{A0}$ . Thus, it is concluded that the driven reconnection process is almost independent of resistivity (within the uncertainty of the onset time, of the order of  $T_{A0}$ ) and that the evolution time is described by  $(V_{A0}/V)T_{A0}$ .

## 7. CONCLUSIONS

The fundamental physical process governing MHD relaxation is 'driven' (non-linear) reconnection, which is essentially different from spontaneous tearing reconnection. Because of the participation of driven reconnection, a non-minimum energy state can relax towards the minimum energy state, stepwise with the falling time of the MHD time-scale.

The relaxation can be categorized into two types global and local relaxation. In global relaxation, 'total' reconnection participates, in which case the global magnetic topology is changed. At reconnection points of total reconnection, where the physical quantity can dissipate selectively, local magnetic helicity vanishes; hence, total magnetic helicity is nearly conserved during the process, while the magnetic energy dissipates. RFP relaxation is a typical example for global relaxation.

In the local relaxation, on the other hand, 'partial' reconnection does take part. Partial reconnection contributes to a partial redistribution of the current distribution, but does not change the global magnetic topology. Since a field component exists, perpendicular to the reconnection plane at the reconnection points, local magnetic helicity does not vanish. Therefore, in local relaxation, magnetic helicity is not conserved. Tokamak relaxation (including low  $q$  tokamak relaxation) is a typical example for local relaxation.

## REFERENCES

- [1] TAYLOR, J.B., *Phys. Rev. Lett.* **33** (1974) 1139.
- [2] HORIUCHI, R., SATO, T., *Phys. Fluids* **29** (1986) 1161.
- [3] HORIUCHI, R., SATO, T., *Phys. Fluids* **29** (1986) 1304.
- [4] KUSANO, K., SATO, T., *Nucl. Fusion* **26** (1986) 1051.
- [5] SATO, T., HAYASHI, T., *Phys. Fluids* **22** (1979) 1189.
- [6] SATO, T., in *Plasma Physics (Proc. Int. Conf. 1986)*, Commission of the European Communities, Brussels (1986) 963.
- [7] MIN, K., OKUDA, H., SATO, T., *J. Geophys. Res.* **90** (1985) 4035.
- [8] SATO, T., KUSANO, K., *Phys. Rev. Lett.* **54** (1985) 808.

## MODELLING AND TRANSPORT SIMULATIONS OF OSCILLATING FIELD CURRENT DRIVE (F- $\theta$ PUMPING) IN A REVERSED FIELD PINCH\*

R.A. NEBEL, K.A. WERLEY  
Los Alamos National Laboratory,  
Los Alamos, New Mexico

R.A. SCARDOVELLI, G.H. MILEY  
Fusion Studies Laboratory,  
University of Illinois,  
Urbana, Illinois

D.S. HARNED, H.R. STRAUSS  
Courant Institute of Mathematical Sciences,  
New York University,  
New York, New York

D.D. SCHNACK, Z. MIKIĆ  
Science Applications, Inc.,  
La Jolla, California

United States of America

### Abstract

MODELLING AND TRANSPORT SIMULATIONS OF OSCILLATING FIELD CURRENT DRIVE (F- $\theta$  PUMPING) IN A REVERSED FIELD PINCH.

Oscillating field current drive has been proposed earlier as a means of maintaining quasi-steady-state currents in a reversed field pinch. Previous analyses relied on the concepts of helicity injection and relaxation to a force-free state. The paper presents an investigation of the associated MHD processes which uses combinations of a one-dimensional transport model, a linear resistive MHD stability model, Kadomtsev's nonlinear global reconnection model, a one-dimensional model including hyper-resistive terms derived from the nonlinear interaction of tearing modes, and a three-dimensional nonlinear MHD model.

**INTRODUCTION.** Oscillating field current drive (OFCD) has been proposed [1,2] as a means of maintaining quasi-steady-state currents in an RFP. Previous analyses relied on the concepts of helicity injection and relaxation to a force-free (Taylor [3]) state. We investigate the associated MHD processes using combinations of a 1-D transport model, a linear resistive MHD stability model, Kadomtsev's nonlinear global reconnection

---

\*Work performed under the auspices of the United States Department of Energy.

model, a 1-D model including hyper-resistive terms derived from the nonlinear interaction of tearing modes, and a 3-D nonlinear MHD model.

### 1. $M = 1$ MODES FOR OFCD

In this section we derive a relation between the mean toroidal current density and the  $\mathbf{V} \times \mathbf{B}$  term on axis, which indicates the instabilities needed for an efficient current drive. The torus is approximated as a periodic cylinder of length  $2\pi R$  and radius  $a$ .

Integration of Faraday's law on  $\theta = \theta' = \text{constant}$  surface from the magnetic axis at  $r = 0$  to the conducting wall at  $r = a$  leads to

$$\frac{\partial \phi_p(\theta', t)}{\partial t} = \int_0^{2\pi R} \left( E_z(a, \theta', z', t) - E_z(0, \theta', z', t) \right) dz' \quad (1)$$

where  $\phi_p(\theta', t)$  is the poloidal flux through the considered surface and  $E_z$  is the toroidal electric field.

OFCD requires the time-averaged toroidal electric field at the wall to vanish and the time-averaged poloidal flux to be a constant. Consequently, taking the time average of Eq. (1) yields

$$\lim_{\tau \rightarrow \infty} \frac{1}{\tau} \int_t^{t+\tau} dt' \int_0^{2\pi R} E_z(0, \theta', z', t') dz' = 0 \quad (2)$$

We now consider the  $z$ -component of the resistive MHD Ohm's law on axis, which reads

$$[E_z + (\mathbf{V} \times \mathbf{B})_z]_{r=0} = [\eta J_z]_{r=0} \quad (3)$$

with the resistivity  $\eta$  a time-independent scalar function.

Expanding each term in Eq. (3) in Fourier components, substituting them into Eq. (2) and integrating over a toroidal period in the  $z$ -direction yields the following expression for the time-averaged ( $m = 0, n = 0$ ) component:

$$\lim_{\tau \rightarrow \infty} \frac{1}{\tau} \left[ \eta \int_t^{t+\tau} J_{z00} dt' - \frac{1}{2} \int_t^{t+\tau} \sum_{m=0}^{\infty} \sum_{n=-\infty}^{+\infty} (\mathbf{v}_{m,n} \times \mathbf{B}_{m,n}^*)_z dt' \right]_{r=0} = 0$$

(4)

Regularity conditions at  $r = 0$  constrain the radial and poloidal components of  $\mathbf{V}$  and  $\mathbf{B}$  such that only the  $m = 1$  modes

TABLE I. RELATION BETWEEN POLOIDAL FLUX AND INTERACTION REGION

Increase in poloidal flux (%)	Interaction region (%)
0.5	36.0
1.0	42.6
2.0	48.0
5.9	65.0
12.74	73.7
16.1	81.2

do not vanish as  $r \rightarrow 0$ . Since OFCD requires that the first integral in (4) be greater than 0, a necessary criterion for OFCD is that the second integral in Eq. (4) also be greater than 0. Note that all of the terms under the second integral in Eq. (4) vanish identically, due to regularity constraints, except for those components with  $m = 1$ . Consequently,  $m = 1$  modes are required for OFCD within the resistive MHD model in a finite cylinder.

A class of  $m = 1$  tearing modes have been identified that satisfy the necessary criterion of Eq. (4). The linear and nonlinear behavior of these modes was described in detail in a paper by Caramana, Nebel and Schnack[4]. These modes are driven unstable by off-axis peaks in the  $\lambda$  profile ( $\lambda \equiv J_{\parallel}/B$ ) and nonlinearly result in an increase in the poloidal flux. Single helicity nonlinear simulations[4] have shown that the final globally reconnected state is well described by Kadomtsev's reconnection model [5].

In order to determine if these instabilities can significantly increase the poloidal flux in the plasma, we have performed a stability and reconnection study with various off-axis peaked  $\lambda$  profiles.  $\lambda$  was parameterized as a power series with  $\lambda$  vanishing at the wall. Parameters were chosen so that  $F$  and  $\theta$  are close to ZT-40M values. Table I shows that a significant increase in the poloidal flux (1%—10%) can be achieved with an interaction region of less than 70% of the plasma radius.

## 2. SIMULATIONS OF THE EXPERIMENTAL DATA

Simulations of OFCD discharges have been performed, utilizing three different models: 1-D transport, 1-D hyper-resistive, and 3-D MHD. A standard 150 kA, 200 eV OFCD

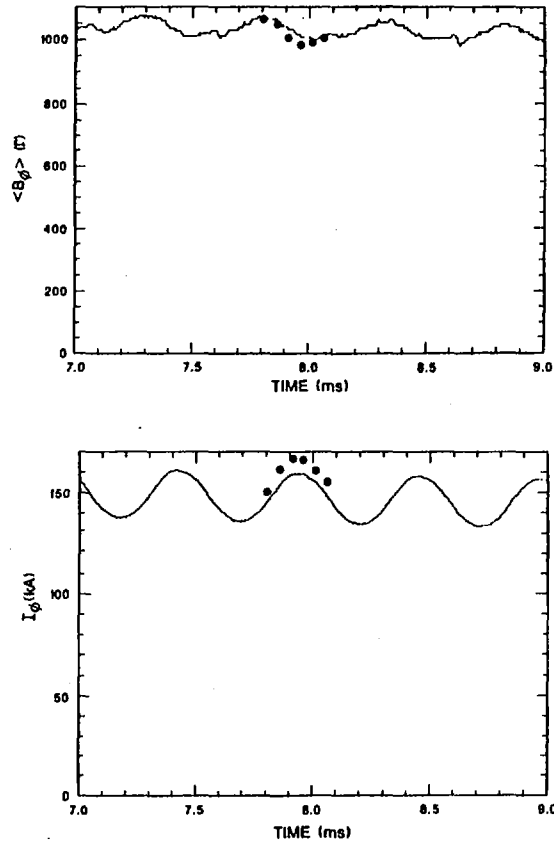


FIG. 1.  $\langle B_\phi \rangle$  and  $I_\phi$  versus time for the transport simulation (dots) compared with the experimental data (solid curves).

discharge from ZT-40M was simulated. Details of the experiment are described in Refs [6, 7].

The purpose of the 1-D transport simulations is to determine if the  $m = 1$  modes required for OFCD are present in the experimental data. Since complete experimental information on temperature and impurity profiles is not yet available, we have assumed these profiles and calculated the resistivity from them. Our model contains no "dynamo" term; thus agreement with experimental data indicates that the dynamo is not active. Similarly, disagreement between simulation and experiment strongly suggests that a dynamo mechanism is present [8]. The applied boundary conditions are the experimentally measured toroidal magnetic field and electric field at the wall. The dynamical evolution of the 1-D model of the plasma then determines the toroidal current  $I_\phi$  and the toroidal flux  $\phi_t$

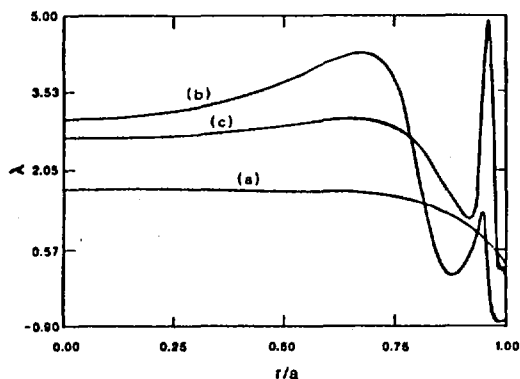


FIG. 2.  $\lambda(r)$  at (a)  $t = 7.80$  ms, (b)  $t = 7.925$  ms, and (c)  $t = 8.05$  ms, from 1-D transport.

which can be compared with the experimental values. We also monitor the linear stability of the tearing modes as the profiles evolve.

Our best transport simulation of the base case OFCD discharge is shown in Fig. 1. The only phase we were able to simulate was the flux decay phase due to the presence of the RFP "dynamo" during the other phase. A reasonable match to experimental data required flat temperature profiles over 95% of the plasma radius, with the temperature falling to 10 eV at the wall.

$\lambda$ -profiles at various times in the simulation are shown in Fig. 2. Note that there are two off-axis peaks: the innermost is a result of plasma compression driven by  $V_\phi$ , while the outermost is a skin current driven by  $V_\theta$ . Stability analysis of these profiles indicates that they are weakly unstable to high  $k$  ( $n \sim 20-25$ )  $m = 1$  tearing modes. This is a result of the peaks in  $\lambda$  residing in a region where high  $k$  modes are resonant.

Helical flux values for these high  $k$  modes are larger on the axis than at the wall; hence the instability cannot reconnect to the axis as is necessary for the generation of poloidal flux (and current drive). Reconnections to the wall, however, would tend to flatten the  $\lambda$ -profile outward and may account for our difficulty in exactly matching the experimental values of the toroidal flux and toroidal current. Consequently, we do not see any indication of current-drive related modes in the data. This is apparently because the peaks in  $\lambda$  are too far out in radius for the discharge simulated.

Theories have been developed recently in which the evolution of the RFP is described by a modified OHM's law. (See, for instance, Refs [9 and 10].) From fluctuating fields (due to the nonlinear interaction of tearing modes) one obtains a hyper-resistive term that modifies Ohm's law for the mean

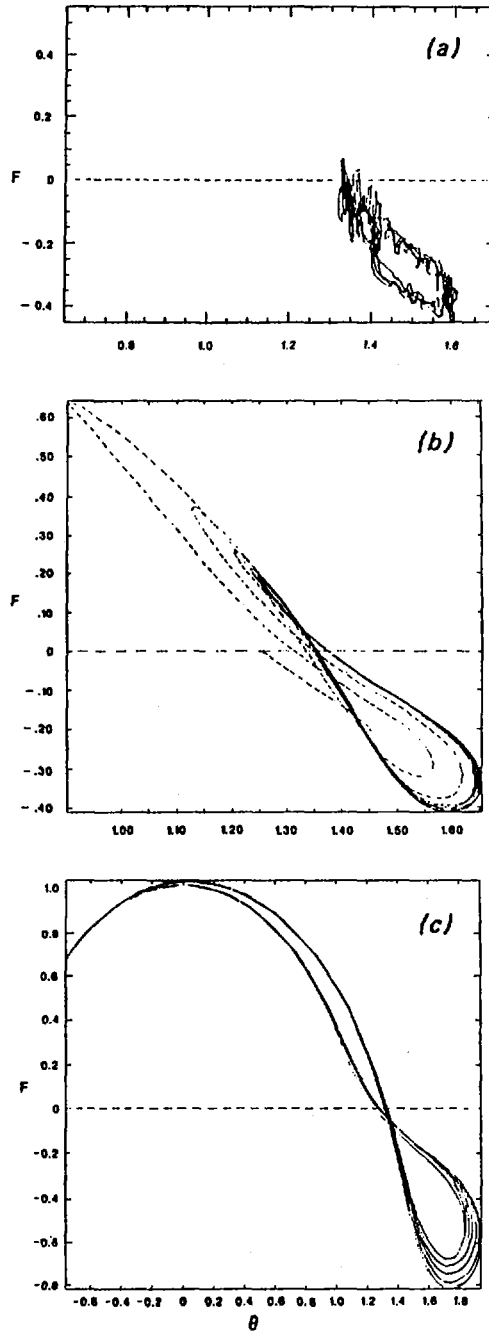


FIG. 3. (a) Experimental  $F$ - $\theta$  diagram.  
 (b) Base case (super-FOT) hyper-resistive simulation  $F$ - $\theta$  diagram.  
 (c) Sub-FOT hyper-resistive  $F$ - $\theta$  diagram.

fields. The hyper-resistive term is of the form  $\mathbf{B} \nabla \cdot (D \nabla \lambda)$ , where the hyper-resistivity  $D$  is given by  $(B_{rk} \nabla r)^2 / (k \cdot \mathbf{B})^2$ . Here  $B_{rk}$  represents the radial magnetic perturbation of mode  $k$ . Close to the rational surfaces the denominators are modified by resistivity and inertia. The hyper-resistive terms in Ohm's law have the property that they dissipate energy while conserving total magnetic helicity. The equations are described in detail in the Refs [9 and 11]. The model is well suited for modeling OFCD because it provides a method of performing inexpensive one-dimensional computations that may approximate the complicated three-dimensional interactions that produce relaxation.

The form of the hyper-resistivity profile is determined by matching a steady driven discharge to the experimentally observed values of  $F$  and  $\theta$ . For the case of the ZT-40M discharge described above, we find that when the hyper-resistivity is such that  $D = \eta a^2$ , the plasma relaxes to a state close to that measured in ZT-40M in which  $F = -0.13$  and  $\theta = 1.47$ . The experimentally measured  $F$ - $\theta$  diagram is given in Fig. 3a. The  $F$ - $\theta$  diagram from the hyper-resistive model is given in Fig. 3b. Note that this limit cycle is similar to that of the experiment and earlier 0-D simulations [2]. The form of the hyper-resistivity profile is determined by matching a steady driven discharge to the experimentally observed values of  $F$  and  $\theta$ . For these parameters, as expected, the oscillating fields do not produce a large effect. The plasma relaxation time due to hyper-resistivity is near the oscillation period. This result indicates that the plasma in ZT-40M was not fully relaxed during the oscillations. In order to see the effect of a given oscillation period on the plasma response, we have varied the frequency while holding the remaining plasma parameters fixed. There appears to be a frequency operation threshold (FOT) below which the plasma undergoes large oscillations. The FOT corresponds roughly to the point where the oscillation period is comparable to the hyper-resistive relaxation time. An  $F$ - $\theta$  diagram for a case in which the oscillation frequency has been reduced by a factor of three, so that the oscillation period exceeds the relaxation time, is shown in Fig. 3c. A similar effect to that shown in Fig. 3c occurs if the hyper-resistivity is increased beyond the computed value for the experiment.

The one-dimensional hyper-resistive model has the advantage of computational efficiency, but it cannot model the full dynamics of the three-dimensional nonlinear evolution of the plasma. Three-dimensional nonlinear computations for the RFP are difficult because features such as compressibility, which are important for an accurate model, produce time step constraints that are too severe to allow simulations on the resistive time scales. A new computational method for three-dimensional MHD [12,13] has been developed using semi-implicit techniques [14] that make such long-time simulations practical. The semi-implicit method has been used

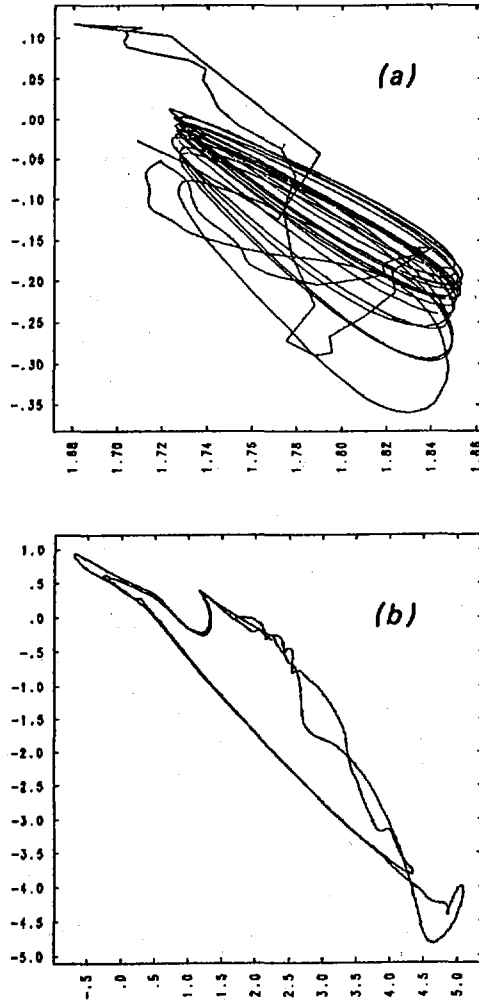


FIG. 4. (a)  $\tau = 50 \tau_A$  (super-FOT).  
 (b)  $\tau = 700 \tau_A$  (sub-FOT).

to eliminate both the fast compressional and the shear Alfvén time-step constraints.

Using the semi-implicit method, we have performed 3-D MHD simulations of OFCD for many periods of the oscillating applied voltage (typically significant fractions of the resistive diffusion time at  $S = 10^4$ ). The code is resistive, compressible, and uses the pseudospectral approximation for the poloidal and axial (toroidal) directions [15]. We employ 100 radial mesh points, and retain 3 poloidal ( $m = 0, 1, 2$ ) and 11 axial ( $-5 \leq n \leq 5$ ) modes. The resistivity profile is the same

as that used in the hyper-resistive calculations described previously.

The results of these 3-D simulations are shown in Figs 4a and 4b, where we display the variations in  $F$  and  $\theta$  for driving periods of 50 and 700 Alfvén times, respectively. Note that large oscillations occur unless the frequency exceeds the FOT. The qualitative agreement of these relatively coarse 3-D results with those obtained with the 1-D hyper-resistive model indicates that the experimentally significant relaxation processes occur at long wavelengths. 3-D simulations with finer resolution are in progress, and will be reported in future publications.

### REFERENCES

- [1] BEVIR, M.K., GRAY, J.W., in Reversed Field Pinch Theory (Proc. Workshop, 1980) Paper IIIA-3 (1980).
- [2] SCHOENBERG, K.F., GRIBBLE, R.F., BAKER, D.A., J. Appl. Phys. **56** (1984) 2519; Rep. LA-9161-MS, Los Alamos National Lab., NM (1984).
- [3] TAYLOR, J.B., Phys. Rev. Lett. **35** (1974) 1139.
- [4] CARAMANA, E.J., NEBEL, R.A., SCHNACK, D.D., Phys. Fluids **26** (1983) 1305.
- [5] KADOMTSEV, B.B., Fiz. Plazmy **1** (1975) 710; Sov. J. Plasma Phys. **1** (1975) 389.
- [6] SCHOENBERG, K.F., et al., Phys. Fluids **27** (1984) 548.
- [7] SCHOENBERG, K.F., et al., Paper IAEA-CN-47/D-II-3, these Proceedings, Vol. 2.
- [8] WERLEY, K.A., NEBEL, R.A., WURDEN, G.A., Phys. Fluids **28** (1985) 1450.
- [9] STRAUSS, H.R., Phys. Fluids **28** (1986) 2786.
- [10] BOOZER, A.H., J. Plasma Phys. **35** (1986) 133.
- [11] STRAUSS, H.R., HARNED, D.S., to be published in Phys. Fluids.
- [12] HARNED, D.S., KERNER, W., J. Comput. Phys. **60** (1985) 62.
- [13] HARNED, D.S., SCHNACK, D.D., J. Comput. Phys. **65** (1986) 57.
- [14] ROBERT, A.J., in Proc. WMO/IUGG Symp. on Numerical Weather Prediction, Tokyo (1969).
- [15] SCHNACK, D.D., BARNES, D.C., MIKIĆ, Z., HARNED, D.S., CARAMANA, E.J., to be published in J. Comput. Phys.



## RELAXATION PHENOMENA IN REVERSED FIELD PINCHES AND TOKAMAKS

A. BHATTACHARJEE, C.K. CHU, Y.-C. KWOK

Department of Applied Physics and Nuclear Engineering,  
Columbia University,  
New York, New York

E. HAMEIRI, H.R. STRAUSS

Courant Institute of Mathematical Sciences,  
New York University,  
New York, New York

A.H. BOOZER

Princeton Plasma Physics Laboratory,  
Princeton University,  
Princeton, New Jersey

United States of America

### Abstract

#### RELAXATION PHENOMENA IN REVERSED FIELD PINCHES AND TOKAMAKS.

A self-consistent theory is given for the field  $\vec{\epsilon} = \langle \vec{v}_1 \times \vec{B}_1 \rangle$  generated by fluctuations ( $\vec{v}_1$  and  $\vec{B}_1$  are the velocity and magnetic fields, respectively) within the framework of resistive MHD, including the effects of plasma compressibility. Rigorous functional forms of  $\vec{\epsilon}$  due to tearing and resistive interchange modes are given. It is shown that, in reversed field pinches,  $\vec{\epsilon}$  produces relaxed states with reversed toroidal field in the vicinity of the 'Taylor state'  $\vec{J} = \lambda_0 \vec{B}$ , but with finite pressure gradients. In tokamaks, the theory is applied to calculate the turbulent resistivity governing current relaxation and to investigate MHD current drive ('F -  $\theta$  pumping') and steady state operation using bootstrap currents. Numerical results on finite beta plasmas, based on reduced MHD equations, are presented.

#### INTRODUCTION

The purpose of this paper is to give a self-consistent theory for  $\vec{\epsilon} \equiv \langle \vec{v}_1 \times \vec{B}_1 \rangle$ , conventionally known as the "dynamo" field in astrophysics, due to resistive modes. The theory is applied to describe relaxation phenomena in reversed-field pinches (RFP's) and tokamaks.

#### 1. MEAN FIELD $\vec{\epsilon}$ IN INCOMPRESSIBLE PLASMAS

We consider an incompressible plasma inside a perfectly conducting cylindrical shell (aligned with the z-axis) to

which the velocity and magnetic fields are tangential. All mean quantities depend only on the radius  $r$ , and the mean magnetic field lies on surfaces  $r = \text{constant}$ . Superimposed on the mean field, denoted by subscript 0, are fluctuations of zero mean, denoted by subscript 1. We will use the following assumptions: (1) the mean state, containing only small flows induced by diffusion, evolves on a resistive time-scale and varies spatially on the scale of the minor radius  $a$  of the torus, i.e.,  $a|\vec{v}_0| = 0(\eta)$ ,  $a^2\partial/\partial t = 0(\eta)$ ,  $a|\nabla| = 0(1)$ , where  $\eta$  is the resistivity of the plasma; (2) the energy of the fluctuations, be it magnetic, kinetic or thermal, is smaller than the mean magnetic energy, i.e.,  $\vec{B}_1^2, \rho\vec{v}_1^2, p_1 \ll \vec{B}_0^2$ ; and (3) the fluctuations vary on a smaller space-scale and a faster time-scale than the mean quantities, i.e.,  $a^2\partial/\partial t \gg 0(\eta)$ ,  $a|\nabla| \gg 0(1)$ . Since  $\vec{J}_1 = \nabla \times \vec{B}_1$ , the fluctuating current may be large; we allow  $a|\vec{J}_1|/|\vec{B}_0| = 0(1)$ . Averaging Ohm's law, we get

$$\partial\vec{B}_0/\partial t - \nabla \times (\eta\vec{J}_0 - \vec{\epsilon}) = 0, \quad \vec{\epsilon} \equiv \langle \vec{v}_1 \times \vec{B}_1 \rangle \quad (1)$$

The average is either over an ensemble, or is a space-time average over the scales of fluctuations. We note that  $\vec{v}_0$  does not enter Eq. (1) for an incompressible plasma

It can be shown that  $\vec{\epsilon}$  obeys the following Theorems:

Theorem 1:  $\int d\tau \vec{\epsilon} \cdot \vec{J}_0 = - \int d\tau \eta \langle \vec{J}_1^2 \rangle$ , to  $0(\eta)$

Theorem 2:  $\int d\tau \vec{\epsilon} \cdot \vec{B}_0 = 0$ , to  $0(\eta)$

where the integrals are taken over the total volume of the plasma. Theorem 1 may be proved by averaging the energy equation

$$\partial/\partial t (B^2/2 + \rho v^2/2) + \nabla \cdot (\rho v^2 \vec{v}/2 + p \vec{v} + (\eta \vec{J} - \vec{v} \times \vec{B}) \times \vec{B}) + \eta \vec{J}^2 = 0 \quad (2)$$

( $\rho$  is the density and  $p$ , the plasma pressure), and keeping terms to  $0(\eta)$ . We get

$$\partial/\partial t (\vec{B}_0^2/2) = -\eta \vec{J}_0^2 - \eta \langle \vec{J}_1^2 \rangle + \nabla \cdot \vec{C}_1 \quad (3)$$

where  $C_1$  represents an energy flux. Now, from Eq. (2), we get

$$\partial/\partial t (\vec{B}_0^2/2) = \vec{\epsilon} \cdot \vec{J}_0 - \eta \vec{J}_0^2 + \nabla \cdot \vec{C}_2 \quad (4)$$

The surface integral  $\int (\vec{C}_1 - \vec{C}_2) \cdot d\vec{s}$  represents the energy flux due to fluctuations which vanishes on a perfectly conducting wall. From (3) and (4), Theorem 1 follows. For a proof of Theorem 2, the reader is referred to Ref. 1. Also, both Theorems 1 and 2 can be shown to carry over to the case of the compressible plasma, with  $\vec{v}_0$  and  $\vec{\epsilon}$  redefined<sup>2</sup>.

## 2. HEURISTIC DERIVATION OF $\vec{\epsilon}$ ,<sup>1,3</sup>

From Theorem 2, we may write  $\vec{\epsilon} = |\vec{B}_0|^{-2} (\nabla \cdot \vec{\zeta}) \vec{B}_0$ , where  $\vec{\zeta}$  is a vector function representing the flux of helicity due to the fluctuations, and satisfying  $\oint \vec{\zeta} \cdot d\vec{s} = 0$  on the plasma boundary.

For a nearly force-free plasma, Theorem 1 now implies  $\int \vec{\zeta} \cdot \nabla \lambda d\tau > 0$ , where  $\lambda \equiv \int \vec{J}_0 \cdot \vec{B}_0 / B_0^2$ . We envision the turbulence as generated by a bath of local resistive modes, where it is known that each mode behaves non-ideally only in the vicinity of some resonant magnetic surface. Therefore,  $\int \vec{\zeta} \cdot \nabla \lambda d\tau > 0$  has to be satisfied pointwise, that is,  $\vec{\zeta} \cdot \nabla \lambda \geq 0$ . We expect that  $\vec{\zeta} = K^2 \nabla \lambda$ , where  $K^2$  is a positive function; thus

$$\vec{\epsilon}_{\parallel} = \vec{B}_0 / |\vec{B}_0|^2 \cdot \nabla \cdot (K^2 \nabla \lambda) \quad (5)$$

The functional form (7) encompasses the calculations of  $\vec{\epsilon}_{\parallel}$  in Refs. 4 and 5, which are based, respectively, on a kinetic and a quasi-linear fluid model. In the next section, we strengthen the heuristic argument by explicitly deriving  $\vec{\epsilon}_{\parallel}$  from the dynamical equations of tearing modes.

### 3. CALCULATION OF $\vec{\epsilon}_{\parallel}$ FOR TEARING MODES

We envision the fluctuations to be due to tearing modes, each resonant on some magnetic surface, and ignore the non-linear interaction between them. The mean fields now represent equilibrium fields, and the fluctuations are the linearized perturbations. For a particular mode with the Fourier dependence  $\exp(qt + i\vec{k} \cdot \vec{r})$ ,  $\vec{k} = k_z \hat{z} + m\hat{\theta}/r$ , the dominant contribution to  $\vec{\epsilon}$  comes from the resonance layer  $\vec{k} \cdot \vec{B}_0 = 0$ . Outside the layer the mode behaves ideally, with zero contribution to  $\vec{\epsilon}$ . It is seen<sup>1,2</sup> that to leading order

$$\vec{\epsilon} \cdot \vec{B}_0 = \nabla \cdot \left[ \frac{i \vec{B}_0^2}{\vec{r} \times \vec{k} \cdot \vec{B}_0} \langle (\hat{r} \cdot \vec{B}_1) (\hat{r} \cdot \vec{v}_1) \rangle \hat{r} \right] \quad (6)$$

Using the notation of Ref. 6, we may rewrite Eq. (6) as  $\vec{\epsilon} \cdot \vec{B}_0 = -\nabla \cdot (nr^{-2} \vec{B}_0^2 \mu' Q \langle \Psi_0 \Xi \rangle \hat{r})$ , where  $\mu \equiv rB_z/B_{\theta 0}$ , primes denote  $r$ -derivatives and  $Q$ ,  $\Psi_0$ , and  $\Xi$  are the normalized growth rate, the radial components of  $\vec{B}_1$  and the displacement vector, respectively. The average is now interpreted as an integral over the dimensionless inner layer variable. Since  $\Psi_0 = \text{constant}$ , only the even part of  $\Psi$  contributes. We finally obtain<sup>1,2</sup>

$$\vec{\epsilon} \cdot \vec{B}_0 = \nabla \cdot (\alpha n \vec{B}_0^2 \lambda' \hat{r}) \quad (7)$$

where  $\alpha = Q^{-1/2} \Psi_0 f(\mu')$ , and  $f(\mu')$  is some positive function.  $\alpha$  has the dimensions of length squared and depends on the global equilibrium profile through the mode amplitude  $\Psi_0$  and  $Q$ , both of which depend on  $\Delta'$ . In a model calculation, such as the one presented later in the paper,  $\alpha$  is taken to be  $\alpha_0 a^2$ , where  $\alpha_0$  is a positive constant.

We have shown thus, from the linear theory of tearing modes, that the functional form for  $\vec{\epsilon}_{\parallel}$  is given by Eq. (5), and an explicit impression has been obtained for  $K^2$ , which we propose to call "eddy"<sup>2</sup> (or "hyper"<sup>7</sup>) resistivity. The calculation

given above has been extended<sup>7</sup> using the direct interaction approximation<sup>8</sup>, and estimates show that eddy resistivity can be more important than the enhancement of the classical resistivity due to tearing mode turbulence.

The tearing mode model described in this section may also be used to calculate  $\vec{\epsilon}_\perp$ . The calculation, however, is much more tedious and seems unprofitable for linear theory. It is more rewarding to derive an exact expression for  $\vec{\epsilon}$  for non-linear resistive interchange modes. We summarize our principal findings in the next section; for details, the reader is referred to Refs. 1 and 2.

#### 4. CALCULATION OF $\vec{\epsilon}_\perp$ FOR RESISTIVE INTERCHANGE MODES

Recently, the nonlinear evolution of resistive interchange modes and the consequences for energy confinement in RFP's, have been studied<sup>9,10</sup>. These studies, however, suffer from using an ad hoc pressure equation<sup>9,10</sup> and inconsistent approximations in the treatment of perturbed fields<sup>10</sup>. We have, therefore, developed an independent treatment of the problem<sup>2</sup>, and shown that previous scaling laws derived by similarity methods<sup>10</sup> are incorrect. The correct dynamical equations can be solved exactly in a low-pressure, weak-shear limit to obtain an analytic expression for  $\vec{\epsilon}$ . Since  $\epsilon_\parallel = 0$  to leading order for these modes, the only surviving component of  $\epsilon$  is perpendicular to B, and given by

$$\vec{\epsilon}_\perp = \beta_0 \eta \frac{B\theta^4}{r^2 p' B^2} \left[ \frac{rp'}{B\theta^2} + \frac{2\gamma p}{B^2} \right]^2 \hat{r} \times \vec{B} \quad (8)$$

where  $\beta_0$  is a positive, dimensionless constant,  $\gamma$  is the specific heat and we have dropped the subscript 0 on mean quantities.

#### 5. STEADY-STATE SOLUTIONS IN RFP's

We consider an RFP plasma in a bath of resistive modes, with tearing modes contributing primarily to  $\epsilon_\parallel$  and resistive interchange modes, to  $\vec{\epsilon}_\perp$ . The relaxed state is given by  $\eta \vec{J} - \vec{\epsilon} = E \hat{z}$ , where the constant E is the applied toroidal voltage per unit length, and  $\vec{\epsilon}_\parallel$  is given by Eq. (5), with  $K^2 = \alpha_0 a^2 \eta B^2$ , and  $\vec{\epsilon}_\perp$  by Eq. (8). Thus, we solve the equation

$$\eta \vec{J} - \alpha_0 \frac{1}{rB^2} (\eta a^2 r B^2 \lambda')' \vec{B} - \beta_0 \frac{\eta B\theta^4}{r^2 p' B^2} \left[ \frac{rp'}{B\theta^2} + \frac{2\gamma p}{B^2} \right]^2 \hat{r} \times \vec{B} = E \hat{z} \quad (9)$$

where the pressure p, for given B, is determined from the equilibrium condition  $(p + B^2/2)' + B_\theta^2/r = 0$ , with  $p(a) = 0$ .

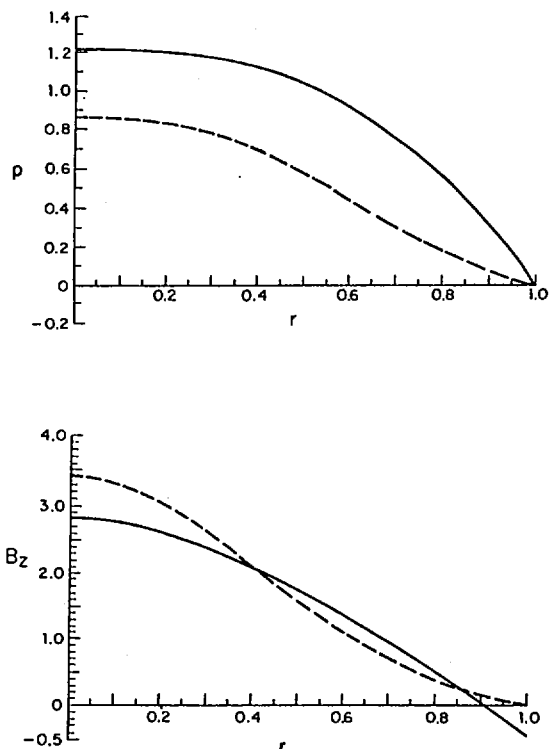


FIG. 1. Pressure and  $B_z$  profiles for  $\alpha_0 = 0$  and  $\beta_0 = 50$  (dotted lines) and  $\alpha_0 = 20$  and  $\beta_0 = 50$  (solid lines). In both cases,  $E = 12$ . ( $B_z$  is normalized to the volume averaged  $B_z (= \bar{B}_z)$ ,  $p$  to  $\bar{B}_z^2$ ,  $r$  to  $a$  and  $E$  to  $\bar{B}_z \eta / a$ ).

We impose the boundary condition  $\lambda' = 0$  at  $r = a$ , in conformity with Theorem 2.

If  $\alpha_0 = 0$ , no solutions with toroidal field reversal are possible. This is because the  $\theta$ -component of Eq. (9) is of the form  $B_z' + f B_z = 0$ ,  $f \geq 0$ , which implies that  $B_z$  decays exponentially from the center, but is never negative. Also, large  $\alpha_0$  and  $\beta_0$  imply that  $\lambda' = 0$  ( $\alpha_0^{-1}$ ),  $p \sim \frac{1}{2}(\beta_0^{-1})$ , and correspond asymptotically to the Taylor state  $\vec{J} = \lambda_0 \vec{B}$ , with constant  $\lambda_0$ . We note that, in reality, the plasma pressure will be determined by additional loss mechanisms, most importantly, by anomalous electron heat conduction, which has to be modelled separately. While the dominant effect of  $\beta_0$  causes  $B_z$  to decay exponentially from the center, a finite value of  $\alpha_0$  is necessary to explain reversal of  $B_z$ <sup>1,2</sup>. This is seen in Fig. 1, which is computed for typical ZT-40 parameters.

## 6. STEADY-STATE SOLUTIONS IN TOKAMAKS

Eq. (9) also yields relaxed states in tokamaks. Whereas in ZT-40, to the extent it is known, the electron temperature profile  $T_e$  is almost flat, in TFTR, under a wide variety of operating conditions,  $T_e(r) = T_e(0) \exp(-2Ar^2/3)$ , where  $A = q(a) + 0.5^{11}$ . This gives  $\eta(r) = \eta(0) \exp(Ar^2)$ . It can be shown<sup>12</sup> then that for small  $\alpha_0$  (which is consistent with a low level of magnetic fluctuations in tokamaks), the effect of  $\epsilon_{||}$  leads to an enhancement of the classical resistivity by approximately a factor of 2 for TFTR, which is not of great importance, given the large uncertainties in the measurement of  $Z_{\text{eff}}$ . What is important is that the theory<sup>12</sup> explains why this enhancement of resistivity does not necessarily lead to RFP-like profiles.

7. HELICITY CONTENT AND TOKAMAK APPLICATIONS OF HELICITY<sup>13</sup>

The definition of magnetic helicity  $K_0 = \int d\tau \vec{A} \cdot \vec{B}$  ( $\vec{B} = \nabla \times \vec{A}$ ) for an integration volume bounded by a magnetic surface, can be extended to the case when the bounding surface has an arbitrary shape and time dependence, for which the proper definition is<sup>14</sup>

$$K_0 = \int d\tau \vec{A} \cdot \vec{B} - \oint_p \vec{A} \cdot d\vec{x} \oint_t \vec{A} \cdot d\vec{x} \quad (10)$$

provided the gauge is chosen correctly, where the line integrals are in the poloidal (p) and toroidal (t) directions. It can be shown<sup>13</sup> that the time-derivation of  $K_0$  is given by

$$dK_0/dt = 2V\psi - 2 \int d\tau \vec{E} \cdot \vec{B} - 2 \int (\phi - \partial \vec{r} / \partial t \cdot \vec{A}) \vec{B} \cdot d\vec{s} \quad (11)$$

where  $V$  is the average loop voltage,  $\psi$ , the toroidal flux enclosed by the bounding region,  $\vec{E}$ , the electric field, and  $\phi$ , the scalar potential ( $\vec{E} = -\partial \vec{A} / \partial t - \nabla \phi$ ).

We investigate the possibility of MHD current drive ("F -  $\theta$  pumping"). From (11) we get

$$dK_0/dt = 2(V - R_\Omega I) \psi \quad (12)$$

where  $R_\Omega \equiv (\int d\tau \vec{E} \cdot \vec{B}) / I\psi$  is the resistivity of the plasma in Ohms and  $I$ , the plasma current in amperes. Assuming that  $I = I_0 \exp(-t/\tau)$ , with  $\tau$  constant, and oscillating the loop voltage and the toroidal flux so that  $V = V_1 \cos \omega t$  and  $\psi = \psi_0 + \psi_1 \cos \omega t$ , one can show from (12) that the conditions  $K_0 \geq 0$  and  $\psi_1 \leq \psi_0$  can be satisfied if  $\omega\tau \geq 2.326$ . We remark that a critical assumption in the analysis is the rigidity of the current profile, which may be difficult to obtain experimentally.

The second application of helicity is to the possible existence of an intrinsically steady-state tokamak due to the

interaction of the bootstrap current and tearing modes. It can be shown<sup>13</sup> from the neoclassical equations that a strong bootstrap effect distorts the current distribution into a hollow profile and makes the q-profile non-monotonic, which are known to be unstable to tearing modes. These modes, however, may be beneficial since they create additional poloidal flux. In fact, it can be shown<sup>13</sup> that if  $r = b$  is the edge of the tearing unstable region, the condition for poloidal flux maintenance through the bootstrap effect is  $2\langle\eta\rangle = \eta(b)$ , where  $\langle\eta\rangle$  is the volume average of the resistivity inside  $r = b$ .

### 8. NUMERICAL SIMULATION OF FINITE BETA RFP PLASMAS<sup>15</sup>

Reduced mean-field equations have been derived for resistive MHD with classical collisional transport. The evolution of the mean profiles is treated without any essential approximation except neglect of inertia. The fluctuations satisfy linear equations, except that parallel gradients are calculated with the total magnetic field. The main benefits of the approach are that it is tractable analytically, and that it requires less computation than the full MHD equations.

Numerical computations in 1-D show a thermal instability due to the temperature dependence of the transport coefficients. In 3-D, the transport due to  $m=1$  tearing modes gives a stationary state which agrees qualitatively with experiment in several respects. The F- $\theta$  diagram is qualitatively consistent with experiment. The value of  $\beta_\theta \approx 0.5$ , which is not unreasonably larger than in the OHTE experiment. Finally,  $|\vec{B}_1|/|\vec{B}| \sim S^{-1/3}$ , where  $S$  is the magnetic Reynolds number, for relaxation dominated by a few  $m=1$  modes, which is consistent with experimental data on HBTX - 1A.

### ACKNOWLEDGMENTS

This research is supported by U.S.D.O.E. Grant Nos. DE-FG02-86ER53222, DE-FG02-86ER53223 and DE-AC02-76-CH -3073.

### REFERENCES

- [1] BHATTACHARJEE, A., HAMEIRI, E., Phys. Rev. Lett. **57** (1986) 206.
- [2] HAMEIRI, E., BHATTACHARJEE, A., submitted to Phys. Fluids.
- [3] BOOZER, A.H., to be published in J. Plasma Phys.
- [4] JACOBSON, A.R., MOSES, R.W., Jr., Phys. Rev., A **29** (1984) 3335.
- [5] STRAUSS, H.R., Phys. Fluids **28** (1985) 2786.

- [6] COPPI, B., GREENE, J.M., JOHNSON, J.L., Nucl. Fusion **6** (1966) 101.
- [7] STRAUSS, H.R., to be published in Phys. Fluids.
- [8] KRAICHNAN, R.H., J. Fluid Mech. **5** (1959) 497.
- [9] AN, Z.G., DIAMOND, P.H., CHIEUH, T.H., in US-Japan Workshop on Compact Toroid Research, Princeton University, Princeton, NJ (1984).
- [10] CONNOR, J.W., TAYLOR, J.B., Phys. Fluids **27** (1984) 2676.
- [11] MURAKAMI, M., et al., to be published in Nucl. Fusion.
- [12] BHATTACHARJEE, A., HAMEIRI, E., submitted to Phys. Fluids.
- [13] BOOZER, A.H., to be published.
- [14] BEVIR, M., GRAY, J., in Reversed Field Pinch Theory (Proc. Workshop, 1980), Vol. 3, Los Alamos National Lab., NM (1980).
- [15] STRAUSS, H.R., Phys. Fluids **29** (1986) 3008.

# PHYSICS CONSIDERATIONS ON A FUSION PLASMA IN A FIELD REVERSED CONFIGURATION

H. MOMOTA, M. OKAMOTO, Y. NOMURA  
Institute of Plasma Physics,  
Nagoya University, Nagoya

K. YOSHIKAWA, M. OHNISHI  
Institute of Atomic Energy,  
Kyoto University, Uji, Kyoto

A. ISHIDA  
Department of Physics,  
Niigata University, Niigata

K. SATO  
Department of Electricity,  
Himeji Institute of Technology, Himeji

S. OHI  
Plasma Physics Laboratory,  
Faculty of Technology,  
Osaka University, Suita, Osaka

Japan

H.L. BERK, T. TAJIMA  
Institute of Fusion Studies,  
University of Texas at Austin,  
Austin, Texas,  
United States of America

## Abstract

### PHYSICS CONSIDERATIONS ON A FUSION PLASMA IN A FIELD REVERSED CONFIGURATION.

FRC/DD-<sup>3</sup>He fusion has advantages such as a smaller neutron fraction and a higher overall plant efficiency. Physics issues inherent in FRC/DD-<sup>3</sup>He fusion reactors are discussed, particularly, achievement of ignited plasma, current sustainment by fusion produced protons, and stabilization of tilt modes by means of plasma rotation.

## 1. INTRODUCTION

In thermonuclear fusion based on deuterium and tritium fuel, most of the fusion energy is released as 14 MeV neutrons. The engineering requirements for a commercial reactor are, accordingly, very hard to achieve. Advanced fuels have been studied so as to mitigate these engineering problems and, possibly, to provide a reasonable reactor system with higher plant efficiency.

In advanced fuels such as Cat. D [1], DD-<sup>3</sup>He [2], and D-<sup>3</sup>He fuel cycles, no tritium breeding is necessary, and a reduction of the 14 MeV neutrons is possible. This permits a large degree of freedom in the selection of structural reactor materials. The DD-<sup>3</sup>He fuel cycle is very similar to Cat. D. The fusion plasma is fed with deuterium, which yields tritium and <sup>3</sup>He together with other fusion products through D-D reactions. A certain amount of tritium and <sup>3</sup>He is burned in situ, and the remainder diffuses out of the plasma. The extracted tritium is stored in a bank where tritium is converted to <sup>3</sup>He through the beta decay process. <sup>3</sup>He produced in this bank is refuelled into the plasma, together with the extracted <sup>3</sup>He so as to promote D-<sup>3</sup>He reactions.

The confinement parameter, the radiation parameter [3], and the 14 MeV neutron fraction for self-ignited DD-<sup>3</sup>He fusion plasmas are shown in Fig. 1 as functions of temperature T. The corresponding curves for D-T and Cat. D plasmas are also drawn, for the convenience of comparison. Both the required confinement parameter and the temperature for the DD-<sup>3</sup>He fusion are higher than the corresponding values for D-T fusion. On the other hand, the radiation parameter is very large, and the 14 MeV neutron fraction is very small in a high beta plasma. The overall plant efficiency, thus, can be expected to be as high as 70%, with a high efficiency direct energy converter of the multistage venetian blind type (DEC) [2].

Very high values of plasma beta, plasma temperature, and accessibility to a high power DEC are required in order to utilize the favourable characteristics of the DD-<sup>3</sup>He fuel cycle. Hence, one finds that an FRC is the most promising candidate for a DD-<sup>3</sup>He reactor. The representative parameters of an FRC plasma and its favourable features are shown in Table I.

As far as physics and engineering are concerned, there are many problems to be solved for DD-<sup>3</sup>He FRC fusion. Some physics key issues are as follows: heating the plasma up to 100 keV, realizing steady burn, and achieving stability of the burning FRC plasma.

In Section 2, we discuss plasma evolution from D-T to DD-<sup>3</sup>He without any external heating. Section 3 deals with the steady maintenance of FRC with applied seed current and fuelling. The plasma current sustained by fusion products in DD-<sup>3</sup>He ignited plasmas and resulting plasma rotation are studied in Section 4. In Section 5, the effects of plasma rotation on tilt mode stability are analysed. Summary and discussions are presented in the last section.

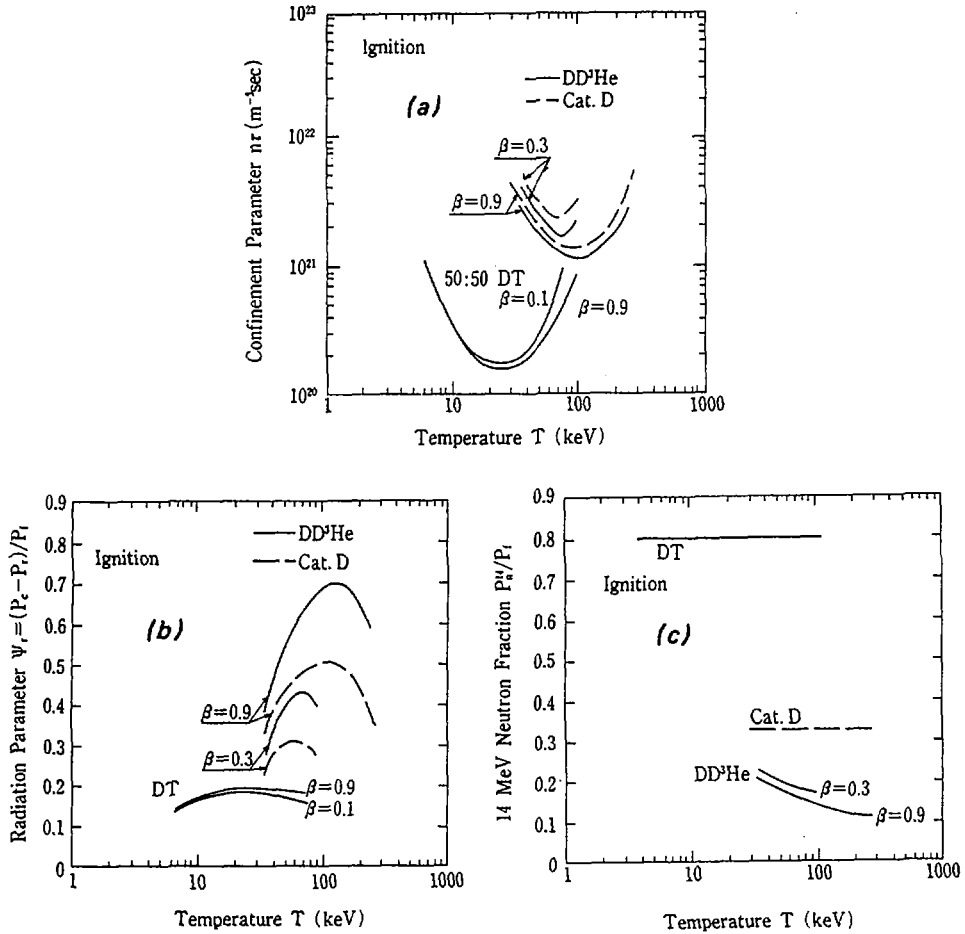


FIG. 1. (a) Confinement parameter  $n\tau$  versus temperature  $T$ ; (b) radiation parameter  $\psi_r$  versus temperature  $T$ ; (c) 14 MeV neutron fraction normalized by fusion power versus temperature  $T$ .

## 2. TRANSITION OF PLASMA OPERATION FROM D-T TO DD-<sup>3</sup>He

The operating temperature of a DD-<sup>3</sup>He reactor is required to be as high as 100 keV, from the viewpoint of overall plant efficiency. Although plasma heating up to such a high temperature seems to be formidable, efficient use of alpha particles produced by the D-T reactions may make this difficult task easier. Then, we study the transition of plasma operation from D-T to DD-<sup>3</sup>He only controlling the externally applied magnetic field and the fuelling rate, without any external heating.

TABLE I. REPRESENTATIVE PARAMETERS AND FAVOURABLE FEATURES OF DD-<sup>3</sup>He FUEL

	D-T	Cat. D	DD- <sup>3</sup> He
Required confinement (s·m <sup>-3</sup> )	2.2 × 10 <sup>20</sup>	4 × 10 <sup>21</sup>	10 <sup>21</sup>
Temperature (keV)	14	40	100
Obtainable plant efficiency (%)	40	51	71
14 MeV neutrons in 1 GW plant (GW)	1.8	0.65	0.18

The basic equations used for this study are: scaling of the average beta,  $\langle\beta\rangle$ , in long, thin equilibrium approximation; the relation between the trapped magnetic flux,  $\varphi_i$ , and the magnetic field at the wall,  $B_w$ , derived from a high flux, sharp boundary model; the energy balance equation in a non-adiabatic situation; and the particle balance equations for the ions of species  $j$ , i.e.

$$\langle\beta\rangle = 1 - \frac{1}{2}x_s^2 \quad (1)$$

$$\varphi_i = \frac{\pi}{2\sqrt{2}} r_w^2 B_w x_s^2 \quad (2)$$

$$\dot{E} = -\dot{W} + \dot{Q} \quad (3)$$

$$\dot{n}_j = S_j - n_j/\tau_p - S_i^{(j)} + S_p^{(j)} - n_j \dot{V}/V \quad (4)$$

where  $x_s$  denotes the ratio of the separatrix radius  $r_s$ , to the wall radius,  $r_w$ . The rest of the notations is conventional. The fuelling rates are given by

$$S_D = n_D/\tau_p + S_i^{(D)} \quad (5)$$

$$S_T = g(n_T/\tau_p + S_i^{(T)}) \quad (6)$$

$$S_{3He} = (1-g)n_T/\tau_p + n_{3He}/\tau_p \quad (7)$$

where  $S_D$ ,  $S_T$  and  $S_{3He}$  are the fuelling rates of D, T and <sup>3</sup>He respectively, and  $g$  stands for the tritium refuelling parameter. For the D-T fuel cycle,  $g \cong 1$  and for the DD-<sup>3</sup>He fuel cycle,  $g = 0$ .

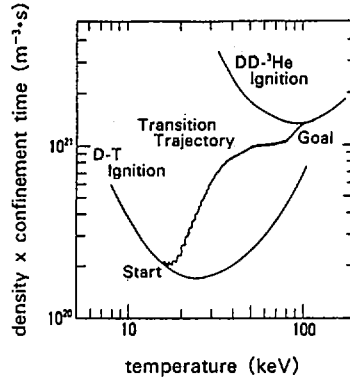


FIG. 2. Trajectory of transition from D-T to DD-<sup>3</sup>He in  $n\tau$ - $T$  diagram.

To increase the plasma temperature in a controlled manner, the following feedback control of the external magnetic field is applied to the plasma [4]:

$$\tau_d \dot{B}_w / B_w = -G(T - T_0) / T_0 \quad (8)$$

where  $\tau_d$  and  $G$  are the time constant of the change in the magnetic field and the gain of the feedback control.  $T_0$  denotes an 'objective' temperature, which is, for example in this study, changed stepwise from 15 keV to 100 keV, by 1 keV every second.

When the tritium refuelling parameter  $g$  is changed from  $g \cong 1$  to  $g = 0$ , simultaneously with magnetic field control, the plasma temperature faithfully follows the objective temperature, and the density of each ion species approaches the value obtained in the DD-<sup>3</sup>He fuel cycle. The trajectory of the transition in the  $n\tau$ - $T$  diagram is shown in Fig. 2: The trapped flux is supplied intermittently during the transition so as to keep the plasma length constant. It is demonstrated that transition from D-T to DD-<sup>3</sup>He can be attained mainly by fusion product heating. Then, in a DD-<sup>3</sup>He fusion plasma, there may not be any essential difficulty once a D-T self-ignited plasma has been attained.

### 3. STEADY STATE FRC

A method is considered for sustaining the diamagnetic plasma current by externally supplying a seed current at a field null point. The steady state solution is obtained by solving the fluid equations, including equilibrium and transport on the following assumptions: 1) injected beam ions such that the seed (Ohkawa current) does not impart any significant momentum to the plasma;

2) ion and electron temperatures are spatially uniform; 3) the FRC plasma is elongated in the axial ( $z$ -) direction; 4) a particle source,  $S_p$ , is introduced, compensating for the particle diffusion loss. The equations are then reduced to a radial, one-dimensional problem. The stationary equation in cylindrical co-ordinates ( $r, \theta, z$ ) are given by

$$J_\theta = -\frac{1}{\eta} v_r B_z + J_\theta^*, \quad \frac{dp}{dr} = J_\theta B_z$$

$$\frac{1}{r} \frac{d}{dr} (r p v_r) = S_p - \rho \frac{w}{L}, \quad \mu_0 J_\theta = -\frac{dB_z}{dr} \quad (9)$$

The magnetic flux function is defined by

$$\psi = (1/B_w) \int_0^y B_z dy$$

where

$$y = r^2 / r_s^2$$

From Eq. (9), we obtain

$$\left\{ \frac{1-\psi'^2}{\psi'} \eta_R (4y\psi' + \sqrt{y} J_*) \right\} = \Sigma - \sigma (1-\psi'^2) \quad (10)$$

Here, we have decomposed the resistivity  $\eta$  into

$$\eta = \eta_R(y) \eta_0$$

where  $\eta_R(y)$  is the spatially varying part of the resistivity and  $\eta_0$  is constant. The other new variables are defined by

$$\sigma = \frac{\mu_0 r_s^2}{\eta_0 L} w, \quad \Sigma = \frac{2\mu_0^2 r_s^2}{\eta_0 B_w^2} S_p \Theta, \quad J_* = \frac{2\mu_0 r_s}{B_w} J_\theta^* \quad (11)$$

where  $\sigma$ ,  $\Sigma$ , and  $J_*$  are 'virtual sink', normalized particle source, and seed current density, respectively. By using parity properties, Eq. (10) can be decomposed into even and odd parts to produce

$$\left\{ \frac{1-\psi'^2}{\psi'} \eta_R \left( 2\psi' + \frac{J_*}{\sqrt{2}} \right) \right\} = \Sigma \quad (12)$$

$$\sigma = -\frac{4}{1-\psi'^2} \left\{ \eta_R \left( y - \frac{1}{2} \right) \frac{1-\psi'^2}{\psi'} \left( \psi' + \frac{J_*}{4\sqrt{2}} \right) \right\} \quad (13)$$

Equation (12) determines  $\psi$ , and subsequently  $\sigma$  is calculated from Eq. (13).  
Integration of Eq. (12) yields

$$f'(y) = \frac{S(y)}{2} \frac{f(y)}{1-f^2(y)} - \frac{1}{2\sqrt{2}} J_*(y) \quad (14)$$

with

$$\psi'(y) = f(y)$$

and

$$S(y) = (1/\eta_R(y)) \int_{1/2}^y \Sigma(y) dy$$

The boundary condition for Eq. (14) is

$$f(1) = \sqrt{1-\beta_s}, \quad \psi(1) = 0 \quad \text{and} \quad \psi(0) = 0$$

where  $\beta_s$  is the plasma beta value at the separatrix

$$(\beta_s = \beta(1) = 1 - \psi'^2(1))$$

$S(y)$  is associated with the particle source  $S_p$  and is proportional to  $S_0$ :

$$S_0 = \frac{2\mu_0^2 r_s^2}{\eta_0 B_w^2} \Theta \langle S_p \rangle = \langle \beta \rangle \frac{\tau_B}{\tau_N} \quad (15)$$

Here,  $\tau_B$  and  $\tau_N$  are the magnetic diffusion and particle confinement times, respectively. The numerical calculation shows that the seed current needed to keep the specified steady configuration depends strongly on the value of  $S_0$ . It should be emphasized that the energy balance equation imposes a constraint on the value of  $S_0$ .

#### 4. ROLE OF FUSION PRODUCTS

A large amount of fusion protons is generated in a DD-<sup>3</sup>He burning plasma, which may stabilize FRC plasmas [5]. In this section, we demonstrate another important role of the energetic fusion protons: they can also contribute a large fraction of the current needed to support the configuration.

Protons are likely to be lost immediately when they intersect the separatrix of the FRC. Thus, some of the energetic protons will be lost directly while others will be trapped. The direct loss allows a directed flow of the fusion proton component that is trapped, and this flow gives rise to an electric current if a certain shortening mechanism exists, preventing radial electric fields from growing. The distribution function of trapped protons in an axisymmetric FRC equilibrium can be described as a function of the speed  $v$  and canonical angular momentum

$$p = rv + U \quad (U = e\phi/M)$$

The kinetic equation for the distribution function  $f(v, p)$  of protons in a steady state is found to be

$$\begin{aligned} & \frac{\partial}{\partial v} \{ (v^3 + v_c^3) f \} + \frac{1}{v} \left\{ p - \frac{\langle vU \rangle}{\langle v \rangle} \right\} (v^3 + v_c^3) \frac{\partial}{\partial p} f \\ & = - \frac{\langle S_p^{(p)} \rangle}{4\pi \langle v \rangle} \delta(v - v_0) h(p - av) \end{aligned} \quad (16)$$

where

$$a = r_s, \quad \langle Q \rangle = \int_{rv > |p-U|} Q(r, z) dr dz / \int_{rv > |p-U|} dr dz$$

is the function of  $p$  and  $v$ ,

$$S_p^{(p)}(r, z)$$

is the source density of the fusion protons per unit time,  $\nu(r, z)$  is the electron drag rate, and  $v_c$  is the speed at which the drags due to the background electrons and the pitch angle scattering on the plasma ions are equal.

The trapping condition is described by Heaviside's function  $h(p - av)$ . The solution for  $f(r, z)$  is easily obtained through the path integral, and the resulting current density carried by the protons is given by the formula:

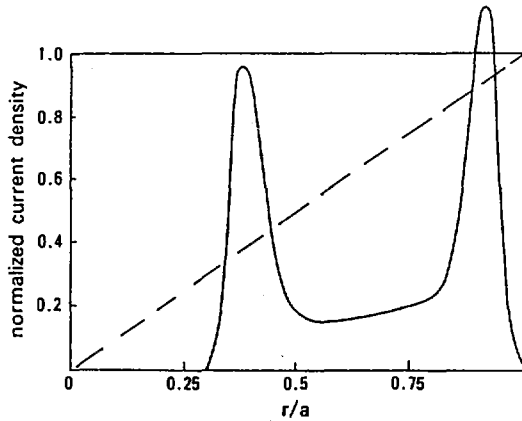


FIG. 3. Current density carried by energetic protons in  $DD-^3\text{He}$  fusion plasma.

$$j_f(r,z) = (q/4r^2) \int_0^{v_0} \frac{v dv}{v^3 + v_c^3} \int_{U(r,z)-rv}^{U(r,z)+rv} [p-U(r,z)] \times \left[ \frac{\langle S_p^{(p)} \rangle}{\langle v \rangle} \right]_{p_0(p,v), v_0} h [p_0(p,v) - av_0] dp \quad (17)$$

where  $p_0 = p_0(p,v)$  is the birth angular momentum of a proton born with speed  $v_0$ , that reaches the point  $(r,v)$  along the characteristics.

The expression for this current density has been evaluated numerically by a reasonable choice of

$$\langle S_p^{(p)} \rangle / \langle v \rangle$$

in an extremely elongated Hill's vortex model. The resulting proton current density produced in a  $DD-^3\text{He}$  fusion plasma is shown in Fig. 3, where the maximum value is approximately 1.2 of the edge plasma current density. Consistent results have been obtained with a Monte Carlo code.

We find the possibility of obtaining a large fraction of the current needed to support the configuration from fusion produced protons. At the same time, the drag due to plasma particles is found to give rise to a radial electric field and, consequently, to cause an azimuthal rotation of the plasma. This will be studied in the next section.

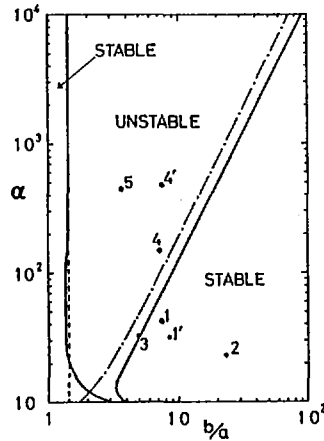


FIG. 4. Internal tilt stability as a function of scale factor  $\alpha$  and elongation  $b/a$ . Plotted are experimental data: 1 and 1' for PIACE [7], 2 for NUCTE [8], 3 for FRX-B [9], 4 and 4' for FRX-C [9], and 5 for FRX-C-LSM [10].

## 5. TILT STABILITY

In this section, we investigate the tilt stability of FRC plasmas. Previous theoretical studies [6] have predicted that the internal tilt mode in elongated FRCs is violently unstable while long lived elongated FRCs have been observed in a number of experiments [7-9]. This discrepancy can be explained by taking into account the rotation of the plasma. This rotation may be more significant in a self-ignited  $DD-^3He$  plasma in an FRC, as was mentioned in the previous section.

We have adopted the two-fluid model in which the ions are described as a rigidly rotating fluid with finite temperature and the electrons as a cold fluid at rest. Adopting Hill's vortex-like solution as an equilibrium and prescribing the displacements for the internal tilt mode,

$$\eta = (1 - r^2/\alpha^2 - z^2/b^2)^{\lambda-1} (\bar{r}z/b^2 + \bar{\theta}iz/b^2 - \bar{z}r/\alpha^2) e^{i\theta}$$

we have a cubic dispersion relation that includes an elongation factor  $b/a$  and a scale factor  $\alpha = (a/\delta)^2$  as parameters. Here,  $b$  is the half-length of the separatrix,  $\lambda$  the shaping parameter, and  $\delta$  the collisionless skin depth of the ion fluid.

The results are shown in Fig. 4, where we have reasonably chosen  $\lambda = 2$ . The two solid lines are the stability boundaries. On the left (right) hand side of the dashed line, the usual MHD potential  $W_{\text{mhd}}$  is positive (negative). Note that

$W_{\text{mhd}}$  depends on the parameter  $\lambda$  and is positive (negative) for  $b/a < (>) 1$  when  $\lambda = 1$ . On the right (left) hand side of the dot-dashed line the 'ion fluid itself', by which we mean the rotating ion fluid including no interaction with the electrons, is stable (unstable). The newly found stable region on the right hand side, which is given by  $b/a > 0.93\sqrt{\alpha}$  for  $\alpha \geq 20$ , is sustained by the rotation of the ion fluid while the left hand side, conventionally stable region is sustained by the usual MHD potential energy. Since the ratio of rotational to thermal energy of the ion fluid at the field null point is nearly equal to  $8/\alpha$ , this ratio is small enough to yield a new stable region. To compare the above results with experiments, several experimental data are plotted in Fig. 4. The present theory can hardly explain the long stable periods observed in FRX-C (4 and 4' of Fig. 4) because the growth periods of the internal tilt instability for the parameters relevant to these are much shorter than the corresponding observed stable periods [9]. It seems, however, to explain well the other experimental results shown in the figure.

## 6. SUMMARY AND DISCUSSIONS

In developing a DD-<sup>3</sup>He fusion reactor of FRC configuration, some physics issues inherent in the FRC plasma have been studied. Once a D-T ignited plasma has been obtained, a self-ignited plasma of 100 keV is found to be subsequently achieved by controlling the fuelling of the components and the magnetic field. The steady state operation of the FRC plasma is examined, showing that the current is sustained by an applied seed current and is also carried by fusion produced protons when the DD-<sup>3</sup>He plasma is ignited. The effects of the plasma rotation on the internal tilt mode stability are also studied in connection with plasma configuration of a spheroid shape. It is found that the mode can be suppressed solely by plasma rotation when both elongation and scale factors are chosen suitably.

Further physics issues should be studied such as kinetic and rotational effects on the plasma stability, ambient plasma behaviour, ambipolar potential buildup, plasma equilibrium consistent with transport including fusion products, and achievement of D-T ignited FRC plasma.

## REFERENCES

- [1] McNALLY, J.R., Jr., in Engineering Problems of Fusion Research (Proc. 6th Symp. San Diego, CA, 1985), IEEE Publ., Piscataway (1976) 1012.
- [2] MOMOTA, H., et al., to be published in Fusion Technol.
- [3] MILEY, G.H., in Fusion Energy Conversion, American Nuclear Society, LaGrange Park, IL, (1976) Ch. 2.
- [4] OKAMOTO, M., OHNISHI, M., J. Nucl. Sci. Tech. **20** (1983) 366.

- [5] FINN, J.M., SUDAN, R.N., Nucl. Fusion 22 (1982) 1443.
- [6] SHESTAKOV, A.I., et al., in Compact Toruses and Energetic Particle Injection (Proc. Japan-US Joint Symp. Princeton, NJ, 1979), Plasma Physics Lab., Princeton Univ., NJ, (1979) 126.  
CLEMENTE, R.A., MILOVICH, J.L., Phys. Lett., A 85 (1981) 148.  
SCHWARZMEIER, J.L., et al., Phys. Fluids 26 (1983) 1295.  
CLEMENTE, R.A., MILOVICH, J.L., Phys. Fluids 26 (1983) 1874.  
BARNES, D.C., et al., Phys. Fluids 29 (1985) 2616.
- [7] OHI, S., et al., Phys. Rev. Lett. 51 (1983) 1042.
- [8] TANJO, M., et al., in Plasma Physics and Controlled Nuclear Fusion Research 1984 (Proc. 10th Int. Conf. London, 1984), Vol. 2, IAEA, Vienna (1985) 523.
- [9] SIEMON, R.E., et al., Fusion Technol. 9 (1986) 13.
- [10] CHRIEN, R.E., Bull. Am. Phys. Soc. 30 (1985) 1456.

# PRELIMINARY EXPERIMENTS IN A COMPACT TOROID FORMED BY FOUR C-GUNS

S. SINMAN

Plasma Engineering Laboratory,  
Electrical and Electronics Engineering Department,  
Middle East Technical University

A. SINMAN

Nuclear Fusion Laboratory,  
Nuclear Research and Training Centre

Ankara, Turkey

## Abstract

### PRELIMINARY EXPERIMENTS IN A COMPACT TOROID FORMED BY FOUR C-GUNS.

Experiments have been performed in a compact toroid (CT) formation system with four C-guns located in an octagonal floating flux conserver. The C-gun is similar to the electromagnetically driven shock tube. As the conventional T-tube, the C-gun has a pair of vertical electrodes and backstrap components, but the vertical electrodes are located inside the flux conserver. Two different CT production schemes have been realized with the C-gun, depending upon the operational mode. In the under-damping mode (UDM) a stable toroid is obtained which begins at the onset of cyclotron wave damping and lasts exponentially for 2.8 ms. The critical damping mode (CDM) also begins at the onset of the ion cyclotron instability; however, in this case the instability is not damped but is transformed to a drift wave instability of 26 kHz, in the same way as in the current drive method. In the CDM it has been possible to generate a toroid, originating from the modulated current channel, for a maximum duration of 20 ms. The duration is strongly dependent upon the background helium gas pressure, which is in the range of 0.05–0.07 torr. The results obtained with Spitzer's resistivity formula and the measurements with the plasma resistivity probe showed that the electron temperature is in the range of 50–75 eV in the CDM. However, a maximum electron temperature of about 90 eV has been measured with a paramagnetic loop of an area of 24 cm<sup>2</sup>. In the UDM, these values are lower. For instance, depending upon the background helium gas pressure in the range of 0.1–0.2 torr, the electron temperature ranges between 20 and 35 eV. According to the Langmuir probe results in the UDM and CDM schemes, the electron densities are  $5 \times 10^{15}$  cm<sup>-3</sup> and  $10^{14}$ – $10^{15}$  cm<sup>-3</sup>, respectively. The loop current of the C-gun is about 100–150 kA and the helical toroidal current is about 6 kA.

## 1. INTRODUCTION

In view of the recent rapid development of toroidal confinement systems towards a breakeven plasma state, the question arises whether the final goal of a commercially feasible nuclear fusion reactor can indeed be reached with the

present tokamak approach. Research on compact toroids (CT) [1, 2] is complementary to tokamak research and will improve the understanding of plasma physics in toroidal devices, with CTs permitting an overall optimization of the toroidal experimental arrangements.

In 1985, we presented a conceptual system design for the realization of a CT, using four magnetized T-tubes, and discussed the results to be expected [3]. Further, we constructed a small-scale device with a single magnetized T-tube and presented preliminary experimental results [4]. Subsequently, modifying the conventional T-tube, we developed a C-gun and showed that a CT may be produced with four C-guns inserted into an octagonal floating flux conserver. In the latest study [5] the findings were evaluated in the light of recent knowledge.

In the present study, the formation of a CT with four C-guns is investigated in more detail. The modes of operation of the C-guns are determined and the effects of these modes on CT generation investigated by experiments. The CT production mechanisms of the proposed alternative schemes are interpreted.

## 2. SYSTEM

### 2.1. General

The experimental arrangement has a 40 L octagonal floating flux conserver which is also the vacuum chamber. The back-pressure in the flux conserver is  $5 \times 10^{-6}$  torr. Four C-guns,  $90^\circ$  apart, are arranged around the flux conserver.

The system consists of a capacitor bank of 2 kJ for each C-gun, spark-gap switches controlled by a self-generated UV ring, and other diagnostic equipment.

### 2.2. The C-gun and its operational modes

The C-gun is a modification of the conventional T-tube. Since the plasma is in electromagnetically driven shock tubes, the plasma column is pushed out by the backstrap. The vertical electrodes of the C-gun are located inside the flux conserver; suitable insulation is used. In this structure there are no horizontal or vertical legs as in a T-tube. The backstrap is directly attached to the external wall of the flux conserver; this has been made possible by a special insulation.

The discharge circuit consists of the capacitor bank, the controlled spark-gap switch, the backstrap and the vertical electrodes. Under the influence of the magnetic field generated by the backstrap, the current belt between the vertical electrodes is pushed out towards the centre of the flux conserver. Since this configuration has the shape of the letter C, this injector is called a C-gun. The C-gun has two modes of operation – the under-damping mode and the critical damping mode.

### 2.2.1. *Under-damping mode (UDM)*

When the background gas pressure is selected to be in the range of 0.07–0.2 torr, the discharge is in the UDM and passes only through the vertical electrodes. Characteristically, this discharge consists of the well known exponentially damping sinusoidal waves (voltage or current).

Under the experimental conditions, the period of this discharge is about 10–12 ms and the logarithmic decrement is 0.58. The working voltage range of the C-gun is 10–15 kV and the maximum current of the operating loop is 150 kA.

### 2.2.2. *Critical damping mode (CDM)*

When the distance between the vertical electrodes is not changed according to the background gas pressure in the critical range of 0.04–0.07 torr, the discharge through the vertical electrodes of the C-gun occurs with the aid of the inner walls of the flux conserver. This result is very natural, since the distance between the vertical electrodes is larger than the distance from these electrodes to the wall. In this condition, the currents passing through the inner wall and the backstrap are in opposite directions. Because of the mutual inductance between the wall and the backstrap, the serial leakage inductance of the capacitor bank circuit becomes smaller. Thus the discharge ends as can be expected in the CDM.

## 2.3. **Diagnostics used**

Generally, in this study, diagnostic techniques as used in high beta systems have been applied. These techniques may be divided into two main groups, namely internal and external diagnostics.

For the internal techniques, toroidal and poloidal magnetic loops, movable magnetic probes at an angle of  $135^\circ$  in the poloidal plane with respect to the C-gun, Langmuir probes, resistivity probes and paramagnetic loops have been used.

For the external techniques, charge exchange cells, Rogowski coils, external magnetic loops, voltage dividers, fast integrators and visible light detectors with filters have been used.

In addition, analog-to-digital data processing systems have been applied.

## 3. **FORMATION OF THE COMPACT TOROID**

### 3.1. **UDM scheme**

Under the influence of the self-generated toroidal magnetic field of the C-gun of about 10 kG, warm electrons (5–15 eV) are produced in the shock

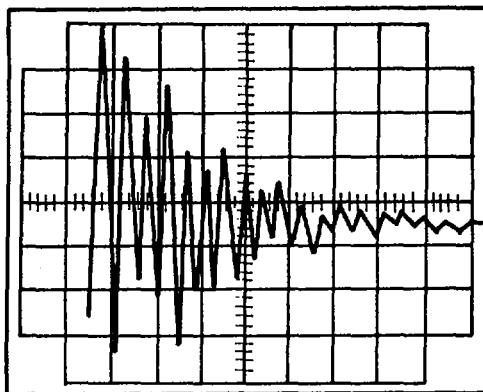


FIG. 1. Ion cyclotron wave damping in the UDM scheme.  
Time-scale: 200 ns/div., vertical scale: relative units.

heated paraboloid plasma volume, drawing a helical orbit around this toroidal magnetic field and reconnecting a CT.

According to measurements carried out by the magnetic probe, with an area of  $31.4 \times 10^{-3} \text{ cm}^2$  and an angular position of  $135^\circ$  on the poloidal plane, a total mean magnetic flux density of about 650 G is found. The corresponding helical toroidal current is approximately 6 kA. In this mode an exponentially decaying stable CT with 2.5–3.0 ms lifetime is obtained.

### 3.2. CDM scheme

By means of a passive conducting rod, located near the centre of the flux conserver and parallel to the vertical wall of the C-gun, the upper and lower walls of the flux conserver are short circuited; also, the current passing through the wall (Section 2.2.2) is transformed to a closed-loop current, the discharge on the capacitor bank circuit is suddenly cut off and a potential difference between the electrodes of the C-gun of up to 70 kV occurs. This voltage decays exponentially in 1.5  $\mu\text{s}$  to 6–8 kV, which is the minimum threshold voltage of the capacitors; according to the time constant of the external discharge circuit (250 ms), this value continues for the lifetime of the CT. In other words, the inductive coupling between the toroidal current of the flux conserver and the capacitor bank is completely exhausted.

In this mode, microinstabilities are effective and the toroidal current channel is modulated by a drift wave of 26 kHz with a lifetime of up to 20 ms, depending upon the background gas pressure, which is in the range of 0.04–0.06 torr.

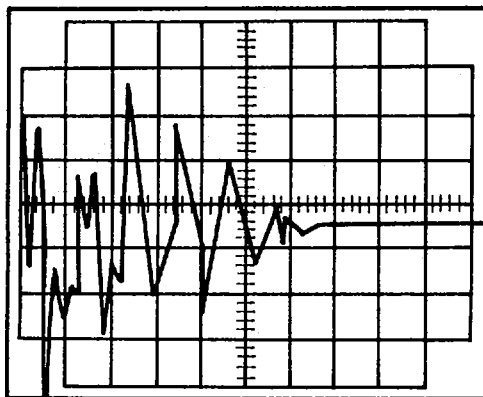


FIG. 2. Typical magnetic probe data in the UDM scheme. Variations of the toroidal magnetic field generated by the C-gun for  $60 \mu\text{s}$ , after ion cyclotron wave damping. Successively, a part of the toroidal magnetic field variation of the stable CT decays exponentially in 2.8 ms. Time-scale:  $10 \mu\text{s}/\text{div.}$ , vertical scale: relative units.

#### 4. EXPERIMENTAL OBSERVATIONS

Preliminary experiments have been carried out with a single C-gun. The modes of operation of the C-gun in the UDM and CDM schemes depend upon the background helium gas pressure. In the pressure range of 0.05–0.07 torr the C-gun is operated in the CDM scheme and in the range of 0.07–0.2 torr the C-gun is operated in the UDM scheme. These modes of operation lead to the production of two separate CTs.

According to the data from the magnetic probes, the CT generated by the UDM scheme shows generally MHD behaviour, whereas in the CDM scheme drift wave instabilities become effective during CT formation.

##### 4.1. MHD behaviour in the UDM

In the UDM scheme, the first operational half-period of the C-gun of between 5 and 6 ms changes in dependence of the gas pressure.

The oscillograms taken by the magnetic probes, moving through the toroidal and poloidal planes at an angular distance of  $135^\circ$  from the C-gun, show that at the end of 2–3 ms a damping ion cyclotron wave occurs (Fig. 1).

From time dependent evaluations it is seen that at the end of the first half-period a wave form is obtained which has both poloidal and toroidal magnetic field components and damping in 40–60  $\mu\text{s}$ , with an exponential zero average (Fig. 2). The derivation of the exponential portion of this magnetic probe signal lasted 600  $\mu\text{s}$ .

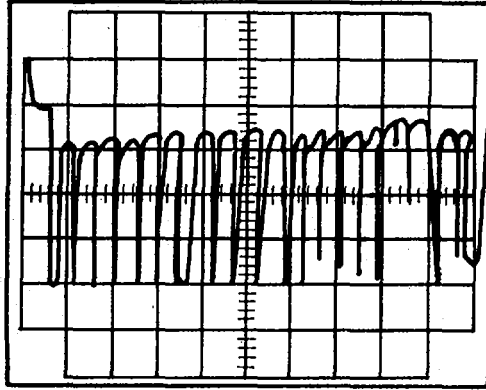


FIG. 3. Oscillogram taken from the charge exchange cell in the CDM scheme. Time-scale: 0.1 ms/div., vertical scale: relative units.

At 7 cm distance from the wall of the flux conserver, the toroidal and poloidal magnetic flux densities are almost the same, namely about 600–700 G. The decay times of the fields change between 2.2 and 2.8 ms; they are calculated with the expression  $t_B = B/(dB/dt)$ .

#### 4.2. Drift wave instability in the CDM

In this scheme, shortly after the occurrence of the undamped ion cyclotron wave instability (10–15 MHz) of a duration of 5 ms, drift wave instabilities commence.

The data taken from the charge exchange cell (Fig. 3) illustrate that this instability has a low frequency (26 kHz). In the analysis of the oscillograms obtained from magnetic probes or from toroidal and poloidal magnetic loops with an effective area of 3 cm<sup>2</sup> and located at a distance of 2 cm from the wall of the flux conserver, 135° from the C-gun on the poloidal plane, it is found that this instability depends on the background gas pressure and that the closed loop configuration continues for 5–20 ms.

At the end of this instability, a toroidal current channel modulated completely with a frequency of 26 kHz (wave electron ring) comes into existence. This mechanism is similar to low frequency self-generated current drive.

The signals from the integrated paramagnetic loop and the Langmuir probe recorded by the sampling technique are shown in Fig. 4. In these experiments the paramagnetic loop and the Langmuir probe were at an angular position of 135° in the poloidal plane with respect to the C-gun.

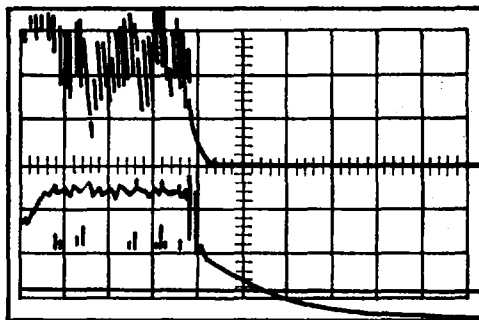


FIG. 4. Signals from the integrated paramagnetic loop and the Langmuir probe versus time in the CDM scheme. Time-scale: 5 ms/div., vertical scale: relative units.

## 5. CONCLUDING REMARKS

A new electromagnetically driven shock tube – the C-gun – has been developed. Without the use of crowbaring techniques the operational regime of this gun can be transformed from the UDM scheme to the CDM scheme, only by changing the background gas pressure.

By means of the self-magnetic field of the C-gun it has been possible to generate ion cyclotron waves in the two operational modes – the UDM scheme and the CDM scheme. In the UDM scheme, which occurs in the magnetic beach model, the ion cyclotron wave is damped, causing thermalization. In the CDM scheme, on the other hand, the ion cyclotron wave is transformed to the drift wave instability, with a current channel modulated by 26 kHz.

These processes have led to the two different ways of CT formation in the floating octagonal flux conserver under background gas pressure. The CT with MHD behaviour was stable and had a lifetime of 2.8 ms. The CT formed by a toroidal current loop modulated by the drift wave kept its properties for about 20 ms, although instabilities existed.

The electron temperature range for the UDM scheme was 20–35 eV and the range for the CDM scheme was 50–75 eV. The electron density changed between  $10^{14} \text{ cm}^{-3}$  and  $5 \times 10^{15} \text{ cm}^{-3}$ .

## ACKNOWLEDGEMENT

This work was performed under a co-operative agreement between the Turkish Atomic Energy Authority and the IAEA, Contract No. 3823/R1/RB.

## REFERENCES

- [1] KATSURAI, M., YAMADA, M., Nucl. Fusion 22 (1982) 1407.
- [2] YAMADA, M., in Advances in Compact Torus Research (Proc. IAEA Tech. Comm. Mtg Sydney, 1985), IAEA-TECDOC-399, IAEA, Vienna (1986) 175.
- [3] SINMAN, S., SINMAN, A., in Controlled Fusion and Plasma Physics (Proc. 12th Europ. Conf. Budapest, 1985), Vol. 9F, Part I, European Physical Society (1985) 642.
- [4] SINMAN, A., SINMAN, S., in Controlled Fusion and Plasma Heating (Proc. 13th Europ. Conf. Schliersee, 1986), Vol. 10C, Part I, European Physical Society (1986) 377.
- [5] SINMAN, S., SINMAN, A., *ibid.*, p. 381.

# LINEAR, HIGH BETA, $\ell = 1$ AND HELIAC STELLARATOR EXPERIMENTS

F.L. RIBE, M.E. KOEPKE, E.R. HEDIN, C.M. GREENFIELD  
 University of Washington,  
 Seattle, Washington,  
 United States of America

## Abstract

### LINEAR, HIGH BETA, $\ell = 1$ AND HELIAC STELLARATOR EXPERIMENTS.

High beta, linear stellarator plasma is produced in a low compression, 3 m theta pinch whose compression coils (22 cm inner diameter) are modified to have a helical offset of 2 cm and an axial helical period of 40 cm. This  $\ell = 1$  stellarator configuration is easily transformed to a heliac configuration by installing a current-carrying conductor along the cylindrical axis. — For the  $\ell = 1$  stellarator, internal probes were used to measure the spatial structure and temporal behaviour of the magnetic field, which agree well with the predictions of ideal MHD equilibrium theory. The higher temperature, lower density, diffuse profile quasi-equilibria are observed to be perturbed by a stable,  $m = 1$ ,  $k \approx 0$ , oscillatory mode. Measured properties of the mode agree with predictions based on a particle-fluid model which includes finite ion Larmor radius (FLR) effects. Cooler, higher density, sharp boundary plasma can also be produced and is observed to be unstable to an exponentially growing ( $0.5 \mu\text{s}$  e-folding time)  $m = 1$ ,  $k \approx 0$  mode. This agrees with ideal MHD sharp boundary theory. The higher temperature, diffuse profiles provide FLR stabilization in the presence of a nearby conducting wall. At lower temperatures, the profile has a sharp boundary with  $\beta \approx 1$ , and the mode becomes MHD unstable. — For the heliac, similar measurements were made for the purpose of experimentally determining flux contours and other plasma properties during formation and quasi-equilibrium. As expected from theory, there is no indication of MHD mode activity.

## 1. Apparatus and Measurements

We investigate the high-beta properties of the heliac and  $\ell = 1$  stellarator in the limit of infinite aspect ratio. For the present work, the High Beta Q Machine<sup>1</sup> (HBQM) is modified to permit plasma production about a helical axis.

The 90-kV HBQM high-voltage theta-pinch discharge is produced in a 3-meter segmented aluminum compression coil whose inner surface is helical with wall radius  $r_w = 11$  cm and closely resembles an  $\ell = 1$  stellarator flux surface with no interior separatrix (Fig. 1). The discharge inside a helical quartz discharge tube produces fully-ionized high-beta deuterium plasma with  $n \approx 10^{15} \text{ cm}^{-3}$ ,  $T_e + T_i \approx 50\text{-}200$  eV,  $\langle \beta \rangle = 0.1\text{-}0.4$ , with particle end-loss times of the order of 30  $\mu\text{sec}$ . The longitudinal compression

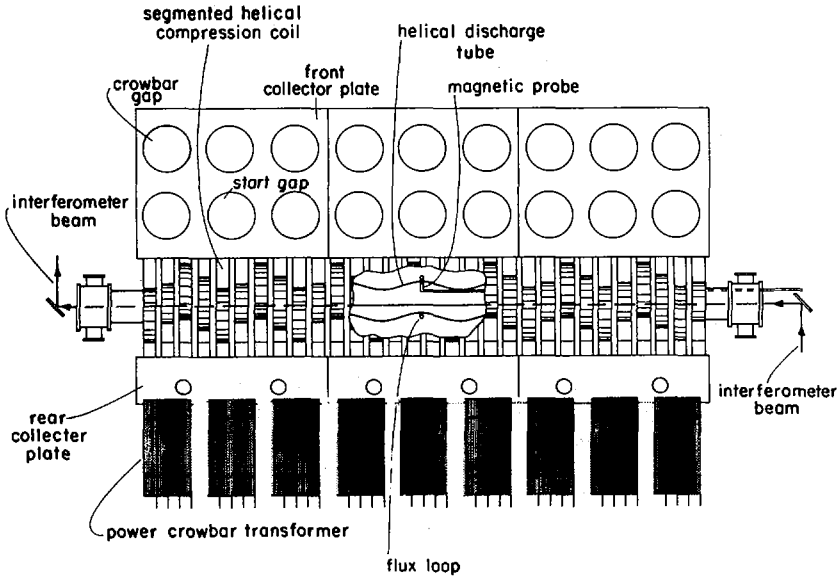


FIG. 1. Top view of High Beta Q Machine showing nine start spark gaps, nine passive crowbar gaps, helically displaced compression coil segments, helical discharge tube, and nine power crowbar transformer modules.

field  $B_0 \approx 4.5$  kG has a rise time of 450 nsec and is power-crowbarred to give a nearly constant field for  $\sim 30$   $\mu$ sec.

Diagnostic equipment (Fig. 1) includes internal field magnetic probes for  $B_r$ ,  $B_\theta$ , and  $B_z$ , axial fractional-fringe laser interferometry, and diamagnetic loop-magnetic probe combinations to measure average plasma beta. Helical symmetry is invoked to associate various  $(r, z, \theta)$  magnetic probe positions with corresponding points  $(r, \theta+hz)$  on a common plane perpendicular to the axis.

## 2. The $\ell = 1$ Stellarator Experiments

The purpose of these experiments is to measure the internal magnetic fields, plasma current, and plasma beta as functions of  $r$  and  $u \equiv hz + \theta$  at various values of average beta  $\bar{\beta}$ , density  $n$ , and temperature  $T$  and to compare them with theoretical predictions of equilibrium and stability. Figure 2 shows traces of  $B_r$ ,  $B_\theta$  and  $B_z$  at  $u = 90^\circ$  where there should be no  $B_r$  component. (The oscillation before the main discharge at 14.5  $\mu$ sec is the preionization B field.) At a filling pressure  $p_F = 7$  mT,  $B_r$  shows an

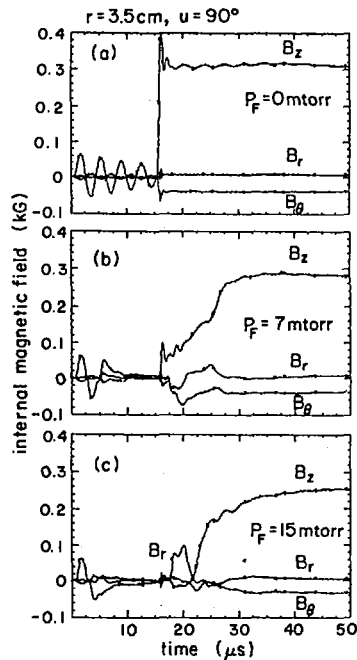


FIG. 2. Internal magnetic field waveforms of  $B_r(t)$ ,  $B_\theta(t)$ , and  $B_z(t)$ , in  $\ell = 1$  stellarator: (a) vacuum, (b) 7 mtorr, and (c) 15 mtorr discharges.

oscillation [Fig. 2(b)], while at  $p_F = 15$  mT, colder, denser plasma is produced and the  $B_r$  perturbation rises quickly to saturation while the  $B_z$  field is almost entirely excluded from the plasma interior. Measurements show that the longitudinal wavenumber  $k_z \gg h$  in both cases.

In Fig. 2(b) and Fig. 2(c) the internal  $B_z$  field is much smaller than the external field, represented approximately by the vacuum case of Fig. 2(a), because of the large plasma diamagnetism ( $\beta_{\max} > 0.8$ ). The loss of  $\beta$  in approximately 10  $\mu\text{sec}$  is due to electron thermal conduction to the ends. Figure 3(a) shows the quasiequilibrium  $B_z$  fields taken at 8  $\mu\text{sec}$  after the main discharge, at the zero of the oscillation of Fig. 2(b). Figure 3(b) shows the  $\ell = 1$  component of  $B_z$ , obtained by taking the component of  $B_z$  in Fig. 3(a) that is antisymmetric about  $x = 0$ . The theoretical curves are from the ideal MHD theory of Freidberg.<sup>2</sup> Also, we observe an antisymmetric component of  $B_\theta$ , comparable in magnitude to the (symmetric) equilibrium component, that can be accounted for by the axial plasma current produced by flux (or iota) conservation during the

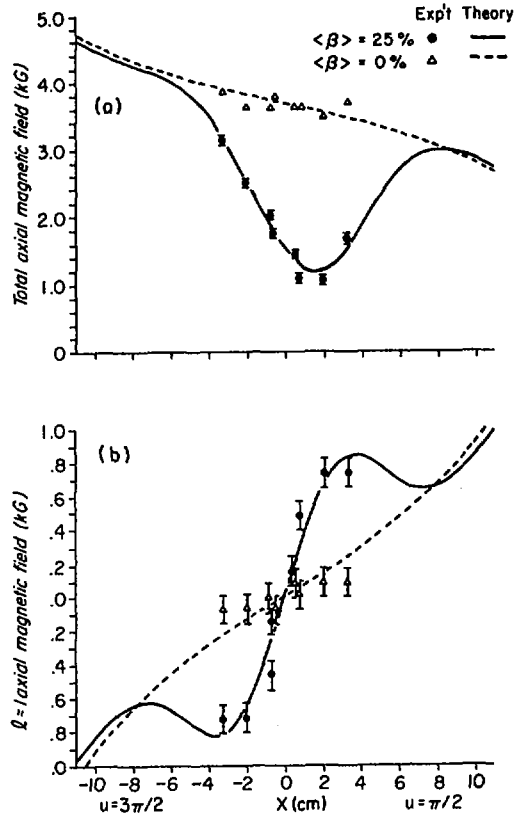


FIG. 3. Measured and analytically predicted axial magnetic field profiles for plasma and vacuum discharges: (a) total,  $B_z = B_{0z} - B_{1z}$ , (b) antisymmetric component,  $B_{1z}$ .

initial formation of the helical plasma (magnetic axis radius = 2.6 cm at  $\beta = 25\%$ ).

An analysis of the stable oscillation shows that it corresponds to a ( $k_z \approx 0$ ,  $m = 1$ ) rotation of the plasma about the cylindrical axis. The radial structure of the mode is that of incompressible flow with no radial node of the stream function  $\chi(r)$  between the cylindrical axis and plasma edge. The stream function is given by  $\vec{\xi} = \vec{e}_z \times \nabla \chi$ , where  $\xi$  is the displacement vector. The perturbation field is  $\vec{B}_p = \nabla \times (\vec{\xi} \times \vec{B}_e)$ , where  $\vec{B}_e$  is the equilibrium field. Observations of the mode agree well with predictions from MHD theory as corrected by Schmidt and Miller<sup>3</sup> for finite Larmor radius (FLR) effects according to the method of Pearstein and Freidberg.<sup>4</sup> The prediction for the experimental case of Fig. 2(b) is

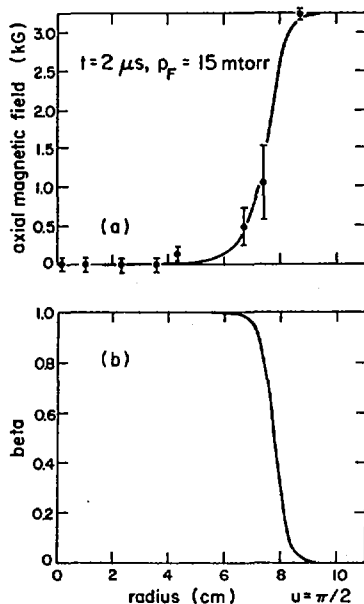


FIG. 4. Sharp boundary plasma profiles: (a) axial magnetic field measurements at various radii with best fit sharp boundary profile; (b) beta profile calculated from magnetic field profile of (a).

$\omega_I = 0$ , and  $\omega_R = 600 \text{ sec}^{-1}$ . The stabilizing effect is that of a diffuse plasma in proximity to the conducting compression-coil wall, where FLR effects act upon the internal structure of the mode.

The unstable mode for  $p_F = 15 \text{ mT}$  exhibits exponential growth with  $\omega_I = 0.5 \text{ μsec}$ . The plasma column excludes virtually all of the axial field, characteristic of  $\beta \approx 1.0$ , until  $t \approx 22 \text{ μsec}$  in Fig. 2(c), when the plasma is cooled by wall contact. Figure 4 shows that during the instability at  $t = 2 \text{ μsec}$  the plasma has a very sharp boundary with  $\beta \approx 1$ . For  $\beta = 0.98$ , sharp-boundary theory<sup>3</sup> predicts a growth rate of  $0.54 \text{ μsec}$ .

### 3. Heliac Experiments

In order to produce a heliac configuration<sup>5,6</sup> a "hard core" current conductor, consisting of a tensioned, 1-cm O.D., aluminum rod inside a 1.4-cm O.D. quartz tube, is installed along the axis of the  $\ell = 1$  system of Fig. 1. A crowbarred  $I_z$  current with a rise time of  $8 \text{ μsec}$  is driven by a  $7.2 \text{ μF}$  capacitor bank and initiated  $21 \text{ μsec}$  before the main capacitor bank discharge. As in the  $\ell = 1$  case,  $B_r$ ,  $B_\theta$ , and  $B_z$  fields are measured simultaneously at four  $r$ -values and at various  $\theta$ - and  $z$ -values for

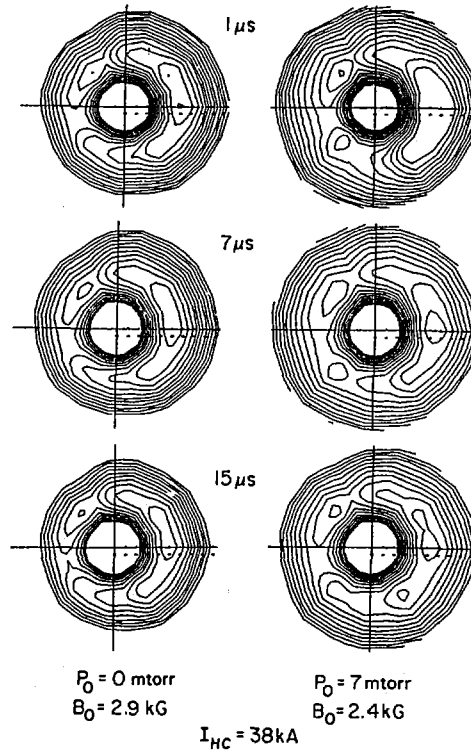


FIG. 5. Magnetic flux contours derived from probe measurements. Flux values associated with contours have constant  $\Delta\psi$  spacing.

successive discharges. Helical symmetry is invoked to map all of the probe positions to a single  $z = \text{constant}$  plane. The experimental values of the helical flux function  $\psi = \int dr(B_\theta + hrB_z)$  are calculated at various  $(r, u)$  values. After a bicubic spline interpolator produces a regularly spaced grid from the original irregularly spaced grid, contours of constant  $\psi$  are then plotted on this  $r$ - $u$  plane.

Figure 5 shows experimental flux contours for vacuum and  $p_F = 7 \text{ mT}$  filling pressure for  $I_z = 38 \text{ kA}$ , a case which corresponds to  $B_z \approx 2.7 \text{ kG}$  and  $(B_{1\theta})_{\text{max}} = 320 \text{ G}$ . In the vacuum case, the bean-shaped flux contours around the helical axis at  $r = 5 \text{ cm}$  do not change as functions of time. In the high-beta plasma case, the wider spacing of the flux contours at earlier times is evident, disappearing at later times as the plasma beta decays by thermal conduction to the ends. An axial measurement<sup>7</sup> of the deuterium ion temperature by Doppler broadening of the CV line from 10%

methane in the filling gas gives  $T_i = 90 \pm 20$  eV, averaged along a paraxial line at  $r \approx 2$  cm. There is no indication of MHD instability or oscillation of a magnitude similar to those of the  $k = 1$  stellarator.

### ACKNOWLEDGEMENTS

We are indebted to G.C. Harper for technical support of these experiments. The work was performed under the auspices of the U.S. Department of Energy.

### REFERENCES

- [1] KNOX, S.O., MEUTH, H., RIBE, F.L., SEVILLANO, E., *Phys. Fluids* **25** (1982) 262.
- [2] FREIDBERG, J.P., *Rev. Mod. Phys.* **54** (1982) 845.
- [3] SCHMIDT, M.J., MILLER, G., *Phys. Fluids* **24** (1981) 2306.
- [4] PEARLSTEIN, L.D., FREIDBERG, J.P., *Phys. Fluids* **20** (1977) 2128.
- [5] FURTH, H.P., KILLEEN, J., ROSENBLUTH, M.N., COPPI, B., in *Plasma Physics and Controlled Nuclear Fusion Research (Proc. 2nd Int. Conf. Culham, 1965)*, Vol. 1, IAEA, Vienna (1966) 103.
- [6] SOLOVEV, L.S., SHAFRANOV, V.D., in *Reviews of Plasma Physics*, Vol. 2, Consultants Bureau, New York (1966) 195.
- [7] CEKIC, M., private communication, 1986.



## CHAIRMEN OF SESSIONS

### *Volume 2*

Session E-I	D.B. NELSON	USA
Session E-II	R.R. PARKER	USA
Session C-I	D.D. RYUTOV	USSR
Session D-I	L.M. KOVRIZHNYKH	USSR
Session D-II	T. UCHIDA	Japan
Session D-III	G. GRIEGER	Germany, Fed. Rep.
Session D-IV	F.L. RIBE	USA

## SECRETARIAT OF THE CONFERENCE

Scientific Secretaries:	M. LEISER A.A. SHURYGIN	Division of Research and Laboratories, IAEA
Administrative Secretary:	Edith PILLER	Division of External Relations, IAEA
Editors:	J.W. Weil Maria DEMIR	Division of Publications, IAEA
Records Officer:	J. RICHARDSON	Division of Languages, IAEA

# HOW TO ORDER IAEA PUBLICATIONS

An exclusive sales agent for IAEA publications, to whom all orders and inquiries should be addressed, has been appointed in the following country:

UNITED STATES OF AMERICA    BERNAN – UNIPUB, 4611-F Assembly Drive, Lanham, MD 20706-4391

In the following countries IAEA publications may be purchased from the sales agents or booksellers listed or through major local booksellers. Payment can be made in local currency or with UNESCO coupons.

ARGENTINA	Comisión Nacional de Energía Atómica, Avenida del Libertador B250, RA-1429 Buenos Aires
AUSTRALIA	Hunter Publications, 58 A Gipps Street, Collingwood, Victoria 3066
BELGIUM	Service Courrier UNESCO, 202, Avenue du Roi, B-1060 Brussels
CHILE	Comisión Chilena de Energía Nuclear, Venta de Publicaciones, Amunategui 95, Casilla 188-D, Santiago
CHINA	IAEA Publications in Chinese: China Nuclear Energy Industry Corporation, Translation Section, P.O. Box 2103, Beijing IAEA Publications other than in Chinese: China National Publications Import & Export Corporation, Deutsche Abteilung, P.O. Box 88, Beijing
CZECHOSLOVAKIA	S.N.T.L., Mikulandska 4, CS-116 86 Prague 1 Alfa, Publishers, Hurbanovo námestie 3, CS-815 89 Bratislava
FRANCE	Office International de Documentation et Librairie, 48, rue Gay-Lussac, F-75240 Paris Cedex 05
HUNGARY	Kultura, Hungarian Foreign Trading Company, P.O. Box 149, H-1389 Budapest 62
INDIA	Oxford Book and Stationery Co., 17, Park Street, Calcutta-700 016 Oxford Book and Stationery Co., Scindia House, New Delhi-110 001
ISRAEL	Heiliger & Co. Ltd. 23 Keren Hayesod Street, Jerusalem 94188
ITALY	Libreria Scientifica, Dott. Lucio de Biasio "aeiou", Via Meravigli 16, I-20123 Milan
JAPAN	Maruzen Company, Ltd, P.O. Box 5050, 100-31 Tokyo International
PAKISTAN	Mirza Book Agency, 65, Shahrah Quaid-e-Azam, P.O. Box 729, Lahore 3
POLAND	Ars Polona-Ruch, Centrala Handlu Zagranicznego, Krakowskie Przedmiescie 7, PL-00-068 Warsaw
ROMANIA	Ilexim, P.O. Box 136-137, Bucharest
SOUTH AFRICA	Van Schaik Bookstore (Pty) Ltd, P.O. Box 724, Pretoria 0001
SPAIN	Díaz de Santos, Lagasca 95, E-28006 Madrid Díaz de Santos, Balmes 417, E-08022 Barcelona
SWEDEN	AB Fritzes Kungl. Hovbokhandel, Fredsgatan 2, P.O. Box 16356, S-103 27 Stockholm
UNITED KINGDOM	Her Majesty's Stationery Office, Publications Centre, Agency Section, 51 Nine Elms Lane, London SW8 5DR
USSR	Mezhdunarodnaya Kniga, Smolenskaya-Sennaya 32-34, Moscow G-200
YUGOSLAVIA	Jugoslovenska Knjiga, Terazije 27, P.O. Box 36, YU-11001 Belgrade

Orders from countries where sales agents have not yet been appointed and requests for information should be addressed directly to:



Division of Publications  
International Atomic Energy Agency  
Wagramerstrasse 5, P.O. Box 100, A-1400 Vienna, Austria



INTERNATIONAL  
ATOMIC ENERGY AGENCY  
VIENNA, 1987

SUBJECT GROUP: III  
Physics/Plasma Physics, Fusion  
PRICE: Austrian Schillings 1520,-